INSTITUT POLYTECHNIQUE DE PARIS

ÉCOLE POLYTECHNIQUE

IP PARIS

NNT : 2025IPPAX040

Thèse de doctorat

Redox behaviour investigation of a photoactive cerium(III) complex for the chemical reduction of pollutants

Thèse de doctorat de l'Institut Polytechnique de Paris
préparée à l'École Polytechnique

École doctorale n°626 École Doctorale de l'Institut Polytechnique de Paris (ED IP Paris)
Spécialité de doctorat: Chimie

Thèse présentée et soutenue à Palaiseau, le 24 juin 2025, par

Adrien COMBOURIEU

Composition du Jury :

Carole DUBOC Directrice de recherche, Université Grenoble Alpes (DCM)	Présidente
Sami LAKHDAR Directeur de recherche, Université Paul Sabatier (LHFA)	Rapporteur
Antoine SIMMONEAU Chargé de recherche, Université Paul Sabatier (LCC)	Rapporteur
Lucile ANTHORE-DALION Chargée de recherche, CEA Saclay (Institut IRAMIS)	Examinatrice
Grégory NOCTON Directeur de recherche, Institut Polytechnique de Paris (LCM)	Directeur de thèse
Grégory DANOUN Chargé de recherche, Institut Polytechnique de Paris (LCM)	Co-Encadrant de thèse

Institut Polytechnique de Paris
91120 Palaiseau, France

Redox behaviour investigation of a photoactive cerium(III) complex for the chemical reduction of pollutants

Adrien COMBOURIEU

Laboratoire de Chimie Moléculaire, Ecole Polytechnique, Institut Polytechnique de Paris

Thesis submitted for the degree of Doctor of Philosophy

24th June 2025

Composition of the jury

Sami LAKHDAR Directeur de recherche, Université Paul Sabatier, Toulouse	Rapporteur
Antoine SIMONNEAU Chargé de recherche, Université Paul Sabatier, Toulouse	Rapporteur
Lucile ANTHORE-DALION Chargée de recherche, CEA Saclay	Examinatrice
Carole DUBOC Directrice de recherche, Université Grenoble-Alpes	Examinatrice
Grégory DANOUN Chargé de recherche, Ecole Polytechnique	Encadrant de thèse
Grégory NOCTON Directeur de recherche, Ecole Polytechnique	Directeur de thèse

Acknowledgements

Supervision : I would like to thank Dr. Grégory DANOUN for supervising this project and in particular for the many valuable ideas he contributed.

Students and post-docs who worked on the cerium project : I would like to express my sincere gratitude to Eachann ASSENDJEE, François LACOMBE, Sixtine CHARPY, Nancy MAZEAU and Dr. Bich Tuyen PHUNG who contributed greatly to this project and helped me a lot to develop the chemistry presented in the first two chapters of this manuscript. It was a real pleasure working with them, and I wish them all the best for the future !

XRD measurements : I cannot thank warmly enough Dr. Nicolas CASARETTO for spending unfathomable amounts of time teaching me all the secrets of XRD, with an unrivalled patience and kindness. It was a pleasure and an honour to meet you in the lab !

EPR measurements : I would like to express my sincere thanks to Lhoussain KROUZ, with whom I had the privilege of working on my first EPR measurements. His help with the data analysis was extremely valuable, as were our discussions about it. It was a real pleasure working with you ! I would also like to thank Dr. Antonino ALESSI and Audrey COURPRON, who taught me how to use the EPR at École Polytechnique.

Luminescence measurements : I am grateful to Dr. Olivier MAURY and Dr. Akos BANYASZ for their work on luminescence measurements on the $Ce^{III}TREN^{TIPS}$ and for their valuable explanations of the techniques they employed.

Technical support : I would like to thank Olivier BEC, Dr. Joseph YOUSSEF and Jean-Michel WIERNIEZKY for their invaluable support with the 3D printing of the photoredox boxes and glassblowing, which were crucial to the development of the projects. Thank you to Karim Hammad for taking care of the 'LCM NMR' after me and for creating the new NMR platform. Thank you to Gilles ALLA (former captain) for managing the IT stock.

Lab 1 team : I would particularly like to thank Dr. Thomas SIMLER, who introduced me to lanthanide chemistry in 2020 (the time of the pandemic !), and for his constant and unfailing help and kindness throughout this period. It was always a pleasure to talk to him, and I have no doubt that he will continue to produce such impressive and original chemistry in the future ! I would also like to thank Lucie PEDUSSAUT profusely for her good humour during our three-year collaboration, and for all the conversations and board game parties. Finally, I would like to thank the rest of the LCM team, Dr. Luca DEMONTI, Dr. Claire SQUARZONI (and Upsie !), Dr. Angus Charles Gordon SHEPARD for the correction of my last chapter, Linda DE MARCHI, Mahdi BERRO, Harsh SINGH PRATAP, Mohamed MOUNIR, Dr. Hugh SANDERSON and Disha BHATTACHARJEE, and will them all the best for their journey.

Former students and post-docs : I would like to express my gratitude to the former students of lab 1, especially Dr. Nolwenn MAHIEU for her invaluable help during the early times of my master internship. I would also like to thank the former lab interns, particularly Ysée LAPLANCHE, Evangelos PAPANGELIS (*bitchaki*), Camille CHARTIER and Thomas RECOULY.

LCM team : I would like to thank the whole LCM team, and especially Dr. Ingrid POPOVICI (who hopefully had a nice stay in our office), Sa Majesté Dr. Edith NICOL, Sophie BOURCIER, Dr. Duncan CARMACHIAEL (thanks for all the interesting talks !), Robin WISSON, Paul RENQUET (Captain'), Marie-Sophie DIAS FERNANDES, Laureen BUSSON, Vaibhav KHUMBAR (French kaïra), Dr. David TOUBOUL, Dr. Gaël ZUCCHI, Dr. Audrey AUFFRANT and Theodor RADU.

Administrative support : I am especially grateful to Dr. Véronique GIRARD, Dr. Cédric TARD, Elodie DUBOIS and Maria MARTINEZ for the management of the lab and the substantial administrative support they provided during my time there.

Teaching : No words could express how grateful I am to the teaching staff at the IUT d'Orsay, especially Dr. Eve DE COCK-SCHWERER and Dr. Caroline VERGNE, for their warm welcome and support in helping me settle into this new environment. I am very grateful for their help and kindness, which enabled me to make the most of my time there !

Financing : I am grateful to Ecole Polytechnique for the three-year financing of the project through the *Financement anticipé*.

Jury members : I thank the jury members for accepting to evaluate this work and for the discussion during my defence.

Family : I would like to finish by thanking my family, for their constant support throughout these three years.

Outline

List of Abbreviations 8
Introduction 11
Chapter I Synthesis of $Ce^{III}(TREN^{TIPS})$, structural and spectroscopic features 55
Chapter II Photochemical remediation of chlorinated and fluorinated Persistent Organic Pollutants . 87
Chapter III Towards the degradation of explosive surrogates 113
Chapter IV Reduction of nitrogen cycle species and small molecule activation 141
Conclusion and Perspectives 191
Experimental Section 193
Appendix 463

List of Abbreviations

12-c-4	12-crown-4
BARF	$B(3,5\text{-}(CF_3)_2\text{-}C_6H_3)_4$
BDE	Bond Dissociation Energy
Boc	*Tert*-butoxycarbonyl ($-CO_2{}^tBu$)
Bu	Butyl ($-CH_2CH_2CH_2CH_3$)
ca.	*circa* (around)
cf.	*confere* (see)
Cp	Cyclopentadienyl ($C_5H_5^-$)
DBAD	Di-*tert*-butyl azodicarboxylate
DFT	Density Functional Theory
DHA	Dihydroanthracene
DMPO	5,5-Dimethyl-1-pyrroline N-oxide
DMSO	Dimethylsulfoxide
DPA	Diphenylanthracene
EPA	Environmental Protection Agency (United States)
EPR	Electron Paramagnetic Resonance
e.g.	*exemplum gratia* (for instance)
eq.	Equivalent(s)
et al.	*et alii* (and others)
etc.	*et caetera* (literally "and others things [that are missing]")
Et	Ethyl
Fc	Ferrocene (Cp_2Fe)
fs	Femtosecond
FWHM	Full Width at Half-Maximum
GC	Gas chromatography
HAT	Hydrogen Atom Transfer
HMDS	Hexamethyldisilazane ($-N(SiMe_3)_2$)
HOCs	Halogen Organic Compounds
IARC	International Agency for Research on Cancer
IEA	International Energy Agency
IRENA	International Renewable Energy Agency
i.e.	*id est* (which means)
IPCC	The Intergovernmental Panel on Climate Change
^{i}Pr	Isopropyl ($-CH(CH_2)_2$)
IUPAC	International Union for Pure and Applied Chemistry
J	Joule
kg	Kilogram
LDA	Lithium diisopropylamide
LED	Light-Emitting Diode
LIH	Light Induced Homolysis
LMCT	Ligand-to-metal Charge Transfer
lwpp	Linewidth peak-to-peak
NBO	Natural Bond Orbital
NHE	Normal Hydrogen Electrode
nm	Nanometer
NMO	N-methylmorpholine-N-oxide
ns	Nanosecond
NTO	Natural Transition Orbital

µs	Microsecond
Me	Methyl (-CH_3)
MLCT	Metal-to-Ligand Charge Transfer
MOF	Metal-Organic Framework
OECD	Organisation for Economic Co-operation and Development
-OTf	Triflate (-OSO_2CF_3)
PBN	N-*tert*-butyl-α-phenylnitrone
PDT	Photodynamic therapy
PETN	Pentaerythritol tetranitrate
PFAA	Perfluoroalkyl acid
PFAS	Perfluoro Alkyl Substances
PFHX	Perfluorohexane Substances
PFOA	Perfluorooctanoic acid
PFOS	Perfluorooctanesulfonic acid
PhBpin	Phenylboronic acid pinacol ester
pin	Pinacolato ($C_6H_{12}O_2$)
POP	Persistent Organic Pollutant
PVC	Polyvinyl chloride
QTAIM	Quantum Theory of Atoms-In-Molecules
REO	Rare-earth oxide
ROS	Reactive Oxygen Species
TAS	Transient Absorption Spectroscopy
TBACl	*n*-tetrabutylammonium chloride
-TBDMS	*Tert*-butyl dimethylsilyl (-$SiMe_2{}^tBu$)
TCSPC	Time-Correlated Single Photon Counting
TD-DFT	Time-Dependent Density Functional Theory
THF	Tetrahydrofuran
-TIPS	Triisopropylsilyl (-Si^iPr_3)
TMAO	Trimethylamine N-oxide
-TMS	Trimethylsilyl (-$SiMe_3$)
TNT	1,3,5-Trinitrotoluene
TREN	Tris-(2-aminoethyl)amine
TTMSS	Tris(trimethylsilyl)silane
SADI	Same Distance restraint
SET	Single Electron Transfer
UNEP	United Nations Environmental Program
USGS	United States Geological Survey
UV	Ultraviolet
V	Volt
VLIH	Visible Light Induced Homolysis
XRD	X-Ray Diffraction

Education, n.: That which discloses to the wise and disguises from the foolish their lack of understanding

Ambrose Bierce, 1906

Introduction

I. Lanthanides 12
  a) Definition and history of lanthanides 12
  b) General Properties 13
  c) Applications of lanthanides 15
  d) Abundancy and extraction 17
  e) Economical and geopolitical concerns 20
    1) Rare earths as critical minerals 20
    2) Geopolitical aspects of rare earth production 21
II. Photochemical reactivity of cerium complexes 23
  a) Why photochemistry ? 23
    1) Chemical reactions and activation energy 23
    2) Selection rules 24
    3) Chemistry in the excited state 25
  b) Light Induced Homolysis using cerium(IV) complexes 28
    1) Photoinduced decarboxylation 29
    2) Alkoxy radical formation 31
  c) Single Electron Transfer reactivity with cerium(III) complexes 39
References 43

I. Lanthanides

a) Definition and history of lanthanides

Two lines of 30 elements with atomic number (Z) ranging from 57 to 71, and Z = 89 to 103 constitute the family of f-block elements, which is divided between the family of lanthanides (Z = 57 → 71) and actinides (Z = 89 → 103, see **Figure 1**). The International Union for Pure and Applied Chemistry (IUPAC) promotes the use of *lanthanoids* and *actinoids* to prevent any confusion with the *-ide* suffix used for negatively charged ions (*e.g.* fluoride F^-), but these families will be referred to as *lanthanides* and *actinides* in this manuscript considering their widespread usage among the community. Although the name *lanthanide* means "like lanthanum", the family does not include lanthanum in principle, but it is often considered as one owing to several similar properties.[1,2] Associated with scandium and yttrium, lanthanides form the *rare earth* elements family.

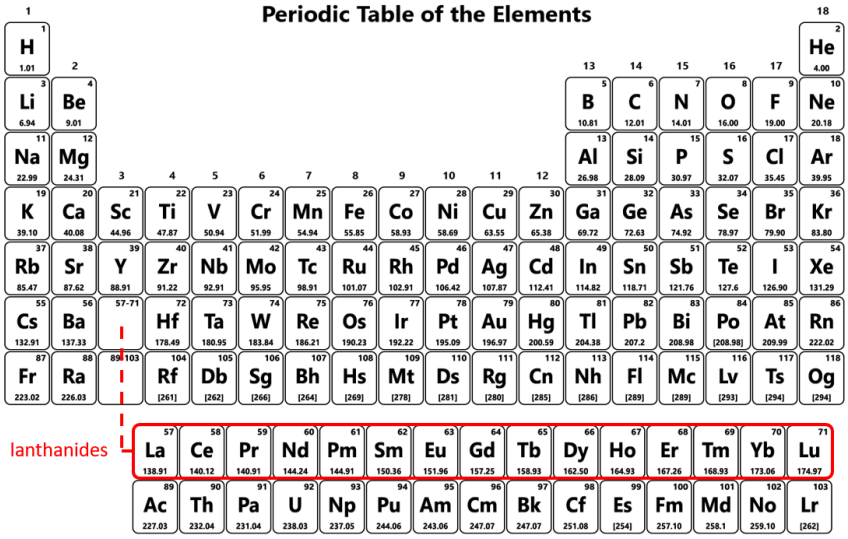

Figure 1. Periodic table of the elements. Adapted from sciencesnotes.org

The discovery of lanthanide dates back to 1751, when A. F. Crondstedt, a Swedish mineralogist, discovered a new heavy mineral from which was isolated in 1803 a new putative oxide (or "earth") named *ceria*, after the recently discovered asteroid Ceres.[3] It was only 40 years later that this oxide was shown to be a mixture of many similar oxides, which could be separated and isolated in 1907.

Contrary to most actinides which are mainly radioactive elements, lanthanides are stable elements (except for promethium). Both families share some structural and reactivity similarities owing to their peculiar electronic properties.

Element	Date of discovery	Origin of name
Lanthanum	1839	λανθάνειν , to escape notice
Cerium	1839	Asteroid Ceres
Praseodymium	1885	πράσον + δίδυμος , leek + twin
Neodymium	1885	νεός + δίδυμος, new + twin
Promethium	1945	Προμηθεύς, Prometheus
Samarium	1879	Mineral samarskite
Europium	1901	Europe
Gadolinium	1880	J. Gadolin, Finnish chemist
Terbium	1843	Ytterby, Swedish village
Dysprosium	1886	δυσπρόσιτος, “hard to get”
Holmium	1879	*Holmia*, Latin name of Stockholm
Erbium	1843	Ytterby
Thulium	1879	*Thule*, Latin for “most northerly land”
Ytterbium	1878	Ytterby
Lutetium	1907	*Lutecia*, latin name of Paris

Table 1. Discovery date and origin of the name of each lanthanide element. Adapted from Greenwood[3]

b) General Properties

Most lanthanides in 0 oxidation state have an electronic structure $[Xe]6s^2 4f^n$ ($n = 0 \rightarrow 14$). 4f orbitals of lanthanide elements are often called *inner orbitals*, as the maximum of the 4f electron density of their wavefunction is closer to the nucleus than the outermost $5s^2 5p^6$ electrons, and are not therefore participating in the bonding with ligands (see **Figure 2**). This feature allows for a degeneracy of the f orbitals, which is exploited to synthesise powerful single-molecule magnets.[4,5]

The gradual filling of the 4f orbitals results in a quicker decrease in atomic and ionic radii compared to other elements, known as *lanthanide contraction*. This phenomenon is caused by the poor shielding of the nuclear charge by 4f electrons, increasing the effective charge felt by outer $5s^2 5p^6$ electrons and therefore diminishing the radius as Z increases.[4,5]

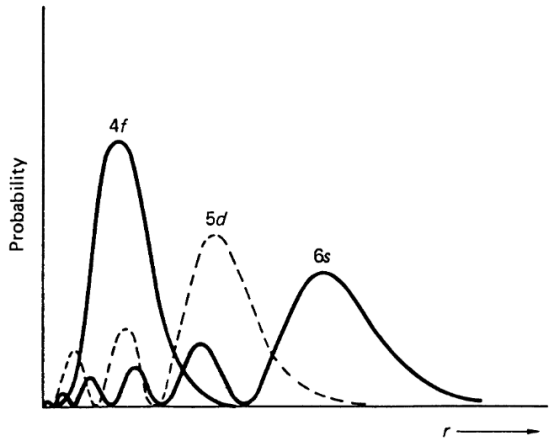

Figure 2. Radial part of the hydrogenic wave functions for the 4f, 5d and 6s orbitals of cerium. Reproduced from Cotton[2]

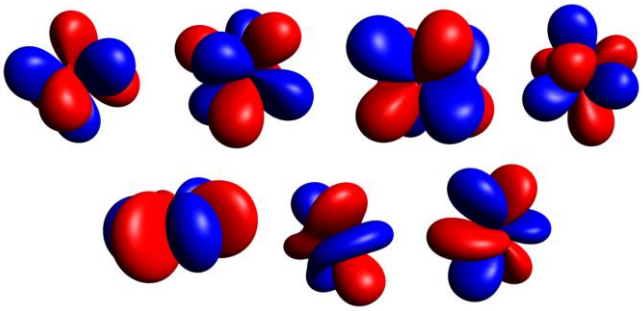

Figure 3. Calculated 4*f* orbitals of cerium(0) (PBE0, def2-TZVP level)

Lanthanides are all stable in +III oxidation (see **Figure 4**).[2] Some of them can nevertheless display a certain stability in +II oxidation state where the 4f level is either half-filled or close to half-filled ([Xe]$6s^0 4f^6$ for Sm^{II} and [Xe]$6s^0 4f^7$ for Eu^{II}) or completely filled ([Xe]$6s^0 4f^{14}$ for Yb^{II}), which allowed these elements to be used as reductants (especially for SmI_2).[6] Other lanthanides in +II oxidation state (referred to as *non-classical divalent lanthanides*) are often highly reducing, and need for specific ligands to stabilize them.[7] Cerium is unique among lanthanide ions because of its naturally occurring +IV oxidation state, having a similar electronic structure to xenon.

Rare-earth elements also tend to reach much higher coordination number than transition metals (often 6 at minimum, and can go as high as 12). This feature makes challenging the synthesis of lanthanide complexes with low coordination number (called *low-valent lanthanide complexes*).[7]

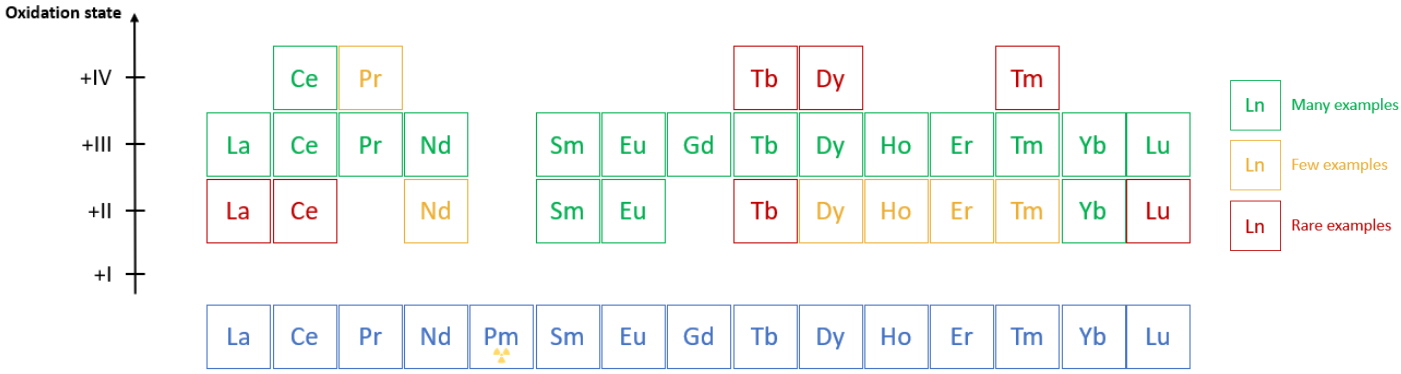

Figure 4. Accessible oxidation states for lanthanide complexes

The spectroscopy of lanthanide ions differs significantly from that of d-metals. In the framework of the perturbation theory, the first splitting of energy levels is due to coulombic interactions (among one of the possible electronic configurations), in the order of magnitude of 10^5 cm^{-1}. Upon approaching ligands, considered as point charges in the crystal field theory,[8] the J-states of each energy level of a d-block element are divided ($\vec{J} = \vec{L} + \vec{S}$, where $\vec{L}$ is the orbital magnetic moment and $\vec{S}$ is the spin magnetic moment). Without external magnetic field, spin-orbit coupling splits the m_J states into $2J$+1 energy levels for each electronic configuration.

In the case of lanthanide ions, 4f orbitals are weakly interacting with the ligands, which makes the contribution of the spin-orbit coupling (about 10^3 cm^{-1}) more important than crystal field splitting (about 10^2 cm^{-1}, see **Figure 5**).

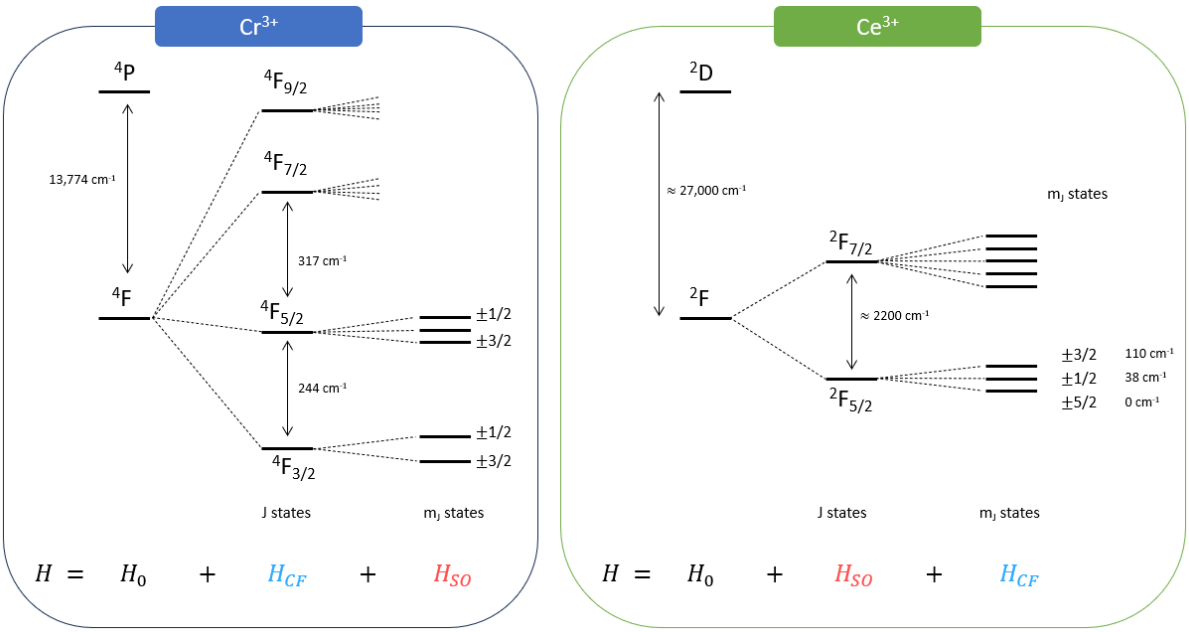

Figure 5. Comparison of perturbation theory applied to d-block elements (chromium(III), left) and f-block elements (cerium(III), right). Adapted from Bünzli *et al.*, and Chilton *et al.*[9,10]

This peculiarity is important in the luminescence of lanthanide complexes : given that 4f orbitals are not influenced by the presence of ligands, the emission wavelength and intensity of f-f transitions are very similar to those of the free ion, which makes them interesting candidates in light-emitting devices.

c) Applications of lanthanides

Rare-earth metals were initially found to be excellent lighter flints under the form of pyrophoric *mischmetall*, an alloy of rare-earth (approximately 50% Ce, 25% La and 25% other lanthanides) and 30% of iron, a mixture that is still used nowadays.[3]

Their use has expanded to many different areas, and their unique structural, luminescent and magnetic properties have turned them into critical elements to a wide range of applications (see **Figure 6**).

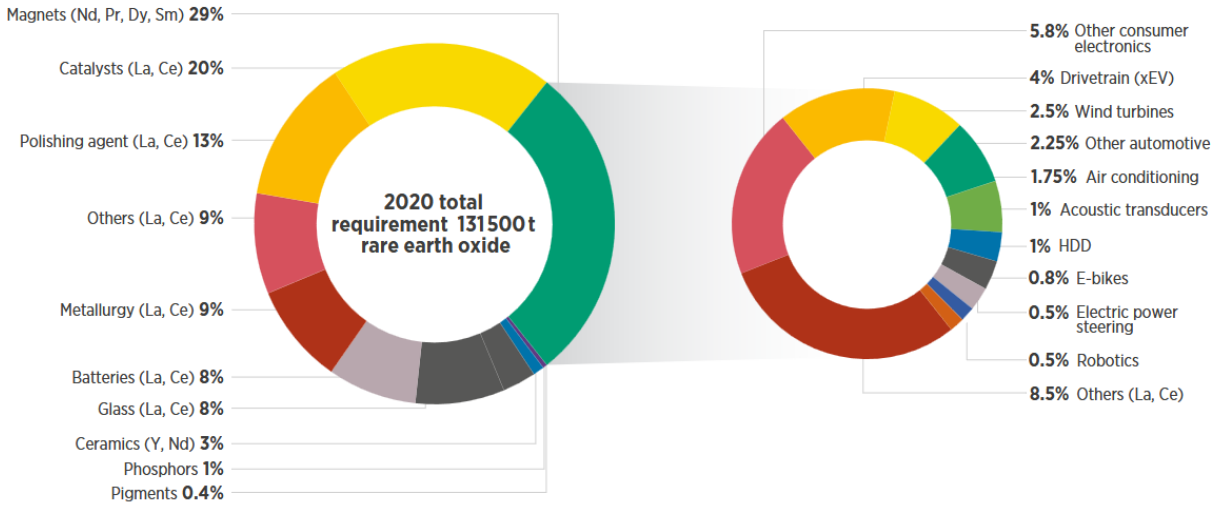

Figure 6. Rare earth demand by end use sectors (left) and breakdown of magnet demand by mass (right). Reproduced from Lyons and Gielen[11]

One of the critical uses of lanthanides is the production of permanent magnets, which constituted 29% of the global demand of rare-earth oxides (REO) in 2020. These magnets are used in many devices ranging from wind turbines to electric vehicles, the latter containing between 2 and 5 kg permanent magnet (NdFeB) per vehicle and making up to half the cost of the motor. As the demand for clean technologies is rising in compliance with environmental policies, the demand for these magnets is expected to increase in 5-fold between 2020 and 2030 for electric vehicles (see **Figure 7**).[11]

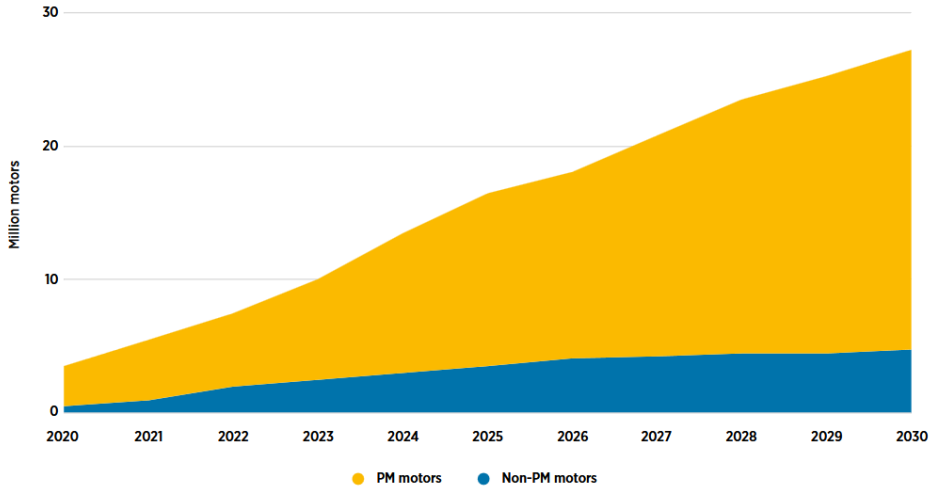

Figure 7. Projections for rare earth permanent magnet use in electric vehicles from 2020 to 2030 (PM = permanent magnet). Reproduced from Lyons and Gielen[11]

Among lanthanides, lanthanum and cerium are by far the most used for a wide variety of application fields. They are used for many catalytic reactions, including catalytic combustion of fossil fuels, purification of industrial waste air, olefin polymerization and production of sulfuric acid.[12] Rare-earths are also found in lithium batteries to enhance their capacity and stability.[13]

In the glass industry, rare-earths (mainly cerium(IV) oxide) are used as polishing reagents but are also part of the chemical composition of optical and photochromic glasses.[14] Metallurgists also add rare-earths to metallic alloys to improve significantly their temperature stability and resistance to deformation over time (*e.g.* cerium added to aluminium alloys).[15]

Finally, the interesting luminescent properties of rare-earths have turned them into key elements for light emission in Light-Emitting Diode (LED) screens, thanks to their ability to transform efficiently energy into visible-light. Each pixel of a LED screen is constituted by three sub-pixels of different colour : red (Pr^{3+} and Eu^{3+}), green (Tb^{3+} and Er^{3+}) and blue (Ce^{3+} and Tm^{3+}) as shown in **Figure 8**. High-end applications also include solid state lasers made up with neodymium, holmium, thulium or yttrium similar to the widely used Nd-YAG laser.[16] Erbium(III) is also used as coating agent in optical fibres to amplify the signal.[17–20]

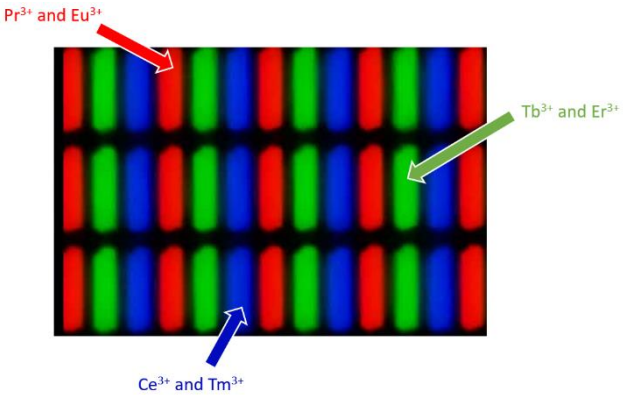

Figure 8. Detail of a Liquid Crystal Display (LCD)

d) Abundancy and extraction

Although their name might suggest otherwise, rare-earth elements are actually quite abundant compared to many elements commonly used in catalysis or in daily life. For instance, the least abundant lanthanide element, lutecium, is 10 times more abundant (0.8 ppm) than silver (0.075 ppm). Cerium (66.5 ppm) is the 25th most abundant element in earth's upper crust, even more abundant than copper (60 ppm, see **Figure 9**).[21]

The name *rare earth* was forged by European scientists due to very limited availability in Europe in the 19th century, due to the absence of important deposits. Later, many reservoirs of rare earths were uncovered, especially in China and Russia which hold together close to two-third of world's estimated reserve of rare-earth oxides (see **Figure 10**).

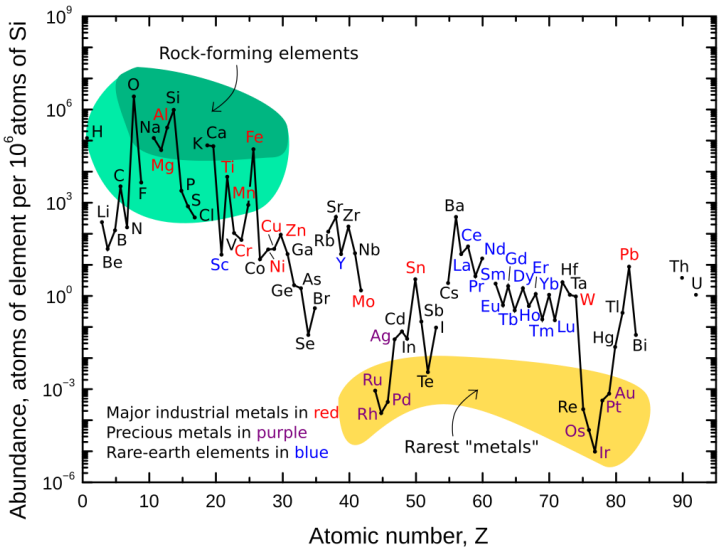

Figure 9. Evolution of the abundance of elements in earth's upper crust as a function of atomic number. Reproduced from United States Geological Surveys[22] and vectorized by a Wikipedia contributor[23]

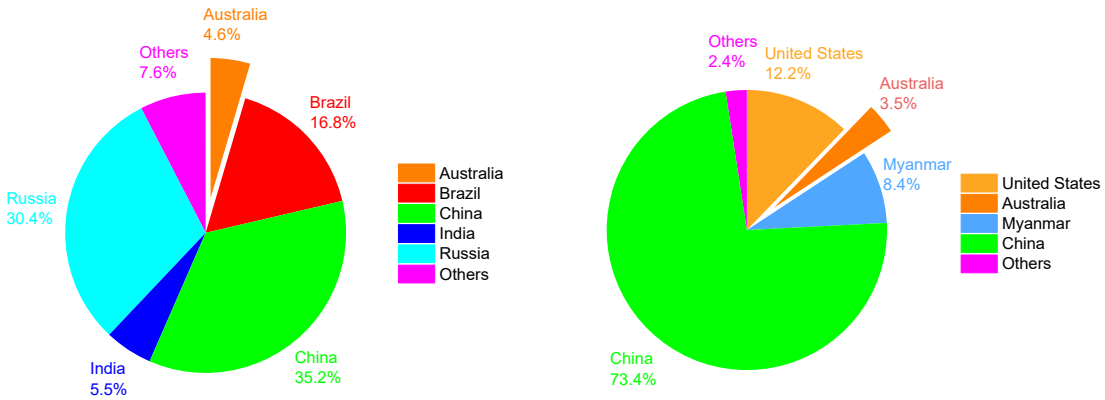

Figure 10. Estimated worldwide rare-earth oxide reserves in percentage of total metric tons (left) and production repartition (right). Data were extracted from USGS Geological survey, 2025[24]

The relative abundancy of the lanthanides follows the Oddo-Harkins effect, which states that elements with an even atomic number are more abundant that those with odd atomic numbers.[25,26] This feature is also reflected by the relative prices of rare-earth oxides of lanthanides, that follows the inverse tendency (see **Figure 11**).

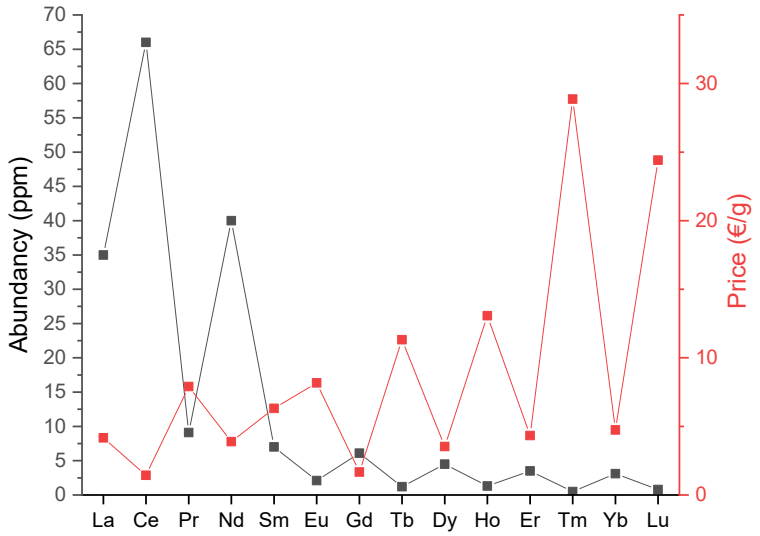

Figure 11. Prices of lanthanide oxides (Ln_2O_3 or CeO_2, purity 99.9% or 99.99%) at ThermoFischer Scientific on February 17th, 2025. Prices were taken for 100 g, 50 g or 25 g of oxide are divided by the total weight of the sample. Abundancy values were taken from literature[27]

Although lanthanides are fairly abundant, their extraction is tedious owing to very similar ionic radii at +III oxidation state within the series. Rare-earth are mostly extracted from two minerals : bastnaesite (containing 75% of REO) and monazite (65% of REO, containing La, Ce, Nd, Th as phosphates).[28] A variety of purification and extraction processes have been developed for different types of rare-earth mineral, particularly those originating from various parts of the world due to the slight geochemical variations between ores from different locations.[29] Cerium is more easily extracted than other rare-earth elements due to its easily accessible +IV oxidation state (bottom right in **Figure 12**). Other rare-earth elements have to be further separated using the difference in solubility of different type of complexes (amine, carboxylic acids, *etc.*).

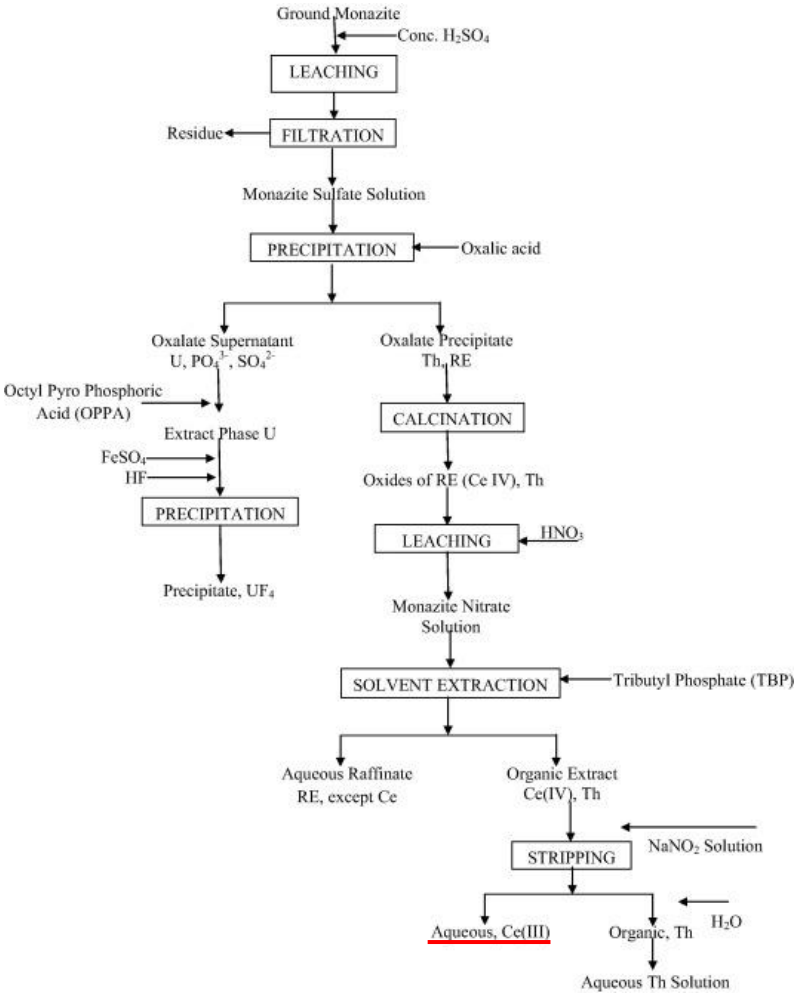

Figure 12. Extraction of cerium and thorium from monazite sand through the acid leaching process. Reproduced from Kumari *et al.*[28]

Extraction of rare-earths generates important amounts of chemical waste, about 2,000 tons per ton of extracted mineral. In addition to the release of radiochemicals, metals, residues from acid mine drainage and dust generated by their extraction, rare-earths' processing also raises environmental concerns.[30] It is also susceptible to creating social disruptions near mining sites, as poor working conditions and increase in small scale mining by indigenous communities can exacerbate local tensions.[31]

Growing demand for theses elements tends to worsen the international relationships between governments, and raises strategical and governance concerns related to their supply.

e) Economical and geopolitical concerns

1) Rare earths as critical minerals

Rare-earth elements have been listed as “critical minerals” by the US government. Critical minerals refer to “any non-fuel mineral, element, substance, or material that the Secretary of Energy determines: (i) has a high risk of supply chain disruption; and (ii) serves an essential function in one or more energy technologies, including technologies that produce, transmit, store, and conserve energy”.[32] They are also registered in this way at the Federal register by the Department of Energy.[33]

These elements are central to the energy production as exposed previously. They are already considered as in short-term danger for supply shortage, which is expected to increase in medium-term (see **Figure 13**).

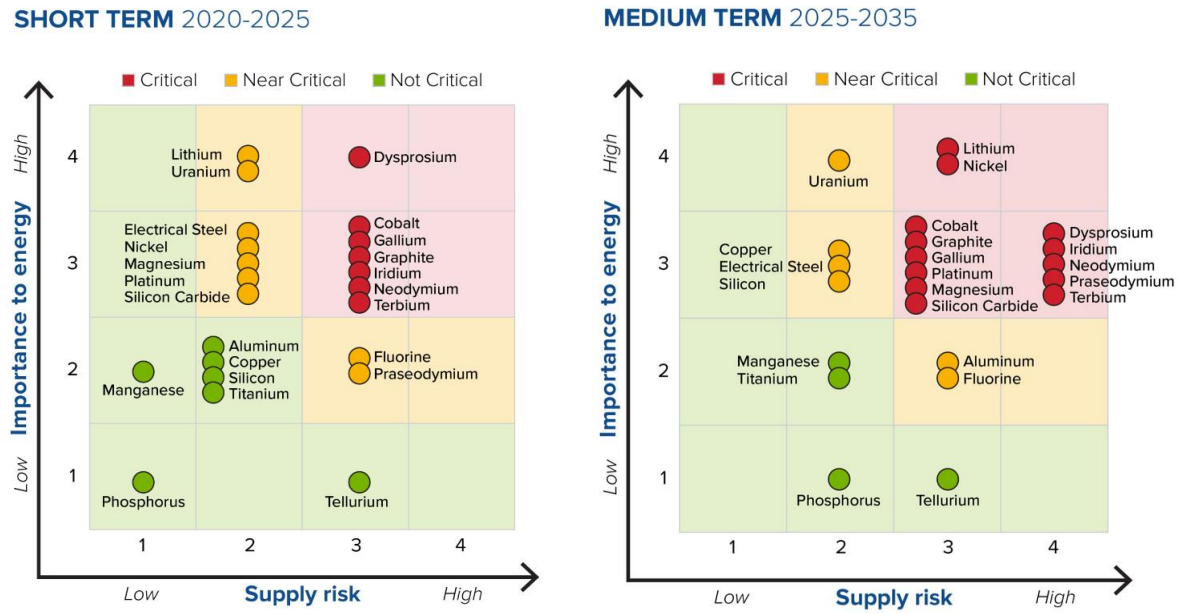

Figure 13. Criticality matrix of critical elements in short term (2020-2025, left) and medium term (2025-2035, right). Reproduced from US Department of Energy[32]

2) Geopolitical aspects of rare earth production

Due to the heterogeneity of rare earth deposits around the globe, some countries find themselves in a quasi-monopoly situation. Taking the example of dysprosium, China holds about 50% of the world production of dysprosium, and is the only country to purify it (see **Figure 14**). This hegemony means that REO-producing countries are still prone to trade disruption, which would affect companies relying on even small quantities of rare-earth precursors and therefore reverberate throughout the economy.[31]

Production

Dysprosium (66 Dy)	
China	48.7%
Myanmar	23.1%
Australia	7.6%
United States	2.9%
Canada	2.7%
Others	15.0%

Neodymium (60 Nd)	
China	45.8%
Australia	23.1%
Greenland*	8.2%
Myanmar	7.4%
Brazil	4.4%
India	2.1%
Others	9.0%

Processing

Dysprosium (66 Dy)	
China	100%

Neodymium (60 Nd)	
China	88.0%
Malaysia	11.0%
Estonia	1.0%

Figure 14. Percentages of world mining production (top) for dysprosium (top left) and neodymium (top right), and world mining processing (bottom) for dysprosium (bottom left) and neodymium (bottom right). Reproduced from International Renewable Agency (IRENA)[31]



Figure 15. Sources of concerns about critical mineral supply. Reproduced from IRENA[31]

The density of producers can raise concerns over several situations as highlighted by the International Renewable Energy Agency (IRENA, see **Figure 15**).[31]

External factors, such as climatic events or pandemic outburst, can cause fluctuations in the production and exchanges of critical minerals. For instance, COVID-19 pandemic has caused the closing of a platinum mine for 21 days in South Africa, which has disrupted 75% of the global platinum supply and led to a dramatic increase in prices in 2020. Similarly, the price for rare-earth oxides has also increased during the pandemic due to limited production and exportations.

In order to develop resource-based industries, many governments from producing countries have established restrictions, which is an ongoing tendency according to the Organisation for Economic Co-operation and Development (OECD).[34] For instance, 41% of rare-earth elements were subjected to export restriction in 2020-2022 period.[35] In 2012, a series of limitations in export duties, export quotas, and limitations on companies allowed to export, set by Chinese government, led to a surge in the price for REO, up to a 5-fold increase for dysprosium oxide in one year (see **Figure 16**). The dispute between China on one-side and European union, Japan and the United States on the other side had to be settled (in favour of the latter group) by the World Trade Organization, as many export restrictions are illegal regarding Article XI of the General Agreement on Tariffs and Trade.[36]

Political and social instabilities in mining countries have also led to perturbations of global markets, as exemplified by the socials strikes in South Africa in 2014 which decreased the worldwide production of platinum by 40%. Myanmar has also experienced a drop in 80% of export earnings (mainly from rare-earth elements) due to social protests against a *coup d'état*. Recent outbreak of war in Ukraine caused a supply shortage of rare-earth precursors in Europe as Russia was one of the main trading partners of the European Union for these elements.

Special care must be taken to ensure future uninterrupted supply of these highly strategical elements, as they also display very interesting photochemical properties.

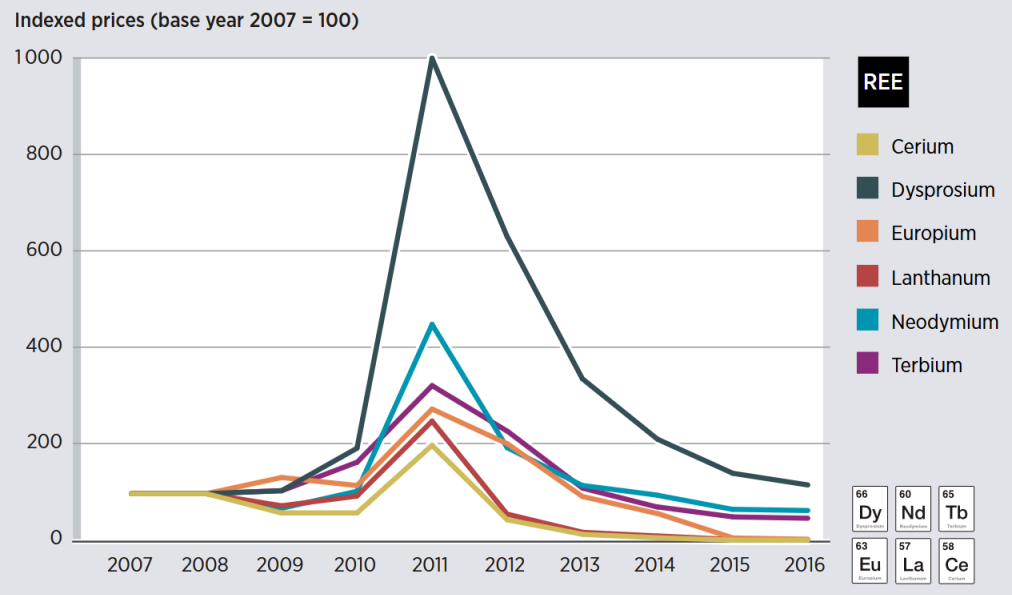

Figure 16. Evolution of prices of rare-earth oxides between 2007 and 2016. Reproduced from IRENA[31]

II. Photochemical reactivity of cerium complexes

a) Why photochemistry ?

1) Chemical reactions and activation energy

Chemistry is defined as “the study of matter and the changes it can undergo” by the American Chemical Society.[37] Atoms, or their agglomerates known as *molecules*, can transform into other compounds. This process is however not free: a toll must be paid for the change to occur, *energy*. This *activation energy* is usually provided to the system through the thermal agitation of the molecules (*heat*), which can as well help the human body to function properly, as a piece of meat to cook on a stove. This method is attractive as it does not require specific characteristics of the chemicals involved, or high-end equipment.

Thermal chemical reactions can nonetheless reach upper limits when targeting high activation energies. Heating at high temperatures may favour undesired degradation pathways. Provided a target temperature at 273 K for a desired reaction, reactions with lower activation energy (*e.g.* 200 K) may occur first. This lack of selectivity and inability to provide important amounts of energy without decomposition may impede the development of highly challenging reactions.

Photochemistry is an interesting way to provide a precise amount of energy to a reaction medium. One of the first source of artificial light without combustion were spectral lamps, made up with a gas element which emits very fine bands upon heating (width lower than 50 cm^{-1} approximatively), at designated wavelengths, meaning that selecting a limited spectral range will only allow reactions that can take place within this energy range. More energy saving and modern Light-Emitting Diodes (LED) emit on larger range (Full Width at Half Maximum (FWHM) of 1126.9 cm^{-1} in **Figure 17**), but their use is facilitated by the much lower heat emission and by the lower cost (≈ 300 € *vs.* more than 700 € for a xenon lamp).[38]

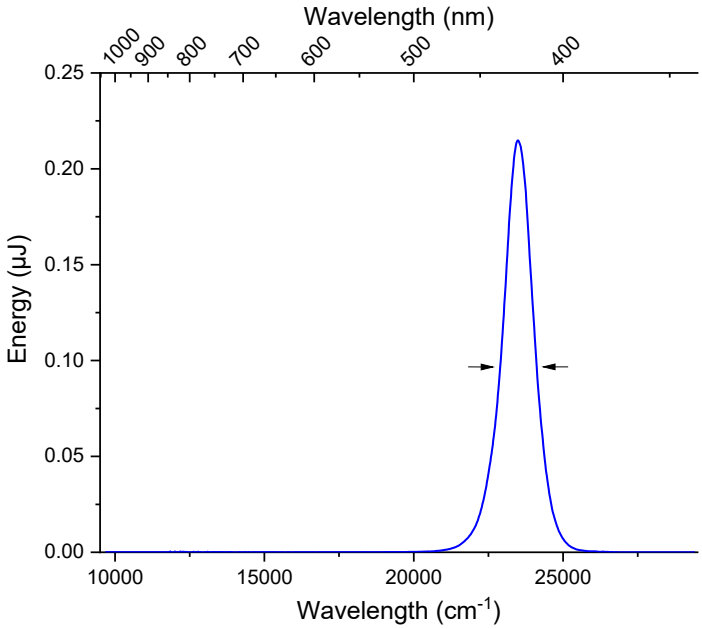

Figure 17. Emission spectra of a Kessil PR160L-427 lamp. Adapted from the data provided with the courtesy of Kessil©

Light absorption is also an interesting way to transfer considerable amount of energy to a reaction medium. The energy carried by one mole of blue photons at λ = 427 nm corresponds to $N_A \frac{hc}{\lambda} \approx 300\ \mathrm{kJ.mol^{-1}}$, which corresponds to the amount of energy needed to heat one mole of chlorobenzene from 0 K to about 1980 K ($C_{p,m}(PhCl_{(l)}) = 150.6\ \mathrm{J.K^{-1}.mol^{-1}}$).[39–41]

Upon light excitation, the electronic configuration of the system changes. Given that chemical and physical properties are deeply correlated with the electronic structure, every excited state will have a unique reactivity (see **Table 2**).

		Ground state		Excited state
HCN	H-C bond distance (pm)	106	→	114
	Bond angle (°)	180	→	125
Formaldehyde	Geometry	Planar	→	Tetrahedral
4-Amino-4'-nitro-p-diphenyl	Dipole moment (D)	5	→	16
Phenol	pKa	10	→	4
$[Ru(bpy)_3]^{2+}$	Reduction potential (V *vs.* NHE)	-1.28	→	+0.84

Table 2. Variation of geometric and chemical parameters between the ground state and the first excited state of several molecules. Adapted from Balzani *et al.*[39]

2) Selection rules

Not any light source can take a molecule to one of its excited states. Two conditions have to be met : (i) the energy of the targeted transition needs to be contained in the emission spectrum of the irradiation source, and (ii) the compound needs to absorb enough light at this wavelength. The absorption of the light by a compound is correlated with the probability of the transition to occur, called the oscillator strength f :

$$f = 4.315 \times 10^{-9} \int_0^{+\infty} \varepsilon(\nu)\, d\nu$$

where ν refers to the frequency and ε is the molar absorptivity coefficient. This expression can be further simplified as followed:

$$f = 1.085 \times 10^{11} \langle \psi_{excited} \,|\hat{\mu}|\, \psi_{ground} \rangle^2$$

where $\hat{\mu}$ is the electric dipole moment operator, ψ_{ground} and $\psi_{excited}$ respectively to the ground state and excited state wavefunctions. The expression $\langle \psi_{excited} \,|\hat{\mu}|\, \psi_{ground} \rangle^2$ is a short form of $\int \psi^*_{excited}\, \hat{\mu}\, \psi_{ground}\, d\tau$ where τ is a volume and * indicates the complex conjugate of the wavefunction.

Applying the Born-Oppenheimer approximation to the wavefunctions combined with further developments and simplifications show that the oscillator strength (without the rotational part) can be written as :

Equation 1. $$f = \langle \psi_{vib,excited} | \psi_{vib,ground} \rangle \langle \psi_{e,excited} | \hat{\mu} | \psi_{e,ground} \rangle \langle \psi_{s,excited} | \psi_{s,ground} \rangle$$

where ψ_{vib}, ψ_e and ψ_s respectively correspond to the vibrational, electronic and spin parts of wavefunction ψ.[42] Ignoring the vibrational selection rules, we can conclude from **Equation 1** that several conditions (called *selection rules*) need to be complied with for the transition to occur :

- Spin state has to be conserved on the transition, meaning that the initial and the final states must have the same spin (ΔS = 0)
- Orbital moment selection rule (also known as *Laporte rule*) states that $\langle \psi_{e,excited} | \hat{\mu} | \psi_{e,ground} \rangle \neq 0$, *i.e.* that the direct product of the irreducible representations of the wavefunctions with the electric dipolar moment $\Gamma(\psi_{ground}) \otimes \Gamma(\hat{\mu}) \otimes \Gamma(\psi_{excited})$ contains the totally symmetric representation A_1 (or A_{1g})

These selection rules are responsible for the very low probability of singlet to triplet excitations (ΔS = 3/2), and for the low absorption coefficient of d-d transitions (Laporte rule), while Ligand-to-Metal Charge Transfer (LMCT) are usually very intense (all conditions are met). They are nonetheless not absolute, as relaxation of Laporte and spin rule can occur through several mechanisms such as vibronic coupling, orbital mixing, and spin-orbit coupling. This fact makes improper the use of *allowed* and *forbidden transition*.

3) Chemistry in the excited state

Once in the highly-energetic excited state, the molecule requires to release the energy excess accumulated upon absorption of a photon. Two major pathways exist :

- deexcitation to the ground state through radiative or non-radiative decay
- transferring this energy to another molecule or engaging into a chemical reaction

a. Radiative and non-radiative decay

Following on this part, we shall consider a close-shell organic molecule in its S_0 ground state (S_n spectroscopic terms correspond to a total spin value S = 0 for a closed-shell molecule). Absorption of one photon (10^{-15} s) at a suitable wavelength excites the molecule into one of the S_n states (n ≥ 1) following the spin selection rule detailed above. According to Kasha's rule,[43] the molecule often quickly loses energy to reach the first excited state S_1 by relaxation through vibrations (≈ 10^{-11} s) and internal conversion (≈ 10^{-10} s, see **Figure 18**). In the S_1 state, three decay pathways are possible :

- radiative decay (fluorescence, ≈ 10^{-9} s) by emission of a photon
- vibrational relaxation (≈ 10^{-11} s) to S_0 state
- inter-system crossing (10^{-10} - 10^{-8} s) and vibrational relaxation to a triplet state T_1, from which a radiative decay (phosphorescence, 10^{-6} - 10 s) or vibrational relaxation can occur

It is important noticing that the time scale of these processes is correlated with the probability of each process to take place (a faster process is more probable). Fluorescence is more likely to happen due to the spin selection rule (ΔS = 0) than phosphorescence (triplet T_1 final state, therefore ΔS = 1), which makes the fluorescence decay faster than phosphorescence.

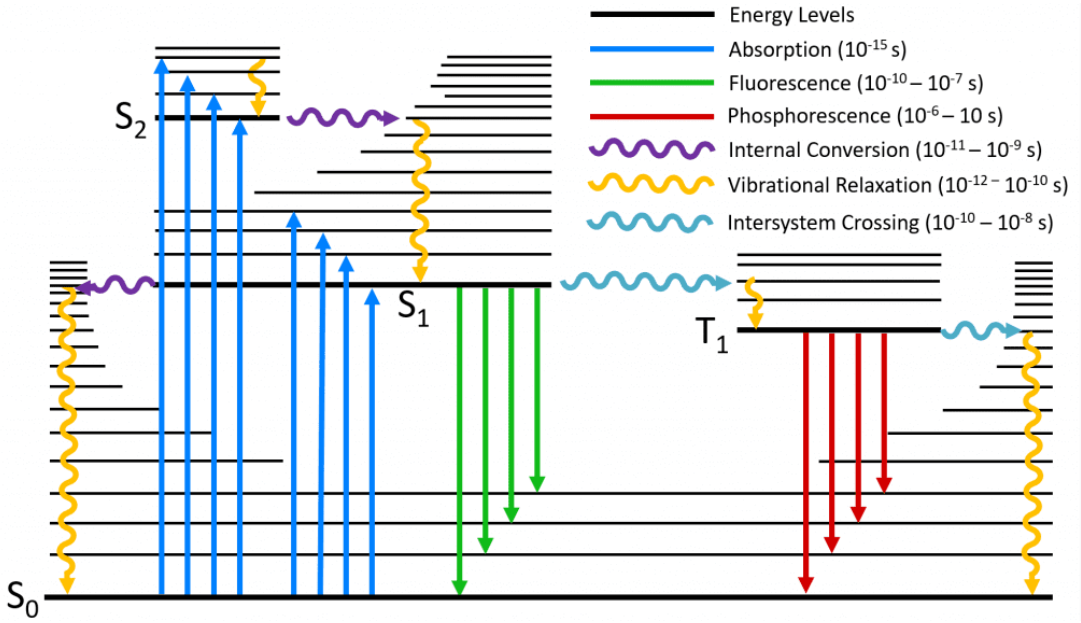

Figure 18. Perrin-Jablonski diagram. Reproduced from Direct Industry[44]

Fluorescence and phosphorescence are part of the broader *luminescence* category, which also includes radiative decay for species emitting from non-singlet excited states (*e.g.* lanthanide ions). Luminescence phenomena are characterised by their lifetime τ ranging from 0.1 ns to almost 1 µs, and the quantum yield Φ which quantifies the probability of a photon emission upon absorption of an incident photon. Together, these values allow to determine the radiative ($k_r = \frac{\Phi}{\tau}$) and other ($k_{other} = 1 - \frac{\Phi}{\tau}$) decay kinetics. The Stokes shift, *i.e.* the energy difference between the absorption maximum and emission maximum is also an interesting parameter to report as it quantifies the reorganisation energy between the ground and excited state. This parameter is useful to explain the unusual narrowness of 4f-4f lanthanide emission bands (see **Figure 19**).

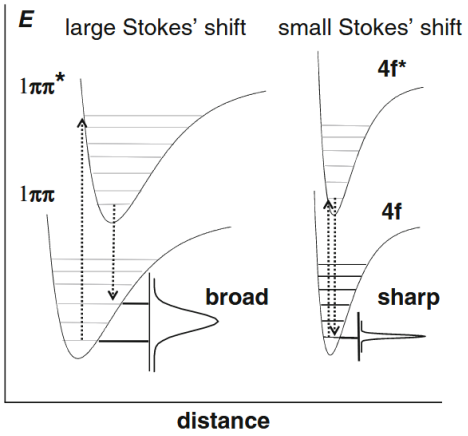

Figure 19. Comparison of the width of emission bands in the cases of large and small Stokes shift. Reproduced from Bünzli *et al.*[2]

Apart from non-radiative and radiative decay, molecules can also undergo chemical reactions in their excited state.

b. Chemical reactions in the excited state

Owing to the different physical and chemical properties of a molecule in its excited states as highlighted in **Table 2**, excitation of an electron into an orbital higher in energy can unravel some new reaction pathways.

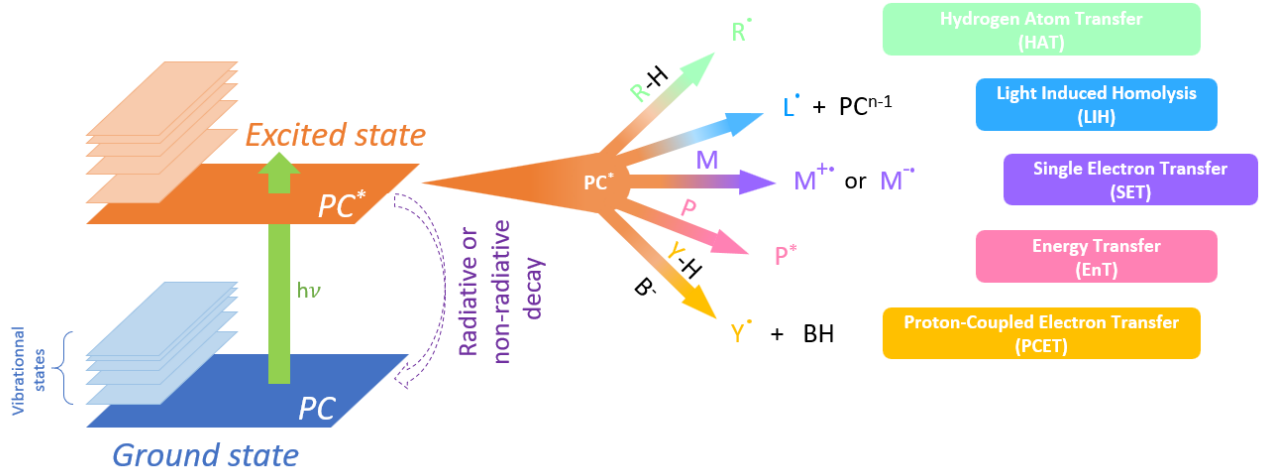

Figure 20. Schematic representation of the energy levels of a molecule and the different processes. Adapted from Balzani *et al.*[39] and Ravelli *et al.*[45]

Direct Hydrogen Atom Transfer (HAT, light green path in **Figure 20**) can occur through the formation of a highly reactive species, which can abstract one hydrogen from a substrate. Irradiation of aromatic ketones with UV-C light can form a biradical species through a π-π* excitation of the C=O bond, which was reported to engage into HAT reactions such as Norrish II reaction.[46,47] Similar HAT behaviour was described for decatungstate anion ($W_{10}O_{32}^{4-}$), which was hypothesised to proceed through a charge transfer in the W-O bond.[48–50]

Charge transfer excitations in metal complexes can induce an homolytic cleavage of a metal-ligand bond (*e.g.* metal-oxygen bond), leading to a reduction of the metal centre and to the release of a highly reactive ligand-based radical (*e.g.* RO•) which can then engage into a HAT reaction with another substrate.[46] The Light induced Homolysis (LIH, blue path) reactivity has been extensively studied,[51] and will be described in more details in the following section.

Light excitation can also enhance the redox properties of the photocatalyst, making easier either the acceptance or the release of one electron to a substrate by Single Electron Transfer (SET, purple path). This reactivity is of particular interest with cerium(III) complexes and will be reviewed at the end of the introduction.

Energy Transfer (EnT, pink path) is especially useful to transfer the excess of energy (and not electrons) to another substrate that does not absorb light.[52] This feature allowed for the development of photodynamic therapy (PDT) which uses a photosensitizer to excite dioxygen in its more reactive singlet state (Type II PDT) or to generate radicals from another redox partner (Type I PDT).[53,54] Intramolecular energy transfer through *antenna effect* was also shown to enhance the sensitivity of improbable transitions on metals, and particularly low intensity f-f transitions on lanthanides ions.[55–57]

Photoinduced Proton-Coupled Energy Transfer (PCET, yellow path) consists in the concerted transfer of one proton and one electron (formally H•), which plays a vital role in biology in photosystem II enzyme which oxidises water in dioxygen and protons that are then used for the phosphorylation of adenosine diphosphate.[58,59]

Compared to organic photocatalysts, metal photocatalysts might seem appealing due to the mild irradiation energies needed (often in visible or near-UV region), long-lived excited states, decent quantum yields and high fatigue resistance under irradiation.[60,61] Recent reports have highlighted the potential of lanthanides[62–64] and especially cerium[65] to catalyse challenging reactions under irradiation.

b) Light Induced Homolysis using cerium(IV) complexes

Light Induced Homolysis (LIH) reactivity is an elegant tool to generate highly reactive species, such as alkoxy radicals (Bond Dissociation Energy, BDE(O-H) 104 kcal.mol^{-1} in MeOH) or halide radicals (H-Cl 103 kcal.mol^{-1})[66] which can easily abstract hydrogens even from challenging substrates like alkanes (C-H 100 kcal.mol^{-1} in ethane).[46]

LIH reactivity with transition metals have been widely studied, owing to their ability to both harness photon energy and directly catalyse bond breaking and bond formation.[51,67,68] Ruthenium(II) and iridium(III) catalysts have been extensively used as SET agent and photosensitizers,[60,61,69,70] but no example of LIH reactivity using these metals has been reported to the best of my knowledge.

3d-transition metals have aroused interest in visible-LIH (VLIH) reactivity, owing to their high degree of ligand lability, a much higher abundancy (60 ppm for Cu, 25 ppm for Co)[71] compared to ruthenium and iridium (0.001 ppm for both)[71] and their lower toxicity.[72–75] 3d-metal photocatalyzed LIH also occurs in natural processes with iron(III) aqua complexes for the formation of hydroxyl radical HO$^{\bullet}$, copper(II) to form various ligand-based radicals, and chromium(VI) compounds to transform alcohols in alkoxy radicals.[76]Copper(II) complexes have been used in VLIH photochemistry[77] to produce highly energetic radicals such as chlorine radical Cl$^{\bullet}$ from simple $CuCl_2$, which is able to react with multiple bonds through a Giese addition,[78] or to activate C-H bonds.[79]

Few examples of nickel LIH-cross-coupling reactions have been reported, mostly using easily accessible nickel(II) precursors (*e.g.* $NiCl_2$, $Ni(C_8H_{12})_2$)[80,81] which are oxidized in nickel(III) by a co-photocatalyst and generates a halide radical by VLIH that can engage in HAT reaction with a C-H bond, creating a C-centred radical. The C-centred radical then coordinates to nickel(II) centre, which finally releases the coupling product upon reductive elimination.[51]

Interestingly, chemist drew their inspiration from vitamin B12 (cobalt(III)) photochemical release of alkyl radicals to develop new strategies to create C-C bonds using the weak intensity of the Co-C bond (BDE(Co-C) = 39.8 kcal.mol^{-1}).[82,83] This feature allowed for the development of photocatalyzed cross coupling reactions through the transient formation of alkyl[84,85] and acyl[86,87] radicals.

Iron photochemistry gathered significant efforts to find organic chemistry applications, given the exceedingly short excited state lifetime of the MLCT state (about 50 fs).[51] Iron(III) complexes have been used to initiate radical decarboxylation reactions to create acyl[88] or alkyl[89,90] radicals that engage in cross-coupling reactions. Biphenyl-benzoic acids do not decarboxylate upon LIH, and create aryloxy radicals which undergo cyclisation into a lactone scaffold.[91]

Thanks to their oxophilicity, lanthanides ions have been considered as interesting candidates to form O-centred radicals. While four examples of VLIH reactivity with europium(III) have been reported by Ishida's group,[62,92–95] cerium(IV) complexes were extensively studied for their possibility to generate highly energetic radicals.[96–98] In +IV oxidation state, the electronic configuration of cerium is [Xe]$6s^0 4f^0 5d^0$, and can easily engage in LIH reactions induced by LMCT upon irradiation with blue light or near-UV LEDs.

1) Photoinduced decarboxylation

Similarly to iron(III) complexes, cerium(IV) was shown to be able to induce decarboxylation reactions with carboxylic acids,[96,97,99–110] and intramolecular cyclization with benzoic acids.[108,111]

Decarboxylation is especially interesting regarding the volatility of CO_2 which provides a strong thermodynamic driving force, meaning that forming alkyl radicals through this pathway is more thermodynamically favourable than direct C-H activation.[106]

Cerium(IV) decarboxylation chemistry started in 1965 with the report of a photoinduced decarboxylation of glacial acetic acid into CO_2 and CH_4 by cerium(IV) ammonium nitrate by Henshall *et al.* (reaction a in **Figure 21**),[99] following the report of Patnaik and Panda on the photosensitivity of cerium(IV) acetate.[112,113] Further studies between 1968 and 1984 focusing on cerium(IV) acetate, cerium(IV) ammonium nitrate and cerium(IV) sulfate allowed to give more insight into the reaction and to expand the scope of carboxylic acids.[100–105]

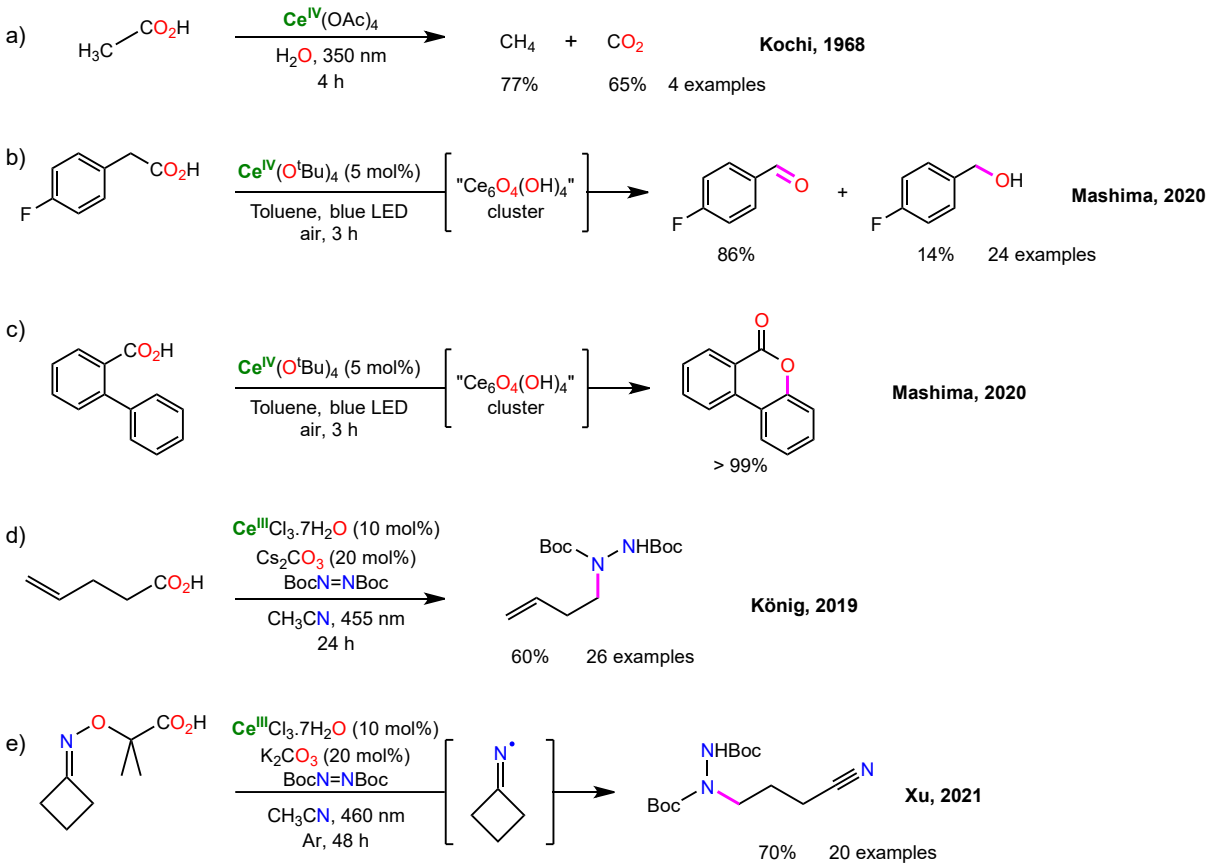

Figure 21. Selected decarboxylation reactions using cerium complexes[100,106,108,109]

In 2019, new developments in cerium(IV) decarboxylation reactions were reported by the teams of Mashima's and König's groups among others.[97,106,108,114,115] Mashima and co-workers used the alkyl radical produced by decarboxylation in synergy with O_2 bubbling to produce a decarboxylative oxygenation, which allowed for the formation of "dehomologation" products (reaction b).[108] Interestingly, the reaction was shown to proceed through the formation of an hexanuclear cerium(IV) oxocluster "$Ce_6O_4(OH)_4$" which can be isolated by mixing cerium(IV) *tert*-butoxide with an excess of pivalic acid.[108] In the case of 2-biphenylcarboxylic acid, a similar lactonization reaction to iron photochemistry was reported (reaction c).[108]

Instead of using a cerium(IV) precursor, König's group used hydrated cerium(III) chloride as a catalyst in the presence of di-*tert*butylazodicarboxylate (DBAD) to photochemically form *in situ* a cerium(IV) precursor (reaction d).[106] This precursor reacts with a carboxylic acid, and that can engage into a photoinduced decarboxylation (see **Figure 22**).

Further developments in this reactivity allowed to expand its range of applications, including an elegant cascade decarboxylation forming a cyclobutaniminyl radical which subsequently rearranges to form linear nitriles (reaction e).[109,116]

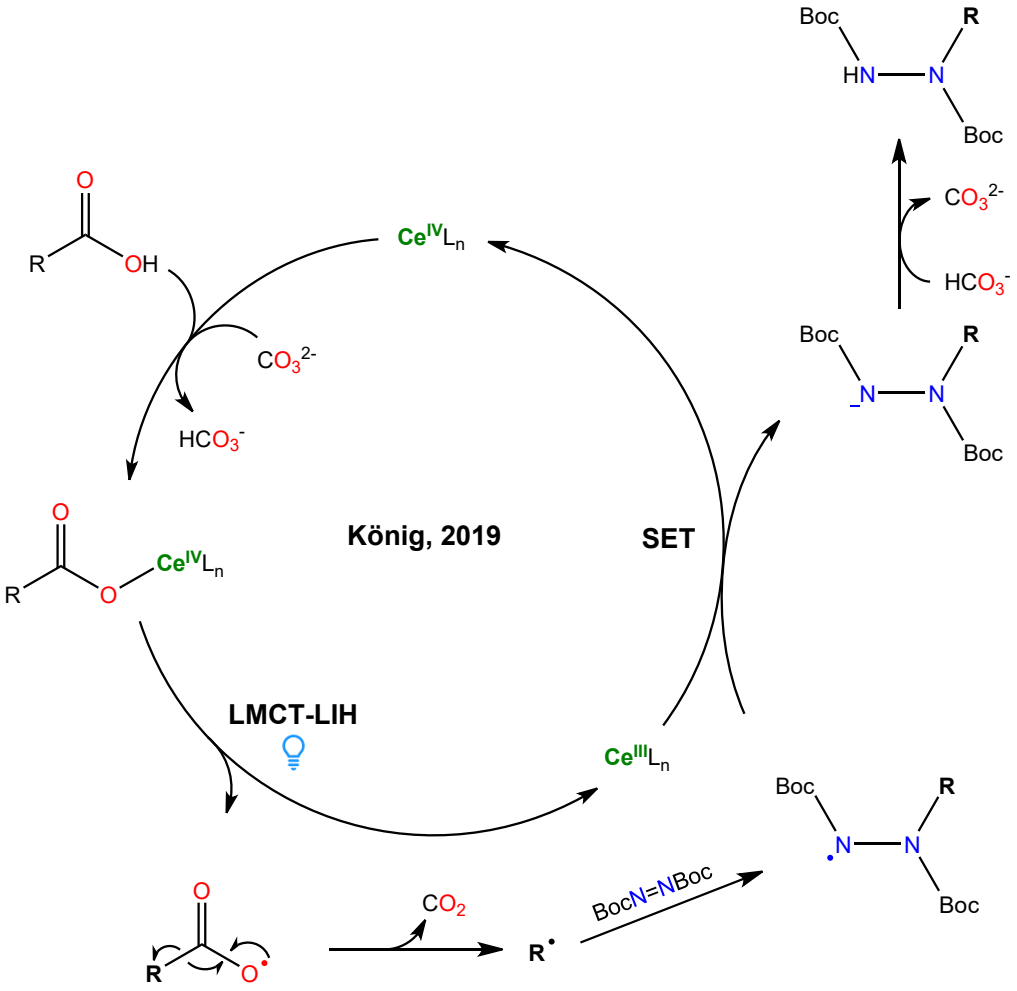

Figure 22. Mechanism of the photoinduced decarboxylation proposed by König and coworkers[106]

2) Alkoxy radical formation

In the presence of alcohols, photoactivation of cerium(IV) complexes leads to the formation of highly reactive alkoxy radicals RO$^{\bullet}$ that can engage in different types of reactivity depending on the structure of the alcohol (see **Figure 23**) :

- Long-chain alcohols are susceptible to engage in two competitive reactions :
  - **β-scission** of the alkoxy radical that creates an alkyl radical[117–122]
  - Intramolecular **1,5-HAT** which forms a C-centred radical in δ position and allows for functionalization in this usually unreactive position[123]
- shorter alcohols tend to engage into **intermolecular HAT**, even able to activate light alkanes such as methane[124–127]

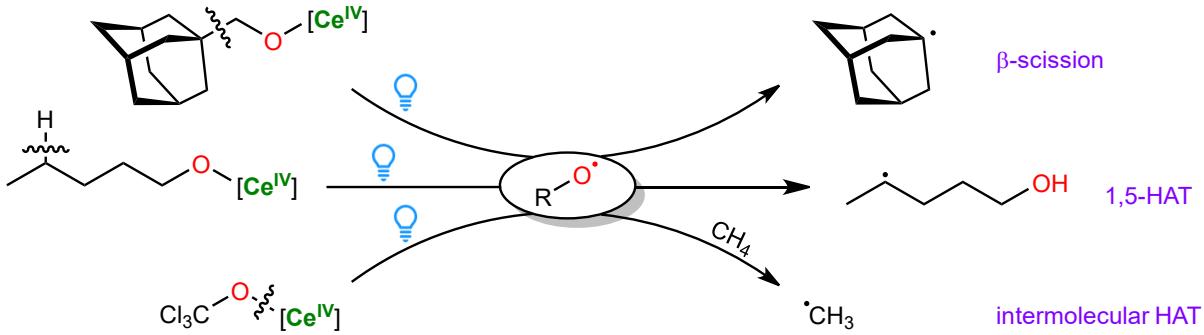

Figure 23. Possible chemical reactions from a LIH-generated alkoxy radical

Traditionally, alkoxy radicals were formed by the photochemical homolysis of hydroperoxides,[128] nitrites[129], hypochlorites,[130] N-alkoxy phtalimides,[131] N-alkoxypyridinethiones[132] and 4-nitrobenzene sulfonates.[133] These substrates nonetheless suffer from security issues (peroxides are explosives), undesired side reactions (oxidations upon formation of nitrosyl radical) or tedious prefunctionalisation of the alcohol.[134]

a. β-scission *vs.* 1,5-HAT

β-scission of alcohols is an interesting type of reactivity, as alcohols can easily be derived from various feedstock compounds through simple oxidation, and the generation of O-centred radical could enable an economic and straightforward pathway to access a wide variety of chemical scaffolds.[135] The first reported example of such a reactivity for ketones is the Norrish I reaction, which can occur upon irradiation of ketones with UV-C light.[136]

Zuo and co-workers investigated the reactivity of alkoxy radicals generated by cerium complexes under irradiation.[134] In 2016, Zuo *et al.* reported the photoinduced β-scission of cyclic alkanols (aliphatic alcohols) using catalytic amounts of cerium(III) chloride, which led to the formation of a variety of linear ketones (reaction a in **Figure 24**).[137] Similar reactivity on cyclic strained alcohols in the presence of diphenylanthracene (DPA) and a Giese acceptor showed the formation of products of a formal cycloaddition with alkenes (reaction b).[122] Further developments on this reactivity afforded the lactamization of cyclic ketones using cerium(IV) *tert*-butoxide and titanium(IV) chloride (Lewis acid) to transform *in situ* the ketone into an alcohol (reaction c).[117] β-scission from 2-alkanol-ketones in the presence of dioxygen led to the formation of macrocyclic lactone through an original mechanism (reaction d).[138]

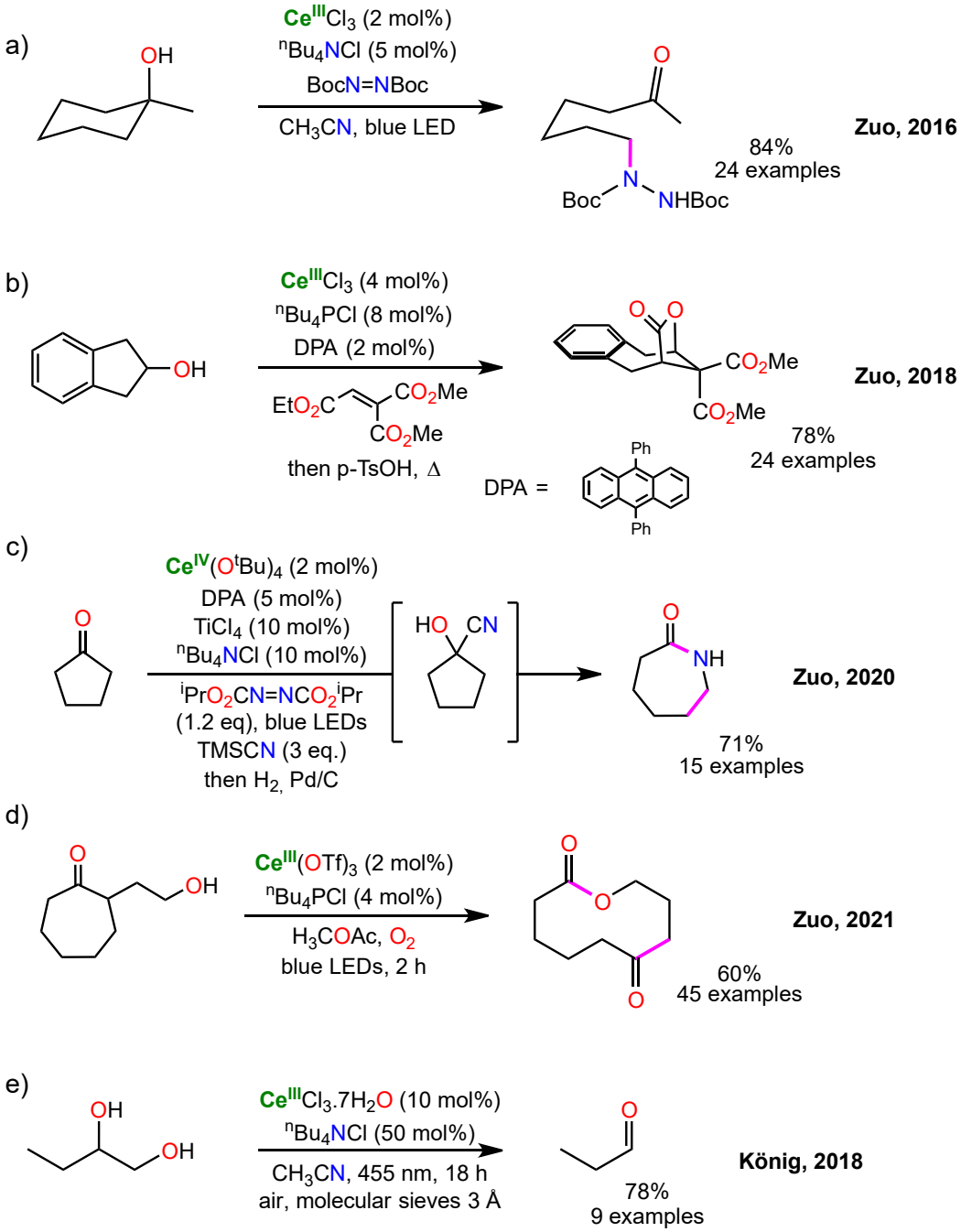

Figure 24. Examples of β-scission reactivity using cerium complexes[117,118,120,122,137]

Similarly, König and co-workers reported an oxidative cleavage of several non-cyclic vicinal diols using a cerium(III) catalyst under blue light irradiation, leading to a cleavage into two aldehydes moieties.[120]

The team of Zuo further investigated the β-scission reactivity on non-cyclic compounds, and reported the dehydroxymethylation of several alkanols into the corresponding C-centred radical which can be trapped on Giese acceptors (reaction a in **Figure 25**). This reactivity was further investigated three years later by Zuo and co-workers to provide an interesting example of synergistic cerium-nickel catalysis, using a nickel(II) complex as a radical scavenger and a cross-coupling catalyst (reaction b).[139] The development of this reaction was especially tedious (190 co-ligands screened by high-throughput platform), due to the decoordination of the co-ligand from the nickel centre.

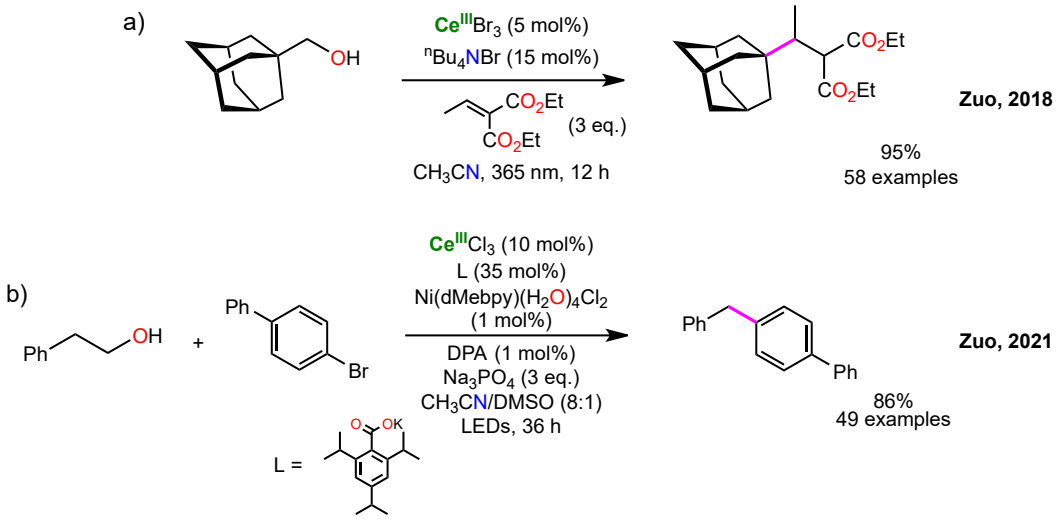

Figure 25. Examples of dehydroxymethylation of alkanols using cerium(III) complexes.[121,139] dMebpy = 4,4'-dimethyl-2,2'-bipyridine

Interestingly, the authors highlighted a competition between dehydroxymethylation of alkanols and 1,5-HAT reactivity.[121] The study of the reaction showed an influence of sterics on the selectivity : bulkier substituents close to the alcohol (α and β positions from the alcohol) led to higher yields in dehydroxymethylated product, while increased hindrance in δ-position facilitated the formation of 1,5-HAT product (see **Figure 26**).

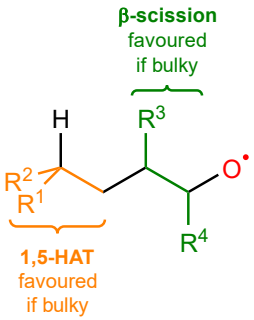

Figure 26. Sterics influence on dehydroxymethylation and 1,5-HAT reactivity

This difference could originate from the stability of the C-centred radical formed after each process, as well as the stability of the pseudo-chair conformation in the transition state during the 1,5-HAT reaction (see **Figure 27**). 1,5-HAT reactivity was also explored on a set of linear alcohols, including complex scaffolds such as steroids and terpenoids (see **Figure 28**).[123]

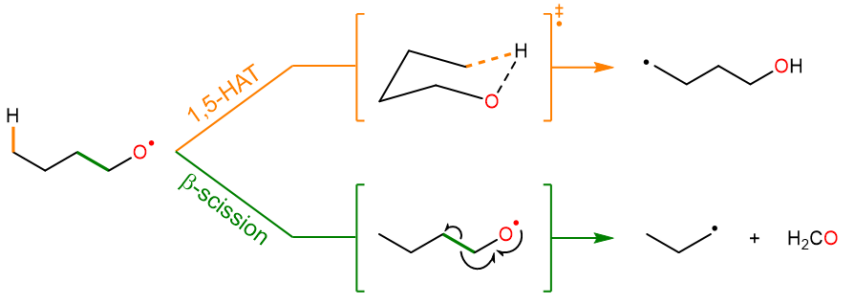

Figure 27. Competition between dehydroxymethylation and 1,5-HAT reactivity on alkanols. Adapted from Zuo *et al.*[123]

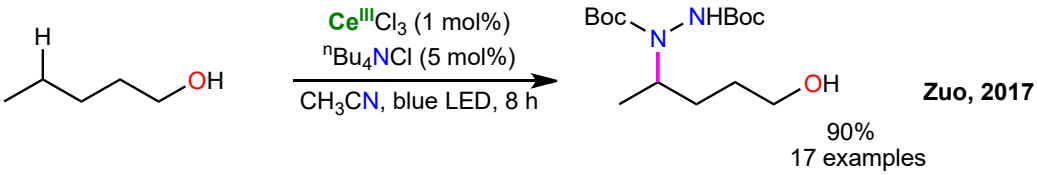

Figure 28. δ-functionalization of linear alkanols[123]

1,5-HAT is nonetheless limited to intramolecular reactions on adapted substrates. Using the alkoxy radical to promote intermolecular HAT could significantly expand the range of reaction possibilities.

b. Short-chain alcohols as potent intermolecular HAT agents

HAT reactions on inert substrates are a key tool for synthetic chemists as they can enable new synthetic opportunities using simple and abundant chemicals.[45] C-H activation is particularly interesting for late stage functionalisation[140–142] and to develop new reactions with unreactive substrates,[67] for instance C-C bond formation on light alkanes considering their abundancy. Nevertheless, activation of alkanes is particularly difficult : methane and ethane are considered among the most challenging substrates in C-H activation, owing to the high BDE of the C-H bond (105 and 100 kcal.mol^{-1} respectively, see **Figure 29**).[143] This inertness brings challenges not only on the harsh conditions needed to overcome the activation barrier, but also in the chemoselectivity and the monofunctionalization of the substrate.[144]

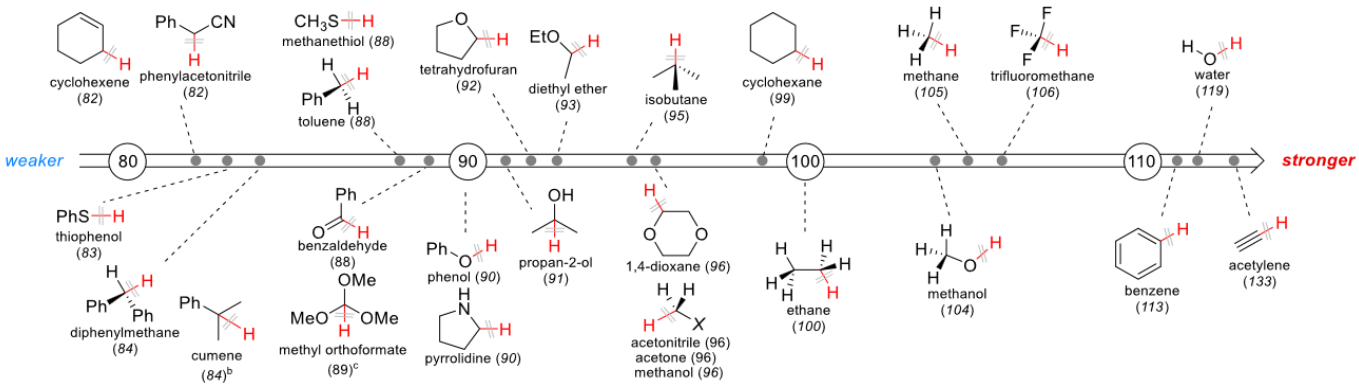

Figure 29. Bond dissociation energies of X-H bonds (in red) in kcal.mol^{-1}. Reproduced from Fagnoni *et al*.[143]

Zuo and co-workers investigated the use of short-chain alcohols as alkoxy radical precursors with cerium complexes under irradiation to engage into intermolecular HAT reactions with non-activated light alkanes in fairly mild conditions.[124]

In their 2018 report, catalytic amounts cerium(IV) or cerium(III) complexes were used in presence of 5 equivalents of *n*-tetrabutylammonium chloride (TBACl) relative to cerium, with an alcohol reagent and di-tert-butyl azodicarboxylate (DBAD) as a radical trapper in acetonitrile under 400 nm irradiation. The use of a highly polar solvent such as acetonitrile was needed to solubilise the cerium salt, but significantly complexified the experimental conditions as high pressures of alkanes (50 bars for CH_4) were applied to partially solubilize them in polar solvents.[145] This nonetheless allowed for the isolation of the aminated alkanes in good yields (70-97%), including methylhydrazine which is an important chemical in rocket propellants. On longer alkanes (propane and butane), no selectivity was observed with 2,2,2-trichloroethanol or 2,2,2-trifluoroethanol on terminal C-H bonds and methylene C-H bonds (which have a slightly lower BDE than CH_3 bonds). The use of methanol led to an increase in selectivity on the methylene bonds up to 1:3.9 ratio, which was attributed to the less electrophilic nature of MeO$^{\bullet}$. Radical-trapping experiments on styrene showed the formation of alkoxy radical trapping products with every alcohol studied, and the generation of the alkoxy radical was confirmed two years later by Transient-Absorption Spectroscopy (TAS) measurements, which also showed no formation of chlorine radical at 330 nm from $[NEt_4]_2[Ce^{IV}Cl_5(OR)]$ complexes (R = alkyl).[146]

Altogether, these results tended to converge to the generation of an alkoxy radical able to react with CH_4 by HAT, as proposed by Zuo and co-workers (see **Figure 30**). Under light irradiation, an *in-situ* generated cerium(IV)-alkoxide complex reacts through LIH to produce an alkoxy radical that can engage into HAT reaction with an alkane and create an alkyl radical, trapped by DBAD as a hydrazyl radical. The latter radical is finally reduced by cerium(III) which forms the aminated product in the presence of protons, and forms back the cerium(IV) complex initially introduced.

One year later, Schelter, Walsh and co-workers reported their mechanistic study of the amination of alkanes, in which they claimed the reaction to proceed through the formation of a chlorine radical Cl• (see **Figure 30**).[125] Starting from cerium(IV) hexachlorocerate $[NEt_4]_2[Ce^{IV}Cl_6]$, the authors managed to functionalize similar alkanes to the one studied by Zuo *et al.* both with and without alcohol catalyst, which questioned the hypothesis of the alkoxy radical generation. Extensive study of the overall kinetics of the reaction showed no influence of alcohol, DBAD and alkane concentrations, which was likely to indicate that the photochemical generation of the active species was the rate-determining step. In addition to spectroscopic studies that showed no change in the absorption spectrum upon addition of alcohols, radical trapping experiments indicated the formation of chlorine radical trapping products in the presence of protons, and formation of chloroacetonitrile in the absence of both alkane and trapping agent. The selectivity of chlorine radical being quite low, the authors postulated that the selectivity observed in the presence of alcohol arose from the formation of a chlorine radical-alcohol complex as supported by DFT calculations which showed a decreasing radical stability from methanol to acetonitrile (MeOH > 2,2,2-trichloroethanol > MeCN).[147,148]

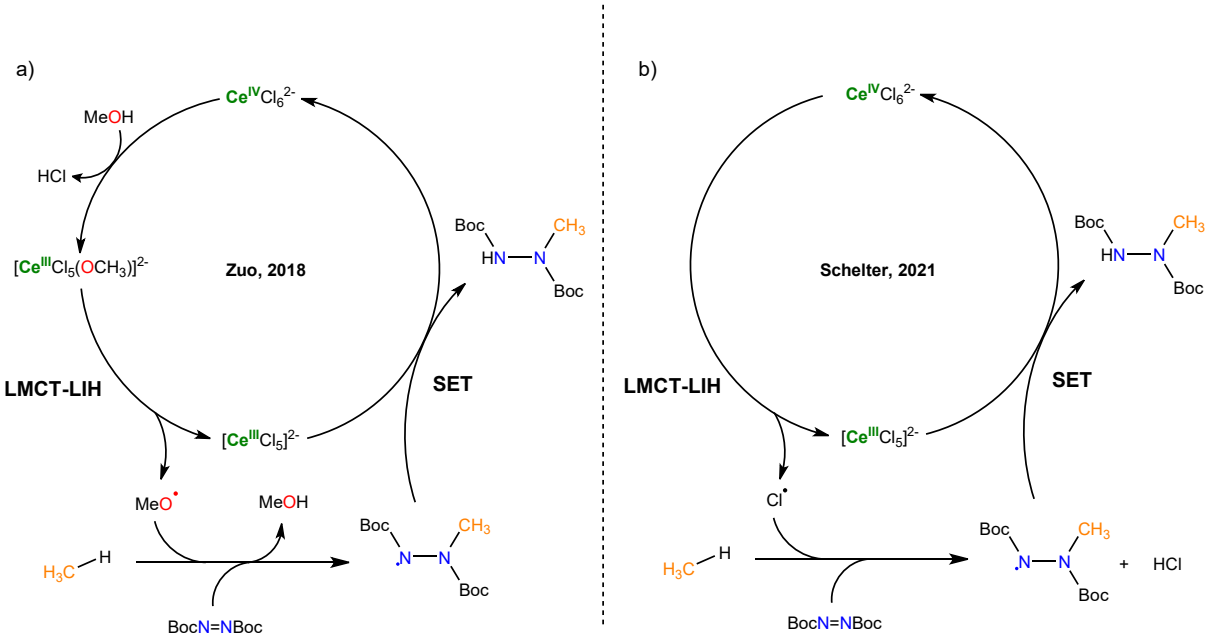

Figure 30. Mechanisms proposed by Zuo (a) and Schelter (b) and co-workers. Adapted from Zuo *et al.*[124] and Schelter *et al.*[125]

In 2023, Zuo and co-workers investigated further their hypothesis of alkoxy radical generation using a variety of characterisation techniques.[126] Synthesis of several pentachloro cerium(IV)-alkoxo complexes $[NEt_4]_2[Ce^{IV}Cl_5(OR)]$ and subsequent radical trapping experiments under irradiation followed by Electron Paramagnetic Resonance (EPR) spectroscopy in the presence of 5,5-dimethyl-1-pyrroline N-oxide (DMPO) and N-*tert*-butyl-α-phenylnitrone (PBN) showed the formation of alkoxy radical trapping products rather than chlorine radical trapping products. Femtosecond TAS neither highlighted the formation of any chlorine radical-alcohol complex nor the transient appearance of a chloride radical from the pentachloro cerium(IV)-alkoxo complexes synthesized. Regioselectivity studies in chloride-free conditions (using cerium(IV) ammonium nitrate or cerium(IV) triflate as cerium(IV) precursor) showed similar behaviour for methane amination. Finally, DFT calculations did not allow to find a productive reaction pathway through the generation of a chlorine radical, and indicated a higher participation of the oxygen into the LMCT process than the chloride ligand.

The complex mechanistic discussion between the teams of Zuo and Schelter showed that each team presented legitimate arguments to support their proposed mechanism, but did not allow for an agreement on the nature of the active species.

In a last paper published in 2025, Walsh, Schelter and co-workers proposed a unified version of both mechanistic proposals through a highly detailed study of the influence of each compound and parameter in the reactivity.[127] As clearly highlighted in their introduction, there were two major differences between their system and Zuo's catalytic systems, related to the initial oxidation state of the cerium catalyst and the use of alcohol as additives. Through many converging proofs that will not be detailed here, they managed to show that, in the presence of alcohol, the speciation of cerium complexes oxidized from $[NEt_4]_2[Ce^{III}Cl_5(HOMe)]$ by excited DBAD was dependent on the basicity of the conditions : basic conditions favoured the formation of $[NEt_4]_2[Ce^{IV}Cl_5(OMe)]$, which can produce methoxy radical upon absorption of a photon, while acidic conditions advantaged $[NEt_4]_2[Ce^{IV}Cl_6]$ as a major species, which creates chlorine radicals under irradiation (see **Figure 31** and **Figure 32**).

Settling this debate was particularly important to the understanding of the photochemistry of cerium(IV) complexes, and should facilitate developments of such reactivity in the future. Meanwhile, the reactivity of cerium(III) complexes was also extensively studied by the team of Schelter as powerful reductant under irradiation.

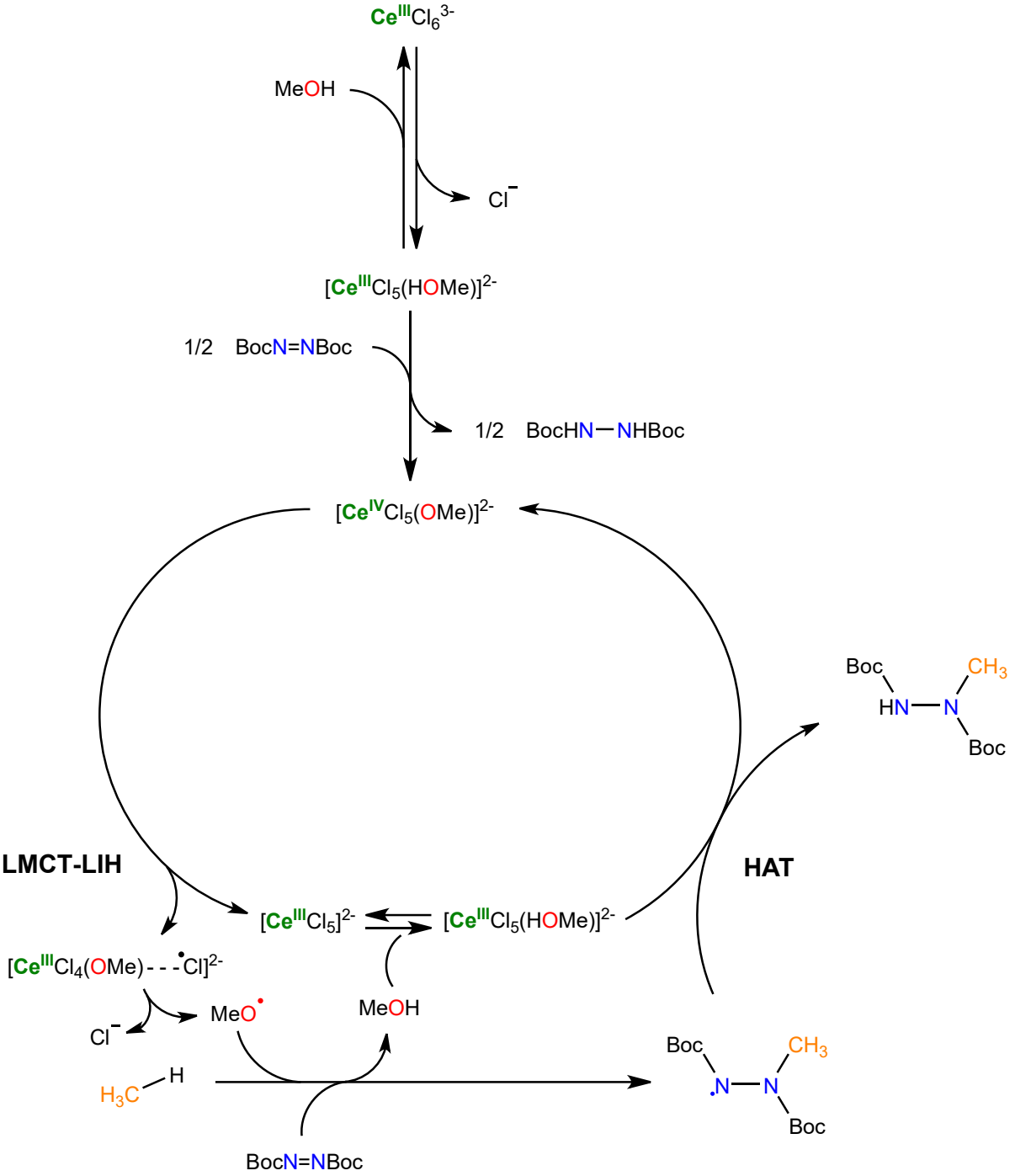

Figure 31. Mechanism proposed by Schelter *et al.* for the photochemical generation of alkoxy radical by light irradiation in basic conditions. Adapted from Schelter *et al.*[127]

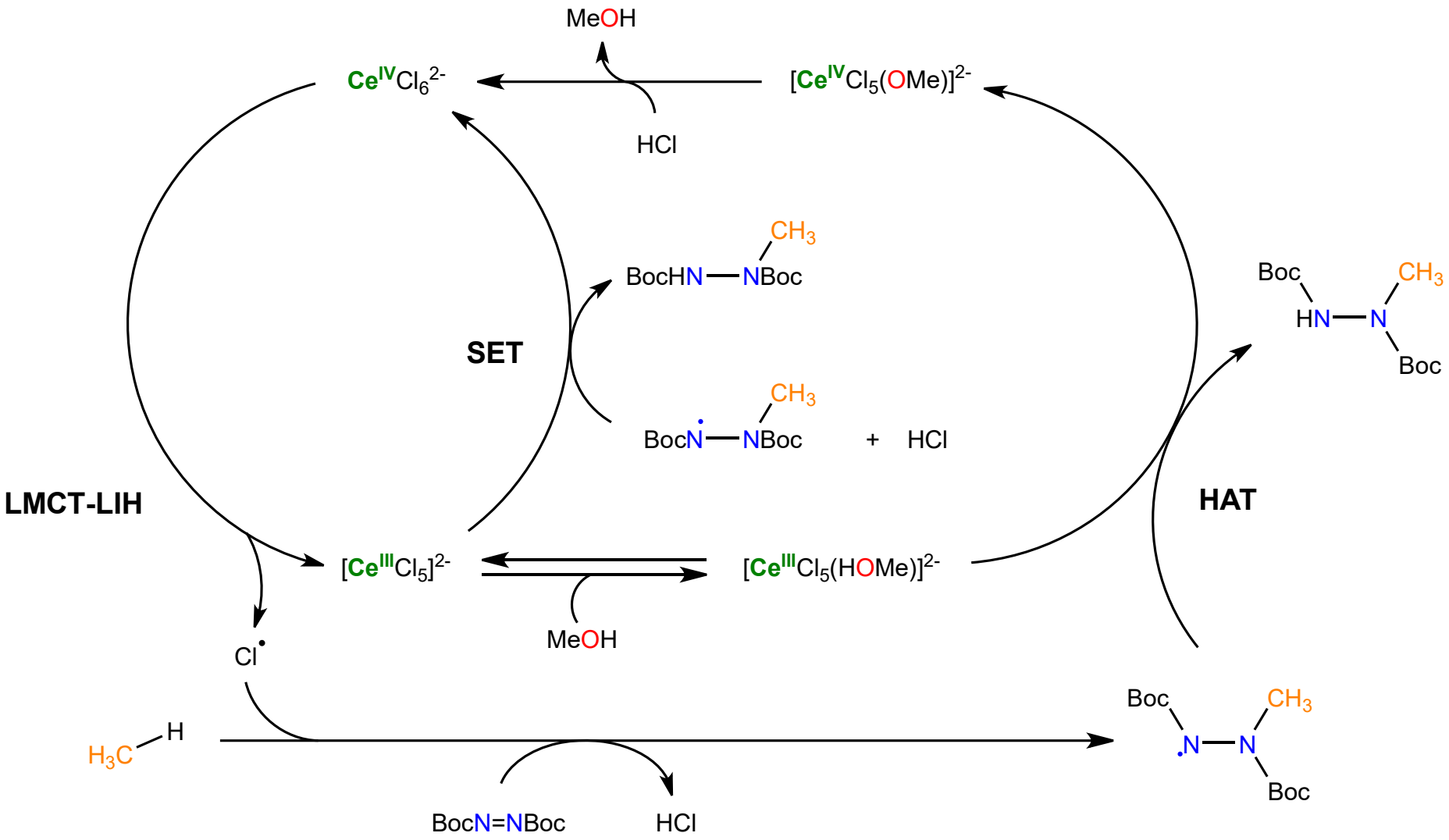

Figure 32. Mechanism proposed by Schelter *et al.* for the photochemical generation of chlorine radical by light irradiation in basic conditions. Adapted from Schelter *et al.*[127]

c) Single Electron Transfer reactivity with cerium(III) complexes

Metal complexes can often accept or donate a single electron more easily than close-shell organic substrates, as two-electron oxidations or reductions are needed to reach another close-shell electronic structure. Single Electron Transfer (SET) reactivity is particularly interesting for its ability to generate highly reactive radical intermediates.

Several families of organic photocatalysts were developed to catalyse oxidation or reductions of organic substrates, but they tend to degrade faster and display very short lifetimes than metal photocatalysts (see **Figure 33**).[149]

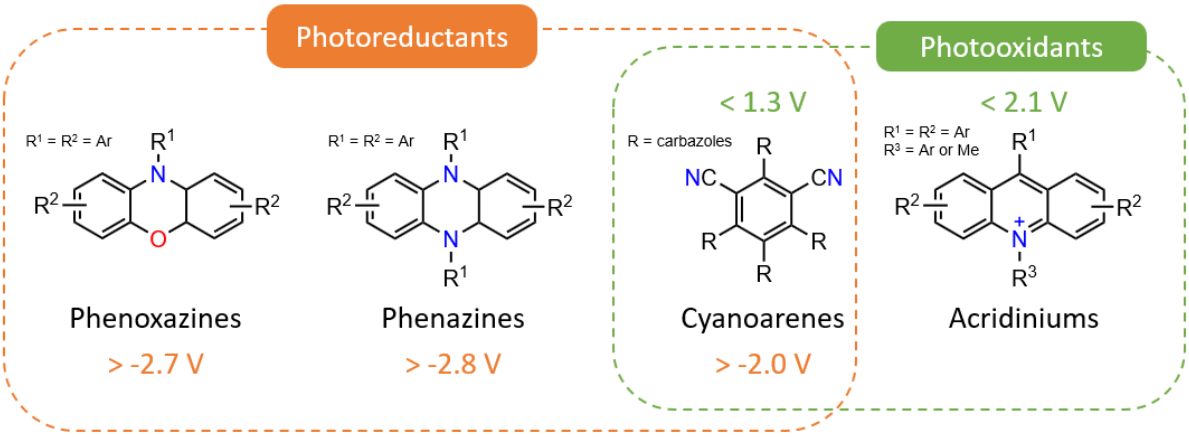

Figure 33. Families of organic photoreductants and photooxidants. Data obtained from Kwon and Lee,[150] and potential values are given relative to Fc/Fc^+

Metal complexes, especially ruthenium(II) and iridium(III) catalysts, have raised interest for the last five decades owing to their long-lived excited state and their absorption of visible light.[60,61,149,151] In $Ru(bpy)_3^{2+}$, the six valence electrons occupy a t_{2g} orbital and the π^* orbital is unoccupied (see **Figure 34**). Upon excitation at 375 nm and subsequent inter-system crossing, the complex reaches a triplet state with a valence electronic configuration $(t_{2g})^5(\pi^*)^1$. In this electronic configuration, accepting an electron is easier compared to the ground state, which makes the excited complex more oxidant in the excited state ($E_{1/2}(Ru^{I}/Ru^{II*}) = 0.46$ V *vs.* $Fe^{II}(C_5H_5)_2/Fe^{III}(C_5H_5)_2$ noted Fc/Fc^+ compared to $E_{1/2}(Ru^{I}/Ru^{II}) = -1.64$ V). Similarly, the unpaired electron in the π^* orbital can be more easily transferred to another substrate compared to the ground state ($E_{1/2}(Ru^{II*}/Ru^{III}) = -1.12$ V *vs.* Fc/Fc^+ compared to $E_{1/2}(Ru^{II}/Ru^{III}) = 1.29$ V).[152] These enhanced redox properties in the excited state are of interest regarding selective activation of challenging compounds, but using ruthenium and iridium complexes raise long-term issues considering the scarcity of the metals and low fatigue resistance of the complexes.

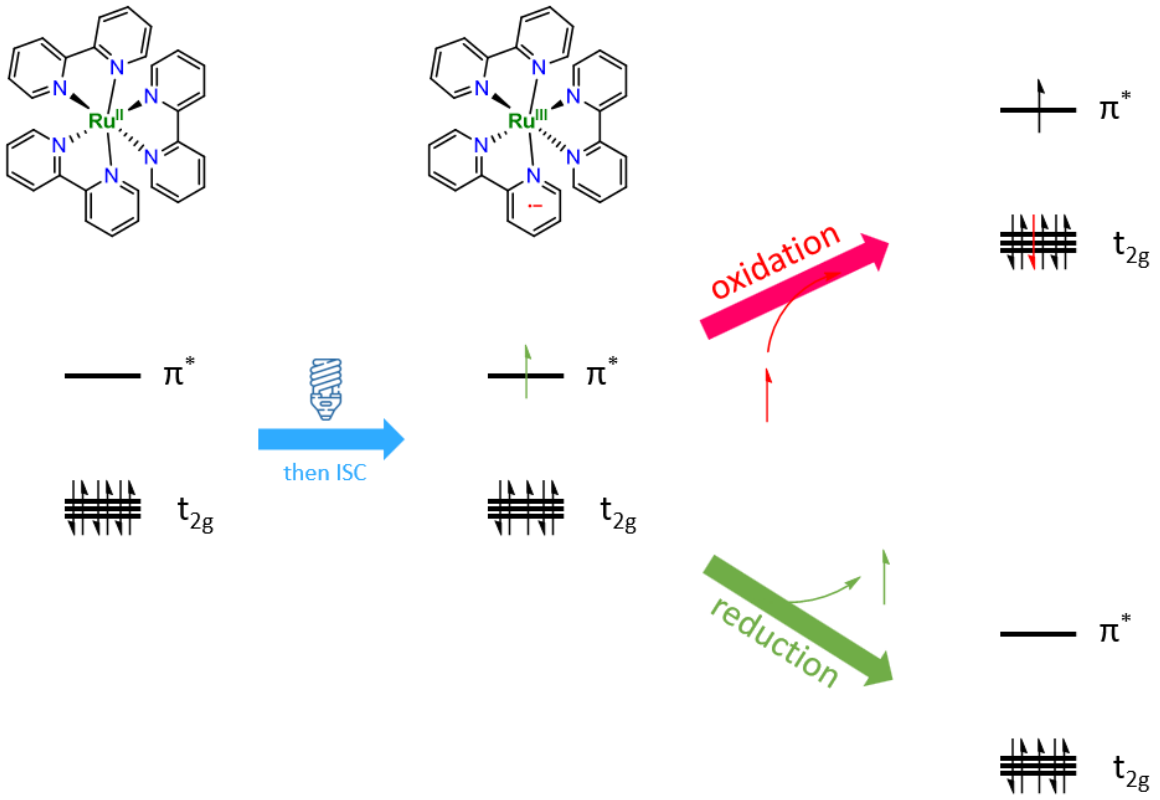

Figure 34. Simplified molecular diagram of Ru(2,2'-bipyridine)$_3^{2+}$ upon light excitation. Adapted from MacMillan *et al.*[152]

Few examples of iron[153,154] and copper[155] photoinduced SET have been reported. Lanthanides are known for their interesting redox behaviour, especially in reductive chemistry in +II oxidation state.[7,62,156–158] Examples of photoinduced reduction by samarium(II/III),[159,160] ytterbium(II),[159] dysprosium(II)[161] and *in situ* generated europium(II) halides[161–164] have been reported, but are often limited to highly polar solvents due to the poor solubility of lanthanide salts. First examples of cerium(III) photoinduced reductions originated in 1953, with the report from Heidt and McMillan of the photochemical reduction of water by cerium(III) ions.[165] While in-depth research was done on photochemical reduction of cerium(IV) ions in water,[166–172] few examples made use of the reducing ability of cerium(III) ions under irradiation.[173–177]

Schelter and co-workers started investigating again the photochemical and luminescence properties of cerium(III) complexes around 2015.[178] They especially took interest on the influence of the ligand on the photochemical and photophysical properties, which will be discussed later in Chapter I.

Synthesis of two families of cerium(III) complexes, guanidinate **G0** and hexamethyldisilazane (HMDS) **G3** (see **Figure 35**), and their subsequent photoreduction analysis showed that only the homoleptic HMDS complex **G0** was able to reduce benzyl chloride under UVA irradiation in C_6D_6.[179] According to the redox potentials of both complexes, this result would tend to indicate an inner-sphere electron transfer.

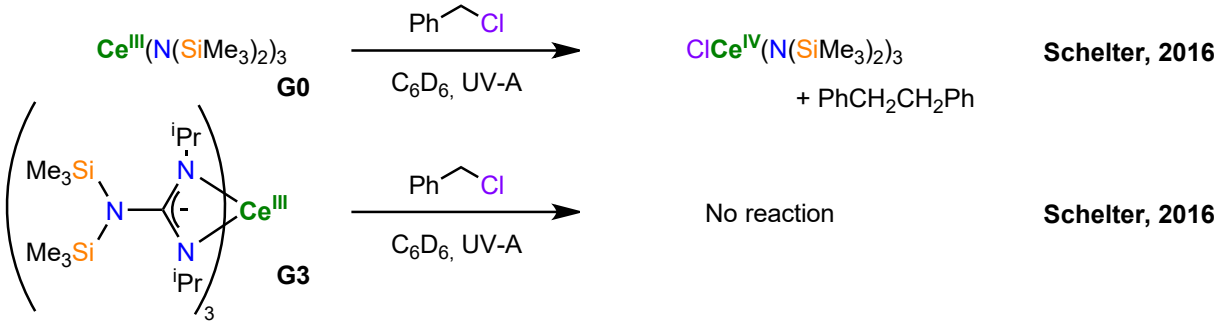

Figure 35. Hexamethyldisilazane and guanidinate complexes studied by Schelter and coworkers[179]

In order to make the reaction catalytic, the authors found that NaHMDS was an efficient reductant to reduce the cerium(IV) complex in Et_2O. Nevertheless, poor yields (22% in Et_2O for **G0**) were attributed to the accumulation of N-centred aminyl radicals ($R_2N^{\bullet}$), which was addressed by adding Ce^0 powder in the reaction medium (68% yield, see **Figure 36**). For complex **G3**, the presence of excess amounts of the ligand is needed for the catalysis.[179,180]

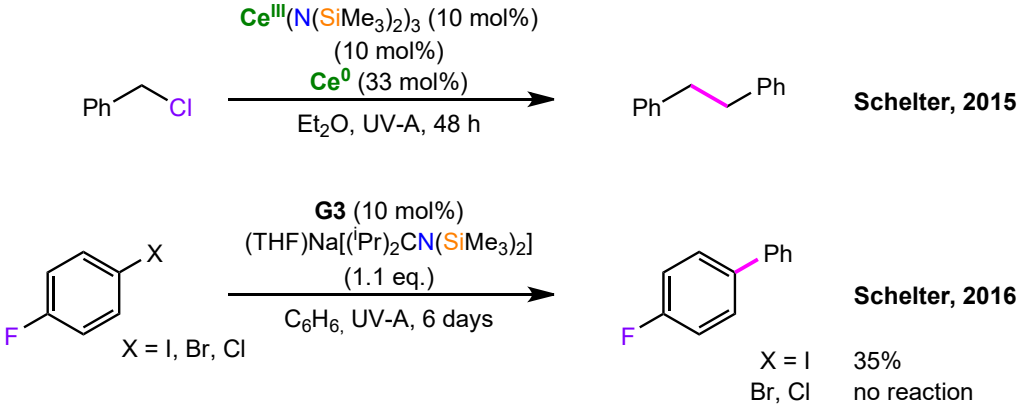

Figure 36. Activation of aryl halide using a cerium(III) guanidinate complex[178]

Parallel to the development of cerium(III) complexes bearing organic ligands, Schelter and co-workers investigated the properties and the reactivity of cerium(III) hexachlorocerate,[181] which was synthesized by LIH of cerium(IV) hexachlorocerate in the presence of excess chloride source (triethylammonium chloride) as reported by Costanzo *et al.*.[182]

To estimate the reduction power of the excited form of a complex, Rehm-Weller formalism can be used :[183]

$$E_{1/2}(D^*/D^{\cdot+}) = E_{1/2}(D/D^{\cdot+}) - E_{0\rightarrow0} - \omega$$

where $E_{1/2}(D^*/D^{\cdot+})$ is the halfwave redox potential of the species in the excited state, $E_{1/2}(D/D^{\cdot+})$ the halfwave redox potential of the species in the ground state, $E_{0\rightarrow0}$ the transition between zeroth vibrational electronic ground state and excited state (sometimes mistakenly approximated as the emission band energy) and ω is the work function. Details and demonstration of the above-mentioned equation are provided in Appendix.

For cerium(III) hexachlorocerate, the redox potential was estimated at -3.45 V *vs.* Fc/Fc^+, which is far lower than the estimated values for $Ce^{III}(HMDS)_3$ **G0** (-2.19 V) and **G3** (-2.92 V), [179,181] and also lower than commonly used alkali reductants as potassium and lithium (-3.10 V *vs.* Fc/Fc^+ for KC_8 in THF and -3.04 V for Na^0).[184] This indicated that highly challenging halide substrates such as 4-chloroanisole (E_{red} < -3.0 V) could be targeted.

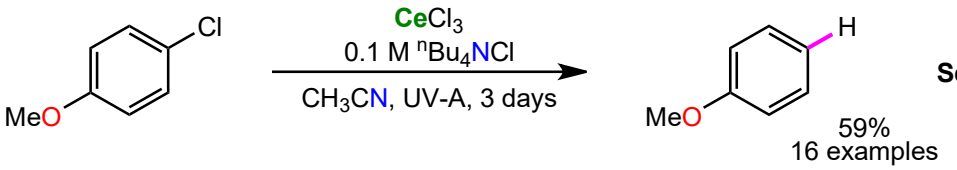

Figure 37. Stoichiometric dehalogenation of aryl chlorides using cerium(III) hexachlorocerate reported by Schelter *et al.* [181]

This complex was successfully used by Schelter *et al.* in the dehalogenation of a variety of aryl chlorides, including aforementioned 4-chloroanisole in good yields (59%, see **Figure 37**). Upon reduction of the halide derivative, cerium(III) hexachlorocerate is oxidized into cerium(IV) hexachlorocerate, which is also photoactive as highlighted by Costanzo *et al.*.[182] LMCT-LIH of Ce-Cl bond in $[Ce^{IV}Cl_6]^{2-}$ allowed for the production of a chlorine radical, which, in the presence of acetonitrile, abstracted one hydrogen to form HCl and $[Ce^{III}Cl_6]^{3-}$, therefore closing the catalytic cycle (see **Figure 38**).

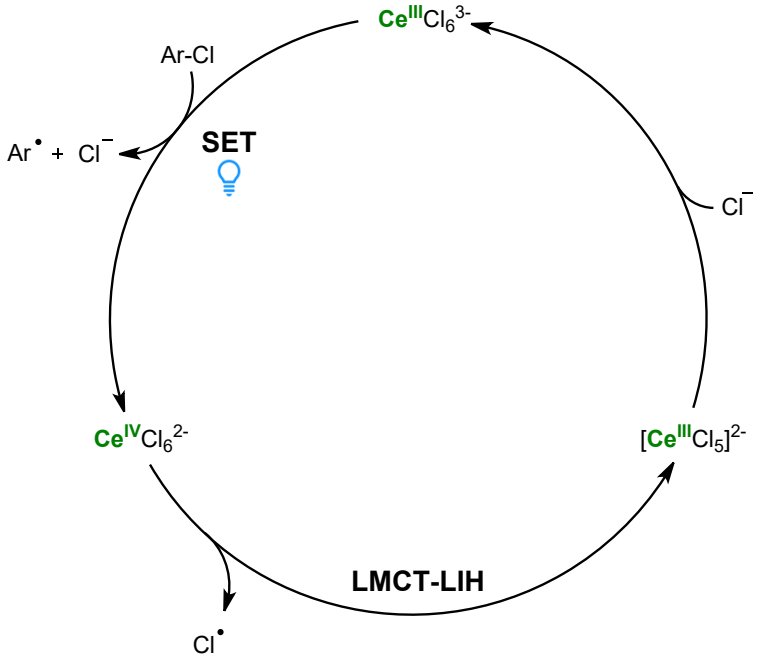

Figure 38. Mechanism of the catalytic dehalogenation of aryl chlorides by Schelter and coworkers

The authors later made use of the production of highly reactive aryl radicals to synthesize borylated products in good yields in the presence of diboron reagents, which corresponded to an overall Miyaura borylation.[185]

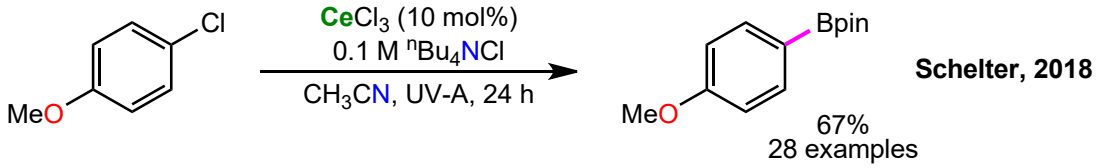

Figure 39. Photoinduced Miyaura borylation reported by Schelter *et al.*[185]

Nevertheless, the use of hexachlorocerate salts is limited to highly polar solvents such as acetonitrile, which hampers the range of its applications. In view of the interesting results reported for cerium hexachlorocerate, we sought to investigate cerium photochemistry and use a ligand that would enable better solubility in apolar media without sacrificing the reducing power of the complex under irradiation.

References

(1) Moeller, T. 44 - The Lanthanides. In *The Chemistry of the Lanthanides*; Moeller, T., Ed.; Pergamon Texts in Inorganic Chemistry; Pergamon, 1973; pp 1–101. https://doi.org/10.1016/B978-0-08-018878-2.50005-2.

(2) Cotton, S. The Lanthanides. In *Lanthanides and actinides*; Cotton, S., Ed.; Macmillan Education UK: London, 1991; pp 10–84. https://doi.org/10.1007/978-1-349-11904-2_2.

(3) 30 - The Lanthanide Elements (Z = 58–71). In *Chemistry of the Elements (Second Edition)*; Greenwood, N. N., Earnshaw, A., Eds.; Butterworth-Heinemann: Oxford, 1997; pp 1227–1249. https://doi.org/10.1016/B978-0-7506-3365-9.50036-5.

(4) McClain, K. R.; Kwon, H.; Chakarawet, K.; Nabi, R.; Kragskow, J. G. C.; Chilton, N. F.; Britt, R. D.; Long, J. R.; Harvey, B. G. A Trinuclear Gadolinium Cluster with a Three-Center One-Electron Bond and an S = 11 Ground State. *J. Am. Chem. Soc.* **2023**, *145* (16), 8996–9002. https://doi.org/10.1021/jacs.3c00182.

(5) Rinehart, J. D.; Long, J. R. Exploiting Single-Ion Anisotropy in the Design of f-Element Single-Molecule Magnets. *Chem. Sci.* **2011**, *2* (11), 2078–2085. https://doi.org/10.1039/C1SC00513H.

(6) Molander, G. A. Reductions with Samarium(II) Iodide. In *Organic Reactions*; John Wiley & Sons, Ltd, 2004; pp 211–367. https://doi.org/10.1002/0471264180.or046.03.

(7) Nief, F. Non-Classical Divalent Lanthanide Complexes. *Dalton Trans.* **2010**, *39* (29), 6589–6598. https://doi.org/10.1039/C001280G.

(8) Bethe, H. Termaufspaltung in Kristallen. *Ann. Phys.* **1929**, *395* (2), 133–208. https://doi.org/10.1002/andp.19293950202.

(9) Bünzli, J.-C. G.; Eliseeva, S. V. Basics of Lanthanide Photophysics. In *Lanthanide Luminescence: Photophysical, Analytical and Biological Aspects*; Hänninen, P., Härmä, H., Eds.; Springer: Berlin, Heidelberg, 2011; pp 1–45. https://doi.org/10.1007/4243_2010_3.

(10) Parker, D.; Suturina, E. A.; Kuprov, I.; Chilton, N. F. How the Ligand Field in Lanthanide Coordination Complexes Determines Magnetic Susceptibility Anisotropy, Paramagnetic NMR Shift, and Relaxation Behavior. *Acc. Chem. Res.* **2020**, *53* (8), 1520–1534. https://doi.org/10.1021/acs.accounts.0c00275.

(11) Gielen, D.; Lyons, M. *Critical Materials For The Energy Transition: Rare-Earth Elements*; International Renewable Energy Agency, 2022. https://www.irena.org/-/media/Files/IRENA/Agency/Technical-Papers/IRENA_Rare_Earth_Elements_2022.pdf.

(12) Zhan, W.; Guo, Y.; Gong, X.; Guo, Y.; Wang, Y.; Lu, G. Current Status and Perspectives of Rare Earth Catalytic Materials and Catalysis. *Chin. J. Catal.* **2014**, *35* (8), 1238–1250. https://doi.org/10.1016/S1872-2067(14)60189-3.

(13) Zhao, H.; Xia, J.; Yin, D.; Luo, M.; Yan, C.; Du, Y. Rare Earth Incorporated Electrode Materials for Advanced Energy Storage. *Coord. Chem. Rev.* **2019**, *390*, 32–49. https://doi.org/10.1016/j.ccr.2019.03.011.

(14) Locardi, B.; Guadagnino, E. Rare Earths in Glass Technology. *Mater. Chem. Phys.* **1992**, *31* (1), 45–49. https://doi.org/10.1016/0254-0584(92)90151-W.

(15) *Application of Rare Earth Metals in the Metallurgy Industry*. Stanford Materials. https://www.stanfordmaterials.com/blog/application-of-rare-earth-metals-in-the-metallurgy-industry.html (accessed 2025-03-24).

(16) Huber, G.; Duczynski, E. W.; Petermann, K. Laser Pumping of Ho, Tm, Er-Doped Garnet Lasers at Room-Temperature. In *Advanced Solid State Lasers (1987), paper MC1*; Optica Publishing Group, 1987; p MC1. https://doi.org/10.1364/ASSL.1987.MC1.

(17) Nakazawa, M.; Kimura, Y.; Suzuki, K. Efficient Er3+-doped Optical Fiber Amplifier Pumped by a 1.48 Mm InGaAsP Laser Diode. *Appl. Phys. Lett.* **1989**, *54* (4), 295–297. https://doi.org/10.1063/1.101448.

(18) Balestrieri, M. Transparent Conductive Oxides with Photon Converting Properties in View of Photovoltaic Applications : The Cases of Rare Earth-Doped Zinc Oxide and Cerium Oxide. phdthesis, Université de Strasbourg, 2014. https://theses.hal.science/tel-01132180 (accessed 2025-03-24).

(19) Harris, I. R.; Jewell, G. W. 19 - Rare-Earth Magnets: Properties, Processing and Applications. In *Functional Materials for Sustainable Energy Applications*; Kilner, J. A., Skinner, S. J., Irvine, S. J. C.,

Edwards, P. P., Eds.; Woodhead Publishing Series in Energy; Woodhead Publishing, 2012; pp 600–639. https://doi.org/10.1533/9780857096371.4.600.
(20) Tanabe, S. Rare-Earth-Doped Glasses for Fiber Amplifiers in Broadband Telecommunication. *Comptes Rendus Chim.* **2002**, *5* (12), 815–824. https://doi.org/10.1016/S1631-0748(02)01449-2.
(21) *CRC Handbook of Chemistry and Physics*, 97th ed.; Haynes, W. M., Lide, D. R., Bruno, T. J., Eds.; CRC Press, 2016. https://doi.org/10.1201/9781315380476.
(22) Haxel, G. B.; Hedrick, J. B.; Orris, G. J. *Rare-Earth's Abundancy*; United States Geological Surveys, 2005. https://pubs.usgs.gov/fs/2002/fs087-02/ (accessed 2023-04-03).
(23) Abundance of the Chemical Elements. *Wikipedia*; 2025.
(24) *United States Geological Survey*; United States Geological Surveys, 2025.
(25) Harkins, W. D. The Evolution of the Elements and the Stability of Complex Atoms. I. A New Periodic System Which Shows a Relation between the Abundance of the Elements and the Structure of the Nuclei of Atoms. *J. Am. Chem. Soc.* **1917**, *39* (5), 856–879. https://doi.org/10.1021/ja02250a002.
(26) Oddo, G. Die Molekularstruktur Der Radioaktiven Atome. *Z. Für Anorg. Chem.* **1914**, *87* (1), 253–268. https://doi.org/10.1002/zaac.19140870118.
(27) Cotton. Introduction to the Lanthanides. In *Lanthanide and Actinide Chemistry*; John Wiley & Sons, Ltd, 2006; pp 1–7. https://doi.org/10.1002/0470010088.ch1.
(28) Kumari, A.; Panda, R.; Jha, M. K.; Kumar, J. R.; Lee, J. Y. Process Development to Recover Rare Earth Metals from Monazite Mineral: A Review. *Miner. Eng.* **2015**, *79*, 102–115. https://doi.org/10.1016/j.mineng.2015.05.003.
(29) Cen, P.; Bian, X.; Liu, Z.; Gu, M.; Wu, W.; Li, B. Extraction of Rare Earths from Bastnaesite Concentrates: A Critical Review and Perspective for the Future. *Miner. Eng.* **2021**, *171*, 107081. https://doi.org/10.1016/j.mineng.2021.107081.
(30) *Rare Earth Elements: A Review of Production, Processing, Recycling, and Associated Environmental Issues*; EPA/600/R-12/572; Environmental Protection Agency, 2012. https://nepis.epa.gov/Exe/ZyPURL.cgi?Dockey=P100EUBC.txt.
(31) *Geopolitics of the Energy Transition: Critical Materials*. https://www.irena.org/Publications/2023/Jul/Geopolitics-of-the-Energy-Transition-Critical-Materials (accessed 2025-03-24).
(32) *What Are Critical Materials and Critical Minerals?*. Energy.gov. https://www.energy.gov/cmm/what-are-critical-materials-and-critical-minerals (accessed 2025-03-25).
(33) Federal Register. *Notice of Final Determination on 2023 DOE Critical Materials List*; 2023. https://www.federalregister.gov/documents/2023/08/04/2023-16611/notice-of-final-determination-on-2023-doe-critical-materials-list (accessed 2025-03-25).
(34) *Methodological Note to the Inventory of Export Restrictions on Industrial Raw Materials*; Organisation for Economic Co-operation and Development, 2022. https://www.oecd.org/content/dam/oecd/en/topics/policy-sub-issues/export-restrictions-on-critical-raw-materials/methodological-note-inventory-export-restrictions-industrial-raw-materials.pdf.
(35) OECD. *OECD Inventory of Export Restrictions on Industrial Raw Materials 2024: Monitoring the Use of Export Restrictions amid Market and Policy Tensions*; OECD, 2024. https://doi.org/10.1787/5e46bb20-en.
(36) World Trade Organization. *General Agreement on Tariffs and Taxes*; 1950. https://treaties.un.org/doc/Publication/UNTS/Volume%2055/volume-55-I-814-English.pdf.
(37) *Chemistry Is Everywhere*. American Chemical Society. https://www.acs.org/education/whatischemistry/everywhere.html (accessed 2025-02-19).
(38) *PR160L | Kessil LED*. Kessil. https://www.Kessil.com/products/science_PR160L.php (accessed 2025-02-24).
(39) Balzani, V.; Ceroni, P.; Juris, A. Photochemistry and Photophysics : Concepts, Research, Applications. 502.
(40) Klán, P.; Wirz, J. *Photochemistry of Organic Compounds: From Concepts to Practice*, 1st ed.; Wiley, 2009. https://doi.org/10.1002/9781444300017.

(41) Beck, U.; Löser, E. Chlorinated Benzenes and Other Nucleus-Chlorinated Aromatic Hydrocarbons. In *Ullmann's Encyclopedia of Industrial Chemistry*; John Wiley & Sons, Ltd, 2011. https://doi.org/10.1002/14356007.o06_o03.
(42) Atkins, P. W.; de Paula, J.; Keeler, J. J. *Atkins' Physical Chemistry*, Twelfth edition.; Oxford University Press: Oxford, 2023.
(43) Kasha, M. Characterization of Electronic Transitions in Complex Molecules. *Discuss. Faraday Soc.* **1950**, *9* (0), 14–19. https://doi.org/10.1039/DF9500900014.
(44) *What is a Jablonski Diagram (Perrin-Jablonski Diagram)?* https://trends.directindustry.fr/edinburgh-instruments/project-25178-193661.html (accessed 2025-03-25).
(45) Capaldo, L.; Ravelli, D. Hydrogen Atom Transfer (HAT): A Versatile Strategy for Substrate Activation in Photocatalyzed Organic Synthesis. *Eur. J. Org. Chem.* **2017**, *2017* (15), 2056–2071. https://doi.org/10.1002/ejoc.201601485.
(46) Fagnoni, M.; Dondi, D.; Ravelli, D.; Albini, A. Photocatalysis for the Formation of the C−C Bond. *Chem. Rev.* **2007**, *107* (6), 2725–2756. https://doi.org/10.1021/cr068352x.
(47) Scaiano, J. C.; Lissi, E. A.; Encina, M. V. Chemistry of the Biradicals Produced in the Norrish Type II Reaction. *Rev. Chem. Intermed.* **1978**, *2* (2), 139–196. https://doi.org/10.1007/BF03155998.
(48) Lykakis, I. N.; Evgenidou, E.; Orfanopoulos, M. Photo-catalysis and Polyoxo-anion Decatungstate in Organic Chemistry: A Manifold Concept for Green Chemistry. *Curr. Org. Chem.* **2012**, *16* (20), 2400–2414. https://doi.org/10.2174/138527212803520092.
(49) Tzirakis, M. D.; Lykakis, I. N.; Orfanopoulos, M. Decatungstate as an Efficient Photocatalyst in Organic Chemistry. *Chem. Soc. Rev.* **2009**, *38* (9), 2609–2621. https://doi.org/10.1039/B812100C.
(50) Waele, V. D.; Poizat, O.; Fagnoni, M.; Bagno, A.; Ravelli, D. Unraveling the Key Features of the Reactive State of Decatungstate Anion in Hydrogen Atom Transfer (HAT) Photocatalysis. *ACS Catal.* **2016**, *6* (10), 7174–7182. https://doi.org/10.1021/acscatal.6b01984.
(51) Abderrazak, Y.; Bhattacharyya, A.; Reiser, O. Visible-Light-Induced Homolysis of Earth-Abundant Metal-Substrate Complexes: A Complementary Activation Strategy in Photoredox Catalysis. *Angew. Chem. Int. Ed.* **2021**, *60* (39), 21100–21115. https://doi.org/10.1002/anie.202100270.
(52) Pei, D.; Luan, J. Development of Visible Light-Responsive Sensitized Photocatalysts. *Int. J. Photoenergy* **2012**, *2012*, 1–13. https://doi.org/10.1155/2012/262831.
(53) Quina, F. H.; Silva, G. T. M. The Photophysics of Photosensitization: A Brief Overview. *J. Photochem. Photobiol.* **2021**, *7*, 100042. https://doi.org/10.1016/j.jpap.2021.100042.
(54) Turksoy, A.; Yildiz, D.; Akkaya, E. U. Photosensitization and Controlled Photosensitization with BODIPY Dyes. *Coord. Chem. Rev.* **2019**, *379*, 47–64. https://doi.org/10.1016/j.ccr.2017.09.029.
(55) Sy, M.; Nonat, A.; Hildebrandt, N.; Charbonnière, L. J. Lanthanide-Based Luminescence Biolabelling. *Chem. Commun.* **2016**, *52* (29), 5080–5095. https://doi.org/10.1039/C6CC00922K.
(56) Hasegawa, Y.; Kitagawa, Y.; Nakanishi, T. Effective Photosensitized, Electrosensitized, and Mechanosensitized Luminescence of Lanthanide Complexes. *NPG Asia Mater.* **2018**, *10* (4), 52–70. https://doi.org/10.1038/s41427-018-0012-y.
(57) Harvey, P.; Nonat, A.; Platas-Iglesias, C.; Natrajan, L. S.; Charbonnière, L. J. Sensing Uranyl(VI) Ions by Coordination and Energy Transfer to a Luminescent Europium(III) Complex. *Angew. Chem.* **2018**, *130* (31), 10069–10072. https://doi.org/10.1002/ange.201805316.
(58) Wenger, O. S. Proton-Coupled Electron Transfer Originating from Excited States of Luminescent Transition-Metal Complexes. *Chem. – Eur. J.* **2011**, *17* (42), 11692–11702. https://doi.org/10.1002/chem.201102011.
(59) Bonin, J.; Robert, M. Photoinduced Proton-Coupled Electron Transfers in Biorelevant Phenolic Systems. *Photochem. Photobiol.* **2011**, *87* (6), 1190–1203. https://doi.org/10.1111/j.1751-1097.2011.00996.x.
(60) Tucker, J. W.; Stephenson, C. R. J. Shining Light on Photoredox Catalysis: Theory and Synthetic Applications. *J. Org. Chem.* **2012**, *77* (4), 1617–1622. https://doi.org/10.1021/jo202538x.
(61) Narayanam, J. M. R.; Stephenson, C. R. J. Visible Light Photoredox Catalysis: Applications in Organic Synthesis. *Chem Soc Rev* **2011**, *40* (1), 102–113. https://doi.org/10.1039/B913880N.

(62) Prieto, A.; Jaroschik, F. Recent Applications of Rare Earth Complexes in Photoredox Catalysis for OrganicSynthesis. *Curr. Org. Chem.* **2022**, *26* (1), 6–41. https://doi.org/10.2174/1385272825666211126123928.
(63) Li, L.; Wang, Z.; Zhao, L.; Liu, H.; Li, Y. Lanthanide-Based Photocatalysts for CO2 Conversion: Are They a Better Choice for Realizing Sustainability? *Coord. Chem. Rev.* **2025**, *522*, 216223. https://doi.org/10.1016/j.ccr.2024.216223.
(64) Tomar, M.; Bhimpuria, R.; Kocsi, D.; Thapper, A.; Borbas, K. E. Photocatalytic Generation of Divalent Lanthanide Reducing Agents. *J. Am. Chem. Soc.* **2023**, *145* (41), 22555–22562. https://doi.org/10.1021/jacs.3c07508.
(65) Qiao, Y.; Schelter, E. J. Lanthanide Photocatalysis. *Acc. Chem. Res.* **2018**, *51* (11), 2926–2936. https://doi.org/10.1021/acs.accounts.8b00336.
(66) Luo, Y.-R. *Handbook of Bond Dissociation Energies in Organic Compounds*, 0 ed.; CRC Press, 2002. https://doi.org/10.1201/9781420039863.
(67) Kancherla, R.; Muralirajan, K.; Sagadevan, A.; Rueping, M. Visible Light-Induced Excited-State Transition-Metal Catalysis. *Trends Chem.* **2019**, *1* (5), 510–523. https://doi.org/10.1016/j.trechm.2019.03.012.
(68) Cheung, K. P. S.; Sarkar, S.; Gevorgyan, V. Visible Light-Induced Transition Metal Catalysis. *Chem. Rev.* **2022**, *122* (2), 1543–1625. https://doi.org/10.1021/acs.chemrev.1c00403.
(69) Davia, K.; King, D.; Hong, Y.; Swavey, S. A Porphyrin–Ruthenium Photosensitizer as a Potential Photodynamic Therapy Agent. *Inorg. Chem. Commun.* **2008**, *11* (5), 584–586. https://doi.org/10.1016/j.inoche.2008.02.023.
(70) Yin, J.-F.; Velayudham, M.; Bhattacharya, D.; Lin, H.-C.; Lu, K.-L. Structure Optimization of Ruthenium Photosensitizers for Efficient Dye-Sensitized Solar Cells – A Goal toward a "Bright" Future. *Coord. Chem. Rev.* **2012**, *256* (23), 3008–3035. https://doi.org/10.1016/j.ccr.2012.06.022.
(71) *CRC Handbook of Chemistry and Physics*, 97th ed.; Haynes, W. M., Ed.; CRC Press: Boca Raton, 2016. https://doi.org/10.1201/9781315380476.
(72) Iavicoli, I.; Fontana, L.; Marinaccio, A.; Bergamaschi, A.; Calabrese, E. J. Iridium Alters Immune Balance between t Helper 1 and t Helper 2 Responses. *Hum. Exp. Toxicol.* **2010**, *29* (3), 213–219. https://doi.org/10.1177/0960327109360215.
(73) Fast, O. G.; Gentry, B.; Strouth, L.; Niece, M. B.; Beckford, F. A.; Shell, S. M. Polynuclear Ruthenium Organometallic Compounds Induce DNA Damage in Human Cells Identified by the Nucleotide Excision Repair Factor XPC. *Biosci. Rep.* **2019**, *39* (7), BSR20190378. https://doi.org/10.1042/BSR20190378.
(74) Vedeanu, N.; Voica, C.; Magdas, D. A.; Kiss, B.; Stefan, M.-G.; Simedrea, R.; Georgiu, C.; Berce, C.; Vostinaru, O.; Boros, R.; Fizesan, I.; Rusu, M. E.; Grozav, A.; Loghin, F.; Popa, D.-S. Subacute Co-Exposure to Low Doses of Ruthenium(III) Changes the Distribution, Excretion and Biological Effects of Silver Ions in Rats. *Environ. Chem.* **2019**, *17* (2), 163–172. https://doi.org/10.1071/EN19249.
(75) Iavicoli, I.; Cufino, V.; Corbi, M.; Goracci, M.; Caredda, E.; Cittadini, A.; Bergamaschi, A.; Sgambato, A. Rhodium and Iridium Salts Inhibit Proliferation and Induce DNA Damage in Rat Fibroblasts *in Vitro*. *Toxicol. In Vitro* **2012**, *26* (6), 963–969. https://doi.org/10.1016/j.tiv.2012.03.014.
(76) Cieśla, P.; Kocot, P.; Mytych, P.; Stasicka, Z. Homogeneous Photocatalysis by Transition Metal Complexes in the Environment. *J. Mol. Catal. Chem.* **2004**, *224* (1), 17–33. https://doi.org/10.1016/j.molcata.2004.08.043.
(77) Reichle, A.; Reiser, O. Light-Induced Homolysis of Copper(II)-Complexes – a Perspective for Photocatalysis. *Chem. Sci.* **2023**, *14* (17), 4449–4462. https://doi.org/10.1039/D3SC00388D.
(78) Kochi, J. K. Photolyses of Metal Compounds: Cupric Chloride in Organic Media. *J. Am. Chem. Soc.* **1962**, *84* (11), 2121–2127. https://doi.org/10.1021/ja00870a025.
(79) Treacy, S. M.; Rovis, T. Copper Catalyzed C(Sp3)–H Bond Alkylation via Photoinduced Ligand-to-Metal Charge Transfer. *J. Am. Chem. Soc.* **2021**, *143* (7), 2729–2735. https://doi.org/10.1021/jacs.1c00687.
(80) Santos, M. S.; Corrêa, A. G.; Paixão, M. W.; König, B. C(Sp3)−C(Sp3) Cross-Coupling of Alkyl Bromides and Ethers Mediated by Metal and Visible Light Photoredox Catalysis. *Adv. Synth. Catal.* **2020**, *362* (12), 2367–2372. https://doi.org/10.1002/adsc.202000167.

(81) Shields, B. J.; Doyle, A. G. Direct C(Sp3)–H Cross Coupling Enabled by Catalytic Generation of Chlorine Radicals. *J. Am. Chem. Soc.* **2016**, *138* (39), 12719–12722. https://doi.org/10.1021/jacs.6b08397.

(82) Chambers, D. R.; Juneau, A.; Ludwig, C. T.; Frenette, M.; Martin, D. B. C. C–O Bond Cleavage of Alcohols via Visible Light Activation of Cobalt Alkoxycarbonyls. *Organometallics* **2019**, *38* (24), 4570–4577. https://doi.org/10.1021/acs.organomet.9b00552.

(83) Jones, A. R. The Photochemistry and Photobiology of Vitamin B12. *Photochem. Photobiol. Sci.* **2017**, *16* (6), 820–834. https://doi.org/10.1039/C7PP00054E.

(84) Giedyk, M.; Goliszewska, K.; Proinsias, K. ó; Gryko, D. Cobalt(I)-Catalysed CH-Alkylation of Terminal Olefins, and Beyond. *Chem. Commun.* **2016**, *52* (7), 1389–1392. https://doi.org/10.1039/C5CC07363D.

(85) Ociepa, M.; Wierzba, A. J.; Turkowska, J.; Gryko, D. Polarity-Reversal Strategy for the Functionalization of Electrophilic Strained Molecules via Light-Driven Cobalt Catalysis. *J. Am. Chem. Soc.* **2020**, *142* (11), 5355–5361. https://doi.org/10.1021/jacs.0c00245.

(86) Ociepa, M.; Baka, O.; Narodowiec, J.; Gryko, D. Light-Driven Vitamin B12-Catalysed Generation of Acyl Radicals from 2-S-Pyridyl Thioesters. *Adv. Synth. Catal.* **2017**, *359* (20), 3560–3565. https://doi.org/10.1002/adsc.201700913.

(87) Potrząsaj, A.; Ociepa, M.; Baka, O.; Spólnik, G.; Gryko, D. Vitamin B12 Enables Consecutive Generation of Acyl and Alkyl Radicals from One Reagent. *Eur. J. Org. Chem.* **2020**, *2020* (10), 1567–1571. https://doi.org/10.1002/ejoc.201901137.

(88) Chinchole, A.; Henriquez, M. A.; Cortes-Arriagada, D.; Cabrera, A. R.; Reiser, O. Iron(III)-Light-Induced Homolysis: A Dual Photocatalytic Approach for the Hydroacylation of Alkenes Using Acyl Radicals via Direct HAT from Aldehydes. *ACS Catal.* **2022**, *12* (21), 13549–13554. https://doi.org/10.1021/acscatal.2c03315.

(89) Sugimori, A.; Yamada, T. Visible Light- and Radiation-Induced Alkylation of Pyridine Ring with Alkanoic Acid. Effective Alkylation in the Presence of Iron(III) Sulfate. *Bull. Chem. Soc. Jpn.* **1986**, *59* (12), 3911–3915. https://doi.org/10.1246/bcsj.59.3911.

(90) Sugimori, A.; Yamada, T. Visible Light- And Gamma Ray-Induced Alkylation In Pyridine Ring. Effective Alkylation With Visible Light In The Presence Of Iron(Iii) Sulfate. *Chem. Lett.* **1986**, *15* (3), 409–412. https://doi.org/10.1246/cl.1986.409.

(91) Xia, S.; Hu, K.; Lei, C.; Jin, J. Intramolecular Aromatic C–H Acyloxylation Enabled by Iron Photocatalysis. *Org. Lett.* **2020**, *22* (4), 1385–1389. https://doi.org/10.1021/acs.orglett.0c00002.

(92) Ishida, A.; Toki, S.; Takamuku, S. Photochemical Reactions Of A-Methylstyrene Induced By Eu(III)/Eu(II) Photoredox System In Methanol. *Chem. Lett.* **1985**, *14* (7), 893–896. https://doi.org/10.1246/cl.1985.893.

(93) Brandys, M.; Stein, G. Photochemical Evolution of Hydrogen from Aqueous Solutions of Europium Ions at .Lambda. >310 Nm. The Role of Europium(II). *J. Phys. Chem.* **1978**, *82* (8), 852–854. https://doi.org/10.1021/j100497a002.

(94) Ishida, A.; Toki, S.; Takamuku, S. Hydroxymethylation of 1,3-Dimethyluracil and Its Derivatives Induced by a Photoredox System of EuIII/EuII in MeOH. *J. Chem. Soc. Chem. Commun.* **1985**, No. 21, 1481–1483. https://doi.org/10.1039/C39850001481.

(95) Ishida, A.; Takamuku, S. One-Electron Reduction of Eu3+ Ions Induced by the Irradiation of γ-Ray or UV-Light. The Fluorescence Properties of Eu2+ Ions in an Ethanol Matrix. *Chem. Lett.* **1988**, *17* (9), 1497–1500. https://doi.org/10.1246/cl.1988.1497.

(96) An, Q.; Chang, L.; Pan, H.; Zuo, Z. Ligand-to-Metal Charge Transfer (LMCT) Catalysis: Harnessing Simple Cerium Catalysts for Selective Functionalization of Inert C–H and C–C Bonds. *Acc. Chem. Res.* **2024**, *57* (19), 2915–2927. https://doi.org/10.1021/acs.accounts.4c00510.

(97) Tsurugi, H.; Mashima, K. Renaissance of Homogeneous Cerium Catalysts with Unique Ce(IV/III) Couple: Redox-Mediated Organic Transformations Involving Homolysis of Ce(IV)–Ligand Covalent Bonds. *J. Am. Chem. Soc.* **2021**, *143* (21), 7879–7890. https://doi.org/10.1021/jacs.1c02889.

(98) Morris, A. O.; Barriault, L. Redox-Neutral Multicatalytic Cerium Photoredox-Enabled Cleavage of O–H Bearing Substrates. *Chem. – Eur. J.* **2024**, *30* (26), e202400642. https://doi.org/10.1002/chem.202400642.

(99) Martin, T. W.; Burk, J. M.; Henshall, A. Ligand Sensitization. I. The Photo- and Oxidation-Reduction Activated Decomposition of Glacial Acetic Acid with Ceric Ammonium Nitrate1. *J. Am. Chem. Soc.* **1966**, *88* (6), 1097–1104. https://doi.org/10.1021/ja00958a002.

(100) Sheldon, R. A.; Kochi, J. K. Photochemical and Thermal Reduction of Cerium(IV) Carboxylates. Formation and Oxidation of Alkyl Radicals. *J. Am. Chem. Soc.* **1968**, *90* (24), 6688–6698. https://doi.org/10.1021/ja01026a022.

(101) Hay, N. E.; Kochi, J. K. Cerium(IV) Acetate. *J. Inorg. Nucl. Chem.* **1968**, *30* (3), 884–886. https://doi.org/10.1016/0022-1902(68)80451-8.

(102) Trahanovsky, W. S.; Cramer, J.; Brixius, D. W. Oxidation of Organic Compounds with Cerium(IV). XVIII. Oxidative Decarboxylation of Substituted Phenylacetic Acids. *J. Am. Chem. Soc.* **1974**, *96* (4), 1077–1081. https://doi.org/10.1021/ja00811a022.

(103) Sala, L. F.; Cirelli, A. F.; Lederkremer, R. M. de. Oxidative Decarboxylation of Aldonolactones by Cerium(IV) Sulphate in Aqueous Sulphuric Acid; Synthesis of D-Arabinose. *J. Chem. Soc. Perkin Trans. 2* **1977**, No. 5, 685–688. https://doi.org/10.1039/P29770000685.

(104) Hanna, S. B.; Sarac, S. A. Metal-Ion Oxidative Decarboxylations. 10. Substituent Effects in the Cerium(IV)-Benzilic Acids Reaction. *J. Org. Chem.* **1977**, *42* (12), 2069–2073. https://doi.org/10.1021/jo00432a006.

(105) Perry, D. L.; Tsao, L.; Brittain, H. G. X-Ray Photoelectron and Infrared Spectroscopic Studies of the Decarboxylation/Oxidation of Cerium(III) Carbonate Octahydrate. *J. Mater. Sci. Lett.* **1984**, *3* (11), 1017–1019. https://doi.org/10.1007/BF00720345.

(106) Yatham, V. R.; Bellotti, P.; König, B. Decarboxylative Hydrazination of Unactivated Carboxylic Acids by Cerium Photocatalysis. *Chem. Commun.* **2019**, *55* (24), 3489–3492. https://doi.org/10.1039/C9CC00492K.

(107) Lai, X.-L.; Shu, X.-M.; Song, J.; Xu, H.-C. Electrophotocatalytic Decarboxylative C−H Functionalization of Heteroarenes. *Angew. Chem. Int. Ed.* **2020**, *59* (26), 10626–10632. https://doi.org/10.1002/anie.202002900.

(108) Shirase, S.; Tamaki, S.; Shinohara, K.; Hirosawa, K.; Tsurugi, H.; Satoh, T.; Mashima, K. Cerium(IV) Carboxylate Photocatalyst for Catalytic Radical Formation from Carboxylic Acids: Decarboxylative Oxygenation of Aliphatic Carboxylic Acids and Lactonization of Aromatic Carboxylic Acids. *J. Am. Chem. Soc.* **2020**, *142* (12), 5668–5675. https://doi.org/10.1021/jacs.9b12918.

(109) Yan, X.; Li, X.; Wang, Y.; Dai, Y.; Yan, X.; Zhao, D.; Xu, X. Iminyl-Radical-Mediated C–C Cleavage/Amination and Alkene Iminoamination Enabled by Visible-Light-Induced Cerium Catalysis. *ACS Sustain. Chem. Eng.* **2021**, *9* (1), 101–105. https://doi.org/10.1021/acssuschemeng.0c07850.

(110) Pham, H.-L.; Jiang, X.; Yan, Q.; So, Y.-M.; Chan, W.; Sung, H. H. Y.; Williams, I. D.; Leung, W.-H. Redox and Photochemical Reactivity of Cerium(IV) Carbonate and Carboxylate Complexes Supported by a Tripodal Oxygen Ligand. *Inorg. Chem.* **2025**, *64* (3), 1433–1442. https://doi.org/10.1021/acs.inorgchem.4c04602.

(111) Wadedkar, K.; Aswale, S.; Yatham, V. R. Cerium Photocatalyzed Dehydrogenative Lactonization of 2-Arylbenzoic Acids. *Org. Biomol. Chem.* **2020**, *18*, 983–987. https://doi.org/10.1039/C9OB02676B.

(112) Patnaik, D.; Panda, S. Preparation of Ceric Acetate in the Anhydrous State and Its Photo and Thermal Decompositions. *Curr. Sci. (India)* **1956**, *25* (9), 287–288.

(113) Patnaik, D.; Sahoo, B. The Preparation of Anhydrous Ceric Oxyadetates. *Curr. Sci. (India)* **1957**, *26* (11), 355−356.

(114) Shirase, S.; Shinohara, K.; Tsurugi, H.; Mashima, K. Oxidation of Alcohols to Carbonyl Compounds Catalyzed by Oxo-Bridged Dinuclear Cerium Complexes with Pentadentate Schiff-Base Ligands under a Dioxygen Atmosphere. *ACS Catal.* **2018**, *8* (8), 6939–6947. https://doi.org/10.1021/acscatal.8b01718.

(115) Paul, M.; Shirase, S.; Morimoto, Y.; Mathey, L.; Murugesapandian, B.; Tanaka, S.; Itoh, S.; Tsurugi, H.; Mashima, K. Cerium-Complex-Catalyzed Oxidation of Arylmethanols under Atmospheric Pressure of Dioxygen and Its Mechanism through a Side-On μ-Peroxo Dicerium(IV) Complex. *Chem. – Eur. J.* **2016**, *22* (12), 4008–4014. https://doi.org/10.1002/chem.201503846.

(116) Singh, S.; Dagar, N.; Roy, S. R. Photoinduced Ligand to Metal Charge Transfer Enabling Cerium Mediated Decarboxylative Alkylation of Quinoxalin-2(1H)-Ones. *Chem. Commun.* **2022**, *58* (23), 3831–3834. https://doi.org/10.1039/D2CC00840H.
(117) Zuo, Z.; Chen, Y.; Du, J. Selective C-C Bond Scission of Ketones via Visible-Light-Mediated Cerium Catalysis. *Chem* **2020**, *6* (1), 266–279. https://doi.org/10.1016/j.chempr.2019.11.009.
(118) Du, J.; Yang, X.; Wang, X.; An, Q.; He, X.; Pan, H.; Zuo, Z. Photocatalytic Aerobic Oxidative Ring Expansion of Cyclic Ketones to Macrolactones by Cerium and Cyanoanthracene Catalysis. *Angew. Chem. Int. Ed.* **2021**, *60* (10), 5370–5376. https://doi.org/10.1002/anie.202012720.
(119) Wang, Y.; He, J.; Zhang, Y. CeCl3-Promoted Simultaneous Photocatalytic Cleavage and Amination of Cα–Cβ Bond in Lignin Model Compounds and Native Lignin. *CCS Chem.* **2020**, *2* (3), 107–117. https://doi.org/10.31635/ccschem.020.201900076.
(120) Schwarz, J.; König, B. Visible-Light Mediated C–C Bond Cleavage of 1,2-Diols to Carbonyls by Cerium-Photocatalysis. *Chem. Commun.* **2019**, *55* (4), 486–488. https://doi.org/10.1039/C8CC09208G.
(121) Zhang, K.; Chang, L.; An, Q.; Wang, X.; Zuo, Z. Dehydroxymethylation of Alcohols Enabled by Cerium Photocatalysis. *J. Am. Chem. Soc.* **2019**, *141* (26), 10556–10564. https://doi.org/10.1021/jacs.9b05932.
(122) Zuo, Z.; Hu, A.; Chen, Y.; Guo, J.-J.; Yu, N.; An, Q. Cerium-Catalyzed Formal Cycloaddition of Cycloalkanols with Alkenes through Dual Photoexcitation. *J. Am. Chem. Soc.* **2018**, *140* (42), 13580. https://doi.org/10.1021/jacs.8b08781.
(123) Hu, A.; Guo, J.-J.; Pan, H.; Tang, H.; Gao, Z.; Zuo, Z. δ-Selective Functionalization of Alkanols Enabled by Visible-Light-Induced Ligand-to-Metal Charge Transfer. *J. Am. Chem. Soc.* **2018**, *140* (5), 1612–1616. https://doi.org/10.1021/jacs.7b13131.
(124) Hu, A.; Guo, J.-J.; Pan, H.; Zuo, Z. Selective Functionalization of Methane, Ethane, and Higher Alkanes by Cerium Photocatalysis. *Science* **2018**, *361* (6403), 668–672. https://doi.org/10.1126/science.aat9750.
(125) Schelter, E. J.; Yang, Q.; Wang, Y.-H.; Qiao, Y.; Gau, M.; Carroll, P. J.; Walsh, P. J. Photocatalytic C–H Activation and the Subtle Role of Chlorine Radical Complexation in Reactivity. *Science* **2021**, *372* (6544), 847–852. https://doi.org/10.1126/science.abd8408.
(126) An, Q.; Xing, Y.-Y.; Pu, R.; Jia, M.; Chen, Y.; Hu, A.; Zhang, S.-Q.; Yu, N.; Du, J.; Zhang, Y.; Chen, J.; Liu, W.; Hong, X.; Zuo, Z. Identification of Alkoxy Radicals as Hydrogen Atom Transfer Agents in Ce-Catalyzed C–H Functionalization. *J. Am. Chem. Soc.* **2023**, *145* (1), 359–376. https://doi.org/10.1021/jacs.2c10126.
(127) Yang, Q.; Song, E.; Wu, Y.; Li, C.; Gau, M. R.; Anna, J. M.; Schelter, E. J.; Walsh, P. J. Mechanistic Investigation of the Ce(III) Chloride Photoredox Catalysis System: Understanding the Role of Alcohols as Additives. *J. Am. Chem. Soc.* **2025**, *147* (2), 2061–2076. https://doi.org/10.1021/jacs.4c15627.
(128) Leffler, J. E. Cleavages and Rearrangements Involving Oxygen Radicals and Cations. *Chem. Rev.* **1949**, *45* (3), 385–417. https://doi.org/10.1021/cr60142a001.
(129) Barton, D. H. R.; Beaton, J. M.; Geller, L. E.; Pechet, M. M. A New Photochemical Reaction. *J. Am. Chem. Soc.* **1960**, *82* (10), 2640–2641. https://doi.org/10.1021/ja01495a061.
(130) Walling, Cheves.; Padwa, Albert. Positive Halogen Compounds. VI. Effects of Structure and Medium on the β-Scission of Alkoxy Radicals. *J. Am. Chem. Soc.* **1963**, *85* (11), 1593–1597. https://doi.org/10.1021/ja00894a012.
(131) Kim, S.; Lee, T. A.; Song, Y. Facile Generation of Alkoxy Radicals from N-Alkoxyphthalimides. *Synlett* **1998**, *1998* (05), 471–472. https://doi.org/10.1055/s-1998-1711.
(132) Beckwith, A. L. J.; Hay, B. P. Generation of Alkoxy Radicals from N-Alkoxypyridinethiones. *J. Am. Chem. Soc.* **1988**, *110* (13), 4415–4416. https://doi.org/10.1021/ja00221a051.
(133) Pasto, D. J.; Cottard, F. Demonstration of the Synthetic Utility of the Generation of Alkoxy Radicals by the Photo-Induced Homolytic Dissociation of Alkyl 4-Nitrobenzenesulfenates. *Tetrahedron Lett.* **1994**, *35* (25), 4303–4306. https://doi.org/10.1016/S0040-4039(00)73339-9.
(134) Chang, L.; An, Q.; Duan, L.; Feng, K.; Zuo, Z. Alkoxy Radicals See the Light: New Paradigms of Photochemical Synthesis. *Chem. Rev.* **2022**, *122* (2), 2429–2486. https://doi.org/10.1021/acs.chemrev.1c00256.

(135) Patehebieke, Y.; Charaf, R.; Bryce-Rogers, H. P.; Ye, K.; Ahlquist, M.; Hammarström, L.; Wallentin, C.-J. β-Scission of Secondary Alcohols via Photosensitization: Synthetic Utilization and Mechanistic Insights. *ACS Catal.* **2024**, *14* (1), 585–593. https://doi.org/10.1021/acscatal.3c05150.
(136) Albini, A. Norrish' Type I and II Reactions and Their Role in the Building of Photochemical Science. *Photochem. Photobiol. Sci.* **2021**, *20* (1), 161–181. https://doi.org/10.1007/s43630-020-00003-9.
(137) Zuo, Z.; Guo, J.-J.; Hu, A.; Chen, Y.; Sun, J.; Tang, H. Photocatalytic C−C Bond Cleavage and Amination of Cycloalkanols by Cerium(III) Chloride Complex. *Angew. Chem. Int. Ed.* **2016**, *55* (49), 15319–15322. https://doi.org/10.1002/anie.201609035.
(138) Du, J.; Yang, X.; Wang, X.; An, Q.; He, X.; Pan, H.; Zuo, Z. Photocatalytic Aerobic Oxidative Ring Expansion of Cyclic Ketones to Macrolactones by Cerium and Cyanoanthracene Catalysis. *Angew. Chem. Int. Ed.* **2021**, *60* (10), 5370–5376. https://doi.org/10.1002/anie.202012720.
(139) Chen, Y.; Wang, X.; He, X.; An, Q.; Zuo, Z. Photocatalytic Dehydroxymethylative Arylation by Synergistic Cerium and Nickel Catalysis. *J. Am. Chem. Soc.* **2021**, *143* (13), 4896–4902. https://doi.org/10.1021/jacs.1c00618.
(140) Cernak, T.; Dykstra, K. D.; Tyagarajan, S.; Vachal, P.; Krska, S. W. The Medicinal Chemist's Toolbox for Late Stage Functionalization of Drug-like Molecules. *Chem. Soc. Rev.* **2016**, *45* (3), 546–576. https://doi.org/10.1039/C5CS00628G.
(141) Shang, W.; Sun, H.; Chen, W.; Liu, J. Diversification of Pharmaceutical Molecules *via* Late-Stage C(Sp2)–H Functionalization. *Green Synth. Catal.* **2023**, *4* (2), 104–123. https://doi.org/10.1016/j.gresc.2022.12.007.
(142) Douglas, J. J.; Sevrin, M. J.; Stephenson, C. R. J. Visible Light Photocatalysis: Applications and New Disconnections in the Synthesis of Pharmaceutical Agents. *Org. Process Res. Dev.* **2016**, *20* (7), 1134–1147. https://doi.org/10.1021/acs.oprd.6b00125.
(143) Capaldo, L.; Ravelli, D.; Fagnoni, M. Direct Photocatalyzed Hydrogen Atom Transfer (HAT) for Aliphatic C–H Bonds Elaboration. *Chem. Rev.* **2022**, *122* (2), 1875–1924. https://doi.org/10.1021/acs.chemrev.1c00263.
(144) Crabtree, R. H. Aspects of Methane Chemistry. *Chem. Rev.* **1995**, *95* (4), 987–1007. https://doi.org/10.1021/cr00036a005.
(145) Lannung, A.; Gjaldbæk, J. Chr.; Rundqvist, S.; Varde, E.; Westin, G. The Solubility of Methane in Hydrocarbons, Alcohols, Water, and Other Solvents. *Acta Chem. Scand.* **1960**, *14*, 1124–1128. https://doi.org/10.3891/acta.chem.scand.14-1124.
(146) An, Q.; Wang, Z.; Chen, Y.; Wang, X.; Zhang, K.; Pan, H.; Liu, W.; Zuo, Z. Cerium-Catalyzed C–H Functionalizations of Alkanes Utilizing Alcohols as Hydrogen Atom Transfer Agents. *J. Am. Chem. Soc.* **2020**, *142* (13), 6216–6226. https://doi.org/10.1021/jacs.0c00212.
(147) Russell, G. A. Solvent Effects In The Reactions Of Free Radicals And Atoms. *J. Am. Chem. Soc.* **1957**, *79* (11), 2977–2978. https://doi.org/10.1021/ja01568a085.
(148) Russell, G. A. Solvent Effects in the Reactions of Free Radicals and Atoms. III. Effects of Solvents in the Competitive Photochlorination of Hydrocarbons and Their Derivatives1. *J. Am. Chem. Soc.* **1958**, *80* (18), 4997–5001. https://doi.org/10.1021/ja01551a057.
(149) Romero, N. A.; Nicewicz, D. A. Organic Photoredox Catalysis. *Chem. Rev.* **2016**, *116* (17), 10075–10166. https://doi.org/10.1021/acs.chemrev.6b00057.
(150) Lee, Y.; Kwon, M. S. Emerging Organic Photoredox Catalysts for Organic Transformations. *Eur. J. Org. Chem.* **2020**, *2020* (38), 6028–6043. https://doi.org/10.1002/ejoc.202000720.
(151) Bitterwolf, T. E. Organometallic Photochemistry at the End of Its First Century. *J. Organomet. Chem.* **2004**, *689* (24), 3939–3952. https://doi.org/10.1016/j.jorganchem.2004.06.023.
(152) Prier, C. K.; Rankic, D. A.; MacMillan, D. W. C. Visible Light Photoredox Catalysis with Transition Metal Complexes: Applications in Organic Synthesis. *Chem. Rev.* **2013**, *113* (7), 5322–5363. https://doi.org/10.1021/cr300503r.
(153) de Groot, L. H. M.; Ilic, A.; Schwarz, J.; Wärnmark, K. Iron Photoredox Catalysis–Past, Present, and Future. *J. Am. Chem. Soc.* **2023**, *145* (17), 9369–9388. https://doi.org/10.1021/jacs.3c01000.
(154) Wu, C.; Bian, Q.; Ding, T.; Tang, M.; Zhang, W.; Xu, Y.; Liu, B.; Xu, H.; Li, H.-B.; Fu, H. Photoinduced Iron-Catalyzed Ipso-Nitration of Aryl Halides via Single-Electron Transfer. *ACS Catal.* **2021**, *11* (15), 9561–9568. https://doi.org/10.1021/acscatal.1c02272.

(155) Reiser, O. Shining Light on Copper: Unique Opportunities for Visible-Light-Catalyzed Atom Transfer Radical Addition Reactions and Related Processes. *Acc. Chem. Res.* **2016**, *49* (9), 1990–1996. https://doi.org/10.1021/acs.accounts.6b00296.
(156) Simler, T.; McCabe, K. N.; Maron, L.; Nocton, G. CO Reductive Oligomerization by a Divalent Thulium Complex and CO2-Induced Functionalization. *Chem. Sci.* **2022**, *13* (25), 7449–7461. https://doi.org/10.1039/D2SC01798A.
(157) Aretz, C. Selective Carbon-Carbon Bond Formation Promoted by Divalent Samarium Reagents. *Univ. Denver* **2018**, 1403.
(158) Masson, G.; Py, S.; Vallée, Y. Samarium Diiodide-Induced Reductive Cross-Coupling of Nitrones with Aldehydes and Ketones. *Angew. Chem. Int. Ed.* **2002**, *41* (10), 1772–1775. https://doi.org/10.1002/1521-3773(20020517)41:10<1772::AID-ANIE1772>3.0.CO;2-Q.
(159) Kondo, T.; Akazome, M.; Watanabe, Y. Lanthanide(II) Iodide Catalysed Photochemical Allylation of Aldehydes with Allylic Halides. *J. Chem. Soc. Chem. Commun.* **1991**, No. 11, 757–758. https://doi.org/10.1039/C39910000757.
(160) Ogawa, A.; Ohya, S.; Doi, M.; Sumino, Y.; Sonoda, N.; Hirao, T. Photoinduced Reduction of Group 16 Heteroatom Compounds with the Aid of Samarium Diiodide. *Tetrahedron Lett.* **1998**, *39* (35), 6341–6342. https://doi.org/10.1016/S0040-4039(98)01347-1.
(161) Basal, L. A.; Kajjam, A. B.; Bailey, M. D.; Allen, M. J. Systematic Tuning of the Optical Properties of Discrete Complexes of EuII in Solution Using Counterions and Solvents. *Inorg. Chem.* **2020**, *59* (14), 9476–9480. https://doi.org/10.1021/acs.inorgchem.0c01516.
(162) Jenks, T. C.; Bailey, M. D.; Hovey, J. L.; Fernando, S.; Basnayake, G.; Cross, M. E.; Li, W.; Allen, M. J. First Use of a Divalent Lanthanide for Visible-Light-Promoted Photoredox Catalysis. *Chem. Sci.* **2018**, *9* (5), 1273–1278. https://doi.org/10.1039/C7SC02479G.
(163) Kuda-Wedagedara, A. N. W.; Wang, C.; Martin, P. D.; Allen, M. J. Aqueous EuII-Containing Complex with Bright Yellow Luminescence. *J. Am. Chem. Soc.* **2015**, *137* (15), 4960–4963. https://doi.org/10.1021/jacs.5b02506.
(164) Jenks, T. C.; Bailey, M. D.; Corbin, B. A.; Kuda-Wedagedara, A. N. W.; Martin, P. D.; Schlegel, H. B.; Rabuffetti, F. A.; Allen, M. J. Photophysical Characterization of a Highly Luminescent Divalent-Europium-Containing Azacryptate. *Chem. Commun.* **2018**, *54* (36), 4545–4548. https://doi.org/10.1039/C8CC01737A.
(165) Heidt, L. J.; McMillan, A. F. Conversion of Sunlight into Chemical Energy Available in Storage for Man's Use. *Science* **1953**, *117* (3030), 75–76. https://doi.org/10.1126/science.117.3030.75.
(166) Weiss, J.; Porret, D. Photochemical Reduction of Ceric Ions by Water. *Nature* **1937**, *139* (3528), 1019–1020. https://doi.org/10.1038/1391019a0.
(167) Rabinowitch, E. Electron Transfer Spectra and Their Photochemical Effects. *Rev. Mod. Phys.* **1942**, *14* (2–3), 112–131. https://doi.org/10.1103/RevModPhys.14.112.
(168) Heidt, L. J.; Smith, M. E. Quantum Yields of the Photochemical Reduction of Ceric Ions by Water and Evidence for the Dimerization of Ceric Ions. *ACS Publ.* **2002**. https://doi.org/10.1021/ja01187a050.
(169) Sworski, T. J. A Mechanism for the Photo-Oxidation of Water by Ceric Ion. *J. Am. Chem. Soc.* **1955**, *77* (4), 1074–1075. https://doi.org/10.1021/ja01609a106.
(170) Sworski, T. J. Photoreduction of Ceric Ion in Sulfuric Acid Solutions. Effect of Thallous Ion2a. *J. Am. Chem. Soc.* **1957**, *79* (14), 3655–3657. https://doi.org/10.1021/ja01571a011.
(171) Martin, T. W.; Henshall, Alan.; Gross, R. C. Spectroscopic and Chemical Evidence for the NO3 Free Radical in Solution at Room Temperature. *J. Am. Chem. Soc.* **1963**, *85* (1), 113–114. https://doi.org/10.1021/ja00884a027.
(172) Martin, T. W.; Rummel, R. E.; Gross, R. C. Electron Exchange Kinetics of the NO3 Free Radical in Solution. *J. Am. Chem. Soc.* **1964**, *86* (13), 2595–2600. https://doi.org/10.1021/ja01067a016.
(173) Rosenfeld-Grunwald, T.; Brandeis, M.; Rabani, J. Photochemical Electron Transfer from Cerous Ions to the Lowest Excited State of Uranyl Ions in Aqueous Media, Studied by Laser Photolysis. *J. Phys. Chem.* **1982**, *86* (24), 4745–4750. https://doi.org/10.1021/j100221a020.
(174) Edgecombe, F. H. C.; Norrish, R. G. W. Vinyl Polymerization Photochemically Initiated by Cerous Ions. *Nature* **1963**, *197* (4864), 282–283. https://doi.org/10.1038/197282a0.

(175) Hussain, F.; Norrish, R. G. W. The Photo-Initiation of the Polymerization of Vinyl Compounds by Means of Cerous Ions. *Proc. R. Soc. Lond. Ser. Math. Phys. Sci.* **1963**, *275* (1361), 161–174.
(176) Donohue, T. Photochemical Separation of Cerium from Rare Earth Mixtures in Aqueous Solution. *Chem. Phys. Lett.* **1979**, *61* (3), 601–604. https://doi.org/10.1016/0009-2614(79)87181-X.
(177) Matthews, R. W.; Sworski, T. J. Photooxidation and Fluorescence of Cerium(III) in Aqueous Sulfuric Acid Solutions. *J. Phys. Chem.* **1975**, *79* (7), 681–686. https://doi.org/10.1021/j100574a003.
(178) Yin, H.; Schelter, E. J.; Carroll, P. J.; Anna, J. M. Luminescent Ce(III) Complexes as Stoichiometric and Catalytic Photoreductants for Halogen Atom Abstraction Reactions. *J. Am. Chem. Soc.* **2015**, *137* (29), 9234–9237. https://doi.org/10.1021/jacs.5b05411.
(179) Yin, H.; Schelter, E. J.; Carroll, P. J.; Manor, B. C.; Anna, J. M. Cerium Photosensitizers: Structure–Function Relationships and Applications in Photocatalytic Aryl Coupling Reactions. *J. Am. Chem. Soc.* **2016**, *138* (18), 5984–5993. https://doi.org/10.1021/jacs.6b02248.
(180) Qiao, Y.; Cheisson, T.; Manor, B. C.; Carroll, P. J.; Schelter, E. J. A Strategy to Improve the Performance of Cerium(III) Photocatalysts. *Chem. Commun.* **2019**, *55* (28), 4067–4070. https://doi.org/10.1039/C9CC00282K.
(181) Yin, H.; Jin, Y.; Hertzog, J. E.; Mullane, K. C.; Carroll, P. J.; Manor, B. C.; Anna, J. M.; Schelter, E. J. The Hexachlorocerate(III) Anion: A Potent, Benchtop Stable, and Readily Available Ultraviolet A Photosensitizer for Aryl Chlorides. *J. Am. Chem. Soc.* **2016**, *138* (50), 16266–16273. https://doi.org/10.1021/jacs.6b05712.
(182) Costanzo, L. L.; Pistarà, S.; Condorelli, G. Photoreduction of Cerium(IV) Hexachloride in Acetonitrile. *J. Photochem.* **1983**, *21* (1), 45–51. https://doi.org/10.1016/0047-2670(83)80006-9.
(183) Rehm, D.; Weller, A. Kinetics of Fluorescence Quenching by Electron and H-Atom Transfer. *Isr. J. Chem.* **1970**, *8* (2), 259–271. https://doi.org/10.1002/ijch.197000029.
(184) Rice, N. T.; Su, J.; Gompa, T. P.; Russo, D. R.; Telser, J.; Palatinus, L.; Bacsa, J.; Yang, P.; Batista, E. R.; La Pierre, H. S. Homoleptic Imidophosphorane Stabilization of Tetravalent Cerium. *Inorg. Chem.* **2019**, *58* (8), 5289–5304. https://doi.org/10.1021/acs.inorgchem.9b00368.
(185) Qiao, Y.; Schelter, E. J.; Yang, Q. Photoinduced Miyaura Borylation by a Rare-Earth-Metal Photoreductant: The Hexachlorocerate(III) Anion. *Angew. Chem. Int. Ed.* **2018**, *57* (34), 10999–11003. https://doi.org/10.1002/anie.201804022.

Education is the kindling of a flame, not the filling of a vessel.

Socrates, 5th century B.C.

Chapter I
Synthesis of $Ce^{III}(TREN^{TIPS})$, structural and spectroscopic features

I. Literature review of photoactive cerium complexes 56
a) Electronic structure of cerium(III) luminescent complexes 56
b) Cerium complexes bearing tripodal ligand 60
II. Synthesis of starting complex 63
a) Synthesis of the complex 63
b) Spectroscopies of $Ce^{III}TREN^{TIPS}$ 68
1) Investigating the ground state 68
2) Electronic transitions in 1 69
3) Luminescence studies and lifetime measurements 69
c) Investigation of the redox behaviour 71
1) Electrochemical measurements 71
2) Oxidations to cerium(IV)-halides 72
3) UV-visible spectroscopy for complexes 2-F, 2-Br and 2-Cl 76
4) Ligand exchange using trimethylsilyl reagents 76
5) Oxidations using organic oxidants 77
References 80

I. Literature review of photoactive cerium complexes

a) Electronic structure of cerium(III) luminescent complexes

Cerium displays a different behaviour from other lanthanide ions. While all lanthanides are stable at +III oxidation state,[1] and sometimes +II,[2–6] cerium also exhibits a particular stability in +IV oxidation state.[7] This peculiarity is illustrated by the remarkable resistance of ceria CeO_2 to reducing conditions, and allows for an easier separation of cerium from other rare-earth elements by a simple oxidation step.[1]

The ^2F ground state of cerium(III) ion is split into three Kramers doublets $^2F_{5/2}$, $^2F_{3/2}$ and $^2F_{1/2}$ as it possesses an odd number of electrons.[8] The first electronic excited state is a low-lying ^2D state, which makes possible the excitation of one 4f electron to a 5d orbital in visible or near-UV region. Contrary to f → f transitions for other lanthanides, this transition is electron-dipole allowed ($\Delta S = 0$ and $\Delta J < 7$),[9] and displays broader and more intense absorption bands ($\varepsilon \approx 10^2$ $M^{-1}.cm^{-1}$) compared to f-f transitions, but shorter fluorescence lifetimes (≈ 10-100 ns).

The involvement of the 5d orbital in this electronic transition should in principle enable a modulation in both the absorption properties of cerium(III) and its emission properties. Schelter and co-workers carried out several highly detailed studies about the influence of the ligand on the spectroscopic features (Stokes shift, luminescence lifetime, quantum yield, absorption and emission maxima), but also on the redox behaviour of the corresponding cerium complex.[10–12] These studies were focused on two families : guanidinate (**G0-G3** in **Figure 40**) and aryloxide (**ArO1-ArO3**) cerium(III) complexes.

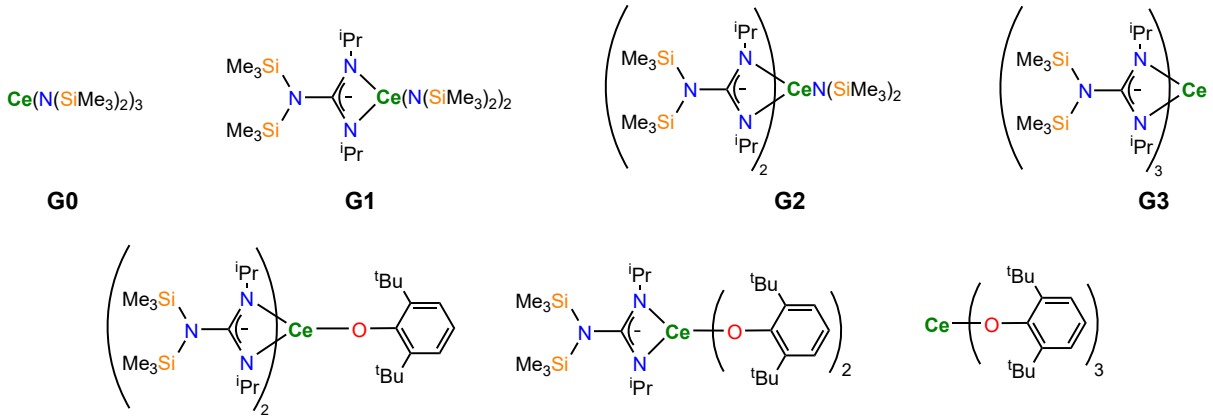

Figure 40. First series of cerium complexes studied by Schelter *et al.*.[11]

Electronic absorption spectra of all complexes in **Figure 40** showed a nearly identical absorption band *ca.* 420 nm (± 20 nm), which indicated a negligible effect of the ligand in the excitation process. Time-Dependent Density Functional Theory (TD-DFT) calculations and subsequent projection as Natural Transition Orbitals (NTO) identified the transition as 4f → 5dz² (see **Figure 41**). In these complexes, 5dz² orbital does not participate in bonding with the ligands, which makes the transition energy independent from the ligand field.[13]

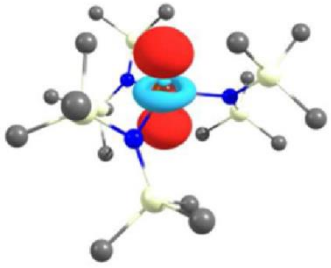

Figure 41. Acceptor orbital for **G0** complex corresponding to the transition close to 420 nm. Reproduced from Schelter *et al.*[6]

Nevertheless, increase in the number of bulkier guanidinate ligands in **G0-G3** and **ArO1-ArO3** led to a significant decrease in the Stokes shift between absorption and emission bands (see **Figure 42**). It is important reporting Stokes shift values in energy unit and not in nm, given that the corresponding transition energy depends on the spectral domain (40 nm difference between 400 and 440 nm corresponds to 2273 cm^{-1} while a Stokes shift from 700 nm to 740 nm corresponds to 772 cm^{-1}).

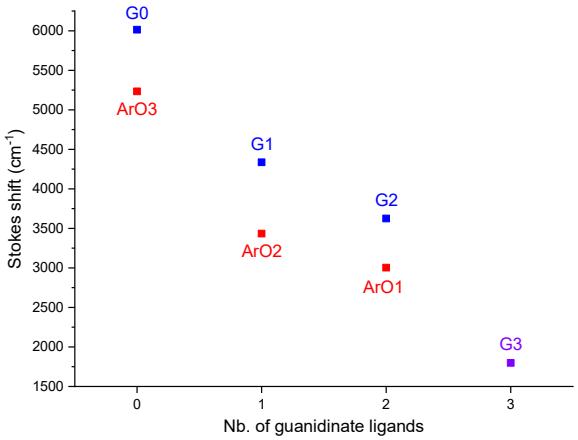

Figure 42. Evolution of Stokes shift as a function of number of guanidinate ligands in complexes **G0-G3** and **ArO0-ArO3**

The difference in Stokes shift indicates here a difference in relaxation process from ^{2}D excited state, which is likely to proceed through vibration of C-H bonds close to the cerium. The authors postulated that replacement of a hexamethyldisilazane (HMDS, $N(SiMe_3)_2$) by a rigid guanidinate removed C-H agostic interactions and prevented energy loss through vibration of Ce-N and N-Si bonds, which led to a decrease in dissipated energy. TD-DFT calculations on complexes **G0-G3** highlighted smaller structural changes between the ground state and excited state as more guanidinate are bound to cerium centre, indicating an overall more rigid scaffold than in **G0**.[10]

This Stokes shift evolution is consistent with the increase in quantum yield and luminescence lifetime with the amount of guanidinate bound to cerium, which indicates that non-radiative decay pathways are less efficient as the number of guanidinate increases (see **Figure 43**). Calculation of the observed radiative and non-radiative decay constants (respectively k_r^{obs} and k_{nr}^{obs}) from the luminescence data confirmed the decrease in the efficiency of non-radiative decay goes along with the amount of guanidinates.

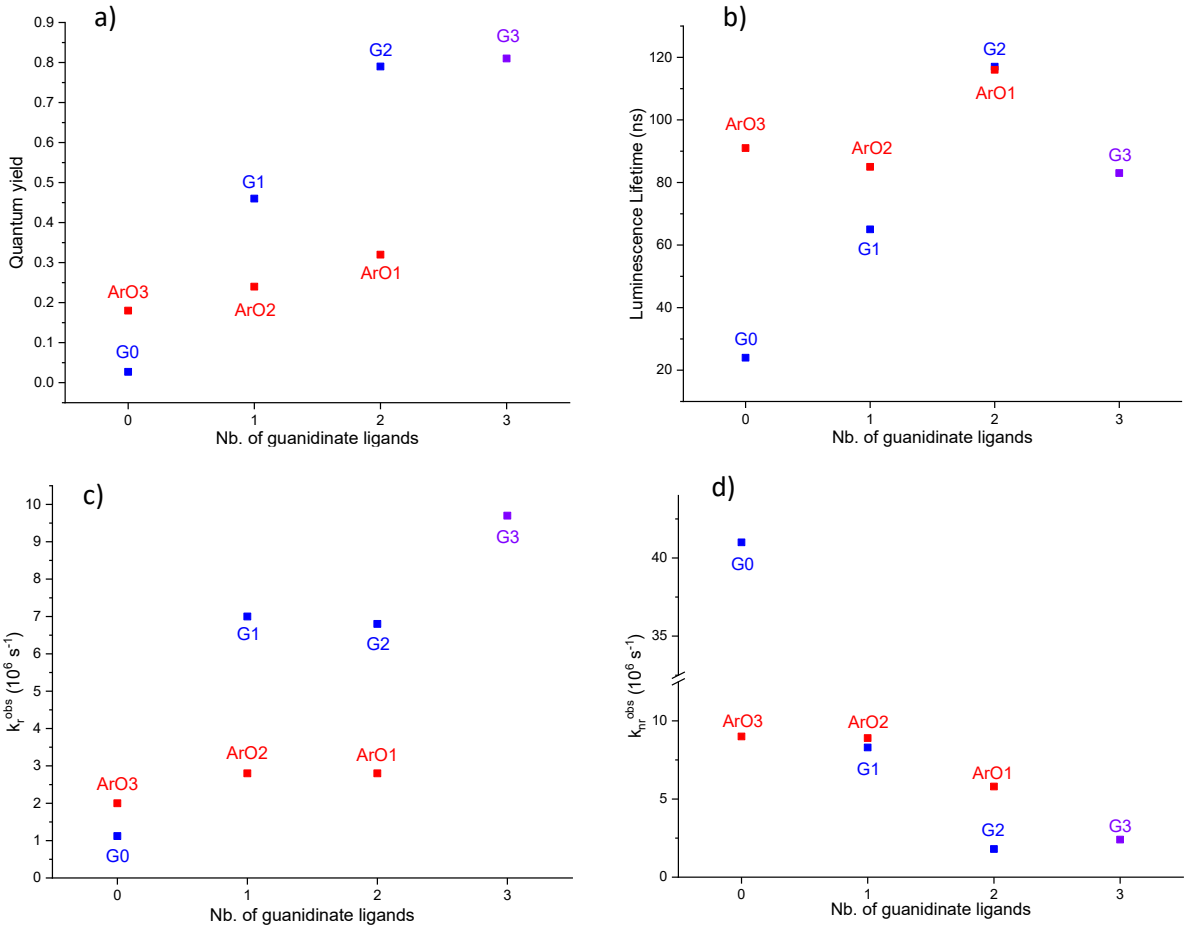

Figure 43. Evolution of a) Quantum yield ; b) Luminescence lifetime ; c) Observed radiative decay constant k_r^{obs} ; d) Observed non-radiative decay constant k_{nr}^{obs} as a function of number of guanidinate ligands in complexes **G0-G3** and **ArO1- ArO3** synthesized by Schelter *et al.*. Adapted from Schelter *et al.*.[12]

To further probe the fine influence of the parameters of the coordination sphere on the spectroscopic properties of cerium(III) complexes, Schelter *et al.* synthesized another series of cerium(III) guanidinate complexes bearing different substituents on the non-coordinating nitrogen (see **Figure 44**).[10]

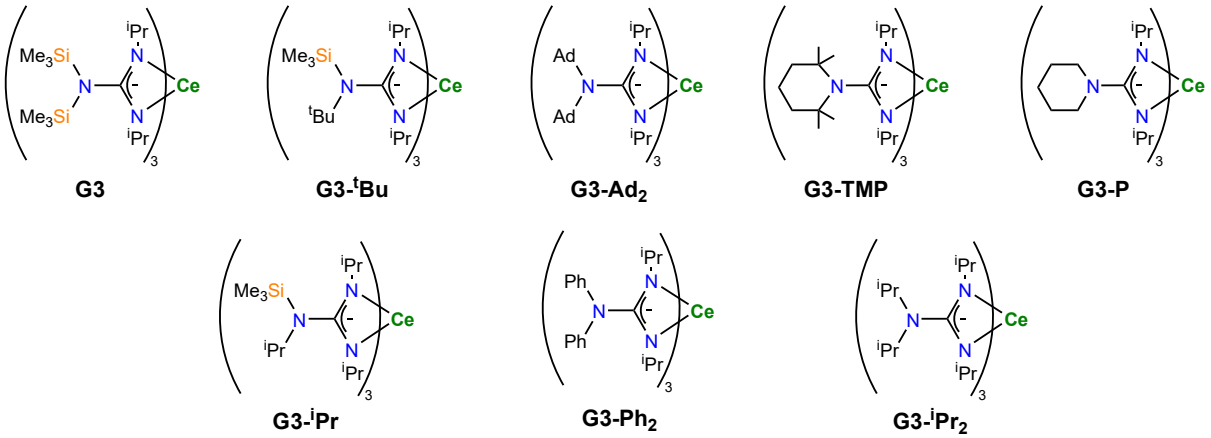

Figure 44. Second series of cerium(III) complexes synthesized by Schelter *et al.*.[10]

Considering that complexes **G3-P**, **G3-^{i}Pr**, **G3-Ph$_2$** and **G3-iPr$_2$** were not luminescent contrary to **G3**, **G3-^{t}Bu**, **G3-Ad$_2$** and **G3-TMP**, the authors envisioned that steric shielding of the cerium centre was a key parameter to design luminescent cerium(III) complexes.

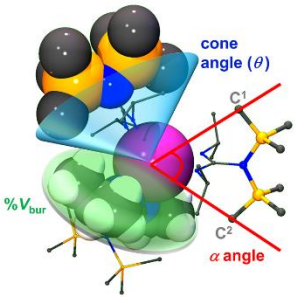

Figure 45. Definition of steric parameters exemplified on complex **G3**. Reproduced from Schelter *et al.*.[6]

Investigation of solid-state structure of these complexes provided a valuable insight on the fine steric effects on the spectroscopic properties. Estimation of the percent buried volume (%V_{bur}, green in **Figure 45**), *i.e.* the total volume of a sphere centred around the metal centre occupied by the ligands, did not emphasize significant differences (84-89%) in quantum yield for the cerium complexes described in **Figure 44**. This result indicated that the first coordination sphere did not influence the spectroscopy of this series of cerium(III) complexes.

On the contrary, a clear correlation was found between the luminescence quantum yield and both the cone angle θ and α angle as defined in **Figure 45**. When α > 57°, the complex was found to be luminescent (see **Figure 46**). The authors attributed this result to a better shielding of the 5dz² orbital for large α values. This result was confirmed by replacing toluene with toluene-d$_8$, as replacing hydrogens with deuterium was reported to probe the C-H/D luminescence quenching in lanthanide(III) complexes.[14] For complexes with large α value, the difference in k_{nr}^{obs} between toluene and toluene-d$_8$ is small, indicating a good shielding from exogenous molecules.

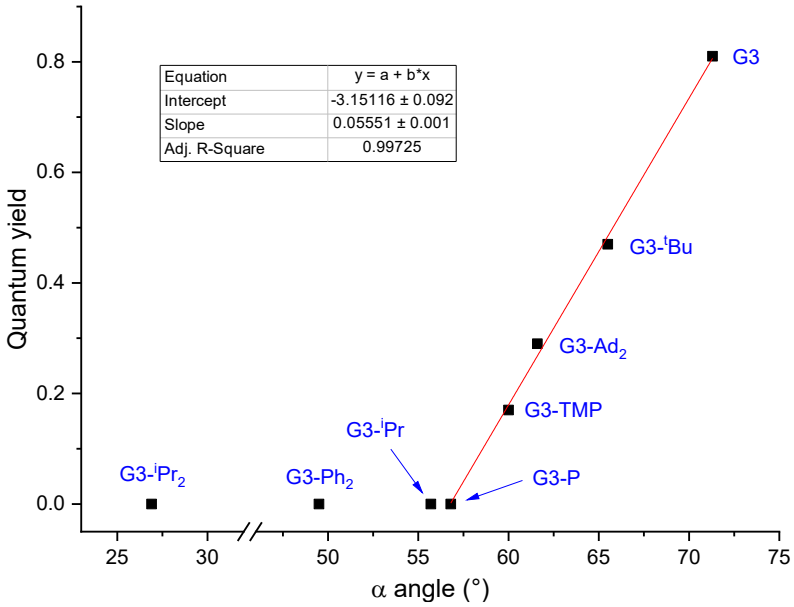

Figure 46. Evolution of the α angle in the series of complexes described in **Figure 44**. Adapted from Schelter *et al.*.[10]

The nature of the coordination sphere also influences the redox reactivity of cerium(III) complexes. Cyclic voltammetry experiments on complexes **G0-G3** (see **Figure 40**) showed that more guanidinate ligands on the cerium centre increased the reducing power of the complex ($E_{1/2}$ = 0.05 V *vs.* Fc/Fc$^+$ for **G0**, -0.22 V for **G3**).

Using the Rehm-Weller formalism,[15] excited-state redox potential of complexes **G0-G3** could be evaluated from -2.19 V for **G0** to -2.92 V *vs.* Fc/Fc$^+$ for **G3**, indicating a higher donating ability of guanidinate ligands. More in depth study of the influence of the structural changes on the redox behaviour of cerium(III) complexes would provide an interesting insight on the reactivity of cerium compounds.

Designing highly reducing cerium(III) complexes goes together with using highly donating ligands to stabilize the +IV oxidation state after oxidation.

b) Cerium complexes bearing tripodal ligand

Owing to the important Lewis acidity in +IV oxidation state, the organometallic chemistry of cerium(IV) complexes was underdeveloped for a long time, due to the need for highly donating ligands. This result contrasts with the particular stability of cerium(IV) in water, which might be due to kinetic factors.

Recent developments on cerium coordination chemistry brought original examples of tripodal ligands bearing aromatic rings in apical position which interacted with the cerium centre. In addition to stabilizing +IV oxidation state, the aryl-cerium interaction was proven useful to stabilize cerium(II) ions (see **Figure 47**) through a δ bond with the aromatic ring, based on the known ability of rare-earth elements and actinides to transfer electrons to aromatic rings.[16]

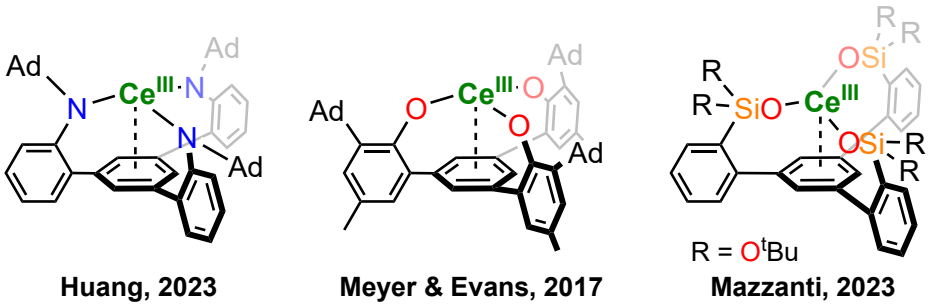

Figure 47. Selected examples of cerium(III) tripodal complexes stabilised by an aromatic ring in apical position[17–19]

Cerium(II) complexes are highly reducing, and were shown to activate several small molecules. For the tris(amido)arene complex reported by Huang *et al.*, two elegant examples of two-electron reductions of pyridine-N-oxide and an aromatic azide were reported.[19] The tris(siloxide)arene ligand reported simultaneously by Mazzanti *et al.* and Cui *et al.* was also proven very efficient towards the stabilization of the +IV oxidation state for cerium and terbium (see **Figure 48**), the latter being especially challenging due to the high oxidation potentials of terbium(III)/terbium(IV) (2.5 V *vs.* Fc/Fc$^+$).[18,20–22]

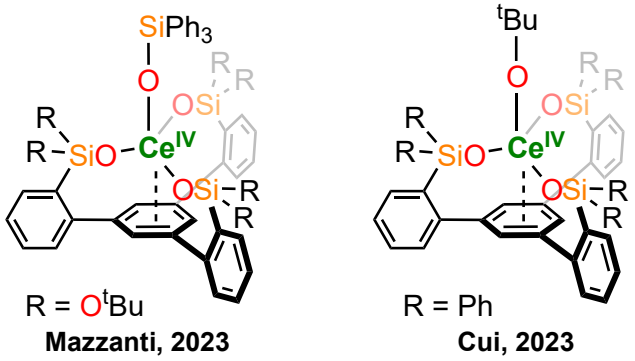

Figure 48. Tris(siloxide)arene cerium(IV) complexes reported by Mazzanti *et al.*[18] and Cui *et al.* [22]

Electron rich and donating ligands are key to easily access high-valent lanthanides. Although alkoxide ligands have been shown to stabilize cerium(IV) ions, their limited steric hindrance is often insufficient to counter the high coordination numbers of lanthanide ions and leads to the formation of multimeric assemblies.[7,23,24]

Bulky amide ligands, especially silylamides, have been extensively used for the past 50 years in lanthanide coordination chemistry to provide highly soluble solvent-free precursors.[25] As shown by the easy oxidation of $Ce^{III}(HMDS)_3$ by $TeCl_4$,[26] and the recent report from Schelter *et al.* of the oxidation of heteroleptic cerium(III)-silylamide-guanidinate complexes (**G0** and **G1** in **Figure 40**) by Fc^+BARF^- (BARF = $B(3,5\text{-}(CF_3)_2\text{-}C_6H_3)_4$) or trityl chloride (trityl = CPh_3),[12] silylamide ligands are able to lower the oxidation potential of cerium(III)/cerium(IV) to accessible values ($E_{1/2}$ = 0.35 V *vs.* Fc/Fc$^+$).[27] Nevertheless, oxidation

of cerium(III)-silylamide complexes was shown to be highly dependent on the reorganization of the ligand, which hampered the isolation of several cerium(IV)-silylamide derivatives.[28–30] Considering the similarities between cerium(III) and uranium(III), examining the coordination chemistry and the reactivity of uranium(III) complexes should provide interesting inspiration.

Extensive developments in uranium coordination chemistry and reactivity initiated by the group Scott[31–35] followed by Liddle and co-workers[36–38] highlighted the particular interest of robust TREN-based ligands (TREN = $N(CH_2CH_2NH_2)_3$) to stabilize uranium complexes from +III to +VI oxidation states.[36] In addition to the thermodynamic and kinetic stability arising from the chelation, TREN ligands also enable easy modification of the steric hindrance in equatorial position through the introduction of different silylated groups, while keeping available one apical coordination site (see **Figure 49**).

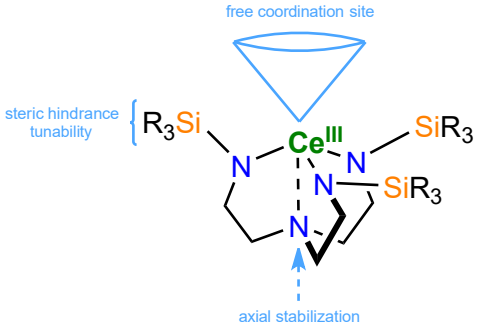

Figure 49. TREN silylated ligand design. Adapted from Gardner and Liddle[36]

These developments led Scott *et al.* them to investigate the reactivity of $Ce^{III}TREN^{TBDMS}$ (TBDMS = $Si((C(CH_3)_3)(CH_3)_2)$, see **Figure 50**).[28] Interestingly, $ICe^{IV}TREN^{TBDMS}$ could be formed by direct oxidation using I_2, which did not work with $Ce^{III}(HMDS)_3$. Oxidations with Cl_2 and Br_2 afforded dissymmetrical dimeric complex, while the addition of Cl_2 to $Ce^{III}(NHSiMe_3)_3$ led to the formation of $Ce^{IV}(NHSiMe_3)_4$ or $Ce^{III}_5(NHSiMe_3)_8Cl_7$ clusters.[30] Hayton and co-workers later used the $TREN^{TBDMS}$ scaffold for the reduction of nitrate ion, which will be presented in Chapter IV.

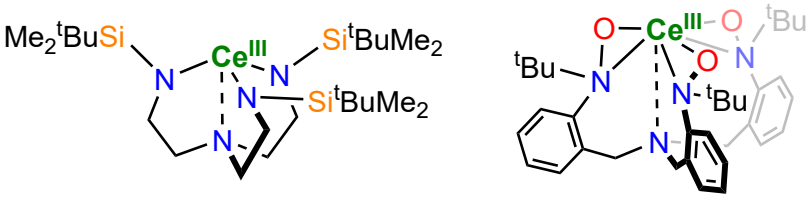

Figure 50. Cerium(III) tripodal amide complexes reported by Scott *et al.*[28] and Schelter *et al.*[29]

The interesting tripodal scaffold motivated the synthesis of a tripodal ligand bearing highly donating nitroxide moieties by Schelter and co-workers, based on a previous study in which they demonstrated the particular ability of nitroxide ligands to stabilize cerium(IV) owing to the much lower reduction potential of the synthesised complex (-1.95 V *vs.* Fc/Fc^+ *vs.* about +1.7 V in water).[29,39] Extensive studies related to the reactivity of this cerium(IV)-TriNOx complex (TriNOx = $\{(2\text{-}^t BuNO)C_6H_4CH_2\}_3N]^{3-}$) brought many examples of interesting reactivities, including the formation of imido and oxo cerium(IV) complexes.[40–46]

These interesting examples of cerium reactivity with tripodal ligands led us to combine the interesting structural and electronic properties of TREN-based ligands with the unique photochemical properties of cerium ions into a new cerium tripodal complex : $Ce^{III}TREN^{TIPS}$.

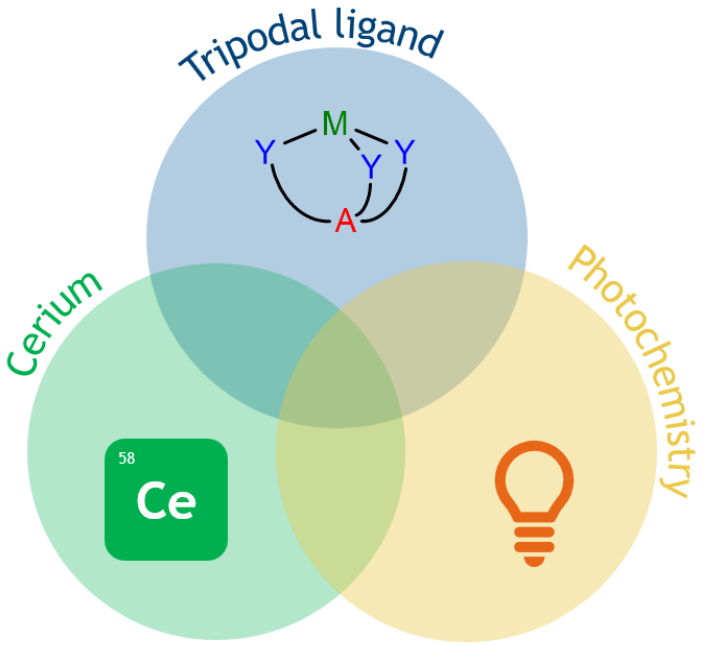

Figure 51. Combination of tripodal ligand with cerium properties and photochemical reactivity

II. Synthesis of starting complex

Our initial project was to synthesize a variety of cerium(IV) complexes bearing different ligand in apical position, in order to improve the understanding related to the VLIH of the cerium(IV)-ligand bond following the debate presented in Introduction. Therefore, a highly donating ligand was envisioned to stabilize the +IV oxidation state. Moreover, the studies of the functionalization of light alkanes by Zuo and co-workers[47,48] and Schelter and co-workers[49,50] were carried out in acetonitrile, preventing an efficient solubilization of alkanes and therefore limiting the reactivity. We targeted the synthesis of a highly bulky complex to enhance the solubility while keeping one apical position available to graft a single ligand.

In addition to the study of the cerium(IV) reactivity, we also sought to investigate further the SET ability of cerium(III), to prevent the use of excess ligand (NEt_4Cl for $CeCl_6^{3-}$ or Na-guanidinate/ NaHMDS for **G0-G1**) in the photoinduced reduction reactions reported by Schelter and co-workers, due to the unproductive ligand decoordination and activation pathways.[11,13,51]

In regards of the interesting properties of TREN-based ligands highlighted in the previous section, we considered $TREN^{TIPS}$ ligand as a good candidate to explore cerium(III) and cerium(IV) reactivity.

a) Synthesis of the complex

Li_3TREN^{TIPS} was synthesized according to a protocol reported by Liddle and co-workers,[37] and later scaled-up to 83 mmol scale in 74% yield (39.4 g).

Anhydrous cerium(III) chloride was initially considered as a suitable cerium(III) precursor for it was available in our laboratory. The reaction was first tried by heating a mixture of $CeCl_3$ and Li_3TREN^{TIPS} at 80 °C in THF for 2 days. Subsequent extraction with pentane, thorough drying at 70 °C under vacuum overnight to remove THF followed by crystallization in a supersaturated solution in pentane at -40 °C overnight afforded yellow crystals which corresponded to $Ce^{III}TREN^{TIPS}$ (**1**, see **Figure 53**).



Figure 52. Crystals of **1**

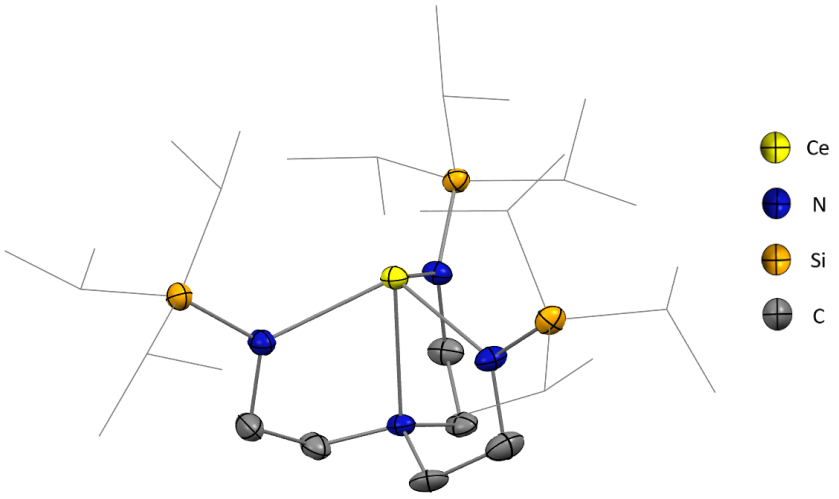

Figure 53. Structure of **1** obtained by X-Ray Diffraction (XRD). Ellipsoids were represented at 50% probability. Hydrogen atoms were omitted for clarity, and isopropyl groups were represented in wireframe style

Pleasingly, no solvent molecule was coordinated to cerium(III) centre in this structure, which indicated that cerium(III) was stabilized enough by the donating ability of amide moieties and protected by the bulky environment to allow for THF to decoordinate.

3D structure of **1** showed slightly longer cerium-nitrogen bonds for equatorial nitrogens (2.361(3) Å) compared to $Ce^{III}(HMDS)_3$ **G0** (2.320(3) Å),[52] and longer nitrogen-silicon bonds (1.720(3) Å *vs.* 1.702(3) Å in **G0**). Cerium-nitrogen-silicon angles are slightly more important in **1**, concomitant with the significantly

shorter distance between cerium and the plane defined by equatorial nitrogen (0.798 Å *vs.* 0.310 Å in **G0**), indicating a more open coordination sphere.

^{1}H NMR spectrum of the yellow crystals displayed four main mildly broad peaks in toluene-d_8, which was consistent with the report of $U^{III}TREN^{TIPS}$ by Liddle and co-workers (see **Figure 54** and **Figure S11**).[37]

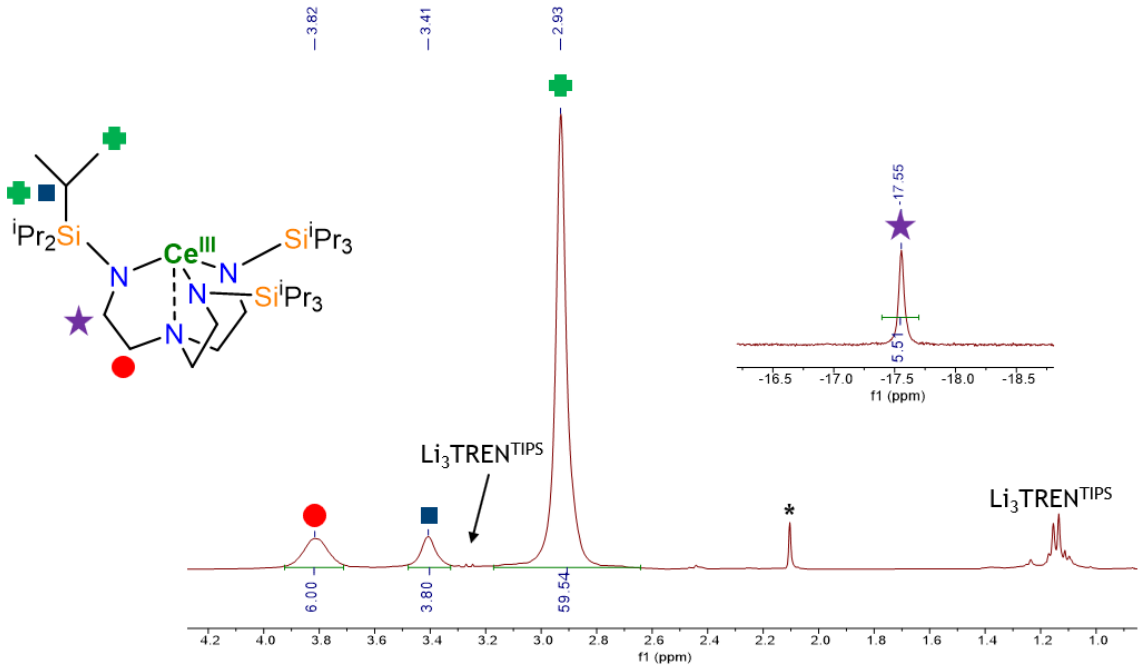

Figure 54. ^{1}H NMR spectrum in toluene-d_8 of crystals of **1** obtained through the first synthesis process

The presence of a peak in the negative ppm region around -17.5 ppm was likely due to a paramagnetic system, consistent with the attribution as cerium(III). Variable Temperature (VT) ^{1}H NMR was recorded to study the paramagnetism of the species. Upon cooling the reaction medium, the chemical shifts of the peaks corresponding to **1** started to change (see **Figure 55** and **Figure S16**). Interestingly, the coalescence temperature of the TREN peak at -17.5 ppm (at 25 °C) was found to be between -50 °C and -60 °C. Given that this peak corresponded to the three CH_2 of TREN moiety close to cerium, the magnetic equivalence at room temperature of these hydrogens was thought to proceed through the "wiggling" movement of TREN branch. Upon reaching temperatures lower than -50 °C, this movement was not thermalized anymore, lifting the magnetic equivalence of each hydrogen.

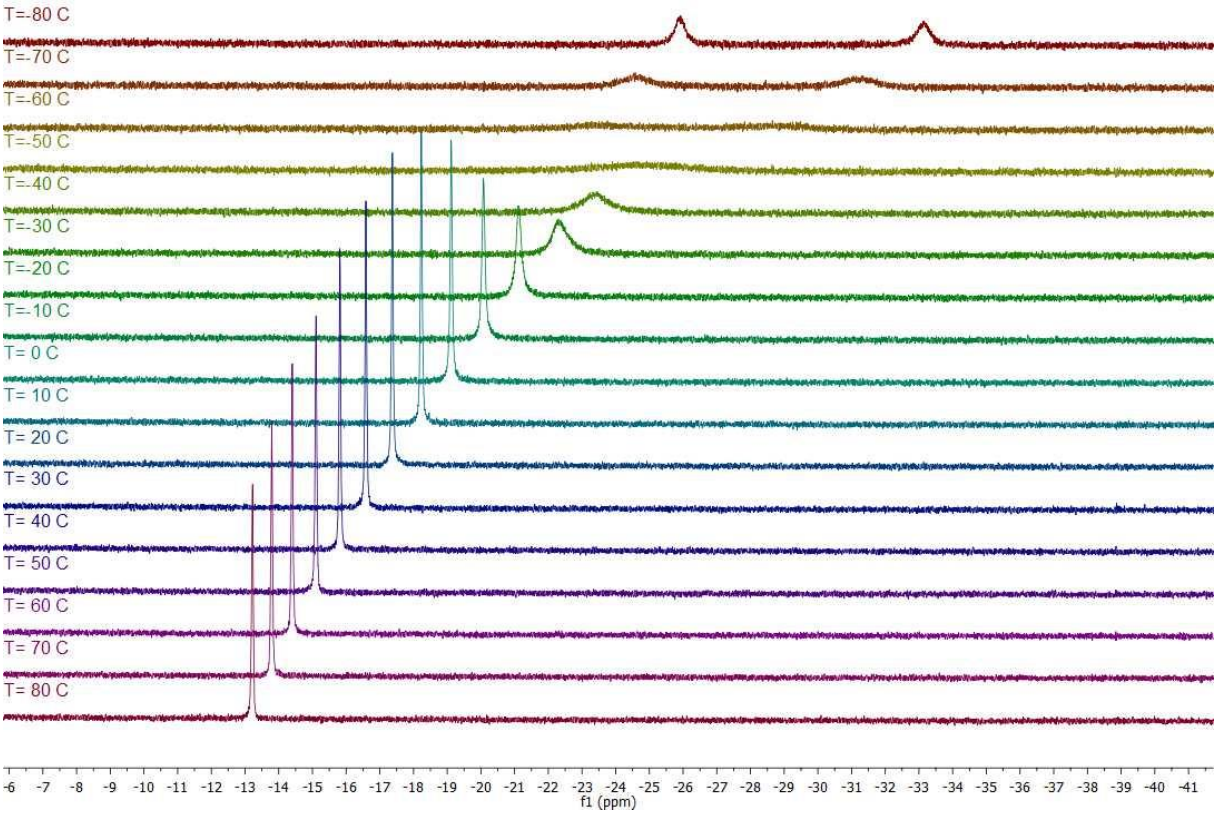

Figure 55. VT ^{1}H NMR spectrum of **1** in toluene-d_8 from -80 to 80 °C. Zoom into the region between -6 and -40 ppm

Several residual peaks could be observed at 1.1 and 3.2 ppm, which fitted perfectly to the ^{1}H NMR spectrum of Li_3TREN^{TIPS}. The presence of this impurity was later confirmed by the isolation of cocrystallization product of Li_3TREN^{TIPS} and **1** (see **Figure 56**), despite the difference in cell parameters between the two crystals in pentane (see **Table S1**).

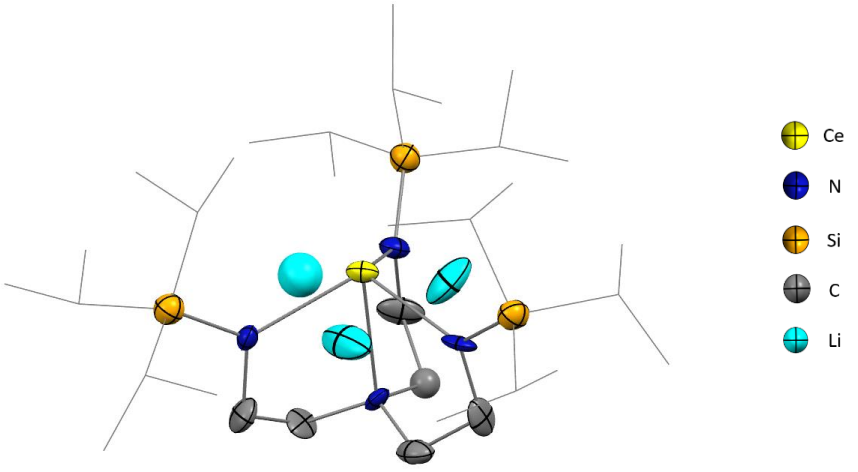

Figure 56. Cocrystallization product of **1** and Li_3TREN^{TIPS}

In order to purify the complex from this impurity, several attempts to change solvent for the metathesis (toluene, pentane), led to similar results. During reactivity studies, complex **1-LiCl-THF$_3$** could be crystallized (see **Figure 57**), showing the possibility for LiCl to coordinate to cerium(III) while being stabilized by THF molecules thanks to the important bond enthalpy of Li-O bond (340.5 ± 6.3 kJ.mol^{-1}).[53]

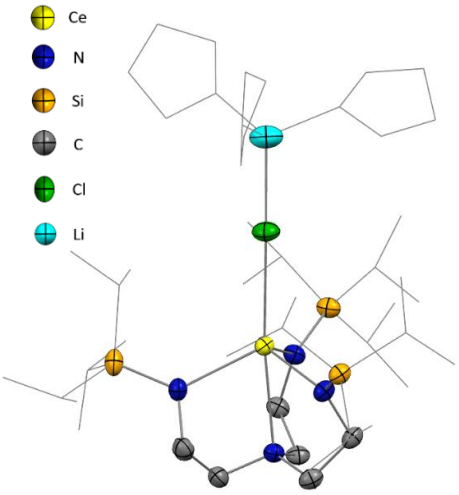

Figure 57. Structure of **1-LiCl-THF$_3$**

As the purity issue was thought to arise from small amounts of LiCl, cerium(III) precursor was changed to cerium(III) triflate (OTf, trifluoromethanesulfonate), due to the much higher solubility of Ce(OTf)$_3$ in THF. Upon mixing a solution of Li$_3$TREN^{TIPS} in THF with Ce(OTf)$_3$, the colour changed to yellow within 10 minutes, indicating that the salt metathesis was much faster than with CeCl$_3$. Nevertheless, after overnight stirring, evaporation of THF at room temperature and extraction with pentane, whitish crystals could be obtained from a supersaturated solution of pentane stored overnight at -40 °C corresponded to Li$_3$TREN^{TIPS}. Further attempts to heat the reaction at 60 °C overnight, removal of volatiles followed by an extraction in pentane and subsequent evaporation, and final drying in vacuo overnight at 60 °C afforded crystals of bridged **1-LiOTf-THF$_2$** after extraction in pentane and storage overnight at -40 °C (see **Figure 59**). Nevertheless, Li$_3$TREN^{TIPS} could still be identified in ^{1}H NMR.

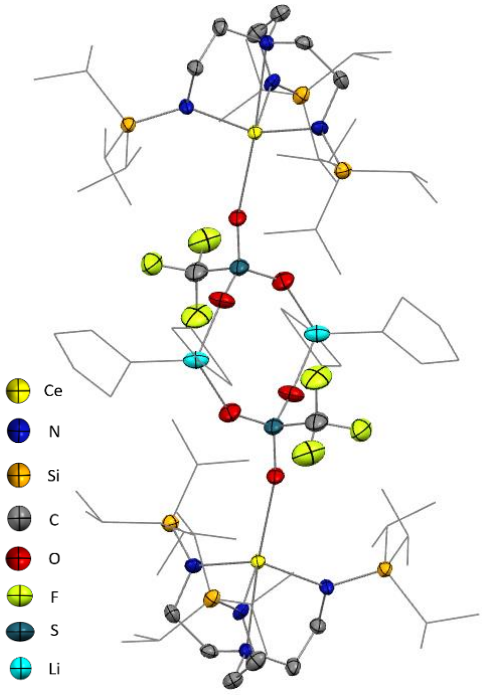

Figure 59. Structure of **1-LiOTf-THF$_2$**

Changing the synthesis strategy to use Ce^{III}(HMDS)$_3$ to deprotonate *in situ* H$_3$TREN^{TIPS} was proven unsuccessful, as the pK$_A$ of the mono-silylamide in TREN (≈ 30) was higher than the one of a bis-silylamide (≈ 25). The cerium(III) precursor was once again changed to cerium(III) iodide, used by Schelter and co-workers for their coordination chemistry of cerium(III) compounds.[11,13]

Similarly, the reaction done with CeI$_3$ in the same conditions than Ce(OTf)$_3$ led to an immediate change in colour to yellow. ^{1}H NMR monitoring of the reaction showed that the reaction was finished within 2 hours. Extraction of the slightly orange mixture with pentane and subsequent crystallization at -40 °C afforded white crystals of **1-LiI-THF$_4$** (see **Figure 58**), where the lithium ion was not coordinated to the iodide, presumably due to lower BDE of LiI bond (345.2 ± 4.2 kJ.mol^{-1}) compared to LiCl (469 ± 13 kJ.mol^{-1}).[53] Given that **1-LiI-THF$_4$** had a very different cell than the one of **1** and Li$_3$TREN^{TIPS}, crystallization of **1-LiI-THF$_4$** occurred without any traces of Li$_3$TREN^{TIPS}. Further drying *in vacuo* at 60 °C overnight followed by an extraction in pentane yielded an intense yellow-orange solution, from which crystals of **1** could be grown at -40 °C. Pleasingly, the corresponding ^{1}H NMR of the crystals did not show any trace of Li$_3$TREN^{TIPS}, but small traces of H$_3$TREN^{TIPS} thought to arise from the hydrolysis of the **1** with very small amounts of water in solvents.

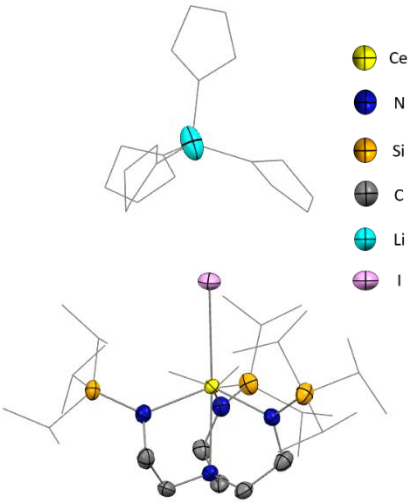

Figure 58. Structure of **1-LiI-THF$_4$**

The synthetic pathway to **1** was therefore adapted to form **1-LiI-THF$_4$** as an intermediate to remove unreacted Li_3TREN^{TIPS}, which can be then used to form **1** in good yields (67% isolated yield on 3.8 mmol scale, 2.29 g, see **Figure 60**).

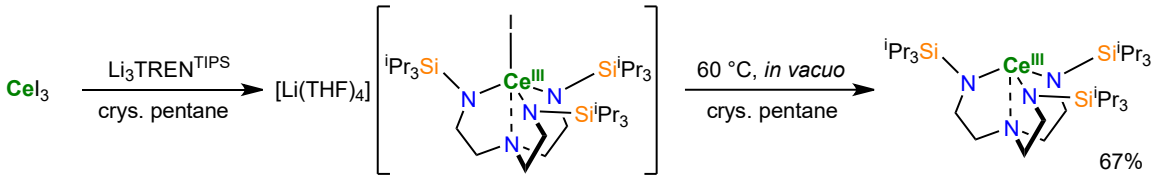

1-LiI-THF$_4$ **1**

Figure 60. Final synthetic scheme for **1**

By investigating the purification of **1**, acetonitrile was found to degrade the complex and to form both H_3TREN^{TIPS} and a powder that could not be identified. The degradation of **1** was thought to proceed through a concerted metalation deprotonation, considering the low pK_A of acetonitrile (≈ 25). To confirm this hypothesis, **1** was reacted with trimethylacetonitrile (^{t}BuCN), having no "acidic" protons in α position from the nitrile. No degradation was occurred, but a change in chemical shift for the peak from -17.1 to -8.0 ppm in C_6D_6 which was likely to correspond to a coordination of the nitrile to **1**. Crystallization in cold pentane afforded light yellow crystals of the adduct **1-^{t}BuCN** (see **Figure 61**).

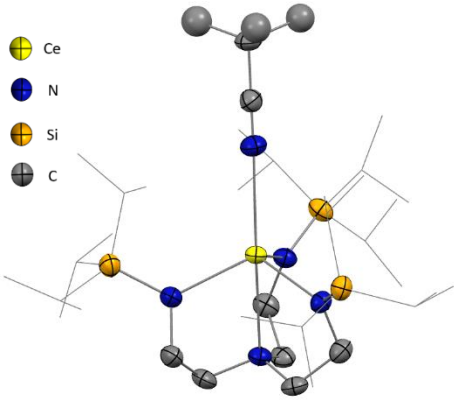

Figure 61. Structure of **1-^{t}BuCN**

These coordination information were useful towards the understanding of the binding possibilities offered by **1**. The first step of our initial project being the study of photoinduced SET reactivity using our complex, we investigated the spectroscopic and redox properties of **1**.

b) Spectroscopies of $Ce^{III}TREN^{TIPS}$

1) Investigating the ground state

To confirm experimentally the electronic structure of **1** in the ground state, X-band Electron Paramagnetic Resonance (EPR) spectroscopy of **1** as powder was recorded at 10 K by Christian Herrero (see **Figure 62**). Two systems could be observed at this temperature : one system displaying an axial symmetry with $g_1 = g_2 = 4.320$ corresponding to an effective magnetic moment $\mu_{eff} = 3.06\ \mu_B$ (μ_B is the Bohr magneton), following the formula $4\mu_{eff}^2 = g_1^2 + g_2^2 + g_3^2$.[54] This species could not be identified, but might result from insufficient grinding of the powder. Recording an EPR spectrum of a frozen solution of **1** could provide understanding on the origin of this species.

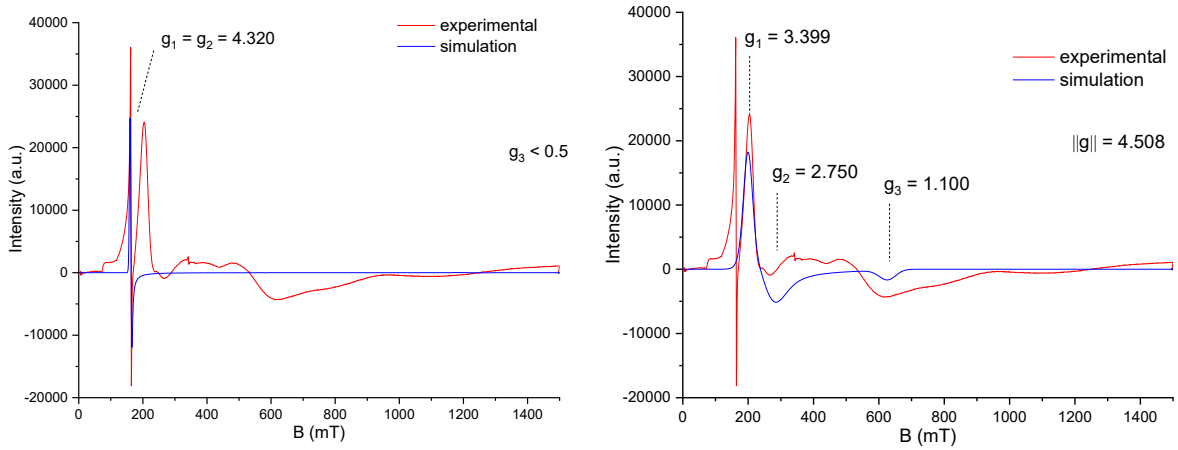

Figure 62. X-band EPR spectra of **1** in powder at 10 K with the corresponding simulations for the "axial" system (left) and **1** (right)

The second species corresponded to a rhombic system with $\mu_{eff} = 2.25\ \mu_B$, which was in accordance with the value obtained by Evans method (2.58 μ_B) done by Grégory Danoun. The theoretical value expected for the effective magnetic moment for a cerium(III) ion is $\mu_{eff} = g(J,L,S)\sqrt{J(J+1)}$, where g is the Lande factor expressed as followed :

$$g(J,L,S) = \frac{3}{2} + \frac{1}{2}\left(\frac{S(S+1) - L(L+1)}{J(J+1)}\right)$$

and $J = L + S$. A 4f electron with $L = 3$ and $S = 1/2$ in the $J = 5/2$ ground state, should therefore have an effective magnetic moment $\mu_{eff} = 2.54\ \mu_B$, which is consistent with the measured value. Therefore, the single electron of **1** was confirmed to be located in a 4f orbital, corresponding to a $^2F_{5/2}$ electronic ground state.

As mentioned in the introduction of this manuscript, the ground state of cerium(III) ion is J = 5/2, divided in three Kramers' doublets by the crystal field with $m_J = \pm 1/2, \pm 3/2, \pm 5/2$ with $m_J = \pm 1/2$ as ground state.[8,54] Theoretical values for this m_J state in axial symmetry are $g_1 = g_2 = 0.86$ and $g_3 = 2.57$, which are quite different from the values obtained for **1**. This difference might either be due to a mixing with another m_J state or to an actual symmetry too different to theoretical axial symmetry.[55] Nevertheless, the rhombic species in **Figure 62** was attributed to **1** considering the similarity to reported cerium(III) complexes.[56]

2) Electronic transitions in 1

As the nature of ground state was unveiled using EPR spectroscopy, the electronic absorption properties of **1** were then investigated.

UV-visible analysis of a solution of **1** in pentane showed the presence of two large bands centred around 415 nm and 335 nm (see **Figure 64**), exhibiting low extinction coefficient values (ε ≈ 400 L.mol^{-1}.cm^{-1}) that is comparable to reported values for f-d transitions.[11,12] Dissymmetry of the former band was likely indicative of the presence of a hidden band, which was confirmed by the deconvolution of the spectrum using Fityk[57] software as shown by the presence of a third band around 379 nm. As the reactions presented in Chapter II were done in THF-d_8, the UV-visible spectrum of **1** was also recorded in THF, which showed little shifts in the bands at 415 and 379 nm to 416 and 384 nm respectively, and a complete disappearance of the band at 335 nm (see **Figure S71**).

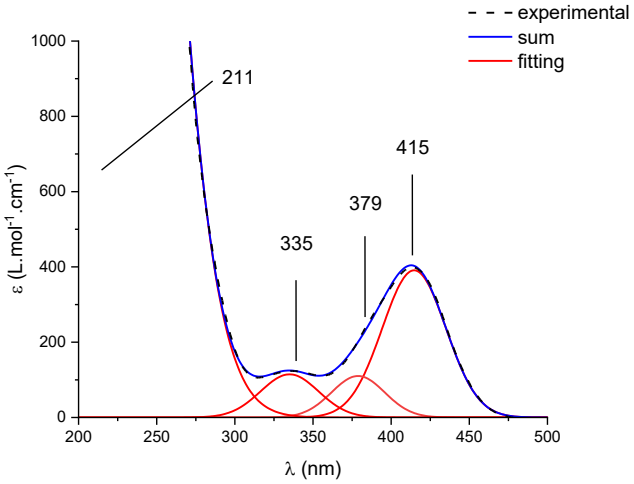

Figure 64. Deconvoluted UV-visible spectrum of **1** in pentane

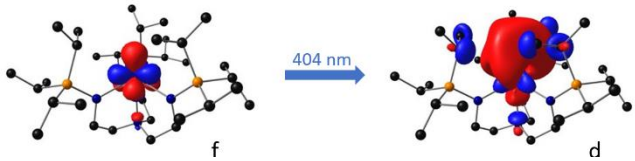

Figure 63. Transition in **1** calculated at 405 nm by TDDFT. Orbitals plotted by S.C. and L.M.

In order to attribute the nature of these bands, Time Dependent-Density Functional Theory (TD-DFT) calculations were performed on **1** by Stella Christodoulou (S.C.) and Laurent Maron (L.M.). The main transition in the visible region was calculated at 405 nm, which corresponded to a f-d transition as shown in **Figure 63**.

To further understand the chemical behaviour of **1**, the redox properties of the complex were studied.

3) Luminescence studies and lifetime measurements

As the nature of ground state was unveiled using EPR spectroscopy, the excited state electronic structure of **1** were probed using luminescence measurements.

Upon irradiation at 427 nm, solutions of **1** exhibited an intense green fluorescence at *ca.* 515 nm from a ^{2}D electronic state with a Stokes shift Δ_{SS} = 5369 cm^{-1}, slightly higher that the reported values for cerium(III) complexes.[11,13] This higher value can be related to the bigger size of the ligand, which can lead to more important reorganization energy in the excited state. Electronic transition between the zeroth vibrational states of the ground state and excited state was approximated as the crossing of excitation and emission bands, which occurred at E_{00} = 21552 cm^{-1} corresponding to 463 nm (*cf.* **Figure 65**). Fitting of the emission band using lognorm functions by Olivier Maury and Akos Banyasz indicated the presence of two emission bands. Interestingly, the emission properties were dependant on the temperature : luminescence spectra recorded in 2-methyl-THF (2-MeTHF) showed a shift and splitting into two emission bands, which were attributed to a $^2D \longrightarrow {}^2F_{7/2}$ and $^2D \longrightarrow {}^2F_{5/2}$.

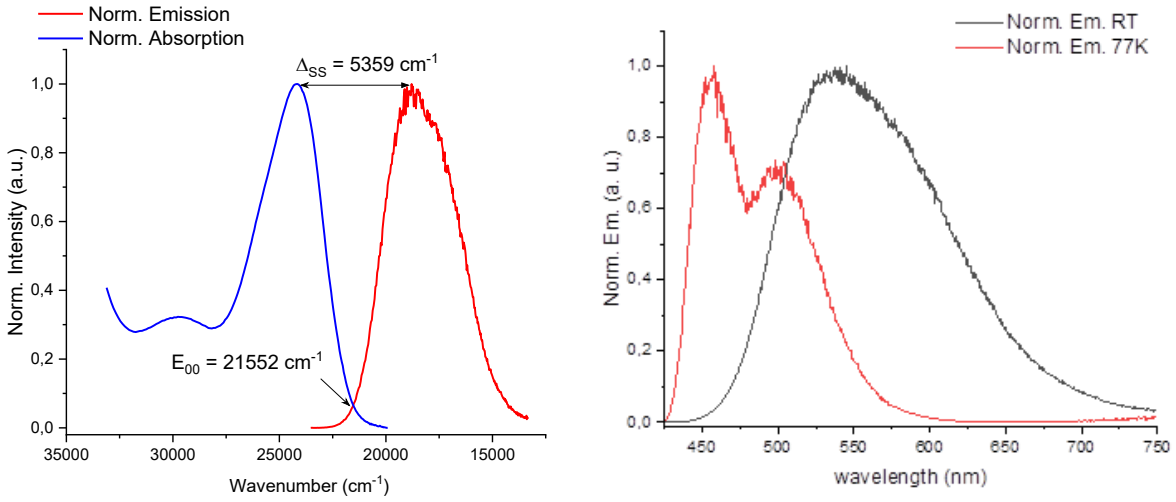

Figure 65. Normalized emission and absorption spectra of **1** in pentane, including measurements of Stokes shift and zero-zero electronic transition (left) and emission curves at room temperature (right, black) and 77 K in 2-MeTHF glass (right, red). Figure plots by Akos Banyasz and Olivier Maury

Fluorescence quantum yield was calculated to be 34% in pentane (using Coumarin 515 as standard), which is more important than in $Ce^{III}(HMDS)_3$ **G0** (about 4%). Luminescence lifetime of **1** has also been measured using Time-Correlated Single Photon Counting (TCSPC, see Appendix) to be 88 ns in pentane and 70 ns in 2-MeTHF, which is much longer than **G0** (about 23 ns). Apparent kinetic radiative (k_r^{obs}) and non-radiative constants (k_{nr}^{obs}) can be calculated using luminescence lifetime and luminescence quantum yields, which were respectively k_r^{obs} = 4.2 10^6 s^{-1} and k_{nr}^{obs} = 9.4 10^6 s^{-1} (comparable to the values for **G3-Ad$_2$**). These differences highlighted the influence of $TREN^{TIPS}$ effect on the luminescence properties to enhance the reactivity under irradiation.

In order to ensure that ^{2}D excited state was responsible for the SET reactions under irradiation, Transient Absorption Spectroscopy (TAS, see Appendix) studies were conducted to probe for the presence of a hypothetical "dark state" (see **Figure 66**). In very general terms, TAS records the evolution of the absorbance at a designated wavelength after a very short delay after pulsed irradiation, which allows for the detection of so-called transient species. The only signal detected by TAS of a solution of **1** in pentane was the luminescence decay of **1**, even after applying a correction to annihilate luminescence. Upon scanning different emission wavelengths and different excitation intensities, no residual signal other than luminescence could be detected, which that would tend to indicate the absence of a dark state.



Figure 66. General scheme for energy transfer to a dark state from an excited state

c) Investigation of the redox behaviour

1) Electrochemical measurements

Determination of the redox potential of **1** by Cyclic Voltammetry (CV) analysis was the first step to probe the redox behaviour of the complex. Given that acetonitrile could not be used as solvent for electrochemical measurements, CVs were carried out in THF.

Initially, *n*-tetrabutylammonium tetrafluoroborate ($TBABF_4$) was chosen as supporting electrolyte for its good solubility in THF, but it was shown to react with **1** upon electrochemical oxidation to cerium(IV). Therefore, *n*-tetrabutylammonium trifluoromethanesulfonimidate (TBATFSI) was chosen as supporting electrolyte owing to its particular inertness. This feature was verified with the absence of reaction with **1**, both in oxidation and reduction sweeping (see **Figure 67**).

The oxidation of **1** was shown to be reversible, occurring at about -0.5 V *vs.* Fc/Fc^+. Even though the difference in potentials between the oxidation and reduction peaks was about 110 mV and would correspond to a slow electron transfer, the analysis of Fc/Fc^+ couple in the same conditions afforded a similar difference in potential, indicating that the apparent slow character of the oxidation of **1** was originating from the experimental conditions, especially due to the non-negligible resistivity of THF compared to acetonitrile.

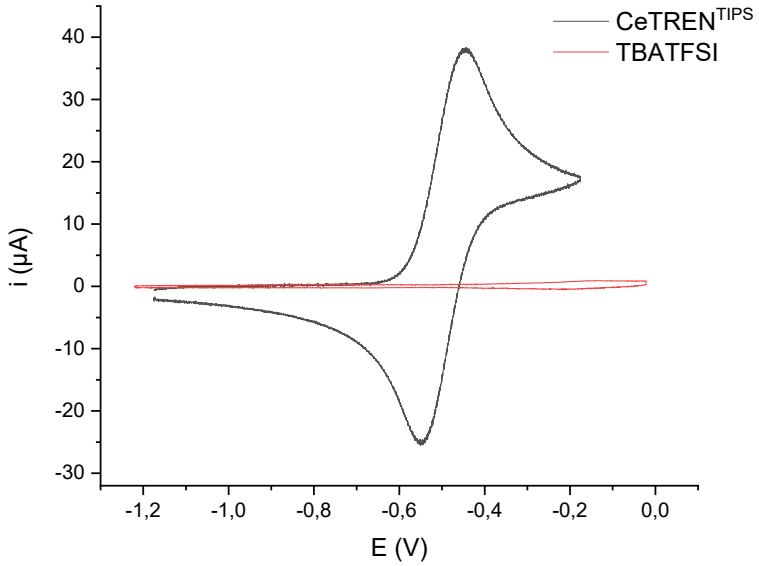

Figure 67. Cyclic voltammogram at 50 $mV.s^{-1}$ scan rate of supporting electrolyte (100 mM) and **1** (4 mM). Potential values are referenced to Fc/Fc^+

In order to evaluate the excited state redox potential $E_{1/2}(1^*/1^+)$ of **1** under irradiation, the Rehm-Weller formalism[15] was applied to **1**. E_{00} = 2.67 eV was determined by luminescence measurements and the work function in THF was estimated to be inferior to 0.1 V (see Appendix). The estimated excited state redox potential of **1** was found to be $E_{1/2}(1^*/1^+)$ = -3.2 V *vs.* Fc/Fc^+, approximately similar to the reducing power of KC_8 in THF (-3.1 V *vs.* Fc/Fc^+)[58] which was significantly lower that most reported cerium(III) complexes[11] but slightly higher than cerium(III) hexachlorocerate (-3.45 V *vs.* Fc/Fc^+).[59]

2) Oxidations to cerium(IV)-halides

The initial developments regarding oxidation of **1** were focusing on the synthesis of cerium(IV) bearing a halide ion in apical position, in view of studying of the possible VLIH of the cerium-halide bond.

Addition of a solution of highly oxidizing hexachloroethane (C_2Cl_6) in pentane to a solution of **1** in pentane afforded an immediate change in colour to intense purple, which was likely to correspond to the formation of a cerium(IV) species. Crystallization in pentane afforded white crystals that corresponded to unreacted hexachloroethane and purple crystals of **2-Cl** (see **Figure 68**). **2-Cl** was perfectly insoluble in acetonitrile, but prolonged storage of the complex in acetonitrile led to degradation after few hours, indicating a possible lability of the Ce-Cl bond. Crystals and solutions of **2-Cl** were both slightly light sensitive and temperature sensitive, decomposing over few hours under ambient light or at room temperature. The crystals were also slowly degrading over the course of several months upon storage in the dark at -40 °C. The isolation of **2-Cl** as a monomer contrasts with the oxidation of $Ce^{III}TREN^{TBDMS}$ reported by Scott and co-workers, who isolated a dissymmetrical dimer upon oxidation with Cl_2 or Br_2.[28]

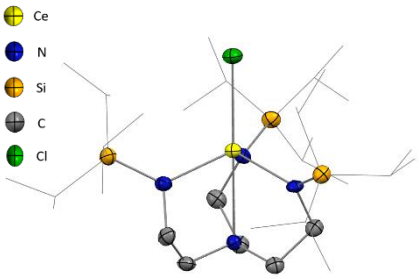

Figure 68. Structure of **2-Cl**

Trityl chloride (Ph_3CCl) was also shown to oxidize **1** in **2-Cl**, but the crystallization of Gomberg's dimer[60] (formed by the dimerization of trityl radicals formed by one-electron reduction of trityl chloride) prevented a clean separation of **2-Cl** from other compounds. Due to the simultaneous crystallization of several organic products with the previous oxidants, liquid tetrachloroethane ($H_2C_2Cl_4$) was successfully used for the oxidation of **1** in **2-Cl** due to its easy purification by washing with MeCN. To prevent the use of highly toxic chloroalkane reagents, a milder oxidation process was developed and will be presented in Chapter II.

The oxidation from **1** into **2-Cl** led to a contraction of the Ce-$N_{equatorial}$ bonds from 2.361(3) to 2.220(3) Å, co-occurring with a shortening of the distance between metal centre and the plane defined by equatorial nitrogens from 0.798 to 0.694 Å, and with a lengthening of the Ce-N_{apical} bond from 2.534(2) to 2.606(3) Å, likely to release the strain from the equatorial contraction. The angle Ce-$N_{equatorial}$-C also decreased significantly upon oxidation from 119.34(16) to 109.39(19)°. Compared to **1-LiCl**, the cerium-chloride distance is significantly shorter (2.8379(8) Å in **1-LiCl** *vs.* 2.625(11) Å in **2-Cl**), which was consistent with the increase in Lewis acidity compared to cerium(III).[61] The Ce-Cl bond length (2.625(11) Å) was slightly longer to the one in $ClCe^{IV}(HMDS)_3$ by Eisenstein *et al.* (2.597(2) Å),[26] possibly caused by important steric hindrance of the metal.

^1H NMR spectrum of crystalline **2-Cl** in C_6D_6 displayed four main peaks in the diamagnetic region (see **Figure 69**). Two triplets at 5.06 and 3.35 ppm accounted for the 12 hydrogens of the TREN base, while the TIPS peaks were split in a septuplet at 1.52 ppm for the 9 hydrogens of the tertiary carbons, and the two singlets at 1.21 and 1.19 ppm corresponding to the 54 hydrogens of methyl groups. No peak was detected outside the region between 0 to 6 ppm, which was coherent with the attribution to a diamagnetic cerium(IV).

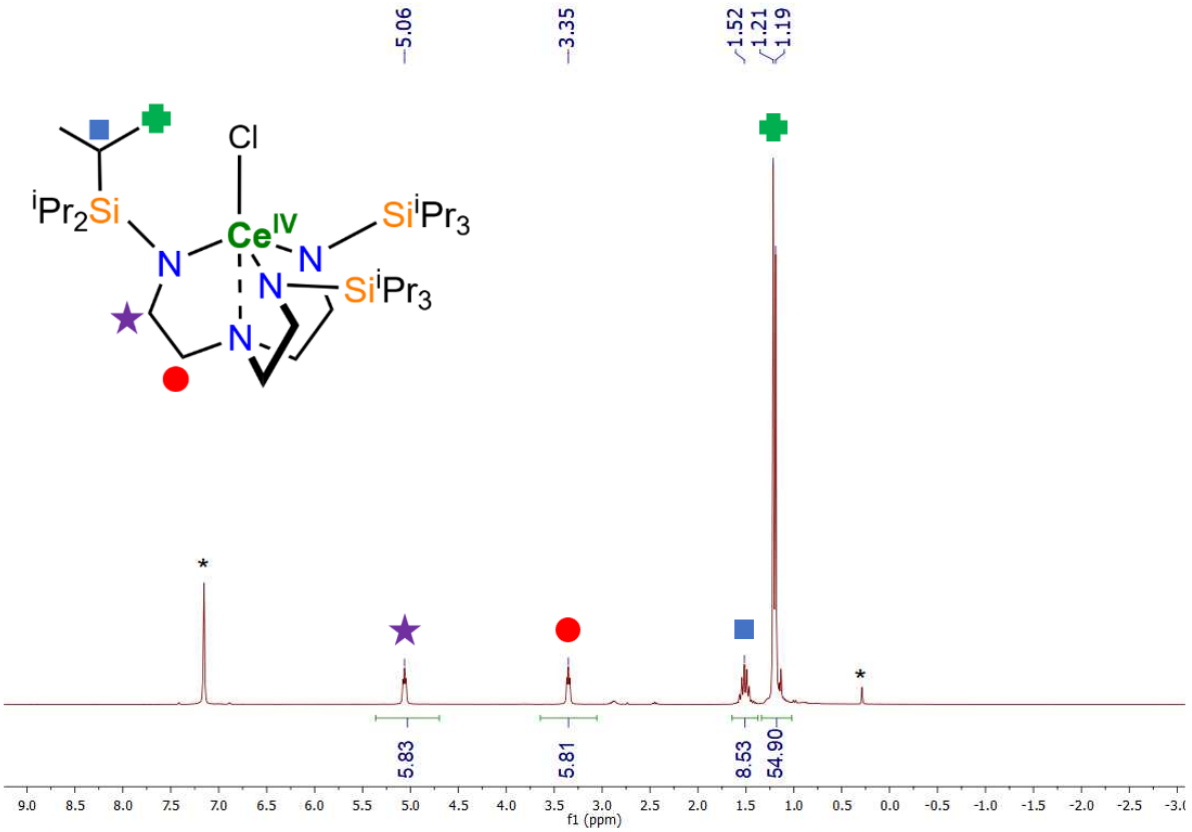

Figure 69. ^{1}H NMR of **2-Cl** in C_6D_6 at 298 K. Solvent residual peak and residues of silicon grease are indicated with *

Similarly, mixing solutions of tetrabromomethane (CBr_4) and **1** in pentane led to an immediate change in colour to deep blue-purple, which corresponded to the formation of **2-Br** as shown by further crystallization in pentane (see **Figure 70**), which suffered from similar crystallization issues to **2-Cl** due to the crystallization of CBr_4 in pentane. **2-Br** was also highly sensitive to light and temperature, even more than **2-Cl**. The Ce-Br bond in **2-Br** was found to be 2.785(3) Å, which is slightly longer than Ce-Br bond in $BrCe^{IV}(HMDS)_3$ (2.766(2) Å).[62]

Following a report from Schelter and co-workers,[27] **2-F** was synthesized using either tritryl (Ph_3C^+) or ferrocenium (Fc^+) salts associated with tetrafluoroborate (BF_4^-) or hexafluorophosphate (PF_6^-) anions in pentane. Both reagents proceed through the one-electron oxidation of cerium(III) into cerium(IV), the latter being a strong Lewis acid that is able to abstract a fluoride from the fluorinated anions to form the corresponding cerium(IV)-fluoride complex. The use of $FcBF_4$ was preferred due to the easier purification step, which consisted in washing the reddish solid obtained after evaporation of pentane with MeCN on a fritted filter to remove salts and ferrocene until the supernatant was colourless, followed by an extraction and crystallization in pentane with one drop of THF. XRD analysis of the reddish crystals afforded the 3D structure of **2-F**, similar to **2-Cl**, with a bond length of 2.0985(18) Å for Ce-F bond. This value is in line with the structure of $FCe^{IV}(HMDS)_3$ by E. J. Schelter and co-workers (2.065(7) Å),[27] and with the U-F bond in $U^{IV}TREN^{TIPS}$ synthesized by Liddle *et al.* (2.124(4) Å),[38] owing to the similarity between ionic radii of cerium(IV) and uranium(IV).[61]

Attempts to synthesize $ICe^{IV}TREN^{TIPS}$ using iodine following the report from Scott and co-workers[28] were unsuccessful, due to a probable high thermal sensitivity of the complex. A transient deep blue colour was observed upon addition of I_2, but faded within seconds. No attempt at low temperature was tried yet.

The XRD structures of the three complexes were very similar to each other (see **Table S16**). The main difference was found in the Ce-X bond (X = Cl, Br, F) which was increasingly elongated from **2-F** to **2-Br** (2.0985(18) Å for Ce-F bond in **2-F**, 2.625(11) Å for Ce-Cl bond in **2-Cl** and 2.785(3) Å for Ce-Br bond in

2-Br). This difference is consistent with the increase in ionic radii of the halide,[61] and with the bond enthalpy of cerium-halide bond (582 ± 42 kJ.mol^{-1} for Ce-F, 457.0 kJ.mol^{-1} for Ce-Cl and 333.8 kJ.mol^{-1} for Ce-I),[53] which could explain the increasing sensitivity to light and thermal degradation from **2-F** to **2-Br**. ^{1}H NMR spectra were similar, although small chemical shifts differences could be noticed for the triplet around 5 ppm and the sextuplet close to 1.5 ppm depending on the nature of the halide (see **Figure 71**).

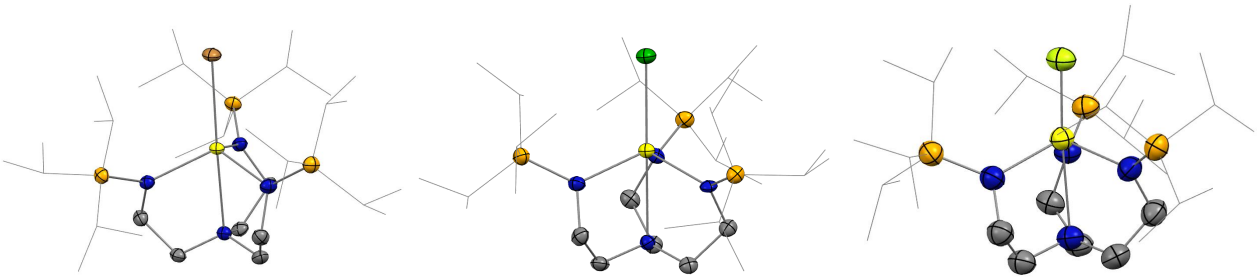

Figure 70. Structures of **2-Br** (left), **2-Cl** (middle) and **2-F** (right)

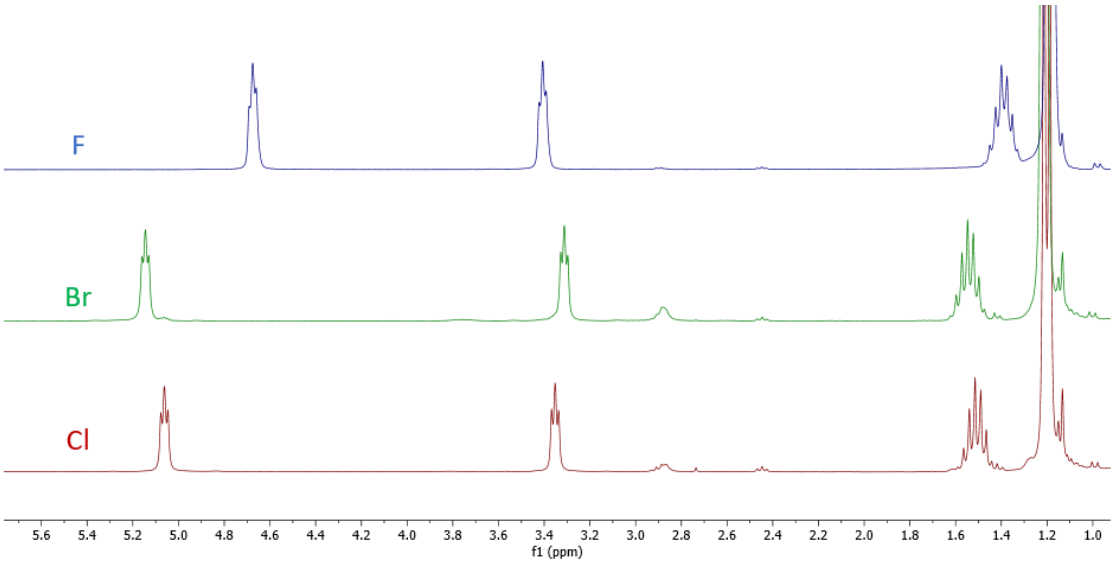

Figure 71. Comparison of ^{1}H NMR spectra of **2-F**, **2-Br** and **2-Cl** in C_6D_6

In order to access new cerium(IV) complexes, in particular bearing heteroatom ligands in apical position, new synthetic pathways were explored.

Silver salts are commonly used in organometallic chemistry and coordination chemistry to easily perform one-electron oxidation while concomitantly providing an anionic ligand to equilibrate charges. A wide variety of counter-anions is available, mostly through salt metathesis with silver(I) nitrate or silver(I) triflate. Several silver oxidants were prepared (AgNCO, $AgBPh_4$) and some already available in the laboratory were tested in reaction with **1**. Surprisingly, several salts did not lead to any tractable results (AgCN, AgO_2CCF_3), while AgOTf, AgI and AgNCO led to colour changes which were consistent with cerium(IV) species. No clean protocol could be extracted from these investigations, due to the inconvenient removal of silver nanoparticles.

Following a recent and elegant report from Walensky *et al.*[63] using copper(I) halides as oxidants for cerium(III) complexes, a few copper precursors in +I and +II oxidation states ($CuCl_2$, CuCl, $CuBr_2$, CuBr, $Cu(OTf)_2$, CuOTf) were tested in reaction with **1**. Pleasingly, all precursors reacted instantly with **1** to give a purple solution (blue for triflate reagents), which could be consistent to the formation of **2-X** compounds (X = Cl, Br, OTf). Nevertheless, neither copper(II) acetate nor copper(I) iodide did afford any change. This strategy is under development, especially to access the cerium(IV)-triflate complex.

In the same idea, several ferrocenium salts were investigated owing to the easier purification of ferrocene compared to silver particles. Ferrocenium triflate was obtained through oxidation of ferrocene by silver triflate in the dark, following a literature protocol.[64] Mixing solutions of FcOTf and **1** in pentane afforded an immediate colour change to deep blue, which would be consistent with the formation of a cerium(IV) compound. Nevertheless, neither clean synthesis nor XRD suitable crystals could be obtained after several trials (the blue solid is decomposed upon washing with MeCN). Similarly, FcBARF (BARF = 3,5-$(CF_3)_2C_6H_3)_4B^-$) was synthesised by salt metathesis from $FcBF_4$ and NaBARF according to a reported procedure,[65] but no interesting result, except a change in colour that was consistent with the colour of **2-F**, arose from the reactivity tests which were not investigated further.

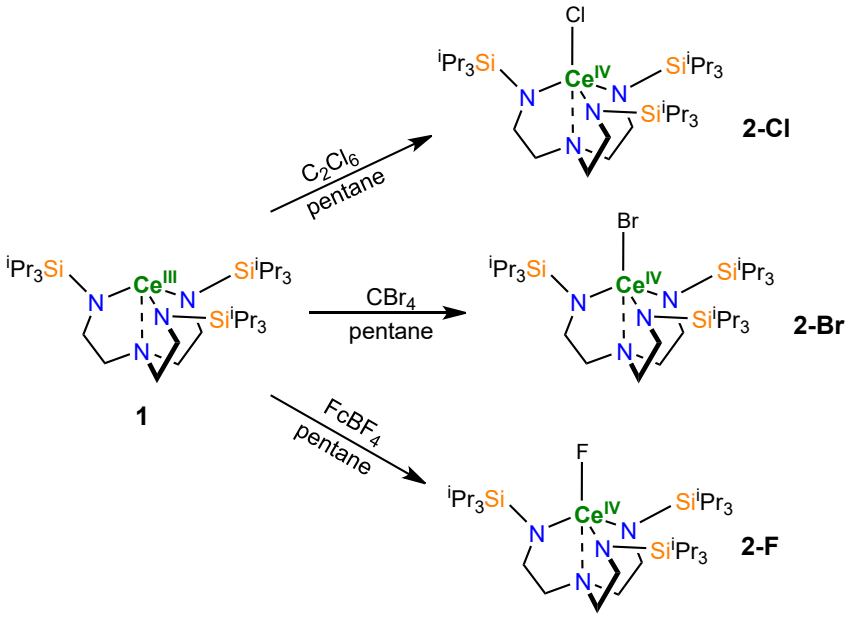

Figure 72. Oxidation pathways of **1** into **2-Cl**, **2-Br** and **2-F**

3) UV-visible spectroscopy for complexes 2-F, 2-Br and 2-Cl

Upon oxidation to cerium(IV), the UV-visible spectra substantially changed, exhibiting broad and intense bands (ε ≈ 2500 L.mol^{-1}.cm^{-1}) around 350 and 520 nm for **2-F**, **2-Cl** and **2-Br**. While little changes could be noticed from **2-Br** to **2-Cl** in extinction molar coefficient ($\varepsilon_{\mathbf{2\text{-}Br},556}$ = 2229 L.mol^{-1}.cm^{-1} *vs.* 2644 for **2-Cl**) and position of the bands, the broad band shifted significantly to 500 nm for **2-F** with $\varepsilon_{\mathbf{2\text{-}F},500}$ = 2844 L.mol^{-1}.cm^{-1} (see **Figure 73**). The extinction molar coefficient values are in line with reported values for cerium(IV) compounds.[66]

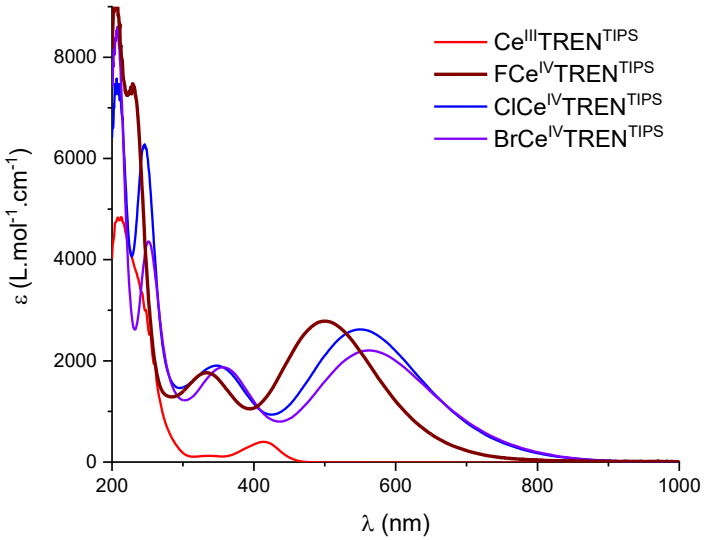

Figure 73. Superimposition of absorption spectra of **1**, **2-F**, **2-Cl** and **2-Br** in pentane at 298 K

High values of extinction molar coefficient for the transitions around 500-550 nm were likely correspond to a charge transfer within the complex. Given that the electronic structure of cerium(IV) is [Xe]4f^{0}5d^0, the transition would therefore be a Ligand-to-Metal Charge Transfer (LMCT). To confirm this hypothesis, TDDFT calculations were run on **2-F**, **2-Cl**, and **2-Br** by S.C. and L.M., which confirmed that the transition occurred from a TREN-based orbital to a pure metal orbital for the three cerium(IV) complexes investigated (see **Figure 74**). No reaction was observed upon irradiation at 525 nm for several hours, which would be consistent with this attribution. A similar shifting trend along the series (while shifted by ≈ +50 nm) was also found in the calculations, as well as the decomposition of the broad band into two smaller bands, that was not observed upon deconvolution.

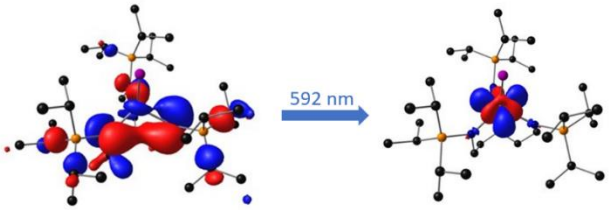

Figure 74. Transition in **2-Cl** calculated at 592 nm by TDDFT. Orbitals plotted by S.C. and L.M.

4) Ligand exchange using trimethylsilyl reagents

Schelter and co-workers developed a new strategy to access a variety of cerium(IV) precursors using trimethylsilyl reagents on cerium(IV)-fluoride complexes to induce a ligand exchange, taking advantage of the highly energetic silicon-fluoride bond (576.4 ± 17 kJ.mol^{-1}).[53,66]

First applying this strategy to ligand exchange from **2-F** with TMS-Br in THF-d$_8$ showed the clean formation of **2-Br**, proving the strategy to be applicable to CeTREN^{TIPS}. Attempts to exchange fluoride anion with TMS-I, TMS-OTf, TMS-N$_3$ and TMS-NCS also led to a detection of new cerium(IV) species by ^{1}H NMR (see **Figure 75**). Trying to expand even further the scope of ligands with TMS-CF$_3$, TMS-CN and TMS-NCO were unsuccessful, even after few days of stirring.

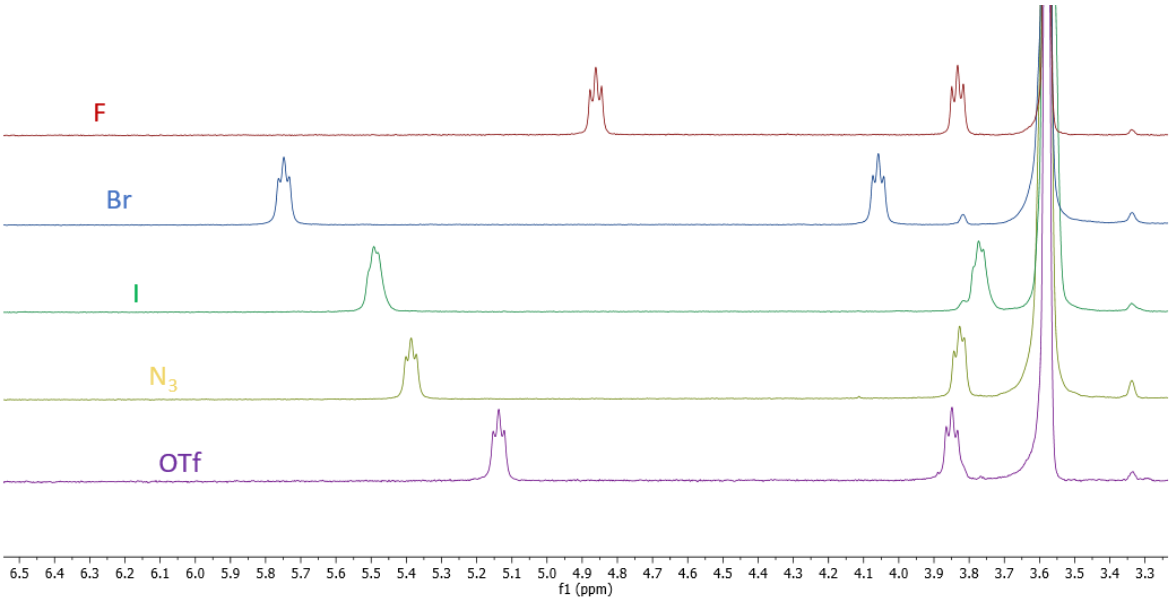

Figure 75. Comparison of ^{1}H spectra of the reactions with TMS-X derivatives in THF-d^{8}. Nature of X is indicated near each spectrum

5) Oxidations using organic oxidants

Following our previous study that was focusing on the synthesis of cerium(IV)-halide complexes, other oxidants that did not contain any halide were considered. Inspired by the detailed study of oxidation of cerium(III) complexes by simple quinone derivatives, reported by Anwander and coworkers[67] and based on previous reports from Rheingold *et al.*,[24] Schelter *et al.*[68] and their group,[69] the same reactivity was investigated with **1**.

Addition of 0.5 equivalents of 1,4-benzoquinone (Bq) to a solution of **1** in pentane afforded an immediate change in colour from yellow to intense purple. ^{1}H NMR monitoring of the reaction medium showed the consumption of **1** and the appearance of cerium(IV) typical signature with two triplets at 4.72 and 3.31 ppm. Concentration and storage at -40 °C in presence of one drop of THF afforded XRD suitable purple crystals, which corresponded to the dimeric cerium(IV) complex **2-Bq** obtained by two-electron reduction of benzoquinone (see **Figure 76**).

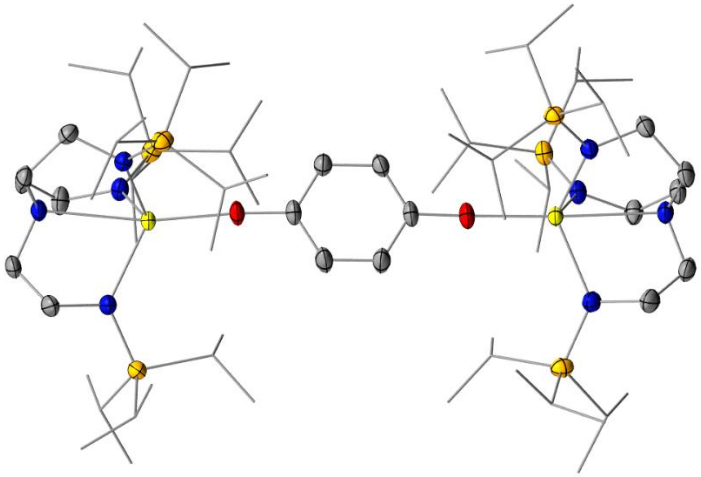

Figure 76. Structure of **2-Bq.** Hydrogen atoms have been omitted for clarity, and isopropyl groups have been represented in wireframe style. One THF molecule is present in the cell but it was not depicted here

The structure was almost perfectly symmetrical and exhibited very similar structural parameters in both CeTREN^{TIPS} moieties, comparable to the report of Anwander and co-workers.[70] Bond lengths in

CeTREN^{TIPS} were similar to those in **2-X** (X = F, Cl, Br), and C-C bonds of the bridging ligand were of comparable length (1.388(3)-1.396(3) Å) to aromatic C-C bonds,[67] confirming that benzoquinone was reduced by two electrons into a hydroquinolato ligand. X-band EPR spectrum of **2-Bq** crystals dissolved in pentane was silent, and the corresponding ^{1}H NMR spectrum in THF-d_8 was diamagnetic and very similar to the other cerium(IV) complexes reported in this manuscript (see **Figure S39**).

The diamagnetic ^{1}H NMR, colour and electron balance of crystalline **2-Bq** in pentane converged towards the attribution of +IV oxidation state to the cerium centre.

To study the influence of the steric hindrance on the oxidation behaviour, the reactivity with 2,6-di-*tert*-butylquinone (^{t}Bu$_2$Bq) was put under scrutiny. Mixing **1** and ^{t}Bu$_2$Bq induced an immediate shift in colour to deep purple, but the corresponding ^{1}H NMR spectrum was displaying broad signals around 1.3 ppm, which could be related to the presence of a highly paramagnetic species. Purple crystals grown from a concentrated solution in pentane and one drop of THF afforded crystals of monomeric **2-^{t}Bu$_2$Bq** (see **Figure 77**).

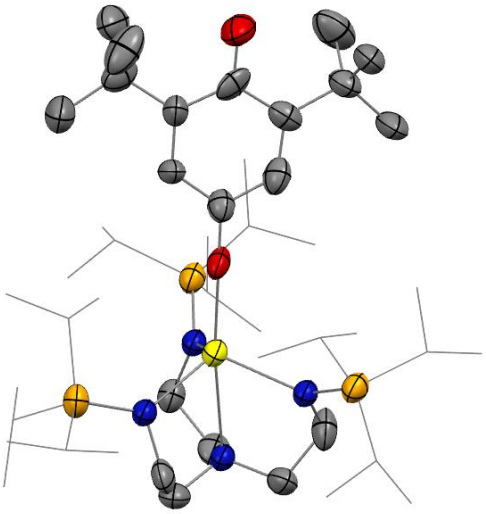

Figure 77. Structure of **2-^{t}Bu$_2$Bq.** Hydrogen atoms have been omitted for clarity, and isopropyl groups have been represented in wireframe style. One THF molecule is present in the cell but it was not depicted here

This solid-state structure was especially interesting, for it indicated that one-electron reduction of the semiquinone ^{t}Bu$_2$Bq$^{\bullet-}$ was either kinetically blocked or thermodynamically not favoured, probably owing to the important steric hindrance of the second anchoring site. EPR measurement of the crystalline **2-^{t}Bu$_2$Bq** in pentane displayed a broad unstructured band centred around 330.3 mT, that was attributed to a delocalized radical on the aryl moiety (see **Figure 78**).

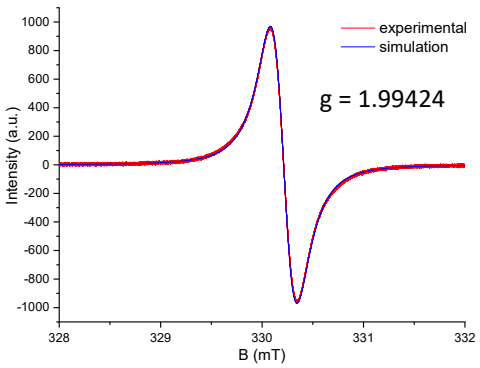

Figure 78. X-band EPR spectrum of a solution of crystals of **2-^{t}Bu$_2$Bq** in pentane

Colour, bond metrics, EPR spectroscopy and electron balance of the complex coincided to the attribution to +IV oxidation state for the metal, which corresponded to a one-electron reduction of ^{t}Bu$_2$Bq to a semiquinone. This behaviour is reminiscent of the one-electron reduction of ^{t}Bu$_2$Bq by samarium(II) trispyrazolylborate, which was also shown to stabilize the semiquinolato radical.[71]

These preliminary investigations of spectroscopic and redox behaviour of **1** were crucial to provide a better understanding of the properties and reactivity of the complex, which was decisive in the further exploration of photochemical reactivity using **1**.

References

(1) Cotton. Introduction to the Lanthanides. In *Lanthanide and Actinide Chemistry*; John Wiley & Sons, Ltd, 2006; pp 1–7. https://doi.org/10.1002/0470010088.ch1.

(2) Simler, T.; McCabe, K. N.; Maron, L.; Nocton, G. CO Reductive Oligomerization by a Divalent Thulium Complex and CO2-Induced Functionalization. *Chem. Sci.* **2022**, *13* (25), 7449–7461. https://doi.org/10.1039/D2SC01798A.

(3) Moutet, J.; Schleinitz, J.; La Droitte, L.; Tricoire, M.; Pointillart, F.; Gendron, F.; Simler, T.; Clavaguéra, C.; Le Guennic, B.; Cador, O.; Nocton, G. Bis-Cyclooctatetraenyl Thulium(II): Highly Reducing Lanthanide Sandwich Single-Molecule Magnets. *Angew. Chem.* **2021**, *133* (11), 6107–6111. https://doi.org/10.1002/ange.202015428.

(4) Yadav, R.; Hossain, M. E.; Paramban, R. P.; Simler, T.; Schoo, C.; Wang, J.; Deacon, G. B.; Junk, P. C.; Roesky, P. W. 3d–4f Heterometallic Complexes by the Reduction of Transition Metal Carbonyls with Bulky LnII Amidinates. *Dalton Trans.* **2020**, *49* (23), 7701–7707. https://doi.org/10.1039/D0DT01271H.

(5) Nief, F. Non-Classical Divalent Lanthanide Complexes. *Dalton Trans.* **2010**, *39* (29), 6589–6598. https://doi.org/10.1039/C001280G.

(6) Nicholas, H. M.; Mills, D. P. Lanthanides: Divalent Organometallic Chemistry. In *Encyclopedia of Inorganic and Bioinorganic Chemistry*; John Wiley & Sons, Ltd, 2017; pp 1–10. https://doi.org/10.1002/9781119951438.eibc2453.

(7) So, Y.-M.; Leung, W.-H. Recent Advances in the Coordination Chemistry of Cerium(IV) Complexes. *Coord. Chem. Rev.* **2017**, *340*, 172–197. https://doi.org/10.1016/j.ccr.2016.12.009.

(8) Abragam, A.; Bleaney, B. *Electron Paramagnetic Resonance of Transition Ions*; Oxford classic texts in the physical sciences; Oxford University Press: Oxford, 2012.

(9) Bünzli, J.-C. G.; Eliseeva, S. V. Basics of Lanthanide Photophysics. In *Lanthanide Luminescence: Photophysical, Analytical and Biological Aspects*; Hänninen, P., Härmä, H., Eds.; Springer: Berlin, Heidelberg, 2011; pp 1–45. https://doi.org/10.1007/4243_2010_3.

(10) Qiao, Y.; Sergentu, D.-C.; Yin, H.; Zabula, A. V.; Cheisson, T.; McSkimming, A.; Manor, B. C.; Carroll, P. J.; Anna, J. M.; Autschbach, J.; Schelter, E. J. Understanding and Controlling the Emission Brightness and Color of Molecular Cerium Luminophores. *J. Am. Chem. Soc.* **2018**, *140* (13), 4588–4595. https://doi.org/10.1021/jacs.7b13339.

(11) Yin, H.; Schelter, E. J.; Carroll, P. J.; Manor, B. C.; Anna, J. M. Cerium Photosensitizers: Structure–Function Relationships and Applications in Photocatalytic Aryl Coupling Reactions. *J. Am. Chem. Soc.* **2016**, *138* (18), 5984–5993. https://doi.org/10.1021/jacs.6b02248.

(12) Qiao, Y.; Yin, H.; Moreau, L. M.; Feng, R.; Higgins, R. F.; Manor, B. C.; Carroll, P. J.; Booth, C. H.; Autschbach, J.; Schelter, E. J. Cerium(IV) Complexes with Guanidinate Ligands: Intense Colors and Anomalous Electronic Structures. *Chem. Sci.* **2021**, *12* (10), 3558–3567. https://doi.org/10.1039/D0SC05193D.

(13) Yin, H.; Schelter, E. J.; Carroll, P. J.; Anna, J. M. Luminescent Ce(III) Complexes as Stoichiometric and Catalytic Photoreductants for Halogen Atom Abstraction Reactions. *J. Am. Chem. Soc.* **2015**, *137* (29), 9234–9237. https://doi.org/10.1021/jacs.5b05411.

(14) Yanagida, S.; Hasegawa, Y.; Murakoshi, K.; Wada, Y.; Nakashima, N.; Yamanaka, T. Strategies for Enhancing Photoluminescence of Nd3+ in Liquid Media. *Coord. Chem. Rev.* **1998**, *171*, 461–480. https://doi.org/10.1016/S0010-8545(98)90069-8.

(15) Rehm, D.; Weller, A. Kinetics of Fluorescence Quenching by Electron and H-Atom Transfer. *Isr. J. Chem.* **1970**, *8* (2), 259–271. https://doi.org/10.1002/ijch.197000029.

(16) Kotyk, C. M.; Fieser, M. E.; Palumbo, C. T.; Ziller, J. W.; Darago, L. E.; Long, J. R.; Furche, F.; Evans, W. J. Isolation of +2 Rare Earth Metal Ions with Three Anionic Carbocyclic Rings: Bimetallic Bis(Cyclopentadienyl) Reduced Arene Complexes of La2+ and Ce2+ Are Four Electron Reductants. *Chem. Sci.* **2015**, *6* (12), 7267–7273. https://doi.org/10.1039/C5SC02486B.

(17) Palumbo, C. T.; Halter, D. P.; Voora, V. K.; Chen, G. P.; Chan, A. K.; Fieser, M. E.; Ziller, J. W.; Hieringer, W.; Furche, F.; Meyer, K.; Evans, W. J. Metal versus Ligand Reduction in Ln^{3+} Complexes of a

Mesitylene-Anchored Tris(Aryloxide) Ligand. *Inorg. Chem.* **2018**, *57* (5), 2823–2833. https://doi.org/10.1021/acs.inorgchem.7b03236.
(18) Hsueh, F.-C.; Rajeshkumar, T.; Maron, L.; Scopelliti, R.; Sienkiewicz, A.; Mazzanti, M. Isolation and Redox Reactivity of Cerium Complexes in Four Redox States. *Chem. Sci.* **2023**, *14* (22), 6011–6021. https://doi.org/10.1039/D3SC01478A.
(19) Wang, Y.; Liang, J.; Deng, C.; Sun, R.; Fu, P.-X.; Wang, B.-W.; Gao, S.; Huang, W. Two-Electron Oxidations at a Single Cerium Center. *J. Am. Chem. Soc.* **2023**, *145* (41), 22466–22474. https://doi.org/10.1021/jacs.3c06613.
(20) Nugent, L. J.; Baybarz, R. D.; Burnett, J. L.; Ryan, J. L. Electron-Transfer and f-d Absorption Bands of Some Lanthanide and Actinide Complexes and the Standard (II-III) Oxidation Potential for Each Member of the Lanthanide and Actinide Series. *J. Phys. Chem.* **1973**, *77* (12), 1528–1539. https://doi.org/10.1021/j100631a011.
(21) Tricoire, M.; Hsueh, F.-C.; Keener, M.; Rajeshkumar, T.; Scopelliti, R.; Zivkovic, I.; Maron, L.; Mazzanti, M. Siloxide Tripodal Ligands as a Scaffold for Stabilizing Lanthanides in the +4 Oxidation State. *Chem. Sci.* **2024**, *15* (18), 6874–6883. https://doi.org/10.1039/D4SC00051J.
(22) Guo, H.; Hong, D.; Cui, P. Tripodal Tris(Siloxide) Ligand Supported Trivalent Rare-Earth Metal Complexes and Redox Reactivity. *Dalton Trans.* **2023**, *52* (43), 15672–15676. https://doi.org/10.1039/D3DT02519E.
(23) Friedrich, J.; Schneider, D.; Bock, L.; Maichle-Mössmer, C.; Anwander, R. Cerium(IV) Neopentoxide Complexes. *Inorg. Chem.* **2017**, *56* (14), 8114–8127. https://doi.org/10.1021/acs.inorgchem.7b00828.
(24) Sen, A.; Stecher, H. A.; Rheingold, A. L. Synthesis, Structure, and Reactivity of Homoleptic Cerium(IV) and Cerium(III) Alkoxides. *Inorg. Chem.* **1992**, *31* (3), 473–479. https://doi.org/10.1021/ic00029a025.
(25) Ortu, F. Rare Earth Starting Materials and Methodologies for Synthetic Chemistry. *Chem. Rev.* **2022**, *122* (6), 6040–6116. https://doi.org/10.1021/acs.chemrev.1c00842.
(26) Eisenstein, O.; Hitchcock, P. B.; Hulkes, A. G.; Lappert, M. F.; Maron, L. Cerium Masquerading as a Group 4 Element: Synthesis, Structure and Computational Characterisation of [CeCl{N(SiMe3)2}3]. *Chem. Commun.* **2001**, No. 17, 1560–1561. https://doi.org/10.1039/b103634n.
(27) Williams, U. J.; Robinson, J. R.; Lewis, A. J.; Carroll, P. J.; Walsh, P. J.; Schelter, E. J. Synthesis, Bonding, and Reactivity of a Cerium(IV) Fluoride Complex. *Inorg. Chem.* **2014**, *53* (1), 27–29. https://doi.org/10.1021/ic402769u.
(28) Morton, C.; Alcock, N. W.; Lees, M. R.; Munslow, I. J.; Sanders, C. J.; Scott, P. Stabilization of Cerium(IV) in the Presence of an Iodide Ligand: Remarkable Effects of Lewis Acidity on Valence State. *J. Am. Chem. Soc.* **1999**, *121* (48), 11255–11256. https://doi.org/10.1021/ja9920563.
(29) Bogart, J. A.; Lippincott, C. A.; Carroll, P. J.; Booth, C. H.; Schelter, E. J. Controlled Redox Chemistry at Cerium within a Tripodal Nitroxide Ligand Framework. *Chem. – Eur. J.* **2015**, *21* (49), 17850–17859. https://doi.org/10.1002/chem.201502952.
(30) Crozier, A. R.; Bienfait, A. M.; Maichle-Mössmer, C.; Törnroos, K. W.; Anwander, R. A Homoleptic Tetravalent Cerium Silylamide. *Chem. Commun.* **2012**, *49* (1), 87–89. https://doi.org/10.1039/C2CC37404H.
(31) Roussel, P.; Scott, P. Complex of Dinitrogen with Trivalent Uranium. *J. Am. Chem. Soc.* **1998**, *120* (5), 1070–1071. https://doi.org/10.1021/ja972933+.
(32) Kaltsoyannis, N.; Scott, P. Evidence for Actinide Metal to Ligand π Backbonding. Density Functional Investigations of the Electronic Structure of [{(NH2)3(NH3)U}2(M2-H2:H2-N2)]. *Chem. Commun.* **1998**, No. 16, 1665–1666. https://doi.org/10.1039/A803833C.
(33) Roussel, P.; Hitchcock, P. B.; Tinker, N. D.; Scott, P. Alkoxide and Aryloxide Derivatives of a (Triamidoamine)Uranium Complex. *Inorg. Chem.* **1997**, *36* (25), 5716–5721. https://doi.org/10.1021/ic970856d.
(34) Roussel, P.; Hitchcock, P. B.; Tinker, N.; Scott, P. A Mixed-Valence Uranium(III/IV) Bimetallic; Structure, Magnetism and Reactivity. *Chem. Commun.* **1996**, No. 17, 2053–2054. https://doi.org/10.1039/CC9960002053.

(35) Roussel, P.; Alcock, N. W.; Boaretto, R.; Kingsley, A. J.; Munslow, I. J.; Sanders, C. J.; Scott, P. Complexes of Triamidoamines with the Early Actinides. Synthetic Routes to Monomeric Compounds of Tetravalent Uranium and Thorium Containing Halide and Amide Ligands. *Inorg. Chem.* **1999**, *38* (16), 3651–3656. https://doi.org/10.1021/ic990563f.

(36) Gardner, B. M.; Liddle, S. T. Uranium Triamidoamine Chemistry. *Chem. Commun.* **2015**, *51* (53), 10589–10607. https://doi.org/10.1039/C5CC01360G.

(37) King, D. M.; Tuna, F.; McInnes, E. J. L.; McMaster, J.; Lewis, W.; Blake, A. J.; Liddle, S. T. Synthesis and Structure of a Terminal Uranium Nitride Complex. *Science* **2012**, *337* (6095), 717–720. https://doi.org/10.1126/science.1223488.

(38) King, D. M.; Tuna, F.; McInnes, E. J. L.; McMaster, J.; Lewis, W.; Blake, A. J.; Liddle, S. T. Isolation and Characterization of a Uranium(VI)–Nitride Triple Bond. *Nat. Chem.* **2013**, *5* (6), 482–488. https://doi.org/10.1038/nchem.1642.

(39) Bogart, J. A.; Lewis, A. J.; Medling, S. A.; Piro, N. A.; Carroll, P. J.; Booth, C. H.; Schelter, E. J. Homoleptic Cerium(III) and Cerium(IV) Nitroxide Complexes: Significant Stabilization of the 4+ Oxidation State. *Inorg. Chem.* **2013**, *52* (19), 11600–11607. https://doi.org/10.1021/ic401974t.

(40) Solola, L. A.; Zabula, A. V.; Dorfner, W. L.; Manor, B. C.; Carroll, P. J.; Schelter, E. J. Cerium(IV) Imido Complexes: Structural, Computational, and Reactivity Studies. *J. Am. Chem. Soc.* **2017**, *139* (6), 2435–2442. https://doi.org/10.1021/jacs.6b12369.

(41) Cheisson, T.; Solola, L. A.; Gau, M. R.; Carroll, P. J.; Schelter, E. J. Silyl Transfer Pathway to a Ce(IV) Imido Complex. *Organometallics* **2018**, *37* (23), 4332–4335. https://doi.org/10.1021/acs.organomet.8b00366.

(42) Cole, B. E.; Falcones, I. B.; Cheisson, T.; Manor, B. C.; Carroll, P. J.; Schelter, E. J. A Molecular Basis to Rare Earth Separations for Recycling: Tuning the TriNOx Ligand Properties for Improved Performance. *Chem. Commun.* **2018**, *54* (73), 10276–10279. https://doi.org/10.1039/C8CC04409K.

(43) Solola, L. A.; Zabula, A. V.; Dorfner, W. L.; Manor, B. C.; Carroll, P. J.; Schelter, E. J. An Alkali Metal-Capped Cerium(IV) Imido Complex. *J. Am. Chem. Soc.* **2016**, *138* (22), 6928–6931. https://doi.org/10.1021/jacs.6b03293.

(44) Wilson, H. H.; Yu, X.; Cheisson, T.; Smith, P. W.; Pandey, P.; Carroll, P. J.; Minasian, S. G.; Autschbach, J.; Schelter, E. J. Synthesis and Characterization of a Bridging Cerium(IV) Nitride Complex. *J. Am. Chem. Soc.* **2023**, *145* (2), 781–786. https://doi.org/10.1021/jacs.2c12145.

(45) Cole, B. E.; Cheisson, T.; Higgins, R. F.; Nakamaru-Ogiso, E.; Manor, B. C.; Carroll, P. J.; Schelter, E. J. Redox-Driven Chelation and Kinetic Separation of Select Rare Earths Using a Tripodal Nitroxide Proligand. *Inorg. Chem.* **2020**, *59* (1), 172–178. https://doi.org/10.1021/acs.inorgchem.9b00975.

(46) Cheisson, T.; Kersey, K. D.; Mahieu, N.; McSkimming, A.; Gau, M. R.; Carroll, P. J.; Schelter, E. J. Multiple Bonding in Lanthanides and Actinides: Direct Comparison of Covalency in Thorium(IV)- and Cerium(IV)-Imido Complexes. *J. Am. Chem. Soc.* **2019**, *141* (23), 9185–9190. https://doi.org/10.1021/jacs.9b04061.

(47) Hu, A.; Guo, J.-J.; Pan, H.; Zuo, Z. Selective Functionalization of Methane, Ethane, and Higher Alkanes by Cerium Photocatalysis. *Science* **2018**, *361* (6403), 668–672. https://doi.org/10.1126/science.aat9750.

(48) An, Q.; Xing, Y.-Y.; Pu, R.; Jia, M.; Chen, Y.; Hu, A.; Zhang, S.-Q.; Yu, N.; Du, J.; Zhang, Y.; Chen, J.; Liu, W.; Hong, X.; Zuo, Z. Identification of Alkoxy Radicals as Hydrogen Atom Transfer Agents in Ce-Catalyzed C–H Functionalization. *J. Am. Chem. Soc.* **2023**, *145* (1), 359–376. https://doi.org/10.1021/jacs.2c10126.

(49) Schelter, E. J.; Yang, Q.; Wang, Y.-H.; Qiao, Y.; Gau, M.; Carroll, P. J.; Walsh, P. J. Photocatalytic C–H Activation and the Subtle Role of Chlorine Radical Complexation in Reactivity. *Science* **2021**, *372* (6544), 847–852. https://doi.org/10.1126/science.abd8408.

(50) Yang, Q.; Song, E.; Wu, Y.; Li, C.; Gau, M. R.; Anna, J. M.; Schelter, E. J.; Walsh, P. J. Mechanistic Investigation of the Ce(III) Chloride Photoredox Catalysis System: Understanding the Role of Alcohols as Additives. *J. Am. Chem. Soc.* **2025**, *147* (2), 2061–2076. https://doi.org/10.1021/jacs.4c15627.

(51) Qiao, Y.; Schelter, E. J. Lanthanide Photocatalysis. *Acc. Chem. Res.* **2018**, *51* (11), 2926–2936. https://doi.org/10.1021/acs.accounts.8b00336.

(52) William S. Rees, J.; Just, O.; Derveer, D. S. V. Molecular Design of Dopant Precursors for Atomic Layer Epitaxy of SrS:Ce. *J. Mater. Chem.* **1999**, *9* (1), 249–252. https://doi.org/10.1039/A805757E.
(53) Luo, Y.-R. *Handbook of Bond Dissociation Energies in Organic Compounds*, 0 ed.; CRC Press, 2002. https://doi.org/10.1201/9781420039863.
(54) Walter, M. D.; Booth, C. H.; Lukens, W. W.; Andersen, R. A. Cerocene Revisited: The Electronic Structure of and Interconversion Between Ce2(C8H8)3 and Ce(C8H8)2. *Organometallics* **2009**, *28* (3), 698–707. https://doi.org/10.1021/om7012327.
(55) Mchenry, M. E.; Laughlin, D. E. Magnetic Moment And Magnetization, 2012. https://www.contrib.andrew.cmu.edu/~dl0p/laughlin/pdf/441.pdf.
(56) Hsueh, F.-C.; Rajeshkumar, T.; Maron, L.; Scopelliti, R.; Sienkiewicz, A.; Mazzanti, M. Isolation and Redox Reactivity of Cerium Complexes in Four Redox States. *Chem. Sci.* **2023**, *14* (22), 6011–6021. https://doi.org/10.1039/D3SC01478A.
(57) Wojdyr, M. *Fityk* : A General-Purpose Peak Fitting Program. *J. Appl. Crystallogr.* **2010**, *43* (5), 1126–1128. https://doi.org/10.1107/S0021889810030499.
(58) Rice, N. T.; Su, J.; Gompa, T. P.; Russo, D. R.; Telser, J.; Palatinus, L.; Bacsa, J.; Yang, P.; Batista, E. R.; La Pierre, H. S. Homoleptic Imidophosphorane Stabilization of Tetravalent Cerium. *Inorg. Chem.* **2019**, *58* (8), 5289–5304. https://doi.org/10.1021/acs.inorgchem.9b00368.
(59) Yin, H.; Jin, Y.; Hertzog, J. E.; Mullane, K. C.; Carroll, P. J.; Manor, B. C.; Anna, J. M.; Schelter, E. J. The Hexachlorocerate(III) Anion: A Potent, Benchtop Stable, and Readily Available Ultraviolet A Photosensitizer for Aryl Chlorides. *J. Am. Chem. Soc.* **2016**, *138* (50), 16266–16273. https://doi.org/10.1021/jacs.6b05712.
(60) Bochkarev, L. N.; Molosnova, N. E.; Zakharov, L. N.; Fukin, G. K.; Yanovsky, A. I.; Struchkov, Y. T. 1-Diphenylmethylene-4-(Triphenylmethyl)Cyclohexa-2,5-Diene Benzene Solvate. *Acta Crystallogr. C* **1995**, *51* (3), 489–491. https://doi.org/10.1107/S0108270194009005.
(61) Shannon, R. D. Revised Effective Ionic Radii and Systematic Studies of Interatomic Distances in Halides and Chalcogenides. *Acta Crystallogr. A* **1976**, *32* (5), 751–767. https://doi.org/10.1107/S0567739476001551.
(62) Hitchcock, P. B.; Hulkes, A. G.; Lappert, M. F. Oxidation in Nonclassical Organolanthanide Chemistry: Synthesis, Characterization, and X-Ray Crystal Structures of Cerium(III) and -(IV) Amides. *Inorg. Chem.* **2004**, *43* (3), 1031–1038. https://doi.org/10.1021/ic035100v.
(63) Gremillion, A. J.; Ross, J.; Yu, X.; Ishtaweera, P.; Anwander, R.; Autschbach, J.; Baker, G. A.; Kelley, S. P.; Walensky, J. R. Facile Oxidation of Ce(III) to Ce(IV) Using Cu(I) Salts. *Inorg. Chem.* **2024**, *63* (21), 9602–9609. https://doi.org/10.1021/acs.inorgchem.3c04337.
(64) Tanabe, Y.; Nakajima, K.; Nishibayashi, Y. Phosphine Oxidation with Water and Ferrocenium(III) Cation Induced by Visible-Light Irradiation. *Chem. – Eur. J.* **2018**, *24* (70), 18618–18622. https://doi.org/10.1002/chem.201805129.
(65) Chávez, I.; Alvarez-Carena, A.; Molins*, E.; Roig, A.; Maniukiewicz, W.; Arancibia, A.; Arancibia, V.; Brand, H.; Manuel Manríquez*, J. Selective Oxidants for Organometallic Compounds Containing a Stabilising Anion of Highly Reactive Cations: (3,5(CF3)2C6H3)4B−)Cp2Fe+ and (3,5(CF3)2C6H3)4B−)Cp*2Fe+. *J. Organomet. Chem.* **2000**, *601* (1), 126–132. https://doi.org/10.1016/S0022-328X(00)00044-9.
(66) Williams, U. J.; Carroll, P. J.; Schelter, E. J. Synthesis and Analysis of a Family of Cerium(IV) Halide and Pseudohalide Compounds. *Inorg. Chem.* **2014**, *53* (12), 6338–6345. https://doi.org/10.1021/ic500969r.
(67) Bayer, U.; Werner, D.; Berkefeld, A.; Maichle-Mössmer, C.; Anwander, R. Cerium–Quinone Redox Couples Put under Scrutiny. *Chem. Sci.* **2021**, *12* (4), 1343–1351. https://doi.org/10.1039/D0SC04489J.
(68) Robinson, J. R.; Booth, C. H.; Carroll, P. J.; Walsh, P. J.; Schelter, E. J. Dimeric Rare-Earth BINOLate Complexes: Activation of 1,4-Benzoquinone through Lewis Acid Promoted Potential Shifts. *Chem. – Eur. J.* **2013**, *19* (19), 5996–6004. https://doi.org/10.1002/chem.201300026.
(69) Werner, D.; Bayer, U.; Schädle, D.; Anwander, R. Emergence of a New [NNN] Pincer Ligand via Si–H Bond Activation and β-Hydride Abstraction at Tetravalent Cerium. *Chem. – Eur. J.* **2020**, *26* (53), 12194–12205. https://doi.org/10.1002/chem.202000625.

(70) Bayer, U.; Werner, D.; Berkefeld, A.; Maichle-Mössmer, C.; Anwander, R. Cerium–Quinone Redox Couples Put under Scrutiny. *Chem. Sci.* **2021**, *12* (4), 1343–1351. https://doi.org/10.1039/D0SC04489J.

(71) Domingos, Â.; Lopes, I.; Waerenborgh, J. C.; Marques, N.; Lin, G. Y.; Zhang, X. W.; Takats, J.; McDonald, R.; Hillier, A. C.; Sella, A.; Elsegood, M. R. J.; Day, V. W. Trapping of Anionic Organic Radicals by (TpMe2)2Ln (Ln = Sm, Eu). *Inorg. Chem.* **2007**, *46* (22), 9415–9424. https://doi.org/10.1021/ic701364k.

Learning is a treasure that will follow its owner everywhere.

Chinese proverb

Chapter II
Photochemical remediation of chlorinated and fluorinated Persistent Organic Pollutants

Introduction 88

I. Dechlorination of inert organochloride compounds 93

a) Activation without irradiation 93

b) Photoinduced degradation 94

1) Photochemical activation of chlorinated substrates 94

2) Degradation and reduction of 2-Cl 98

3) Towards photocatalytic dechlorination of POPs 100

c) Photoinduced Miyaura borylation 100

II. Photochemical activation of C-F bonds 103

References 107

Introduction

Following the exponential increase in industrialisation processes during the 20th century, increasing number of chemicals were synthesized. In particular, Halogen Organic Compounds (HOCs) have been used for a wide variety of applications, ranging from fire retardants (brominated compounds)[1] to pesticides and dielectrics (chlorinated substances), and antiadhesive materials (perfluorinated molecules).[2] Nevertheless, HOCs display many harmful adverse effects on health and environment, reported as early as 1980s, caused by their lipophilicity which tends to facilitate the accumulation in fatty tissues of living organisms and resist biological degradation.[3] The *in-vivo* pollutant concentrations can reach dangerous toxicological thresholds upon chronic exposure (bioaccumulation) or through accumulation in organisms upper in the food chain (biomagnification, see **Figure 79**, left), even if the concentrations in HOC remain below acceptable levels in organisms low in the food chain (see **Figure 79**, right).

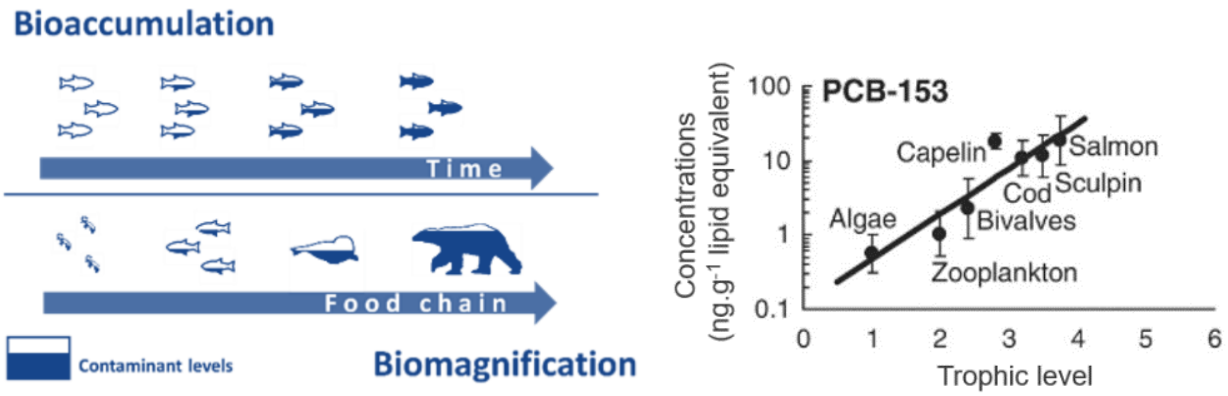

Figure 79. Schematic representations of bioaccumulation and biomagnification processes (left) and evolution of concentration of a polychlorobiphenyl (PCB) at different trophic levels (right). Reproduced from Stockholm Convention[4] and Gobas *et al.*[5]

Most HOCs are labelled as "Contaminants of Emerging Concerns" by experts as they display many negative effects on human health, including cancer, birth defects, immune systems dysfunctions, obesity, lower fertility and specific organ failure among others.[6] Owing to their important persistence, these compounds can slowly volatilise and travel long distances in gaseous form or bound to particles (aerosols), creating accumulation in regions where they were not directly introduced.[5]

Following the growing concern about their omnipresence and toxicity issues, the Rotterdam Convention (on the Prior Informed Consent Procedure for Certain Hazardous Chemicals and Pesticides in International Trade) was signed in 1998 to promote exchange of information regarding hazardous chemicals.[7] Among the 43 families of compounds mentioned, 26 of them belonged to HOCs category.

Three years later, the Stockholm convention (2001) listed a series of Persistent Organic Pollutants (POPs) known as the *dirty dozen* (35 compounds nowadays) to outlaw the use of several particularly harmful anthropogenic substances (see **Figure 80**).[8] The chemicals targeted by the convention had to see their production stopped (Annex A), and/or strictly regulated and used for very specific applications (Annex B), and/or their unintentional generation reduced (Annex C).

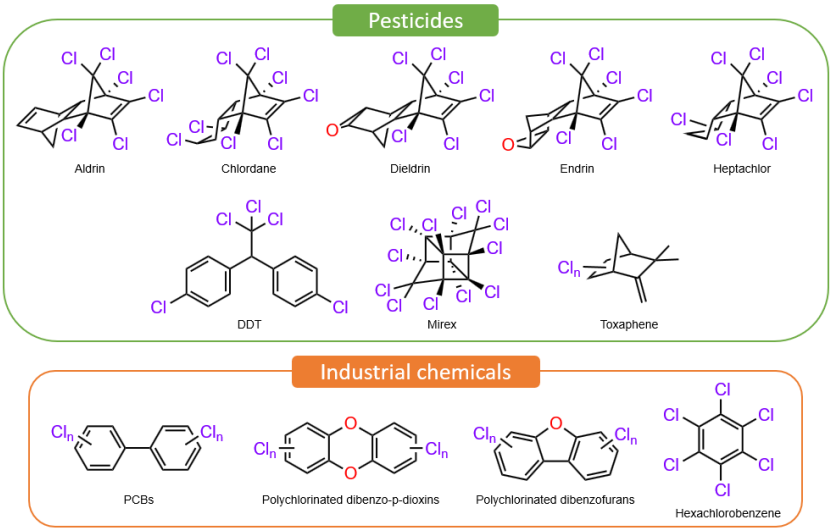

Figure 80. Chemicals (*Dirty dozen*) listed in the initial Stockholm convention (2001)[2]

Article 16 of the Convention moreover required a globalized collection of data to follow their evolution over time, which was monitored by the United Nations Environment Program (UNEP) with different collaborators between 2000 and 2019 in 42 countries from South America, Africa, Asia and Pacific.[9] The reports highlighted a global measurable decrease in POPs levels during the period in both air[10] and human milk,[11] showing a positive effect of the Stockholm convention.

So far, the chemical treatment of POPs in water has been problematic. While conventional water treatment methods by coagulation-flocculation are able to remove high concentrations in pollutants, they struggle to eliminate traces of chemicals. Innovative absorption methods such as Metal-Organic-Frameworks (MOFs)[12] or with biodegradable guar gum and xanthan[13] enable the concentration of problematic substances at low cost, but do not allow for their elimination and also risk undesired desorption on the long term.[14] Several treatment methods including bioremediation,[15] photochemical oxidation using reactive oxygen species[16] and electrochemical oxidations[17] have been investigated,[18] but no system specifically designed to directly reduce these substances has been reported to my knowledge, possibly due to technical limitations to generate strong reductants in water. Therefore, the highly reductive redox potential of **1** under irradiation was envisioned to enable the efficient degradation of such species.

The vast majority of POPs contain several carbon-chloride bonds, which were initially introduced in pesticides to enhance the lipophilicity and the resistance to degradation through hydrolysis and photolysis, owing to a strong C-Cl bond (BDE 394.9 ± 13.4 kJ.mol^{-1})[19] which makes them difficult to reduce (E_{red} < -2.5 V *vs.* Fc/Fc^{+}).[20,21] The high lipophilicity prevented solubilization in water and increased the penetration in living organisms to ensure a long-time effect, but this persistence in the environment and in animals was shown to create ecological and/or health issues among exposed populations. Most of POPs were evaluated by the International Agency for Research on Cancer (IARC) and listed among one of the three major groups of IARC classification (group 1 : known carcinogenic, group 2A : probably carcinogenic, group 2B : possibly carcinogenic, see **Figure 81**).[22–24]

While some methodologies have been investigated to target specifically the degradation of chlorinated POPs in water,[25–28] they form oxidation products of the POPs which can be even more harmful than the initial compound (*e.g.* hexachlorobenzene degraded in pentachlorophenol, a known carcinogen).

Photocatalysis was envisioned as an attractive tool to dehalogenate organochlorinated compounds,[20] but was not extensively targeting *real-life* problematic chemicals as POPs. E. J. Schelter and co-workers already provided a proof of concept to the cerium(III)-catalysed photodehalogenation of many chlorinated derivatives,[29,30] but focused mainly on aryl halides and benzyl halides. Extending the scope to

the reduction of alkyl chlorides by **1** was an important target towards the degradation of POPs, as many of them contain several alkyl-chloride bonds (*e.g.* Aldrin-related compounds).

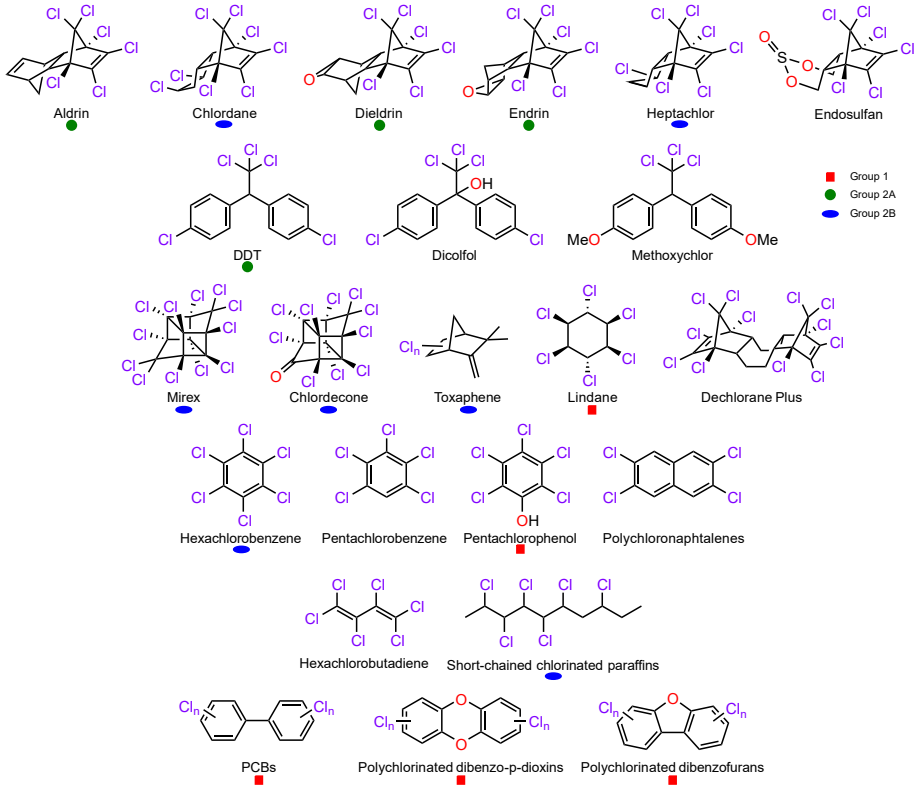

Figure 81. Chlorinated Persistent Organic Pollutants defined by the revised Stockholm Convention (2023).[2] Carcinogenicity data were obtained from IARC[31]

Per- and polyfluoroalkyl (PFASs) are a group of about 4700 anthropogenic chemicals containing partially or completely fluorinated carbon chains of different lengths (see **Figure 79**) used in a variety of applications, ranging from cosmetics[32] to food packaging,[33] used since 1950s for their interesting antiadhesive and waterproofing properties (see **Figure 83**).[34] The harmful potential on health of PFASs was known since late 1980s[35] from industrial studies led by 3M®[36,37] which highlighted the carcinogenicity, genotoxicity and immunotoxicity of several PFASs.[35,38] Recent IARC reports from 2023 classified two surfactants used in firefighting foam compounds, perfluorooctanesulfonic acid (PFOS) and perfluorooctanoic acid (PFOA, see **Figure 82**) in respectively group 2B (possibly carcinogenic) and 1 (carcinogenic), especially towards prostate, testicular, liver and kidney cancers,[4,39] and could induce developmental misfunctions on foetuses or breastfed babies.

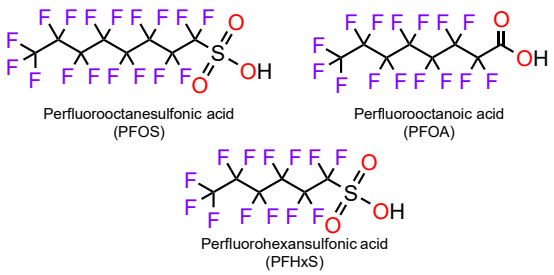

Figure 82. Most commonly encountered PFASs

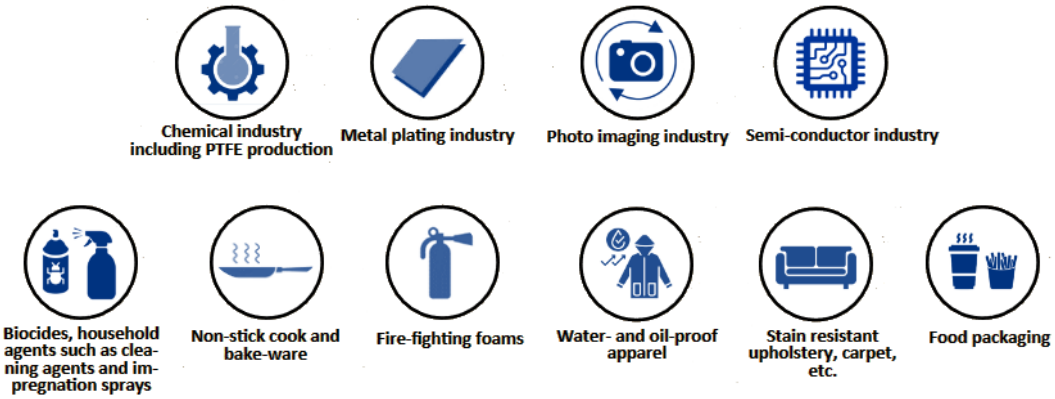

Figure 83. Area of use for PFAS substances. Reproduced from UNEP[40]

PFASs tend to accumulate in the environment due to their extreme resistance to almost all degradation pathways due to the very strong C-F bond (513.8 ± 10.0 $kJ.mol^{-1}$),[19] which earned them the name of *eternal pollutants*.[41,42] They are most exclusively transformed into per- and polyfluoroalkyl acids (PFAAs), which can escape water treatment facilities for short-chained PFAAs.[43] This problem of water contamination is especially serious as a study conducted in 2016 showed that more than 6 million of US residents were exposed to drinking water with PFASs levels higher than US Environmental Protection Agency (EPA) standards (70 $ng.L^{-1}$), up to 30,000 times higher.[44] The treatment cost for PFASs-contaminated water is moreover important, as the US Air Force estimated a 2-billion dollar cost to clean up PFASs-contaminated water.[45]

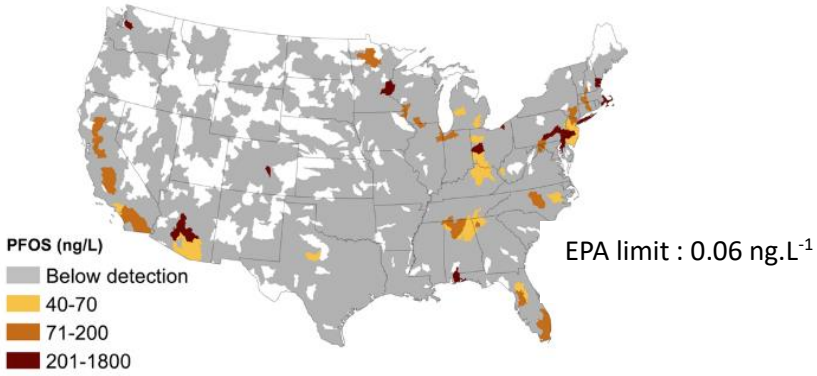

Figure 84. Concentrations of perfluorooctanesulfonic acid (PFOS) in different areas in the United States. Reproduced from Sunderland *el al.*[44], and EPA limit value was obtained from Federal Register[46]

As well as chlorinated POPs, the widespread presence of PFASs is especially concerning regarding the low environmental degradability of the compounds, and difficulty of treatment. Most perfluorinated wastes are nowadays destroyed by incineration, which can produce harmful incomplete combustion products.[47]

Current non-chemical treatment procedures include classical absorption, filtration, bioremediation and sonochemical degradation among others.[48] Reported chemical degradation of PFASs mostly focused on the oxidative degradation, using high valent iron species or Reactive Oxygen Species (ROS, *e.g.* hydroxyl radical $HO^{\bullet}$) through Fenton-like reaction. Photolytic degradation of PFASs in contaminated water was also studied in direct photolysis (overall slow), photochemical oxidation using highly reactive ROS in Fenton-like reactions and persulfate radicals or with TiO_2.[49]

Reduction of PFASs was less investigated due to the need for highly reductive species to break the strong C-F bonds. Main strategies include reduction by zero valent iron at high temperatures (> 350 °C), sonochemical and electrochemical degradations.[48,50,51] Photoinduced reduction pathways have also been reported through the generation of a solvated electron in water from the oxidation of iodide anion under

UV irradiation.[52] Operational costs of these photochemical methods could nonetheless reach important amounts : for about 4000 L of wastewater, the costs ranged from 82 $ by UV/H_2O_2 system, to 5000 $ for Fenton-like system and 2000 $ for UV-TIO_2.[53]

Most investigations nevertheless use concentrations order of magnitudes higher (µg to mg.L^{-1}) than legal thresholds and actual PFASs concentrations (50 ng-µg.L^{-1}), which raises the question of applicability of these methods to removal of PFAS traces.

Following the finding of PFASs' omnipresence in the environment in early 2000s and growing concerns about related health issues, several perfluorinated compounds were added to the Stockholm Convention in 2009 as POPs in Annex A (elimination), with the latest addition in 2022 (perfluorohexanesulfonic acid, PFHXs).[2] Initiatives to raise awareness about the danger of PFASs were also taken, as the Madrid Statement[54] signed in 2015 by over 200 scientists.

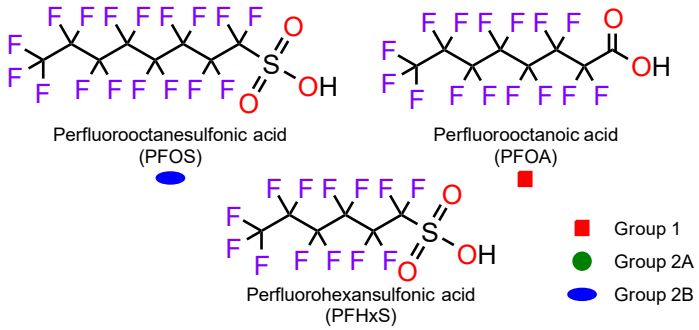

Figure 85. PFASs listed on the Stockholm Convention[2]

Considering the highly reducing potential of **1** under visible-light irradiation (-3.2 V *vs.* Fc/Fc^+), we envisioned that the photodehalogenation of both chlorinated and fluorinated substrates could be achieved with our complex.

I. Dechlorination of inert organochloride compounds

As initial scope, we targeted the photochemical reduction of different families of compounds, including unactivated chloroalkanes alkanes on primary, secondary and tertiary carbons including polyvinylchloride (PVC), and a series of para-substituted chloroarenes (see **Figure 86**).

The reactivity was first investigated in C_6D_6 given the simple NMR signature of the solvent and to ensure a good solubilisation of apolar substrates. Kessil PR160L-427 was chosen as irradiation source, as it was a powerful LED source emitting around 427 nm, displaying the best overlap with absorption band of **1** (see **Figure S1**). Prior to irradiation, a ^{1}H NMR spectrum of the mixture between **1** and the substrate was taken 30 minutes after addition to ensure that no reaction was occurring without irradiation.

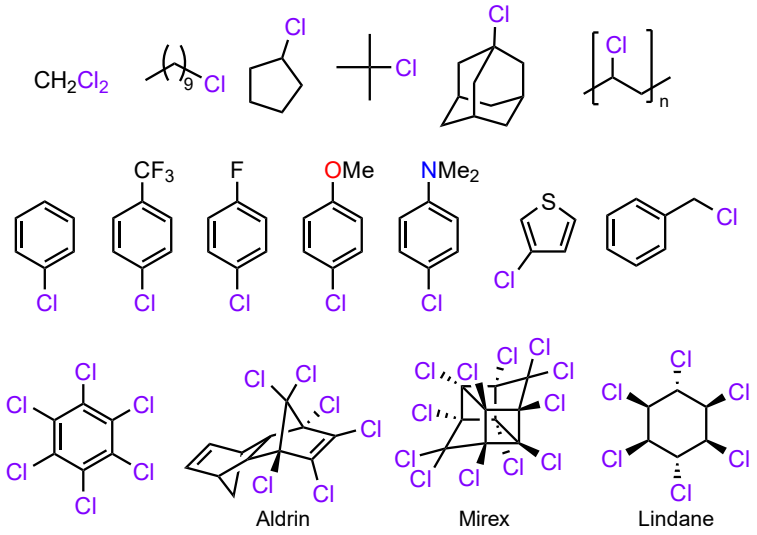

Figure 86. Scope of chlorinated substrates for the dehalogenation reaction

a) Activation without irradiation

No reaction occurred in the dark for most substrates, except for benzyl chloride which led to a change in colour from yellow to deep purple within 5 minutes. ^{1}H NMR spectrum showed the slow appearance of **2-Cl**.

This result was promising, given that cerium(III) hexachlorocerate could activate benzyl chloride only in the presence of irradiation.[55] The important difference between the redox potentials of **1** (-0.5 V *vs.* Fc/Fc$^+$) and $PhCH_2Cl$ (peak potential E_p = -2.56 V *vs.* Fc/Fc$^+$ in MeCN),[56] could indicate an inner sphere electron transfer in this case. 1,2-diphenylethane ($PhCH_2CH_2Ph$) was detected in gas chromatography-mass spectrometry (GC-MS), which was formed by the dimerization of two benzyl radicals generated by SET from **1** (see **Figure 87**).

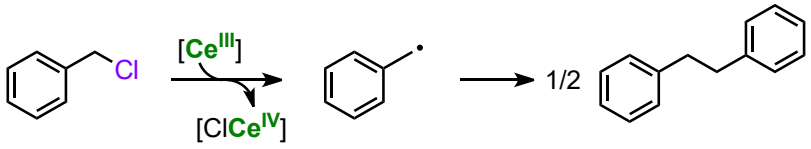

Figure 87. Mechanism of benzyl chloride reduction by **1** and subsequent formation of 1,2-diphenylethane

The oxidation of **1** by benzyl chloride was especially interesting as it opened a convenient synthetic pathway to synthesize **2-Cl** in pentane without purification issues. 1,2-diphenylethane and unreacted benzyl chloride could be removed by washing with MeCN and afford pure **2-Cl** as purple solid in medium yields (55%). Benzyl bromide was also envisioned as a substitute to CBr_4 for the synthesis of **2-Br** as it is even more easily reduced than benzyl chloride (E_p = -2.11 *vs.* Fc/Fc$^+$ in MeCN).[56] Similarly, **2-Br** was successfully obtained as deep purple powder (66%) using the same protocol as described for **2-Cl** (see **Figure 88**).

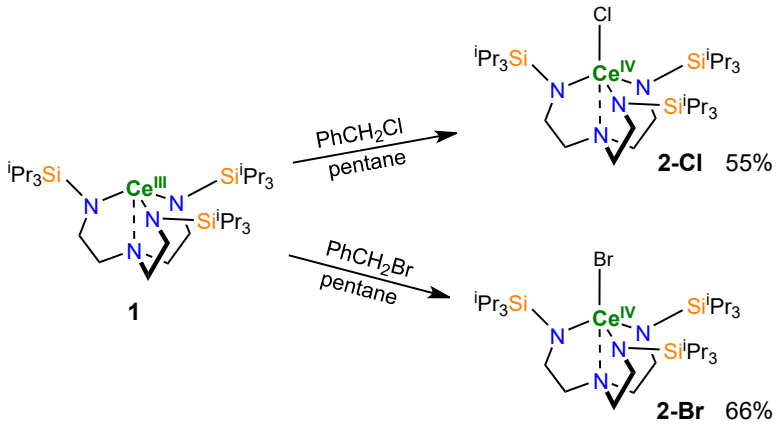

Figure 88. New synthetic pathways for **2-Cl** and **2-Br**

b) Photoinduced degradation

1) Photochemical activation of chlorinated substrates

Pleasingly, C_6D_6 solutions of **1** in presence of all substrates in **Figure 86** led to a change in colour after few minutes of irradiation at 427 nm (*cf.* **Figure 89**). The oxidation of **1** was confirmed by detection of the distinct signature of **2-Cl** by ^{1}H NMR spectroscopy, but quantification of most of products in **Figure 86** in ^{1}H NMR spectroscopy was difficult due to many overlaps with other peaks both for the reagent and the product(s).

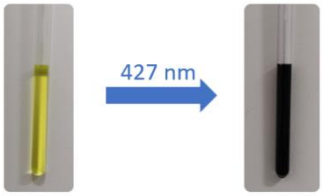

Figure 89. Reaction between **1** and chlorinated substrates before (left) and after irradiation (right)

In order to find a suitable way to quantify the reduction products, chlorobenzene was chosen as optimization candidate. GC-MS analysis of the reaction medium after overnight photoirradiation of a solution of **1** and chlorobenzene in C_6D_6 highlighted the formation of a hemi-deuterated biphenyl product in **Figure 90**. The dimer would likely arise from the addition of an aryl radical on C_6D_6, formally releasing a deuterium radical D$^\bullet$ (see **Figure 90**). The detection of this product was in line with the report from Schelter and co-workers of catalytic arylation of 4-fluorobromobenzene and 4-fluoroiodobenzene with $Ce^{III}(HMDS)_3$ **G0** in benzene under UV irradiation for 6 days.[29]

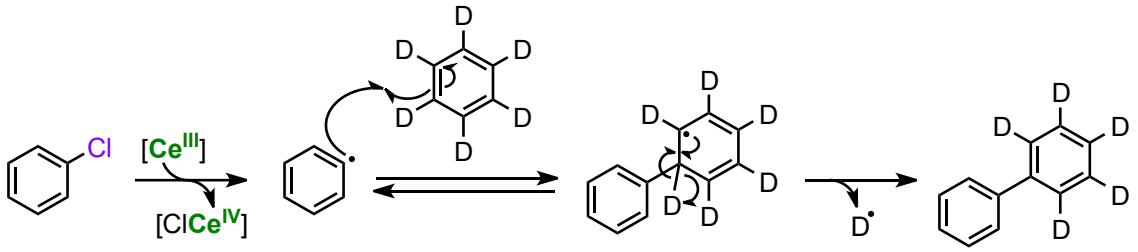

Figure 90. Possible mechanism of C_6D_6 activation by an aryl radical generated through the photochemical reduction of chlorobenzene by **1**

To confirm that the activation of chlorobenzene was proceeding through SET, radical clock experiments were carried out. Photoirradiation of a solution of **1** and 6-bromo-hex-1-ene in C_6D_6 did not lead to the cyclization product expected after formation of the corresponding alkyl radical. Nevertheless, changing the substrate to 2-allyloxychlorobenzene and the solvent to THF-d_8 in the presence of dihydroanthracene (DHA) allowed for the detection of the cyclization product depicted in **Figure 91** in ^{1}H NMR spectroscopy (see **Figure S96**), formed by thermodynamically favoured 5-exo cyclisation of the aryl radical (Baldwin's rules).[57]

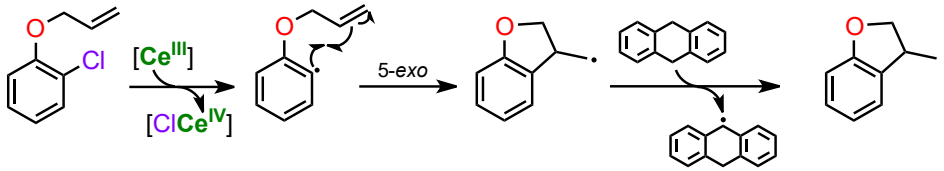

Figure 91. Radical clock experiment with 2-allyloxychlorobenzene in the presence of DHA in THF-d_8

As no chelation was detected by ^{1}H NMR both in C_6D_6 and THF-d_8, and no stable structure could be calculated in DFT when the coordination of chlorobenzene was forced, the electron transfer was hypothesized to occur by outer sphere transfer. TDDFT calculations on a system made up with **1** and an uncoordinated chlorobenzene found a transition at 407 nm that corresponded to an electron transfer from a pure metal orbital to the antibonding σ* orbital of the carbon-chloride bond (see **Figure 92**).

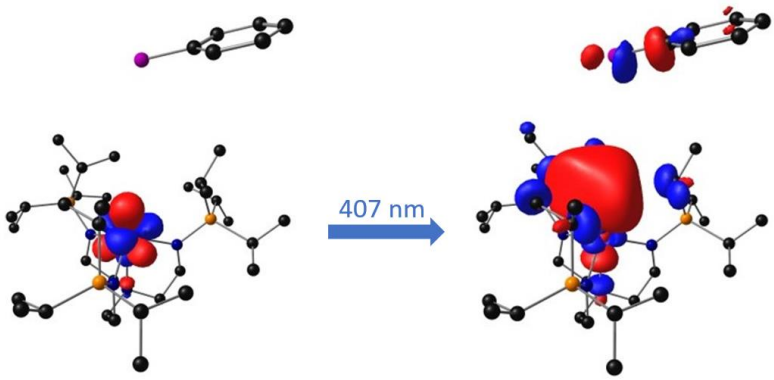

Figure 92. TDDFT transition calculated on a system made up with **1** and an uncoordinated chlorobenzene. Molecular orbitals plotted by L.M. and S.C.

Assuming that an outer-sphere electron transfer takes place, the activation of the carbon-chloride bond might occur first through the acceptance of the electron forming $PhCl^{\bullet -}$, followed by its heterolytic cleavage to form a chloride anion (which coordinates to $Ce^{IV}TREN^{TIPS}$ to form **2-Cl**) and an aryl radical, similar to electrochemical mechanistic studies.[58,59]

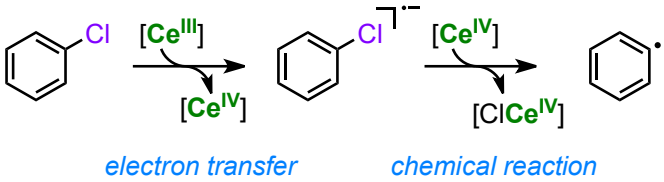

Figure 93. Possible activation mechanism (EC) of chlorobenzene by **1**

Given that the dehalogenation of HOCs was targeted, the arylation of chloroarenes was not further explored. To prevent this unproductive reaction, solvent was changed to THF-d_8 which has a lower BDE than benzene (385 kJ.mol^{-1} for THF *vs.* 472 kJ.mol^{-1} for benzene),[60] but could *a priori* prevent undesired addition from aryl radicals to THF due to polarity mismatching of the substrates.[61]

Upon testing the reactivity of the chlorinated molecules shown in **Figure 86**, the same identification issue of the organic products persisted in the monitoring of the reaction by ^{1}H NMR spectroscopy in THF-d_8. Attempts to quantify the products by gas chromatography with a flame ionization detector (GC-FID) were unsuccessful due to a non-linearity response of the detector for many substrates within the scale of the reaction.

In light of mechanistic evidence of the chlorinated substrate activation by SET, it was decided to follow the evolutions of **1** and **2-Cl** (referenced to trimethoxybenzene) to compare the reactivity with the different substrates, considering that the formation of one molecule of **2-Cl** corresponded to the

consumption of one molecule of substrate. It is important underlining that this methodology is an approximation.

To limit possible solvent activation, tributyltin hydride (Bu_3SnH) was added as a hydrogen donor due to its weak Sn-H bond BDE (309 $kJ.mol^{-1}$)[62] quenching the aryl/alkyl radical formed and to confirm concomitantly its formation by detection of hexabutylditin ($Bu_3Sn\text{-}SnBu_3$) in GC-MS, formed by dimerization of two $Bu_3Sn^{\bullet}$ radicals. The possibility of a radical chain reaction was investigated for every substrate by letting the reaction medium in the dark overnight after 1 h 20 of irradiation prior to restarting irradiation (*start and stop* experiments), in order to quantify the evolution of the species overnight.

Interestingly, all substrates were activated upon significantly shorter irradiation compared to the reports of Schelter and co-workers (24 h to several days),[29,30,55] possibly owing to a better solubility of the compounds. Hexabutylditin as well as the dehalogenation product were detected upon GC-MS analysis after each reaction, and no significant evolution of the quantities of **1** and **2-Cl** were observed after overnight storage in the dark, except a small decrease in **2-Cl** which was attributed to temperature decomposition.

Among the series of alkane compounds (see **Figure 94**), no clear reactivity trend could be identified for different substitution levels of the carbon bearing the chloride. Dichloromethane was activated faster than chlorodecane, and formed small amounts of ethylene. PVC was also activated within short times under the studied conditions, and significantly faster than the photoinduced reduction of PVC by a cerium(III) sandwich complex with dibenzyl magnesium(II) reported by Arnold and co-workers (24 h).[63] At the end of the reaction, a transparent elastic solid was obtained.

As observed for chloroadamantane and dichloromethane, the quantity of **2-Cl** (red curves on **Figure 94**) slowly decreased upon long irradiation durations in favour of H_3TREN^{TIPS}, indicating a degradation of **2-Cl**. The degradation of **2-Cl** will be discussed later in this part.

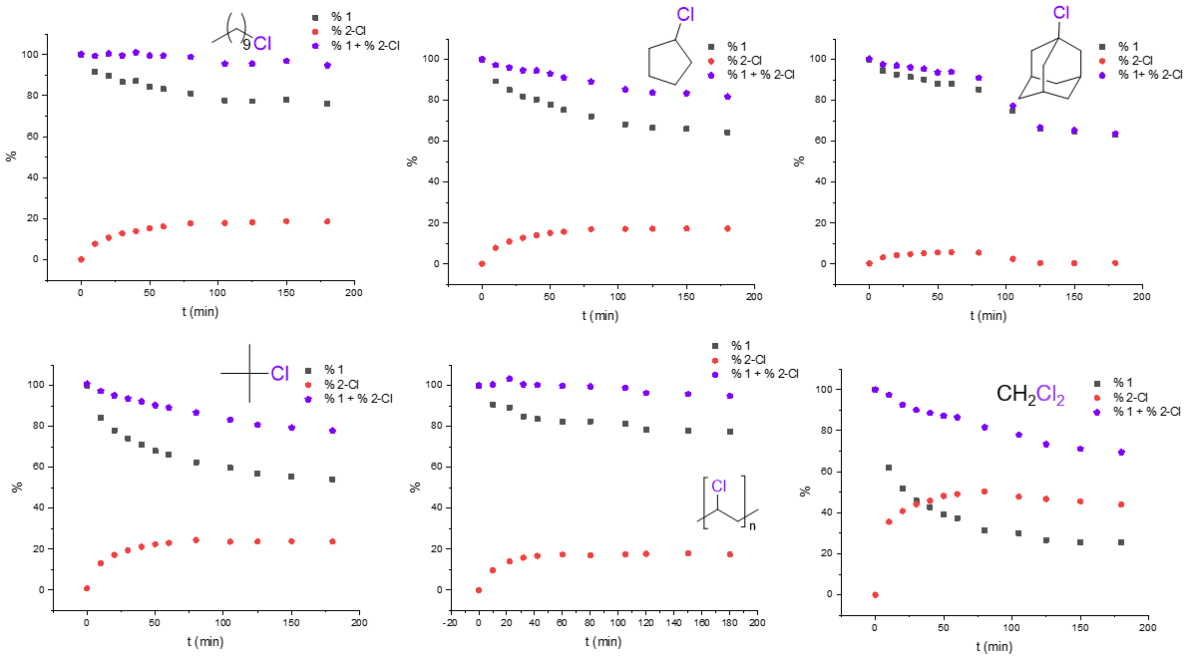

Figure 94. Kinetic studies of the photochemical reduction of alkyl chlorides at 427 nm by **1** in THF-d_8

Chloroarene derivatives were overall activated more slowly than chloroalkanes. A small negative trend could be identified between the electron donating ability of the para-group and the speed of the reduction : the more donating group, the slower the activation (see **Figure 95**).

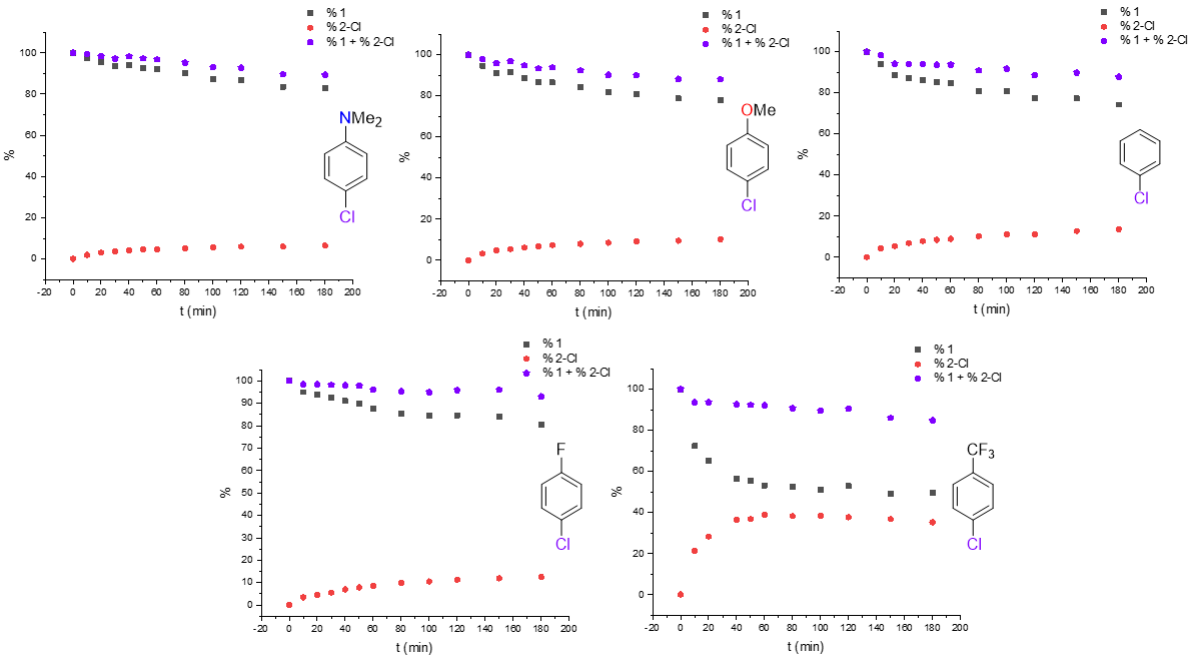

Figure 95. Kinetic studies of the photochemical reduction of aryl chlorides at 427 nm by **1** in THF-d_8

This trend could be explained in the frame of the Marcus theory for electron transfer.[64] Assuming an outer-sphere electron transfer between **1** and the halide derivative (RX), the kinetic constant of the redox reaction k_{act} follows the Arrhenius law :

$$k_{act} = A.e^{\frac{-\Delta G^{\ddagger}}{RT}}$$

where $\Delta G^{\ddagger}$ is the free enthalpy of the redox reaction, A a constant, R the gas constant (6.314 J.K^{-1}.mol^{-1}) and T the temperature in Kelvin. $\Delta G^{\ddagger}$ is linked to the solvent reorganization energy λ_0 and the free enthalpy change $\Delta G°$:

$$\Delta G^{\ddagger} = \frac{(\lambda_0 + \Delta G°)^2}{4\lambda_0}$$

Assuming the reorganization of solvent around the different chloroarene derivatives is similar, the difference between the reduction kinetics (k_{act}) of two chloroaryl derivatives would therefore be dictated by the difference in free enthalpy change $\Delta G°$, which is linked to the redox potentials of the substrates ($\Delta G° = -nFE°$ where n is the number of electrons exchanged, F the Faraday constant $F = 96485\ C$ and $E°$ the standard redox potential of the species, here $RX^{\bullet -}$/RX). $\Delta G°$ therefore depends to the stability of the radical anion formed, which is influenced by electron-withdrawing or donating nature of the group in the para position in the series of chloroarene compounds studied here. To confirm this analysis, determination of the redox potentials of the chloroarene studied here would be interesting, as well as more in depth electrochemical studies to confirm the stepwise EC mechanism (electron transfer followed by chemical reaction) postulated in **Figure 93**.

Finally, the reactivity of **1** was investigated on chlorinated POPs. Pleasingly, all four POPs studied (Aldrin, Mirex, Lindane and hexachlorobenzene) were rapidly degraded by **1** under irradiation at 427 nm. After 1 h of irradiation, a minimum of 50% of all four pesticides were degraded, which is particularly faster than all other substrates presented previously, probably caused by the numerous chloride atoms on each POP compound. Neither the nature of the products nor the selectivity have yet been elucidated (except for the reduction of hexachlorobenzene which formed pentachlorobenzene), but are under investigation using GC-MS.

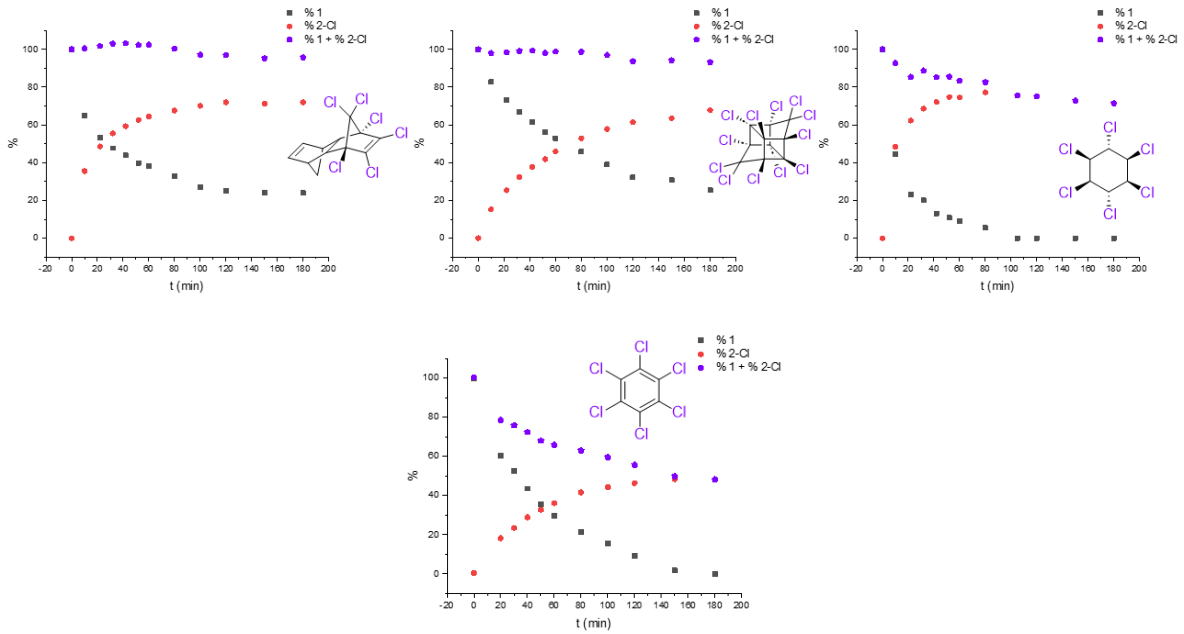

Figure 96. Kinetic studies of the photochemical reduction of chlorinated POPs (left to right, top to bottom : Aldrin, Mirex, Lindane, hexachlorobenzene) at 427 nm by **1** in THF-d_8

2) Degradation and reduction of 2-Cl

As noticed earlier, the quantity of **2-Cl** was slowly decreasing under irradiation, which could correspond to another LMCT transition than the one presented in **Figure 74** (TREN to cerium) that would here take place from the chloride to the cerium. This would lead to a LIH, forming a chlorine radical and regenerating **1**. Nevertheless, the overall cerium amount decreases as shown in each graph by showing the sum of **1** and **2-Cl**, decreasing slowly over time, which could correspond to a reaction with another reactive molecule (*e.g.* a radical).

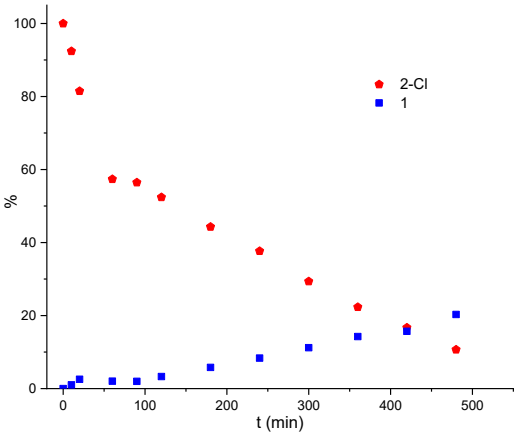

Figure 97. Photochemical degradation of **2-Cl**. NB : between 20 and 60 min, and 240 and 300 min of irradiation, the NMR tube was stored at 0 °C overnight

To confirm this hypothesis, a solution of **2-Cl** in THF-d_8 was irradiated and monitored by ^{1}H NMR spectroscopy (see **Figure 97**). The quantity of **2-Cl** was decreasing over long irradiation durations, and small quantities of **1** slowly appeared in low yield. This reaction would be consistent with the hypothesis of a LIH of cerium-chloride bond, but the overall decrease in cerium quantity (**1** + **2-Cl**) over time highlighted the poor efficiency of this kind of reactivity.

Attempts to trap the chlorine radical or to indirectly detect its formation using substrates prone to HAT (having low C-H BDE) such as DHA (about 326 kJ.mol^{-1}), or to directly detect its formation by TAS were unsuccessful.

In order to progress towards the catalytic dechlorination of POPs (see **Figure 98**), the reduction of **2-Cl** was studied. Silane reagents (triethylsilane, tris(trimethylsilyl)silane (TTMSS) and triphenylsilane) were first considered as reductants, but no reduction of **2-Cl** was observed.

As shown by Schelter and co-workers,[29,65] silylamides were able to reduce cerium(IV) complexes back into cerium(III). A small scope of amide reagents was chosen, including sodium amide, lithium

diisopropyl amide (LDA), lithium tertbutyl amide, lithium diethylamide and two HMDS salts (LiHMDS and KHMDS) both in C_6D_6 and THF-d_8.

All reagents (except sodium amide) were shown to rapidly reduce **2-Cl** in **1** in THF-d_8 (within minutes), while only some of them worked slowly in C_6D_6 (LDA, LiHMDS, KHMDS), possibly caused by their low solubility in C_6D_6. Nevertheless, most reductants did not allow for good yields in **1** except for LDA and LiHMDS, which were considered as suitable candidates for the following reactions. Given the better solubility of LiHMDS in C_6D_6 and THF-d_8, it was favoured over LDA.

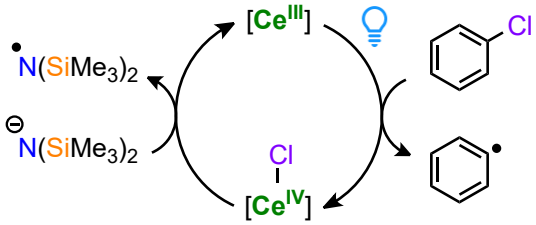

Figure 98. Catalytic cycle of the chloroarene activation and reduction by LiHMDS

3) Towards photocatalytic dechlorination of POPs

In order to avoid the use of toxic tin reagents, the scope of hydrogen donors for the dehalogenation reaction was studied. Silane reagents were again considered as interesting partners in this reaction given the low BDE of the Si-H bond (330 kJ.mol^{-1} in $(TMS)_3Si$-H, 371 kJ.mol^{-1} in Ph_3Si-H, 376 kJ.mol^{-1} in Et_3Si-H).[66] Considering that the silicon-centred radical formed after HAT should be fairly nucleophilic,[61] I hypothesized that it might be able to reduce **2-Cl** back into **1**. Two examples of such behaviour were reported in photochemistry, where $(TMS)_3Si^{\bullet}$ was used to reduce iridium(IV)[67] and ruthenium(III)[68] photocatalysts into the starting complexes.[69] With the help of Bich Tuyen Phung (post-doctorate student), we investigated the feasibility of this reaction.

Pleasingly, the reaction was shown to work catalytically at 5 mol% in **1** on various polychlorinated substrates (1,4-dichlorobenzene, Lindane, hexachlorobenzene) in THF-d_8 (see **Figure 99**). The different silane reagents were shown to work in the catalytic reaction, with an increased activity for TTMSS. Formation of Cl-Si(TMS)$_3$ was confirmed by ^{1}H NMR spectroscopy, as well as traces of the dimer $(TMS)_3$Si-Si(TMS)$_3$.

Reduction step from **2-Cl** to **1** was studied by irradiating **2-Cl** in the presence of TTMSS, which led to a decrease in **2-Cl** but neither to a consumption of TTMSS nor a detection of $(TMS)_3$Si-Si(TMS)$_3$ or Cl-Si(TMS)$_3$. This should indicate that the silicon-centred radical was not formed by photolysis of cerium(IV)-chloride bond, and that no HAT reaction was taking place between putative $Cl^{\bullet}$ and TTMSS. No cross-coupling product between the aryl radical and $(TMS)_3Si^{\bullet}$ was detected.

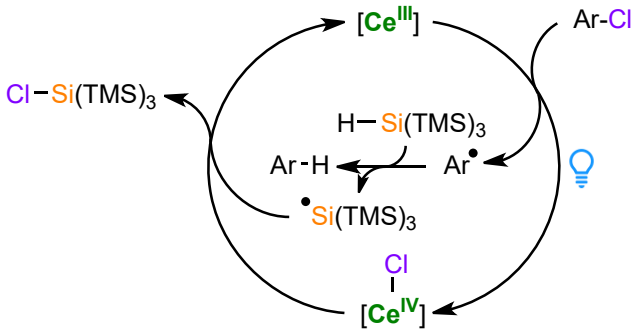

Figure 99. Catalytic cycle of chlorinated substrates photochemical activation by **1** in with tris(trimethylsilyl)silane

Several investigations on the trapping of the aryl radical were conducted with triethylphosphite, trimethylphosphite and several alkenes, but no significant result could be extracted from these experiments. This reactivity is still in need for further investigations to fully develop its potential for the reduction of POPs in mild conditions.

c) Photoinduced Miyaura borylation

Following the report of Schelter and co-workers on the photoinduced Miyaura borylation by cerium(III) hexachlorocerate,[30] diboron reagents were considered as trapping agents for the generated aryl radical.

Irradiation of equimolar mixtures of **1**, chlorobenzene and bispinacolato-diboron (B_2pin_2) at 427 nm in THF-d_8 allowed for the detection of phenylboronic acid pinacol ester (PhBpin), evidencing the feasibility of the reaction. To ensure the fast reduction of **2-Cl**, LiHMDS was chosen on the base of previous studies due to its solubility in THF-d_8.

The reaction was optimized on 4-chloroanisole with LiHMDS and B_2pin_2 in THF-d_8 at 0.5 M on 0.4 mmol scale, considering that it was one of the most difficult chloroarene substrate to activate in our scope. Monitoring was done by ^{1}H NMR spectroscopy, given that GC-FID analysis was hampered by the same non-

linearity issue as reported previously. Overall, the optimisation process suffered from several reproducibility issues, and many experiments had to be redone to ensure fairly reproducible results. Overall, the reaction afforded approximately 50% of borylated product after irradiation for 5 h in the standard conditions with more than 90% conversion.

The nature of the reductant was first screened between LiHMDS, NaHMDS and KHMDS. Due to the poor solubility of the two latter reagents, the yields of MeOPhBpin were much lower than for LiHMDS (15 and 13% for KHMDS and NaHMDS *vs.* 47% for LiHMDS). Excess zinc powder was also tested, but afforded very low yields (10% after 6 h). Two other diboron reagents were studied, namely bis(neopentyl glycolato)diboron B_2neo_2 and bis(catecholato)diboron B_2cat_2. For B_2neo_2, the yield was lower (19%) than for B_2pin_2, and B_2cat_2 gave comparable results (47%) to B_2pin_2.

Optimisation of the catalyst loading showed similar kinetics and yields between 1% and 10% of **1**. At 0.5%, the reaction was slower and final yield slightly smaller. A small positive correlation was found between the concentration of chlorinated derivative and the yield, increasing from 0.25 to 0.75 M. On the contrary, adding more LiHMDS decreased the yield, possible due to side reactivity of the aminyl radical $^{\bullet}N(HMDS)_2$. Interestingly, substoichiometric amounts of LiHMDS were tested, and did not lead to a significant decrease in yields for 0.5 and 0.7 equivalents (respectively 40 and 51% *vs.* 47% for one equivalent).

Overall, the best conditions were chosen to 2 mol% of **1**, 0.5 M of halide derivative and one equivalent of LiHMDS and B_2pin_2.

Given that preliminary borylation tests on chloroalkanes were unfruitful, the scope was limited to chloroarenes (see **Figure 100**), with substrates bearing different types of substituents (electron donating or withdrawing groups) in para position as well as three different isomers of chloroanisole and 2-chloro-meta-xylene to assess a possible influence of sterics on the electron transfer.

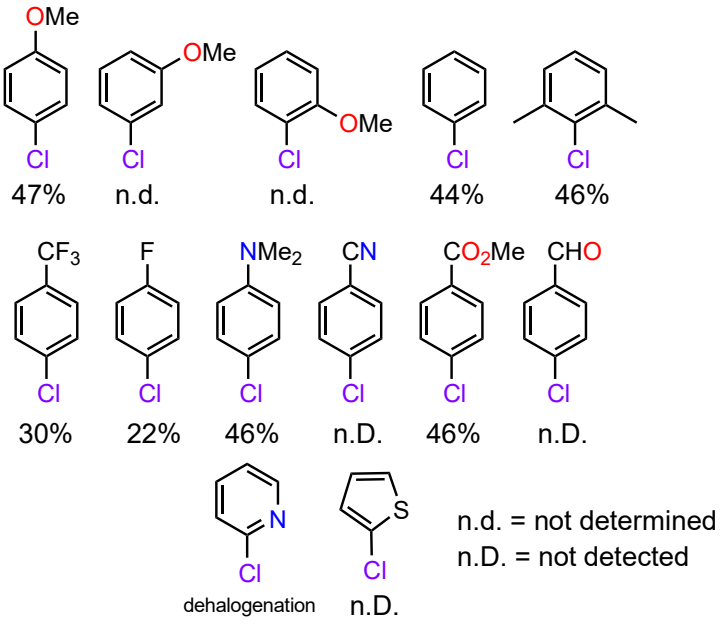

Figure 100. Scope of substrates considered for photoinduced Miyaura borylation

Unfortunately, several substrates could not be analysed by ^1H NMR spectroscopy due to overlaps between the signal of the reagent and the hypothetic product (see **Figure 100**).

NMR yields were similar for most activated substrates, even for challenging 4-chloro-dimethylaniline, but significantly lower for 4-fluoro-chlorobenzene and 4-chloro-trifluoromethyl-benzene (22 and 30% respectively). 4-chloro-benzonitrile and 4-chloro-benzaldehyde were not consumed by **1**

under irradiation, which is surprising considering the additional stabilization of the radical on the aromatic cycle induced by the electron withdrawing groups.

Several substrates did not react at all for the borylation reaction. For 2-chlorothiophene, overnight storage of the mixture of all reagents in THF-d_8 formed a white powder prior to irradiation, which prevented clear analysis of ^{1}H NMR spectrum. Upon irradiation, the colour faintly turned to light purple, but no signal corresponding to a possible borylated product could be identified. For 2-chloropyridine, only dehalogenation could be detected by ^{1}H NMR spectroscopy.

For each substrate that was successfully borylated, GC-MS analysis after reaction indicated the formation of BpinHMDS (see **Figure 101**), that was initially thought to proceed through a nucleophilic activation of B_2pin_2 by LiHMDS. To test this hypothesis, both reagents were mixed in THF-d_8, but no change could be noticed in the ^{1}H NMR spectrum after several days. Analysis of this reaction by GC-MS neither led to the detection of BpinHMDS, indicating that the product was formed during the borylation reaction. This product could therefore be generated either by homocoupling of two •Bpin and HMDS• radicals (unlikely considering the concentration), or by the addition of HMDS• radical to B_2pin_2 creating BpinHMDS and •Bpin.

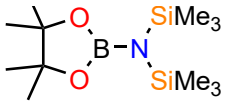

Figure 101. Structure of BpinHMDS

Interestingly, $PhN(TMS)_2$ was reproducibly detected by GC-MS from the borylation reaction of chlorobenzene (see **Figure 102**), which could be formed by a reaction with an aminyl radicals to form a product of a "photoinduced Buchwald-Hartwig amination". To obtain the ^{1}H NMR signature of this compound, $PhN(TMS)_2$ was synthesized from distilled aniline by two successive deprotonation-nucleophilic substitutions cycles with ^{n}BuLi and TMS-Cl in THF at -78 °C. ^{1}H NMR analysis of the product after distillation under reduced pressure did not match with other peaks in the ^{1}H NMR spectrum obtained after the borylation reaction with chlorobenzene in the standard conditions, which indicated that the product was present in very low quantity.

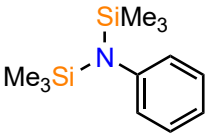

Figure 102. Structure of $PhN(TMS)_2$

No detailed mechanistic analysis was performed, precluding a detailed discussion on the borylation mechanism. Considering the results obtained in this part, a simplified version of the mechanism is proposed in **Figure 103**.

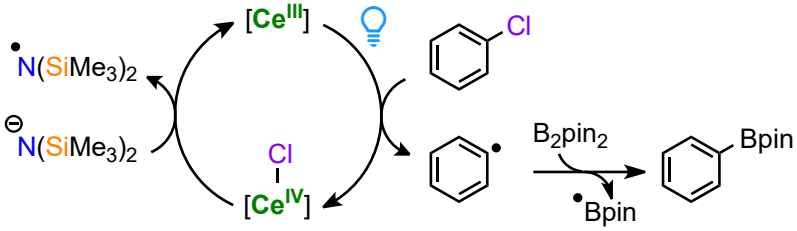

Figure 103. Simplified Miyaura borylation mechanism

Further optimizations should be carried on this reaction to enhance the reactivity and reach higher yields while addressing reproducibility issues.

Considering the encouraging results on chlorinated POPs and non-activated chlorinated substrates activation, photochemical reduction of highly challenging fluorinated substrates was targeted.

II. Photochemical activation of C-F bonds

C-F activation by lanthanide complexes is a well-known reactivity.[70–72] Considering the high reducing power of cerium(III) hexachlorocerate under irradiation (-3.45 V *vs.* Fc/Fc^+ in MeCN),[55] the absence of example of defluorination reactivity to the best of my knowledge is very surprising. The opportunity to elucidate this reactivity with **1** was therefore taken.

Fluorinated compounds are overall harder to reduce than their chlorinated counterparts : fluorobenzene (-3.28 V *vs.* Fc/Fc^+)[73] is more difficult to reduce than chlorobenzene (-3.13 V, see **Figure 104**).[58]

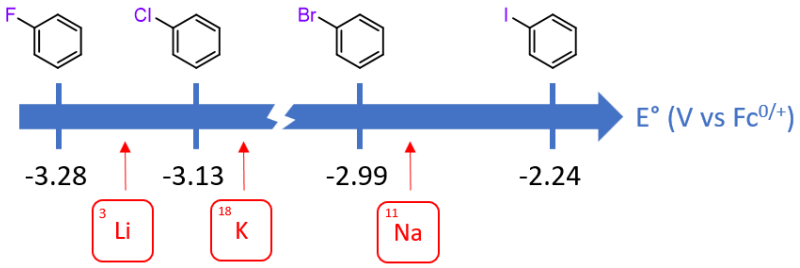

Figure 104. Redox potential scale of halobenzenes referenced to Fc/Fc^+. Values were obtained from Grimshaw and Savéant *et al.*[58,73]

In order to study the possible C-F activation of fluorinated substrates with **1** under irradiation, a scope mainly centred around aromatic fluorinated derivatives (see **Figure 105**) was chosen, considering the higher BDE for C-F bond in fluorobenzene (532 $kJ.mol^{-1}$) than in 2-fluoropropane (462 $kJ.mol^{-1}$).[74] A series of polyfluorinated fluorobenzenes was also contemplated, to compare the possible differences in kinetics with different substitution levels. Activation of poly-trifluoromethyl aromatic compounds was also investigated, owing to the very interesting potential of selective benzylic C-F functionalization.

PFOS, PFOA and PFHxs could not be directly investigated in the dehalogenation reactivity, due to the acidity of carboxylic and sulfonic acid moieties, and perfluorononane was therefore chosen as alternative due to its similar carbon chain length to PFOS and PFOA.

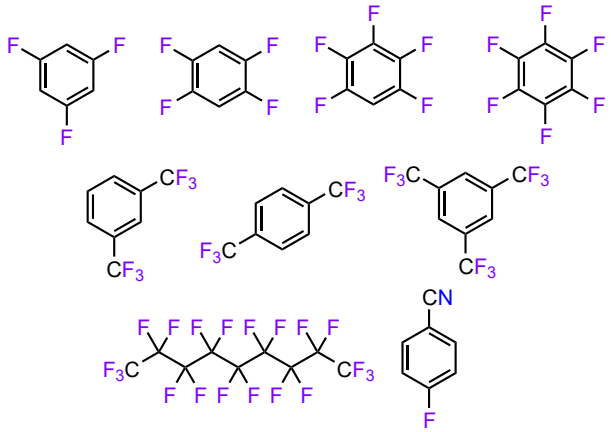

Figure 105. Scope of fluorinated substrates for the photoinduced dehalogenation with **1**

The defluorination reactivity was studied in the same conditions as the dechlorination of POPs, and followed in tandem ^1H NMR and ^{19}F NMR during irradiation at 427 nm for most substrates. Similar one-to-one conversion hypothesis from one molecule of substrate to one **2-F** was assumed. Analysis of the products by GC-MS was hampered by the volatility of both substrates and products, but ^{19}F NMR was proven very useful towards the attribution of several new compounds. As fluorobenzene and trifluoromethylbenzene did not react with **1** under irradiation, ^{19}F NMR quantification with these substrates

was envisioned. Nevertheless, quantification attempts afforded inconsistent results even with long relaxation delays (5 s) between each pulse.

All substrates presented in **Figure 105** were activated by **1** under irradiation for various amounts of time (see **Figure 106** and **Figure 107**). For the polyfluorobenzene series, a clear positive trend was found between the amount of fluorine groups and the kinetics of the reaction, which could be explained in the same way as previously described through the lens of Marcus theory. For instance, 32% of hexafluorobenzene were consumed after 4 h of irradiation, compared to less than 5 % of 1,2,4,5-tetrafluorobenzene.

1,3,5-trifluorobenzene was successfully reduced into 1,3-difluorobenzene during very long irradiation (20% after 20 h), the latter was shown not to react with **1** even after several days of irradiation in a separated experiment. Reduction of 1,2,4,5-tetrafluorobenzene occurred upon long irradiation times, but was not studied by ^{19}F NMR. Pentafluorobenzene was selectively reduced into 1,2,4,5-tetrafluorobenzene. Finally, hexafluorobenzene was shown to be converted to pentafluorobenzene, and further reduced into 1,2,4,5-tetrafluorobenzene, consistent with the reduction of both previous substrates.

Study of this series of compounds highlighted the potential of sequential photochemical reduction of polyfluorinated aromatic compound over reasonable amount of time in mild conditions.

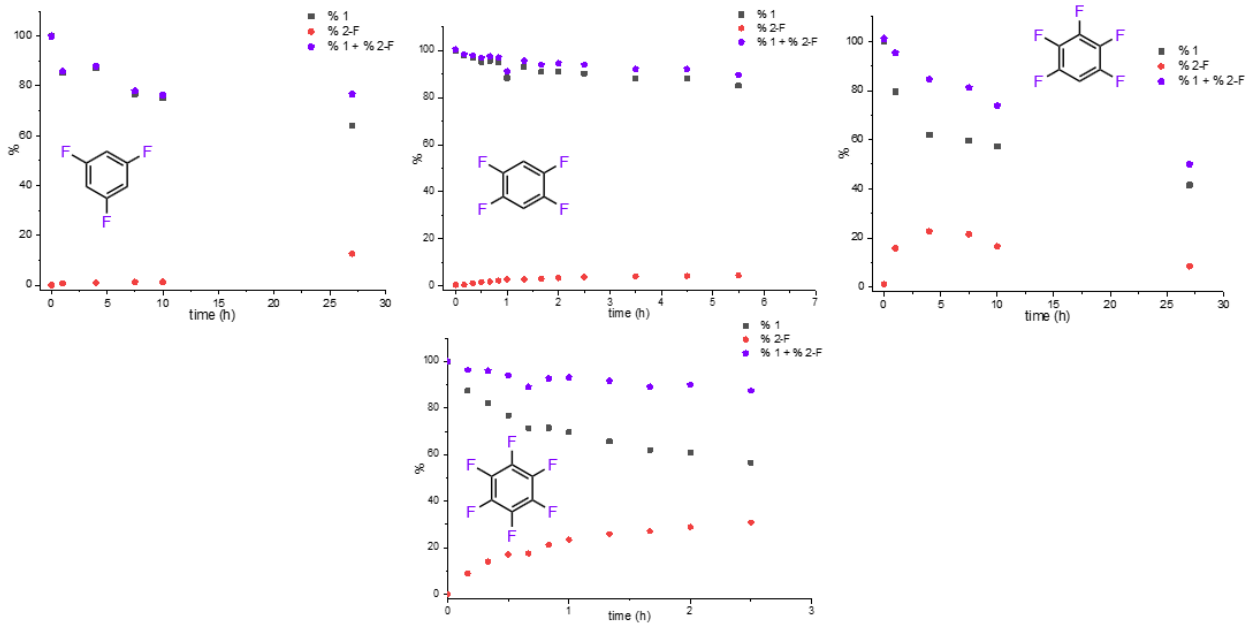

Figure 106. ^{1}H NMR monitoring of the evolution of **1** and **2-F** over irradiation time for the series of polyfluorobenzenes

Investigation of the poly-trifluoromethylbenzene series also showed activation of the three substrates studied, in significantly longer time scale than for polyfluorobenzenes (see **Figure 107**). ^{19}F NMR analysis was more difficult than for the previous series, as differences in chemical shifts between the peaks of reagents and products was very small (< 0.5 ppm). Surprisingly, reduction of 1,3,5-tris-(trifluoromethyl)benzene was slower than 1,3 and 1,4-bis-(trifluoromethyl)benzene, which could be explained by uncertainties on the quantity of reagents.

Perfluorononane was pleasantly activated by **1** under irradiation (see **Figure 107**). Reduction already started after 40 minutes of irradiation, and proceeded slowly upon ongoing irradiation. This feature is especially interesting, as it may be considered as a proof of concept in the photochemical reduction of PFASs in mild conditions.

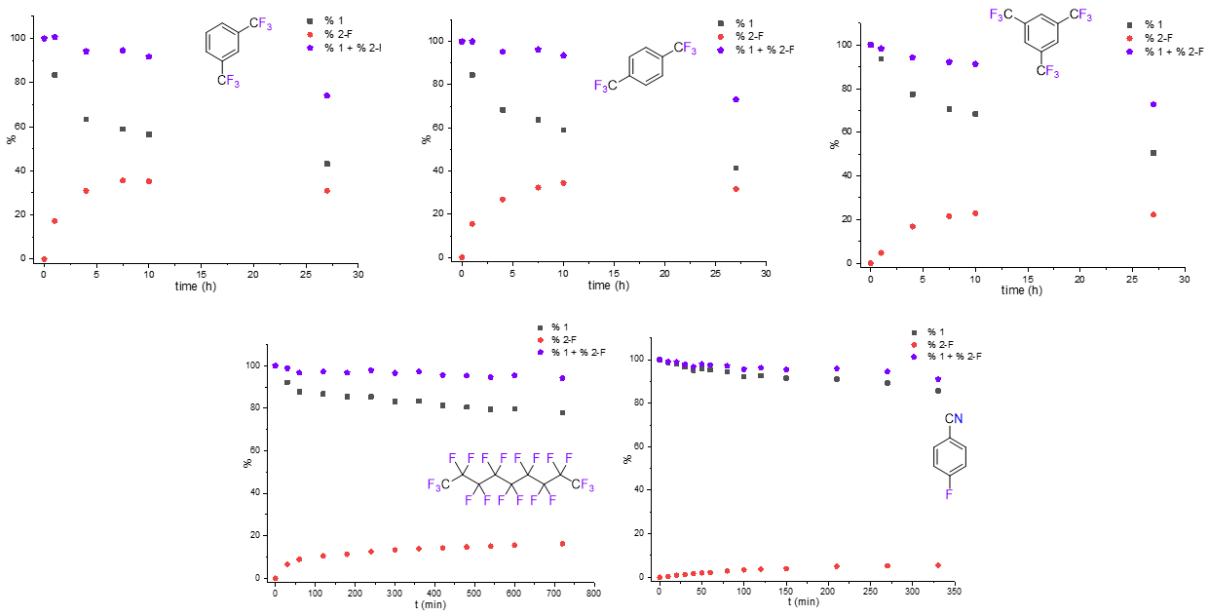

Figure 107. ^{1}H NMR monitoring of the evolution of **1** and **2-F** over irradiation time for the series of poly-trifluoromethyl-benzenes, perfluorononane and 4-fluorobenzonitrile

In the same idea than PVC reduction, defluorination of polytetrafluoroethylene (PTFE), commonly used as antiadhesive commercially know as Teflon©, was also investigated in both THF-d_8 and C_6D_6 due to the very poor solubility of the compound. No reaction was nonetheless observed, even after a week of irradiation at 427 nm. Considering the structural similarity with perfluorononane, the absence of reaction is hypothesized to originate more likely from the insolubility of PTFE than from the hypothetical redox potential mismatch between **1** and PTFE.

Possibility of Miyaura borylation was also investigated, but mixing most aryl fluorides with B_2pin_2 with LiHMDS afforded precipitation of a white powder (no change could be noticed in ^{1}H NMR and ^{19}F NMR). Irradiation of the mixtures did not lead to the detection of any borylated product, precluding further investigations of the reactivity.

As noticed in the kinetic monitoring of pentafluorobenzene reduction, the quantity of **2-F** slowly decreased over time (see **Figure 108**). Assuming a similar photochemical degradation pathway as **2-Cl**, ^{1}H NMR monitoring of the irradiation of crystalline **2-F** dissolved in THF-d_8 was recorded. Photochemical degradation of **2-F** was much slower than decay of **2-Cl** under irradiation, consistent with the stability observations made during the synthesis exploration of **2-X** compounds (X = F, Cl, Br). Trapping experiments of putative F$^{\bullet}$ radical with alkenes and nitrones were unsuccessful, mainly leading to the formation of one peak in ^{19}F NMR spectrum which was attributed to TIPS-F.

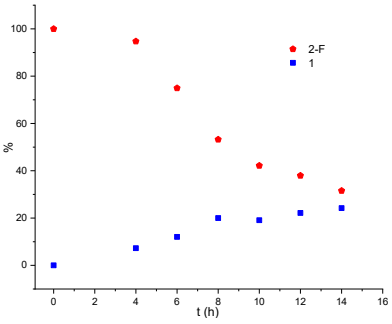

Figure 108. Photochemical degradation of **2-F** at 427 nm in THF-d_8

Synthesis of **1** described in Chapter I allowed for the investigations of reductive reactivity under irradiation on many inactivated chlorinated derivatives (arenes and alkyls), and was applied to the reduction of three POPs to offer new possibilities for environmental remediation for problematic pollutants in mild conditions. [22]

Following the preliminary interesting results on chlorinated substrates, exploration of new substrates was pushed one step further by examining the reduction of fluorinated compounds. Several polyfluorobenzenes, poly-trifluoromethyl-benzenes and perfluorononane (surrogate for PFASs) were

shown to be reduced by **1** within one day of irradiation, which paved the way for new possible degradation pathways for *eternal pollutants*.

References

(1) *Brominated flame retardants | EFSA*. https://www.efsa.europa.eu/en/topics/topic/brominated-flame-retardants (accessed 2025-04-04).

(2) *Stockholm Convention on Persistent Organic Pollutants (POPs)*. https://www.pops.int/Implementation/Alternatives/Overview/tabid/5834/Default.aspx (accessed 2025-04-04).

(3) Kodavanti, P. R. S.; Costa, L. G.; Aschner, M. Perspective on Halogenated Organic Compounds. In *Advances in Neurotoxicology*; Kodavanti, P. R. S., Aschner, M., Costa, L. G., Eds.; Neurotoxicity of Halogenated Organic Compounds; Academic Press, 2023; Vol. 10, pp 1–25. https://doi.org/10.1016/bs.ant.2023.06.001.

(4) United Nations Environment Programme. PFASs under the Stockholm Convention, 2022. https://www.pops.int/Portals/0/download.aspx?d=UNEP-POPS-PUB-factsheet-PFAS-2022.English.pdf.

(5) Kelly, B. C.; Ikonomou, M. G.; Blair, J. D.; Morin, A. E.; Gobas, F. A. P. C. Food Web-Specific Biomagnification of Persistent Organic Pollutants. *Science* **2007**, *317* (5835), 236–239. https://doi.org/10.1126/science.1138275.

(6) Loganathan, B. G.; Ahuja, S.; Subedi, B. Synthetic Organic Chemical Pollutants in Water: Origin, Distribution, and Implications for Human Exposure and Health. In *Contaminants in Our Water: Identification and Remediation Methods*; ACS Symposium Series; American Chemical Society, 2020; Vol. 1352, pp 13–39. https://doi.org/10.1021/bk-2020-1352.ch002.

(7) *Rotterdam Convention*; 1998. https://www.pic.int/Portals/5/download.aspx?d=UNEP-FAO-RC-CONVTEXT-2023.English.pdf.

(8) *Stockholm Convention*; 2001. https://www.pops.int/Portals/0/download.aspx?d=UNEP-POPS-COP-CONVTEXT-2023.English.pdf.

(9) United Nations Environment Programme. *A Brief Summary of Monitoring Reports Prepared under the POPs Global Monitoring Plan Projects of UNEP*; United Nations Environment Programme, 2024.

(10) United Nations Environment Programme. *Results of Air Monitoring of Persistent Organic Pollutants - Sectoral Report*; United Nations Environment Programme, 2024. https://doi.org/10.59117/20.500.11822/45466.

(11) United Nations Environment Programme. *Results of the 2016-2019 WHO/UNEP Human Milk Survey on Persistent Organic Pollutants*; United Nations Environment Programme, 2023. https://doi.org/10.59117/20.500.11822/44829.

(12) Naghdi, S.; Shahrestani, M. M.; Zendehbad, M.; Djahaniani, H.; Kazemian, H.; Eder, D. Recent Advances in Application of Metal-Organic Frameworks (MOFs) as Adsorbent and Catalyst in Removal of Persistent Organic Pollutants (POPs). *J. Hazard. Mater.* **2023**, *442*, 130127. https://doi.org/10.1016/j.jhazmat.2022.130127.

(13) Pariatamby, A.; Kee, Y. L. Persistent Organic Pollutants Management and Remediation. *Procedia Environ. Sci.* **2016**, *31*, 842–848. https://doi.org/10.1016/j.proenv.2016.02.093.

(14) Sun, B.; Li, Q.; Zheng, M.; Su, G.; Lin, S.; Wu, M.; Li, C.; Wang, Q.; Tao, Y.; Dai, L.; Qin, Y.; Meng, B. Recent Advances in the Removal of Persistent Organic Pollutants (POPs) Using Multifunctional Materials:A Review. *Environ. Pollut.* **2020**, *265*, 114908. https://doi.org/10.1016/j.envpol.2020.114908.

(15) Matsumoto, E.; Kawanaka, Y.; Yun, S.-J.; Oyaizu, H. Bioremediation of the Organochlorine Pesticides, Dieldrin and Endrin, and Their Occurrence in the Environment. *Appl. Microbiol. Biotechnol.* **2009**, *84* (2), 205–216. https://doi.org/10.1007/s00253-009-2094-5.

(16) Nguyen, V.-H.; Smith, S. M.; Wantala, K.; Kajitvichyanukul, P. Photocatalytic Remediation of Persistent Organic Pollutants (POPs): A Review. *Arab. J. Chem.* **2020**, *13* (11), 8309–8337. https://doi.org/10.1016/j.arabjc.2020.04.028.

(17) Wacławek, S.; Antoš, V.; Hrabák, P.; Černík, M.; Elliott, D. Remediation of Hexachlorocyclohexanes by Electrochemically Activated Persulfates. *Environ. Sci. Pollut. Res.* **2016**, *23* (1), 765–773. https://doi.org/10.1007/s11356-015-5312-y.

(18) Akhtar, A. B. T.; Naseem, S.; Yasar, A.; Naseem, Z. Persistent Organic Pollutants (POPs): Sources, Types, Impacts, and Their Remediation. In *Environmental Pollution and Remediation*; Prasad, R., Ed.; Environmental and Microbial Biotechnology; Springer Singapore: Singapore, 2021; pp 213–246. https://doi.org/10.1007/978-981-15-5499-5_8.
(19) Luo, Y.-R. *Handbook of Bond Dissociation Energies in Organic Compounds*, 0 ed.; CRC Press, 2002. https://doi.org/10.1201/9781420039863.
(20) Cybularczyk-Cecotka, M.; Szczepanik, J.; Giedyk, M. Photocatalytic Strategies for the Activation of Organic Chlorides. *Nat. Catal.* **2020**, *3* (11), 872–886. https://doi.org/10.1038/s41929-020-00515-8.
(21) Lambert, F. L.; Ingall, G. B. Voltammetry of Organic Halogen Compounds. IV. The Reduction of Organic Chlorides at the Vitreous (Glassy) Carbon Electrode. *Tetrahedron Lett.* **1974**, *15* (36), 3231–3234. https://doi.org/10.1016/S0040-4039(01)91870-2.
(22) IARC. *DDT, Lindane, and 2,4-D*.
(23) IARC. *Pentachlorophenol and Some Related Compounds*.
(24) IARC. *Polychlorinated Biphenyls and Polybrominated Biphenyls*.
(25) Martin, E. T.; McGuire, C. M.; Mubarak, M. S.; Peters, D. G. Electroreductive Remediation of Halogenated Environmental Pollutants. *Chem. Rev.* **2016**, *116* (24), 15198–15234. https://doi.org/10.1021/acs.chemrev.6b00531.
(26) Shoiful, A.; Ueda, Y.; Nugroho, R.; Honda, K. Degradation of Organochlorine Pesticides (OCPs) in Water by Iron (Fe)-Based Materials. *J. Water Process Eng.* **2016**, *11*, 110–117. https://doi.org/10.1016/j.jwpe.2016.02.011.
(27) Yu, B.; Zeng, J.; Gong, L.; Zhang, M.; Zhang, L.; Chen, X. Investigation of the Photocatalytic Degradation of Organochlorine Pesticides on a Nano-TiO2 Coated Film. *Talanta* **2007**, *72* (5), 1667–1674. https://doi.org/10.1016/j.talanta.2007.03.013.
(28) Hisanaga, T.; Harada, K.; Tanaka, K. Photocatalytic Degradation of Organochlorine Compounds in Suspended TiO2. *J. Photochem. Photobiol. Chem.* **1990**, *54* (1), 113–118. https://doi.org/10.1016/1010-6030(90)87015-4.
(29) Yin, H.; Schelter, E. J.; Carroll, P. J.; Anna, J. M. Luminescent Ce(III) Complexes as Stoichiometric and Catalytic Photoreductants for Halogen Atom Abstraction Reactions. *J. Am. Chem. Soc.* **2015**, *137* (29), 9234–9237. https://doi.org/10.1021/jacs.5b05411.
(30) Qiao, Y.; Schelter, E. J.; Yang, Q. Photoinduced Miyaura Borylation by a Rare-Earth-Metal Photoreductant: The Hexachlorocerate(III) Anion. *Angew. Chem. Int. Ed.* **2018**, *57* (34), 10999–11003. https://doi.org/10.1002/anie.201804022.
(31) *List of Classifications*. https://monographs.iarc.who.int/list-of-classifications (accessed 2025-04-06).
(32) Whitehead, H. D.; Venier, M.; Wu, Y.; Eastman, E.; Urbanik, S.; Diamond, M. L.; Shalin, A.; Schwartz-Narbonne, H.; Bruton, T. A.; Blum, A.; Wang, Z.; Green, M.; Tighe, M.; Wilkinson, J. T.; McGuinness, S.; Peaslee, G. F. Fluorinated Compounds in North American Cosmetics. *Environ. Sci. Technol. Lett.* **2021**, *8* (7), 538–544. https://doi.org/10.1021/acs.estlett.1c00240.
(33) Schaider, L. A.; Balan, S. A.; Blum, A.; Andrews, D. Q.; Strynar, M. J.; Dickinson, M. E.; Lunderberg, D. M.; Lang, J. R.; Peaslee, G. F. Fluorinated Compounds in U.S. Fast Food Packaging. *Environ. Sci. Technol. Lett.* **2017**, *4* (3), 105–111. https://doi.org/10.1021/acs.estlett.6b00435.
(34) United Nations Environment Programme. *PFASs listed under the Stockholm Convention*. https://www.pops.int/Implementation/IndustrialPOPs/PFAS/Overview/tabid/5221/Default.aspx (accessed 2025-04-05).
(35) Sunderland, E. M.; Hu, X. C.; Dassuncao, C.; Tokranov, A. K.; Wagner, C. C.; Allen, J. G. A Review of the Pathways of Human Exposure to Poly- and Perfluoroalkyl Substances (PFASs) and Present Understanding of Health Effects. *J. Expo. Sci. Environ. Epidemiol.* **2019**, *29* (2), 131–147. https://doi.org/10.1038/s41370-018-0094-1.
(36) Griffith, F. D.; Long, J. E. Animal Toxicity Studies with Ammonium Perfluorooctanoate. *Am. Ind. Hyg. Assoc. J.* **1980**, *41* (8), 576–583. https://doi.org/10.1080/15298668091425301.
(37) Ubel, F. A.; Sorenson, S. D.; Roach, D. E. Health Status of Plant Workers Exposed to Fluorochemicals - a Preliminary Report. *Am. Ind. Hyg. Assoc. J.* **1980**, *41* (8), 584–589. https://doi.org/10.1080/15298668091425310.

(38) Bline, A. P.; DeWitt, J. C.; Kwiatkowski, C. F.; Pelch, K. E.; Reade, A.; Varshavsky, J. R. Public Health Risks of PFAS-Related Immunotoxicity Are Real. *Curr. Environ. Health Rep.* **2024**, *11* (2), 118–127. https://doi.org/10.1007/s40572-024-00441-y.
(39) IARC. *Perfluorooctanoic Acid (PFOA) and Perfluorooctanesulfonic Acid (PFOS)*.
(40) Environment, U. N. *Per- and Polyfluoroalkyl Substances (PFASs) | UNEP - UN Environment Programme*. https://www.unep.org/topics/chemicals-and-pollution-action/pollution-and-health/persistent-organic-pollutants-pops/and (accessed 2025-04-09).
(41) US EPA, O. *Per- and Polyfluoroalkyl Substances (PFAS)*. https://www.epa.gov/pfas (accessed 2025-04-09).
(42) CDC. *Per- and Polyfluoroalkyl Substances (PFAS) and Your Health*. Per- and Polyfluoroalkyl Substances (PFAS) and Your Health. https://www.atsdr.cdc.gov/pfas/index.html (accessed 2025-04-09).
(43) Cousins, I. T.; Ng, C. A.; Wang, Z.; Scheringer, M. Why Is High Persistence Alone a Major Cause of Concern? *Environ. Sci. Process. Impacts* **2019**, *21* (5), 781–792. https://doi.org/10.1039/C8EM00515J.
(44) Hu, X. C.; Andrews, D. Q.; Lindstrom, A. B.; Bruton, T. A.; Schaider, L. A.; Grandjean, P.; Lohmann, R.; Carignan, C. C.; Blum, A.; Balan, S. A.; Higgins, C. P.; Sunderland, E. M. Detection of Poly- and Perfluoroalkyl Substances (PFASs) in U.S. Drinking Water Linked to Industrial Sites, Military Fire Training Areas, and Wastewater Treatment Plants. *Environ. Sci. Technol. Lett.* **2016**, *3* (10), 344–350. https://doi.org/10.1021/acs.estlett.6b00260.
(45) Air Force Civil Engineer Center. *Per- and Polyfluoroalkl Substances*. https://www.afcec.af.mil/WhatWeDo/Environment/Perfluorinated-Compounds/ (accessed 2025-04-09).
(46) *Draft National Recommended Ambient Water Quality Criteria for the Protection of Human Health for Perfluorooctanoic Acid, Perfluorooctane Sulfonic Acid, and Perfluorobutane Sulfonic Acid*; 2024. https://www.federalregister.gov/documents/2024/12/26/2024-30637/draft-national-recommended-ambient-water-quality-criteria-for-the-protection-of-human-health-for (accessed 2025-04-11).
(47) Longendyke, G. K.; Katel, S.; Wang, Y. PFAS Fate and Destruction Mechanisms during Thermal Treatment: A Comprehensive Review. *Environ. Sci. Process. Impacts* **2022**, *24* (2), 196–208. https://doi.org/10.1039/D1EM00465D.
(48) Kucharzyk, K. H.; Darlington, R.; Benotti, M.; Deeb, R.; Hawley, E. Novel Treatment Technologies for PFAS Compounds: A Critical Review. *J. Environ. Manage.* **2017**, *204*, 757–764. https://doi.org/10.1016/j.jenvman.2017.08.016.
(49) Gar Alalm, M.; Boffito, D. C. Mechanisms and Pathways of PFAS Degradation by Advanced Oxidation and Reduction Processes: A Critical Review. *Chem. Eng. J.* **2022**, *450*, 138352. https://doi.org/10.1016/j.cej.2022.138352.
(50) Cui, J.; Gao, P.; Deng, Y. Destruction of Per- and Polyfluoroalkyl Substances (PFAS) with Advanced Reduction Processes (ARPs): A Critical Review. *Environ. Sci. Technol.* **2020**, *54* (7), 3752–3766. https://doi.org/10.1021/acs.est.9b05565.
(51) King, J. F.; Chaplin, B. P. Electrochemical Reduction of Per- and Polyfluorinated Alkyl Substances (PFAS): Is It Possible? Applying Experimental and Quantum Mechanical Insights from the Reductive Defluorination Literature. *Curr. Opin. Chem. Eng.* **2024**, *44*, 101014. https://doi.org/10.1016/j.coche.2024.101014.
(52) Yu, K.; Li, X.; Chen, L.; Fang, J.; Chen, H.; Li, Q.; Chi, N.; Ma, J. Mechanism and Efficiency of Contaminant Reduction by Hydrated Electron in the Sulfite/Iodide/UV Process. *Water Res.* **2018**, *129*, 357–364. https://doi.org/10.1016/j.watres.2017.11.030.
(53) Yadav, S.; Ibrar, I.; Al-Juboori, R. A.; Singh, L.; Ganbat, N.; Kazwini, T.; Karbassiyazdi, E.; Samal, A. K.; Subbiah, S.; Altaee, A. Updated Review on Emerging Technologies for PFAS Contaminated Water Treatment. *Chem. Eng. Res. Des.* **2022**, *182*, 667–700. https://doi.org/10.1016/j.cherd.2022.04.009.
(54) Blum, A.; Balan, S. A.; Scheringer, M.; Trier, X.; Goldenman, G.; Cousins, I. T.; Diamond, M.; Fletcher, T.; Higgins, C.; Lindeman, A. E.; Peaslee, G.; De Voogt, P.; Wang, Z.; Weber, R. The Madrid Statement

on Poly- and Perfluoroalkyl Substances (PFASs). *Environ. Health Perspect.* **2015**, *123* (5). https://doi.org/10.1289/ehp.1509934.

(55) Yin, H.; Jin, Y.; Hertzog, J. E.; Mullane, K. C.; Carroll, P. J.; Manor, B. C.; Anna, J. M.; Schelter, E. J. The Hexachlorocerate(III) Anion: A Potent, Benchtop Stable, and Readily Available Ultraviolet A Photosensitizer for Aryl Chlorides. *J. Am. Chem. Soc.* **2016**, *138* (50), 16266–16273. https://doi.org/10.1021/jacs.6b05712.

(56) Isse, A. A.; De Giusti, A.; Gennaro, A.; Falciola, L.; Mussini, P. R. Electrochemical Reduction of Benzyl Halides at a Silver Electrode. *Electrochimica Acta* **2006**, *51* (23), 4956–4964. https://doi.org/10.1016/j.electacta.2006.01.039.

(57) Gilmore, K.; Mohamed, R. K.; Alabugin, I. V. The Baldwin Rules: Revised and Extended. *WIREs Comput. Mol. Sci.* **2016**, *6* (5), 487–514. https://doi.org/10.1002/wcms.1261.

(58) Grimshaw, J. *Electrochemical Reactions and Mechanisms in Organic Chemistry*, 1st ed.; Elsevier: Amsterdam ; New York, 2000.

(59) Andrieux, C. P.; Blocman, C.; Dumas-Bouchiat, J. M.; Saveant, J. M. Heterogeneous and Homogeneous Electron Transfers to Aromatic Halides. An Electrochemical Redox Catalysis Study in the Halobenzene and Halopyridine Series. *J. Am. Chem. Soc.* **1979**, *101* (13), 3431–3441. https://doi.org/10.1021/ja00507a002.

(60) Fagnoni, M.; Dondi, D.; Ravelli, D.; Albini, A. Photocatalysis for the Formation of the C−C Bond. *Chem. Rev.* **2007**, *107* (6), 2725–2756. https://doi.org/10.1021/cr068352x.

(61) Garwood, J. J. A.; Chen, A. D.; Nagib, D. A. Radical Polarity. *J. Am. Chem. Soc.* **2024**, *146* (41), 28034–28059. https://doi.org/10.1021/jacs.4c06774.

(62) Chatgilialoglu, C.; Griller, D.; Lesage, M. Tris(Trimethylsilyl)Silane. A New Reducing Agent. *J. Org. Chem.* **1988**, *53* (15), 3641–3642. https://doi.org/10.1021/jo00250a051.

(63) Kynman, A. E.; Christodoulou, S.; Ouellette, E. T.; Peterson, A.; Kelly, S. N.; Maron, L.; Arnold, P. Photocatalytic Dechlorination of Unactivated Chlorocarbons Including PVC Using Organolanthanide Complexes. *Chem. Commun.* **2023**, *59* (73), 10924–10927. https://doi.org/10.1039/D3CC02906A.

(64) Marcus, R. A. On the Theory of Oxidation-Reduction Reactions Involving Electron Transfer. I. *J. Chem. Phys.* **1956**, *24* (5), 966–978. https://doi.org/10.1063/1.1742723.

(65) Qiao, Y.; Schelter, E. J. Lanthanide Photocatalysis. *Acc. Chem. Res.* **2018**, *51* (11), 2926–2936. https://doi.org/10.1021/acs.accounts.8b00336.

(66) Wang, H.-J.; Fu, Y. Designing New Free-Radical Reducing Reagents: Theoretical Study on Si–H Bond Dissociation Energies of Organic Silanes. *J. Mol. Struct. THEOCHEM* **2009**, *893* (1), 67–72. https://doi.org/10.1016/j.theochem.2008.09.017.

(67) Zhang, M.; Ruzi, R.; Xi, J.; Li, N.; Wu, Z.; Li, W.; Yu, S.; Zhu, C. Photoredox-Catalyzed Hydroacylation of Olefins Employing Carboxylic Acids and Hydrosilanes. *Org. Lett.* **2017**, *19* (13), 3430–3433. https://doi.org/10.1021/acs.orglett.7b01391.

(68) Lalevée, J.; Blanchard, N.; Tehfe, M.-A.; Morlet-Savary, F.; Fouassier, J. P. Green Bulb Light Source Induced Epoxy Cationic Polymerization under Air Using Tris(2,2'-Bipyridine)Ruthenium(II) and Silyl Radicals. *Macromolecules* **2010**, *43* (24), 10191–10195. https://doi.org/10.1021/ma1023318.

(69) Chatgilialoglu, C.; Ferreri, C.; Landais, Y.; Timokhin, V. I. Thirty Years of (TMS)3SiH: A Milestone in Radical-Based Synthetic Chemistry. *Chem. Rev.* **2018**, *118* (14), 6516–6572. https://doi.org/10.1021/acs.chemrev.8b00109.

(70) Deacon, G. B.; Junk, P. C.; Werner, D. Lanthanoid Induced C–F Activation of All Fluorine Atoms of One CF3 Group. *Eur. J. Inorg. Chem.* **2015**, *2015* (9), 1484–1489. https://doi.org/10.1002/ejic.201500137.

(71) Jaroschik, F. Picking One out of Three: Selective Single C−F Activation in Trifluoromethyl Groups. *Chem. – Eur. J.* **2018**, *24* (55), 14572–14582. https://doi.org/10.1002/chem.201801702.

(72) Träff, A. M.; Janjetovic, M.; Ta, L.; Hilmersson, G. Selective C-F Bond Activation: Substitution of Unactivated Alkyl Fluorides Using YbI3. *Angew. Chem. Int. Ed.* **2013**, *52* (46), 12073–12076. https://doi.org/10.1002/anie.201306104.

(73) Andrieux, C. P.; Blocman, C.; Savéant, J. M. Characterization of Electrochemical Reactions Hidden in the Background Discharge the Redox Catalyzed Reduction of Fluorobenzene. *J. Electroanal. Chem. Interfacial Electrochem.* **1979**, *105* (2), 413–417. https://doi.org/10.1016/S0022-0728(79)80139-4.

(74) Liu, X.; Sau, A.; Green, A. R.; Popescu, M. V.; Pompetti, N. F.; Li, Y.; Zhao, Y.; Paton, R. S.; Damrauer, N. H.; Miyake, G. M. Photocatalytic C–F Bond Activation in Small Molecules and Polyfluoroalkyl Substances. *Nature* **2025**, *637* (8046), 601–607. https://doi.org/10.1038/s41586-024-08327-7.

Curiosity is the wick in the candle of learning.

William Arthur Ward, 20th century

Chapter III
Towards the degradation of explosive surrogates

Introduction 113
I. Chemical formation of nitro and nitroso radicals 117
a) Reductive coupling of nitrosobenzene 117
b) Single Electron Transfer on nitro derivatives 120
1) Formation of nitroarene radicals 120
2) Stability of nitroarene radical 123
3) Reactivity with nitroalkanes 124
II. Reduction of N-O bond in organic nitrites, amine oxides and nitrones 126
a) Organic Nitrites 126
b) Reactivity with amine-oxides 127
c) Monoelectronic reduction of nitrones 128
References 131

Introduction

Nitrogen is a central element in many biological processes. It displays a variety of oxidation states from -III to +V, where almost all of them can be found in the nitrogen cycle (see Chapter IV). Oxidized nitrogen species (oxidation state > 0) often contain nitrogen-oxygen bonds, which are interesting given their involvement in many biological systems and for their various anthropic uses. For instance, organic nitrates (R-ONO_2, +V) are used as potent vasodilators in cardiovascular therapy, due to the *in vivo* formation of nitric oxide NO,[1] similarly to organic nitrites (R-ONO, +III) which are used as recreational drug for their vasodilatation properties (see **Figure 109**).[2] Nitrates are also used as explosives under the form of pentaerythritol tetranitrate (PETN), a military-grade explosive, nitroglycerin and nitrocellulose.[3]

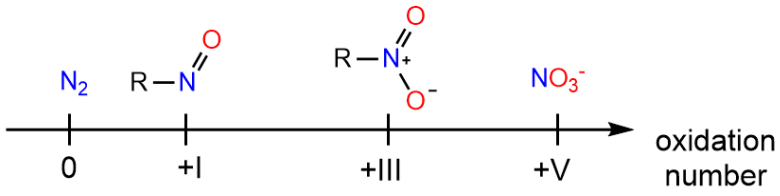

Figure 109. Usual oxidation states of oxidized nitrogen species

Generally speaking, most explosives substances contain several N-O bonds, which allows for a better oxygen balance and the formation of strong intermolecular and intramolecular hydrogen bonds which enabled better crystal packing.[4,5] This increased stability was especially well embodied by N-oxide based explosive 2,6-diamino-3,5-dinitropyrazine-1-oxide (LLM-105, see **Figure 110**), which displayed a more important explosion energy (detonation velocity of 8560 $m.s^{-1}$), increased thermal stability (decomposition temperature of 356 °C) and lower impact sensitivity (H_{50} = 117 cm, H_{50} is the drop height of 2.5 kg weight at which 50% of samples detonates)[6] compared to widely used trinitrotoluene (TNT, respectively 6940 $m.s^{-1}$, 295 °C and 59 cm).[4] Given these promising properties, the use for N-oxide based compounds is soon expected to soar, as well as their dispersion into the environment which can cause pollution and health problems.[7]

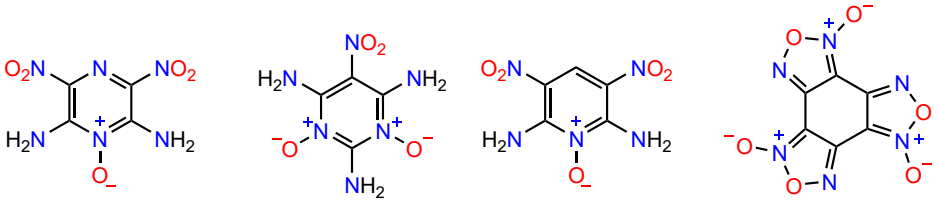

Figure 110. N-oxide based explosives[4,5]

In vivo studies of small N-oxide molecules such as trimethylamine N-oxide (TMAO) have highlighted the role of TMAO in preventing protein denaturation, and the increased risk of cardiovascular disease, renal failure, diabetes mellitus, heart failure, atherosclerosis, hypertension, metabolic syndrome and dyslipidaemia.[8–11] Nevertheless, their high polarity hampered interaction with lipophilic media such as DNA, and were used as directing groups in C-H activation,[12] which are both interesting features for drug design.[13]

Reduction of N-oxides has been extensively studied using oxophilic reagents (phosphines,[14,15] sulfur oxides,[16–19] silicon reagents[20,21] and boron derivatives)[22] as well as d-block compounds[23–31] and p-block derivatives,[32–36] but only one example of reduction using a lanthanide complex (SmI_2) has been reported to the best of my knowledge.[37] On the contrary, several examples of photochemical activation of N-oxide compounds have been reported with d-block complexes,[38–40] or without any metal.[21,41–45]

Low bond dissociation energy (BDE) of N-O σ bonds (about 63 $kcal.mol^{-1}$ in NH_2OH, similarly to 60.5 $kcal.mol^{-1}$ for highly reactive NH_2Cl),[46] allows for a wide variety of reactivity patterns.[47] Despite the frailty of N-O bond, reduction of aromatic N-oxide derivatives in corresponding pyridines is quite challenging as indicated by the low redox potential of pyridine N-oxide (-0.49 V *vs*. Fc/Fc^+).[48]

Most of reduction processes of N-oxide chemicals proceed through two-electron transfer reduction of N-oxides derivatives, and the several reports of one-electron reduction with or without irradiation either use fairly rare metals or UV irradiation to allow for the reduction to happen. An alternative visible-light induced one-electron reduction pathway on these compounds with an abundant metal would be interesting.

Nitro compounds (R-NO_2, +III), especially nitroaromatic compounds, display various application fields, ranging from bioactive substances (as pesticides or drugs), to synthesis intermediates towards the production of aniline building blocks (see **Figure 111**).[49,50] Nitroaromatic compounds have been especially used for their highly explosives properties, as trinitrotoluene (TNT) for instance, which is used as starting compound for the synthesis of several nitroaromatic explosives materials (see **Figure 112**).[51]

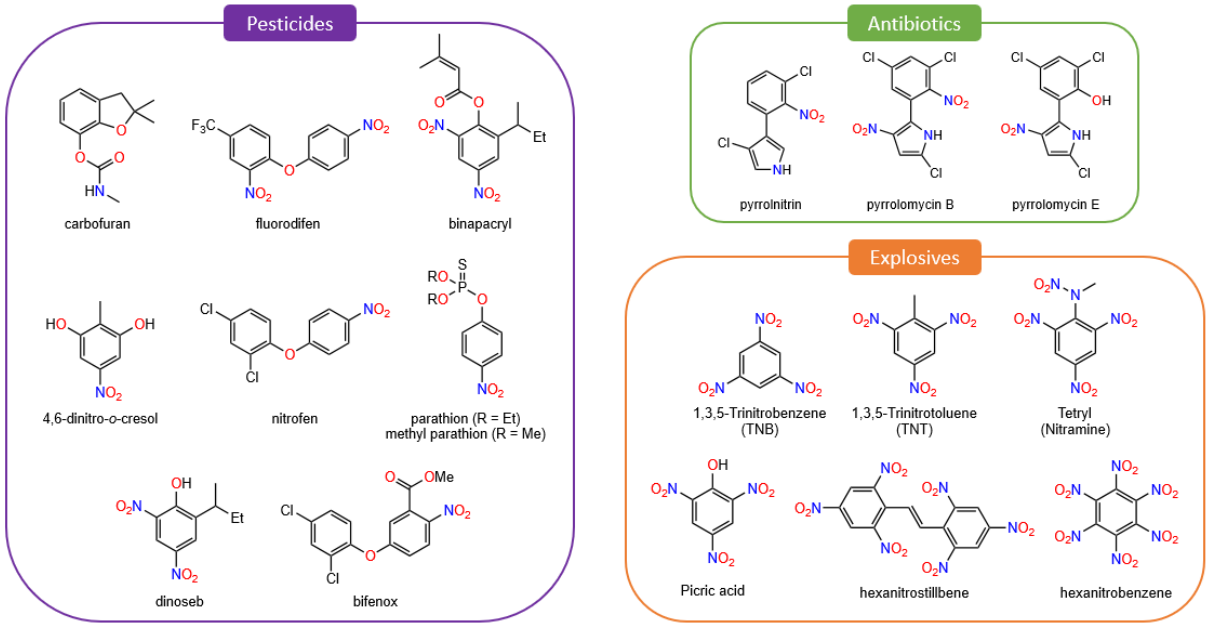

Figure 111. Families of nitroaromatic compounds sorted out by field of use. Adapted from Ju and Parales[51]

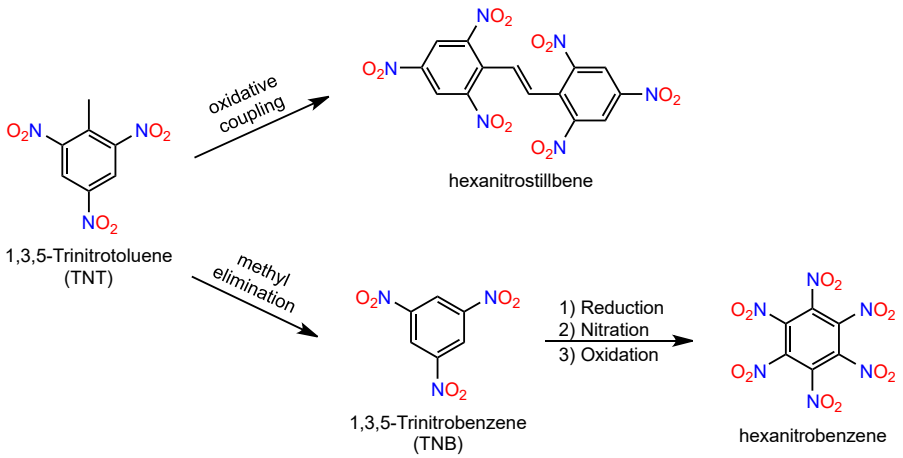

Figure 112. Synthesis of nitroaromatic explosives starting from TNT[51]

Nevertheless, industrial production of TNT is particularly polluting, releasing close to 340 kg of waste water called *red water* per ton of TNT produced, which corresponds to the production of almost 2 million litres of red water per year.[52] This polluted water contains dinitrotoluenes derivatives, particularly persistent in the environment and highly toxic as they are prone to induce a variety of diseases such as methemoglobinemia, anaemia, or bile duct hyperplasia.[53,54] The American Environmental Protection Agency (EPA) therefore listed TNT and dinitrotoluenes as priority pollutant.[55] In general, nitroaromatic compounds such as *o*-nitroanisole (precursor of *o*-anisidine), nitropyrenes (exhaust gas from cars),

nitrofluoranthenes (incomplete combustion), nitrofurans (drugs) or nitrobiphenyls (industrial subsproduct) are known to display either mutagenic or carcinogenic activity.[56,57]

Military use of nitroaromatic explosives has decreased nowadays and is mostly replaced by non-aromatic nitro chemicals such as High Melting-point eXplosive (HMX) and Research Department eXplosive (RDX, see **Figure 113**), which are used as anti-tank ammunitions and rocket propellant, even if environmental toxicity issues have been reported.[58,59] Nevertheless, pre-existing polluted sites and current production of TNT still raise the issue about effluent treatment.[60,61]

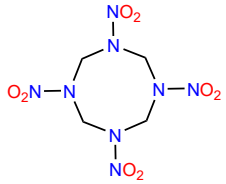

High Melting point eXplosive (HMX)



Research Department eXplosive (RDX)

Figure 113. Non-aromatic nitro explosives

Current degradation methods mostly rely on biological processes due a fairly low cost,[62–64] or to some oxidation process using or mimicking Fenton reaction.[65–71] Electrochemical six-electron reduction of nitroaromatics has also been studied to form the corresponding anilines.[72–76]

Reduction of nitroaromatics to aniline proceeds through the formation of several intermediates. One-electron reduction of nitrobenzene allows for the formation of nitrobenzene radical (see **Figure 114**), unstable in water[77] but detectable by *in situ* EPR in acetonitrile.[78] *In vivo*, nitrobenzene radical reduces dioxygen to form superoxide radical $O_2^{\bullet -}$, a Reactive Oxygen Species (ROS) which displays acute *in vivo* toxicity.[56,79]

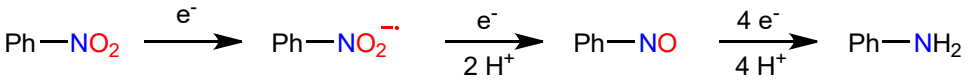

Figure 114. Stepwise reduction of nitrobenzene. Adapted from Mason and Holtzman[80]

Further one-electron reduction of nitrobenzene radical in the presence of proton affords nitrosobenzene PhNO as a stable product, which is harmful to human due to its binding with haemoglobin.[81] Final 4-electron-4-proton reduction of nitrosobenzene leads to the formation of aniline.

While many examples of materials reducing nitroaromatic to anilines have been reported, [76,82–90] reactivity with molecular complexes is surprisingly under-investigated, with only few examples of hydrogenations into anilines with $NaBH_4$ or H_2 using iron,[91] palladium[92] and molybdenum[93] complexes.

Considering the powerful reducing properties of cerium(III) complexes under irradiation and the oxophilicity of lanthanides, the reactivity with N-oxide, nitro and nitroso compounds was investigated in the presence of complex **1**.

I. Chemical formation of nitro and nitroso radicals

a) Reductive coupling of nitrosobenzene

Given that nitrosobenzene is an intermediate in reducing nitrobenzene to aniline in non-aqueous conditions, its reduction has been extensively studied by several groups.[94–100] Mechanistic investigations pointed out the difference in reduction first step whether the reaction was carried out in aqueous solvent (two-electrons),[101] or in organic aprotic solvents (one-electron). In the presence of hydrogen donors such as ammonium ions[102] or acetic anhydride in aprotic media,[103] the first reduction step involves two electrons. One-electron reduction of nitrosobenzene in aprotic solvents allows for the formation of nitrosobenzene radical which has been unambiguously characterized by EPR,[94,100,104,105] but the relative instability of the radical makes difficult in depth analysis of the reactivity.

Nitroso compounds are also interesting non-innocent ligands for coordination chemistry. In addition to the rich coordination patterns of the nitroso group,[106,107] different oxidation states of this ligand (0, 1 or 2) enabled ligand based redox chemistry.[108] Nevertheless, metal-$(RNO)^{\bullet -}$ complexes have been described as unstable,[109] and few examples of mono-reduced nitrosoarene complexes have been reported.[108,110] To the best of my knowledge, no reactivity of nitroso derivatives was reported with lanthanide complexes.

Addition of one equivalent of nitrosobenzene to a solution of **1** in THF-d_8 or C_6D_6 led to an immediate change of colour from yellow to dark brown. ^{1}H NMR spectrum monitoring of the reaction medium showed a complete consumption of PhNO and a shift of aromatic peaks (see **Figure 115**). Nevertheless, NMR signature of **1** was still detected, even upon further additions of PhNO.

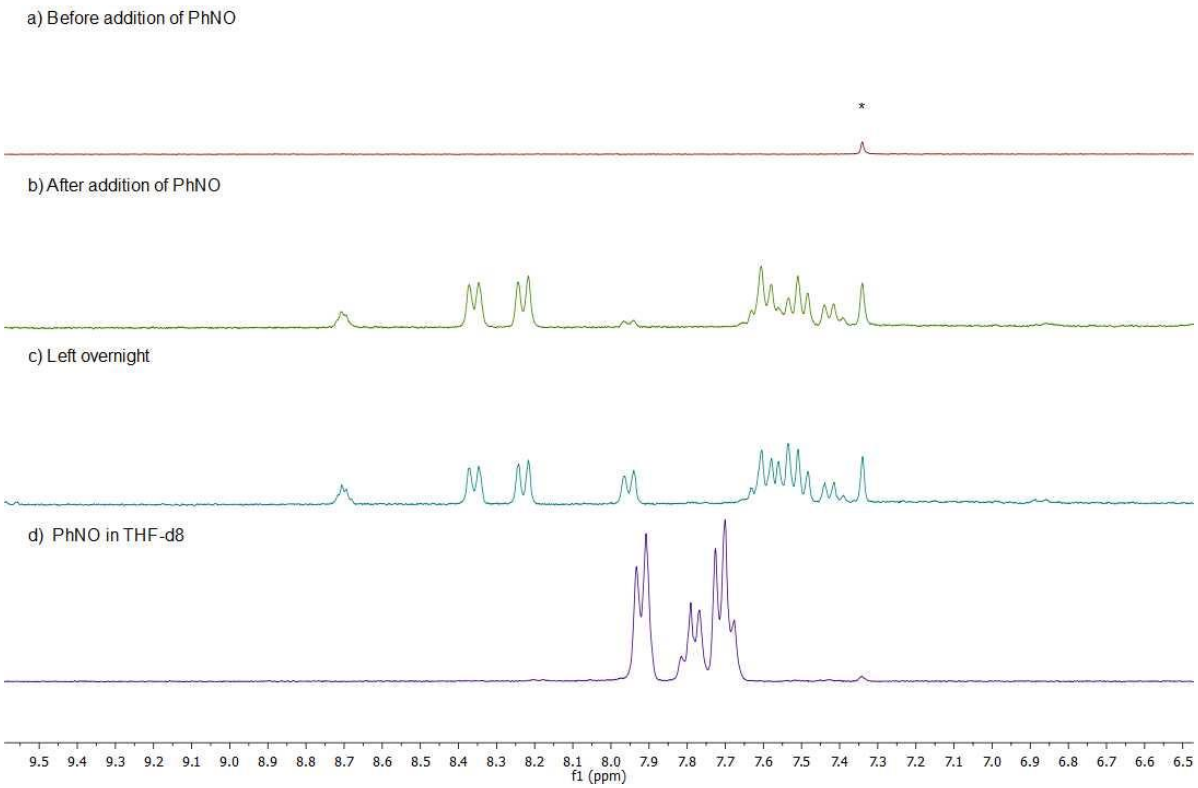

Figure 115. ^{1}H NMR spectrum monitoring of the reaction between **1** and PhNO in THF-d_8. Solvent residual peak indicated with *

Solvent evaporation, dissolution in pentane with one drop of THF afforded XRD suitable brown crystals, which corresponded to the reductive coupling of nitrosobenzene coordinating to cerium centre in η^2 fashion.

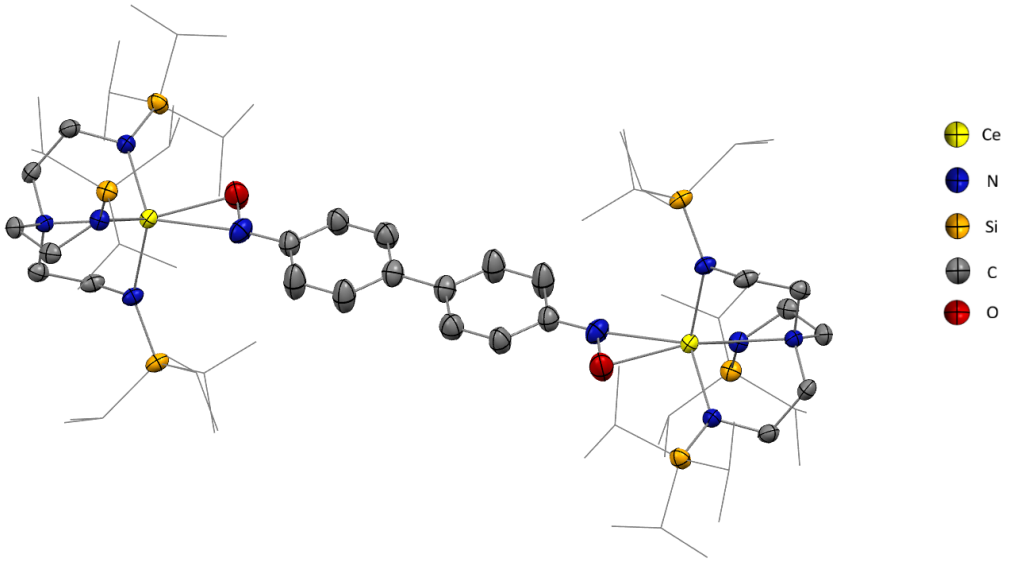

Figure 116. 3D structure of **2-PhNO**. Ellipsoids are represented at 50% probability, and TIPS groups are shown in wireframe style for clarity

Coordination and reaction of PhNO led to a contraction of the coordination sphere in equatorial nitrogen-cerium bonds from 2.366(2) to 2.265(2) Å in **2-PhNO** that induced a significant elongation of Ce-N_{axial} bond from 2.354(2) to 2.651(2) Å. Asymmetric unit of the crystal was made up with one cerium complex bearing one reduced nitrosobenzene (half of the structure in **Figure 116**), and did not show the coupling of the two moieties. The right moiety in **Figure 117** was generated by symmetry from the asymmetric unit, and therefore displayed exact same parameters than the left one. Structural features of $CeTREN^{TIPS}$ moiety in **2-PhNO** were similar to those of **2-Cl**, **2-Br** and **2-F**, which might indicate a +IV oxidation state for both metals. Coupled nitrosobenzene moieties were planar, pointing out sp^2 hybridisation for all carbons of the cycles. C-C bonds of the cycle had different lengths, significantly shorter for C_{36}-C_{37} and C_{39}-C_{40} (1.340(4) and 1.353(4) Å) compared to the four other bonds (1.421(4)-1.428(4) Å), demonstrating the non-aromaticity of the cycle (see **Figure 117**). This result was in line with the C_{35}-N_{PhNO} bond length of 1.318(4), typical of a C=N double bond. [111] The C-C bond bridging the two nitrosobenzene molecules was measured to 1.425(6) Å, closer to the value of a single C-C bond.

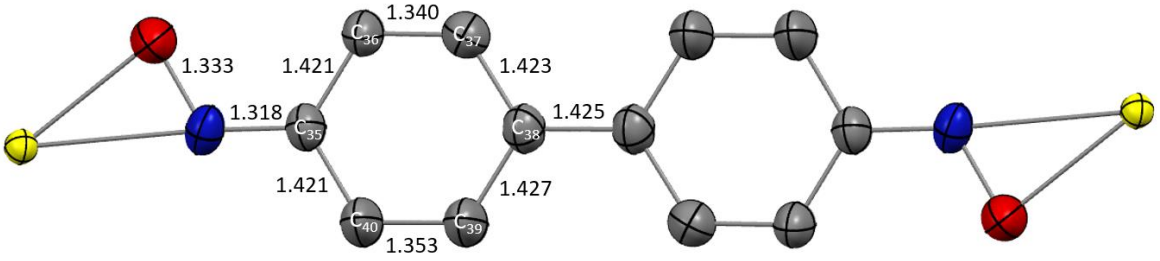

Figure 117. Bond lengths of nitrosobenzene moieties in **2-PhNO**

N-O bond was 1.333(3) Å and co-planar with the cycle, indicative of a single bond considering literature values of about 1.4 Å for N-O single bond in nitrosobenzene complexes.[112] Planarity of the O-N-C atoms indicated a sp^2 hybridization state of the nitrogen atom. X-band EPR spectrum of the crystalline complex dissolved in pentane was silent, but low temperature measurements were not done to confirm the +IV oxidation state of **2-PhNO**. Nevertheless, a representation problem of the bridging C-C bond

persisted, as the bond length was in favour of a single bond, whereas valence, hybridization and resonance structures should lean towards a double bond. Considering the three latter features, the bridging bond was chosen to be represented as a double bond.

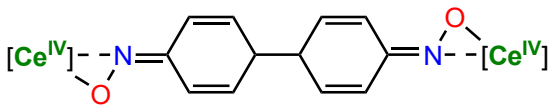

Figure 118. Representation of **2-PhNO**

Reaction monitoring using *in situ* EPR highlighted the formation of a radical in the reaction medium upon addition of PhNO to a solution of **1** in pentane (see **Figure 119**). g-value (2.0027) and hyperfine coupling constants ($A(^{14}N)$ = 1.127 mT, $A(^{1}H_o)$ = 0.400 and 0.388 mT, $A(^{1}H_m)$ = 0.148 and 0.109 mT, $A(^{1}H_p)$ = 0.356 mT) are consistent with a N-centred nitrosobenzene radical interacting with an electrophilic atom, given the higher hyperfine coupling constant with nitrogen atom compared to literature values (around 0.8 mT).[104,105] Nitrosobenzene radical was therefore supposed to interact with $CeTREN^{TIPS}$.

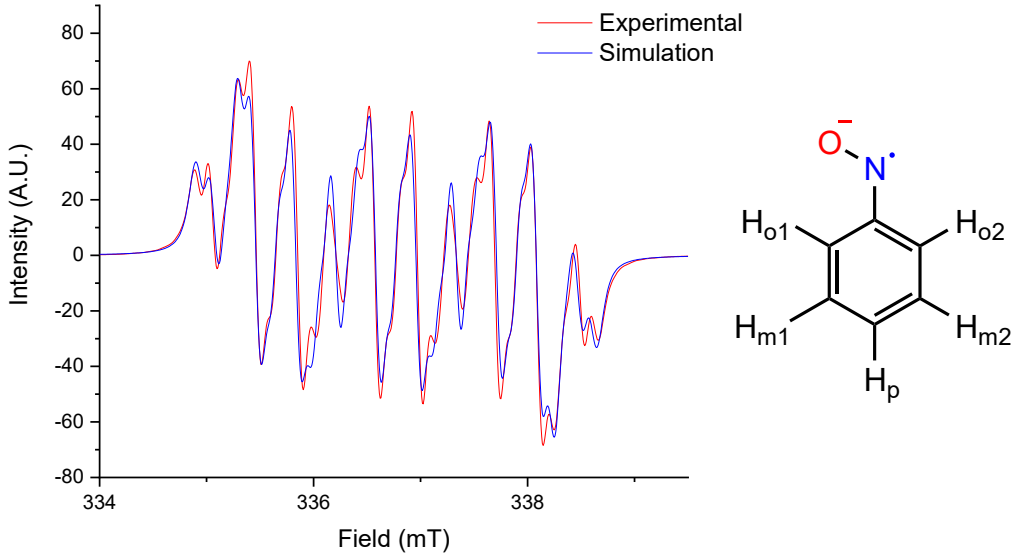

Figure 119. X-band EPR spectrum of the reaction between **1** and PhNO in pentane

Therefore, the coupling of nitrosobenzene moieties is thought to procced through the following mechanism: (i) SET on nitrosobenzene molecule, creating a nitrosobenzene radical partially delocalized in para position ; (ii) addition of the radical on the para position of another reduced nitrosobenzene coordinated with $Ce^{IV}TREN^{TIPS}$ (see **Figure 120**). Computational mechanistic studies should be carried out to confirm this hypothesis.

In this part, complex **1** was shown to reduce nitrosobenzene in the corresponding radical, which is a key step in the reduction of nitroarenes to aniline derivatives. In order to study the possible direct full reduction of nitroarenes, the reactivity of **1** with nitroarene derivatives was investigated.

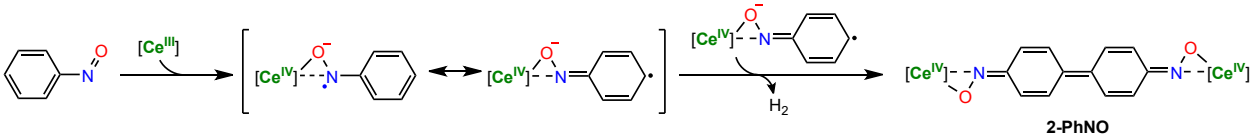

Figure 120. Mechanism hypothesis for the formation of **2-PhNO**

b) Single Electron Transfer on nitro derivatives

1) Formation of nitroarene radicals

Equimolar reaction between **1** and $PhNO_2$ immediately led to a change in colour from yellow to deep purple, which could be consistent with the presence of a cerium(IV) species.

UV-visible analysis of the reaction showed the formation of a large absorption band centred around 590 nm, which would likely correspond to a LMCT transition in a cerium(IV) complex similarly to **2-X** (X = Br, Cl, F, see Chapter I).

^{1}H NMR monitoring of the reaction showed the complete and immediate consumption of **1** and the formation of a new species exhibiting broad resonance peaks around 2.0, 3.4 and 6.5 ppm (see **Figure 121**). This species was unstable and after 6 h of reaction, aromatic compounds bearing highly deshielded hydrogen atoms (about 8.2 ppm) were formed, alongside about 30% of H_3TREN^{TIPS}. While the nature of the new aromatic compounds is still under investigation, the production of H_3TREN^{TIPS} could possibly indicate that a HAT reaction had occurred (see **Figure 121**).

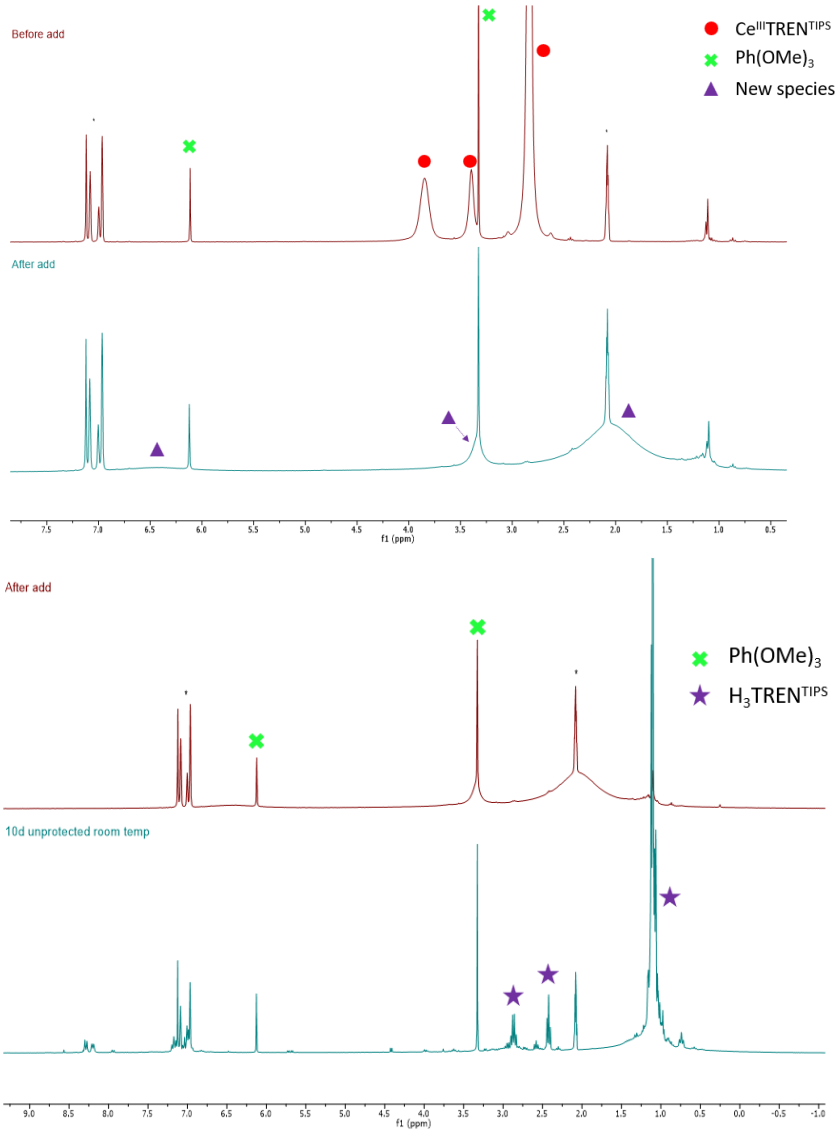

Figure 121. ^{1}H NMR spectrum of the reaction between **1** and $PhNO_2$ after addition (top) and after reaction overnight (bottom) in toluene-d_8. Zoom between 0.5 and 8.0 ppm. (right) Solvent residual peaks are indicated with *

This result could be consistent with the intermediate formation of a radical. To test this hypothesis, the reaction was studied using *in situ* X-band EPR spectroscopy at room temperature. The spectrum obtained from a mixture of **1** and $PhNO_2$ in pentane was dissymmetrical (see **Figure 122**). Formation of an anisotropic radical was precluded due to the temperature at which the spectrum was recorded. The dissymmetry of the spectrum was therefore attributed to the presence of multiple radicals in the reaction medium. Collaborative fitting of the spectrum with EasySpin software[115] by Lhoussain Krouz and I showed the presence of two radicals in 1/3 ratio, herein respectively referred to as system α and system β, which were likely to correspond to nitrobenzene radicals in different chemical environments (see **Figure 122**). Hyperfine coupling constants are in good agreement, while slightly higher, with reported values for nitrobenzene radical in acetonitrile.[78,113,114] This difference might be partly explained by the difference in solvation of the radical and the different chemical environment of the radical (presence of an electrophilic metal).

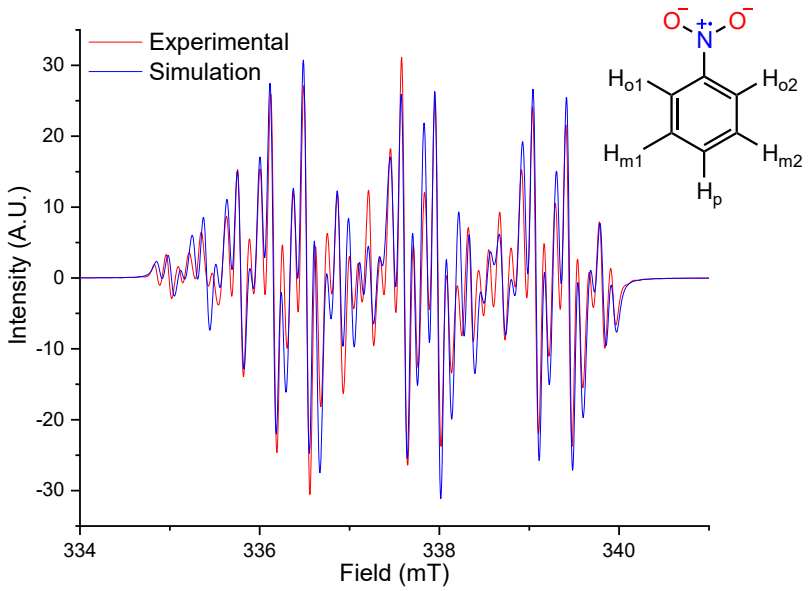

Figure 122. EPR spectrum of the reaction between $PhNO_2$ and **1** in pentane

Parameter	Value
System α	
g	2.0021
$A(^{14}N)$	1.223
$A(^{1}H_{o1})$	0.388
$A(^{1}H_{o2})$	0.388
$A(^{1}H_{m1})$	0.120
$A(^{1}H_{m2})$	0.132
$A(^{1}H_{p})$	0.405
weight	23.9%
System β	
g	1.9963
$A(^{14}N)$	1.459
$A(^{1}H_{o1})$	0.371
$A(^{1}H_{o2})$	0.368
$A(^{1}H_{m1})$	0.113
$A(^{1}H_{m2})$	0.119
$A(^{1}H_{p})$	0.375
weight	75.5%
Litterature[78,113,114]	
$A(^{14}N)$	1.032(3)
$A(^{1}H_{o})$	0.339(2)
$A(^{1}H_{m})$	0.109(1)
$A(^{1}H_{p})$	0.397(2)

Table 3. Fitting values associated with EPR spectrum of the reaction between **1** and $PhNO_2$ in pentane, alongside literature references. A values are given in mT

g-value for system α (2.0021) was similar to the expected value for an N-centred radical (2.003), and much smaller than that for an O-centred nitroxide radical ($R_2NO^{\bullet}$, 2.006),[116] which was also in accordance with $A(^{14}N)$ value (1.223 mT). System α was therefore attributed to be an uncoordinated N-centred $PhNO_2^{\bullet-}$ radical (see **Figure 120**).

System β displayed a much lower g-value (1.996) and a higher $A(^{14}N)$ hyperfine constant. By analogy to system α, the radical was attributed to be N-centred and coordinated to cerium, which could explain the deviation from the values of system α according to literature report.[114] In order to elucidate this reactivity, other para-substituted nitro compounds were investigated given the delocalization of the radical in ortho and para positions (see **Figure 124**).

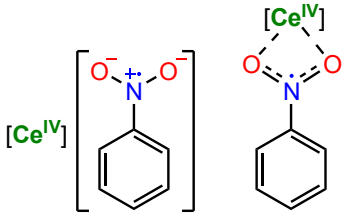

Figure 123. Description of the two systems

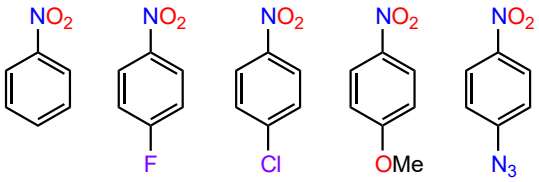

Figure 124. Scope of studied nitro compounds

Similar two-species systems were obtained for 4-fluoronitrobenzene and 4-chloronitrobenzene with comparable hyperfine coupling constants (except for para-substituent given the difference in nuclei, see **Table S47**), with higher A-values for A(^{14}N) and A(^{1}H$_o$). System β was the favoured species for these substrates, with relative weight of 85% in FPhNO$_2$ and 93% in ClPhNO$_2$, compared to 75% for PhNO$_2$ (see **Figure 125**). From these ratios, electron-poor nitroarenes seemed to be thermodynamically more stable in association with cerium cation than in the uncoordinated form.

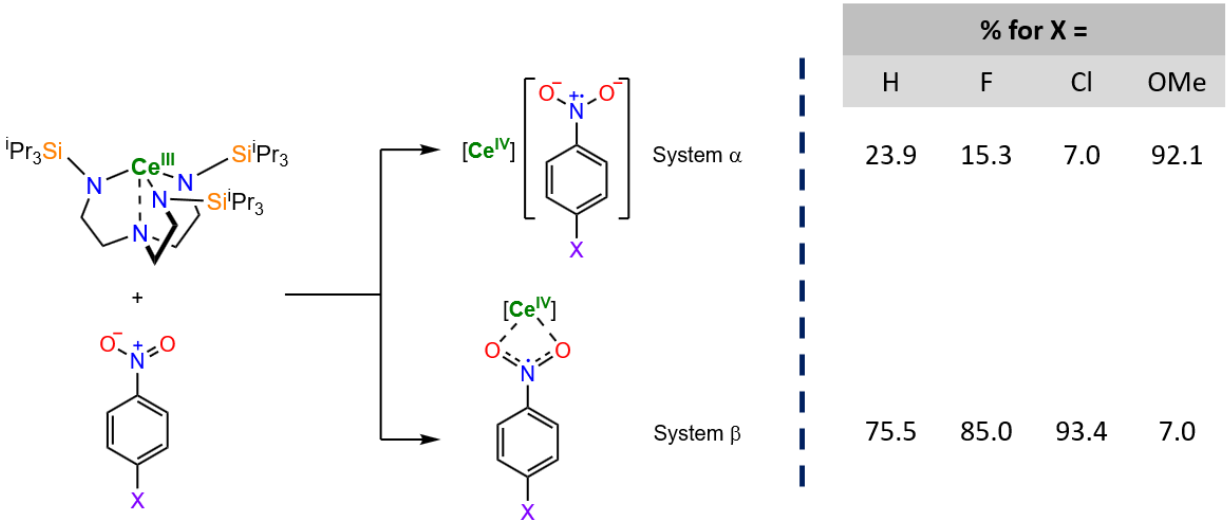

	% for X =			
	H	F	Cl	OMe
System α	23.9	15.3	7.0	92.1
System β	75.5	85.0	93.4	7.0

Figure 125. Formation of both systems α and β, and proportions of each system for every different X group after addition of the nitro derivative

4-nitroanisole showed an opposite behaviour : major species was found to be the uncoordinated radical system α, displaying super-hyperfine coupling with hydrogen of methoxy group. System β featured broad peaks which precluded determination of all A-values, and thus prevented the direct identification of of system β. Electron-rich nitroarene radicals therefore seem to be thermodynamically more stable in uncoordinated form, provided that the attribution of system β is identical to the one of other nitroarene compounds.

Surprisingly, 4-azidonitrobenzene did not react with **1**. Upon irradiation at 427 nm for 1 minute in pentane, a slight change of colour to orange could be noticed, but no radical was detected in EPR. This change in colour could be attributed to a reactivity with the azido group, as preliminary investigations into the activation of aromatic azides by **1** suggest (not presented in this manuscript).

Ratio of system α and system β were not influenced by the initial amount of PhNO$_2$ introduced, as reactions with 0.5 and 2 equivalents in similar conditions gave perfectly identical results. *In situ* light irradiation of the sample at 405 nm neither did lead to a change in the ratio between the two species.

To further probe a possible difference in reactivity, the time stability of the different species was investigated.

2) Stability of nitroarene radical

Over the course of time, system β converted into system α, meaning that the hypothetical coordinated radical slowly degraded over time and converts into an uncoordinated radical (see **Figure 126**) as shown by EPR kinetics on the four nitroarenes (see **Figure 127**).

UV-visible monitoring of the reaction over 24 h showed a decrease in absorbance of the band at 556 nm and the concomitant appearance of two new bands at 477 and 459 nm. Isosbestic point at 504 nm indicated a conversion of the initial species to a new one (see **Figure 128**). By comparing with the EPR monitoring data, the absorption band around 590 nm was attributed to the absorption of major system β, which should be expected to exhibit a high ε value similarly to **2-X** (X = F, Cl, Br).

Conversion of system β is occurring on a fairly long-time scale ($t_{1/2} \approx 6$ h). Small kinetic differences can be noticed in **Figure 127**, but might not be significant due to the overlap of the spectra of both species. Further kinetic studies could provide insight into the order of the reaction and the conversion mechanism.

Attempts to trap the radical with 1,1'-(2-Propenylidene)bis[benzene], bis(pinacolato)diboron, norbornene, tris(*tert*-butyl)phenol, dihydroanthracene, diphenylacetylene, diphenyl disulphide (PhS-SPh), hexamethyldisilane (Me_3Si-$SiMe_3$), triethylsilane (Et_3SiH) and tri(isopropyl)phosphite ($P(O^iPr)_3$) were unsuccessful (see **Figure 129**). No change could be observed in EPR in the presence of N-*tert*-butyl-α-phenylnitrone (PBN).

To extend the scope of the reactivity of **1** with nitro derivatives, nitroalkanes were investigated.

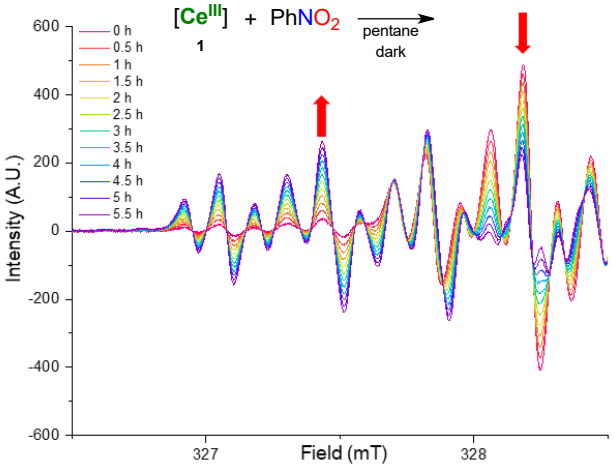

Figure 126. EPR kinetic monitoring of the reaction between $PhNO_2$ and **1** in pentane at 10^{-4} M. Zoom on the region between 326.5 and 328.7 mT

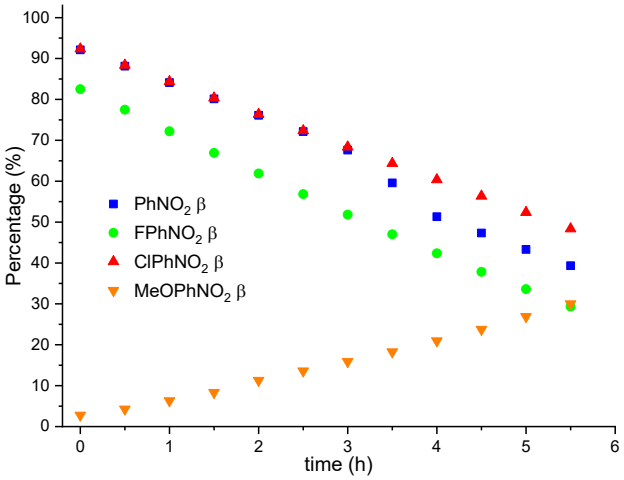

Figure 127. Superimposition of appearance of system β in the reactions of several nitro compounds with **1** in pentane at 10^{-4} M.

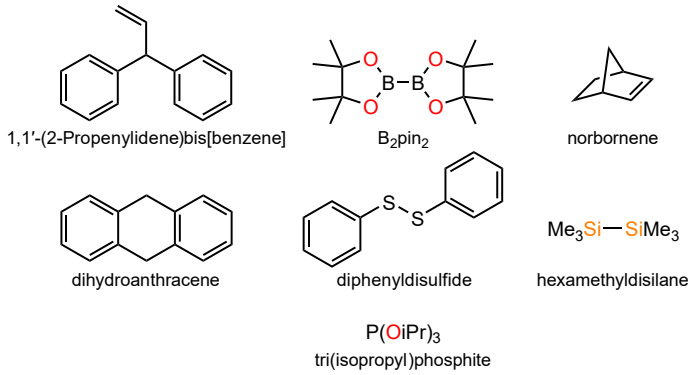

Figure 129. Substrates attempted for radical trapping experiments with nitrobenzene radicals

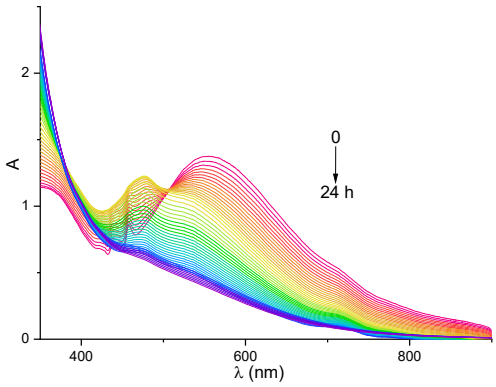

Figure 128. Kinetic UV-visible monitoring of the degradation of the species formed by the reaction between **1** and $PhNO_2$ in pentane

3) Reactivity with nitroalkanes

Addition of $MeNO_2$ to a solution of **1** in THF-d_8 or toluene-d_8 led to an immediate change in colour to purple, which turned within seconds to a colourless solution and led to a precipitation of a whitish solid. ^{1}H NMR monitoring of the reaction in C_6D_6 showed the immediate formation of H_3TREN^{TIPS}, which could not be controlled even when the reaction was performed at -40 °C in toluene-d_8.

Given the immediate colour change to purple upon addition, it could be reasonably envisaged that an electron transfer occurs on $MeNO_2$. This would lead to the formation of $MeNO_2^{\bullet-}$ which could polymerise, thereby explaining the formation of the solid.

To rule out any possibility of purely acid-base reaction given the low pK_A of protons in nitromethane (pK_A = 10.21 in H_2O),[117] 2-methyl-2-nitropropane was selected due to the absence of acidic protons in α position. Upon mixing one equivalent of 2,2-dimethylnitropropane with a solution of **1** in either THF-d_8 or C_6D_6, no change in colour could be observed. ^{1}H NMR spectrum indicated a small shift in the peaks of **1** in C_6D_6 (see **Figure 130**), possibly caused by a coordination of ^{t}BuNO$_2$. No EPR signal could be detected in the dark.

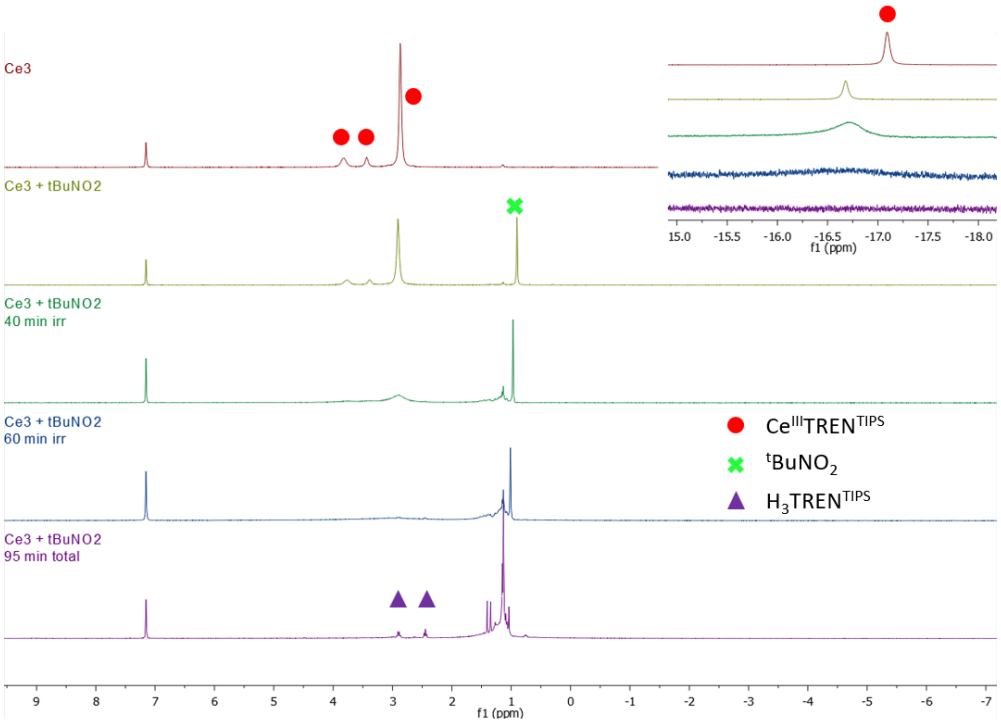

Figure 130. ^{1}H NMR of the equimolar reaction between **1** and 2-methyl-2-nitropropane under irradiation at 427 nm

Storage of the mixture under ambient light allowed for a progressive change in colour to purple. After 5 minutes under ambient light, EPR spectrum of the reaction in pentane showed a low intensity triplet centred around g = 2.0015 with A = 1.365 mT, which were similar to the abovementioned free N-centred nitroarene radicals (see **Figure 131**). Nevertheless, no hyperfine coupling could be detected with hydrogens, which is consistent with the absence of delocalization of the radical. Contrary to the reduction of nitroarenes, only one system was observed with ^{t}BuNO$_2$. Irradiation at 427 nm for 5 minutes caused a dramatic increase in triplet intensity, which is likely to correspond to a photoinduced reduction of ^{t}BuNO$_2$ by **1**.

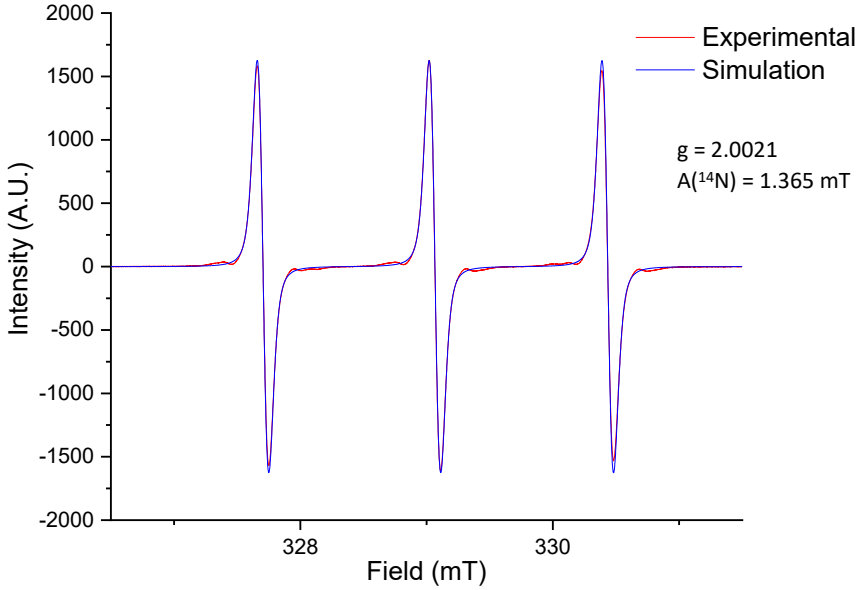

Figure 131. EPR spectrum of the reaction between $^{t}BuNO_2$ and **1** in pentane at 10^{-4} M after 5 minutes in ambient light

Monitoring of the irradiation of the reaction by ^{1}H NMR spectroscopy showed a clear decrease in **1** and a shift of $^{t}BuNO_2$ singlet from 0.90 ppm to 0.97 ppm after 40 minutes of irradiation (see **Figure 130**). Simultaneously, the appearance of a broad peak centred around 3 ppm could correspond to the formation of the nitroalkane radical. After irradiating for 95 minutes, **1** was consumed and non-negligible quantities of H_3TREN^{TIPS} were present. Two singlets at 1.40 and 1.35 ppm might indicate the formation of 2,2'-azobis(2-methylpropane) $^{t}BuN{=}N^{t}Bu$ and 2-methyl-2-nitrosopropane $^{t}BuNO$.

Need for irradiation for 2-methyl-2-nitropropane activation compared to nitroarene is in line with reported redox potentials respectively of -1.25 V in THF and -0.71 V in H_2O *vs*. Fc/Fc^{+} for $PhNO_2$.[118,119] This might be explained by the radical anion stabilization in the latter case, which enables an electron transfer without external stimuli.

To gain more insight into the formation of radicals on N-O bonds, the scope of reactivity was extended to include other families of compounds with different types of N-O bonds.

II. Reduction of N-O bond in organic nitrites, amine oxides and nitrones

a) Organic Nitrites

Among the possible candidates of N-O groups, nitrite reagents were considered as they are constitutional isomers of nitro compounds. We were especially interested in the reactivity of **1** with *tert*-butyl nitrite ^{t}BuONO. Known for its use as nitrosation agents on secondary amides,[120] the weaker O-N bond compared to nitro derivatives would likely be reduced by **1** without any external stimuli.

Reaction between **1** and ^{t}BuONO in THF-d_8 led to an immediate change in colour from yellow to orange. ^{1}H NMR analysis of the reaction medium showed the formation of important amounts of H_3TREN^{TIPS}.

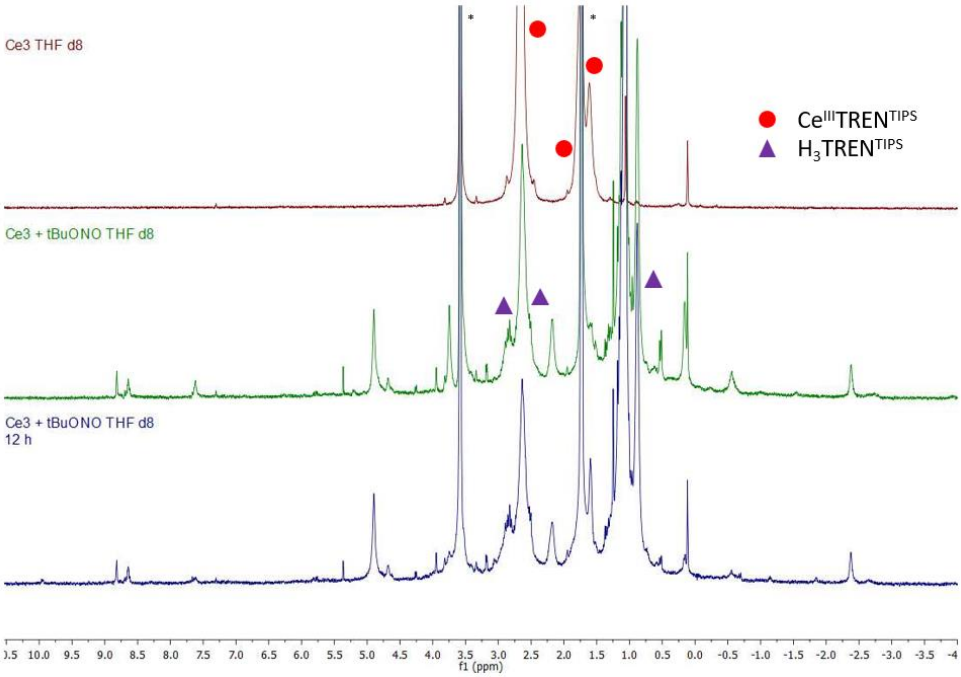

Figure 132. ^{1}H NMR spectrum of the reaction between **1** and *tert*-butyl nitrite in THF-d_8. Zoom between -4.0 and 11.5 ppm. Solvent peaks are indicated with *

The reaction was incomplete, as important quantities of **1** remained after reaction. This was attributed to the important uncertainty of the quantity of nitrite injected in the tube given the small scale of the reaction. No major product could be identified : traces of ethylene (5.36 ppm) and ^{t}BuOH (3.16 and 1.17 ppm) could be found after reaction.

At first sight, formation of ^{t}BuOH might be rationalized through the transient generation of a ^{t}BuO$^{\bullet}$ radical from the reduction of ^{t}BuONO by **1** followed by a HAT reaction. Nevertheless, ^{t}BuO$^{\bullet}$ should also generate methane and acetone through β-scission of the alkoxy radical and subsequent HAT reaction. No traces of these two latter compounds could be found in the NMR spectra after reaction, therefore ruling out the possibility of ^{t}BuO$^{\bullet}$ generation. The formation of ethylene remains unexplained so far.

To further investigate the reactivity of **1** with N-O bonds, amine-oxide derivatives (R_3N^{+}-O^{-}) were considered as the oxidation state of the nitrogen (-I) is lower than in the previously studied compounds.

b) Reactivity with amine-oxides

In order to study the reactivity of **1** with amine-oxide derivatives, the reaction between **1** and ^{1}H NMR simple trimethylammonium-oxide (TMAO) in THF-d_8. Upon addition, TMAO is immediately completely consumed. Several singlets around 1.1 ppm appear, and a singlet at 2.16 ppm that could correspond to trimethylamine.

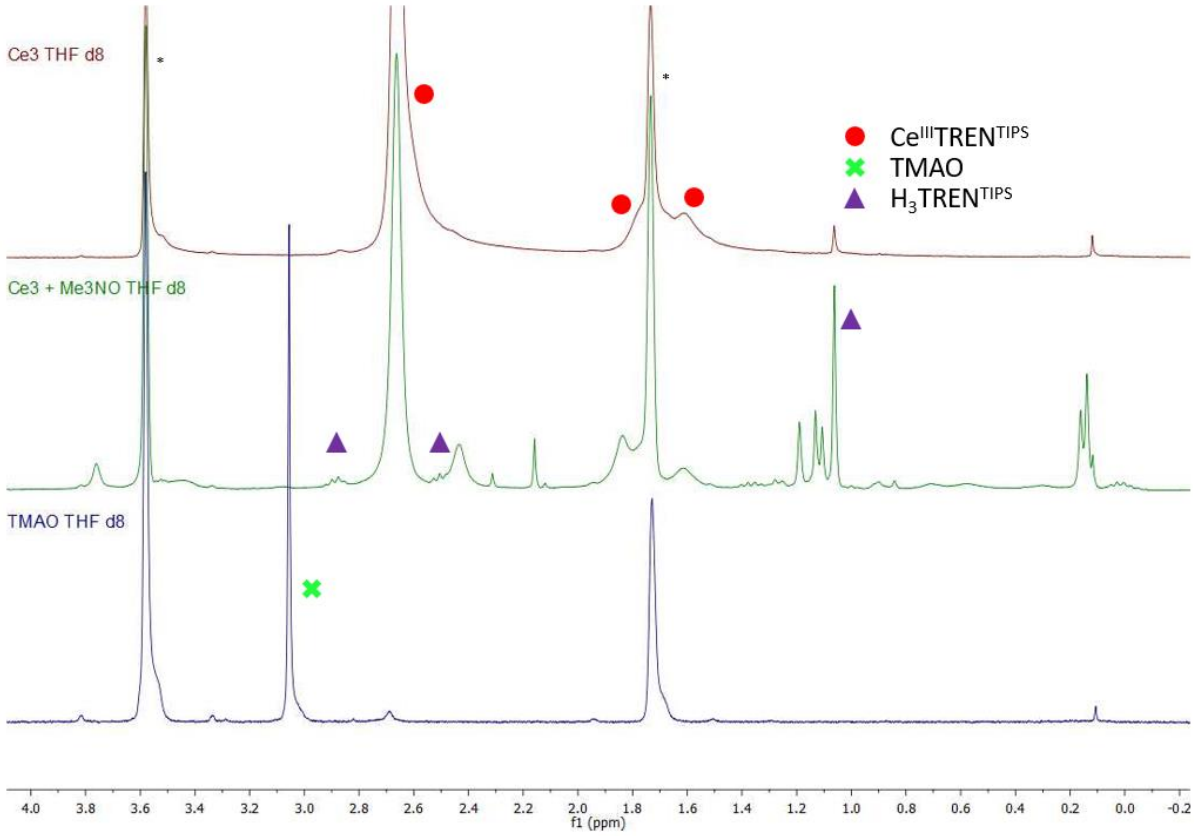

Figure 133. ^{1}H NMR spectrum of the reaction between **1** and TMAO in THF-d_8. Zoom between -0.2 and 4.5 ppm region. Solvent peaks are indicated with *

Probing the reactivity with other amine oxides such as N-methylmorpholine-N-oxide (NMO) afforded similar results with the production of small quantities of N-methylmorpholine.

Reaction of pyridinium-N-oxide with **1** afforded nevertheless slightly different results. Pyridine was not identified as a product from the reaction, but other similar aromatic compounds were formed. In the presence of B_2pin_2, initially introduced to attempt to trap any oxygen based reactive species, small amounts of pyridine could be detected by ^{1}H NMR spectroscopy.

Following on the nitrogen species to study and considering the importance of EPR reactivity analysis in the project, the reactivity of **1** with nitrone radical trappers was studied, as PBN and 5,5-dimethyl-1-pyrroline *N*-oxide (DMPO) are the most widely used radical trappers.

c) Monoelectronic reduction of nitrones

Nitrones (R-C=N$^+$(O$^-$)-R') are interesting building blocks for organic synthesis. They can engage in [3+2] dipolar cycloadditions with multiple bonds to form isoxazolidine groups,[121,122] which are often part of biologically active compounds.[123–125]

Nitrones are also well-known for their ability to react with radicals to form long-lived nitroxyl radicals which can be detected using EPR spectroscopy. This specific behaviour allowed for the developments of many studies relative to *in vivo* generated short-lived radicals such as reactive oxygen species and reactive nitrogen species.[126–130] Chemical trapping and detection of short-lived radical intermediates is of interest, as it can provide crucial insights on mechanism for a given reaction.[131,132] Their therapeutic potential to trap radicals generated by oxidative stress is also thoroughly investigated, as many serious conditions including Parkinson disease, Alzheimer disease, acute ischemia and cancer development, tend to increase the generation of free radicals.[133–136]

Two nitrones have mainly been used to trap radicals : *N-tert*-Butyl-α-phenylnitrone (PBN) for C-centred radicals, and 5,5-dimethyl-1-pyrroline *N*-oxide (DMPO) for O-centred radicals (see **Figure 134**).[137–140]

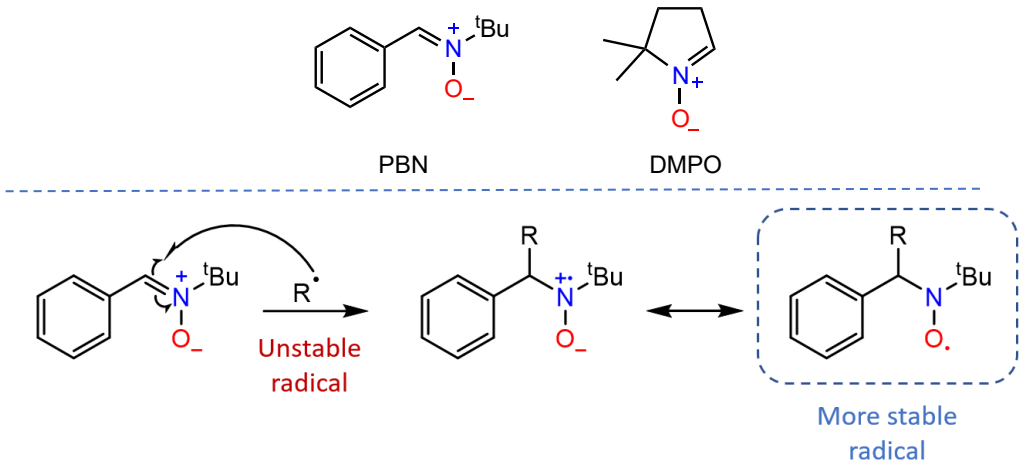

Figure 134. Nitrone spin trappers *N-tert*-Butyl-α-phenylnitrone (PBN) and 5,5-dimethyl-1-pyrroline *N*-oxide (DMPO) (top), and example of spin-trapping mechanism on PBN (bottom)

While several metal complexes bearing nitrone ligands have been reported,[141–143] no example of nitrone-bearing lanthanide complex has been reported to the best of my knowledge. Spin trapping technique have nevertheless been used to study radical production induced by lanthanides (cerium and samarium mainly).[144–157]

Equimolar mixture of **1** and DMPO in THF-d_8 immediately changed colour to orange upon addition. ^{1}H NMR spectrum of the reaction medium showed a degradation of DMPO and **1**, concomitant with the production of H_3TREN^{TIPS}. This reactivity could be explained by the instability of the radical hypothetically formed in a similar way to N-oxide derivatives, which prevented further use of DMPO in radical trapping experiments.

Mixing **1** with PBN in THF-d_8 did not induce significant change in the ^{1}H NMR spectrum. Cold storing of a concentrated mixture of **1** and PBN in pentane afforded extremely light sensitive crystals which corresponded to the adduct complex **1-PBN** (see **Figure 135**, any direct light on the crystal during XRD measurement led to degradation). No significant change could be observed in the 3D structure of the complex from the metrics of **1**.

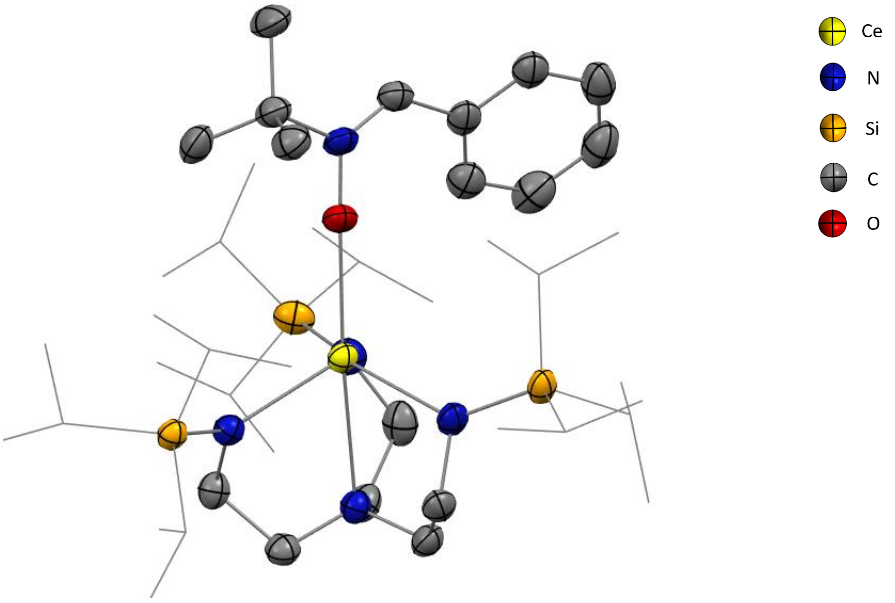

Figure 135. Structure of **1-PBN**. Displacement ellipsoids are represented at 50% probability. Hydrogen atoms have been omitted for clarity, and isopropyl groups have been represented in wireframe style

Nevertheless, a slow change in colour to light orange was observed upon storage of the solution at room temperature under ambient light. Irradiation of the sample at 427 nm led to a significant decrease in both **1** and PBN, and the progressive generation of H_3TREN^{TIPS} (see **Figure S195**).

Analysis of the reaction using *in situ* EPR allowed to probe further this reaction. Before irradiation, a triplet with very low intensity was detected at g = 2.002 with A = 1.367 mT, which would be consistent with a N-centred radical very similar to nitroalkane $^tBuNO_2^{\bullet-}$ radical described earlier in this manuscript. Upon irradiation at 405 nm, intensity of the triplet quickly soared, and slowly decreased upon prolonged irradiation.

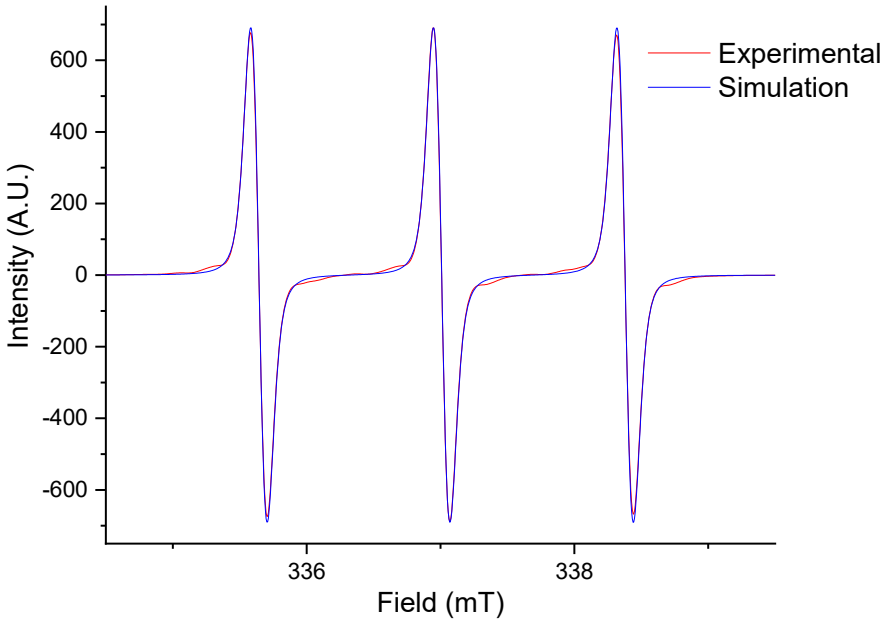

Figure 136. EPR spectrum of the reaction between PBN and **1** in pentane at 10^{-4} M after 12 min irradiation at 405 nm

These results converged towards the one-electron reduction of PBN, creating a radical anion of PBN. While some reduction of nitrones have been reported in the literature,[31,33,35,158,159] it is the only evidence of PBN radical anion formation in the literature to the best of my knowledge.

Attempts to trap the radical with 1,1'-(2-propenylidene)bis[benzene] and 1,1-diphenylethylene by irradiation at 427 nm in THF-d_8 were proven unsuccessful (see **Figure 137**).

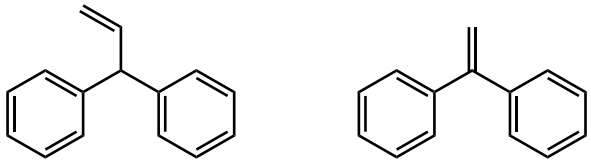

1,1'-(2-Propenylidene)bis[benzene] 1,1-diphenylethylene

Figure 137. Substrates investigated for radical trapping in the photoinduced reaction between **1** and PBN

Together, the results presented in this chapter showcased the versatility of complex **1** to activate a wide variety of N-O bonds in different families of compounds through unusual mechanisms. While the analysis of products is often made difficult by a lack of selectivity of the reactions and by unproductive ligand collapse, this work initiated possible developments of original reactivities.

To further complete the study of species involved in the nitrogen cycle, the reactivity of inorganic nitrogen compounds as nitrates and nitrites alongside nitrous oxide activation will be discussed in the next chapter.

References

(1) Fung, H.-L.; Chung, S.-J.; Bauer, J. A.; Chong, S.; Kowaluk, E. A. Biochemical Mechanism of Organic Nitrate Action. *Am. J. Cardiol.* **1992**, *70* (8), B4–B10. https://doi.org/10.1016/0002-9149(92)90588-P.

(2) Brambilla, G.; Martelli, A. Genotoxic and Carcinogenic Risk to Humans of Drug–Nitrite Interaction Products. *Mutat. Res. Mutat. Res.* **2007**, *635* (1), 17–52. https://doi.org/10.1016/j.mrrev.2006.09.003.

(3) Klapötke, T. M.; Lemarchand, G.; Lenz, T.; Mühlemann, M.; Stierstorfer, J.; Weber, R. Impact and Friction Sensitivities of PETN: I. Sensitivities of the Pure and Wetted Material. *Propellants Explos. Pyrotech.* **2022**, *47* (9), e202200150. https://doi.org/10.1002/prep.202200150.

(4) Jia, J.; Chen, J.; Ding, H.; Xue, X.; Li, S.; Huang, J.; Liu, Y. A Comprehensive Study of the Dissolution Process of *N*-Oxide Based Explosives in Deep Eutectic Solvents. *J. Mol. Liq.* **2021**, *340*, 117170. https://doi.org/10.1016/j.molliq.2021.117170.

(5) Zhuang, S.; Jia, J.; Lin, Y.; He, Y.; Liu, Y.; Huang, H.; Chen, J.-B. A Two-in-One Sensing Solvent for Green Extraction and Analysis of *N*-Oxide Based Explosives. *Microchem. J.* **2022**, *180*, 107542. https://doi.org/10.1016/j.microc.2022.107542.

(6) Marrs, F. W.; Davis, J. V.; Burch, A. C.; Brown, G. W.; Lease, N.; Huestis, P. L.; Cawkwell, M. J.; Manner, V. W. Chemical Descriptors for a Large-Scale Study on Drop-Weight Impact Sensitivity of High Explosives. *J. Chem. Inf. Model.* **2023**, *63* (3), 753–769. https://doi.org/10.1021/acs.jcim.2c01154.

(7) Sikder, A. K.; Sikder, N. A Review of Advanced High Performance, Insensitive and Thermally Stable Energetic Materials Emerging for Military and Space Applications. *J. Hazard. Mater.* **2004**, *112* (1), 1–15. https://doi.org/10.1016/j.jhazmat.2004.04.003.

(8) Al-Rubaye, H.; Perfetti, G.; Kaski, J.-C. The Role of Microbiota in Cardiovascular Risk: Focus on Trimethylamine Oxide. *Curr. Probl. Cardiol.* **2019**, *44* (6), 182–196. https://doi.org/10.1016/j.cpcardiol.2018.06.005.

(9) Kałużna-Czaplińska, J.; Gątarek, P. Trimethylamine N-Oxide (TMAO) in Human Health. *EXCLI J.* **2021**, *20*, 301–319. https://doi.org/10.17179/excli2020-3239.

(10) Thomas, M. S.; Fernandez, M. L. Trimethylamine N-Oxide (TMAO), Diet and Cardiovascular Disease. *Curr. Atheroscler. Rep.* **2021**, *23* (4), 12. https://doi.org/10.1007/s11883-021-00910-x.

(11) Li, D.; Lu, Y.; Yuan, S.; Cai, X.; He, Y.; Chen, J.; Wu, Q.; He, D.; Fang, A.; Bo, Y.; Song, P.; Bogaert, D.; Tsilidis, K.; Larsson, S. C.; Yu, H.; Zhu, H.; Theodoratou, E.; Zhu, Y.; Li, X. Gut Microbiota–Derived Metabolite Trimethylamine-N-Oxide and Multiple Health Outcomes: An Umbrella Review and Updated Meta-Analysis. *Am. J. Clin. Nutr.* **2022**, *116* (1), 230–243. https://doi.org/10.1093/ajcn/nqac074.

(12) Wang, Y.; Zhang, L. Recent Developments in the Chemistry of Heteroaromatic N-Oxides. *Synthesis* **2015**, *47* (3), 289–305. https://doi.org/10.1055/s-0034-1379884.

(13) Wilson, W. R.; Denny, W. A.; Pullen, S. M.; Thompson, K. M.; Li, A. E.; Patterson, L. H.; Lee, H. H. Tertiary Amine N-Oxides as Bioreductive Drugs: DACA N-Oxide, Nitracrine N-Oxide and AQ4N. *Br. J. Cancer. Suppl.* **1996**, *27*, S43–S47.

(14) Lutz, W. B.; Lazarus, S.; Klutchko, S.; Meltzer, R. I. Amino Derivatives of Pyrazine N-Oxides1. *J. Org. Chem.* **1964**, *29* (6), 1645–1647. https://doi.org/10.1021/jo01029a517.

(15) Howard, E. Jr.; Olszewski, W. F. The Reaction of Triphenylphosphine with Some Aromatic Amine Oxides1. *J. Am. Chem. Soc.* **1959**, *81* (6), 1483–1484. https://doi.org/10.1021/ja01515a050.

(16) Biffin, M. E. C.; Bocksteiner, G.; Miller, J.; Paul, D. B. Reduction by Sulphoxides : The Mechanism of Deoxygenation of Heterocyclic N-Oxides and Tertiary Amine N-Oxide. *Aust. J. Chem.* **1974**, *27* (4), 789–799. https://doi.org/10.1071/ch9740789.

(17) Daniher, F. A.; Hackley, B. E. Jr. Deoxygenation of Pyridine N-Oxides with Sulfur Dioxide. *J. Org. Chem.* **1966**, *31* (12), 4267–4268. https://doi.org/10.1021/jo01350a524.

(18) Bonini, B. F.; Maccagnani, G.; Mazzanti, G.; Pedrini, P. Deoxygenation of Pyridine N-Oxides with Sulphur Monoxide Generated from Trans-2,3-Diphenylthiiran-1-Oxide. *Tetrahedron Lett.* **1979**, *20* (20), 1799–1800. https://doi.org/10.1016/S0040-4039(01)86221-3.

(19) Kagami, H.; Motoki, S. Deoxygenation of Amine N-Oxides or C-Nitroso Compounds by Dialkyl Sulfoxylates. *J. Org. Chem.* **1978**, *43* (6), 1267–1268. https://doi.org/10.1021/jo00400a061.
(20) Chandrasekhar, S.; Reddy, C. R.; Rao, R. J.; Rao, J. M. Efficient and Chemoselective Deoxygenation of Amine N-Oxides Using Polymethylhydrosiloxane. *Synlett* **2002**, *2002* (02), 0349–0351. https://doi.org/10.1055/s-2002-19751.
(21) Lecroq, W.; Schleinitz, J.; Billoue, M.; Perfetto, A.; Gaumont, A.-C.; Lalevée, J.; Ciofini, I.; Grimaud, L.; Lakhdar, S. Metal-Free Deoxygenation of Amine N-Oxides: Synthetic and Mechanistic Studies. *ChemPhysChem* **2021**, *22* (12), 1237–1242. https://doi.org/10.1002/cphc.202100108.
(22) Kokatla, H. P.; Thomson, P. F.; Bae, S.; Doddi, V. R.; Lakshman, M. K. Reduction of Amine N-Oxides by Diboron Reagents. *J. Org. Chem.* **2011**, *76* (19), 7842–7848. https://doi.org/10.1021/jo201192c.
(23) Alonso, F.; Radivoy, G.; Yus, M. Reduction of Hydrazines, Azo and Azoxy Compounds, and Amine *N*-Oxides with the NiCl2·2H2O–Li–DTBB (Cat.) Combination. *Tetrahedron* **2000**, *56* (44), 8673–8678. https://doi.org/10.1016/S0040-4020(00)00797-3.
(24) Balicki, R.; Cybulski, M.; Maciejewski, G. An Efficient Deoxygenation of Heteroaromatic N-Oxides Using Zinc Dust/Ammonium Formate Reagent System. *Synth. Commun.* **2003**, *33* (23), 4137–4141. https://doi.org/10.1081/SCC-120026355.
(25) Jousseaume, B.; Chanson, E. Mild Selective Deoxygenation of Amine Oxides by Tin-Tin Bonded Derivatives. *Synthesis* **1987**, *1987* (01), 55–56. https://doi.org/10.1055/s-1987-27842.
(26) Yoo, B. W.; Choi, J. W.; Yoon, C. M. A Facile and Efficient Deoxygenation of Amine-*N*-Oxides with Mo(CO)6. *Tetrahedron Lett.* **2006**, *47* (1), 125–126. https://doi.org/10.1016/j.tetlet.2005.10.143.
(27) Saini, A.; Kumar, S.; Sandhu, J. S. An Efficient and General Method for the Deoxygenation of Organic N-Oxides Using Zn(OTf)2 and Cu(OTf)2. *Synlett* **2006**, *2006* (3), 395–398. https://doi.org/10.1055/s-2006-926269.
(28) Kano, S.; Tanaka, Y.; Sugino, E.; Hibino, S. Reduction of Some Functional Groups with Titanium(IV) Chloride/Sodium Borohydride. *Synthesis* **1980**, *1980* (09), 695–697. https://doi.org/10.1055/s-1980-29174.
(29) Kumar, S.; Saini, A.; Sandhu, J. S. A General Method for the Deoxygenation of Aromatic *N*-Oxides Using RuCl3·*x*H2O. *Tetrahedron Lett.* **2005**, *46* (50), 8737–8739. https://doi.org/10.1016/j.tetlet.2005.10.047.
(30) Wang, Y.; Espenson, J. H. Efficient Catalytic Conversion of Pyridine N-Oxides to Pyridine with an Oxorhenium(V) Catalyst. *Org. Lett.* **2000**, *2* (22), 3525–3526. https://doi.org/10.1021/ol006595k.
(31) Ilankumaran, P.; Chandrasekaran, S. Chemoselective Deoxygenation of Nitrones and N-Oxides with Tetrathiomolybdate. *Tetrahedron Lett.* **1995**, *36* (27), 4881–4882. https://doi.org/10.1016/0040-4039(95)00875-D.
(32) Yoon, N. M. Selective Reduction of Organic Compounds with Aluminum and Boron Hydrides. *Pure Appl. Chem.* **1996**, *68* (4), 843–848. https://doi.org/10.1351/pac199668040843.
(33) Barton, D. H. R.; Fekih, A.; Lusinchi, X. Selective Reduction of the N-O Bond in N-Oxides and in Nitrones by Sodium Hydrogen Telluride. *Tetrahedron Lett.* **1985**, *26* (38), 4603–4606. https://doi.org/10.1016/S0040-4039(00)98763-X.
(34) Yadav, J. S.; Subba Reddy, B. V.; Reddy, M. M. Indium-Mediated Deoxygenation of Amine-*N*-Oxides in Aqueous Media†. *Tetrahedron Lett.* **2000**, *41* (15), 2663–2665. https://doi.org/10.1016/S0040-4039(00)00218-5.
(35) Ilias, M.; Barman, D. C.; Prajapati, D.; Sandhu, J. S. An Indium Mediated Efficient Chemoselective Deoxygenation of *N*-Oxides and Nitrones. *Tetrahedron Lett.* **2002**, *43* (10), 1877–1879. https://doi.org/10.1016/S0040-4039(02)00020-5.
(36) Han, J. H.; Il Choi, K.; Kim, J. H.; Yoo, B. W. Facile and Efficient Deoxygenation of Amine-N-oxides with Gallium in Water. *Synth. Commun.* **2004**, *34* (17), 3197–3201. https://doi.org/10.1081/SCC-200028619.
(37) Zhang, Y.; Lin, R. Some Deoxygenation and Reducation Reactions with Samarium Diiodide. *Synth. Commun.* **1987**, *17* (3), 329–332. https://doi.org/10.1080/00397918708077313.
(38) Jeong, J.; Suzuki, K.; Hibino, M.; Yamaguchi, K.; Mizuno, N. Selective Deoxygenation of Pyridine N-Oxides through Photoredox Catalysis of a Dilacunary Silicotungstate. *ChemistrySelect* **2016**, *1* (15), 5042–5048. https://doi.org/10.1002/slct.201601146.

(39) Kjellberg, M.; Ohleier, A.; Thuéry, P.; Nicolas, E.; Anthore-Dalion, L.; Cantat, T. Photocatalytic Deoxygenation of N–O Bonds with Rhenium Complexes: From the Reduction of Nitrous Oxide to Pyridine N-Oxides. *Chem. Sci.* **2021**, *12* (30), 10266–10272. https://doi.org/10.1039/D1SC01974K.

(40) Kim, K. D.; Lee, J. H. Visible-Light Photocatalyzed Deoxygenation of N-Heterocyclic N-Oxides. *Org. Lett.* **2018**, *20* (23), 7712–7716. https://doi.org/10.1021/acs.orglett.8b03446.

(41) Sako, Magoichi.; Shimada, Kaoru.; Hirota, Kosaku.; Maki, Yoshifumi. Photochemical Oxygen-Atom Transfer Reaction by Heterocycle N-Oxides Involving a Single-Electron Transfer Process: Oxidative Demethylation of N,N-Dimethylaniline. *J. Am. Chem. Soc.* **1986**, *108* (19), 6039–6041. https://doi.org/10.1021/ja00279a063.

(42) Ryu, H. K.; Song, Y. D.; Lee, J. H. Deoxygenation of N-Heterocyclic N-Oxides Using Isopropanol as a Recyclable Reductant. *Org. Chem. Front.* **2024**, *11* (8), 2249–2268. https://doi.org/10.1039/D4QO00208C.

(43) Konev, M. O.; Cardinale, L.; Jacobi von Wangelin, A. Catalyst-Free N-Deoxygenation by Photoexcitation of Hantzsch Ester. *Org. Lett.* **2020**, *22* (4), 1316–1320. https://doi.org/10.1021/acs.orglett.9b04632.

(44) Albini, A.; Fasani, E.; Moroni, M.; Pietra, S. Photochemical Decomposition of 4-Arylazo- and 4-Arylazoxy-N,N-Dialkylaniline N-Oxides. *J. Chem. Soc. Perkin Trans. 2* **1986**, No. 9, 1439–1443. https://doi.org/10.1039/P29860001439.

(45) Maki, Y.; Shimada, K.; Sako, M.; Hirota, K. Photo-Oxidative Cyclisation of 2'-Hydroxychalcones Leading to Flavones Induced by heterocycleN-Oxides : High Efficiency of Pybimido[54-g]Pteridine N-Oxide for the Photochemical Dehydrogenation. *Tetrahedron* **1988**, *44* (11), 3187–3194. https://doi.org/10.1016/S0040-4020(01)85950-0.

(46) Luo, Y.-R. *Comprehensive Handbook of Chemical Bond Energies*; CRC Press: Boca Raton, 2007. https://doi.org/10.1201/9781420007282.

(47) Todorović, U.; Martin Romero, R.; Anthore-Dalion, L. Activation of N−O σ Bonds with Transition Metals: A Versatile Platform for Organic Synthesis and C−N Bonds Formation. *Eur. J. Org. Chem.* **2023**, *26* (31), e202300391. https://doi.org/10.1002/ejoc.202300391.

(48) Kubota, T.; Miyazaki, H. The Effect of Substituents on the Half-Wave Potential of the Polarographic Reduction of Pyridine N-Oxide Derivatives. *Bull. Chem. Soc. Jpn.* **1966**, *39* (10), 2057–2062. https://doi.org/10.1246/bcsj.39.2057.

(49) Strauss, M. J. The Nitroaromatic Group in Drug Design. Pharmacology and Toxicology (for Nonpharmacologists). *Ind. Eng. Chem. Prod. Res. Dev.* **1979**, *18* (3), 158–166. https://doi.org/10.1021/i360071a002.

(50) Xavier, J. A.; Silva, T. L.; Torres-Santos, E. C.; de Vasconcelos, C. C.; Boane, A.; dos Santos, R. A.; Xavier, A. F. A.; Goulart, M. O. F. Unveiling the Relevance of the Redox Character of Nitroaromatic and Nitroheteroaromatic Compounds as Potential Medicines. *Curr. Opin. Electrochem.* **2021**, *29*, 100740. https://doi.org/10.1016/j.coelec.2021.100740.

(51) Ju, K.-S.; Parales, R. E. Nitroaromatic Compounds, from Synthesis to Biodegradation. *Microbiol. Mol. Biol. Rev.* **2010**, *74* (2), 250–272. https://doi.org/10.1128/mmbr.00006-10.

(52) Serrano-González, M. Y.; Chandra, R.; Castillo-Zacarias, C.; Robledo-Padilla, F.; Rostro-Alanis, M. de J.; Parra-Saldivar, R. Biotransformation and Degradation of 2,4,6-Trinitrotoluene by Microbial Metabolism and Their Interaction. *Def. Technol.* **2018**, *14* (2), 151–164. https://doi.org/10.1016/j.dt.2018.01.004.

(53) Zhang, M.; Liu, G.; Song, K.; Wang, Z.; Zhao, Q.; Li, S.; Ye, Z. Biological Treatment of 2,4,6-Trinitrotoluene (TNT) Red Water by Immobilized Anaerobic–Aerobic Microbial Filters. *Chem. Eng. J.* **2015**, *259*, 876–884. https://doi.org/10.1016/j.cej.2014.08.041.

(54) Zhao, W.; Yang, X.; Feng, A.; Yan, X.; Wang, L.; Liang, T.; Liu, J.; Ma, H.; Zhou, Y. Distribution and Migration Characteristics of Dinitrotoluene Sulfonates (DNTs) in Typical TNT Production Sites: Effects and Health Risk Assessment. *J. Environ. Manage.* **2021**, *287*, 112342. https://doi.org/10.1016/j.jenvman.2021.112342.

(55) *Code of Federal Law - Toxic Pollutants*; 1981. https://www.ecfr.gov/current/title-40/part-401/section-401.15 (accessed 2025-02-04).

(56) Purohit, V.; Basu, A. K. Mutagenicity of Nitroaromatic Compounds. *Chem. Res. Toxicol.* **2000**, *13* (8), 673–692. https://doi.org/10.1021/tx000002x.
(57) Padda, R. S.; Wang, C.; Hughes, J. B.; Kutty, R.; Bennett, G. N. Mutagenicity of Nitroaromatic Degradation Compounds. *Environ. Toxicol. Chem.* **2003**, *22* (10), 2293–2297. https://doi.org/10.1897/02-220.
(58) *Ecotoxicology of Explosives*. Routledge & CRC Press. https://www.routledge.com/Ecotoxicology-of-Explosives/Sunahara-Lotufo-Kuperman-Hawari/p/book/9780367385590 (accessed 2025-02-03).
(59) Lima, D. R. S.; Bezerra, M. L. S.; Neves, E. B.; Moreira, F. R. Impact of Ammunition and Military Explosives on Human Health and the Environment. **2011**, *26* (2), 101–110. https://doi.org/10.1515/reveh.2011.014.
(60) Kalderis, D.; Juhasz, A. L.; Boopathy, R.; Comfort, S. Soils contaminated with explosives: Environmental fate and evaluation of state-of-the-art remediation processes (IUPAC Technical Report). *Pure Appl. Chem.* **2011**, *83* (7), 1407–1484. https://doi.org/10.1351/PAC-REP-10-01-05.
(61) Bilal, M.; Bagheri, A. R.; Bhatt, P.; Chen, S. Environmental Occurrence, Toxicity Concerns, and Remediation of Recalcitrant Nitroaromatic Compounds. *J. Environ. Manage.* **2021**, *291*, 112685. https://doi.org/10.1016/j.jenvman.2021.112685.
(62) Gerth, A.; Hebner, A.; Thomas, H. Natural Remediation of TNT-Contaminated Water and Soil. *Acta Biotechnol.* **2003**, *23* (2–3), 143–150. https://doi.org/10.1002/abio.200390022.
(63) Esteve-Núñez, A.; Caballero, A.; Ramos, J. L. Biological Degradation of 2,4,6-Trinitrotoluene. *Microbiol. Mol. Biol. Rev.* **2001**, *65* (3), 335–352. https://doi.org/10.1128/mmbr.65.3.335-352.2001.
(64) Snellinx, Z.; Nepovím, A.; Taghavi, S.; Vangronsveld, J.; Vanek, T.; van der Lelie, D. Biological Remediation of Explosives and Related Nitroaromatic Compounds. *Environ. Sci. Pollut. Res.* **2002**, *9* (1), 48–61. https://doi.org/10.1007/BF02987316.
(65) Li, Z. M.; Peterson, M. M.; Comfort, S. D.; Horst, G. L.; Shea, P. J.; Oh, B. T. Remediating TNT-Contaminated Soil by Soil Washing and Fenton Oxidation. *Sci. Total Environ.* **1997**, *204* (2), 107–115. https://doi.org/10.1016/S0048-9697(97)00158-7.
(66) Li, Z. M.; Comfort, S. D.; Shea, P. J. Destruction of 2,4,6-Trinitrotoluene by Fenton Oxidation. *J. Environ. Qual.* **1997**, *26* (2), 480–487. https://doi.org/10.2134/jeq1997.00472425002600020020x.
(67) Barreto-Rodrigues, M.; Silva, F. T.; Paiva, T. C. B. Optimization of Brazilian TNT Industry Wastewater Treatment Using Combined Zero-Valent Iron and Fenton Processes. *J. Hazard. Mater.* **2009**, *168* (2), 1065–1069. https://doi.org/10.1016/j.jhazmat.2009.02.172.
(68) Matta, R.; Hanna, K.; Chiron, S. Fenton-like Oxidation of 2,4,6-Trinitrotoluene Using Different Iron Minerals. *Sci. Total Environ.* **2007**, *385* (1), 242–251. https://doi.org/10.1016/j.scitotenv.2007.06.030.
(69) Yardin, G.; Chiron, S. Photo–Fenton Treatment of TNT Contaminated Soil Extract Solutions Obtained by Soil Flushing with Cyclodextrin. *Chemosphere* **2006**, *62* (9), 1395–1402. https://doi.org/10.1016/j.chemosphere.2005.05.019.
(70) Li, Z. M.; Shea, P. J.; Comfort, S. D. Nitrotoluene Destruction by UV-Catalyzed Fenton Oxidation. *Chemosphere* **1998**, *36* (8), 1849–1865. https://doi.org/10.1016/S0045-6535(97)10073-X.
(71) Matta, R.; Hanna, K.; Kone, T.; Chiron, S. Oxidation of 2,4,6-Trinitrotoluene in the Presence of Different Iron-Bearing Minerals at Neutral pH. *Chem. Eng. J.* **2008**, *144* (3), 453–458. https://doi.org/10.1016/j.cej.2008.07.013.
(72) Doppalapudi, R. B.; Sorial, G. A.; Maloney, S. W. Electrochemical Reduction of Simulated Munitions Wastewater in a Bench-Scale Batch Reactor. *Environ. Eng. Sci.* **2002**, *19* (2), 115–130. https://doi.org/10.1089/10928750252953741.
(73) Palaniswamy, D. K.; Sorial, G. A.; Maloney, S. W. Electrochemical Reduction of 2,4,6-Trinitrotoluene. *Environ. Eng. Sci.* **2004**, *21* (2), 203–218. https://doi.org/10.1089/10928750477308737 2.
(74) Grigoriants, I.; Markovsky, B.; Persky, R.; Perelshtein, I.; Gedanken, A.; Aurbach, D.; Filanovsky, B.; Bourenko, T.; Felner, I. Electrochemical Reduction of Trinitrotoluene on Core–Shell Tin–Carbon Electrodes. *Electrochimica Acta* **2008**, *54* (2), 690–697. https://doi.org/10.1016/j.electacta.2008.07.005.

(75) Ni, X.; Zhao, Y.; Song, Q. Electrochemical Reduction and In-Situ Electrochemiluminescence Detection of Nitroaromatic Compounds. *Electrochimica Acta* **2015**, *164*, 31–37. https://doi.org/10.1016/j.electacta.2015.02.174.

(76) Macías-Ruvalcaba, N. A.; Telo, J. P.; Evans, D. H. Studies of the Electrochemical Reduction of Some Dinitroaromatics. *J. Electroanal. Chem.* **2007**, *600* (2), 294–302. https://doi.org/10.1016/j.jelechem.2006.10.003.

(77) Čėnas, N.; Nemeikaitė-Čėnienė, A.; Kosychova, L. Single- and Two-Electron Reduction of Nitroaromatic Compounds by Flavoenzymes: Mechanisms and Implications for Cytotoxicity. *Int. J. Mol. Sci.* **2021**, *22* (16), 8534. https://doi.org/10.3390/ijms22168534.

(78) Geske, D. H.; Maki, A. H. Electrochemical Generation of Free Radicals and Their Study by Electron Spin Resonance Spectroscopy; the Nitrobenzene Anion Radical. *J. Am. Chem. Soc.* **1960**, *82* (11), 2671–2676. https://doi.org/10.1021/ja01496a004.

(79) Moreno, S. N.; Schreiber, J.; Mason, R. P. Nitrobenzyl Radical Metabolites from Microsomal Reduction of Nitrobenzyl Chlorides. *J. Biol. Chem.* **1986**, *261* (17), 7811–7815. https://doi.org/10.1016/S0021-9258(19)57473-7.

(80) Mason, R. P.; Holtzman, J. L. Mechanism of Microsomal and Mitochondrial Nitroreductase. Electron Spin Resonance Evidence for Nitroaromatic Free Radical Intermediates. *Biochemistry* **1975**, *14* (8), 1626–1632. https://doi.org/10.1021/bi00679a013.

(81) Murayama, M. The Combining Power of Normal Human Hemoglobin for Nitrosobenzene. *J. Biol. Chem.* **1960**, *235* (4), 1024–1028. https://doi.org/10.1016/S0021-9258(18)69473-6.

(82) Xia, C.; Jin, X.; Parandoust, A.; Sheibani, R.; Khorsandi, Z.; Montazeri, N.; Wu, Y.; Le, Q. V. Chitosan-Supported Metal Nanocatalysts for the Reduction of Nitroaromatics. *Int. J. Biol. Macromol.* **2023**, *239*, 124135. https://doi.org/10.1016/j.ijbiomac.2023.124135.

(83) Rezaei, F.; Dinari, M. Cu Nanoparticles Embedded in the Porous Organic Polymer as Highly Effective Catalysts for Nitroaromatics Reduction. *Microporous Mesoporous Mater.* **2021**, *325*, 111339. https://doi.org/10.1016/j.micromeso.2021.111339.

(84) Rezaei, F.; Dinari, M. Novel Covalent Organic Polymer-Supported Ag Nanoparticles as a Catalyst for Nitroaromatics Reduction. *Colloids Surf. Physicochem. Eng. Asp.* **2021**, *618*, 126441. https://doi.org/10.1016/j.colsurfa.2021.126441.

(85) Pandey, A.; Twinkle; Sonkar, S. K.; Dalal, C. Copper Nanoparticles-Decorated Carbon Nanoflakes as a Catalyst for Nitroaromatic Reduction. *ACS Appl. Nano Mater.* **2024**, *7* (22), 26238–26247. https://doi.org/10.1021/acsanm.4c05839.

(86) Li, J.; Ma, R.; Lu, Y.; Wu, Z.; Liu, R.; Su, M.; Jin, X.; Zhang, R.; Bao, Y.; Chen, Y.; Qin, D.; Yang, D.; Jiang, Z. Bamboo-Inspired Design of a Stable and High-Efficiency Catalytic Capillary Microreactor for Nitroaromatics Reduction. *Appl. Catal. B Environ.* **2022**, *310*, 121297. https://doi.org/10.1016/j.apcatb.2022.121297.

(87) Ji, T.; Chen, L.; Mu, L.; Yuan, R.; Knoblauch, M.; Bao, F. S.; Zhu, J. *In-Situ* Reduction of Ag Nanoparticles on Oxygenated Mesoporous Carbon Fabric: Exceptional Catalyst for Nitroaromatics Reduction. *Appl. Catal. B Environ.* **2016**, *182*, 306–315. https://doi.org/10.1016/j.apcatb.2015.09.024.

(88) Devlin, J. F.; Klausen, J.; Schwarzenbach, R. P. Kinetics of Nitroaromatic Reduction on Granular Iron in Recirculating Batch Experiments. *Environ. Sci. Technol.* **1998**, *32* (13), 1941–1947. https://doi.org/10.1021/es970896g.

(89) Devlin, J. F.; Allin, K. O. Major Anion Effects on the Kinetics and Reactivity of Granular Iron in Glass-Encased Magnet Batch Reactor Experiments. *Environ. Sci. Technol.* **2005**, *39* (6), 1868–1874. https://doi.org/10.1021/es040413q.

(90) Qin, L.; Zeng, G.; Lai, C.; Huang, D.; Zhang, C.; Cheng, M.; Yi, H.; Liu, X.; Zhou, C.; Xiong, W.; Huang, F.; Cao, W. Synthetic Strategies and Application of Gold-Based Nanocatalysts for Nitroaromatics Reduction. *Sci. Total Environ.* **2019**, *652*, 93–116. https://doi.org/10.1016/j.scitotenv.2018.10.215.

(91) Naka, D.; Kim, D.; Strathmann, T. J. Abiotic Reduction of Nitroaromatic Compounds by Aqueous Iron(II)−Catechol Complexes. *Environ. Sci. Technol.* **2006**, *40* (9), 3006–3012. https://doi.org/10.1021/es060044t.

(92) Santra, P. K.; Sagar, P. Dihydrogen Reduction of Nitroaromatics, Alkenes, Alkynes Using Pd(II) Complexes Both in Normal and High Pressure Conditions. *J. Mol. Catal. Chem.* **2003**, *197* (1), 37–50. https://doi.org/10.1016/S1381-1169(02)00600-3.

(93) Guo, K.; Jiao, J.; Zhang, L.; Sun, H.; Miao, X.; Li, J.; Han, Q. Constructing an Isopolymolybdate-Based Bifunctional Photocatalyst for Promoting Nitroaromatic Reduction and C–H Oxidation. *Inorg. Chem.* **2025**, *64* (1), 58–66. https://doi.org/10.1021/acs.inorgchem.4c04145.

(94) Núñez-Vergara, L. J.; Squella, J. A.; Olea-Azar, C.; Bollo, S.; Navarrete-Encina, P. A.; Sturm, J. C. Nitrosobenzene: Electrochemical, UV-Visible and EPR Spectroscopic Studies on the Nitrosobenzene Free Radical Generation and Its Interaction with Glutathione. *Electrochimica Acta* **2000**, *45* (21), 3555–3561. https://doi.org/10.1016/S0013-4686(00)00477-1.

(95) Asirvatham, M. R.; Hawley, M. D. Electron-Transfer Processes: The Electrochemical and Chemical Behavior of Nitrosobenzene. *J. Electroanal. Chem. Interfacial Electrochem.* **1974**, *57* (2), 179–190. https://doi.org/10.1016/S0022-0728(74)80021-5.

(96) Smith, W. H.; Bard, A. J. Electrochemical Reactions of Organic Compounds in Liquid Ammonia. II. Nitrobenzene and Nitrosobenzene. *J. Am. Chem. Soc.* **1975**, *97* (18), 5203–5210. https://doi.org/10.1021/ja00851a030.

(97) Zuman, P.; Shah, B. Addition, Reduction, and Oxidation Reactions of Nitrosobenzene. *Chem. Rev.* **1994**, *94* (6), 1621–1641. https://doi.org/10.1021/cr00030a007.

(98) Hutton, J.; Waters, W. A. The Mechanism of Reduction of Nitrosobenzene by Alcohols. *J. Chem. Soc. B Phys. Org.* **1968**, No. 0, 191–195. https://doi.org/10.1039/J29680000191.

(99) Palacios-Ramírez, J. I.; González, F. J. Revisiting the Electrochemical Reduction Mechanism of Nitrosobenzene in Acetonitrile. Concomitant Reactions and Voltammetric Simulation. *ChemElectroChem* **2024**, *11* (3), e202300486. https://doi.org/10.1002/celc.202300486.

(100) Brezová, V.; Tarábek, P.; Dvoranová, D.; Staško, A.; Biskupič, S. EPR Study of Photoinduced Reduction of Nitroso Compounds in Titanium Dioxide Suspensions. *J. Photochem. Photobiol. Chem.* **2003**, *155* (1), 179–198. https://doi.org/10.1016/S1010-6030(02)00357-X.

(101) Bard, A. J.; Ketelaar, J. a. A. Encyclopedia of Electrochemistry of the Elements. *J. Electrochem. Soc.* **1976**, *123* (10), 348Ca. https://doi.org/10.1149/1.2132649.

(102) Lipsztajn, M.; Krygowski, T. M.; Laren, E.; Galus, Z. Electrochemical Investigations of Intermediates in Electroreduction of Aromatic Nitro and Nitroso Compounds in DMF: Part I. Electrochemical Behaviour of Azoxybenzene. *J. Electroanal. Chem. Interfacial Electrochem.* **1974**, *54* (2), 313–320. https://doi.org/10.1016/S0022-0728(74)80404-3.

(103) Stridsberg, B.; Allenmark, S.; Daasvatn, K.; Liaaen-Jensen, S.; Enzell, C. R.; Mannervik, B. Intramolecular Transfer of Chirality from Sulfur to Carbon: Dehydrocyclization of Optically Active o-Benzylsulfinylbenzoic Acid with Dicyclohexylcarbodiimide. *Acta Chem. Scand.* **1974**, *28b*, 591–593. https://doi.org/10.3891/acta.chem.scand.28b-0591.

(104) Ayscough, P. B.; Sargent, F. P.; Wilson, R. Electron Spin Resonance Studies of Radicals and Radical-Ions in Solution. Part IV. Further Intermediates in the Reduction of Aromatic Nitro- and Nitroso-Compounds. *J. Chem. Soc. B Phys. Org.* **1966**, No. 0, 903–906. https://doi.org/10.1039/J29660000903.

(105) Russell, G. Allan.; Geels, E. J.; Smentowski, F. J.; Chang, K.-Yuan.; Reynolds, James.; Kaupp, Gerd. Reactions of Resonance Stabilized Anions. XXIX. Electron-Transfer Processes. 7. Formation of Paramagnetic and Condensation Products from Nitrosobenzene in Basic Solution. *J. Am. Chem. Soc.* **1967**, *89* (15), 3821–3828. https://doi.org/10.1021/ja00991a025.

(106) Lee, J.; Chen, L.; West, A. H.; Richter-Addo, G. B. Interactions of Organic Nitroso Compounds with Metals. *Chem. Rev.* **2002**, *102* (4), 1019–1066. https://doi.org/10.1021/cr0000731.

(107) Cameron, M.; Gowenlock, B. G.; Vasapollo, G. Coordination Chemistry of C-Nitroso-Compounds. *Chem. Soc. Rev.* **1990**, *19* (4), 355–379. https://doi.org/10.1039/CS9901900355.

(108) Tomson, N. C.; Labios, L. A.; Weyhermüller, T.; Figueroa, J. S.; Wieghardt, K. Redox Noninnocence of Nitrosoarene Ligands in Transition Metal Complexes. *Inorg. Chem.* **2011**, *50* (12), 5763–5776. https://doi.org/10.1021/ic2005979.

(109) Rehorek, D. Spin Trapping of Inorganic Radicals. *Chem. Soc. Rev.* **1991**, *20* (3), 341. https://doi.org/10.1039/cs9912000341.

(110) Iwasa, T.; Shimada, H.; Takami, A.; Matsuzaka, H.; Ishii, Y.; Hidai, M. Preparation of Cationic Dinuclear Hydrido Complexes of Ruthenium, Rhodium, and Iridium with Bridging Thiolato Ligands and Their Reactions with Nitrosobenzene. *Inorg. Chem.* **1999**, *38* (12), 2851–2859. https://doi.org/10.1021/ic981274e.
(111) Sandorfy, C. General and Theoretical Aspects. In *Carbon–Nitrogen Double Bonds (1970)*; John Wiley & Sons, Ltd, 1970; pp 1–60. https://doi.org/10.1002/9780470771204.ch1.
(112) Liebeskind, L. S.; Sharpless, K. B.; Wilson, R. D.; Ibers, J. A. The First D0 Metallooxaziridines. Amination of Olefins. *ACS Publ.* **1978**, *100* (22), 7061–7063. https://doi.org/10.1021/ja00490a047.
(113) Lendzian, F.; Plato, M.; Möbius, K. 14N ENDOR of the Nitrobenzene Radical Anion in Solution. *J. Magn. Reson. 1969* **1981**, *44* (1), 20–31. https://doi.org/10.1016/0022-2364(81)90185-2.
(114) Ling, C.; Gendell, J. ESR Studies of Nitrobenzene, o-Dinitrobenzene, and m-Dinitrobenzene Alkali-Metal Salts. *J. Chem. Phys.* **1967**, *47* (9), 3475–3484. https://doi.org/10.1063/1.1712413.
(115) Stoll, S.; Schweiger, A. EasySpin, a Comprehensive Software Package for Spectral Simulation and Analysis in EPR. *J. Magn. Reson.* **2006**, *178* (1), 42–55. https://doi.org/10.1016/j.jmr.2005.08.013.
(116) Walton, J. C. Analysis of Radicals by EPR. In *Encyclopedia of Radicals in Chemistry, Biology and Materials*; John Wiley & Sons, Ltd, 2012. https://doi.org/10.1002/9781119953678.rad001.
(117) *CRC Handbook of Chemistry and Physics*, 97th ed.; Haynes, W. M., Lide, D. R., Bruno, T. J., Eds.; CRC Press, 2016. https://doi.org/10.1201/9781315380476.
(118) Li, Y.-P.; Cao, H.-B.; Liu, C.-M.; Zhang, Y. Electrochemical Reduction of Nitrobenzene at Carbon Nanotube Electrode. *J. Hazard. Mater.* **2007**, *148* (1), 158–163. https://doi.org/10.1016/j.jhazmat.2007.02.021.
(119) Tanner, D. D.; Harrison, D. J.; Chen, J.; Kharrat, A.; Wayner, D. D. M.; Griller, D.; McPhee, D. J. The Mechanism of the Radical Chain Transformation of Nitroalkanes to Alkanes Using Triaryl- or Trialkyltin Hydrides. *J. Org. Chem.* **1990**, *55* (10), 3321–3325. https://doi.org/10.1021/jo00297a061.
(120) Yedage, S. L.; Bhanage, B. M. Tert-Butyl Nitrite-Mediated Synthesis of N-Nitrosoamides, Carboxylic Acids, Benzocoumarins, and Isocoumarins from Amides. *J. Org. Chem.* **2017**, *82* (11), 5769–5781. https://doi.org/10.1021/acs.joc.7b00570.
(121) Brandi, A.; Cardona, F.; Cicchi, S.; Cordero, F. M.; Goti, A. [3 + 2] Dipolar Cycloadditions of Cyclic Nitrones with Alkenes. In *Organic Reactions*; John Wiley & Sons, Ltd, 2017; pp 1–321. https://doi.org/10.1002/0471264180.or094.01.
(122) Murahashi, S.-I.; Imada, Y. Synthesis and Transformations of Nitrones for Organic Synthesis. *Chem. Rev.* **2019**, *119* (7), 4684–4716. https://doi.org/10.1021/acs.chemrev.8b00476.
(123) Kumar, K. R. R.; Mallesha, H.; Rangappa, K. S. Synthesis of Novel Isoxazolidine Derivatives and Their Antifungal and Antibacterial Properties. *Arch. Pharm. (Weinheim)* **2003**, *336* (3), 159–164. https://doi.org/10.1002/ardp.200390015.
(124) Ghannay, S.; Bakari, S.; Msaddek, M.; Vidal, S.; Kadri, A.; Aouadi, K. Design, Synthesis, Molecular Properties and *in Vitro* Antioxidant and Antibacterial Potential of Novel Enantiopure Isoxazolidine Derivatives. *Arab. J. Chem.* **2020**, *13* (1), 2121–2131. https://doi.org/10.1016/j.arabjc.2018.03.013.
(125) Loh, B.; Vozzolo, L.; Mok, B. J.; Lee, C. C.; Fitzmaurice, R. J.; Caddick, S.; Fassati, A. Inhibition of HIV-1 Replication by Isoxazolidine and Isoxazole Sulfonamides. *Chem. Biol. Drug Des.* **2010**, *75* (5), 461–474. https://doi.org/10.1111/j.1747-0285.2010.00956.x.
(126) Mojović, M.; Vuletić, M.; Bačić, G. G. Detection of Oxygen-Centered Radicals Using EPR Spin-Trap DEPMPO: The Effect of Oxygen. *Ann. N. Y. Acad. Sci.* **2005**, *1048* (1), 471–475. https://doi.org/10.1196/annals.1342.069.
(127) Mason, R. P. Imaging Free Radicals in Organelles, Cells, Tissue, and in Vivo with Immuno-Spin Trapping. *Redox Biol.* **2016**, *8*, 422–429. https://doi.org/10.1016/j.redox.2016.04.003.
(128) Berliner, L. J.; Fujii, H. In Vivo Spin Trapping of Nitric Oxide. *Antioxid. Redox Signal.* **2004**, *6* (3), 649–656. https://doi.org/10.1089/152308604773934413.
(129) Berliner, L. J.; Khramtsov, V.; Fujii, H.; Clanton, T. L. Unique in Vivo Applications of Spin Traps. *Free Radic. Biol. Med.* **2001**, *30* (5), 489–499. https://doi.org/10.1016/S0891-5849(00)00491-3.
(130) Berliner, L. J. Assessment of Nitrones as In Vivo Redox Sensors. *Appl. Magn. Reson.* **2009**, *36* (2), 157–170. https://doi.org/10.1007/s00723-009-0034-2.

(131) Lemercier, J. N.; Squadrito, G. L.; Pryor, W. A. Spin Trap Studies on the Decomposition of Peroxynitrite. *Arch. Biochem. Biophys.* **1995**, *321* (1), 31–39. https://doi.org/10.1006/abbi.1995.1364.
(132) Shichiri, T.; Toriumi, M.; Tanaka, K.; Yamabe, T.; Yamauchi, J.; Deguchi, Y. ESR Study for the Oxidation of Pyrrole in the Presence of a Spin Trap. *Synth. Met.* **1989**, *33* (3), 389–397. https://doi.org/10.1016/0379-6779(89)90484-0.
(133) Floyd, R. A.; Kopke, R. D.; Choi, C.-H.; Foster, S. B.; Doblas, S.; Towner, R. A. Nitrones as Therapeutics. *Free Radic. Biol. Med.* **2008**, *45* (10), 1361–1374. https://doi.org/10.1016/j.freeradbiomed.2008.08.017.
(134) Rosselin, M.; Poeggeler, B.; Durand, G. Nitrone Derivatives as Therapeutics: From Chemical Modification to Specific-Targeting. *Curr. Top. Med. Chem.* **2017**, *17* (18), 2006–2022. https://doi.org/10.2174/1568026617666170303115324.
(135) Villamena, F. A.; Das, A.; Nash, K. M. Potential Implication of The Chemical Properties and Bioactivity of Nitrone Spin Traps for Therapeutics. *Future Med. Chem.* **2012**, *4* (9), 1171–1207. https://doi.org/10.4155/fmc.12.74.
(136) Floyd, R. A.; Castro Faria Neto, H. C.; Zimmerman, G. A.; Hensley, K.; Towner, R. A. Nitrone-Based Therapeutics for Neurodegenerative Diseases: Their Use Alone or in Combination with Lanthionines. *Free Radic. Biol. Med.* **2013**, *62*, 145–156. https://doi.org/10.1016/j.freeradbiomed.2013.01.033.
(137) Baum, S. L.; Anderson, I. G. M.; Baker, R. R.; Murphy, D. M.; Rowlands, C. C. Electron Spin Resonance and Spin Trap Investigation of Free Radicals in Cigarette Smoke: Development of a Quantification Procedure. *Anal. Chim. Acta* **2003**, *481* (1), 1–13. https://doi.org/10.1016/S0003-2670(03)00078-3.
(138) Davies, M. J. Detection and Characterisation of Radicals Using Electron Paramagnetic Resonance (EPR) Spin Trapping and Related Methods. *Methods* **2016**, *109*, 21–30. https://doi.org/10.1016/j.ymeth.2016.05.013.
(139) Nash, K. M.; Rockenbauer, A.; Villamena, F. A. Reactive Nitrogen Species Reactivities with Nitrones: Theoretical and Experimental Studies. *Chem. Res. Toxicol.* **2012**, *25* (8), 1581–1597. https://doi.org/10.1021/tx200526y.
(140) Supranovich, V. I.; Levin, V. V.; Struchkova, M. I.; Dilman, A. D. Photocatalytic Reductive Fluoroalkylation of Nitrones. *Org. Lett.* **2018**, *20* (3), 840–843. https://doi.org/10.1021/acs.orglett.7b03987.
(141) Villamena, F. A.; Crist, D. R. Metal–Nitrone Complexes: Spin Trapping and Solution Characterization†. *J. Chem. Soc. Dalton Trans.* **1998**, No. 23, 4055–4062. https://doi.org/10.1039/A806162I.
(142) Villamena, F. A.; Dickman, M. H.; Crist, D. R. Nitrones as Ligands in Complexes of Cu(II), Mn(II), Co(II), Ni(II), Fe(II), and Fe(III) with N-Tert-Butyl-α-(2-Pyridyl)Nitrone and 2,5,5-Trimethyl-1-Pyrroline-N-Oxide. *Inorg. Chem.* **1998**, *37* (7), 1446–1453. https://doi.org/10.1021/ic9709741.
(143) Villamena, F. A.; Horak, V.; Crist, D. R. Cyclic Voltammetry of Metal Complexes of Nitrones and Nitroxides. *Inorganica Chim. Acta* **2003**, *342*, 125–130. https://doi.org/10.1016/S0020-1693(02)01154-4.
(144) Huang, H.-M.; He, Q.; Procter, D. J. Samarium Diiodide Catalyzed Radical Cascade Cyclizations That Construct Quaternary Stereocenters. *Synlett* **2020**, *31* (1), 45–50. https://doi.org/10.1055/s-0039-1690196.
(145) Aretz, C. Selective Carbon-Carbon Bond Formation Promoted by Divalent Samarium Reagents. *Univ. Denver* **2018**, 1403.
(146) Durand, G.; Polidori, A.; Ouari, O.; Tordo, P.; Geromel, V.; Rustin, P.; Pucci, B. Synthesis and Preliminary Biological Evaluations of Ionic and Nonionic Amphiphilic α-Phenyl-N-Tert-Butylnitrone Derivatives. *J. Med. Chem.* **2003**, *46* (24), 5230–5237. https://doi.org/10.1021/jm030873e.
(147) Sono, M.; Hanamura, S.; Furumaki, M.; Murai, H.; Tori, M. First Direct Evidence of Radical Intermediates in Samarium Diiodide Induced Cyclization by ESR Spectra. *Org. Lett.* **2011**, *13* (21), 5720–5723. https://doi.org/10.1021/ol202403q.
(148) Heckert, E. G.; Karakoti, A. S.; Seal, S.; Self, W. T. The Role of Cerium Redox State in the SOD Mimetic Activity of Nanoceria. *Biomaterials* **2008**, *29* (18), 2705–2709. https://doi.org/10.1016/j.biomaterials.2008.03.014.

(149) Babu, S.; Velez, A.; Wozniak, K.; Szydlowska, J.; Seal, S. Electron Paramagnetic Study on Radical Scavenging Properties of Ceria Nanoparticles. *Chem. Phys. Lett.* **2007**, *442* (4), 405–408. https://doi.org/10.1016/j.cplett.2007.06.026.
(150) Caputo, F.; Nicola, M. D.; Sienkiewicz, A.; Giovanetti, A.; Bejarano, I.; Licoccia, S.; Traversa, E.; Ghibelli, L. Cerium Oxide Nanoparticles, Combining Antioxidant and UV Shielding Properties, Prevent UV-Induced Cell Damage and Mutagenesis. *Nanoscale* **2015**, *7* (38), 15643–15656. https://doi.org/10.1039/C5NR03767K.
(151) Shukla, A. K.; Rakhmatullin, R. EPR Studies of Cerium Dioxide Nanoparticles. In *EMR/ESR/EPR Spectroscopy for Characterization of Nanomaterials*; Shukla, A. K., Ed.; Springer India: New Delhi, 2017; pp 135–149. https://doi.org/10.1007/978-81-322-3655-9_6.
(152) Culcasi, M.; Benameur, L.; Mercier, A.; Lucchesi, C.; Rahmouni, H.; Asteian, A.; Casano, G.; Botta, A.; Kovacic, H.; Pietri, S. EPR Spin Trapping Evaluation of ROS Production in Human Fibroblasts Exposed to Cerium Oxide Nanoparticles: Evidence for NADPH Oxidase and Mitochondrial Stimulation. *Chem. Biol. Interact.* **2012**, *199* (3), 161–176. https://doi.org/10.1016/j.cbi.2012.08.007.
(153) Dunnick, K. M.; Pillai, R.; Pisane, K. L.; Stefaniak, A. B.; Sabolsky, E. M.; Leonard, S. S. The Effect of Cerium Oxide Nanoparticle Valence State on Reactive Oxygen Species and Toxicity. *Biol. Trace Elem. Res.* **2015**, *166* (1), 96–107. https://doi.org/10.1007/s12011-015-0297-4.
(154) Caputo, F.; Mameli, M.; Sienkiewicz, A.; Licoccia, S.; Stellacci, F.; Ghibelli, L.; Traversa, E. A Novel Synthetic Approach of Cerium Oxide Nanoparticles with Improved Biomedical Activity. *Sci. Rep.* **2017**, *7* (1), 4636. https://doi.org/10.1038/s41598-017-04098-6.
(155) Singh, N.; Amateis, E.; Mahaney, J. E.; Meehan, K.; Rzigalinski, B. A. The Antioxidant Activity of Cerium Oxide Nanoparticles Is Size Dependant and Blocks Aβ1-42-Induced Free Radical Production and Neurotoxicity. *FASEB J.* **2008**, *22* (S1), 624.2-624.2. https://doi.org/10.1096/fasebj.22.1_supplement.624.2.
(156) Heckert, E. G.; Seal, S.; Self, W. T. Fenton-Like Reaction Catalyzed by the Rare Earth Inner Transition Metal Cerium. *Environ. Sci. Technol.* **2008**, *42* (13), 5014–5019. https://doi.org/10.1021/es8001508.
(157) An, Q.; Xing, Y.-Y.; Pu, R.; Jia, M.; Chen, Y.; Hu, A.; Zhang, S.-Q.; Yu, N.; Du, J.; Zhang, Y.; Chen, J.; Liu, W.; Hong, X.; Zuo, Z. Identification of Alkoxy Radicals as Hydrogen Atom Transfer Agents in Ce-Catalyzed C–H Functionalization. *J. Am. Chem. Soc.* **2023**, *145* (1), 359–376. https://doi.org/10.1021/jacs.2c10126.
(158) Masson, G.; Py, S.; Vallée, Y. Samarium Diiodide-Induced Reductive Cross-Coupling of Nitrones with Aldehydes and Ketones. *Angew. Chem. Int. Ed.* **2002**, *41* (10), 1772–1775. https://doi.org/10.1002/1521-3773(20020517)41:10<1772::AID-ANIE1772>3.0.CO;2-Q.
(159) Masson, G.; Cividino, P.; Py, S.; Vallée, Y. SmI2-Induced Umpolung of the C-N Bond: First Reductive Conjugate Addition of Nitrones to α,β-Unsaturated Esters. *Angew. Chem. Int. Ed.* **2003**, *42* (20), 2265–2268. https://doi.org/10.1002/anie.200250480.

If you look for a meaning, you will miss everything that happens.

Andrei Tarkovsky, 1979

Chapter IV
Reduction of nitrogen cycle species and small molecule activation

Introduction 142

I. Photochemical nitrate reduction 146

a) Photochemical reduction of nitrates 147

1) Formation of cerium-nitrate complex 148

2) Photochemical formation of a cerium-oxo complex 153

b) Reactivity with sodium nitrite and nitrous oxide 156

1) Reactivity with sodium nitrite 157

2) Reactivity with N_2O 159

II. Carbon capture by a cerium(III) tripodal complex 161

III. Superoxide radical formation under dioxygen atmosphere 165

a) Introduction 165

1) Dioxygen transport in proteins 165

2) Reactivity of dioxygen with complexes 166

b) Reactivity with 1 169

c) Reactivity of 2-O_2 173

References 175

Introduction

The increase of anthropogenic activities throughout the 19th and 20th century had a profound impact on the environment, especially on the disruption of the cycles of elements on the surface of Earth.[1]

Among all elements, nitrogen is particularly important due to its ubiquity within all life forms. For instance, plants require nitrogen intake for their growth, as nitrate ions.[2] These ions may come from nitrogen fixation by bacteria or archaea which occurs by reducing atmospheric N_2 into NH_3 using a heterodimeric enzyme complex (nitrogenase).[3] Nevertheless, most plants cannot directly fix nitrogen and have to rely on other sources of NO_3^- ions, mostly through the oxidation of NH_4^+ ions released upon organic matter decomposition.[4]

In the environment, nitrate ions (NO_3^-) are in equilibrium with reactive species such as nitrite ions (NO_2^-), nitric oxide (NO) and nitrous oxide (N_2O, see **Figure 138**). These 4 species have raised health and environmental concerns over the past 20 years :

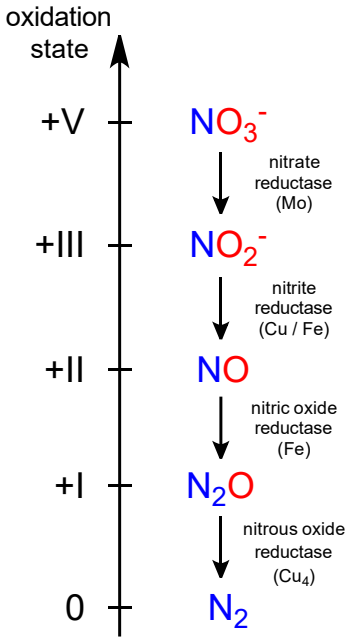

Figure 138. Simplified anaerobic reduction of nitrates in dinitrogen. Metal centre(s) of each enzyme in indicated between brackets. Adapted from Falkowski *et al.*, Fout *et al.* and Lee *et al.*.[3,5,6]

- Nitrate intake has been associated with higher risks of cardiovascular diseases (atherosclerosis, coronary artery disease and myocardial infarction),[5] increased chances of colorectal cancer,[6,7] methemoglobinemia, diabetes and eruption of infectious disorders.[8] Accumulation of nitrates in water due to leaching from agricultural fields is responsible for eutrophication, *i.e.* an excessive growth of plants and algae which deplete oxygen from water and cause the ecosystem to die off[9]
- Nitrite's influence on human health is still unclear due to the very limited amount of studies,[6] but they are thought to form carcinogenic N-nitrosamines *in vivo*,[10] which questions their use as red meat preservatives[11]
- Nitric oxide acts as a mediator in the cardiovascular system and nerve cells[12] and a vasodilator, while also involved in immune response.[13] High concentrations of this species may cause peptic ulcers, chronic gastritis, gastrointestinal cancer, bacterial gastroenteritis, celiac disease or chronic inflammatory bowel disease[14]
- Nitrous oxide is known to inhibit the activity of vitamin B_{12} (involved in the synthesis of neurotransmitters) and long-term exposure may be responsible for bone-marrow depression and neuropathologies.[15] It is also a strong greenhouse gas (300 times more powerful than CO_2 and 12 times more than methane, see **Table 4**) and can be degraded into NO_x (NO + NO_2) species which degrade the ozone layer in Earth's stratosphere[16]

Greenhouse gas	Chemical formula	Lifetime (years)	Global Warming Potential at 100 years
Carbon dioxide	CO_2	/	1
Methane	CH_4	12	25
Nitrous oxide	N_2O	114	298

Table 4. Several greenhouse gases lifetimes and global warming potentials (integrated radiative forcing over time from a unit mass pulse emission). Adapted from IPCC 2007[17]

Over a total of 15.3 Tg of nitrogen of N_2O emitted per year in 2005, 33% were arising from anthropogenic emissions, among which 77% were induced by agriculture[18] (see **Figure 139**). Together with industry, energy and transport, they add up to 94% of N_2O emissions due to anthropic activities.

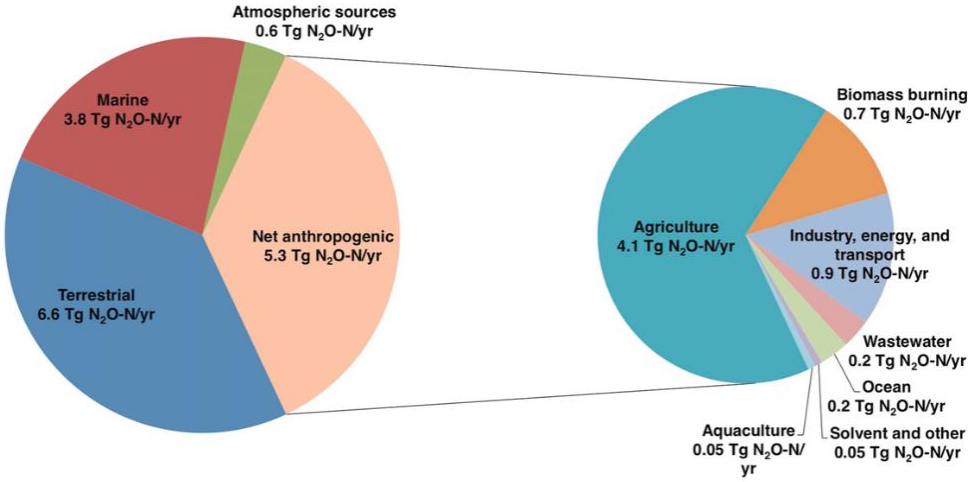

Figure 139. Natural *vs.* anthropogenic N_2O emissions in 2005. Reproduced from Davidson and Kanter[19]

N_2O concentration in the atmosphere has increased by 20% since 1850,[16] and without change in current politics, human emissions of N_2O are foreseen to reach between 9 and 10.10^{12} g of N_2O nitrogen per year by 2050 (see **Figure 140**).[19–22]

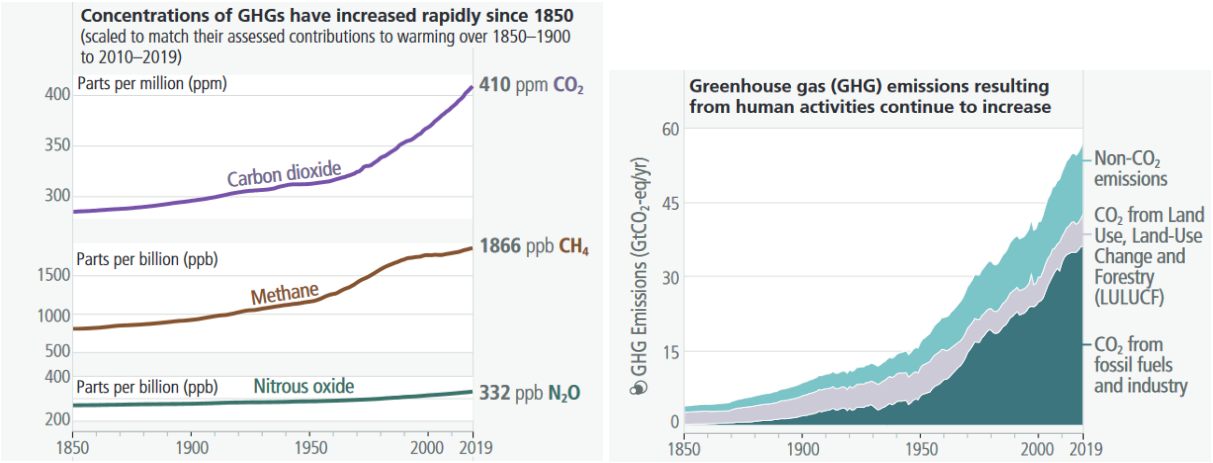

Figure 140. Evolution of concentrations in the atmosphere (left) and worldwide emissions (right) of several greenhouse gases from 1850 to 2019. Reproduced from IPCC 2023[23]

In addition to perturbing the nitrogen cycle, anthropogenic activities induced profound changes in the carbon cycle, involving species such as carbon dioxide (CO_2), hydrogenocarbonate (HCO_3^-), carbonate (CO_3^{2-}) and methane (CH_4). While the two first species are directly available carbon source for biological systems, carbonate and methane are bio-unavailable, implying a need for transformation (respectively into HCO_3^- and CO_2) prior to use by living organisms.[24]

The beginning of the Industrial Revolution at the end of the 18th century led to significant economic, scientific and social developments, which gave access to new fuel sources such as coal. Extensive use of these new fuels increased significantly atmospheric levels of combustion products (among which CO_2 and CH_4) over the course of time, that was not slowed down by the popularisation of oil, used as gasoline to meet the demand for the growing transportation of goods and humans. Between 1900 and 2019, CO_2 emissions from fossil fuel and industry have risen in more than 30-times fold (see **Figure 140**),

leading to an increase in 47% in atmospheric CO_2 concentrations compared to 1750, the highest ever since 2 million years.[23]

The impact of CO_2 on climate and on average temperatures around the globe has been extensively documented.[25–30] The relationship between carbon dioxide and climate change dates back as early as 1824, when Joseph Fourier highlighted the importance of the atmosphere on ground temperature.[31,32] Eunice Newton Foote later found out that carbon dioxide was a good heat conductor and hypothesized that a CO_2 atmosphere "would give to our earth a high temperature" (1857).[33] In 1896, Svante Arrhenius proposed the first estimation of the impact of carbon dioxide concentrations on earth's temperature, estimating that doubling its concentration would lead to a 5 °C increase of average temperature.[34] In 2023, the International Panel on Climate Change (IPCC) estimated that the global surface temperature had increased by about 1.1 °C compared to 1850-1900 period, and could reach +4 °C without any change in trend for the global emissions.[23]

The increase in atmospheric CO_2 concentration previously depicted in **Figure 140** could accelerate the growth of plants, inducing a higher water consumption in the soil and therefore a change in the microbiology of the rhizosphere and soil.[35] This faster growth rate would also lead to a more important nitrogen supply through decay of dead plants and would disrupt the nitrogen cycle.[36] Indirect temperature and climate changes (heatwaves and freezing waves) may also put plants in a stress situation which can hamper their development.[37]

Furthermore, the main part of anthropogenic CO_2 is absorbed by oceans[80–82] and transformed into carbonates, which has resulted in a decrease in pH by 0.1 units in the past 200 years (which corresponds to 30% more H^+ ions), and is expected to further decrease by 0.5 units (threefold increase in H^+ concentration) by 2100.[41] This acidification process causes the partial dissolution and weakening of the calcium carbonate shells of shellfish (see **Figure 141**).[40,42] Coral reefs are also expected to be severely damaged due to this intense acidification, as well as disrupting calcification process of phytoplanktons and zooplanktons which are at the bottom of ocean's food chain.[41]

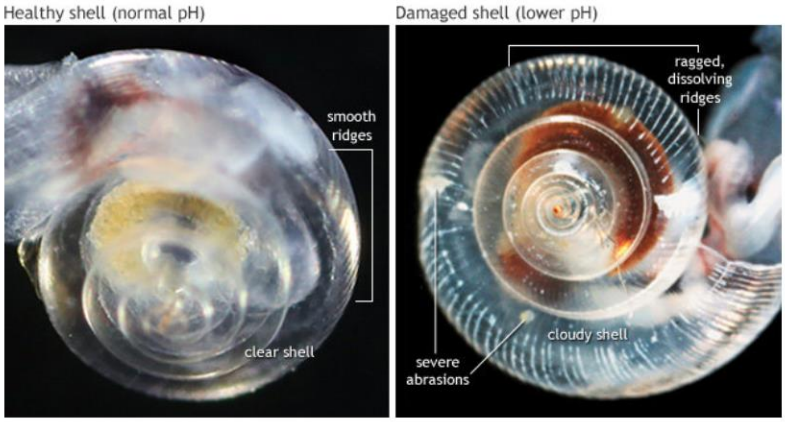

Figure 141. Comparison of the shell of an ocean snail living at a normal pH (left), and exposed to a more acidic medium (right). Reproduced from Lindsey[43]

While being harmful to the environment, carbon dioxide is also noxious to health. In the human body, CO_2 is produced by respiration and transported through the bloodstream as a carbamate in carbaminohemoglobin (23% of total CO_2 transport), or transformed into bicarbonate by carbonic anhydrase enzymes and carried in plasma (70%).[44] Overexposure to atmospheric CO_2 (hypercapnia) can lead to various troubles, including respiratory acidosis (which can cause bowel or kidney problems), central nervous system overstimulation and teratogenic effects.[45,46]

Different evolutions *scenarii* have been envisioned by the IPCC to predict the evolution of carbon dioxide emissions, and therefore the average temperature change which is expected to be around 3.2 °C with current environmental policies (see **Figure 142**).[23] Such a dramatic increase in temperature is likely to create more frequent climate catastrophes such as drought, flooding and extreme heats which may lead to difficulties in food growth (see **Figure 143**).[47]

For all these reasons, carbon dioxide activation and remediation are key topics to facilitate the targeted decrease in CO_2 emissions.

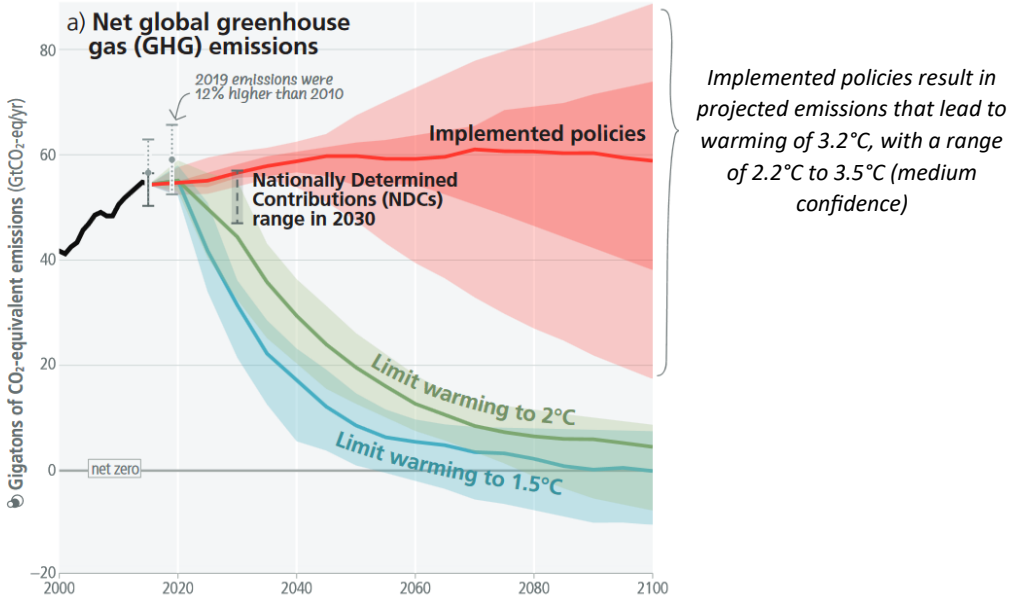

Figure 142. Evolution of worldwide carbon dioxide emissions. Adapted from IPCC 2023[23]

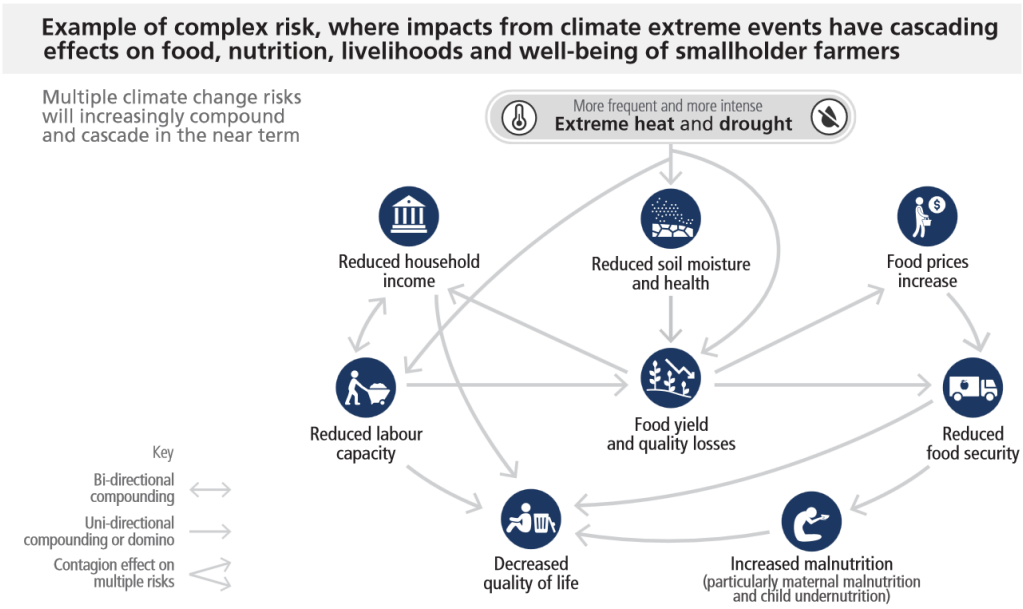

Figure 143. Example of chain of consequences from climate extreme events. Reproduced from IPCC 2023[23]

I. Photochemical nitrate reduction

To meet the growing food demand, the use of fertilizers made with inorganic nitrate source has dramatically increased over the 20th and 21st centuries, and created an increase in overall nitrate concentration in groundwater and drinking water.[6,7,48]

Strategies to extract or degrade nitrates in the environment have therefore been studied. Nitrate ions can be removed from water by ion exchange,[49,50] adsorption, reverse osmosis[51] and electrodialysis,[52] but these processes only concentrate nitrate ions without degrading them.[53,54] Biological denitrification was also studied as a possible candidate, although constant monitoring associated with long reaction durations and sludge production hampered its use.[55] Catalytic hydrogenation has sparked interest due to high reduction yields, but technical limitations and dangers complicated the scale-up of the process.[520–522] Electrochemical reduction is able to selectively reduce nitrates into either hydroxylamine, dinitrogen or ammonium ions,[59] but often relied on noble metals displaying higher electroreduction activity.[60–62] Efforts are nonetheless being made to develop new electrodes made up of abundant metals.[54]

The chemical reduction of nitrate using materials was mostly studied using zero-valent iron materials due to the low redox potential of iron(0)/iron(II) couple (-0.447 V *vs.* NHE) and its availability of iron, but only allowed for limited conversion to N_2 (typically 50% at most), and surface passivation prevented a long term use of this method.[63]

Surprisingly, few studies have investigated nitrate reduction using d-block molecular complexes to the best of my knowledge.[64–74] One example of a nickel(II) complex reported by Lee *et al.* was shown to reduce NO_3^- ions to dinitrogen, using CO as oxygen acceptor to form CO_2. Very recently, Fout *et al.* published the first example of the reduction of nitrate ions to ammonia or dinitrogen using an iron(II) tripodal complex.[64]

F-block elements could be even more interesting candidates, owing to their important oxophilicity,[75] which makes, to the best of my knowledge, the existence of only three examples of nitrate activation using f-block complexes surprising.[76–78]

a) Photochemical reduction of nitrates

The team of Hayton first reported in 2016 the reduction of lithium nitrate using $Ce^{III}TREN^{TBDMS}$ (TBDMS = $SiMe_2{}^tBu$) in presence of 12-crown-4 (12-c-4) in Et_2O for 4 days, which led to the formation of a unique cerium-oxo complex capped with $[Li(12\text{-crown-}4)]^+$ and the supposed release of NO_2 (see **Figure 144**).[76] This reaction proceeded through the transient formation of $[Li(12\text{-crown-}4)][(TREN^{TBDMS})Ce(\kappa^2\text{-}O_2NO)]$ where the nitrate can be reduced by one electron over the course of few days.

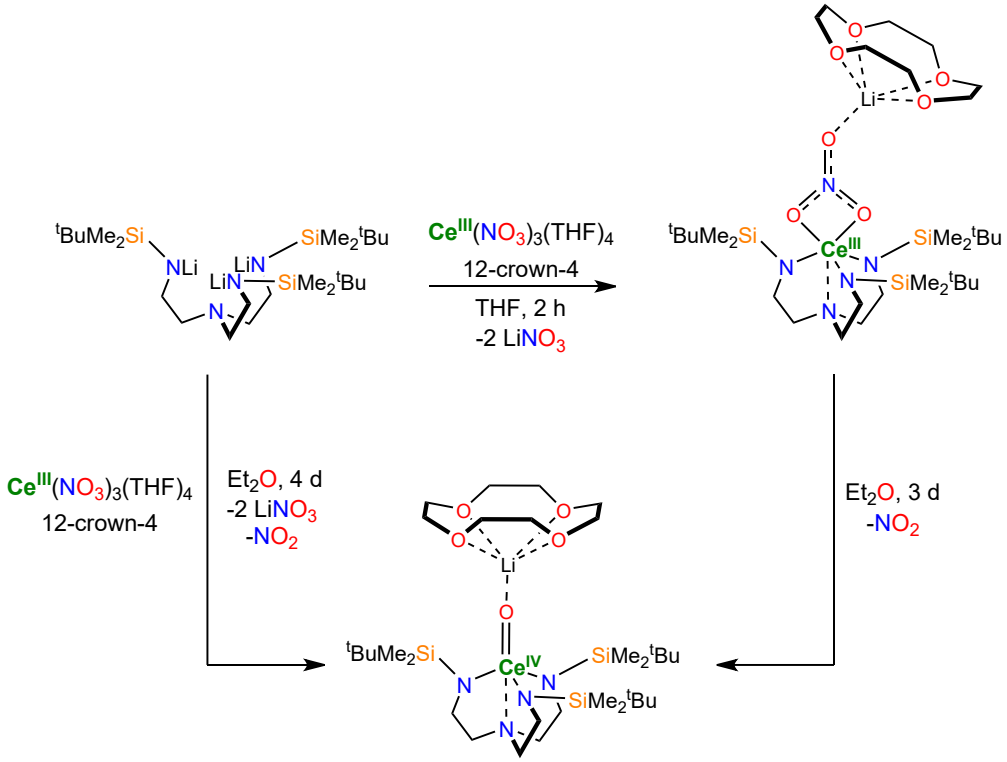

Figure 144. Synthesis of $[Li(12\text{-crown-}4)][(TREN^{TBDMS})Ce(O)]$. Adapted from Hayton *et al.*[76]

They later decided to investigate this interesting reactivity with a more simple cerium precursor, $Ce^{III}(HMDS)_3$ in the presence of 2,2,2-cryptand. While the nitrate reduction did not occur at room temperature for 24 h, the photoirradiation of the sample at 380 nm for 6 h at -5 °C allowed for the formation of three different products as depicted in **Figure 145**.

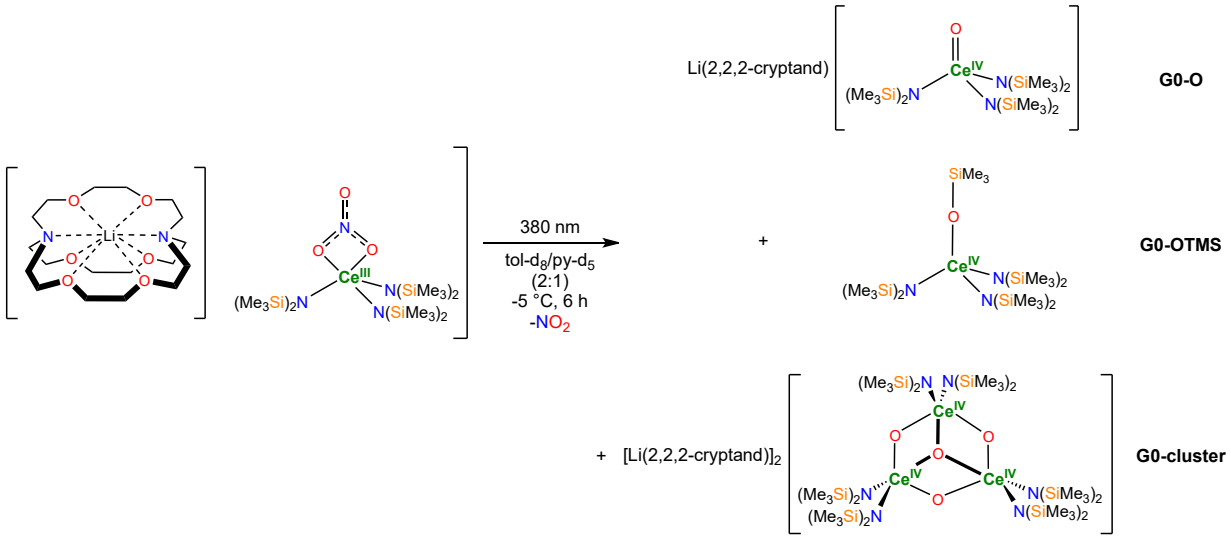

Figure 145. Photoactivation of $[Li(2,2,2\text{-cryptand})][(HMDS)_3Ce(\kappa^2\text{-}O_2NO)]$. Reproduced from Hayton *et al.*[77]

Formation of products **G0-OTMS** and **G0-cluster** are thought to arise from decomposition of product **G0-O**, by a concerted abstraction of $^{\bullet}SiMe_3$ by the oxo species to form compound **G0-OTMS**, and ligand scrambling to form **G0-cluster**.[76] These results made interesting the optimization of nitrate reduction using the interesting redox and solubility properties of a TREN base ligand with light irradiation in mild conditions. In light of these promising investigations, the same reactivity was studied with **1**.

1) Formation of cerium-nitrate complex

Addition of one equivalent of $LiNO_3$ to a solution of **1** in THF-d_8 led to an immediate colour change to orange, and to a shift in the paramagnetic peaks at 2.7 ppm, 1.8 ppm, 1.6 ppm and -6.25 ppm to 2.6 ppm, 2.0 ppm, 1.8 ppm and -6.1 ppm in the ^{1}H NMR spectrum, indicating a geometry change within the coordination sphere of the complex.

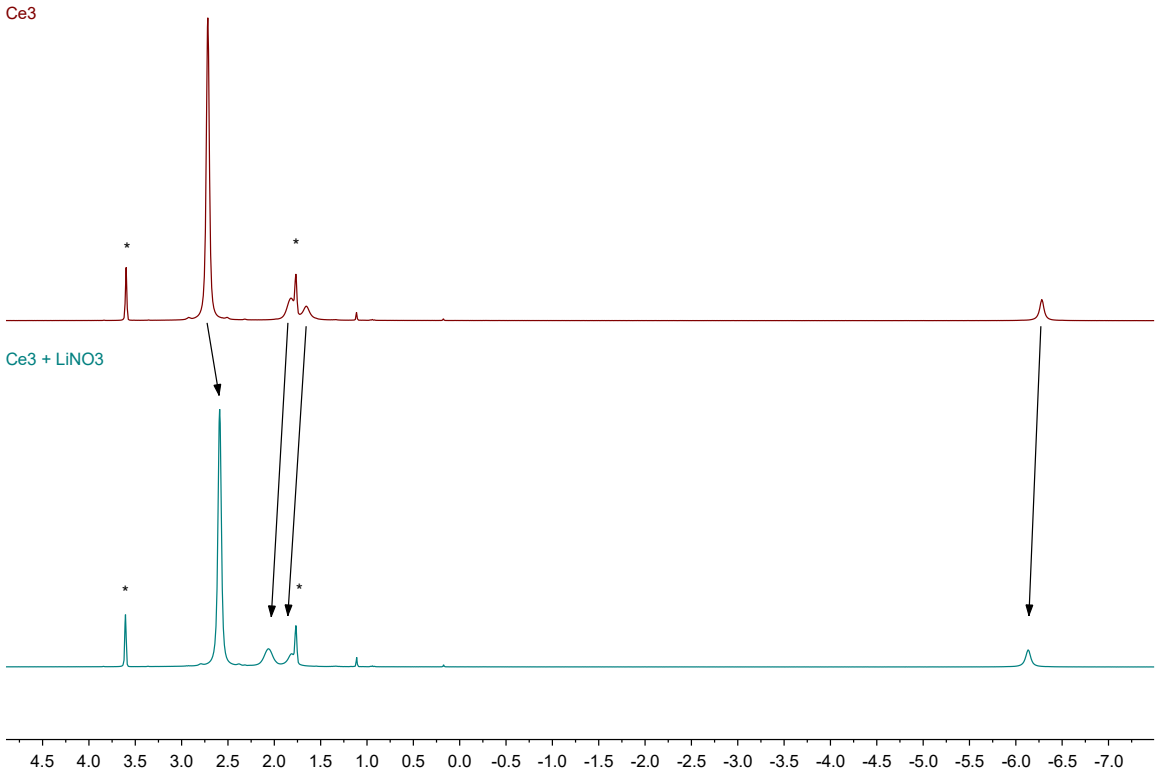

Figure 146. ^{1}H NMR spectra before and after the addition of $LiNO_3$ to a solution of **1** in THF-d_8. Solvent residual peaks are indicated with *

The shift of paramagnetic peaks was found to depend on the amount of $LiNO_3$ introduced in the reaction medium up to about two equivalents of nitrate (except for the broad singlet around -6.0 ppm which continued to shift slowly after adding more than 2 equivalents of $LiNO_3$, see **Figure 147** and **Figure 148**). This result may correspond to a coordination equilibrium between the nitrate anion and **1**.

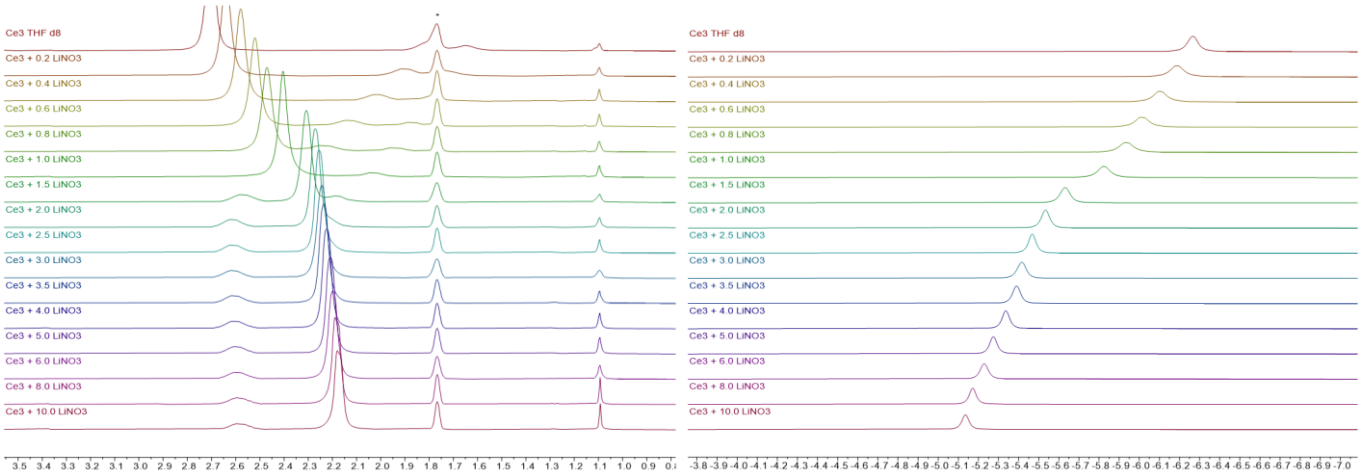

Figure 147. Successive additions of amounts of $LiNO_3$ to a solution of **1** in THF-d_8. Zoom on the region between 2.5 ppm and 0.8 ppm (left) and between -3.8 ppm and -7.0 ppm (right)

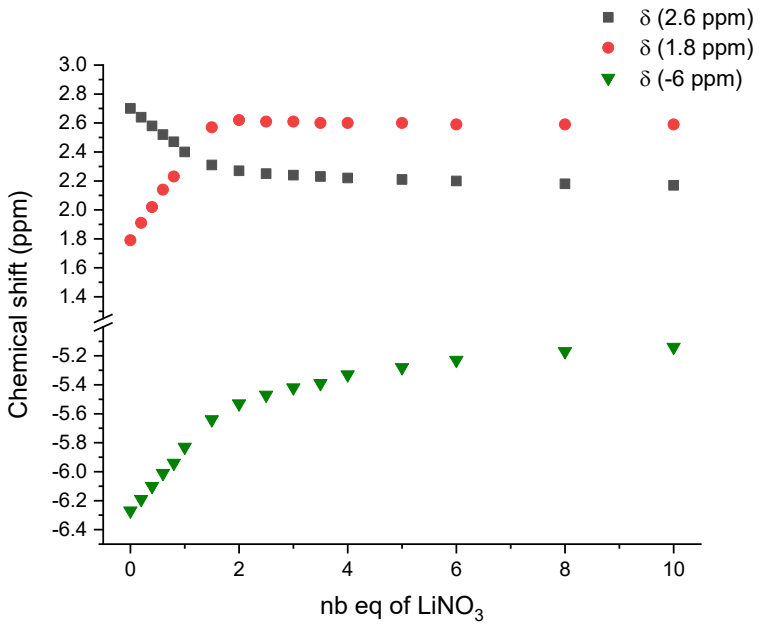

Figure 148. Evolution of chemical shifts of several paramagnetic peaks upon successive additions of $LiNO_3$ to a solution of **1** in THF-d_8

Evaporation of THF, addition of minimal amounts of pentane and one drop of THF allowed for the growth of dark orange crystals at -40 °C overnight. The 3D structure of the complex showed the coordination of one nitrate anion in κ^2 fashion to the cerium centre, stabilized by a lithium cation and three molecules of THF (see **Figure 149**). This stabilization of lithium with THF molecules allowed for the crystallization of the species without using costly 12-crown-4 as in [Li(12-crown-4)][(TREN^{TBDMS})Ce(κ^2-O_2NO)].[76]

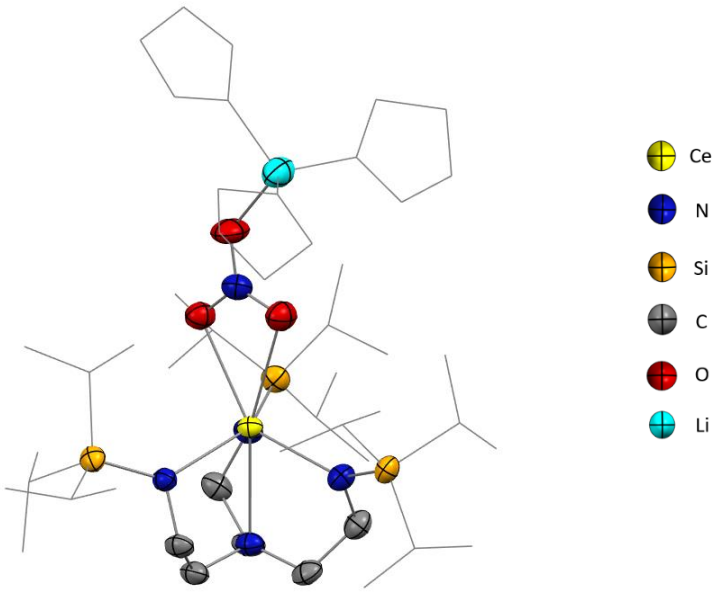

Figure 149. XRD structure of **1-NO₃** [Li(THF)$_3$][TREN^{TIPS}Ce(κ^2-O$_2$NO)]. Ellipsoids are represented at 50% probability, and TIPS moieties and THF molecules are shown in wireframe style for clarity.

Coordination of [NO$_3$-Li(THF)$_3$)] to **1** did not change significantly the three-dimensional structure of the complex : only a small lengthening of Ce-N$_{equatorial}$ bonds from 2.361(3) for **1** to 2.381(5) for **1-NO₃** and a decrease in Ce-N$_{equatorial}$-C angle from 119.1(3) in **1** to 109.3(4) Å in **1-NO₃** could be noticed. Ce-O bonds were respectively 2.656(3) and 2.743(3) Å (average 2.700(4) Å), which were slightly longer in average than in [Li(12-crown-4)][(TREN^{TBDMS})Ce(κ^2-O$_2$NO)] (2.735(8) Å on average). N-O bonds in nitrate anion were 1.249(7) Å in average, with slightly shorter bonds with oxygens bound to cerium (1.261(4) and 1.246(4) Å *vs.* 1.237(4) Å for the non-coordinating bonding N-O bond). This difference in N-O bond length could be explained by a delocalization of electrons with the cerium centre, which weakens the N-O bonds of oxygen atoms bound to cerium.

UV-visible recording of *in situ* generated **1-NO₃** showed a splitting of the absorption band of **1** at 416 nm into two apparent bands at 413 and 357 nm (see **Figure 150** and **Figure S297**) which indicated a change in the electronic structure of the complex. A rough estimation of the ε value of these transitions to about 400 L.mol^{-1}.cm^{-1} would not be consistent with MLCT transitions (ε > 1000 L.mol^{-1}.cm^{-1}), and may either correspond to a f-d transition similarly to **1** or to a more complex electronic transition that could be elucidated by TD-DFT calculations.

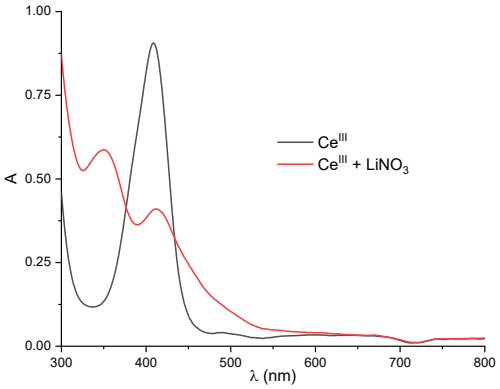

Figure 150. UV-visible spectrum of the reaction between **1** and 1 equivalent of LiNO$_3$ in THF at 1.5 mmol.L^{-1}

In order to compare this system with the one of Hayton *et al.*, the effect of 12-crown-4 addition was investigated. Upon addition of 12-crown-4 to a solution of **1-NO₃** in THF-d$_8$, the paramagnetic peaks in ^{1}H NMR slightly shifted.

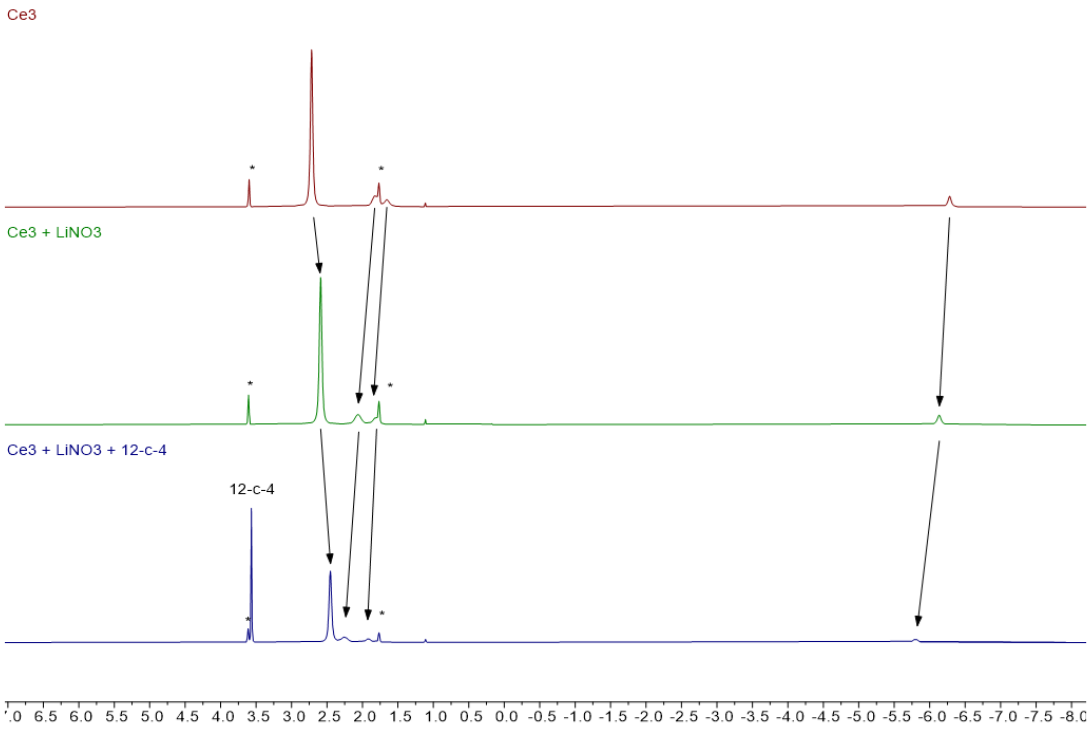

Figure 151. Successive additions of $LiNO_3$ and 12-crown-4 to a solution of **1** in THF-d_8. Solvent peaks are marked with *

The same purification protocol as previously described led to the isolation of highly photosensitive crystals of **1-NO₃-12c4** $[Li(12\text{-}c\text{-}4)_2][TREN^{TIPS}Ce^{III}(\kappa^2\text{-}O_2NO)]$ (see **Figure 152**), where the lithium ion was placed in the outer sphere (any direct light on the crystal during XRD measurement led to degradation). This structure differed from the structure of $[Li(12\text{-crown-}4)][(TREN^{TBDMS})Ce^{III}(\kappa^2\text{-}O_2NO)]$ obtained by Hayton *et al.*, and was more similar to $[Li(2,2,2\text{-cryptand})][(HMDS)_3Ce^{III}(\kappa^2\text{-}O_2NO)]$ (see **Figure 145**). This bis-chelated lithium ion with 12-crown-4 is quite rare in lanthanide[79–81] and actinide chemistry,[82–87] and unique in cerium chemistry. Compared to $[Li(2,2,2\text{-cryptand})][(HMDS)_3Ce(\kappa^2\text{-}O_2NO)]$, Ce-O bonds are slightly shorter in the complex reported by Hayton *et al.* (2.608(3) *vs.* 2.654(3) Å in **1-NO₃-12c4**), and N-O bonds displayed a similar behaviour and similar distances to **1-NO₃** and **1-NO₃-12c4** (average of 1.266(5) Å for N-O bonds with oxygen bound to cerium, 1.223(3) Å for the free N-O bond).

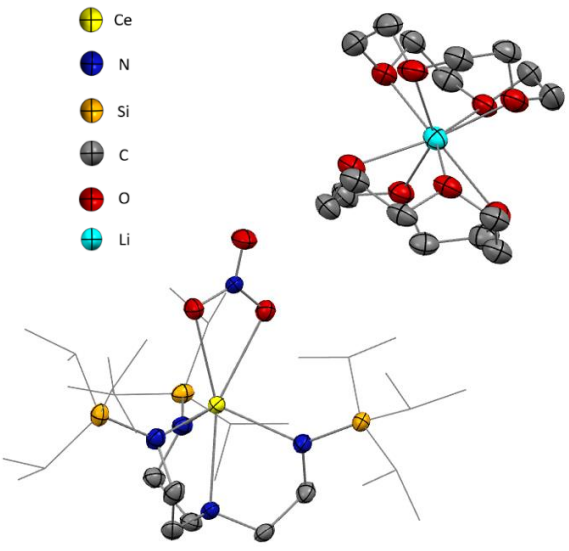

Figure 152. Structure of **1-NO₃-12c4**

Compared to **1-NO₃**, no major structural change in **1-NO₃-12c4** bond lengths and angles were observed. The N-O bonds in the nitrate are similar in average, but longer for oxygen atoms bound to the cerium centre (1.267(3) Å on average for **1-NO₃-12c4** compared to 1.253(6) Å in **1-NO₃**) and shorter for the uncoordinated N-O bond (1.237(4) *vs.* 1.213(3) Å), which could be explained by the abstraction of an electrophilic Li^+ cation.

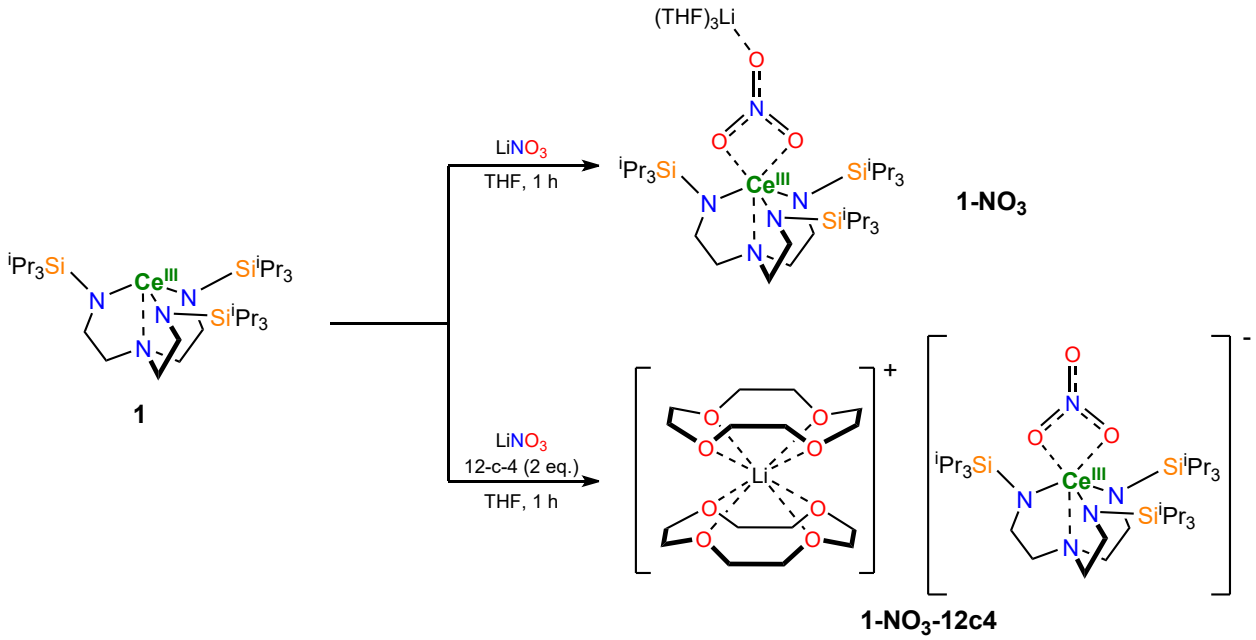

Figure 153. Reaction scheme for the synthesis of complexes **1-NO₃** and **1-NO₃-12c4**

Attempts to synthesize complex **1-NO₃** using sodium nitrate and potassium nitrate only allowed for a ^{1}H NMR characterization of each hypothetical complex after long time of stirring, due to the poor solubility of both salts even in the presence of 15-crown-5 and 18-crown-6 respectively.

Two different cerium(III)-nitrate complexes were synthesised both in presence and absence of stabilizing crown ether, which is different from the report of Hayton and co-workers, and were then irradiated to study their photochemical reactivity presented in the following section.

2) Photochemical formation of a cerium-oxo complex

a. Formation of cerium-oxo complex

In analogy with Hayton and co-workers' report on nitrate photoreduction using $Ce(HMDS)_3$, the photoinduced reduction of nitrate ions with **1** was investigated.

Irradiation of an equimolar mixture of **1** and $LiNO_3$ in THF-d_8 for 10 minutes led to a change in colour from orange to dark yellow, and to the partial consumption of **1** and appearance of a new cerium(IV) compound, as shown by the typical signature of two triplets around 3.7 ppm and 2.6 ppm, and a multiplet around 1.6 ppm (see **Figure 154**). The reaction was monitored using ^{1}H NMR spectroscopy showing the decrease in **1** and the appearance of cerium(IV) over the course of the irradiation time, and it was found that optimal irradiation time to achieve a maximum cerium(IV)/cerium(III) ratio was around 30 minutes. Over longer irradiation times, the amount of cerium(IV) slowly decreased, but no new product could be identified in ^{1}H NMR spectroscopy.

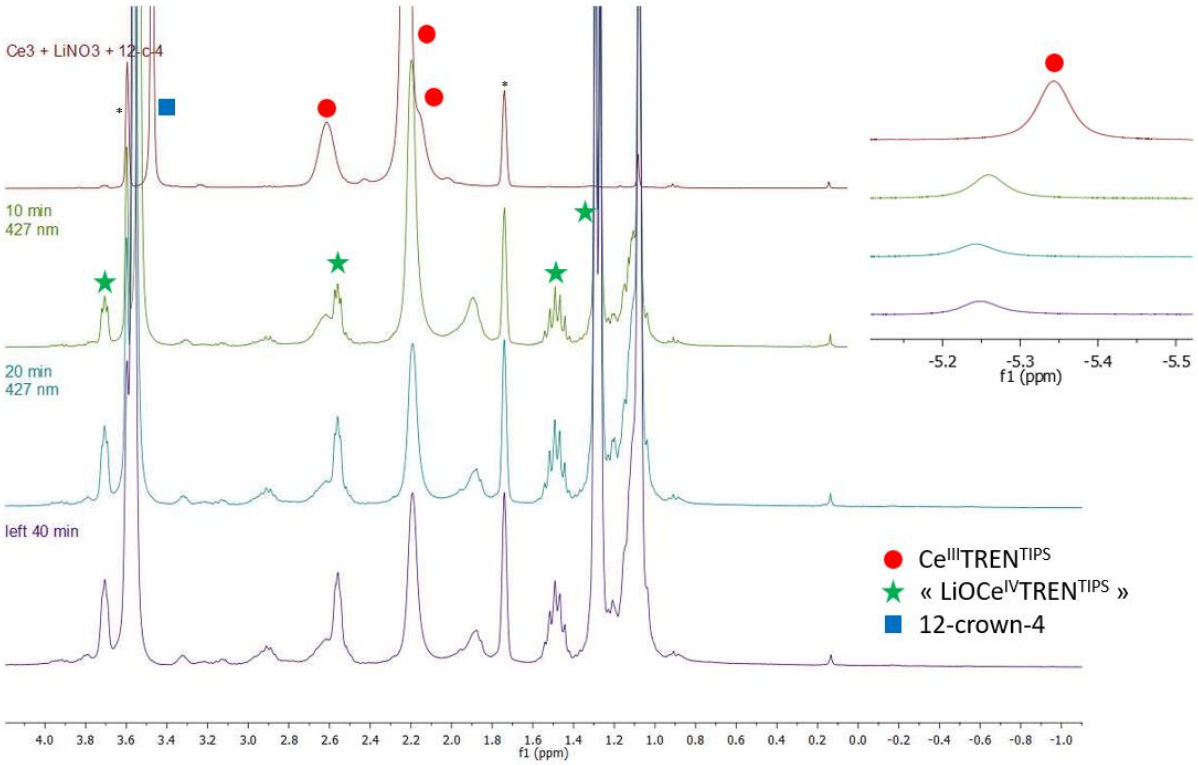

Figure 154. ^{1}H NMR spectra of photoirradiation at 427 nm of a mixture of **1**, $LiNO_3$ and 12-crown-4 in THF-d_8 over time. Zoom between -0.3 and 4.0 ppm. Solvent residual peaks are indicated with *

To identify clearly the nature of the cerium(IV) species, the reaction was scaled-up and irradiated for 45 minutes. THF was evaporated, and a minimal amount of pentane and one drop of THF were added. Storage at -40 °C afforded yellow highly photosensitive crystals corresponding to the structure of complex **2-O** [Li(12-crown-4)][($TREN^{TIPS}$)Ce(O)] (see **Figure 155**).

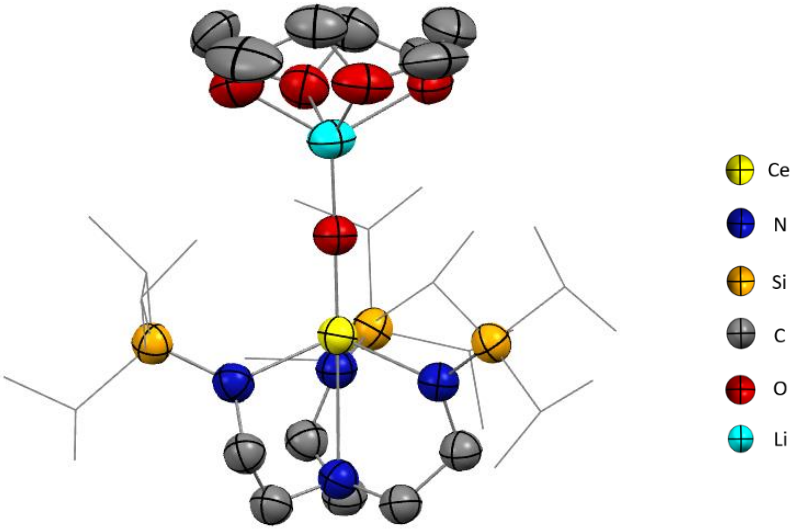

Figure 155. Structure of **2-O**. Hydrogen atoms and THF molecule have been omitted for clarity, and isopropyl groups have been represented in wireframe style. The molecule presents a slight disorder on 12-crown-4 and THF moieties, which was modelled but not plotted for clarity

Formation of **2-O** did not induce major structural changes in the complex compared to **1-NO$_3$** and **1-NO$_3$-12c4**, except a shortening in the Ce-N$_{equatorial}$ bonds from 2.388(4) and 2.381(5) Å to 2.354(4) Å in **2-O**. The Ce-oxo bond length was 1.910(2) Å, comparable to the reported cerium-oxo bond in [Li(12-crown-4)][(TREN^{TBDMS})Ce(O)] (1.902(2) Å),[76] in Ce-O bonds of (TriNOx)Ce-O complexes (1.887(4)-1.902(4) Å)[88] and in Ce-O complex reported by Leung *et al.* (1.857(3) Å).[89]

Considering charge balance, the expected oxidation state of cerium should be +IV. Nevertheless, Ce^{IV}TREN^{TIPS} complexes are usually purple to deep blue, which was strikingly different from the yellowish colour obtained after reduction, and may indicate a more complex electronic structure. Computational investigations led by Hayton *et al.* based on Natural Bond Orbital (NBO) and Quantum Theory of Atoms-In-Molecules (QTAIM) elucidated the triple-bond nature (σ+2π) of the Ce-O bond, similarly to thorium and uranium oxo complexes.[90] Considering the structural similarity of **2-O** with [Li(12-crown-4)][(TREN^{TBDMS})Ce(O)], a similar behaviour could be assumed for our complex. Calculations should be run on this new cerium-oxo complex to confirm this hypothesis.

UV-visible monitoring of the photochemical reaction showed the quick appearance of a broad and intense band in near-UV region which saturated the detector (see **Figure 156**). Upon further irradiation, the intensity of the band slowly decreased (see **Figure S300**).

The mixture of **1** and $NaNO_3$ also led to the formation of a cerium(IV) species highly similar to **2-O** under irradiation at 427 nm, with a small difference in the chemical shift of the triplet at 3.67 ppm compared to 3.71 ppm in the case of **2-O** (see **Figure S284**).

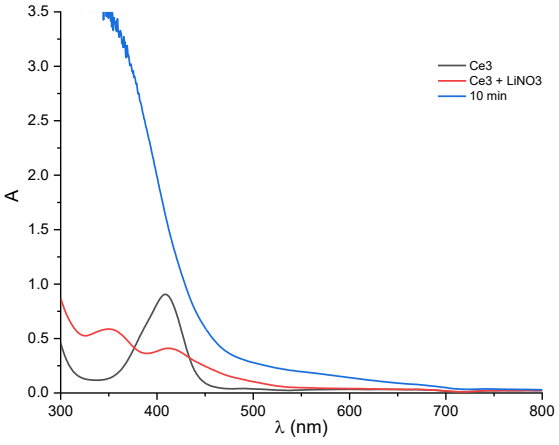

Figure 156. UV-visible monitoring of the photochemical reaction between **1** and $LiNO_3$, and irradiation at 427 nm for 10 minutes (1.5 mmol.L^{-1})

b. Reactivity with electrophiles and PPh_3

To assess the reactivity of the oxo species, reactions with several electrophiles were investigated. Considering the very poor yields of crystallization, the oxo species was generated *in situ* and the electrophiles were added directly to the reaction medium after 45 minutes of irradiation. No reaction was observed with CO, CO_2 or PPh_3. Given the several reports of f-block oxo-complexes silylation using silylated electrophiles,[91–97] the reactivity of this new oxo species was investigated with TIPS-Cl and TMS-OTf.

Addition of TIPS-Cl or TMS-OTf to the **2-O** *in situ* led to an immediate change in colour from orange to dark purple, typical of $Ce^{IV}TREN^{TIPS}$ species. ^1H NMR monitoring of the reaction showed a complete disappearance of **2-O** and the creation of another cerium(IV) species. While no crystal of this new species could be grown, the similarity of the ^1H NMR spectrum to that of Hayton *et al.* combined with the correlation of the 5.1 ppm triplet with the broad apparent singlet at 4.9 ppm in ^1H-^1H COSY (see **Figure S274**) could indicate that a similar species to the siloxy cerium(IV) complex of Hayton *et al.* was formed.

In this first part, the redox reactivity of **1** was applied to the photochemical reduction of nitrate ions. Although the nature of the reduced species has not yet been elucidated, its ability to initiate the reduction of the first step in the nitrogen cycle motivated the study of the reduction of subsequent species in this cycle, such as nitrite ions and nitrous oxide.

b) Reactivity with sodium nitrite and nitrous oxide

Reduction of nitrite anions has gathered efforts to mimic and surpass the activity of nitrite reductase (iron or copper enzyme), reducing *in vivo* NO_2^- into NO. Several tripodal copper(II) model complexes were shown to display similar activities,[98,99] as well as dinuclear complexes of ruthenium(II)[100] and heterobimetallic cobalt-magnesium complexes.[101] Several reports of nitrite electrocatalytic reduction used iron(II) and ruthenium(II) porphyrin complexes[102–104] as well as copper(II) tripodal complexes[105] to reduce NO_2^- into NO or even NH_3. Several examples of lanthanide complexes bearing nitrite ligands in κ^2 fashion (cerium, samarium, neodymium) were reported, exhibiting particular stability with cerium(III) and being readily reduced by SmI_2.[106]

Natural processes involving harmless destruction of nitrous oxide involve nitrous oxide reductase (copper enzyme) reducing N_2O into N_2.[107,108] The seemingly high redox potential of N_2O (1.21 V *vs.* Fc/Fc^+ for N_2/N_2O)[109] should allow for an easy reduction with many substrates, but the reaction is very often blocked by a high kinetic barrier.[110]

Investigations on the chemical reduction of N_2O have highlighted several thermal processes but also many photochemical catalysed systems to degrade N_2O using different materials (*e.g.* zeolites, TiO_2),[111] an many different molecular complexes made of cobalt,[112] titanium,[113] rhodium,[112,114] iridium,[115,116] copper,[117,118] osmium[119], ruthenium[120–122] and rhenium.[109]

A recent elegant report from Cantat *et al.*[123] showed the fast metal-free reduction of N_2O into dinitrogen using stoichiometric amounts of simple disilane reagents in the presence of catalytic amounts of caesium fluoride or potassium trimethylsilanolate in DMSO.

Actinide[124–126] and few lanthanide complexes ($(Me_5C_5)_2M$, M = Yb, Sm)[127] were shown to react with N_2O, to form bridging complexes or oxidize uranium complexes by two electrons.[128–130] To overcome this scarcity of examples of N_2O activation by lanthanides, the reactivity of **1** with N_2O and inorganic nitrites was investigated in THF.

1) Reactivity with sodium nitrite

Addition of sodium nitrite to a solution of **1** in THF-d_8 in the dark did not lead to any significant change, possibly due to the very low solubility of $NaNO_2$ in THF. Upon stirring for about 1 h 30, a broad peak at 2.4 ppm was detected in ^{1}H NMR, which could correspond to the formation of a radical, but this hypothesis was not investigated by EPR of the reaction medium. After overnight stirring in the dark, two triplets at 2.55 and 3.65 ppm started to appear, simultaneously with a multiplet at 1.50 ppm and a doublet at 1.25 ppm, which might correspond to a cerium(IV) species. No crystal could be grown, possibly caused by the very low apparent yield of the reaction.

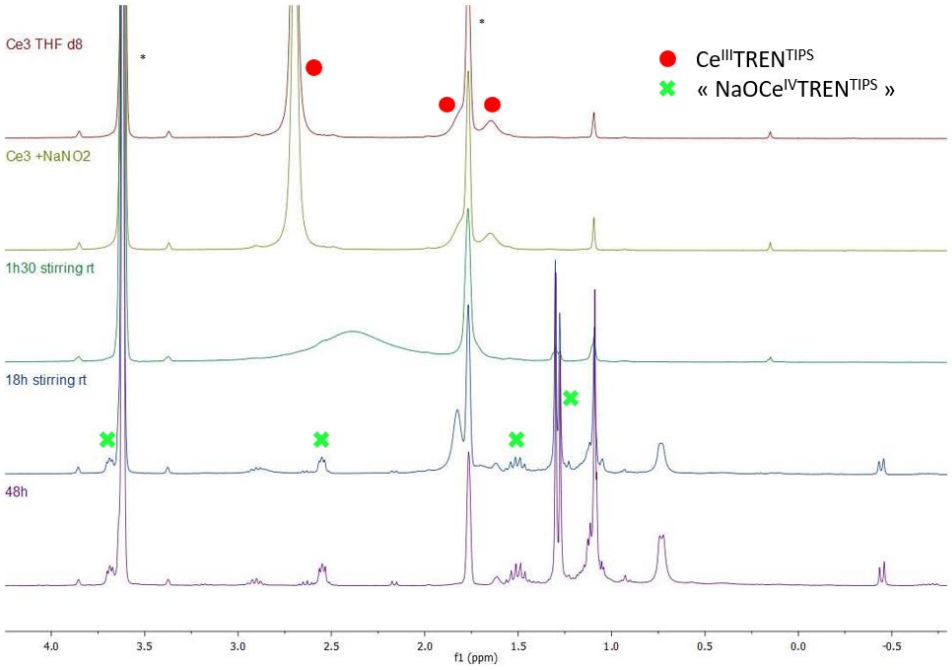

Figure 157. ^{1}H NMR spectrum of the reaction between **1** and $NaNO_2$ in THF-d_8. Zoom between -1.0 and 4.0 ppm. Solvent residual peaks are indicated with *

Due to the similarity of the chemical shifts of this new species with complex **2-O**, the ^{1}H NMR spectrum was compared to the one of the photoirradiation of **1** in the presence of sodium nitrate, as the countercation should play a small role in the chemical shift of the characteristic triplet close to 3.7 ppm as previously highlighted. Pleasingly, the chemical shifts of both species were almost perfectly similar, which would likely indicate that the oxo compound similar to **2-O** was formed in the reaction medium (see **Figure 158**).

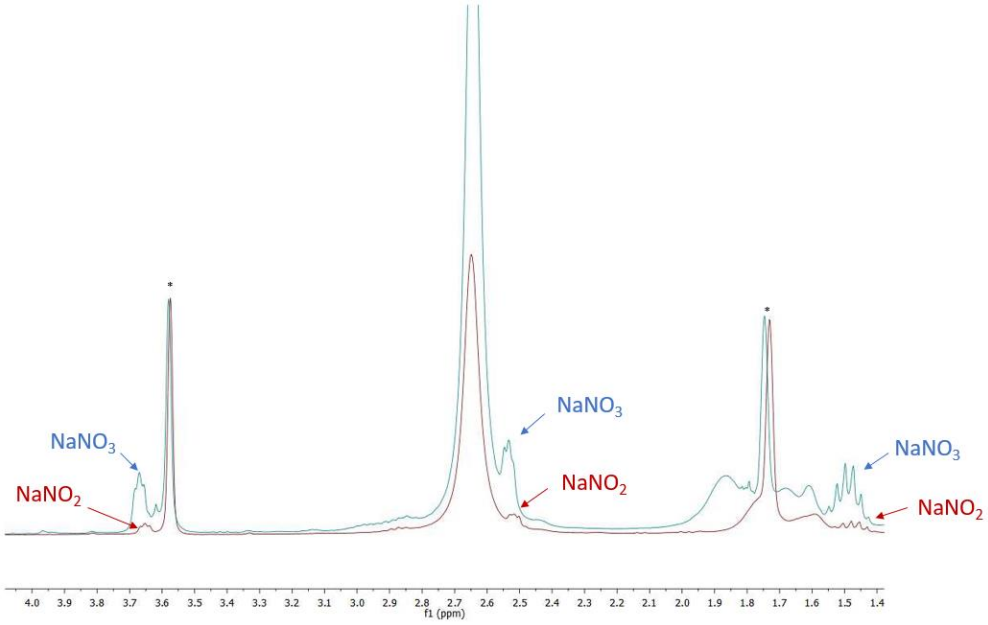

Figure 158. Overlay of the reactions between **1** and $NaNO_2$ after 1 h 30 of irradiation at 427 nm (red) and between **1** and $NaNO_3$ after 30 minutes of irradiation at 427 nm (blue) in THF-d_8. Solvent residual peaks are indicated with *

As the reaction in the dark was proceeding very slowly (probably partly due to the low solubility), a mixture of **1** and $NaNO_2$ was irradiated at 427 nm. The formation of the oxo species was detected after 10 minutes of irradiation, but further irradiation did not allow for the increase in the quantity of the new complex, and ended up forming H_3TREN^{TIPS} after long irradiation times.

Reactivity test on the new cerium(IV) complex attributed to **2-O** with triphenylphosphine did not lead to the formation of triphenylphosphine oxide. More experiments should be run to provide more insight on this reactivity and analyse the degradation products.

Similarly to the cleavage of nitrite ions with uranium(V) complex reported by Schelter and co-workers,[131] the mechanism is probably proceeding through the coordination of NO_2^- ion to the cerium centre, which is then cleaved into nitrogen monoxide and an unstable oxo radical due to the impossibility to form dimers in the case of $CeTREN^{TIPS}$.

As nitric oxide was the next species to study in the nitrogen cycle, the reactivity with NO was envisioned but could not been studied due to unavailability of the gas in our laboratory and the regulations in place which complexify its acquisition. We therefore moved to the investigation of the reduction of nitrous oxide as it follows nitric oxide in the reduction of nitrates.

2) Reactivity with N_2O

Addition of one atmosphere of nitrous oxide to a degassed solution of **1** in THF-d_8 or C_6D_6 did not induce noticeable change in the ^{1}H NMR spectrum, which indicated both the absence of coordination and reduction of N_2O even at higher pressure (up to 3 bar absolute). Nevertheless, the quantity of **1** decreased and H_3TREN^{TIPS} slowly appeared upon irradiation for 30 minutes at 427 nm. An apparent multiplicity of the peaks of H_3TREN^{TIPS} could bring the idea of an activation of the deuterated solvent, but ^{1}H-^{1}H homonuclear decoupling realised with the help of Karim Hammad showed the presence of two different H_3TREN^{TIPS} molecules with a similar structure. The precise nature of the second species was nonetheless not determined.

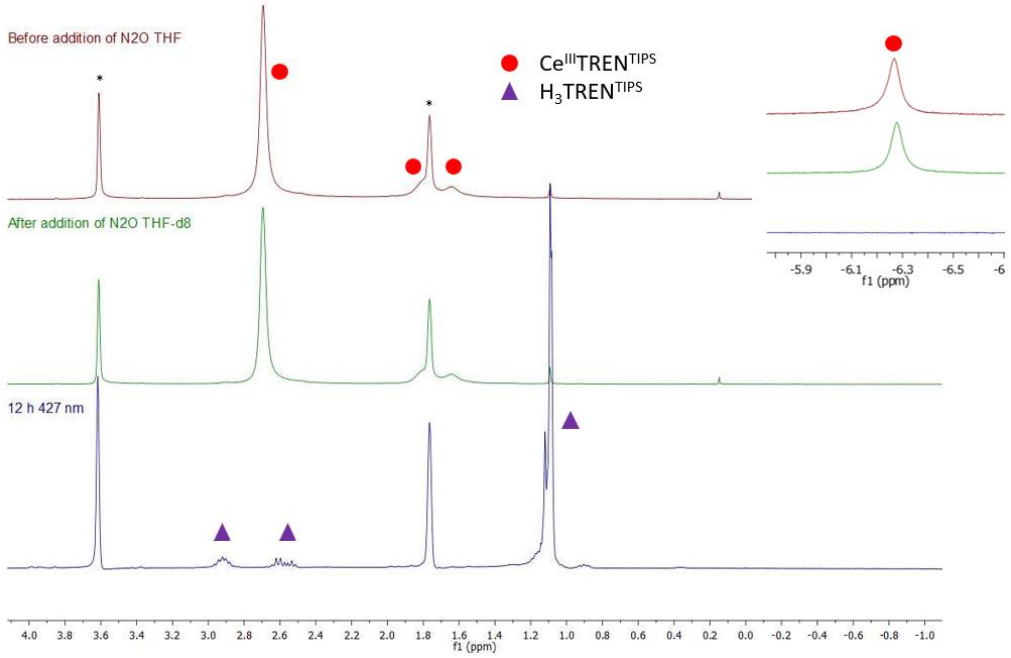

Figure 159. ^{1}H NMR spectrum of the photochemical reaction between **1** and N_2O in THF-d_8. Zoom between -1.0 and 4.2 ppm. Solvent residual peaks are indicated with *

As ^{1}H NMR was not suited for the analysis of the reaction, analysis of the volatile products of the reaction was carried out using a micro-gas chromatograph. To provide relevant analyses, reaction was scaled-up in THF to 40 µmol with an absolute pressure of 1.5 bar of N_2O (3 eq.) into two different tubes : one kept in the dark as a reference and one irradiated at 427 nm for 30 minutes.

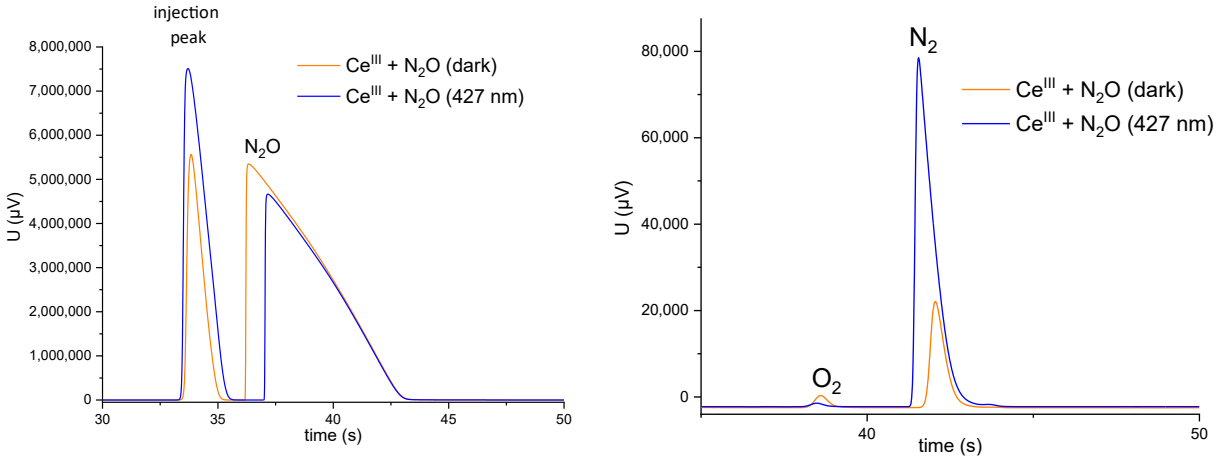

Figure 160. GC analysis of the atmosphere of the reaction medium containing a solution of **1** and N_2O (1.5 bar absolute) in THF left in the dark for 30 min (orange) and irradiated at 427 nm for 30 min (blue). Details are available in Experimental section

GC analysis of the volatile species showed the decrease in nitrous oxide in the reaction medium and the unambiguous increase of dinitrogen in the reaction medium (see **Figure 160**).

In order to trap the intermediary species, reactions in presence of B_2pin_2, hexamethyldisilane, or triphenylphosphine as shown by Cantat *et al.*[109,123] and Anthore-Dalion *et al.*[132] in both THF-d_8 and C_6D_6 were carried out but none of them allowed for the detection of a trapping product (pinB-O-Bpin, hexamethyldisiloxane or triphenylphosphine oxide). This could be explained by the fast degradation of the intermediary species, which could be putatively attributed to a Ce-O$^{\bullet}$ unstable species which degrades quickly (see **Figure 161**).

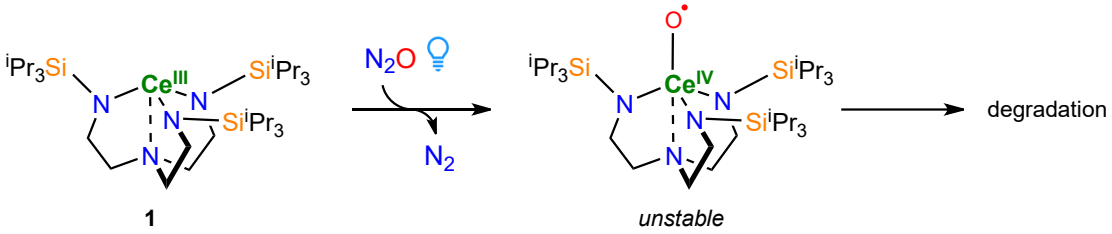

Figure 161. Hypothesis of mechanism for photoinduced N_2O reduction

The absence of cerium-oxo bridged species similar to the previous reports of N_2O activation by lanthanide complexes is not surprising considering the important steric hindrance induced by the bulky TIPS groups from the TREN^{TIPS} moiety (see **Figure 162**).

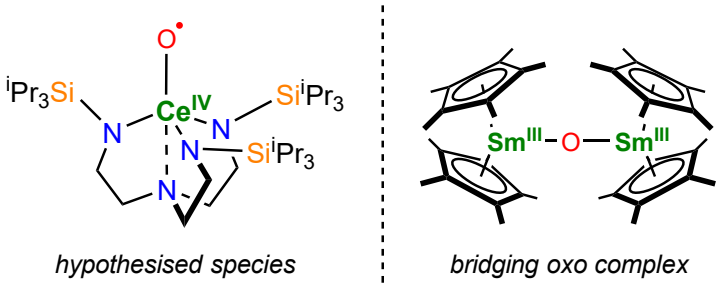

Figure 162. Structures of hypothesised reactive species obtained after N_2O reduction by **1** (left) and example of bridged species obtained after N_2O reduction by $Sm^{II}(C_5Me_5)_2$[127]

Next developments in this kind of this type of reactivity would focus on the trapping of the intermediate species to prevent degradation of the complex, and maybe afford one pot photochemical reduction of nitrate to nitrogen.

II. Carbon capture by a cerium(III) tripodal complex

Storage of CO_2 could be an economically viable solution to decrease quickly the concentration in the atmosphere. Current method involve either pumping carbon dioxide deep into the ground (> 800 m depth),[133] chemical storage with zeolites,[134–136] MOFs,[137,138] and carbon and alkali-carbonate based materials,[139] but this storage is resource limited and enable CO_2 recycling. Amine species, especially under TREN form, are particularly interesting for the CO_2 capture as they lead to lower regeneration costs compared to existing techniques.[140–146]

Electrochemical reduction of CO_2[147,148] into highly value-added products such as methanol,[149–152] formic acid[153–156] or even hydrocarbons[157] is currently a thoroughly investigated field, but up-scaling the process is made difficult by the drop in faradaic efficiency due to the increase in hydrogen evolution reaction at high current densities.[148]

Activation of CO_2 by materials[158–161] and metal complexes in homogenous catalysis is also an active research topic,[162–164] especially due to the possibility to form complex chemical architectures such as cyclic carbonates,[162,165,166] urea,[167] and formic acid[168] among others. Photochemical reductions of CO_2 have also been reported.[169–174]

Given their high oxophilicity, rare-earth elements have shown a wide range of different reactivities with CO_2, ranging from simple insertions in metal-ligand bond,[175] reduction and dimerization,[176,177] to copolymerisation with epoxides[178–186] and unique reactivities.[187]

Insertion of carbon dioxide into rare-earth-amido bond is surprisingly rare. The first example of this reactivity is the report of Bochkarev *et al.* of CO_2 insertion into homoleptic silylamide complexes of $Pr[N(SiMe_3)_2]_3$ and $Nd[N(SiMe_3)_2]_3$, which then decompose into the corresponding siloxy derivatives $Ln(OSiMe_3)_3$[188]. A rare example of stable CO_2 insertion compound in lanthanide-nitrogen bond was reported by Evans *et al.* in a yttrium-caprolactam complex (see **Figure 163**).[189]

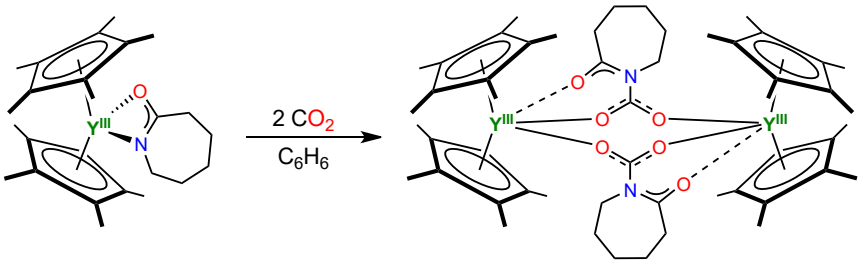

Figure 163. CO_2 insertion in $[(C_5Me_5)_2]Yb(NC_6H_{10}O)$ complex reported by Evans *et al.*[189]

Concerning cerium chemistry, CO_2 was shown to react reversibly with cerium(III)-pyrazolate complexes reported by Anwander *et al.*[190] which was used as a building block to form cyclic carbonates from simple epoxides. In 2019, Schelter and co-workers showed that cerium(III)-amide complexes were activating carbon dioxide to form isocyanates.[191]

Despite their high coordination number, examples of coordination of CO_2 in κ^2 fashion is quite rare among rare-earth complexes, mostly restricted to insertion in lanthanide-carbene bonds as reported by Simler *et al.*,[192] and two other examples of scandium complexes.[193,194] Considering the interesting reactivity of **1** bearing a TREN ligand, the complex was put under a CO_2 atmosphere to examine its behaviour.

Addition of about one equivalent of CO_2 to a solution of **1** in THF-d_8 led to a fading in the pale-yellow colour, which corresponded a partial consumption of the complex and a loss in symmetry, as shown in **Figure 164**. Further addition of CO_2 to about 3 equivalents in total afforded a colourless clear solution

and complete disappearance of **1**. Complete evaporation of the solvent afforded a white powder, which was soluble in THF but not in apolar solvent (pentane and toluene).

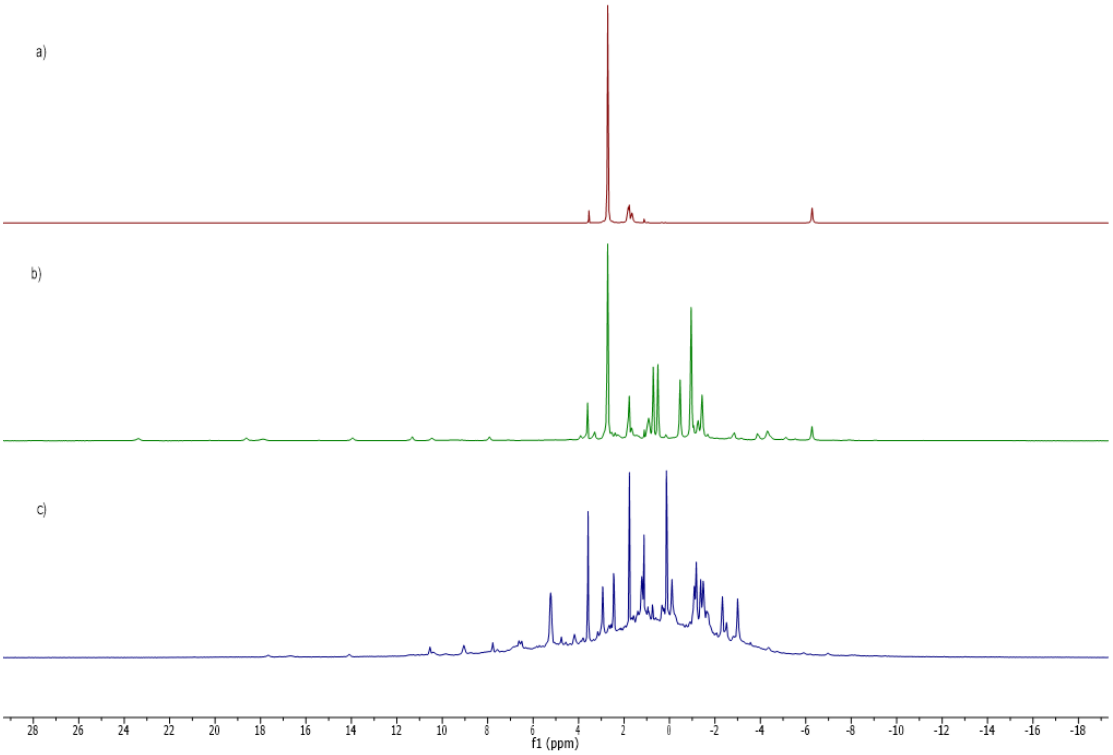

Figure 164. ^{1}H NMR spectra of the addition of 1.25 eq. CO_2 to a solution of **1** in THF-d_8 before (a) and after (b) addition, and (c) after second addition of 1.8 eq. of CO_2

UV-visible analysis of the absorption before and after addition of excess CO_2 to a solution of **1** in THF showed an important shift in absorption from 413 nm for **1** to about 330 nm after addition of CO_2 (see **Figure 165**). No attempt of irradiation at 330 nm was performed due to the unavailability of suitable irradiation source in our laboratory.

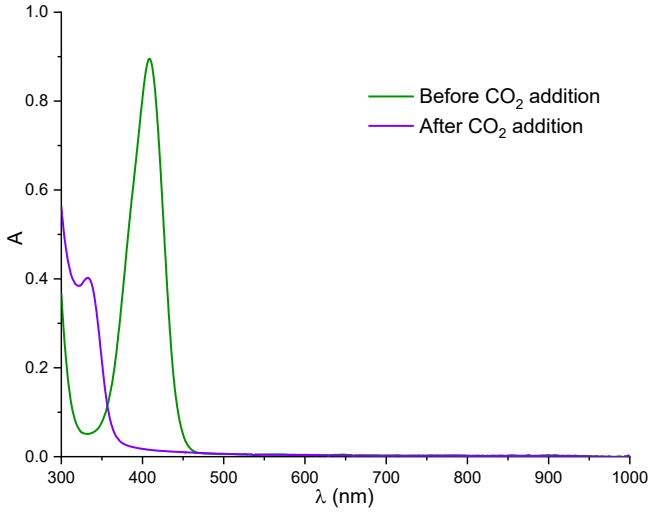

Figure 165. UV-visible spectrum before (green) and after (purple) addition of CO_2 to a solution of **1** in THF (about 1.5 mmol.L^{-1})

In order to identify the species formed, 3 equivalents of CO_2 were added to a solution of **1** in pentane, affording a colourless solution. Attempts to crystallize directly at -80 °C or by slow evaporation at -80 °C were unsuccessful, but led to a precipitation of a fine white powder. The solution was filtrated, concentrated and stored

at -40 °C over 3 days, which yielded colourless crystals that corresponded to a dimeric cerium complex **1-CO_2** bearing 3 CO_2 per cerium (see **Figure 166**).

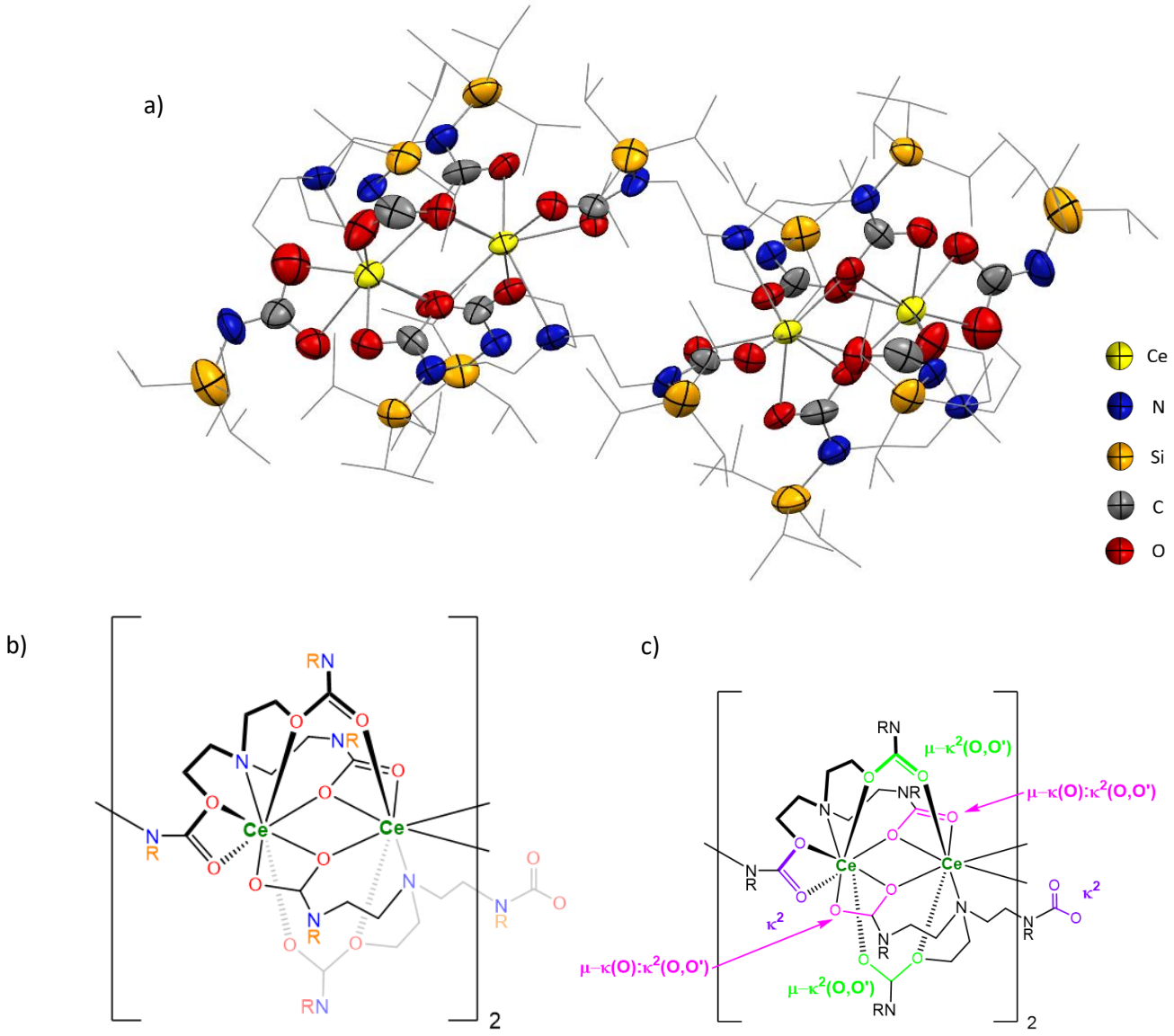

Figure 166. a) XRD structure of **1-CO_2** and schematic representation. Displacement ellipsoids are represented at 50% probability. Hydrogen atoms have been omitted for clarity, and isopropyl groups have been represented in wireframe style. b) Schematic representation of **1-CO_2** (R = TIPS). c) Highlight of the different CO_2 bonding patterns in **1-CO_2**

3D structure of the complex showed a formation of a bimetallic complex where CO_2 was inserted into Ce-N bonds of **1** to form carbamate moieties, and an opening of the TREN coordination sphere with one TREN arm bridging towards another identical bimetallic complex. Three different coordination patterns of CO_2 could be observed: κ^2 bonding (purple in **Figure 166**), end-on bridging μ-κ^2(O,O') (light green) and chelating-bridging μ-κ(O):κ^2(O,O') (pink). It is important noticing that one TREN moiety was better defined than the other (lower uncertainty values) as shown in **Table S63**. Overall, all C-O bonds in **1-CO_2** were longer than C-O bonds in CO_2 (1.1621 Å),[195] which was consistent with the formation of a carbamate group.

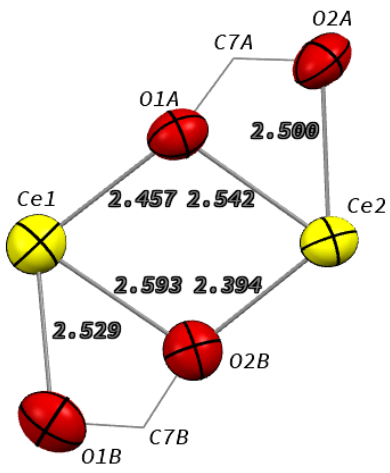

κ^2 CO_2 displayed dissymmetric C-O bonds (*e.g.* 1.27(2) *vs.* 1.37(2) Å), which clearly indicated a C=O and C-O pattern (C-O bond in $CeCl_5(OMe)^{2-}$ is 1.340(5) Å).[196] The two μ-κ^2(O,O')-CO_2 were nevertheless different, with a clear C=O and C-O pattern for the first (1.38(2) and 1.25(2) Å), and a hybrid structure of the second CO_2 moiety (1.273(18) and 1.248(18) Å). Chelating-bridging μ-κ(O):κ^2(O,O')-CO_2 displayed a similar hybrid pattern than the latter. This dissymmetrical feature was surprising given the apparent overall symmetry of **1-CO_2**.

The overall charge in the complex was zero, indicating that oxidation state of the cerium centres was still +III. This is in accordance with the presence of peaks between 0 and -8 ppm in ^{1}H NMR spectrum. Neither computational data nor EPR spectroscopy were run so far to confirm this hypothesis.

Figure 167. Bond distances of the Ce-O diamond core in **1-CO_2**

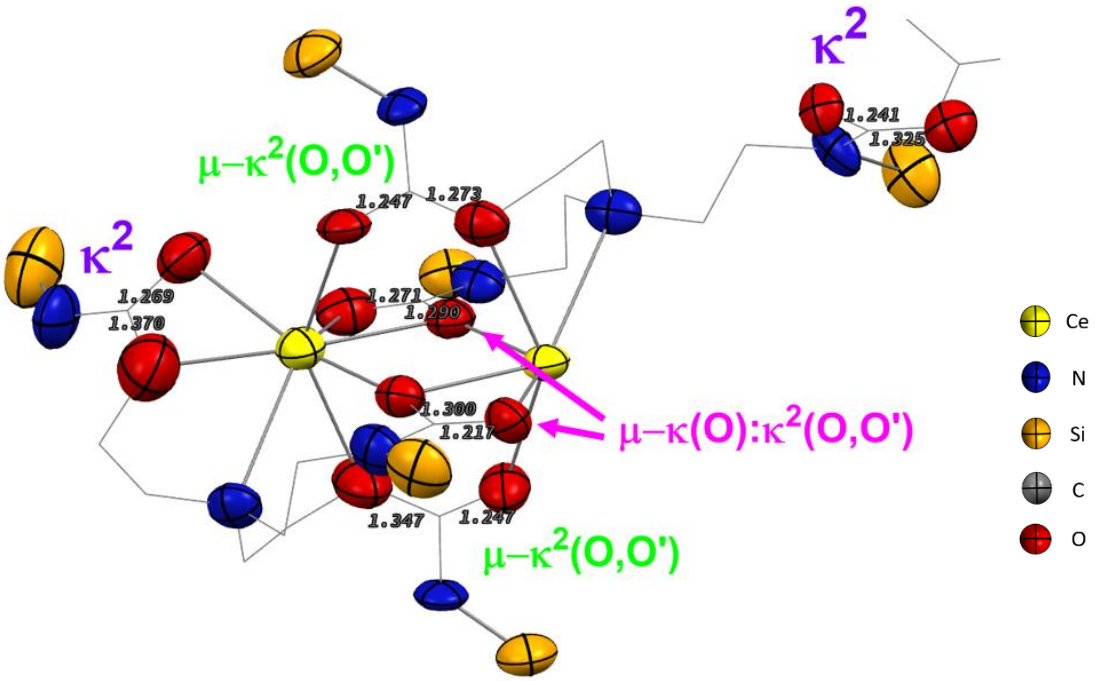

Figure 168. C-O bond distances (in Å) in **1-CO_2**

In this part, complex **1** was shown to react with CO_2 to trap carbon dioxide under the form of carbamate, which mimicked the carbon storage techniques using amine moieties developed in the literature. Further investigations on this project would focus on the regeneration of **1** to make the trapping catalytic, and further optimisations of the reaction conditions.

III. Superoxide radical formation under dioxygen atmosphere

a) Introduction

1) Dioxygen transport in proteins

The ability to harvest and use dioxygen allowed biological organisms to access an unfathomable number of possibilities and improvements. For instance, glucose metabolism delivers 15 times more energy in the presence of dioxygen than in anaerobic conditions.[197] Providing enough dioxygen to the organism is therefore of great importance. Evolution produced two systems to meet the demand for O_2 supply :

- a circulatory system that delivers dioxygen in the organism : haemolymph for arthropods and molluscs and blood for vertebrates
- dioxygen carrying and storage proteins : hemocyanin or hemerythrin for arthropods and molluscs, and haemoglobin and myoglobin for vertebrates

These proteins differ in the reversible or irreversible binding of oxygen to the metallic centre(s). In hemocyanin, dioxygen is reduced by two copper(I) ions to form a side-on μ,η^2,η^2 peroxo complex (two-electron reduction). This change in redox state goes together with a shift in colour from colourless copper(I) to blue copper(II), which is a characteristic colour for hemolymph in molluscs.

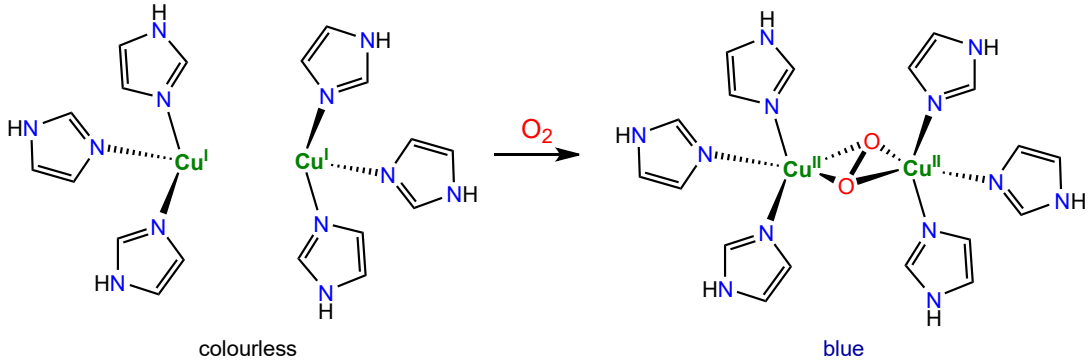

Figure 169. Binding of dioxygen to copper centres of hemocyanin. Only pyrrole cycles from histidine moieties have been showed for clarity

A similar binding mode occurs in hemerythrin, used by marine invertebrates to carry dioxygen. Upon coordination in end-on fashion, colour shifts from colourless to pink-purple.

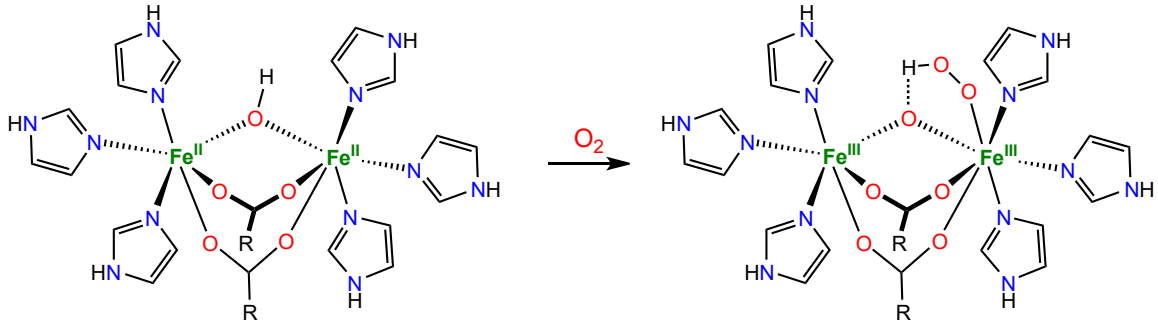

Figure 170. Binding of dioxygen to iron centres of hemerythrin. Only pyrrole cycles from histidine moieties have been shown for clarity. R chains correspond to glutamate or aspartate amino acids

Haemoglobin and myoglobin tend to interact reversibly with dioxygen on a tetrapyrrole ring (haem, from ancient Greek αἷμα, blood) surrounding an iron(II) ion. A *proximal* histidine is located under the macrocycle to stabilize the octahedral geometry of the complex. Upon coordination, O_2 is stabilized by

hydrogen bonding with another *distal* histidine, which also impairs undesired coordination of carbon monoxide.

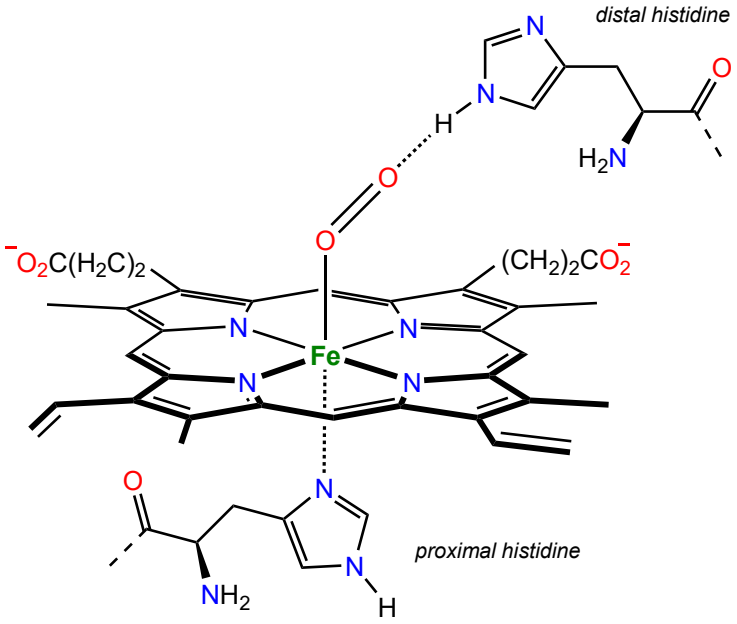

Figure 171. Binding of dioxygen to haem

In this structure, O_2 seems to only coordinate to the iron(II) centre without any redox reaction occurring. Actually, the interaction between iron and oxygen is more complex, and can be considered as a superposition of both Fe(II)-O_2 and Fe(III)-$O_2^{\bullet-}$ where $O_2^{\bullet-}$ is the superoxide radical, the latter form being stabilized by the distal histidine.

2) Reactivity of dioxygen with complexes

Despite a mild reduction potential of -0.33 V *vs.* NHE ($O_2^{\bullet-}/O_2$),[198] dioxygen oxidations with organic molecules are usually extremely slow. This feature is due to the triplet ground state electronic structure of dioxygen, which should prevent it from engaging in thermodynamically feasible reactions with closed-shell species with regard to spin selection rules.[199] These reactions may nonetheless still occur at very low kinetic rates, due to the need for spin interconversion. On the contrary, metals may display a set of unpaired electrons which favours spin-allowed reactions and leverages kinetic and thermodynamic barriers usually preventing uncatalyzed reactions of O_2.[199] In order to investigate and model biological processes, dioxygen activation by transition-metal complexes has been extensively studied.[200–208]

TREN-like base ligands have especially been used with transition metals as they tend to mimic the histidine coordination environment of the copper and iron ions in hemocyanin and hemerythrin,[206,209–217] while allowing for an easy tuning of ligands grafted on equatorial nitrogens. Increase in the stability of superoxide radical and in steric bulk to prevent dimerization was achieved by introducing *tert*-butylated urea onto equatorial nitrogens to provide hydrogen bonding,[212] or bulky guanidinate to significantly increase bulkiness (see **Figure 172**).[213,218]

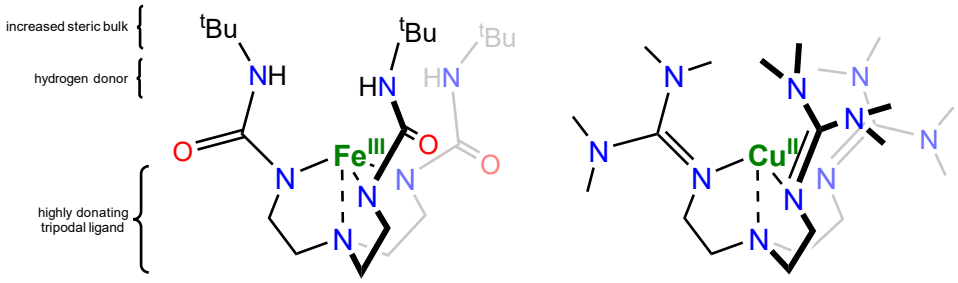

Figure 172. Ligand design for stabilization of reduced oxygen species and example of TREN-guanidinate copper complex. Adapted from Borovik[209] and Saracini[213]

Owing to their oxophilicity and their reducing properties, lanthanide ions have been reported to react with dioxygen.[219–225] Contrary to d-block elements, no end-on coordination of dioxygen has been crystallographically characterized, and only one of the 49 structures reported in the 2021 Cambridge Crystallographic Data Centre was a monomeric species.[226] The absence in end-on species might be explained by the high coordination number of lanthanide ions.

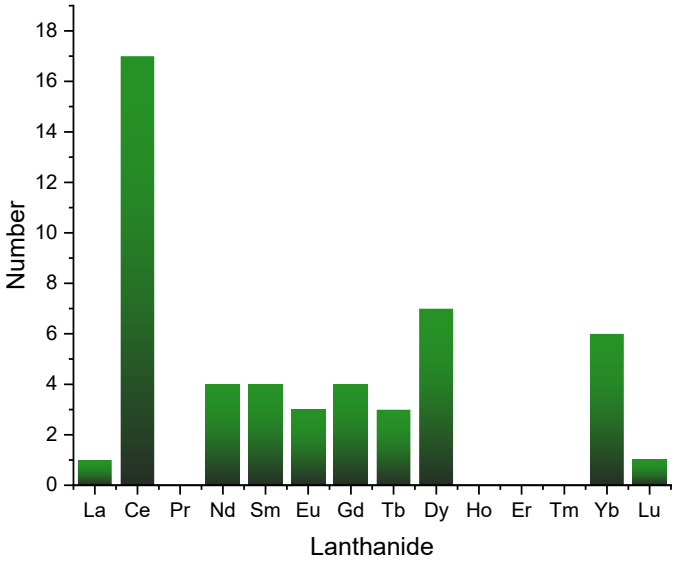

Figure 173. Number of crystal structure reported in the Cambridge Crystallographic Data Centre (2021) involving a lanthanide (including lanthanum) and a O_2^{n-} species (n = 0, 1, 2)

Among lanthanides, cerium is strikingly overrepresented in activation of dioxygen, accounting for about 1/3 of the reported structures (see **Figure 173**).[227] The important disparity in O-O bond length within all the reported peroxo complexes highlights the impossibility to rely in this only metric to determine the peroxo or superoxo nature of the species as mentioned by Protchenko *et al.*.[228]

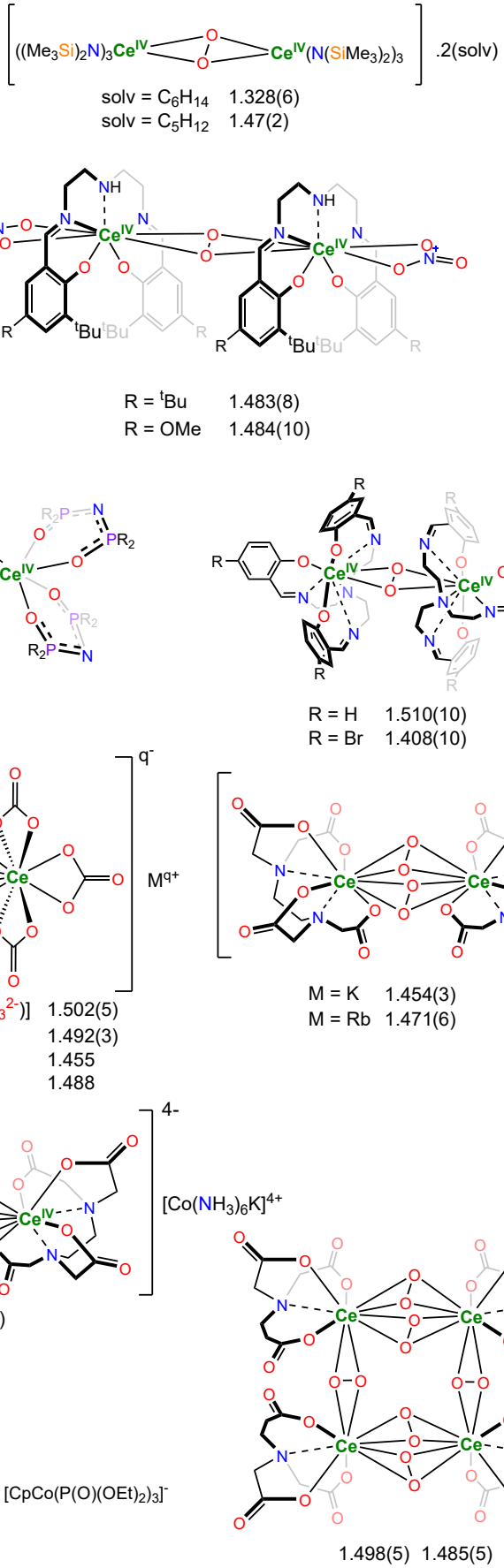

Figure 174. Cerium complexes bearing reduced dioxygen species.[227–235] Values indicated correspond to reported O-O bond distances in Å

b) Reactivity with 1

Upon addition of excess dioxygen to a solution of **1** in THF-d_8 at room temperature, the colour immediately changed to orange. ^{1}H NMR analysis of the reaction medium indicated the complete destruction of **1** and the formation of H_3TREN^{TIPS}, which may have arisen from a HAT reaction induced by a highly reactive species.

In order to identify this species, the same reaction was performed at -78 °C. Repeating the reaction in toluene-d_8 with 1 bar of O_2 afforded an immediate change to deep purple solution, characteristic of cerium(IV) species. Given the low solubility of O_2 in toluene, the reaction medium was left at -78 °C for 24 h prior to analysis.

^{1}H NMR spectrum of the reaction medium showed the consumption of the **1** and the rise of two triplets at 3.14 and 6.17 ppm, in addition to two doublets at 3.28 and 4.17 ppm and two singlets at 1.27 and 1.46 ppm. This signature would likely be the one of a cerium(IV) complex quite different from the ones previously described in this manuscript, especially due to the absence of a typical multiplet around 1.3 ppm. This hypothesis was consistent with the very small shift of the peaks with the temperature, as shown by the VT NMR of the reaction medium in toluene-d_8 between -75 °C and 10 °C. This experiment also allowed to determine the degradation temperature of the complex (about 10 °C, see **Figure S352**).

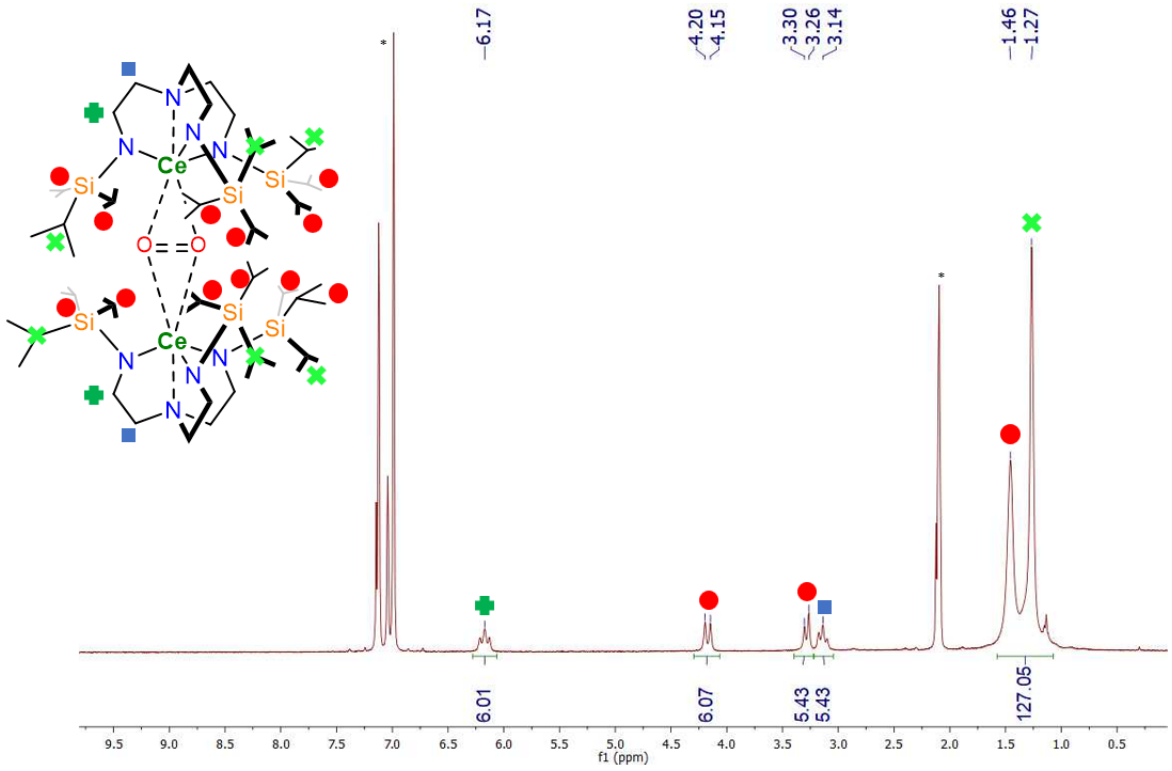

Figure 175. ^{1}H NMR of *in situ* **2-O₂** in toluene-d_8. Green crosses are related to TIPS moiety pointing out from the coordination sphere of the complex, and red circle for the one closer to the reduced dioxygen moiety. Solvent residual peaks are indicated with *

Interestingly, if the warming to room temperature was made quickly after addition (within 10 minutes), the complex degraded at much lower temperature (close to -40 °C), which may indicate a sequential mechanism that could proceed through the formation of an unstable cerium(IV)-$O_2^{\bullet-}$ monomeric species, which further reacts with another molecule of **1** to yield **2-O₂** (see **Figure 176**).

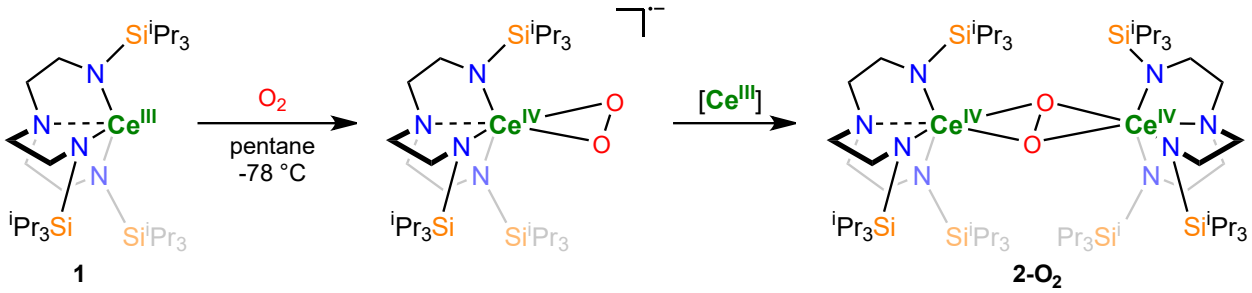

Figure 176. Hypothetical mechanism for the formation of **2-O₂**

Due to the extreme temperature sensitivity, no purification step could be performed, as the reaction medium could not be entered into the glovebox or cannulated into another container. Direct crystallization attempts at -78 °C were therefore made directly from the reaction medium. Attempts to grow crystals from MeCy and THF solutions did not afford any solid nor crystals, and slow evaporation at -78 °C only led to the formation of a waxy purple solid. Storage of a pentane solution for 24 h at -78 °C in a J. Young NMR tube afforded small purple plates which were extremely sensitive to temperature and would tend to quickly degrade into a yellow solid.

XRD analysis of the purple crystals showed the formation of a dimeric cerium complex **2-O₂** bearing a μ,η^2,η^2 bridging disordered dioxygen motif. Using this structural information, the attribution of peaks in ^{1}H NMR depicted in **Figure 175** was proposed.

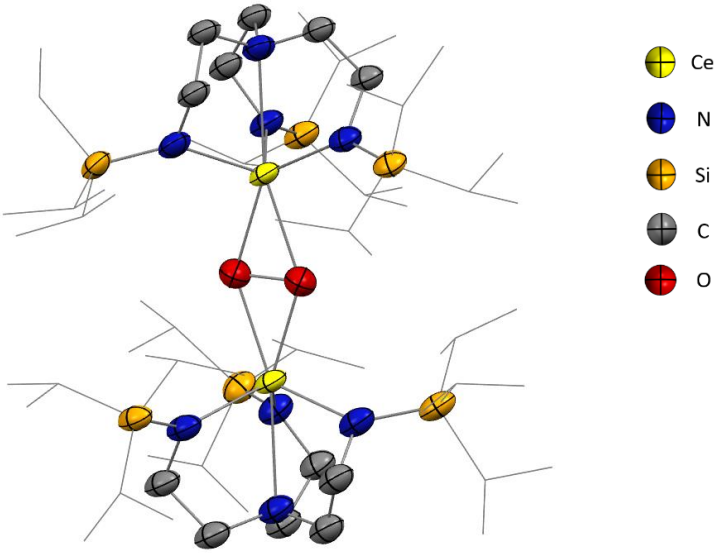

Figure 177. Structure of **2-O₂**. Hydrogen atoms have been omitted for clarity, and isopropyl groups have been represented in wireframe style. The molecule presents a slight disorder on isopropyl groups and dioxygen centre, which was not shown for clarity

Integration values for the two triplets were consistent with a similar attribution to the one for **2-X** (X = Br, Cl, F). TIPS moieties were found to be split in two, attributed to different orientations in space : TIPS pointing out from the coordination sphere (1/3) with a similar chemical shift to TIPS groups in **2-X**, and slightly more deshielded TIPS (2/3) with two “doublets” at 3.28 and 4.17 ppm that were likely to correspond to hydrogens bound to the tertiary carbon of the TIPS. The unusual shifts of these protons might be explained by the steric congestion of the coordination sphere, forcing the C-H bonds of tertiary carbons to points towards the reduced O_2 moiety and shortening the distance to between 2.7 and 4 Å in a static analysis. This spatial proximity and orientation of these bonds could induce an important shift by dipolar coupling through space.

Before analysing bond distances in **2-O_2**, it is worth mentioning that due to the difficult crystal mounting of this species, the quality of the data is not sufficient for in depth structural discussions due to important uncertainties. Some restraints had to be applied using SHELX[236] onto the cerium and oxygen atoms for the structure refinement (other restraints like fixed distances for C-Si and C-C bonds will not be discussed here):[237]

- Same Distance (SADI) restraints on O-O bonds, which restrains the length of all O-O bonds to be the same within standard uncertainty 0.04
- All ellipsoids within 2 Å were forced to be of similar size within standard uncertainty of 0.004 using SIMU restraint

Ce-$N_{equatorial}$ bonds are slightly shortened from 2.361(3) Å in **1** to 2.27(5) Å, which was similar to Ce-$N_{equatorial}$ in cerium(IV)-halide complexes reported in this manuscript (2.222(5), 2.220(3) and 2.222(4) Å respectively for **2-Br**, **2-Cl**, and **2-F**). The distance between the cerium centre and the plane intersecting all equatorial nitrogens was calculated to be 0.828 Å in average, which is significantly longer than in complexes **2-Br**, **2-Cl**, and **2-F** (0.687, 0.694 and 0.722 Å respectively). The Ce-N_{axial} bonds are also significantly elongated compared to the halogenated complexes, 2.74(4) Å in the cerium-dioxygen bridged complex and 2.603(3), 2.606(3) and 2.620(3) Å in **2-Br**, **2-Cl**, and **2-F**. These structural changes indicated that cerium was "pulled out" from the coordination sphere of $TREN^{TIPS}$, and the evolution in bond lengths was attributed to the opposite effects of important oxophilicity of cerium and the steric repulsions between TIPS groups. The Ce-O bonds lengths were found to be 2.37(12) Å in average, which was within the range of the complexes reported in **Figure 174** (2.2 – 2.4 Å).

The O-O bonds of both disordered reduced dioxygen were measured to be 1.50(3) and 1.49(3) Å, which was falling in the upper range of bond lengths for reported complexes. This value was much longer than the double bond of dioxygen (1.12 Å), confirming that a reduction had occurred.

Attributing the nature of the reduced species (superoxo $O_2^{\bullet-}$ or peroxo O_2^{2-}) solely on this criterion would be debatable, but the very long bond distance compared to other reported distances tends to be coherent with a peroxo species. A Raman spectrum would be needed to confirm this attribution, where a signal around 1200 cm^{-1} would correspond to a superoxo species whereas a peroxo species would appear closer to the 750-850 cm^{-1} region.[226,228,238] Attempts of recording a Raman spectrum at low temperature of the in situ reaction of O_2 addition in a LINKAM FTIR600 cell with the help of Simon Delacroix were unfruitful due to air leaks in the system.

EPR analysis of the reaction medium in pentane at 108 K (-165 °C) 24 h after addition allowed for the detection of an anisotropic signal displaying an axial symmetry with $g_{\parallel}$ = 2.038 and $g_{\perp}$ = 2.009 (see **Figure 178**). This pattern was typical of a superoxide radical at low temperature.[239–241] Comparing to the reported g values was nevertheless not relevant, since an important variation occurs with the change in local environment of the radical. A triplet peroxo species was not considered here given the relatively narrow EPR bands, which would be extremely broad in the case of vicinal radicals. Attempts to trap the radical species with PBN or DMPO did not afford any result.

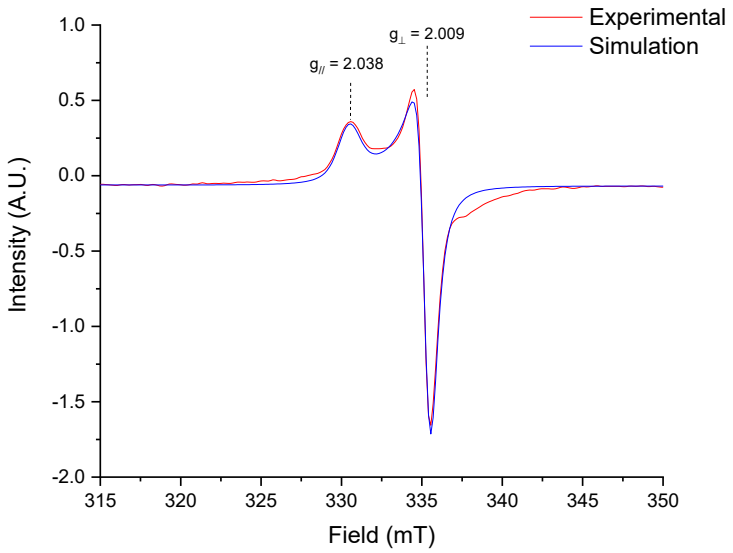

Figure 178. X-band EPR spectrum of the reaction medium at 108 K after addition of 3 equivalents of O_2 to a solution of **1** in pentane

With current data, three systems can be considered (see **Table 5**):

- 2 Ce^{III} + O_2 : this possibility respects the symmetry of the XRD structure, but the long O-O bond, the purple colour and the active EPR spectra obtained of the reaction medium preclude this possibility
- 2 Ce^{IV} + O_2^{2-} : this system would be coherent with colour, the symmetry of the structure and O-O bond length, but not with the EPR data
- 1 Ce^{III} + 1 Ce^{IV} + $O_2^{\bullet-}$: given the much higher extinction coefficient of cerium(IV) species, the colour of such a system would be expected to be purple which is coherent with experimental observations, as well as the radical present in the EPR spectrum, but does not respect the symmetry of the 3D structure

System	Colour	NMR	EPR	Symmetry	O-O bond length
2 Ce^{III} + O_2	✗	✗	✗	✓	✗
2 Ce^{IV} + O_2^{2-}	✓	✓	✗	✓	✓
1 Ce^{III} + 1 Ce^{IV} + $O_2^{\bullet-}$	✓	✗	✓	✗	✗

Table 5. Possible electronic structures of complex **2-O_2**

The cerium(IV)-peroxo system therefore seems to be the most likely to describe the system, but is not in accordance with the EPR data. Another possible explanation for these conflicting data could lie in the electronic structure of **2-O_2**, possibly being a mixed valence complex with two resonance structures Ce^{III} - $O_2^{\bullet-}$ - Ce^{IV} and Ce^{IV} - O_2^{2-} - Ce^{IV}. EPR measurement should be done a second time to confirm the reproducibility of the experiment.



Figure 179. Possible combination of resonance structures in complex **2-O_2**

A second possible hypothesis could be that the species detected in EPR could be an intermediate in the formation of **2-O_2** as depicted in Figure 176. Hypothetical mechanism for the formation of 2-O2**Figure**

176. the detection of the superoxo radical could correspond to the formation of the monomeric species, which later dimerises into **2-O_2**.

c) Reactivity of 2-O_2

Reactivity of complex **2-O_2** with different substrates was briefly studied. Attempts to form a hydroperoxide species using 1,1'-(2-Propenylidene)bis[benzene] and cumene were unsuccessful (see **Figure 180**). Nevertheless, following the report of Takats *et al.* of triphenylphosphine oxidation using a samarium-superoxo complex,[226] the same reaction was investigated.

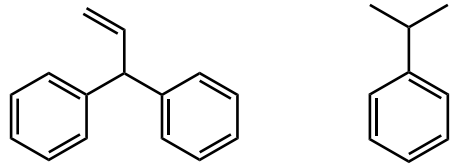

1,1'-(2-propenylidene)bis[benzene] cumene

Figure 180. Trappers attempted in trapping experiments between **1** and O_2

Mixing **1** and PPh_3 did not lead to any change in ^{1}H or ^{31}P NMR spectra (see **Figure 181**). Upon addition of dioxygen at -78 °C, the reaction medium turned blue-green. No NMR was recorded at low temperature, but upon slow warming to room temperature, the ^{31}P NMR spectrum showed the formation of triphenylphosphine oxide in roughly 50% yield. To confirm the influence of the bridged complex in this reaction, a sample of triphenylphosphine was stirred under pure O_2 atmosphere for 18 h. No signal corresponding to $OPPh_3$ could be identified in ^{31}P NMR, confirming that oxidation arose from the reduction of O_2 by **1**.

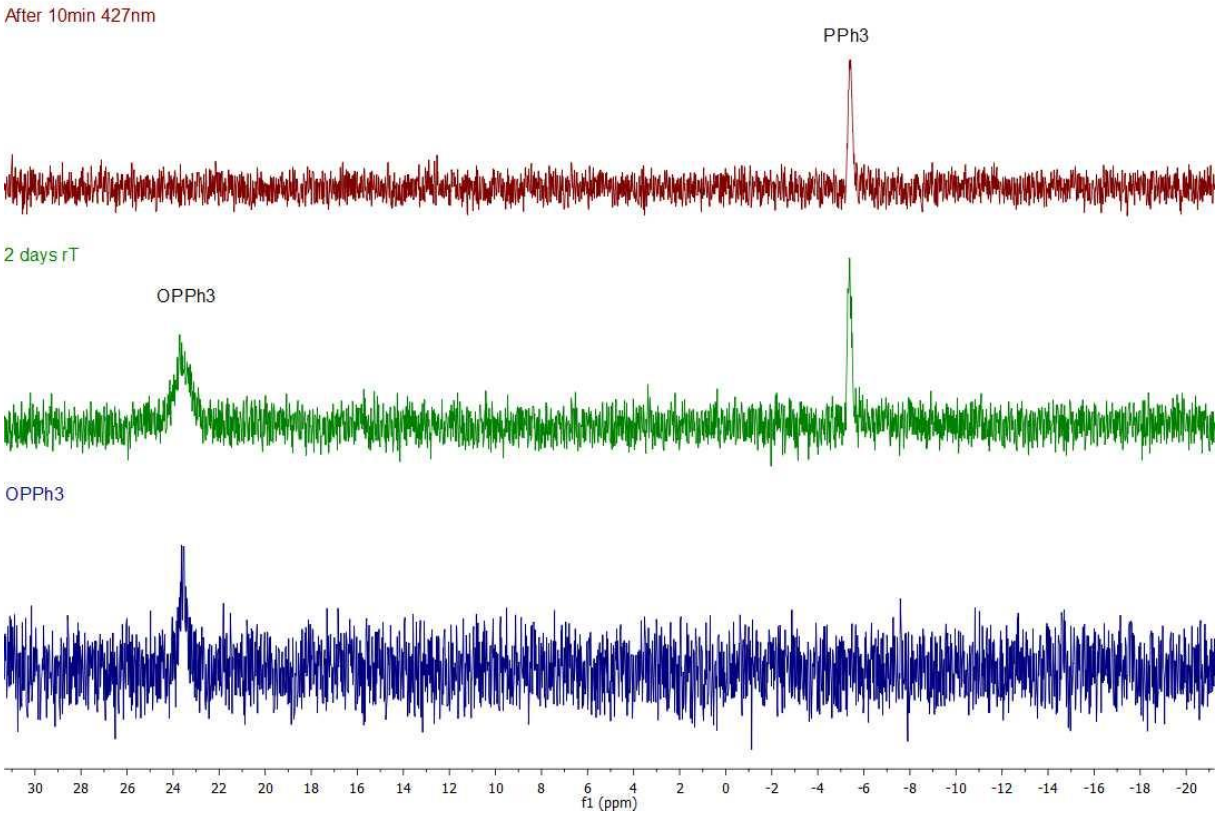

Figure 181. ^{31}P NMR of the reaction medium before (top) and after O_2 addition to a solution of **1** and PPh_3 in THF-d_8, warming up to room temperature, and 2 days of rest. ^{31}P NMR of $OPPh_3$ (bottom) in THF-d_8 is given for reference

Conclusion

In this chapter, the reactivity of $Ce^{III}TREN^{TIPS}$ towards small molecule was demonstrated. Complex **1** was proven useful regarding the photoinduced chemical reduction of inorganic nitrate sources, which was a first step towards the degradation of nitrate to dinitrogen. Further investigations on the reactivity with nitrite ions and nitrous oxide, both part of the nitrogen cycle, showed that **1** could be a suitable candidate for the full reduction of nitrates into dinitrogen, while the reduction of nitric oxide has to be confirmed. Finally, carbon dioxide and dioygen were engaged into original reactions with **1**, which demonstrated the wide range of reactivity of this new cerium(III) complex.

References

(1) Sen, I. S.; Peucker-Ehrenbrink, B. Anthropogenic Disturbance of Element Cycles at the Earth's Surface. *Environ. Sci. Technol.* **2012**, *46* (16), 8601–8609. https://doi.org/10.1021/es301261x.

(2) Kinzig, A. P.; Socolow, R. H. Human Impacts on the Nitrogen Cycle. *Phys. Today* **1994**, *47* (11), 24–31. https://doi.org/10.1063/1.881423.

(3) Canfield, D. E.; Glazer, A. N.; Falkowski, P. G. The Evolution and Future of Earth's Nitrogen Cycle. *Science* **2010**, *330* (6001), 192–196. https://doi.org/10.1126/science.1186120.

(4) Andrews, M.; Raven, J. A.; Lea, P. J. Do Plants Need Nitrate? The Mechanisms by Which Nitrogen Form Affects Plants. *Ann. Appl. Biol.* **2013**, *163* (2), 174–199. https://doi.org/10.1111/aab.12045.

(5) Jackson, J. K.; Patterson, A. J.; MacDonald-Wicks, L. K.; Oldmeadow, C.; McEvoy, M. A. The Role of Inorganic Nitrate and Nitrite in Cardiovascular Disease Risk Factors: A Systematic Review and Meta-Analysis of Human Evidence. *Nutr. Rev.* **2018**, *76* (5), 348–371. https://doi.org/10.1093/nutrit/nuy005.

(6) Picetti, R.; Deeney, M.; Pastorino, S.; Miller, M. R.; Shah, A.; Leon, D. A.; Dangour, A. D.; Green, R. Nitrate and Nitrite Contamination in Drinking Water and Cancer Risk: A Systematic Review with Meta-Analysis. *Environ. Res.* **2022**, *210*, 112988. https://doi.org/10.1016/j.envres.2022.112988.

(7) Hosseini, F.; Majdi, M.; Naghshi, S.; Sheikhhossein, F.; Djafarian, K.; Shab-Bidar, S. Nitrate-Nitrite Exposure through Drinking Water and Diet and Risk of Colorectal Cancer: A Systematic Review and Meta-Analysis of Observational Studies. *Clin. Nutr.* **2021**, *40* (5), 3073–3081. https://doi.org/10.1016/j.clnu.2020.11.010.

(8) Singh, S.; Anil, A. G.; Kumar, V.; Kapoor, D.; Subramanian, S.; Singh, J.; Ramamurthy, P. C. Nitrates in the Environment: A Critical Review of Their Distribution, Sensing Techniques, Ecological Effects and Remediation. *Chemosphere* **2022**, *287*, 131996. https://doi.org/10.1016/j.chemosphere.2021.131996.

(9) Smolders, A. J. P.; Lucassen, E. C. H. E. T.; Bobbink, R.; Roelofs, J. G. M.; Lamers, L. P. M. How Nitrate Leaching from Agricultural Lands Provokes Phosphate Eutrophication in Groundwater Fed Wetlands: The Sulphur Bridge. *Biogeochemistry* **2010**, *98* (1–3), 1–7. https://doi.org/10.1007/s10533-009-9387-8.

(10) Lundberg, J. O.; Weitzberg, E.; Cole, J. A.; Benjamin, N. Nitrate, Bacteria and Human Health. *Nat. Rev. Microbiol.* **2004**, *2* (7), 593–602. https://doi.org/10.1038/nrmicro929.

(11) Sindelar, J. J.; Milkowski, A. L. Human Safety Controversies Surrounding Nitrate and Nitrite in the Diet. *Nitric Oxide* **2012**, *26* (4), 259–266. https://doi.org/10.1016/j.niox.2012.03.011.

(12) Furchgott, R. F.; Ignarro, L. J.; Murad, F. *Nobel Prize in Physiology and Medecine*; Nobelförsamlingen Karolinska Institutet the Nobel assembly at Karolinska Institutet, 1998. https://www.nobelprize.org/prizes/medicine/1998/press-release/.

(13) Änggård, E. Nitric Oxide: Mediator, Murderer, and Medicine. *The Lancet* **1994**, *343* (8907), 1199–1206. https://doi.org/10.1016/S0140-6736(94)92405-8.

(14) Martin, M.; jimenez, M.; Motilva, V. New Issues about Nitric Oxide and Its Effects on the Gastrointestinal Tract. *Curr. Pharm. Des.* **2001**, *7* (10), 881–908. https://doi.org/10.2174/1381612013397645.

(15) Weimann, J. Toxicity of Nitrous Oxide. *Best Pract. Res. Clin. Anaesthesiol.* **2003**, *17* (1), 47–61. https://doi.org/10.1053/bean.2002.0264.

(16) Wuebbles, D. J. Nitrous Oxide: No Laughing Matter. *Science* **2009**, *326* (5949), 56–57. https://doi.org/10.1126/science.1179571.

(17) *Climate Change 2007: Synthesis Report: A Report of the Intergovernmental Panel on Climate Change*; Bernstein, L., IPCC, Eds.; IPCC: Geneva, 2008.

(18) Reay, D. S.; Davidson, E. A.; Smith, K. A.; Smith, P.; Melillo, J. M.; Dentener, F.; Crutzen, P. J. Global Agriculture and Nitrous Oxide Emissions. *Nat. Clim. Change* **2012**, *2* (6), 410–416. https://doi.org/10.1038/nclimate1458.

(19) Davidson, E. A.; Kanter, D. Inventories and Scenarios of Nitrous Oxide Emissions. *Environ. Res. Lett.* **2014**, *9* (10), 105012. https://doi.org/10.1088/1748-9326/9/10/105012.

(20) *Special Report on Emissions Scenarios: A Special Report of Working Group III of the Intergovernmental Panel on Climate Change*, 1. publ.; Nakićenović, N., IPCC, Eds.; Cambridge University Press: Cambridge, 2000.
(21) van Vuuren, D. P.; Stehfest, E.; den Elzen, M. G. J.; Kram, T.; van Vliet, J.; Deetman, S.; Isaac, M.; Klein Goldewijk, K.; Hof, A.; Mendoza Beltran, A.; Oostenrijk, R.; van Ruijven, B. RCP2.6: Exploring the Possibility to Keep Global Mean Temperature Increase below 2°C. *Clim. Change* **2011**, *109* (1), 95. https://doi.org/10.1007/s10584-011-0152-3.
(22) Davidson, E. A. Representative Concentration Pathways and Mitigation Scenarios for Nitrous Oxide. *Environ. Res. Lett.* **2012**, *7* (2), 024005. https://doi.org/10.1088/1748-9326/7/2/024005.
(23) Calvin, K.; Dasgupta, D.; Krinner, G.; Mukherji, A.; Thorne, P. W.; Trisos, C.; Romero, J.; Aldunce, P.; Barrett, K.; Blanco, G.; Cheung, W. W. L.; Connors, S.; Denton, F.; Diongue-Niang, A.; Dodman, D.; Garschagen, M.; Geden, O.; Hayward, B.; Jones, C.; Jotzo, F.; Krug, T.; Lasco, R.; Lee, Y.-Y.; Masson-Delmotte, V.; Meinshausen, M.; Mintenbeck, K.; Mokssit, A.; Otto, F. E. L.; Pathak, M.; Pirani, A.; Poloczanska, E.; Pörtner, H.-O.; Revi, A.; Roberts, D. C.; Roy, J.; Ruane, A. C.; Skea, J.; Shukla, P. R.; Slade, R.; Slangen, A.; Sokona, Y.; Sörensson, A. A.; Tignor, M.; van Vuuren, D.; Wei, Y.-M.; Winkler, H.; Zhai, P.; Zommers, Z.; Hourcade, J.-C.; Johnson, F. X.; Pachauri, S.; Simpson, N. P.; Singh, C.; Thomas, A.; Totin, E.; Arias, P.; Bustamante, M.; Elgizouli, I.; Flato, G.; Howden, M.; Méndez-Vallejo, C.; Pereira, J. J.; Pichs-Madruga, R.; Rose, S. K.; Saheb, Y.; Sánchez Rodríguez, R.; Ürge-Vorsatz, D.; Xiao, C.; Yassaa, N.; Alegría, A.; Armour, K.; Bednar-Friedl, B.; Blok, K.; Cissé, G.; Dentener, F.; Eriksen, S.; Fischer, E.; Garner, G.; Guivarch, C.; Haasnoot, M.; Hansen, G.; Hauser, M.; Hawkins, E.; Hermans, T.; Kopp, R.; Leprince-Ringuet, N.; Lewis, J.; Ley, D.; Ludden, C.; Niamir, L.; Nicholls, Z.; Some, S.; Szopa, S.; Trewin, B.; van der Wijst, K.-I.; Winter, G.; Witting, M.; Birt, A.; Ha, M.; Romero, J.; Kim, J.; Haites, E. F.; Jung, Y.; Stavins, R.; Birt, A.; Ha, M.; Orendain, D. J. A.; Ignon, L.; Park, S.; Park, Y.; Reisinger, A.; Cammaramo, D.; Fischlin, A.; Fuglestvedt, J. S.; Hansen, G.; Ludden, C.; Masson-Delmotte, V.; Matthews, J. B. R.; Mintenbeck, K.; Pirani, A.; Poloczanska, E.; Leprince-Ringuet, N.; Péan, C. *IPCC, 2023: Climate Change 2023: Synthesis Report. Contribution of Working Groups I, II and III to the Sixth Assessment Report of the Intergovernmental Panel on Climate Change [Core Writing Team, H. Lee and J. Romero (Eds.)]. IPCC, Geneva, Switzerland.*, First.; Intergovernmental Panel on Climate Change (IPCC), 2023. https://doi.org/10.59327/IPCC/AR6-9789291691647.
(24) *Industrial Ecology and Global Change*; Socolow, R., Andrews, C., Berkhout, F., Thomas, V., Eds.; Cambridge University Press: Cambridge, 1994. https://doi.org/10.1017/CBO9780511564550.
(25) *Climate Change 2001: The Scientific Basis: Contribution of Working Group I to the Third Assessment Report of the Intergovernmental Panel on Climate Change*; Houghton, J. T., Intergovernmental Panel on Climate Change, Eds.; Cambridge University Press: Cambridge ; New York, 2001.
(26) Heimann, M.; Reichstein, M. Terrestrial Ecosystem Carbon Dynamics and Climate Feedbacks. *Nature* **2008**, *451* (7176), 289–292. https://doi.org/10.1038/nature06591.
(27) *Carbon Dioxide and Terrestrial Ecosystems*; Elsevier, 1996. https://doi.org/10.1016/B978-0-12-505295-5.X5000-9.
(28) Sawyer, J. S. Man-Made Carbon Dioxide and the "Greenhouse" Effect. *Nature* **1972**, *239* (5366), 23–26. https://doi.org/10.1038/239023a0.
(29) *Carbon Dioxide and Environmental Stress*; Elsevier, 1999. https://doi.org/10.1016/B978-0-12-460370-7.X5000-1.
(30) Soon, W.; Baliunas, S. L.; Robinson, A. B.; Robinson, Z. W. Environmental Effects of Increased Atmospheric Carbon Dioxide. *Clim. Res.* **1999**, *13* (2), 149–164. https://doi.org/10.3354/cr013149.
(31) Fourier, J. Remarques Générales Sur Les Températures Du Globe Terrestre et Des Espaces Planétaires. *Annales de Chimie et de Physique* **1824**, 136–167.
(32) Dufresne, J.-L. Jean-Baptiste Joseph Fourier et La Découverte de l'effet de Serre. *La Météorologie* **2006**, 42–46.
(33) Newton Foote, E. Circumstances Affecting the Heat of the Sun's Rays. *The American Journal of Science and Arts* **1857**.
(34) Arrhenius, S. On the Influence of Carbonic Acid in the Air upon the Temperature of the Ground. *Philosophical Magazine and Journal of Science* **1896**, *5* (41), 237–276.

(35) Rogers, H. H.; Runion, G. B.; Prior, S. A.; Torbert, H. A. Response of Plants to Elevated Atmospheric CO2. In *Carbon Dioxide and Environmental Stress*; Elsevier, 1999; pp 215–244. https://doi.org/10.1016/B978-012460370-7/50009-7.
(36) Hungate, B. A. Ecosystem Responses to Rising Atmospheric CO2. In *Carbon Dioxide and Environmental Stress*; Luo, Y., Mooney, H. A., Eds.; Physiological Ecology; Academic Press: San Diego, 1999; pp 265–285. https://doi.org/10.1016/B978-012460370-7/50011-5.
(37) Amthor, J. S. Increasing Atmospheric CO2 Concentration, Water Use, and Water Stress. In *Carbon Dioxide and Environmental Stress*; Luo, Y., Mooney, H. A., Eds.; Physiological Ecology; Academic Press: San Diego, 1999; pp 33–59. https://doi.org/10.1016/B978-012460370-7/50003-6.
(38) Siegenthaler, U.; Sarmiento, J. L. Atmospheric Carbon Dioxide and the Ocean. *Nature* **1993**, *365* (6442), 119–125. https://doi.org/10.1038/365119a0.
(39) Feely, R.; Sabine, C.; Takahashi, T.; Wanninkhof, R. Uptake and Storage of Carbon Dioxide in the Ocean: The Global CO2 Survey. *Oceanography* **2001**, *14* (4), 18–32. https://doi.org/10.5670/oceanog.2001.03.
(40) Talmage, S. C.; Gobler, C. J. Effects of Past, Present, and Future Ocean Carbon Dioxide Concentrations on the Growth and Survival of Larval Shellfish. *Proc. Natl. Acad. Sci.* **2010**, *107* (40), 17246–17251. https://doi.org/10.1073/pnas.0913804107.
(41) Raven, J.; Caldeira, K.; Elderfield, H.; Hoegh-Guldberg, O.; Liss, P.; Riebesell, U.; Shepherd, J.; Turley, C.; Watson, A.; Heap, R.; Banes, R.; Quinn, R. *Ocean Acidification Due to Increasing Atmospheric Carbon Dioxide*; Royal Society, 2005. https://royalsociety.org/-/media/policy/publications/2005/9634.pdf.
(42) Beniash, E.; Ivanina, A.; Lieb, N. S.; Kurochkin, I.; Sokolova, I. M. Elevated Level of Carbon Dioxide Affects Metabolism and Shell Formation in Oysters Crassostrea Virginica. *Mar. Ecol. Prog. Ser.* **2010**, *419*, 95–108. https://doi.org/10.3354/meps08841.
(43) Lindsey, R. Climate Change: Atmospheric Carbon Dioxide. April 9, 2024. https://www.climate.gov/news-features/understanding-climate/climate-change-atmospheric-carbon-dioxide.
(44) Betts, J. G.; DeSaix, P.; Johnson, E.; Johnson, J. E.; Korol, O.; Kruse, D. H.; Poe, B.; Wise, J. A.; Womble, M.; Young, K. A. *Anatomy and Physiology*; Open textbook library; OpenStax College, Rice University: Houston, Texas, 2017.
(45) Guais, A.; Brand, G.; Jacquot, L.; Karrer, M.; Dukan, S.; Grévillot, G.; Molina, T. J.; Bonte, J.; Regnier, M.; Schwartz, L. Toxicity of Carbon Dioxide: A Review. *Chem. Res. Toxicol.* **2011**, *24* (12), 2061–2070. https://doi.org/10.1021/tx200220r.
(46) Langford, N. J. Carbon Dioxide Poisoning: *Toxicol. Rev.* **2005**, *24* (4), 229–235. https://doi.org/10.2165/00139709-200524040-00003.
(47) Feller, U.; Vaseva, I. I. Extreme Climatic Events: Impacts of Drought and High Temperature on Physiological Processes in Agronomically Important Plants. *Front. Environ. Sci.* **2014**, *2*. https://doi.org/10.3389/fenvs.2014.00039.
(48) Chaudhuri, S.; Ale, S.; DeLaune, P.; Rajan, N. Spatio-Temporal Variability of Groundwater Nitrate Concentration in Texas: 1960 to 2010. *J. Environ. Qual.* **2012**, *41* (6), 1806–1817. https://doi.org/10.2134/jeq2012.0022.
(49) Samatya, S.; Kabay, N.; Yüksel, Ü.; Arda, M.; Yüksel, M. Removal of Nitrate from Aqueous Solution by Nitrate Selective Ion Exchange Resins. *React. Funct. Polym.* **2006**, *66* (11), 1206–1214. https://doi.org/10.1016/j.reactfunctpolym.2006.03.009.
(50) Alikhani, M.; Moghbeli, M. R. Ion-Exchange polyHIPE Type Membrane for Removing Nitrate Ions: Preparation, Characterization, Kinetics and Adsorption Studies. *Chem. Eng. J.* **2014**, *239*, 93–104. https://doi.org/10.1016/j.cej.2013.11.013.
(51) Epsztein, R.; Nir, O.; Lahav, O.; Green, M. Selective Nitrate Removal from Groundwater Using a Hybrid Nanofiltration–Reverse Osmosis Filtration Scheme. *Chem. Eng. J.* **2015**, *279*, 372–378. https://doi.org/10.1016/j.cej.2015.05.010.
(52) Banasiak, L. J.; Schäfer, A. I. Removal of Boron, Fluoride and Nitrate by Electrodialysis in the Presence of Organic Matter. *J. Membr. Sci.* **2009**, *334* (1–2), 101–109. https://doi.org/10.1016/j.memsci.2009.02.020.

(53) Huno, S. K. M.; Rene, E. R.; Van Hullebusch, E. D.; Annachhatre, A. P. Nitrate Removal from Groundwater: A Review of Natural and Engineered Processes. *J. Water Supply Res. Technol.-Aqua* **2018**, *67* (8), 885–902. https://doi.org/10.2166/aqua.2018.194.

(54) Zhang, X.; Wang, Y.; Liu, C.; Yu, Y.; Lu, S.; Zhang, B. Recent Advances in Non-Noble Metal Electrocatalysts for Nitrate Reduction. *Chem. Eng. J.* **2021**, *403*, 126269. https://doi.org/10.1016/j.cej.2020.126269.

(55) Ghafari, S.; Hasan, M.; Aroua, M. K. Bio-Electrochemical Removal of Nitrate from Water and Wastewater—A Review. *Bioresour. Technol.* **2008**, *99* (10), 3965–3974. https://doi.org/10.1016/j.biortech.2007.05.026.

(56) Gao, J.; Jiang, B.; Ni, C.; Qi, Y.; Zhang, Y.; Oturan, N.; Oturan, M. A. Non-Precious Co3O4-TiO2/Ti Cathode Based Electrocatalytic Nitrate Reduction: Preparation, Performance and Mechanism. *Appl. Catal. B Environ.* **2019**, *254*, 391–402. https://doi.org/10.1016/j.apcatb.2019.05.016.

(57) Yao, F.; Yang, Q.; Zhong, Y.; Shu, X.; Chen, F.; Sun, J.; Ma, Y.; Fu, Z.; Wang, D.; Li, X. Indirect Electrochemical Reduction of Nitrate in Water Using Zero-Valent Titanium Anode: Factors, Kinetics, and Mechanism. *Water Res.* **2019**, *157*, 191–200. https://doi.org/10.1016/j.watres.2019.03.078.

(58) Zhu, I.; Getting, T. A Review of Nitrate Reduction Using Inorganic Materials. *Environ. Technol. Rev.* **2012**, *1* (1), 46–58. https://doi.org/10.1080/09593330.2012.706646.

(59) Lu, X.; Song, H.; Cai, J.; Lu, S. Recent Development of Electrochemical Nitrate Reduction to Ammonia: A Mini Review. *Electrochem. Commun.* **2021**, *129*, 107094. https://doi.org/10.1016/j.elecom.2021.107094.

(60) Taguchi, S.; Feliu, J. M. Electrochemical Reduction of Nitrate on Pt(S)[n(1 1 1) × (1 1 1)] Electrodes in Perchloric Acid Solution. *Electrochimica Acta* **2007**, *52* (19), 6023–6033. https://doi.org/10.1016/j.electacta.2007.03.057.

(61) Duca, M.; Cucarella, M. O.; Rodriguez, P.; Koper, M. T. M. Direct Reduction of Nitrite to N_2 on a Pt(100) Electrode in Alkaline Media. *J. Am. Chem. Soc.* **2010**, *132* (51), 18042–18044. https://doi.org/10.1021/ja1092503.

(62) Yang, J.; Sebastian, P.; Duca, M.; Hoogenboom, T.; Koper, M. T. M. pH Dependence of the Electroreduction of Nitrate on Rh and Pt Polycrystalline Electrodes. *Chem Commun* **2014**, *50* (17), 2148–2151. https://doi.org/10.1039/C3CC49224A.

(63) Liu, Y.; Wang, J. Reduction of Nitrate by Zero Valent Iron (ZVI)-Based Materials: A Review. *Sci. Total Environ.* **2019**, *671*, 388–403. https://doi.org/10.1016/j.scitotenv.2019.03.317.

(64) Moore, J. M.; Miller, T. J.; Mu, M.; Peñas-Defrutos, M. N.; Gullett, K. L.; Elford, L. S.; Quintero, S.; García-Melchor, M.; Fout, A. R. Selective Stepwise Reduction of Nitrate and Nitrite to Dinitrogen or Ammonia. *J. Am. Chem. Soc.* **2025**, *147* (10), 8444–8454. https://doi.org/10.1021/jacs.4c16585.

(65) Sun, L.; Dai, C.; Wang, T.; Jin, X.; Xu, Z. J.; Wang, X. Modulating the Electronic Structure of Cobalt in Molecular Catalysts via Coordination Environment Regulation for Highly Efficient Heterogeneous Nitrate Reduction. *Angew. Chem. Int. Ed.* **2024**, *63* (15), e202320027. https://doi.org/10.1002/anie.202320027.

(66) Schachner, J. A.; Wiedemaier, F.; Zwettler, N.; Peschel, L. M.; Boese, A. D.; Belaj, F.; Mösch-Zanetti, N. C. Catalytic Reduction of Nitrate by an Oxidorhenium (V) Complex. *J. Catal.* **2021**, *397*, 108–115. https://doi.org/10.1016/j.jcat.2021.03.028.

(67) Xu, S.; Ashley, D. C.; Kwon, H.-Y.; Ware, G. R.; Chen, C.-H.; Losovyj, Y.; Gao, X.; Jakubikova, E.; Smith, J. M. A Flexible, Redox-Active Macrocycle Enables the Electrocatalytic Reduction of Nitrate to Ammonia by a Cobalt Complex. *Chem. Sci.* **2018**, *9* (22), 4950–4958. https://doi.org/10.1039/C8SC00721G.

(68) Ottley, C. J.; Davison, W.; Edmunds, W. M. Chemical Catalysis of Nitrate Reduction by Iron (II). *Geochim. Cosmochim. Acta* **1997**, *61* (9), 1819–1828. https://doi.org/10.1016/S0016-7037(97)00058-6.

(69) Kunkely, H.; Vogler, A. Photochemistry of Nitratobis(Triphenylphosphine)Copper(I). *J. Am. Chem. Soc.* **1995**, *117* (1), 540–541. https://doi.org/10.1021/ja00106a066.

(70) Taylor, R. D.; Todd, P. G.; Chasteen, N. D.; Spence, J. T. Reduction of Nitrate by Monomeric Molybdenum(V) Complexes in Dimethylformamide. *Inorg. Chem.* **1979**, *18* (1), 44–48. https://doi.org/10.1021/ic50191a008.

(71) Suslick, K. S.; Watson, R. A. Photochemical Reduction of Nitrate and Nitrite by Manganese and Iron Porphyrins. *Inorg. Chem.* **1991**, *30* (5), 912–919. https://doi.org/10.1021/ic00005a009.
(72) Spence, J. T.; Taylor, R. D. The Reduction of Nitrate by Molybdenum(V) Complexes in Dimethylformamide. *J. Common Met.* **1977**, *54* (2), 449–457. https://doi.org/10.1016/0022-5088(77)90067-4.
(73) Guymon, E. P.; Spence, J. T. The Reduction of Nitrate by Molybdenum(V)[1]. *J. Phys. Chem.* **1966**, *70* (6), 1964–1969. https://doi.org/10.1021/j100878a044.
(74) Gwak, J.; Ahn, S.; Baik, M.-H.; Lee, Y. One Metal Is Enough: A Nickel Complex Reduces Nitrate Anions to Nitrogen Gas. *Chem. Sci.* **2019**, *10* (18), 4767–4774. https://doi.org/10.1039/C9SC00717B.
(75) Kepp, K. P. A Quantitative Scale of Oxophilicity and Thiophilicity. *Inorg. Chem.* **2016**, *55* (18), 9461–9470. https://doi.org/10.1021/acs.inorgchem.6b01702.
(76) Damon, P. L.; Wu, G.; Kaltsoyannis, N.; Hayton, T. W. Formation of a Ce(IV) Oxo Complex via Inner Sphere Nitrate Reduction. *J. Am. Chem. Soc.* **2016**, *138* (39), 12743–12746. https://doi.org/10.1021/jacs.6b07932.
(77) Assefa, M. K.; Wu, G.; Hayton, T. W. Synthesis of a Terminal Ce(IV) Oxo Complex by Photolysis of a Ce(III) Nitrate Complex. *Chem Sci* **2017**, *8* (11), 7873–7878. https://doi.org/10.1039/C7SC03715E.
(78) Marks, W. R.; Baumgardner, D. F.; Reinheimer, E. W.; Gilbertson, J. D. Complete Denitrification of Nitrate and Nitrite to N2 Gas by Samarium(II) Iodide. *Chem. Commun.* **2020**, *56* (77), 11441–11444. https://doi.org/10.1039/D0CC04115G.
(79) Thomson, R. K.; Monreal, M. J.; Masuda, J. D.; Scott, B. L.; Kiplinger, J. L. Lutetium Gets a Crown: Synthesis, Structure and Reaction Chemistry of the Separated Ion Pair Complex, [Li(12-Crown-4)2][(C5Me5)2LuMe2]. *J. Organomet. Chem.* **2011**, *696* (25), 3966–3973. https://doi.org/10.1016/j.jorganchem.2011.06.017.
(80) Xu, L.; Wang, Y.; Wang, Y.-C.; Wang, Z.; Zhang, W.-X.; Xi, Z. Sandwich Lutetacyclopentadiene with the Coordination of Lithium to the Diene Unit: Synthesis, Structure, and Transformation. *Organometallics* **2016**, *35* (1), 5–8. https://doi.org/10.1021/acs.organomet.5b00957.
(81) Xu, L.; Wang, Y.-C.; Wei, J.; Wang, Y.; Wang, Z.; Zhang, W.-X.; Xi, Z. The First Lutetacyclopentadienes: Synthesis, Structure, and Diversified Insertion/C□H Activation Reactivity. *Chem. – Eur. J.* **2015**, *21* (18), 6686–6689. https://doi.org/10.1002/chem.201500387.
(82) Pattenaude, S. A.; Coughlin, E. J.; Collins, T. S.; Zeller, M.; Bart, S. C. Expanding the Library of Uranyl Amide Derivatives: New Complexes Featuring the Tert-Butyldimethylsilylamide Ligand. *Inorg. Chem.* **2018**, *57* (8), 4543–4549. https://doi.org/10.1021/acs.inorgchem.8b00298.
(83) Bjorklund, J. L.; Pyrch, M. M.; Basile, M. C.; Mason, S. E.; Forbes, T. Z. Actinyl-Cation Interactions: Experimental and Theoretical Assessment of [Np(VI)O2Cl4]2− and [U(VI)O2Cl4]2− Systems. *Dalton Trans.* **2019**, *48* (24), 8861–8871. https://doi.org/10.1039/C9DT01753D.
(84) Smiles, D. E.; Wu, G.; Hayton, T. W. Synthesis of Uranium–Ligand Multiple Bonds by Cleavage of a Trityl Protecting Group. *J. Am. Chem. Soc.* **2014**, *136* (1), 96–99. https://doi.org/10.1021/ja411423a.
(85) Pedrick, E. A.; Seaman, L. A.; Scott, J. C.; Griego, L.; Wu, G.; Hayton, T. W. Synthesis and Reactivity of a U(IV) Dibenzyne Complex. *Organometallics* **2016**, *35* (4), 494–502. https://doi.org/10.1021/acs.organomet.5b00929.
(86) Danis, J. A.; Lin, M. R.; Scott, B. L.; Eichhorn, B. W.; Runde, W. H. Coordination Trends in Alkali Metal Crown Ether Uranyl Halide Complexes: The Series [A(Crown)]2[UO2X4] Where A = Li, Na, K and X = Cl, Br. *Inorg. Chem.* **2001**, *40* (14), 3389–3394. https://doi.org/10.1021/ic0011056.
(87) Cobb, P. J.; Moulding, D. J.; Ortu, F.; Randall, S.; Wooles, A. J.; Natrajan, L. S.; Liddle, S. T. Uranyl-Tri-Bis(Silyl)Amide Alkali Metal Contact and Separated Ion Pair Complexes. *Inorg. Chem.* **2018**, *57* (11), 6571–6583. https://doi.org/10.1021/acs.inorgchem.8b00715.
(88) Solola, L. A.; Zabula, A. V.; Dorfner, W. L.; Manor, B. C.; Carroll, P. J.; Schelter, E. J. Cerium(IV) Imido Complexes: Structural, Computational, and Reactivity Studies. *J. Am. Chem. Soc.* **2017**, *139* (6), 2435–2442. https://doi.org/10.1021/jacs.6b12369.
(89) So, Y.-M.; Wang, G.-C.; Li, Y.; Sung, H. H.-Y.; Williams, I. D.; Lin, Z.; Leung, W.-H. A Tetravalent Cerium Complex Containing a Ce=O Bond. *Angew. Chem. Int. Ed.* **2014**, *53* (6), 1626–1629. https://doi.org/10.1002/anie.201309764.

(90) Smiles, D. E.; Wu, G.; Kaltsoyannis, N.; Hayton, T. W. Thorium–Ligand Multiple Bonds via Reductive Deprotection of a Trityl Group. *Chem. Sci.* **2015**, *6* (7), 3891–3899. https://doi.org/10.1039/C5SC01248A.
(91) Kiernicki, J. J.; Zeller, M.; Bart, S. C. Facile Reductive Silylation of UO22+ to Uranium(IV) Chloride. *Angew. Chem. Int. Ed.* **2017**, *56* (4), 1097–1100. https://doi.org/10.1002/anie.201609838.
(92) Arnold, P. L.; Pécharman, A.-F.; Love, J. B. Oxo Group Protonation and Silylation of Pentavalent Uranyl Pacman Complexes. *Angew. Chem. Int. Ed.* **2011**, *50* (40), 9456–9458. https://doi.org/10.1002/anie.201104359.
(93) Brown, J. L.; Wu, G.; Hayton, T. W. Oxo Ligand Silylation in a Uranyl β-Ketoiminate Complex. *J. Am. Chem. Soc.* **2010**, *132* (21), 7248–7249. https://doi.org/10.1021/ja1013739.
(94) Assefa, M. K.; Wu, G.; Hayton, T. W. Uranyl Oxo Silylation Promoted by Silsesquioxane Coordination. *J. Am. Chem. Soc.* **2020**, *142* (19), 8738–8747. https://doi.org/10.1021/jacs.0c00990.
(95) Arnold, P. L.; Pécharman, A.-F.; Lord, R. M.; Jones, G. M.; Hollis, E.; Nichol, G. S.; Maron, L.; Fang, J.; Davin, T.; Love, J. B. Control of Oxo-Group Functionalization and Reduction of the Uranyl Ion. *Inorg. Chem.* **2015**, *54* (7), 3702–3710. https://doi.org/10.1021/acs.inorgchem.5b00420.
(96) Schnaars, D. D.; Wu, G.; Hayton, T. W. Borane-Mediated Silylation of a Metal–Oxo Ligand. *Inorg. Chem.* **2011**, *50* (11), 4695–4697. https://doi.org/10.1021/ic2008649.
(97) Brown, J. L.; Mokhtarzadeh, C. C.; Lever, J. M.; Wu, G.; Hayton, T. W. Facile Reduction of a Uranyl(VI) β-Ketoiminate Complex to U(IV) Upon Oxo Silylation. *Inorg. Chem.* **2011**, *50* (11), 5105–5112. https://doi.org/10.1021/ic200387n.
(98) Woollard-Shore, J. G.; Holland, J. P.; Jones, M. W.; Dilworth, J. R. Nitrite Reduction by Copper Complexes. *Dalton Trans.* **2010**, *39* (6), 1576–1585. https://doi.org/10.1039/B913463H.
(99) Merkle, A. C.; Lehnert, N. Binding and Activation of Nitrite and Nitric Oxide by Copper Nitrite Reductase and Corresponding Model Complexes. *Dalton Trans.* **2012**, *41* (12), 3355–3368. https://doi.org/10.1039/C1DT11049G.
(100) Arikawa, Y.; Otsubo, Y.; Fujino, H.; Horiuchi, S.; Sakuda, E.; Umakoshi, K. Nitrite Reduction Cycle on a Dinuclear Ruthenium Complex Producing Ammonia. *J. Am. Chem. Soc.* **2018**, *140* (2), 842–847. https://doi.org/10.1021/jacs.7b12020.
(101) Uyeda, C.; Peters, J. C. Selective Nitrite Reduction at Heterobimetallic CoMg Complexes. *J. Am. Chem. Soc.* **2013**, *135* (32), 12023–12031. https://doi.org/10.1021/ja4053653.
(102) Barley, M. H.; Meyer, T. J. Electrocatalytic Reduction of Nitrite to Ammonia Based on a Water-Soluble Iron Porphyrin. *J. Am. Chem. Soc.* **1986**, *108* (19), 5876–5885. https://doi.org/10.1021/ja00279a036.
(103) Rhodes, M. R.; Meyer, T. J. Electrocatalytic Reduction of Nitrite Using Simple Coordination Complexes of Iron and Ruthenium. *Inorg. Chem.* **1988**, *27* (26), 4772–4774. https://doi.org/10.1021/ic00299a019.
(104) Rhodes, M. R.; Barley, M. H.; Meyer, T. J. Electrocatalytic Reduction of Nitrite Ion by Edta Complexes of Iron(II) and Ruthenium(II). *Inorg. Chem.* **1991**, *30* (4), 629–635. https://doi.org/10.1021/ic00004a008.
(105) Zhang, X.; Wang, Y.; Wang, Y.; Guo, Y.; Xie, X.; Yu, Y.; Zhang, B. Recent Advances in Electrocatalytic Nitrite Reduction. *Chem. Commun.* **2022**, *58* (17), 2777–2787. https://doi.org/10.1039/D1CC06690K.
(106) Pouessel, J.; Thuéry, P.; Berthet, J.-C.; Cantat, T. Nitrite Complexes of the Rare Earth Elements. *Dalton Trans.* **2014**, *43* (11), 4415–4425. https://doi.org/10.1039/C3DT52703D.
(107) Pauleta, S. R.; Carepo, M. S. P.; Moura, I. Source and Reduction of Nitrous Oxide. *Coord. Chem. Rev.* **2019**, *387*, 436–449. https://doi.org/10.1016/j.ccr.2019.02.005.
(108) Pauleta, S. R.; Dell'Acqua, S.; Moura, I. Nitrous Oxide Reductase. *Coord. Chem. Rev.* **2013**, *257* (2), 332–349. https://doi.org/10.1016/j.ccr.2012.05.026.
(109) Kjellberg, M.; Ohleier, A.; Thuéry, P.; Nicolas, E.; Anthore-Dalion, L.; Cantat, T. Photocatalytic Deoxygenation of N–O Bonds with Rhenium Complexes: From the Reduction of Nitrous Oxide to Pyridine N-Oxides. *Chem. Sci.* **2021**, *12* (30), 10266–10272. https://doi.org/10.1039/D1SC01974K.
(110) Tran, B.; Smith, J. Nitrogen Oxyanion Deoxygenation: Redox Chemistry and Oxygen Atom Transfer Reactions. *Coord. Chem. Rev.* **2025**, *530*, 216490. https://doi.org/10.1016/j.ccr.2025.216490.

(111) Ming, T.; de_Richter, R.; Shen, S.; Caillol, S. Fighting Global Warming by Greenhouse Gas Removal: Destroying Atmospheric Nitrous Oxide Thanks to Synergies between Two Breakthrough Technologies. *Environ. Sci. Pollut. Res.* **2016**, *23* (7), 6119–6138. https://doi.org/10.1007/s11356-016-6103-9.
(112) S. Banks, R. G.; J. Henderson, R.; M. Pratt, J. Reactions of Gases in Solution. Part III. Some Reactions of Nitrous Oxide with Transition-Metal Complexes. *J. Chem. Soc. Inorg. Phys. Theor.* **1968**, *0* (0), 2886–2889. https://doi.org/10.1039/J19680002886.
(113) Nichols, M. L.; Derbigny, I. A. The Reduction of Nitrous Oxide. *J. Phys. Chem.* **1926**, *30* (4), 491–506. https://doi.org/10.1021/j150262a006.
(114) Gianetti, T. L.; Annen, S. P.; Santiso-Quinones, G.; Reiher, M.; Driess, M.; Grützmacher, H. Nitrous Oxide as a Hydrogen Acceptor for the Dehydrogenative Coupling of Alcohols. *Angew. Chem. Int. Ed.* **2016**, *55* (5), 1854–1858. https://doi.org/10.1002/anie.201509288.
(115) Ortega-Lepe, I.; Sánchez, P.; Santos, L. L.; Lara, P.; Rendón, N.; López-Serrano, J.; Salazar-Pereda, V.; Álvarez, E.; Paneque, M.; Suárez, A. Catalytic Nitrous Oxide Reduction with H2 Mediated by Pincer Ir Complexes. *Inorg. Chem.* **2022**, *61* (46), 18590–18600. https://doi.org/10.1021/acs.inorgchem.2c02963.
(116) Doyle, L. E.; Piers, W. E.; Borau-Garcia, J. Ligand Cooperation in the Formal Hydrogenation of N2O Using a PCsp2P Iridium Pincer Complex. *J. Am. Chem. Soc.* **2015**, *137* (6), 2187–2190. https://doi.org/10.1021/ja512602m.
(117) Esmieu, C.; Orio, M.; Torelli, S.; Pape, L. L.; Pécaut, J.; Lebrun, C.; Ménage, S. N2O Reduction at a Dissymmetric {Cu2S}-Containing Mixed-Valent Center. *Chem. Sci.* **2014**, *5* (12), 4774–4784. https://doi.org/10.1039/C4SC01487A.
(118) Timmons, A. J.; Symes, M. D. Converting between the Oxides of Nitrogen Using Metal–Ligand Coordination Complexes. *Chem. Soc. Rev.* **2015**, *44* (19), 6708–6722. https://doi.org/10.1039/C5CS00269A.
(119) Lee, J.-H.; Pink, M.; Tomaszewski, J.; Fan, H.; Caulton, K. G. Facile Hydrogenation of N2O by an Operationally Unsaturated Osmium Polyhydride. *J. Am. Chem. Soc.* **2007**, *129* (28), 8706–8707. https://doi.org/10.1021/ja071452f.
(120) Kaplan, A. W.; Bergman, R. G. Nitrous Oxide Mediated Oxygen Atom Insertion into a Ruthenium−Hydride Bond. Synthesis and Reactivity of the Monomeric Hydroxoruthenium Complex (DMPE)2Ru(H)(OH). *Organometallics* **1997**, *16* (6), 1106–1108. https://doi.org/10.1021/om960991i.
(121) Kaplan, A. W.; Bergman, R. G. Nitrous Oxide Mediated Synthesis of Monomeric Hydroxoruthenium Complexes. Reactivity of (DMPE)2Ru(H)(OH) and the Synthesis of a Silica-Bound Ruthenium Complex. *Organometallics* **1998**, *17* (23), 5072–5085. https://doi.org/10.1021/om980295d.
(122) Pamplin, C. B.; Ma, E. S. F.; Safari, N.; Rettig, S. J.; James, B. R. The Nitrous Oxide Complex, RuCl2(H1-N2O)(P−N)(PPh3) (P−N = [o-(N,N-Dimethylamino)Phenyl]Diphenylphosphine); Low Temperature Conversion of N2O to N2 and O2. *J. Am. Chem. Soc.* **2001**, *123* (35), 8596–8597. https://doi.org/10.1021/ja0106319.
(123) Anthore-Dalion, L.; Nicolas, E.; Cantat, T. Catalytic Metal-Free Deoxygenation of Nitrous Oxide with Disilanes. *ACS Catal.* **2019**, *9* (12), 11563–11567. https://doi.org/10.1021/acscatal.9b04434.
(124) Berthet, J.-C.; Le Maréchal, J.-F.; Nierlich, M.; Lance, M.; Vigner, J.; Ephritikhine, M. Synthesis and Crystal Structure of the Oxo-Bridged Bimetallic Organouranium Complex [(Me3SiC5H4)3U]2[μ-O]. *J. Organomet. Chem.* **1991**, *408* (3), 335–341. https://doi.org/10.1016/0022-328X(91)83205-I.
(125) Avens, L. R.; Barnhart, D. M.; Burns, C. J.; McKee, S. D.; Smith, W. H. Oxidation Chemistry of a Uranium(III) Aryloxide. *Inorg. Chem.* **1994**, *33* (19), 4245–4254. https://doi.org/10.1021/ic00097a010.
(126) Lam, O. P.; Bart, S. C.; Kameo, H.; Heinemann, F. W.; Meyer, K. Insights into the Mechanism of Carbonate Formation through Reductive Cleavage of Carbon Dioxide with Low-Valent Uranium Centers. *Chem. Commun.* **2010**, *46* (18), 3137–3139. https://doi.org/10.1039/B927142B.
(127) Berg, D. J.; Burns, C. J.; Andersen, R. A.; Zalkin, A. Electron-Transfer Reactions of Divalent Ytterbium Metallocenes. Synthesis of the Series [(Me5C5)2Yb]2[.Mu.-E] (E = Oxygen, Sulfur, Selenium, or

Tellurium) and Crystal Structure of [(Me5C5)2Yb]2[.Mu.-Se]. *Organometallics* **1989**, *8* (8), 1865–1870. https://doi.org/10.1021/om00110a006.
(128) Arney, D. S. J.; Burns, C. J. Synthesis and Properties of High-Valent Organouranium Complexes Containing Terminal Organoimido and Oxo Functional Groups. A New Class of Organo-f-Element Complexes. *J. Am. Chem. Soc.* **1995**, *117* (37), 9448–9460. https://doi.org/10.1021/ja00142a011.
(129) Franke, S. M.; Tran, B. L.; Heinemann, F. W.; Hieringer, W.; Mindiola, D. J.; Meyer, K. Uranium(III) Complexes with Bulky Aryloxide Ligands Featuring Metal–Arene Interactions and Their Reactivity Toward Nitrous Oxide. *Inorg. Chem.* **2013**, *52* (18), 10552–10558. https://doi.org/10.1021/ic401532j.
(130) Severin, K. Synthetic Chemistry with Nitrous Oxide. *Chem. Soc. Rev.* **2015**, *44* (17), 6375–6386. https://doi.org/10.1039/C5CS00339C.
(131) Lewis, A. J.; Carroll, P. J.; Schelter, E. J. Reductive Cleavage of Nitrite to Form Terminal Uranium Mono-Oxo Complexes. *J. Am. Chem. Soc.* **2013**, *135* (1), 511–518. https://doi.org/10.1021/ja311057y.
(132) Todorović, U.; Martin Romero, R.; Anthore-Dalion, L. Activation of N−O σ Bonds with Transition Metals: A Versatile Platform for Organic Synthesis and C−N Bonds Formation. *Eur. J. Org. Chem.* **2023**, *26* (31), e202300391. https://doi.org/10.1002/ejoc.202300391.
(133) Benson, S. M.; Orr, F. M. Carbon Dioxide Capture and Storage. *MRS Bull.* **2008**, *33* (4), 303–305. https://doi.org/10.1557/mrs2008.63.
(134) Rahmah, W.; Kadja, G. T. M.; Mahyuddin, M. H.; Saputro, A. G.; Dipojono, H. K.; Wenten, I. G. Small-Pore Zeolite and Zeotype Membranes for CO2 Capture and Sequestration – A Review. *J. Environ. Chem. Eng.* **2022**, *10* (6), 108707. https://doi.org/10.1016/j.jece.2022.108707.
(135) Gao, X.; Wang, Z.; Chen, T.; Hu, L.; Yang, S.; Kawi, S. State-of-Art Designs and Synthesis of Zeolite Membranes for CO2 Capture. *Carbon Capture Sci. Technol.* **2022**, *5*, 100073. https://doi.org/10.1016/j.ccst.2022.100073.
(136) Usman, M.; Ghanem, A. S.; Niaz Ali Shah, S.; Garba, M. D.; Yusuf Khan, M.; Khan, S.; Humayun, M.; Laeeq Khan, A. A Review on SAPO-34 Zeolite Materials for CO2 Capture and Conversion. *Chem. Rec.* **2022**, *22* (7), e202200039. https://doi.org/10.1002/tcr.202200039.
(137) Zhao, M.; Yang, Y.; Gu, X.-S. MOF Based CO2 Capture: Adsorption and Membrane Separation. *Inorg. Chem. Commun.* **2023**, *152*, 110722. https://doi.org/10.1016/j.inoche.2023.110722.
(138) Avci, G.; Velioglu, S.; Keskin, S. High-Throughput Screening of MOF Adsorbents and Membranes for H2 Purification and CO2 Capture. *ACS Appl. Mater. Interfaces* **2018**, *10* (39), 33693–33706. https://doi.org/10.1021/acsami.8b12746.
(139) Abdalazeez, A.; Li, T.; Wang, W.; Abuelgasim, S. A Brief Review of CO2 Utilization for Alkali Carbonate Gasification and Biomass/Coal Co-Gasification: Reactivity, Products and Process. *J. CO2 Util.* **2021**, *43*, 101370. https://doi.org/10.1016/j.jcou.2020.101370.
(140) Ünveren, E. E.; Monkul, B. Ö.; Sarıoğlan, Ş.; Karademir, N.; Alper, E. Solid Amine Sorbents for CO2 Capture by Chemical Adsorption: A Review. *Petroleum* **2017**, *3* (1), 37–50. https://doi.org/10.1016/j.petlm.2016.11.001.
(141) Yamada, H. Amine-Based Capture of CO2 for Utilization and Storage. *Polym. J.* **2021**, *53* (1), 93–102. https://doi.org/10.1038/s41428-020-00400-y.
(142) Chen, M.; Li, M.; Zhang, F.; Hu, X.; Wu, Y. Fast and Efficient CO2 Absorption in Non-Aqueous Tertiary Amines Promoted by Ethylene Glycol. *Energy Fuels* **2022**, *36* (9), 4830–4836. https://doi.org/10.1021/acs.energyfuels.2c00215.
(143) Darunte, L. A.; Walton, K. S.; Sholl, D. S.; Jones, C. W. CO2 Capture via Adsorption in Amine-Functionalized Sorbents. *Curr. Opin. Chem. Eng.* **2016**, *12*, 82–90. https://doi.org/10.1016/j.coche.2016.03.002.
(144) Chowdhury, F. A.; Okabe, H.; Shimizu, S.; Onoda, M.; Fujioka, Y. Development of Novel Tertiary Amine Absorbents for CO2 Capture. *Energy Procedia* **2009**, *1* (1), 1241–1248. https://doi.org/10.1016/j.egypro.2009.01.163.
(145) Darunte, L. A.; Oetomo, A. D.; Walton, K. S.; Sholl, D. S.; Jones, C. W. Direct Air Capture of CO2 Using Amine Functionalized MIL-101(Cr). *ACS Sustain. Chem. Eng.* **2016**, *4* (10), 5761–5768. https://doi.org/10.1021/acssuschemeng.6b01692.

(146) Olivares-Marín, M.; Maroto-Valer, M. M. Development of Adsorbents for CO2 Capture from Waste Materials: A Review. *Greenh. Gases Sci. Technol.* **2012**, *2* (1), 20–35. https://doi.org/10.1002/ghg.45.
(147) Jitaru, M. Electrochemical Carbon Dioxide Reduction - Fundamental and Applied Topics (Review). *Journal of the University of Chemical Technology and Metallurgy 42* (4), 333–344.
(148) Perry, S. C.; Leung, P.; Wang, L.; Ponce de León, C. Developments on Carbon Dioxide Reduction: Their Promise, Achievements, and Challenges. *Curr. Opin. Electrochem.* **2020**, *20*, 88–98. https://doi.org/10.1016/j.coelec.2020.04.014.
(149) Le, M.; Ren, M.; Zhang, Z.; Sprunger, P. T.; Kurtz, R. L.; Flake, J. C. Electrochemical Reduction of CO2 to CH3OH at Copper Oxide Surfaces. *J. Electrochem. Soc.* **2011**, *158* (5), E45. https://doi.org/10.1149/1.3561636.
(150) Saha, P.; Amanullah, S.; Barman, S.; Dey, A. Electrochemical Reduction of CO2 to CH3OH Catalyzed by an Iron Porphyrinoid. *J. Am. Chem. Soc.* **2025**, *147* (2), 1497–1507. https://doi.org/10.1021/jacs.4c08922.
(151) Ohya, S.; Kaneco, S.; Katsumata, H.; Suzuki, T.; Ohta, K. Electrochemical Reduction of CO2 in Methanol with Aid of CuO and Cu2O. *Catal. Today* **2009**, *148* (3), 329–334. https://doi.org/10.1016/j.cattod.2009.07.077.
(152) Rihko-Struckmann, L. K.; Peschel, A.; Hanke-Rauschenbach, R.; Sundmacher, K. Assessment of Methanol Synthesis Utilizing Exhaust CO2 for Chemical Storage of Electrical Energy. *Ind. Eng. Chem. Res.* **2010**, *49* (21), 11073–11078. https://doi.org/10.1021/ie100508w.
(153) Duarah, P.; Haldar, D.; Yadav, V.; Purkait, M. K. Progress in the Electrochemical Reduction of CO2 to Formic Acid: A Review on Current Trends and Future Prospects. *J. Environ. Chem. Eng.* **2021**, *9* (6), 106394. https://doi.org/10.1016/j.jece.2021.106394.
(154) Lu, X.; Leung, D. Y. C.; Wang, H.; Leung, M. K. H.; Xuan, J. Electrochemical Reduction of Carbon Dioxide to Formic Acid. *ChemElectroChem* **2014**, *1* (5), 836–849. https://doi.org/10.1002/celc.201300206.
(155) Agarwal, A. S.; Zhai, Y.; Hill, D.; Sridhar, N. The Electrochemical Reduction of Carbon Dioxide to Formate/Formic Acid: Engineering and Economic Feasibility. *ChemSusChem* **2011**, *4* (9), 1301–1310. https://doi.org/10.1002/cssc.201100220.
(156) Ewis, D.; Arsalan, M.; Khaled, M.; Pant, D.; Ba-Abbad, M. M.; Amhamed, A.; El-Naas, M. H. Electrochemical Reduction of CO2 into Formate/Formic Acid: A Review of Cell Design and Operation. *Sep. Purif. Technol.* **2023**, *316*, 123811. https://doi.org/10.1016/j.seppur.2023.123811.
(157) Gattrell, M.; Gupta, N.; Co, A. A Review of the Aqueous Electrochemical Reduction of CO2 to Hydrocarbons at Copper. *J. Electroanal. Chem.* **2006**, *594* (1), 1–19. https://doi.org/10.1016/j.jelechem.2006.05.013.
(158) Pinto, M. L.; Mafra, L.; Guil, J. M.; Pires, J.; Rocha, J. Adsorption and Activation of CO2 by Amine-Modified Nanoporous Materials Studied by Solid-State NMR and 13CO2 Adsorption. *Chem. Mater.* **2011**, *23* (6), 1387–1395. https://doi.org/10.1021/cm1029563.
(159) Shah Bacha, R. ullah; Li, L.; Guo, Y.-R.; Jing, L.; Pan, Q.-J. Actinyl-Modified g-C3N4 as CO2 Activation Materials for Chemical Conversion and Environmental Remedy via an Artificial Photosynthetic Route. *Inorg. Chem.* **2020**, *59* (12), 8369–8379. https://doi.org/10.1021/acs.inorgchem.0c00791.
(160) Álvarez, A.; Borges, M.; Corral-Pérez, J. J.; Olcina, J. G.; Hu, L.; Cornu, D.; Huang, R.; Stoian, D.; Urakawa, A. CO2 Activation over Catalytic Surfaces. *ChemPhysChem* **2017**, *18* (22), 3135–3141. https://doi.org/10.1002/cphc.201700782.
(161) Millet, M.-M.; Algara-Siller, G.; Wrabetz, S.; Mazheika, A.; Girgsdies, F.; Teschner, D.; Seitz, F.; Tarasov, A.; Levchenko, S. V.; Schlögl, R.; Frei, E. Ni Single Atom Catalysts for CO2 Activation. *J. Am. Chem. Soc.* **2019**, *141* (6), 2451–2461. https://doi.org/10.1021/jacs.8b11729.
(162) Yin, X.; Moss, J. R. Recent Developments in the Activation of Carbon Dioxide by Metal Complexes. *Coord. Chem. Rev.* **1999**, *181* (1), 27–59. https://doi.org/10.1016/S0010-8545(98)00171-4.
(163) Darensbourg, D. J.; Kudaroski, R. A. The Activation of Carbon Dioxide by Metai Complexes. In *Advances in Organometallic Chemistry*; Stone, F. G. A., West, R., Eds.; Academic Press, 1983; Vol. 22, pp 129–168. https://doi.org/10.1016/S0065-3055(08)60402-5.

(164) Gibson, D. H. Carbon Dioxide Coordination Chemistry: Metal Complexes and Surface-Bound Species. What Relationships? *Coord. Chem. Rev.* **1999**, *185–186*, 335–355. https://doi.org/10.1016/S0010-8545(99)00021-1.
(165) Tyagi, P.; Singh, D.; Malik, N.; Kumar, S.; Singh Malik, R. Metal Catalyst for CO2 Capture and Conversion into Cyclic Carbonate: Progress and Challenges. *Mater. Today* **2023**, *65*, 133–165. https://doi.org/10.1016/j.mattod.2023.02.029.
(166) Paddock, R. L.; Hiyama, Y.; McKay, J. M.; Nguyen, S. T. Co(III) Porphyrin/DMAP: An Efficient Catalyst System for the Synthesis of Cyclic Carbonates from CO2 and Epoxides. *Tetrahedron Lett.* **2004**, *45* (9), 2023–2026. https://doi.org/10.1016/j.tetlet.2003.10.101.
(167) Barzagli, F.; Mani, F.; Peruzzini, M. From Greenhouse Gas to Feedstock: Formation of Ammonium Carbamate from CO2 and NH3 in Organic Solvents and Its Catalytic Conversion into Urea under Mild Conditions. *Green Chem.* **2011**, *13* (5), 1267–1274. https://doi.org/10.1039/C0GC00674B.
(168) Leitner, W. Carbon Dioxide as a Raw Material: The Synthesis of Formic Acid and Its Derivatives from CO2. *Angew. Chem. Int. Ed. Engl.* **1995**, *34* (20), 2207–2221. https://doi.org/10.1002/anie.199522071.
(169) Fujita, E.; Brunschwig, B. S.; Ogata, T.; Yanagida, S. Toward Photochemical Carbon Dioxide Activation by Transition Metal Complexes. *Coord. Chem. Rev.* **1994**, *132*, 195–200. https://doi.org/10.1016/0010-8545(94)80040-5.
(170) Fujita, E. Photochemical Carbon Dioxide Reduction with Metal Complexes. *Coord. Chem. Rev.* **1999**, *185–186*, 373–384. https://doi.org/10.1016/S0010-8545(99)00023-5.
(171) López-Caballero, P.; Hauser, A. W.; Pilar de Lara-Castells, M. Exploring the Catalytic Properties of Unsupported and TiO2-Supported Cu5 Clusters: CO2 Decomposition to CO and CO2 Photoactivation. *J. Phys. Chem. C* **2019**, *123* (37), 23064–23074. https://doi.org/10.1021/acs.jpcc.9b06620.
(172) Zhang, Q.; Mao, M.; Li, Y.; Yang, Y.; Huang, H.; Jiang, Z.; Hu, Q.; Wu, S.; Zhao, X. Novel Photoactivation Promoted Light-Driven CO2 Reduction by CH4 on Ni/CeO2 Nanocomposite with High Light-to-Fuel Efficiency and Enhanced Stability. *Appl. Catal. B Environ.* **2018**, *239*, 555–564. https://doi.org/10.1016/j.apcatb.2018.08.052.
(173) Hædersdal, M.; Katsnelson, J.; Sakamoto, F. h.; Farinelli, W. a.; Doukas, A. g.; Tam, J.; Anderson, R. r. Enhanced Uptake and Photoactivation of Topical Methyl Aminolevulinate after Fractional CO2 Laser Pretreatment. *Lasers Surg. Med.* **2011**, *43* (8), 804–813. https://doi.org/10.1002/lsm.21096.
(174) Zeng, L.; Wang, Z.; Wang, Y.; Wang, J.; Guo, Y.; Hu, H.; He, X.; Wang, C.; Lin, W. Photoactivation of Cu Centers in Metal–Organic Frameworks for Selective CO2 Conversion to Ethanol. *J. Am. Chem. Soc.* **2020**, *142* (1), 75–79. https://doi.org/10.1021/jacs.9b11443.
(175) Bayer, U.; Anwander, R. Carbonyl Group and Carbon Dioxide Activation by Rare-Earth-Metal Complexes. *Dalton Trans.* **2020**, *49* (48), 17472–17493. https://doi.org/10.1039/D0DT03578E.
(176) Xémard, M.; Goudy, V.; Braun, A.; Tricoire, M.; Cordier, M.; Ricard, L.; Castro, L.; Louyriac, E.; Kefalidis, C. E.; Clavaguéra, C.; Maron, L.; Nocton, G. Reductive Disproportionation of CO2 with Bulky Divalent Samarium Complexes. *Organometallics* **2017**, *36* (23), 4660–4668. https://doi.org/10.1021/acs.organomet.7b00630.
(177) Evans, W. J.; Seibel, C. A.; Ziller, J. W. Organosamarium-Mediated Transformations of CO2 and COS: Monoinsertion and Disproportionation Reactions and the Reductive Coupling of CO2 to [O2CCO2]2-. *Inorg. Chem.* **1998**, *37* (4), 770–776. https://doi.org/10.1021/ic971381t.
(178) Qu, L.; Roisnel, T.; Cordier, M.; Yuan, D.; Yao, Y.; Zhao, B.; Kirillov, E. Rare-Earth Metal Complexes Supported by Polydentate Phenoxy-Type Ligand Platforms: C–H Activation Reactivity and CO2/Epoxide Copolymerization Catalysis. *Inorg. Chem.* **2020**, *59* (23), 16976–16987. https://doi.org/10.1021/acs.inorgchem.0c02112.
(179) Yao, Q.; Chen, Y.; Wang, Y.; Yuan, D.; You, H.; Yao, Y. Alternating Copolymerization of CO2 and Cyclohexene Oxide Initiated by Rare-Earth Metal Complexes Stabilized by *o*-Phenylenediamine-Bridged Tris(Phenolate) Ligand. *J. Rare Earths* **2022**, *40* (9), 1471–1479. https://doi.org/10.1016/j.jre.2021.07.007.
(180) Cui, D.; Nishiura, M.; Tardif, O.; Hou, Z. Rare-Earth-Metal Mixed Hydride/Aryloxide Complexes Bearing Mono(Cyclopentadienyl) Ligands. Synthesis, CO2 Fixation, and Catalysis on

Copolymerization of CO2 with Cyclohexene Oxide. *Organometallics* **2008**, *27* (11), 2428–2435. https://doi.org/10.1021/om800170x.
(181) Quan, Z.; Wang, X.; Zhao, X.; Wang, F. Copolymerization of CO2 and Propylene Oxide under Rare Earth Ternary Catalyst: Design of Ligand in Yttrium Complex. *Polymer* **2003**, *44* (19), 5605–5610. https://doi.org/10.1016/S0032-3861(03)00561-5.
(182) Tan, C.-S.; Hsu, T.-J. Alternating Copolymerization of Carbon Dioxide and Propylene Oxide with a Rare-Earth-Metal Coordination Catalyst. *Macromolecules* **1997**, *30* (11), 3147–3150. https://doi.org/10.1021/ma961725j.
(183) Zhang, Z.; Cui, D.; Liu, X. Alternating Copolymerization of Cyclohexene Oxide and Carbon Dioxide Catalyzed by Noncyclopentadienyl Rare-Earth Metal Bis(Alkyl) Complexes. *J. Polym. Sci. Part Polym. Chem.* **2008**, *46* (20), 6810–6818. https://doi.org/10.1002/pola.22989.
(184) Yao, Q.; Shi, Y.; Wang, Y.; Zhu, X.; Yuan, D.; Yao, Y. Bifunctional Rare-Earth Metal Catalysts for Conversion of CO2 and Epoxides into Cyclic Carbonates. *Asian J. Org. Chem.* **2022**, *11* (8), e202200106. https://doi.org/10.1002/ajoc.202200106.
(185) Dong, Y.; Wang, X.; Zhao, X.; Wang, F. Facile Synthesis of Poly(Ether Carbonate)s via Copolymerization of CO2 and Propylene Oxide under Combinatorial Catalyst of Rare Earth Ternary Complex and Double Metal Cyanide Complex. *J. Polym. Sci. Part Polym. Chem.* **2012**, *50* (2), 362–370. https://doi.org/10.1002/pola.25040.
(186) Zhao, Z.; Qin, J.; Zhang, C.; Wang, Y.; Yuan, D.; Yao, Y. Recyclable Single-Component Rare-Earth Metal Catalysts for Cycloaddition of CO2 and Epoxides at Atmospheric Pressure. *Inorg. Chem.* **2017**, *56* (8), 4568–4575. https://doi.org/10.1021/acs.inorgchem.7b00107.
(187) Simler, T.; McCabe, K. N.; Maron, L.; Nocton, G. CO Reductive Oligomerization by a Divalent Thulium Complex and CO_2 -Induced Functionalization. *Chem. Sci.* **2022**, *13* (25), 7449–7461. https://doi.org/10.1039/D2SC01798A.
(188) Bochkarev, M. N.; Fedorova, E. A.; Radkov, Yu. F.; Khorshev, S. Ya.; Kalinina, G. S.; Razuvaev, G. A. Carbon Dioxide Fixaion by Lathanide Complexes. *J. Organomet. Chem.* **1983**, *258* (2), C29–C33. https://doi.org/10.1016/S0022-328X(00)99264-7.
(189) Evans, W. J.; Fujimoto, C. H.; Ziller, J. W. Organolanthanide-Based Coordination and Insertion Reactivity of the Anion Formed by Deprotonation of ε-Caprolactam. *Organometallics* **2001**, *20* (22), 4529–4536. https://doi.org/10.1021/om010403n.
(190) Bayer, U.; Werner, D.; Maichle-Mössmer, C.; Anwander, R. Effective and Reversible Carbon Dioxide Insertion into Cerium Pyrazolates. *Angew. Chem. Int. Ed.* **2020**, *59* (14), 5830–5836. https://doi.org/10.1002/anie.201916483.
(191) Yin, H.; Carroll, P. J.; Schelter, E. J. Reactions of a Cerium(III) Amide with Heteroallenes: Insertion, Silyl-Migration and de-Insertion. *Chem. Commun.* **2016**, *52* (63), 9813–9816. https://doi.org/10.1039/C6CC03719D.
(192) Simler, T.; Feuerstein, T. J.; Yadav, R.; Gamer, M. T.; Roesky, P. W. Access to Divalent Lanthanide NHC Complexes by Redox-Transmetallation from Silver and CO2 Insertion Reactions. *Chem. Commun.* **2018**, *55* (2), 222–225. https://doi.org/10.1039/C8CC08120D.
(193) Zhou, J.; Li, T.; Maron, L.; Leng, X.; Chen, Y. A Scandium Complex Bearing Both Methylidene and Phosphinidene Ligands: Synthesis, Structure, and Reactivity. *Organometallics* **2015**, *34* (2), 470–476. https://doi.org/10.1021/om500997j.
(194) Beh, D. W.; Piers, W. E.; Rosal, I. del; Maron, L.; Gelfand, B. S.; Gendy, C.; Lin, J.-B. Scandium Alkyl and Hydride Complexes Supported by a Pentadentate Diborate Ligand: Reactions with CO2 and N2O. *Dalton Trans.* **2018**, *47* (38), 13680–13688. https://doi.org/10.1039/C8DT03313G.
(195) Linstrom, P. NIST Chemistry WebBook, NIST Standard Reference Database 69, 1997. https://doi.org/10.18434/T4D303.
(196) An, Q.; Xing, Y.-Y.; Pu, R.; Jia, M.; Chen, Y.; Hu, A.; Zhang, S.-Q.; Yu, N.; Du, J.; Zhang, Y.; Chen, J.; Liu, W.; Hong, X.; Zuo, Z. Identification of Alkoxy Radicals as Hydrogen Atom Transfer Agents in Ce-Catalyzed C–H Functionalization. *J. Am. Chem. Soc.* **2023**, *145* (1), 359–376. https://doi.org/10.1021/jacs.2c10126.
(197) Berg, J. M.; Tymoczko, J. L.; Gatto, G. J.; Stryer, L. *Biochemistry*, Eighth edition.; W.H. Freeman & Company, a Macmillan Education Imprint: New York, 2015.

(198) Martell, A. *Oxygen Complexes and Oxygen Activation by Transition Metals*; Springer: New York, NY, 1988.
(199) Ho, R. Y. N.; Liebman, J. F.; Valentine, J. S. Biological Reactions of Dioxygen: An Introduction. In *Active Oxygen in Biochemistry*; Valentine, J. S., Foote, C. S., Greenberg, A., Liebman, J. F., Eds.; Springer Netherlands: Dordrecht, 1995; pp 1–36. https://doi.org/10.1007/978-94-011-0609-2_1.
(200) Costas, M.; Mehn, M. P.; Jensen, M. P.; Que, L. Dioxygen Activation at Mononuclear Nonheme Iron Active Sites: Enzymes, Models, and Intermediates. *Chem. Rev.* **2004**, *104* (2), 939–986. https://doi.org/10.1021/cr020628n.
(201) Hong, S.; Lee, Y.-M.; Ray, K.; Nam, W. Dioxygen Activation Chemistry by Synthetic Mononuclear Nonheme Iron, Copper and Chromium Complexes. *Coord. Chem. Rev.* **2017**, *334*, 25–42. https://doi.org/10.1016/j.ccr.2016.07.006.
(202) Wallar, B. J.; Lipscomb, J. D. Dioxygen Activation by Enzymes Containing Binuclear Non-Heme Iron Clusters. *Chem. Rev.* **1996**, *96* (7), 2625–2658. https://doi.org/10.1021/cr9500489.
(203) Lewis, E. A.; Tolman, W. B. Reactivity of Dioxygen−Copper Systems. *Chem. Rev.* **2004**, *104* (2), 1047–1076. https://doi.org/10.1021/cr020633r.
(204) Tabushi, I. Reductive Dioxygen Activation by Use of Artificial P-450 Systems. *Coord. Chem. Rev.* **1988**, *86*, 1–42. https://doi.org/10.1016/0010-8545(88)85011-2.
(205) Decker, A.; Solomon, E. I. Dioxygen Activation by Copper, Heme and Non-Heme Iron Enzymes: Comparison of Electronic Structures and Reactivities. *Curr. Opin. Chem. Biol.* **2005**, *9* (2), 152–163. https://doi.org/10.1016/j.cbpa.2005.02.012.
(206) Quist, D. A.; Diaz, D. E.; Liu, J. J.; Karlin, K. D. Activation of Dioxygen by Copper Metalloproteins and Insights from Model Complexes. *JBIC J. Biol. Inorg. Chem.* **2017**, *22* (2), 253–288. https://doi.org/10.1007/s00775-016-1415-2.
(207) Simándi, L. I. *Catalytic Activation of Dioxygen by Metal Complexes*; Ugo, R., James, B. R., Series Eds.; Catalysis by Metal Complexes; Springer Netherlands: Dordrecht, 1992; Vol. 13. https://doi.org/10.1007/978-94-011-2850-6.
(208) Sahu, S.; Goldberg, D. P. Activation of Dioxygen by Iron and Manganese Complexes: A Heme and Nonheme Perspective. *J. Am. Chem. Soc.* **2016**, *138* (36), 11410–11428. https://doi.org/10.1021/jacs.6b05251.
(209) Borovik, A. S. Bioinspired Hydrogen Bond Motifs in Ligand Design: The Role of Noncovalent Interactions in Metal Ion Mediated Activation of Dioxygen. *Acc. Chem. Res.* **2005**, *38* (1), 54–61. https://doi.org/10.1021/ar030160q.
(210) Shook, R. L.; Borovik, A. S. Role of the Secondary Coordination Sphere in Metal-Mediated Dioxygen Activation. *Inorg. Chem.* **2010**, *49* (8), 3646–3660. https://doi.org/10.1021/ic901550k.
(211) Shook, R. L.; Borovik, A. S. The Effects of Hydrogen Bonds on Metal-Mediated O2activation and Related Processes. *Chem. Commun.* **2008**, No. 46, 6095–6107. https://doi.org/10.1039/B810957E.
(212) Cook, S. A.; Borovik, A. S. Molecular Designs for Controlling the Local Environments around Metal Ions. *Acc. Chem. Res.* **2015**, *48* (8), 2407–2414. https://doi.org/10.1021/acs.accounts.5b00212.
(213) Saracini, C.; Liakos, D. G.; Zapata Rivera, J. E.; Neese, F.; Meyer, G. J.; Karlin, K. D. Excitation Wavelength Dependent O2 Release from Copper(II)–Superoxide Compounds: Laser Flash-Photolysis Experiments and Theoretical Studies. *J. Am. Chem. Soc.* **2014**, *136* (4), 1260–1263. https://doi.org/10.1021/ja4115314.
(214) Shook, R. L.; Gunderson, W. A.; Greaves, J.; Ziller, J. W.; Hendrich, M. P.; Borovik, A. S. A Monomeric MnIII−Peroxo Complex Derived Directly from Dioxygen. *J. Am. Chem. Soc.* **2008**, *130* (28), 8888–8889. https://doi.org/10.1021/ja802775e.
(215) Parsell, T. H.; Behan, R. K.; Green, M. T.; Hendrich, M. P.; Borovik, A. S. Preparation and Properties of a Monomeric MnIV−Oxo Complex. *J. Am. Chem. Soc.* **2006**, *128* (27), 8728–8729. https://doi.org/10.1021/ja062332v.
(216) Gupta, R.; Taguchi, T.; Lassalle-Kaiser, B.; Bominaar, E. L.; Yano, J.; Hendrich, M. P.; Borovik, A. S. High-Spin Mn–Oxo Complexes and Their Relevance to the Oxygen-Evolving Complex within Photosystem II. *Proc. Natl. Acad. Sci.* **2015**, *112* (17), 5319–5324. https://doi.org/10.1073/pnas.1422800112.

(217) Taguchi, T.; Gupta, R.; Lassalle-Kaiser, B.; Boyce, D. W.; Yachandra, V. K.; Tolman, W. B.; Yano, J.; Hendrich, M. P.; Borovik, A. S. Preparation and Properties of a Monomeric High-Spin MnV–Oxo Complex. *J. Am. Chem. Soc.* **2012**, *134* (4), 1996–1999. https://doi.org/10.1021/ja210957u.
(218) Pfaff, F. F.; Heims, F.; Kundu, S.; Mebs, S.; Ray, K. Spectroscopic Capture and Reactivity of S = 1/2 Nickel(III)–Oxygen Intermediates in the Reaction of a NiII-Salt with mCPBA. *Chem. Commun.* **2012**, *48* (31), 3730–3732. https://doi.org/10.1039/C2CC30716B.
(219) Radecka-Paryzek, W.; Patroniak, V.; Kubicki, M. First Example of Template Synthesis of Pentaaza Macrocyclic Ytterbium(III) Complex and Solvent-Controlled Supramolecular Self-Assembly of Its Dimeric μ-H2:H2 Peroxo-Bridged Derivative. *Inorg. Chem. Commun.* **2004**, *7* (3), 455–458. https://doi.org/10.1016/j.inoche.2003.12.035.
(220) Guo, Z.; Blair, V. L.; Deacon, G. B.; Junk, P. C. Widely Contrasting Outcomes from the Use of Tris(Pentafluorophenyl)Bismuth or Pentafluorophenylsilver as Oxidants in the Reactions of Lanthanoid Metals with N,N'-Diarylformamidines. *Dalton Trans.* **2020**, *49* (39), 13588–13600. https://doi.org/10.1039/D0DT03044A.
(221) van Velzen, N. J. C.; Harder, S. Deca-Arylsamarocene: An Unusually Inert Sm(II) Sandwich Complex. *Organometallics* **2018**, *37* (14), 2263–2271. https://doi.org/10.1021/acs.organomet.8b00254.
(222) Gee, W. J.; MacLellan, J. G.; Forsyth, C. M.; Moubaraki, B.; Murray, K. S.; Andrews, P. C.; Junk, P. C. Caging Peroxide: Anion-Templated Synthesis and Characterization of a Rare-Earth Cluster. *Inorg. Chem.* **2012**, *51* (16), 8661–8663. https://doi.org/10.1021/ic301382r.
(223) Patroniak, V.; Kubicki, M.; Radecka-Paryzek, W. The First Example of μ-H2:H2-Peroxo-Bridged Macrocyclic Lanthanide Complex. The Crystal Structure of [Lu2{Me2pyo[16]trieneN5}2(μ-H2:H2-O2)Cl2](ClO4)2 Dioxane Solvate. *J. Incl. Phenom. Macrocycl. Chem.* **2004**, *49* (1), 121–125. https://doi.org/10.1023/B:JIPH.0000031124.82412.40.
(224) Wang, X.-T.; Dong, H.-M.; Wang, X.-G.; Yang, E.-C.; Zhao, X.-J. Two Oxime-Based LnIII3NiII3 Clusters with Triangular Ln3(M3-O2)7+ Core: Solvothermal Syntheses, Crystal Structures, and Magnetic Properties. *Z. Für Anorg. Allg. Chem.* **2016**, *642* (20), 1166–1172. https://doi.org/10.1002/zaac.201600253.
(225) Deacon, G. B.; Forsyth, C. M.; Freckmann, D.; Junk, P. C.; Konstas, K.; Luu, J.; Meyer, G.; Werner, D. Adventitiously Obtained Rare-Earth Peroxide Complexes and Their Structural Characterisation. *Aust. J. Chem.* **2014**, *67* (12), 1860–1865. https://doi.org/10.1071/CH14410.
(226) Zhang, X.; Loppnow, G. R.; McDonald, R.; Takats, J. {HB(3,5-Me2pz)3}2Sm(.Eta.2-O2): First Example of a Lanthanide Superoxo Complex. *J. Am. Chem. Soc.* **1995**, *117* (29), 7828–7829. https://doi.org/10.1021/ja00134a037.
(227) Shirase, S.; Shinohara, K.; Tsurugi, H.; Mashima, K. Oxidation of Alcohols to Carbonyl Compounds Catalyzed by Oxo-Bridged Dinuclear Cerium Complexes with Pentadentate Schiff-Base Ligands under a Dioxygen Atmosphere. *ACS Catal.* **2018**, *8* (8), 6939–6947. https://doi.org/10.1021/acscatal.8b01718.
(228) Coles, M. P.; Hitchcock, P. B.; Khvostov, A. V.; Lappert, M. F.; Li, Z.; Protchenko, A. V. Crystalline Amidocerium(Iv) Oxides and a Side-on Bridging Dioxygen Complex. *Dalton Trans.* **2010**, *39* (29), 6780. https://doi.org/10.1039/c0dt00349b.
(229) Wang, G.-C.; Sung, H. H. Y.; Williams, I. D.; Leung, W.-H. Tetravalent Titanium, Zirconium, and Cerium Oxo and Peroxo Complexes Containing an Imidodiphosphinate Ligand. *Inorg. Chem.* **2012**, *51* (6), 3640–3647. https://doi.org/10.1021/ic202564h.
(230) Mustapha, A.; Reglinski, J.; Kennedy, A. R. The Use of Hydrogenated Schiff Base Ligands in the Synthesis of Multi-Metallic Compounds. *Inorganica Chim. Acta* **2009**, *362* (4), 1267–1274. https://doi.org/10.1016/j.ica.2008.06.026.
(231) Sang, Y.-L.; Lin, X.-S.; Li, X.-C.; Liu, Y.-H.; Zhang, X.-H. Synthesis, Crystal Structure and Antibacterial Activity of a Novel Phenolato- and Peroxo-Bridged Dinuclear Cerium(IV) Complex with Tripodal Schiff Bases. *Inorg. Chem. Commun.* **2015**, *62*, 115–118. https://doi.org/10.1016/j.inoche.2015.11.003.
(232) Butman, L. A.; Sokol, V. I.; Porai-Koshits, M. A. *Koordinatsionnaia khimiia* **1976**, *2*, 265.
(233) Barnes, J. S.; Blyth, C. S.; Paton, J. D.; Smith, I. G. B. *Lanthanide and Actinide Research*, VCH Publishers.; 1990; Vol. 3.

(234) Sweet, L. E.; Corbey, J. F.; Gendron, F.; Autschbach, J.; McNamara, B. K.; Ziegelgruber, K. L.; Arrigo, L. M.; Peper, S. M.; Schwantes, J. M. Structure and Bonding Investigation of Plutonium Peroxocarbonate Complexes Using Cerium Surrogates and Electronic Structure Modeling. *Inorg. Chem.* **2017**, *56* (2), 791–801. https://doi.org/10.1021/acs.inorgchem.6b02235.
(235) Wang, G.-C.; So, Y.-M.; Wong, K.-L.; Au-Yeung, K.-C.; Sung, H. H.-Y.; Williams, I. D.; Leung, W.-H. Synthesis, Structure, and Reactivity of a Tetranuclear Cerium(IV) Oxo Cluster Supported by the Kläui Tripodal Ligand [Co(H5-C5H5)P(O)(OEt)23]−. *Chem. – Eur. J.* **2015**, *21* (45), 16126–16135. https://doi.org/10.1002/chem.201502173.
(236) Sheldrick, G. M. Crystal Structure Refinement with *SHELXL*. *Acta Crystallogr. Sect. C Struct. Chem.* **2015**, *71* (1), 3–8. https://doi.org/10.1107/S2053229614024218.
(237) Müller, P. Refinement of Disorder with SHELXL. https://web.mit.edu/pmueller/www/ACA2007/WK01/Disorder.pdf (accessed 2025-01-31).
(238) Niemeyer, M. Synthesis and Structural Characterization of Several Ytterbium Bis(Trimethylsilyl)Amides Including Base-Free [YbN(SiMe3)22(μ-Cl)]2 — A Coordinatively Unsaturated Complex with Additional Agostic Yb···(H3C—Si) Interactions. *Z. Für Anorg. Allg. Chem.* **2002**, *628* (3), 647–657. https://doi.org/10.1002/1521-3749(200203)628:3<647::AID-ZAAC647>3.0.CO;2-L.
(239) Sobańska, K.; Krasowska, A.; Mazur, T.; Podolska-Serafin, K.; Pietrzyk, P.; Sojka, Z. Diagnostic Features of EPR Spectra of Superoxide Intermediates on Catalytic Surfaces and Molecular Interpretation of Their g and A Tensors. *Top. Catal.* **2015**, *58* (12–13), 796–810. https://doi.org/10.1007/s11244-015-0420-y.
(240) Mishra, B.; Indira Priyadarsini, K.; Bhide, M. K.; Kadam, R. M.; Mohan, H. Reactions of Superoxide Radicals with Curcumin: Probable Mechanisms by Optical Spectroscopy and EPR. *Free Radic. Res.* **2004**, *38* (4), 355–362. https://doi.org/10.1080/10715760310001660259.
(241) Petr, A.; Kataev, V.; Büchner, B. First Direct In Situ EPR Spectroelectrochemical Evidence of the Superoxide Anion Radical. *J. Phys. Chem. B* **2011**, *115* (42), 12036–12039. https://doi.org/10.1021/jp206540c.

No matter how thin you slice it, there will always be two sides.

Baruch Spinoza, 17th century

Conclusion and Perspectives

The work presented in this manuscript focused the synthesis and the reactivity of a new cerium(III) tripodal complex : $Ce^{III}TREN^{TIPS}$. The complex was extensively characterised using multiple techniques, and was shown to exhibit a particularly low redox potential under blue light irradiation, on par with the reducing power of lithium metal. The photoinduced reducing ability of $Ce^{III}TREN^{TIPS}$ was applied to the reduction of Persistent Organic Pollutants, non-biodegradable chemicals containing several carbon-halide bonds and difficult to activate. Other challenging substrates such as polyfluorobenzenes and surrogate of PFAS (*eternal pollutants*) were also shown to be activated by the complex under irradiation, which paved the way for developments of promising environmental remediation strategies.

$Ce^{III}TREN^{TIPS}$ also displayed an original reactivity with nitro compounds (found in many polluting explosives), reducing these substances by one electron to form fairly stable radical species with and without irradiation. This interesting behaviour did not yet find a chemical outcome, but further investigations could possibly find a use for these unusual radical species.

Finally, the reduction of most species involved in the nitrogen cycle was also investigated, and the complex was once again proven useful towards the reduction of inorganic nitrates and nitrites, but also transforming nitrous oxide (N_2O) into dinitrogen under irradiation. Carbon dioxide and dioxygen were also reacting with $Ce^{III}TREN^{TIPS}$ and showed interesting insertion and reduction reactions respectively.

In addition to this work, accessing new cerium(IV) complexes could also allow for the study of the spectrochemical series (idea suggested by Olivier Maury). Considering that $Ce^{III}TREN^{TIPS}$ only allows for one exogenous substrate to coordinate, and that the electronic transition in the visible region in $Ce^{IV}TREN^{TIPS}$ complexes reported in this manuscript is a charge transfer from the ligand to the metal (LMCT), changing one ligand would also lead to a shift of the LMCT band as shown between fluoride, chloride and bromide ligands. Obtaining new $Ce^{IV}TREN^{TIPS}$ complexes could provide interesting insight on the effects of each ligand and possibly produce a parameter to rank effects of ligands on a scale.

A great amount of works remains nonetheless to go into the depth of all reactivities herein reported. Reduction of organohalogen compounds could be applied to more *real-life molecules*, and especially targeting real PFAS as their degradation remains a global health issue. Activation of N-O bonds is also of interest, regarding their presence in several pollutants including nitrate (agriculture), N-oxide and nitro compounds (explosives).

Taking these reactivities to solving real-life issues goes together with a significantly higher tolerance to air and water, as most pollution problems herein mentioned involve water pollution. This feature would prevent the use of highly sensitive silylamide ligands, and need for extensive ligand design to afford a stable complex without sacrificing the potential of reactivity of $Ce^{III}TREN^{TIPS}$.

Stulti stultos esse nesciunt.

Experimental Section

General methods and materials 194
Experimental Section for Chapter I 197
Experimental section for Chapter II 269
Experimental section for Chapter III 315
Experimental section for Chapter IV 381
Part I.a 381
Part I.b 419
Part II 443
Part III 453

General methods and materials

General methods :

All reactions were performed using standard Schlenk-line techniques under dry N_2 or gloveboxes (MBraun) under N_2 atmosphere with concentrations of O_2 and H_2O lower than 1 ppm. Glassware was dried at 110 °C overnight before use.

Solvents were dried either using either CaH_2 (MeCN, CH_2Cl_2) or sodium, using benzophenone as an indicator (pentane, benzene, THF, C_6D_6, THF-d_8, toluene-d_8), degassed at least thrice using freeze-pump-thaw techniques and distilled under reduced pressure. Deuterated solvents were purchased from Eurisotop and purified similarly to non-deuterated solvents.

All reagents have been distilled on CaH_2 and degassed, or sublimated and before use.

$Ce(OTf)_3$ and $CeCl_3$ were bought from Strem Chemicals and used without purification. CeI_3 was provided by Alfa Aesar and used as provided.

NMR spectroscopy :

NMR spectra were recorded on a Bruker Avance III-300 MHz spectrometer using standard 5 mm NMR tubes with J. Young valves. Chemical shifts are given in parts per million (ppm), and referenced to residual solvent residual peaks or internal reference. Spectra were analysed using MestreNova software, with a systematic baseline correction for integration.

Without any specification, all reactions depicted in NMR spectra are equimolar.

Gas chromatography separation, mass spectrometry and flame ionization detector characterization :

GC-MS and GC-FID were respectively carried out with a Varian 450-GC equipped with Varian 240-MS and a Bruker Scion 436-GC equipped with a split mode, capillary injection system, and flame ionization detector, using an SGE apolar IDBP5 (15 m x 0.25 mm x 0.25 µm) column and helium as carrier gas.

Gaseous substrates were analysed using an Inficon Micro GC fusion.

UV-visible, infrared spectroscopies and luminescence measurements :

UV-visible measurements were carried out in a quartz cuvette bearing a J. Young tape (see Figure S2a) on an Agilent Technologies Carry 60 UV equipped with a Xenon flash lamp (80 Hz) in double beam mode at 300 nm/min from 200 nm to 1000 nm with a baseline correction, using pentane as solvent. Spectra were plotted in wavenumber, fitted with fityk[1] using gaussian functions, and plotted again in wavelength.

Fluorescence spectra were recorded on a Horiba Fluoromax-4 using a 150 W CW ozone-free xenon lamp, from 250 nm to 800 nm with 2 nm for entrance and exit slits at 1 nm/s.

Transient Absorption Spectroscopy measurements were done using a Magnitude envision spectrometer.

Electrochemical measurements :

Cyclic voltammetry experiments were recorded using a Metrohm Autolab PGSTAT302N potentiometer, and the data were processed using OriginLab 2019 software. The experiments were performed inside an N_2-filled glovebox.

The electrochemical cell consisted of a homemade 5-necks 5 mL cell, with a silver wire as quasi-reference electrode, a glassy carbon disk (3 mm diameter) as working electrode and a platinum wire as

counter-electrode. The solution used for electrochemical analysis was 4 mM in analyte and 100 mM in electrolyte (*n*-tetrabutylammonium bis-trifluoromethanesulfonimidate, TBATFSI) in 5 mL of THF.

All data were collected in a positive-feedback IR compensation mode. At the end of the experiment, ferrocene was added as an internal standard for calibration. The potential of the analyte was reported *versus* ferrocene (noted Fc).

EPR measurements:

EPR spectrum were recorded either on a Jeol JES-X310 spectrometer working in X-band with a modulation frequency of 0.01 mT or on a Bruker ESP 500E using a standard rectangular (4102ST) EPR cavity (Bruker ER4131VT). Otherwise mentioned, data have been recorded at 273 K

EPR spectrum of **1** was recorded by Eric Rivière on a Bruker ELEXSYS 500 spectrometer equipped with a Bruker ER 4116DM X band resonator, an Oxford Instruments continuous flow ESR 900 cryostat, and an ITC 503 temperature control system. The conditions used were the following: microwave frequency = 9.636 GHz, microwave power = 4.0 mW, modulation amplitude = 8 Gauss, modulation frequency = 100 KHz, Gain = 50 dB, and temperature = 10 K

EPR data were simulated using EasySpin program in MatLab R2024a, using a homemade program provided in appendix. All atoms included in the simulations were weighted with their natural abundancy, and spectra were simulated using “garlic” sub-program. Line broadening was evaluated using an average of Lorentzian and Gaussian broadenings. Final optimizations of the simulations were done using least-square fitting “esfit” subprogram, with Levenberg-Marquardt algorithm, with optimisation target as “data as if” and scaling set to “maxabs”. Data were exported and plotted using Origin 2019 64 bits.

Elemental analyses :

Elemental analysis samples were analyzed by Mikroanalytisches Labor Pascher in double determination C, H, N under an inert atmosphere.

X-Ray Diffraction measurements :

Single crystal diffraction measurements were carried on a STOE Stadivari diffractometer using a Mo source (λ_{K_α} = 0.710 Å) and an EIGER 2 detector. The crystal was kept at 150 K during data collection using an Oxford Instruments cryostat. Using Olex2[18], the structures were solved with the SHELXT[19,20] structure solution program using Intrinsic Phasing and refined with the SHELXL refinement package using Least Squares minimization.

All structures are represented with displacement ellipsoids are represented at 50% probability, and hydrogen atoms are omitted for clarity. Isopropyl groups are displayed in wireframe style for improved reading of the structure.

All atoms in structures based on $TREN^{TIPS}$ ligand are labelled in a similar way (see **Figure S48** for the labelling in $Ce^{III}TREN^{TIPS}$).

Magnetism measurements :

Magnetic susceptibility data were collected on a powdered sample of the compound with a SQUID-based sample magnetometer Quantum design MPMS5.

Photochemistry setup :

Light irradiations were carried out using Kessil lamps (https://kessil.com/products/science_main.php).

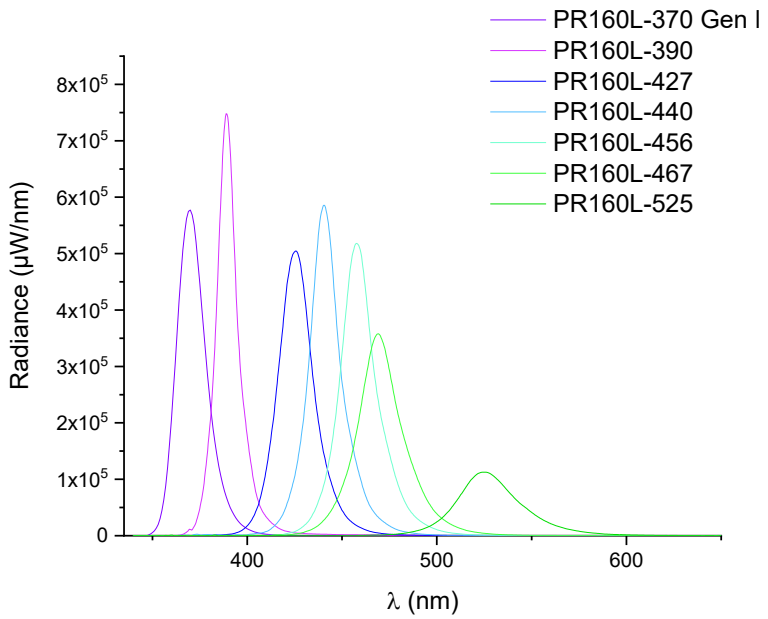

Figure S1. Emission spectra of Kessil photochemistry lamps. Provided with courtesy by Kessil©

Photochemistry experiments were carried out using a homemade 3D-printed box (see **Figure S2b**) designed by Olivier Bec and Joseph Youssef, in which both NMR tubes could be irradiated.

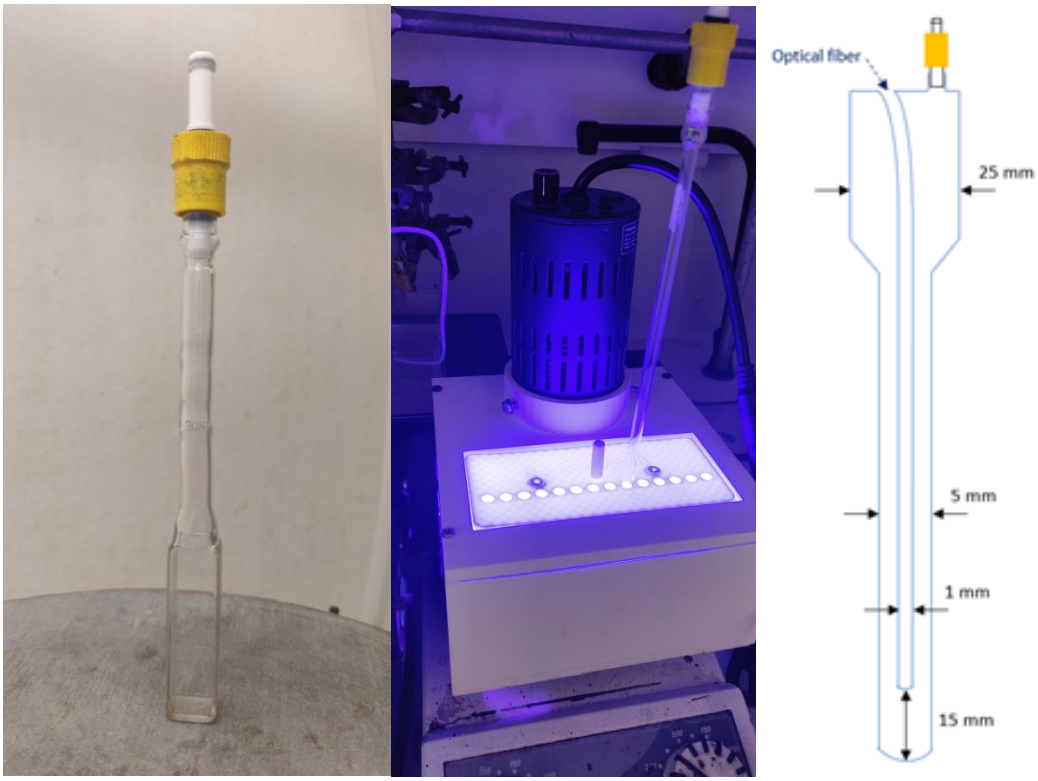

Figure S2. (left) J. Young quartz cuvette used for UV-vis measurements. (middle) Homemade 3D-printed photochemistry box used for irradiation experiments (right). (right) Structure of a prototype of J. Young NMR tube to irradiate inside the NMR spectrometer.

Experimental Section for Chapter I

I. Synthetic procedures 198
II. Spectral data 201
III. X-Ray crystal structures 225
IV. Magnetic measurements 252
V. EPR measurements for Chapter I 253
VII. UV-visible and fluorescence spectra 255
VIII. Electrochemistry 264
References 267

I. Synthetic procedures

a) Synthesis of [Li_3TREN^{TIPS}]

Li_3Tren^{TIPS} was prepared in a similar procedure as previously described in the literature.[2]

In a 250 mL Schlenk flask containing tris-(2-aminoethyl)amine (12.2 g, 83 mmol, 1 equiv.) was added 200 mL of dry THF. The mixture was stirred for 5 minutes and cooled down to -78°C. ^{n}BuLi (100 mL, 250 mmol, 3 equiv., 2.5 M in hexanes) was added dropwise over 15 minutes, and the mixture was left warming up to room temperature for 6 h. Without purification, the reaction medium was cooled to -78°C, and $ClSi^{i}Pr_3$ (53.5 mL, 250 mmol, 3 equiv.) was added dropwise over 10 minutes. The reaction medium gradually turned yellow, and a white solid appeared. The mixture was left warming overnight (approximately 14 h). Volatiles were removed under reduced pressure, and the reaction medium was filtered on a porosity 3 fritted filter to remove LiCl precipitate, then on the Teflon® filter to remove any remaining solid. 40 mL of dry pentane was added to the yellow liquid (to prevent solidification upon further cooling) and cooled down to -78 °C. ^{n}BuLi (100 mL, 250 mmol, 3 equiv., 2.5 M in hexanes) was added dropwise over 15 minutes, yielding a white solid, and the mixture was left warming up to room temperature overnight. A white solid was recovered on a fritted filter and rinsed using cold pentane, yielding 39.4 g of white powder (η = 74%).

^{1}H NMR (300 MHz, C_6D_6, 298 K): δ 3.09 (m, 6H, C**H$_2$**$CH_2Si^{i}Pr_3$), 2.25 (m, 6H, CH_2C**H$_2$**$Si^{i}Pr_3$), 1.16 (m, 63H, $CH_2CH_2Si^{i}$**Pr$_3$**)

^{13}C NMR (300 MHz, C_6D_6, 298 K): δ 57.3 (**C**H_2), 43.2 (**C**H_2), 19.8 ($CH($**C**$H_2)_2$), 12.6 (**C**$H(CH_2)_2$).

FTIR ν (cm^{-1}) (powder): 2931 (s), 2883 (s), 2858 (s), 2774 (m), 1460 (vs), 1362 (s), 1341 (s), 1270 (s), 1073 (s), 1055 (s), 1027 (s), 1005 (s), 991 (vs), 963 (vs), 933 (vs), 878 (vs), 777 (vs), 658 (vs), 638 (vs)

b) Synthesis of [$Li(THF)_4$][$ICeTREN^{TIPS}$] (1-LiI-THF_4)

To a suspension of CeI_3 (2.00 g, 3.8 mmol, 1 eq.) in 30 mL of THF was added a solution of Li_3TREN^{TIPS} (2.43 g, 3.8 mmol, 1 eq.) in 25 mL of THF. The supernatant became readily yellow, and the mixture was left under stirring overnight. Volatiles were removed under reduced pressure (2 evaporation with pentane), extracted with pentane until the supernatant was colourless, filtered using a Teflon® filter, and set to cool at -40 °C in about 40 mL of pentane. After 30 minutes, a large amount of yellowish precipitate appeared, and after removal of the supernatant, the yellowish-beige solid (5.865 g), corresponding to [$Li(THF)_4$][$ICe^{III}TREN^{TIPS}$] (**1-LiI-THF_4**) was obtained.

c) Synthesis of [$Ce^{III}TREN^{TIPS}$] (1)

To a suspension of CeI_3 (2.00 g, 3.8 mmol, 1 eq.) in 30 mL of THF was added a solution of Li_3TREN^{TIPS} (2.43 g, 3.8 mmol, 1 eq.) in 25 mL of THF. The supernatant became readily yellow, and the mixture was left under stirring overnight. Volatiles were removed under reduced pressure (2 evaporation with pentane), extracted with pentane until the supernatant was colourless, filtered using a Teflon® filter, and set to cool at -40°C in about 40 mL of pentane. After 30 minutes, a large amount of yellowish precipitate appeared, and after removal of the supernatant, the yellowish-beige solid (5.865 g), corresponding to [$Li(THF)_4$][$ICe^{III}TREN^{TIPS}$] (**1-LiI-THF_4**), was dried under vacuum at 50°C for 2 days. The yellow solid was then extracted with pentane (total volume of 50 mL), then crystallized at -40 °C overnight. Yellow crystals from the first two fractions were gathered and combined to afford [$Ce^{III}TREN^{TIPS}$] (**1**) (2.286 g, 67 %).

^{1}H NMR (300 MHz, C_6D_6, 298 K) δ 3.81 (s, 6H, C**H$_2$**$CH_2SiPr^{i}_3$), 3.41 (s, 3H, $CH_2CH_2Si($C**H**$(CH_3)_2)_3$), 2.94 (s, 60H, $CH_2CH_2Si($C**H**$(CH_3)_2)_3$ and $CH_2CH_2Si(CH($C**H$_3)_2)_3$), -17.56 (s, 6H, CH_2C**H$_2$**$SiPr^{i}_3$)

^{13}C NMR (300 MHz, C_6D_6, 298 K) δ 19.2 (s), 17.9 (s), -5 (s)

FTIR ν (cm^{-1}) (powder) : 2935 (s), 2881 (s), 2859 (s), 2836 (s), 2820 (s), 1458 (vs), 1092 (vs), 1070 (s), 1002 (vs), 943 (vs), 923 (vs), 913 (s), 877 (vs), 768 (vs), 752 (vs), 738 (vs), 666 (vs), 628 (vs)

Elemental analysis for $CeC_{33}H_{75}N_4Si_3$, Found (Theoretical): C, 52.78 (52.68) H, 10.03 (10.05); N, 7.46 (7.45)

a) Synthesis of [ClCe^{IV}TREN^{TIPS}] (2-Cl)

Given the light sensitivity of **2-Cl**, the reaction should be carried out in the dark.

Benzyl chloride (16 µL, 0.14 mmol, 1 eq.) was added to a solution of **1** (100 mg, 0.14 mmol, 1 eq.) in 2 mL of pentane. The solution turned dark blue within minutes. The mixture was left under stirring in the dark for 2 hours. The volatiles were removed under reduced pressure for 30 minutes, and the deep purple solid was rinsed with 3 x 1 mL of MeCN on a fritted filter. After drying under vacuum for 30 minutes, a purple solid could be recovered (61 mg, 55 %). Deep purple crystals suitable for XRD could be grown from a concentrated solution in THF at -40 °C for a few hours.

^{1}H NMR (300 MHz, C_6D_6, 298 K) δ 5.05 (t (J = 4.8 Hz), 6H, C**H$_2$**$CH_2SiPr^i_3$), 3.34 (t (J = 4.7 Hz), 6H, CH_2C**H$_2$**$SiPr^i_3$), 1.52 (sept (J = 7.5 Hz), 9H, $CH_2CH_2Si(CH(CH_3)_2)_3$); 1.20 (s, 54H, $CH_2CH_2Si(CH(CH_3)_2)_3$

^{13}C NMR (300 MHz, C_6D_6, 298 K) δ 67.2 (s, 3C, **C**$H_2CH_2Si(CH(CH_3)_2)$, 49.2 (s, 3C, CH_2**C**$H_2Si(CH(CH_3)_2)$, 19.4 (s, 18C, CH_2CH_2 $Si(CH($**C**$H_3)_2)$, 13.9 (s, 9C, $CH_2CH_2Si($**C**$H(CH_3)_2)$

FTIR ν (cm^{-1}) (powder) : 2937 (s), 2924 (s), 2885 (s), 2860 (s), 1455 (s), 1037 (vs), 1009 (vs), 917 (vs), 880 (vs), 710 (vs), 371 (vs), 634 (vs), 625 (vs)

Elemental analysis for $ClCeC_{33}H_{75}N_4Si_3$, Found (Theoretical): C, 50.48 (50.31) H, 9.64 (9.60); N, 7.24 (7.11)

b) Synthesis of [BrCe^{IV}TREN^{TIPS}] (2-Br)

Given the high light sensitivity of **2-Br**, the reaction should be carried out in the dark.

Benzyl bromide (16 µL, 0.14 mmol, 1 eq.) was added to a solution of **1** (100 mg, 0.14 mmol, 1 eq.) in 2 mL of pentane. The solution turned dark blue within minutes. The mixture was left under stirring in the dark for 2 hours. The volatiles were removed under reduce pressure for 30 minutes, and the dark blue solid was rinsed with 3 x 1 mL of MeCN on a fritted filter. After drying under vacuum for 30 minutes, a purple solid could be recovered (71.5 mg, 66 %). Deep purple crystals could be grown from a solution in 0.5 mL of THF at -40°C overnight.

^{1}H NMR (300 MHz, C_6D_6, 298 K) δ 5.15 (t (J = 4.7 Hz), 6H, C**H$_2$**$CH_2SiPr^i_3$), 3.32 (t (J = 4.7 Hz), 6H, CH_2C**H$_2$**$SiPr^i_3$), 1.55 (sept (J = 7.5 Hz), 9H, $CH_2CH_2Si(CH(CH_3)_2)_3$); 1.22 (s, 54H, $CH_2CH_2Si(CH(CH_3)_2)_3$

^{13}C NMR (300 MHz, C_6D_6, 298 K) δ 67.7 (s, 3C, **C**$H_2CH_2Si(CH(CH_3)_2)$, 49.1 (s, 3C, CH_2**C**$H_2Si(CH(CH_3)_2)$, 19.6 (s, 18C, CH_2CH_2 $Si(CH($**C**$H_3)_2)$, 14.2 (s, 9C, $CH_2CH_2Si($**C**$H(CH_3)_2)$

FTIR ν (cm^{-1}) (powder) : 2937 (s), 2885 (s), 2860 (s), 1457 (s), 1271 (vs), 1038 (vs), 1009 (vs), 989 (vs), 918 (vs), 880 (vs) 708 (vs) 672 (vs), 629 (vs)

Elemental analysis for $BrCeC_{33}H_{75}N_4Si_3$, Found (Theoretical): C, 47.92 (47.62) H, 9.18 (9.08); N, 6.70 (6.73)

c) Synthesis of [FCe^{IV}TREN^{TIPS}] (2-F)

Compound **1** (100 mg, 0.14 mmol, 1 eq.) was dissolved in 2 mL of pentane and added to ferrocenium tetrafluoroborate (36 mg, 0.14 mmol, 1 eq.). The colour turned immediately dark red, and the reaction was left stirring for 10 hours. The volatiles were removed under reduced pressure, and the dark red solid was rinsed with MeCN until the supernatant was colourless. The remaining solid was finally extracted with pentane, and volatiles were removed under reduced pressure, yielding [FCe^{IV}TREN^{TIPS}] (**2-F**) as a dark red powder (30 mg, 28%). Crystals suitable for XRD could be grown from a saturated solution in THF at -40 °C.

^{1}H NMR (300 MHz, C_6D_6, 298 K) δ 4.68 (t (J = 4.5 Hz), 6H, C**H$_2$**$CH_2SiPr^i_3$), 3.41 (t (J = 4.5 Hz), 6H, CH_2C**H$_2$**$SiPr^i_3$), 1.40 (sept (J = 7.1 Hz), 9H, $CH_2CH_2Si(CH(CH_3)_2)_3$); 1.20 (s, 54H, $CH_2CH_2Si(CH(CH_3)_2)_3$

^{13}C NMR (300 MHz, C_6D_6, 298 K) δ 64.9 (s, 3C, **C**$H_2CH_2Si(CH(CH_3)_2)$, 48.9 (s, 3C, CH_2**C**$H_2Si(CH(CH_3)_2)$, 19.2 (s, 18C, $CH_2CH_2Si(CH($**C**$H_3)_2)$, 13.2 (s, 9C, $CH_2CH_2Si($**C**$H(CH_3)_2)$

^{19}F NMR (300 MHz, THD-d_8, 298 K) δ 311.85 (s, 1F, Ce-**F**)

FTIR ν (cm^{-1}) (powder) : 2939 (s), 2861 (s), 1460 (s), 1052 (vs), 1010 (vs), 919 (vs), 879 (vs), 717 (s), 371 (vs), 672 (vs), 636 (vs)

Elemental analysis for $FCeC_{33}H_{75}N_4Si_3$, Found (Theoretical): C, 50.78 (51.38) H, 9.79 (9.80); N, 7.28 (7.26)

d) Synthesis of μ-(O-C_6H_4-O)[Ce^{IV}TREN^{TIPS}] (2-Bq)

Compound **1** (32 mg, 42 μmol, 1 eq.) was dissolved in 2 mL of pentane, and a solution of 1,4-benzoquinone (2.3 mg, 26 μmol, 0.5 eq.) in 0.5 mL of THF was added. The colour turned immediately deep purple, and the solution was left under stirring for 30 min. Volatiles were removed under reduced pressure, the resulting purple solid was washed with acetonitrile until the supernatant was colourless, and the solid was dissolved in a minimum amount of pentane with one drop of THF. Storage of the purple solution at 640 °C overnight afforded XRD suitable purple crystals.

^{1}H NMR (300 MHz, C_6D_6, 298 K) δ 4.72 (t (J = 4.0 Hz), 6H, C**H$_2$**$CH_2SiPr^i_3$), 3.31 (t (J = 4.7 Hz), 6H, CH_2C**H$_2$**$SiPr^i_3$), 1.45 (sept (J = 7.4 Hz), 9H, $CH_2CH_2Si($**C**$H(CH_3)_2)_3$); 1.24 (2×s, 54H, $CH_2CH_2Si(CH(CH_3)_2)_3$)

e) Synthesis of ferrocenium triflate (FcOTf)

Ferrocenium triflate was synthesized following a literature procedure.[234]

AgOTf (2.465 g, 9.5 mmol, 1 eq.) and ferrocene (1.812 g, 9.7 mmol, 1 eq.) were mixed in dry CH_2Cl_2 at 0 °C. The mixture became blue after 10 minutes of stirring, and the reaction was left overnight in the dark. After filtration on a Celite pad, volatiles were removed under reduced pressure. The blue solid obtained was rinsed first with hexanes, then Et_2O until the organic phase was colourless, and dried overnight *in vacuo*. Redissolution in CH_2Cl_2 followed by filtration on Celite , evaporation of volatiles and drying *in vacuo* afforded a blue powder (1.32 g, 41%).

II. Spectral data

a) Spectral data for Li_3TREN^{TIPS}

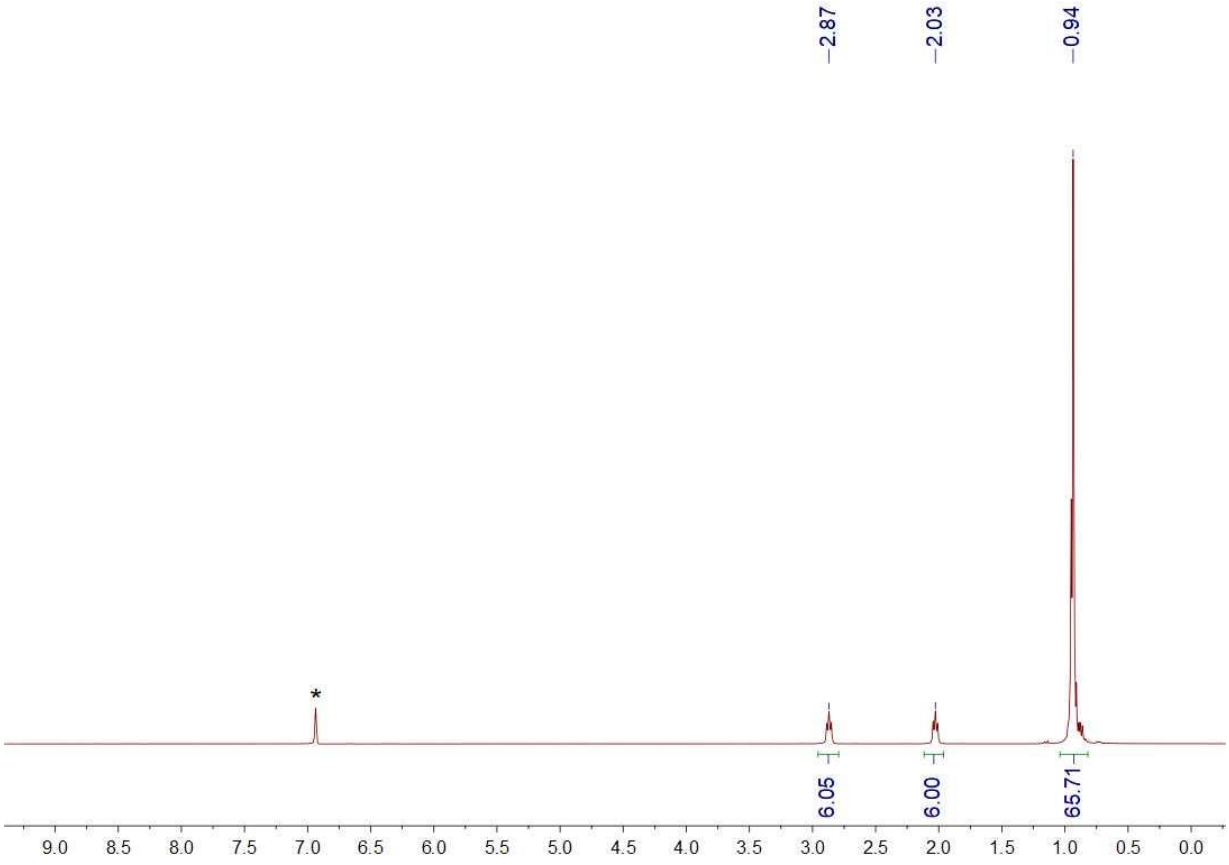

Figure S3. ^{1}H NMR spectrum of [Li_3TREN^{TIPS}] in C_6D_6. Solvent residual peak is indicated with *

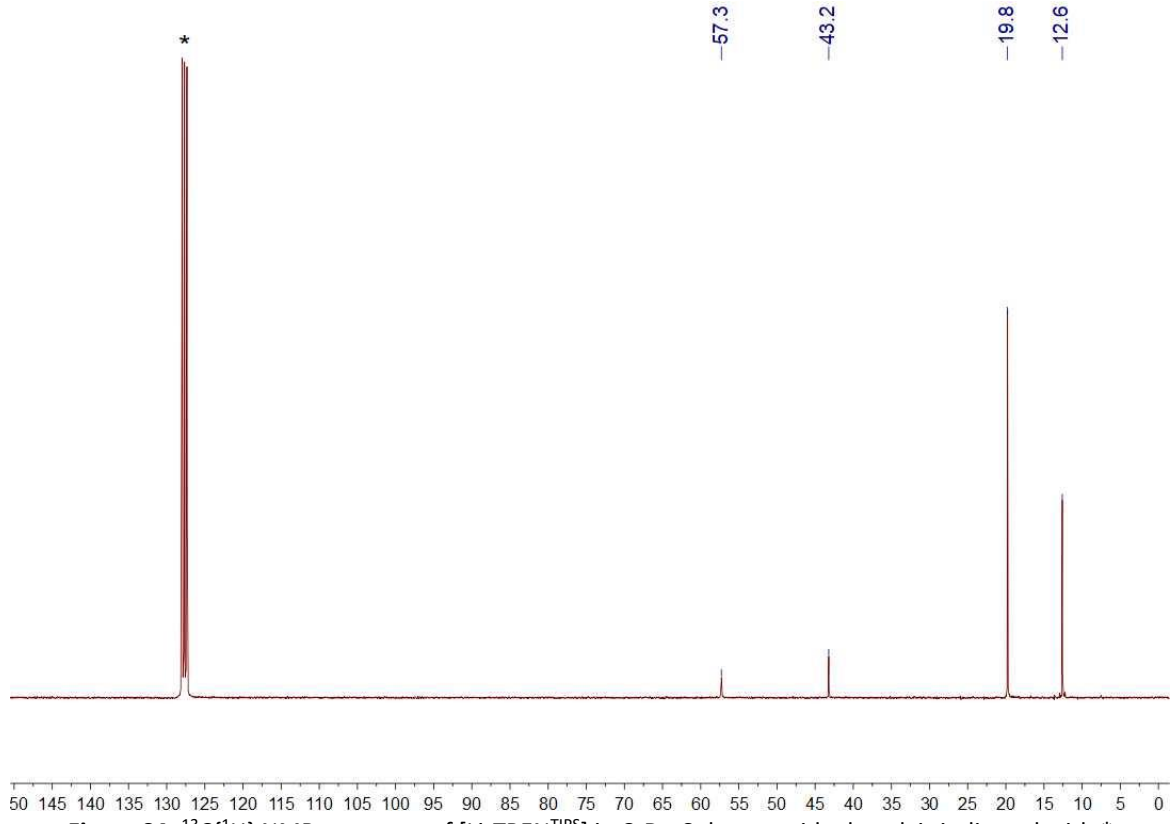

Figure S4. $^{13}C\{^{1}H\}$ NMR spectrum of [Li_3TREN^{TIPS}] in C_6D_6. Solvent residual peak is indicated with *

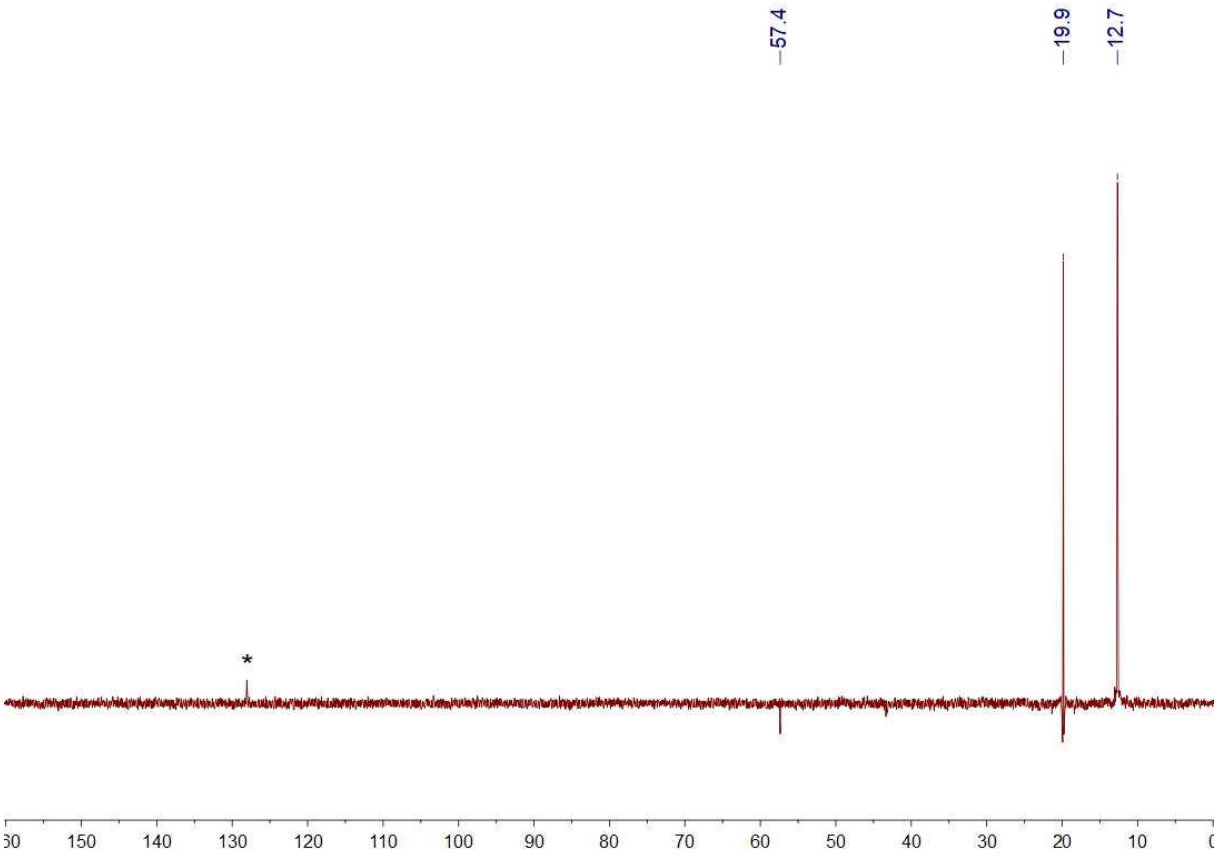

Figure S5. DEPT 135 $^{13}C\{^{1}H\}$ spectrum of [Li_3TREN^{TIPS}] in C_6D_6. Solvent residual peak is indicated with *

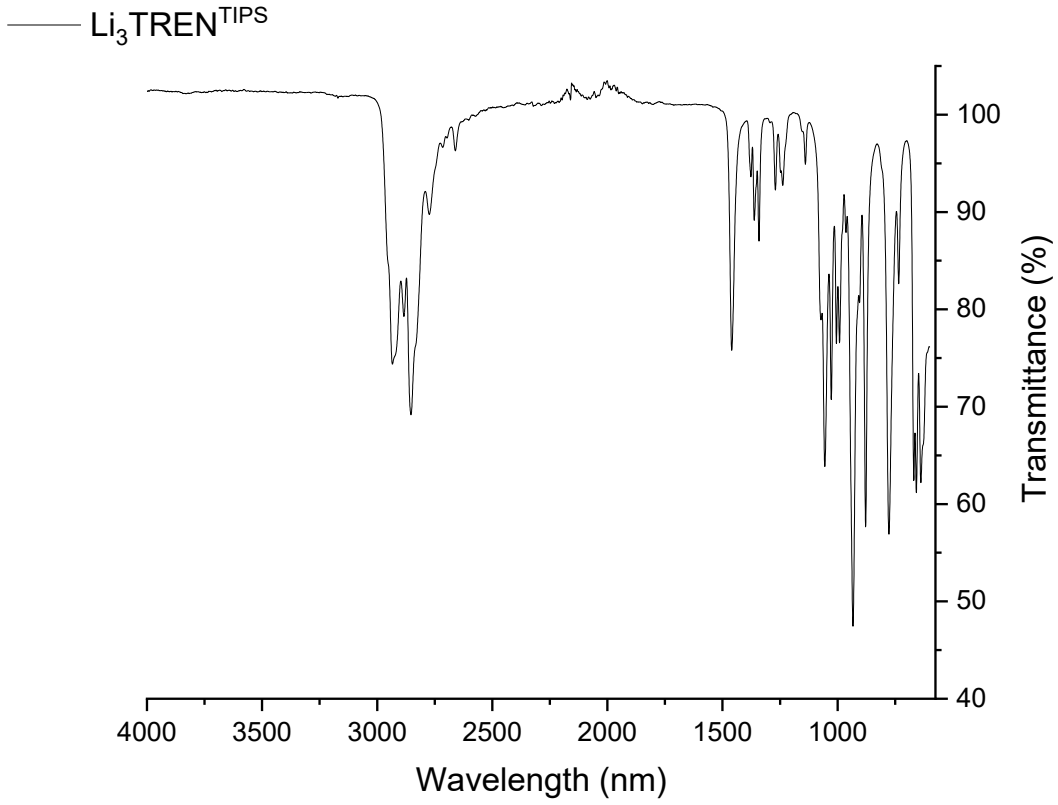

Figure S6. IR spectrum of neat Li_3TREN^{TIPS}

b) Spectral data for [Li(THF)$_4$][ICeTREN^{TIPS}] (1-LiI-THF$_4$)

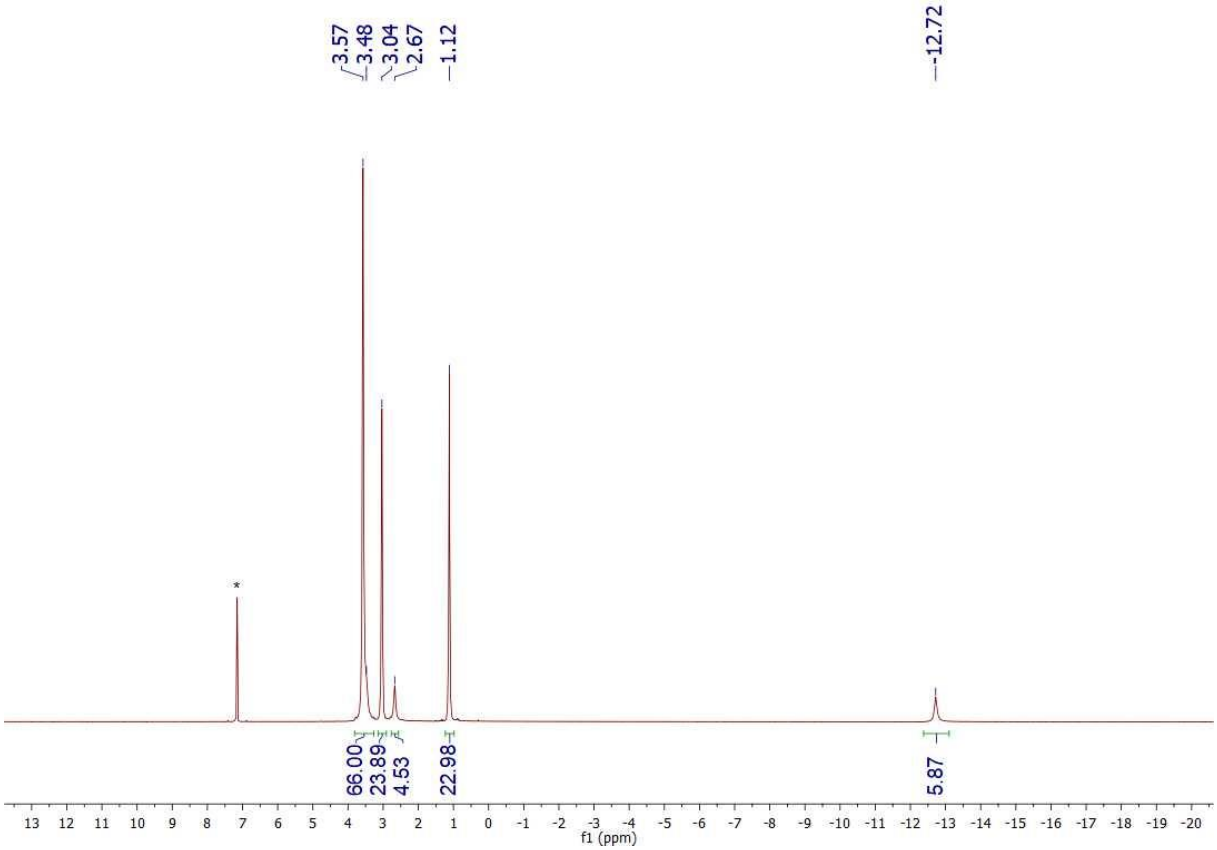

Figure S7. ^{1}H NMR of **1-LiI-THF$_4$** in C_6D_6 at 298 K. Solvent residual peak is indicated with *

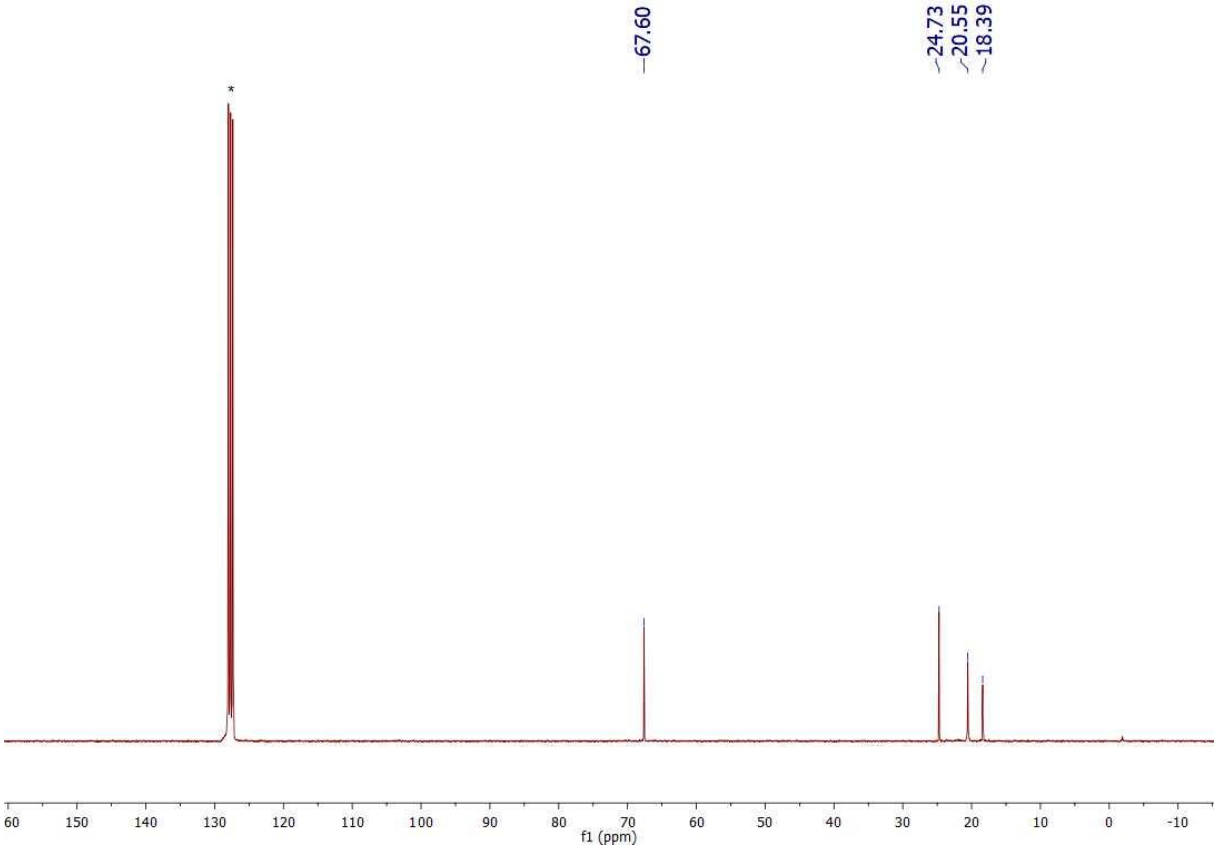

Figure S8. $^{13}C\{^{1}H\}$ NMR of **1-LiI-THF$_4$** in C_6D_6 at 298 K. Solvent residual peak is indicated with *

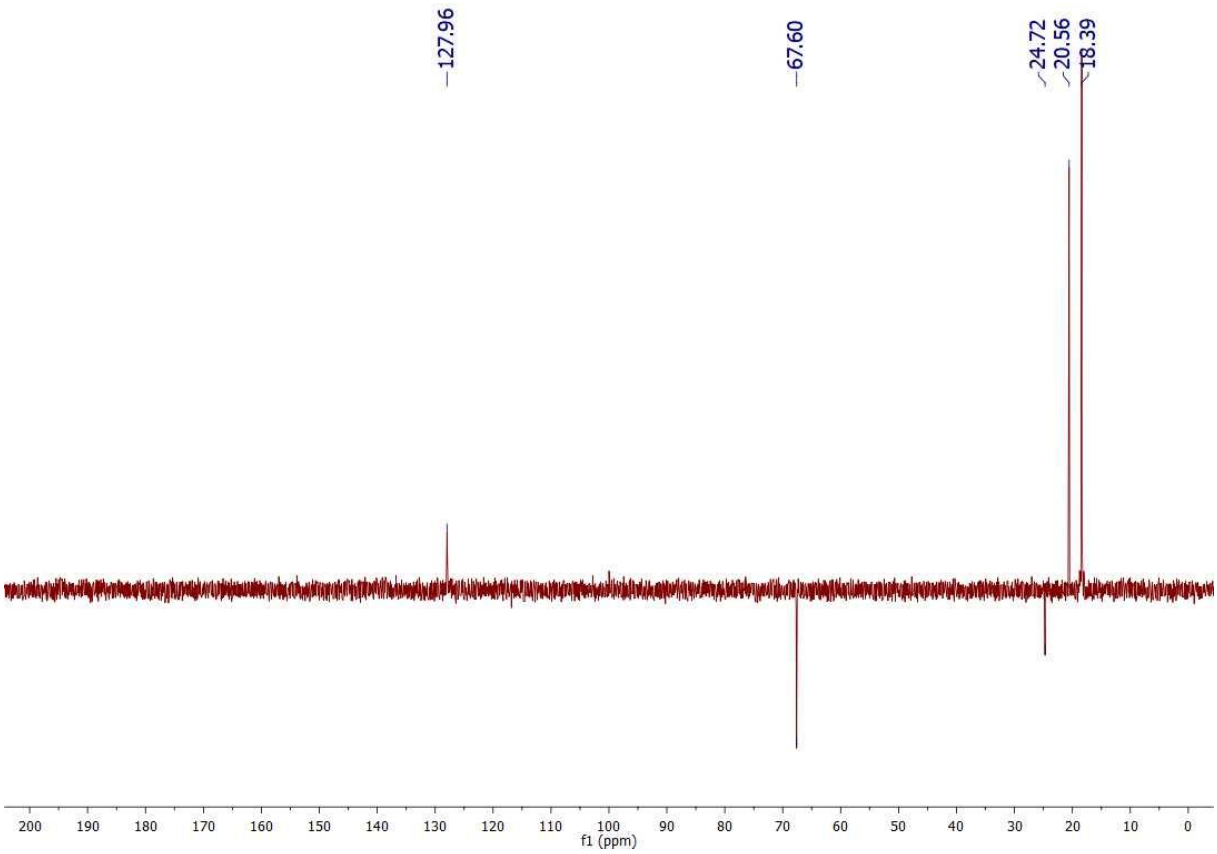

Figure S9. DEPT 135 $^{13}C\{^{1}H\}$ spectrum of 1-LiI-THF_4 in C_6D_6 at 298 K

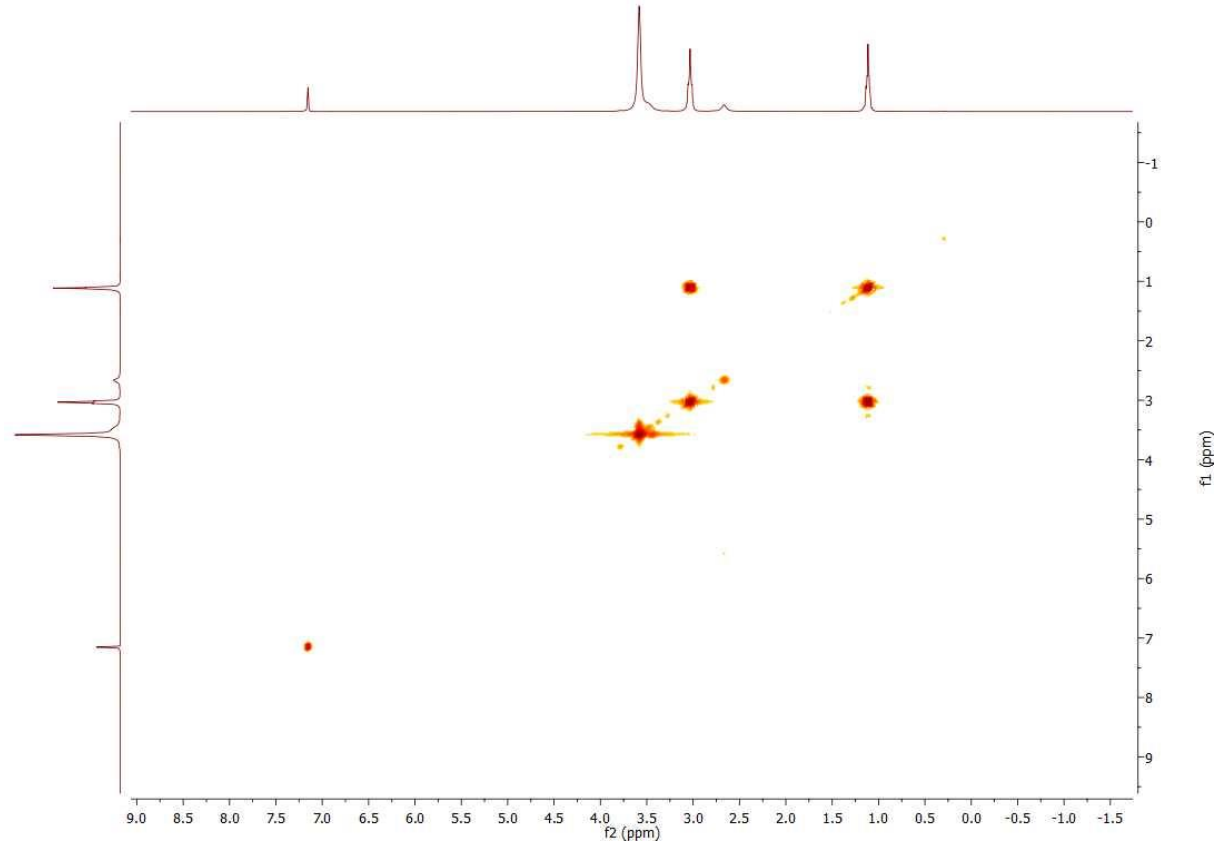

Figure S10. ^{1}H-^{1}H COSY spectrum of **1-LiI-THF_4** in C_6D_6 at 298 K

c) Spectral data for [Ce^{III}TREN^{TIPS}] (1)

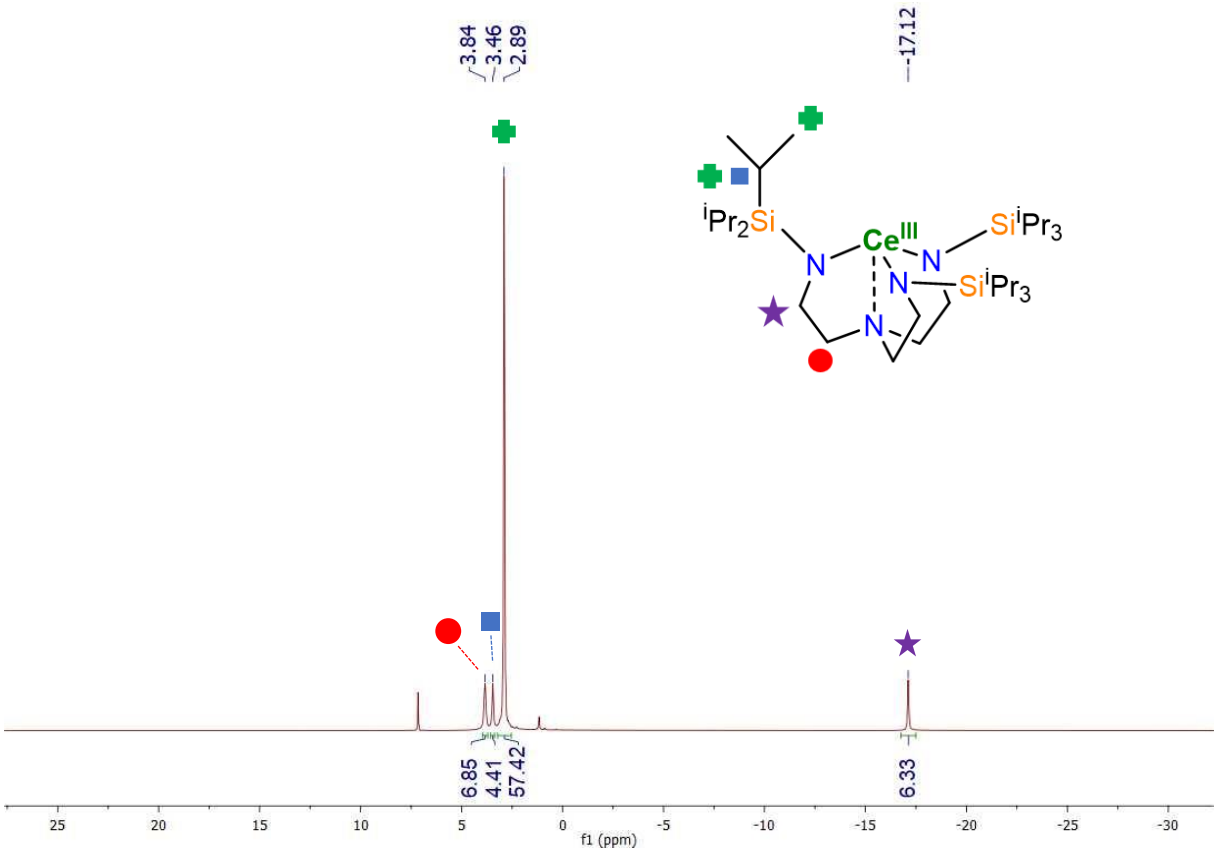

Figure S11. ^{1}H NMR of **1** in C_6D_6 at 298 K. Residual peaks at 2.49 ppm and 1.15 ppm correspond to the formation of H_3TREN^{TIPS}, created by the hydrolysis of the complex by the residual water in the deuterated solvent.

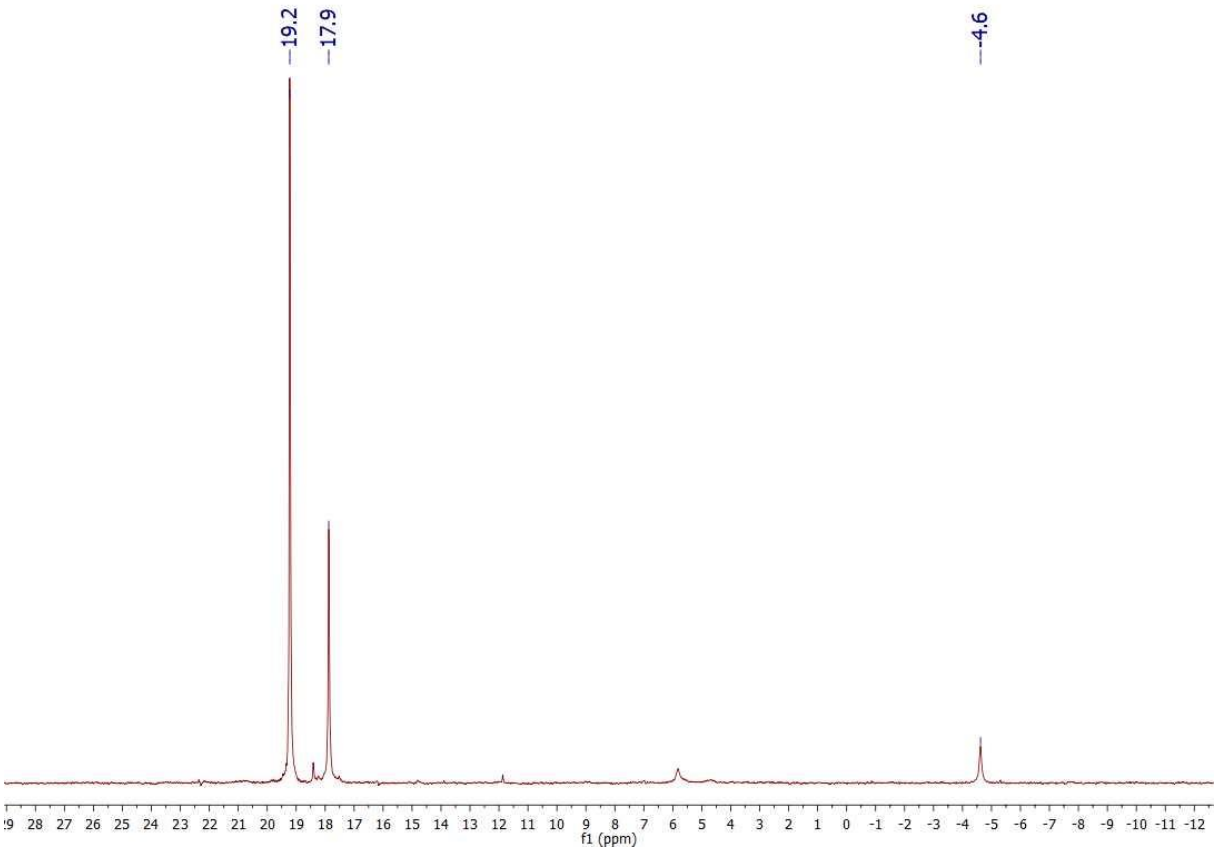

Figure S12. ^{13}C NMR of **1** in C_6D_6 at 298 K

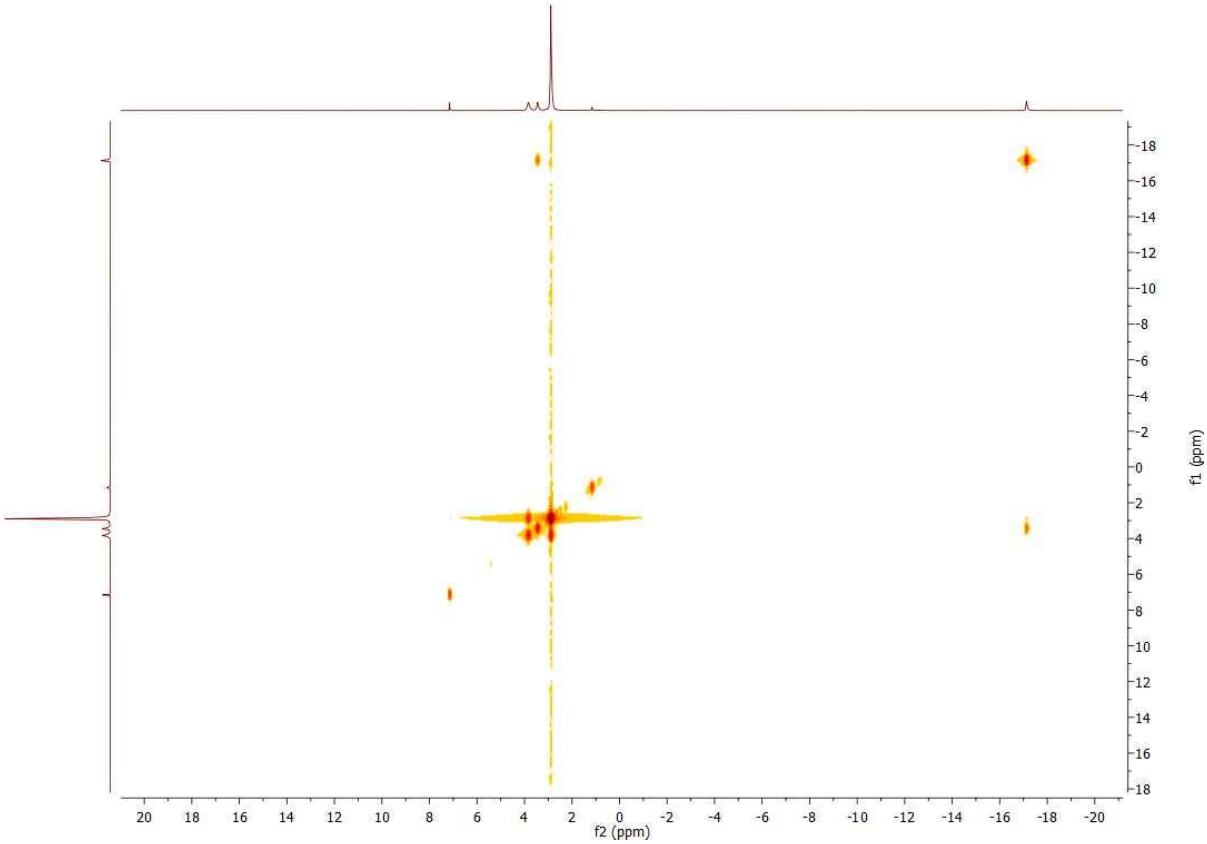

Figure S13. ^{1}H-^{1}H COSY spectrum of **1** in C_6D_6 at 298 K

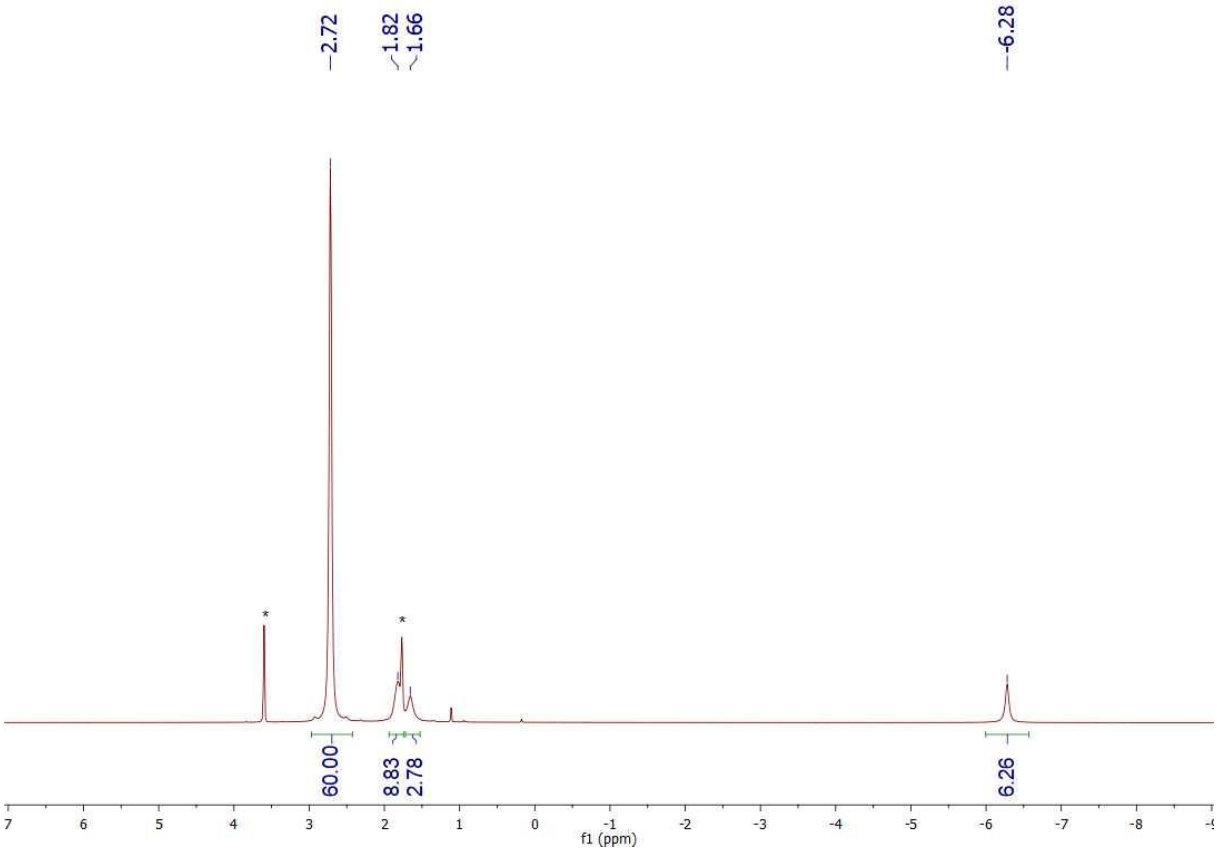

Figure S14. ^{1}H NMR of **1** in THF-d_8 at 298 K

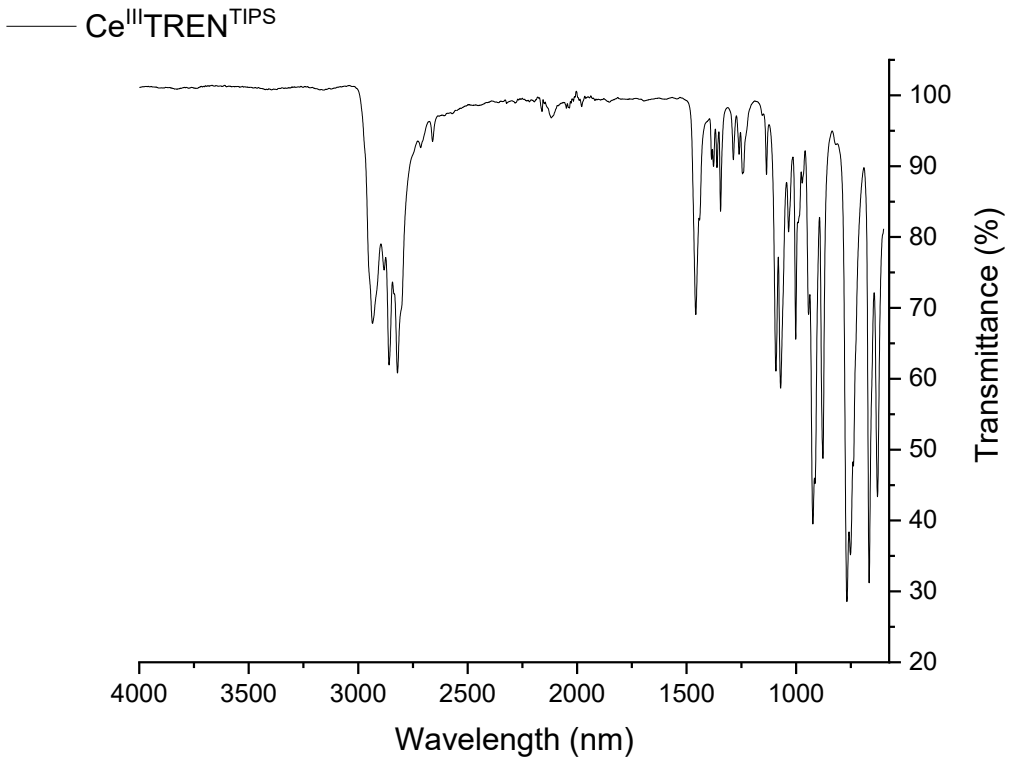

Figure S15. IR spectrum of **1** at 298 K

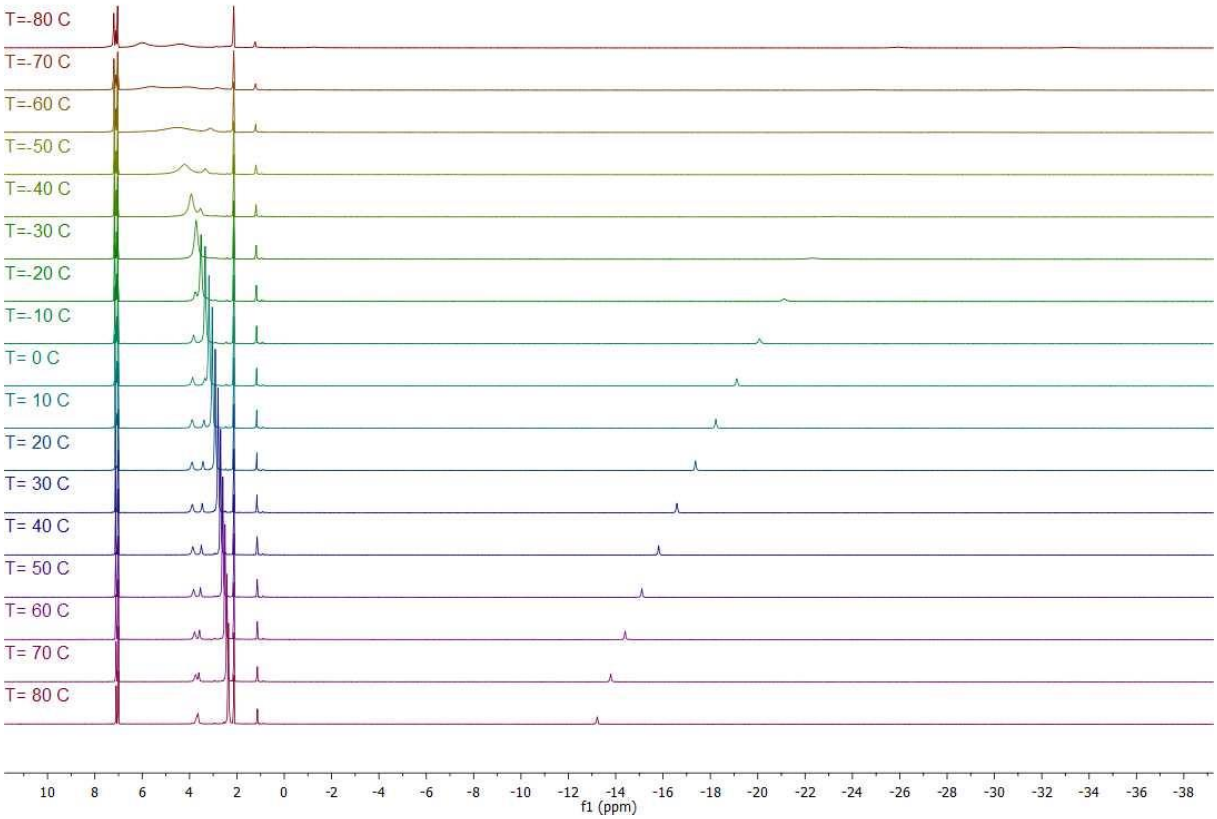

Figure S16. VT NMR of **1** in toluene-d_8 in the -80°C to 80°C temperature range

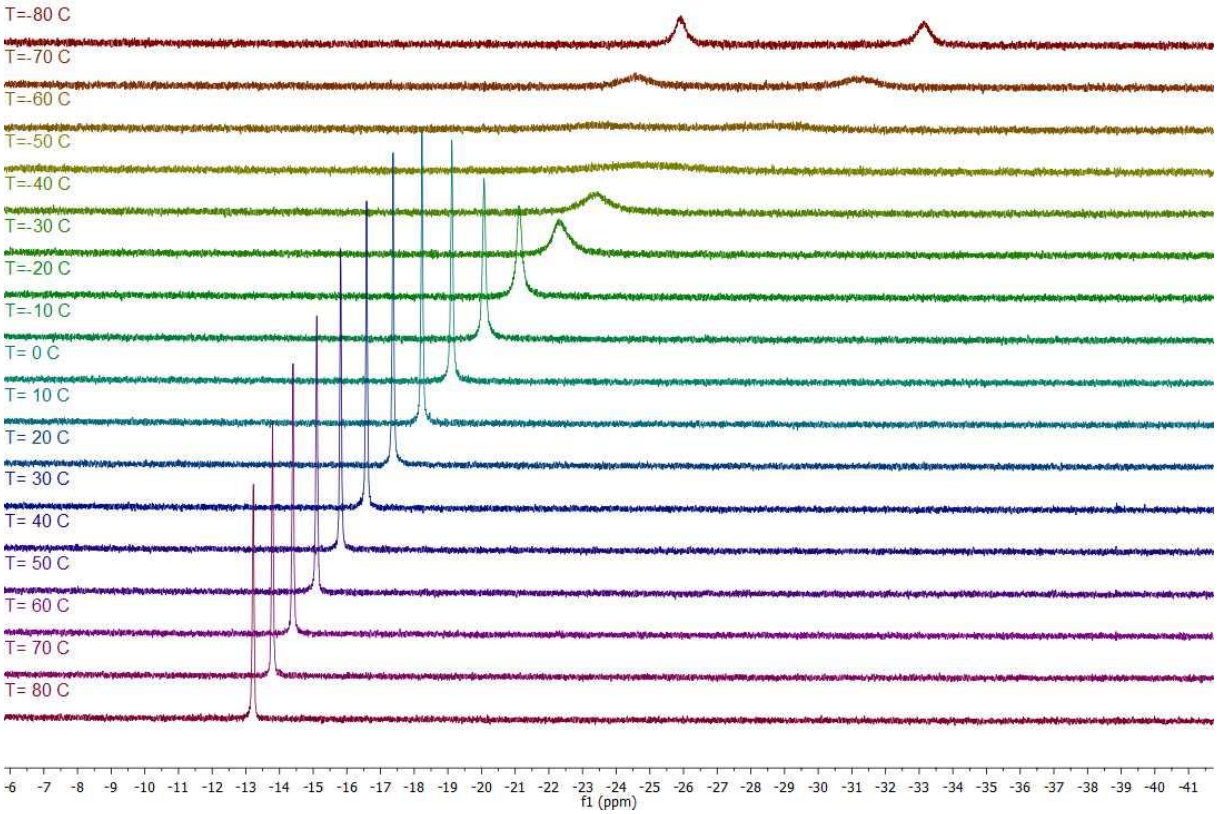

Figure S17. VT NMR of **1** (zoom on the -8 ppm to -38 ppm range) in toluene-d_8 in the -80°C to 20°C temperature range

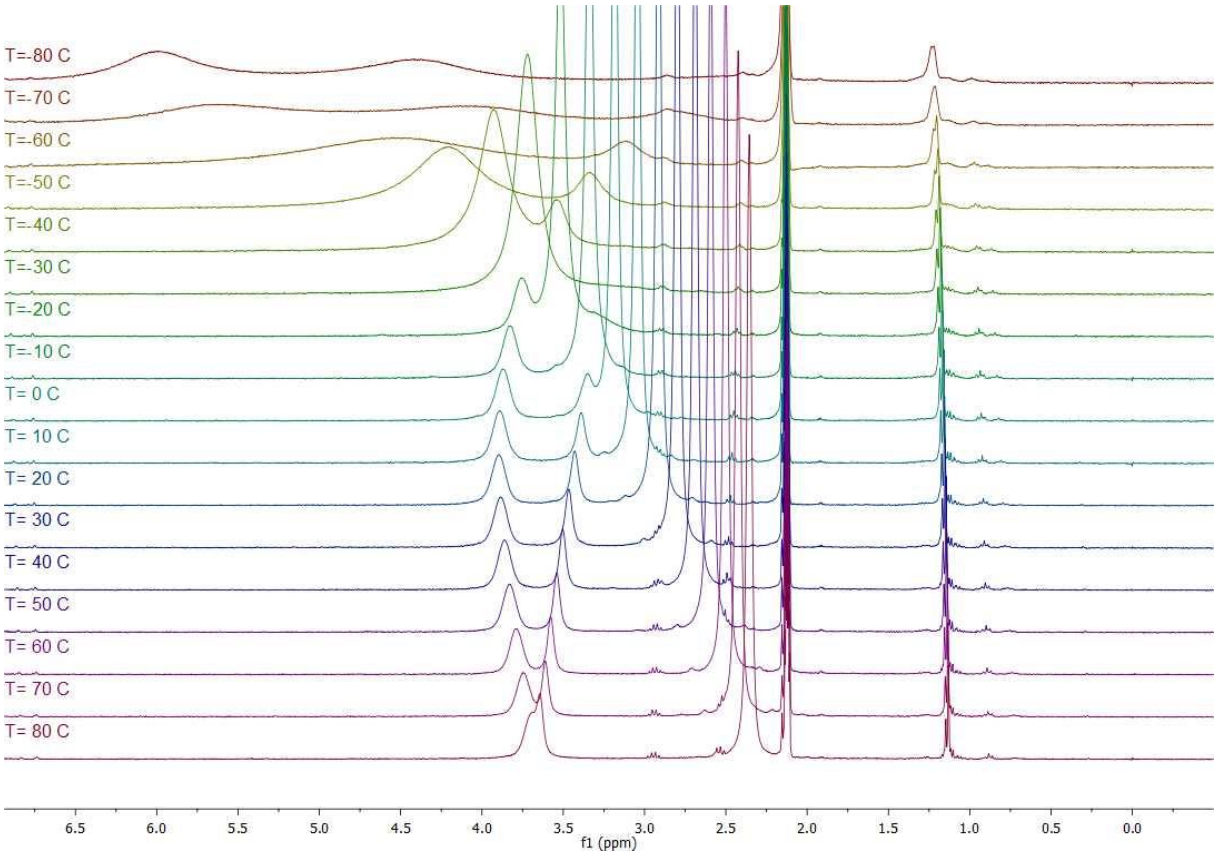

Figure S18. VT NMR of **1** (zoom on the 6 ppm to 0 ppm range) in toluene-d_8 in the -80°C to 20°C temperature range

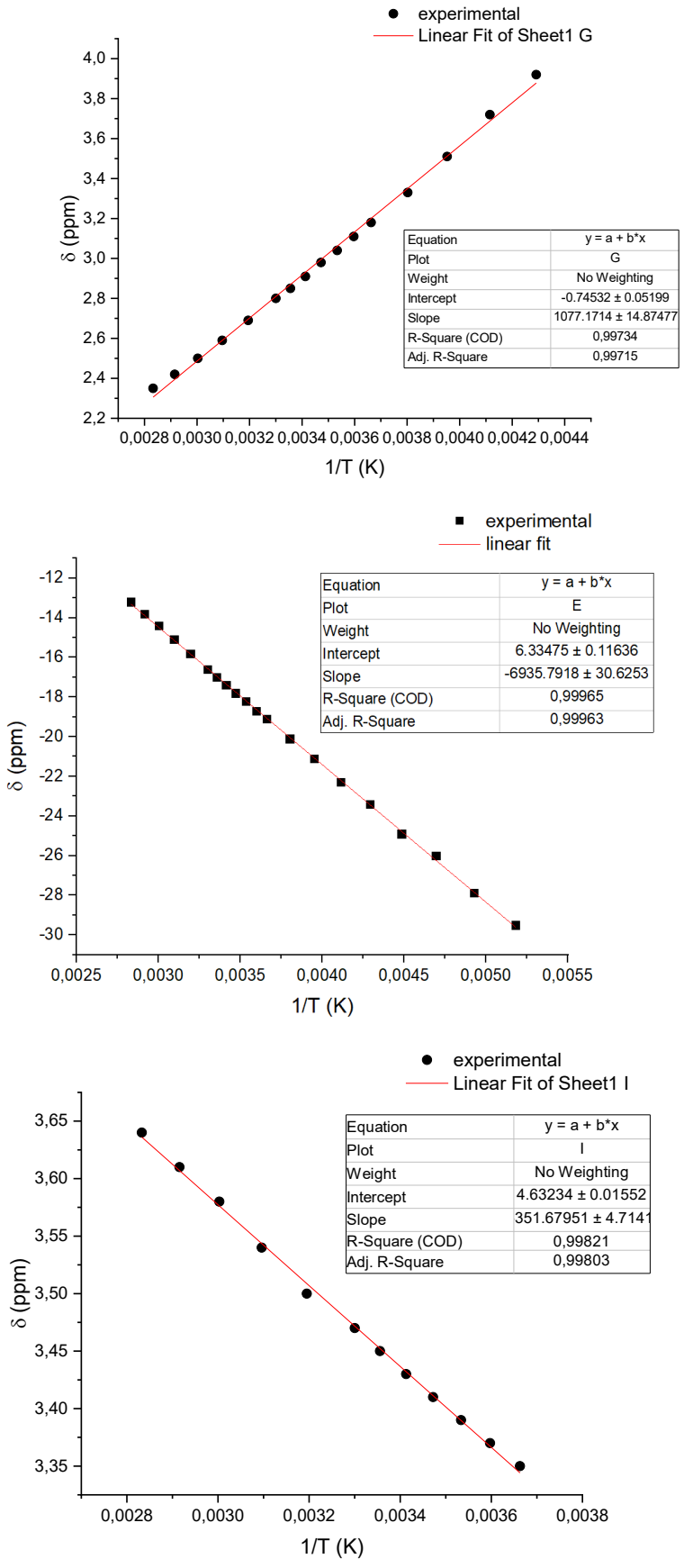

Figure S19. Linear regressions δ=f(1/T) on peaks at -17 ppm, 3.2 ppm, and 3.5 ppm in toluene-d_8 in the -80°C to 80°C temperature range for **1**

d) Spectral data for [ClCe^{IV}TREN^{TIPS}] (2-Cl)

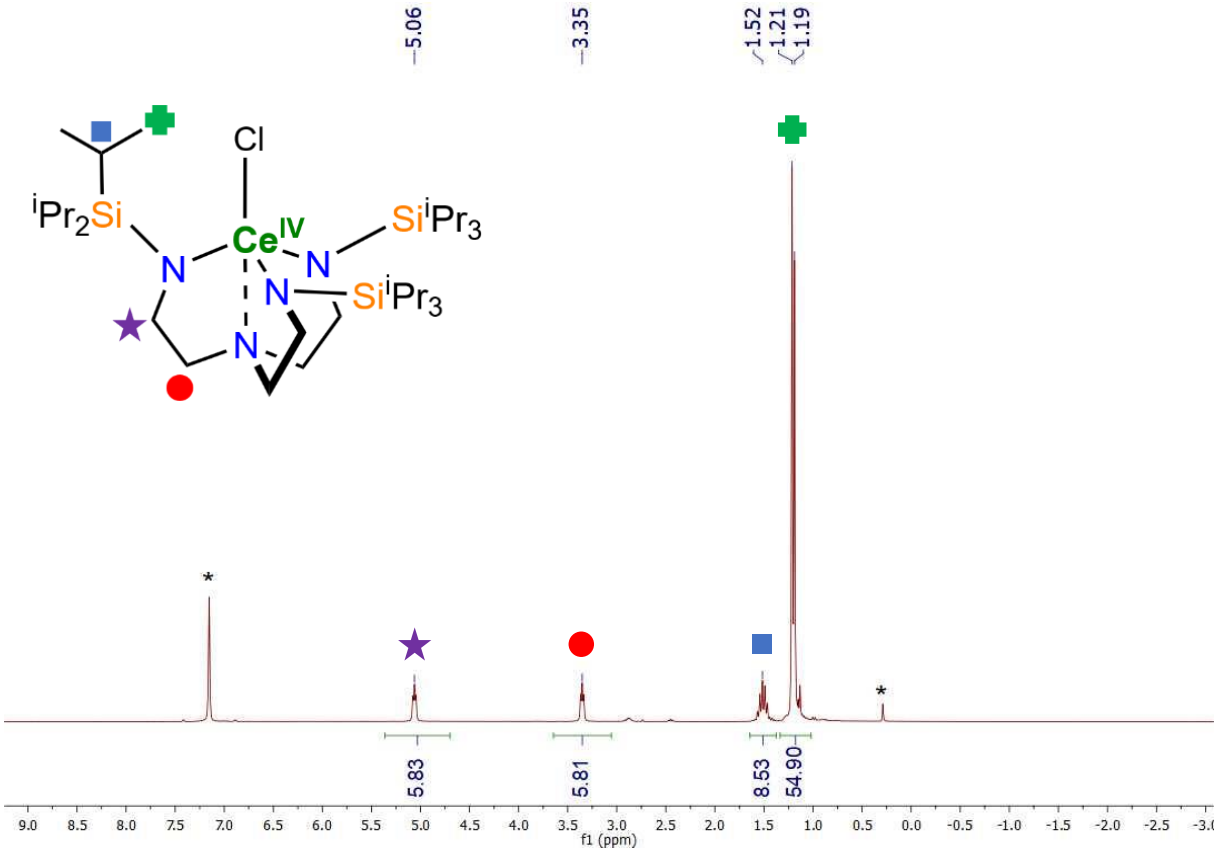

Figure S20. ^{1}H NMR of **2-Cl** in C_6D_6 at 298 K. Residual peaks at 2.86 ppm and 2.45 ppm correspond to the formation of H_3TREN^{TIPS}, created by the hydrolysis of the complex by the residual water in the deuterated solvent. Solvent residual peak and residues of silicon grease are indicated with *

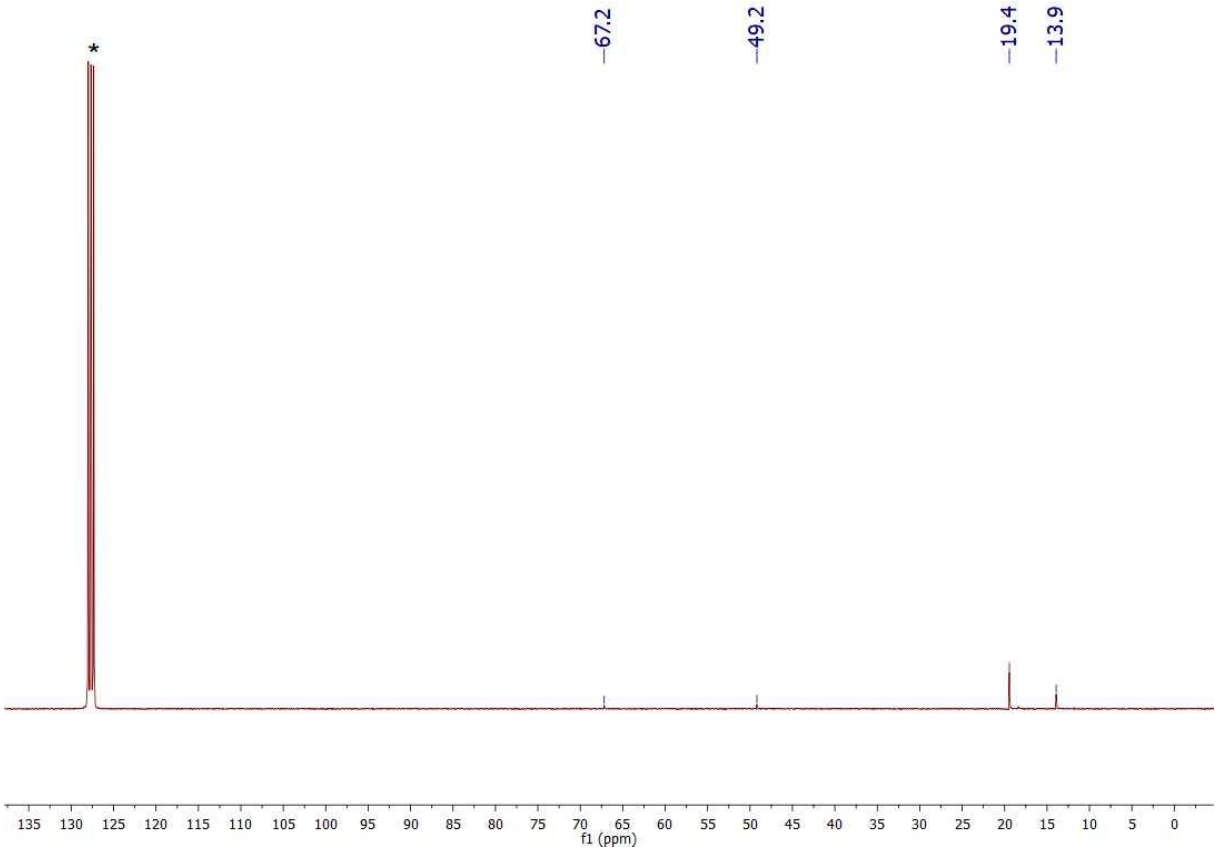

Figure S21. $^{13}C\{^{1}H\}$ spectrum of **2-Cl** in C_6D_6 at 298 K. Solvent residual peak is indicated with *

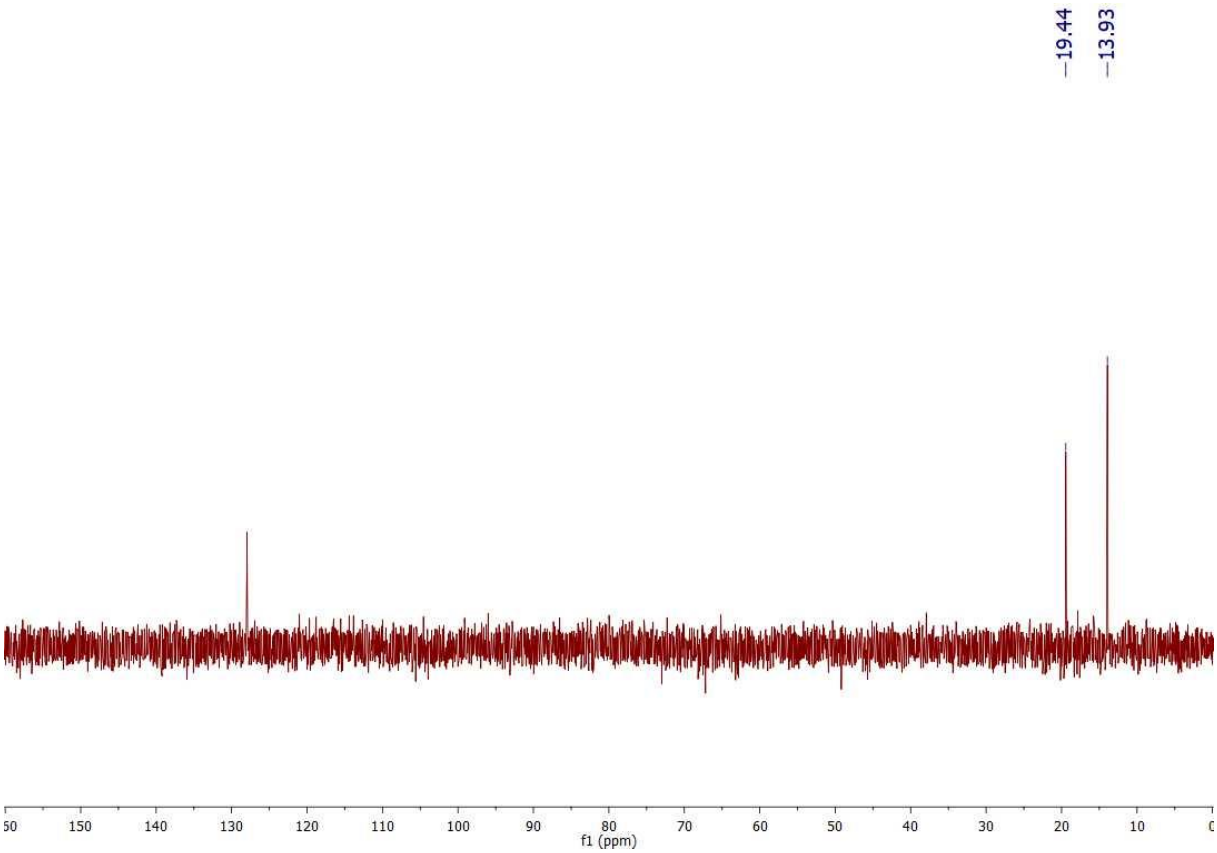

Figure S22. DEPT 135 $^{13}C\{^{1}H\}$ spectrum of **2-Cl** in C_6D_6 at 298 K

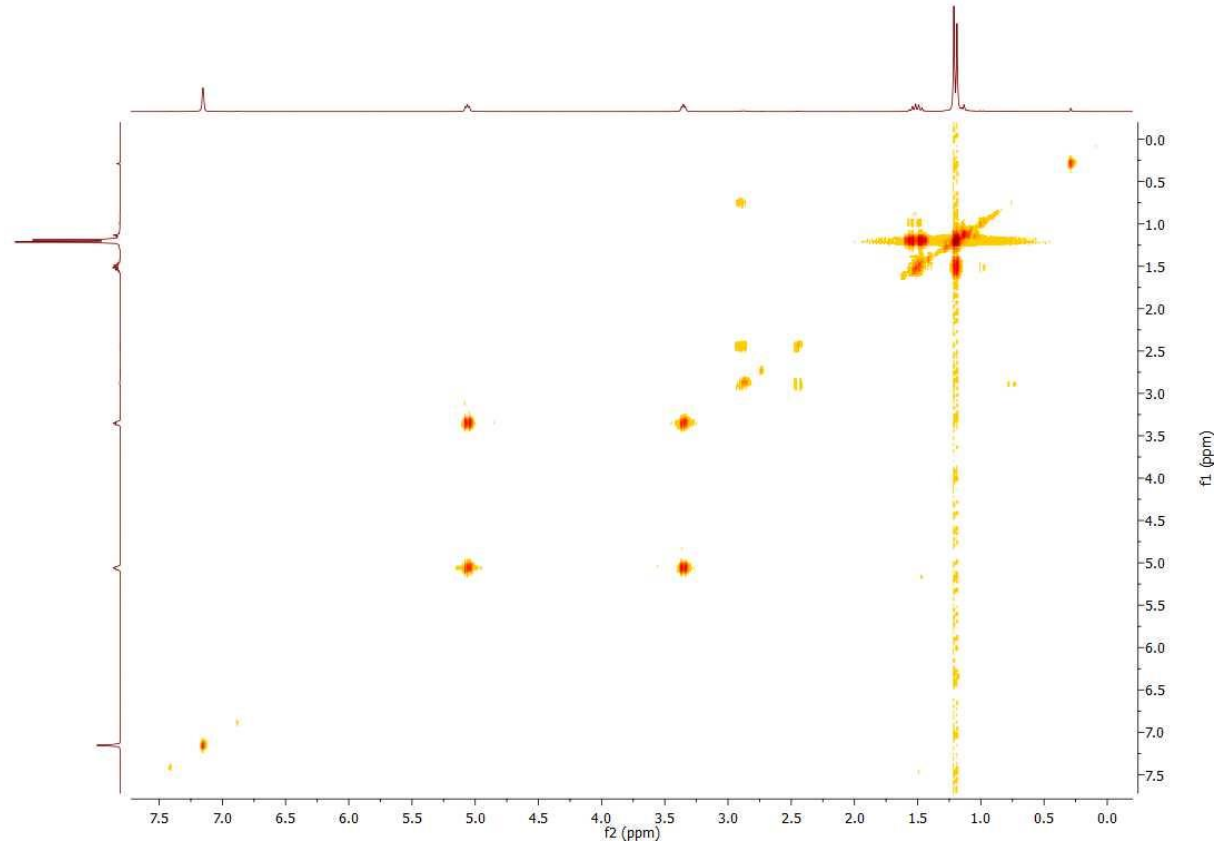

Figure S23. ^{1}H-^{1}H COSY spectrum of **2-Cl** in C_6D_6 at 298 K

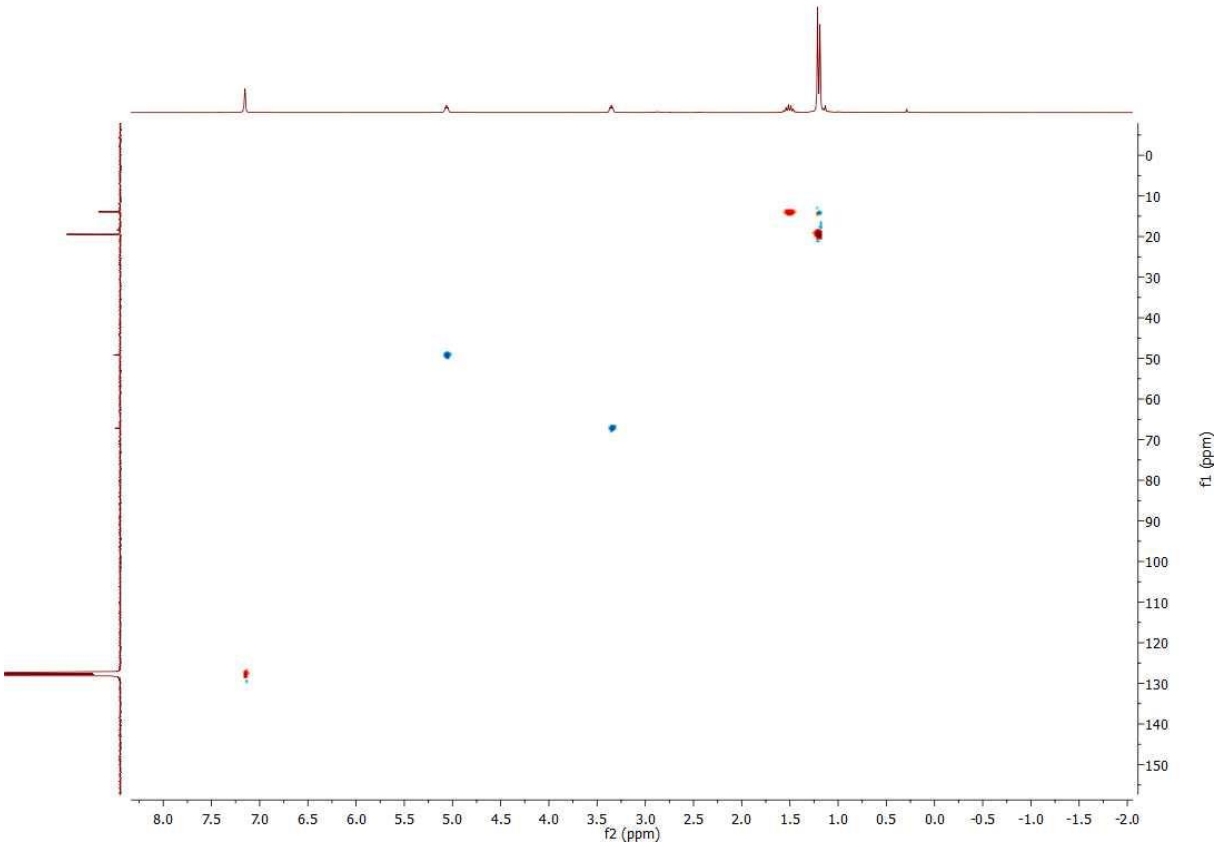

Figure S24. ^{1}H-^{13}C HSQC spectrum of **2-Cl** in C_6D_6 at 298 K

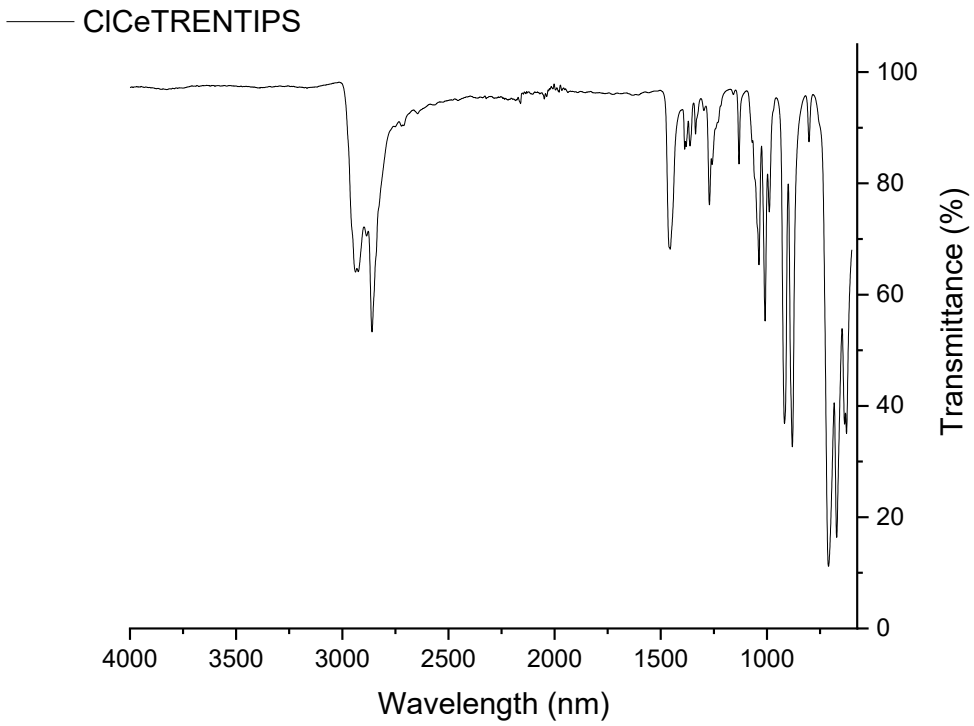

Figure S25. IR spectrum of **2-Cl** at 298 K

e) Spectral data for [BrCe^{IV}TREN^{TIPS}] (2-Br)

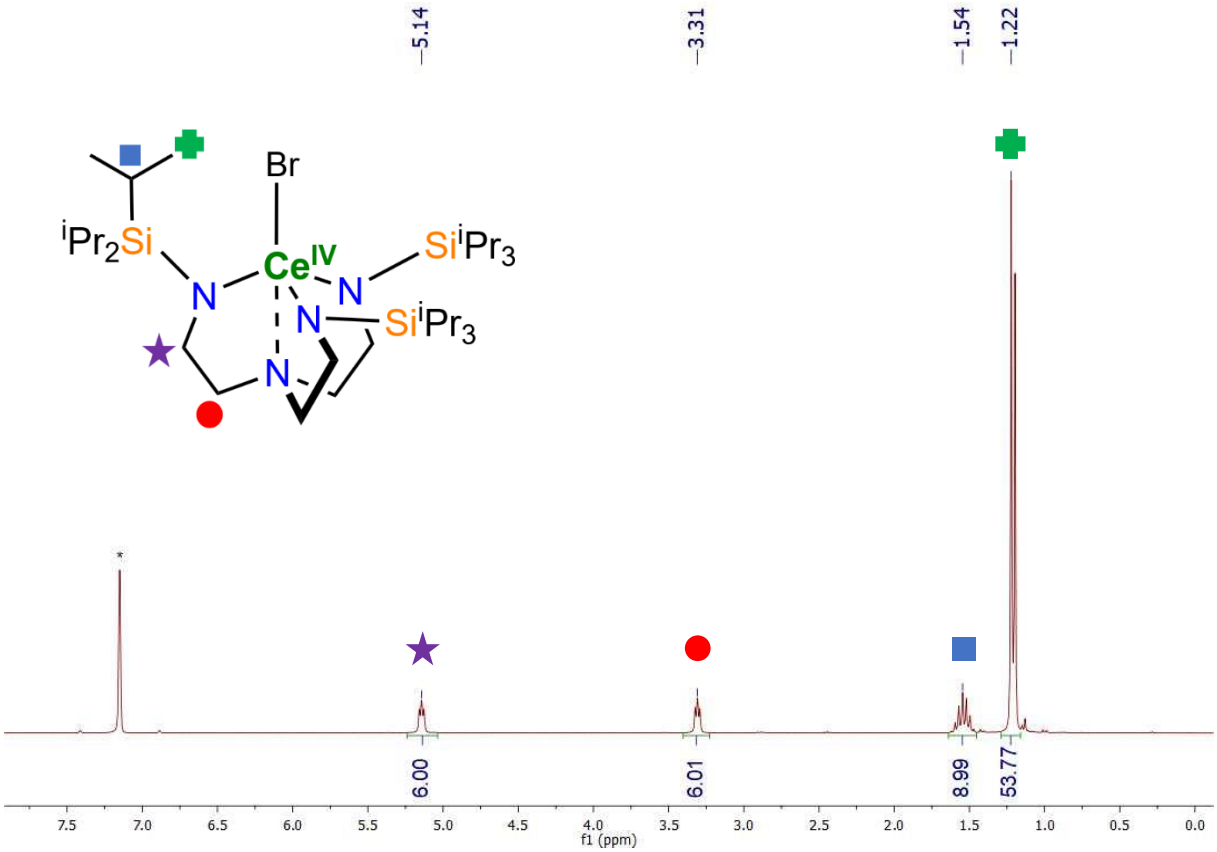

Figure S26. ^{1}H NMR spectrum of **2-Br** in C_6D_6 at 298 K. Solvent residual peak is indicated with *

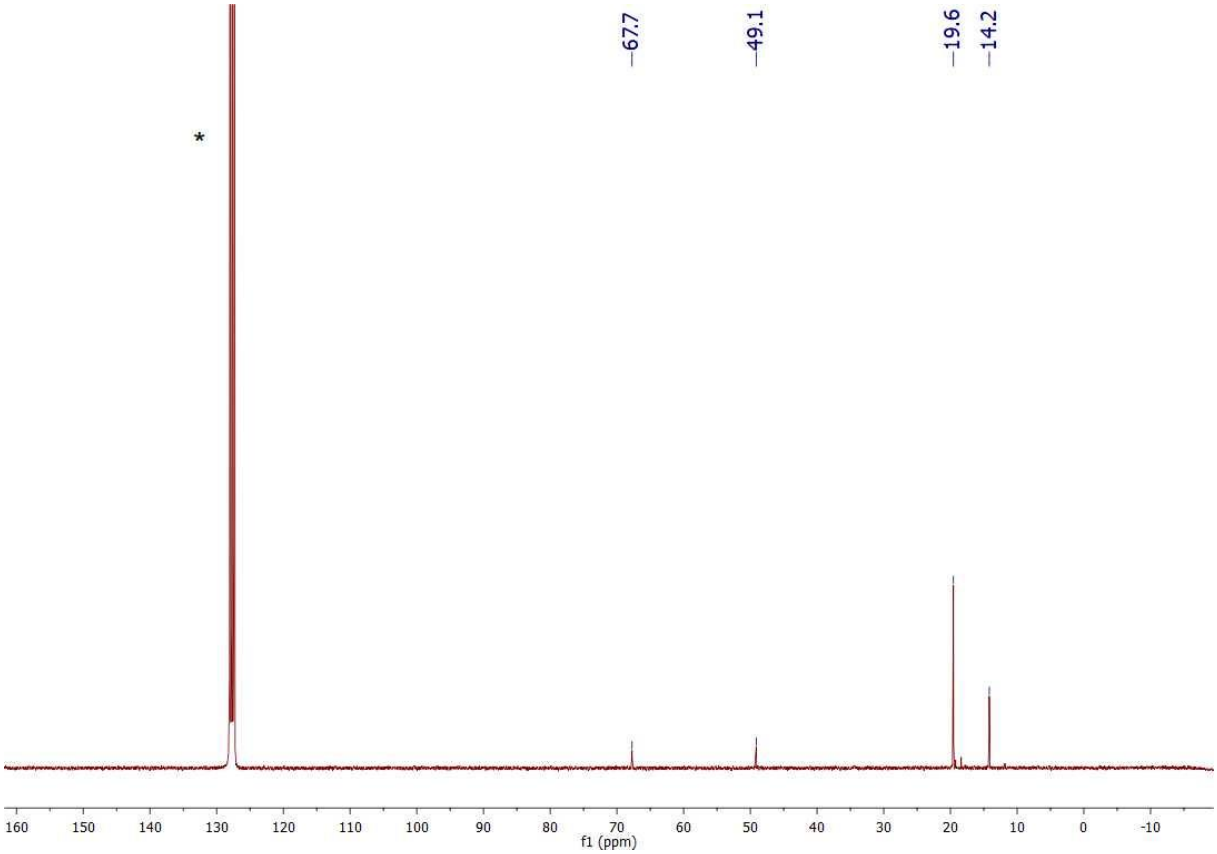

Figure S27. $^{13}C\{^{1}H\}$ NMR spectrum of **2-Br** in C_6D_6 at 298 K. Solvent residual peak is indicated with *

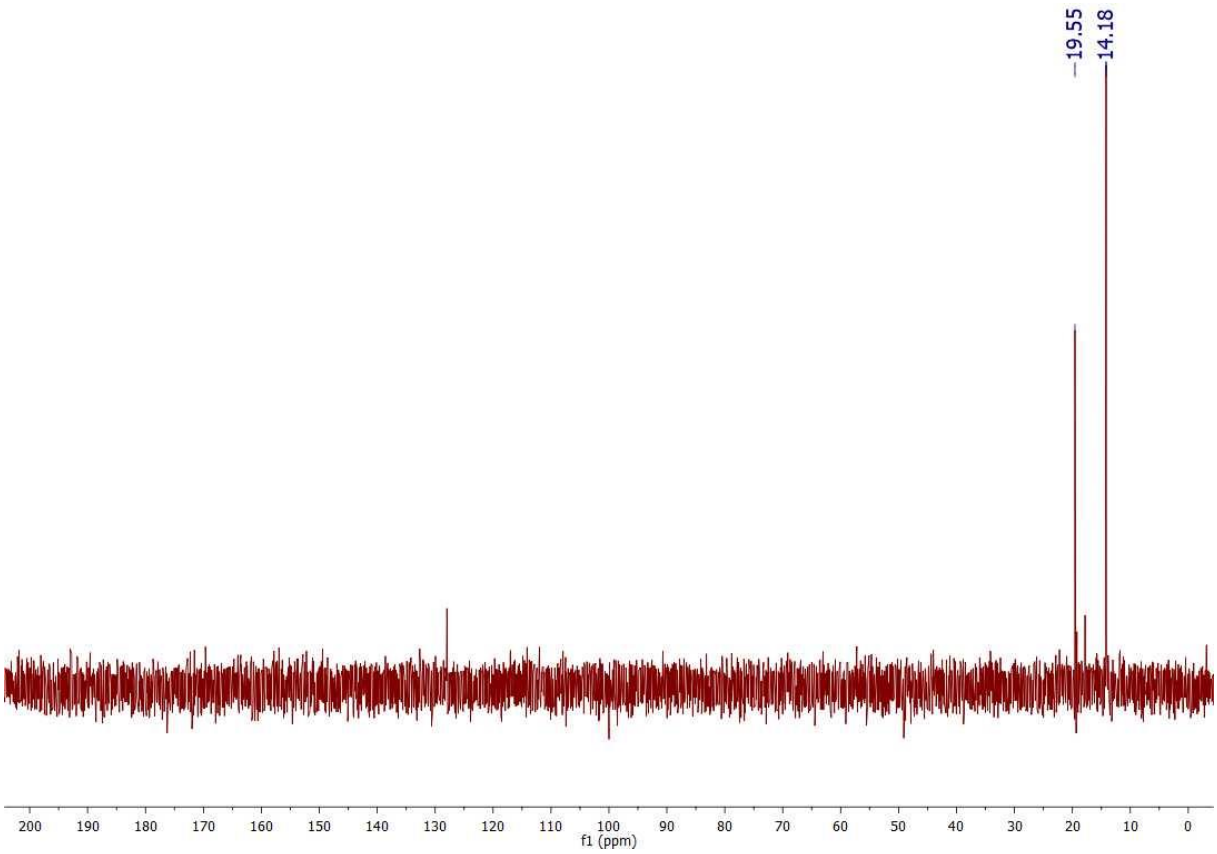

Figure S28. DEPT 135 $^{13}C\{^{1}H\}$ spectrum of **2-Br** in C_6D_6 at 298 K

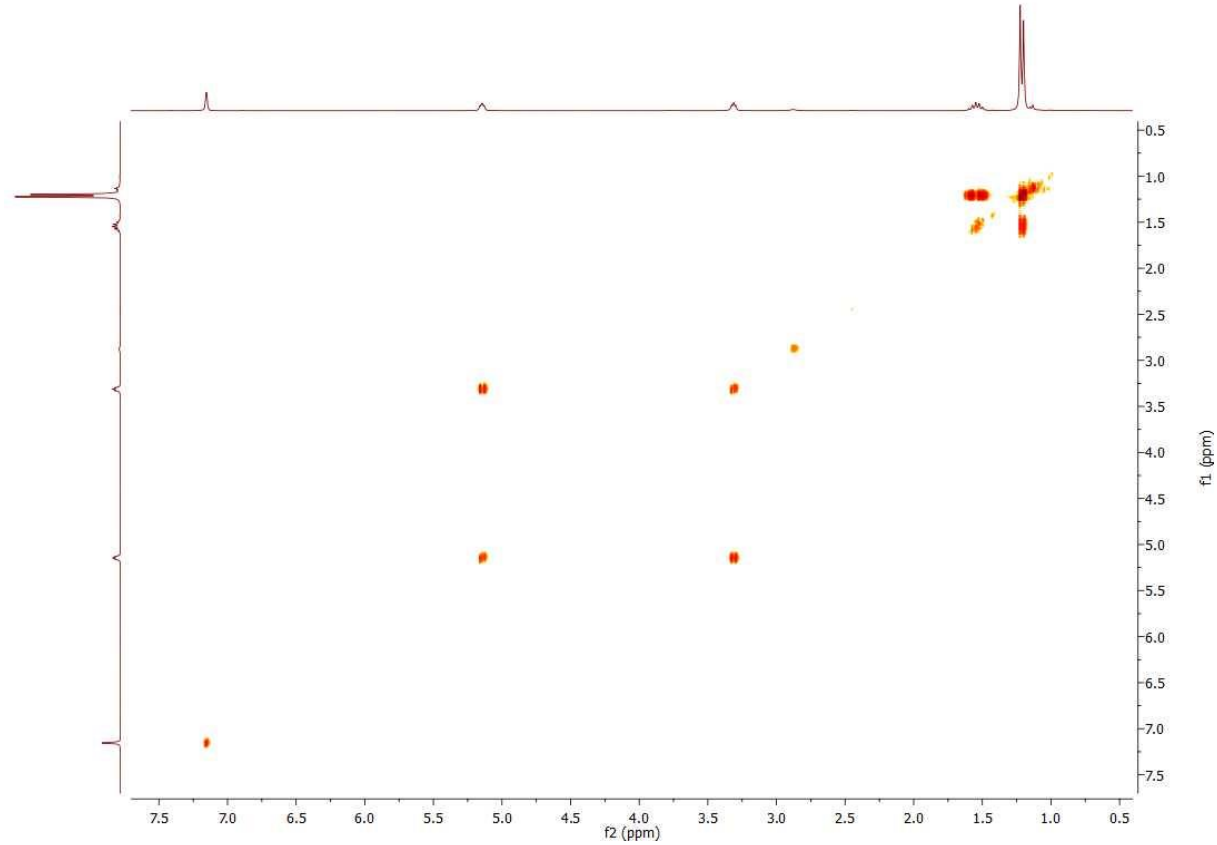

Figure S29. ^{1}H-^{1}H COSY spectrum of **2-Br** in C_6D_6 at 298 K

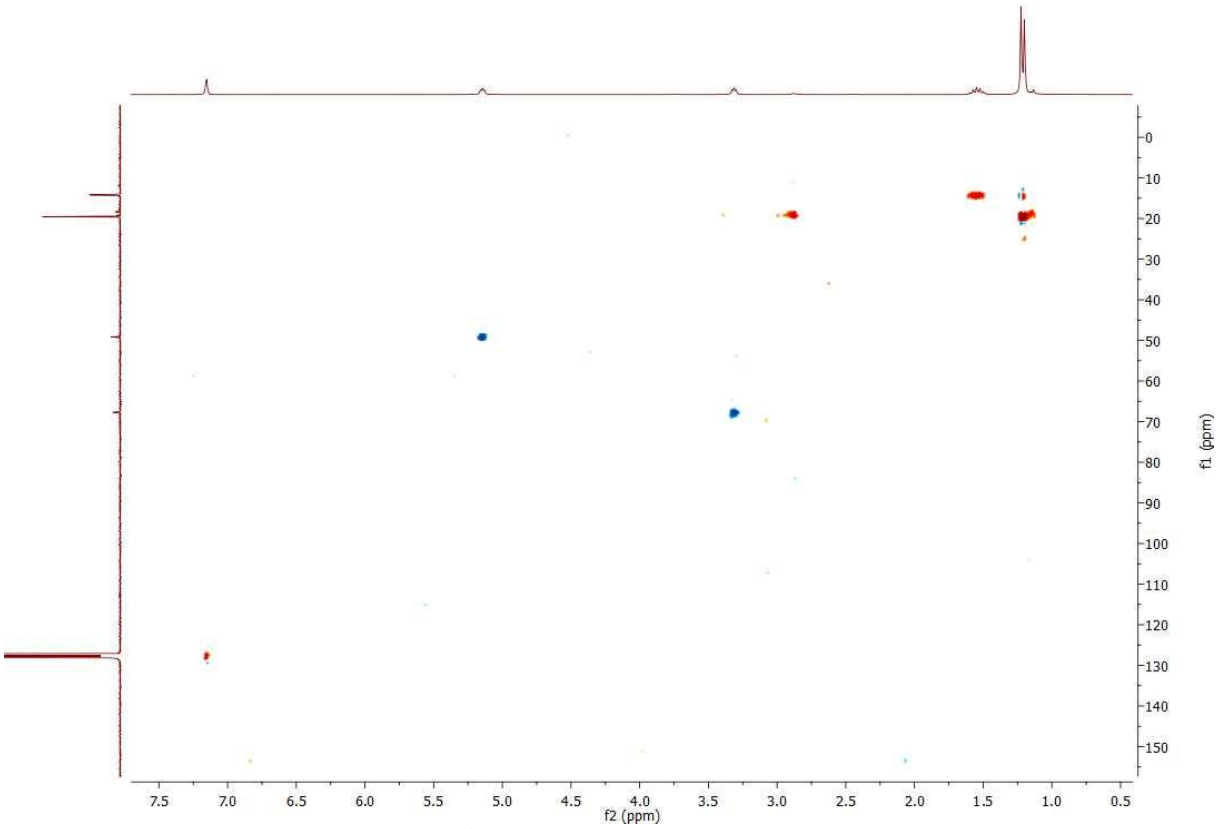

Figure S30. ^{1}H-^{13}C HSQC spectrum of **2-Br** in C_6D_6 at 298 K

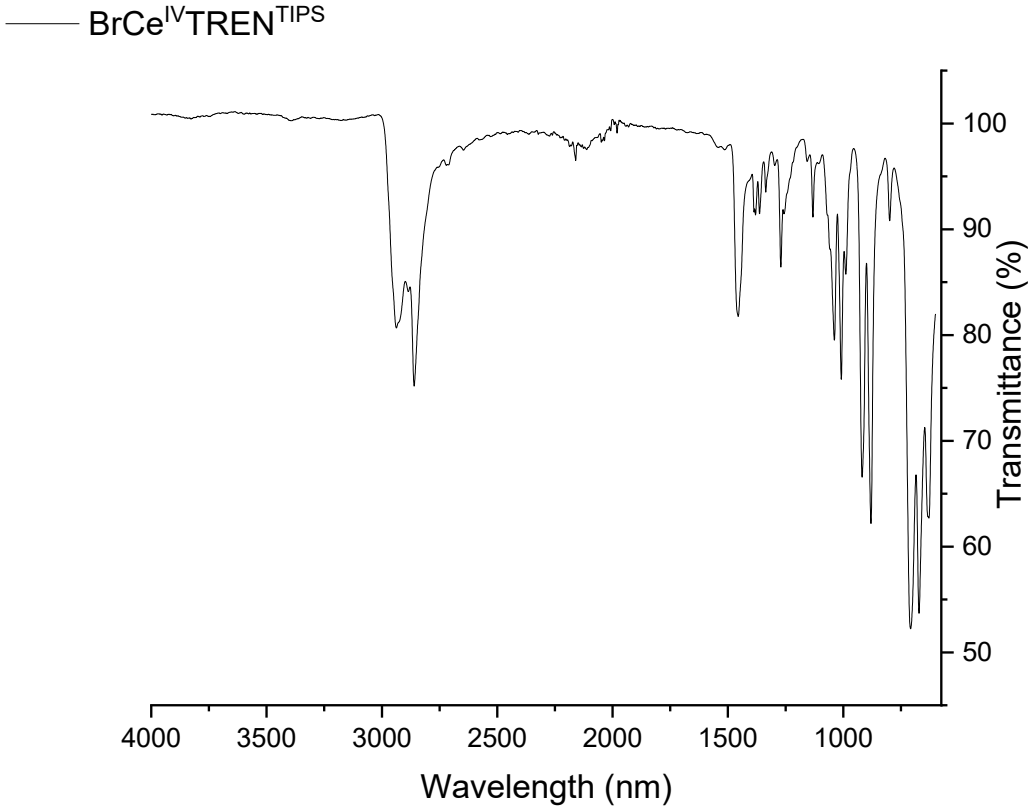

Figure S31. IR spectrum of **2-Br** at 298 K

f) Spectral data for [FCe^{IV}TREN^{TIPS}] (2-F)

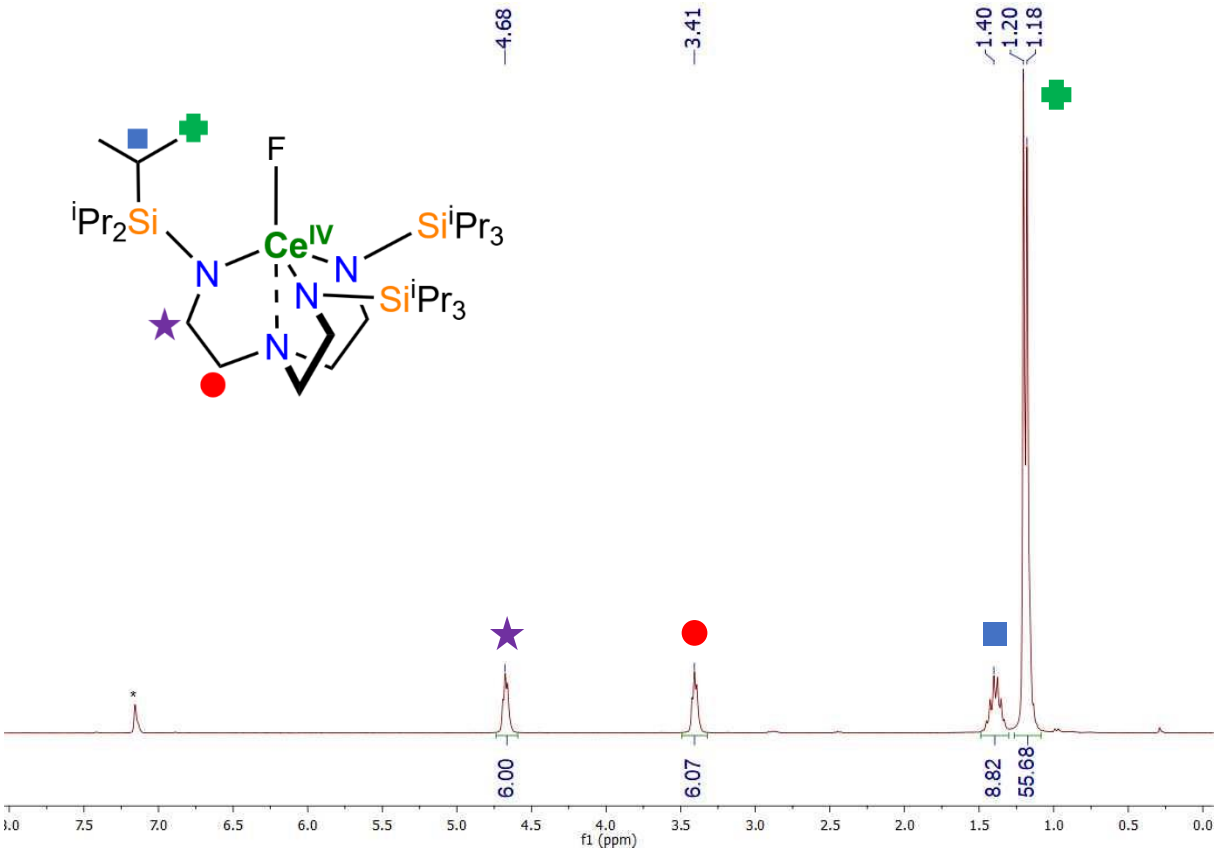

Figure S32. ^{1}H NMR spectrum of **2-F** in C_6D_6 at 298 K. Solvent residual peak is indicated with *

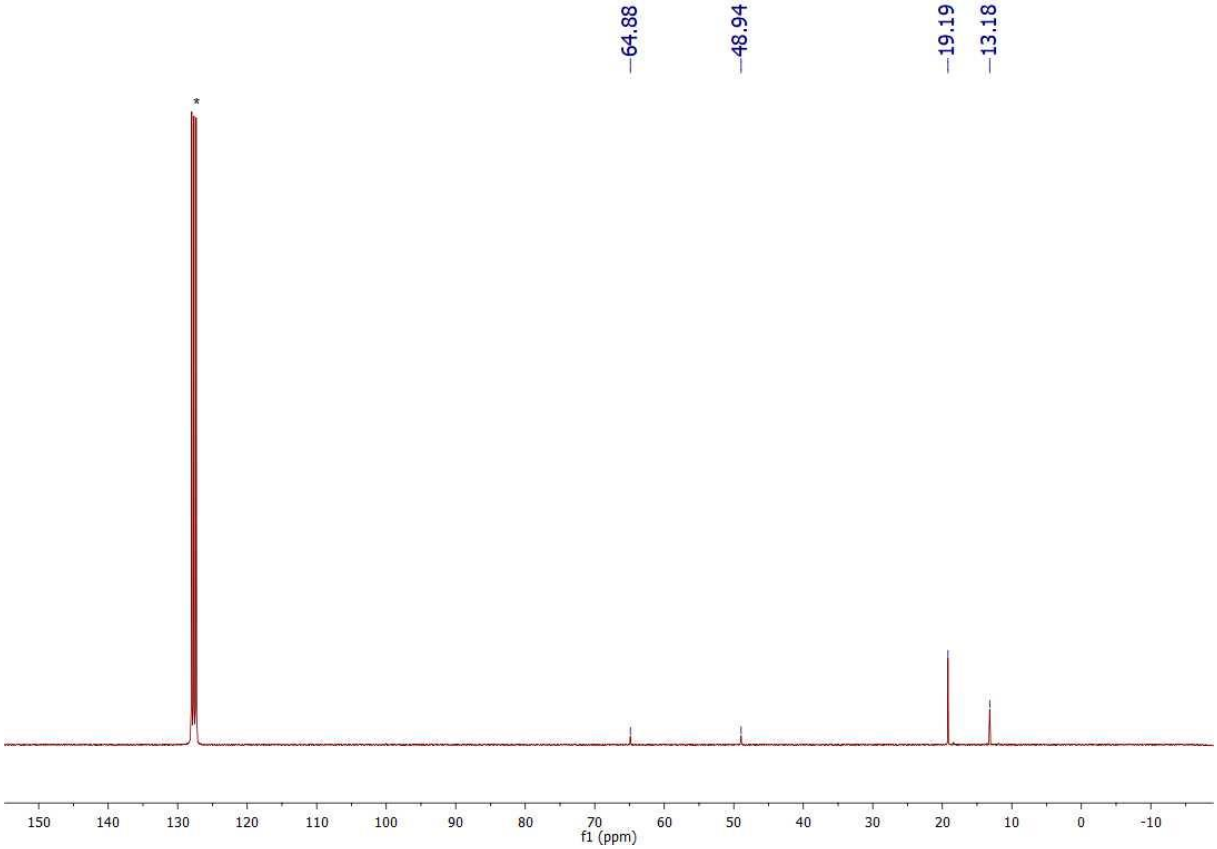

Figure S33. $^{13}C\{^{1}H\}$ NMR spectrum of **2-F** in C_6D_6 at 298 K. Solvent residual peak is indicated with *

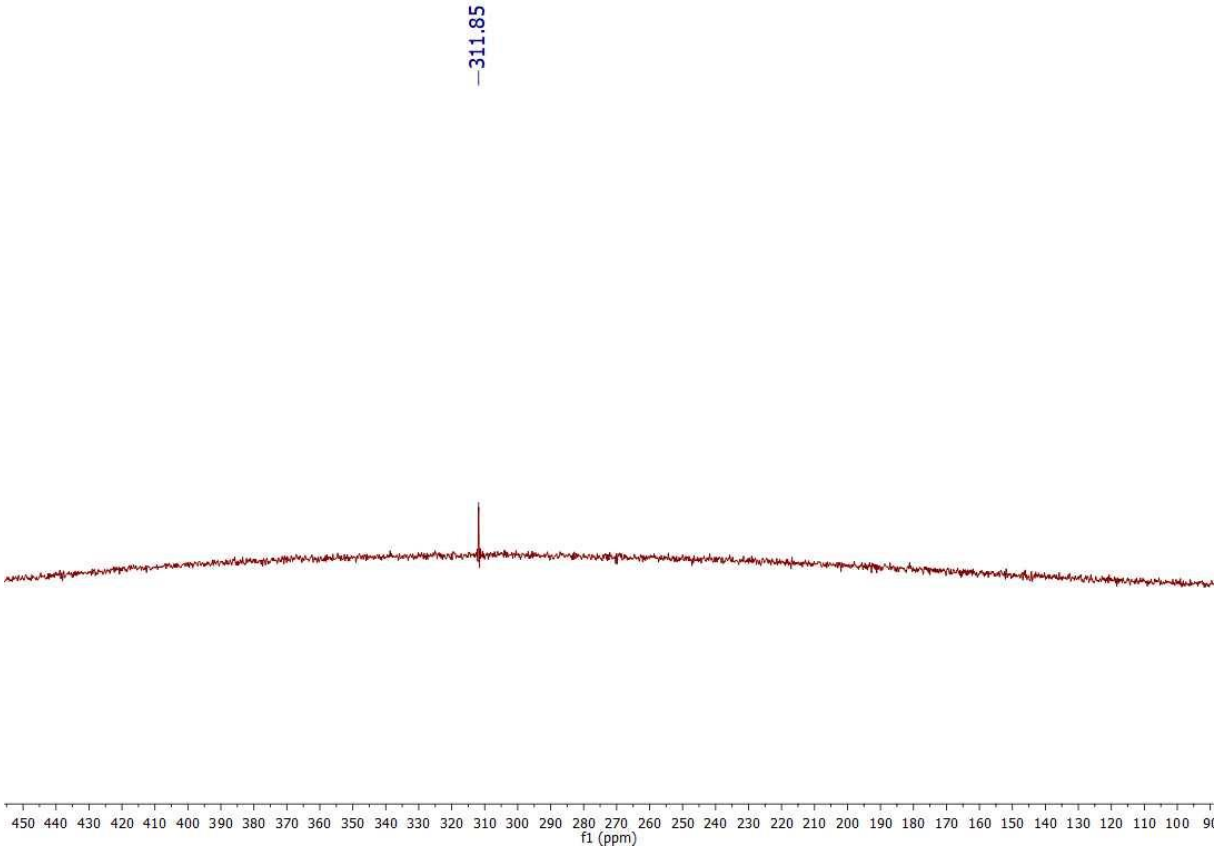

Figure S34. $^{19}F\{^{1}H\}$ NMR spectrum of **2-F** in THF-d_8 at 298 K

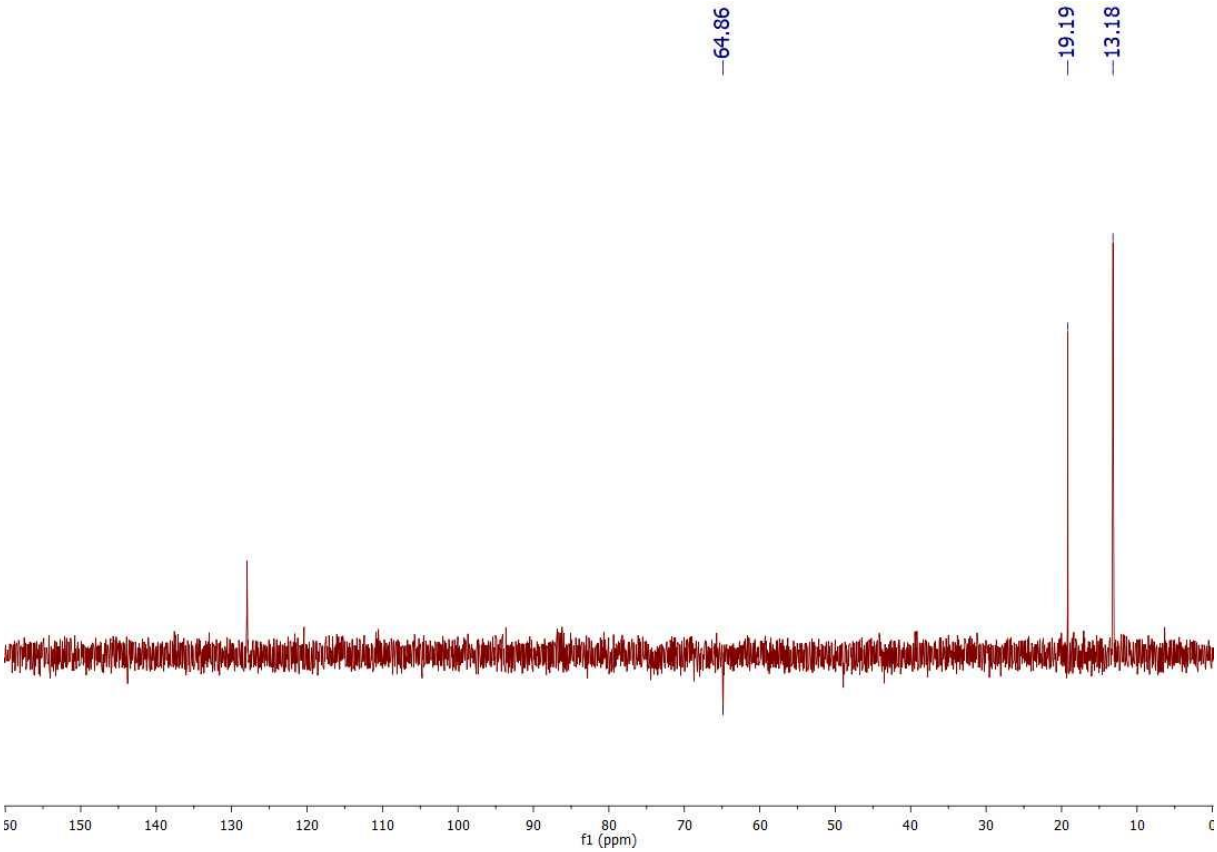

Figure S35. DEPT 135 $^{13}C\{^{1}H\}$ spectrum of **2-F** in C_6D_6 at 298 K. Solvent residual peak is indicated with *

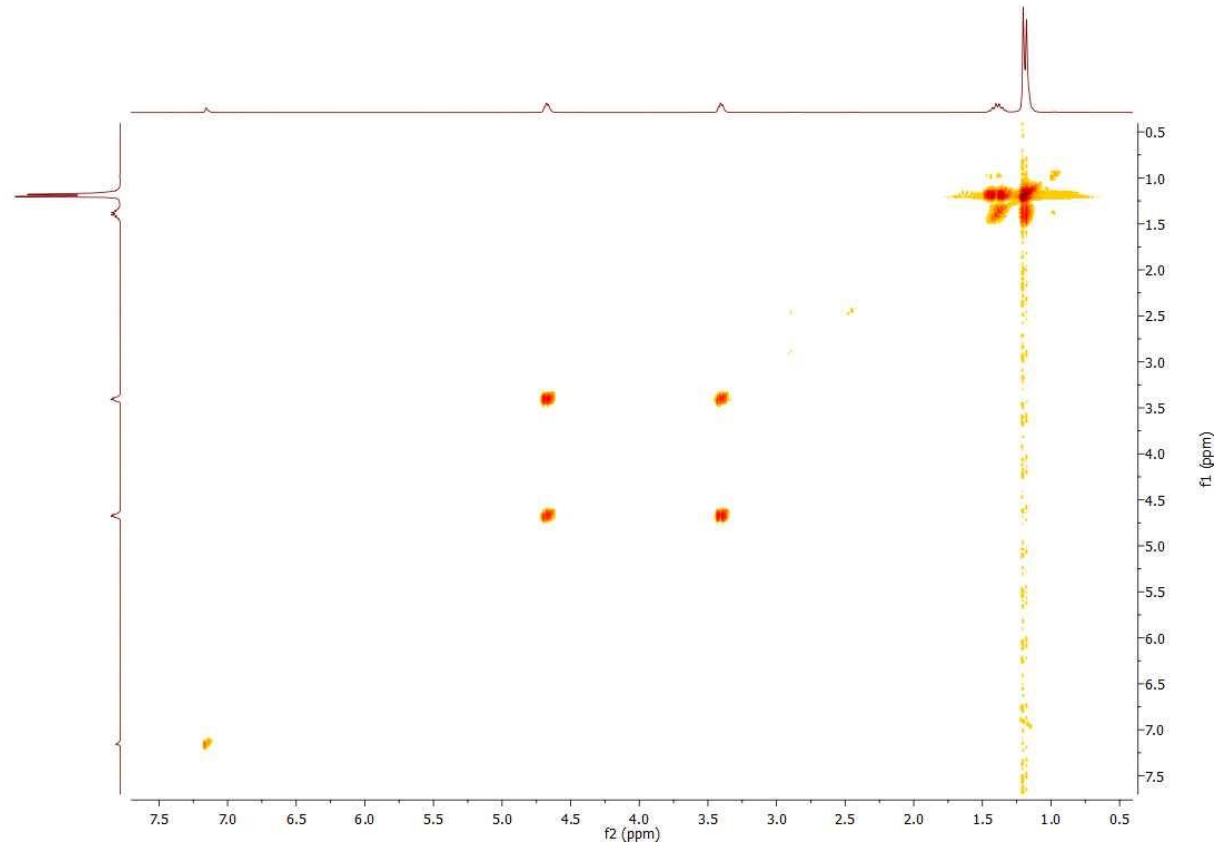

Figure S36. ^{1}H-^{1}H COSY spectrum of **2-F** in C_6D_6 at 298 K

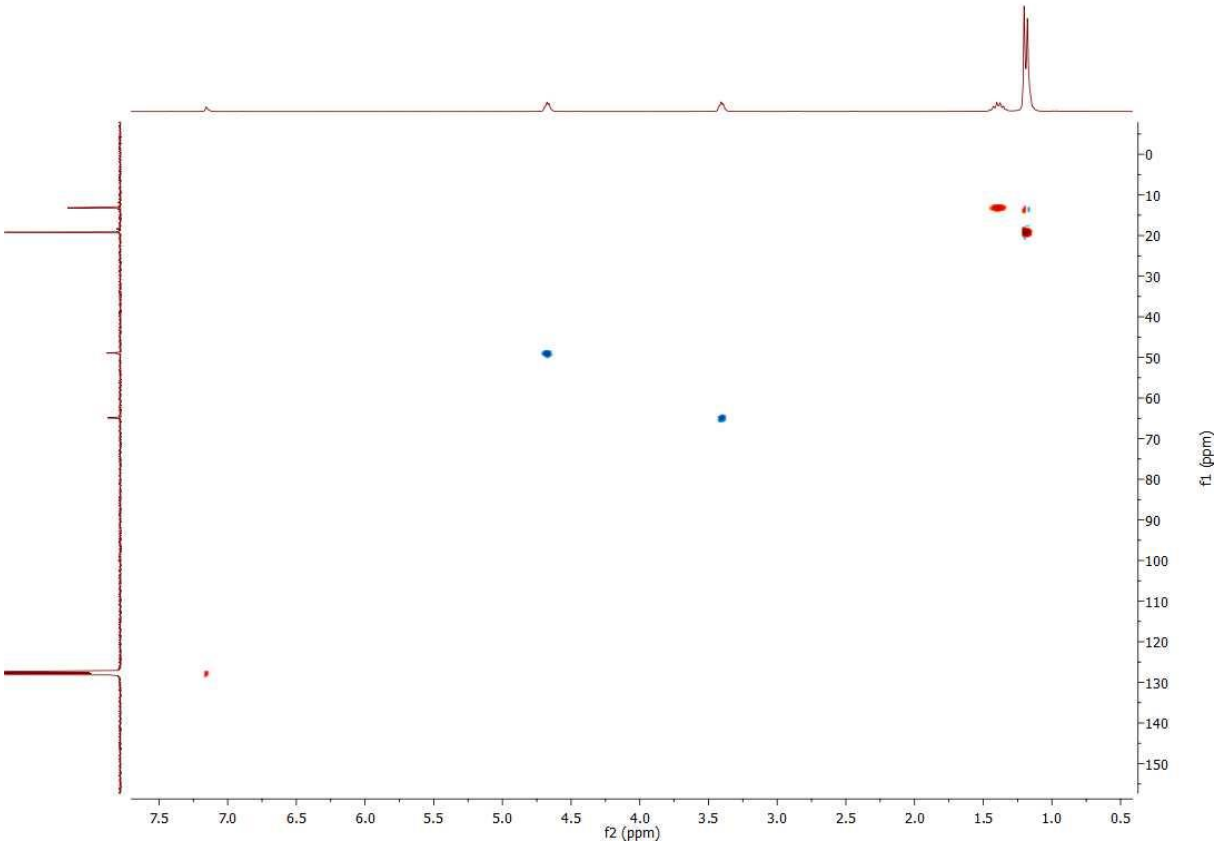

Figure S37. ^{1}H-^{13}C HSQC spectrum of **2-F** in C_6D_6 at 298 K

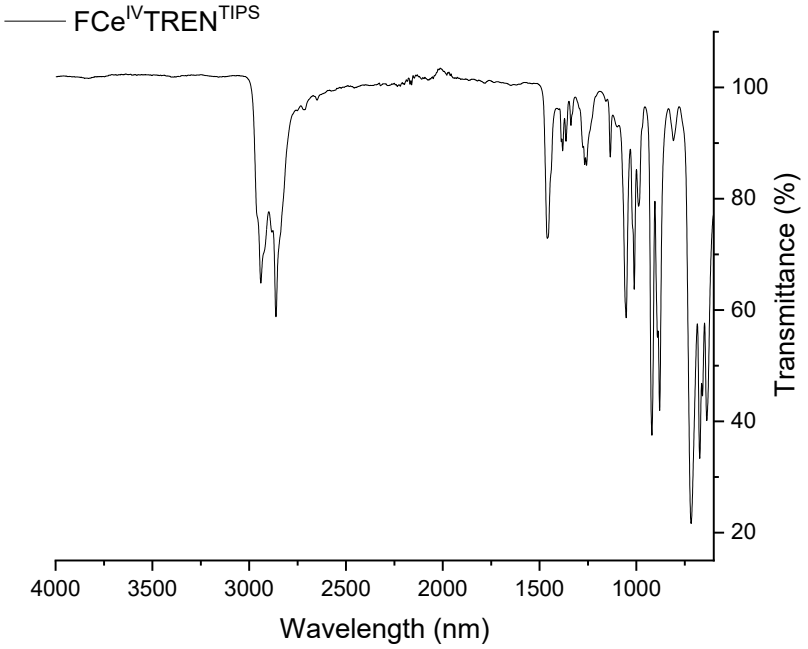

Figure S38. IR spectrum of **2-F** at 298 K

g) Spectral data for μ-(OC$_6$H$_4$-O)[Ce^{IV}TREN^{TIPS}] (2-Bq)

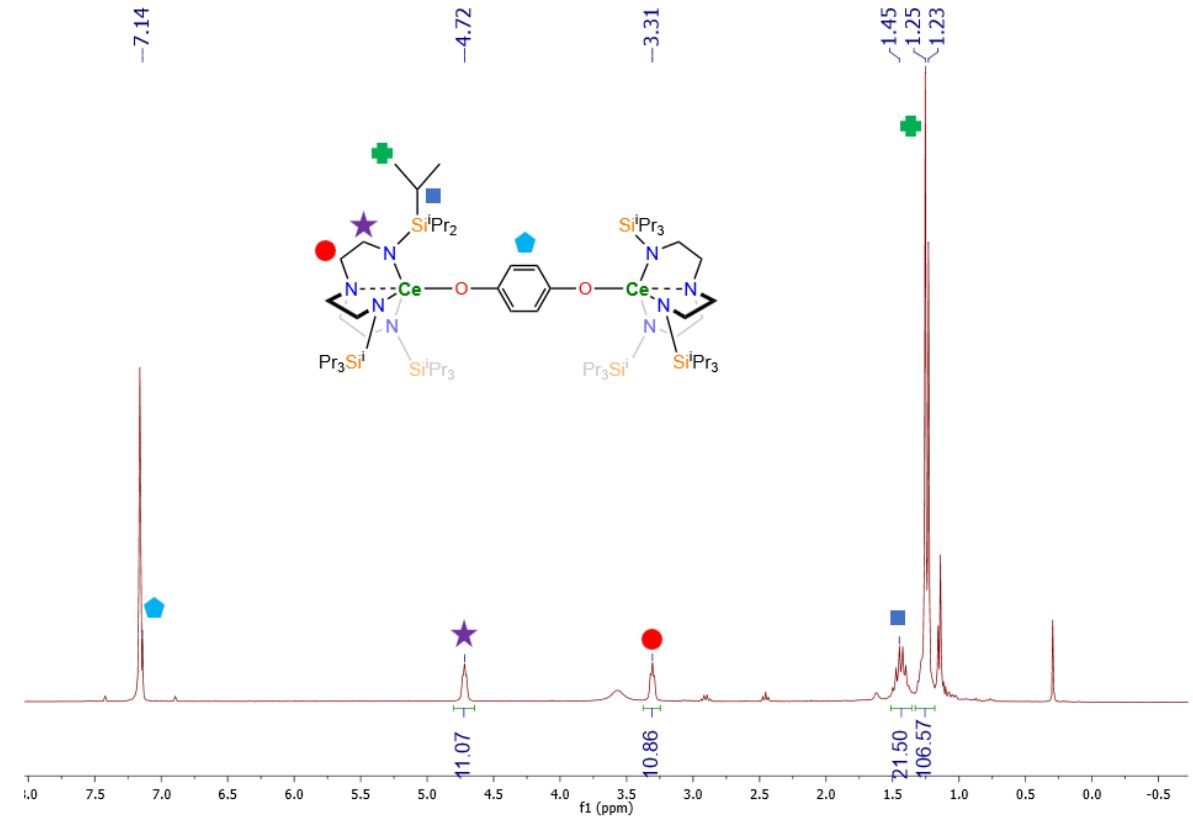

Figure S39. ^{1}H NMR spectrum of **2-Bq** in C_6D_6 at 298 K. Solvent residual peak is indicated with *. Broad peak at 3.5 ppm corresponds to traces of **1**

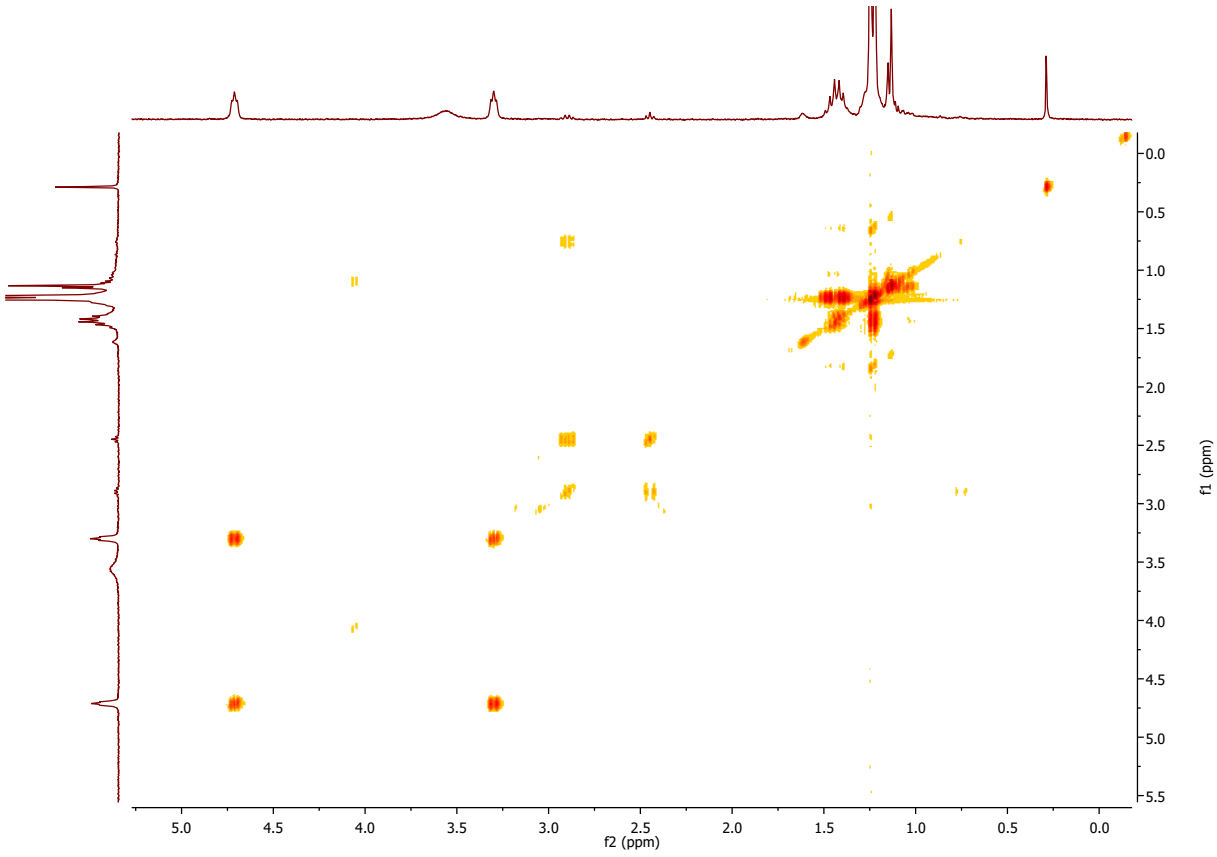

Figure S40. ^{1}H-^{1}H COSY spectrum of **2-Bq** in C_6D_6 at 298 K

h) Spectral data for ($^{t}Bu_2Bq$))[$Ce^{IV}TREN^{TIPS}$] (2-$^{t}Bu_2Bq$)

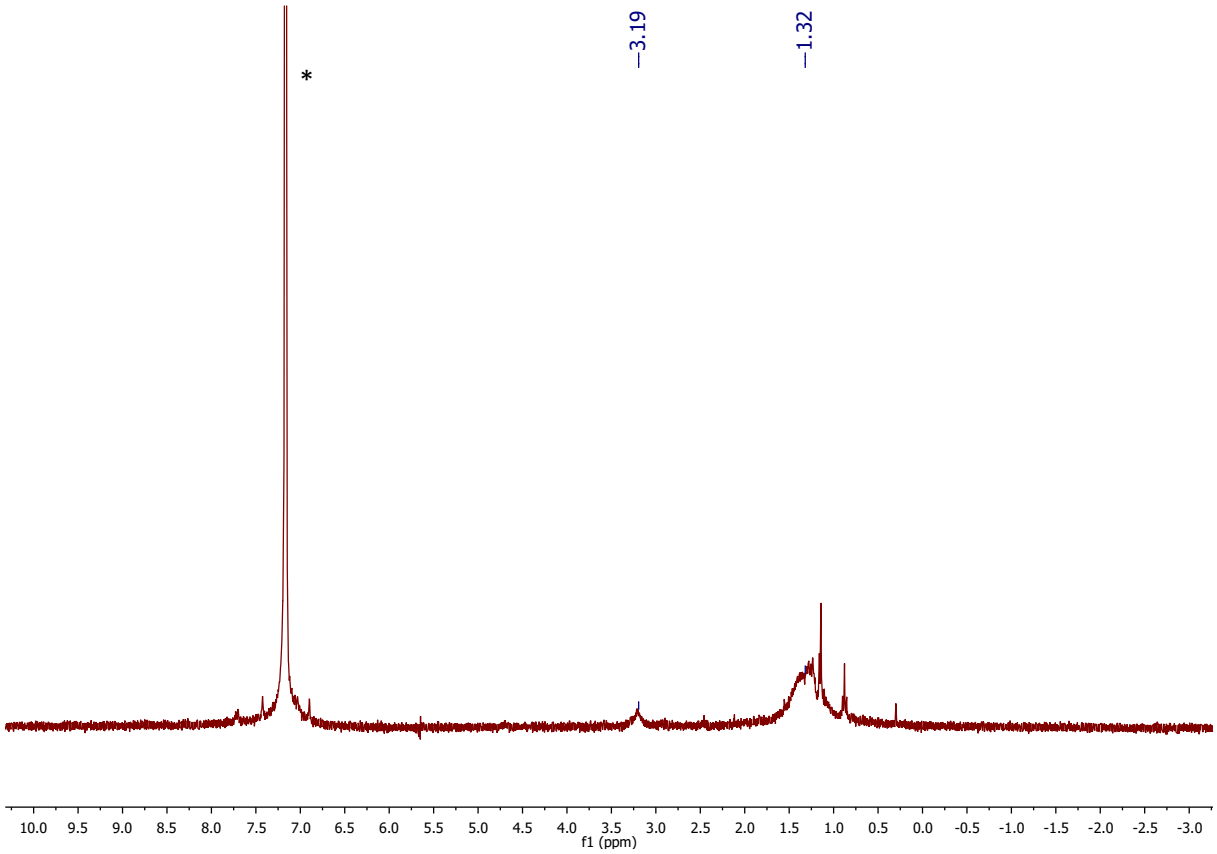

Figure S41. ^{1}H NMR spectrum of **2-Bq** in C_6D_6 at 298 K. Solvent residual peak is indicated with *

i) Spectra of 1-allyloxy-2-chlorobenzene

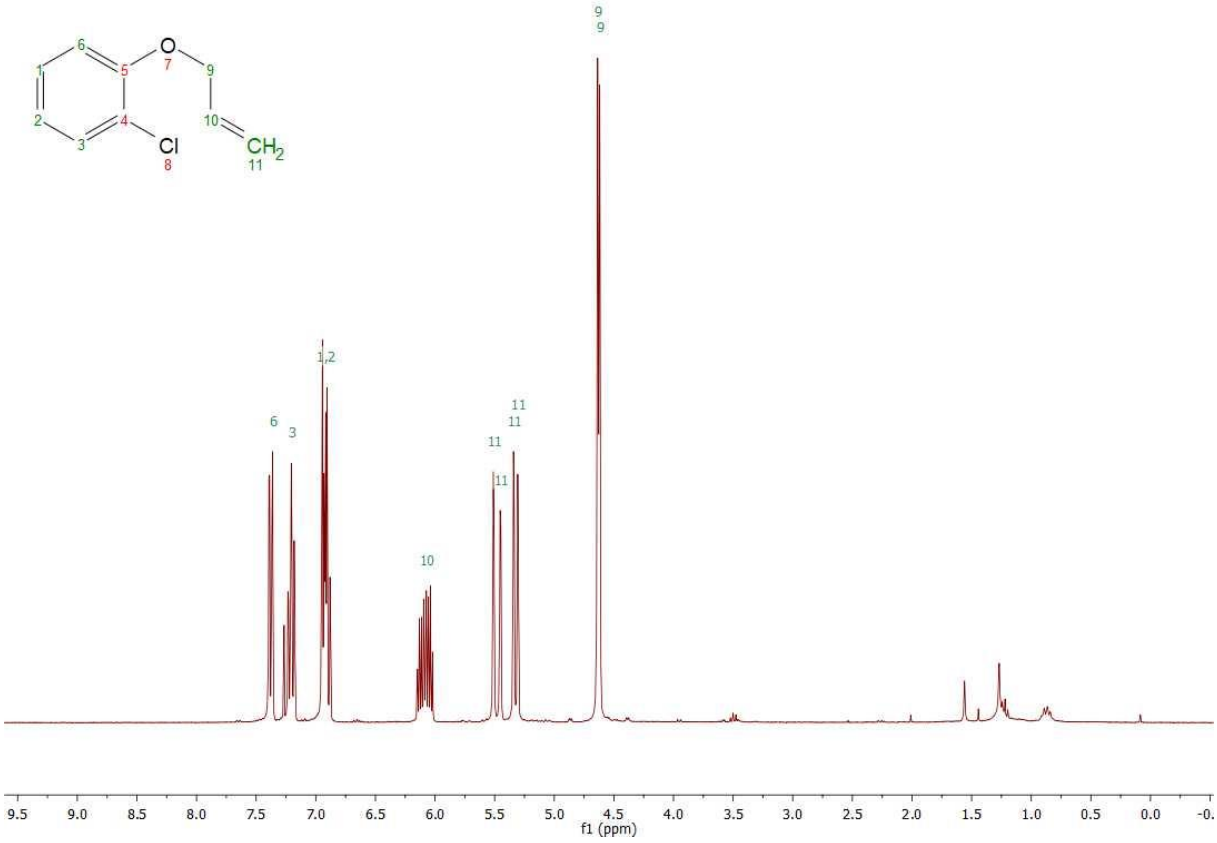

Figure S42. ^{1}H NMR of 1-allyloxy-2-chlorobenzene in $CDCl_3$ at 298 K

j) Reaction between 1 and ^{t}BuCN

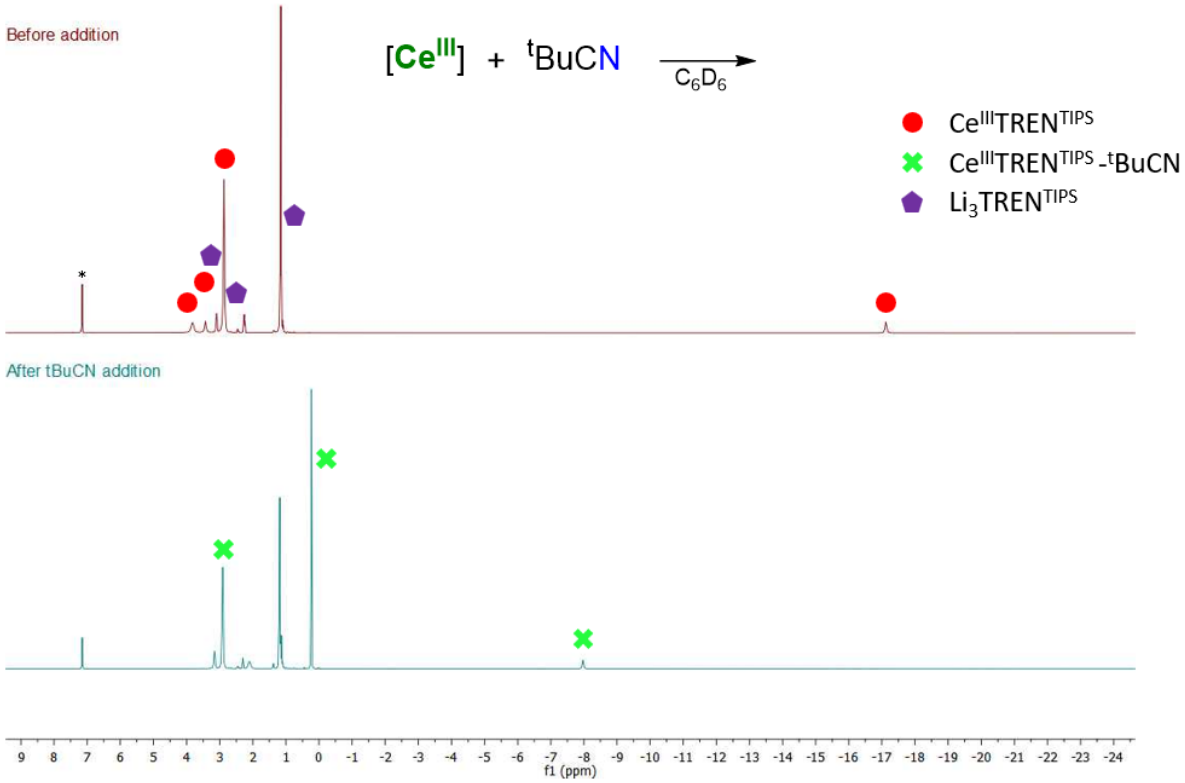

Figure S43. Reaction between **1** and ^{t}BuCN in C_6D_6. Solvent residual signals are indicated with *

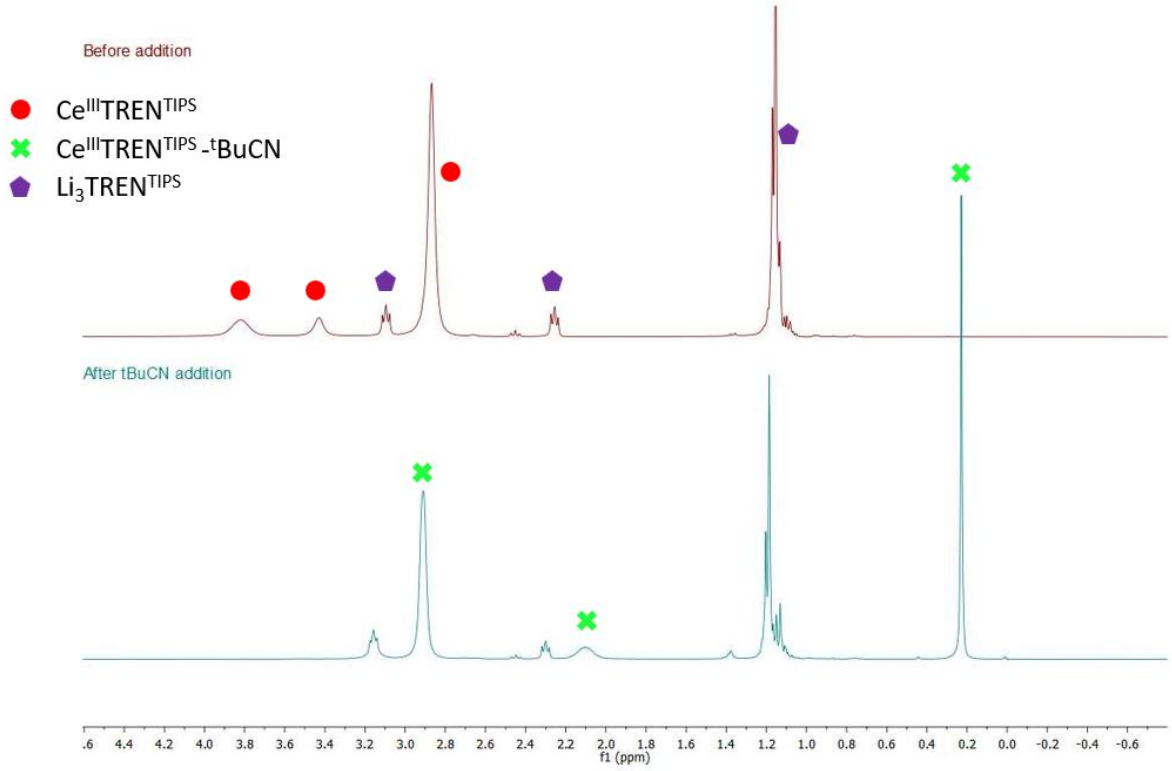

Figure S44. Reaction between **1** and ^{t}BuCN in C_6D_6. Zoom between -0.8 and 4.6 ppm. Solvent residual signals are indicated with *

III. X-Ray crystal structures

Identification code	**Li_3TREN^{TIPS}**	$[Ce^{III}TREN^{TIPS}]$ (**1**)
Empirical formula	$C_{99}H_{224}Li_9N_{12}Si_9$	$C_{33}H_{75}CeN_4Si_3$
Formula weight	7592.63	752.36
Temperature/K	150	150
Crystal system	monoclinic	monoclinic
Space group	$P2_1/c$	$P2_1/n$
a/Å	31.680(2)	9.4990(8)
b/Å	16.5524(12)	22.531(2)
c/Å	23.4351(18)	19.0088(17)
α/°	90	90
β/°	96.896(6)	91.907(3)
γ/°	90	90
Volume/Å^3	12199.8(16)	4066.0(6)
Z	4	4
ρ_{calc} g/cm^3	1.033	1.229
μ/mm^{-1}	0.142	1.233
F(000)	4220.0	1604.0
Radiation	Mo K_α (λ = 0.71073)	Mo K_α (λ = 0.71073)
2Θ range for data collection/°	4.348 to 54.206	4.288 to 52.744
Index ranges	-40 ≤ h ≤ 40, -19 ≤ k ≤ 21, -29 ≤ l ≤ 30	-11 ≤ h ≤ 11, -28 ≤ k ≤ 28, -21 ≤ l ≤ 23
Reflections collected	86385	73441
Independent reflections	26598 [R_{int} = 0.0845, R_{sigma} = 0.1733]	8313 [R_{int} = 0.1032, R_{sigma} = 0.0572]
Data/restraints/parameters	26598/72/1216	8313/0/388
Goodness-of-fit on F2	1.041	0.977
Final R indexes [I>=2σ (I)]	R_1 = 0.1114, wR_2 = 0.3150	R_1 = 0.0318, wR_2 = 0.0729
Final R indexes [all data]	R_1 = 0.2424, wR_2 = 0.3756	R_1 = 0.0443, wR_2 = 0.0767
Largest diff. peak/hole / e Å^{-3}	1.84/-0.61	0.60/-1.12
CCDC number		2387384

Table S1. Crystal data and structure refinement for **Li_3TREN^{TIPS}** and **1**

Identification code	**1-THF**	**1-LiCl**
Empirical formula	$C_{37}H_{83}CeN_4OSi_3$	$C_{45}H_{99}CeClLiN_4O_3Si_3$
Formula weight	824.46	1011.06
Temperature/K	150	150
Crystal system	monoclinic	monoclinic
Space group	$P2_1/c$	$P2_1/n$
a/Å	20.9000(5)	14.8586(13)
b/Å	24.4372(8)	19.4346(16)
c/Å	18.6624(6)	19.6118(16)
α/°	90	90
β/°	108.982(2)	90
γ/°	90	90
Volume/Å^3	9013.3(5)	5663.3(8)
Z	8	4
ρ_{calc} g/cm^3	1.215	1.186
μ/mm^{-1}	1.120	0.951
F(000)	3528.0	2164.0
Radiation	Mo K_α (λ = 0.71073)	Mo K_α (λ = 0.71073)
2Θ range for data collection/°	4.348 to 52	4.028 to 55.956
Index ranges	-24 ≤ h ≤ 25, -30 ≤ k ≤ 30, -23 ≤ l ≤ 23	-19 ≤ h ≤ 19, -25 ≤ k ≤ 25, -25 ≤ l ≤ 25
Reflections collected	87763	211854
Independent reflections	17693 [R_{int} = 0.1102, R_{sigma} = 0.0831]	13467 [R_{int} = 0.0861, R_{sigma} = 0.0328]
Data/restraints/parameters	17693/66/895	13467/122/578
Goodness-of-fit on F2	0.963	1.166
Final R indexes [I>=2σ (I)]	R_1 = 0.0598, wR_2 = 0.1350	R_1 = 0.0389, wR_2 = 0.0865
Final R indexes [all data]	R_1 = 0.0979, wR_2 = 0.1538	R_1 = 0.0637, wR_2 = 0.1048
Largest diff. peak/hole / e Å^{-3}	1.63/-2.09	1.13/-0.91

Table S2. Crystal data and structure refinement for **1-THF** and **1-LiCl**

Identification code	$[Li(THF)_4]$ $[ICe^{III}TREN^{TIPS}]$ (**1-LiI-THF$_4$**)	**1-^{t}BuCN**
Empirical formula	$C_{49}H_{107}CeILiN_4O_4Si_3$	$C_{38}H_{75}CeN_5Si_3$
Formula weight	1174.61	826.42
Temperature/K	150	200
Crystal system	orthorhombic	monoclinic
Space group	$Pna2_1$	$P2_1/n$
a/Å	17.7985(6)	13.542
b/Å	17.8628(8)	19.054
c/Å	19.3154(6)	18.570
α/°	90	90
β/°	90	96.38
γ/°	90	90
Volume/Å^3	6141.0(4)	4761.9
Z	4	4
ρ_{calc} g/cm^3	1.270	1.153
μ/mm^{-1}	1.342	1.059
F(000)	2468.0	1752.0
Radiation	Mo K_α (λ = 0.71073)	Mo K_α (λ = 0.71073)
2Θ range for data collection/°	4.56 to 52.742	4.482 to 61.1
Index ranges	-22≤ h ≤ 21, -22 ≤ k ≤ 22, -24 ≤ l ≤ 24	-19 ≤ h ≤ 14, -26 ≤ k ≤ 26, -26 ≤ l ≤ 22
Reflections collected	42273	37350
Independent reflections	11846 [R_{int} = 0.0214, R_{sigma} = 0.0274]	12978 [R_{int} = 0.0374, R_{sigma} = 0.0627]
Data/restraints/parameters	11846/136/619	12978/2/530
Goodness-of-fit on F2	1.085	0.953
Final R indexes [I>=2σ (I)]	R_1 = 0.0331, wR_2 = 0.0849	R_1 = 0.0360, wR_2 = 0.0782
Final R indexes [all data]	R_1 = 0.0417, wR_2 = 0.0888	R_1 = 0.0715, wR_2 = 0.0869
Largest diff. peak/hole / e Å^{-3}	1.11/-0.92	0.67/-0.34
CCDC number	2387121	

Table S3. Crystal data and structure refinement for **1-LiI-THF$_4$** and **1-^{t}BuCN**

Identification code	**1-N_3-15c5**	[$ClCe^{IV}TREN^{TIPS}$] (**2-Cl**)
Empirical formula	$C_{43}H_{95}CeN_7NaO_5Si_3$	$C_{33}H_{75}CeClN_4Si_3$
Formula weight	1037.63	787.81
Temperature/K	150	150
Crystal system	monoclinic	monoclinic
Space group	$P2_1/c$	$P2_1/n$
a/Å	15.1524(8)	12.9683(8)
b/Å	13.4962(6)	15.5387(9)
c/Å	27.4719(17)	20.3785(12)
α/°	90	90
β/°	96.469(5)	90.572(5)
γ/°	90	90
Volume/$Å^3$	5582.2(5)	4106.3(4)
Z	4	4
ρ_{calc} g/cm^3	1.235	1.274
μ/mm^{-1}	0.931	1.287
F(000)	2212.0	1672.0
Radiation	Mo K_α (λ = 0.71073)	Mo Kα (λ = 0.71073)
2Θ range for data collection/°	4.424 to 58.522	4.54 to 52.04
Index ranges	-11 ≤ h ≤ 20, -18 ≤ k ≤ 18, -37 ≤ l ≤ 37	-15 ≤ h ≤ 16, -19 ≤ k ≤ 18, -14 ≤ l ≤ 25
Reflections collected	64862	31438
Independent reflections	13938 [R_{int} = 0.0239, R_{sigma} = 0.0217]	8013 [R_{int} = 0.0760, R_{sigma} = 0.1053]
Data/restraints/parameters	13938/310/826	8013/0/397
Goodness-of-fit on F2	1.053	0.910
Final R indexes [I>=2σ (I)]	R_1 = 0.0327, wR_2 = 0.0781	R_1 = 0.0378, wR_2 = 0.0667
Final R indexes [all data]	R_1 = 0.0425, wR_2 = 0.0821	R_1 = 0.0806, wR_2 = 0.0737
Largest diff. peak/hole / e $Å^{-3}$	1.12/-0.68	0.72/-0.42
CCDC number		2387124

Table S4. Crystal data and structure refinement for **1-N_3-15c5** and **2-Cl**

Identification code	[BrCe^{IV}TREN^{TIPS}] (**2-Br**)	[FCe^{IV}TREN^{TIPS}] (**2-F**)
Empirical formula	$C_{33}H_{75}CeBrN_4Si_3$	$C_{264}H_{600}Ce_8F_8N_{32}Si_{24}$
Formula weight	832.27	6170.84
Temperature/K	150	150
Crystal system	monoclinic	monoclinic
Space group	$P2_1/n$	$P2_1/n$
a/Å	13.0115(10)	20.3562(10)
b/Å	15.7902(9)	19.9580(9)
c/Å	20.3365(17)	20.6752(11)
α/°	90	90
β/°	90.712(7)	103.739(4)
γ/°	90	90
Volume/Å^3	4177.9(5)	8159.4(7)
Z	4	1
ρ_{calc} g/cm^3	1.323	1.256
μ/mm^{-1}	2.158	1.234
F(000)	1744.0	3280.0
Radiation	Mo K_α (λ = 0.71073)	Mo K_α (λ = 0.71073)
2Θ range for data collection/°	4.506 to 56.564	4.54 to 61.288
Index ranges	-17 ≤ h ≤ 17, -16 ≤ k ≤ 21, -27 ≤ l ≤ 26	-29 ≤ h ≤ 27, -22 ≤ k ≤ 28, -29 ≤ l ≤ 29
Reflections collected	113832	77535
Independent reflections	10348 [R_{int} = 0.0524, R_{sigma} = 0.0264]	22744 [R_{int} = 0.0287, R_{sigma} = 0.0274]]
Data/restraints/parameters	10348/0/413	22744/0/1214
Goodness-of-fit on F2	1.066	1.035
Final R indexes [I>=2σ (I)]	R_1 = 0.0280, wR_2 = 0.0624	R_1 = 0.0371, wR_2 = 0.0869
Final R indexes [all data]	R_1 = 0.0434, wR_2 = 0.0677	R_1 = 0.0609, wR_2 = 0.0998
Largest diff. peak/hole / e Å^{-3}	0.87/-0.42	0.68/-0.87
CCDC number	2387123	2387125

Table S5. Crystal data and structure refinement for **2-Br** and **2-F**

Identification code	**2-Bq**	**2-BqMe$_4$**
Empirical formula	$C_{74}H_{158}Ce_2N_8O_{2.5}Si_6$	$C_{80.5}H_{172}Ce_2N_8O_{2.5}Si_6$
Formula weight	1648.85	1741.03
Temperature/K	150	150
Crystal system	monoclinic	monoclinic
Space group	$P2_1/c$	$P2_1/n$
a/Å	19.0502(10)	24.2636(5)
b/Å	19.2286(7)	17.8818(2)
c/Å	25.5367(13)	24.3384(5)
α/°	90	90
β/°	100.808(4)	108.0400(10)
γ/°	90	90
Volume/Å^3	9188.4(8)	10040.7(3)
Z	4	4
ρ_{calc} g/cm^3	1.192	1.152
μ/mm^{-1}	1.099	1.009
F(000)	3512.0	3724.0
Radiation	Mo K_α (λ = 0.71073)	Mo K_α (λ = 0.71073)
2Θ range for data collection/°	4.354 to 58.34	4.556 to 54.97
Index ranges	-23 ≤ h ≤ 26, -25 ≤ k ≤ 26, -34 ≤ l ≤ 34	-31 ≤ h ≤ 29, 0 ≤ k ≤ 23, 0 ≤ l ≤ 31
Reflections collected	98421	22711
Independent reflections	22662 [R_{int} = 0.0229, R_{sigma} = 0.0204]	22711 [R_{int} = ?, R_{sigma} = 0.0696]
Data/restraints/parameters	22662/0/932	22711/73/914
Goodness-of-fit on F2	1.089	1.074
Final R indexes [I>=2σ (I)]	R_1 = 0.0287, wR_2 = 0.0791	R_1 = 0.0583, wR_2 = 0.1655
Final R indexes [all data]	R_1 = 0.0379, wR_2 = 0.0830	R_1 = 0.0842, wR_2 = 0.1795
Largest diff. peak/hole / e Å^{-3}	1.34/-1.01	1.14/-0.92

Table S6. Crystal data and structure refinement for **2-Bq** and **2-BqMe$_4$**

Identification code	**2-TEMPO**	**$Ce^{III}TREN^{TBDMS}$-LiI-THF_2**
Empirical formula	$C_{84}H_{186}Ce_2N_{10}O_2Si_6$	$C_{32}H_{73}CeILiN_4O_2Si_3$
Formula weight	1817.20	3616.68
Temperature/K	150	150
Crystal system	monoclinic	triclinic
Space group	$P2_1/n$	P-1
a/Å	13.8058(6)	12.0714(6)
b/Å	18.2835(11)	19.3413(9)
c/Å	19.6931(8)	20.1941(9)
α/°	90	97.668(4)
β/°	100.611(3)	95.569(4)
γ/°	90	103.013(4)
Volume/$Å^3$	4885.9(4)	4513.1(4)
Z	2	4
ρ_{calc} g/cm^3	1.235	1.331
μ/mm^{-1}	1.040	1.801
F(000)	1952.0	1860.0
Radiation	Mo K_α (λ = 0.71073)	Mo K_α (λ = 0.71073)
2Θ range for data collection/°	4.552 to 58.504	4.334 to 56.862
Index ranges	-18 ≤ h ≤ 18, -24 ≤ k ≤ 24, -26 ≤ l ≤ 22	-14 ≤ h ≤ 15, -25 ≤ k ≤ 25, -26 ≤ l ≤ 25
Reflections collected	77261	63434
Independent reflections	12336 [R_{int} = 0.0283, R_{sigma} = 0.0226]	19826 [R_{int} = 0.0466, R_{sigma} = 0.0550]
Data/restraints/parameters	12336/0/819	19826/18/823
Goodness-of-fit on F2	1.088	1.039
Final R indexes [I>=2σ (I)]	R_1 = 0.0246, wR_2 = 0.0576	R_1 = 0.0577, wR_2 = 0.1629
Final R indexes [all data]	R_1 = 0.0364, wR_2 = 0.0621	R_1 = 0.0932, wR_2 = 0.1845
Largest diff. peak/hole / e $Å^{-3}$	0.70/-0.40	1.75/-1.24

Table S7. Crystal data and structure refinement for **2-TEMPO** and **$Ce^{III}TREN^{TBDMS}$-LiI-THF_2**

Identification code	**$Tb^{III}TREN^{TIPS}$**
Empirical formula	$C_{33}H_{75}N_4Si_3Tb$
Formula weight	771.16
Temperature/K	150
Crystal system	monoclinic
Space group	$P2_1/n$
a/Å	9.6154(7)
b/Å	22.4374(17)
c/Å	18.5269(12)
α/°	90
β/°	92.098(6)
γ/°	90
Volume/Å^3	3994.4(5)
Z	4
ρ_{calc} g/cm^3	1.282
μ/mm^{-1}	1.886
F(000)	1632
Radiation	Mo K_α (λ = 0.71073)
2Θ range for data collection/°	4.612 to 54.97
Index ranges	-12 ≤ h ≤ 12, -29 ≤ k ≤ 29, -23 ≤ l ≤ 24
Reflections collected	25435
Independent reflections	9030 [R_{int} = 0.0479, R_{sigma} = 0.0821]
Data/restraints/parameters	9030/72/418
Goodness-of-fit on F2	0.994
Final R indexes [I>=2σ (I)]	R_1 = 0.0448, wR_2 = 0.1009
Final R indexes [all data]	R_1 = 0.0853, wR_2 = 0.1121
Largest diff. peak/hole / e Å^{-3}	1.44/-0.64

Table S8. Crystal data and structure refinement for **$Tb^{III}TREN^{TIPS}$**

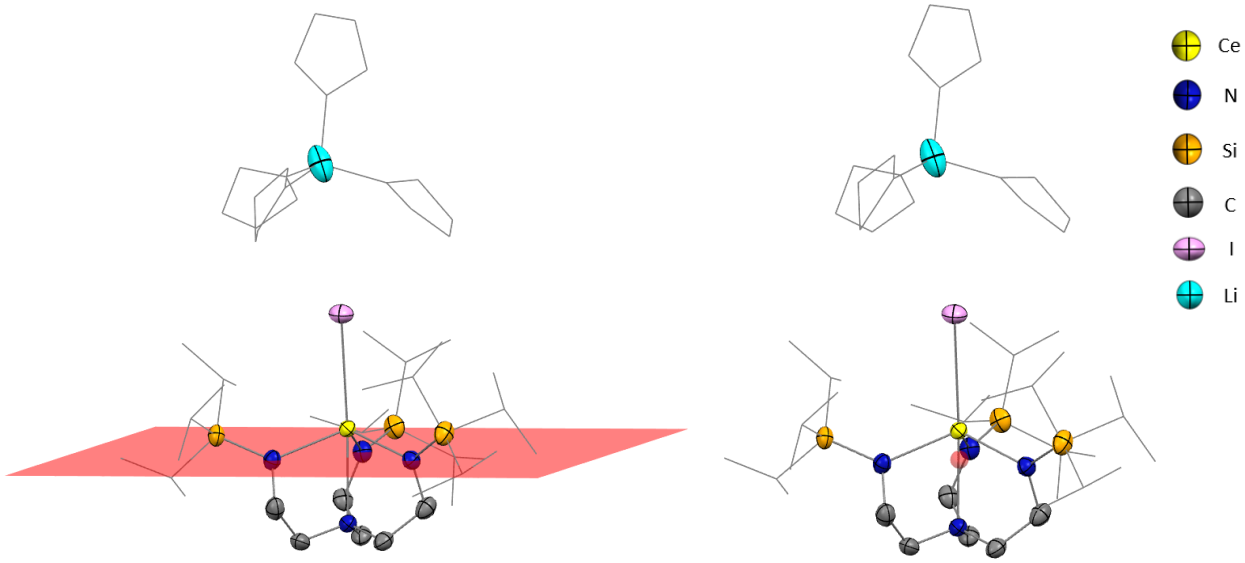

Figure S45. Position of plane (A) and centroid (B) used for distance and bond measurements on **1-LiI-THF$_4$**, [Li(THF)$_4$][ICe^{III}TREN^{TIPS}]

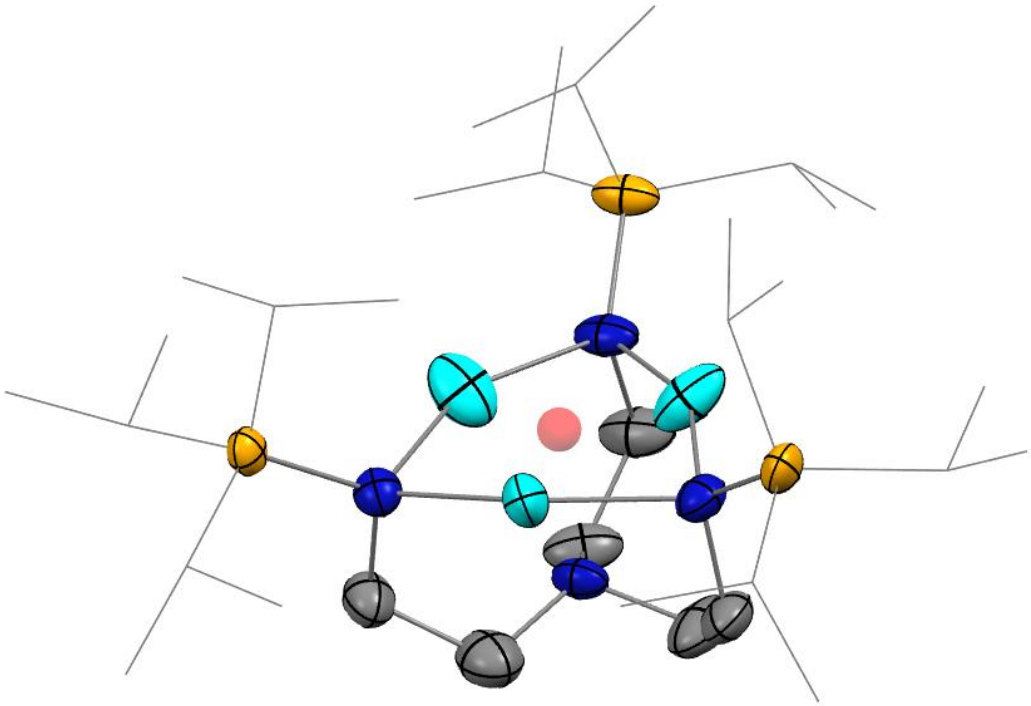

Figure S46. Position of the centroid defined by the three lithium ions in **Li$_3$TREN^{TIPS}**

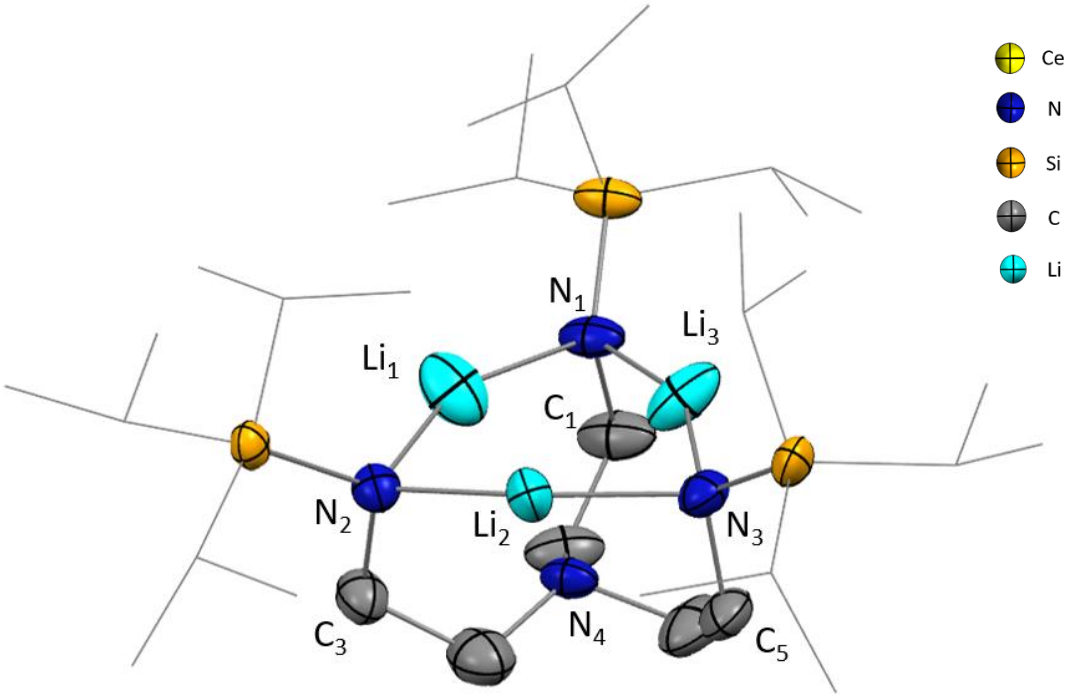

Figure S47. Molecular structure of **Li_3TREN^{TIPS}**. Displacement ellipsoids are represented at 50% probability. Hydrogen atoms have been omitted for clarity, and isopropyl groups have been represented in wireframe style. Three molecules are present per asymmetric unit, but only one was shown for clarity. Values given in **Table S9** were selected on one of the molecules

Bond	Length (Å)	Bonds	Angle (°)
Cent-N_1	2.163	C_1-N_1-Cent	104.00
Cent-N_2	2.183	C_3-N_2-Cent	103.64
Cent-N_3	2.273	C_5-N_3-Cent	105.07
Cent-N_4	2.045		
N_1-Si_1	1.716(5)		
N_2-Si_2	1.706(5)		
N_3-Si_3	1.709(5)	**Bond**	**Mean value (Å)**
N_1-C_1	1.488(7)	Cent-$N_{equatorial}$	2.206
N_2-C_3	1.480(6)	N-Si	1.710(9)
N_3-C_5	1.484(7)		
N_1-Li_1	1.970(11)		
N_1-Li_3	1.965(11)		
N_2-Li_1	1.947(12)		
N_2-Li_2	1.990(12)		
N_3-Li_2	1.976(13)		
N_3-Li_3	1.966(12)		

Table S9. Selected bond lengths and angles for **Li_3TREN^{TIPS}**

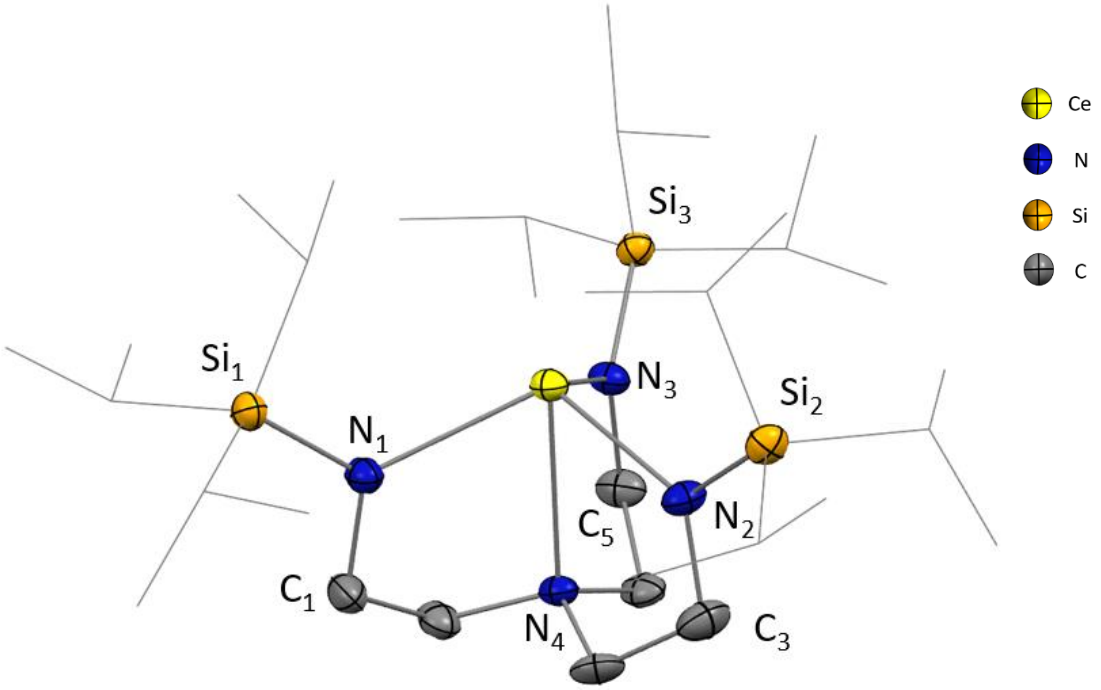

Figure S48. Molecular structure of **1**. Displacement ellipsoids are represented at 50% probability. Hydrogen atoms have been omitted for clarity, and isopropyl groups have been represented in wireframe style

Bond	Length (Å)	Bonds	Angle (°)
Ce-N_1	2.366(2)	C_1-N_1-Ce	119.34(16)
Ce-N_2	2.358(2)	C_3-N_2-Ce	118.64(17)
Ce-N_3	2.359(2)	C_5-N_3-Ce	119.23(17)
Ce-N_4	2.534(2)	Ce-Cent-N_4	177.1
N_1-Si_1	1.716(2)		
N_2-Si_2	1.724(2)		
N_3-Si_3	1.720(2)	**Bond**	**Mean value (Å)**
N_1-C_1	1.469(3)	Ce-$N_{equatorial}$	2.361(3)
N_2-C_3	1.464(3)	Ce-N_{plane}	0.798
N_3-C_5	1.466(3)	N-Si	1.720(3)

Table S10. Selected bond lengths and angles for **1**

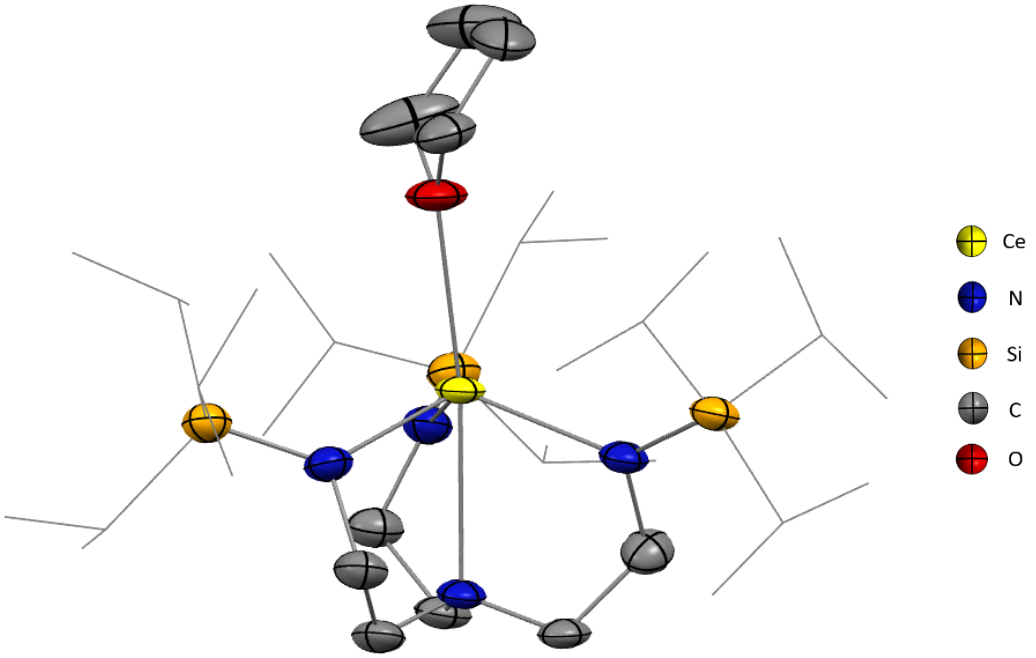

Figure S49. Molecular structure of **1-THF**. Displacement ellipsoids are represented at 50% probability. Hydrogen atoms have been omitted for clarity, and isopropyl groups have been represented in wireframe style. The molecule presents a slight disorder on the isopropyl groups, which was modelled but not plotted for clarity

Bond	Length (Å)	Bonds	Angle (°)
Ce-N_1	2.364(4)	C_1-N_1-Ce	107.5(3)
Ce-N_2	2.351(4)	C_3-N_2-Ce	109.8(3)
Ce-N_3	2.356(4)	C_5-N_3-Ce	105.0(3)
Ce-N_4	2.656(4)	Ce-Cent-N_4	178.8
N_1-Si_1	1.712(4)		
N_2-Si_2	1.719(5)		
N_3-Si_3	1.718(4)	**Bond**	**Mean value (Å)**
N_1-C_1	1.488(6)	Ce-$N_{equatorial}$	2.357(7)
N_2-C_3	1.481(6)	Ce-N_{plane}	0.757
N_3-C_5	1.489(6)	N-Si	1.714(8)

Table S11. Selected bond lengths and angles for **1-THF**

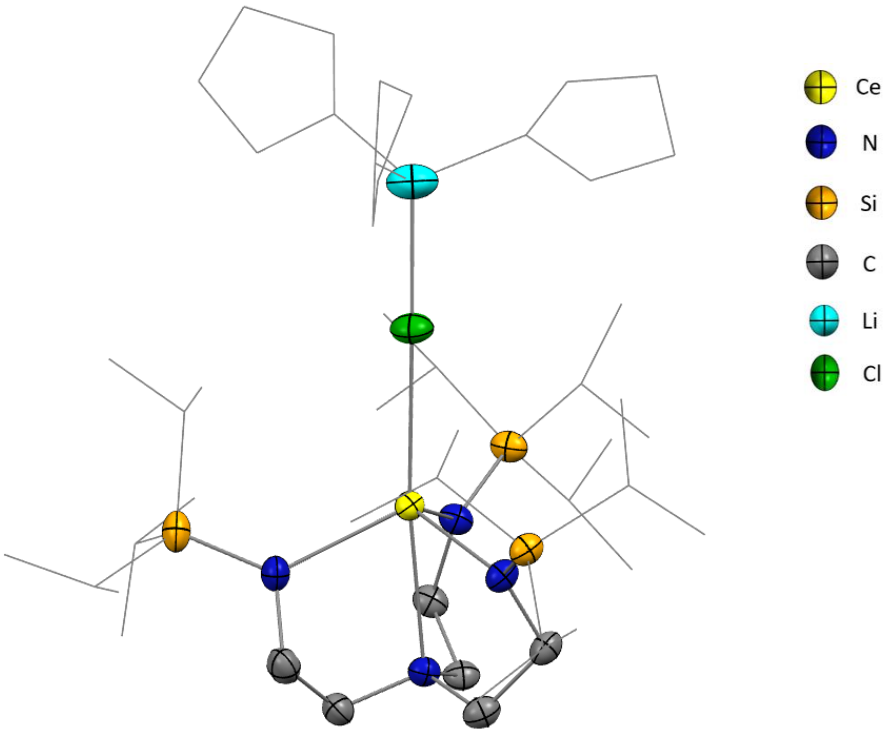

Figure S50. Structure of $[Li(THF)_3][ClCe^{III}TREN^{TIPS}]$ **1-LiCl-THF$_3$**. Displacement ellipsoids are represented at 50% probability. Hydrogen atoms have been omitted for clarity, and isopropyl groups have been represented in wireframe style. The molecule presents a slight disorder on THF molecules, which was modelled but not plotted for clarity

Bond	Length (Å)	Bonds	Angle (°)
Ce-N_1	2.382(2)	C_1-N_1-Ce	112.06(18)
Ce-N_2	2.357(2)	C_3-N_2-Ce	111.93(17)
Ce-N_3	2.361(3)	C_5-N_3-Ce	112.16(19)
Ce-N_4	2.682(2)	Ce-Cent-N_4	175.37
N_1-Si_1	1.721(3)		
N_2-Si_2	1.713(3)		
N_3-Si_3	1.701(3)	**Bond**	**Mean value (Å)**
N_1-C_1	1.468(4)	Ce-$N_{equatorial}$	2.367(5)
N_2-C_3	1.466(4)	Ce-N_{plane}	0.809
N_3-C_5	1.475(4)	N-Si	1.712(6)
Ce-Cl	2.8379(8)		
Li-Cl	2.301(7)		

Table S12. Selected bond lengths and angles for **1-LiCl-THF$_3$**, $[Li(THF)_3][ClCe^{III}TREN^{TIPS}]$

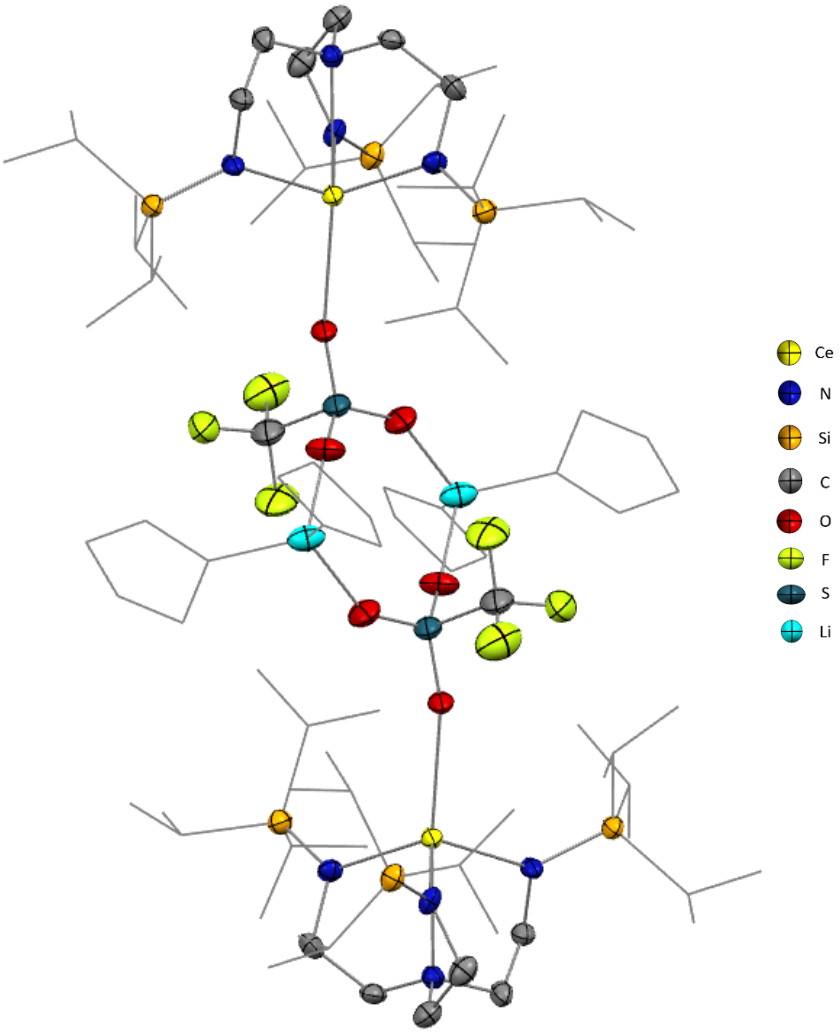

Figure S51. Structure of [Li(THF)2][TfOCe^{III}TREN^{TIPS}] **1-LiCl-THF$_3$**. Displacement ellipsoids are represented at 50% probability. Hydrogen atoms have been omitted for clarity, and isopropyl groups have been represented in wireframe style. Bond distances were not reported due to incomplete data

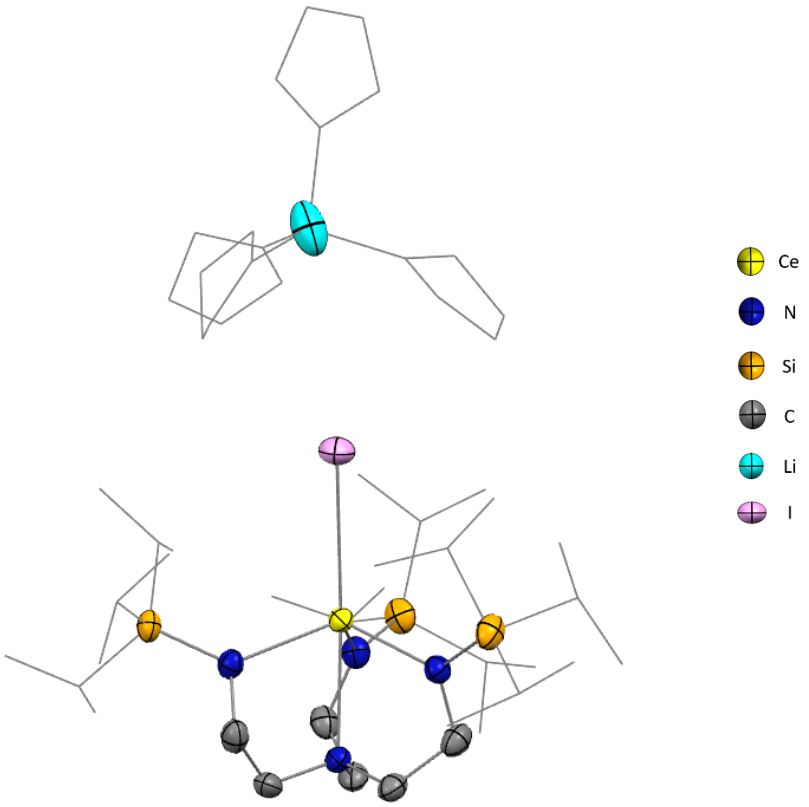

Figure S52. Structure of $[Li(THF)_4][ICe^{III}TREN^{TIPS}]$ (**1-LiI-THF$_4$**). Displacement ellipsoids are represented at 50% probability. Hydrogen atoms have been omitted for clarity, and isopropyl groups have been represented in wireframe style. The molecule presents a slight disorder on the isopropyl ligands which was modelled but not plotted for clarity

Bond	Length (Å)	Bonds	Angle (°)
Ce-N_1	2.380(5)	C_1-N_1-Ce	114.2(4))
Ce-N_2	2.374(5)	C_3-N_2-Ce	110.7(3)
Ce-N_3	2.364(5)	C_5-N_3-Ce	112.7(4)
Ce-N_4	2.664(5)	Ce-Cent-N_4	172.0(3)
N_1-Si_1	1.720(5)		
N_2-Si_2	1.705(5)		
N_3-Si_3	1.711(5)		
N_1-C_1	1.453(9)		
N_2-C_3	1.478(8)	**Bond**	**Mean value (Å)**
N_3-C_5	1.472(9)	Ce-$N_{equatorial}$	2.273(2)
Ce-I	3.2580(5)	Ce-N_{plane}	0.809(5)
Li-I	4.343	N-Si	1.712(1)

Table S13. Selected bond lengths and angles for **1-LiI-THF$_4$**, $[Li(THF)_4][ICe^{III}TREN^{TIPS}]$

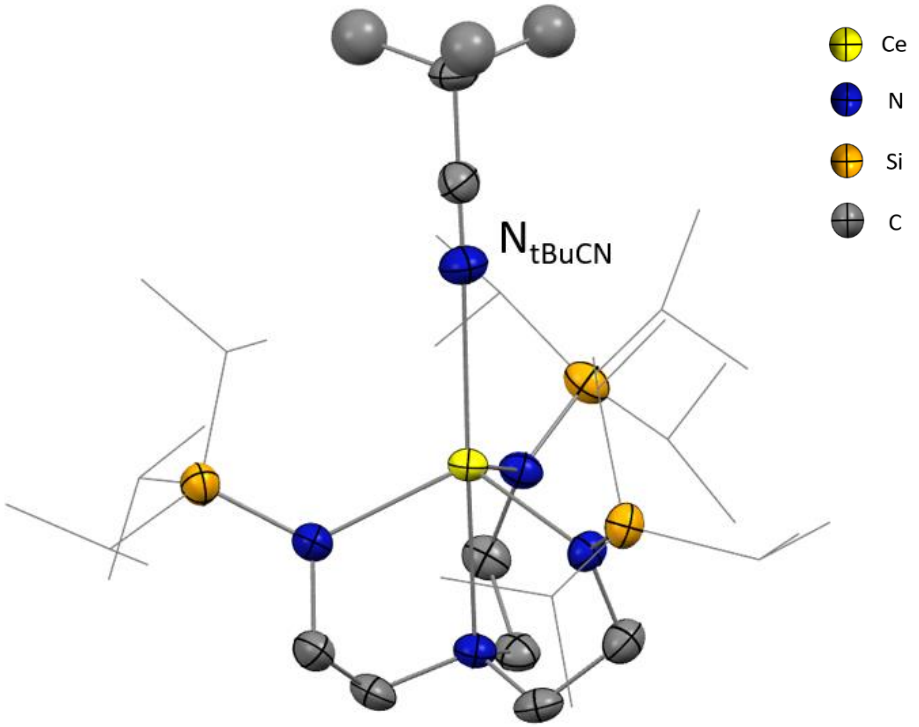

Figure S 53. Structure of ^{t}BuCNCe^{III}TREN^{TIPS} (**1-^{t}BuCN**). Displacement ellipsoids are represented at 50% probability. Hydrogen atoms have been omitted for clarity, and isopropyl groups have been represented in wireframe style. The molecule presents a slight disorder on the ^{t}BuCN moiety which was modelled but not plotted for clarity

Bond	Length (Å)	Bonds	Angle (°)
Ce-N_1	2.365(2)	C_1-N_1-Ce	115.68(16)
Ce-N_2	2.356(2)	C_3-N_2-Ce	112.96(17)
Ce-N_3	2.350(2)	C_5-N_3-Ce	113.94(17)
Ce-N_4	2.646(2)	Ce-Cent-N_4	174.87
N_1-Si_1	1.709(2)		
N_2-Si_2	1.714(2)		
N_3-Si_3	1.708(2)		
N_1-C_1	1.467(3)		
N_2-C_3	1.451(3)	**Bond**	**Mean value (Å)**
N_3-C_5	1.464(3)	Ce-$N_{equatorial}$	2.357(4)
Ce-N_{tBuCN}	2.742(2)	Ce-N_{plane}	0.800
C_{tBuCN}-C_{tBuCN}	1.521(12)-1.693(12)	N-Si	1.710(4)

Table S14. Selected bond lengths and angles for **1-^{t}BuCN**, ^{t}BuCNCe^{III}TREN^{TIPS}

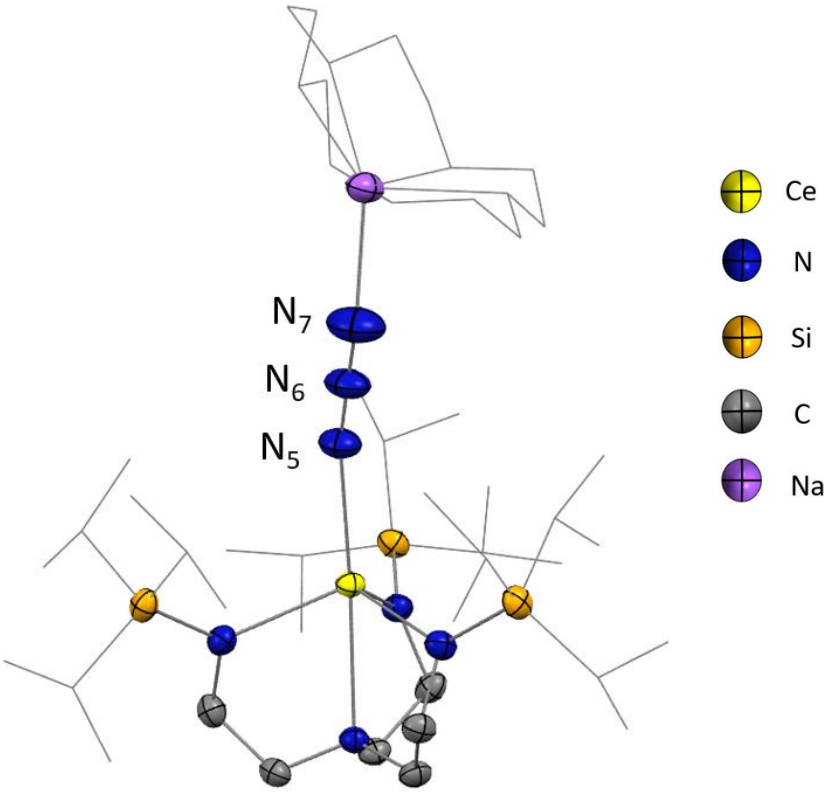

Figure S54. Structure of [Na@15-crown-5][$N_3Ce^{III}TREN^{TIPS}$] (**1-N_3-15c5**). Displacement ellipsoids are represented at 50% probability. Hydrogen atoms have been omitted for clarity, and isopropyl groups have been represented in wireframe style. The molecule presents a slight disorder on 15-crown-5 which was modelled but not plotted for clarity

Bond	Length (Å)	Bonds	Angle (°)
Ce-N_1	2.3616(18)	C_1-N_1-Ce	110.88(13)
Ce-N_2	2.3775(18)	C_3-N_2-Ce	114.60(13)
Ce-N_3	2.3897(19)	C_5-N_3-Ce	110.72(13)
Ce-N_4	2.6749(17)	Ce-Cent-N_4	176.40
N_1-Si_1	1.7071(19)		
N_2-Si_2	1.7050(19)		
N_3-Si_3	1.7102(19)	**Bond**	**Mean value (Å)**
N_1-C_1	1.468(3)	Ce-$N_{equatorial}$	2.376(4)
N_2-C_3	1.473(3)	Ce-N_{plane}	0.806
N_3-C_5	1.464(3)	N-Si	1.707(4)
Ce-N_5	2.495(2)		
N_5-N_6	1.144(3)		
N_6-N_7	1.166(3)		

Table S15. Selected bond lengths and angles for **1-N_3-15c5**, [Na@15-crown-5][$N_3Ce^{III}TREN^{TIPS}$]

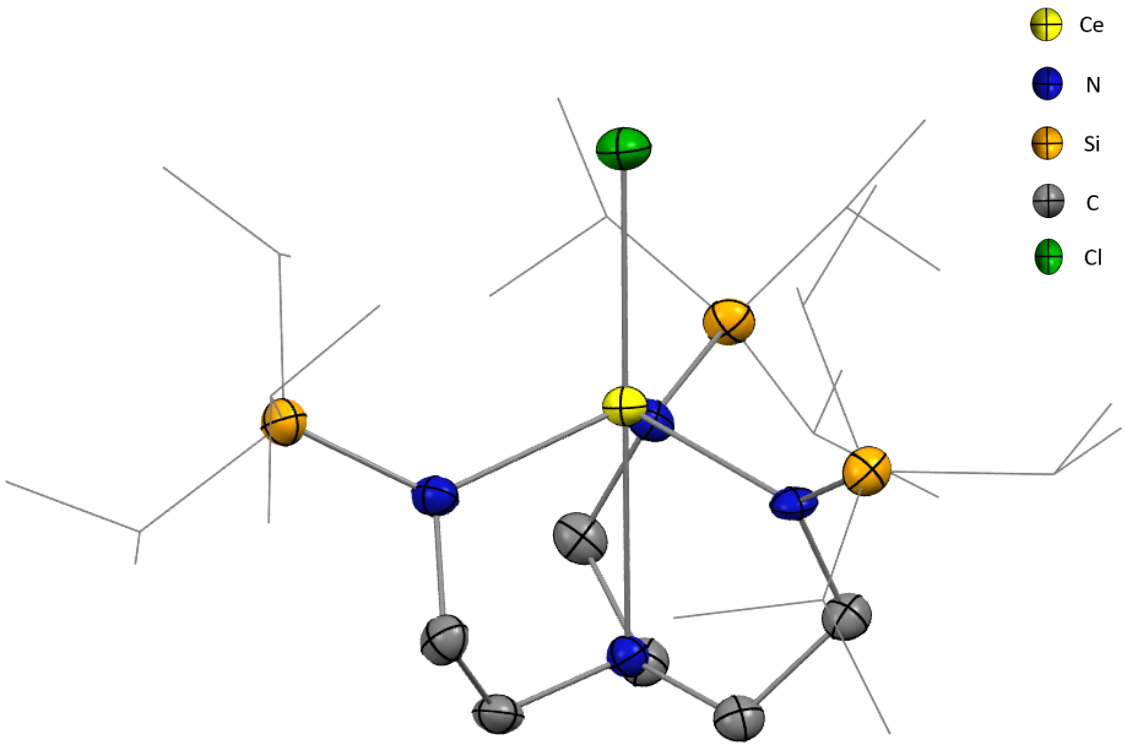

Figure S55. Structure of **2-Cl**. Displacement ellipsoids are represented at 50% probability. Hydrogen atoms have been omitted for clarity, and isopropyl groups have been represented in wireframe style. The molecule presents a slight disorder on the isopropyl ligands, which was modelled but not plotted for clarity

Bond	Length (Å)	Bonds	Angle (°)
Ce-N_1	2.202(3)	C_1-N_1-Ce	109.39(19)
Ce-N_2	2.225(3)	C_3-N_2-Ce	113.8(2)
Ce-N_3	2.233(3)	C_5-N_3-Ce	111.4(2)
Ce-N_4	2.606(3)	Ce-Cent-N_4	177.4
N_1-Si_1	1.746(3)		
N_2-Si_2	1.747(3)		
N_3-Si_3	1.736(3)		
N_1-C_1	1.476(5)	**Bond**	**Mean value (Å)**
N_2-C_3	1.479(5)	Ce-$N_{equatorial}$	2.220(3)
N_3-C_5	1.480(5)	Ce-N_{plane}	0.694
Ce-Cl	2.625(11)	N-Si	1.743(2)

Table S16. Selected bond lengths and angles for **2-Cl**

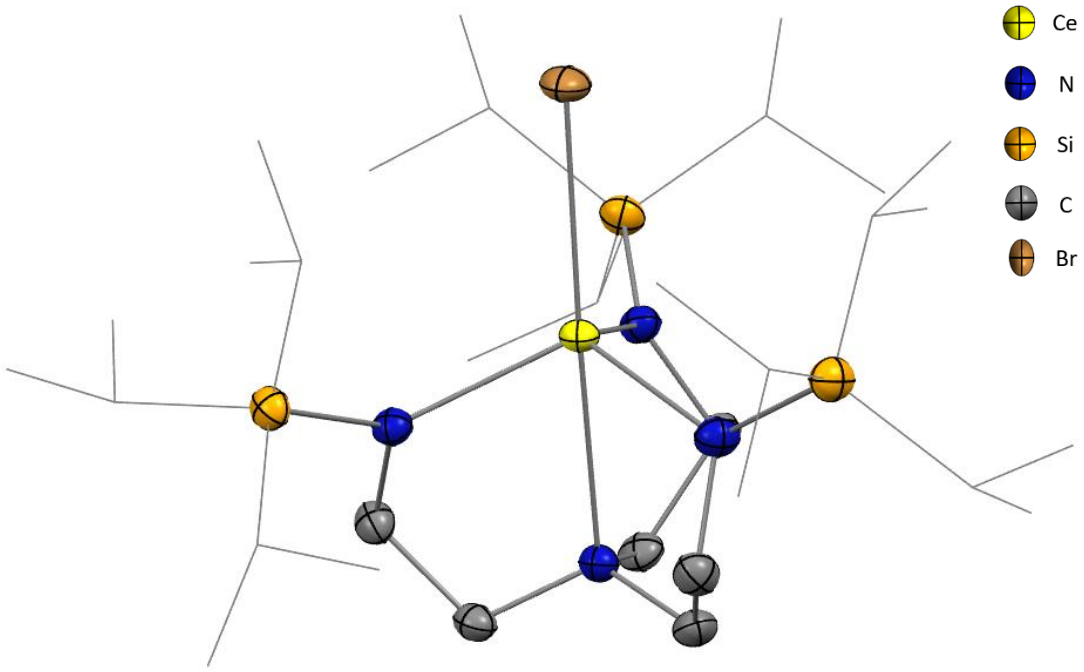

Figure S56. Structure of **2-Br**. Displacement ellipsoids are represented at 50% probability. Hydrogen atoms have been omitted for clarity, and isopropyl groups have been represented in wireframe style. The molecule presents a slight disorder on the isopropyl ligands. The disorder was modelled but not plotted for clarity

Bond	Length (Å)	Bonds	Angle (°)
Ce-N_1	2.229(2)	C_1-N_1-Ce	113.43(15)
Ce-N_2	2.232(2)	C_3-N_2-Ce	111.31(14)
Ce-N_3	2.206(2)	C_5-N_3-Ce	109.03(15)
Ce-N_4	2.603(2)	Ce-Cent-N_4	177.8
N_1-Si_1	1.743(2)		
N_2-Si_2	1.743(2)		
N_3-Si_3	1.750(2)		
N_1-C_1	1.481(3)	**Bond**	**Mean value (Å)**
N_2-C_3	1.483(3)	Ce-$N_{equatorial}$	2.222(5)
N_3-C_5	1.473(3)	Ce-N_{plane}	0.687
Ce-Br	2.785(3)	N-Si	1.754(3)

Table S17. Selected bond lengths and angles for **2-Br**

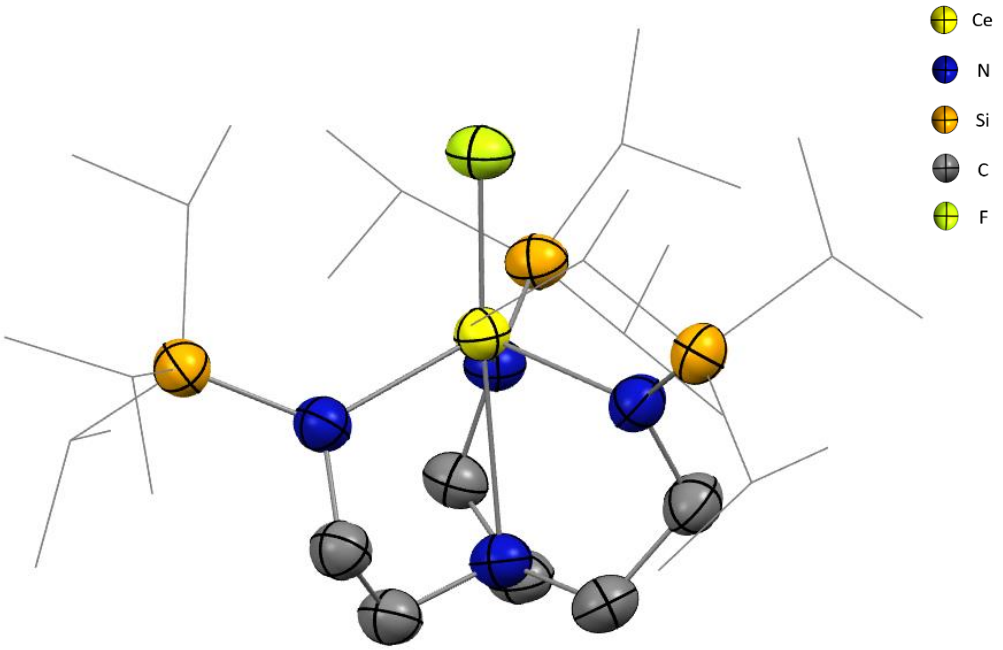

Figure S57. Structure of **2-F.** Displacement ellipsoids are represented at 50% probability. Hydrogen atoms have been omitted for clarity, and isopropyl groups have been represented in wireframe style. The molecule presents a slight disorder on the isopropyl ligands. The disorder was modelled but not plotted for clarity. NB : two molecules are present in the asymmetric unit, but only one was displayed here

Bond	Length (Å)	Bonds	Angle (°)
Ce-N_1	2.227(3)	C_1-N_1-Ce	114.3(2)
Ce-N_2	2.223(3)	C_3-N_2-Ce	111.9(2)
Ce-N_3	2.235(2)	C_5-N_3-Ce	116.21(19)
Ce-N_4	2.620(3)	Ce-Cent-N_4	174.42
N_1-Si_1	1.734(3)		
N_2-Si_2	1.737(3)		
N_3-Si_3	1.738(3)		
N_1-C_1	1.482(4)	**Bond**	**Mean value (Å)**
N_2-C_3	1.477(4)	Ce-$N_{equatorial}$	2.222(4)
N_3-C_5	1.467(4)	Ce-N_{plane}	0.722
Ce-F	2.0985(18)	N-Si	1.736(5)

Table S18. Selected bond lengths and angles for **2-F**

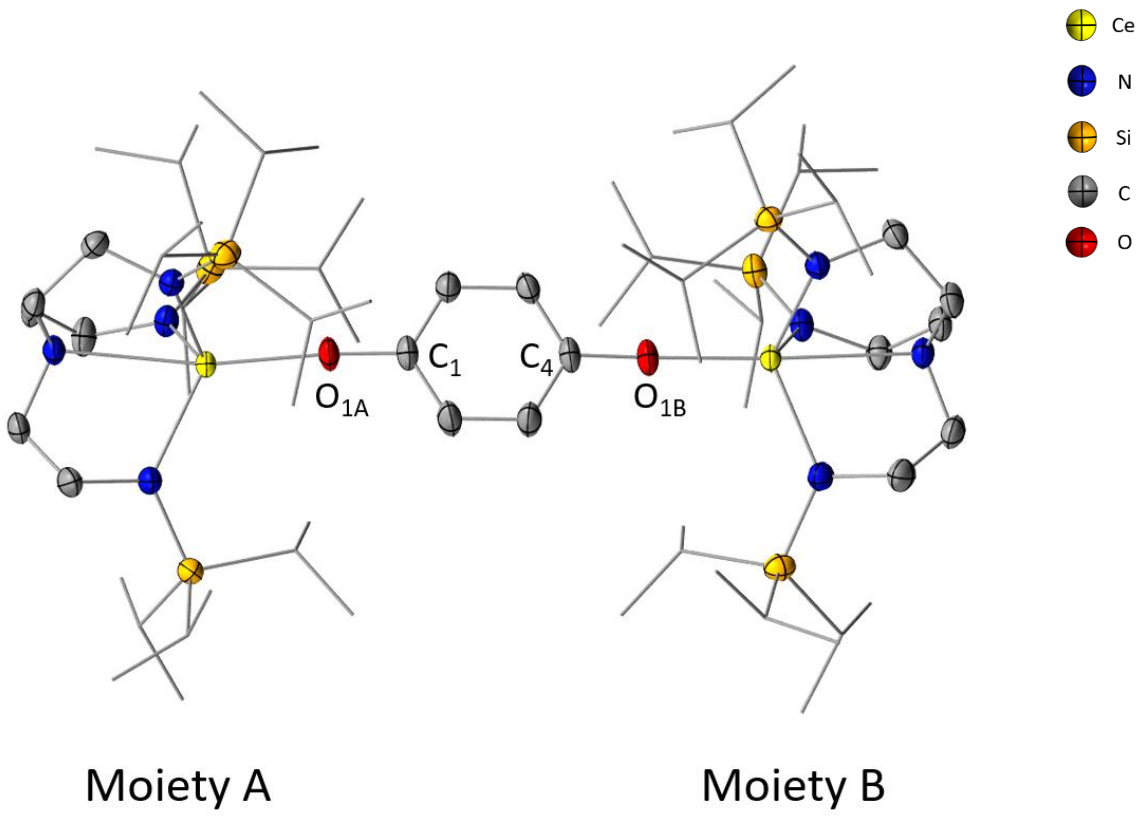

Figure S58. Structure of **2-Bq.** Displacement ellipsoids are represented at 50% probability. Hydrogen atoms have been omitted for clarity, and isopropyl groups have been represented in wireframe style. One THF molecule is present in the cell but it was not represented here.

Bond	Length (Å)	Bonds	Angle (°)
Ce_1-N_4	2.6427(18)	C_1-N_1-Ce_1	118.42(14)
Ce_2-N_8	2.6471(18)	C_{34}-N_5-Ce_2	112.80(14)
N_{1A}-C_{1A}	1.480(3)	Ce_1-$Cent_1$-N_4	174.49
N_{1B}-C_{1B}	1.481(3)	Ce_2-$Cent_2$-N_8	177.54
Ce_A-O_1	2.1423(15)	$N_{plane,1}$-$N_{plane,2}$	9.53
Ce_B-O_2	2.1400(16)		
O_1-C_1	1.360(3)		
O_2-C_4	1.361(3)	**Bond**	**Mean value (Å)**
C_{aro}-C_{aro}	1.388(3)-1.396(3)	Ce_A-$N_{equatorial}$	2.263(33)
		Ce_B-$N_{equatorial}$	2.263(33)
		Ce_A-N_{plane}	0.751
		Ce_B-N_{plane}	0.745
		$(N\text{-}Si)_A$	1.745(4)
		$(N\text{-}Si)_B$	1.743(4)

Table S19. Selected bond lengths and angles for **2-Bq**

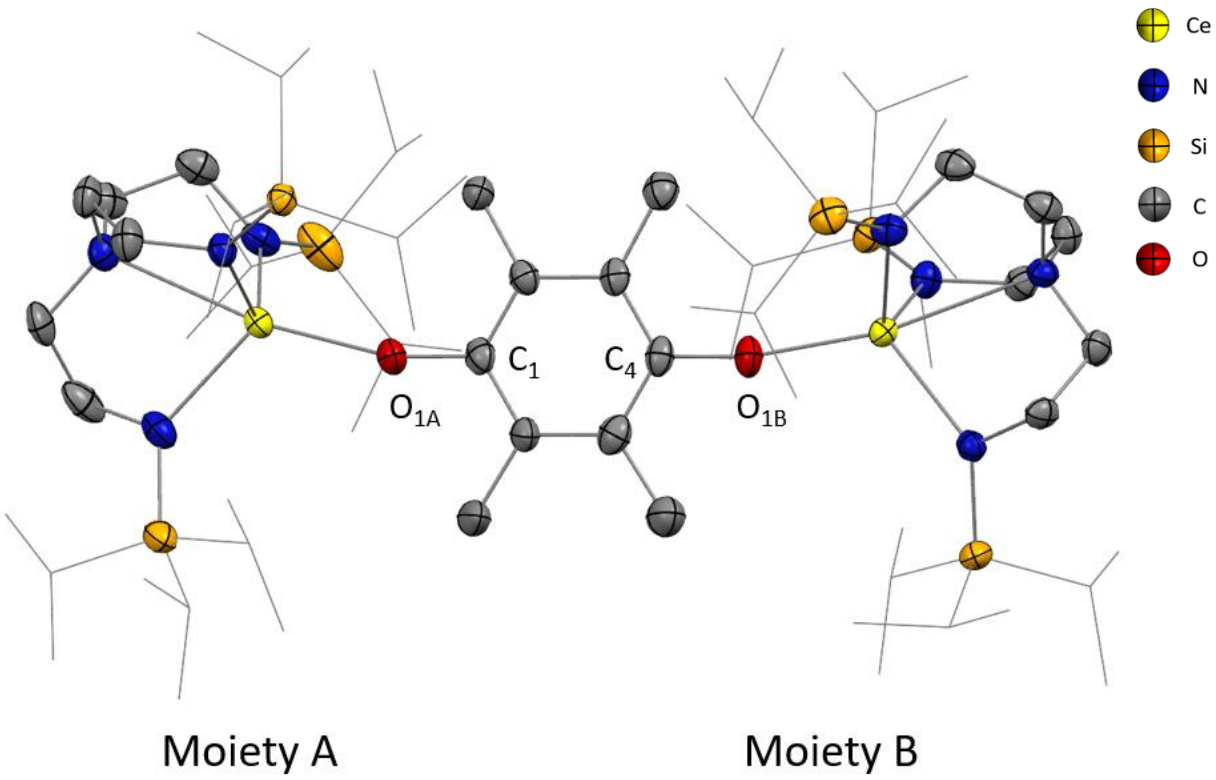

Figure S59. Structure of **2-BqMe$_4$**. Displacement ellipsoids are represented at 50% probability. Hydrogen atoms have been omitted for clarity, and isopropyl groups have been represented in wireframe style. One THF molecule and one molecule of pentane are present in the cell but were not represented here

Bond	Length (Å)	Bonds	Angle (°)
Ce_{1A}-N_{1A}	2.264(4)	C_{1A}-N_{1A}-Ce_{1A}	112.9(3)
Ce_{1B}-N_{2B}	2.266(5)	C_{1B}-N_{1B}-Ce_{1B}	112.9(3)
N_{1A}-C_{1A}	1.487(7)	Ce_{1A}-O_{1A}-C_1	165.0(4)
N_{1B}-C_{1B}	1.458(7)	Ce_{1B}-O_{1B}-C_4	169.4(4)
Ce_{1A}-O_{1A}	2.133(4)		
Ce_{1B}-O_{1B}	2.118(4)	**Bond**	**Mean value (Å)**
O_{1A}-C_1	1.366(7)	Ce_{1A}-$N_{equatorial}$	2.265(7)
O_{1B}-C_4	1.377(6)	Ce_{1B}-$N_{equatorial}$	2.272(9)
C_{aro}-C_{aro}		$(N\text{-}Si)_A$	1.741(9)
		$(N\text{-}Si)_B$	1.742(9)

Table S20. Selected bond lengths and angles for **2-BqMe$_4$**

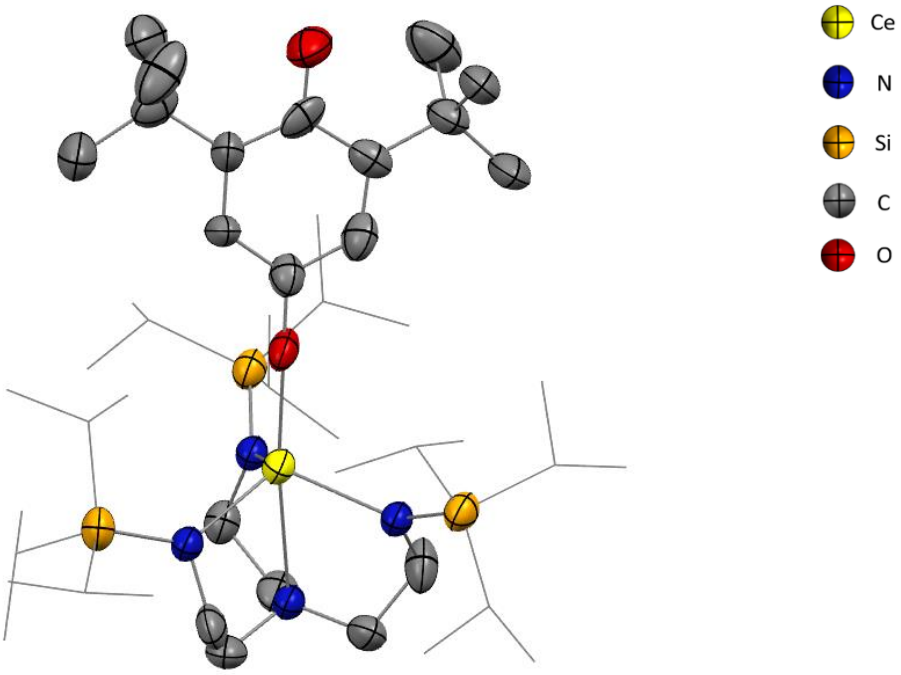

Figure S60. Structure of **2-^{t}Bu$_2$Bq.** Displacement ellipsoids are represented at 50% probability. Hydrogen atoms have been omitted for clarity, and isopropyl groups have been represented in wireframe style. One THF molecule is present in the cell but it was not represented here

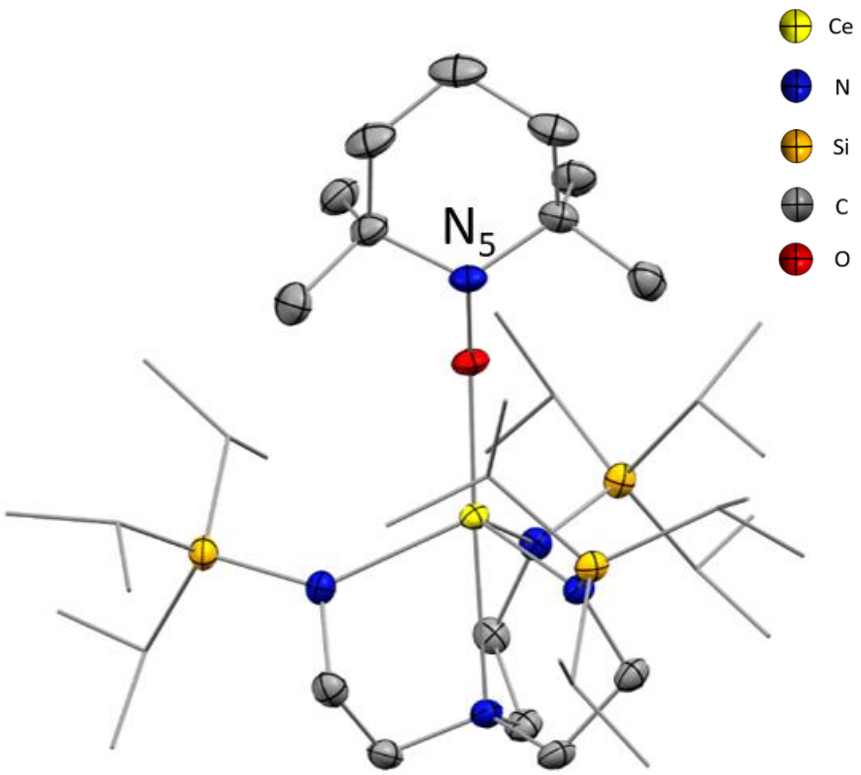

Figure S61. Structure of **2-TEMPO.** Displacement ellipsoids are represented at 50% probability. Hydrogen atoms have been omitted for clarity, and isopropyl groups have been represented in wireframe style

Bond	Length (Å)	Bonds	Angle (°)
Ce-N_1	2.2768(15)	C_1-N_1-Ce	109.49(11)
Ce-N_2	2.2512(14)	C_3-N_2-Ce	112.29(11)
Ce-N_3	2.2841(15)	C_5-N_3-Ce	109.93(11)
Ce-N_4	2.6916(15)	Ce-Cent-N_4	177.02
N_1-Si_1	1.7379(16)	O-Ce-N_4	177.34(5)
N_2-Si_2	1.7398(16)		
N_3-Si_3	1.7358(16)		
N_1-C_1	1.479(2)		
N_2-C_3	1.475(2)	**Bond**	**Mean value (Å)**
N_3-C_5	1.481(2)	Ce-$N_{equatorial}$	0.786
Ce-O	2.1181(13)	Ce-N_{plane}	0.786
O-N_5	1.4386(19)	N-Si	1.7378(28)

Table S21. Selected bond lengths and angles for **2-TEMPO**

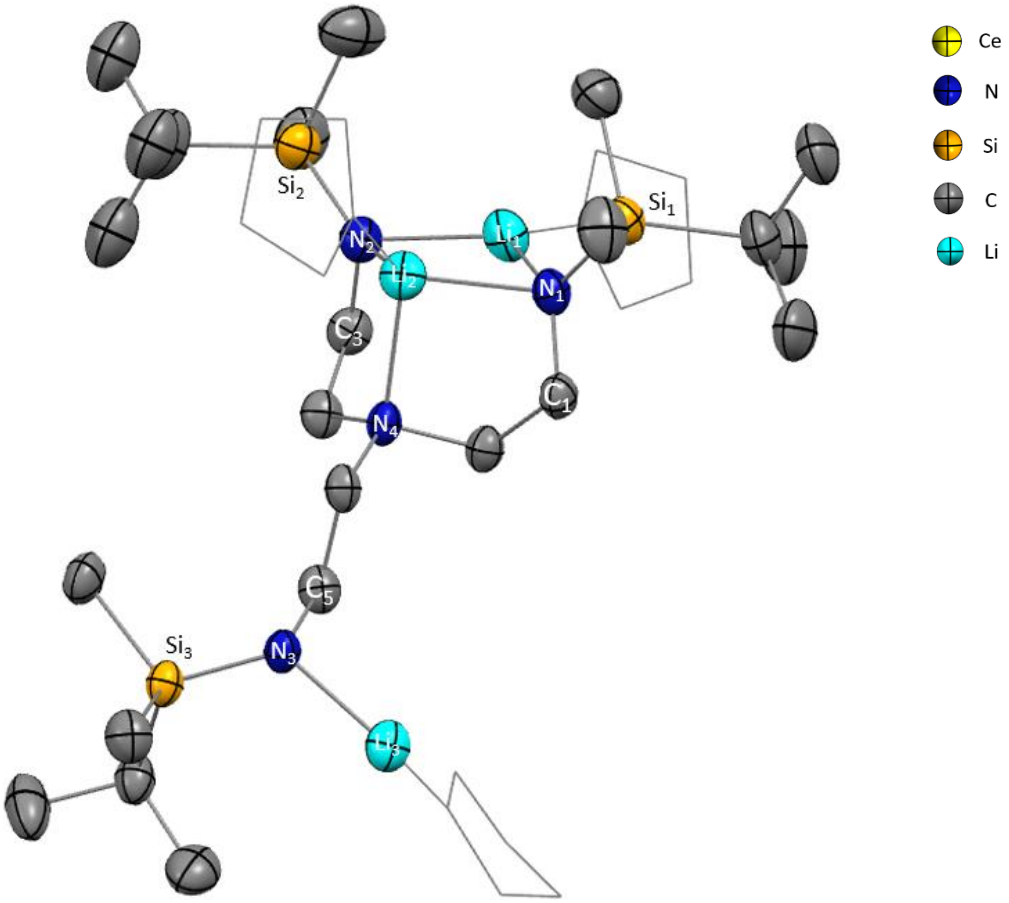

Figure S62. Structure of $Li_3TREN^{TBDMS}(THF)_3$. Displacement ellipsoids are represented at 50% probability. Hydrogen atoms have been omitted for clarity, and THF molecules have been represented in wireframe style

Bond	Length (Å)	Bond	Mean value (Å)
N_1-Si_1	1.691(3)	N-Si	1.691(6)
N_2-Si_2	1.680(3)		
N_3-Si_3	1.704(3)		
N_1-C_1	1.463(5)		
N_2-C_3	1.460(5)		
N_3-C_5	1.480(4)		
N_1-Li_1	1.981(7)		
N_2-Li_2	2.035(6)		
N_3-Li_3	1.977(7)		

Table S22. Selected bond lengths and angles for $Li_3TREN^{TBDMS}(THF)_3$

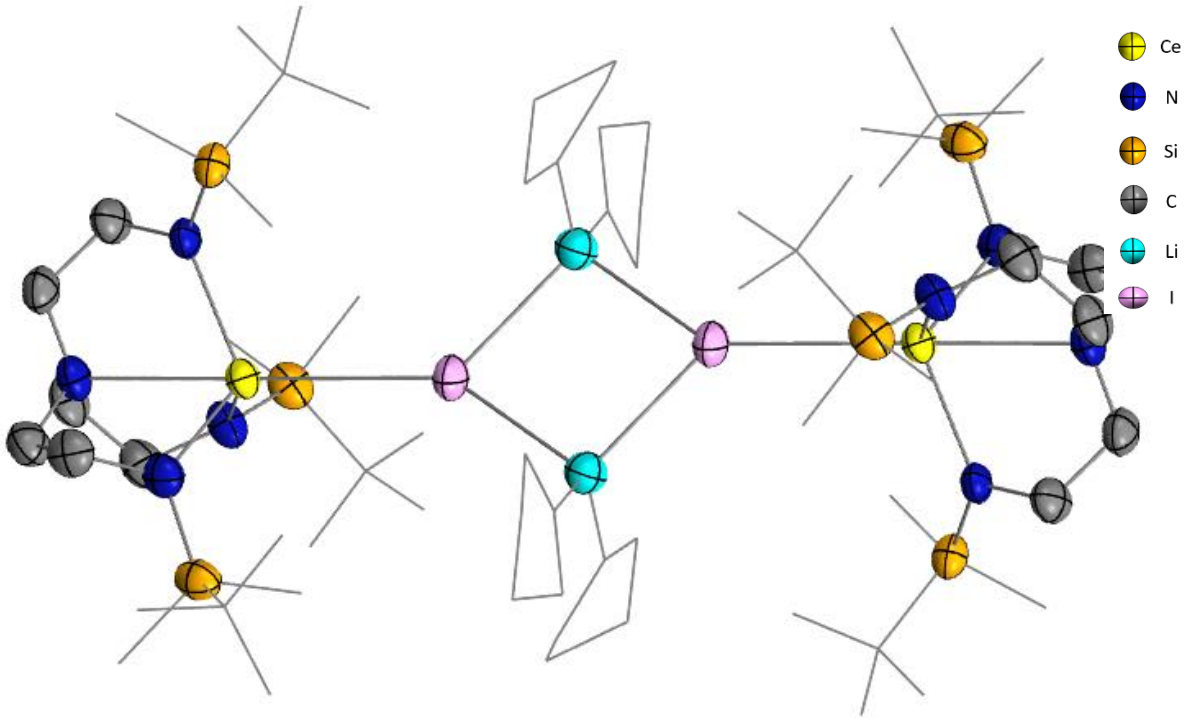

Figure S63. Structure of $[Li(THF)_4][ICe^{III}TREN^{TIPS}]$ (**$Ce^{III}TREN^{TBDMS}$-LiI-THF_2**). Displacement ellipsoids are represented at 50% probability. Hydrogen atoms have been omitted for clarity, and isopropyl groups and THF molecules have been represented in wireframe style. Values reported in **Table S23** were chosen on one of the two molecules present in the unit

Bond	Length (Å)	Bonds	Angle (°)
Ce-N_1	2.329(6)	C_1-N_1-Ce	114.0(5)
Ce-N_2	2.332(7)	C_3-N_2-Ce	114.2(5)
Ce-N_3	2.328(6)	C_5-N_3-Ce	114.5(5)
Ce-N_4	2.685(6)	Ce-Cent-N_4	178.02
N_1-Si_1	1.699(6)		
N_2-Si_2	1.692(7)		
N_3-Si_3	1.698(7)		
N_1-C_1	1.468(9)		
N_2-C_3	1.469(11)	**Bond**	**Mean value (Å)**
N_3-C_5	1.459(10)	Ce-$N_{equatorial}$	0.815
Ce-I	3.3294(6)	Ce-N_{plane}	0.815
Li-I	2.824(14)	N-Si	1.696(12)

Table S23. Selected bond lengths and angles for **$Ce^{III}TREN^{TBDMS}$-LiI-THF_2**

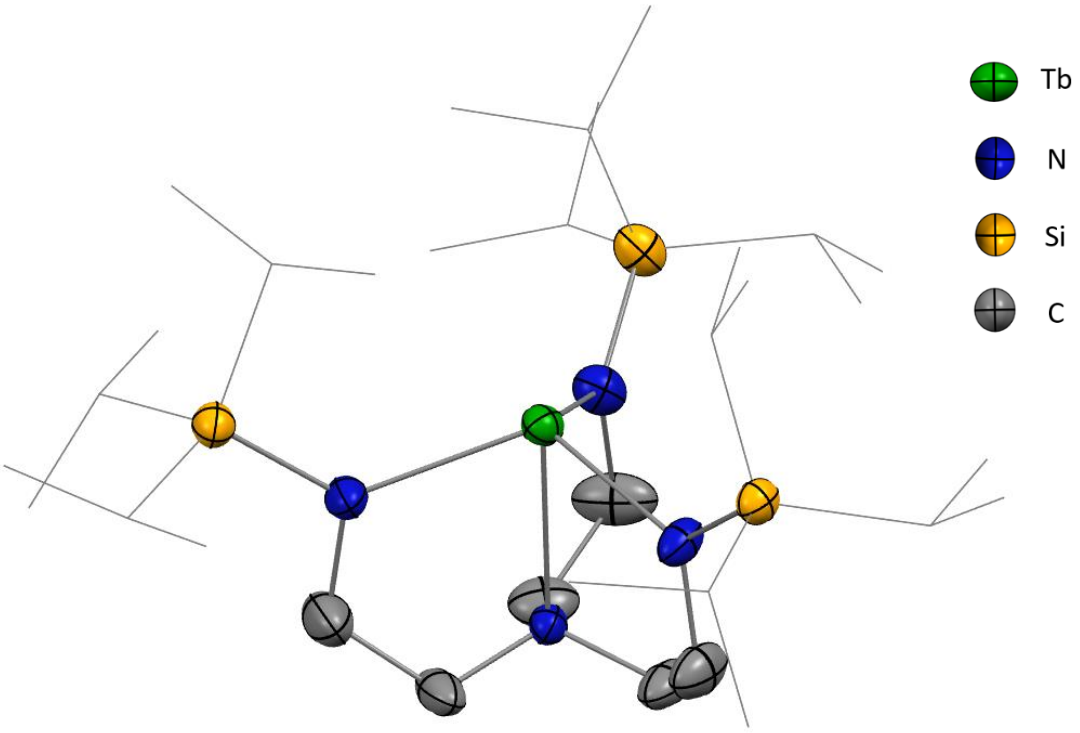

Figure S64. Structure of **$Tb^{III}TREN^{TIPS}$**. Displacement ellipsoids are represented at 50% probability. Hydrogen atoms have been omitted for clarity, and isopropyl groups and THF molecules have been represented in wireframe style

Bond	Length (Å)	Bonds	Angle (°)
Tb-N_1	2.253(4)	C_1-N_1-Tb	117.2(3)
Tb-N_2	2.279(4)	C_3-N_2-Tb	116.4(3)
Tb-N_3	2.269(4)	C_5-N_3-Tb	115.1(3)
Tb-N_4	2.418(4)	Tb-Cent-N_4	
N_1-Si_1	1.716(4)		
N_2-Si_2	1.697(4)		
N_3-Si_3	1.717(4)	**Bond**	**Mean value (Å)**
N_1-C_1	1.479(6)	Tb-$N_{equatorial}$	2.267(3)
N_2-C_3	1.480(6)	Tb-N_{plane}	0.630
N_3-C_5	1.464(6)	N-Si	1.710(7)

Table S24. Selected bond lengths and angles for **$Tb^{III}TREN^{TIPS}$**

IV. Magnetic measurements

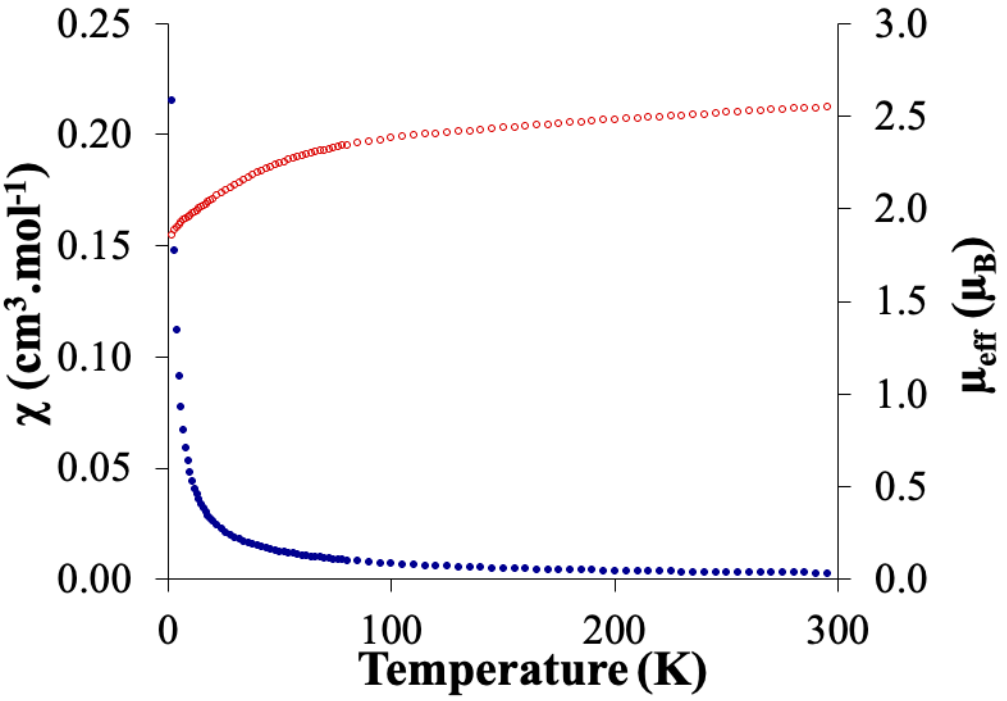

Figure S65. Solid-state temperature-dependent magnetic data of **1** recorded at 0.5 T, χ *vs.* T plot in blue and μ_{eff} *vs.* T plot in red. Data plot by Eric Rivière

V. EPR measurements for Chapter I

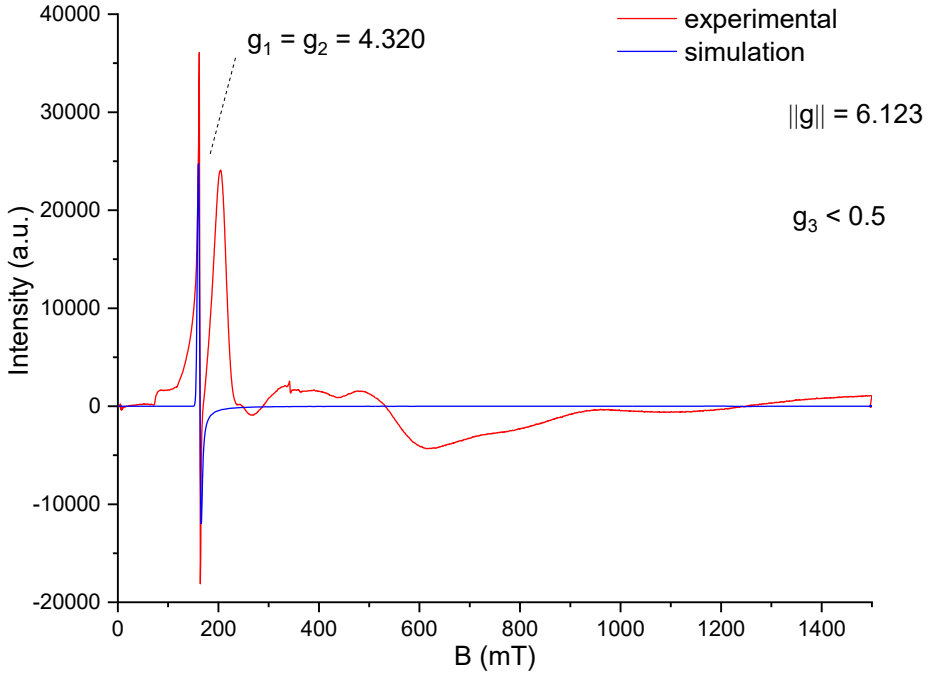

Figure S66. X-band EPR spectrum of powder of **1** at 10 K. Simulation of the "axial" system

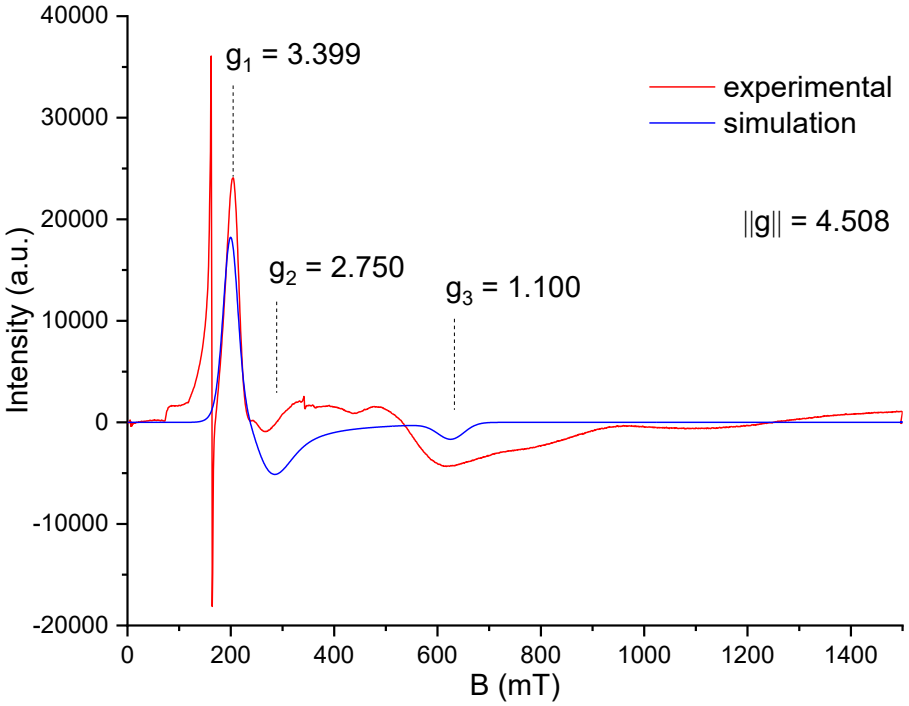

Figure S67. X-band EPR spectrum of powder of **1** at 10 K. Simulation of the second system

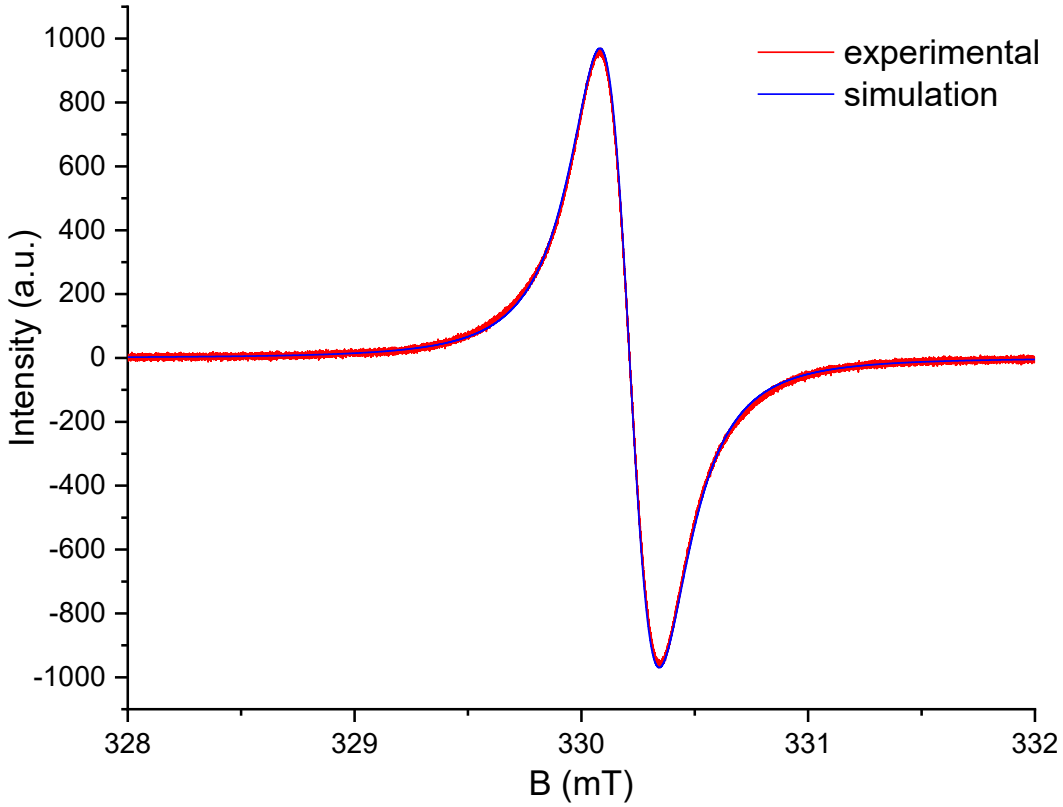

Figure S68. X-band EPR spectrum of a solution of crystals of **2-^{t}Bu$_2$Bq** in pentane

Parameter	Value
g	1.99424
lwpp	[0.081 0.236]

Table S25. Fitting values associated with EPR spectrum of the crystals of **2-^{t}Bu$_2$Bq** in pentane

VII. UV-visible and fluorescence spectra

k) Experimental data

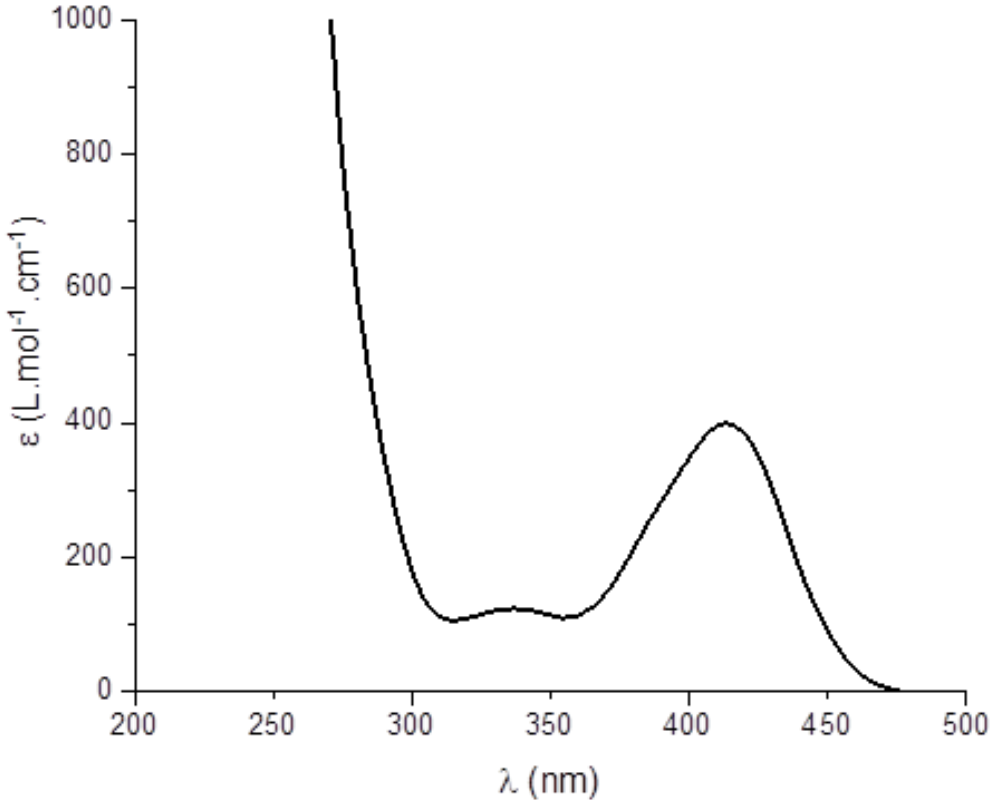

Figure S69. UV-visible spectrum of **1** in pentane at 298 K

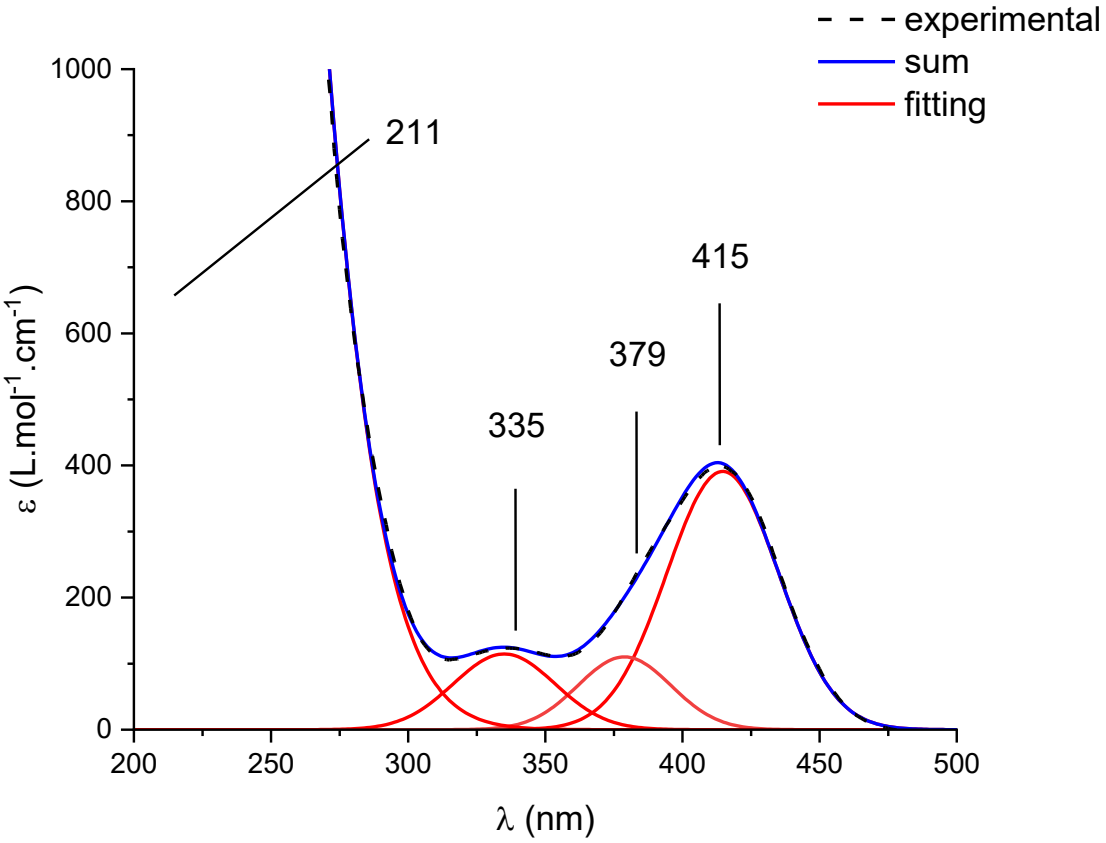

Figure S70. Deconvoluted UV-visible spectrum of **1** in pentane

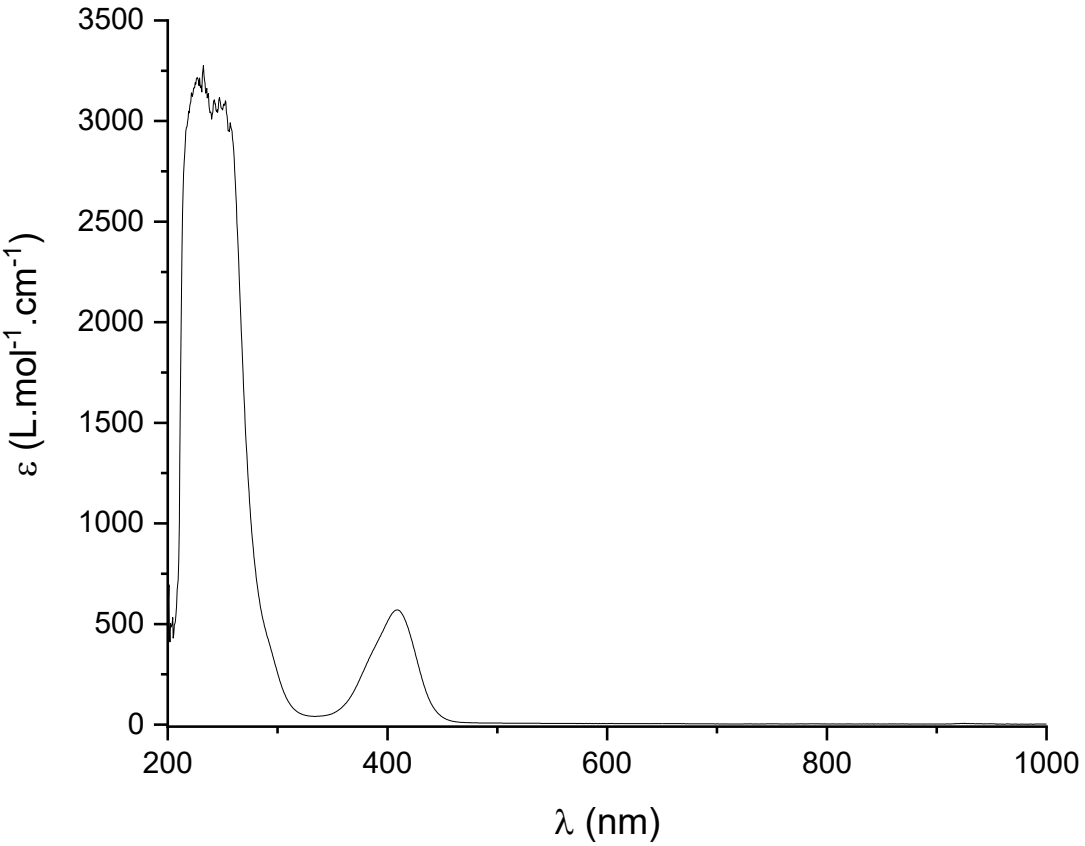

Figure S71. UV-visible spectrum of **1** in THF at 298 K

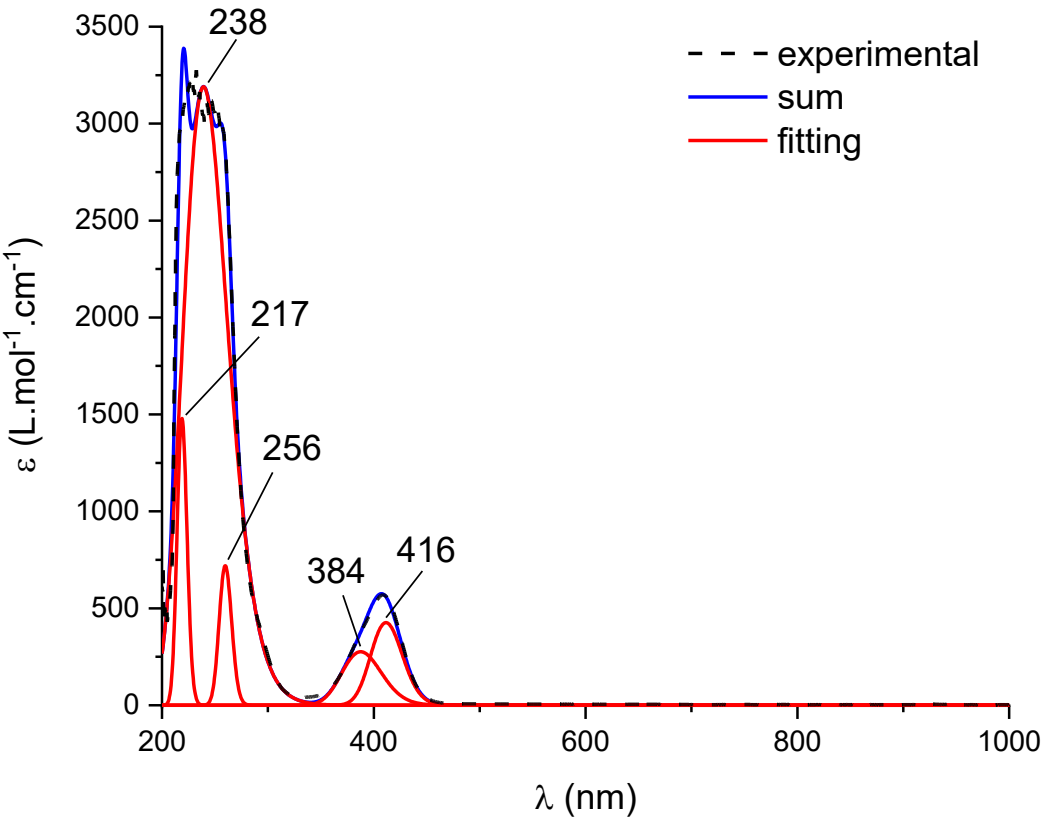

Figure S72. Deconvoluted UV-visible spectrum of **1** in THF at 298 K

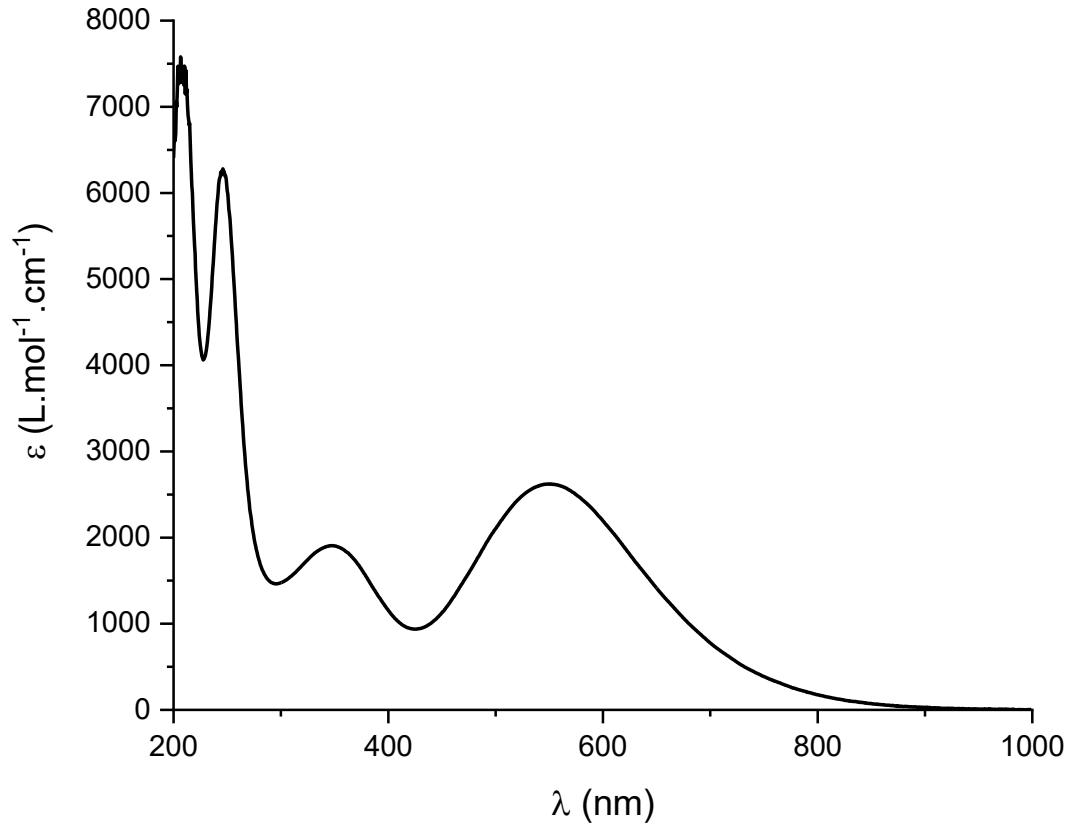

Figure S73. UV-visible spectrum of **2-Cl** in pentane at 298 K

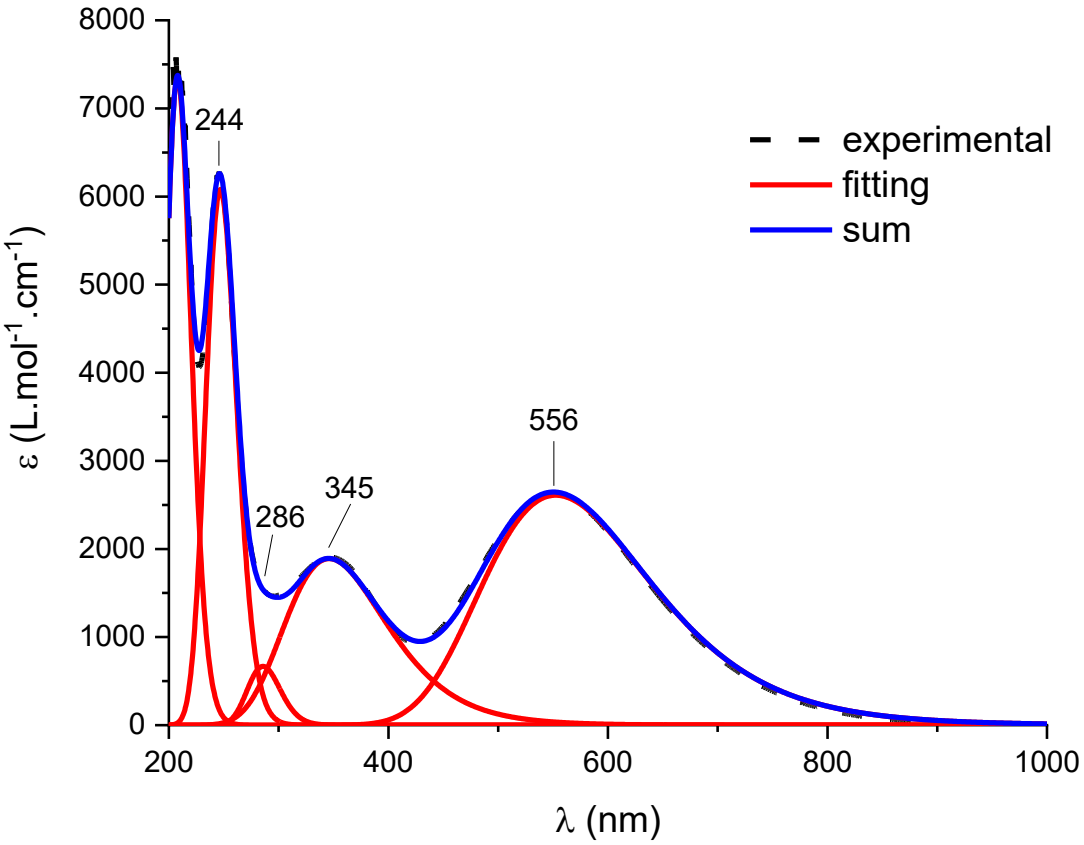

Figure S74. Deconvoluted UV-visible spectrum of **2-Cl** in pentane

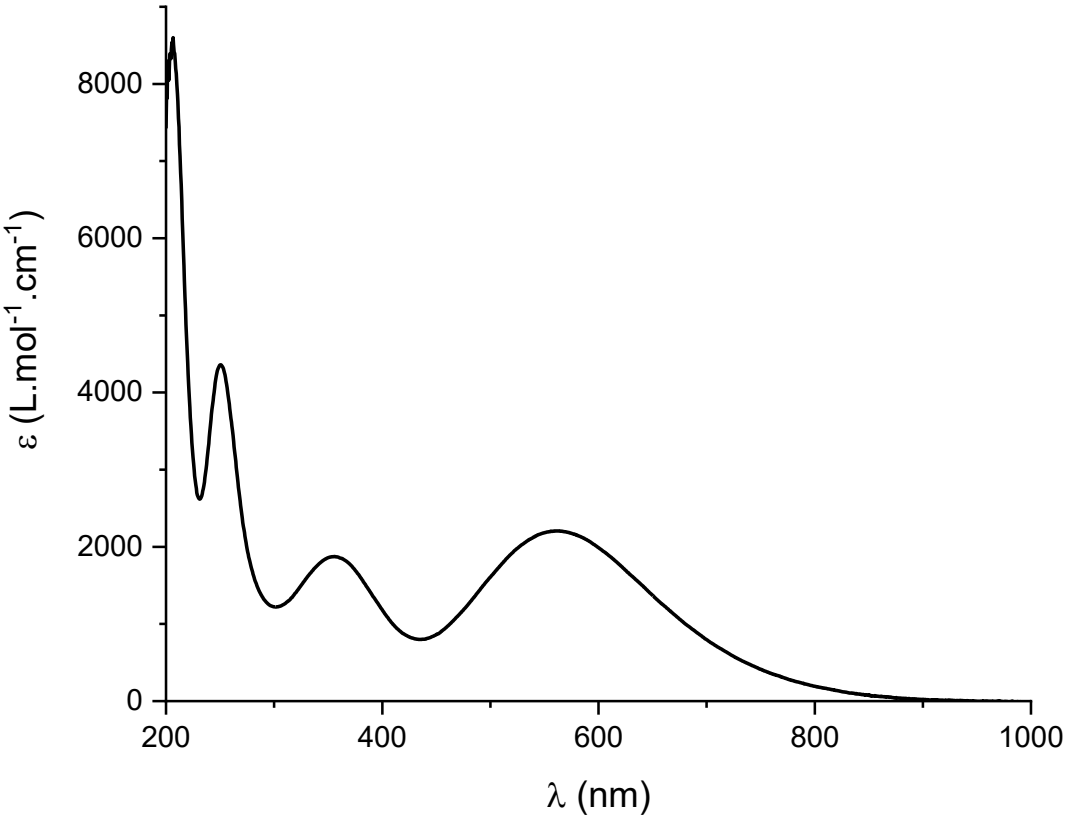

Figure S75. UV-visible spectrum of **2-Br** in pentane at 298 K

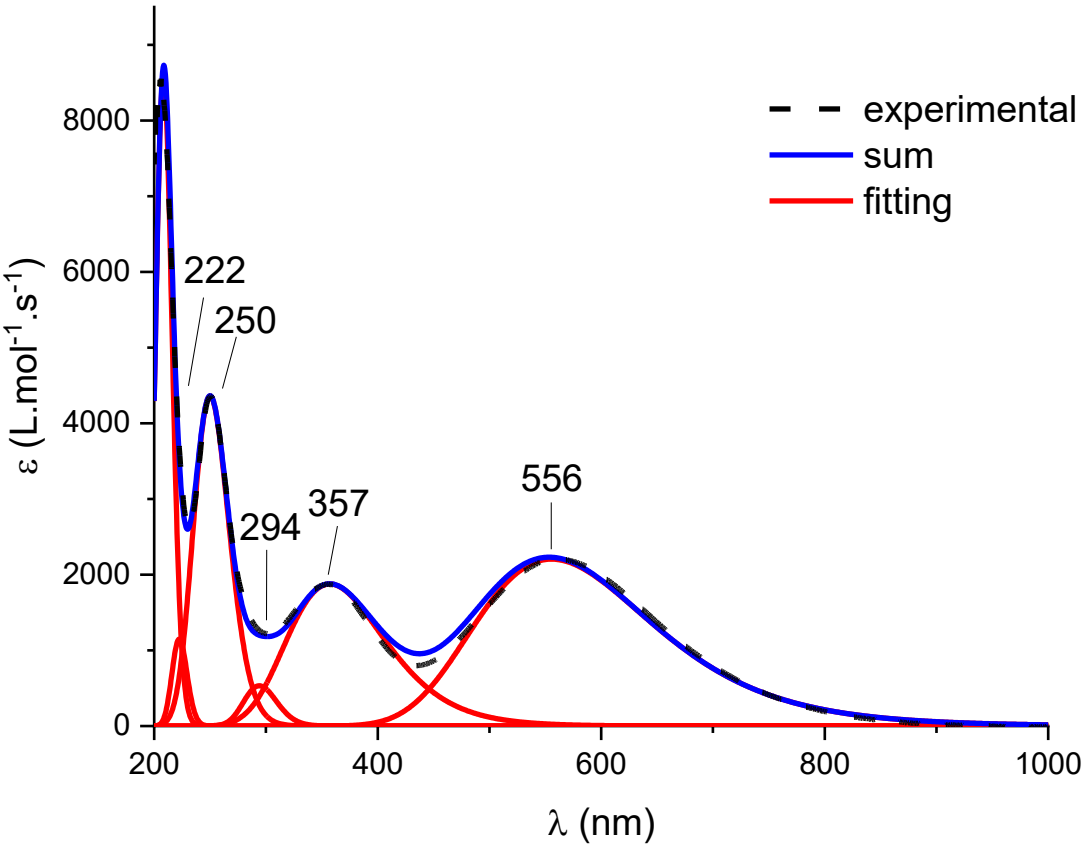

Figure S76. Deconvoluted UV-visible spectrum of **2-Br** in pentane

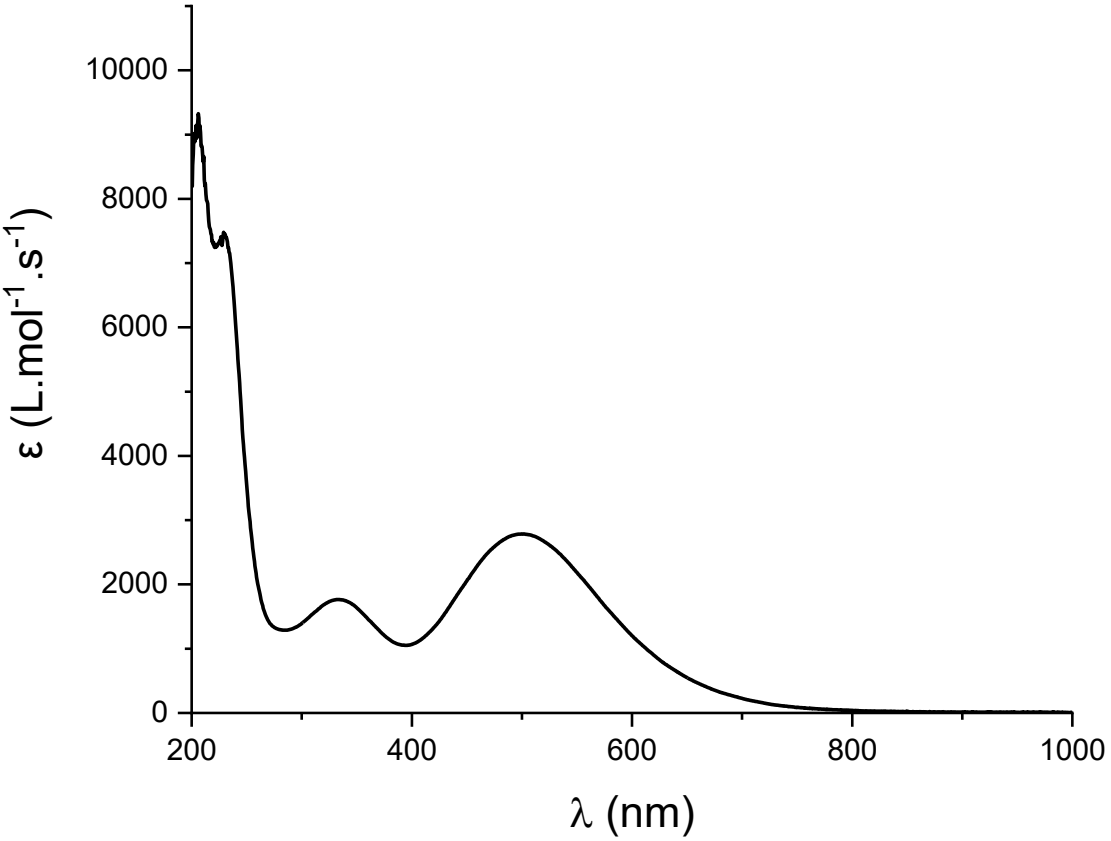

Figure S77. UV-visible spectrum of **2-F** in pentane at 298 K

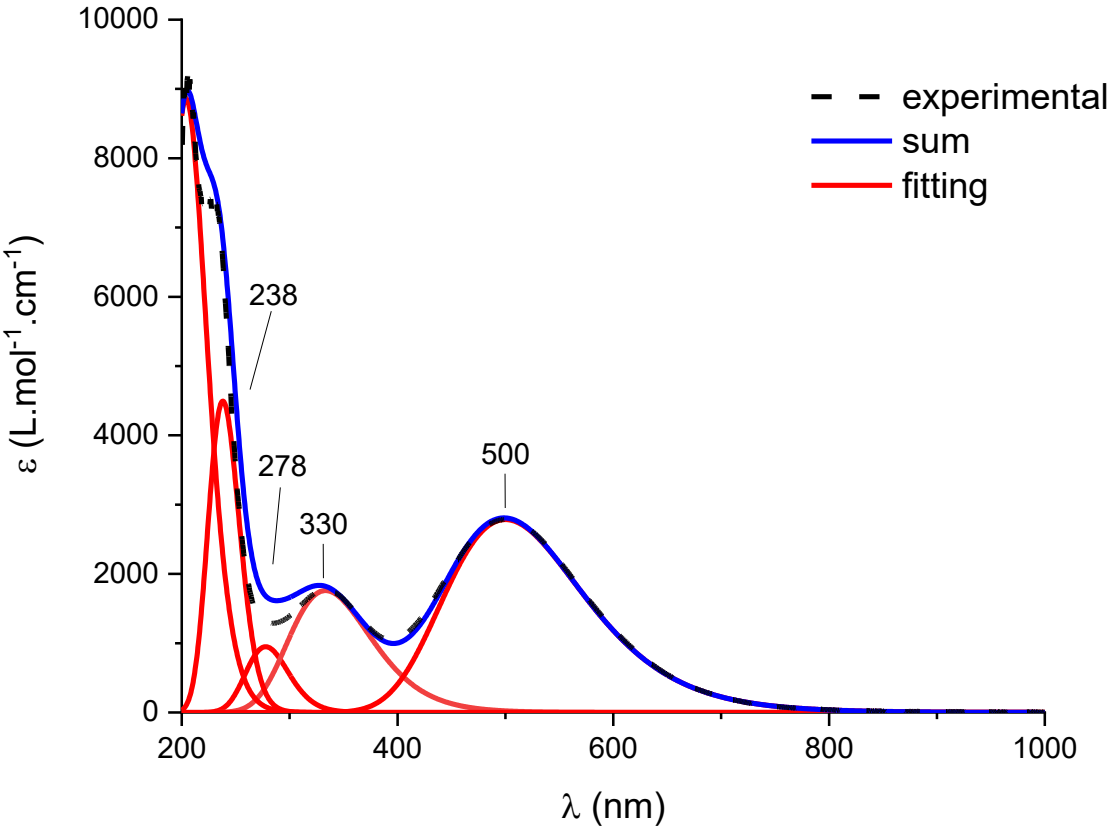

Figure S78. Deconvoluted UV-visible spectrum of **2-F** in pentane

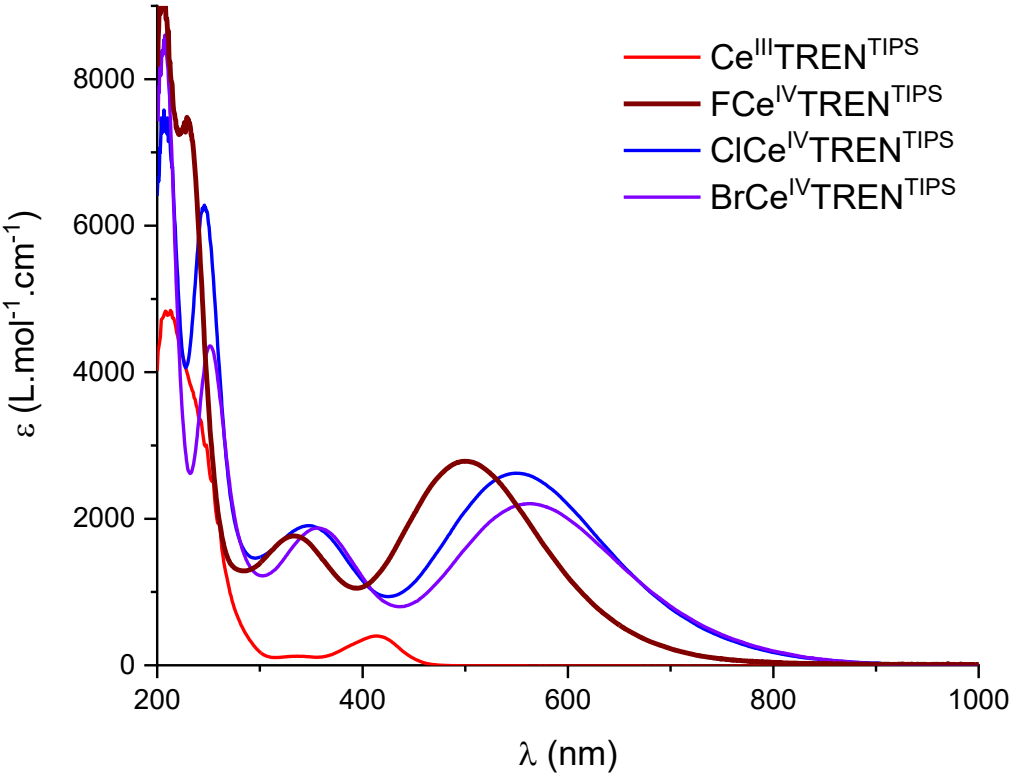

Figure S79. Superimposition of absorption spectra of **1**, **2-Cl**, **2-Br** and **2-F** in pentane at 298 K

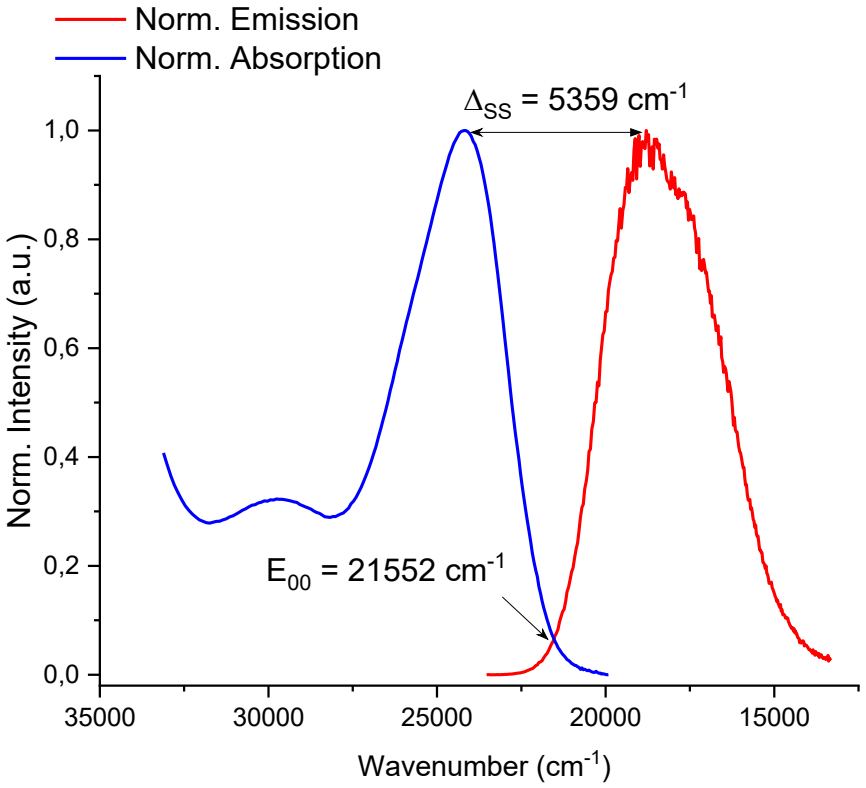

Figure S80. Normalized emission and absorption spectra of **1** in pentane, including measurements of Stokes shift and zero-zero electronic transition. Figure plot by Akos Banyasz and Olivier Maury

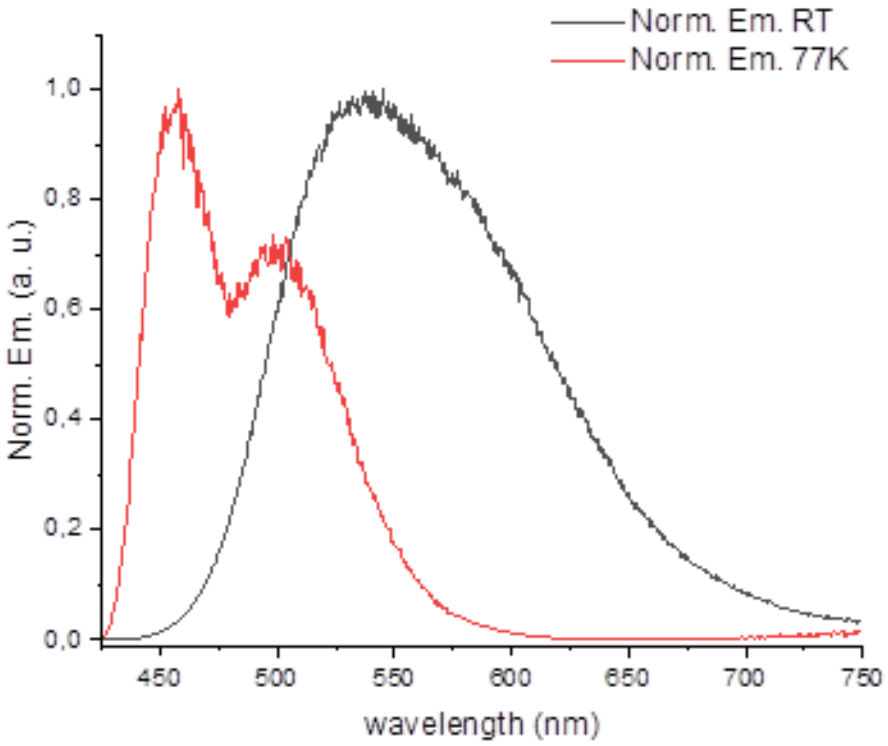

Figure S81. Emission spectra of **1** in 2-MeTHF at room temperature (Black curve) and 77 K (Red curve). Figure plotted by Akos Banyasz and Olivier Maury

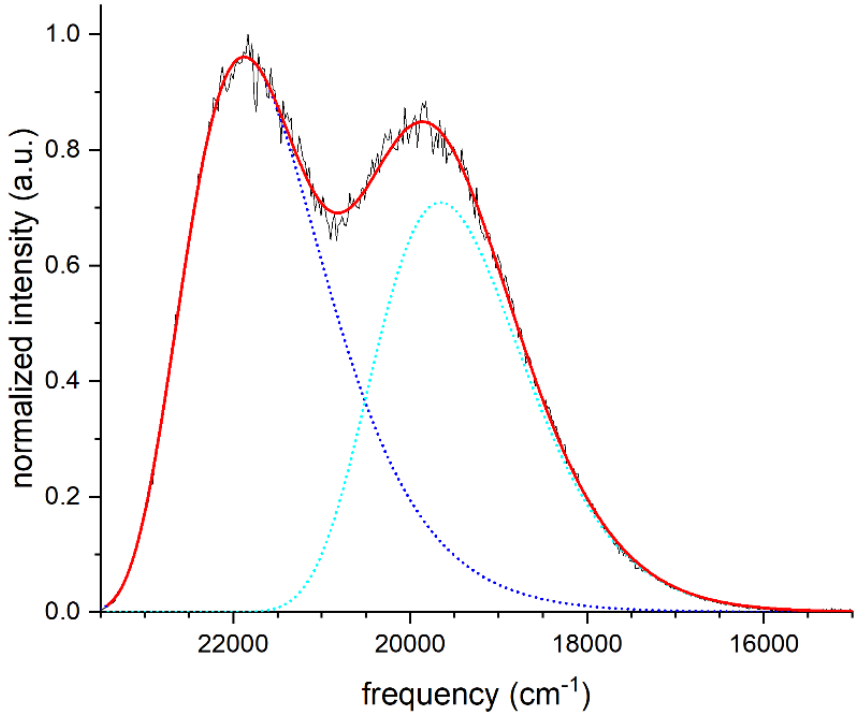

Figure S82. Emission spectra of **1** in 2-MeTHF at 77 K (black) presented on frequency scale along with the lognorm fit of the two-constituting bands (1 in dark and 2 in light blue) and the sum (red) of the two-lognorm functions. Figure realised by Akos Banyasz and Olivier Maury

The 77 K emission spectrum of [$Ce^{III}TREN^{TIPS}$], **1**, was converted to frequency scale then λ^2 correction was applied on the emission intensity. The obtained spectrum was fitted by the sum of two simplified lognorm functions[3] to characterize the parameters of the two involved transitions. The frequencies corresponding to the peak maximum (ν_{max}) and to the full-width at half-maximum (ν_{FWHM}) are calculated according to equations 2 and 3 and presented in **Table S26**.

Equation 1. $$I_\nu = A * \exp\left(-\beta^2\left(ln\left(\frac{a-\nu}{b}\right)\right)^2\right)$$

Equation 2. $$\upsilon_{max} = a - b$$

Equation 3. $$\upsilon_{FWHM} = b\ sinh\left(\sqrt{ln2}/\beta\right)$$

	A	B
A	0.96 (0.01)	0.71 (0.01)
β^2	5.4 (0.3)	10.0 (0.3)
a (10^3 cm^{-1})	24.5 (0.1)	23.4 (0.1)
b (10^3 cm^{-1})	2.6 (0.1)	3.8 (0.1)
ν_{max} (10^3 cm^{-1})	21.9 (0.1)	19.7 (0.1)
ν_{FWHM} (10^3 cm^{-1})	1.9 (0.1)	2.0 (0.1)

Table S26. Result of the lognorm fit of the 77 K emission spectrum of **1** according to equations 1-3. Standard errors are in parenthesis. Data provided by Akos Banyasz and Olivier Maury

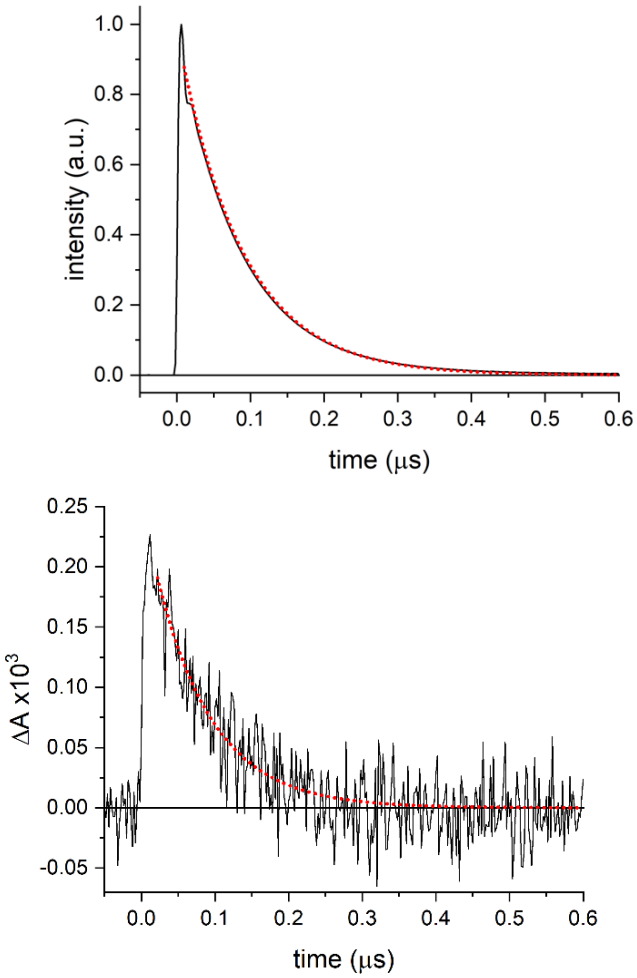

Figure S83. Luminescence (left) and transient absorption (right) decays of **1** obtained at 550 and 400 nm, respectively, upon 354 nm excitation. The dotted red line represents the monoexponential fit. Figure realised by Akos Banyasz and Olivier Maury

a)  b) 

Figure S84. a) **1** under ambient light, b) **1** under irradiation at 427 nm at 298 K

VIII. Electrochemistry

a) Cyclic voltammetry measurements

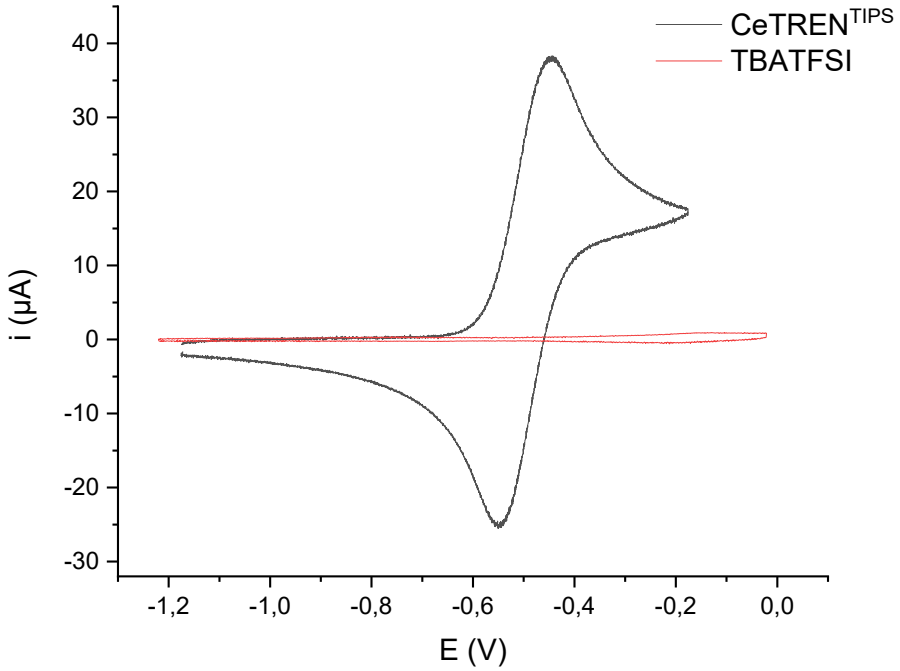

Figure S85. Cyclic voltammogram at 50 mV.s^{-1} scan rate of supporting electrolyte (100 mM) and **1** (4 mM)

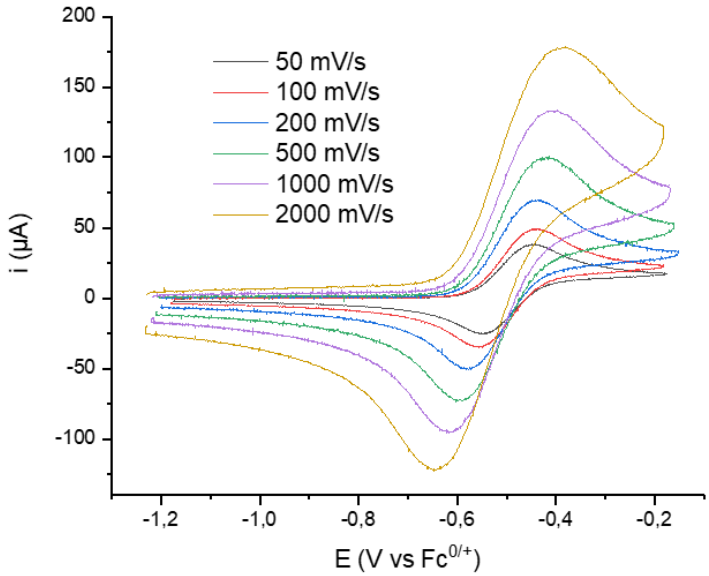

Figure S86. Cyclic voltammograms at various scan rates of 1 (4 mM)

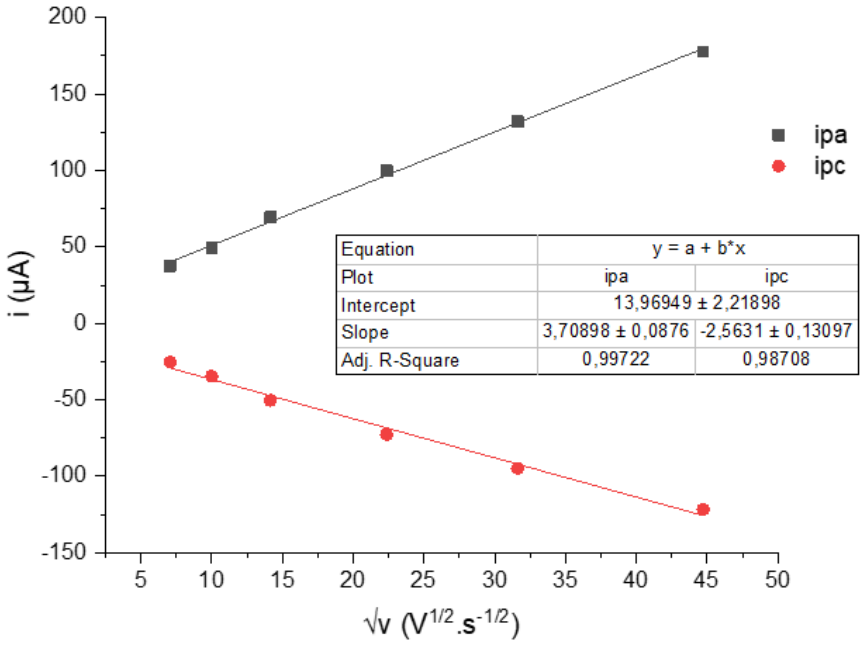

Figure S87. Modelling of the relationship between i_p and square root of scan rate to check the validity of Randles-Ševčík equation

v (mV.s^{-1})	$\sqrt{v}$ (mV$^{1/2}$.s$^{-1/2}$)	i_{pa} (µA)	i_{pc} (µA)	E_{pa} (V)	E_{pc} (V)	ΔV (V)
50	7.07	37.5	-25.3	-0.45	-0.56	0.11
100	10	49.3	-34.6	-0.44	-0.51	0.12
200	14.14	69.4	-50.4	-0.44	-0.58	0.14
500	22.36	99.7	-72.7	-0.42	-0.60	0.18
1000	31.62	132	-95	-0.41	-0.62	0.21
2000	44.72	177.8	-121.8	-0.39	-0.64	0.25

Table S27. Experimental data of the influence of the scan rate over the intensities and the potentials of anodic and cathodic peaks in cyclic voltammetry of **1**

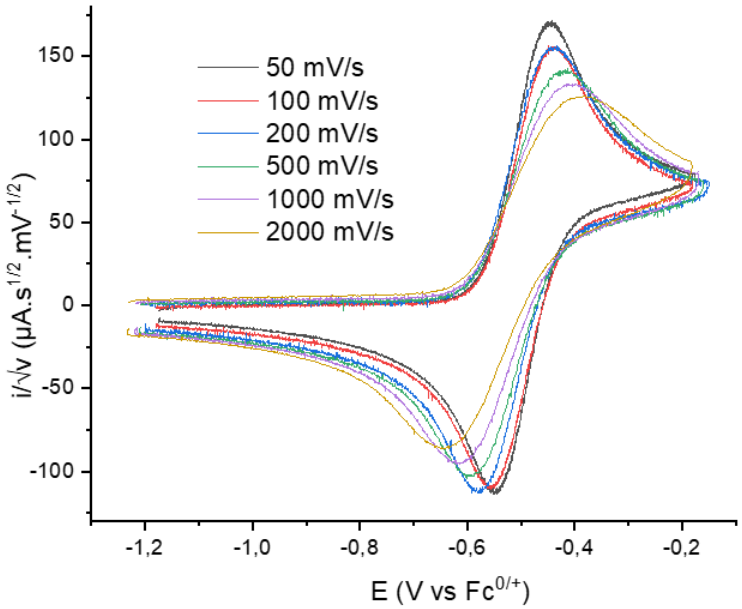

Figure S88. Cyclic voltammograms of **1** at different scan rates, normalized by $\sqrt{v}$

b) Estimation of the work function ω_f

As detailed in Appendix, $\omega_f = \frac{e^2}{\varepsilon a}$ where e is the elementary charge of the electron (e = 1.6 10^{-19} C), ε the dielectric permittivity of the medium and a the ion-radical pair distance.

Considering $\varepsilon = \varepsilon_r \varepsilon_0$ with ε_r being the relative permittivity of the solvent (here THF, $\varepsilon_r = 7.58$)[4] and $\varepsilon_0 = 8.85.10^{-12}\ N.m^2.C^{-2}$, and a being the distance separating the ion-radical pair, it can be assumed that $a \approx 15$ Å that is the size of $Ce^{III}TREN^{TIPS}$ **1**. Thus:

$$\omega_f < 0.09\ V$$

References

(1) Wojdyr, M. *Fityk* : A General-Purpose Peak Fitting Program. *J Appl Crystallogr* **2010**, *43* (5), 1126–1128. https://doi.org/10.1107/S0021889810030499.

(2) King, D. M.; Tuna, F.; McInnes, E. J. L.; McMaster, J.; Lewis, W.; Blake, A. J.; Liddle, S. T. Synthesis and Structure of a Terminal Uranium Nitride Complex. *Science* **2012**, *337* (6095), 717–720. https://doi.org/10.1126/science.1223488.

(3) Siano, D. B.; Metzler, D. E. Band Shapes of the Electronic Spectra of Complex Molecules. *The Journal of Chemical Physics* **1969**, *51* (5), 1856–1861. https://doi.org/10.1063/1.1672270.

(4) Washington University. . https://depts.washington.edu/eooptic/linkfiles/dielectric_chart%5B1%5D.pdf.

Experimental section for Chapter II

I. Synthetic procedures 270
II. Reactivity 271
References 313

I. Synthetic procedures

a) Synthesis of 1-allyloxy-2-chlorobenzene

1-allyloxy-2-chlorobenzene was synthesized according to a literature procedure.[1]

2-chlorophenol (0.8 mL, 8 mmol, 1 eq.), potassium carbonate (2.2 g, 16 mmol, 2 eq.), 3-bromo-1-propene (1.4 mL, 16 mmol, 2 eq.), and 5 mL of dry acetonitrile were mixed in a Schlenk flask and heated for 20 h at 70 °C. The mixture was allowed to cool down to room temperature, and 35 mL of diethyl ether was added. The organic mixture was washed with water, washed twice with a saturated KOH solution, dried with magnesium sulfate, and concentrated in vacuo at 250 mBar for 4 h. 1-allyloxy-2-chlorobenzene could be isolated as a colourless oil (808 mg, 60%).

^{1}H NMR (300 MHz, $CDCl_3$, 298 K) δ 7.38 (dd, J = 7.6, 1.6 Hz, 1H), 7.20 (ddd, J = 8.5, 7.6, 1.6 Hz, 1H), 6.97 – 6.85 (m, 2H), 6.08 (ddt, J = 17.2, 10.3, 5.1 Hz, 1H), 5.48 (dq, J = 17.2, 1.7 Hz, 1H), 5.32 (dq, J = 10.3, 1.7 Hz, 1H), 4.63 (dt, J = 5.1, 1.7 Hz, 3H).

b) Reactivity with chlorinated substrates

Compound **1** (15 mg, 20 µmol), chlorinated substrate (20 µmol), tributyltin hydride (5.3 µL, 20 µmol), and an internal standard, 1,3,5-trimethoxybenzene (3.3 mg, 20 µmol), were mixed in 0.5 mL of THF-d_8, and sealed in a J. Young NMR tube, and irradiated for designated amounts of time. The reaction was followed by ^{1}H spectroscopy.

c) Reactivity with fluorinated substrates

Compound **1** (15 mg, 20 µmol), fluorinated substrate (20 µmol), tributyltin hydride (5.3 µL, 20 µmol), and an internal standard, trimethoxybenzene (3.3 mg, 20 µmol), were mixed in 0.5 mL of THF-d_8, and sealed in a J. Young NMR tube, and irradiated for designated amounts of time. The reaction was followed by ^{1}H and ^{19}F NMR spectroscopy.

II. Reactivity

a) Photochemical degradation of [ClCe^{IV}TREN^{TIPS}] (2-Cl)

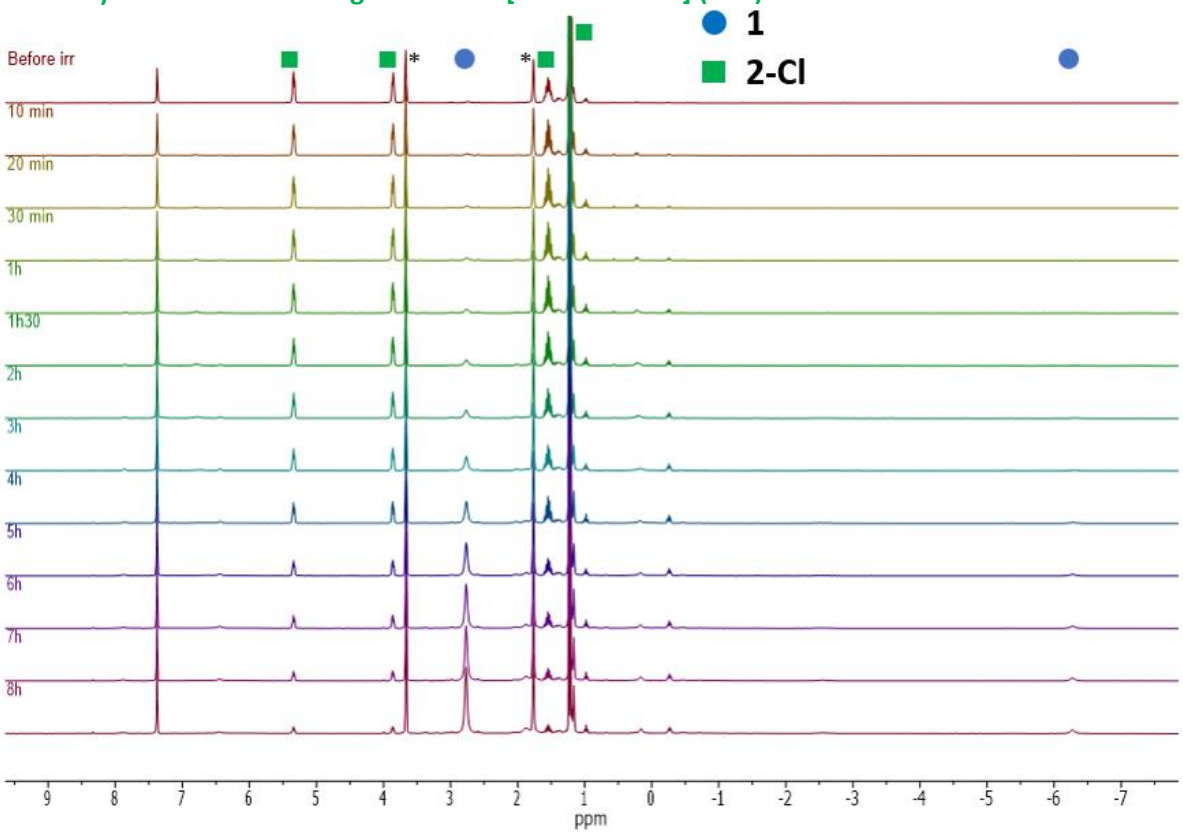

Figure S89. ^{1}H NMR spectra of the photochemical degradation of **2-Cl** (5 mg, 6.3 µmol) in THF-d_8 (0.4 mL). Solvent residual peak is indicated with *

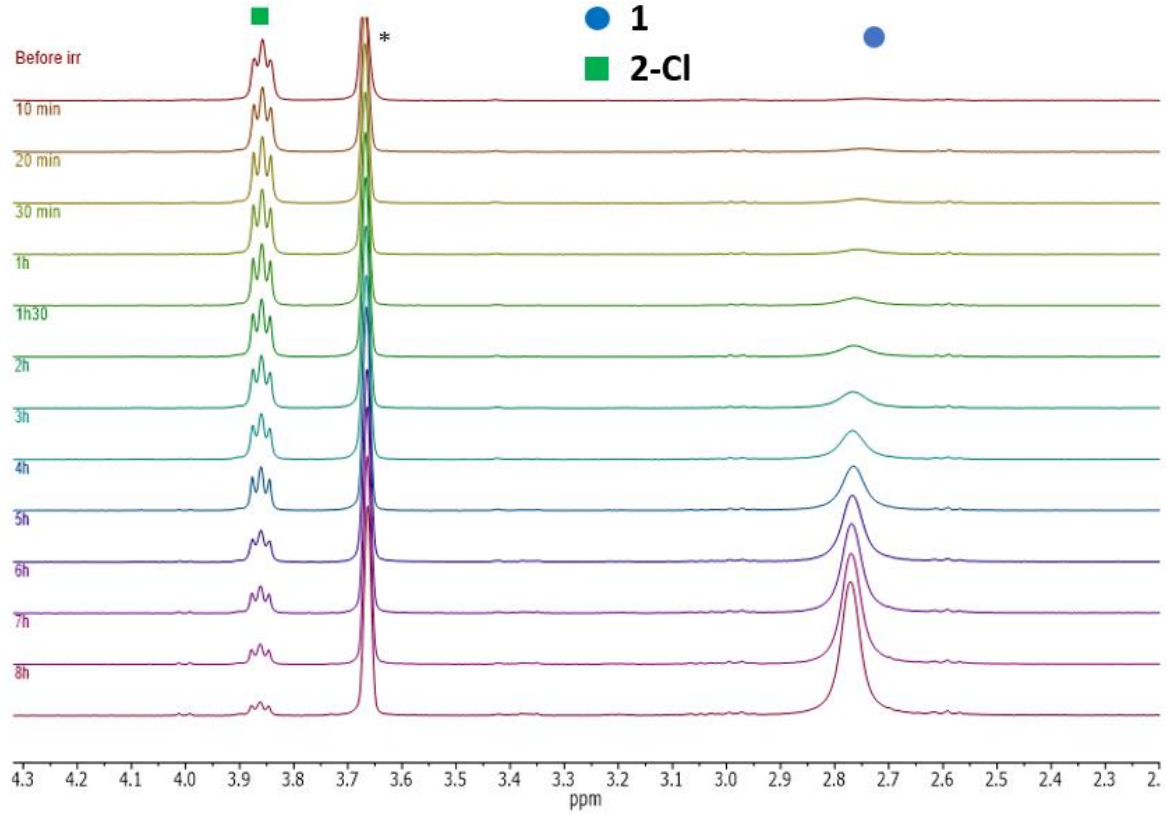

Figure S90. ^{1}H NMR spectra of the photochemical degradation of **2-Cl** (5 mg, 6.3 µmol) in THF-d_8 (0.4 mL). Zoom between 2.2 and 4.3 ppm. Solvent residual peak is indicated with *

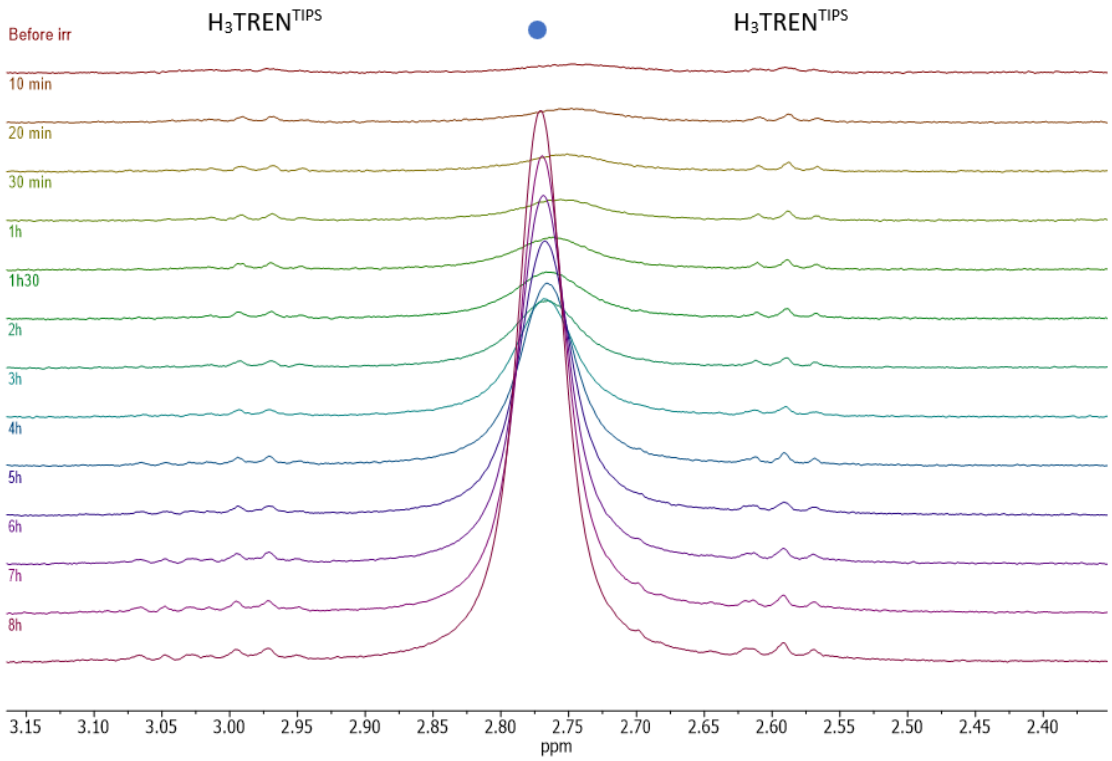

Figure S91. Zoom on the 2.3 and 3.2 ppm range

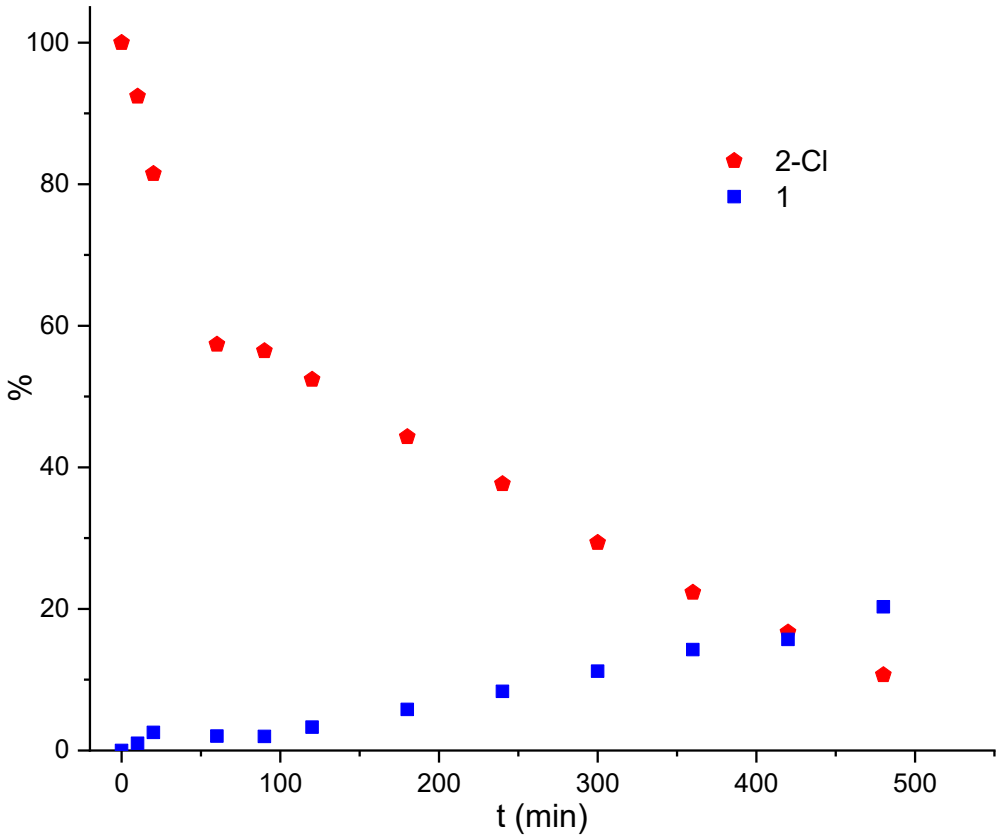

Figure S92. Photochemical degradation of **2-Cl** (5 mg, 6.3 µmol) at 427 nm in THF-d_8 (0.4 mL). NB : between 20 and 60 min, and 240 and 300 min of irradiation, the NMR tube was stored at 0 °C overnight. The point at 60 min seems to be an outlier, which could be due to the insufficient warming up to room temperature before measurement

t (min)	% **2-Cl**	% H_3TREN^{TIPS}	% **1**
0	100	2.2	0
10	92.42	2.43	1.02
20	81.47	1.89	2.55
60	57.37	1.9	2.02
90	56.45	1.87	1.99
120	52.42	1.7	3.29
180	44.3	1.47	5.8
240	37.68	1.69	8.35
300	29.36	1.93	11.2
360	22.33	2.33	14.26
420	16.71	2.47	15.69
480	10.68	2.31	20.3

Table S28. Experimental data of the photochemical degradation of **2-Cl** (5 mg, 6.3 µmol) in THF-d_8 (0.4 mL)

b) Radical clock experiment

Compound **1** (10 mg, 13 µmol, 1 eq.), 1-allyloxy-2-chlorobenzene (2 µL, 13 µmol, 1 eq.), and dihydroanthracene (5 mg, 26 µmol, 2 eq.) were dissolved in THF-d_8 in a J. Young NMR tube, and irradiated for 12 h at 427 nm. After irradiation, the reaction medium was colourless.

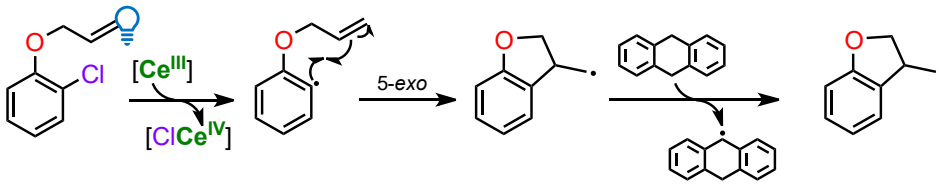

Figure S93. Mechanism of the radical clock experiment using 1-allyloxy-2-chlorobenzene

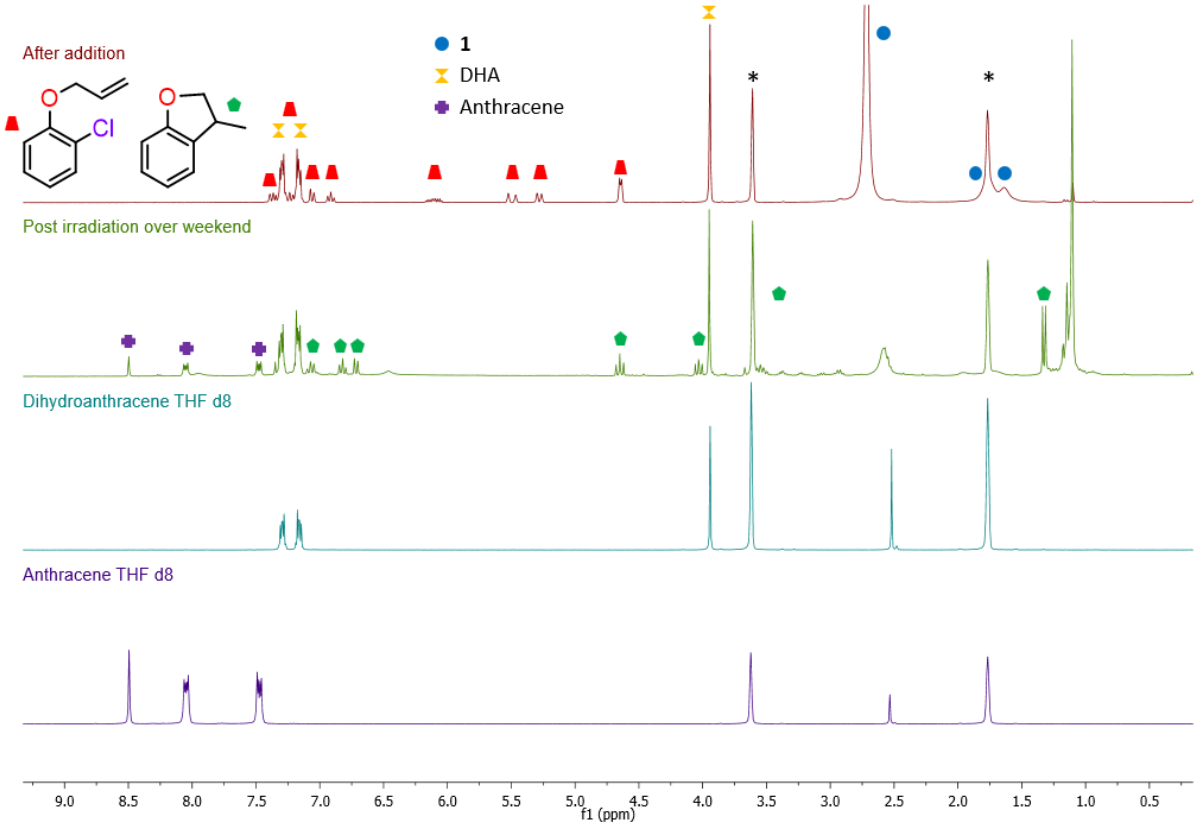

Figure S94. Stacking of spectra before irradiation (red), after irradiation (green) of radical clock experiment, with dihydroanthracene (light blue) and anthracene (purple) in THF d_8. Solvent residual peaks are indicated with *

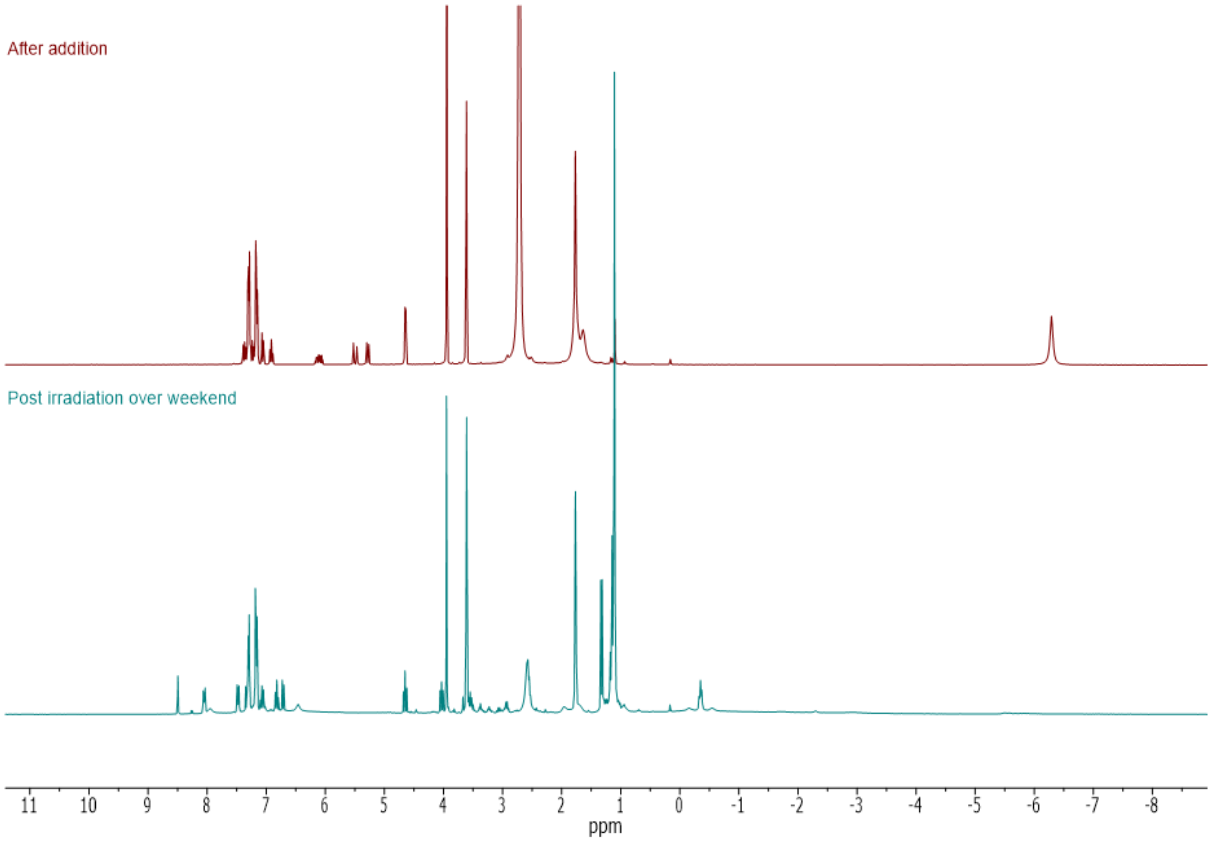

Figure S95. ^{1}H NMR spectra of the reaction medium for radical clock experiment before and after over weekend irradiation at 427 nm

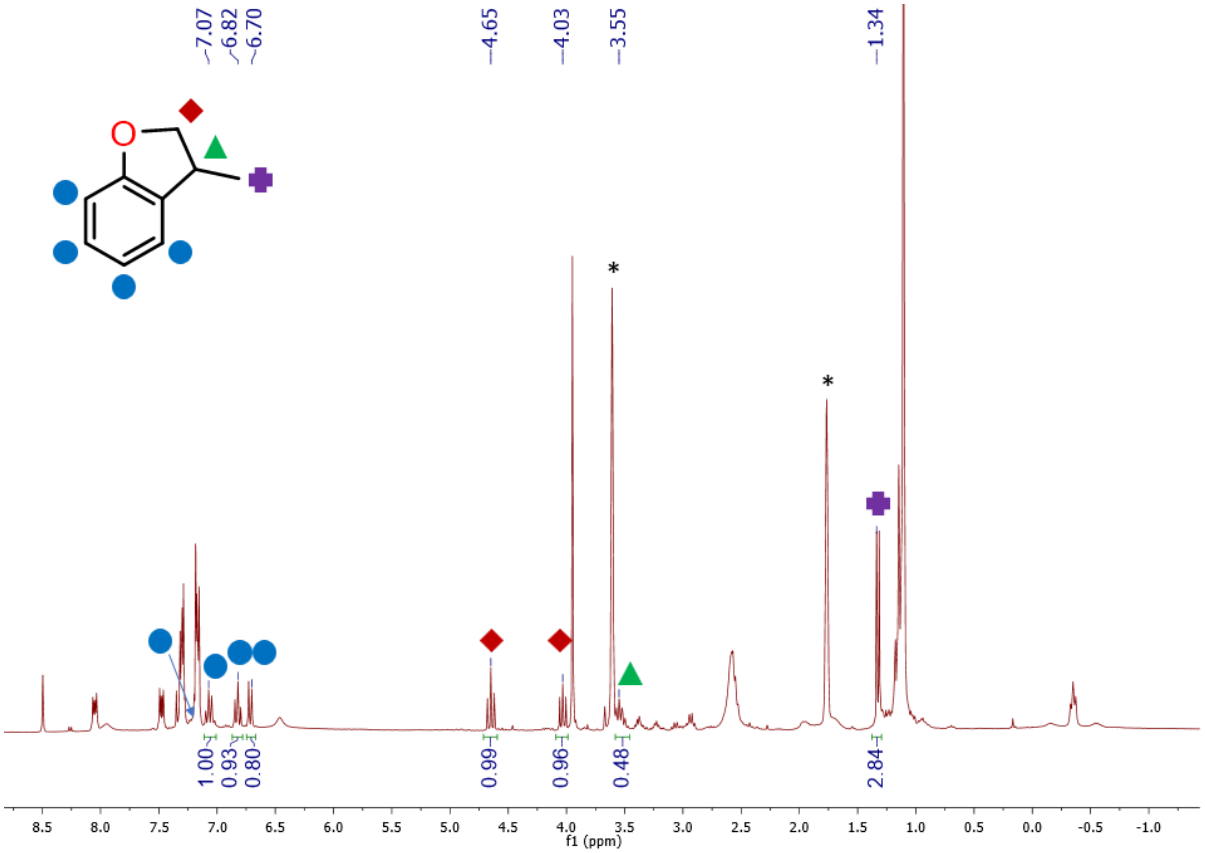

Figure S96. ^{1}H NMR of the reaction medium of the radical clock experiment in THF d_8. The presence of 3-methyl-2,3-dihydrobenzofuran in the spectra correspond to the one reported in the literature[1]

Institut Polytechnique de Paris
91120 Palaiseau, France

c) Reactivity with CH_2Cl_2

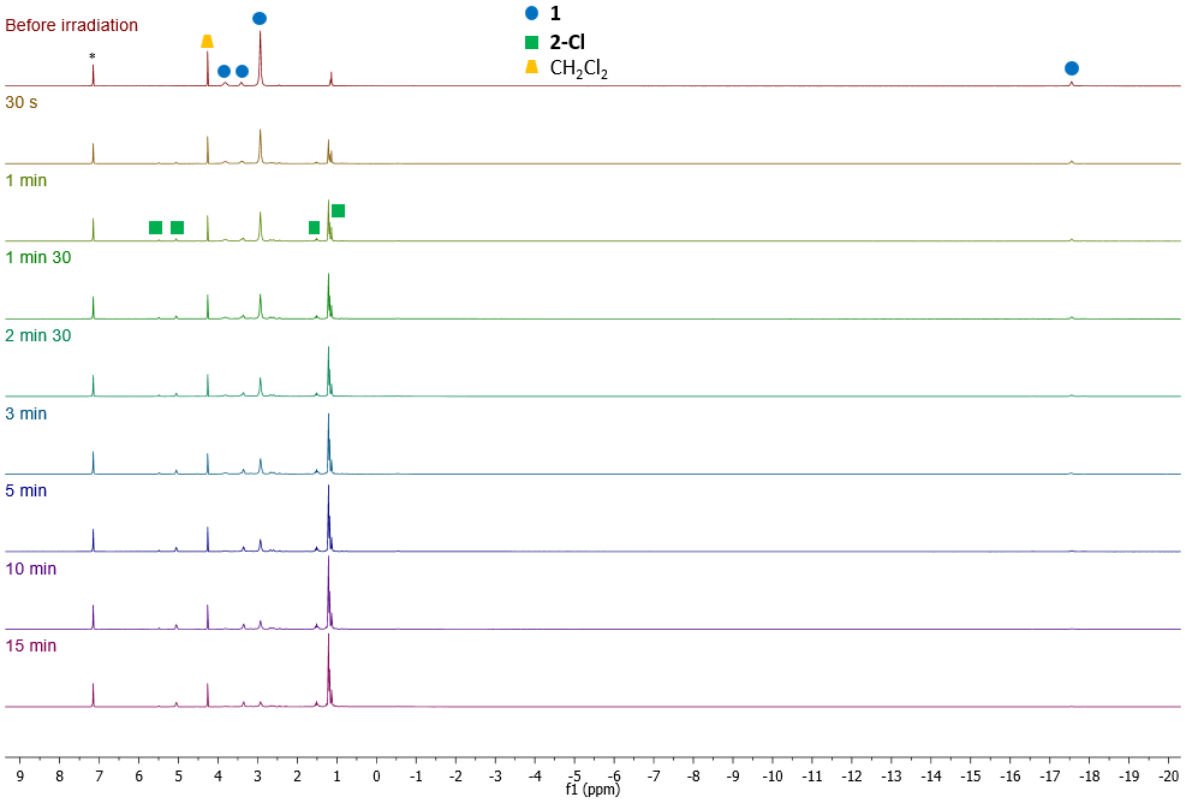

Figure S97. Kinetic study of the photochemical reaction between **1** (12.7 mg, 17 µmol, 1 eq.) and CH_2Cl_2 (2 µL, 13 µmol, 1 eq.) under irradiation at 427 nm in C_6D_6 at 298 K

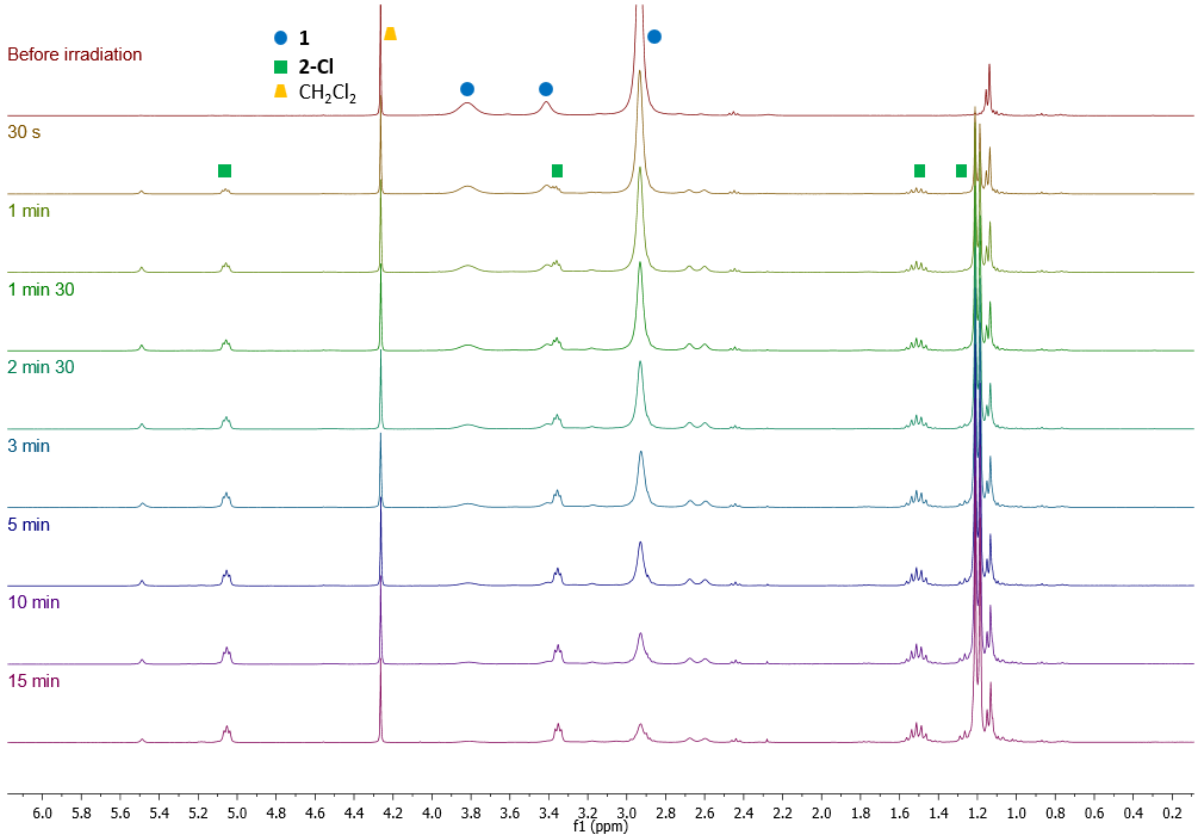

Figure S98. Kinetic study of the photochemical reaction between **1** (12.7 mg, 17 µmol, 1 eq.) and CH_2Cl_2 (2 µL, 13 µmol, 1 eq.) under irradiation at 427 nm in C_6D_6 at 298 K. Zoom on the region between 6.0 ppm and 0.2 ppm. Solvent residual peak is indicated by *

Institut Polytechnique de Paris
91120 Palaiseau, France

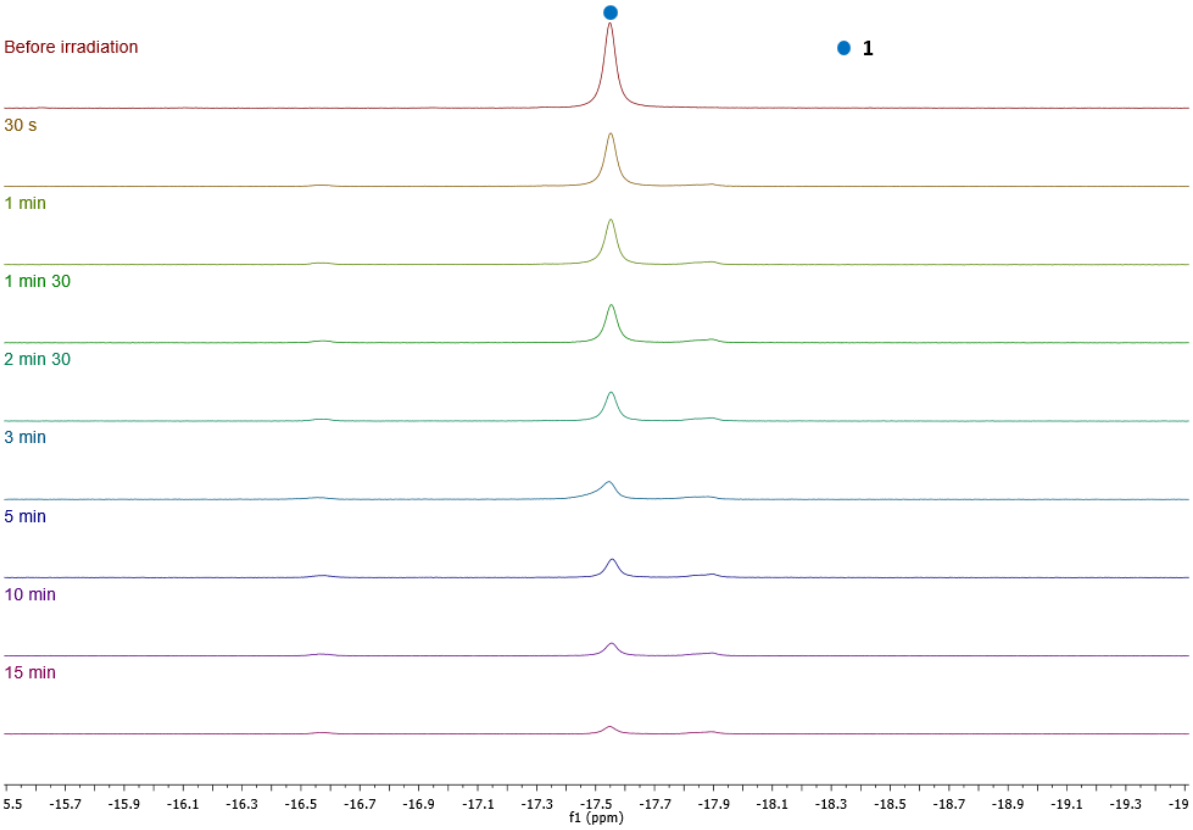

Figure S99. Kinetic study of the photochemical reaction between **1** (12.7 mg, 17 µmol, 1 eq.) and CH_2Cl_2 (2 µL, 13 µmol, 1 eq.) under irradiation at 427 nm in C_6D_6 at 298 K. Zoom on the -15.5 ppm and -19.4 ppm range. Solvent residual peak is indicated by *

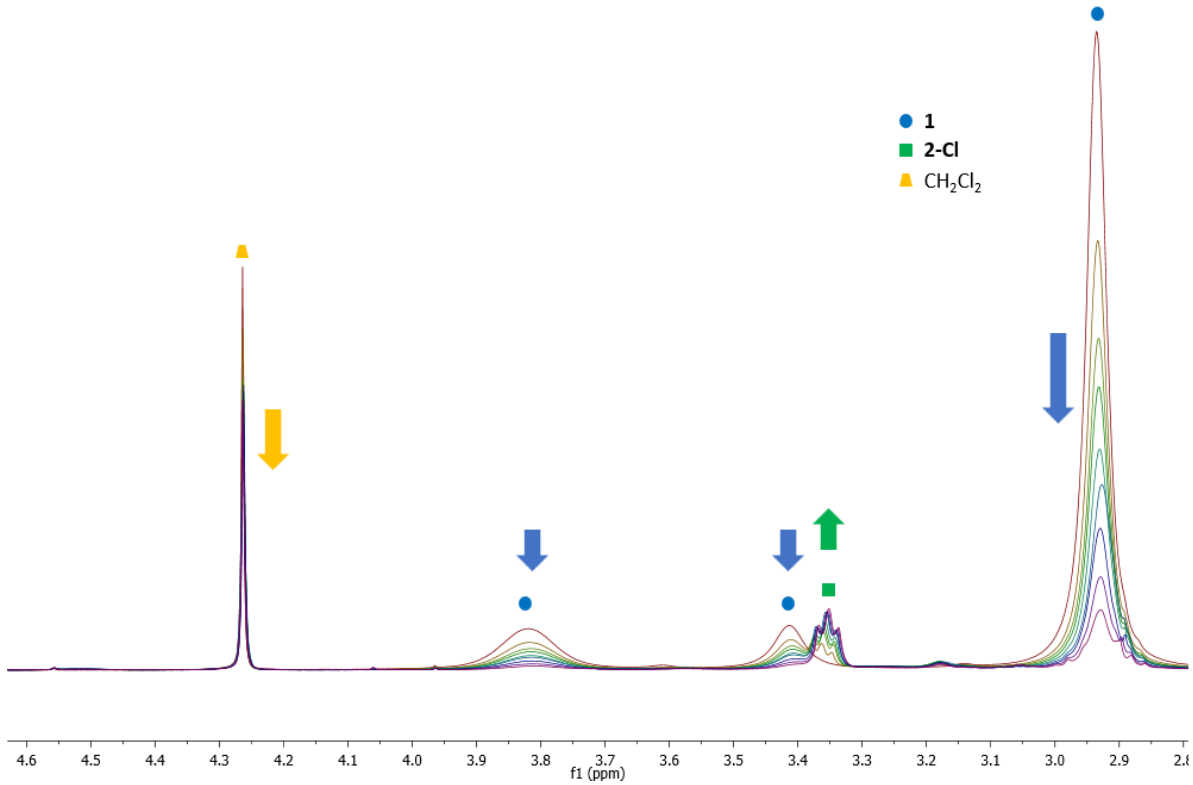

Figure S100. Kinetic study of the photochemical reaction between **1** (12.7 mg, 17 µmol, 1 eq.) and CH_2Cl_2 (2 µL, 13 µmol, 1 eq.) under irradiation at 427 nm for the first 10 minutes at 298 K. Zoom on the region between 4.4 ppm and 2.8 ppm

Institut Polytechnique de Paris
91120 Palaiseau, France

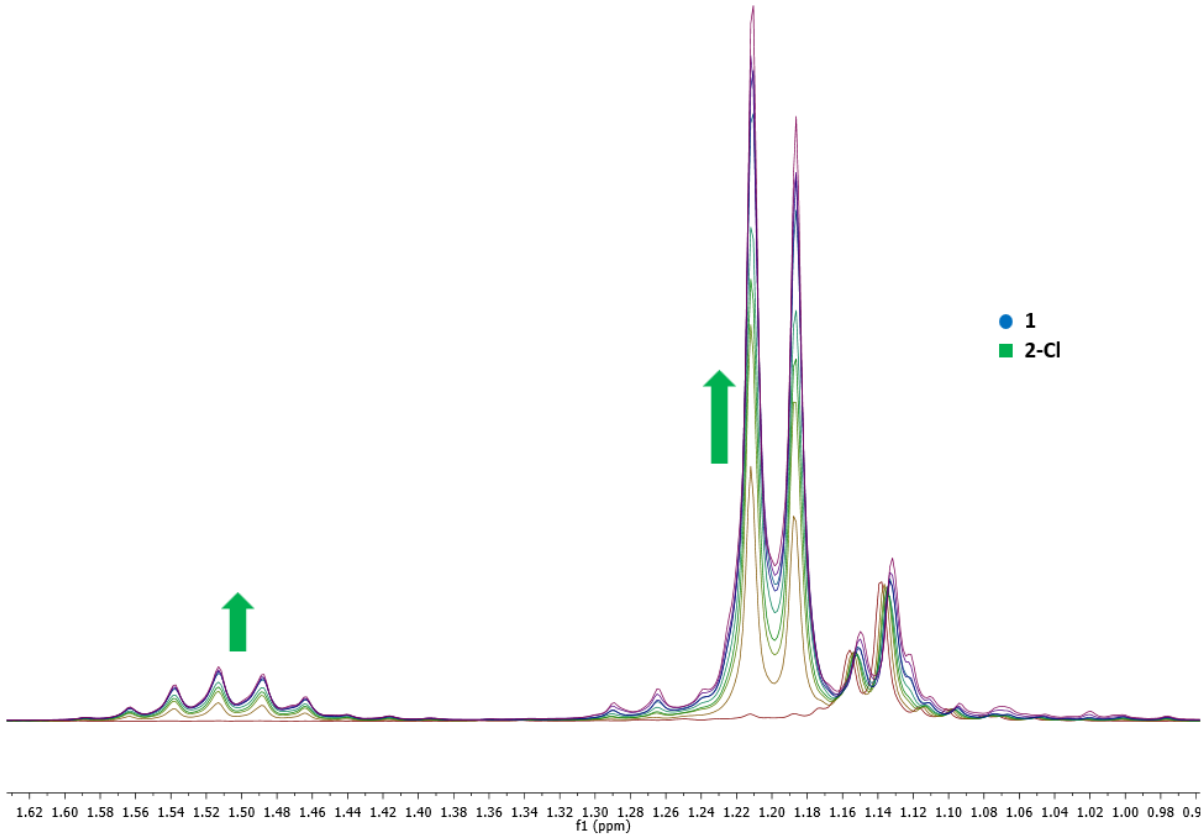

Figure S101. Kinetic study of the photochemical reaction between **1** (12.7 mg, 17 µmol, 1 eq.) and CH_2Cl_2 (2 µL, 13 µmol, 1 eq.) under irradiation at 427 nm for the first 10 minutes at 298 K. Zoom on the region between 1.65 ppm and 0.9 ppm

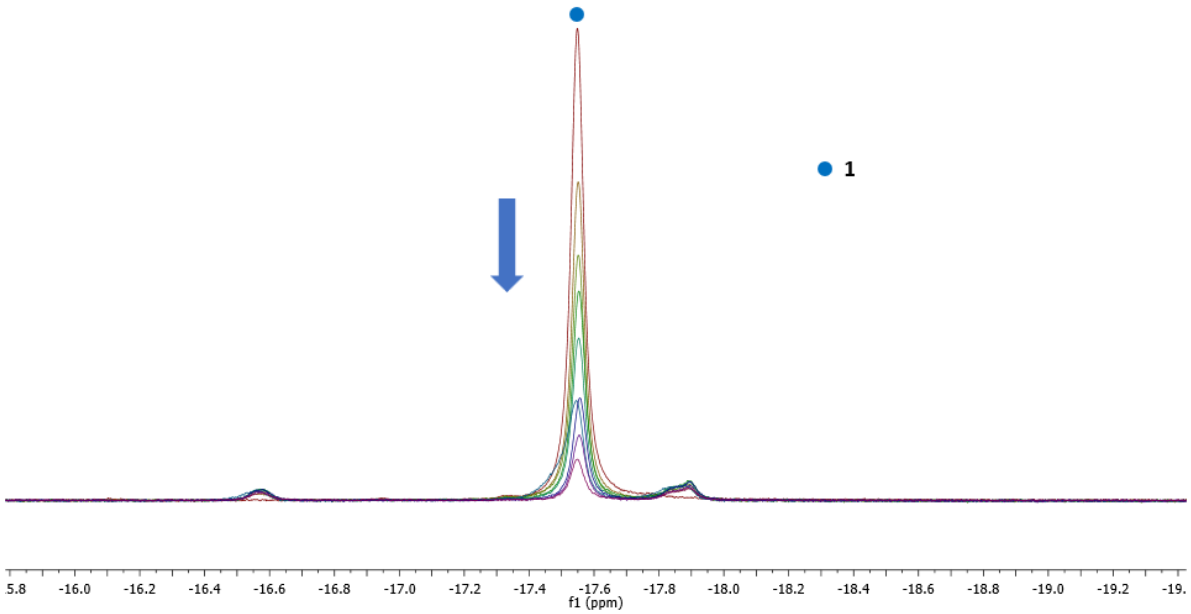

Figure S102. Kinetic study of the photochemical reaction between **1** (12.7 mg, 17 µmol, 1 eq.) and CH_2Cl_2 (2 µL, 13 µmol, 1 eq.) under irradiation at 427 nm for the first 10 minutes at 298 K. Zoom on the region between -15.8 ppm and -19.3 ppm

d) Reactivity with chlorinated substrates

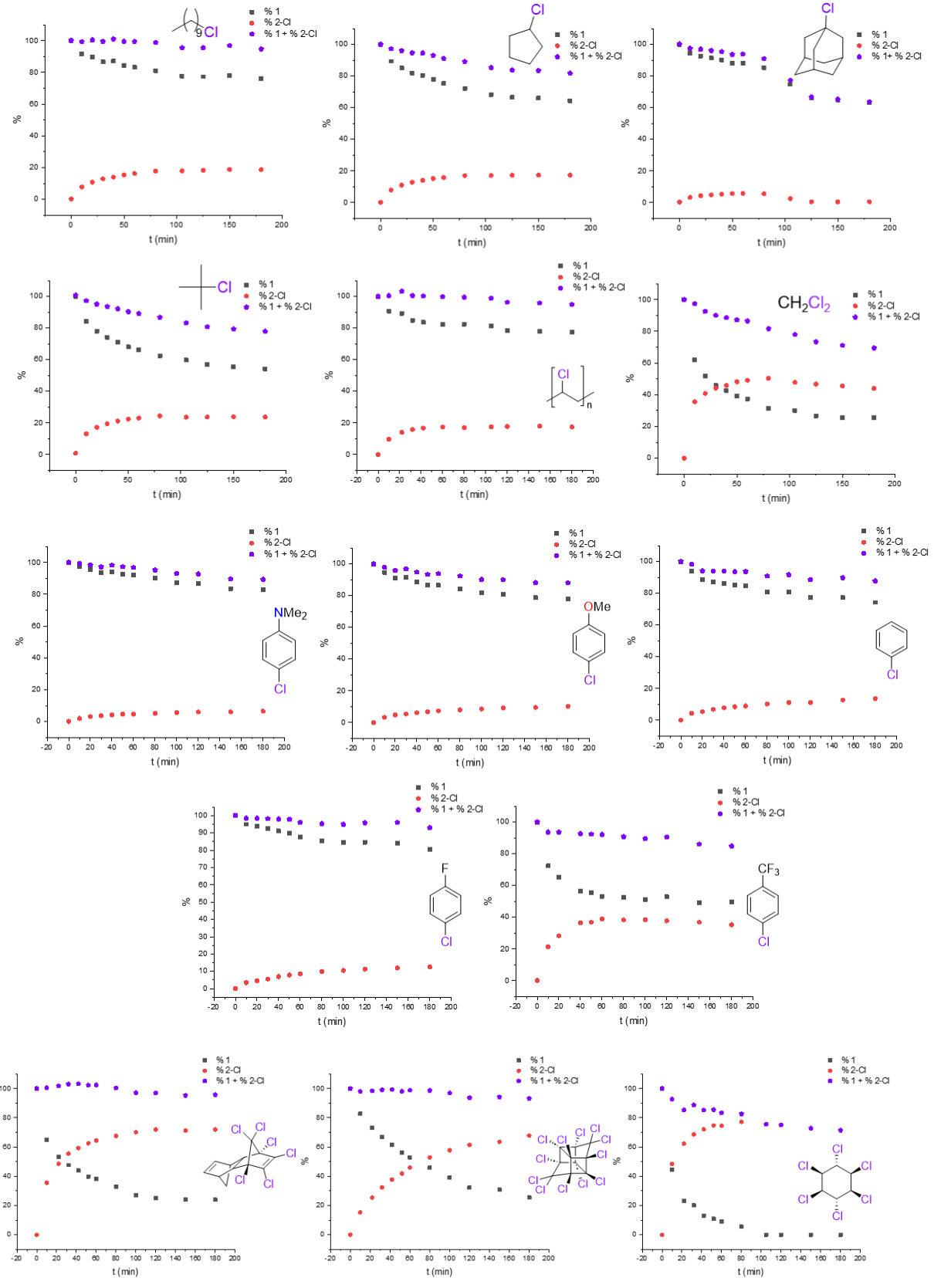

Institut Polytechnique de Paris
91120 Palaiseau, France

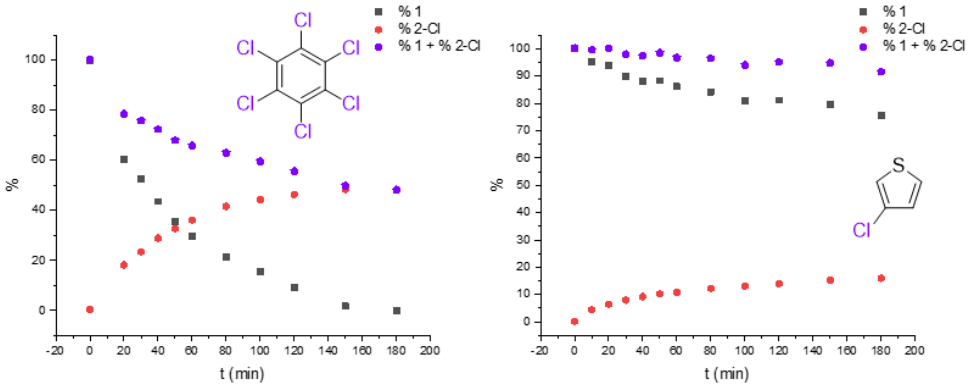

Figure S103. Evolution of quantities of **1**, **2-Cl**, in the function of irradiation time with various chlorinated substrates. Yields of formation of **2-Cl**, were calculated using the integration of a characteristic signal of the internal standard in ^{1}H NMR and calibrated on the initial integration of **1**

Note S1. For **Table S**30, yields of formation of **2-Cl**, were calculated using the integration of a characteristic signal of internal standard in ^{1}H NMR and calibrated on the initial integration of **1**

CH_2Cl_2					$_9$Cl			
t (min)	% **1**	% **2-Cl**	% RX	% **1** + % **2-Cl**	t (min)	% **1**	% **2-Cl**	% **1** + % **2-Cl**
0	100	0	100	100.0	0	100	0.2	100.2
10	61.89	35.55	79.64	97.44	10	91.61	7.77	99.38
20	51.81	40.84	72.16	92.65	20	89.75	10.77	100.5
30	45.94	44.17	69.58	90.11	30	86.69	12.9	99.59
40	42.72	45.88	67.15	88.6	40	87.22	13.95	101.2
E50	39.06	48.18	65.00	87.24	50	84.2	15.41	99.61
60	37.4	49.12	63.58	86.52	60	83.22	16.28	99.5
80	31.47	50.32	60.60	81.79	80	81.15	17.77	98.92
105	30.03	47.86	59.12	77.89	105	77.61	17.96	95.57
125	26.76	46.69	56.11	73.45	125	77.34	18.25	95.59
150	25.54	45.58	53.43	71.12	150	78.04	18.92	96.96
180	25.48	44.05	51.83	69.53	180	76.06	18.71	94.77
240	18.3	39.76	42.85	58.06	240	31.23	3.87	35.10

Table S29. Percentages of compounds **1** and **2-Cl** during photochemical degradation of dichloromethane and 2-1-chlorodecane

Institut Polytechnique de Paris
91120 Palaiseau, France

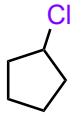

t (min)	% **1**	% **2-Cl**	% **1** + % **2-Cl**
0	100	0.15	100.2
10	89.35	7.95	97.3
20	85.16	10.98	96.14
30	81.95	12.8	94.75
40	80.56	13.98	94.54
50	77.92	15.14	93.06
60	75.28	15.83	91.11
80	72.12	17.04	89.16
105	68.28	17.14	85.42
125	66.48	17.32	83.8
150	66.08	17.42	83.5
180	64.46	17.3	81.76
240	23.73	3.3	27.03

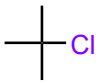

t (min)	% **1**	% **2-Cl**	% **1** + % **2-Cl**
0	100	0.81	100.8
10	84.11	13.14	97.25
20	77.97	17.21	95.18
30	74.19	19.45	93.64
40	71.14	21.14	92.28
50	68	22.41	90.41
60	66.14	23.02	89.16
80	62.41	24.4	86.81
105	59.68	23.6	83.28
125	57.03	23.68	80.71
150	55.49	23.87	79.36
180	54.11	23.72	77.83
240	46.07	22.99	69.06

Table S30. Percentages of compounds **1** and **2-Cl** during photochemical degradation of chlorocyclopentane and 2-methyl-2-chloropropane

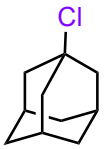

t (min)	% **1**	% **2-Cl**	% RX	% **1** + % **2-Cl**
0	100	0.28	100	100.3
10	94.38	3.21	85.13	97.59
20	92.71	4.3	78.73	97.01
30	91.37	4.84	72.66	96.21
40	90.16	5.29	68.09	95.45
50	88.12	5.63	64.18	93.75
60	88.09	5.79	61.48	93.88
80	85.4	5.58	54.92	90.98
105	74.78	2.51	46.42	77.29
125	66.28	0.5	40.73	66.78
150	64.93	0.44	36.32	65.37
180	63.18	0.54	28.22	63.72
240	60.57	0.39	16.78	60.96

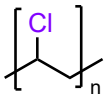

t (min)	% **1**	% **2-Cl**	% **1** + % **2-Cl**
0	100	0	100.0
10	90.78	9.65	100.4
22	89.3	14.03	103.3
32	84.82	15.82	100.6
42	83.54	16.69	100.2
60	82.46	17.39	99.85
80	82.5	17.04	99.54
105	81.38	17.51	98.89
120	78.56	17.72	96.28
150	77.88	17.94	95.82
180	77.46	17.43	94.89

Table S31. Percentages of compounds **1** and **2-Cl** during photochemical degradation of chloroadamantane and PVC

Institut Polytechnique de Paris
91120 Palaiseau, France

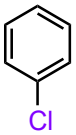

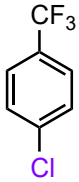

t (min)	% **1**	% **2-Cl**	% **1** + % **2-Cl**
0	100	0.09	100.1
10	94	4.36	98.36
20	88.72	5.47	94.19
30	87.17	6.87	94.04
40	86.23	7.82	94.05
50	85.17	8.47	93.64
60	84.87	8.93	93.8
80	80.7	10.25	90.95
100	80.68	11.13	91.81
120	77.43	11.17	88.6
150	77.2	12.72	89.92
180	74.22	13.63	87.85

t (min)	% **1**	% **2-Cl**	% **1** + % **2-Cl**
0	100	0.16	100.2
10	72.32	21.32	93.64
20	65.45	28.31	93.76
40	56.35	36.4	92.75
50	55.52	36.88	92.4
60	53.25	38.93	92.18
80	52.59	38.26	90.85
100	51.21	38.39	89.6
120	52.85	37.77	90.62
150	49.24	36.81	86.05
180	49.63	35.28	84.91

Table S32. Percentages of compounds **1** and **2-Cl** during photochemical degradation of chlorobenzene and 4-chloro-α,α,α-trifluorotoluene

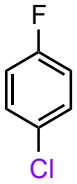

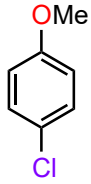

t (min)	% **1**	% **2-Cl**	% **1** + % **2-Cl**
0	100	0.14	100.1
10	95	3.45	98.45
20	93.84	4.61	98.45
30	92.7	5.59	98.29
40	91.05	6.99	98.04
50	89.99	7.89	97.88
60	87.52	8.58	96.1
80	85.53	9.84	95.37
100	84.51	10.54	95.05
120	84.66	11.32	95.98
150	84.12	11.94	96.06
180	80.52	12.56	93.08

t (min)	% **1**	% **2-Cl**	% **1** + % **2-Cl**
0	100	0	100.0
10	94.67	3.2	97.87
20	90.98	4.88	95.86
30	91.44	5.43	96.87
40	88.71	6.15	94.86
50	86.56	6.79	93.35
60	86.51	7.37	93.88
80	84.39	7.97	92.36
100	81.69	8.52	90.21
120	80.84	9.15	89.99
150	78.73	9.49	88.22
180	77.9	10.18	88.08

Table S33. Percentages of compounds **1** and **2-Cl** during photochemical degradation of 4-fluoro-chlorobenzene and 4-chloroanisole

Institut Polytechnique de Paris
91120 Palaiseau, France

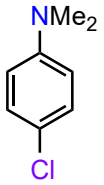

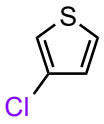

t (min)	% **1**	% **2-Cl**	% **1** + % **2-Cl**
0	100	0.1	100.1
10	97.49	1.97	99.46
20	95.31	3.12	98.43
30	93.54	3.76	97.3
40	94.11	4.21	98.32
50	92.69	4.66	97.35
60	92.28	4.62	96.9
80	90.22	5.11	95.33
100	87.38	5.7	93.08
120	86.85	6.01	92.86
150	83.6	6.04	89.64
180	82.95	6.47	89.42

t (min)	% **1**	% **2-Cl**	% RX	% **1** + % **2-Cl**
0	100	0.22	100	100.2
10	95.24	4.41	93.72	99.65
20	93.77	6.42	90.74	100.19
30	90.06	7.94	90.89	98
40	88.23	9.22	87.91	97.45
50	88.32	10.23	87.91	98.55
60	86.09	10.74	84.93	96.83
80	84.25	12.24	83.91	96.49
100	80.96	13.13	81.71	94.09
120	81.15	14	80.06	95.15
150	79.54	15.32	74.96	94.86
180	75.59	16.03	72.06	91.62

Table S34. Percentages of compounds **1** and **2-Cl** during photochemical degradation of 4-chloro-dimethylaniline and 2-chlorothiophene

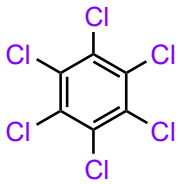

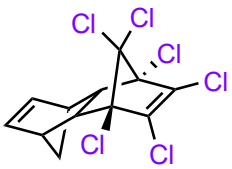

t (min)	% **1**	% **2-Cl**	% **1** + % **2-Cl**
0	100	0.34	100.3
10	82.23	15.56	97.79
20	60.29	18.19	78.48
30	52.41	23.46	75.87
40	43.53	28.9	72.43
50	35.31	32.75	68.06
60	29.8	36.14	65.94
80	21.42	41.64	63.06
100	15.38	44.27	59.65
120	9.33	46.36	55.69
150	1.65	48.31	49.96
180	0	48.2	48.2

t (min)	% **1**	% **2-Cl**	% **1** + % **2-Cl**
0	100	0	100
10	65.05	35.54	100.6
22	53.19	48.56	101.8
32	47.68	55.47	103.2
42	43.94	59.28	103.2
52	39.78	62.58	102.4
60	38.11	64.38	102.5
80	32.82	67.63	100.5
100	27.04	70.12	97.16
120	25.03	72	97.03
150	24.14	71.24	95.38
180	23.86	72	95.86

Table S35. Percentages of compounds **1** and **2-Cl** during photochemical degradation of hexachlorobenzene and Aldrin

Institut Polytechnique de Paris
91120 Palaiseau, France

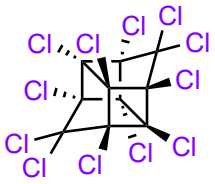

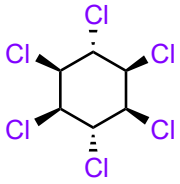

t (min)	% **1**	% **2-Cl**	% **1** + % **2-Cl**
0	100	0	100
10	82.72	15.28	98
22	73.08	25.39	98.47
32	66.78	32.41	99.19
42	61.64	37.77	99.41
52	56.28	41.84	98.12
60	52.92	45.95	98.87
80	45.89	52.86	98.75
100	39.13	57.78	96.91
120	32.26	61.46	93.72
150	30.72	63.52	94.24
180	25.48	67.82	93.3

t (min)	% **1**	% **2-Cl**	% **1** + % **2-Cl**
0	100	0	100.0
10	44.42	48.34	92.76
22	23.07	62.35	85.42
32	20.05	68.68	88.73
42	13.09	72.15	85.24
52	10.88	74.77	85.65
60	8.86	74.54	83.4
80	5.46	77.27	82.73
105	0	75.64	75.64
120	0	75.16	75.16
150	0	72.87	72.87
180	0	71.5	71.5

Table S36. Percentages of compounds **1** and **2-Cl** during photochemical degradation of Mirex and Lindane

Institut Polytechnique de Paris
91120 Palaiseau, France

1) NMR spectra

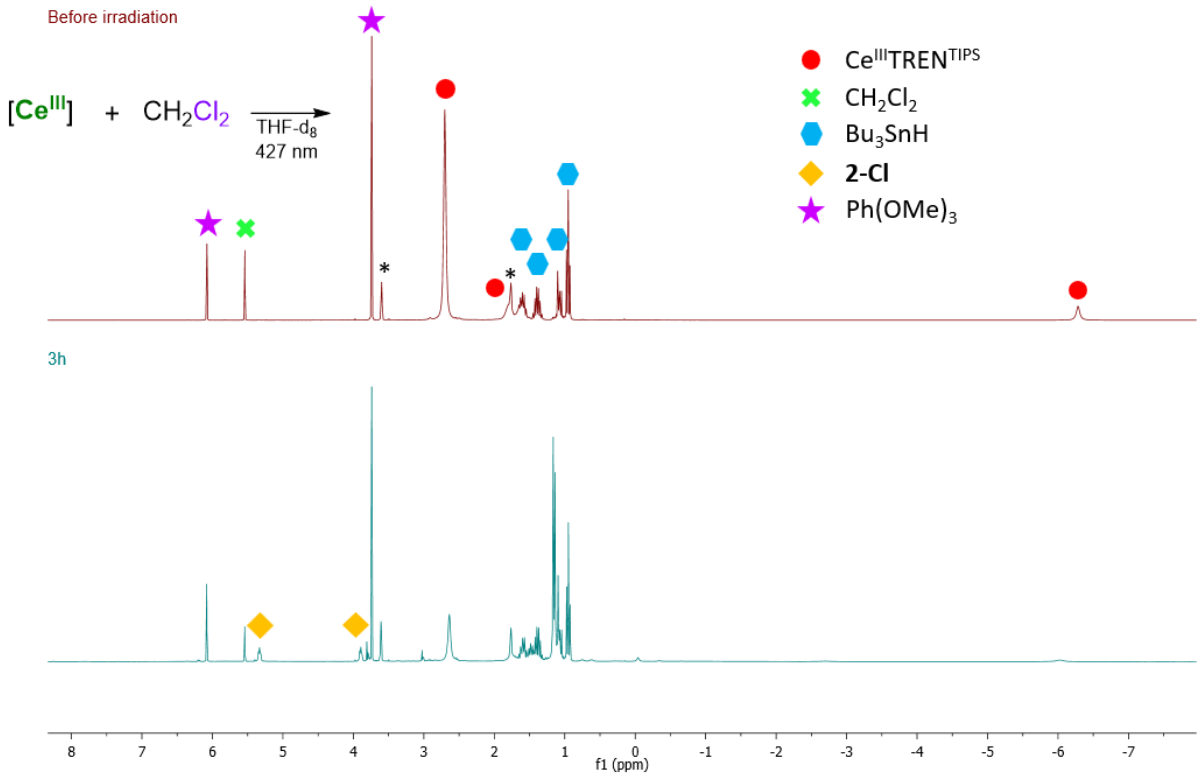

Figure S104. ^{1}H NMR spectrum of the reaction between **1** and dichloromethane under irradiation at 427 nm in THF-d_8. Solvent residual peaks are indicated with *

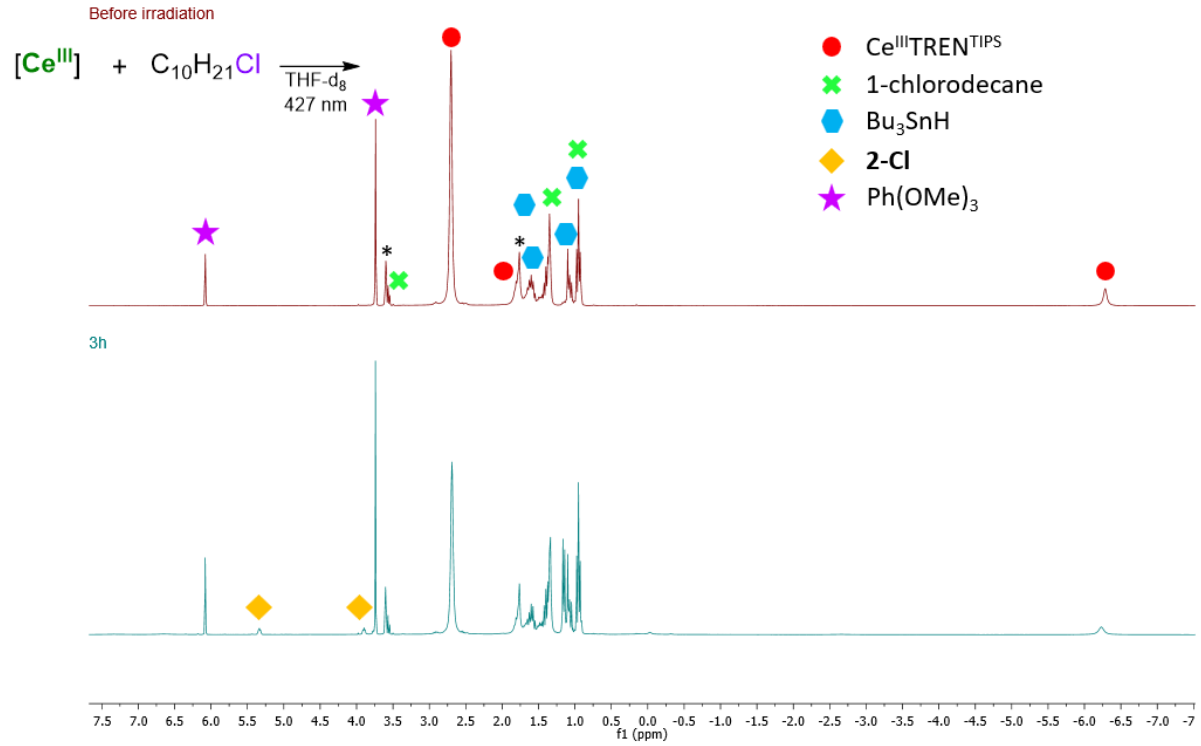

Figure S105. ^{1}H NMR spectrum of the reaction between **1** and 1-chlorodecane under irradiation at 427 nm in THF-d_8. Solvent residual peaks are indicated with *

Institut Polytechnique de Paris
91120 Palaiseau, France

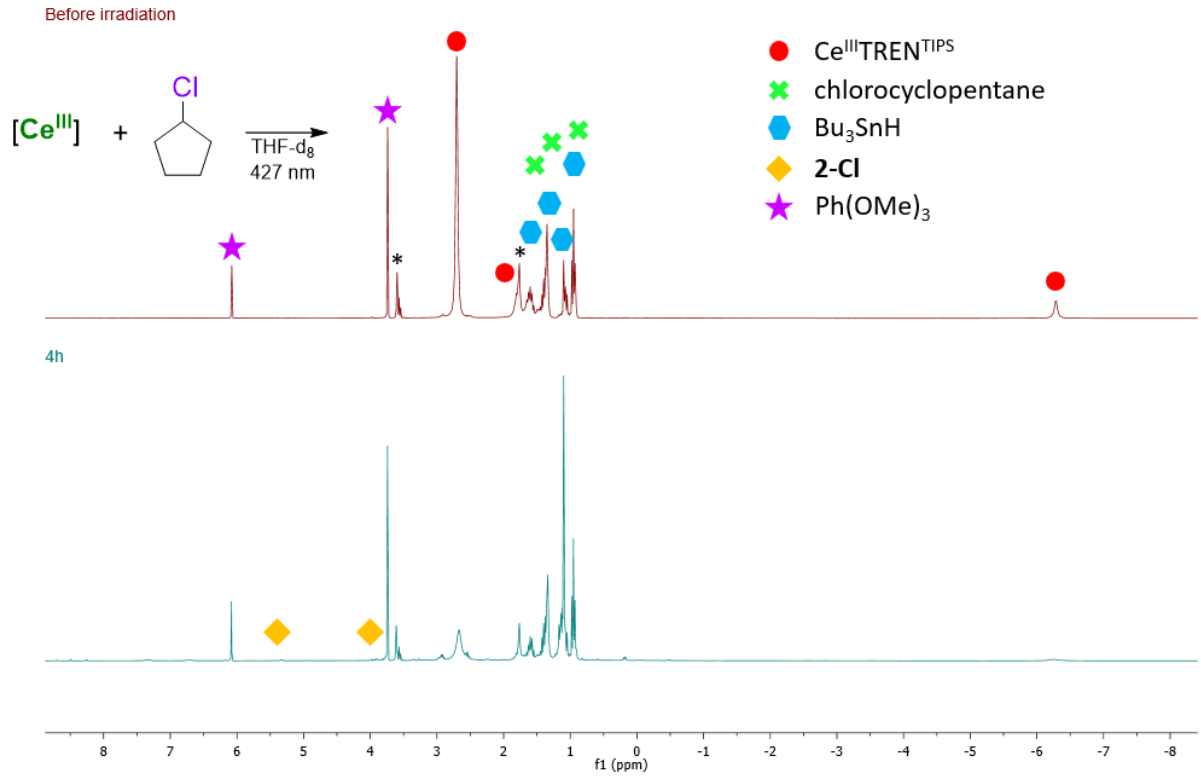

Figure S106. ^{1}H NMR spectrum of the reaction between **1** and chlorocyclopentane under irradiation at 427 nm in THF-d_8. Solvent residual peaks are indicated with *

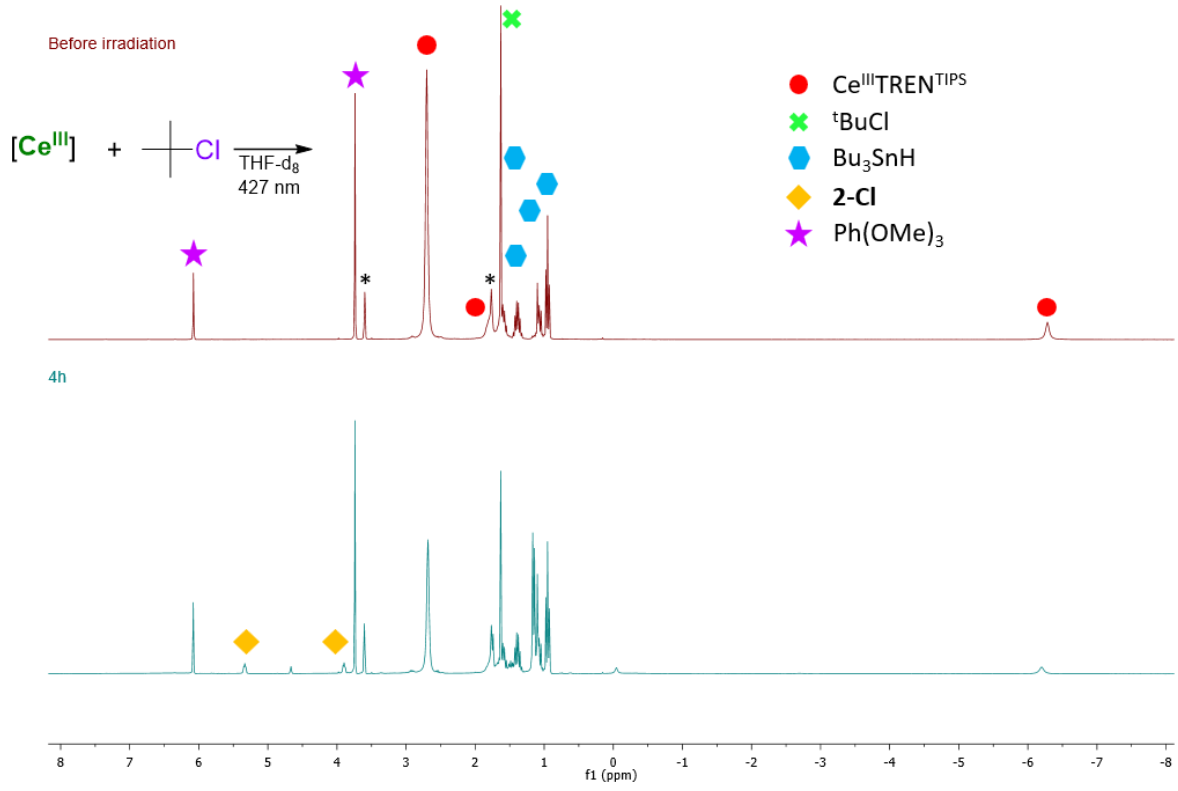

Figure S107. ^{1}H NMR spectrum of the reaction between **1** and 2-chloro-2-methyl-propane under irradiation at 427 nm in THF-d_8. Solvent residual peaks are indicated with *

Institut Polytechnique de Paris
91120 Palaiseau, France

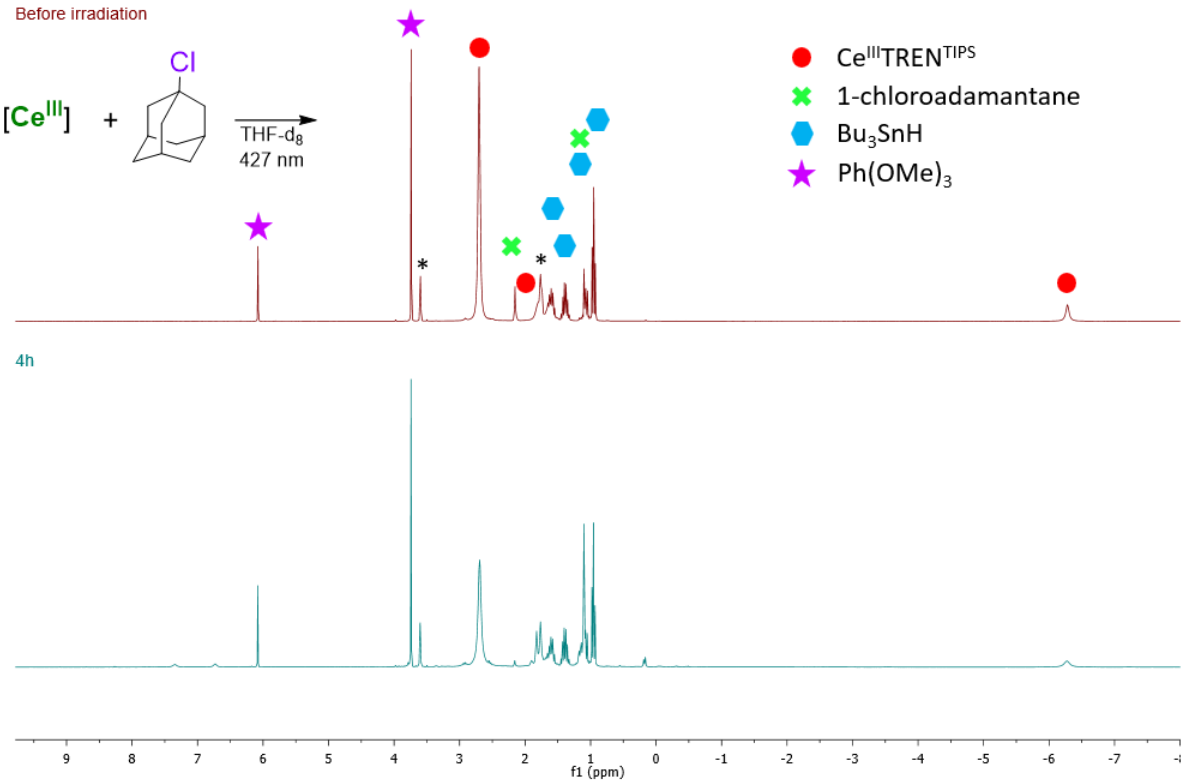

Figure S108. ^{1}H NMR spectrum of the reaction between **1** and 1-chloroadamantane under irradiation at 427 nm in THF-d_8. Solvent residual peaks are indicated with *

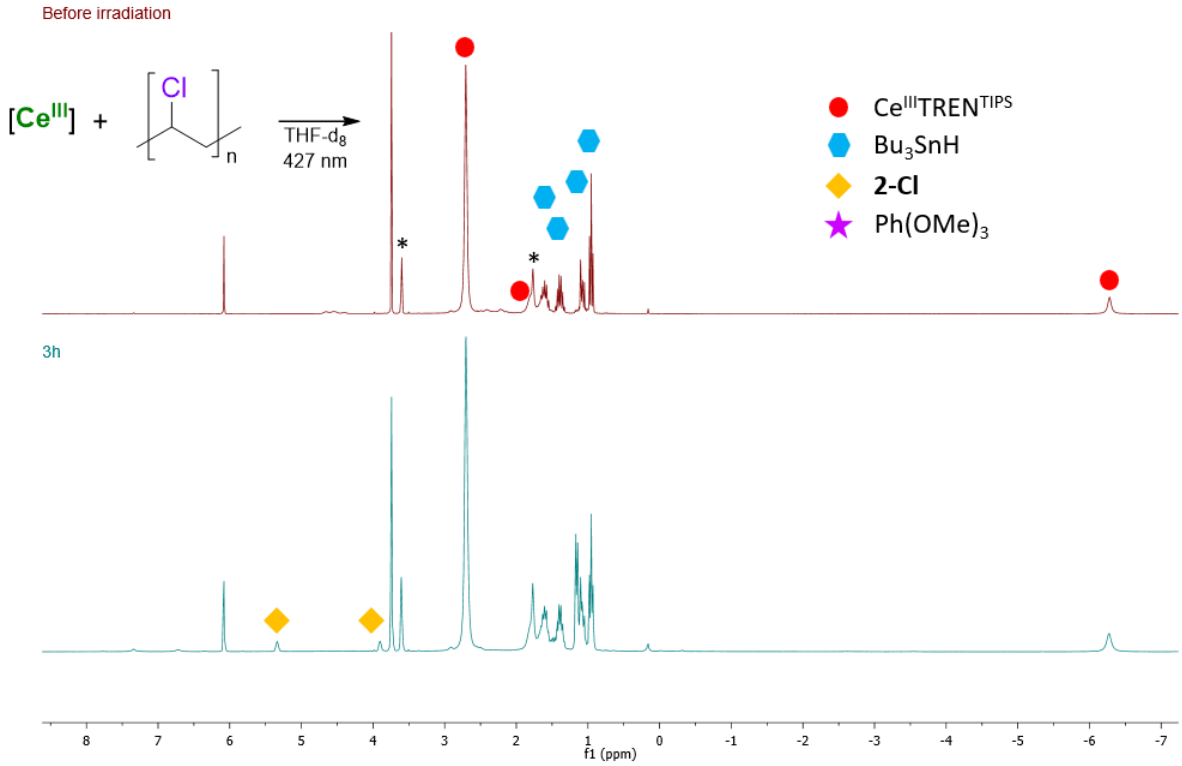

Figure S109. ^{1}H NMR spectrum of the reaction between **1** and PVC under irradiation at 427 nm in THF-d_8. Solvent residual peaks are indicated with *

Institut Polytechnique de Paris
91120 Palaiseau, France

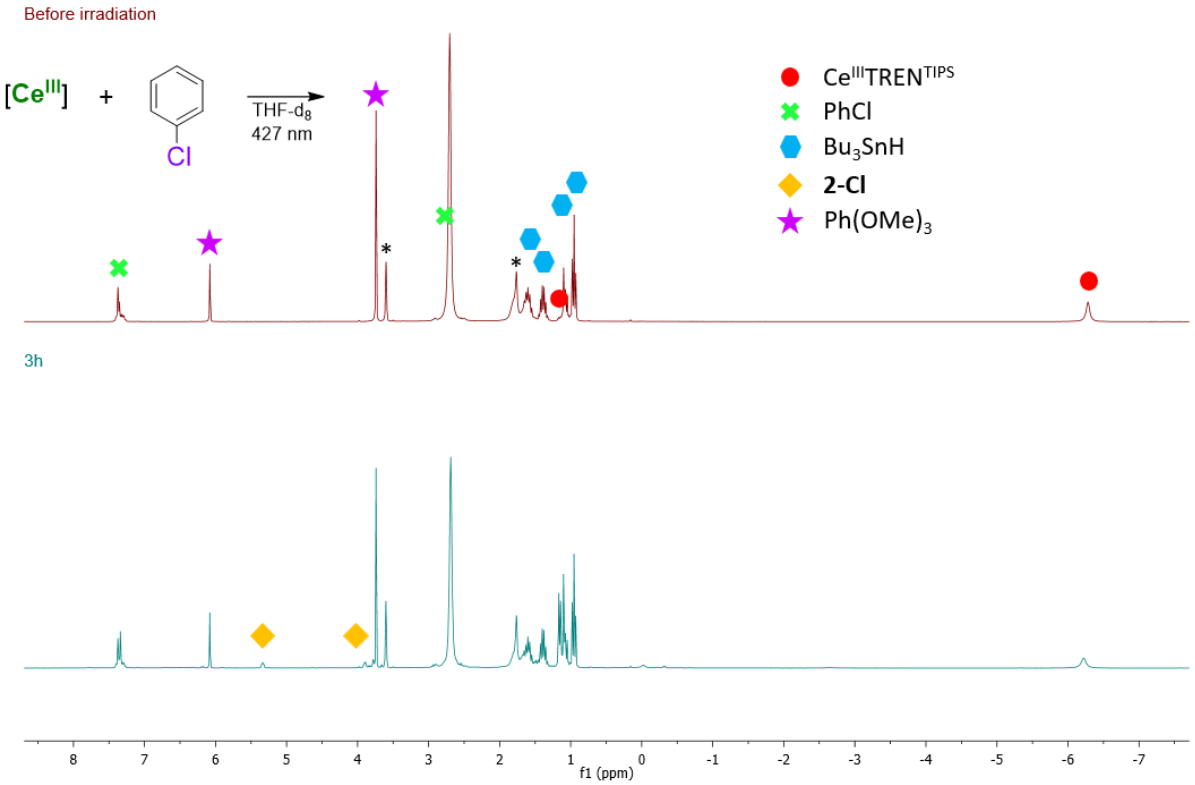

Figure S110. ^{1}H NMR spectrum of the reaction between **1** and chlorobenzene under irradiation at 427 nm in THF-d$_8$. Solvent residual peaks are indicated with *

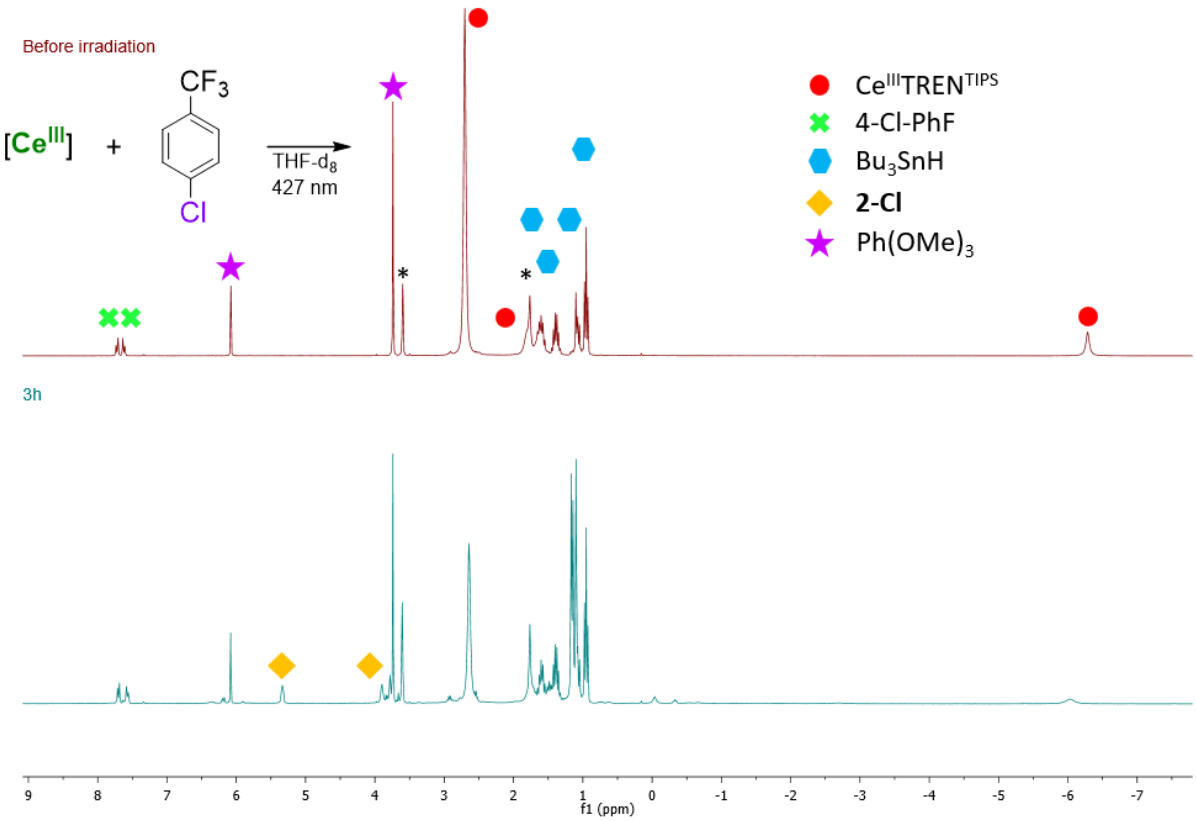

Figure S111. ^{1}H NMR spectrum of the reaction between **1** and 4-chloro-trifluoromethylbenzene under irradiation at 427 nm in THF-d$_8$. Solvent residual peaks are indicated with *

Institut Polytechnique de Paris
91120 Palaiseau, France

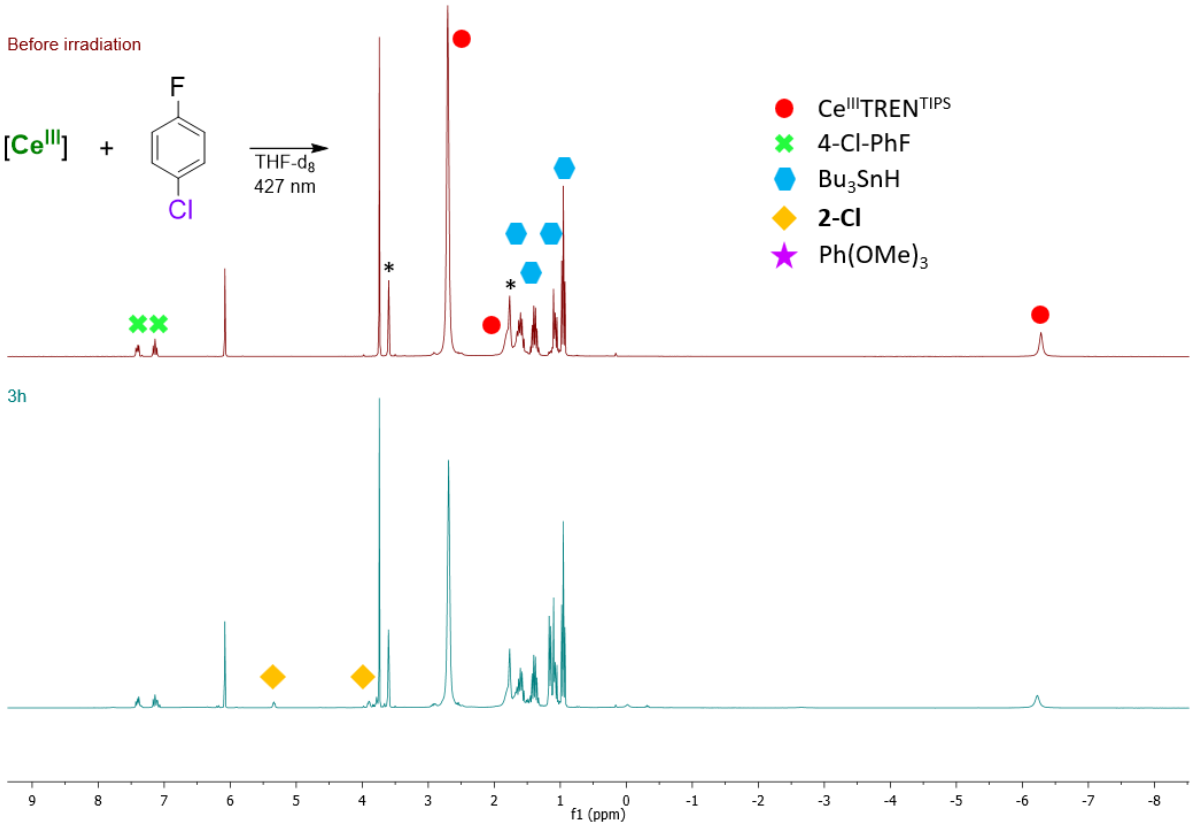

Figure S112. ^{1}H NMR spectrum of the reaction between **1** and 4-fluoro-chlorobenzene under irradiation at 427 nm in THF-d_8. Solvent residual peaks are indicated with *

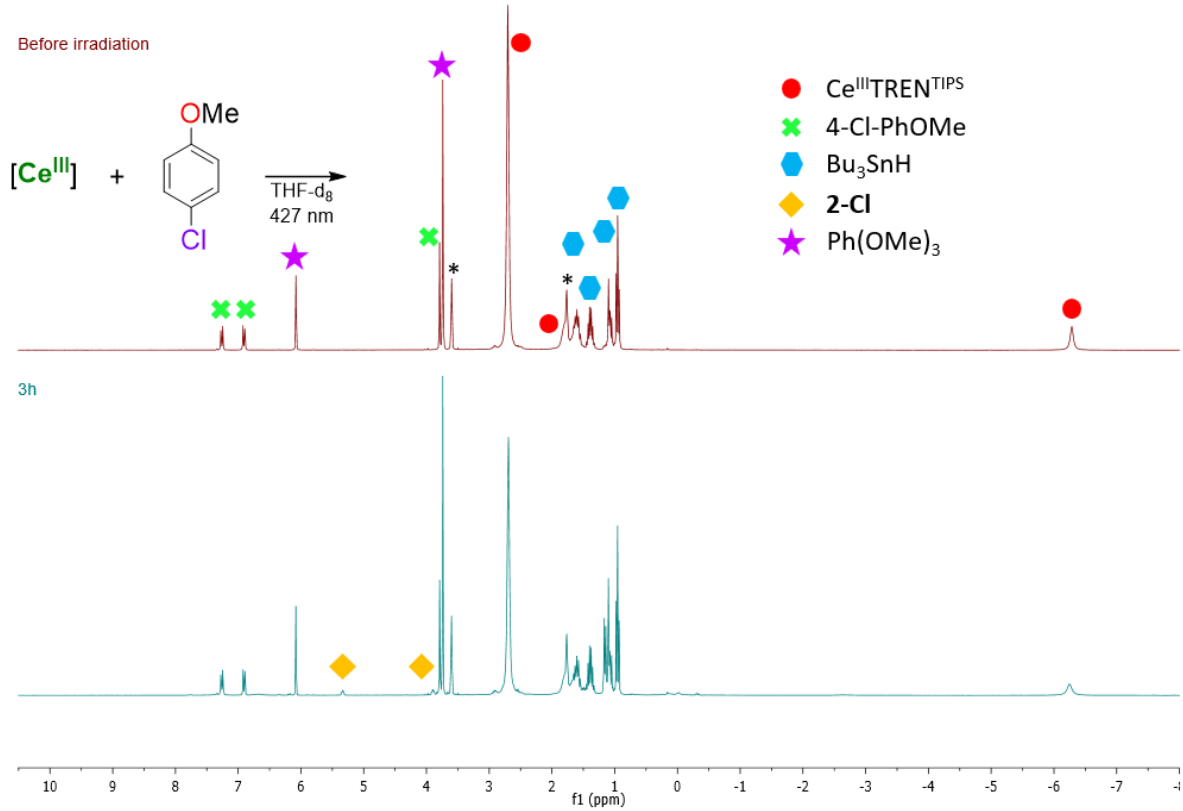

Figure S113. ^{1}H NMR spectrum of the reaction between **1** and 4-chloroanisole under irradiation at 427 nm in THF-d_8. Solvent residual peaks are indicated with *

Institut Polytechnique de Paris
91120 Palaiseau, France

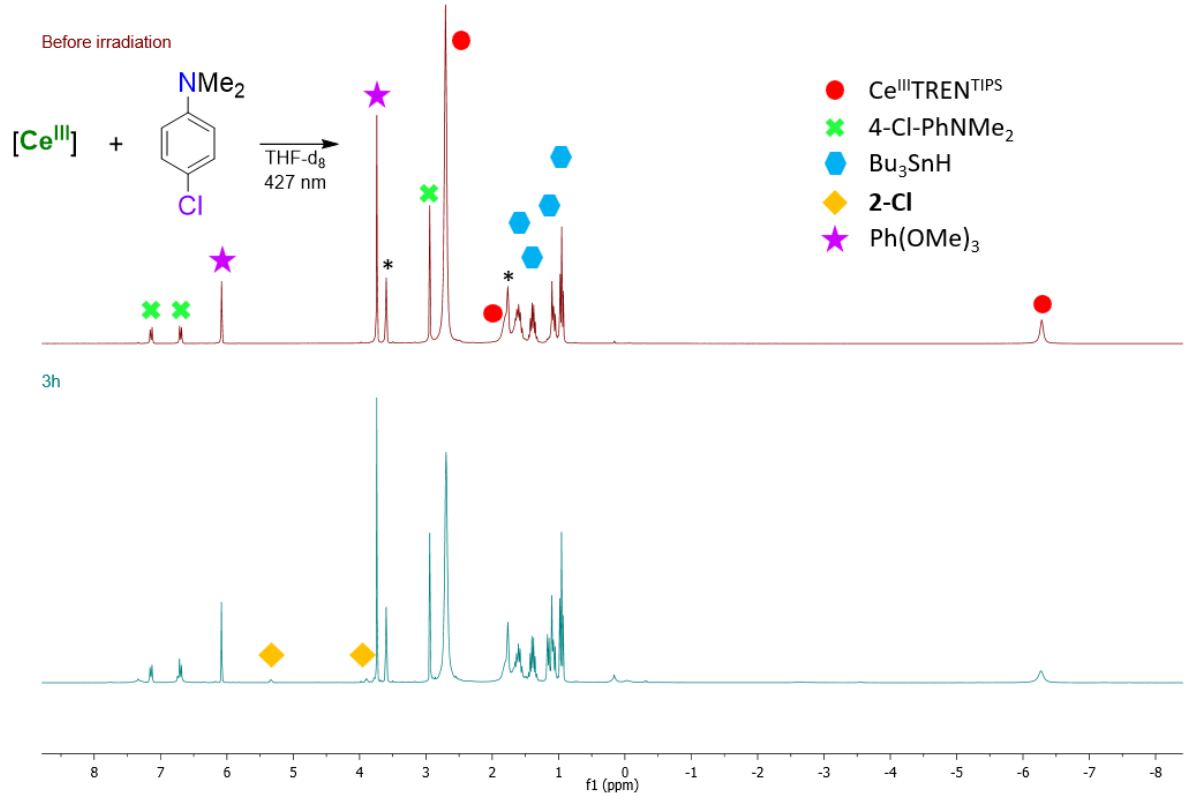

Figure S114. ^{1}H NMR spectrum of the reaction between **1** and 4-chloro-dimethylaniline under irradiation at 427 nm in THF-d_8. Solvent residual peaks are indicated with *

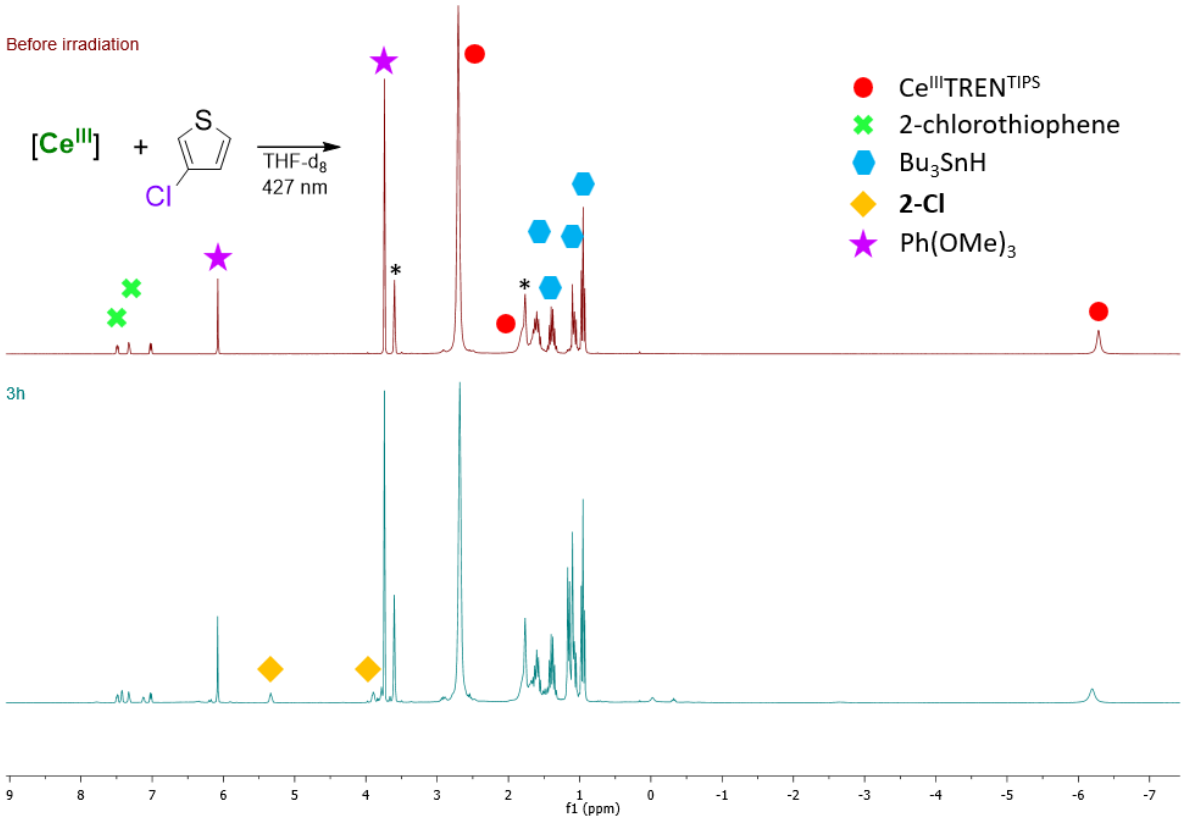

Figure S115. ^{1}H NMR spectrum of the reaction between **1** and 2-chlorothiophene under irradiation at 427 nm in THF-d_8. Solvent residual peaks are indicated with *

Institut Polytechnique de Paris
91120 Palaiseau, France

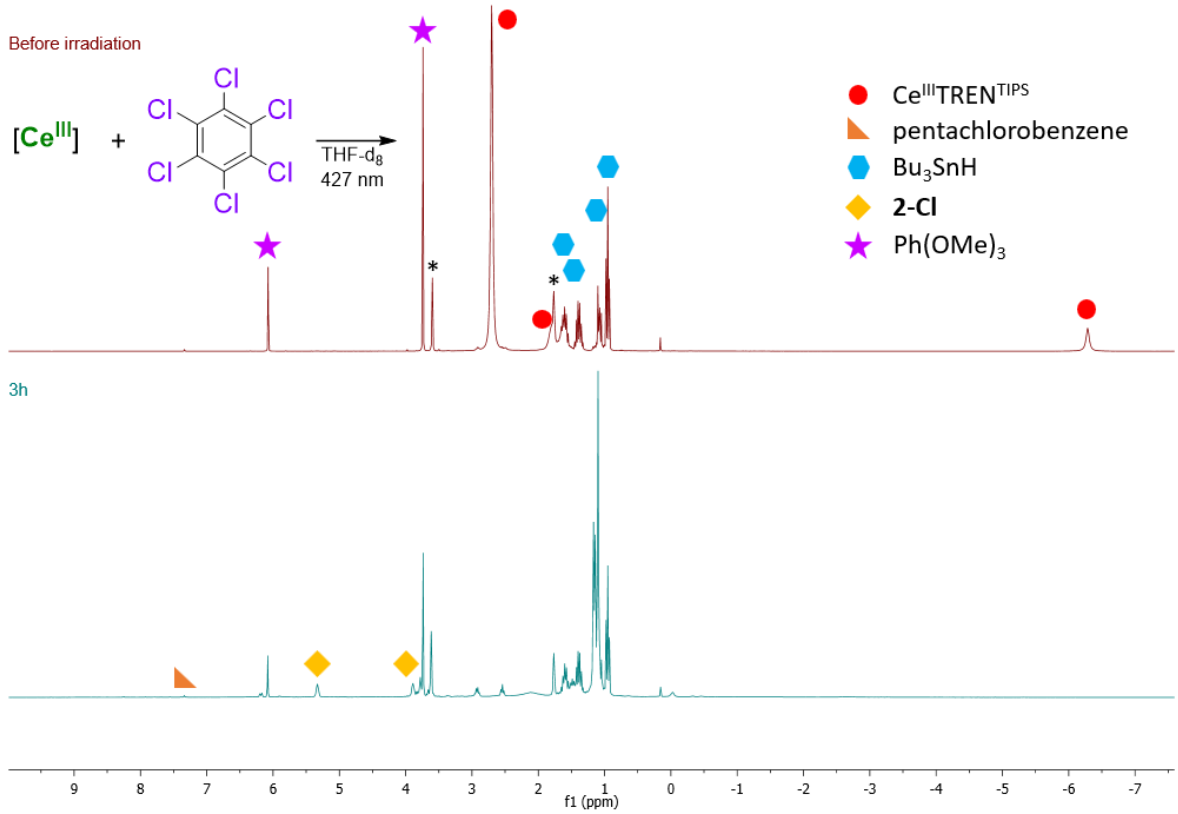

Figure S116. ^{1}H NMR spectrum of the reaction between **1** and hexachlorobenzene under irradiation at 427 nm in THF-d_8. Solvent residual peaks are indicated with *

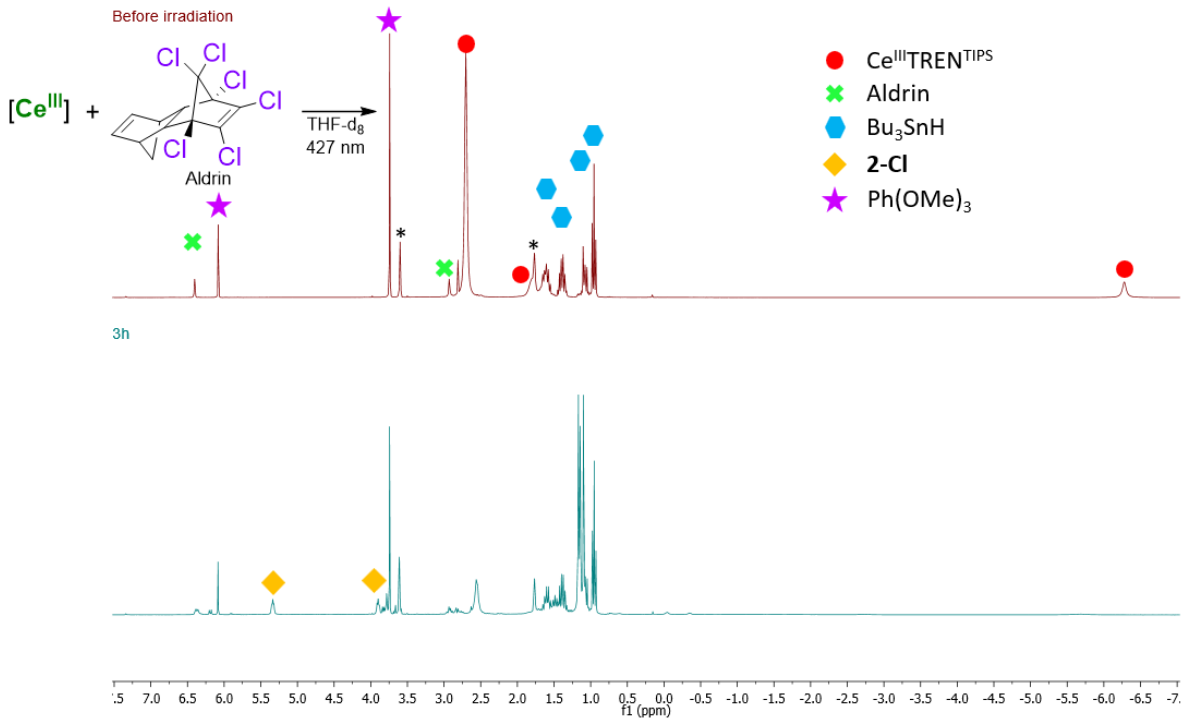

Figure S117. ^{1}H NMR spectrum of the reaction between **1** and Aldrin under irradiation at 427 nm in THF-d_8. Solvent residual peaks are indicated with *

Institut Polytechnique de Paris
91120 Palaiseau, France

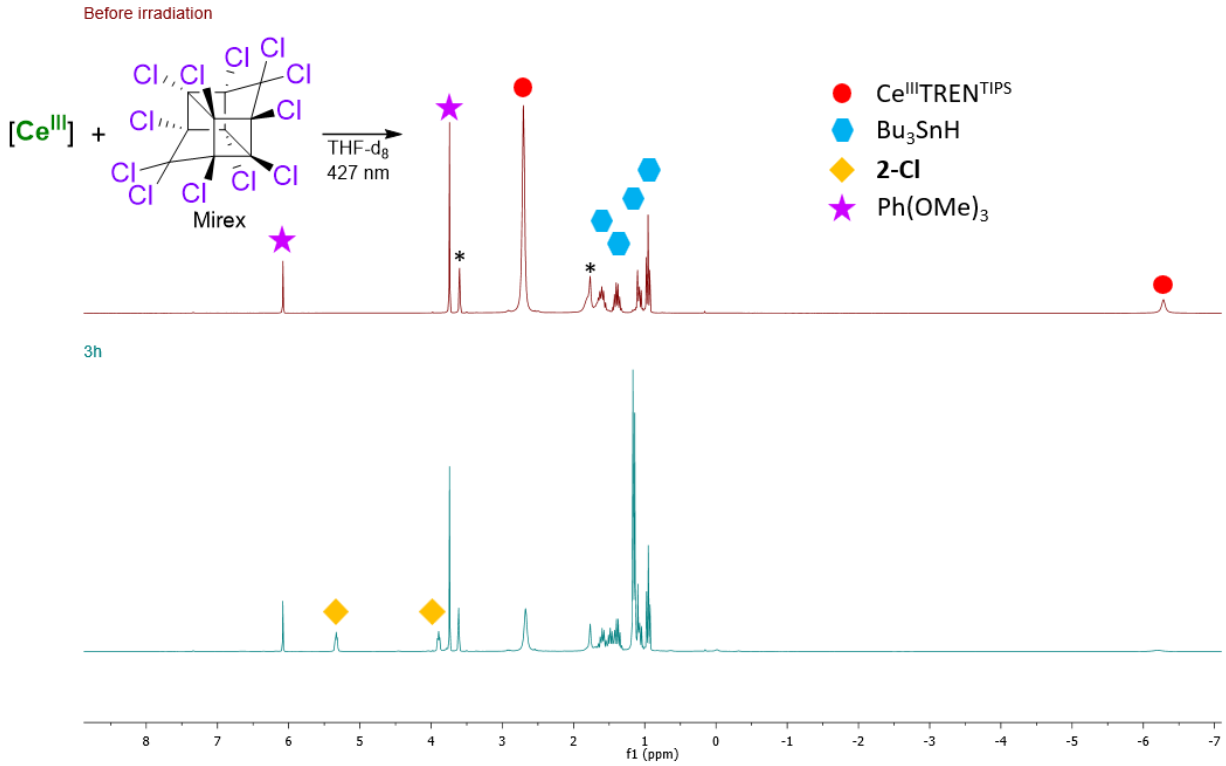

Figure S118. ^{1}H NMR spectrum of the reaction between **1** and Mirex under irradiation at 427 nm in THF-d$_8$. Solvent residual peaks are indicated with *

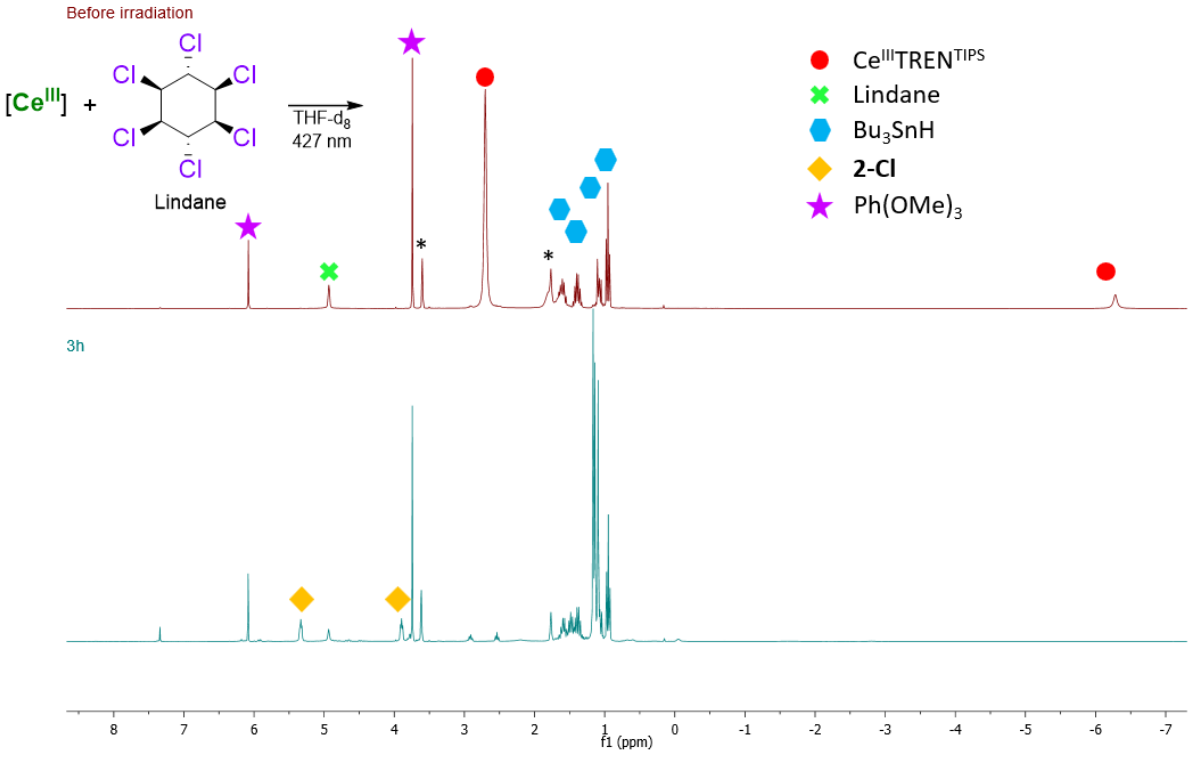

Figure S119. ^{1}H NMR spectrum of the reaction between **1** and Lindane under irradiation at 427 nm in THF-d$_8$. Solvent residual peaks are indicated with *

Institut Polytechnique de Paris
91120 Palaiseau, France

3) Photoinduced Miyaura borylation optimisation

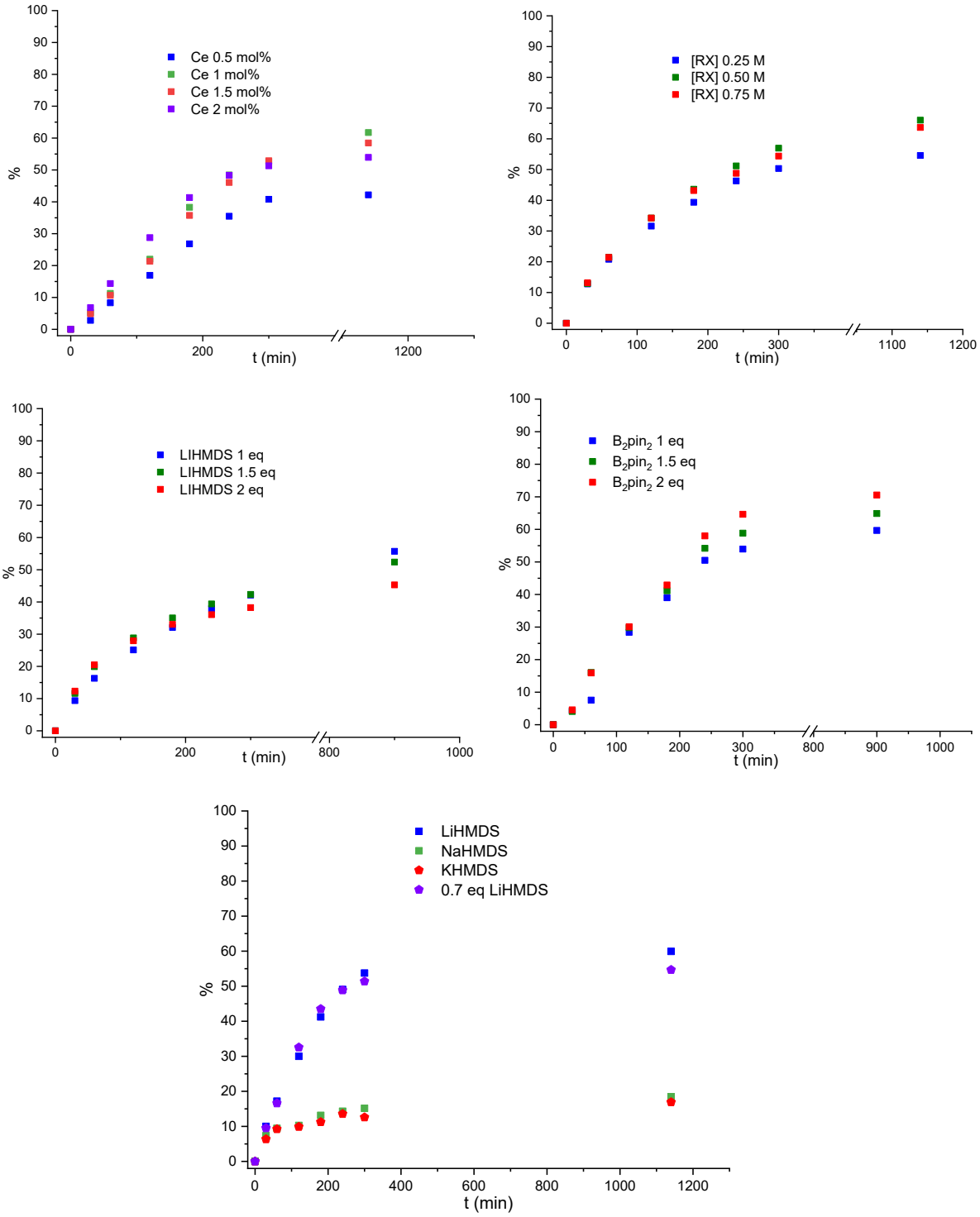

Figure S120. Optimisation reactions for the photoinduced Miyaura borylation. % shown corresponds to the quantity of MeOPhBpin formed, referenced to trimethoxybenzene as internal standard

Conditions		% MeOPhBpin (5 h)
Ce	1 mol%	53
	2 mol%	63
	5 mol%	67
[RX]	0.25 M	50
	0.50 M	57
	0.75 M	54

Conditions		% MeOPhBpin (5 h)	% MeOPhBpin (19 h
LiHMDS	0.5 eq.	40	44
	0.7 eq.	51	55
	1 eq.	47	60
	1.5 eq.	45	55
	2 eq.	43	49
B2pin2	1 eq.	54	
	1.5 eq.	59	
	2 eq.	65	

Conditions	% MeOPhBpin (5 h)	% MeOPhBpin (19 h)
LiHMDS	47	60
NaHMDS	15	19
KHMDS	13	17
Zn (2 eq.) (6h)	10	

Table S37. Optimisation tables for the photoinduced Miyaura borylation reaction

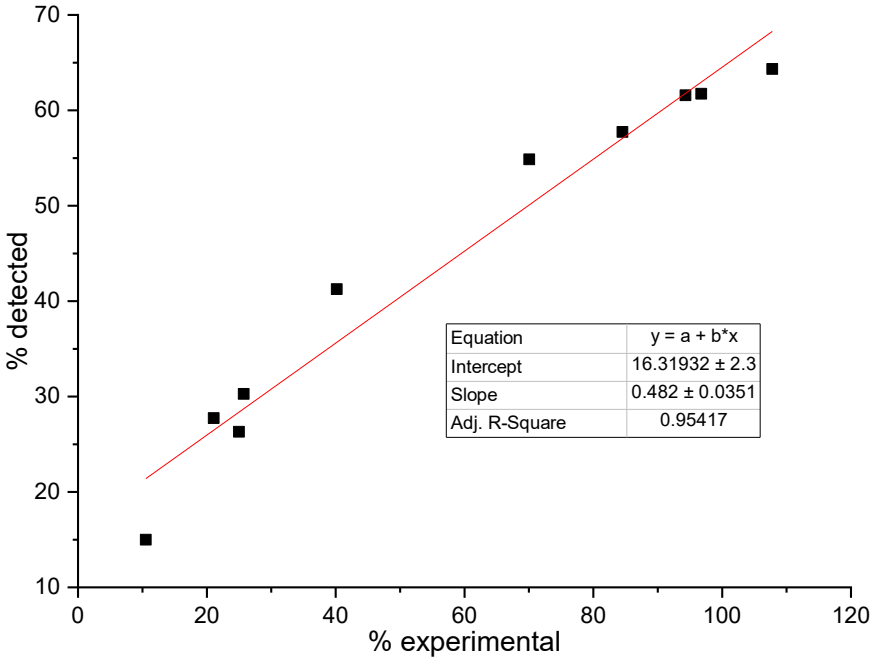

Figure S121. Example of poor calibration curve of PhBpin with dodecane analysed by GC-FID

e) Reactivity with fluorinated substrates

1) Kinetic data

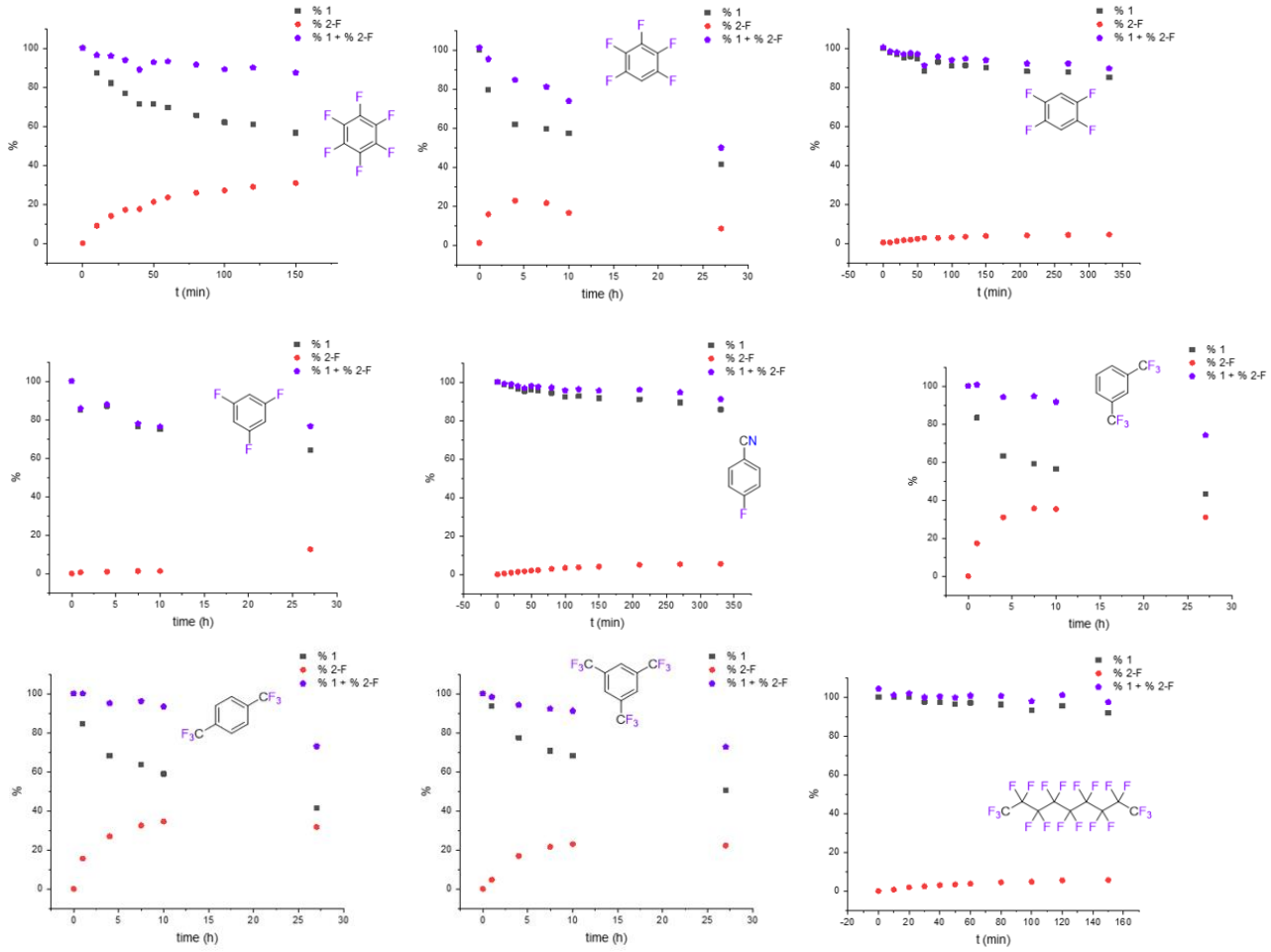

Figure S122. Evolution of quantities of **1**, **2-F** as function of irradiation time with various chlorinated substrates. Yields of formation of **2-F**, were calculated using the integration of a characteristic signal of the internal standard in ^{1}H NMR and calibrated on the initial integration of **1**

Note S1. For **Table S40**, yields of formation of **2-F** were calculated using the integration of a characteristic signal of internal standard in ^{1}H NMR and calibrated on the initial integration of **1**

Institut Polytechnique de Paris
91120 Palaiseau, France

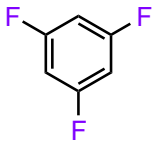

t (h)	% **1**	% **2-F**	% RX	% **1** + % **2-F**
0	100	0	100	100.0
1	85.17	0.63	98.68	85.80
4	87.07	0.95	97.37	88.01
7.5	76.66	1.26	100.00	77.92
10	75.08	1.26	98.68	76.34
27	64.04	12.62	92.11	76.66

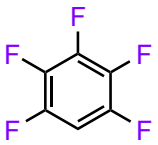

t (h)	% **1**	% **2-F**	% RX	% **1** + % **2-F**
0	100	0	100	100.0
1	79.62	15.77	93.10	95.38
4	61.92	22.69	86.21	84.62
7.5	59.62	21.54	79.31	81.15
10	57.31	16.54	82.76	73.85
27	41.54	8.46	72.41	50.00

Table S38. Percentages of compounds **1** and **2-F** during photochemical degradation of 1,3,5-trifluorobenzene and pentafluorobenzene

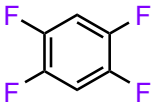

t (min)	% **1**	% **2-F**	% RX	% **1** + % **2-F**
0	100	0.45	100	100.5
10	97.86	0.5	102.51	98.36
20	96.7	1.15	100.04	97.85
30	95.19	1.66	101.44	96.85
40	95.67	1.81	99.33	97.48
50	94.71	2.28	97.49	96.99
60	88.32	2.83	95.49	91.15
80	92.94	2.75	98.00	95.69
100	90.93	3	95.19	93.93
120	91.16	3.39	95.49	94.55
150	90.17	3.74	94.12	93.91
210	88.11	4.04	93.90	92.15
270	87.89	4.29	94.20	92.18
330	85.07	4.48	93.49	89.55

t (min)	% **1**	% **2-F**	% RX	% **1** + % **2-F**
0	100	0	100	100.0
30	98.05	0.22	100.71	98.27
60	95.47	1.02	98.39	96.49
180	91.67	2.63	93.05	94.3
240	89.96	2.88	90.61	92.84
300	89.14	3.12	88.84	92.26
360	87.81	2.93	87.56	90.74
420	87.57	3	84.53	90.57
480	84.52	3	83.83	87.52
540	85.16	2.97	83.31	88.13
600	86	2.05	79.97	88.05
660	84.39	2.22	78.17	86.61
720	83.77	2.43	77.30	86.2

Table S39. Percentages of compounds **1** and **2-F** during photochemical degradation of 1,2,4,5-tetrafluorobenzene

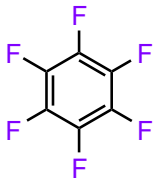

t (min)	% **1**	% **2-F**	% **1** + % **2-F**
0	100	0.04	100.0
10	87.32	9.01	96.33
20	82.01	14.04	96.05
30	76.8	17.17	93.97
40	71.46	17.58	89.04
50	71.48	21.25	92.73
60	69.62	23.54	93.16
80	65.64	25.93	91.57
100	62.03	27.13	89.16
120	61.02	28.97	89.99
150	56.56	30.9	87.46
210	42.86	24.83	67.69
270	36.71	26.08	62.79
330	32.67	26.63	59.3

t (min)	% **1**	% **2-F**	% **1** + % **2-F**
0	100	0	100.0
30	91.24	6.42	97.66
60	79.05	16.42	95.47
120	66.45	24.71	91.16
180	59.93	29.37	89.3
240	56.86	33.25	90.11
300	51.4	34.9	86.3
360	49.39	35.91	85.3
420	46.74	37.43	84.17
480	44.11	38.58	82.69
540	41.59	38.82	80.41
600	41.03	37.76	78.79
660	41.73	38.1	79.83
720	38.17	38.37	76.54

Table S40. Percentages of compounds **1** and **2-F** during photochemical degradation of hexafluorobenzene

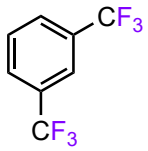

t (min)	% **1**	% **2-F**	% RX	% **1** + % **2-F**
0	100	0	100	100.0
1	83.45	17.27	86.73	100.7
4	63.31	30.94	73.47	94.24
7.5	58.99	35.61	66.33	94.60
10	56.47	35.25	64.29	91.73
27	43.17	30.94	46.94	74.10

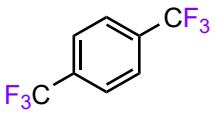

t (min)	% **1**	% **2-F**	% RX	% **1** + % **2-F**
0	100	0	100	100.0
1	84.48	15.52	86.67	100.0
4	68.28	26.90	77.04	95.17
7.5	63.79	32.41	71.85	96.21
10	58.97	34.48	68.15	93.45
27	41.38	31.72	46.67	73.10

Table S41. Percentages of compounds **1** and **2-F** during photochemical degradation of 1,3-bis(trifluoromethyl)benzene and1,4-bis(trifluoromethyl)benzene

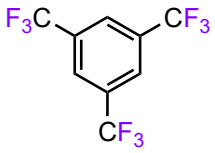

t (min)	% **1**	% **2-F**	% RX	% **1** + % **2-F**
0	100	0	100	100.0
1	93.60	4.71	95.65	98.32
4	77.44	16.84	83.70	94.28
7.5	70.71	21.55	79.35	92.26
10	68.35	22.90	77.17	91.25
27	50.51	22.22	58.70	72.73

Table S42. Percentages of compounds **1** and **2-F** during photochemical degradation of 1,3,5-tris(trifluoromethyl)benzene

Institut Polytechnique de Paris
91120 Palaiseau, France

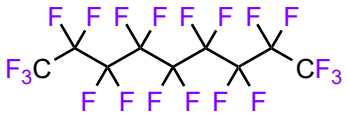

t (min)	% **1**	% 2-F	% **1** + % **2-F**
0	100	0	100.0
10	100.27	0.73	101
20	99.93	1.89	101.8
30	97.54	2.39	99.93
40	97.33	3.01	100.3
50	96.39	3.35	99.74
60	97.1	3.75	100.9
80	96.16	4.43	100.6
100	93.16	4.7	97.86
120	95.56	5.49	101.1
150	91.8	5.67	97.47

t (min)	% **1**	% 2-F	% **1** + % **2-F**
0	100	0	100.0
30	92.21	6.64	98.85
60	87.71	8.93	96.64
120	86.71	10.54	97.25
180	85.38	11.38	96.76
240	85.35	12.56	97.91
300	83.06	13.43	96.49
360	83.26	13.96	97.22
420	81.36	14.23	95.59
480	80.51	14.75	95.26
540	79.49	15.12	94.61
600	79.79	15.63	95.42
720	77.94	16.27	94.21

Table S43. Percentages of compounds **1** and **2-F** during photochemical degradation of perfluorononane

Institut Polytechnique de Paris
91120 Palaiseau, France

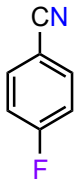

t (min)	% **1**	% 2-F	% **1** + % **2-F**
0	100	0	100.0
10	98.75	0.4	99.15
20	98.06	0.88	98.94
30	96.65	1.3	97.95
40	95.2	1.58	96.78
50	96.09	1.94	98.03
60	95.39	2.18	97.57
80	94.34	2.86	97.2
100	92.36	3.35	95.71
120	92.61	3.7	96.31
150	91.56	4.02	95.58
210	91.04	4.97	96.01
270	89.3	5.27	94.57
330	85.73	5.45	91.18

t (min)	% **1**	% 2-F	% **1** + % **2-F**
0	100	0	100.0
30	97.58	0.21	97.79
120	93.68	1.83	95.51
180	90.79	2.82	93.61
240	90.85	3.12	93.97
300	89.02	3.44	92.46
360	87.94	3.7	91.64
420	88.38	3.81	92.19
480	88.38	3.87	92.25
540	87.25	3.82	91.07
600	86.61	3.47	90.08
660	84.86	3.88	88.74
720	84.74	3.77	88.51

Table S44. Percentages of compounds **1** and **2-F** during photochemical degradation of 4-fluorobenzonitrile

4) NMR spectra

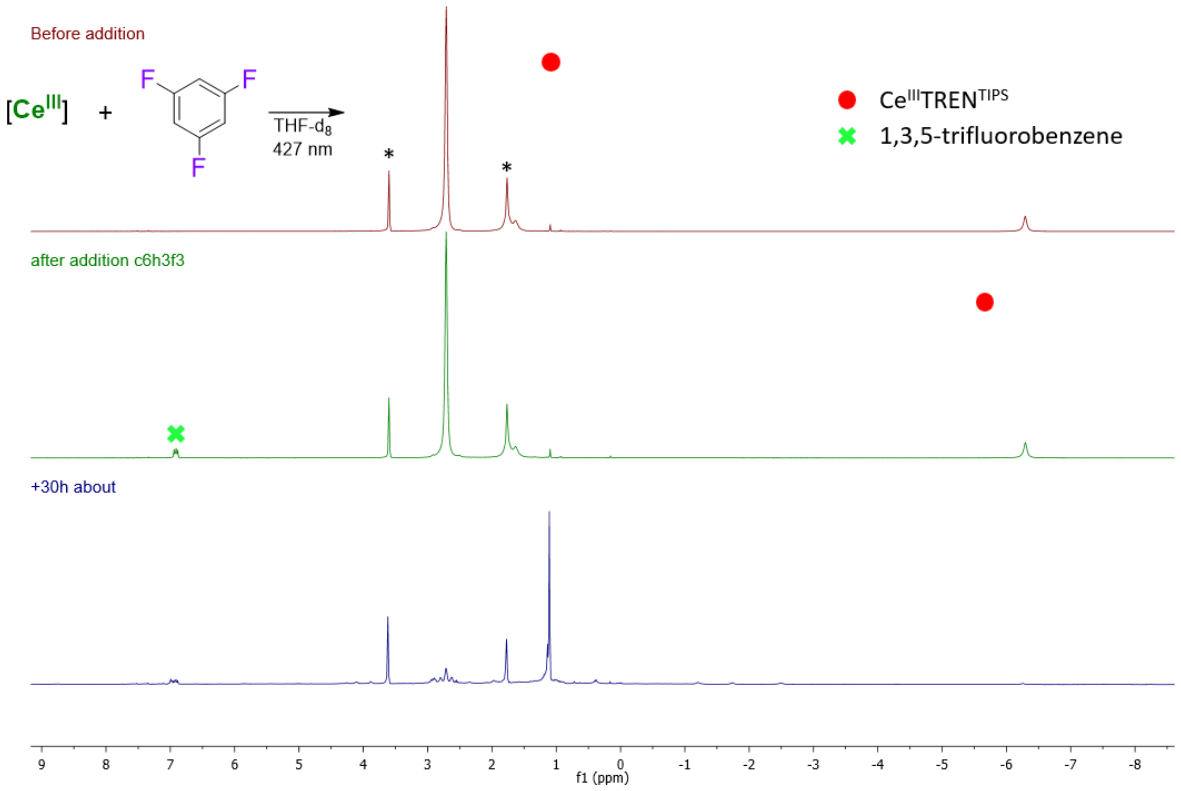

Figure S123. ^{1}H NMR spectrum of the **r**eaction between **1** and 1,3,5-trifluorobenzene under irradiation at 427 nm in THF-d_8. Solvent residual peaks are indicated with *

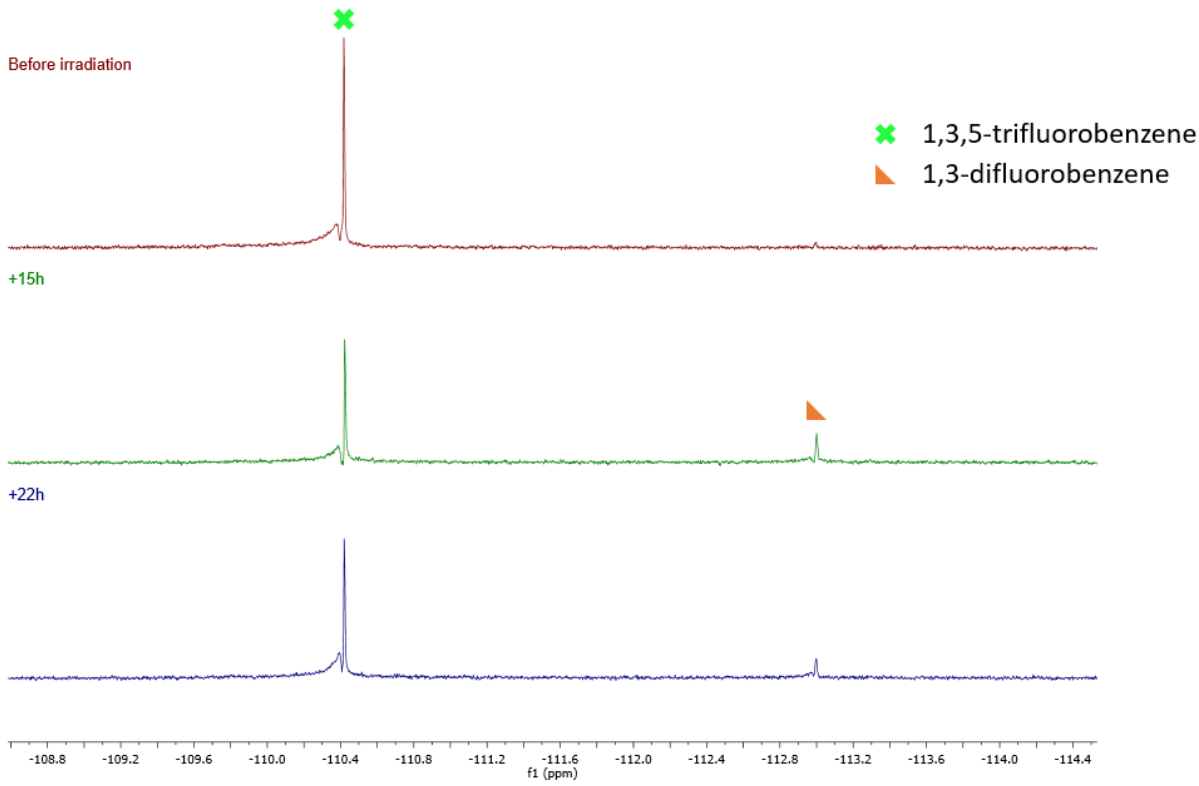

Figure S124. ^{19}F NMR spectrum of the **r**eaction between **1** and 1,3,5-trifluorobenzene under irradiation at 427 nm in THF-d_8

Institut Polytechnique de Paris
91120 Palaiseau, France

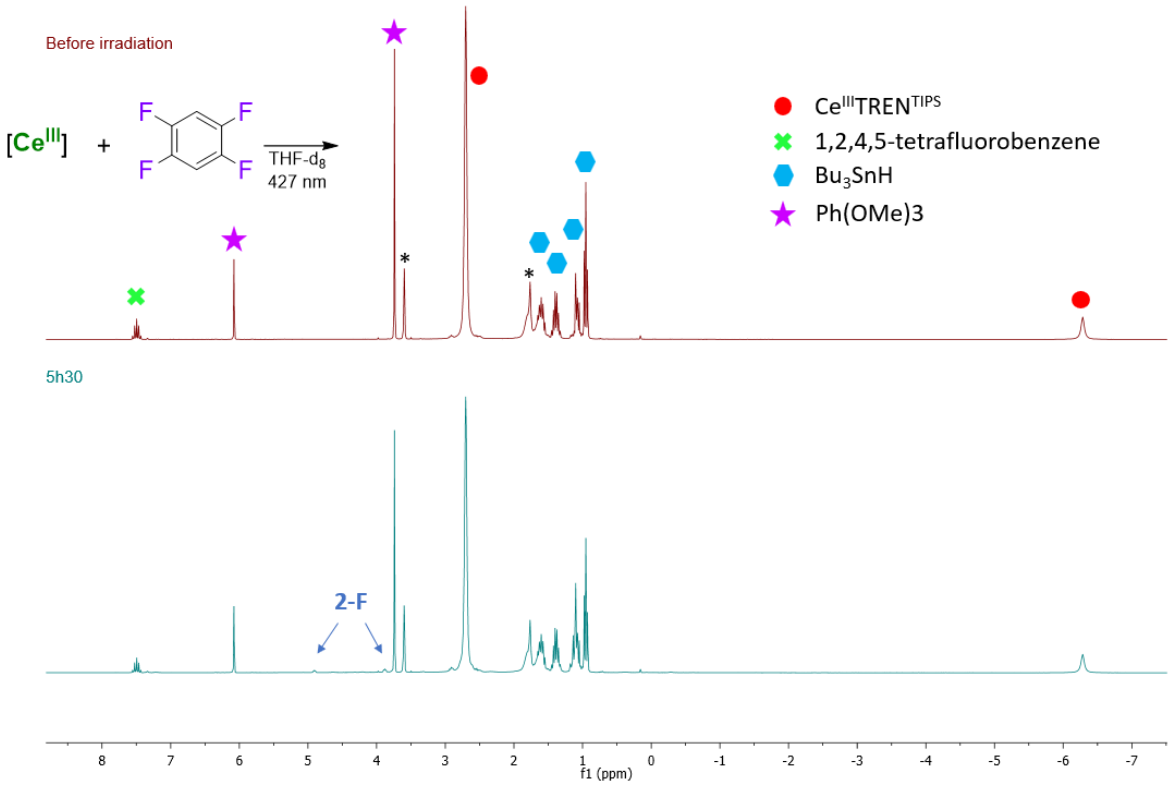

Figure S125. ^{1}H NMR spectrum of the reaction between **1** and 1,2,4,5-tetrafluorobenzene under irradiation at 427 nm in THF-d_8. Solvent residual peaks are indicated with *

Institut Polytechnique de Paris
91120 Palaiseau, France

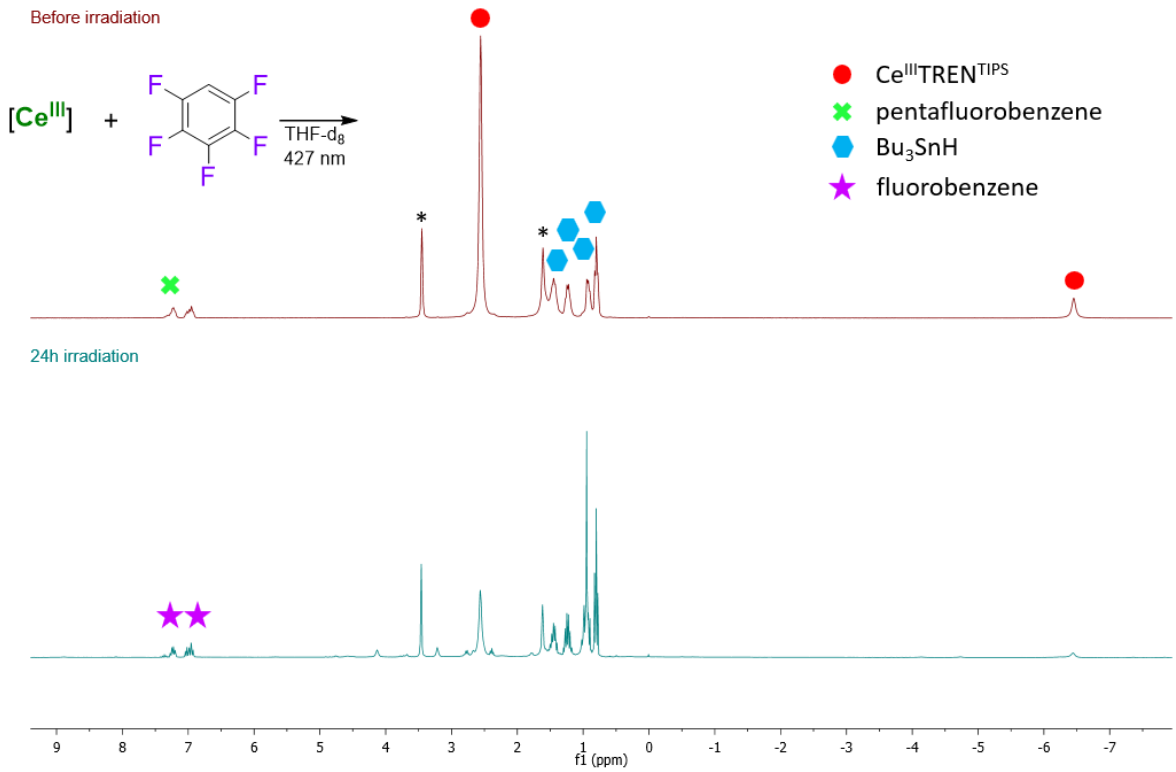

Figure S 126. ^{1}H NMR spectrum of the reaction between **1** and pentafluorobenzene under irradiation at 427 nm in THF-d_8. Solvent residual peaks are indicated with *

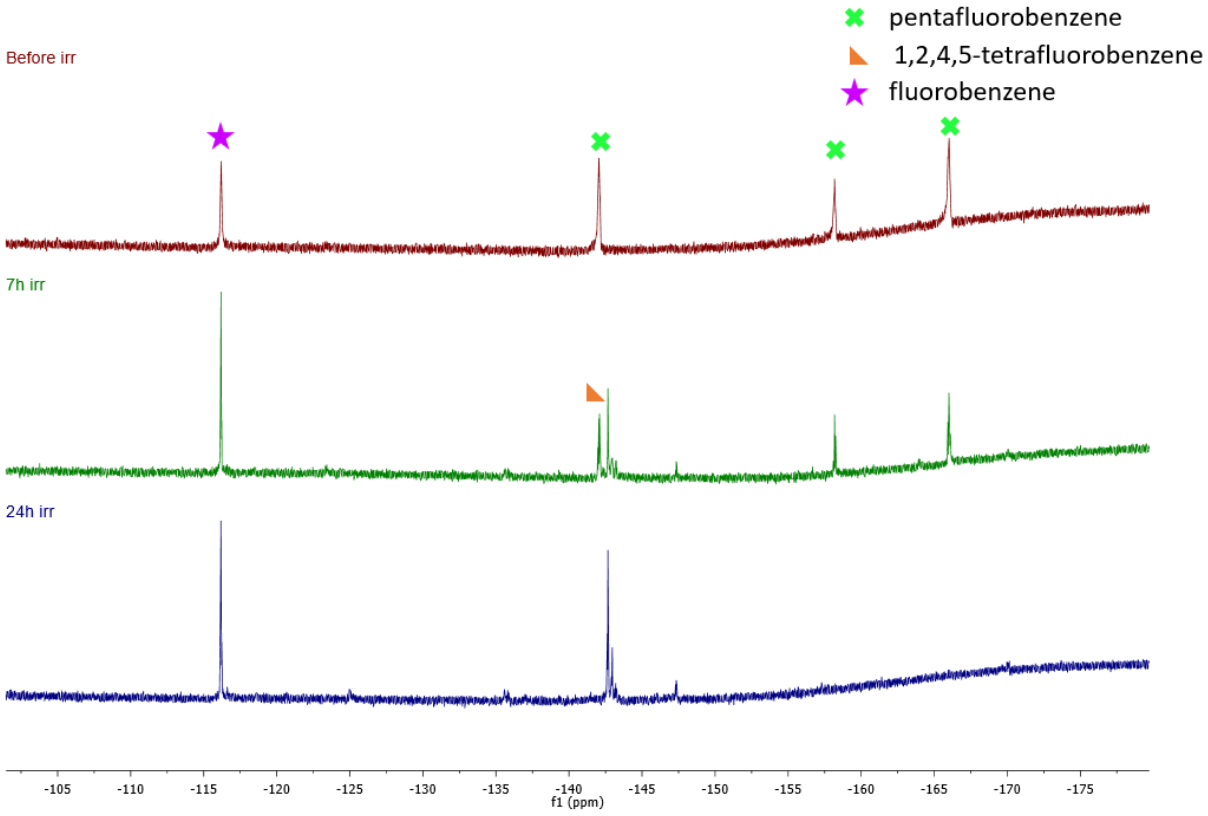

Figure S127. ^{19}F NMR spectrum of the **r**eaction between **1** and pentafluorobenzene under irradiation at 427 nm in THF-d_8

Institut Polytechnique de Paris
91120 Palaiseau, France

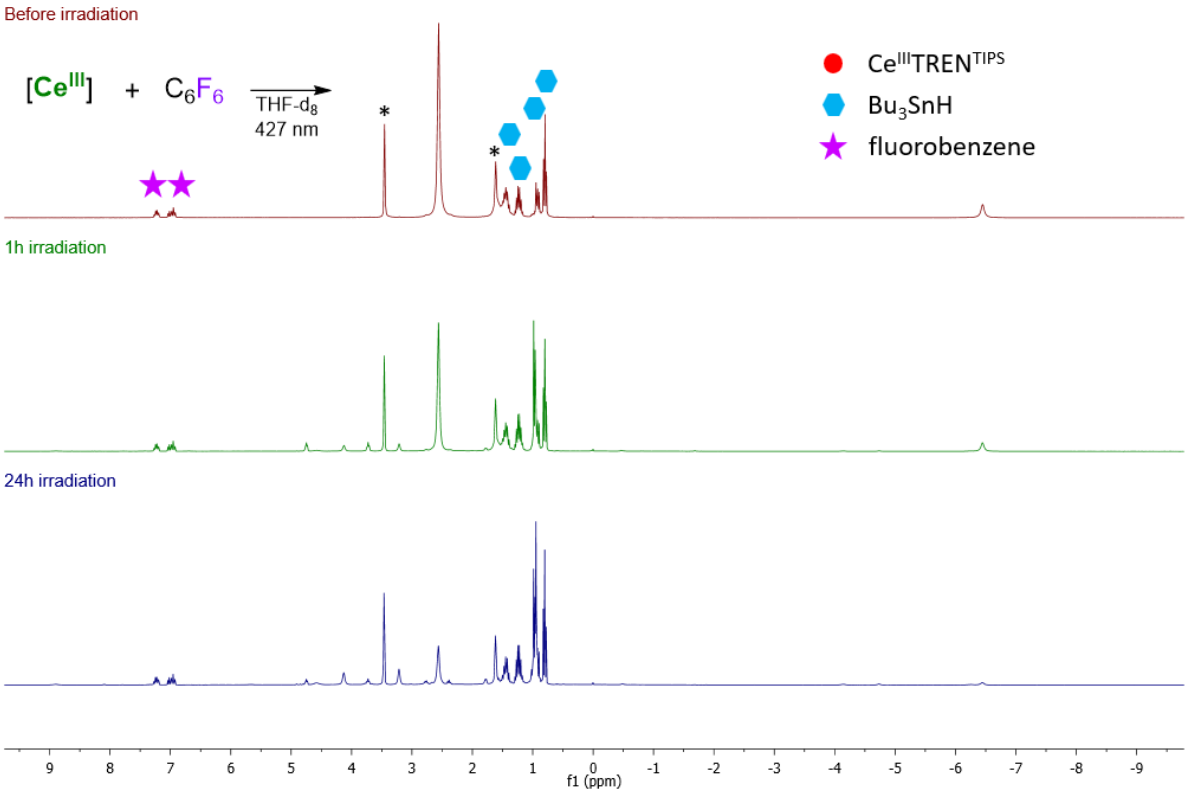

Figure S128. ^{1}H NMR spectrum of the reaction between **1** and hexafluorobenzene under irradiation at 427 nm in THF-d_8. Solvent residual peaks are indicated with *

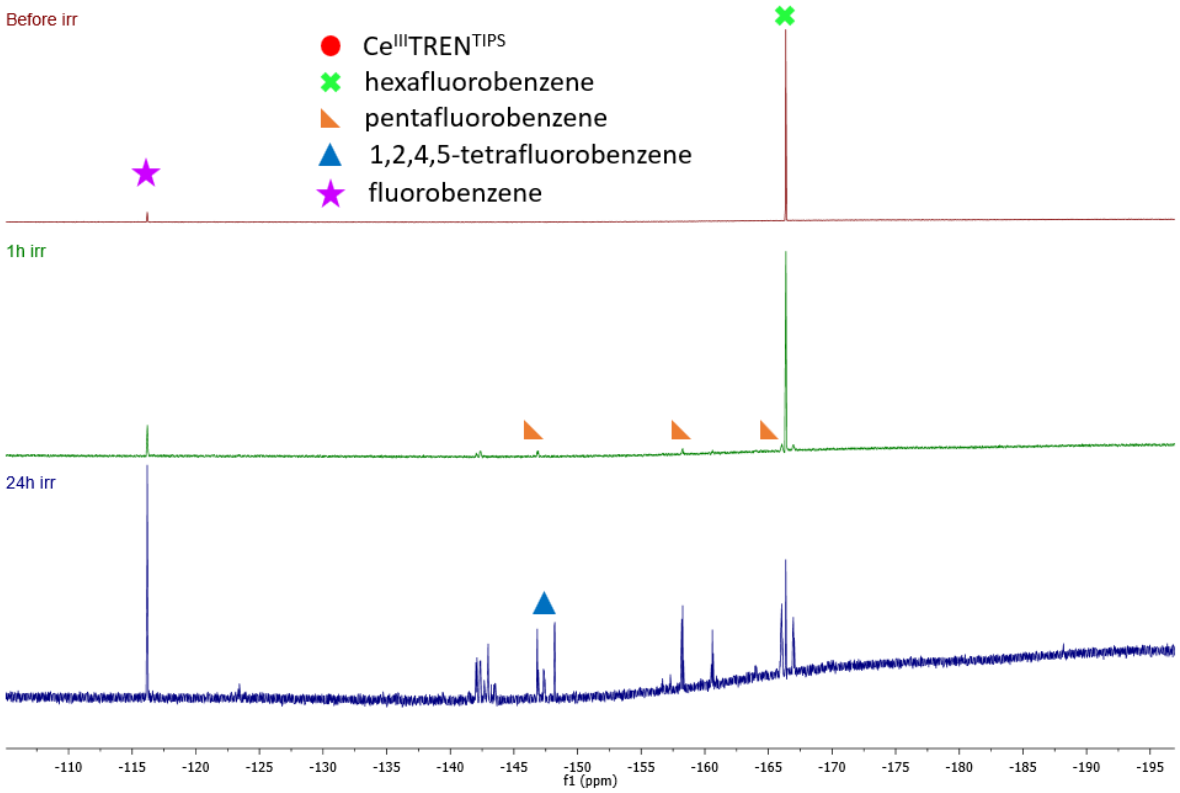

Figure S129. ^{19}F NMR spectrum of the reaction between **1** and hexafluorobenzene under irradiation at 427 nm in THF-d_8

Institut Polytechnique de Paris
91120 Palaiseau, France

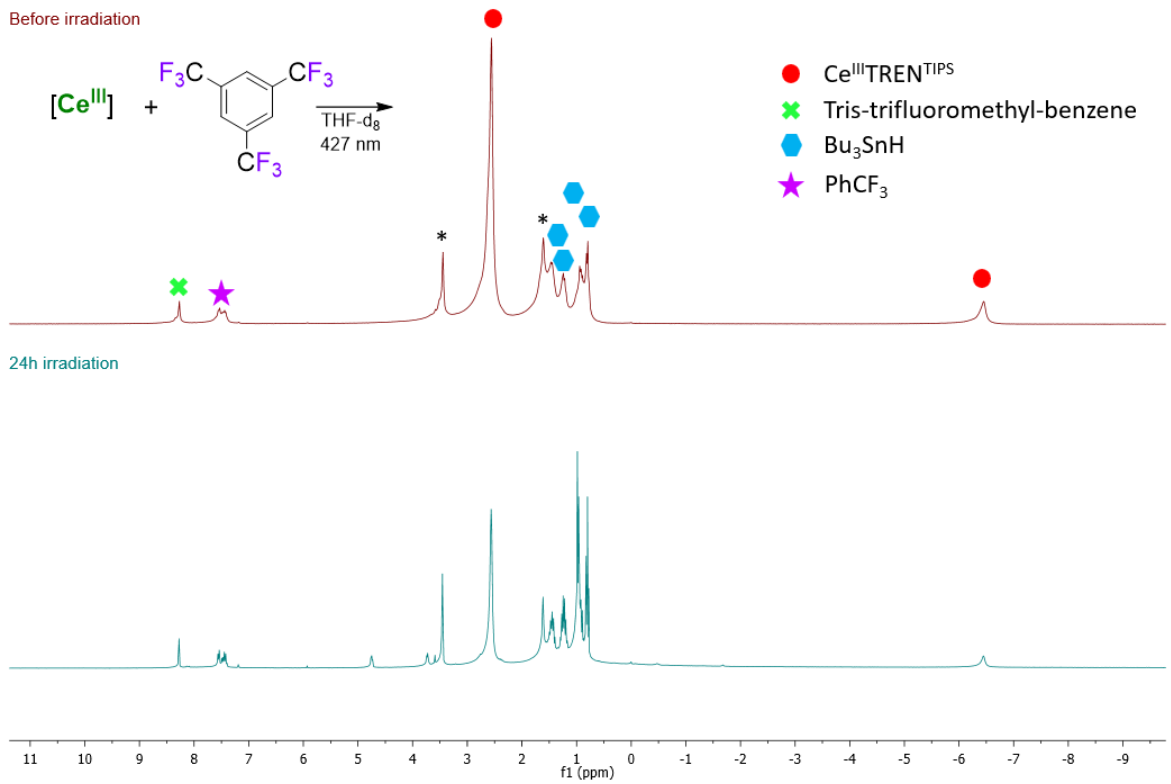

Figure S130. ^{1}H NMR spectrum of the reaction between **1** and tris-trifluoromethyl-benzene under irradiation at 427 nm in THF-d_8. Solvent residual peaks are indicated with *

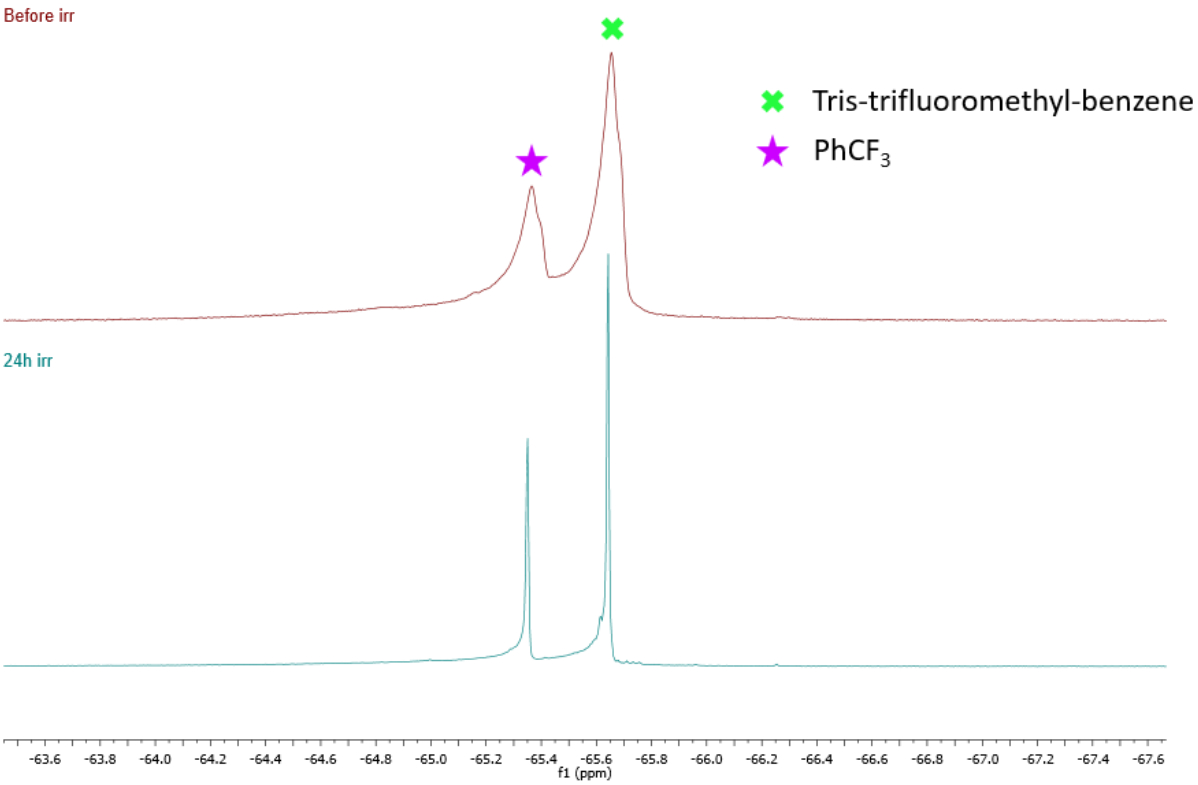

Figure S131. ^{19}F NMR spectrum of the reaction between **1** and tris-trifluoromethyl-benzene under irradiation at 427 nm in THF-d_8

Institut Polytechnique de Paris
91120 Palaiseau, France

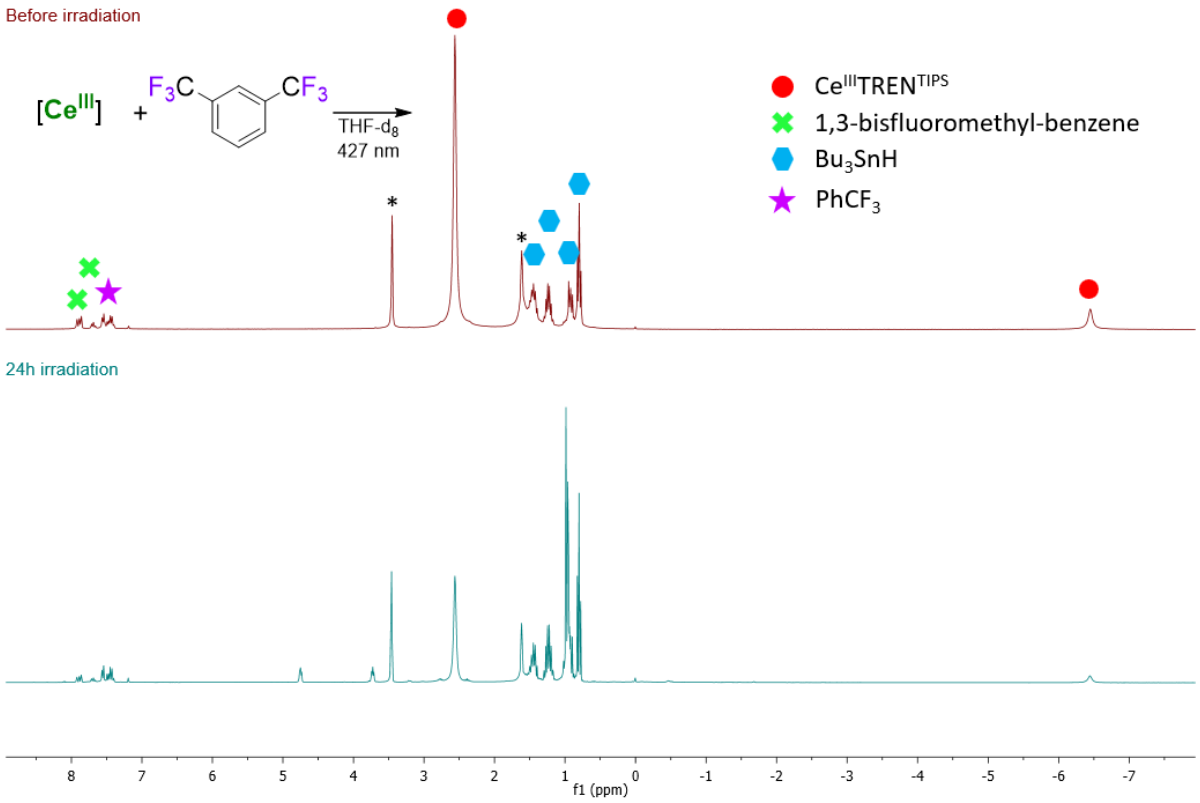

Figure S132. ^{1}H NMR spectrum of the reaction between **1** and 1,3-bis-trifluoromethyl-benzene under irradiation at 427 nm in THF-d_8. Solvent residual peaks are indicated with *

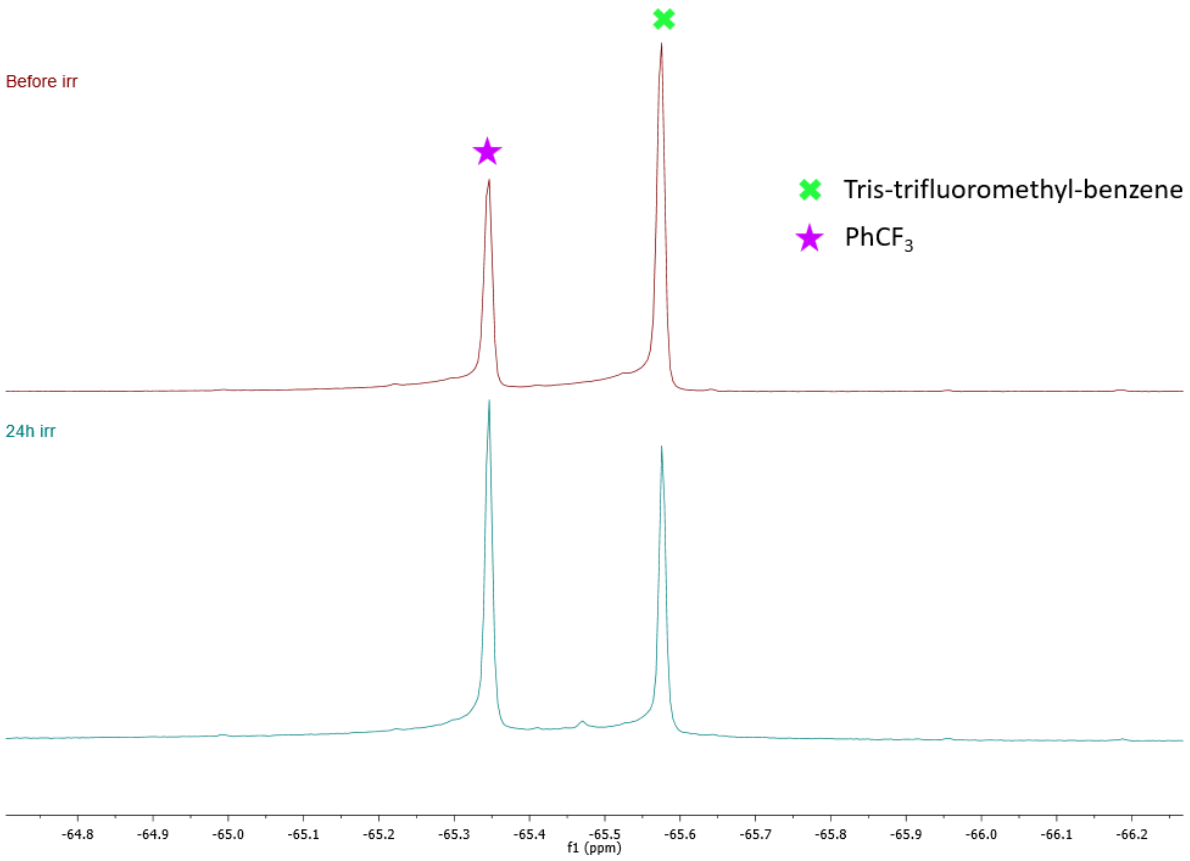

Figure S133. ^{19}F NMR spectrum of the reaction between **1** and 1,3-bis-trifluoromethyl-benzene under irradiation at 427 nm in THF-d_8

Institut Polytechnique de Paris
91120 Palaiseau, France

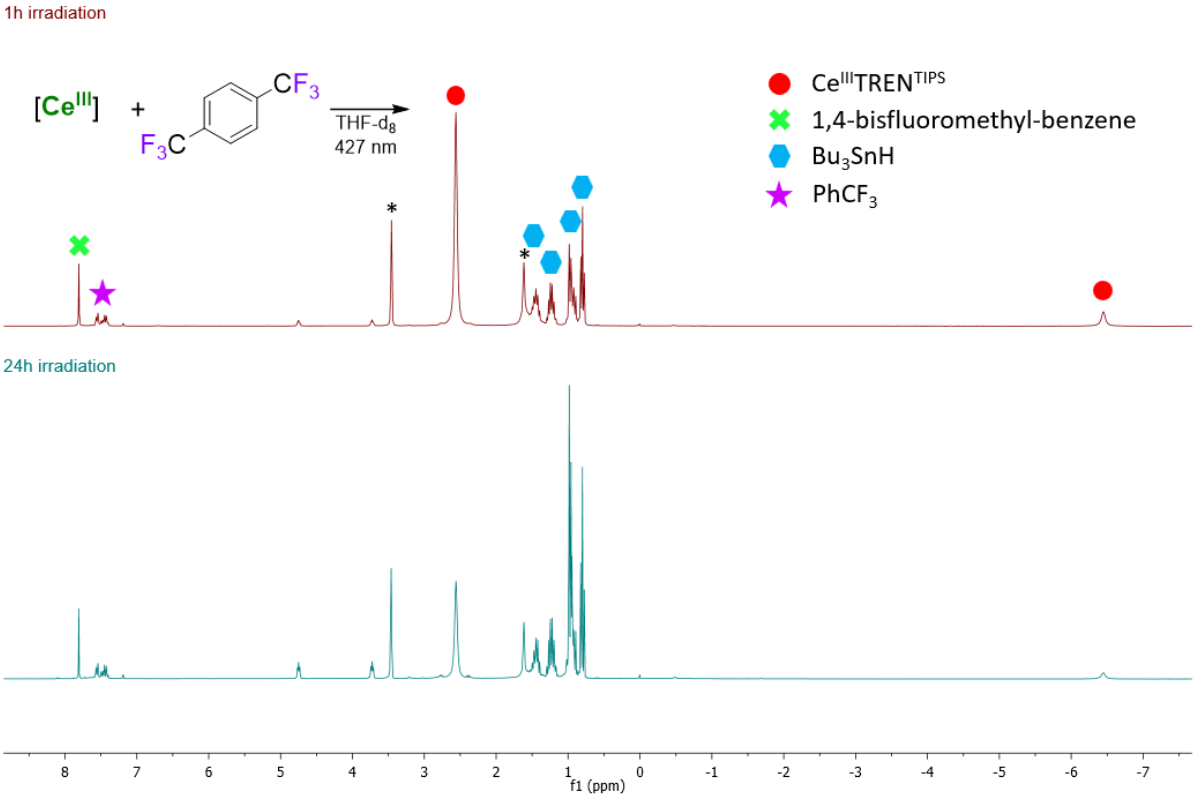

Figure S134. ^{1}H NMR spectrum of the reaction between **1** and 1,4-bis-trifluoromethyl-benzene under irradiation at 427 nm in THF-d_8. Solvent residual peaks are indicated with *

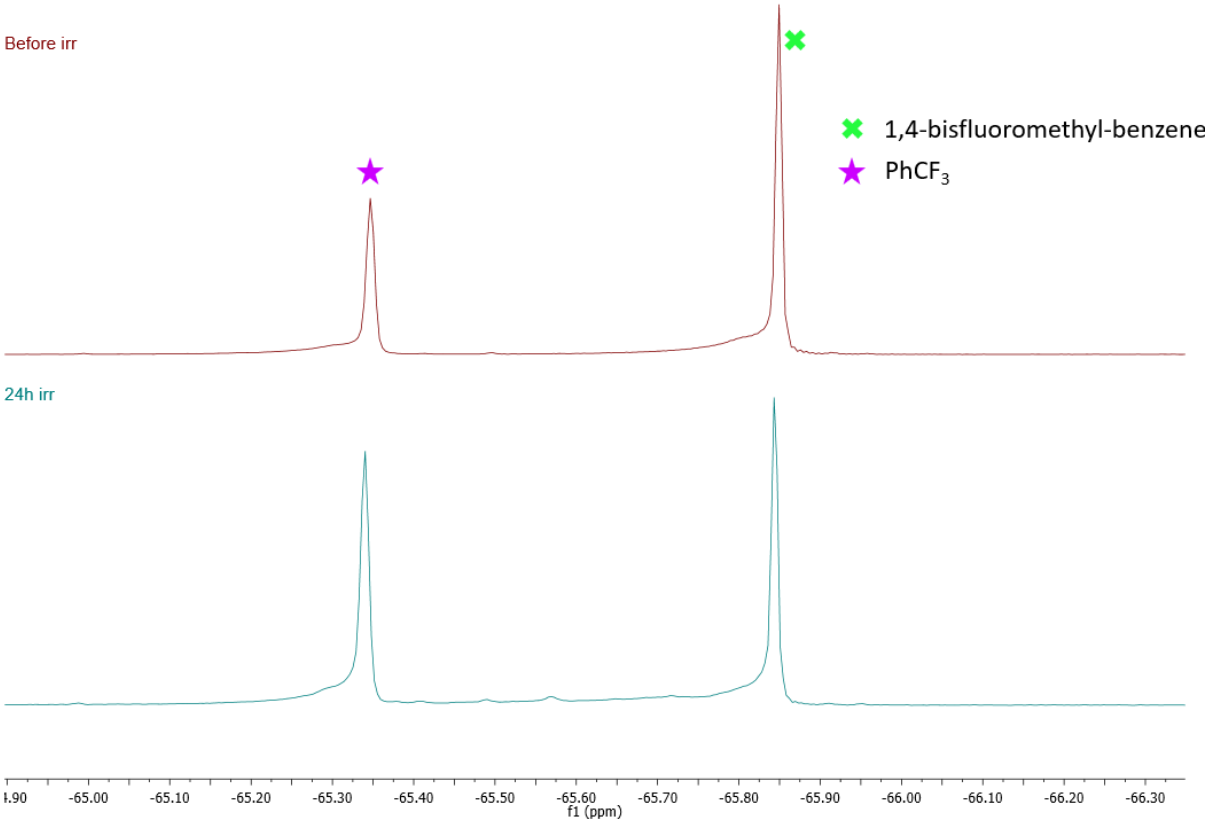

Figure S135. ^{19}F NMR spectrum of the reaction between **1** and 1,4-bis-trifluoromethyl-benzene under irradiation at 427 nm in THF-d_8

Institut Polytechnique de Paris
91120 Palaiseau, France

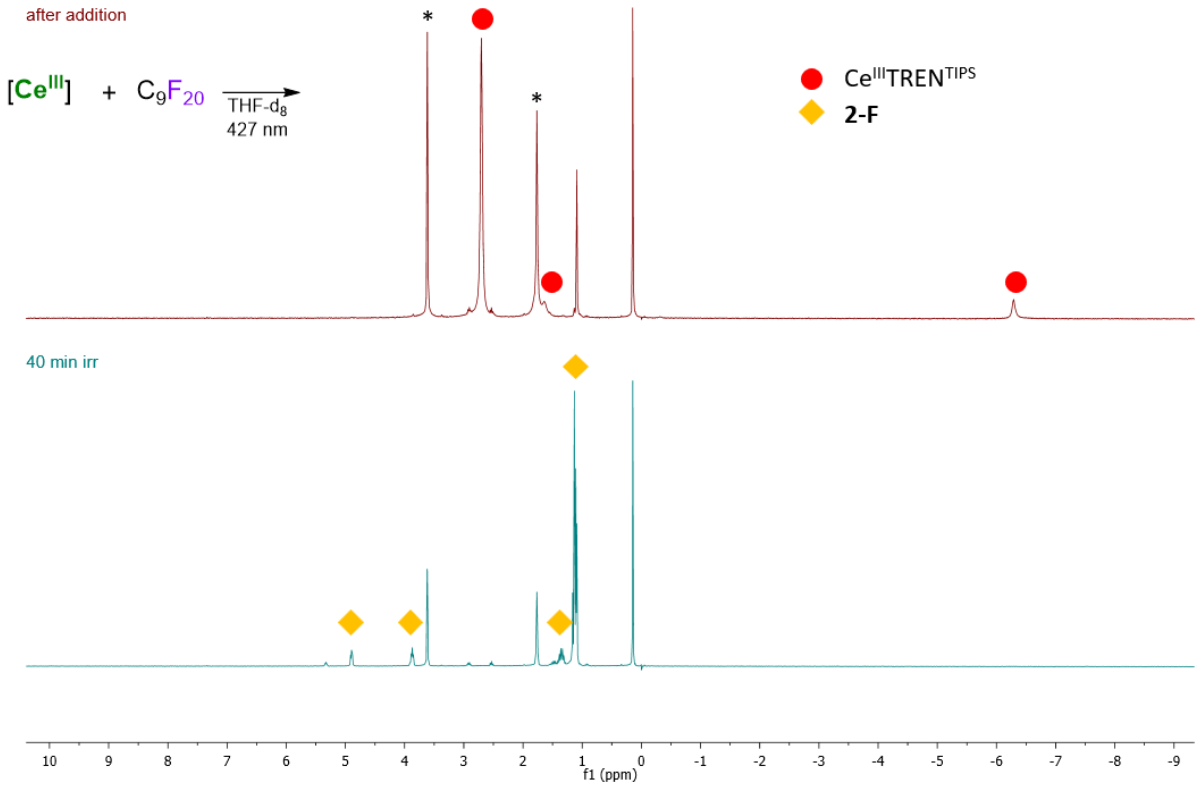

Figure S136. ^{1}H NMR spectrum of the reaction between **1** and perfluorononane under irradiation at 427 nm in THF-d_8. Solvent residual peaks are indicated with *

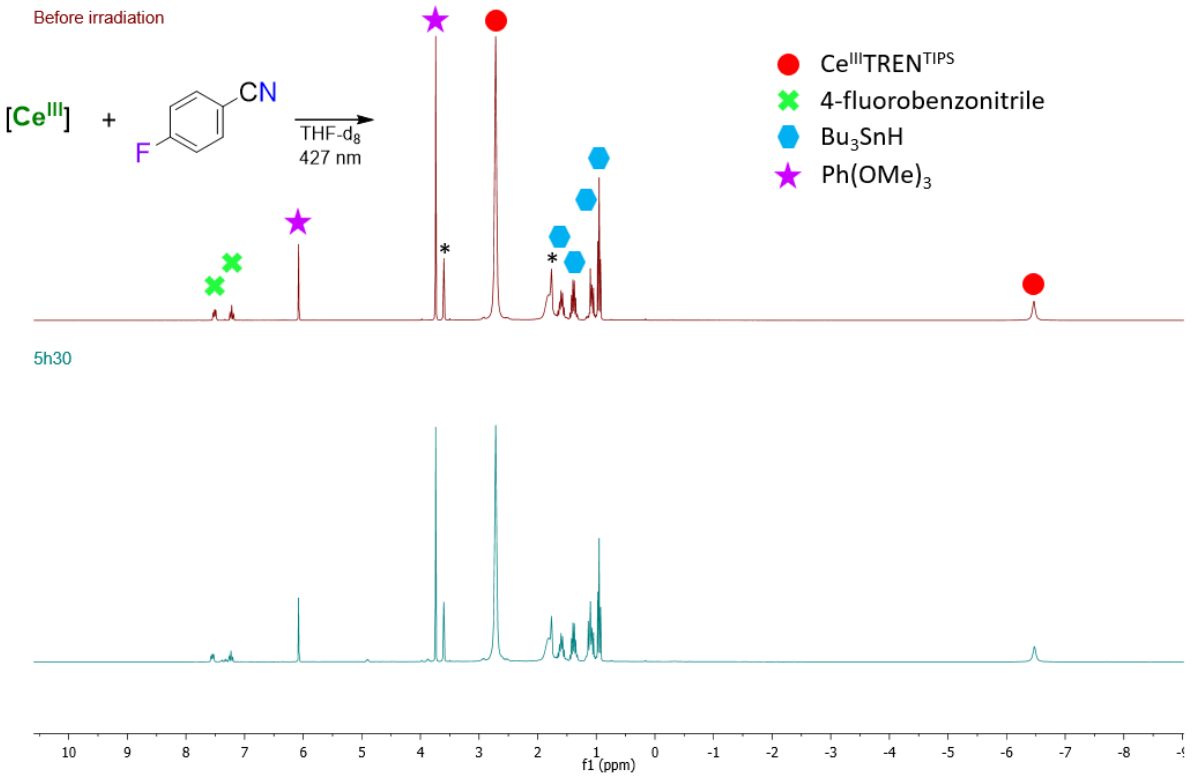

Figure S137. ^{1}H NMR spectrum of the reaction between **1** and 4-fluorobenzonitrile under irradiation at 427 nm in THF-d_8. Solvent residual peaks are indicated with *

Institut Polytechnique de Paris
91120 Palaiseau, France

5) Photochemical degradation of [FCe^{IV}TREN^{TIPS}] (2-F)

Compound **2-F** (5 mg, 6.4 µmol, 1 eq.) was dissolved in 0.4 mL of THF-d_8 with 3 drops of C6D6 in a J. Young NMR tube. The tube was irradiated at 427 nm and analysed by ^{1}H NMR at designated times.

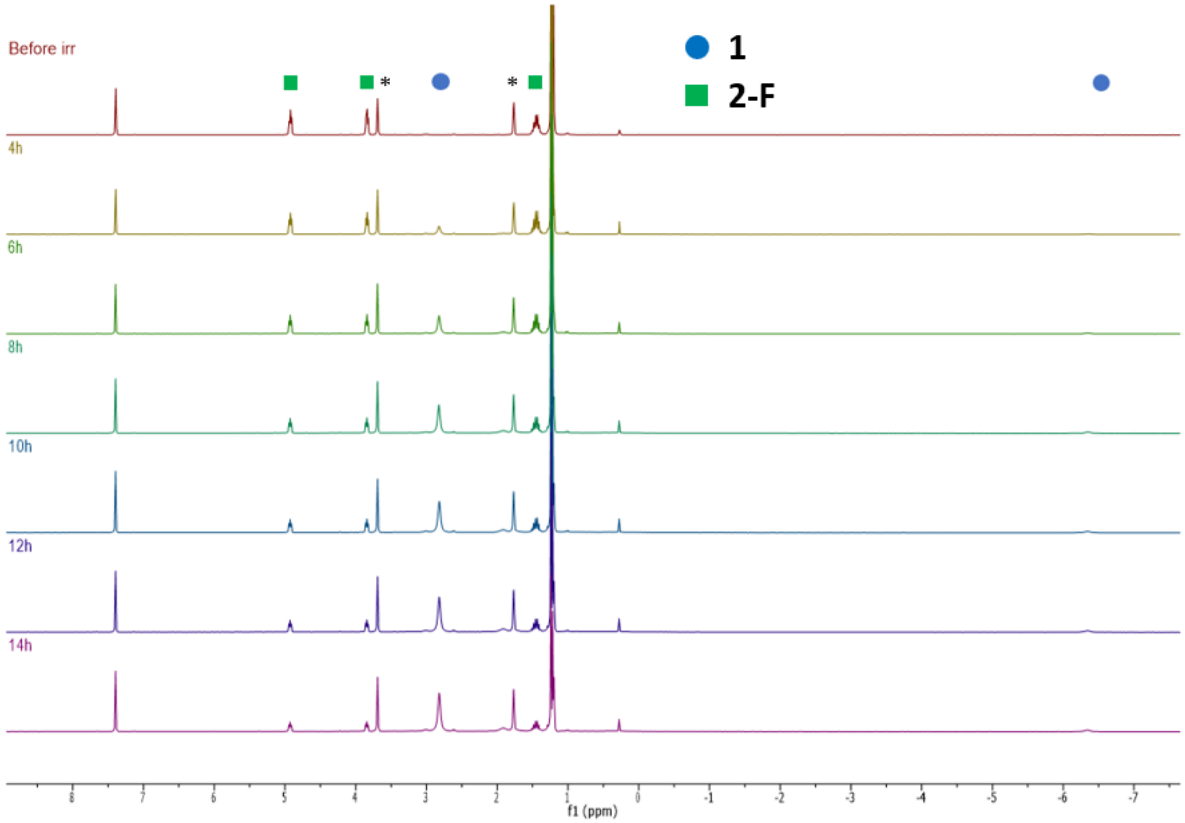

Figure S138. ^{1}H NMR spectra of the photochemical degradation of **2-F** (5 mg, 6.4 µmol) in THF-d_8 (0.4 mL) with 3 drops of C_6D_6. Solvent residual peaks are indicated with *

Institut Polytechnique de Paris
91120 Palaiseau, France

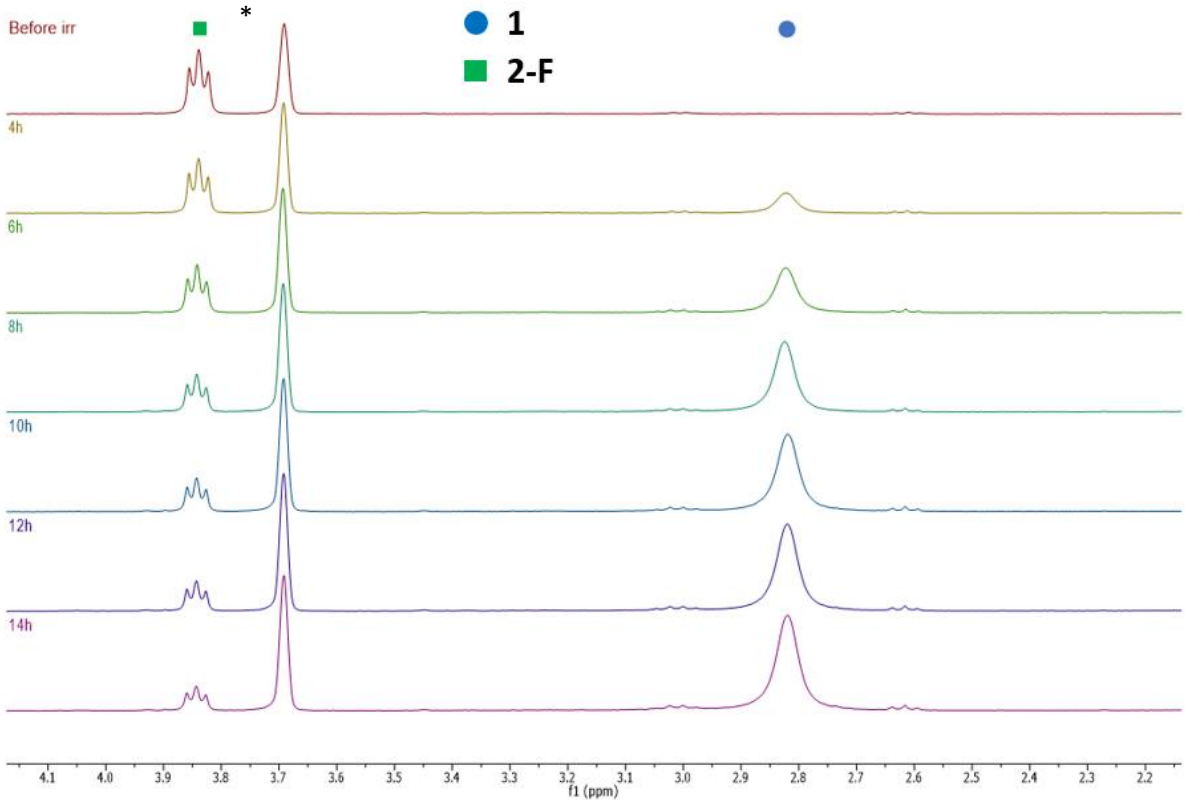

Figure S139. ^{1}H NMR spectra of the photochemical degradation of **2-F** (5 mg, 6.4 µmol) in THF-d_8 (0.4 mL) with 3 drops of C_6D_6. Zoom on the 2.2 ppm and 4.2 ppm region. Solvent residual peak is indicated with *

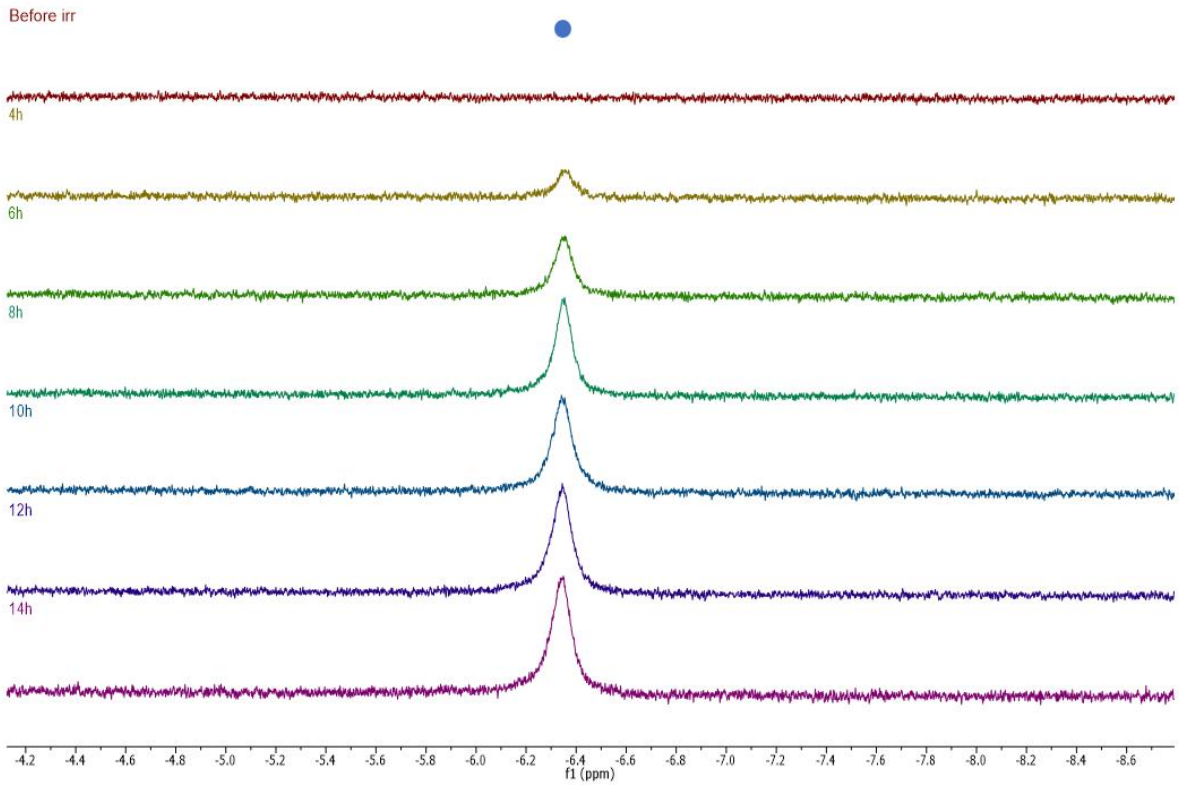

Figure S140. ^{1}H NMR spectra of the photochemical degradation of **2-F** (5 mg, 6.4 µmol) in THF-d_8 (0.4 mL) with 3 drops of C_6D_6. Zoom on the -8.6 ppm and -4.2 ppm region

Institut Polytechnique de Paris
91120 Palaiseau, France

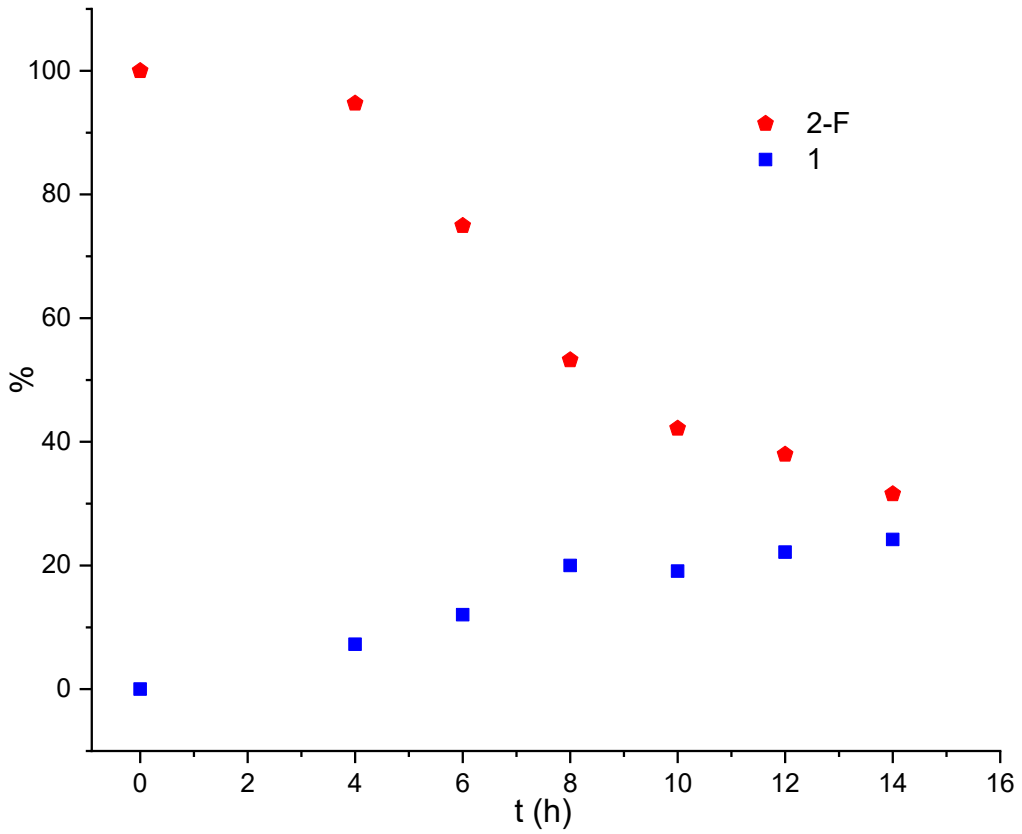

Figure S141. Photochemical degradation of **2-F** (5 mg, 6.4 µmol) with time in THF-d_8 (0.4 mL). NB : between 4 h and 6 h, and 8 and 10 h of irradiation, the NMR tube was stored at 0 °C overnight

t (min)	% **2-Cl**	% **1**
0	100	0
4	94.73	7.25
6	74.94	12.02
8	53.22	19.99
10	42.17	19.08
12	37.96	22.15
14	31.57	24.21

Table S45. Experimental data of the photochemical degradation of **2-F** (5 mg, 6.3 µmol) in THF-d_8 (0.4 mL)

References

(1) Chang, R. K.; Clairmont, B. P.; Lin, S.; MacArthur, A. H. R. Amidation of Aryl Chlorides Using a Microwave-Assisted, Copper-Catalyzed Concurrent Tandem Catalytic Methodology. *Organometallics* **2019**, *38* (22), 4448–4454. https://doi.org/10.1021/acs.organomet.9b00561.

(2) Zhang, J.; Yang, J.-D.; Cheng, J.-P. Exploiting the Radical Reactivity of Diazaphosphinanes in Hydrodehalogenations and Cascade Cyclizations. *Chem. Sci.* **2020**, *11* (18), 4786–4790. https://doi.org/10.1039/D0SC01352H.

Institut Polytechnique de Paris
91120 Palaiseau, France

Institut Polytechnique de Paris
91120 Palaiseau, France

Experimental section for Chapter III

I. Synthetic procedures 316
II. NMR spectra 317
III. EPR spectroscopy data 348
IV. UV-visible and IR spectroscopy data 368
V. Crystal structure data 376
References 379

Institut Polytechnique de Paris
91120 Palaiseau, France

I. Synthetic procedures

a) Synthesis of 4-azidonitrobenzene

4-azidonitrobenzene was synthesized according to a literature procedure.[1]

In a 250 mL round-bottom flask, 3.0 g (22 mmol, 1 eq.) of 4-nitroaniline were dissolved in 22 mL of water, and cooled down to 0°C. 22 mL of HCl (36% w/w, 1 eq.) were slowly added, and $NaNO_2$ (1.8 g, 1.2 eq.) was added portion-wise and left under stirring for 1 h. A solution of NaN_3 (2.1 g, 1.5 eq.) was slowly added to the reaction medium, and the reaction medium was left warming to room temperature. Extraction of the aqueous phase with Et_2O, drying of the organic phase with $MgSO_4$, filtration and concentration under reduced pressure afforded 3.05 g of orange solid (15 mmol, 84%).

^{1}H NMR (300 MHz, $CDCl_3$, 298 K) δ 8.25 (d, 2H), 7.15 (d, 2H)

Institut Polytechnique de Paris
91120 Palaiseau, France

II. NMR spectra

a) Reaction of 1 with nitrosobenzene

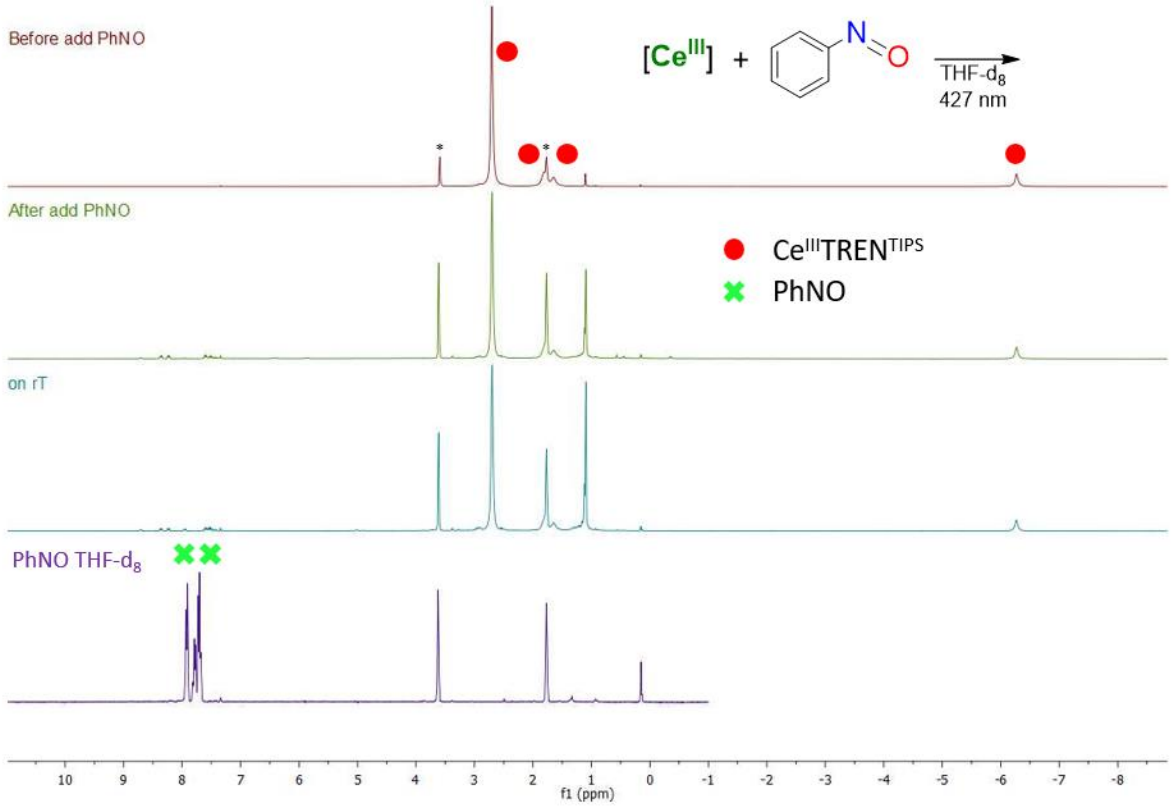

Figure S142. ^{1}H NMR spectrum of the *in-situ* reaction between **1** and PhNO. Solvent residual peaks are indicated with *

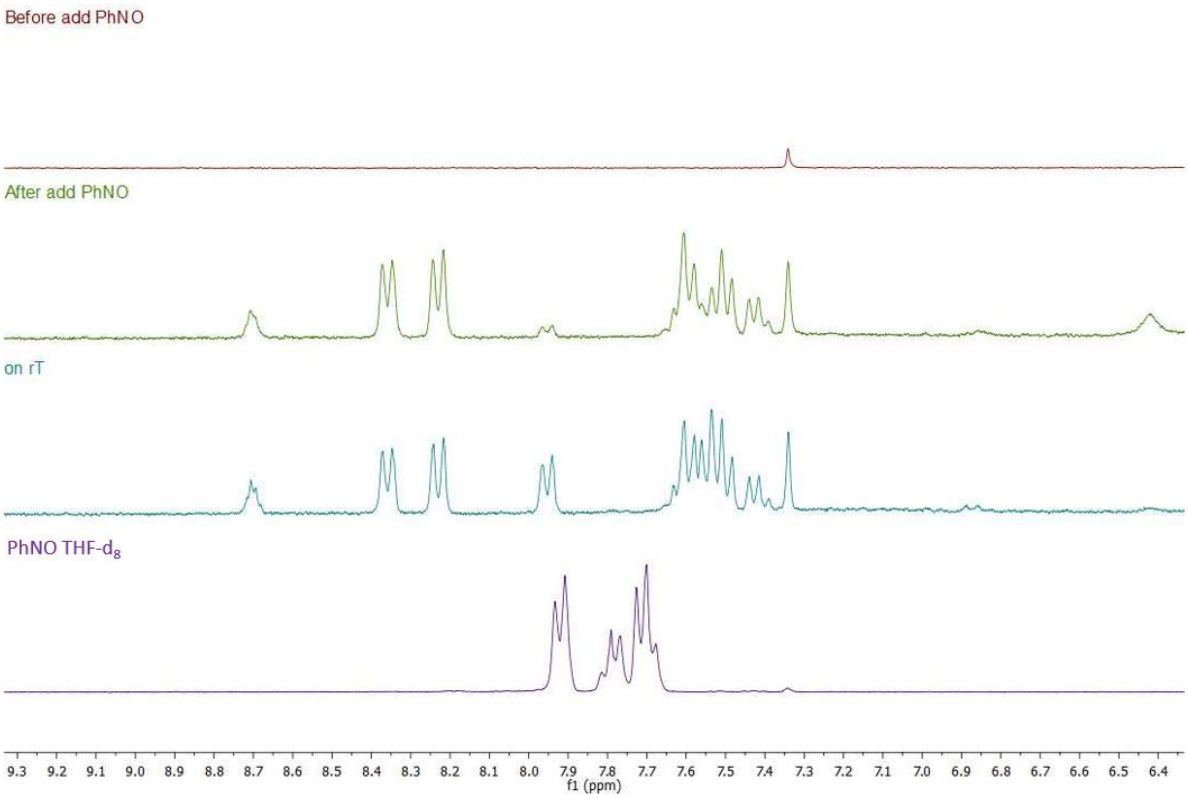

Figure S143. ^{1}H NMR spectrum of the *in-situ* reaction between **1** and PhNO. Zoom between 6.4 and 9.3 ppm. Solvent residual peaks are indicated with *

Institut Polytechnique de Paris
91120 Palaiseau, France

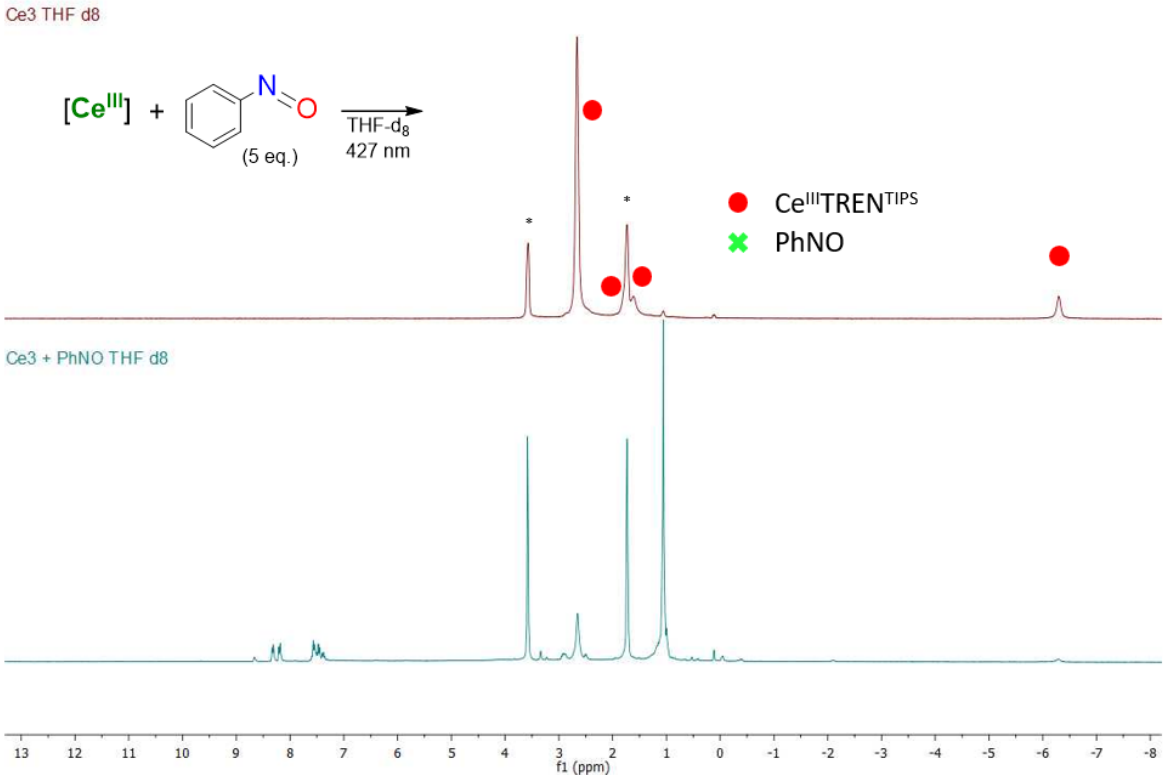

Figure S144. ^{1}H NMR spectrum of the *in-situ* reaction between **1** and 5 equivalents of PhNO. Solvent residual peaks are indicated with *

Institut Polytechnique de Paris
91120 Palaiseau, France

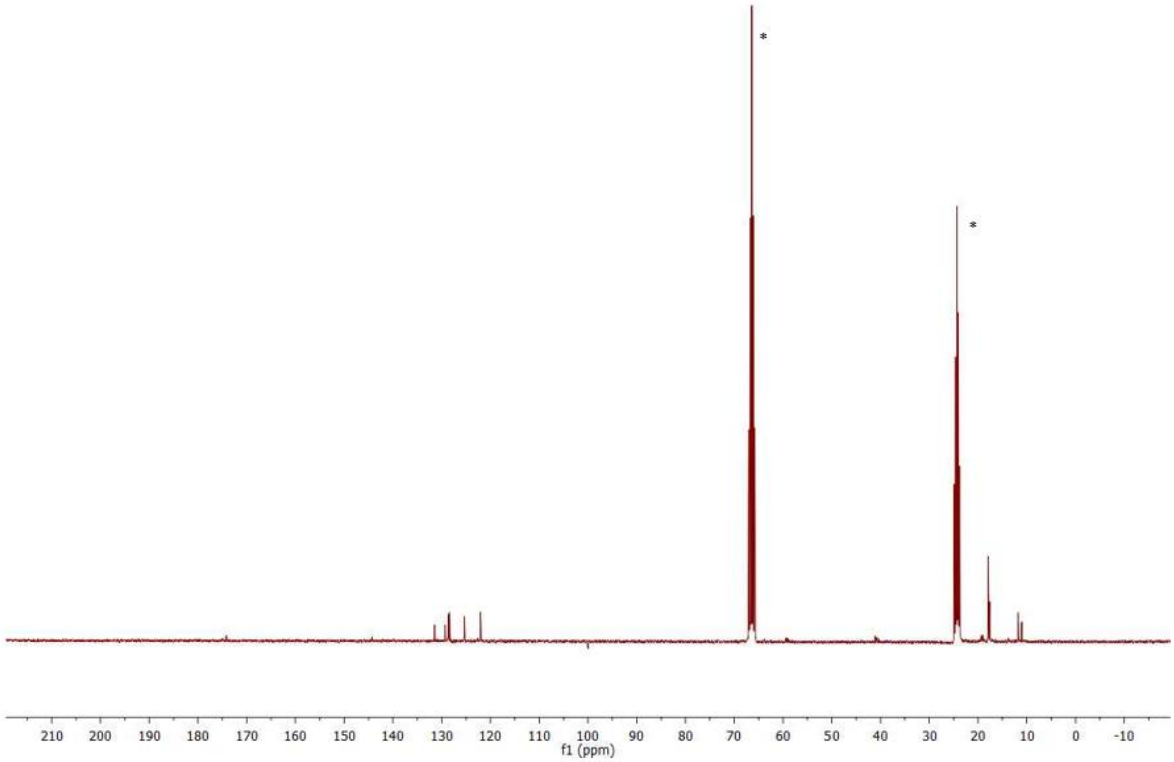

Figure S145. ^{13}C NMR spectrum of the *in-situ* reaction between **1** and 5 equivalents of PhNO. Solvent residual peaks are indicated with *

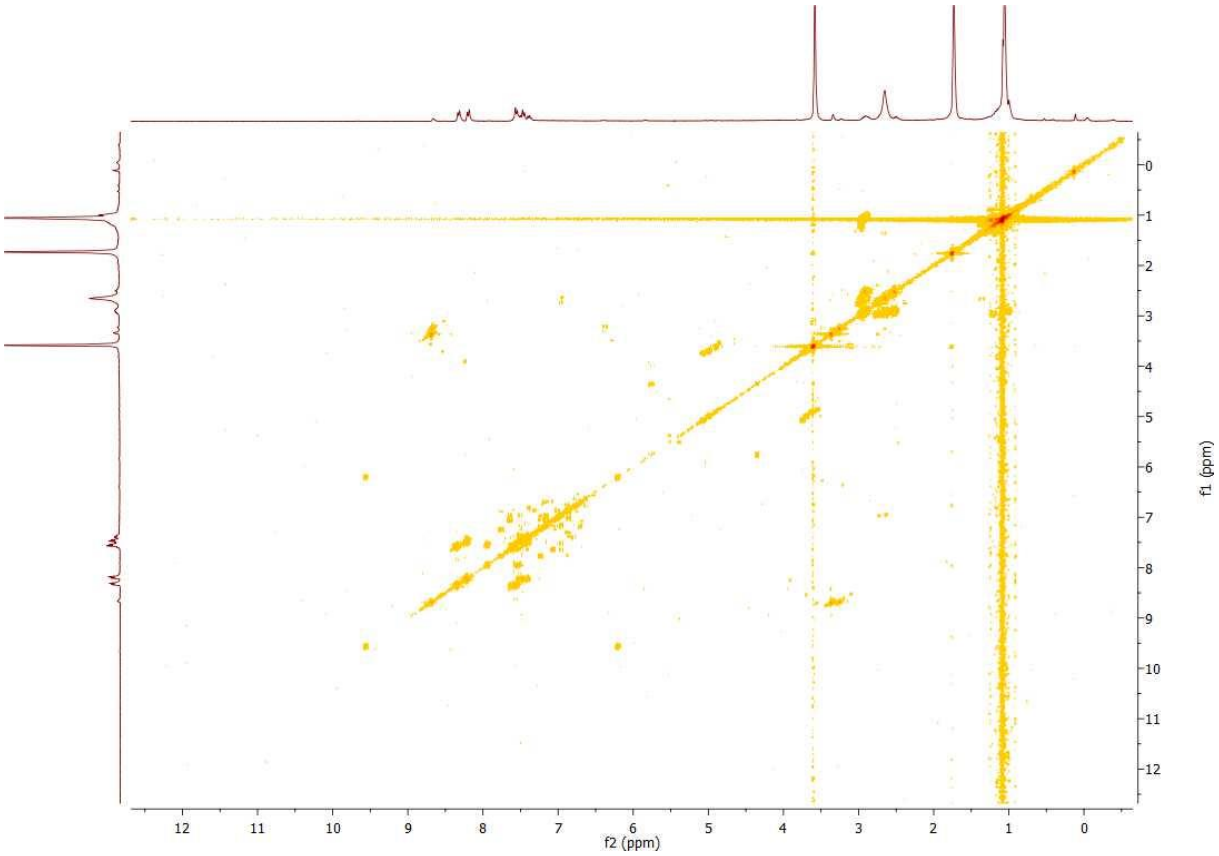

Figure S146. ^{1}H-^{1}H COSY spectrum of the *in-situ* reaction between **1** and 5 equivalents of PhNO

b) Reaction of 1 with nitroaryls

Institut Polytechnique de Paris
91120 Palaiseau, France

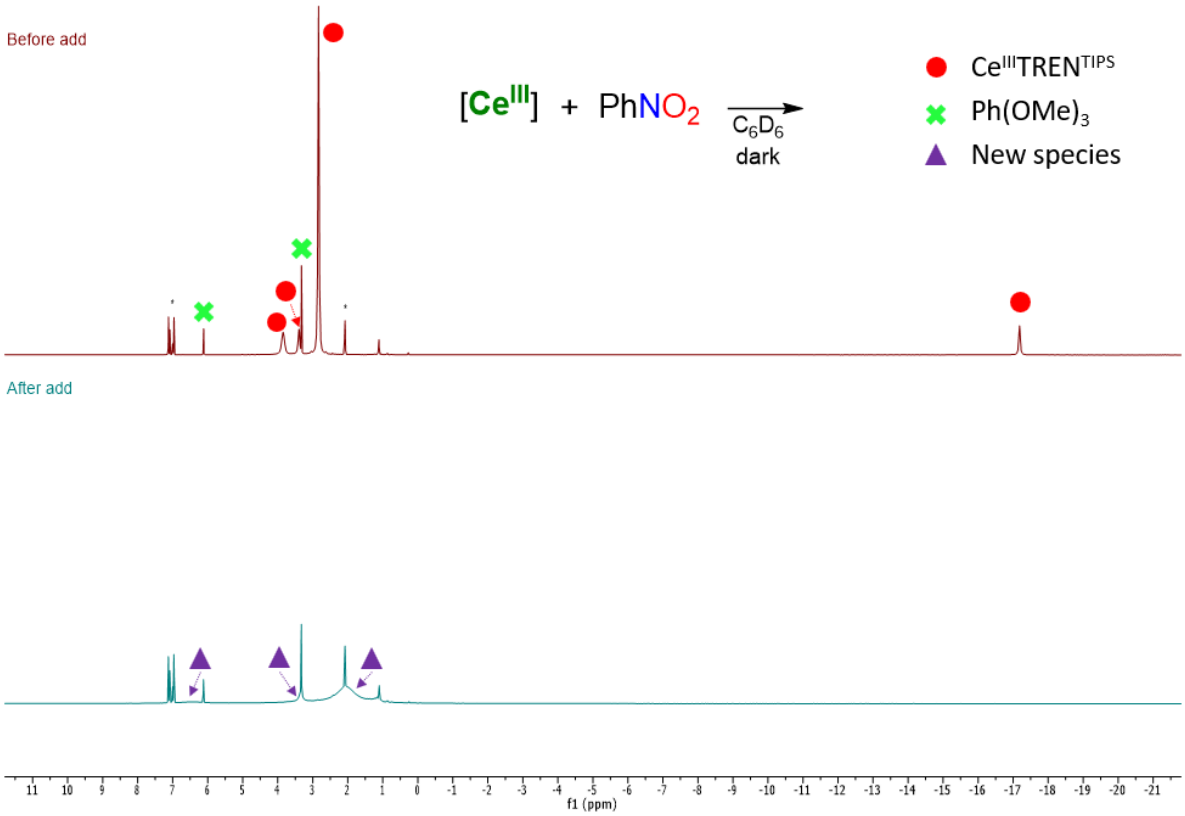

Figure S147. ^{1}H NMR spectrum of the reaction between **1** and $PhNO_2$ in toluene-d_8. Solvent residual peaks are indicated with *

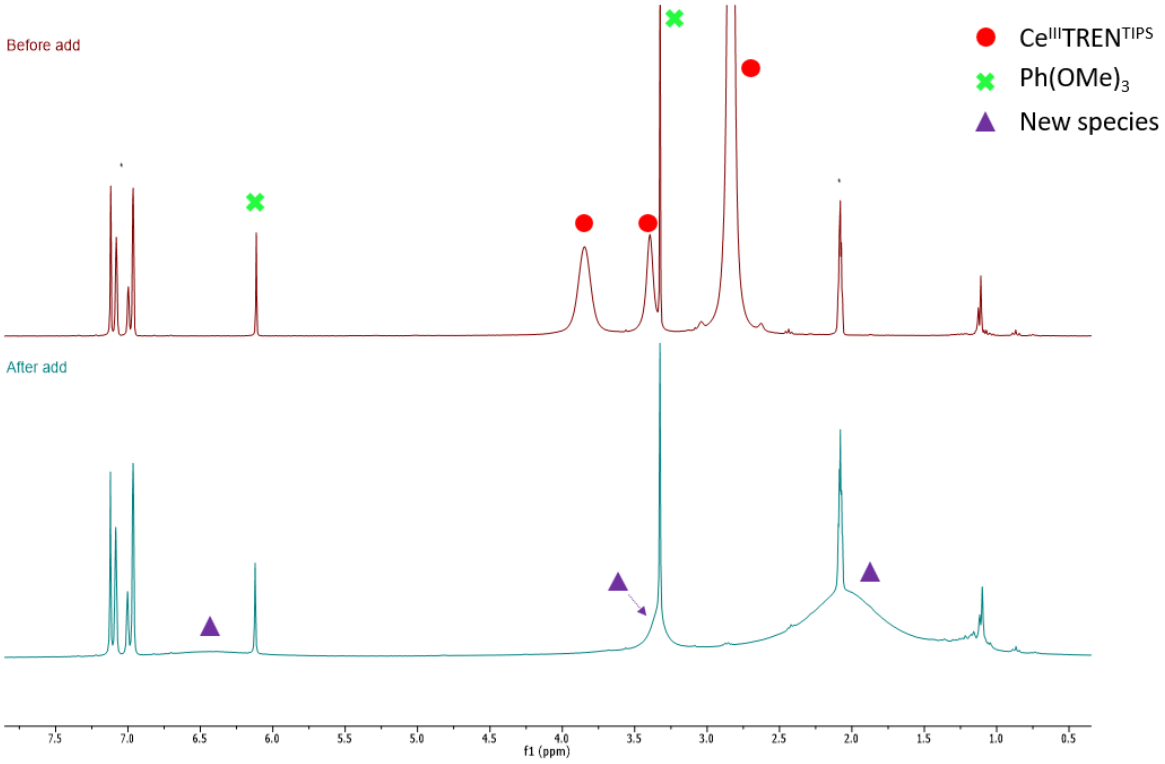

Figure S148. ^{1}H NMR spectrum of the reaction between **1** and $PhNO_2$ in toluene-d_8. Zoom between 0.5 and 7.5 ppm region. Solvent residual peaks are indicated with *

Institut Polytechnique de Paris
91120 Palaiseau, France

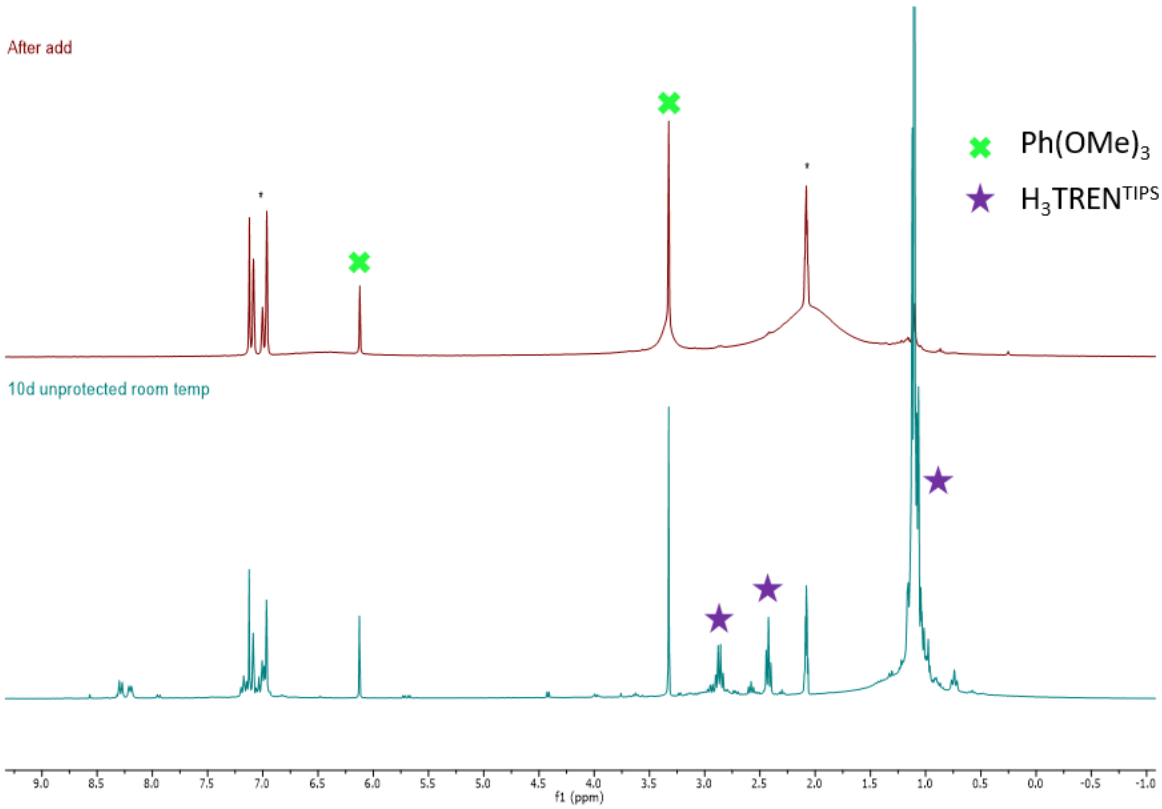

Figure S149. ^{1}H NMR spectrum of the reaction between **1** and $PhNO_2$ in toluene-d_8, left for 10 days at room temperature. Zoom between -1.0 and 9.5 ppm region. Solvent residual peaks are indicated with *

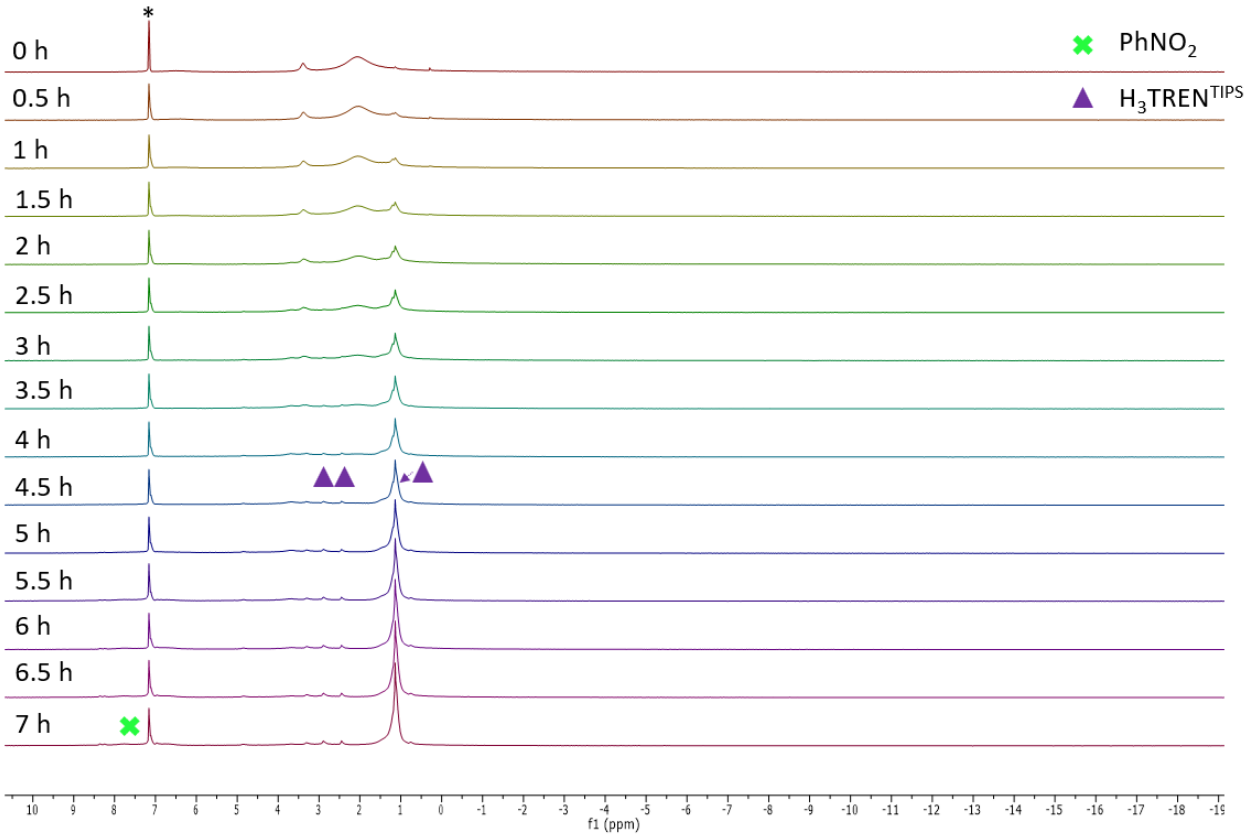

Figure S150. Degradation kinetics of the reaction between **1** and $PhNO_2$ in C_6D_6.Solvent residual signals is indicated with *

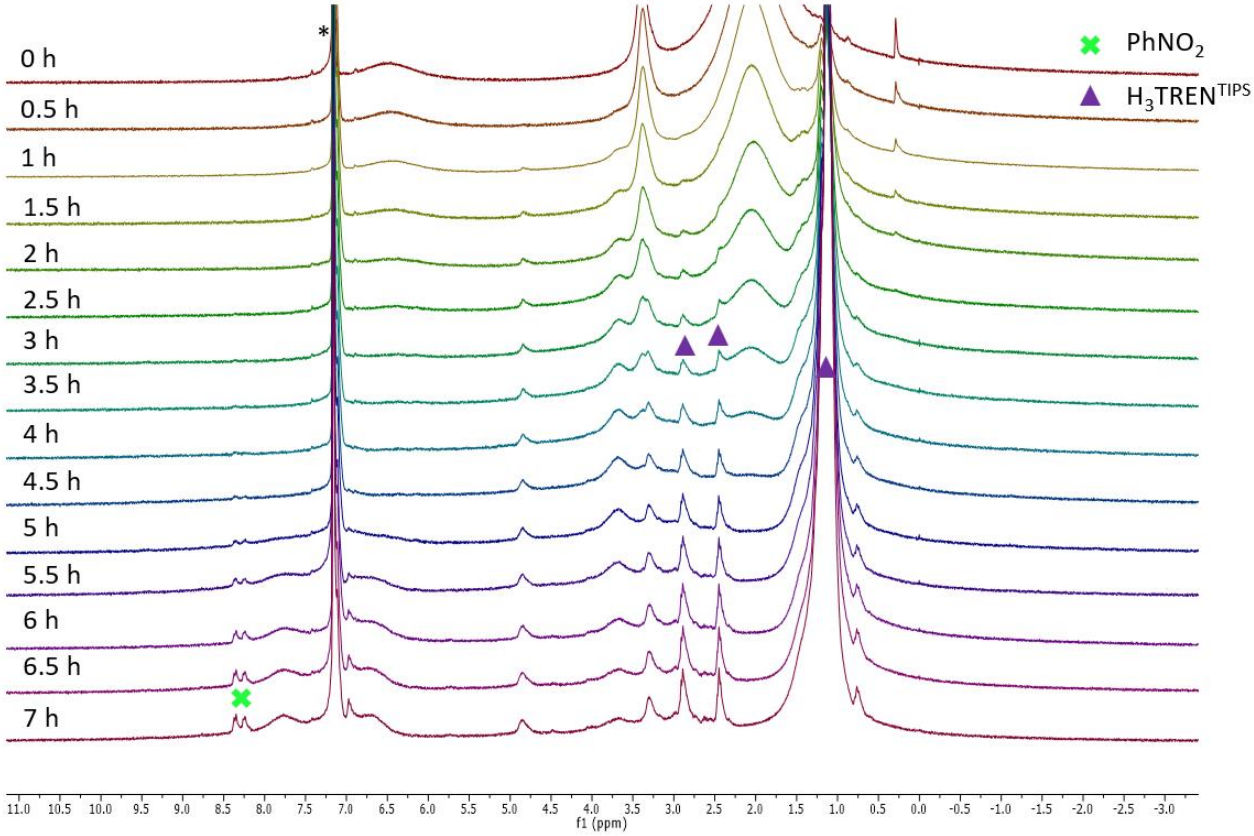

Figure S151. Degradation kinetics of the reaction between **1** and $PhNO_2$ in C_6D_6. Zoom on the region between -3 and 11 ppm. Solvent residual signal is indicated with *

Institut Polytechnique de Paris
91120 Palaiseau, France

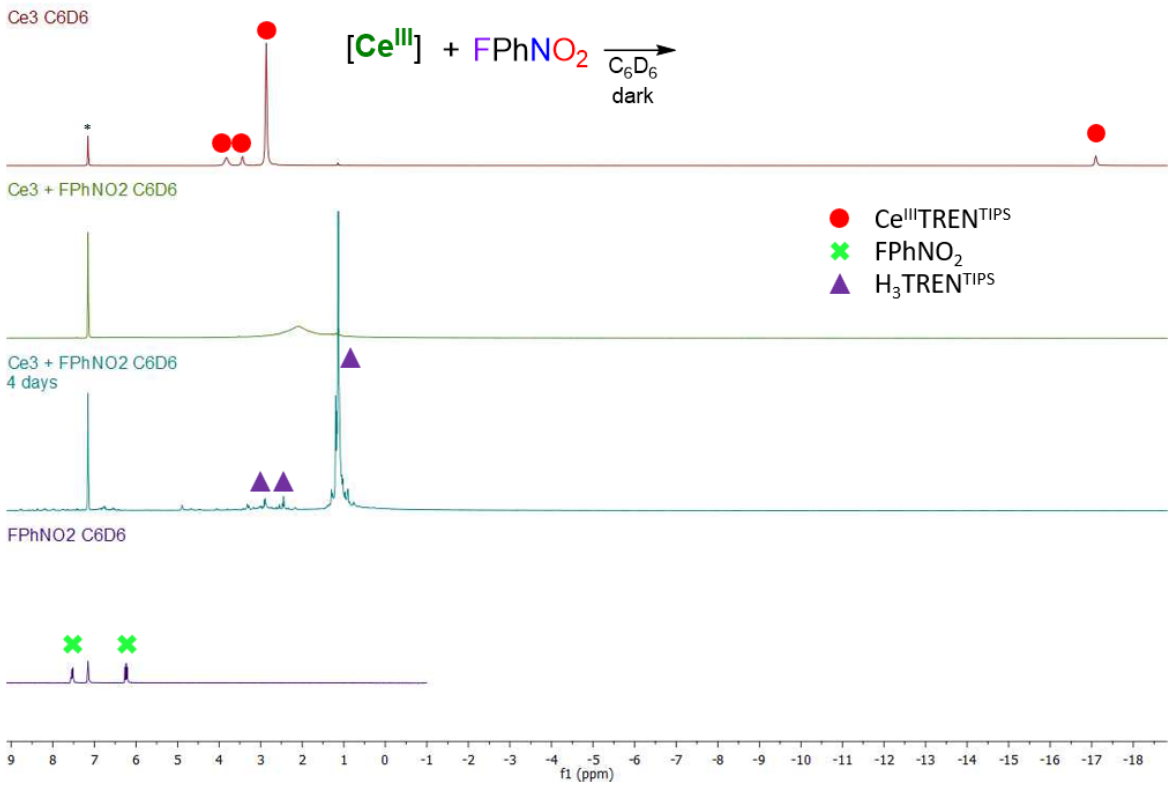

Figure S152. ^{1}H NMR spectrum of the reaction between **1** and $FPhNO_2$ in C_6D_6. Solvent residual peak is indicated with *

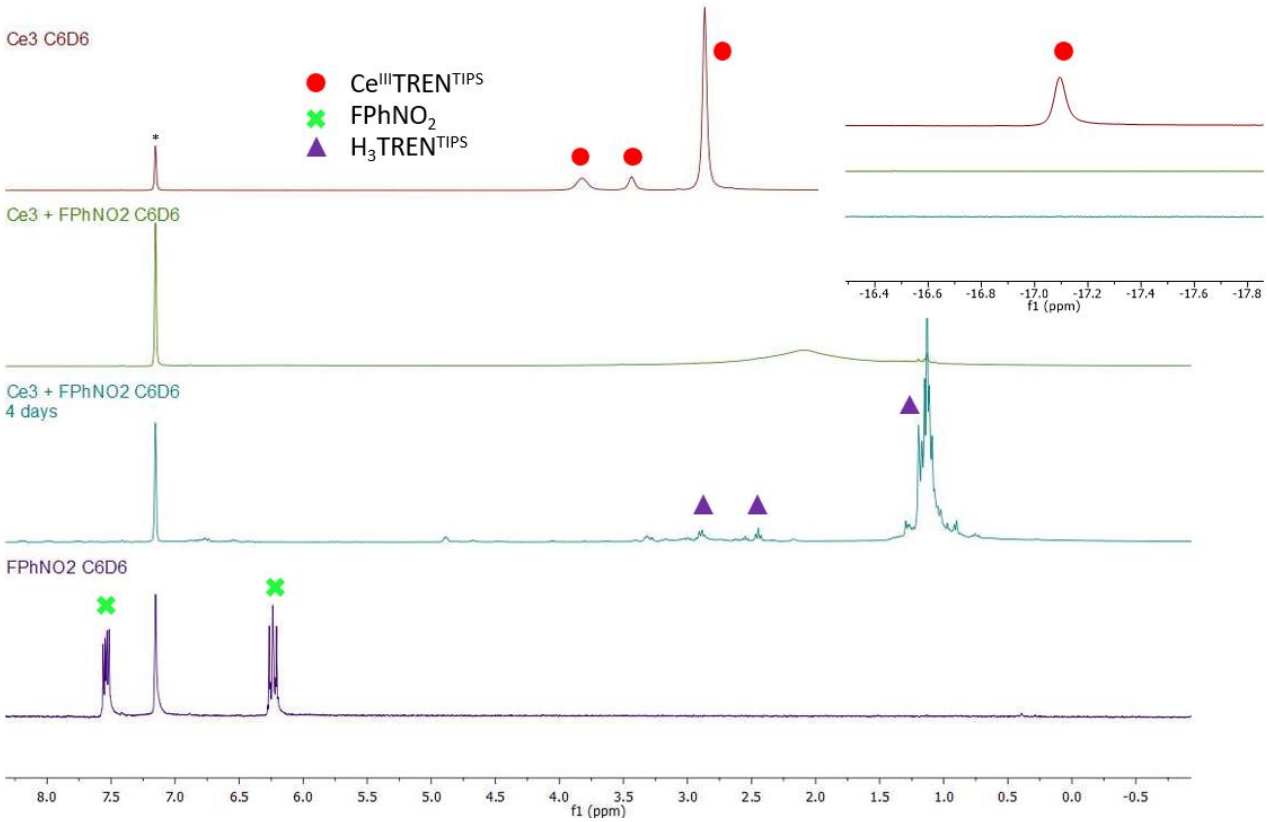

Figure S 153. ^{1}H NMR spectrum of the reaction between **1** and $FPhNO_2$ in C_6D_6. Zoom between -1.0 and 8.5 ppm region. Solvent residual peak is indicated with *

Institut Polytechnique de Paris
91120 Palaiseau, France

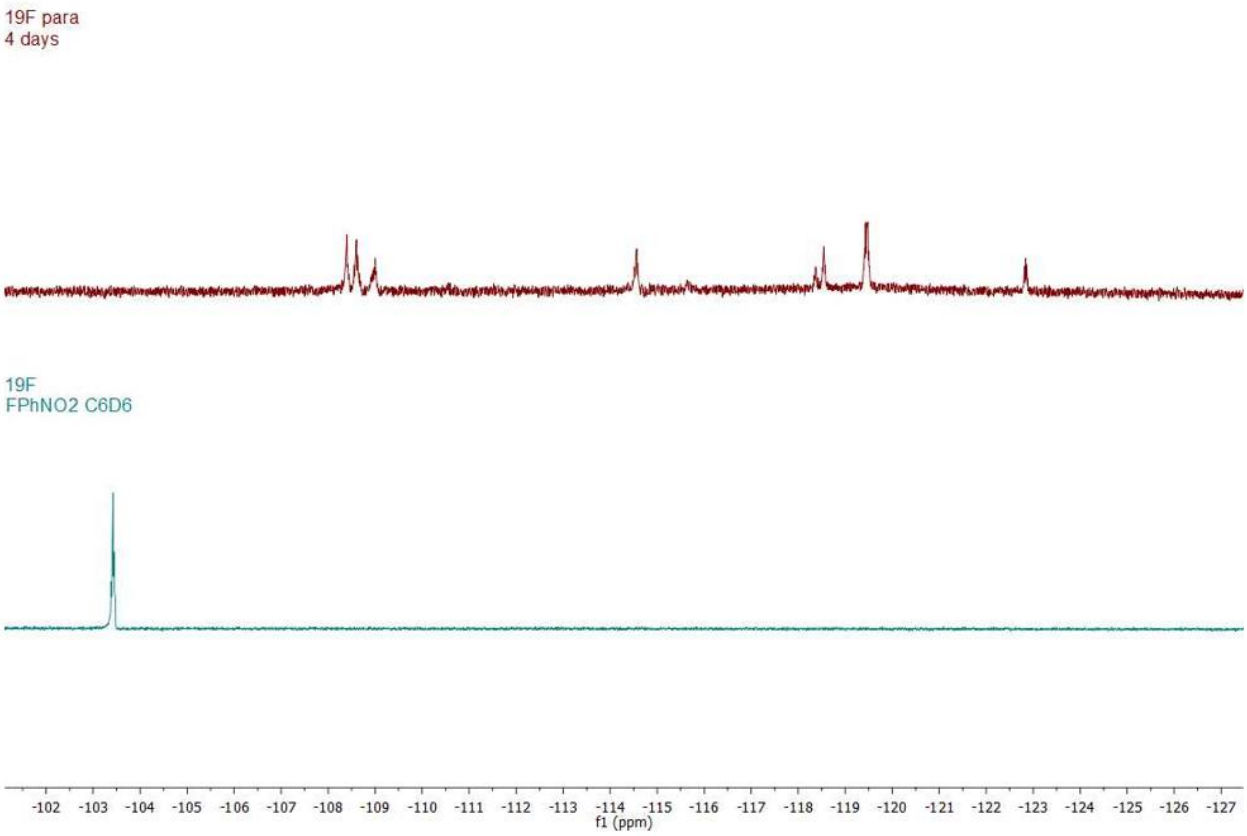

Figure S154. ^{19}F NMR spectrum of the reaction between **1** and $FPhNO_2$ in C_6D_6

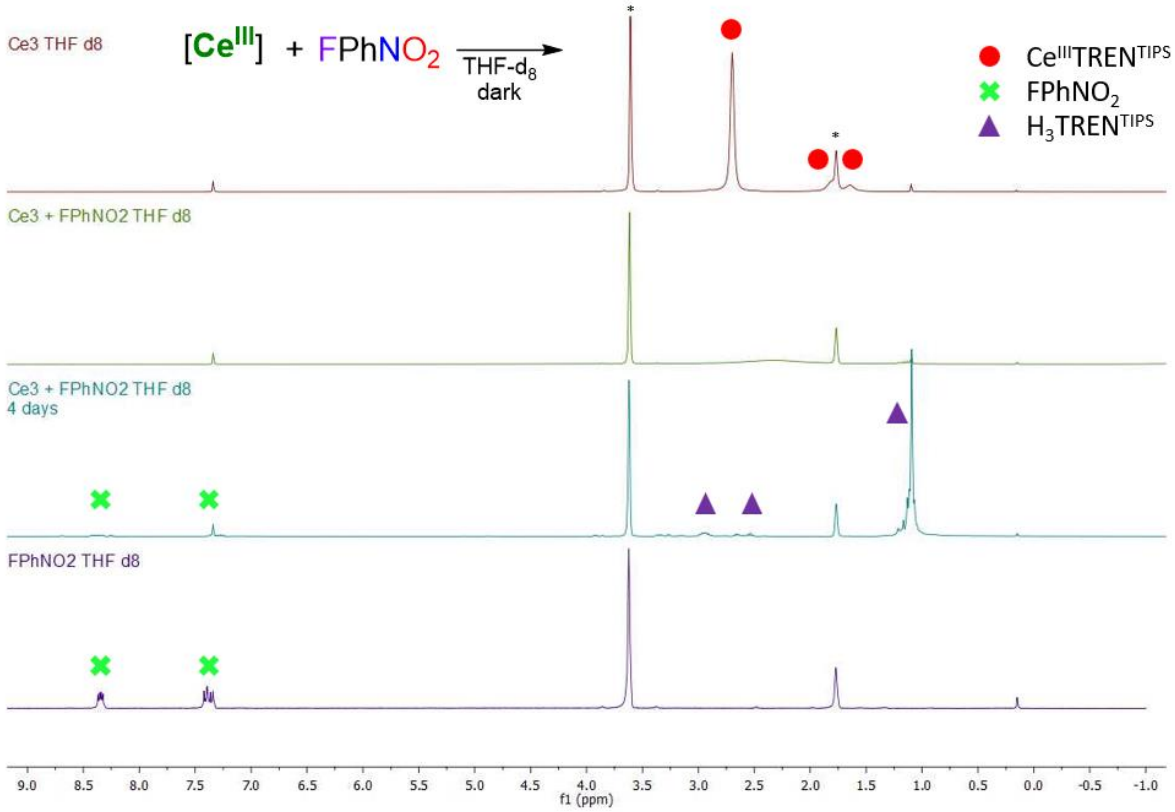

Figure S155. ^{1}H NMR spectrum of the reaction between **1** and $FPhNO_2$ in THF-d_8. Zoom between -1.0 and 9.0 ppm region. Solvent residual peaks are indicated with *

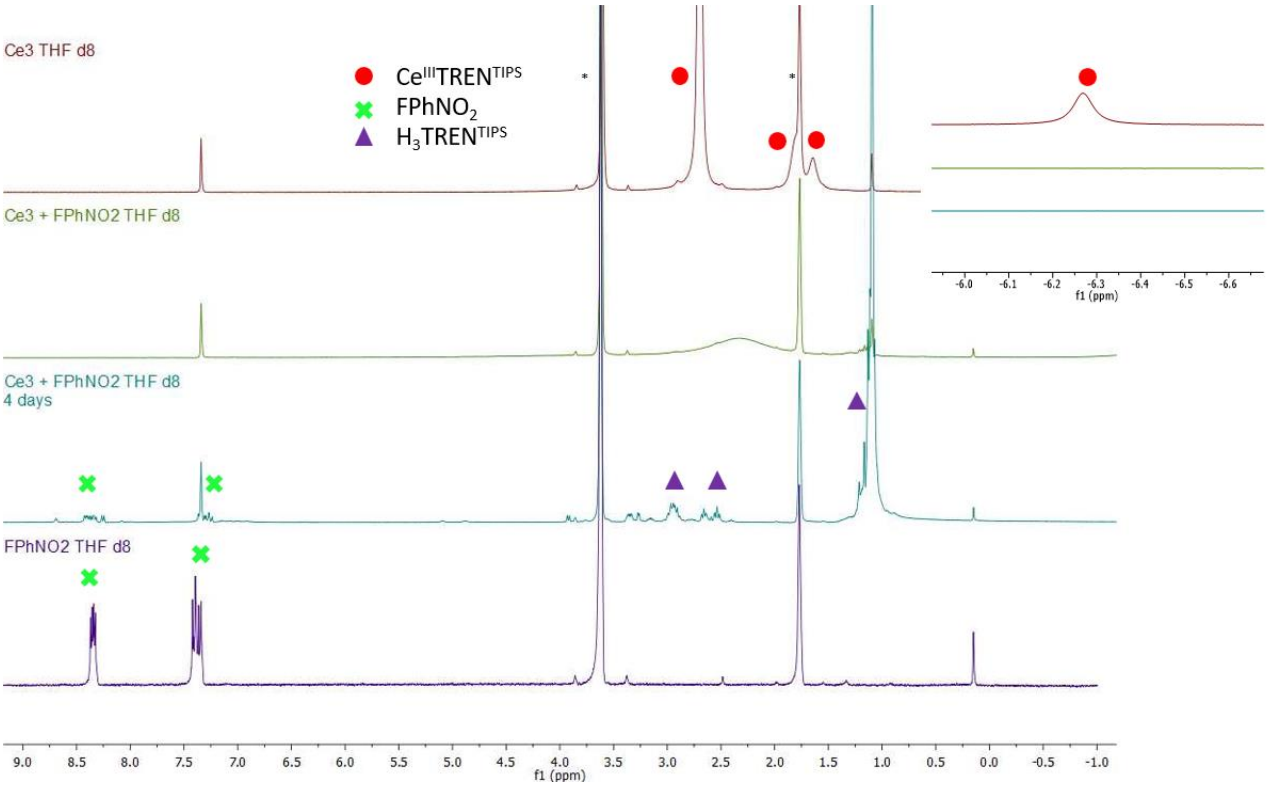

Figure S156. ^{1}H NMR spectrum of the reaction between **1** and $FPhNO_2$ in THF-d_8. Zoom between -1.0 and 9.0 ppm region. Solvent residual peaks are indicated with *

Institut Polytechnique de Paris
91120 Palaiseau, France

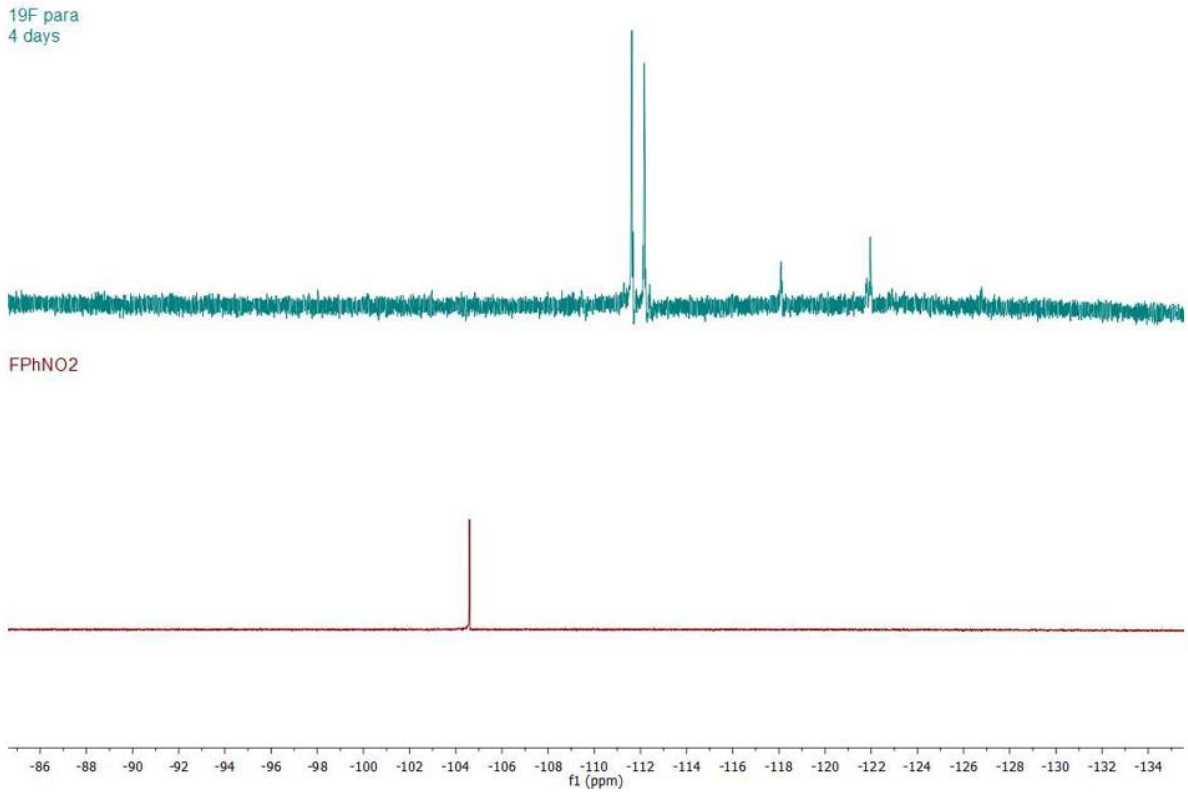

Figure S157. ^{19}F NMR spectrum of the reaction between **1** and $FPhNO_2$ in THF-d_8

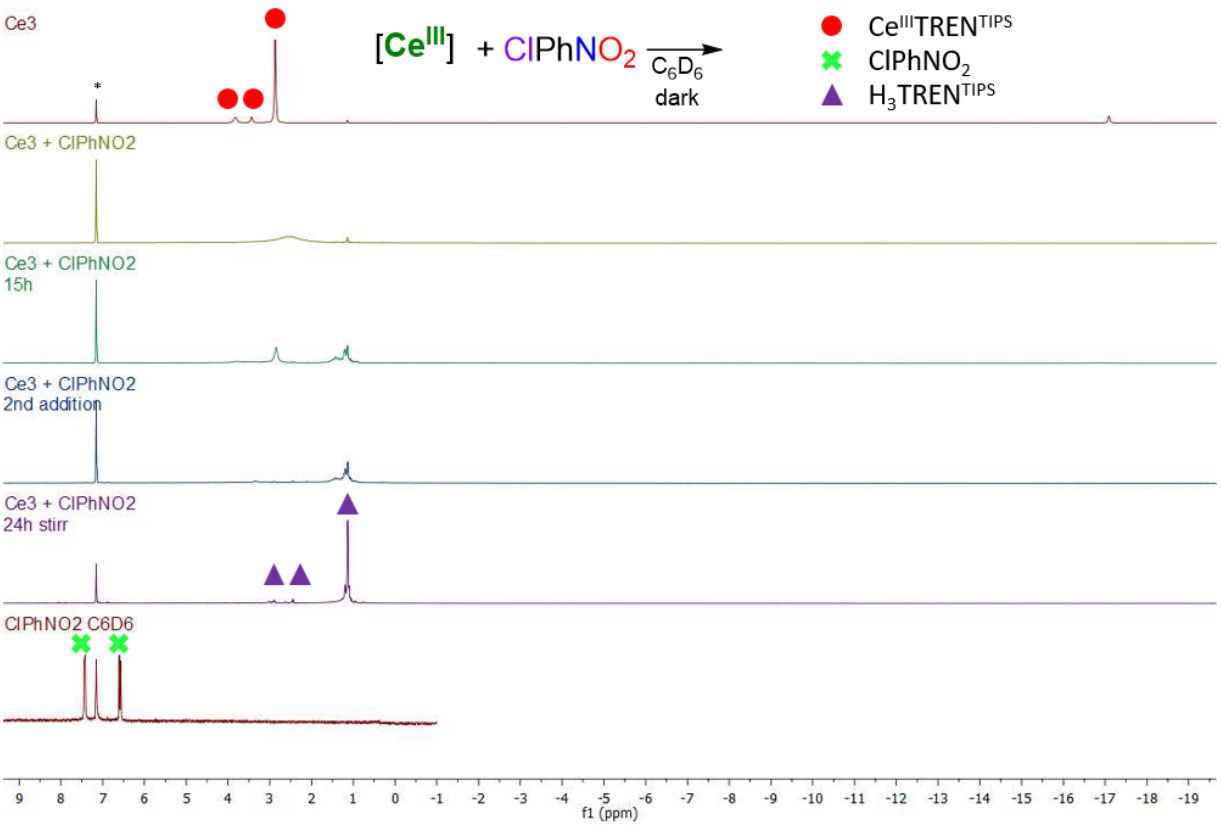

Figure S158. ^{1}H NMR spectrum of the reaction between **1** and ClPhNO$_2$ in C$_6$D$_6$. Solvent residual peak is indicated with *

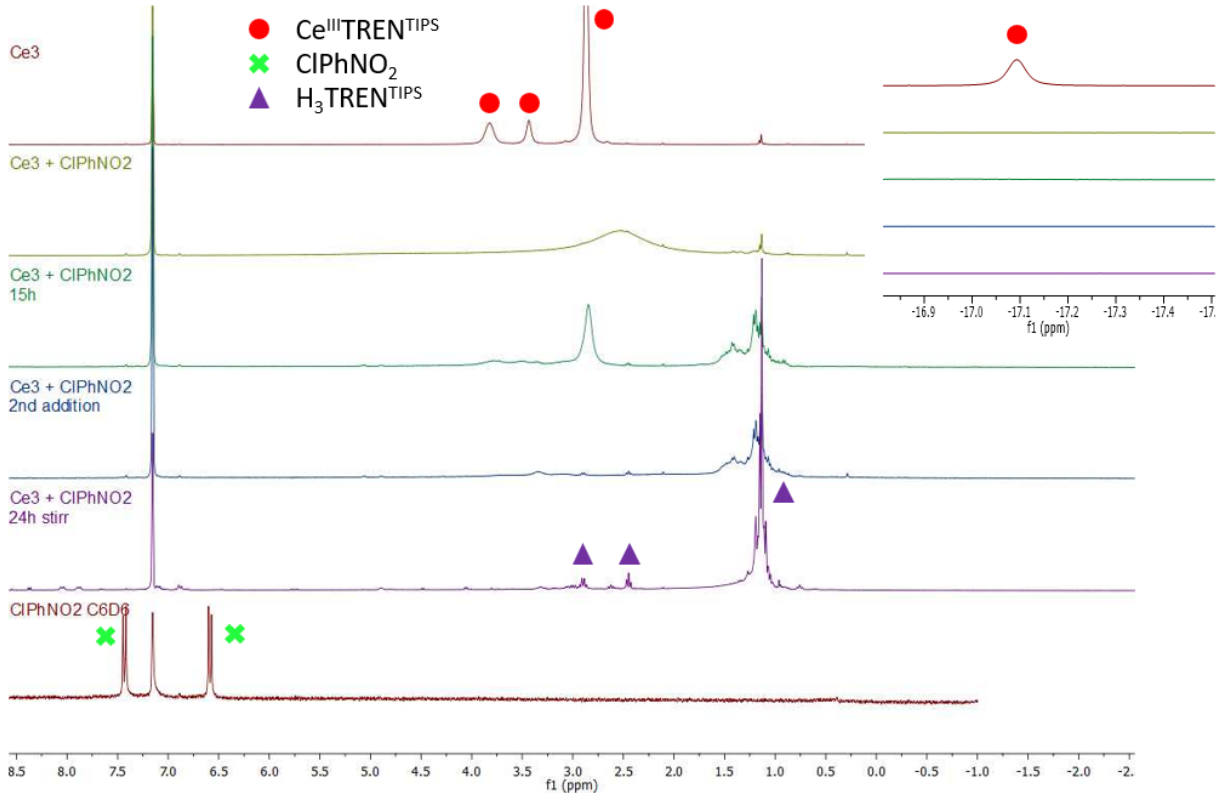

Figure S159. ^{1}H NMR spectrum of the reaction between **1** and ClPhNO$_2$ in C$_6$D$_6$. Solvent residual peak is indicated with *

Institut Polytechnique de Paris
91120 Palaiseau, France

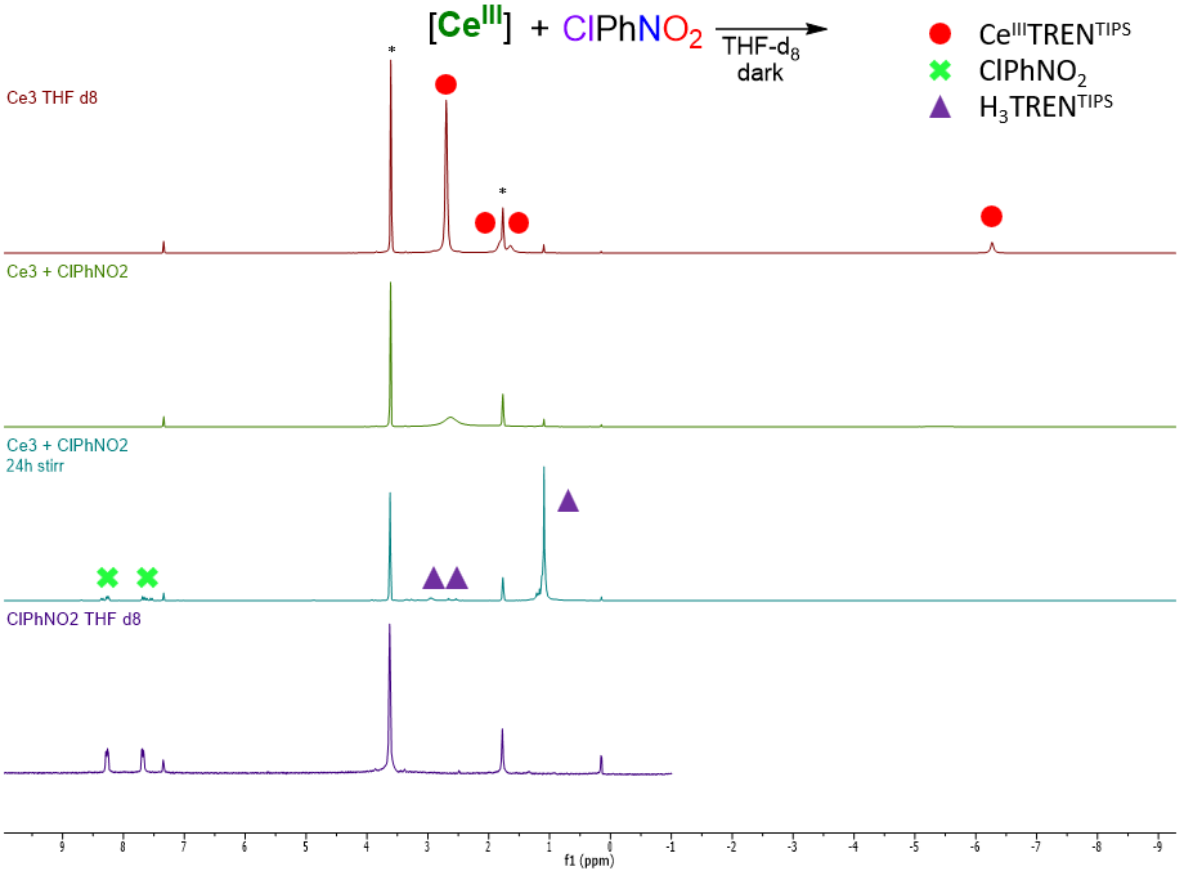

Figure S160. ^{1}H NMR spectrum of the reaction between **1** and $ClPhNO_2$ in THF-d_8. Solvent residual peaks are indicated with *

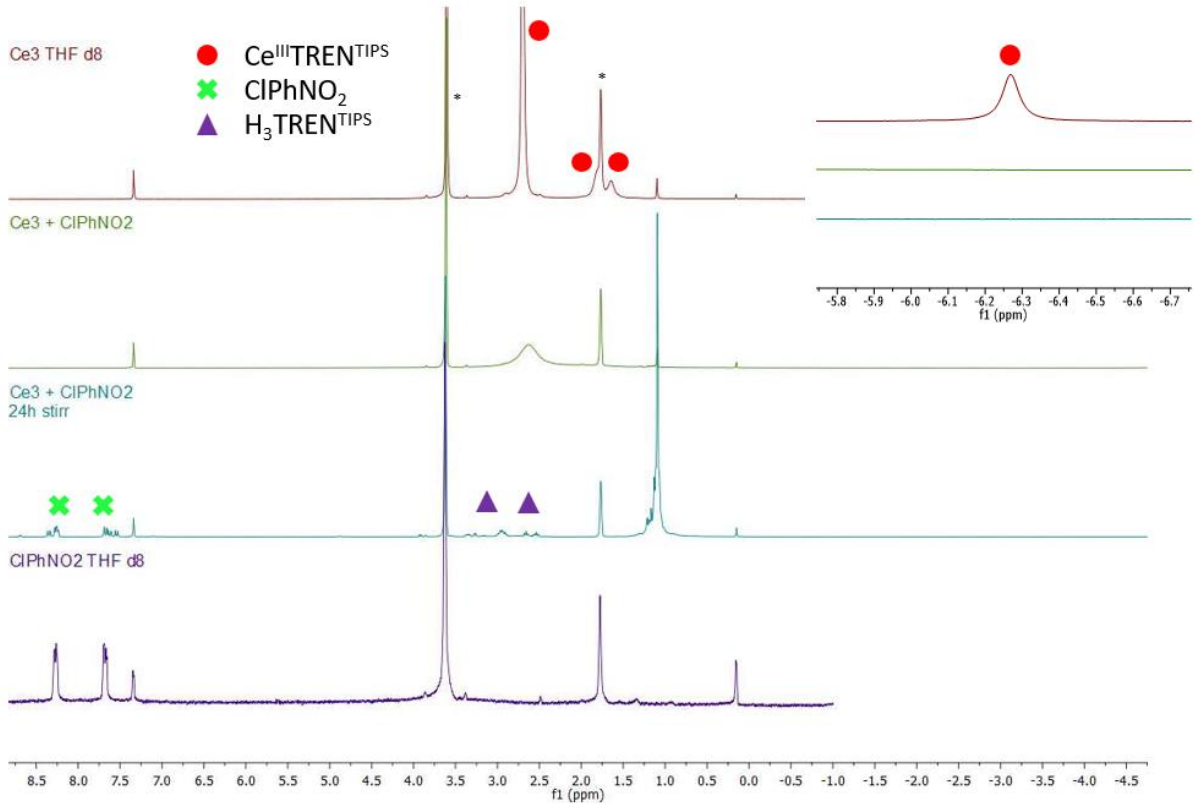

Figure S161. ^{1}H NMR spectrum of the reaction between **1** and $ClPhNO_2$ in THF-d_8. Solvent residual peaks are indicated with *

Institut Polytechnique de Paris
91120 Palaiseau, France

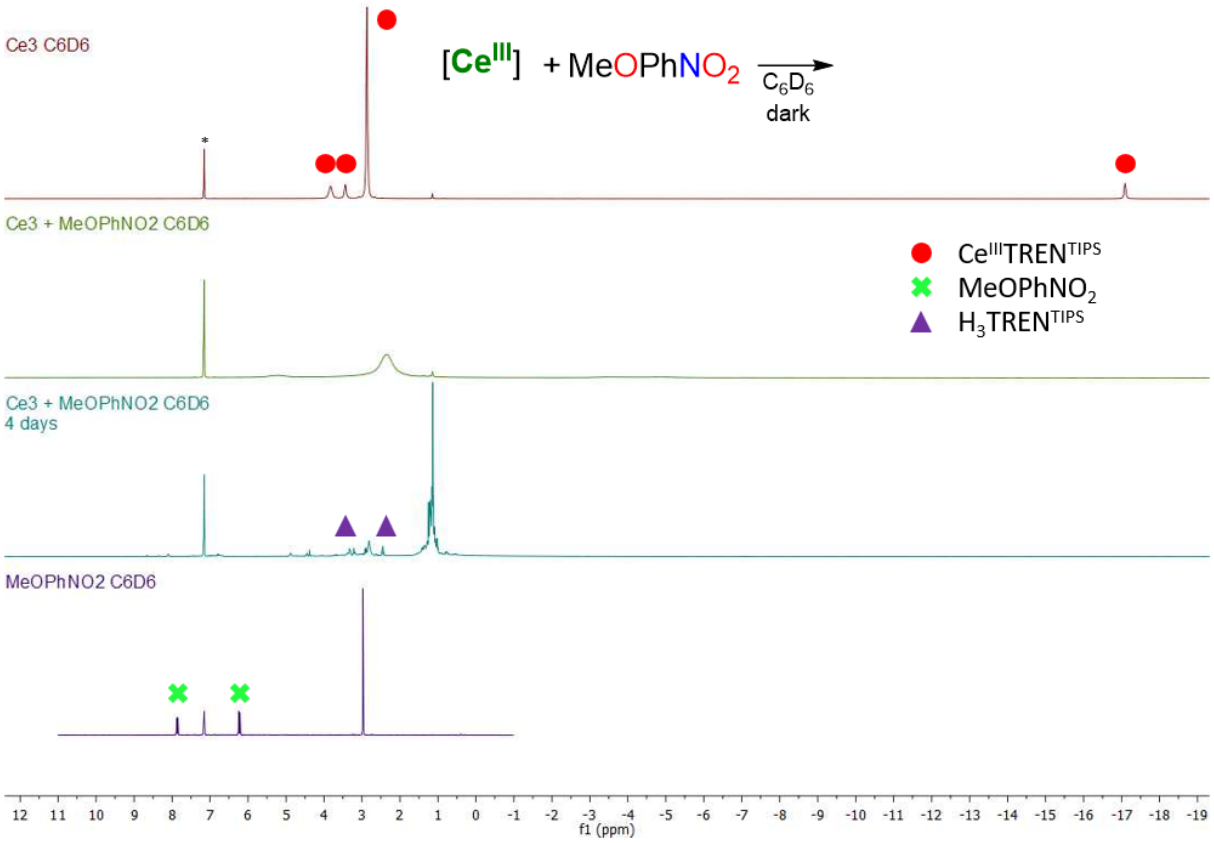

Figure S162. ^{1}H NMR spectrum of the reaction between **1** and $MeOPhNO_2$ in C_6D_6. Solvent residual peak is indicated with *

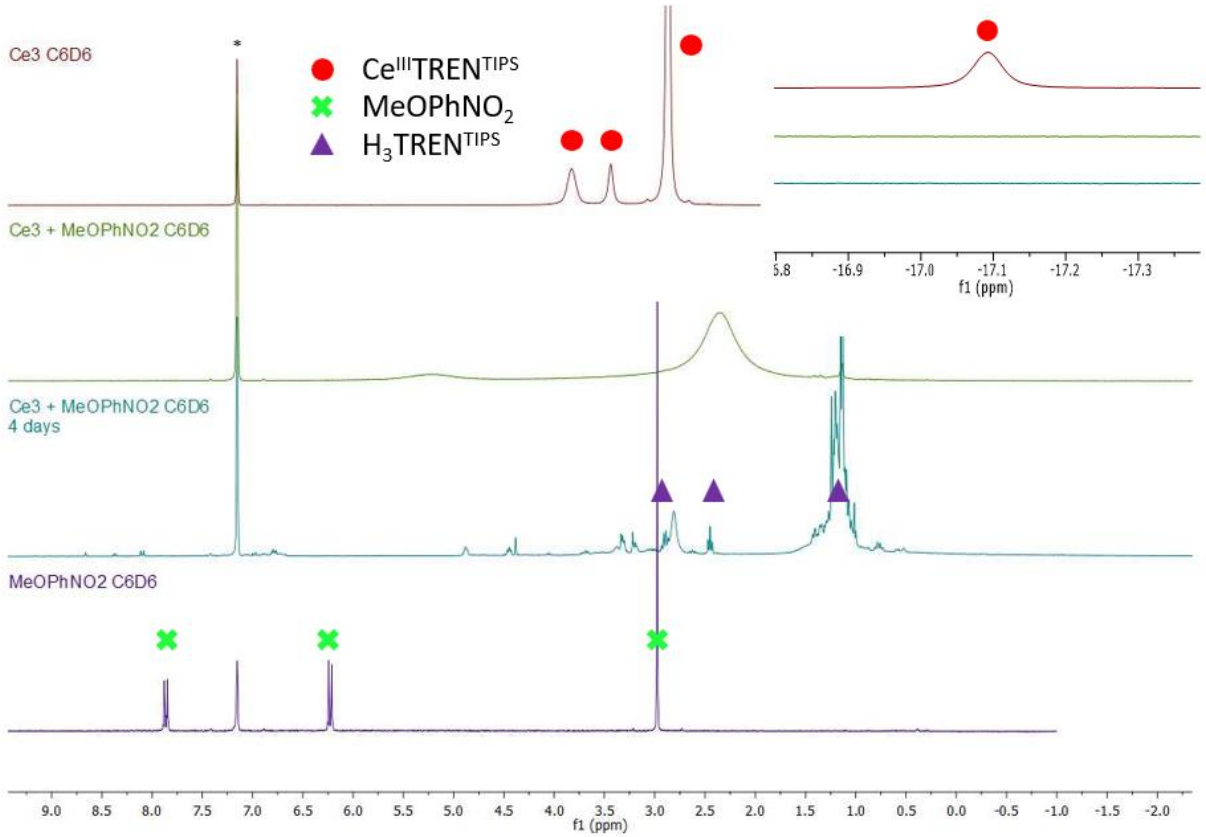

Figure S163. ^{1}H NMR spectrum of the reaction between **1** and $MeOPhNO_2$ in C_6D_6. Zoom between -1.0 and 9.5 ppm region. Solvent residual peak is indicated with *

Institut Polytechnique de Paris
91120 Palaiseau, France

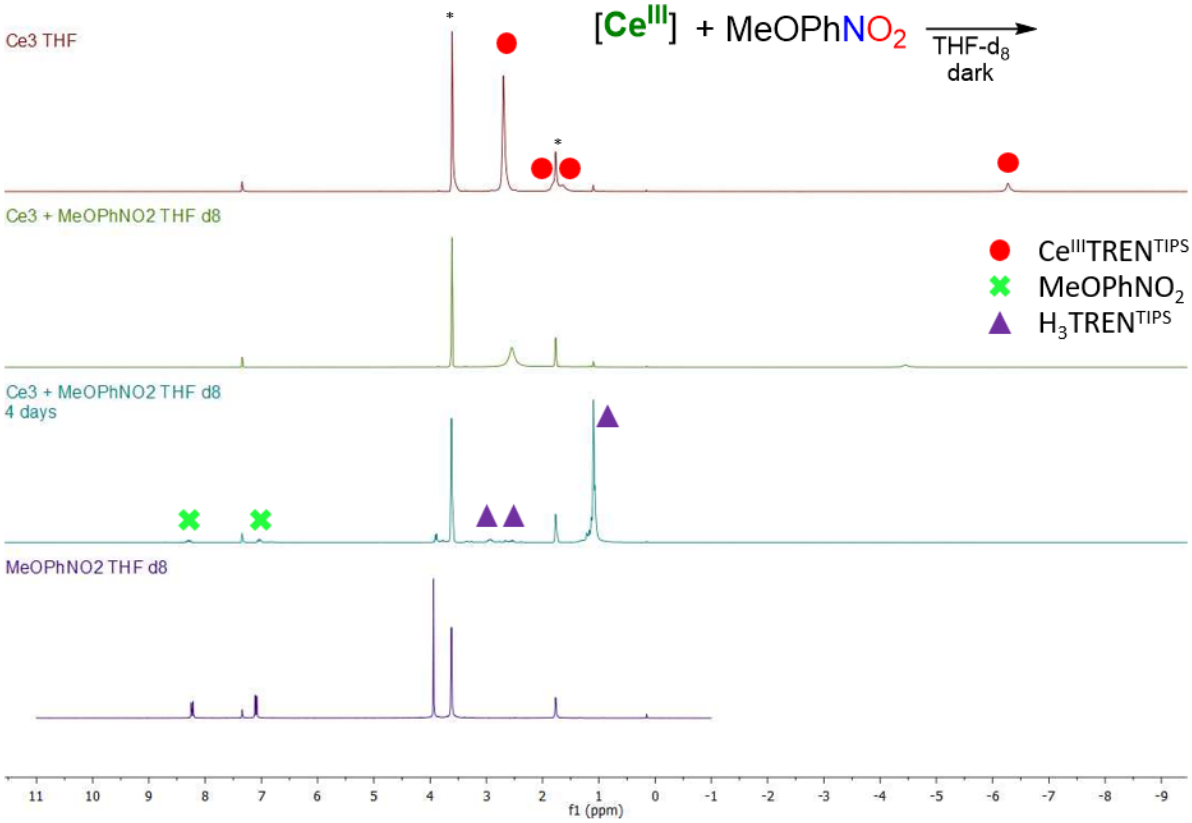

Figure S164. ^{1}H NMR spectrum of the reaction between **1** and $MeOPhNO_2$ in THF-d_8. Solvent residual peaks are indicated with *

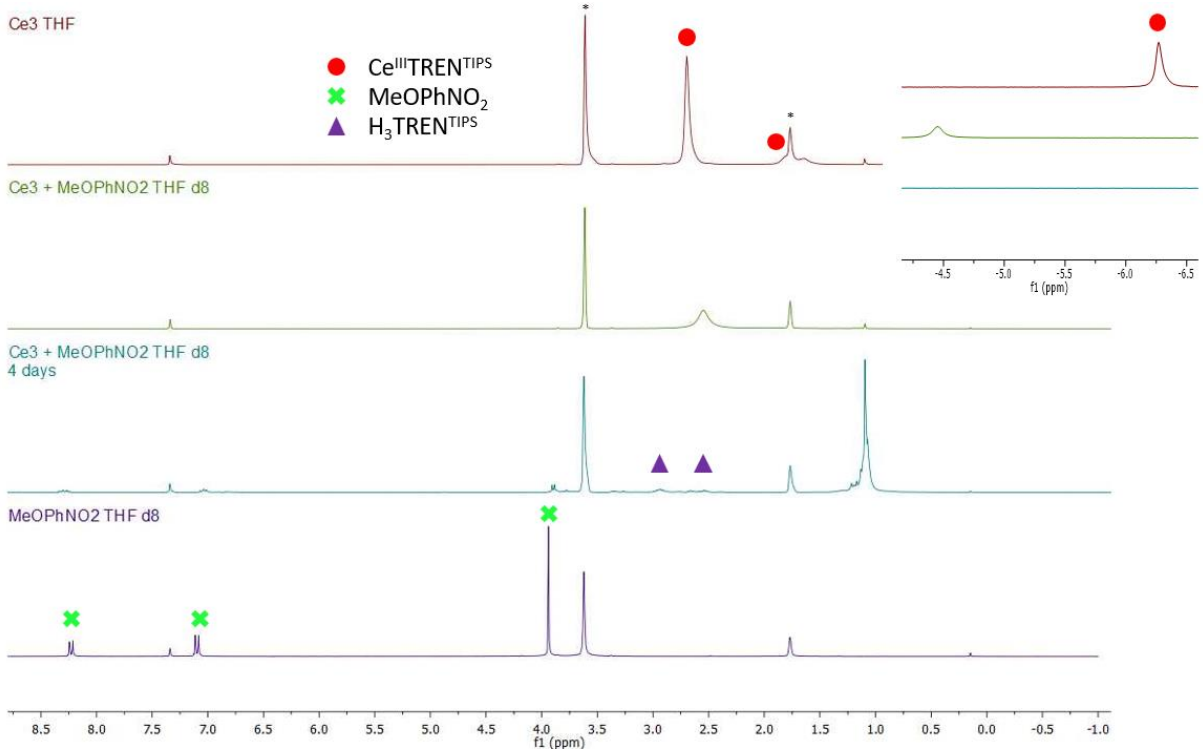

Figure S165. ^{1}H NMR spectrum of the reaction between **1** and $MeOPhNO_2$ in THF-d_8. Solvent residual peaks are indicated with *Zoom between -1.0 and 9.0 ppm region

c) Reaction of 1 with nitroalkanes

Institut Polytechnique de Paris
91120 Palaiseau, France

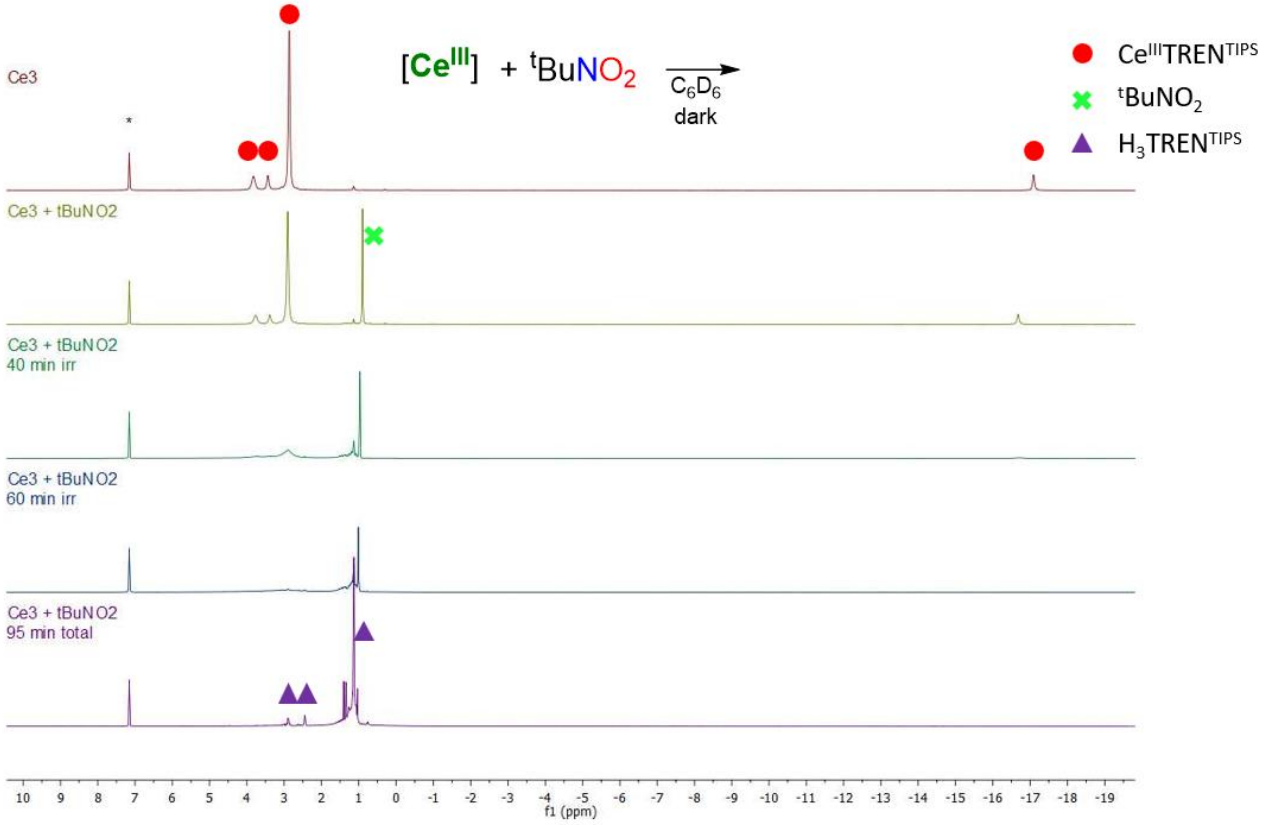

Figure S166. Reaction between **1** and $^{t}BuNO_2$ in C_6D_6. Solvent residual signal is indicated with *

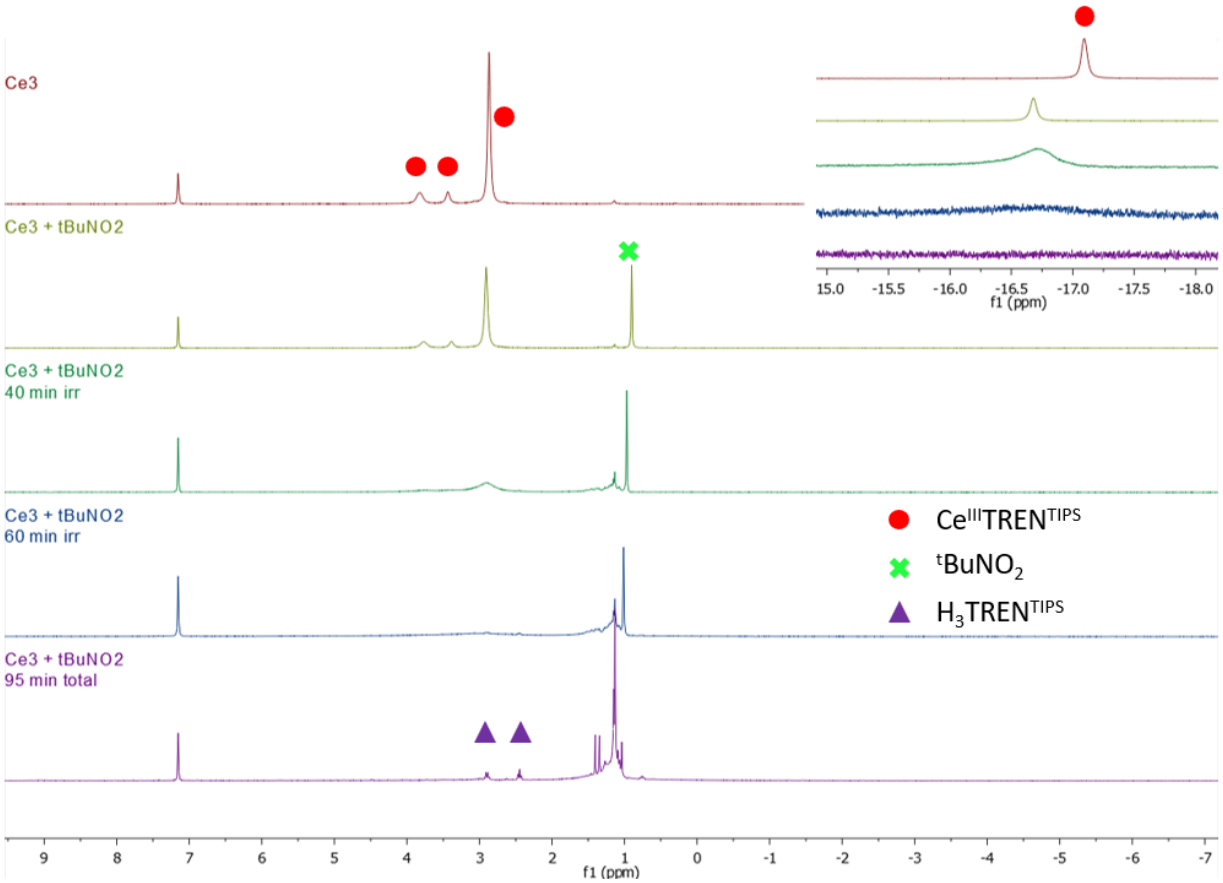

Figure S167. Reaction between **1** and $^{t}BuNO_2$ in C_6D_6. Solvent residual signal is indicated with *

Institut Polytechnique de Paris
91120 Palaiseau, France

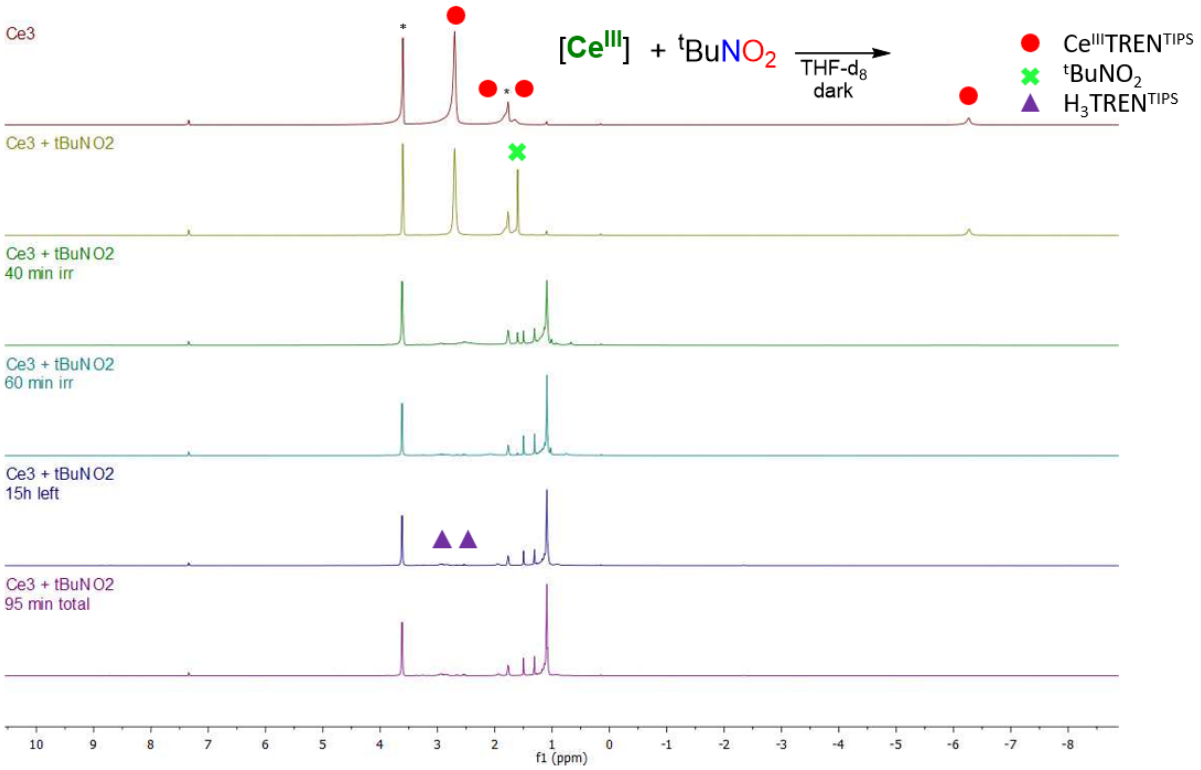

Figure S168. Reaction between **1** and $^{t}BuNO_2$ in THF-d_8. Solvent residual signals are indicated with *

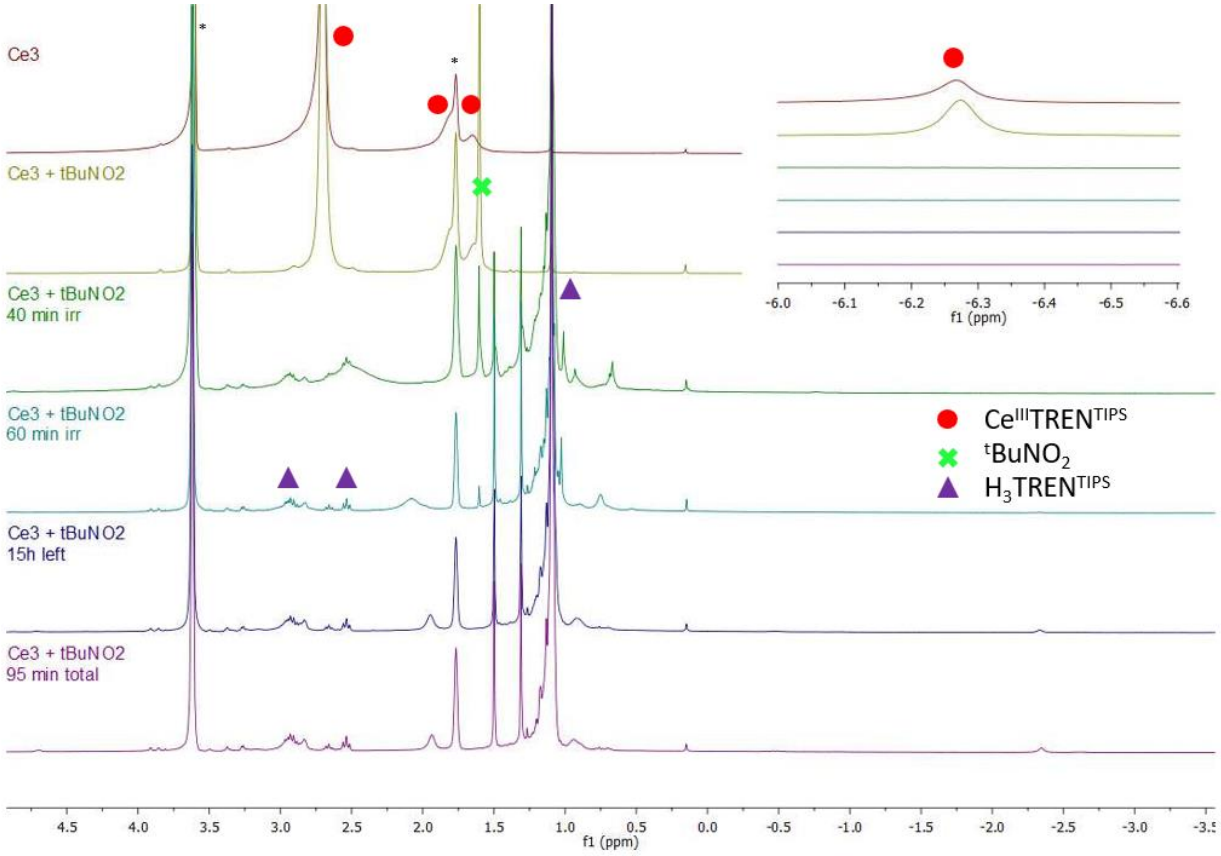

Figure S169. Reaction between **1** and $^{t}BuNO_2$ in THF-d_8. Zoom between -3.5 and 4.8 ppm. Solvent residual signals are indicated with *

Institut Polytechnique de Paris
91120 Palaiseau, France

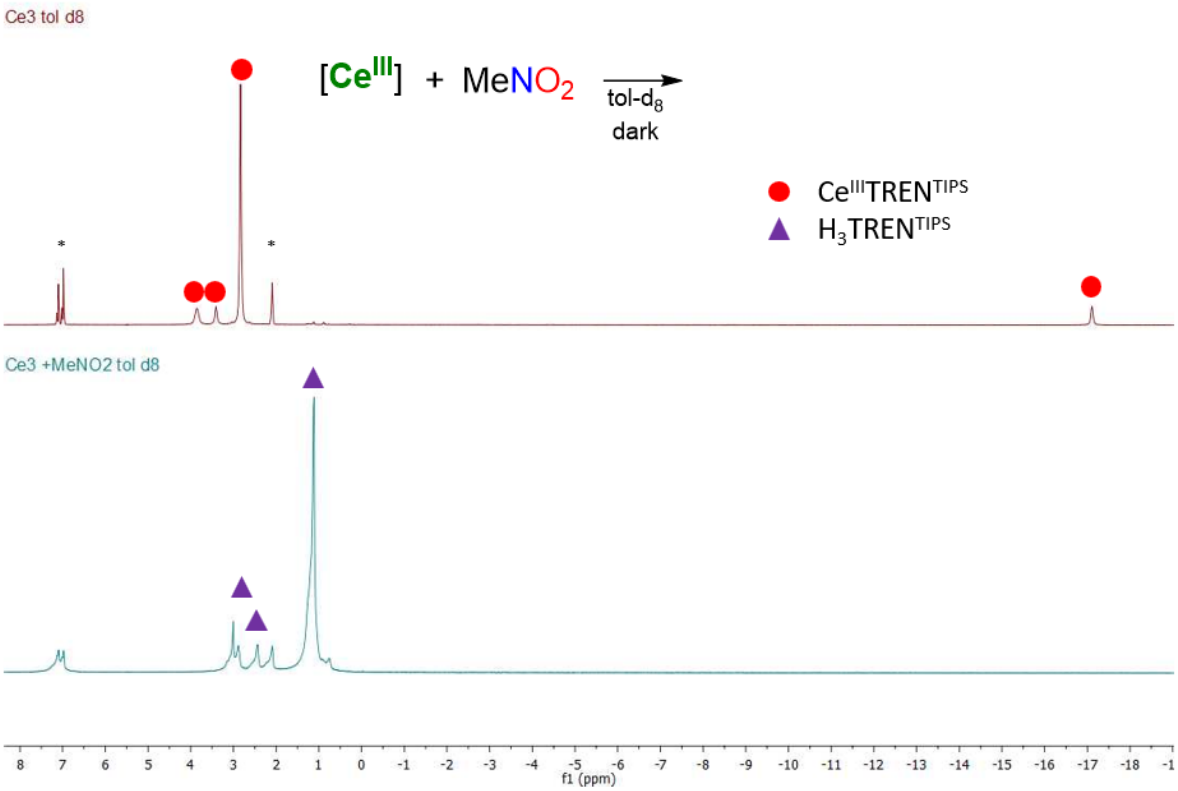

Figure S170. Reaction between **1** and $MeNO_2$ in toluene-d_8. Solvent residual signals are indicated with *

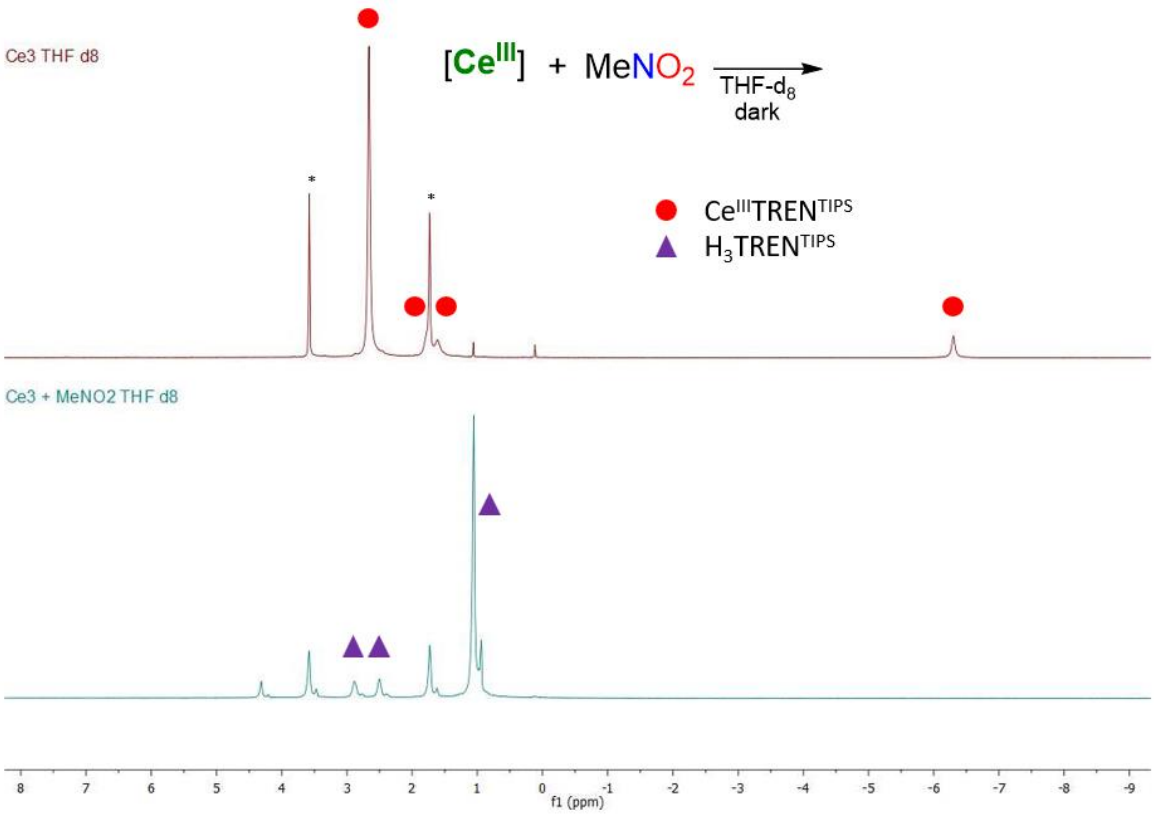

Figure S171. Reaction between **1** and $MeNO_2$ in THF-d_8. Solvent residual signals are indicated with *

Institut Polytechnique de Paris
91120 Palaiseau, France

d) Attempts of radical trapping experiments

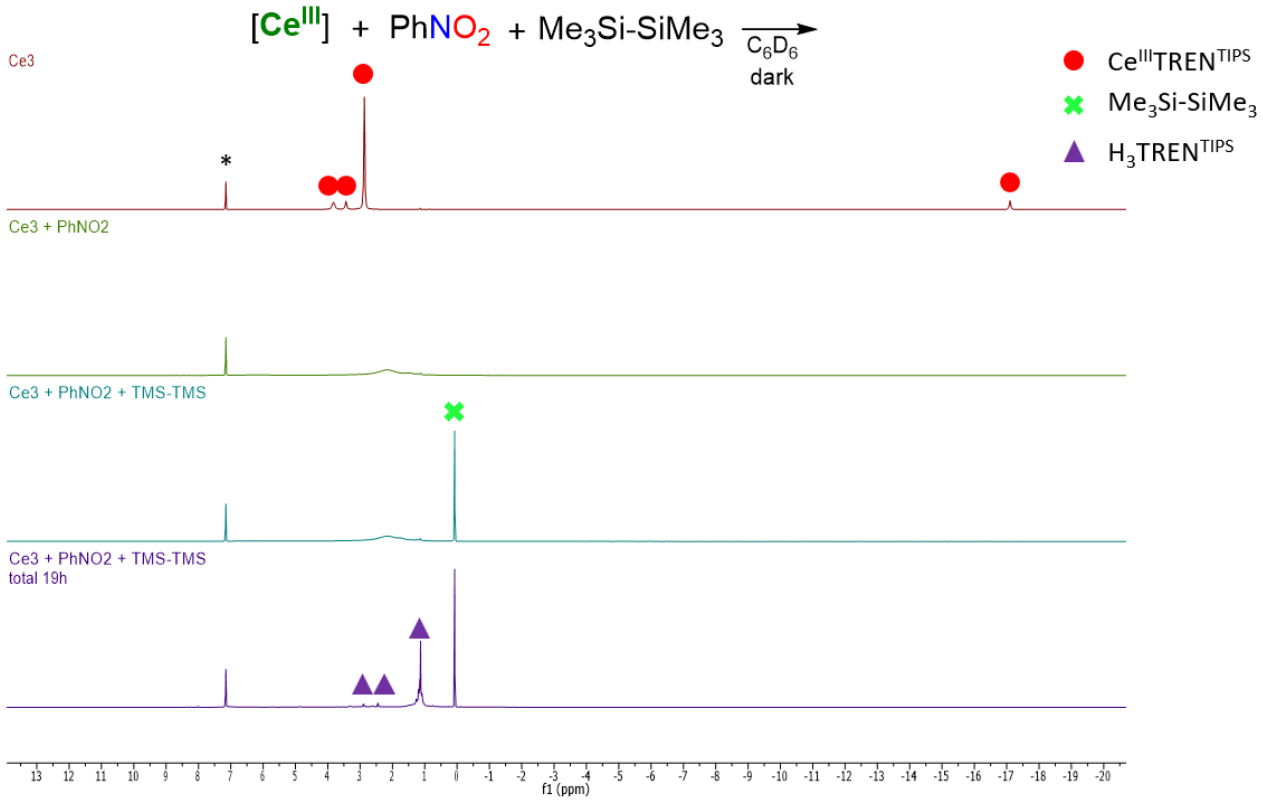

Figure S172. ^{1}H NMR spectrum of the reaction between **1** and $PhNO_2$ with TMS-TMS in C_6D_6. Solvent residual peak is indicated with *

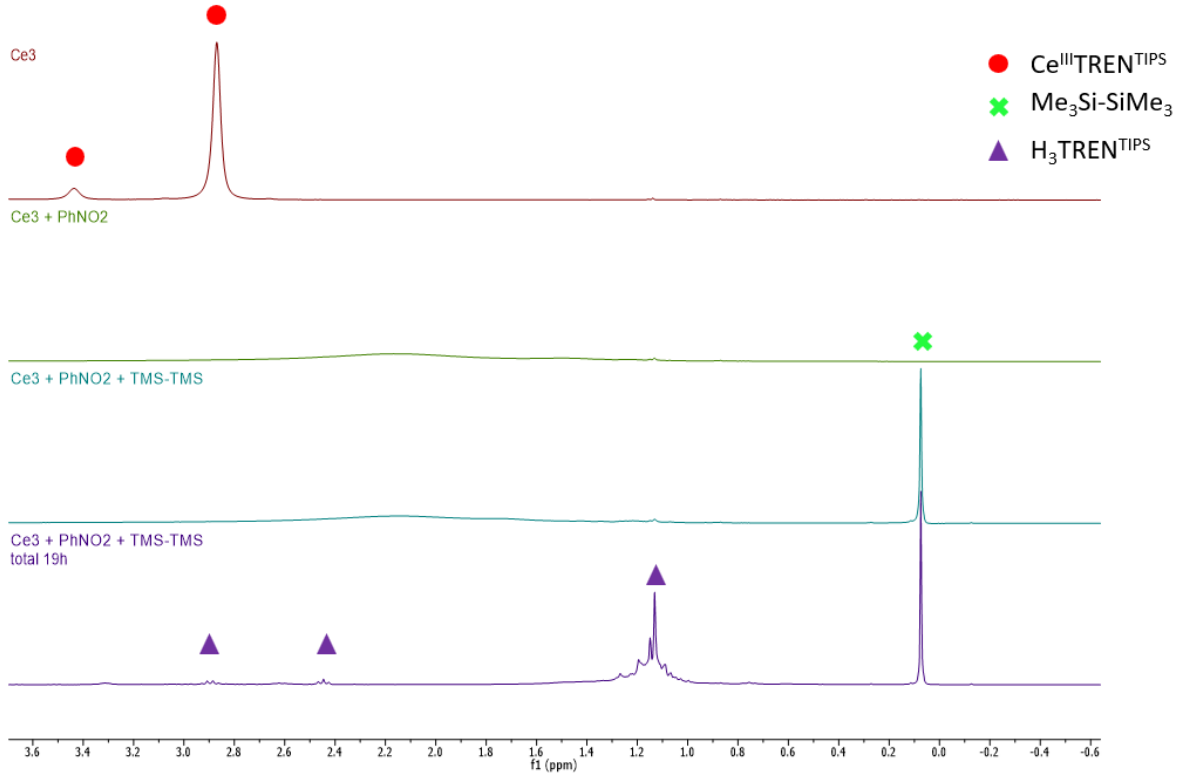

Figure S173. ^{1}H NMR spectrum of the reaction between **1** and $PhNO_2$ with TMS-TMS in C_6D_6. Zoom between -0.6 and 3.6 ppm region. Solvent residual peak is indicated with *

Institut Polytechnique de Paris
91120 Palaiseau, France

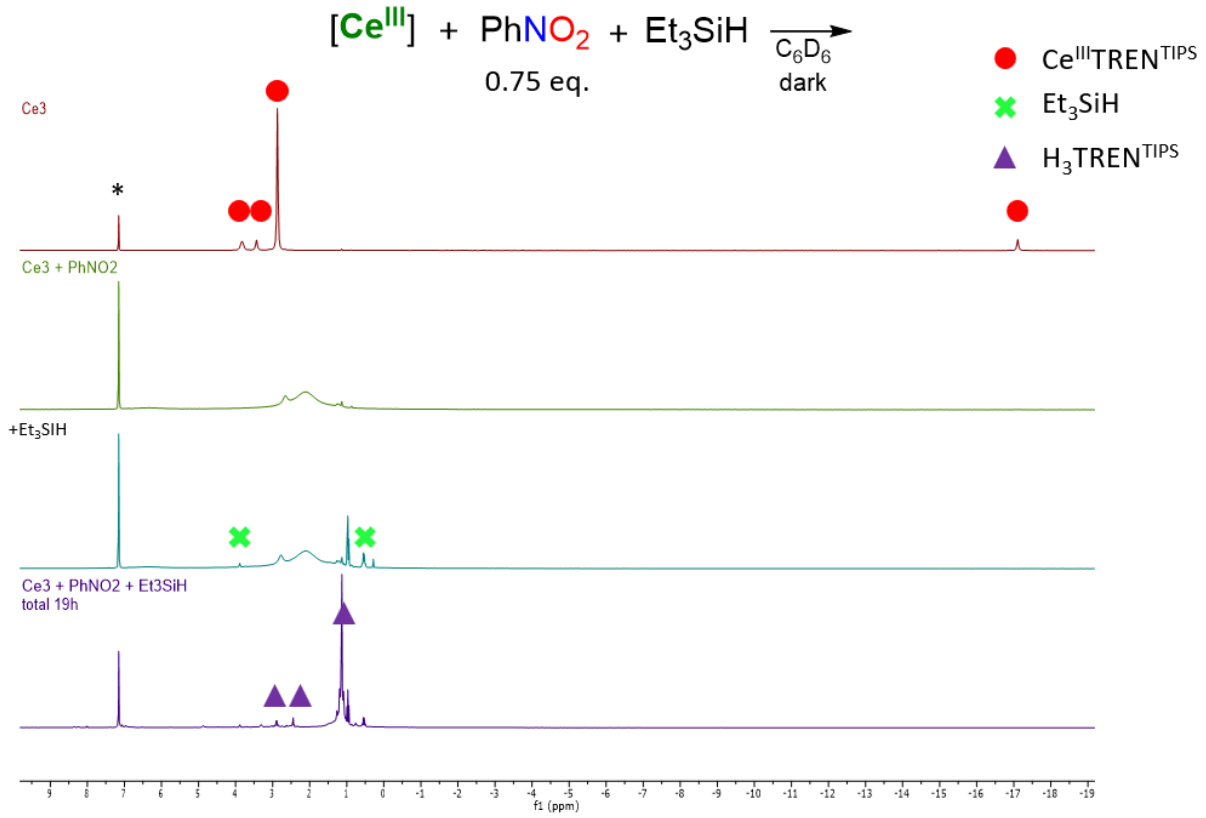

Figure S174. ^{1}H NMR spectrum of the reaction between **1** and $PhNO_2$ with Et_3SiH in C_6D_6. Solvent residual peak is indicated with *

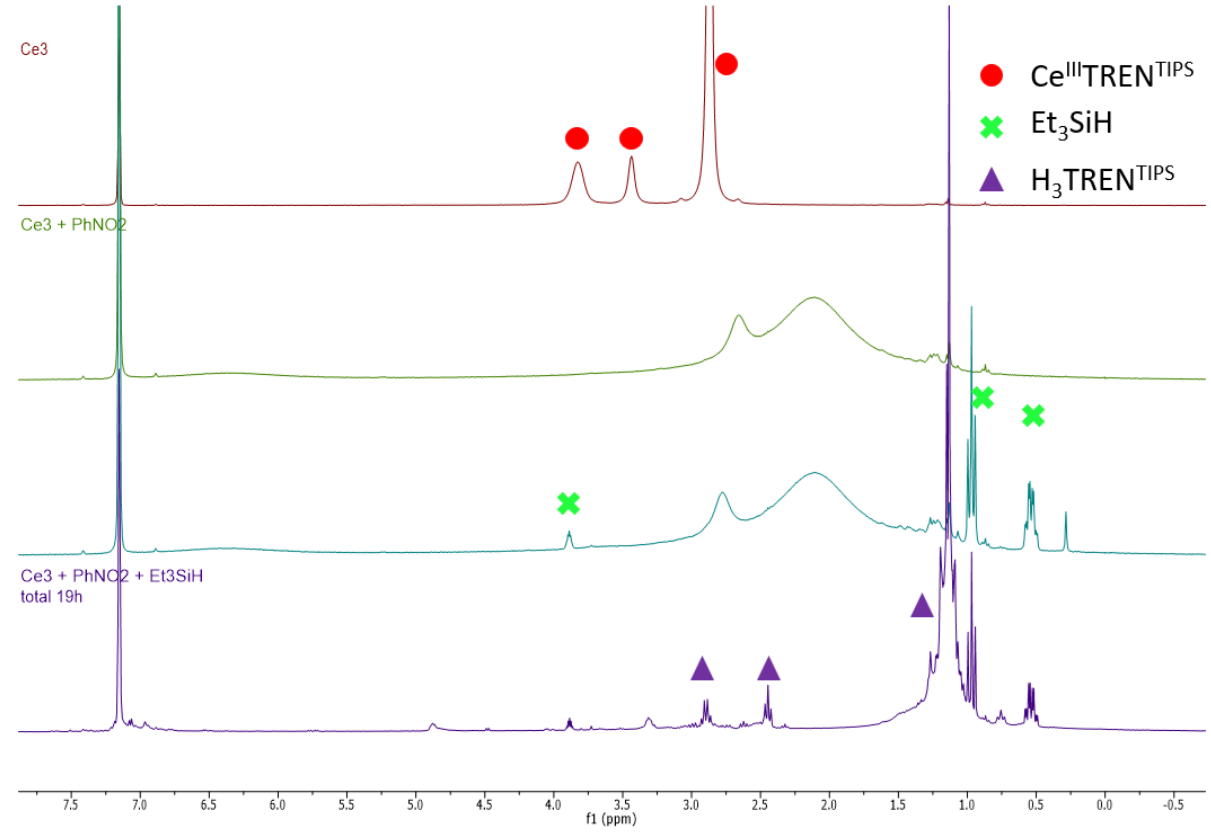

Figure S175. ^{1}H NMR spectrum of the reaction between **1** and $PhNO_2$ with Et_3SiH in C_6D_6. Zoom between -0.5 and 7.5 ppm region. Solvent residual peak is indicated with *

Institut Polytechnique de Paris
91120 Palaiseau, France

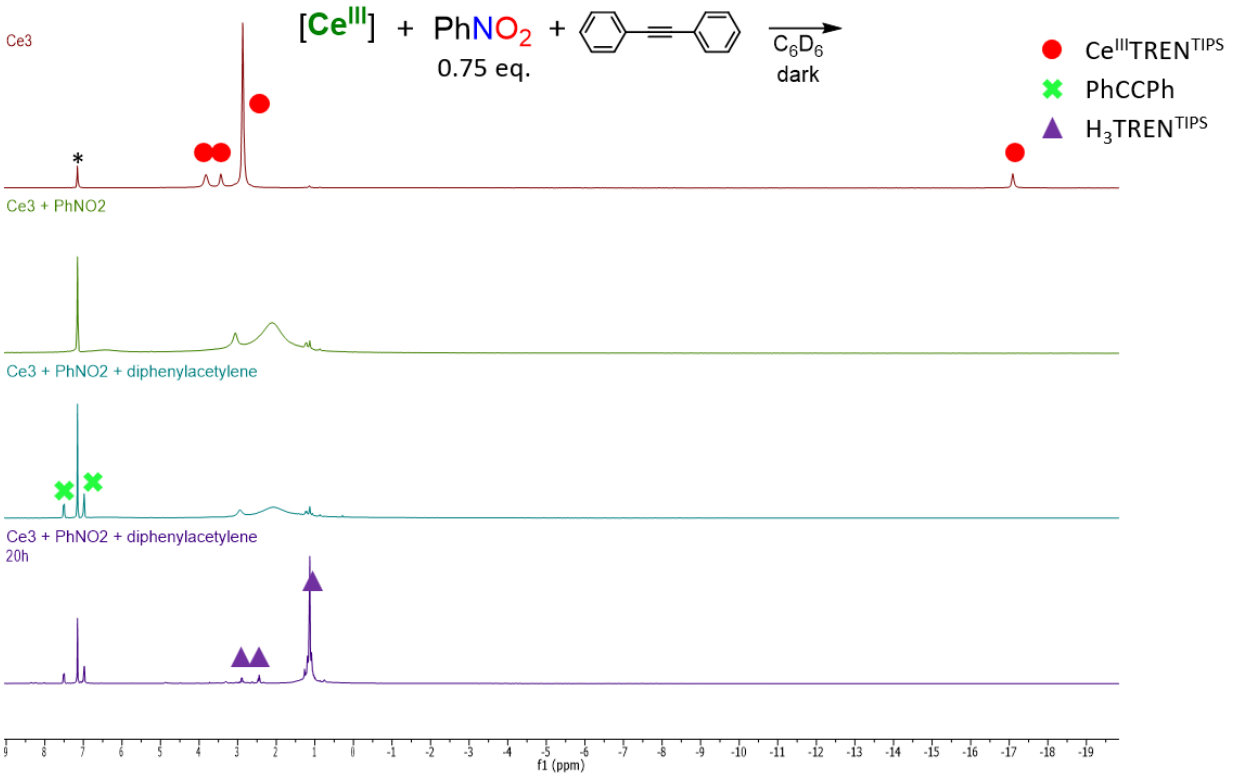

Figure S176. ^{1}H NMR spectrum of the reaction between **1** and $PhNO_2$ with diphenylacetylene in C_6D_6. Solvent residual peak is indicated with *

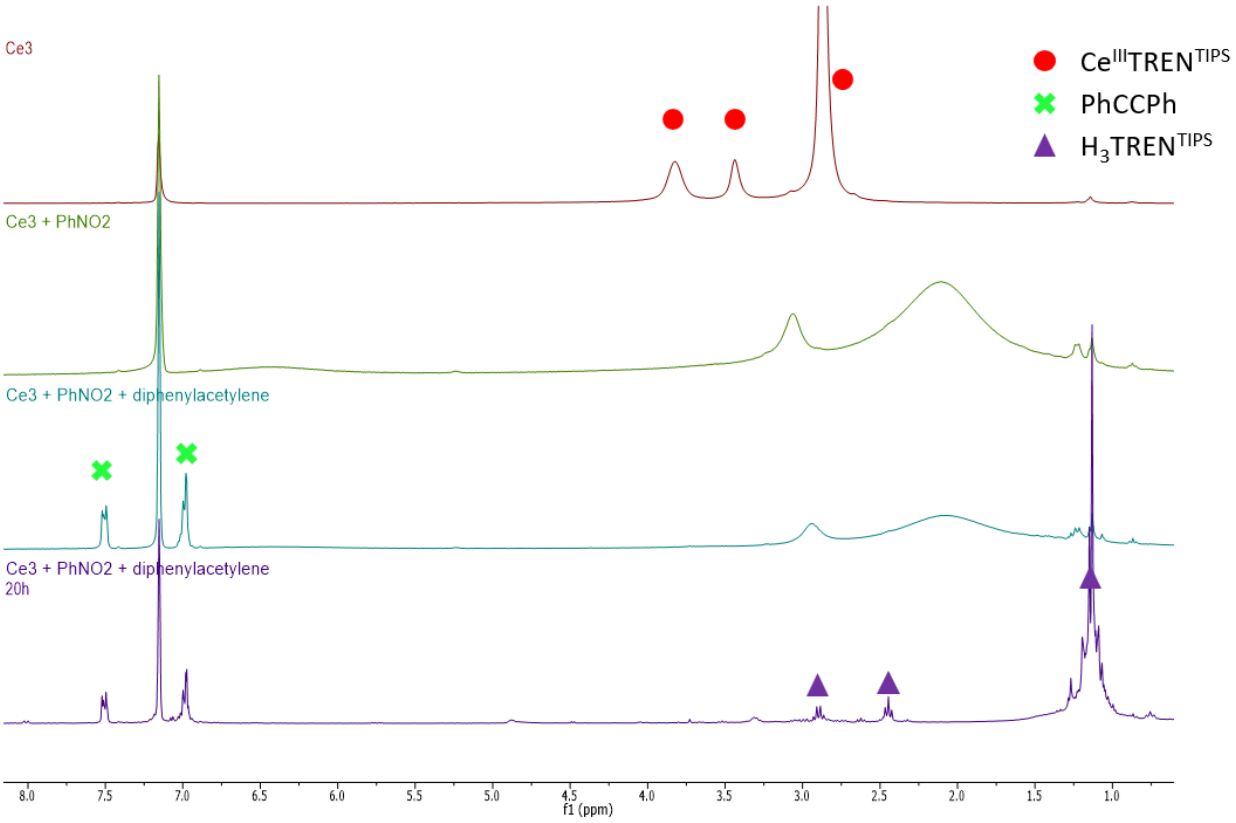

Figure S177. ^{1}H NMR spectrum of the reaction between **1** and $PhNO_2$ with diphenylacetylene in C_6D_6. Zoom between 0.5 and 8.0 ppm region. Solvent residual peak is indicated with *

Institut Polytechnique de Paris
91120 Palaiseau, France

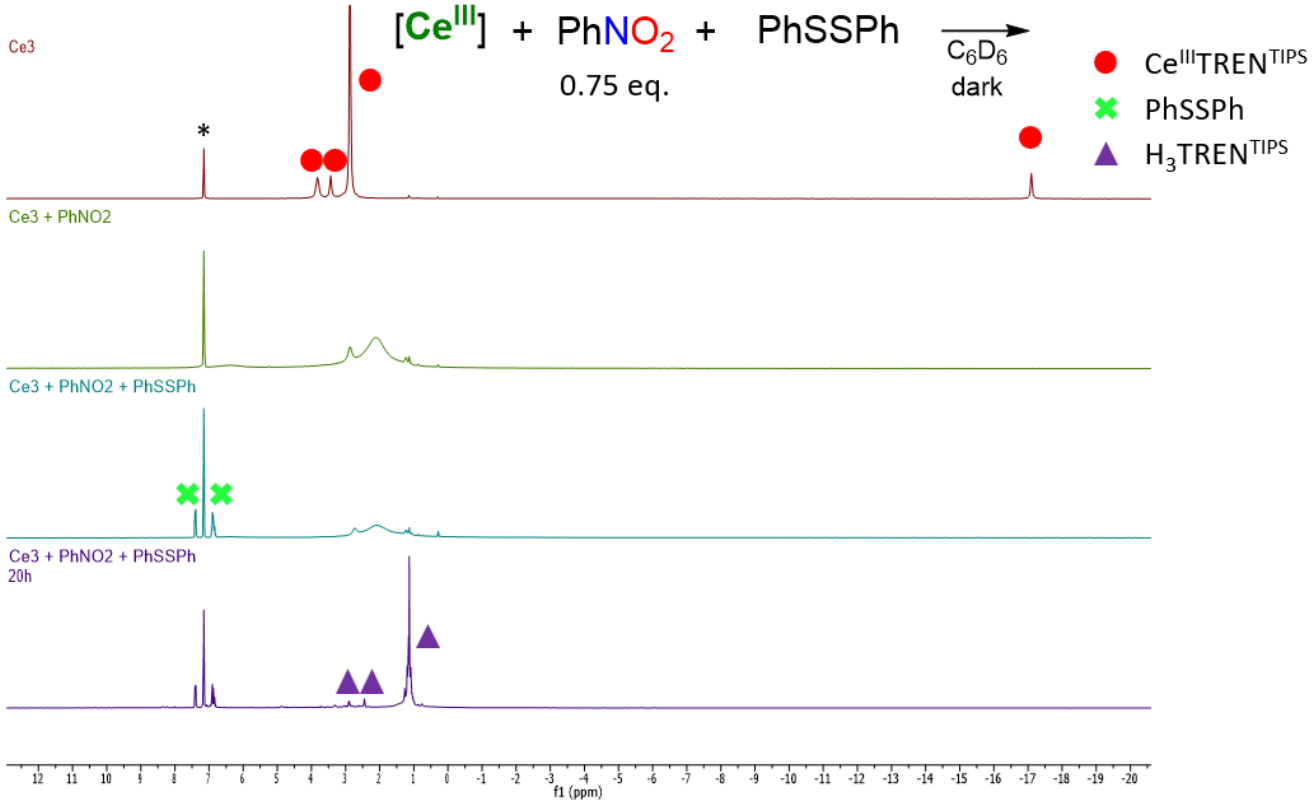

Figure S178. ^{1}H NMR spectrum of the reaction between **1** and $PhNO_2$ with PhSSPh in C_6D_6. Zoom between 0.5 and 8.0 ppm region. Solvent residual peak is indicated with *

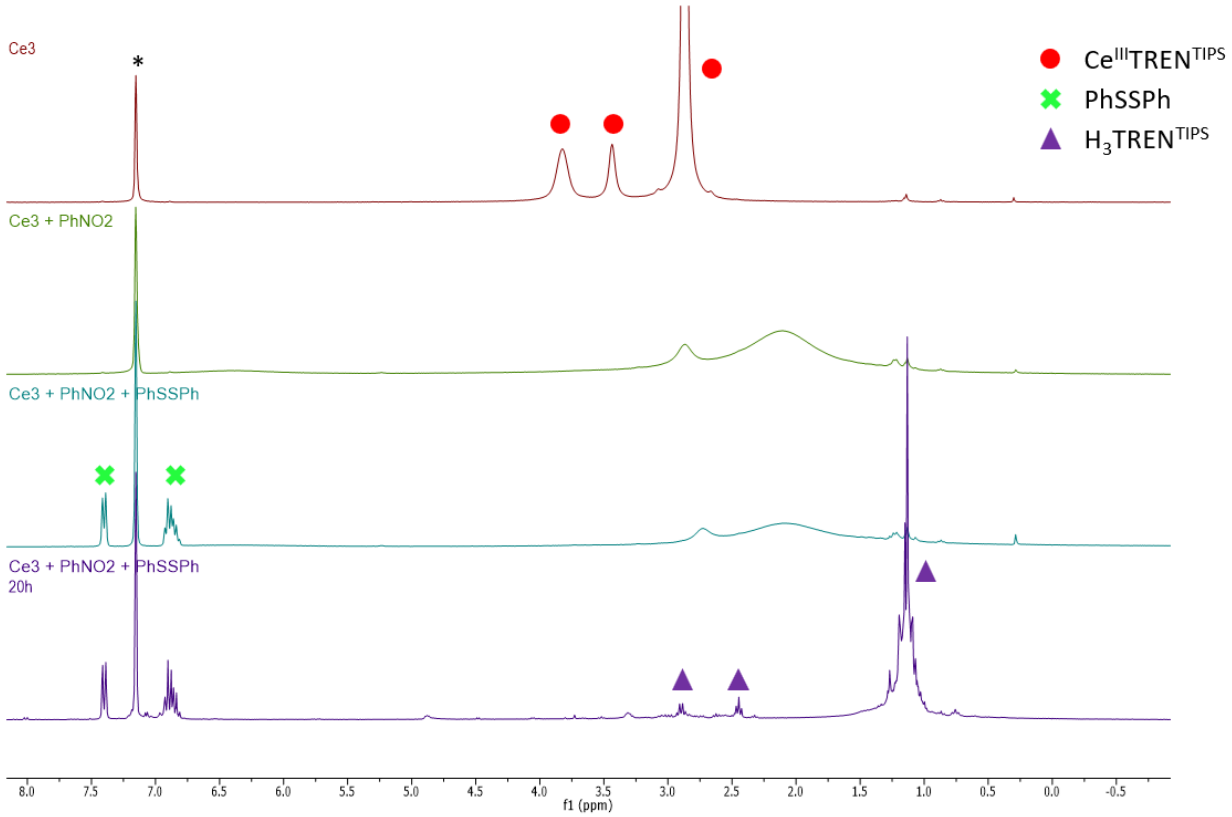

Figure S179. ^{1}H NMR spectrum of the reaction between **1** and $PhNO_2$ with PhSSPh in C_6D_6. Zoom between -0.8 and 8.0 ppm region. Solvent residual peak is indicated with *

Institut Polytechnique de Paris
91120 Palaiseau, France

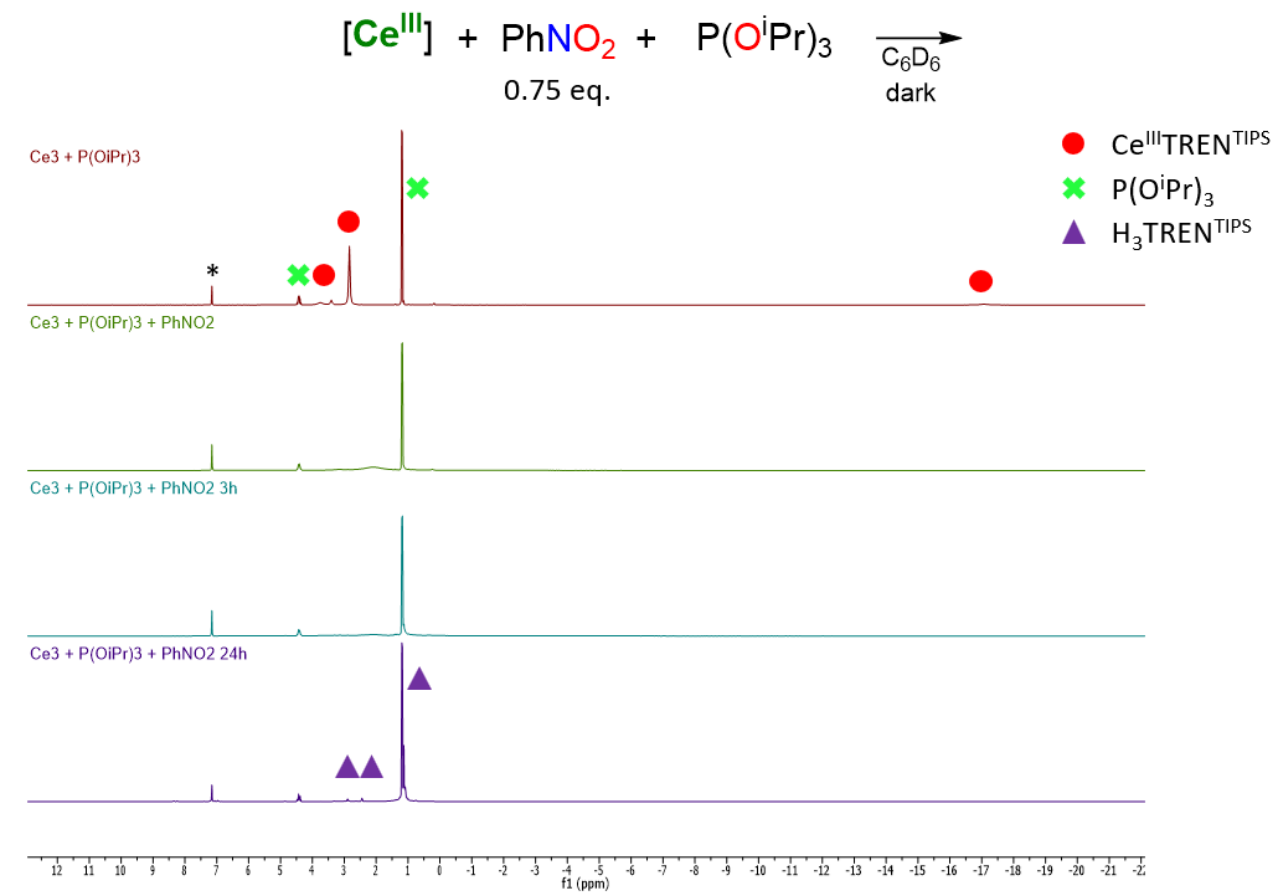

Figure S180. ^{1}H NMR spectrum of the reaction between **1** and $PhNO_2$ with $P(O^iPr)_3$ in C_6D_6. Solvent residual peak is indicated with *

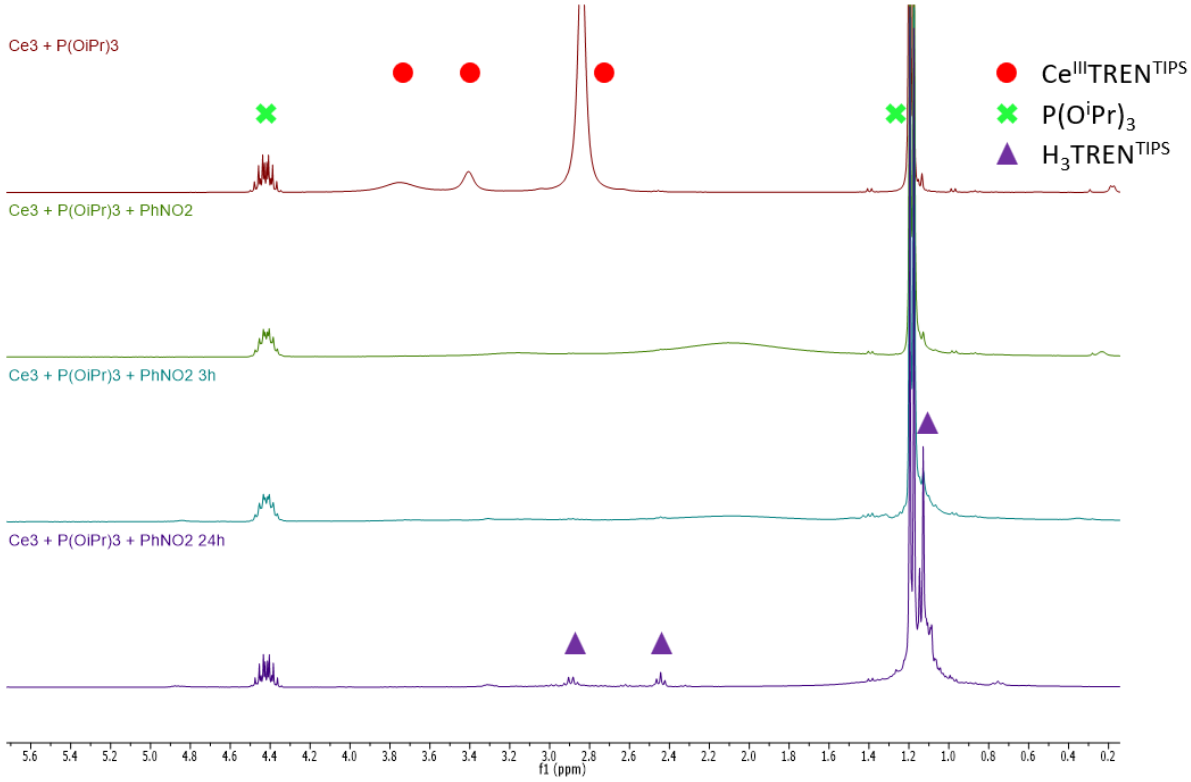

Figure S181. ^{1}H NMR spectrum of the reaction between **1** and $PhNO_2$ with $P(O^iPr)_3$ in C_6D_6. Zoom between 0.2 and 5.6 ppm region. Solvent residual peak is indicated with *

Institut Polytechnique de Paris
91120 Palaiseau, France

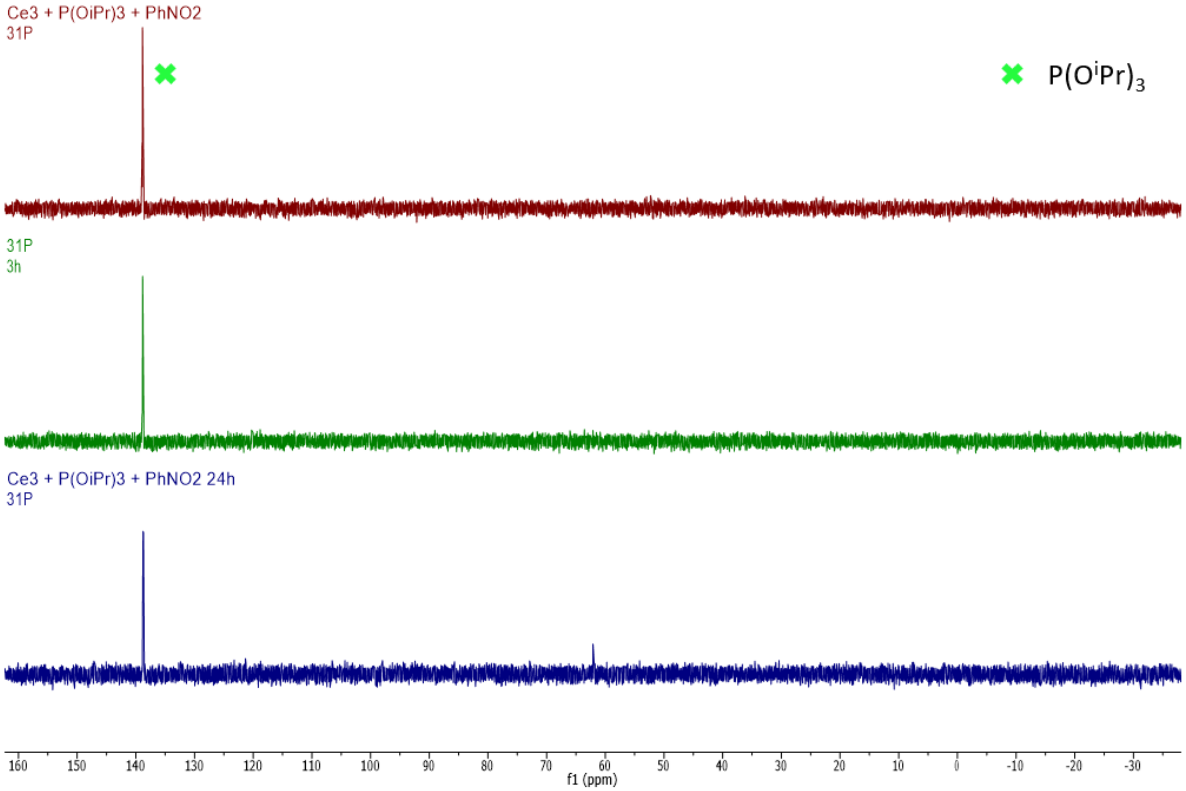

Figure S182. ^{31}P NMR spectrum of the reaction between **1** and $PhNO_2$ with $P(O^iPr)_3$ in C_6D_6

Institut Polytechnique de Paris
91120 Palaiseau, France

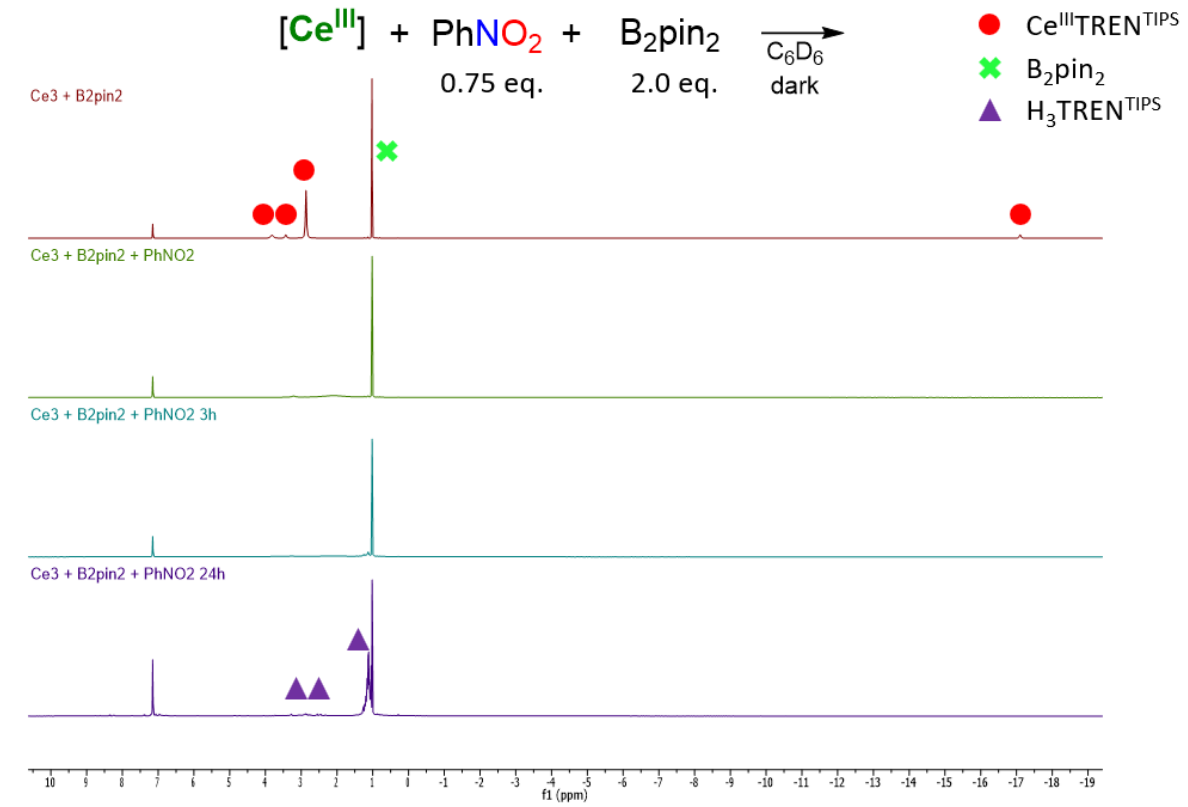

Figure S183. ^{1}H NMR spectrum of the reaction between **1** and $PhNO_2$ with B_2pin_2 in C_6D_6. Solvent residual peak is indicated with *

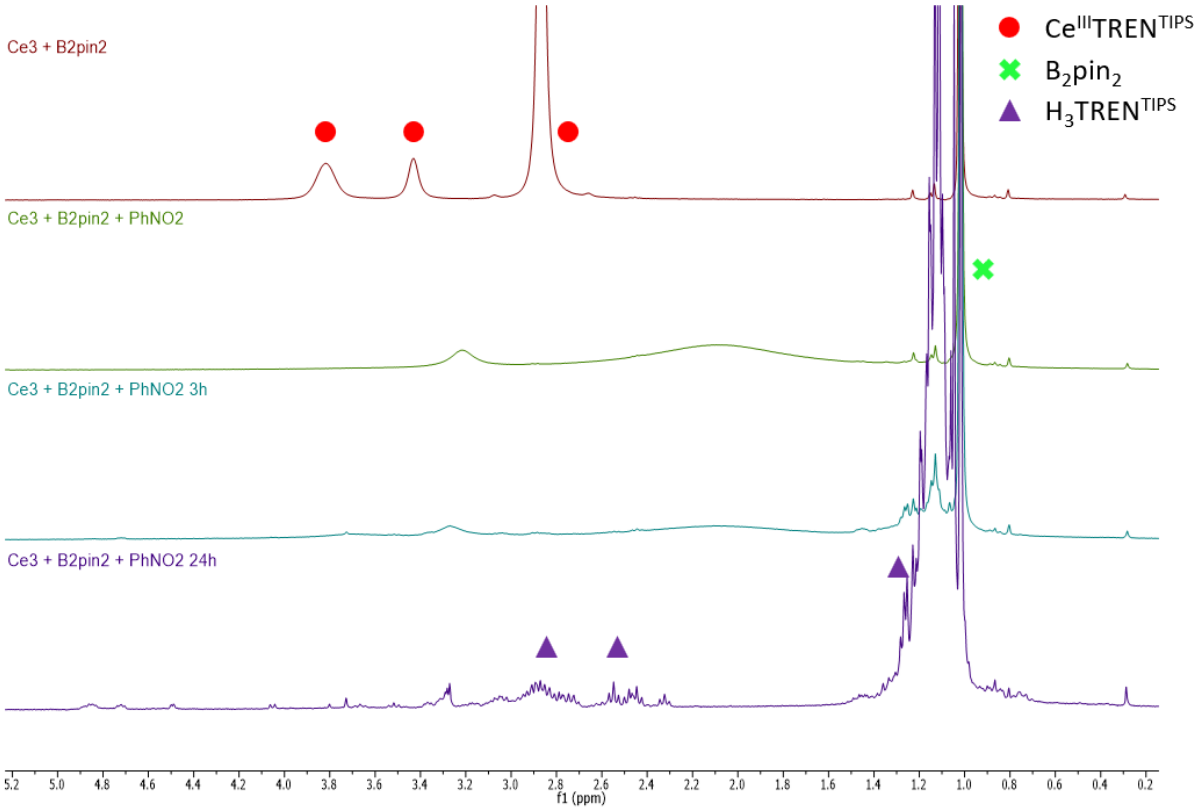

Figure S184. ^{1}H NMR spectrum of the reaction between **1** and $PhNO_2$ with B_2pin_2 in C_6D_6. Zoom between 0.2 and 5.2 ppm region. Solvent residual peak is indicated with *

c) Reactivity of 1 with organic nitrites

Institut Polytechnique de Paris
91120 Palaiseau, France

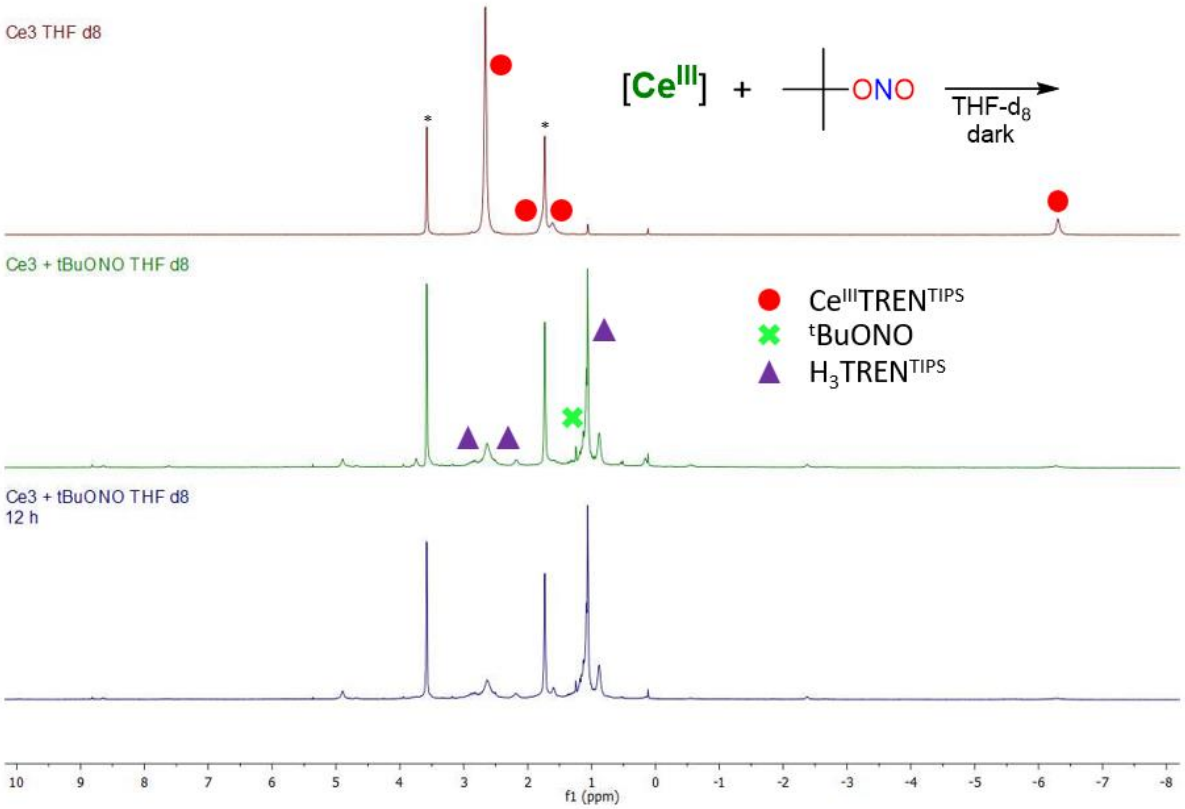

Figure S185. ^{1}H NMR spectrum of the reaction between **1** and *tert*-butyl nitrite in THF-d_8. Solvent residual peaks are indicated with *

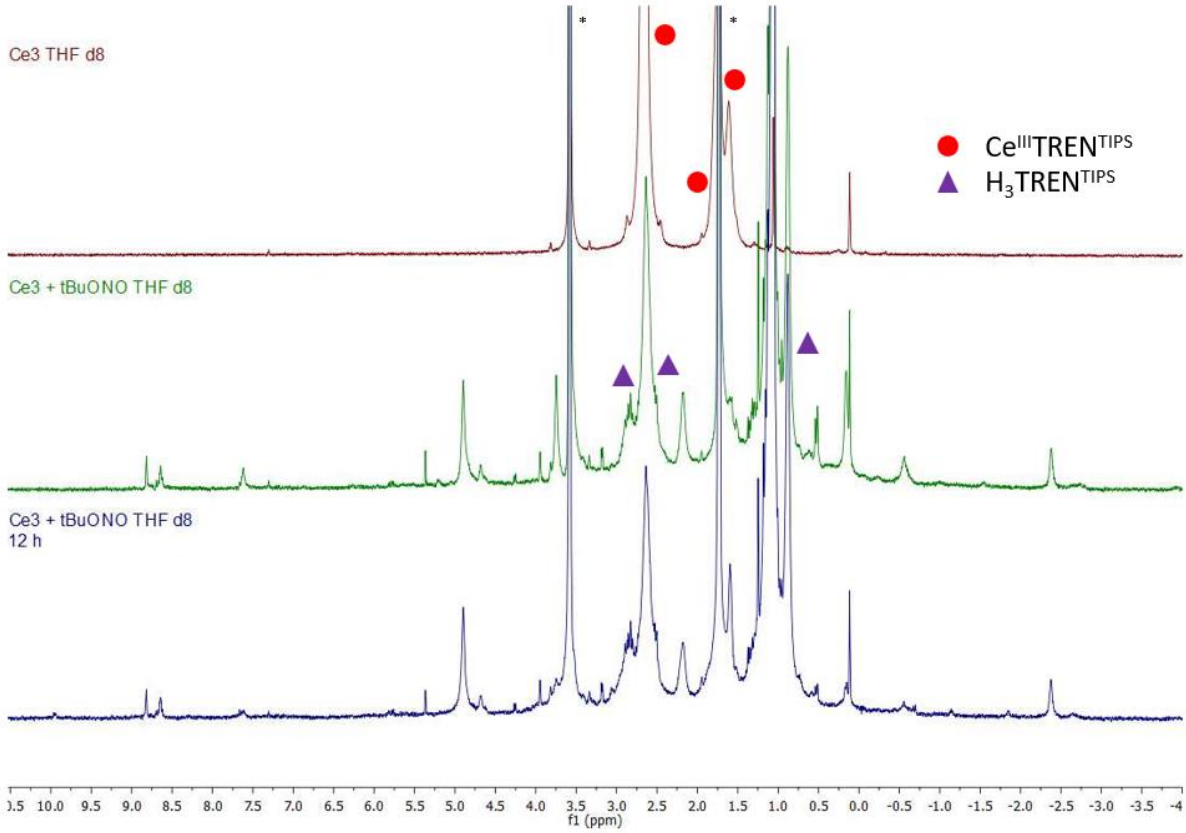

Figure S186. ^{1}H NMR spectrum of the reaction between **1** and *tert*-butyl nitrite in THF-d_8. Zoom between -4.0 and 11.5 ppm. Solvent residual peaks are indicated with *

Institut Polytechnique de Paris
91120 Palaiseau, France

d) Reaction of 1 with amine-oxides

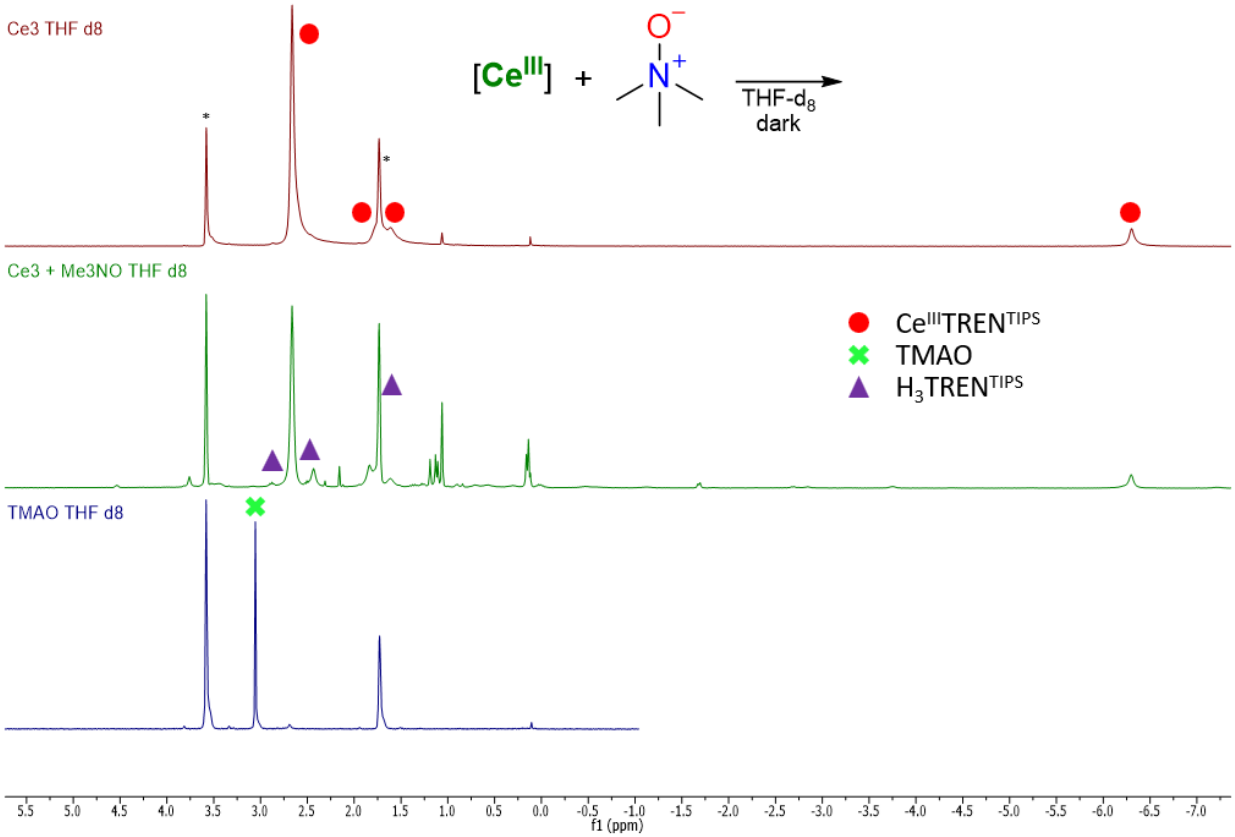

Figure S187. ^{1}H NMR spectrum of the reaction between **1** and TMAO in THF-d_8. Solvent residual peaks are indicated with *

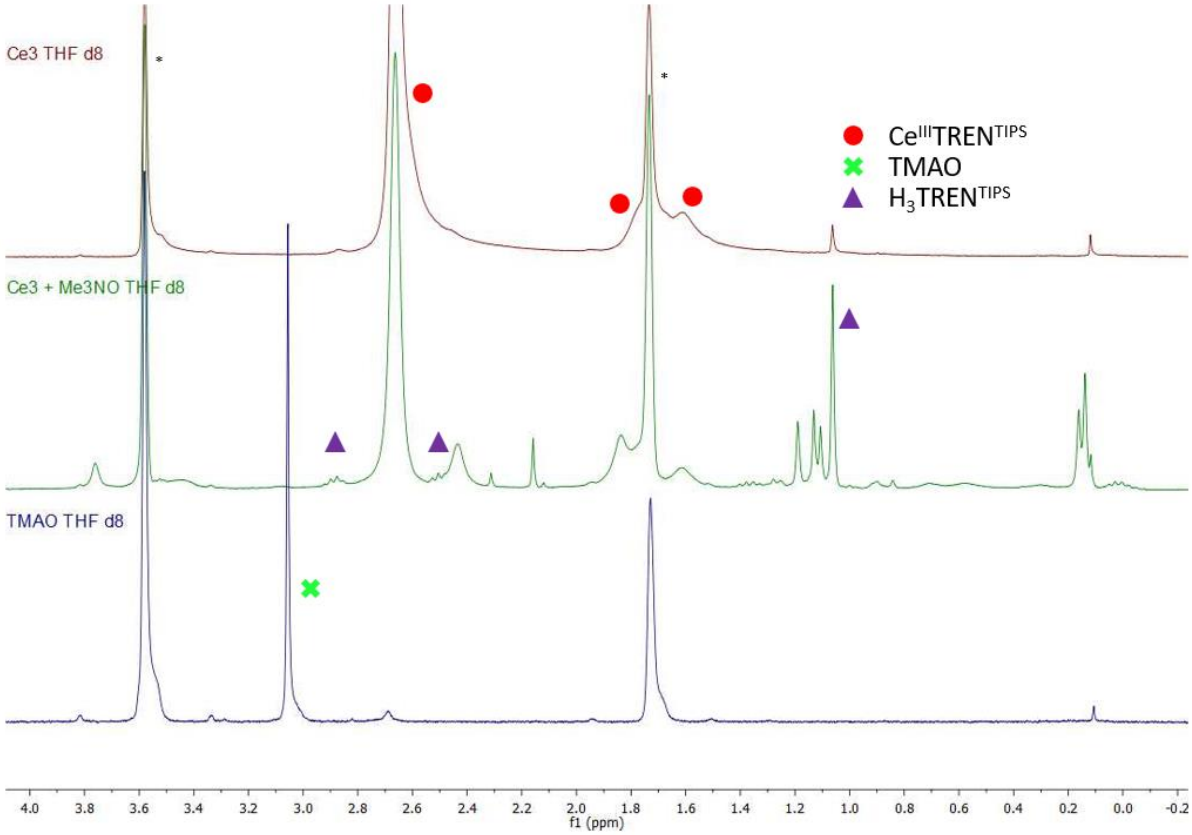

Figure S188. ^{1}H NMR spectrum of the reaction between **1** and TMAO in THF-d_8. Zoom between 0.0 and 4.5 ppm region. Solvent residual peaks are indicated with *

Institut Polytechnique de Paris
91120 Palaiseau, France

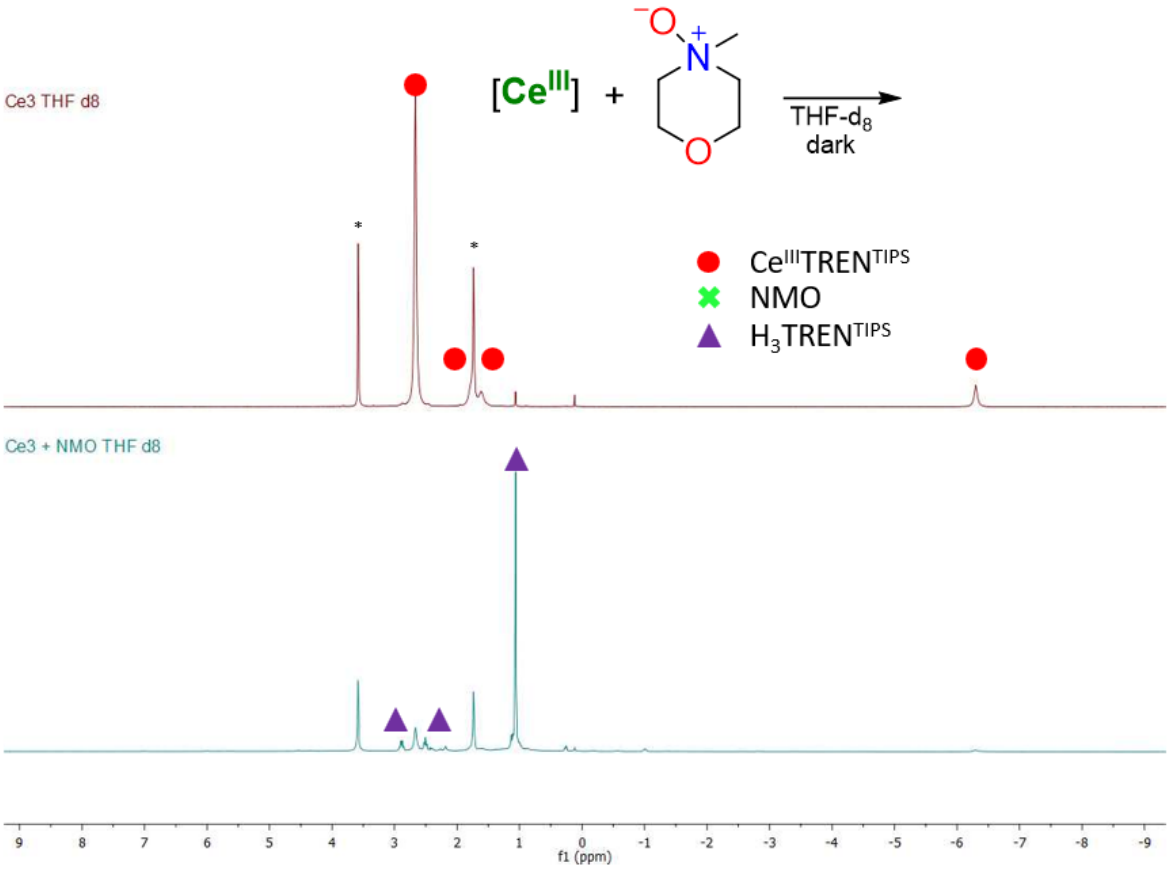

Figure S189. ^{1}H NMR spectrum of the reaction between **1** and NMO in THF-d$_8$. Solvent residual peaks are indicated with *

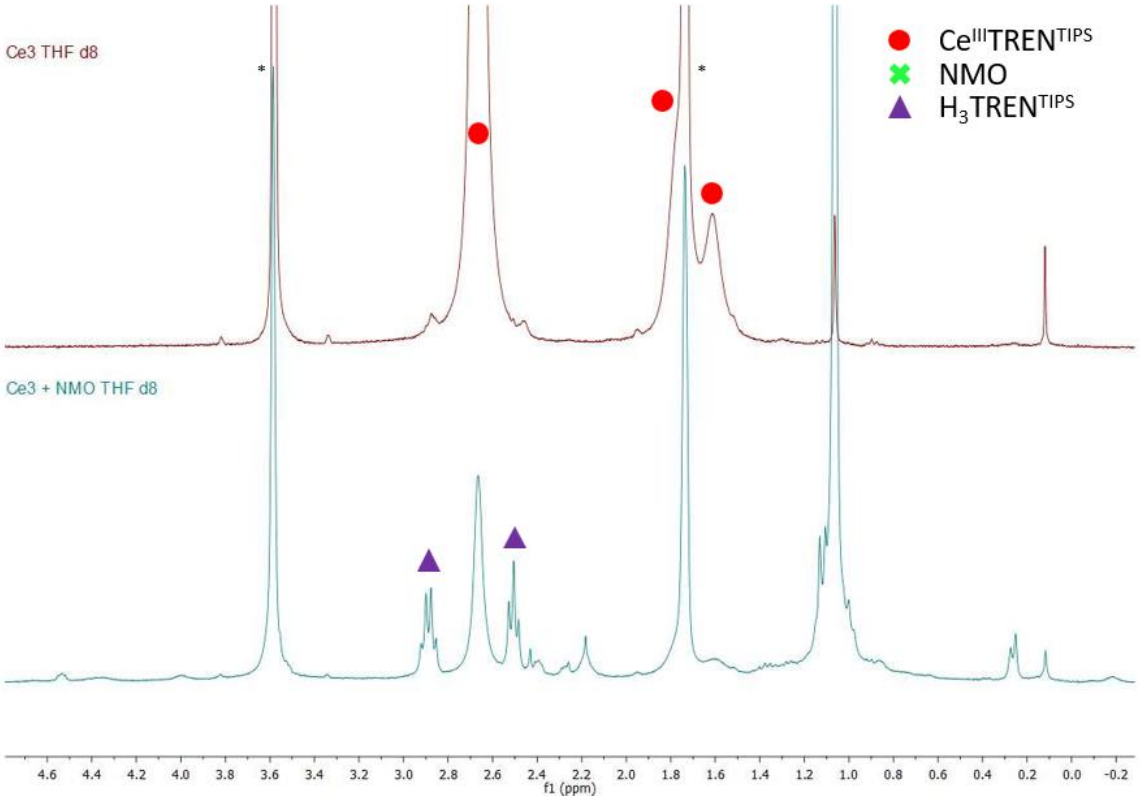

Figure S190. ^{1}H NMR spectrum of the reaction between **1** and NMO in THF-d$_8$. Zoom between -0.2 and 4.8 ppm. Solvent residual peaks are indicated with *

Institut Polytechnique de Paris
91120 Palaiseau, France

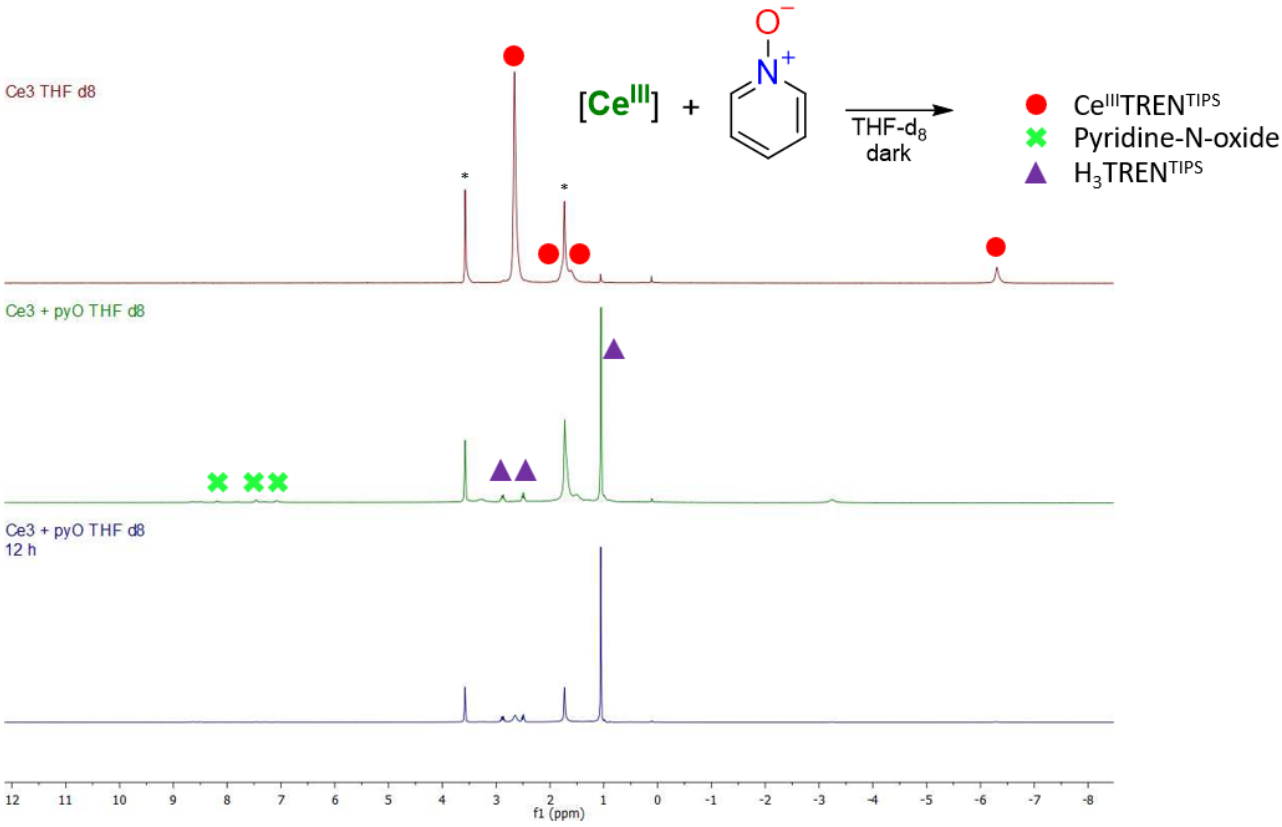

Figure S191. ^{1}H NMR spectrum of the reaction between **1** and pyridine-N-oxide in THF-d$_8$. Solvent residual peaks are indicated with *

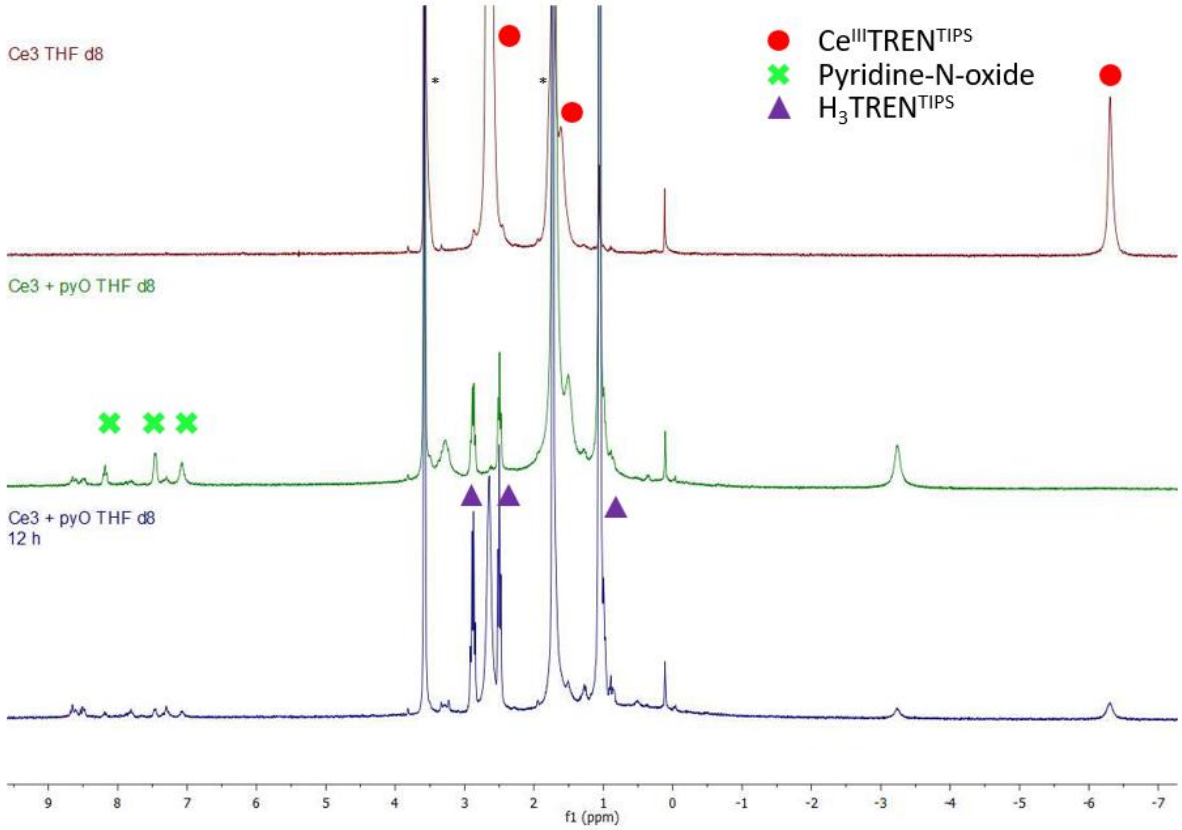

Figure S192. ^{1}H NMR spectrum of the reaction between **1** and pyridine-N-oxide in THF-d$_8$. Zoom between -7.0 and 9.5 ppm region. Solvent residual peaks are indicated with *

Institut Polytechnique de Paris
91120 Palaiseau, France

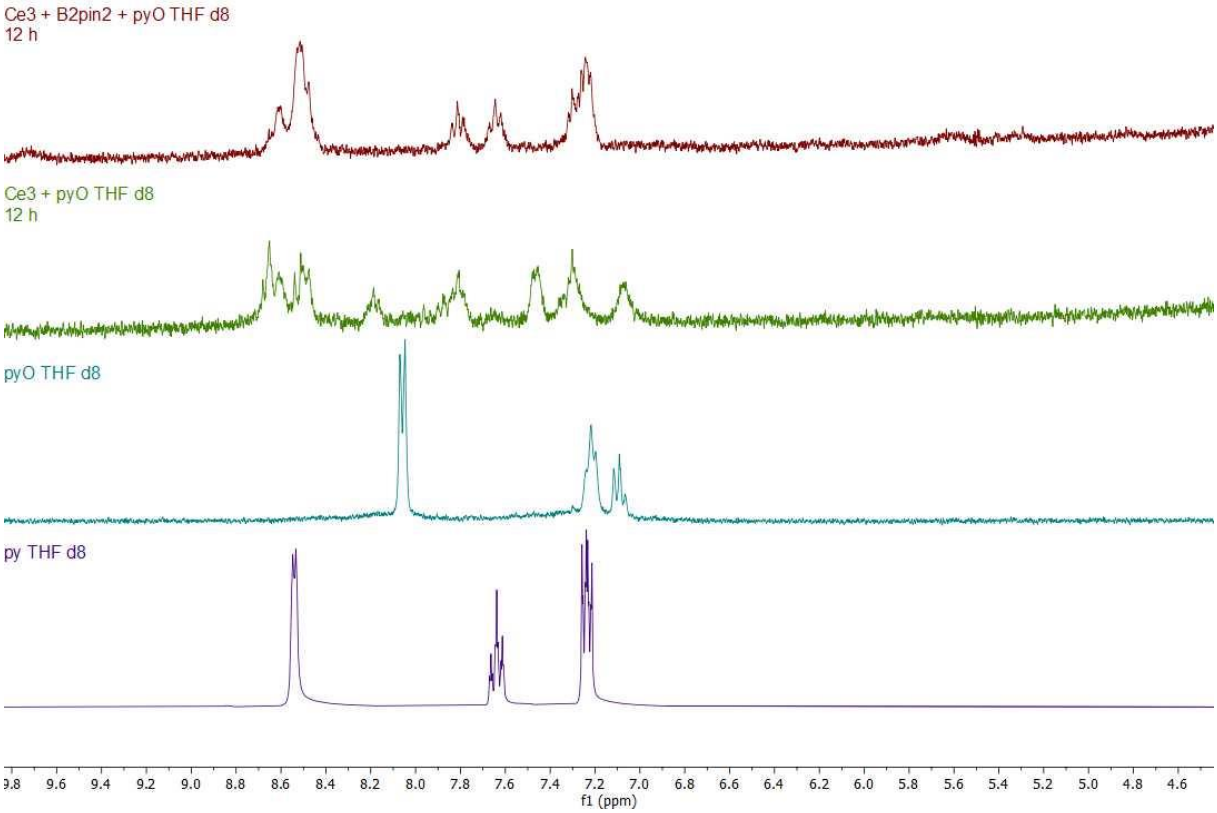

Figure S193. Comparison of experiments between **1** and pyridine-N-oxide with and without B_2pin_2

a) Reaction of 1 with nitrones

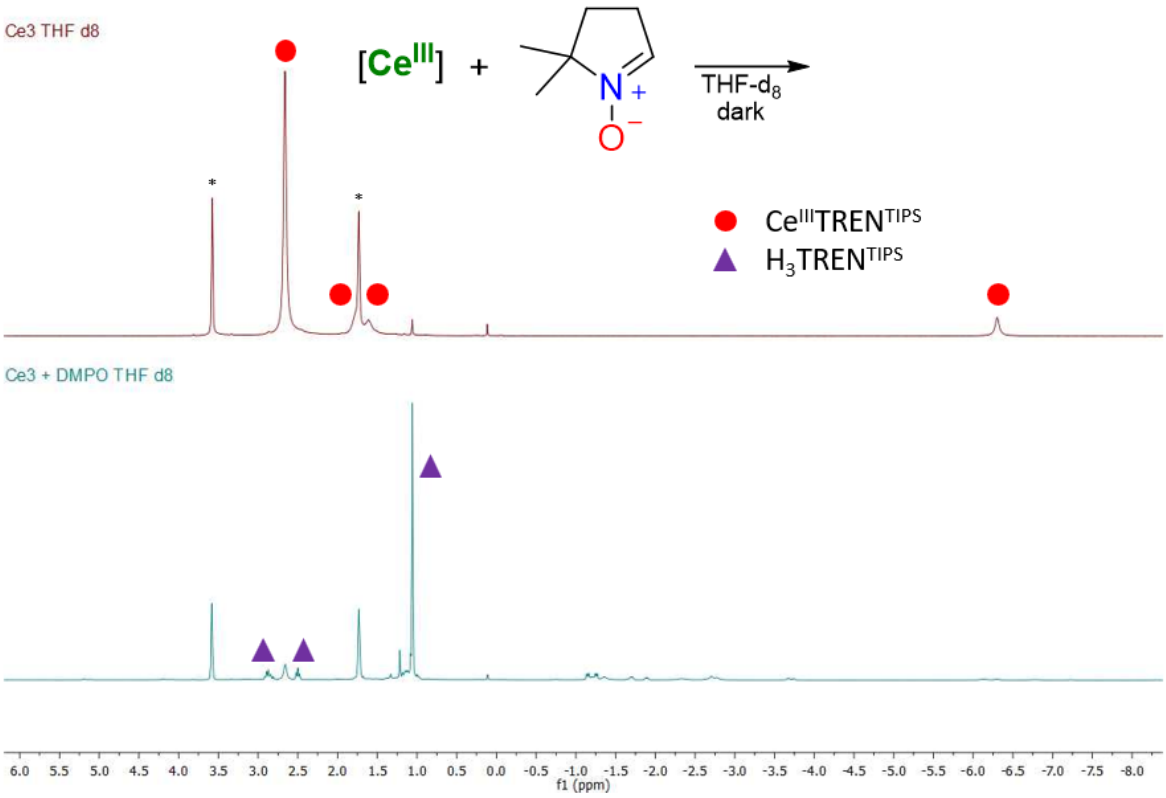

Figure S194. ^{1}H NMR spectrum of the reaction between **1** and DMPO in THF-d$_8$. Solvent residual peak is indicated with *

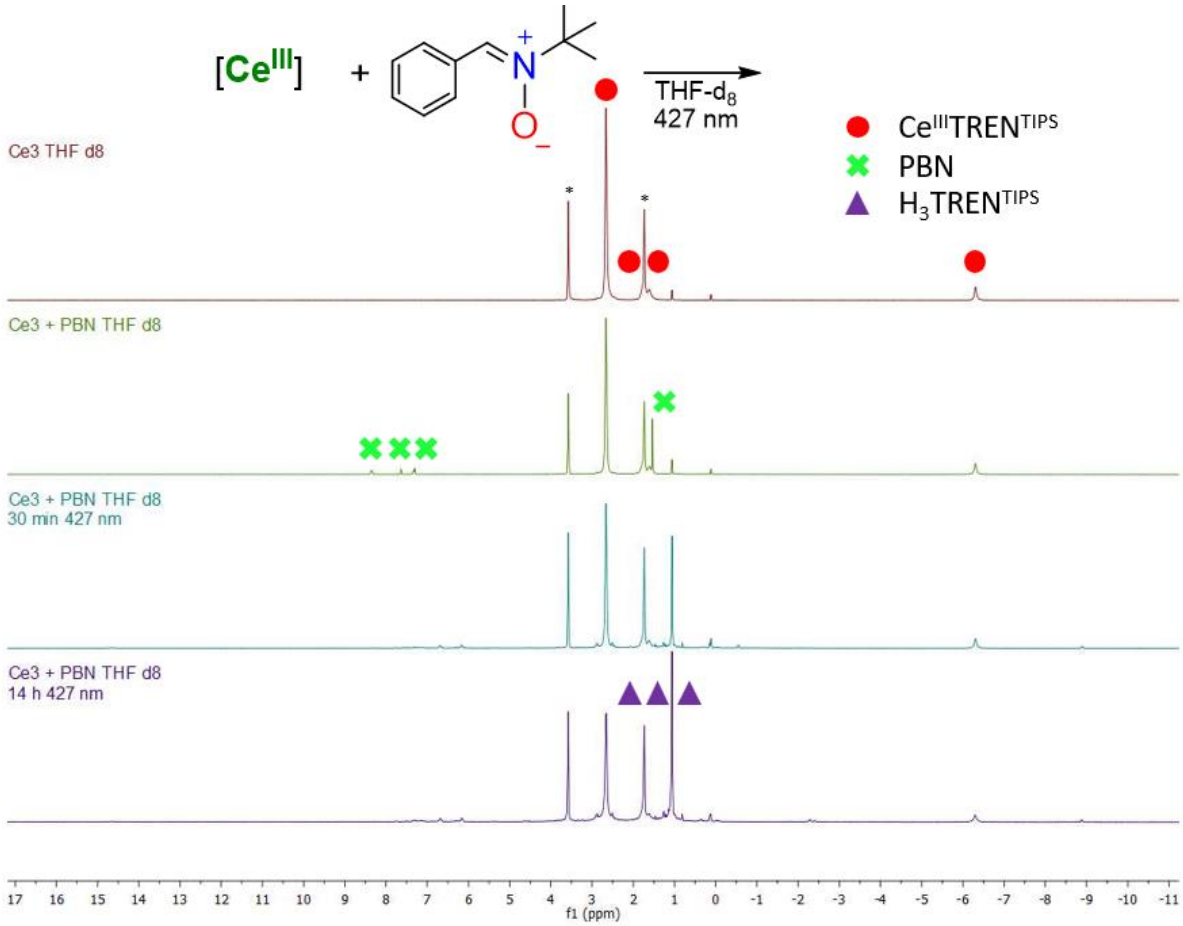

Figure S195. ^{1}H NMR spectrum of the photochemical reaction between **1** and PBN in THF-d_8. Solvent residual peaks are indicated with *

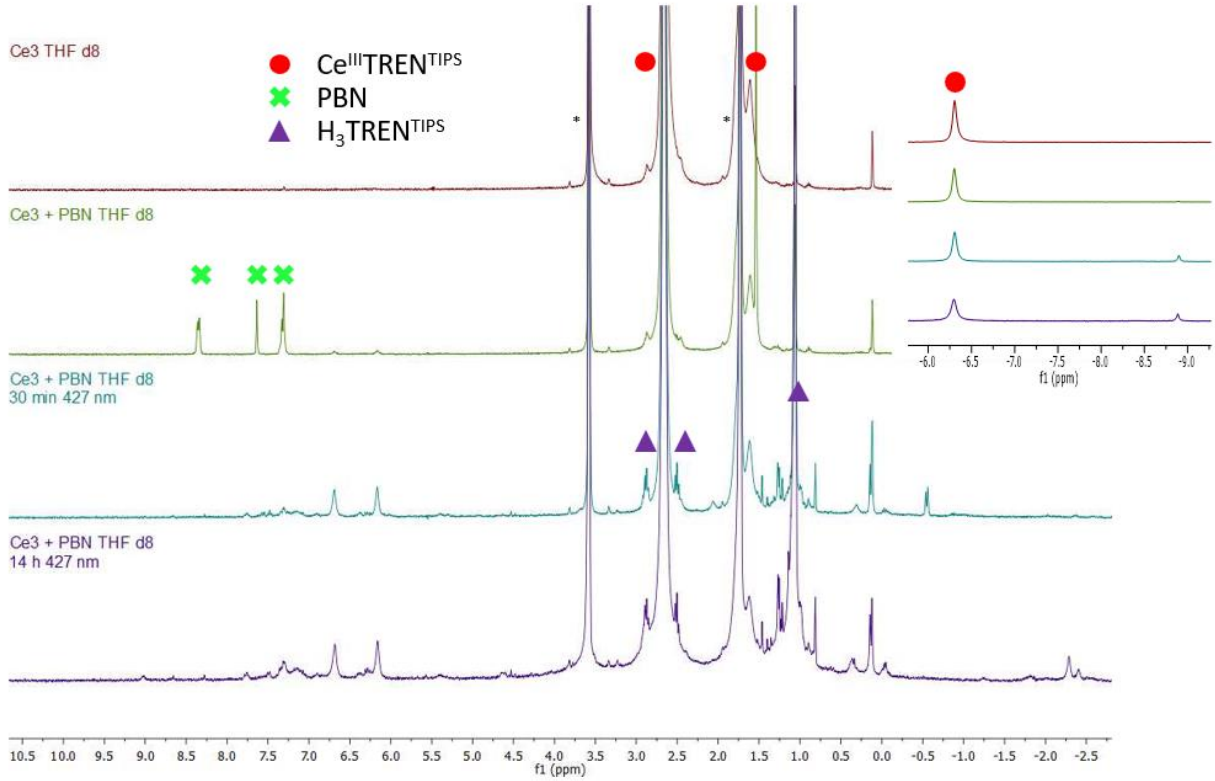

Figure S196. ^{1}H NMR spectrum of the photochemical reaction between **1** and PBN in THF-d_8. Zoom between -2.5 and 10.5 ppm region Solvent residual peaks are indicated with *

Institut Polytechnique de Paris
91120 Palaiseau, France

III. EPR spectroscopy data

a) Reaction of 1 with PhNO

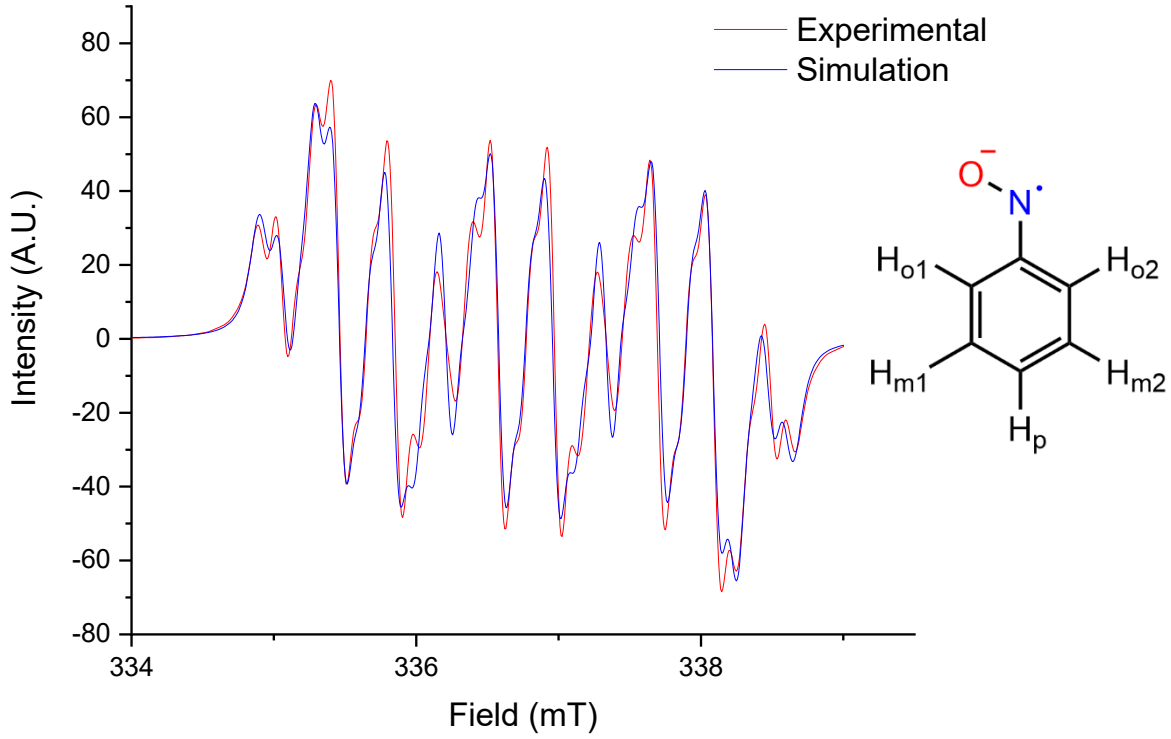

Figure S197. EPR spectrum of the reaction between PhNO and **1** in pentane at 10^{-4} M

Parameter	Value
g	2.0027
A(^{14}N)	1.127
A($^{1}H_{o1}$)	0.400
A($^{1}H_{o2}$)	0.388
A($^{1}H_{m1}$)	0.148
A($^{1}H_{m2}$)	0.109
A($^{1}H_{p}$)	0.356
lwpp	[0.06 0.06]

Table S46. Fitting values associated with EPR spectrum of the reaction between PhNO and **1** in pentane. A values are given in mT

b) Reaction of 1 with $PhNO_2$

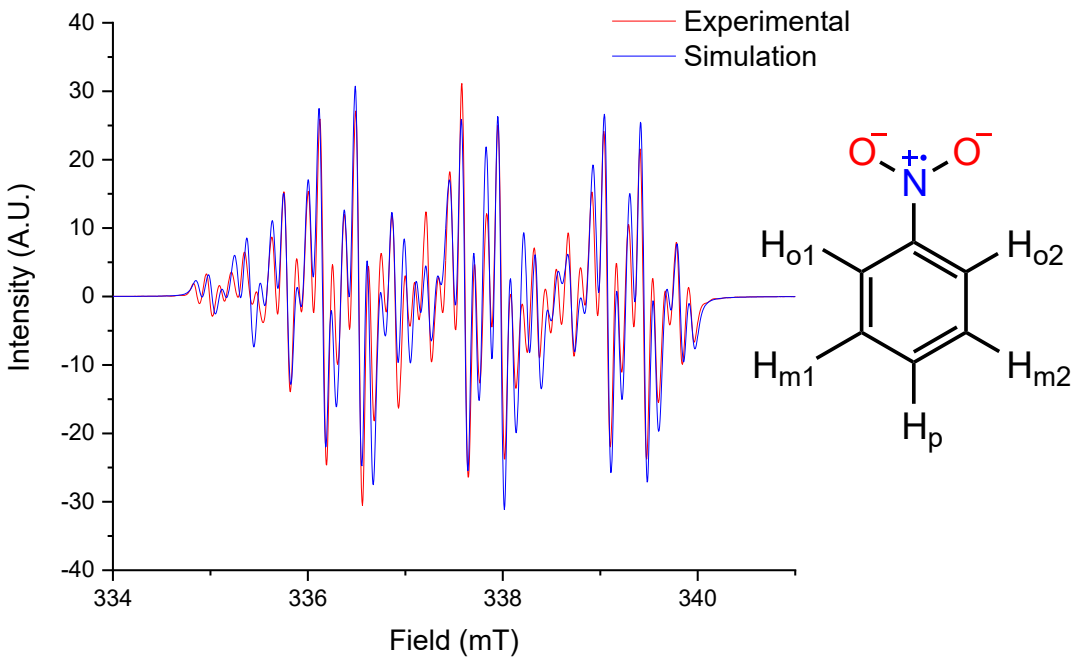

Figure S198. EPR spectrum of the reaction between $PhNO_2$ and **1** in pentane at 10^{-4} M

Parameter	Value
System α	
g	2.0021
A(^{14}N)	1.223
A($^{1}H_{o1}$)	0.388
A($^{1}H_{o2}$)	0.388
A($^{1}H_{m1}$)	0.120
A($^{1}H_{m2}$)	0.132
A($^{1}H_{p}$)	0.405
lwpp	[0.05 0.05]
weight	23.9%
System β	
g	1.9963
A(^{14}N)	1.459
A($^{1}H_{o1}$)	0.371
A($^{1}H_{o2}$)	0.368
A($^{1}H_{m1}$)	0.113
A($^{1}H_{m2}$)	0.119
A($^{1}H_{p}$)	0.375
lwpp	[0.05 0.05]
weight	75.5%

Table S47. Fitting values associated with EPR spectrum of the reaction between $PhNO_2$ and **1** in pentane. A values are given in mT

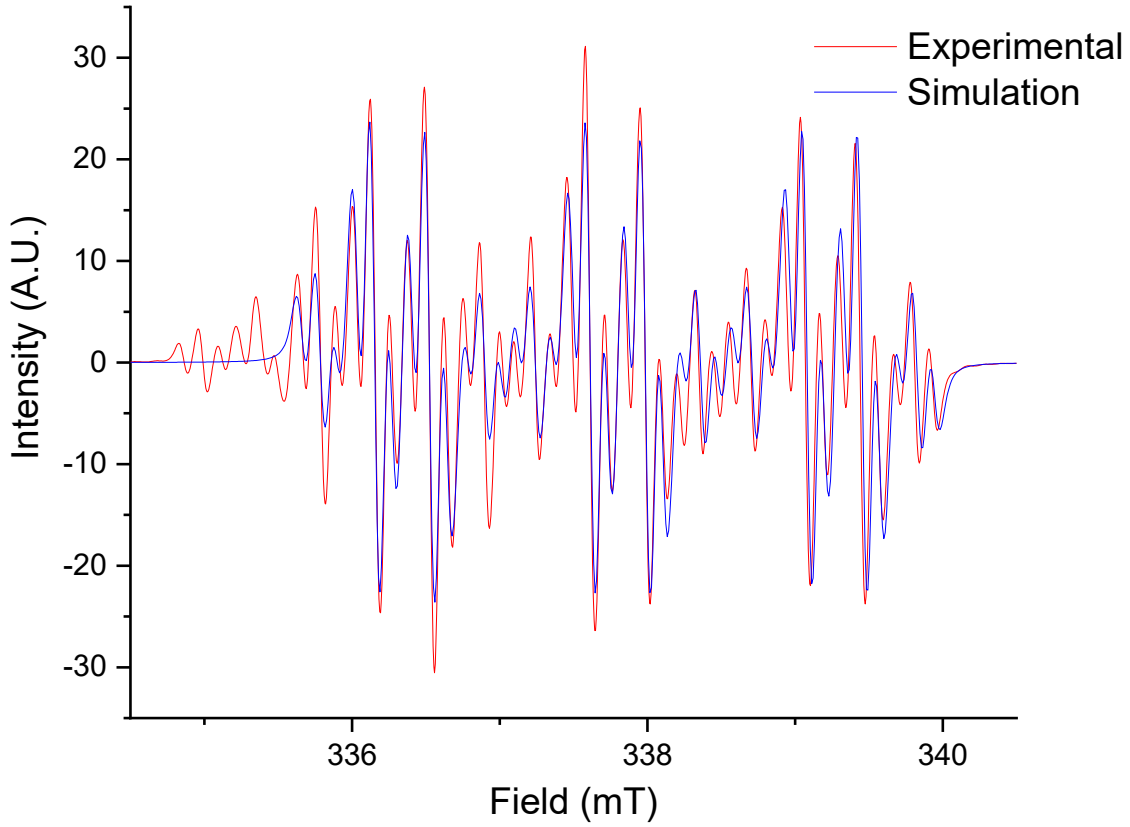

Figure S199. Fitting of system α for the reaction between $PhNO_2$ and **1** in pentane.

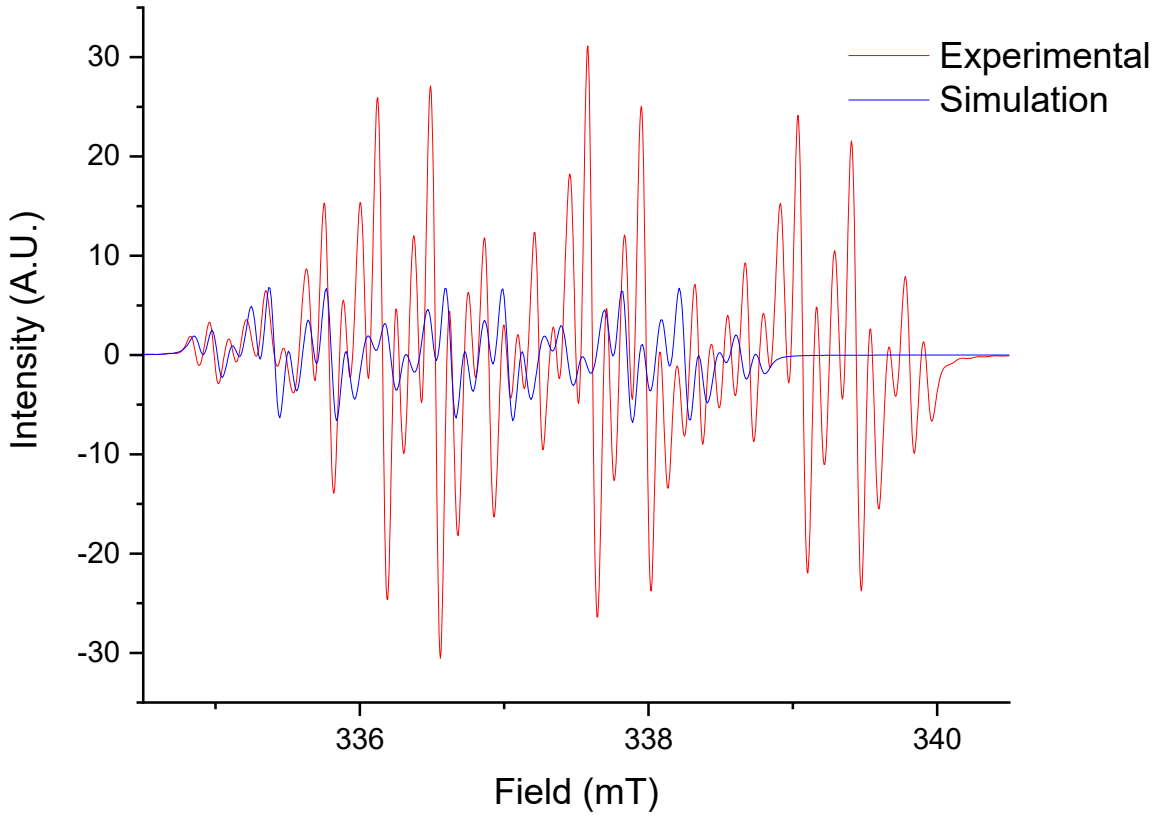

Figure S200. Fitting of system β for the reaction between $PhNO_2$ and **1** in pentane

Institut Polytechnique de Paris
91120 Palaiseau, France

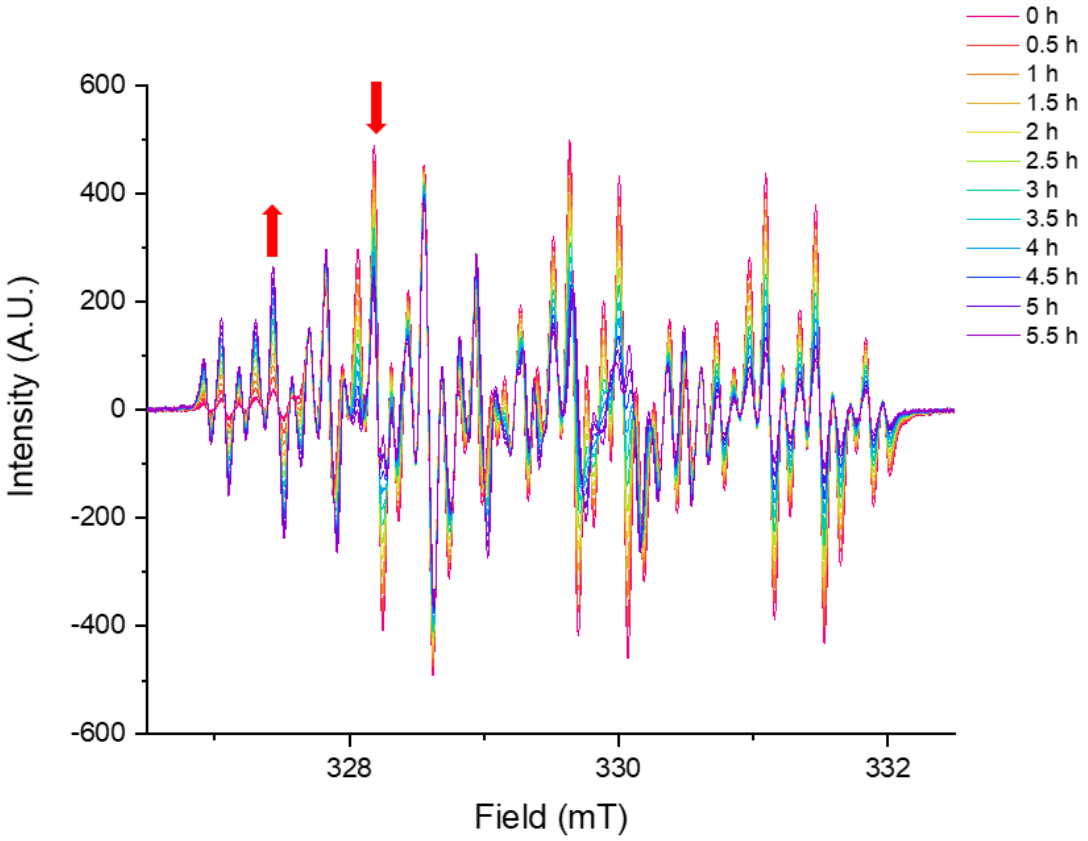

Figure S201. EPR kinetic monitoring of the reaction between $PhNO_2$ and **1** in pentane at 10^{-4} M

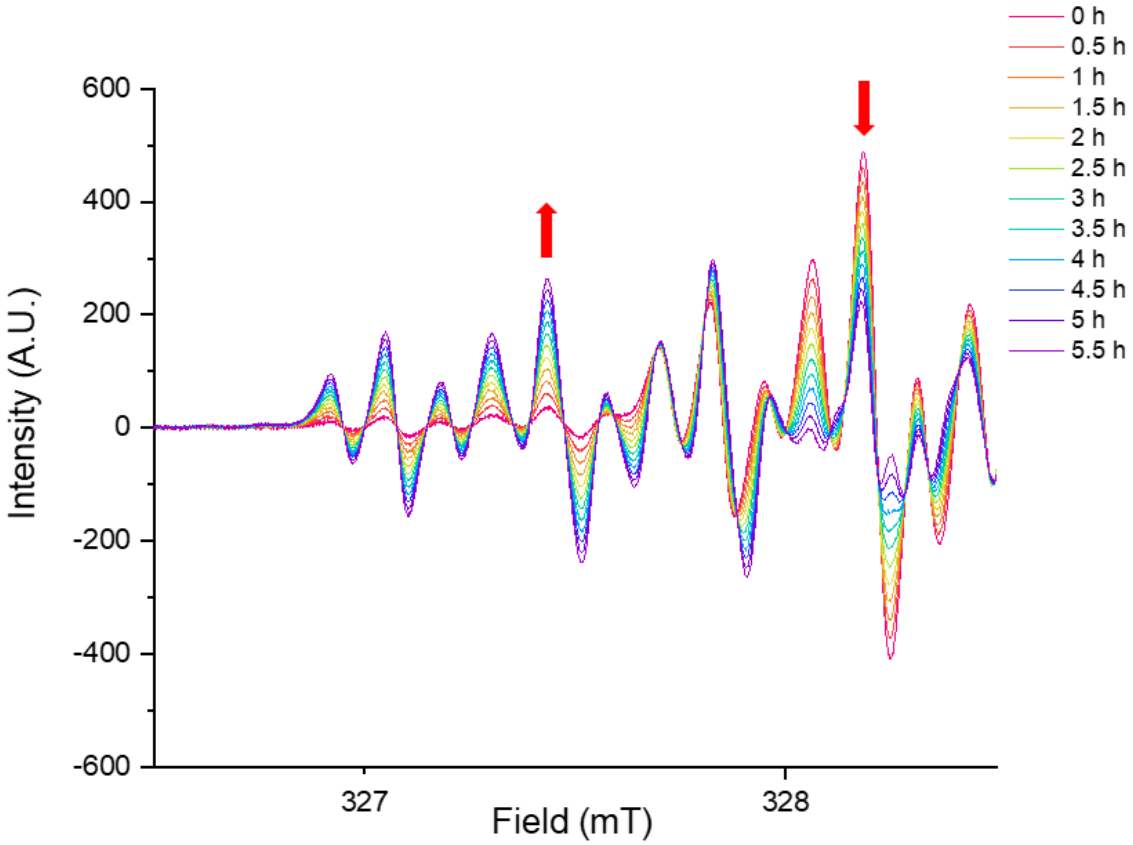

Figure S202. EPR kinetic monitoring of the reaction between $PhNO_2$ and **1** in pentane at 10^{-4} M. Zoom on the region between 326.5 and 328.7 mT

e) Reaction of 1 with $FPhNO_2$

Institut Polytechnique de Paris
91120 Palaiseau, France

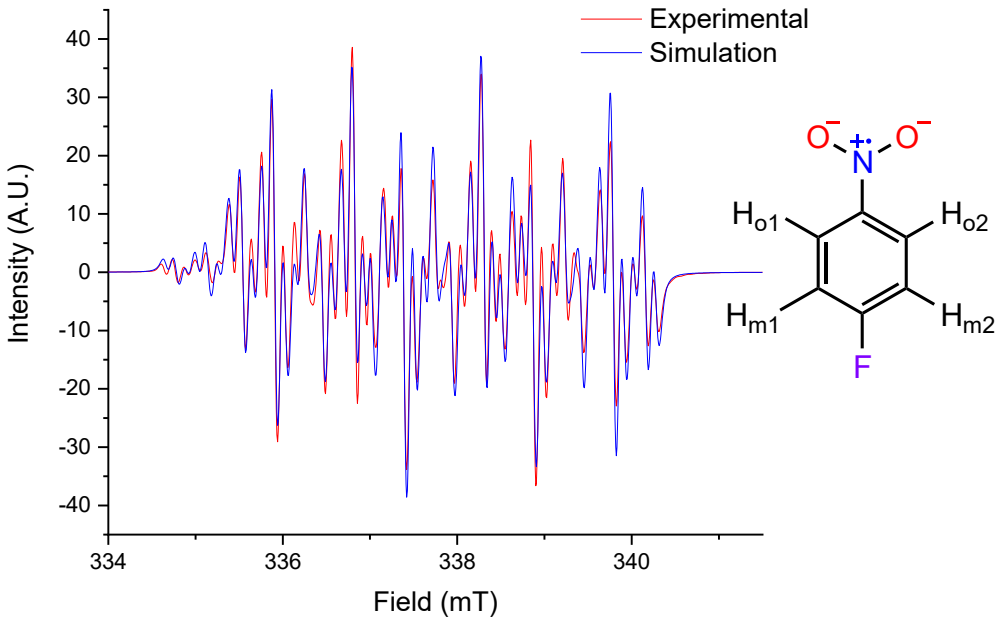

Figure S203. EPR spectrum of the reaction between $FPhNO_2$ and **1** in pentane at 10^{-4} M

Parameter	Value
System α	
g	1.9965
A(^{14}N)	1.4786
A($^{1}H_{o1}$)	0.3718
A($^{1}H_{o2}$)	0.3598
A($^{1}H_{m1}$)	0.1234
A($^{1}H_{m2}$)	0.1161
A(^{19}F)	0.9170
lwpp	[0.050 0.049]
weight	85.0%
System β	
g	2.0017
A(^{14}N)	1.4100
A($^{1}H_{o1}$)	0.3631
A($^{1}H_{o2}$)	0.3620
A($^{1}H_{m1}$)	0.1297
A($^{1}H_{m2}$)	0.1025
A(^{19}F)	0.8424
lwpp	[0.050 0.050]
weight	15.3%

Table S48. Fitting values associated with EPR spectrum of the reaction between $FPhNO_2$ and **1** in pentane. A values are given in mT

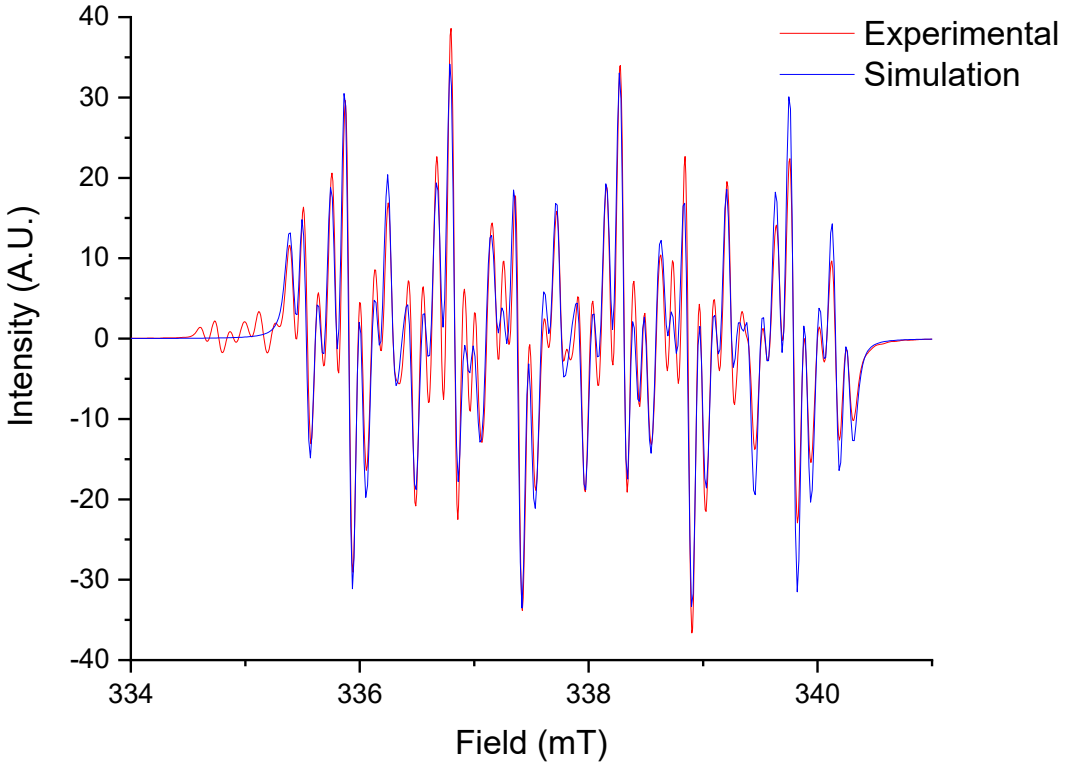

Figure S204. Fitting of system α for the reaction between $FPhNO_2$ and **1** in pentane

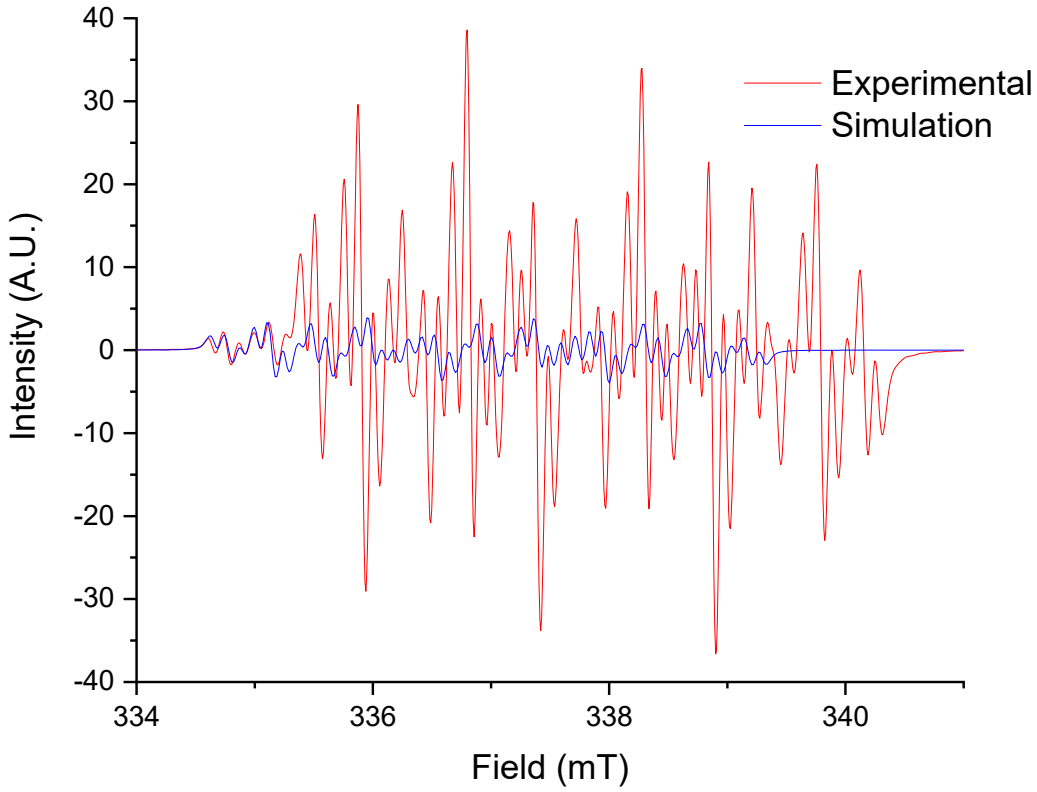

Figure S205. Fitting of system β for the reaction between $ClPhNO_2$ and **1** in pentane

Institut Polytechnique de Paris
91120 Palaiseau, France

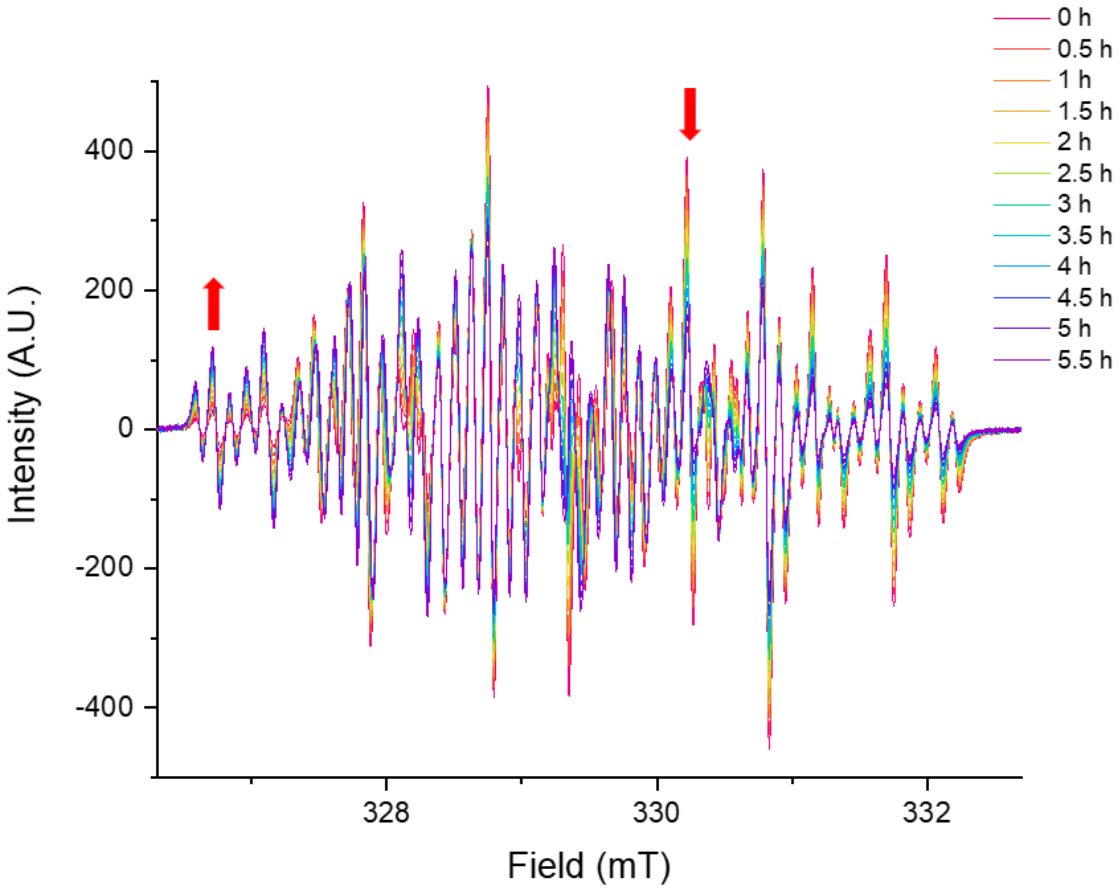

Figure S206. EPR kinetic monitoring of the reaction between $FPhNO_2$ and **1** in pentane at 10^{-4} M

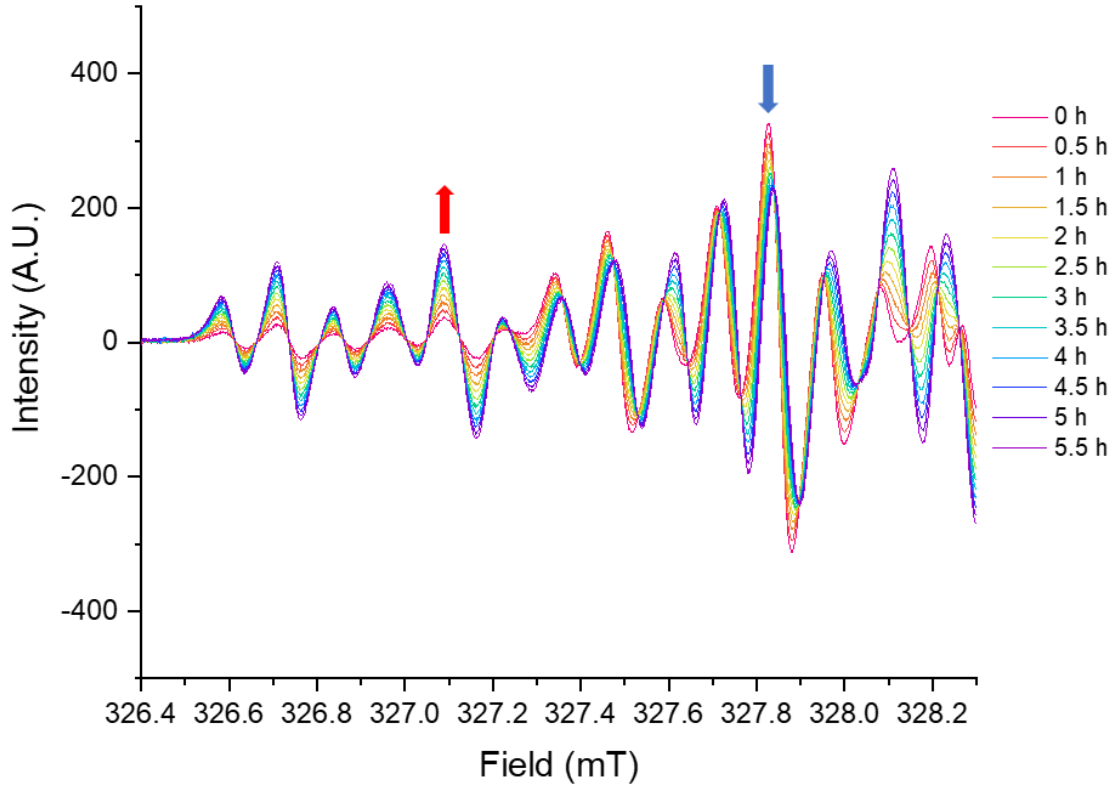

Figure S207. EPR kinetic monitoring of the reaction between $FPhNO_2$ and **1** in pentane at 10^{-4} M. Zoom on the region between 326.4 and 328.3 mT

Institut Polytechnique de Paris
91120 Palaiseau, France

c) Reaction of 1 with $ClPhNO_2$

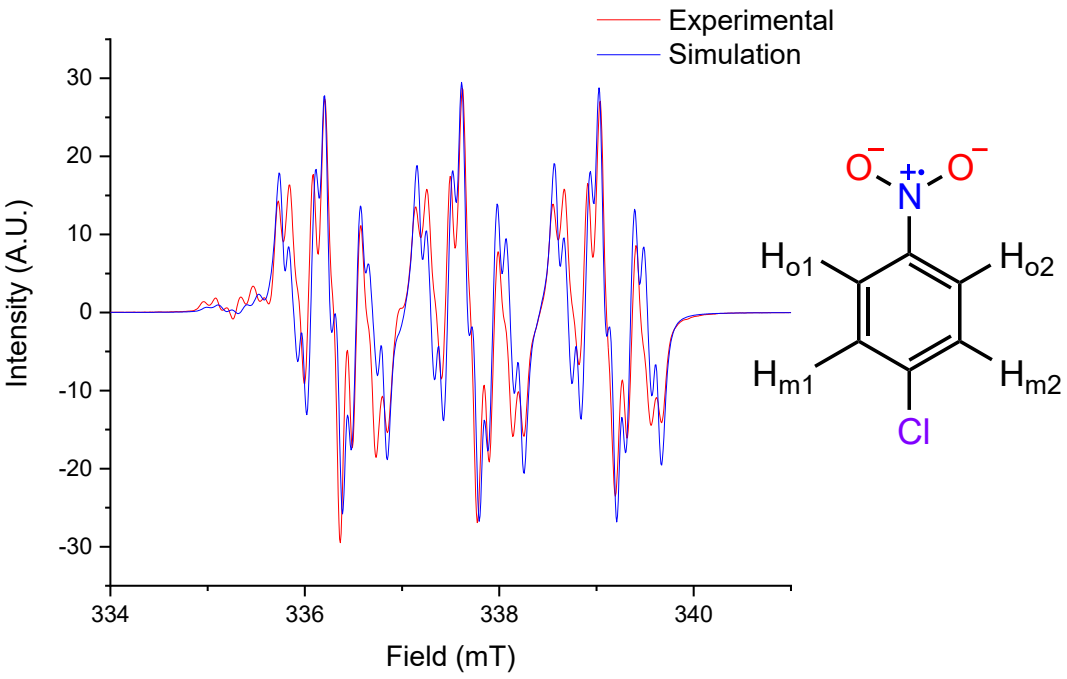

Figure S208. EPR spectrum of the reaction between $ClPhNO_2$ and **1** in pentane at 10^{-4} M

Parameter	Value
System α	
g	1.9973
$A(^{14}N)$	1.404
$A(^{1}H_{o1})$	0.460
$A(^{1}H_{o2})$	0.360
$A(^{1}H_{m1})$	0.135
$A(^{1}H_{m2})$	0.080
$A(^{35}Cl)$	/
lwpp	[0.05 0.05]
weight	93.4%
System β	
g	2.0021
$A(^{14}N)$	1.260
$A(^{1}H_{o1})$	0.410
$A(^{1}H_{o2})$	0.410
$A(^{1}H_{m1})$	0.149
$A(^{1}H_{m2})$	0.120
$A(^{35}Cl)$	0.05
lwpp	[0.05 0.05]
weight	7.0%

Table S49. Fitting values associated with EPR spectrum of the reaction between $ClPhNO_2$ and **1** in pentane. A values are given in mT

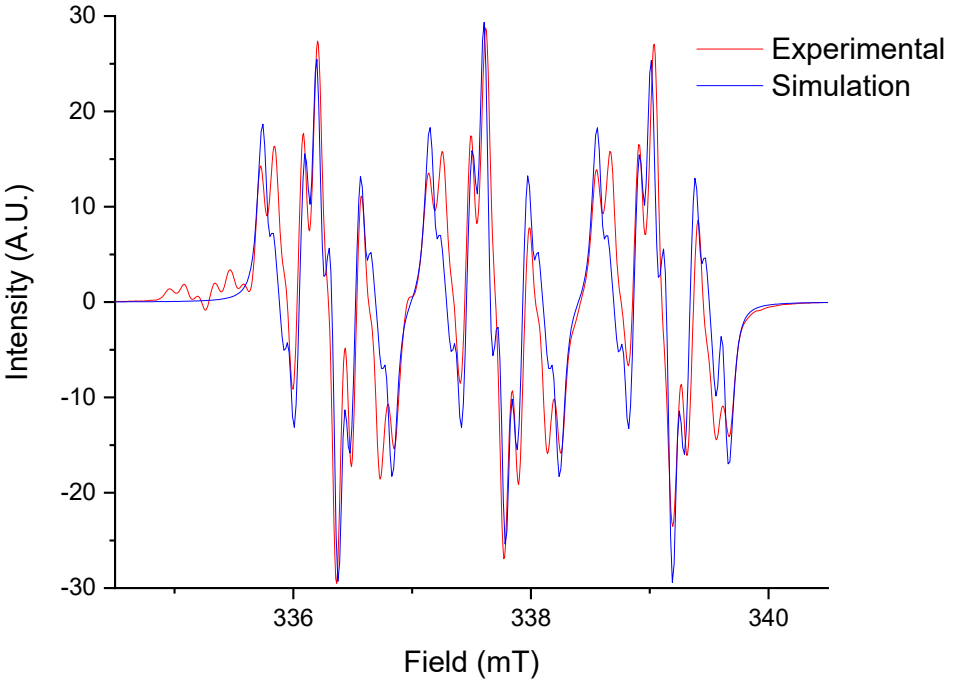

Figure S209. Fitting of system α for the reaction between $ClPhNO_2$ and **1** in pentane

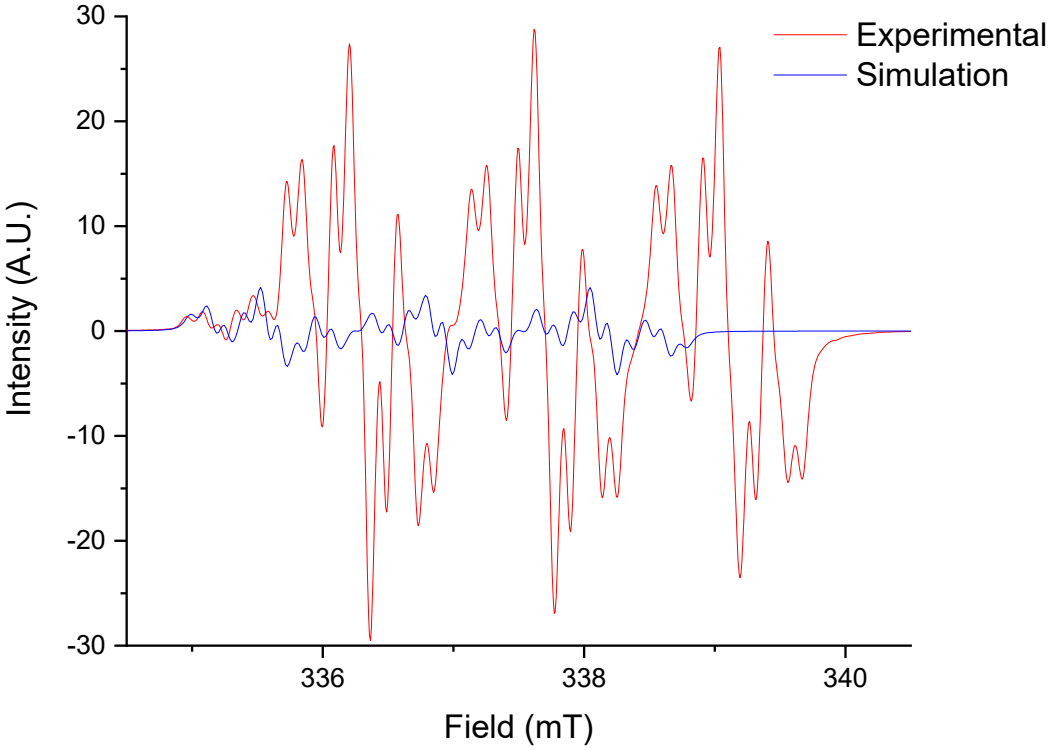

Figure S210. Fitting of system β for the reaction between $ClPhNO_2$ and **1** in pentane

Institut Polytechnique de Paris
91120 Palaiseau, France

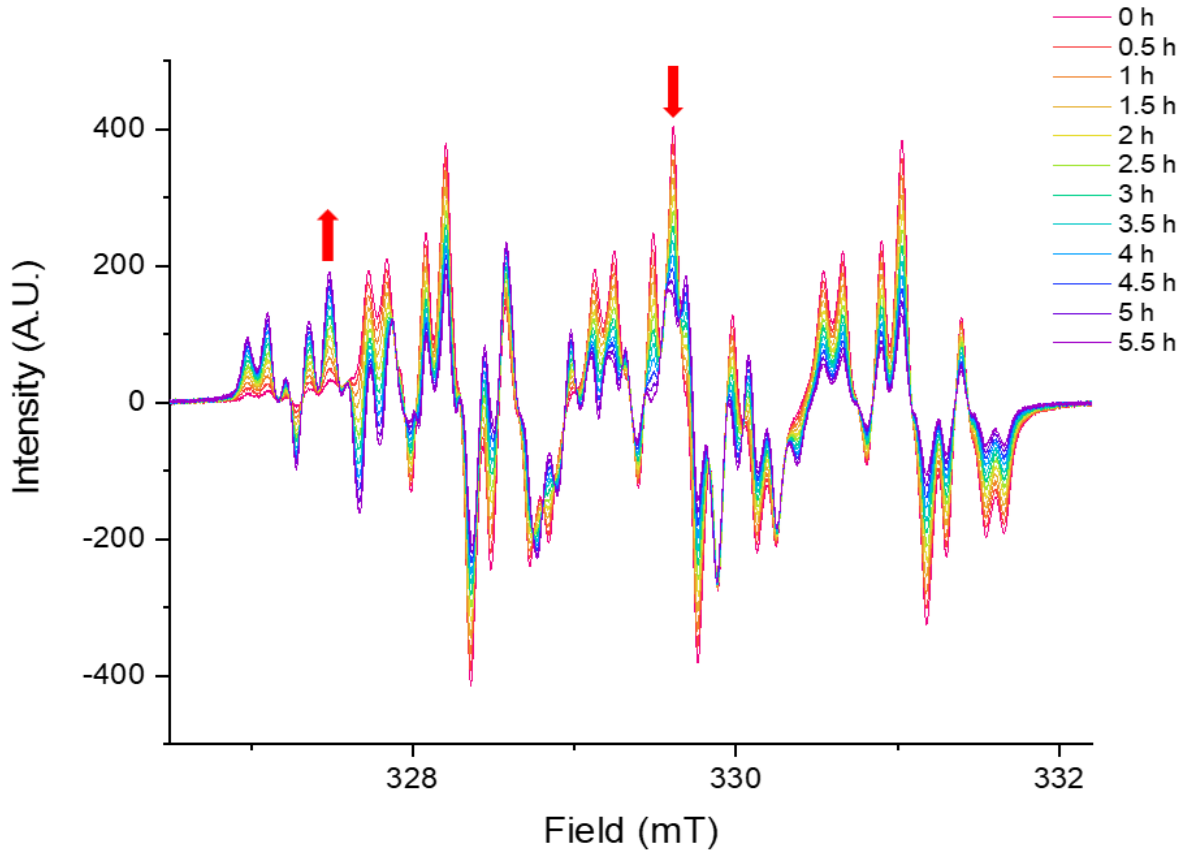

Figure S211. EPR kinetic monitoring of the reaction between $ClPhNO_2$ and **1** in pentane at 10^{-4} M

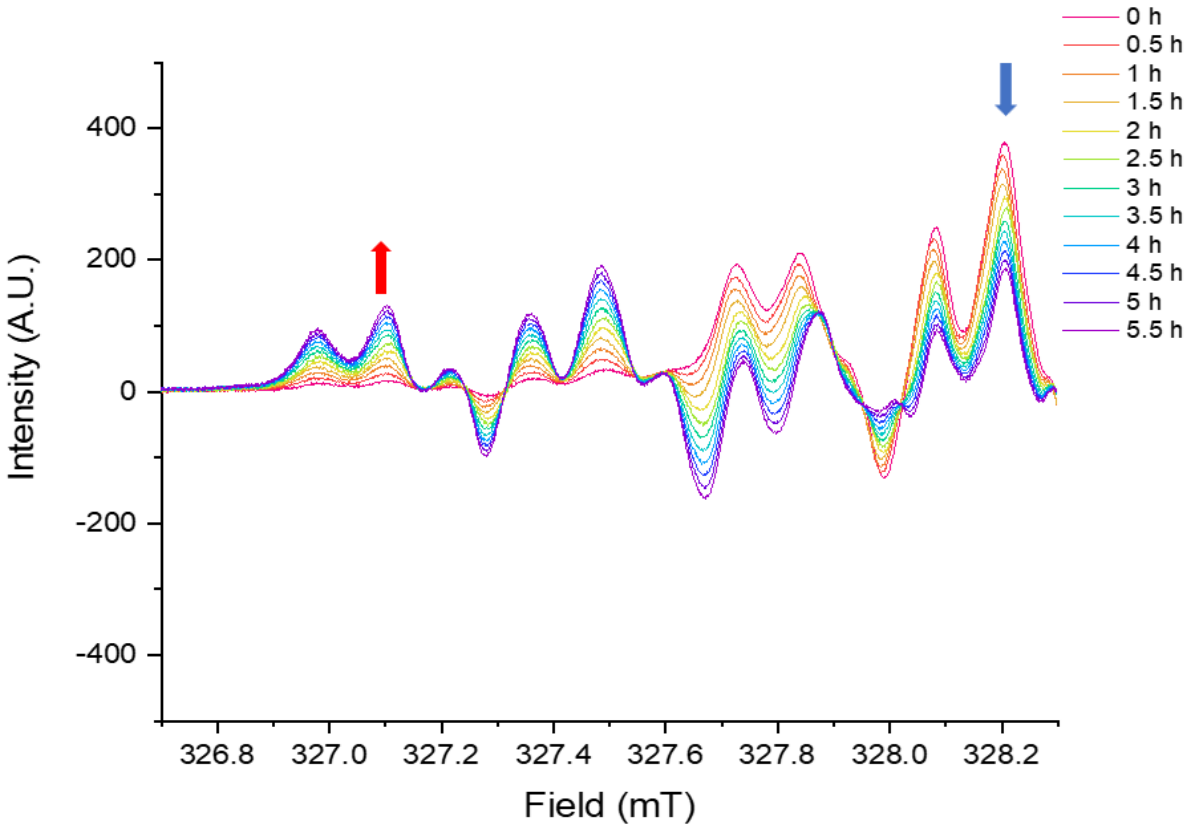

Figure S212. EPR kinetic monitoring of the reaction between $ClPhNO_2$ and **1** in pentane at 10^{-4} M. Zoom on the region between 326.7 and 328.3 mT

d) Reaction of 1 with $MeOPhNO_2$

Institut Polytechnique de Paris
91120 Palaiseau, France

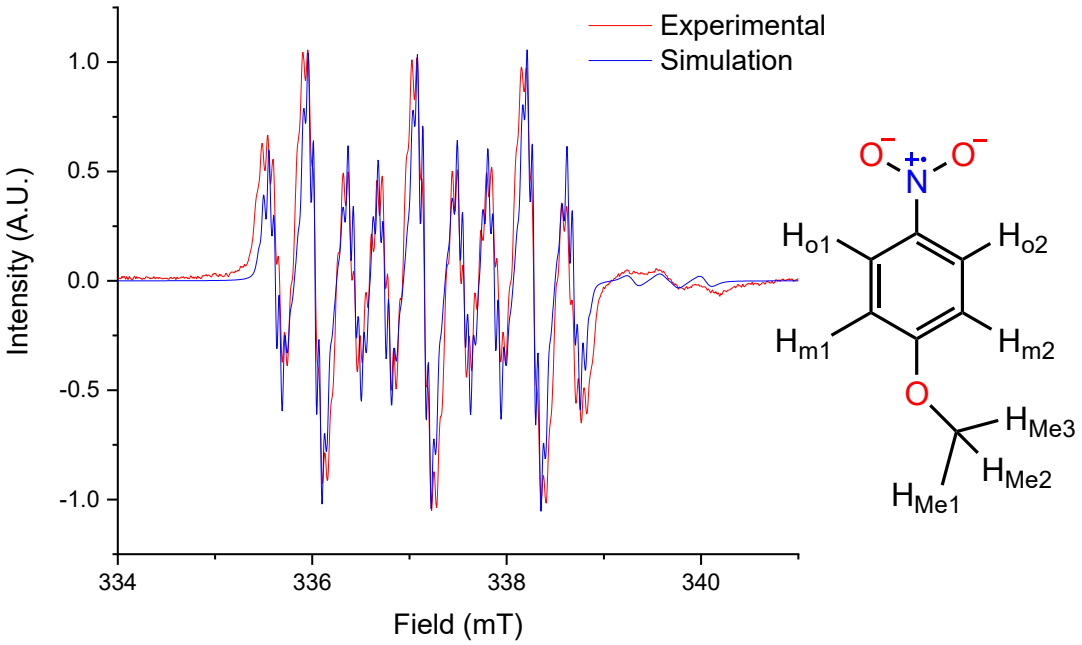

Figure S213. EPR spectrum of the reaction between $MeOPhNO_2$ and **1** in pentane at 10^{-4} M

Parameter	Value
System α	
g	2.0005
A(^{14}N)	1.125
A($^{1}H_{o1}$)	0.401
A($^{1}H_{o2}$)	0.412
A($^{1}H_{m1}$)	0.060
A($^{1}H_{m2}$)	0.060
A($^{1}H_{Me1}$)	0.055
A($^{1}H_{Me2}$)	0.055
A($^{1}H_{Me3}$)	0.041
A($^{1}H_{Me4}$)	0.041
lwpp	[0.027 0.027]
weight	92.1%
System β	
g	1.9956
A(^{14}N)	1.748
A($^{1}H_{o1}$)	0.324
A($^{1}H_{o2}$)	0.418
lwpp	[0.075 0.187]
weight	7.0%

Table S50. Fitting values associated with EPR spectrum of the reaction between $MeOPhNO_2$ and **1** in pentane. A values are given in mT

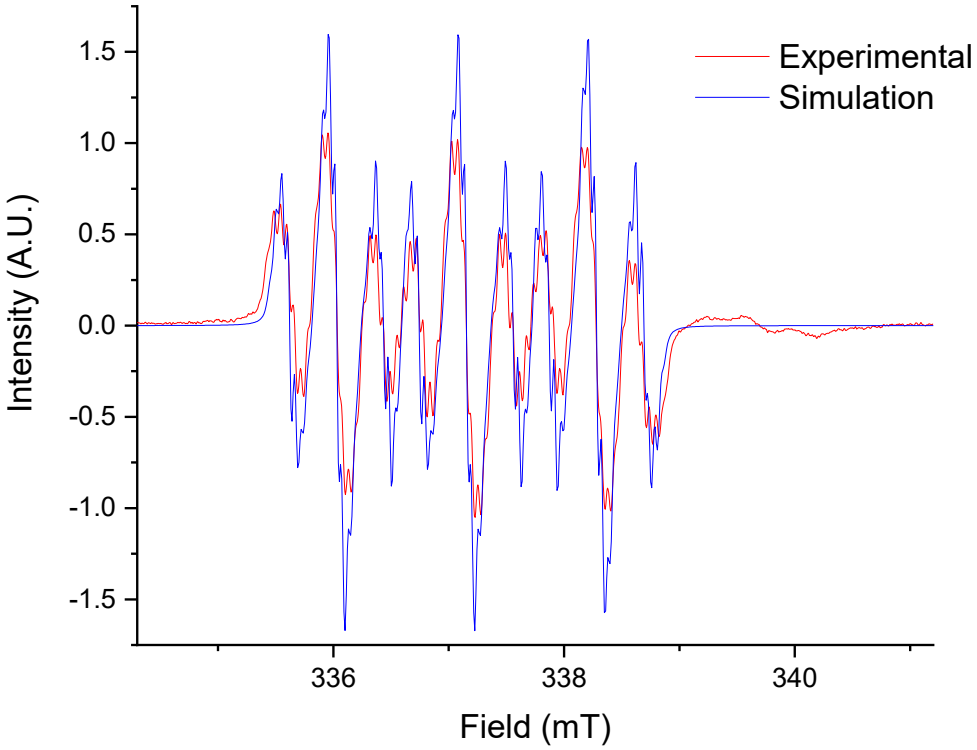

Figure S214. Fitting of system α for the reaction between $MeOPhNO_2$ and **1** in pentane

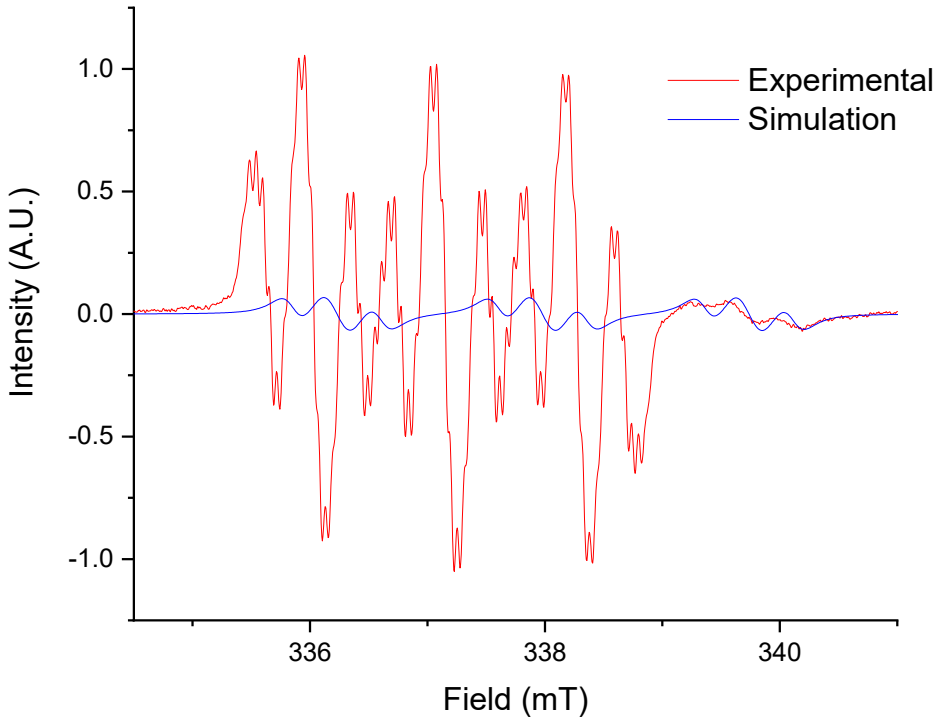

Figure S215. Fitting of system β for the reaction between $MeOPhNO_2$ and **1** in pentane

Institut Polytechnique de Paris
91120 Palaiseau, France

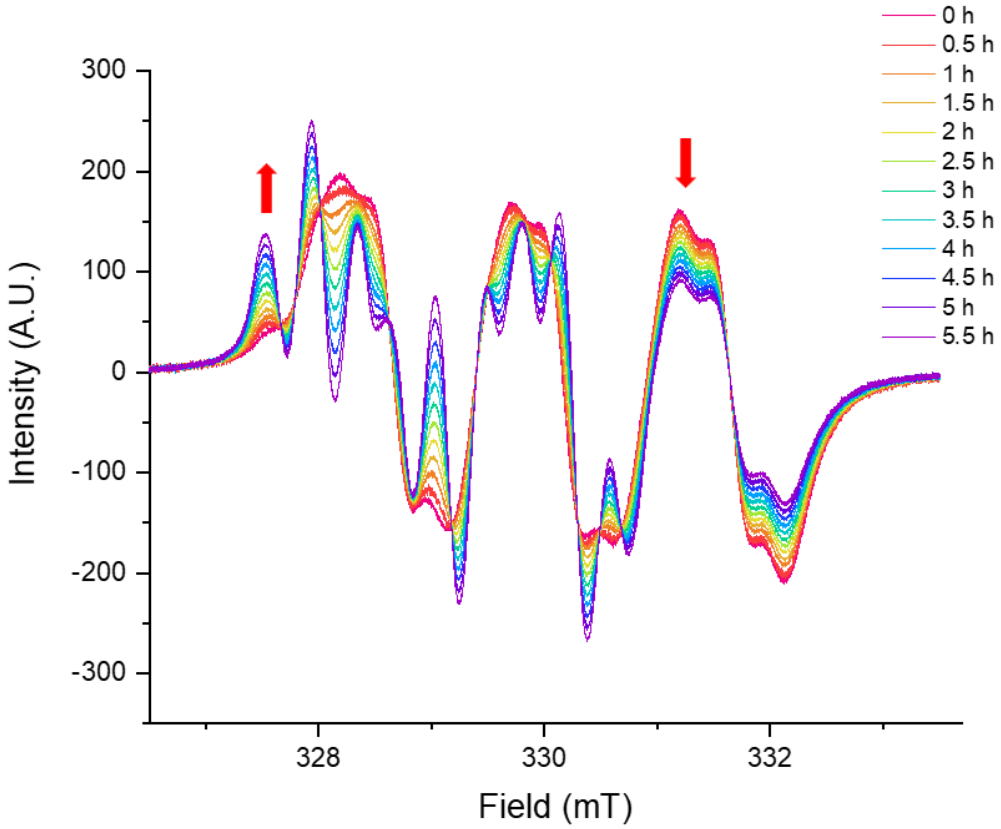

Figure S216. EPR kinetic monitoring of the reaction between $MeOPhNO_2$ and **1** in pentane at 10^{-4} M.

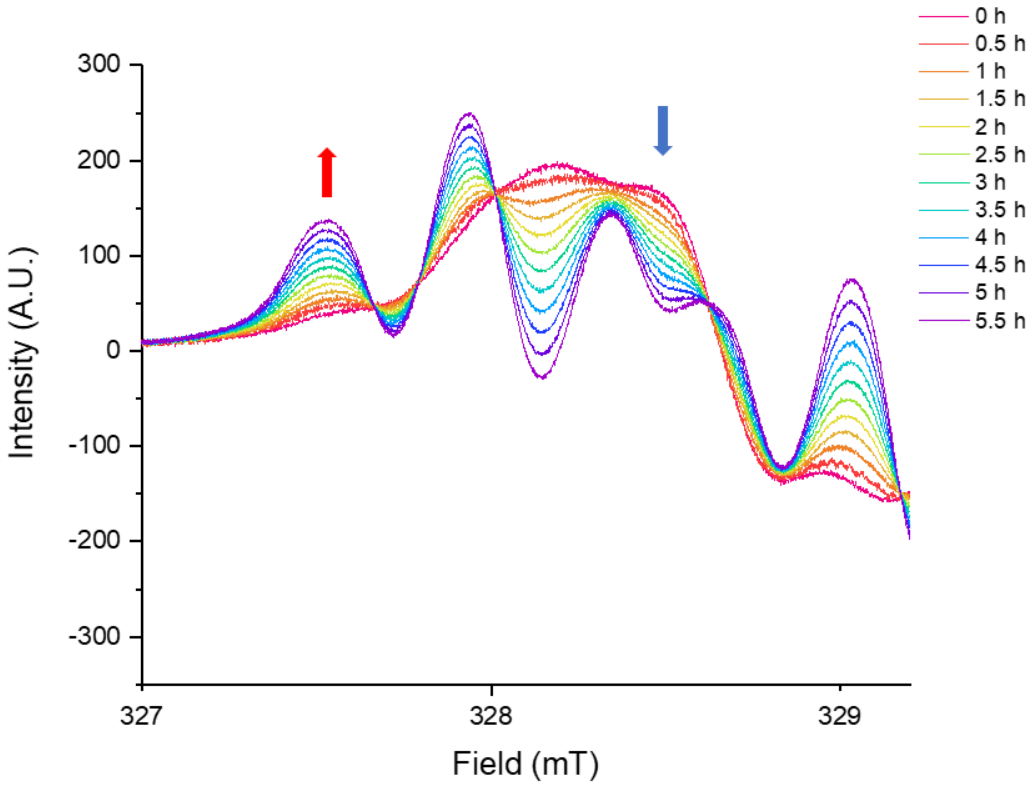

Figure S217. EPR kinetic monitoring of the reaction between $MeOPhNO_2$ and **1** in pentane at 10^{-4} M. Zoom on the region between 327.0 and 329.3 mT

Institut Polytechnique de Paris
91120 Palaiseau, France

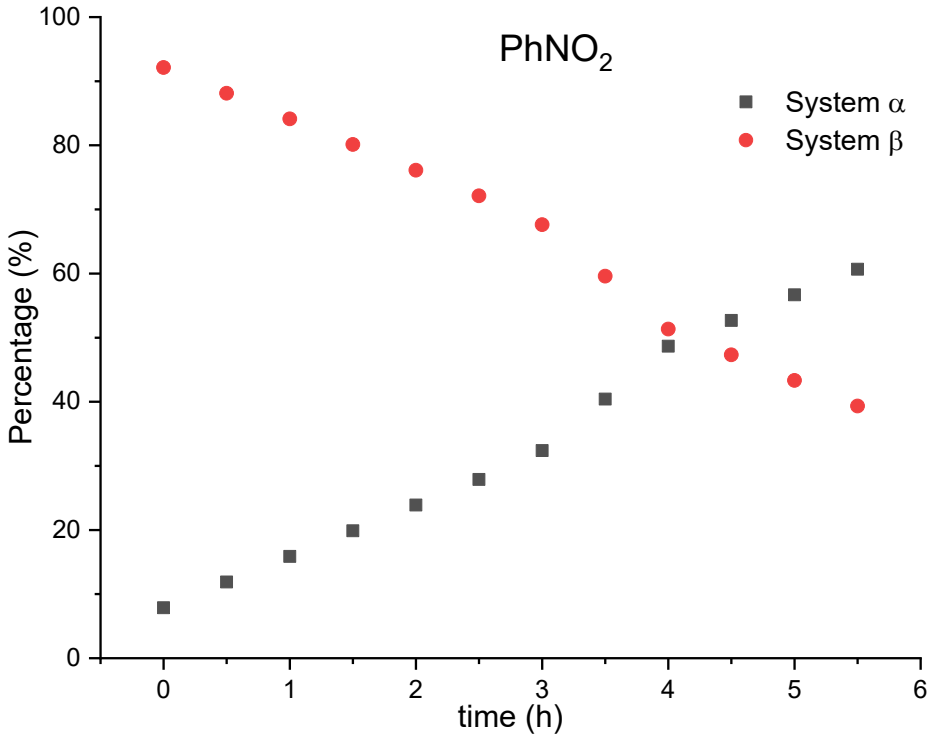

Figure S218. Evolution of relative quantities of system α and system β in the reaction between $PhNO_2$ and **1** in pentane at 10^{-4} M. The quantities were calibrated on the initial intensity value of system β (coordinated radical). Intensities were recorded from characteristic peaks of each system (respectively 327.43 and 328.18 mT, indicated as red arrows on **Figure S201**)

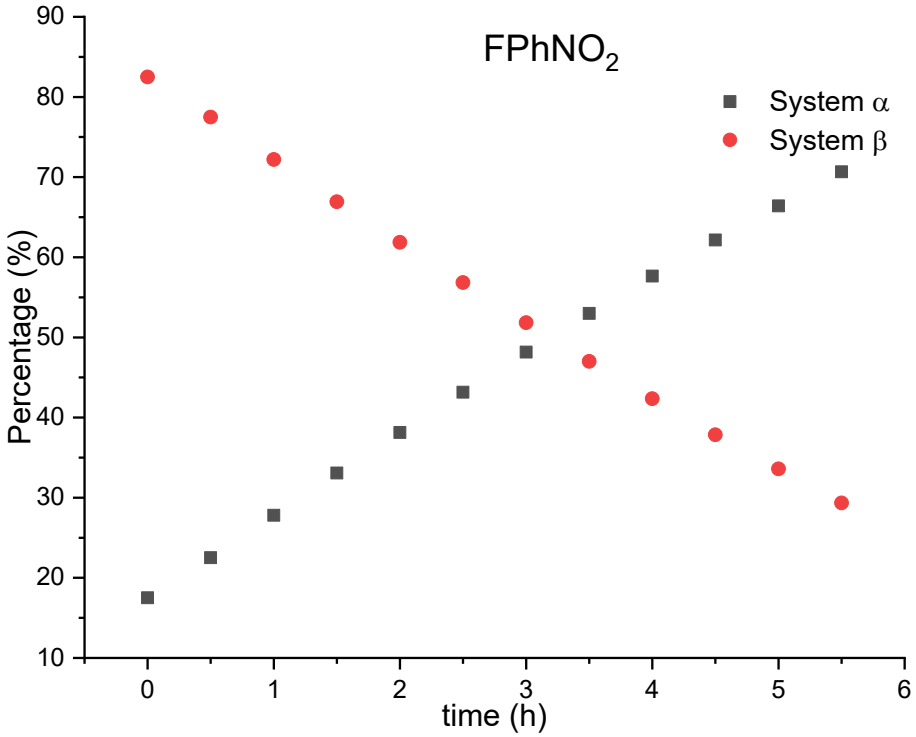

Figure S219. Evolution of relative quantities of system α and system β in the reaction between $FPhNO_2$ and **1** in pentane at 10^{-4} M. The quantities were calibrated on the initial intensity value of system β (coordinated radical). Intensities were recorded from characteristic peaks of each system (respectively 327.08 and 330.22 mT, indicated as red arrows on **Figure S206**)

Institut Polytechnique de Paris
91120 Palaiseau, France

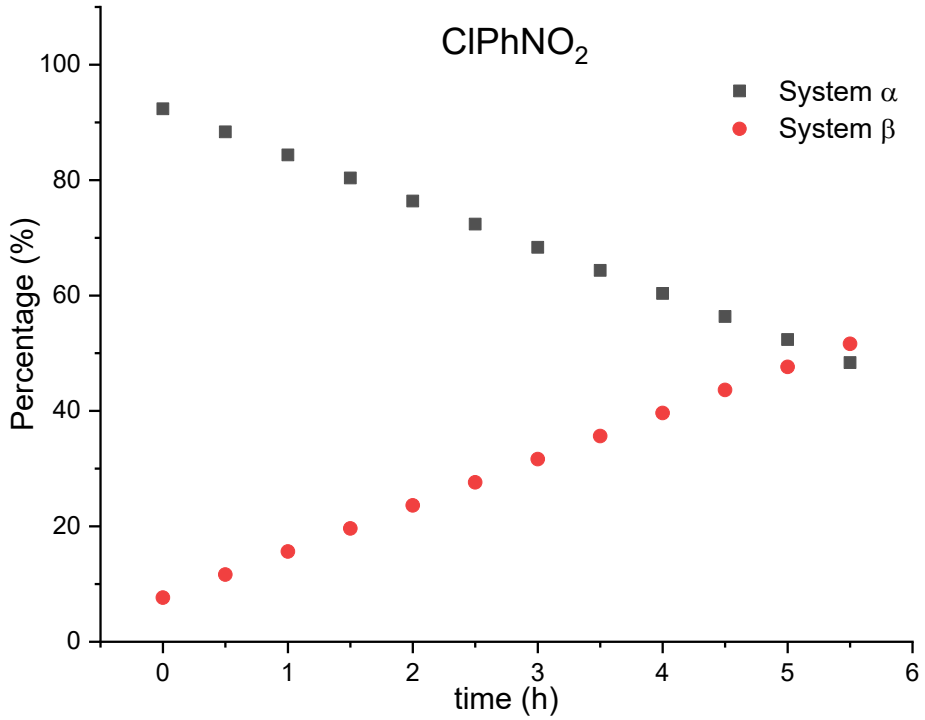

Figure S220. Evolution of relative quantities of system α and system β in the reaction between $ClPhNO_2$ and **1** in pentane at 10^{-4} M. The quantities were calibrated on the initial intensity value of system β (coordinated radical). Intensities were recorded from characteristic peaks of each system (respectively 327.48 and 329.61 mT, indicated as red arrows on **Figure S211**)

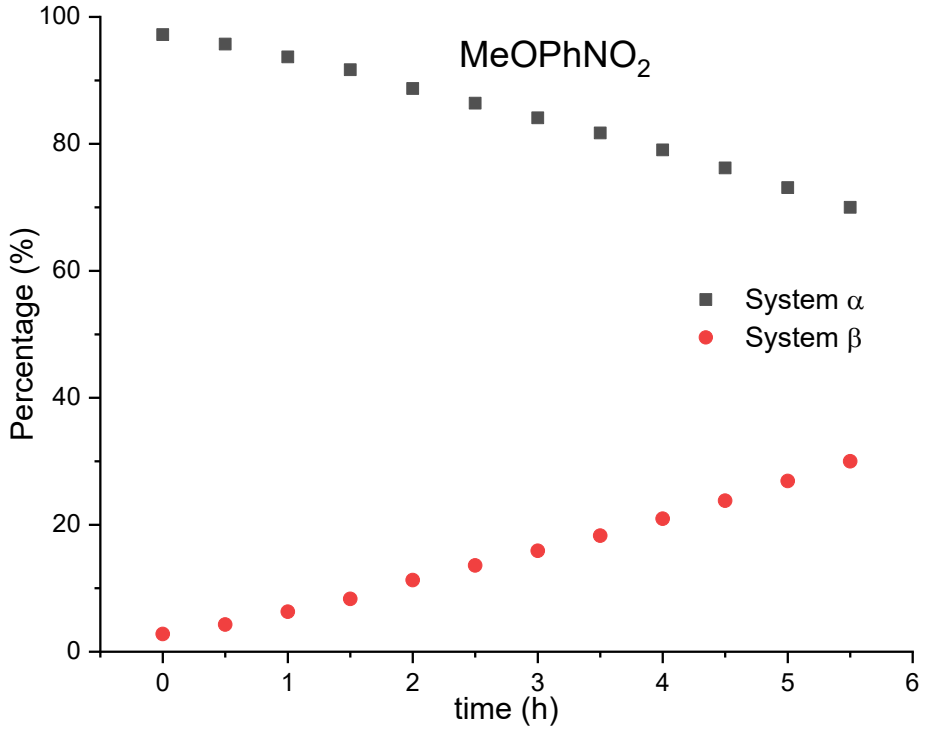

Figure S221. Evolution of relative quantities of system α and system β in the reaction between $MeOPhNO_2$ and **1** in pentane at 10^{-4} M. The quantities were calibrated on the initial intensity value of system β (coordinated radical). Intensities were recorded from characteristic peaks of each system (respectively 327.52 and 331.19 mT, indicated as red arrows on **Figure S216**)

Institut Polytechnique de Paris
91120 Palaiseau, France

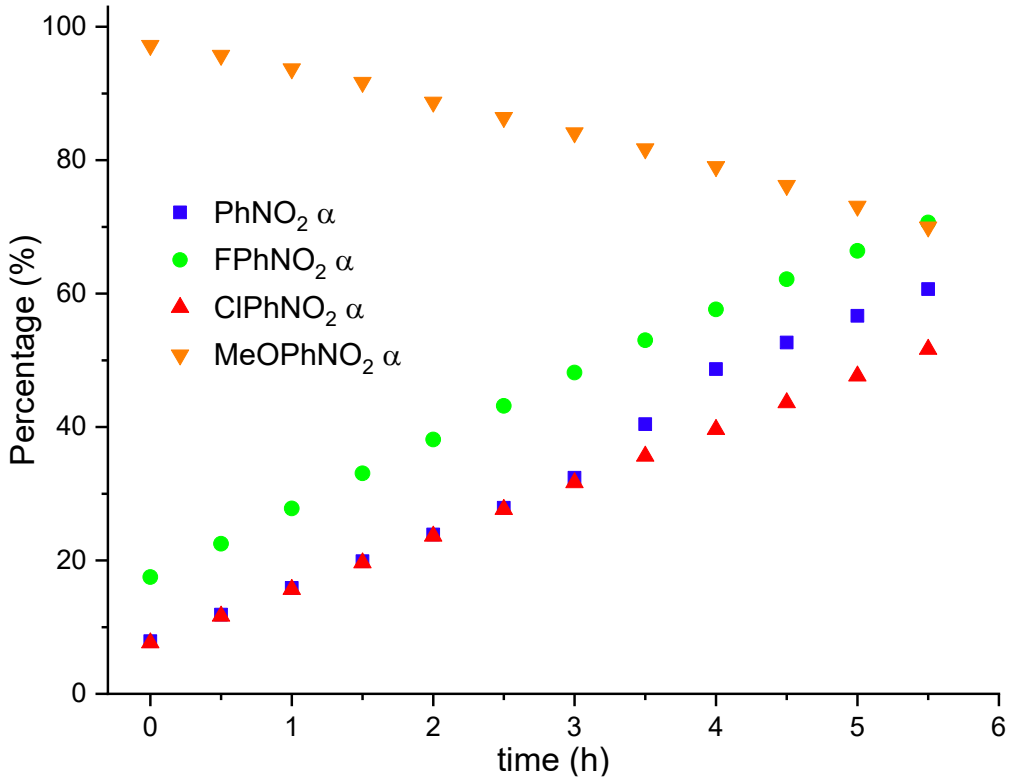

Figure S222. Superimposition of appearance of system α in the reactions of $PhNO_2$, $FPhNO_2$, $ClPhNO_2$ and $MeOPhNO_2$ with **1** in pentane at 10^{-4} M

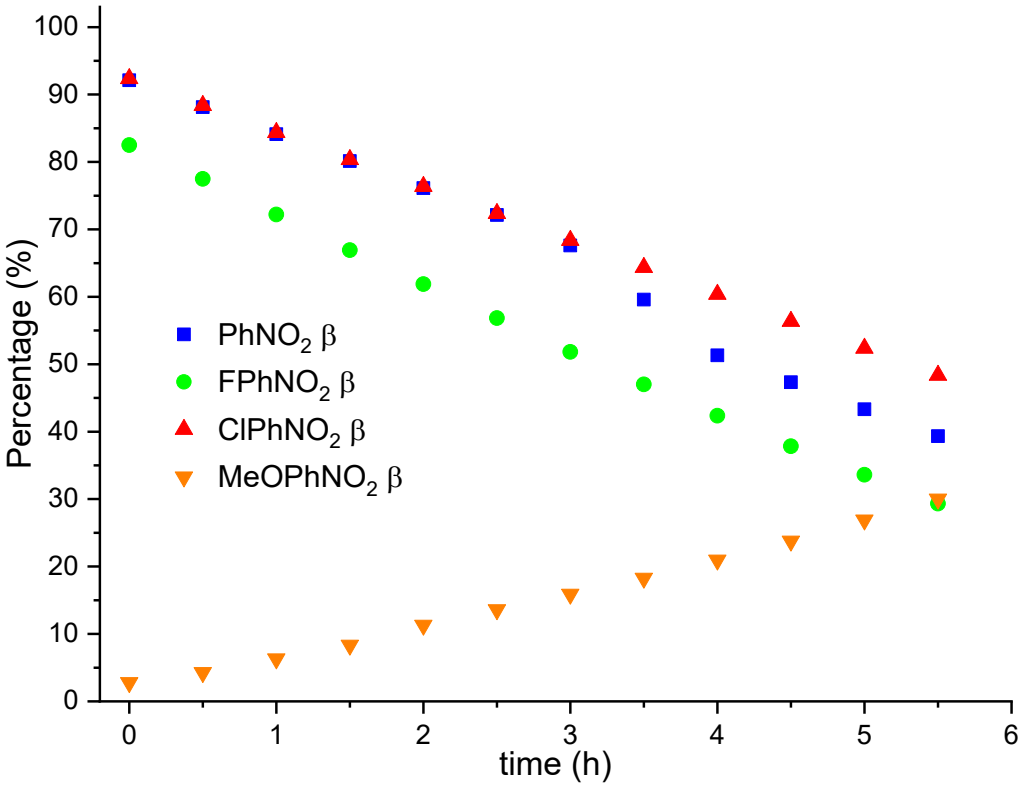

Figure S223. Superimposition of appearance of system β in the reactions of $PhNO_2$, $FPhNO_2$, $ClPhNO_2$ and $MeOPhNO_2$ with **1** in pentane at 10^{-4} M

Institut Polytechnique de Paris
91120 Palaiseau, France

$PhNO_2$		
t (h)	% α	% β
0	7.9	92.1
0.5	11.9	88.1
1	15.9	84.1
1.5	19.9	80.1
2	23.9	76.1
2.5	27.9	72.1
3	32.4	67.6
3.5	40.4	59.6
4	48.7	51.3
4.5	52.7	47.3
5	56.7	43.3

$FPhNO_2$		
t (h)	% α	% β
0	17.5	82.5
0.5	22.5	77.5
1	27.8	72.2
1.5	33.1	66.9
2	38.1	61.9
2.5	43.2	56.8
3	48.2	51.8
3.5	53.0	47.0
4	57.6	42.4
4.5	62.2	37.8
5	66.4	33.6

$ClPhNO_2$		
t (h)	% α	% β
0	7.6	92.4
0.5	11.6	88.4
1	15.6	84.4
1.5	19.6	80.4
2	23.6	76.4
2.5	27.6	72.4
3	31.6	68.4
3.5	35.6	64.4
4	39.6	60.4
4.5	43.6	56.4
5	47.6	52.4

$MeOPhNO_2$		
t (h)	% α	% β
0	97.2	2.8
0.5	95.7	4.3
1	93.7	6.3
1.5	91.7	8.3
2	88.7	11.3
2.5	86.4	13.6
3	84.1	15.9
3.5	81.7	18.3
4	79.0	21.0
4.5	76.2	23.8
5	73.1	26.9

Table S51. Values obtained from the automatic fitting for the relative weights of the two systems α and β for the different nitro derivatives. The corresponding algorithm is provided in Appendix

e) Photoinduced reactivity with $^{t}BuNO_2$

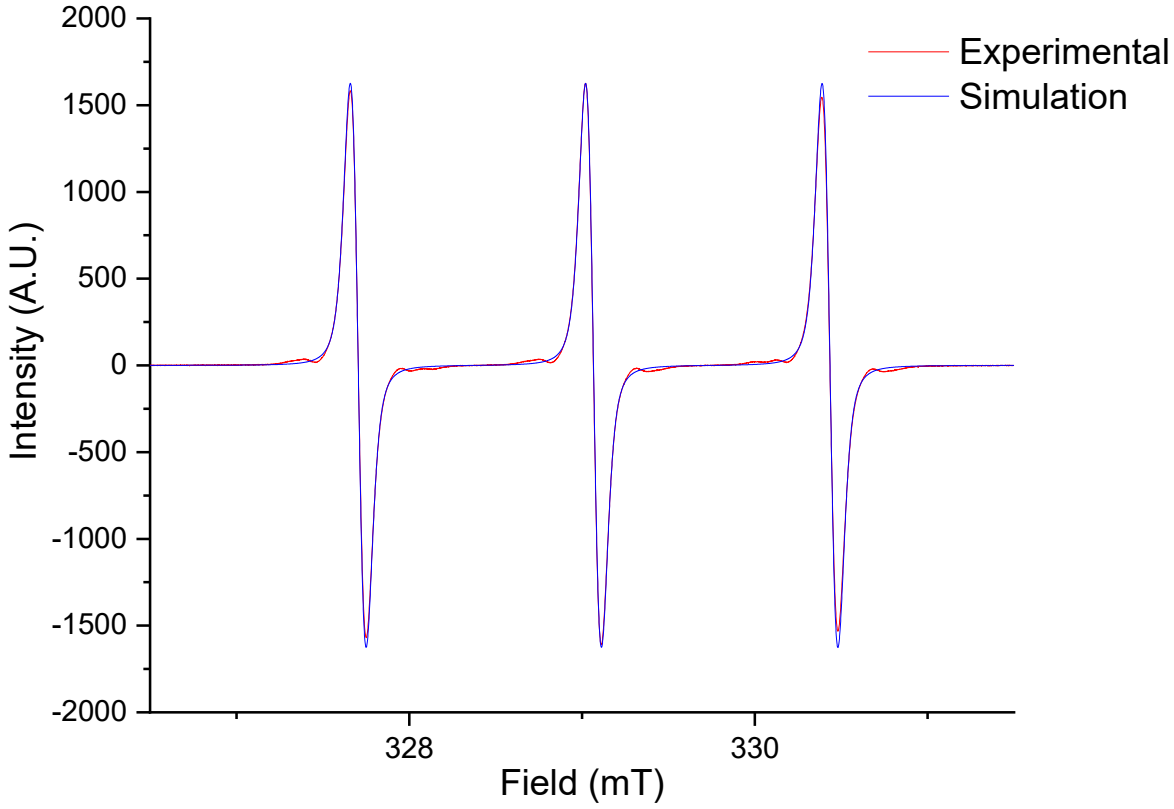

Figure S224. EPR spectrum of the reaction between $^{t}BuNO_2$ and **1** in pentane at 10^{-4} M after 5 minutes in ambient light

Parameter	Value
g	2.0021
A(^{14}N)	1.365
lwpp	[0.0697 0.0379]

Table S52. Fitting values associated with EPR spectrum of the reaction between $^{t}BuNO_2$ and **1** in pentane after 5 minutes in ambient light. A value is given in mT

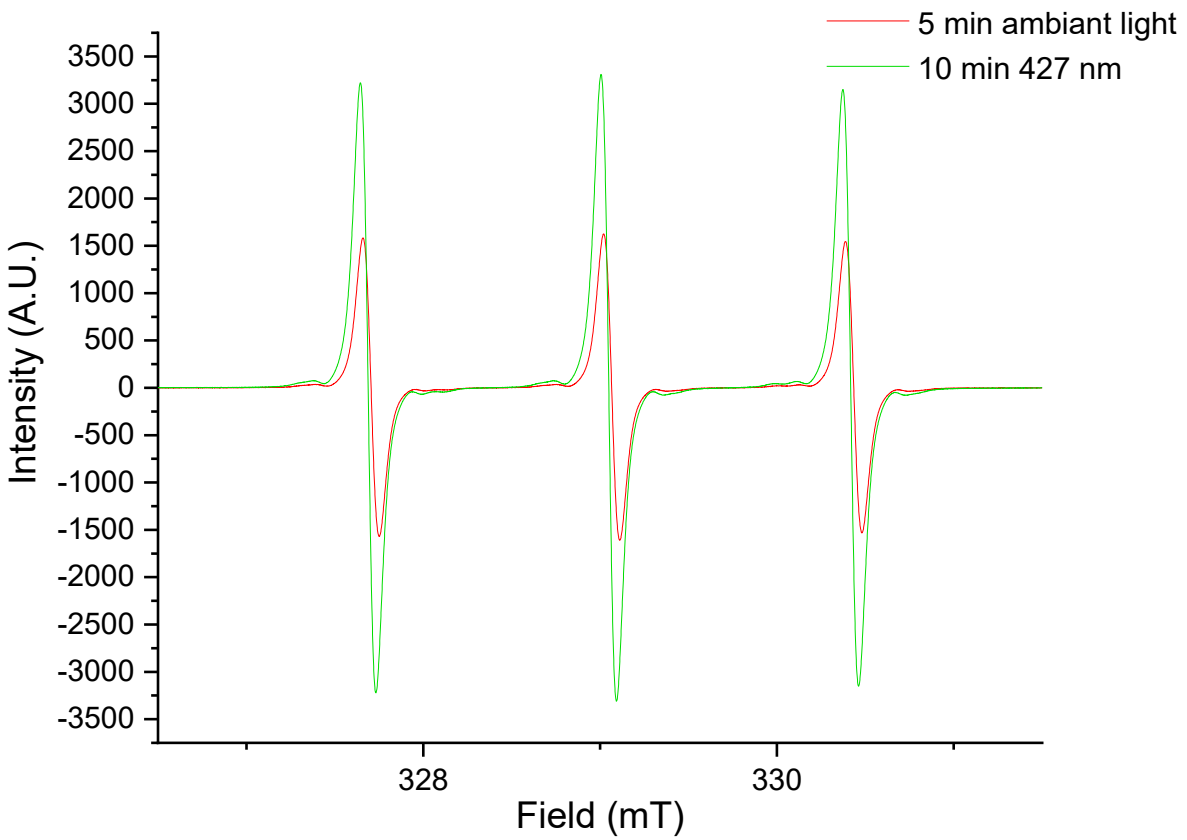

Figure S225. EPR spectrum of the reaction between $^{t}BuNO_2$ and **1** in pentane at 10^{-4} M after 5 minutes in ambient light (red) and after 10 minutes under irradiation at 427 nm

f) Photoinduced reactivity with PBN

Institut Polytechnique de Paris
91120 Palaiseau, France

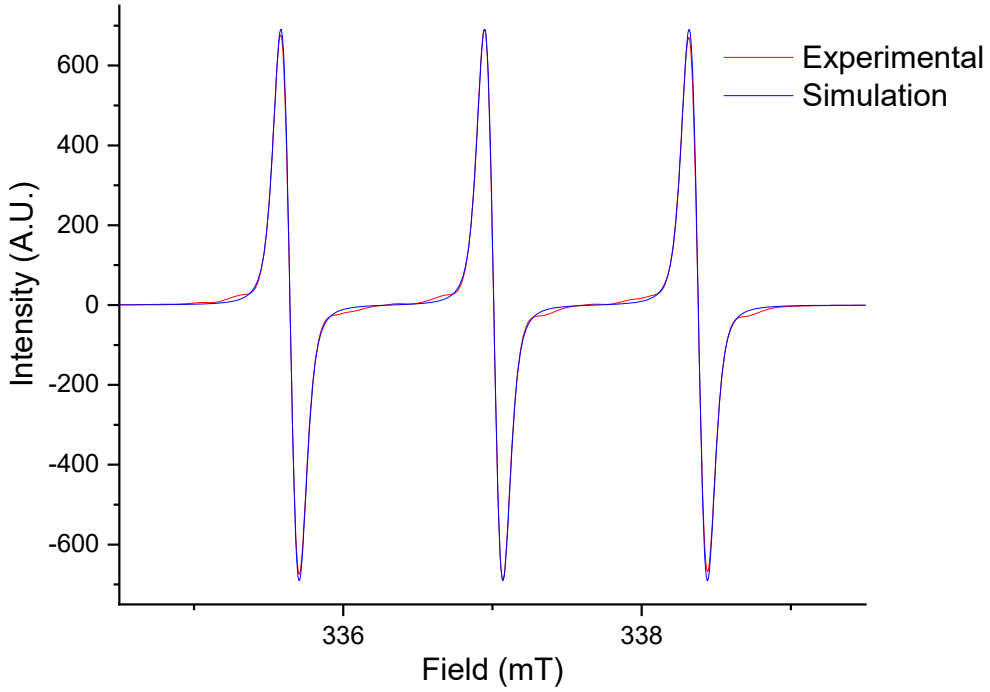

Figure S226. EPR spectrum of the reaction between PBN and **1** in pentane at 10^{-4} M after 12 minutes irradiation at 405 nm

Parameter	Value
g	2.0015
A(^{14}N)	1.367
lwpp	[0.094 0.050]

Table S53. Fitting values associated with EPR spectrum of the reaction between PBN and **1** in pentane. A value is given in mT

Institut Polytechnique de Paris
91120 Palaiseau, France

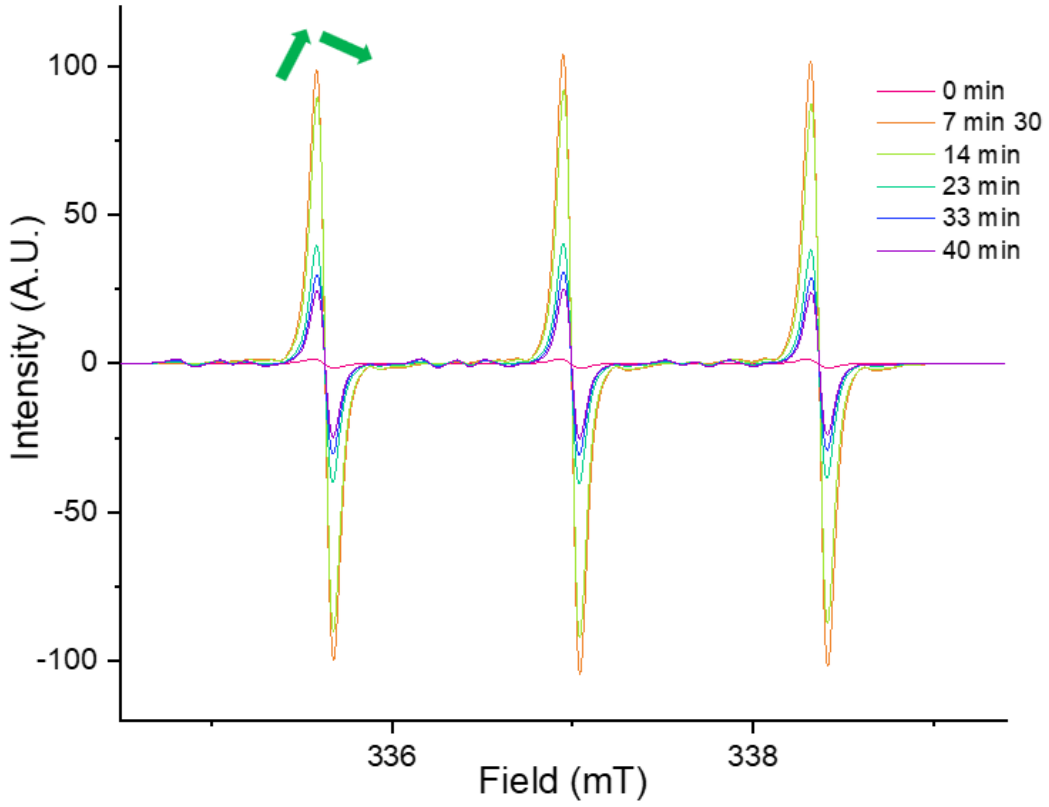

Figure S227. EPR spectrum of the reaction between PBN and **1** in pentane at 10^{-4} M after different irradiation times at 405 nm

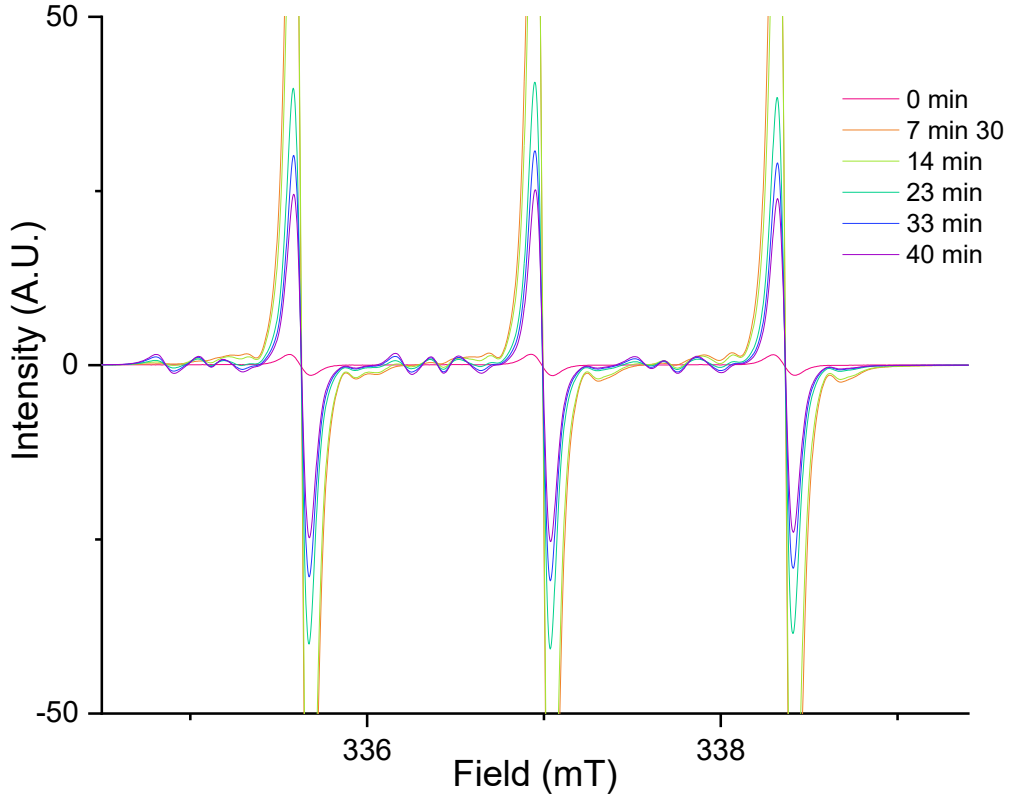

Figure S228. EPR spectrum of the reaction between PBN and **1** in pentane at 10^{-4} M after different irradiation times at 405 nm (zoomed)

IV. UV-visible and IR spectroscopy data

a) UV-visible data

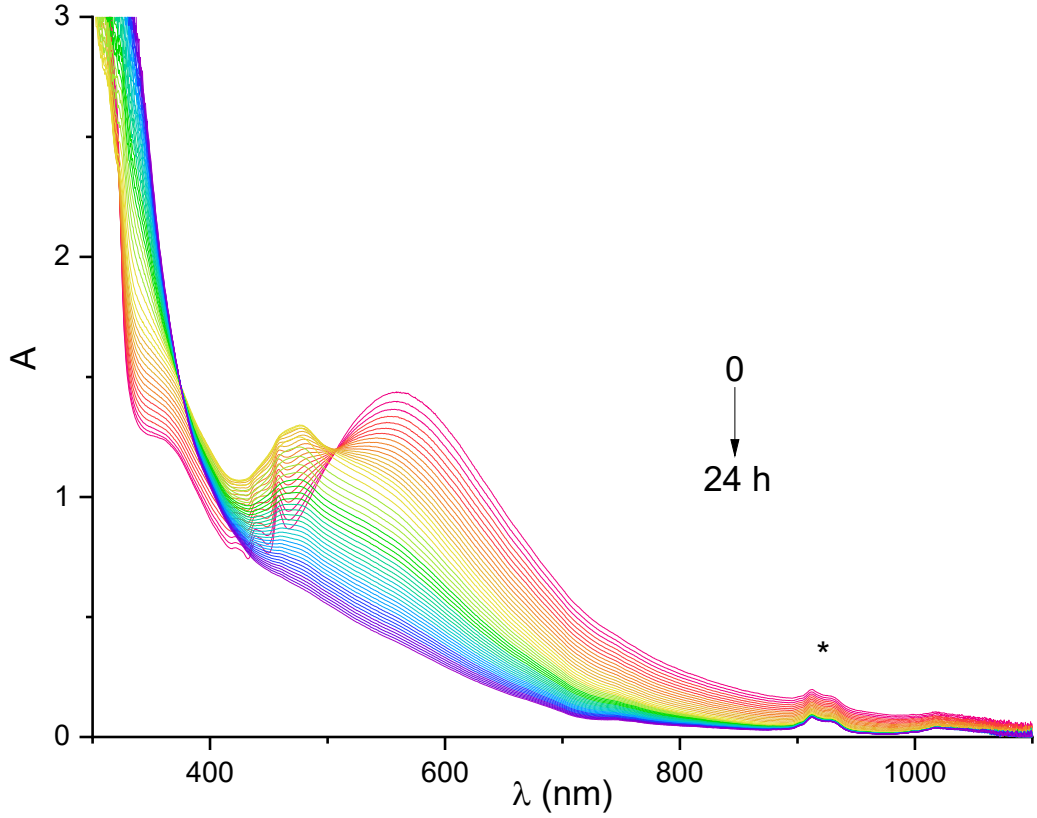

Figure S229. Kinetic UV-visible monitoring of the degradation of the species formed by the reaction between **1** and $PhNO_2$ in pentane (no baseline correction). Residual signal from the blank is indicated with *

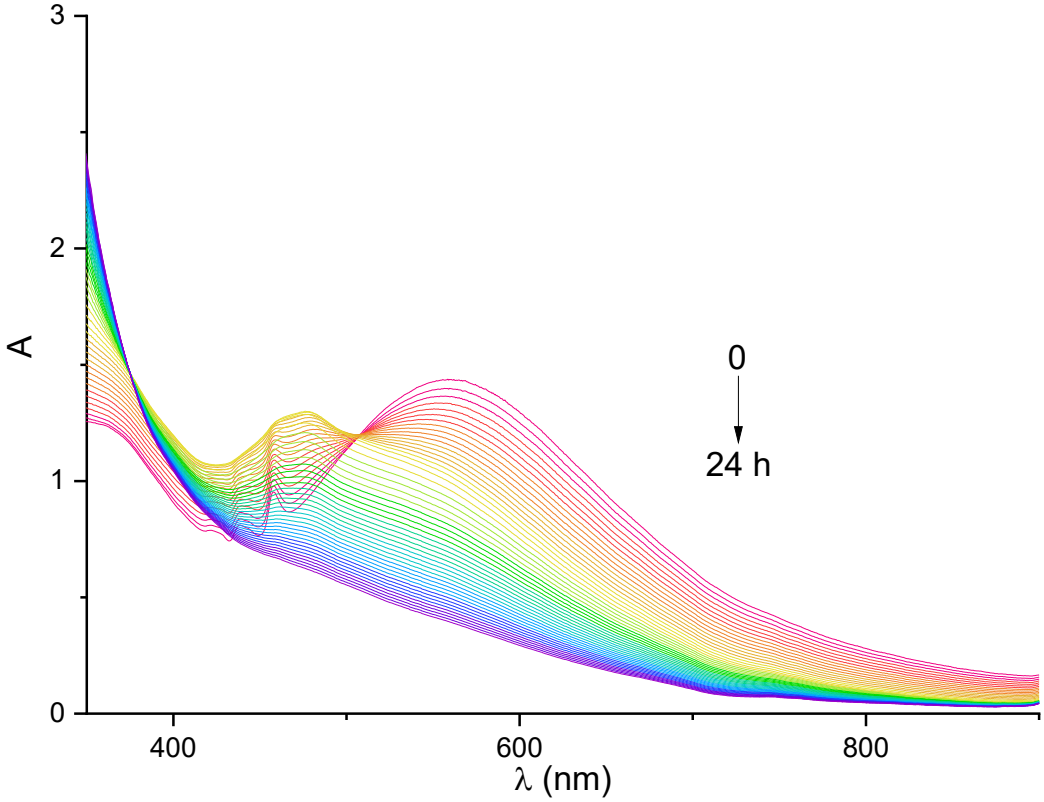

Figure S230. Kinetic UV-visible monitoring of the degradation of the species formed by the reaction between **1** and $PhNO_2$ in pentane (no baseline correction). Zoom between 350 and 900 nm

Institut Polytechnique de Paris
91120 Palaiseau, France

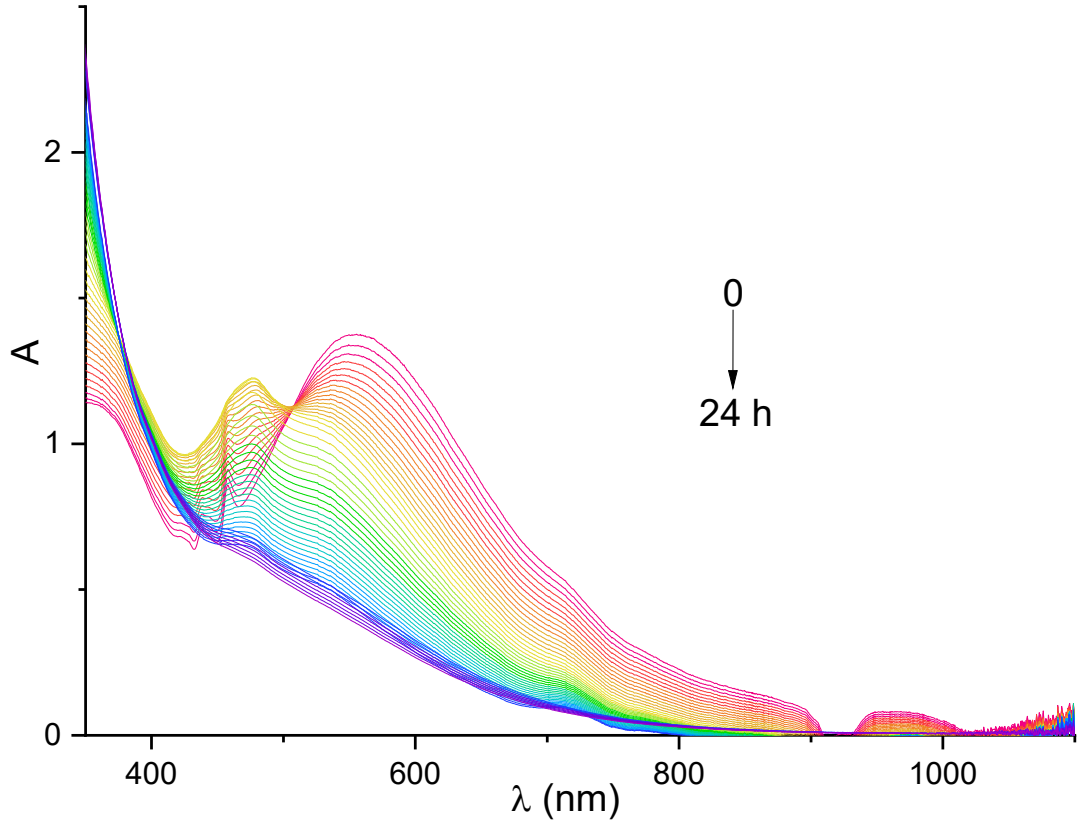

Figure S231. Kinetic UV-visible monitoring of the degradation of the species formed by the reaction between **1** and $PhNO_2$ in pentane (baseline correction)

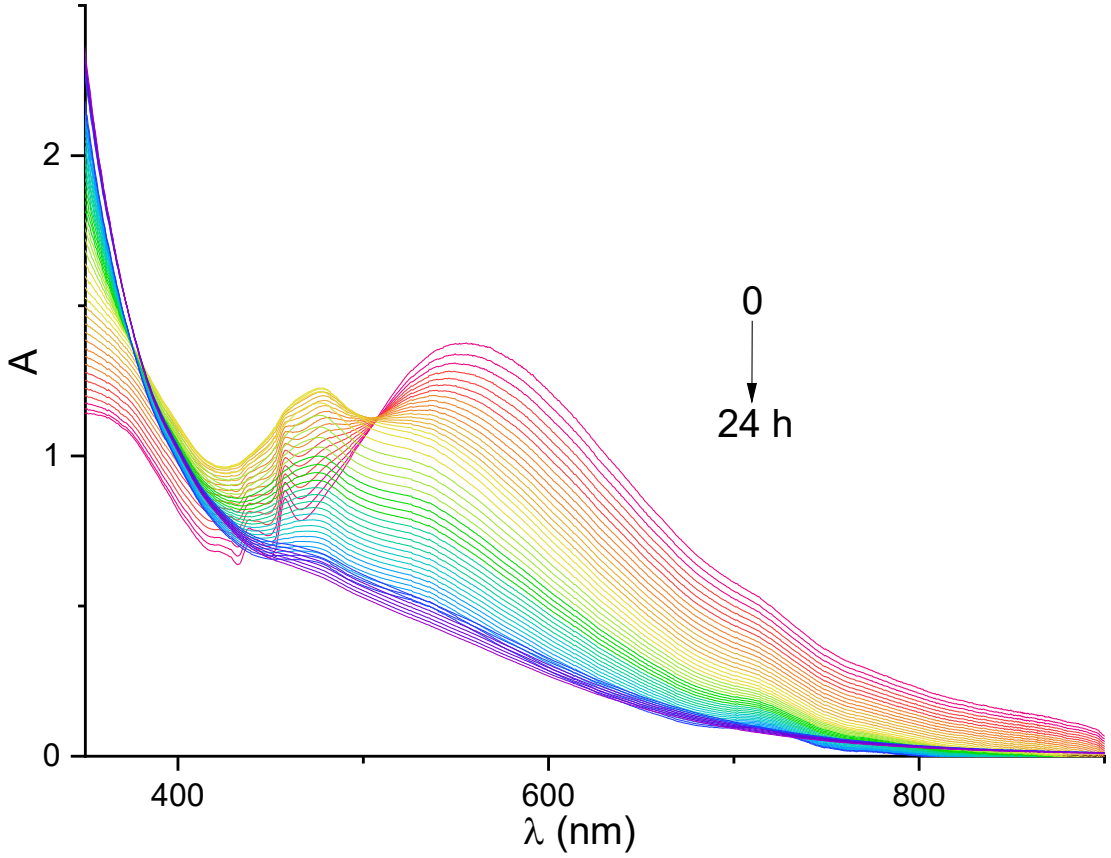

Figure S232. Kinetic UV-visible monitoring of the degradation of the species formed by the reaction between **1** and $PhNO_2$ in pentane (baseline correction). Zoom between 350 and 900 nm

Institut Polytechnique de Paris
91120 Palaiseau, France

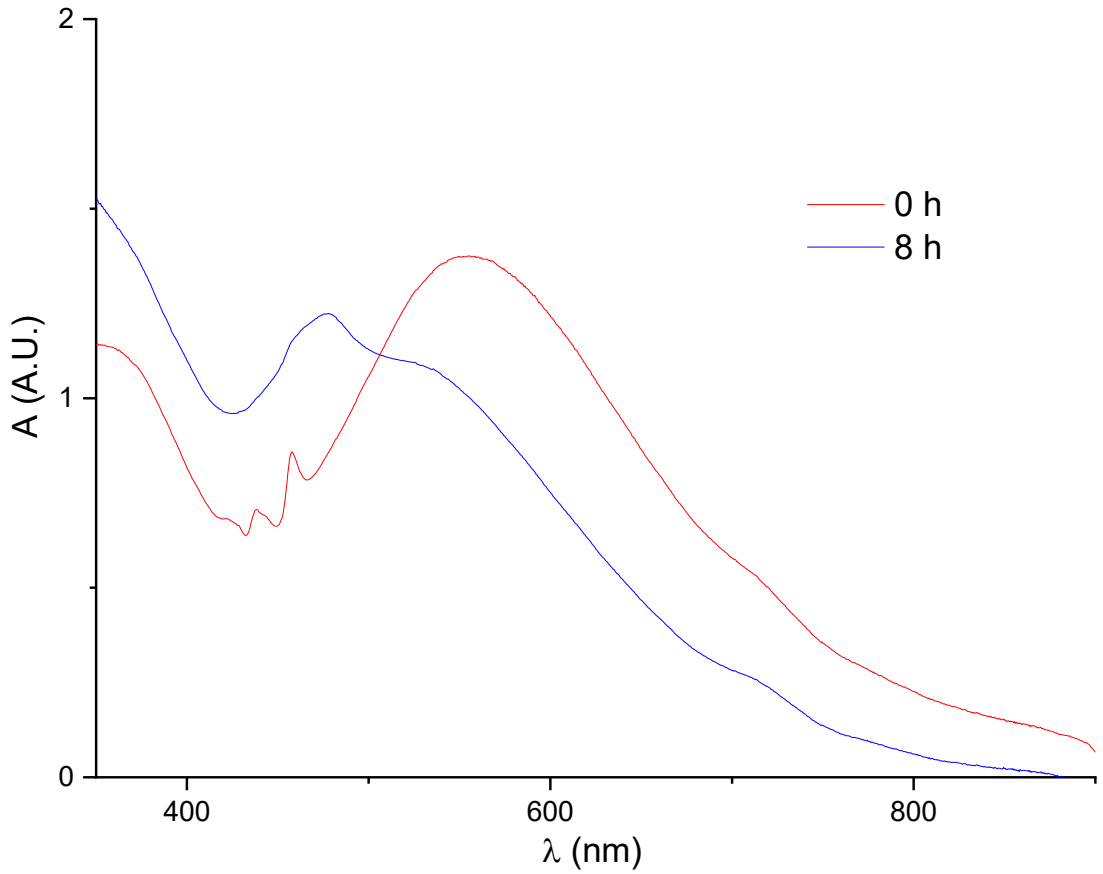

Figure S233. UV-visible spectra of the reaction between **1** and $PhNO_2$ in pentane (baseline correction) at t = 0 h and t = 8 h

Institut Polytechnique de Paris
91120 Palaiseau, France

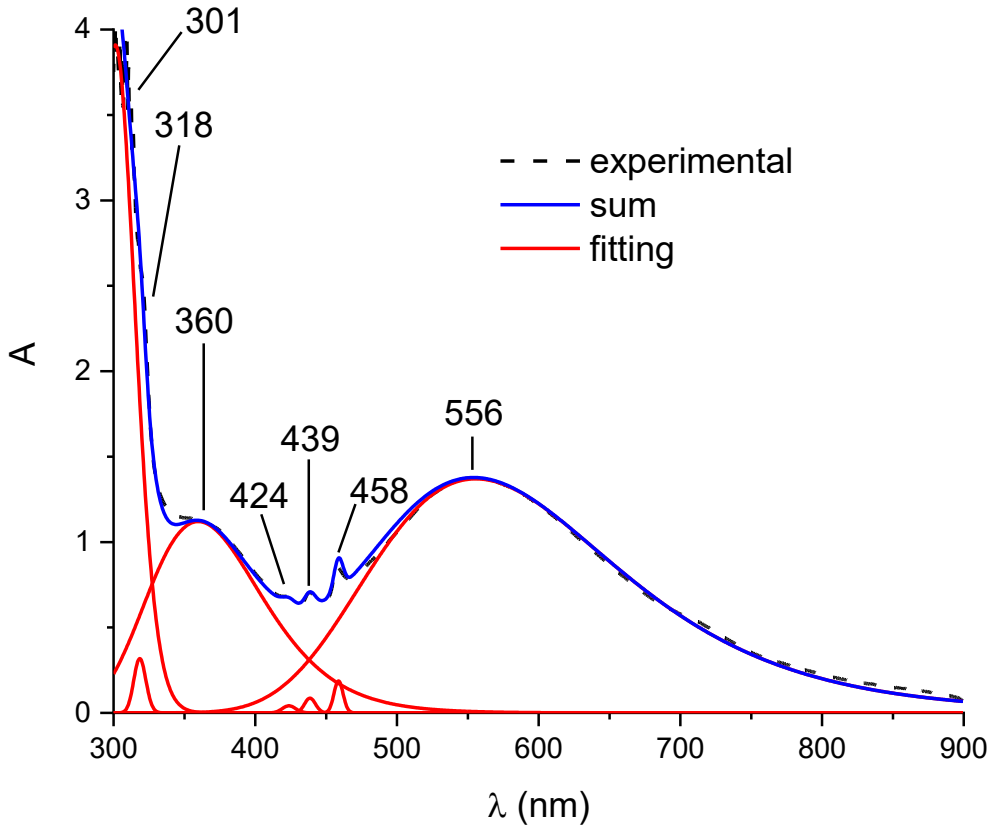

Figure S234. Deconvolution of the UV-visible spectrum of the reaction between **1** and $PhNO_2$ in pentane (baseline correction) at t = 0 h

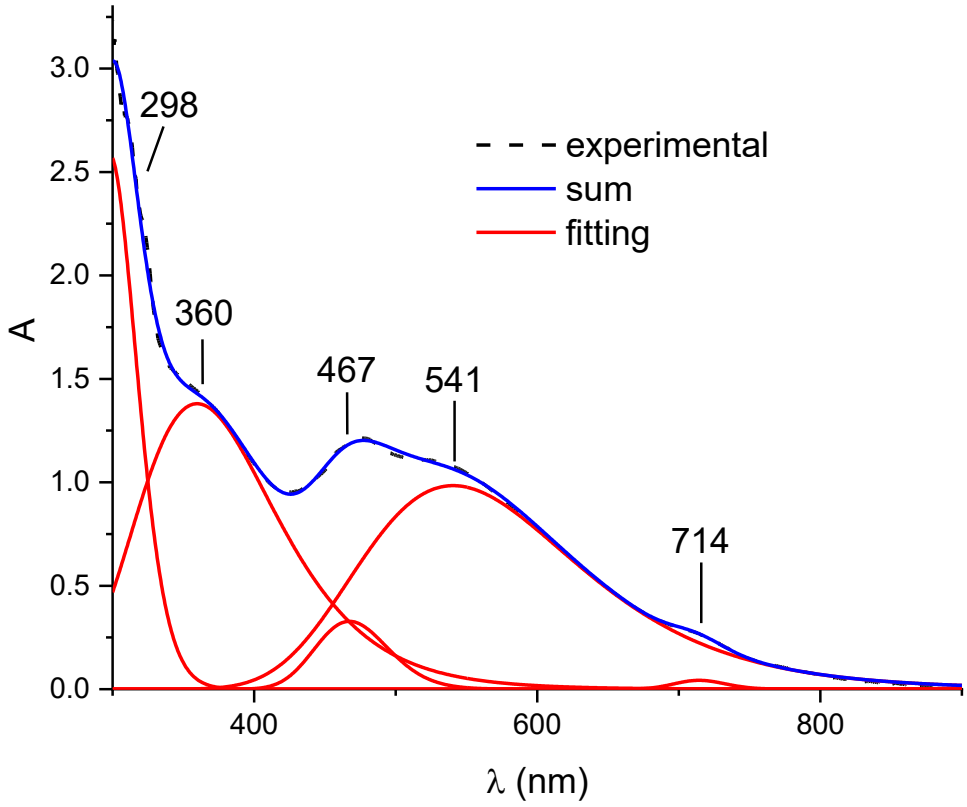

Figure S 235. Deconvolution of the UV-visible spectrum of the reaction between **1** and $PhNO_2$ in pentane (baseline correction) at t = 8 h

Institut Polytechnique de Paris
91120 Palaiseau, France

g) IR spectroscopy data

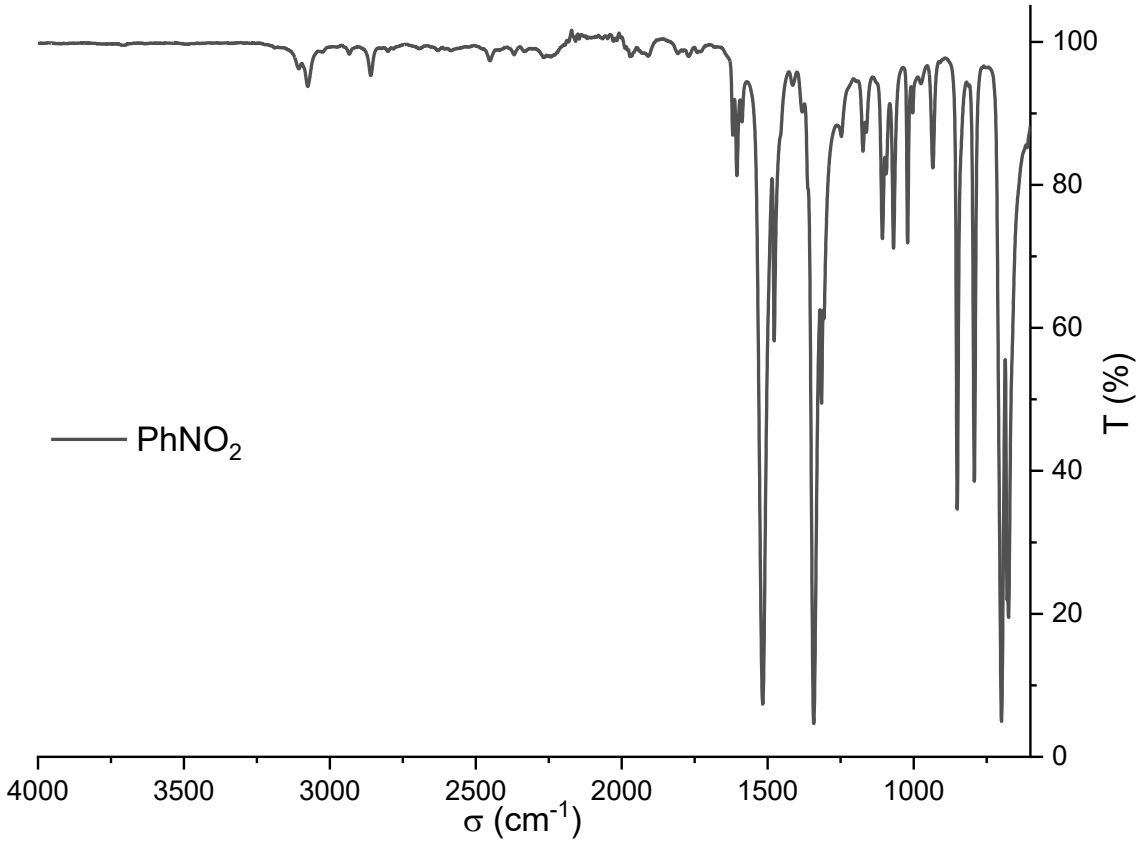

Figure S236. IR spectrum of neat $PhNO_2$

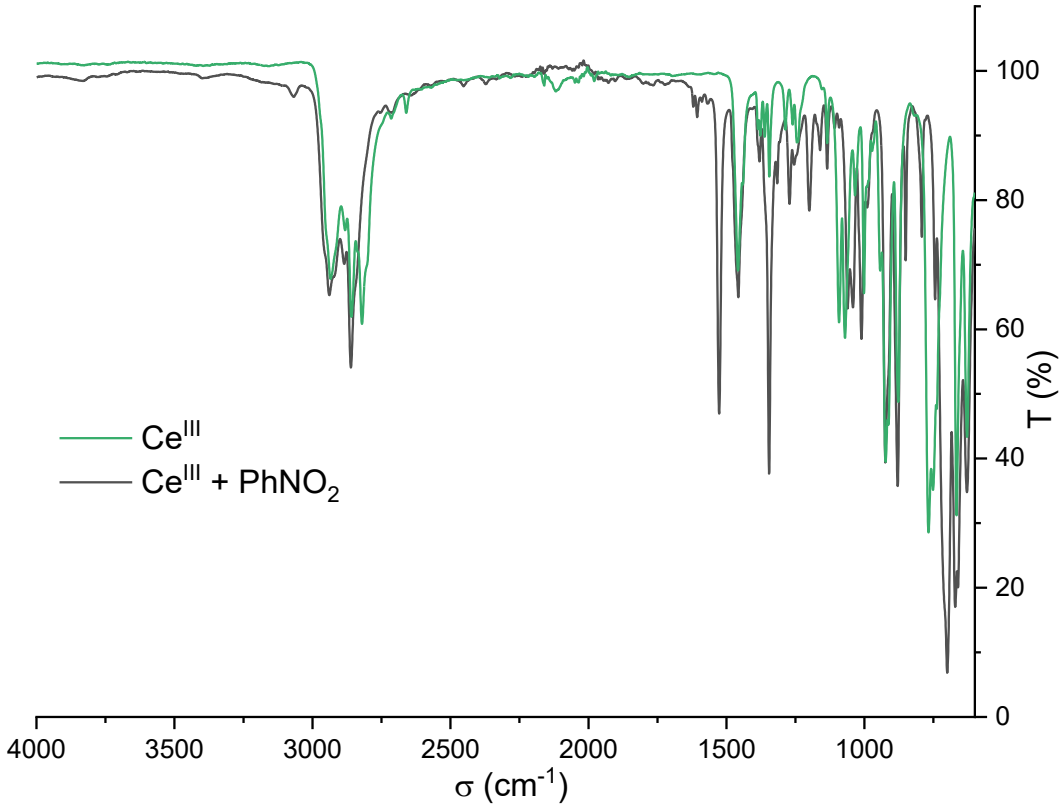

Figure S237. Comparison between IR spectrum of neat **1** and a solution of **1** and $PhNO_2$ in pentane

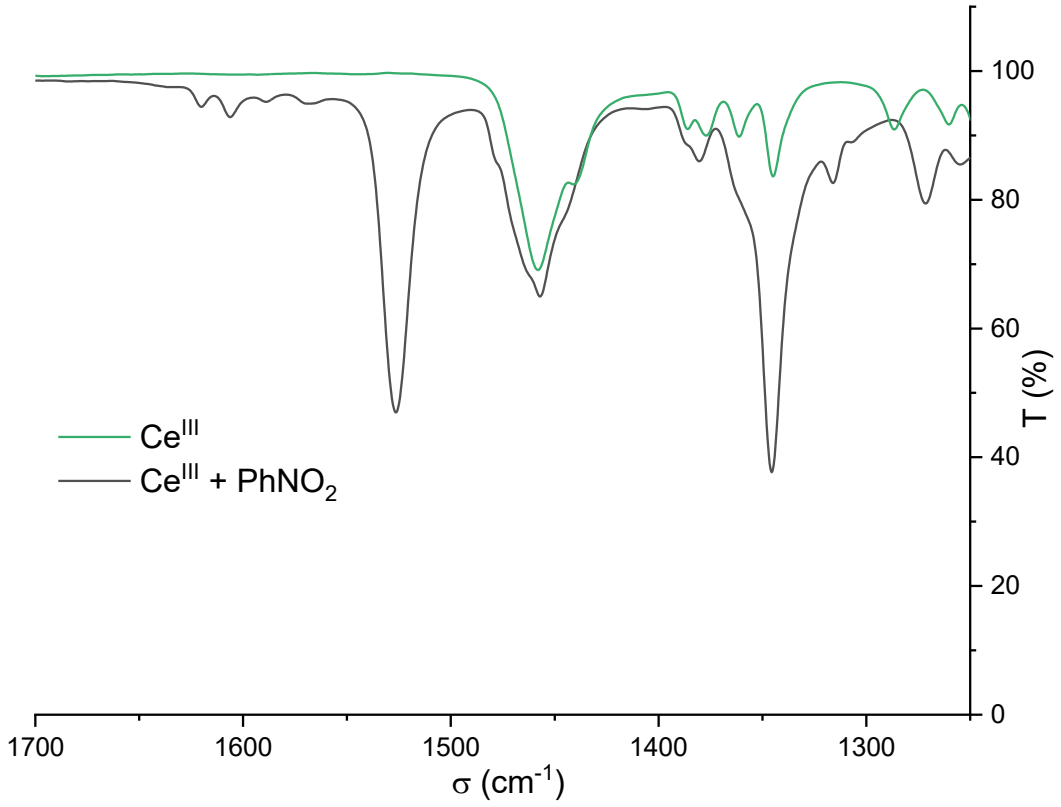

Figure S238. Comparison between IR spectrum of neat **1** and a solution of **1** and $PhNO_2$ in pentane. Zoom between 1250 and 1700 cm^{-1}

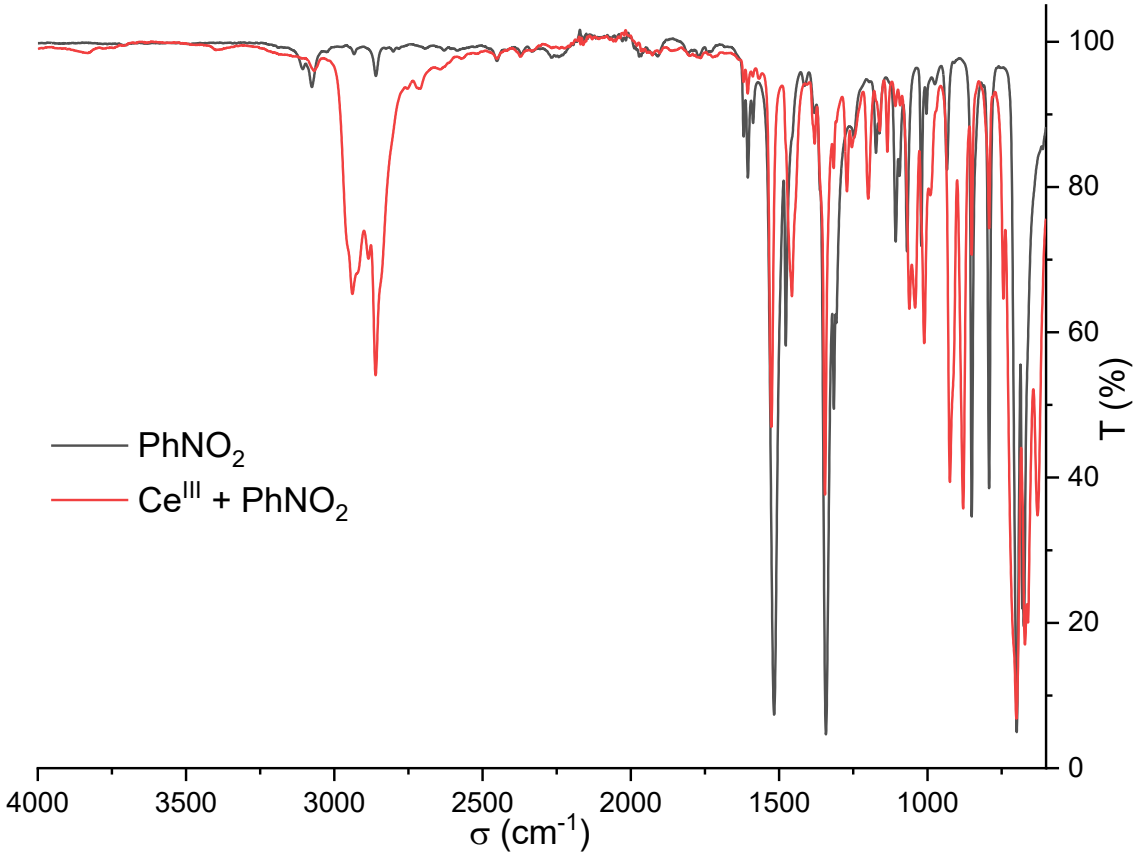

Figure S239. IR spectrum of neat $PhNO_2$ and a solution of **1** and $PhNO_2$ in pentane

Institut Polytechnique de Paris
91120 Palaiseau, France

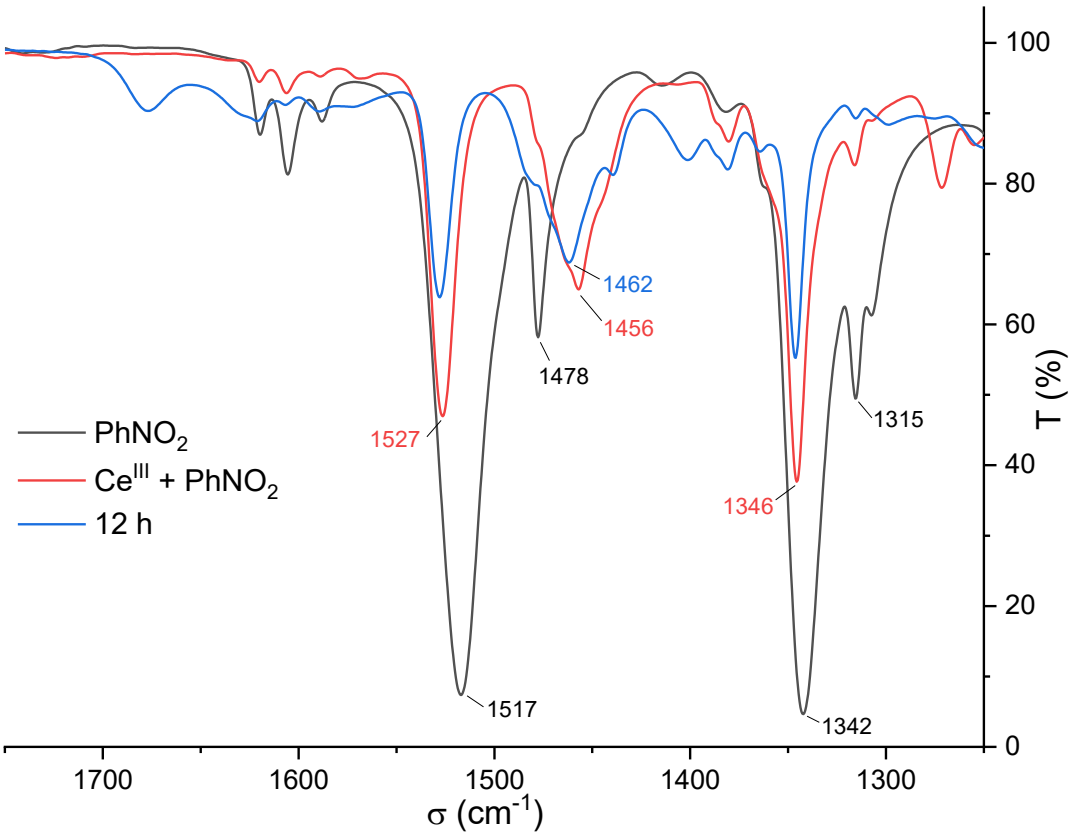

Figure S240. IR spectrum of neat $PhNO_2$ (black), a solution of **1** and $PhNO_2$ in pentane (red) and after being left overnight (blue). Zoom between 1250 and 1700 cm^{-1}

Institut Polytechnique de Paris
91120 Palaiseau, France

V. Crystal structure data

Identification code	2-PhNO	1-PBN
Empirical formula	$C_{78}H_{156}Ce_2N_{10}O_2Si_6$	$C_{49}H_{102}CeN_5OSi_3$
Formula weight	1714.90	1001.74
Temperature/K	150	150
Crystal system	Triclinic	Triclinic
Space group	P-1	P-1
a/Å	11.5040(3)	10.6715(3)
b/Å	12.1854(3)	13.0203(3)
c/Å	17.1940(5)	23.2696(6)
α/°	87.940(2)	73.026(2)
β/°	78.734(2)	81.247(2)
γ/°	73.225(2)	68.949(2)
Volume/Å^3	2262.70(11)	2881.94(14)
Z	1	2
ρ_{calc} g/cm^3	1.259	1.154
μ/mm^{-1}	1.119	0.887
F(000)	910.0	1078.0
Radiation	Mo Kα (λ = 0.71073)	Mo Kα (λ = 0.71073)
2Θ range for data collection/°	4.34 to 58.394	4.318 to 58.564
Index ranges	-12 ≤ h ≤ 15, -16 ≤ k ≤ 16, -23 ≤ l ≤ 22	-14 ≤ h ≤ 14, -17 ≤ k ≤ 17, -31 ≤ l ≤ 29
Reflections collected	36422	30296
Independent reflections	11149 [R_{int} = 0.0381, R_{sigma} = 0.0535]	13745 [R_{int} = 0.0377, R_{sigma} = 0.0544]
Data/restraints/parameters	11149/0/754	13745/0/508
Goodness-of-fit on F2	0.996	1.049
Final R indexes [I>=2σ (I)]	R_1 = 0.0340, wR_2 = 0.0683	R_1 = 0.0435, wR_2 = 0.1102
Final R indexes [all data]	R_1 = 0.0558, wR_2 = 0.0741	R_1 = 0.0555, wR_2 = 0.1139
Largest diff. peak/hole / e Å^{-3}	0.66/-0.41	1.86/-0.75

Table S54. Crystal data and structure refinement for **2-PhNO** and **1-PBN**

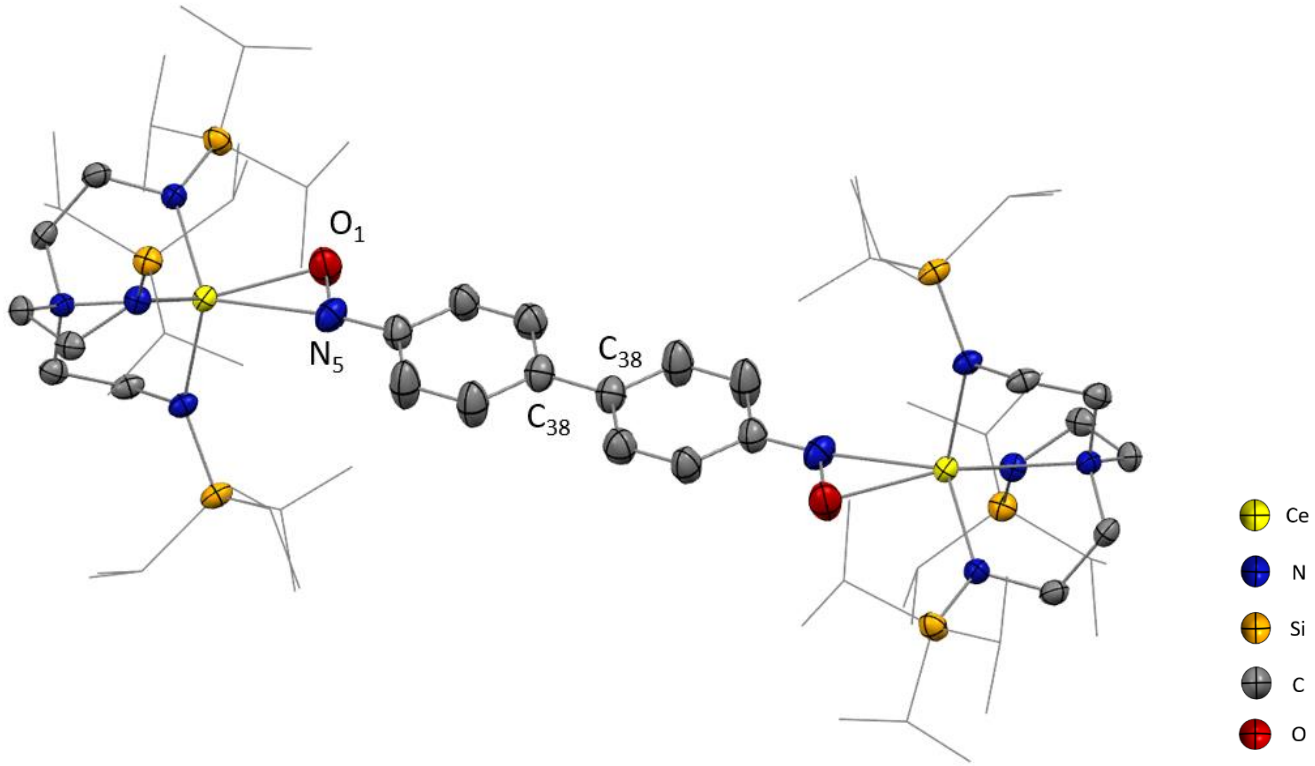

Figure S241. Structure of **2-PhNO**. Displacement ellipsoids are represented at 50% probability. Hydrogen atoms have been omitted for clarity, and isopropyl groups have been represented in wireframe style

Bond	Length (Å)
Ce-O_1	2.252(2)
Ce-N_5	2.457(2)
Ce-N_1	2.2646(19)
Ce-N_2	2.272(2)
Ce-N_3	2.262(2)
Ce-N_4	2.651(2)
N_1-Si_1	1.740(2)
N_2-Si_2	1.735(2)
N_3-Si_3	1.734(2)
N_1-C_1	1.483(3)
N_2-C_3	1.484(3)
N_3-C_5	1.479(3)
O_1-N_5	1.333(3)
N_5-C_{35}	1.318(4)
C_{35}-C_{36}	1.422(4)
C_{36}-C_{37}	1.340(4)
C_{37}-C_{38}	1.423(4)
C_{38}-C_{39}	1.428(4)
C_{39}-C_{40}	1.353(4)
C_{40}-C_{35}	1.421(4)
C_{38}-C_{38}	1.425(6)

Bonds	Angle (°)
C_1-N_1-Ce	108.78(14)
C_3-N_2-Ce	108.29(15)
C_5-N_3-Ce	106.14(14)
Ce-Cent-N_4	175.5
O_1-Ce-N_5	32.53(8)

Bond	Mean value (Å)
Ce-$N_{equatorial}$	2.266(4)
Ce-N_{plane}	0.731
N-Si	1.736(4)

Table S55. Selected bond lengths and angles for **2-PhNO**

Institut Polytechnique de Paris
91120 Palaiseau, France

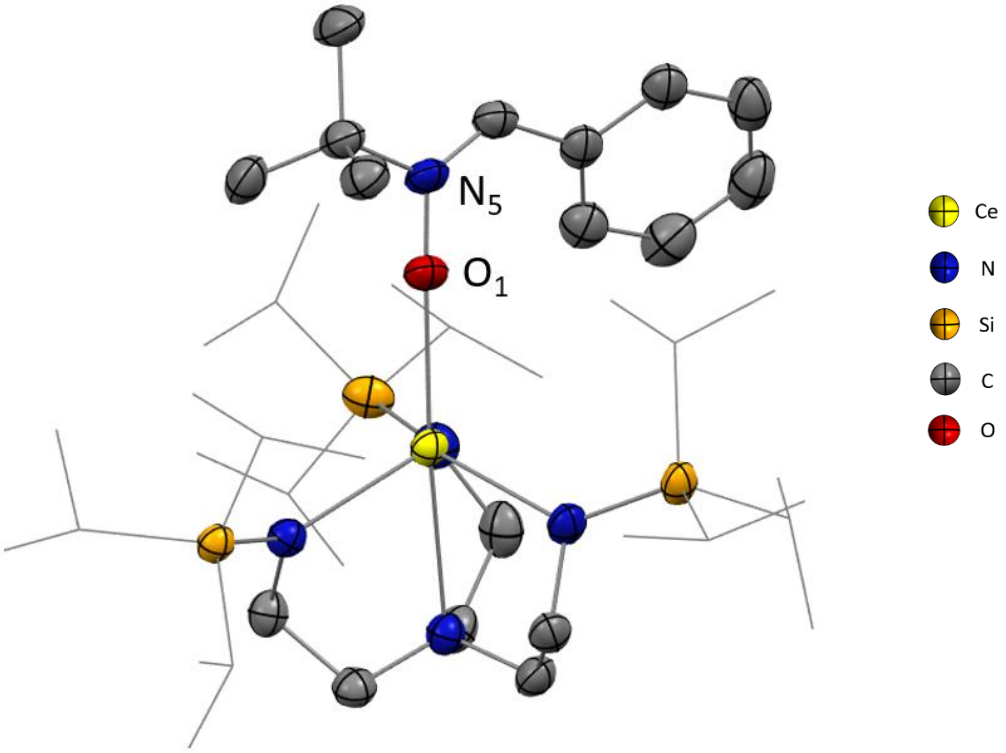

Figure S242. Structure of **1-PBN**. Displacement ellipsoids are represented at 50% probability. Hydrogen atoms have been omitted for clarity, and isopropyl groups have been represented in wireframe style

Bond	Length (Å)	Bonds	Angle (°)
Ce-O_1	2.410(2)	C_1-N_1-Ce	103.85(18)
Ce-N_1	2.394(3)	C_3-N_2-Ce	107.61(17)
Ce-N_2	2.368(2)	C_5-N_3-Ce	109.22(18)
Ce-N_3	2.390(2)	Ce-Cent-N_4	173.1
Ce-N_4	2.660(2)	O_1-Ce-N_5	176.24(18)
N_1-C_1	1.466(4)	O_1-Ce-N_4	172.79(7)
N_2-C_3	1.475(4)		
N_3-C_5	1.486(4)	**Bond**	**Mean value (Å)**
O_1-N_5	1.318(3)	Ce-$N_{equatorial}$	2.384(5)
		Ce-N_{plane}	0.769
		N-Si	1.711(5)

Table S56. Selected bond lengths and angles for **1-PBN**

Institut Polytechnique de Paris
91120 Palaiseau, France

References

(1) Sebest, F.; Casarrubios, L.; Rzepa, H. S.; White, A. J. P.; Díez-González, S. Thermal Azide–Alkene Cycloaddition Reactions: Straightforward Multi-Gram Access to Δ2-1,2,3-Triazolines in Deep Eutectic Solvents. *Green Chem.* **2018**, *20* (17), 4023–4035. https://doi.org/10.1039/C8GC01797B.

Institut Polytechnique de Paris
91120 Palaiseau, France

Institut Polytechnique de Paris
91120 Palaiseau, France

Experimental section for Chapter IV

Part I.a

Institut Polytechnique de Paris
91120 Palaiseau, France

I. Synthetic procedures

a) Synthesis of [(THF)$_3$LiNO$_3$Ce^{III}TREN^{TIPS}] (1-NO$_3$)

In a vial, Ce^{III}TREN^{TIPS} (30 mg, 40 µmol) was dissolved in 1 mL of THF. LiNO$_3$ (2.7 mg, 40 µmol) was added. The mixture was left to stir for 2 hours, and the solvent was removed under reduced pressure. The remaining oil was dissolved in 0.5 mL of pentane with one drop of THF, and stored at -40°C overnight which afforded XRD suitable orange crystals (11 mg, 25%).

^{1}H NMR (300 MHz, THF-d$_8$, 298 K) δ 2.56 (s, 9H), 2.11-2.25 (2 × s, 60H), -5.57 (s, 6H)

Elemental analysis for $CeC_{33}H_{75}N_5O_3Si_3Li$, Found (Theoretical): C, 52.34 (52.09) H, 9.74 (9.62); N, 6.77 (6.75)

b) Synthesis of [Li@2(12-c-4)NO$_3$Ce^{III}TREN^{TIPS}] (1-NO$_3$-12c4)

In a vial, Ce^{III}TREN^{TIPS} (30 mg, 40 µmol) was dissolved in 1 mL of THF. 12-crown-4 (13 µL, 80 µmol) and LiNO$_3$ (2.7 mg, 40 µmol) were added. The mixture was left to stir for 2 hours, and the solvent was removed under reduced pressure. The remaining oil was dissolved in 0.5 mL of pentane with one drop of THF, and stored at -40°C overnight which afforded XRD suitable orange crystals (22 mg, 48%).

^{1}H NMR (300 MHz, THF-d$_8$, 298 K) 2.56 (s, 9H), 2.15-2.23 (2 × s, 60H), -5.45 (s, 6H)

c) Synthesis of [(THF)Li@(12-c-4)OCe^{IV}TREN^{TIPS}] (2-O)

In a J. Young NMR tube, Ce^{III}TREN^{TIPS} (30 mg, 40 µmol) was dissolved in 0.5 mL of THF-d$_8$. 12-crown-4 (13 µL, 80 µmol) and LiNO$_3$ (2.7 mg, 40 µmol) were successively added. The reaction medium was irradiated at 427 nm for 45 minutes. The reaction progress was monitored using ^{1}H NMR spectroscopy. Solvent was removed under reduced pressure, and the remaining orange oil was dissolved in 0.5 mL of pentane + 1 drop of THF, and stored at -40°C overnight. XRD suitable orange crystals (17 mg, 43%) could be isolated.

Institut Polytechnique de Paris
91120 Palaiseau, France

II. NMR data for Part I

a) Spectral data for 1-NO_3 [$(THF)_3LiNO_3Ce^{III}TREN^{TIPS}$]

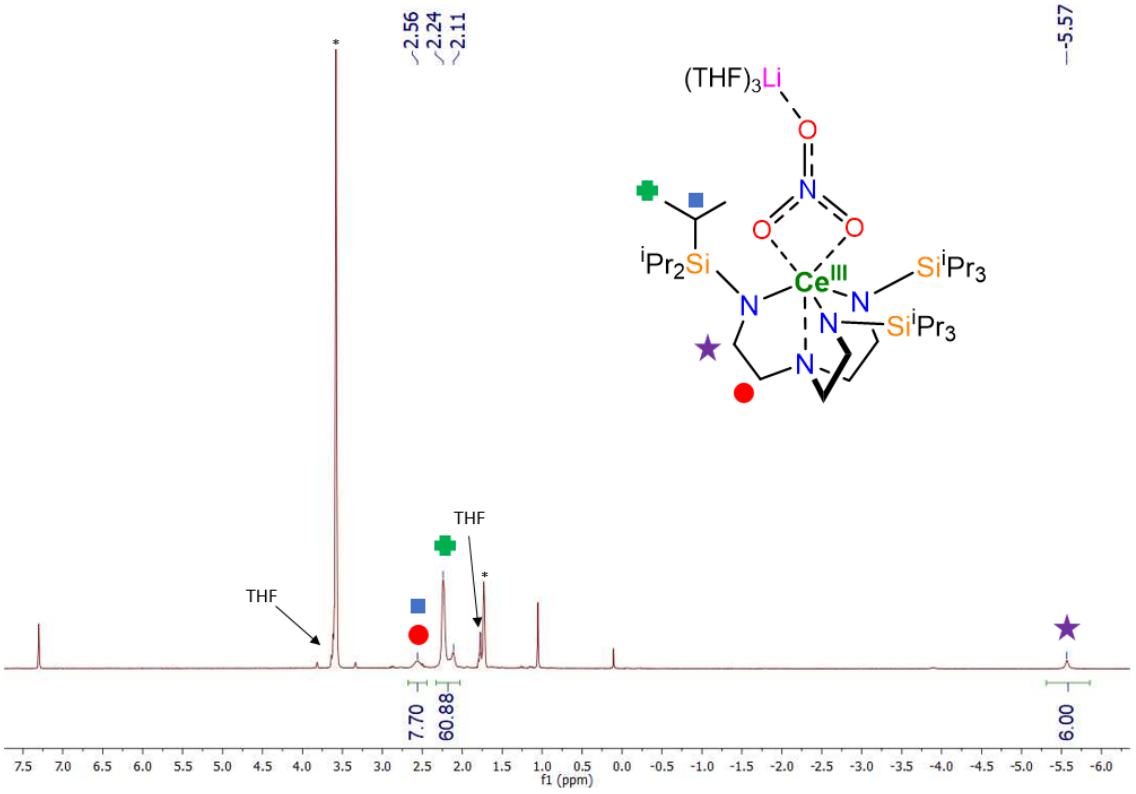

Figure S243. ^{1}H NMR spectrum of **1-NO_3** [$(THF)_3LiNO_3Ce^{III}TREN^{TIPS}$] in THF-$d_8$. * indicates the residual solvent residual peaks

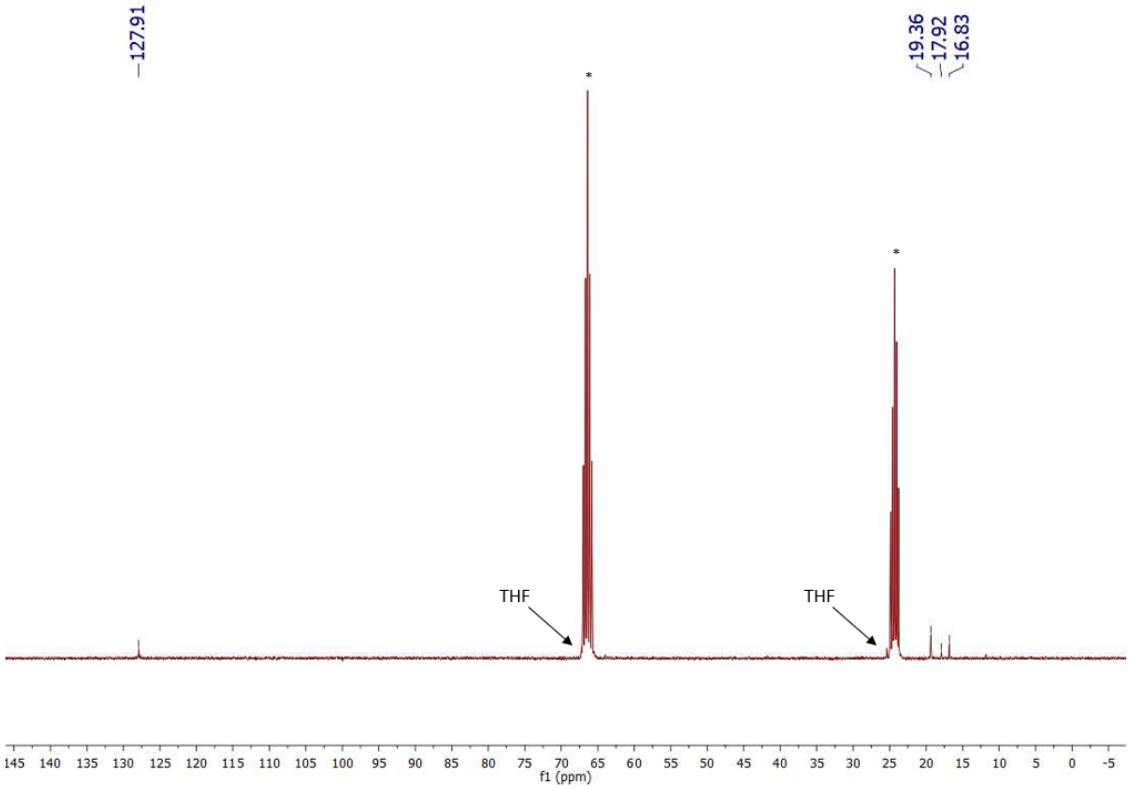

Figure S244. $^{13}C\{^{1}H\}$ NMR spectrum of **1-NO_3** [$(THF)_3LiNO_3Ce^{III}TREN^{TIPS}$] in THF-$d_8$. * indicates solvent residual peaks

Institut Polytechnique de Paris
91120 Palaiseau, France

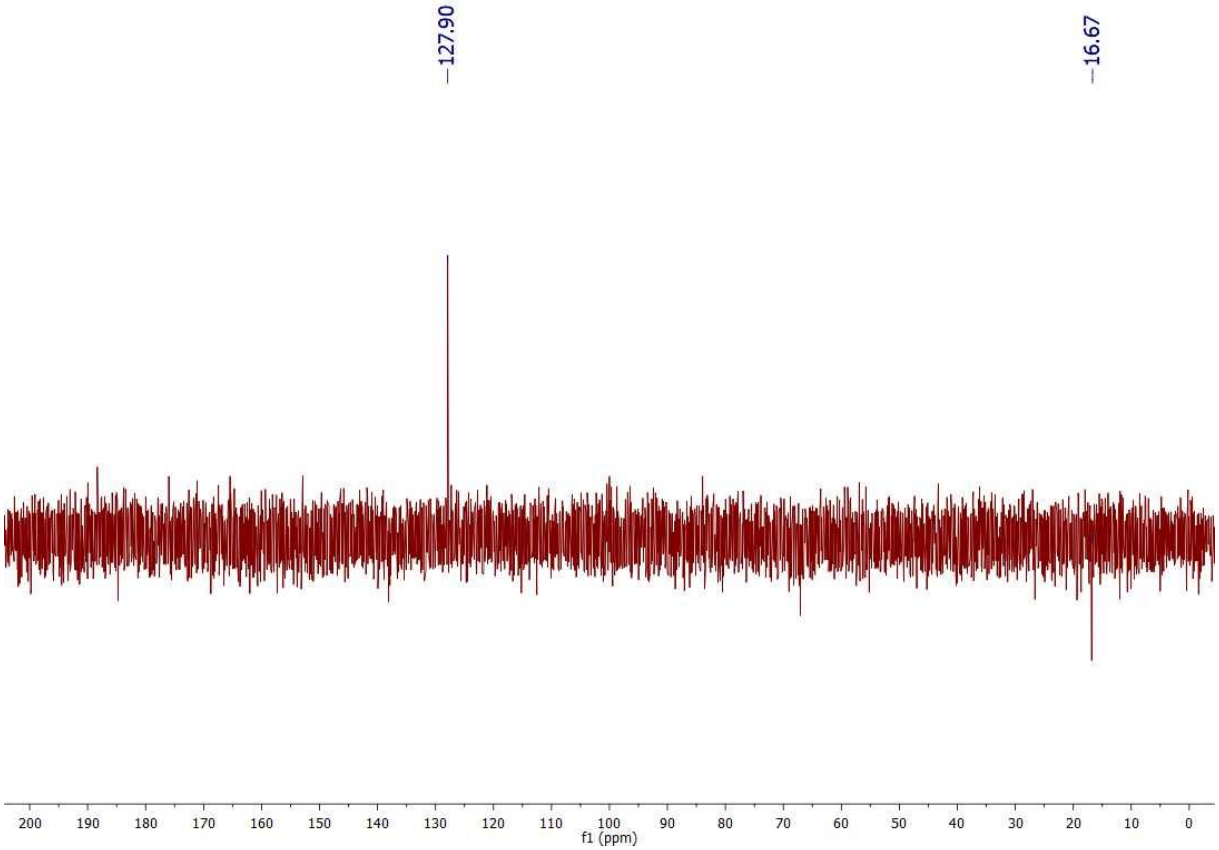

Figure S245. DEPT 135 $^{13}C\{^{1}H\}$ spectrum of **1-NO$_3$** [(THF)$_3$LiNO$_3$Ce^{III}TREN^{TIPS}] in THF-d$_8$

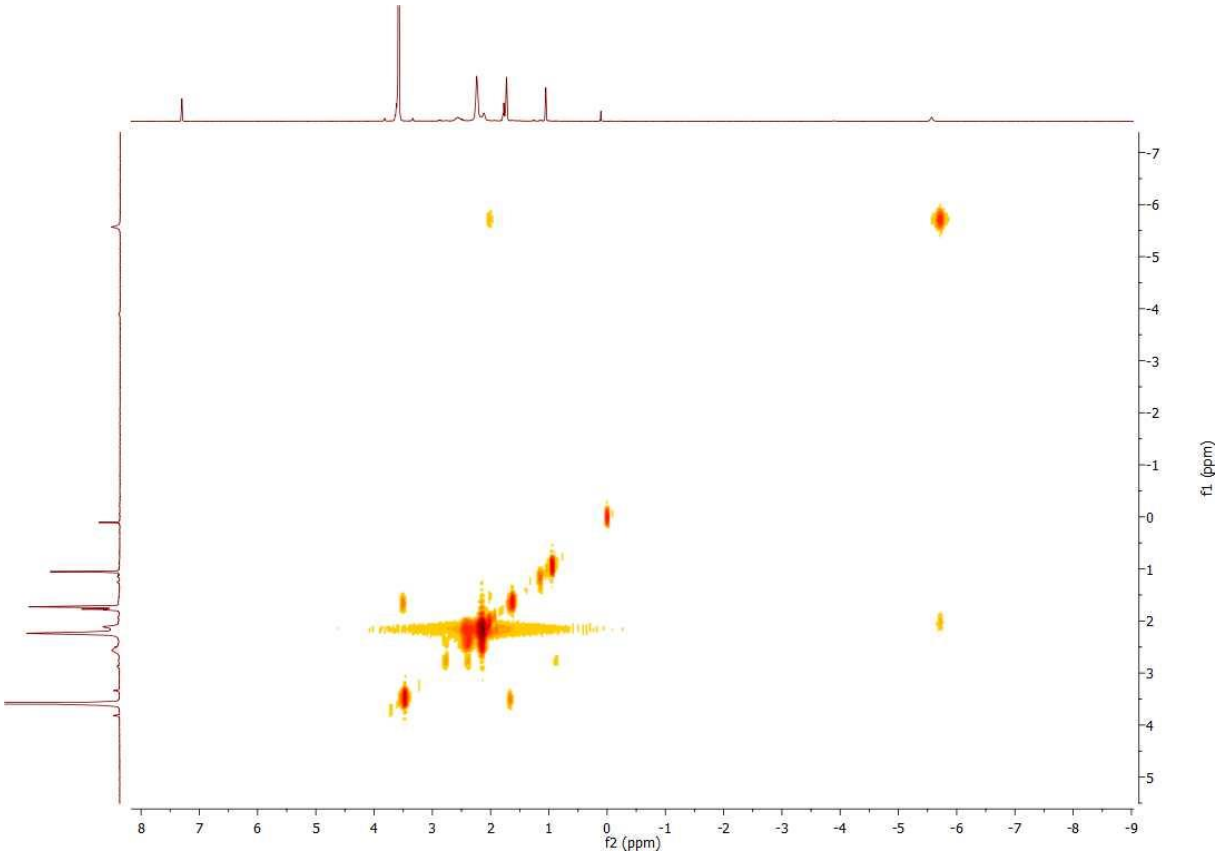

Figure S246. ^{1}H-^{1}H COSY spectrum of **1-NO$_3$** [(THF)$_3$LiNO$_3$Ce^{III}TREN^{TIPS}] in THF-d$_8$

Institut Polytechnique de Paris
91120 Palaiseau, France

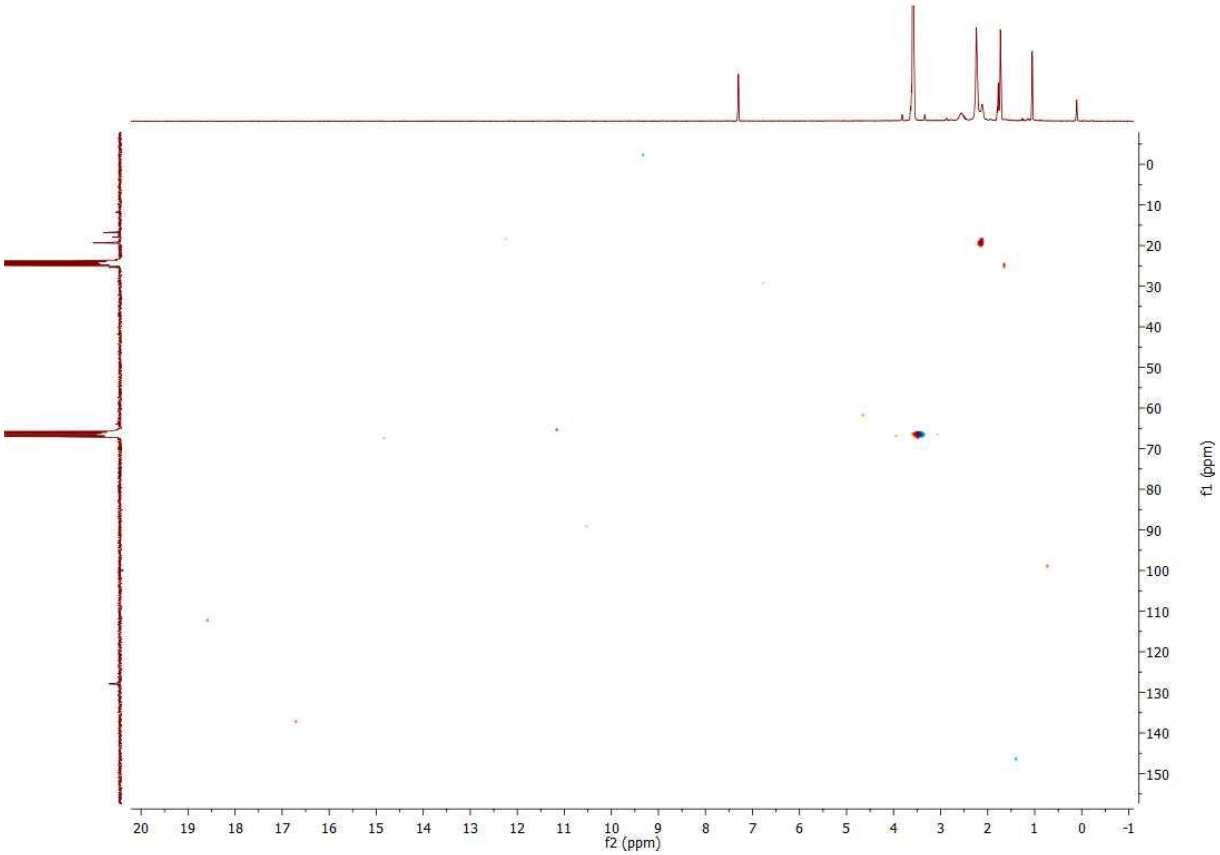

Figure S247. HSQC spectrum of **1-NO$_3$** [(THF)$_3$LiNO$_3$Ce^{III}TREN^{TIPS}] in THF-d$_8$

Institut Polytechnique de Paris
91120 Palaiseau, France

b) Spectral data for [Li@(12-c-4)2NO3CeIIITRENTIPS] 1-NO_3-12c4

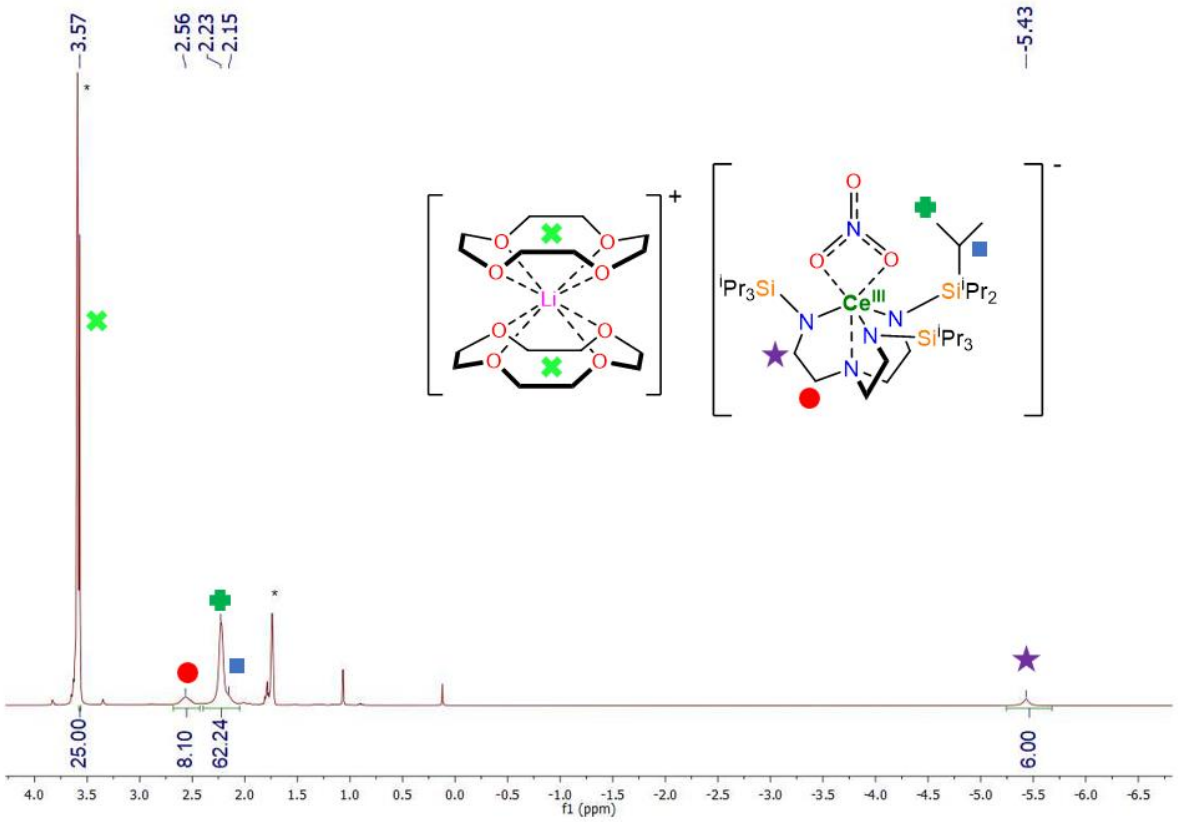

Figure S248. ^{1}H NMR spectrum of **1-NO_3-12c4** [Li@2(12-c-4)$NO_3Ce^{III}TREN^{TIPS}$] in THF-d_8. * indicates the residual solvent residual peaks

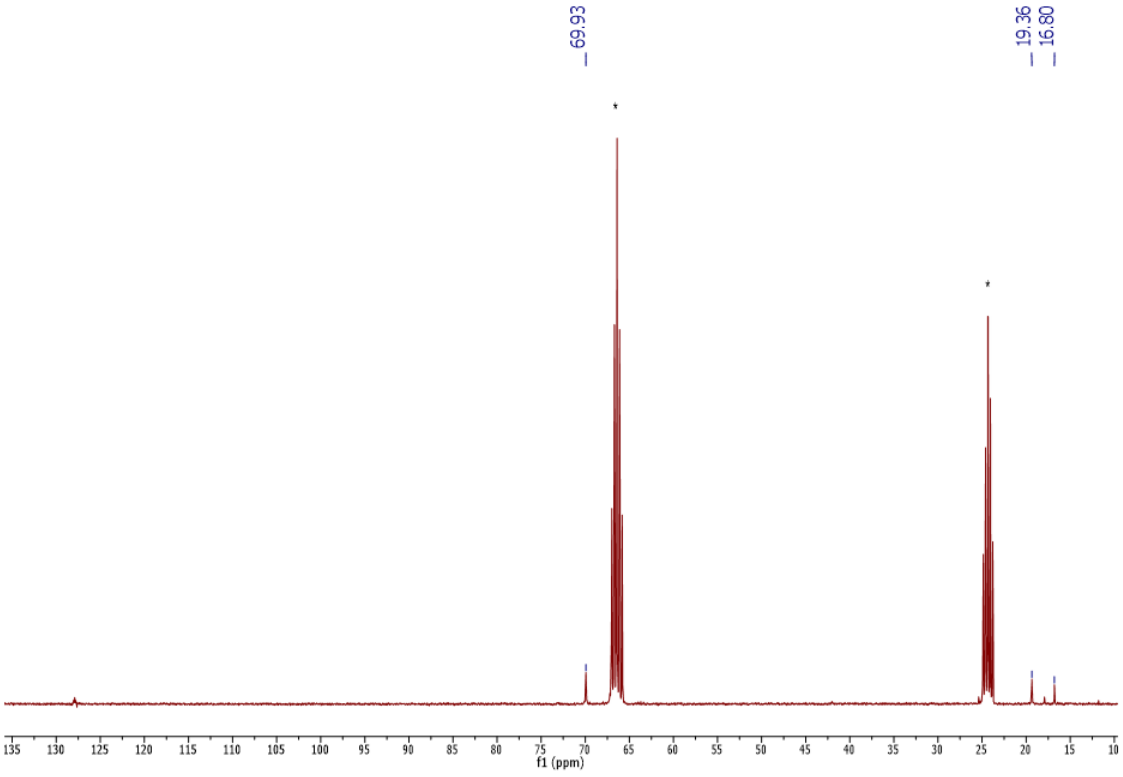

Figure S249. $^{13}C\{^{1}H\}$ NMR spectrum of **1-NO_3-12c4** [Li@2(12-c-4)$NO_3Ce^{III}TREN^{TIPS}$] in THF-d_8. * indicates the solvent residual peaks

Institut Polytechnique de Paris
91120 Palaiseau, France

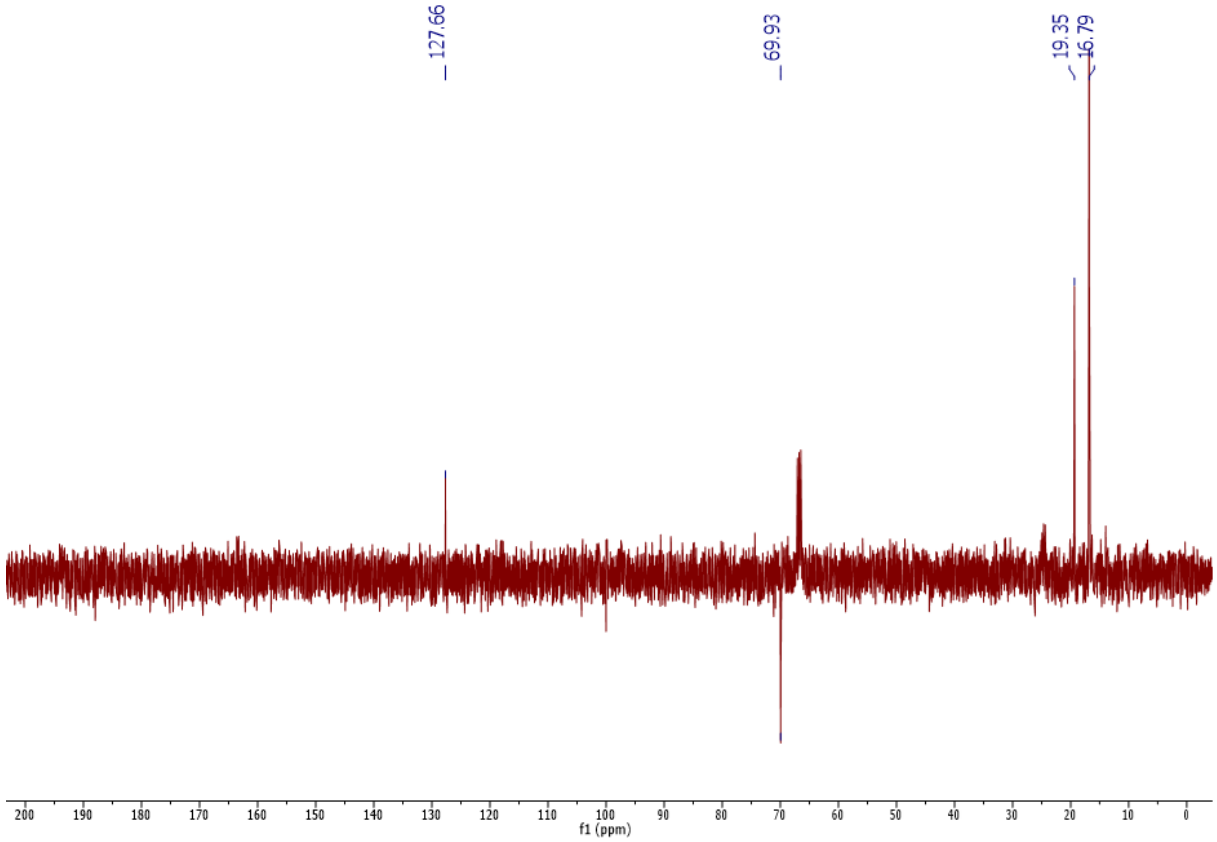

Figure S250. DEPT 135 $^{13}C\{^{1}H\}$ spectrum of **1-NO_3-12c4** [Li@2(12-c-4)$NO_3Ce^{III}TREN^{TIPS}$] in THF-d_8

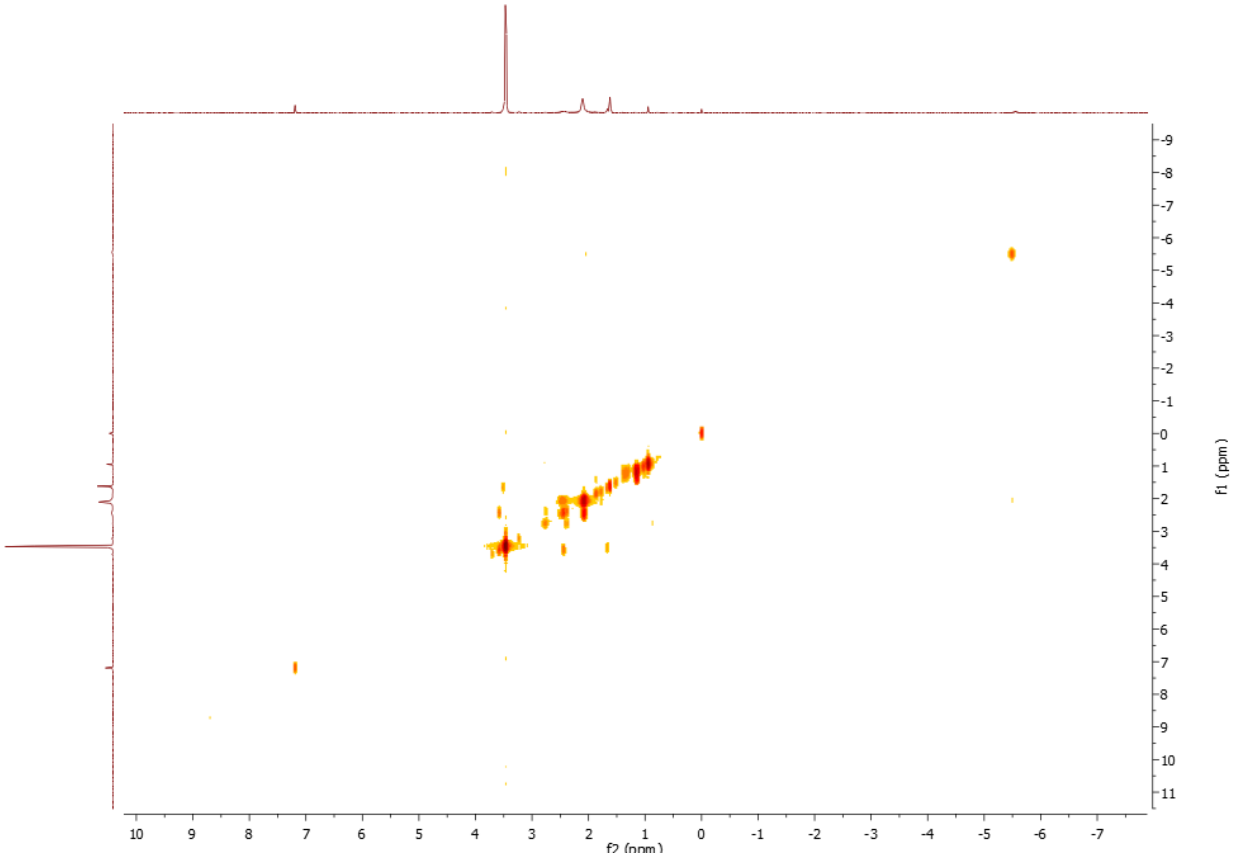

Figure S251. ^{1}H-^{1}H COSY spectrum of **1-NO_3-12c4** [Li@2(12-c-4)$NO_3Ce^{III}TREN^{TIPS}$] in THF-d_8

Institut Polytechnique de Paris
91120 Palaiseau, France

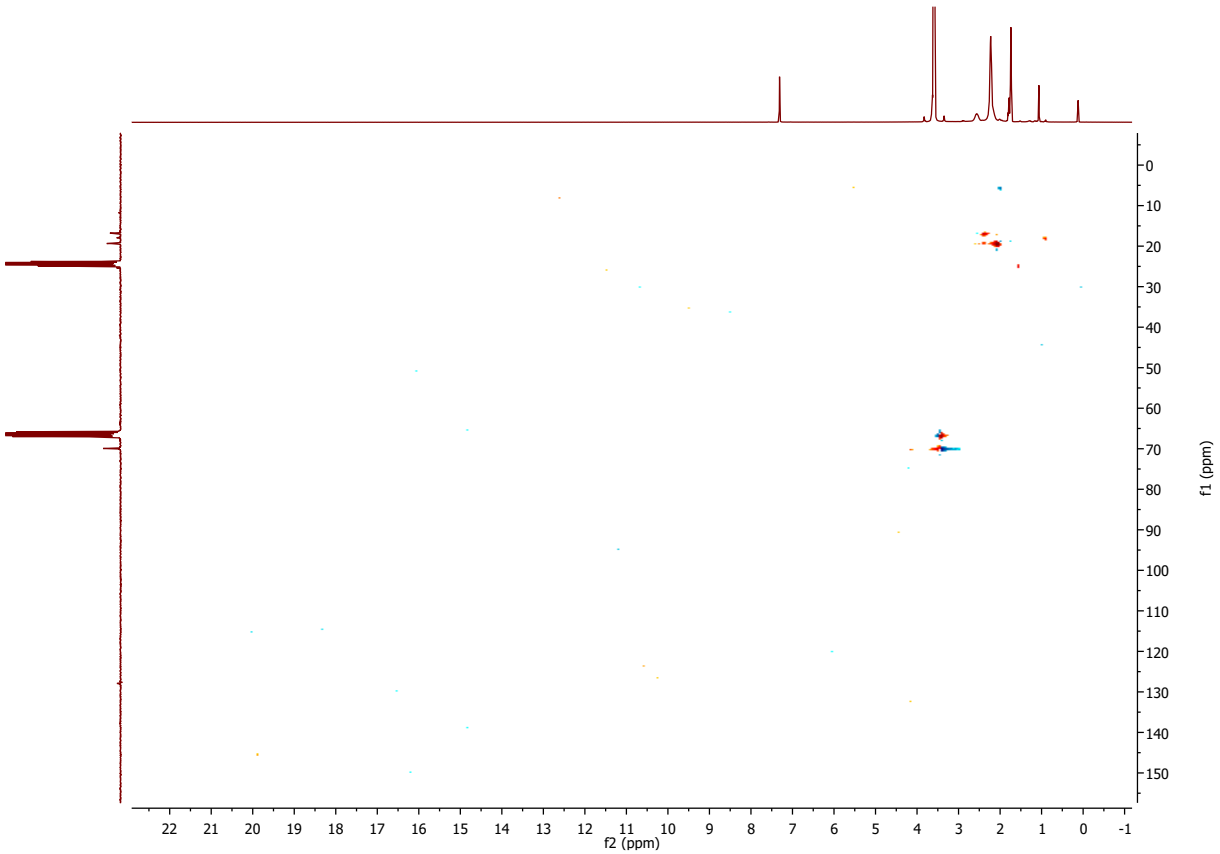

Figure S252. HSQC spectrum of **1-NO_3-12c4** [Li@2(12-c-4)$NO_3$$Ce^{III}TREN^{TIPS}$] in THF-$d_8$

Institut Polytechnique de Paris
91120 Palaiseau, France

c) Reactivity of 1 with $LiNO_3$ in the dark

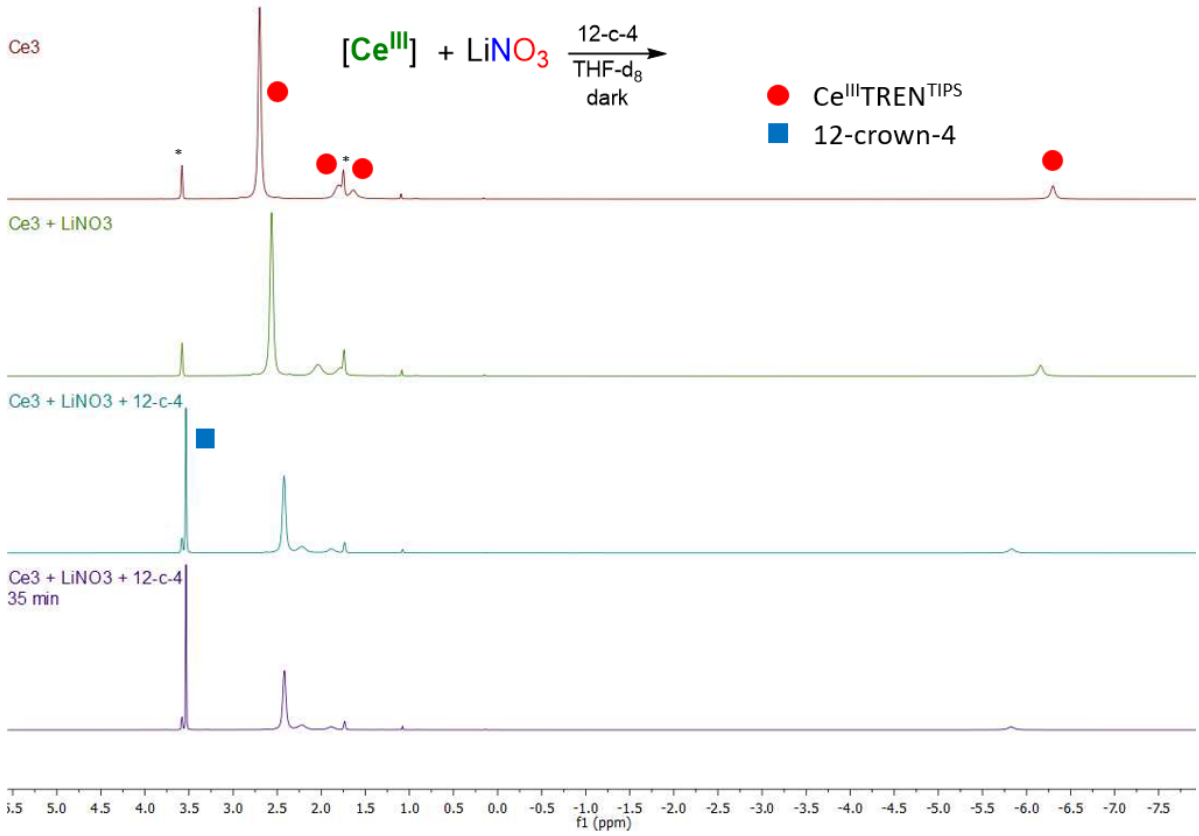

Figure S253. ^{1}H NMR spectra of reaction between **1**, $LiNO_3$ and 12-crown-4 in THF-d_8 over time**.** Solvent residual peaks are indicated with *

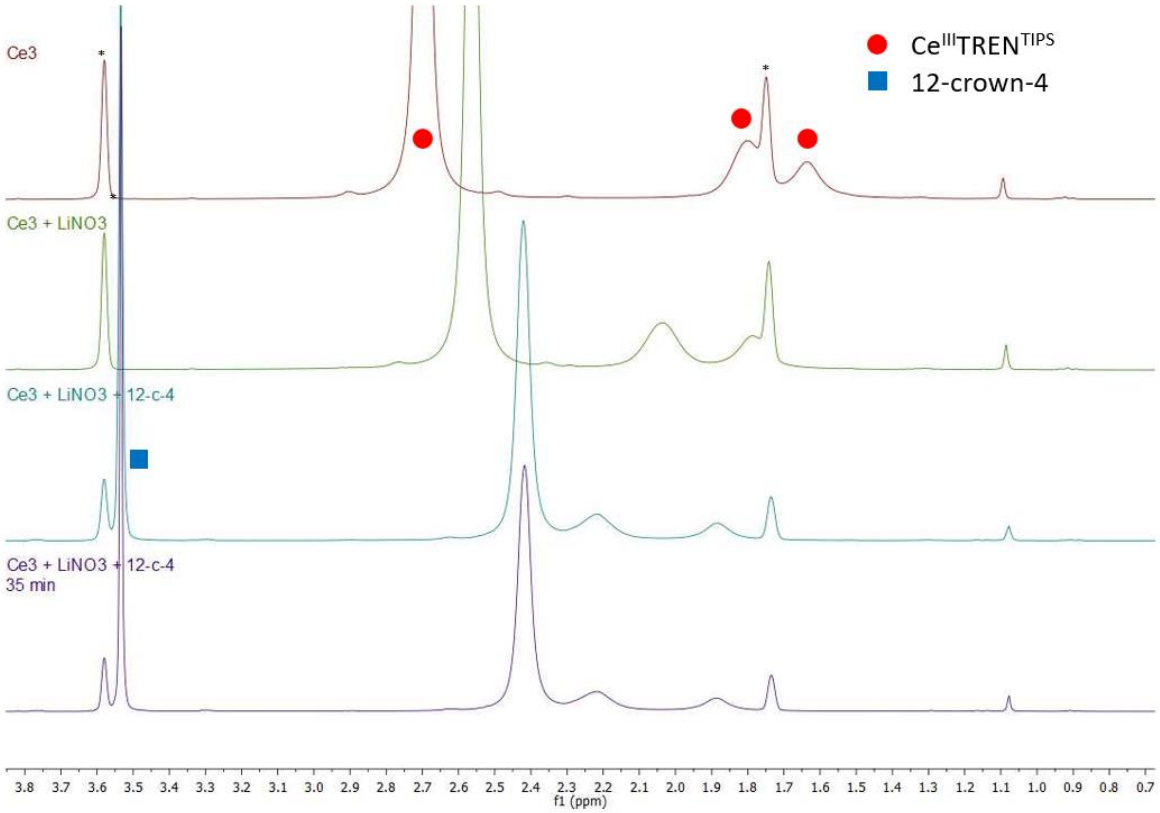

Figure S254. ^{1}H NMR spectra of reaction between **1**, $LiNO_3$ and 12-crown-4 in THF-d_8 over time. Zoom between 0.7 and 3.8 ppm. Solvent residual peaks are indicated with *

Institut Polytechnique de Paris
91120 Palaiseau, France

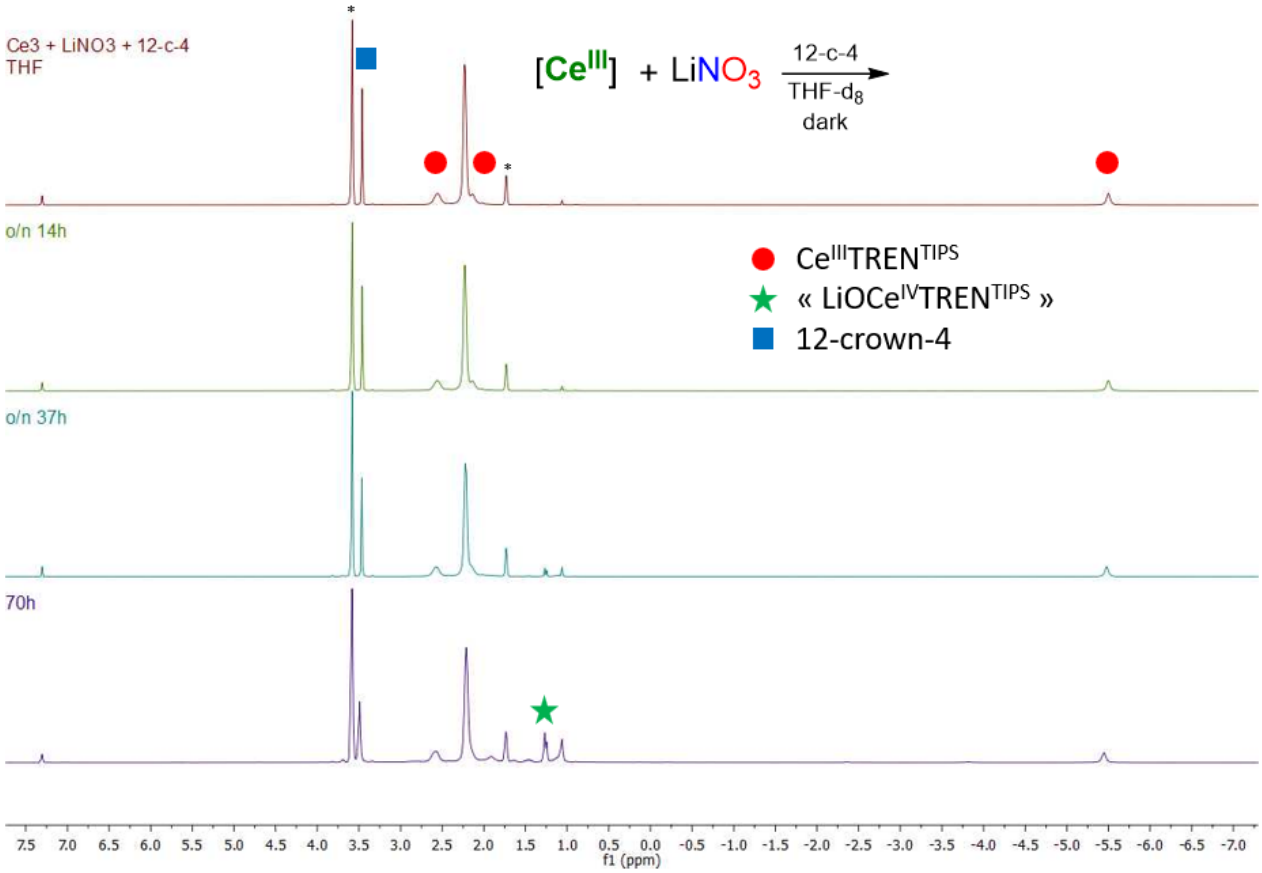

Figure S255. ^{1}H NMR spectra of reaction between **1**, $LiNO_3$ and 12-crown-4 in THF-d_8 over time. Solvent residual peaks are indicated with *

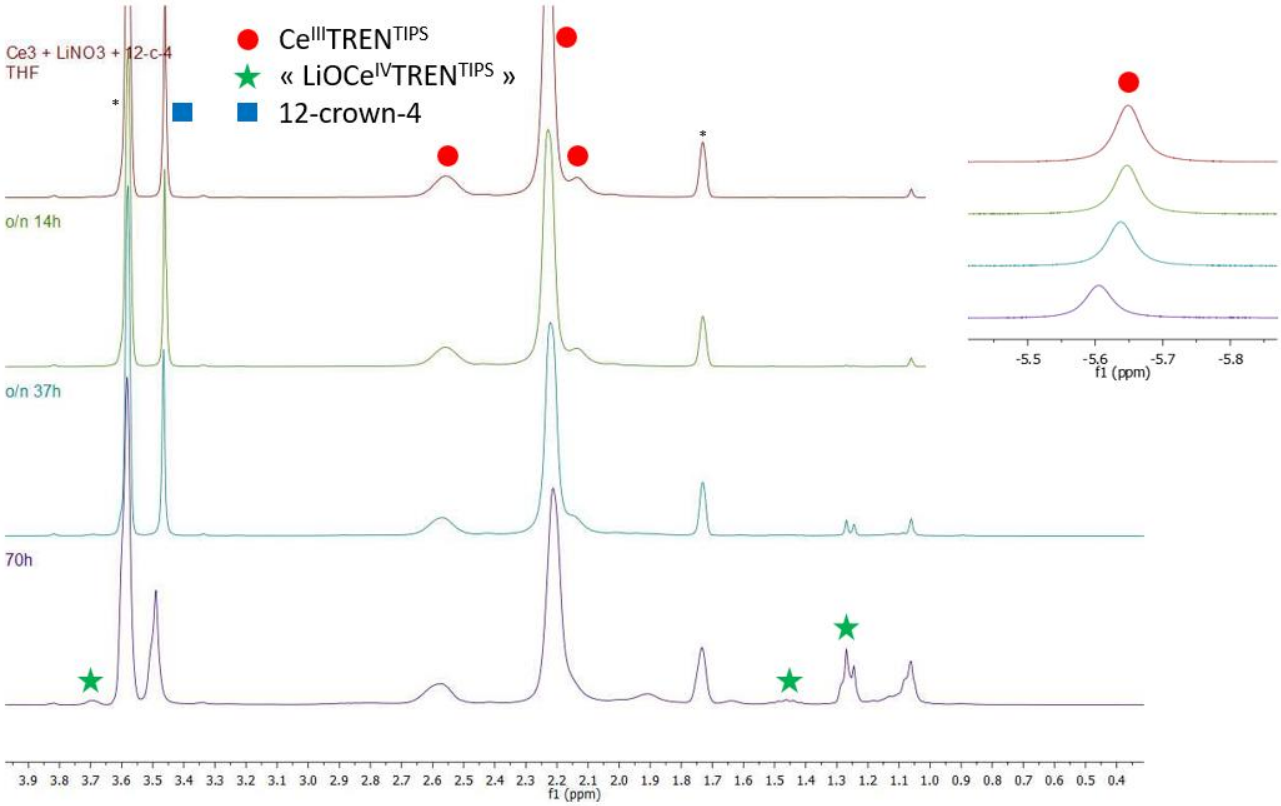

Figure S256. ^{1}H NMR spectra of reaction between **1**, $LiNO_3$ and 12-crown-4 in THF-d_8 over time. Zoom between 0.4 and 3.9 ppm. Solvent residual peaks are indicated with *

Institut Polytechnique de Paris
91120 Palaiseau, France

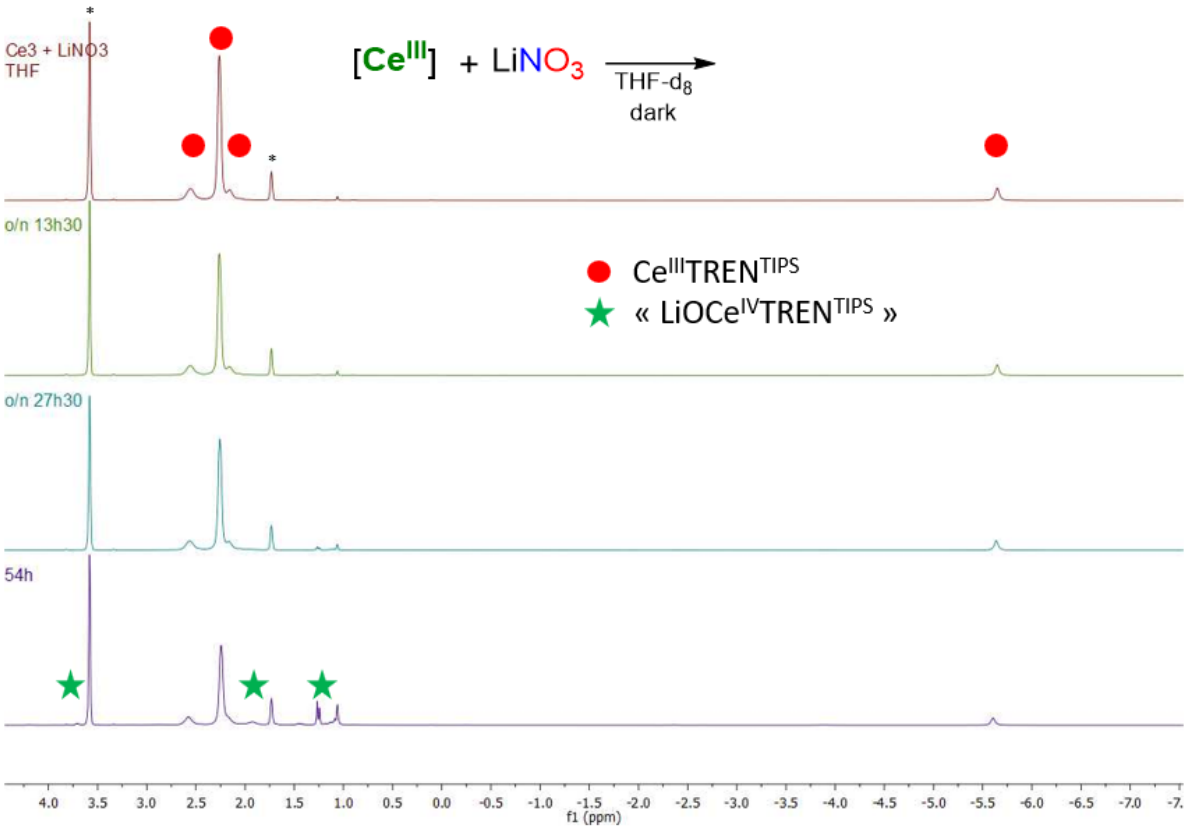

Figure S257. ^{1}H NMR spectra of reaction between **1** and $LiNO_3$ in THF-d_8 over time. Solvent residual peaks are indicated with *

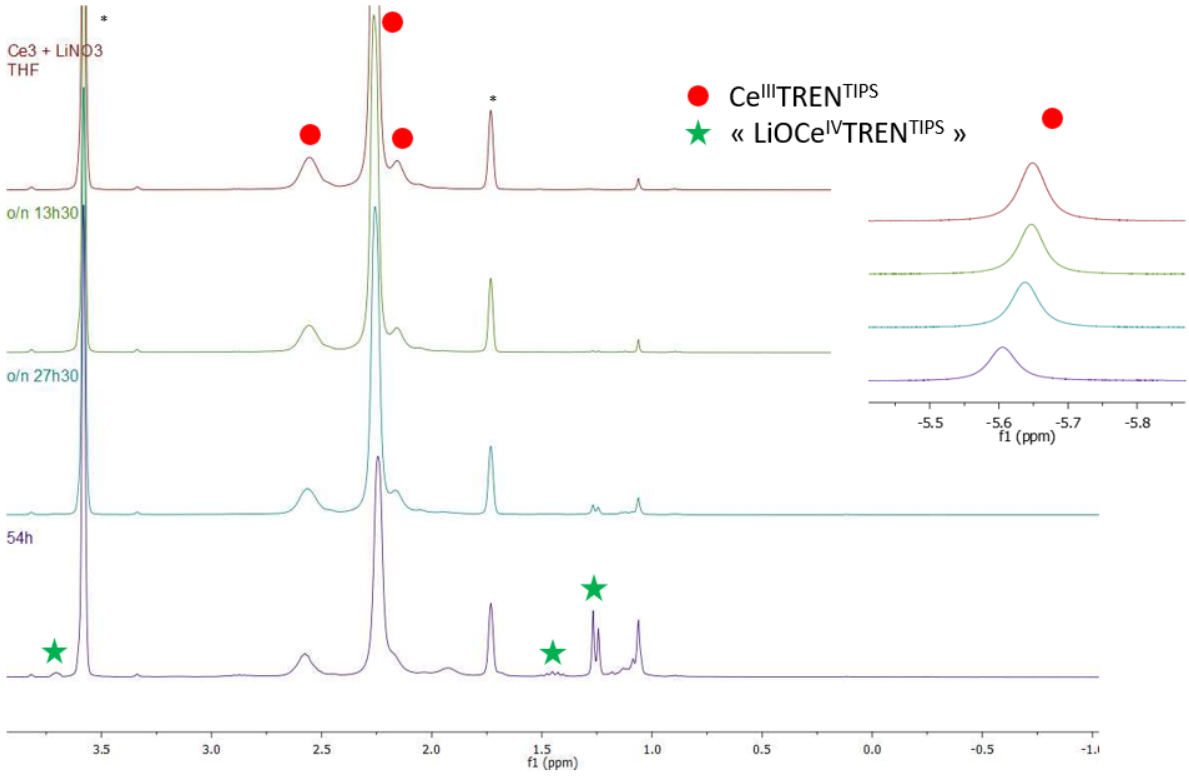

Figure S258. ^{1}H NMR spectra of reaction between **1** and $LiNO_3$ in THF-d_8 over time. Zoom between -1.0 and 3.8 ppm. Solvent residual peaks are indicated with *

Institut Polytechnique de Paris
91120 Palaiseau, France

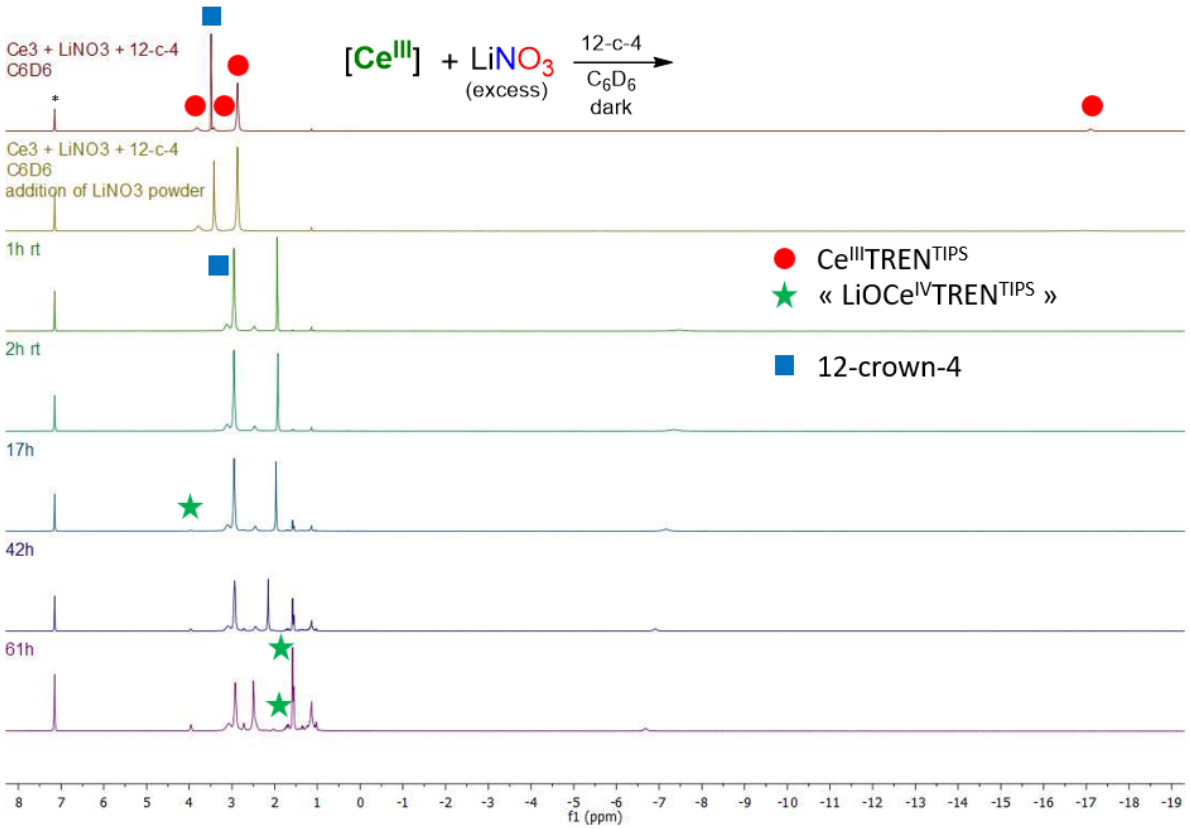

Figure S259. ^{1}H NMR spectra of reaction between **1**, $LiNO_3$ and 12-crown-4 in C_6D_6 over time. Solvent residual peaks are indicated with *

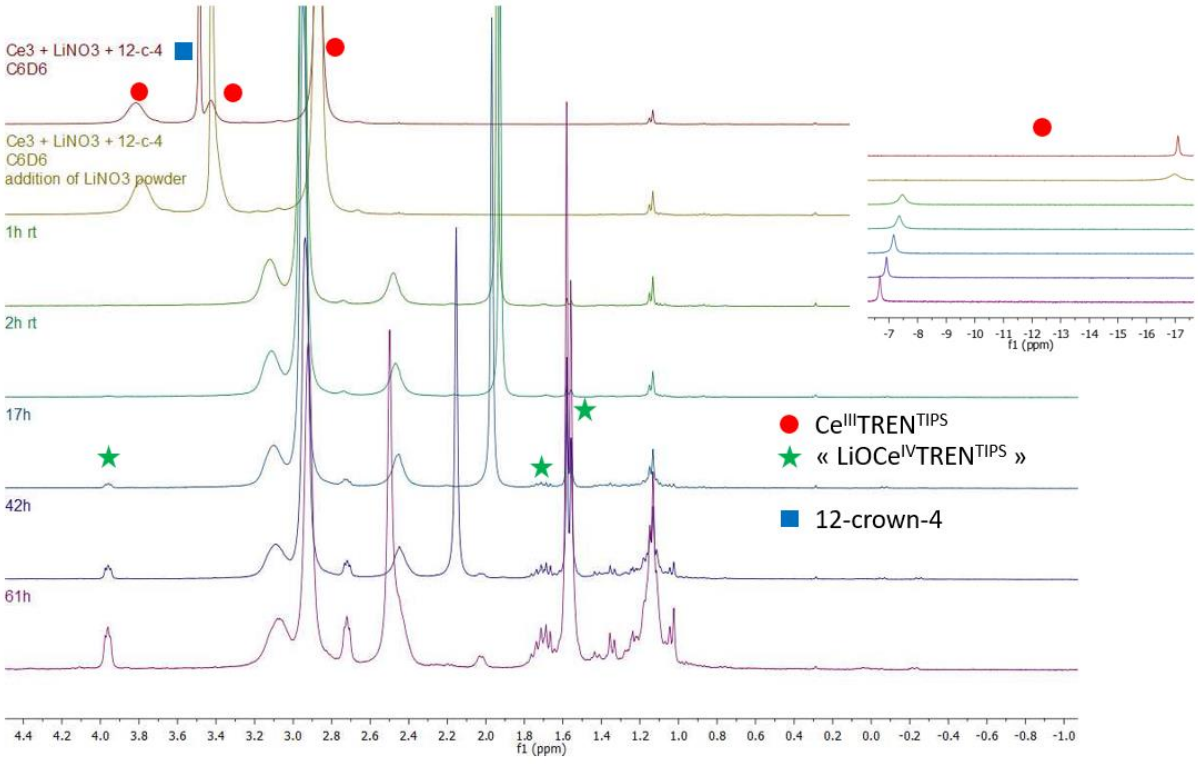

Figure S260. ^{1}H NMR spectra of reaction between **1**, $LiNO_3$ and 12-crown-4 in C_6D_6 over time. Zoom between -1.0 and 4.4 ppm. Solvent residual peaks are indicated with *

d) Reactivity of 1 with $LiNO_3$ under irradiation

Institut Polytechnique de Paris
91120 Palaiseau, France

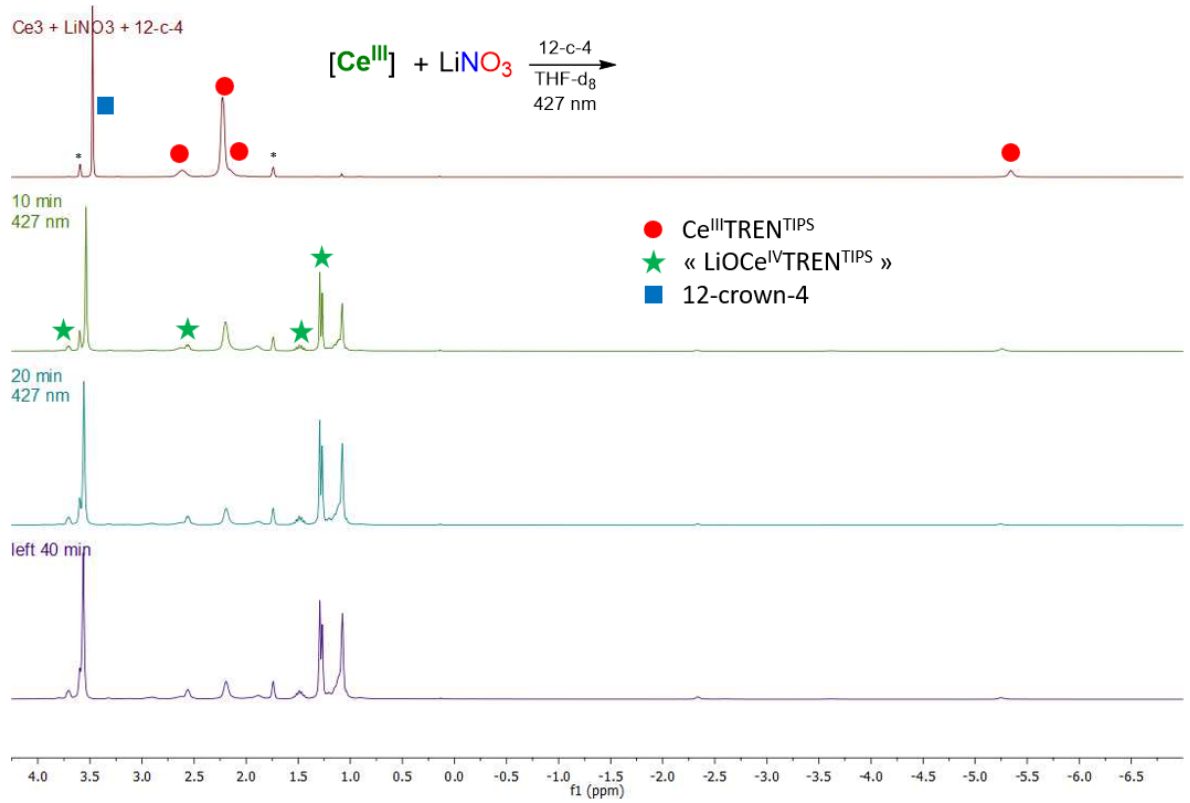

Figure S261. ^{1}H NMR spectra of photoirradiation at 427 nm of a mixture of **1**, $LiNO_3$ and 12-crown-4 in THF-d_8 over time. Solvent residual peaks are indicated with *

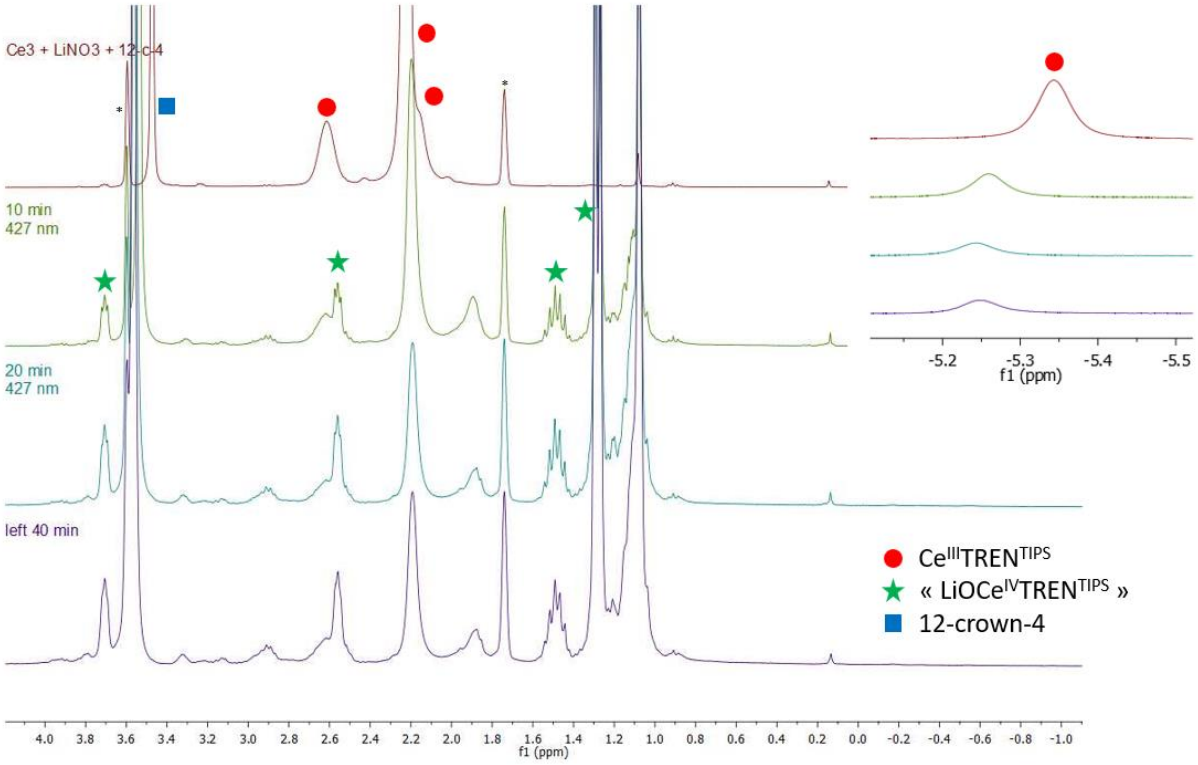

Figure S262. ^{1}H NMR spectra of photoirradiation at 427 nm of a mixture of **1**, $LiNO_3$ and 12-crown-4 in THF-d_8 over time. Zoom between -0.3 and 4.0 ppm. Solvent residual peaks are indicated with *

Institut Polytechnique de Paris
91120 Palaiseau, France

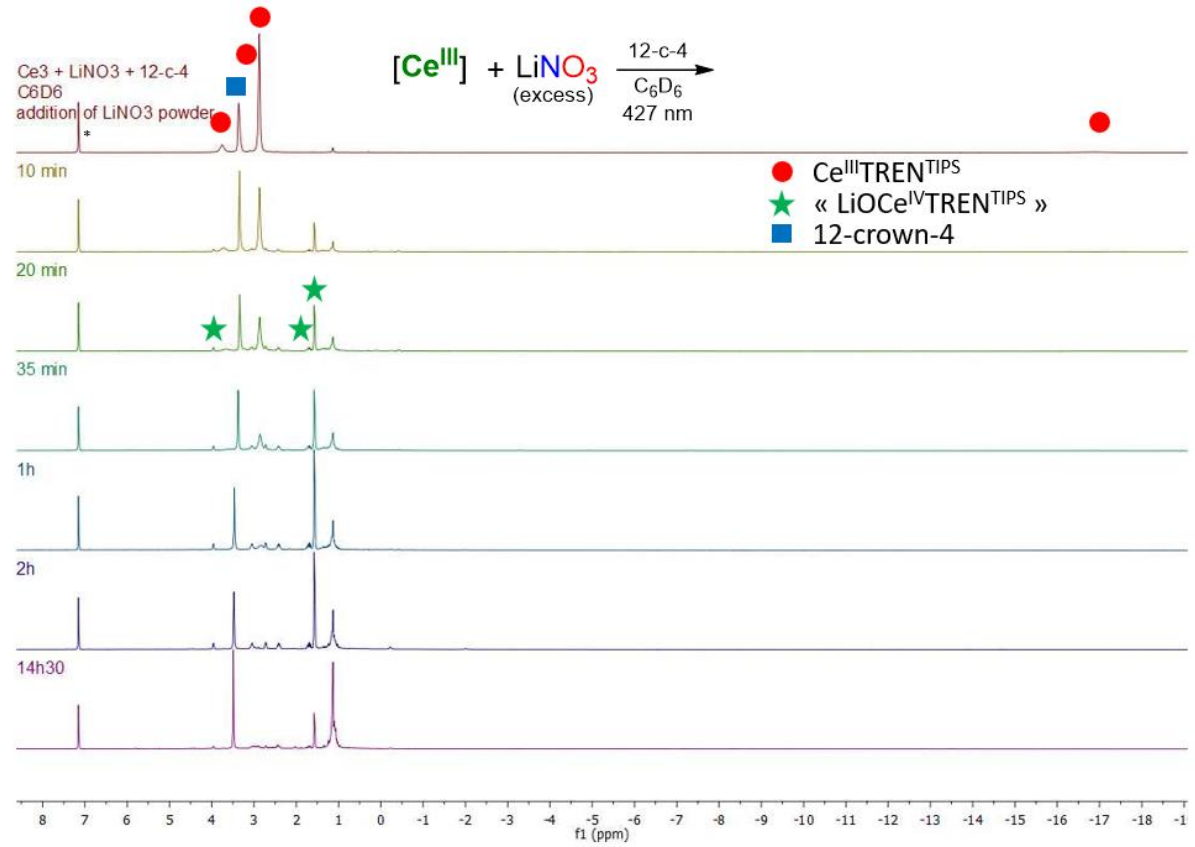

Figure S263. ^{1}H NMR spectra of photoirradiation at 427 nm of a mixture of **1**, $LiNO_3$ and 12-crown-4 in C_6D_6 over time. Solvent residual peak is indicated with *

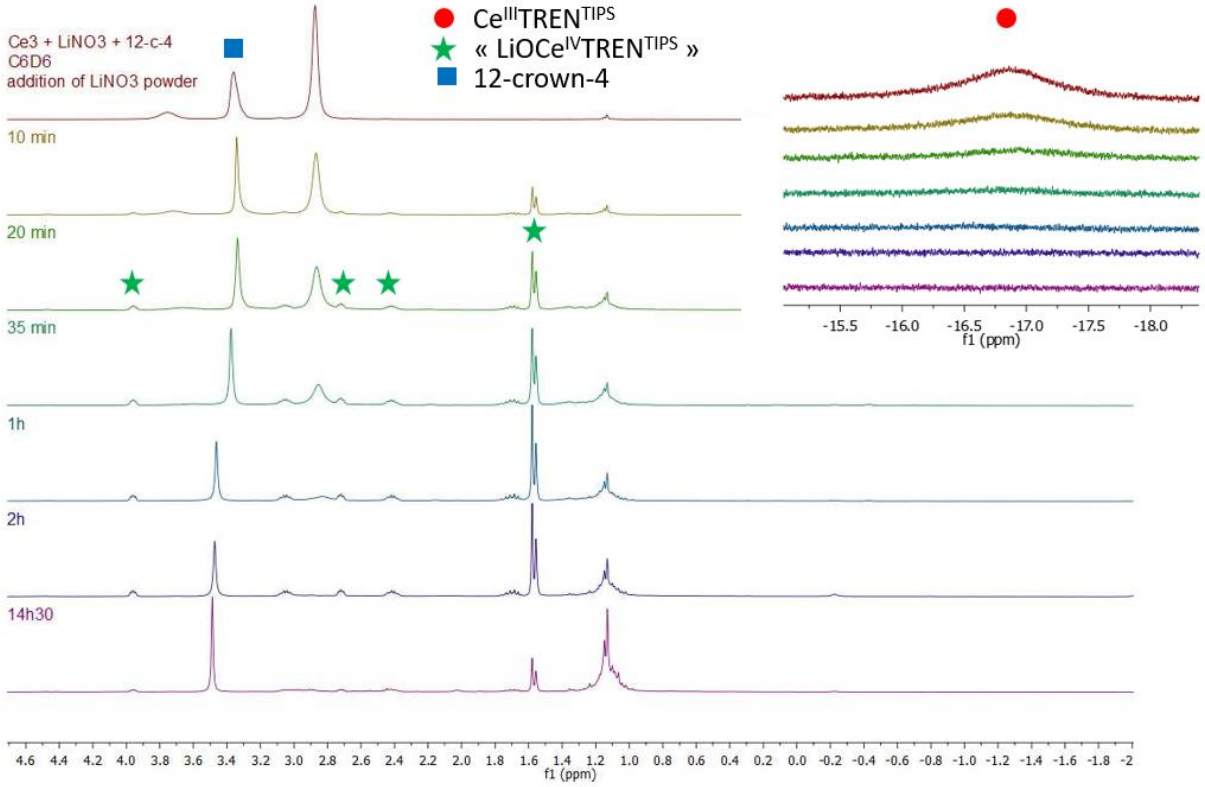

Figure S264. ^{1}H NMR spectra of photoirradiation at 427 nm of a mixture of **1**, $LiNO_3$ and 12-crown-4 in C_6D_6 over time. Zoom between -2.0 and 4.7 ppm. Solvent residual peaks are indicated with *

Institut Polytechnique de Paris
91120 Palaiseau, France

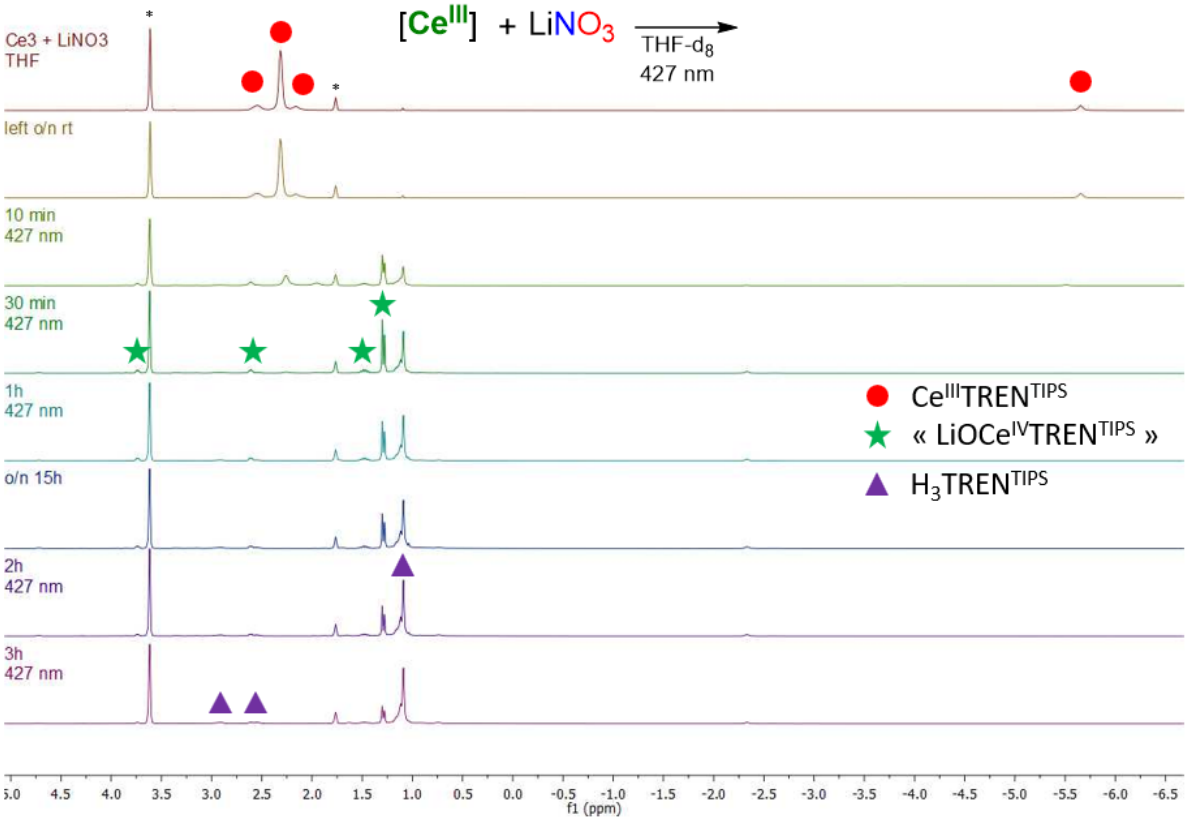

Figure S265. ^{1}H NMR spectra of photoirradiation at 427 nm of a mixture of **1** and $LiNO_3$ without 12-crown-4 in THF-d_8 over time. Zoom from -6.5 to 5.0 ppm. Solvent residual peaks are indicated with *

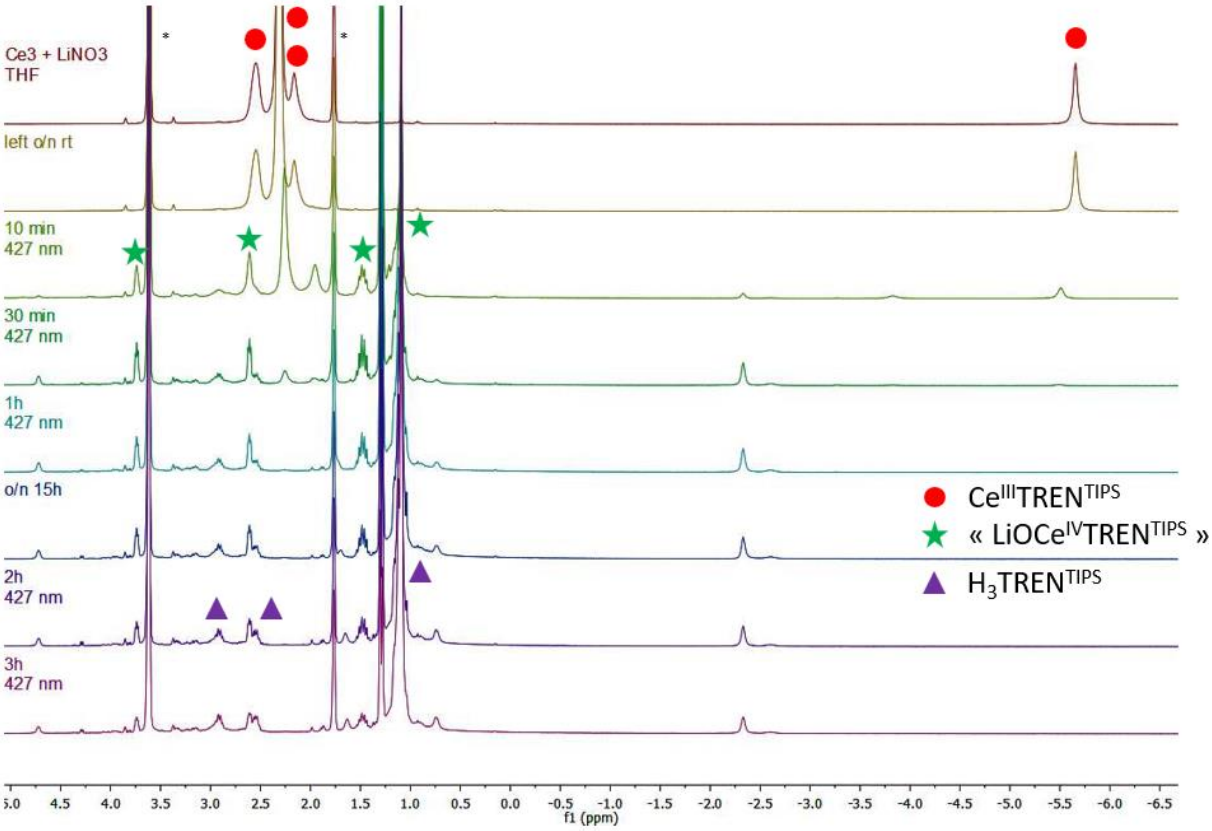

Figure S266. ^{1}H NMR spectra of photoirradiation at 427 nm of a mixture of **1** and $LiNO_3$ without 12-crown-4 in THF-d_8 over time. Zoom from -6.5 to 5.0 ppm. Solvent residual peaks are indicated with *

Institut Polytechnique de Paris
91120 Palaiseau, France

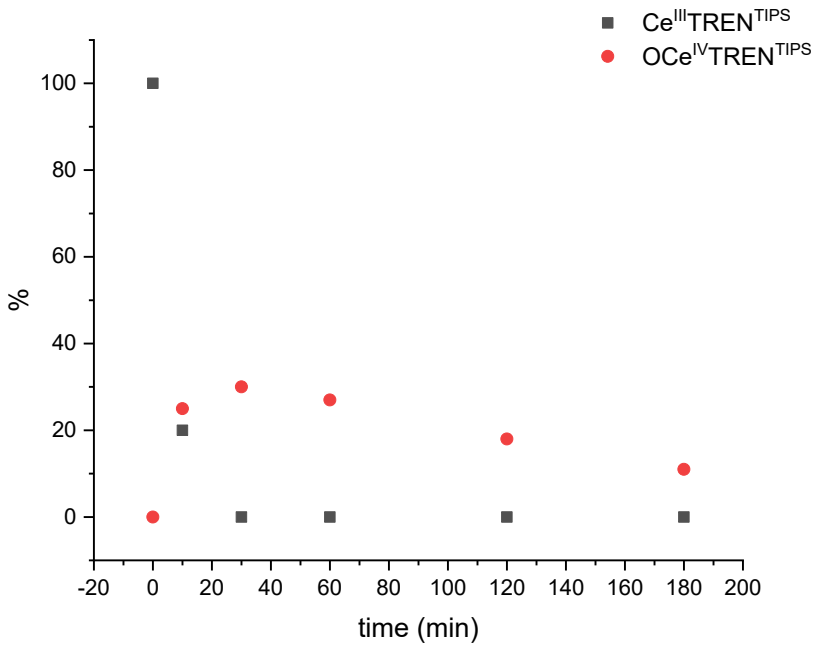

Figure S267. Evolution of $Ce^{III}TREN^{TIPS}$ / $OCe^{IV}TREN^{TIPS}$ ratio over irradiation time at 427 nm

Institut Polytechnique de Paris
91120 Palaiseau, France

e) Attempts of reactivity with 2-O

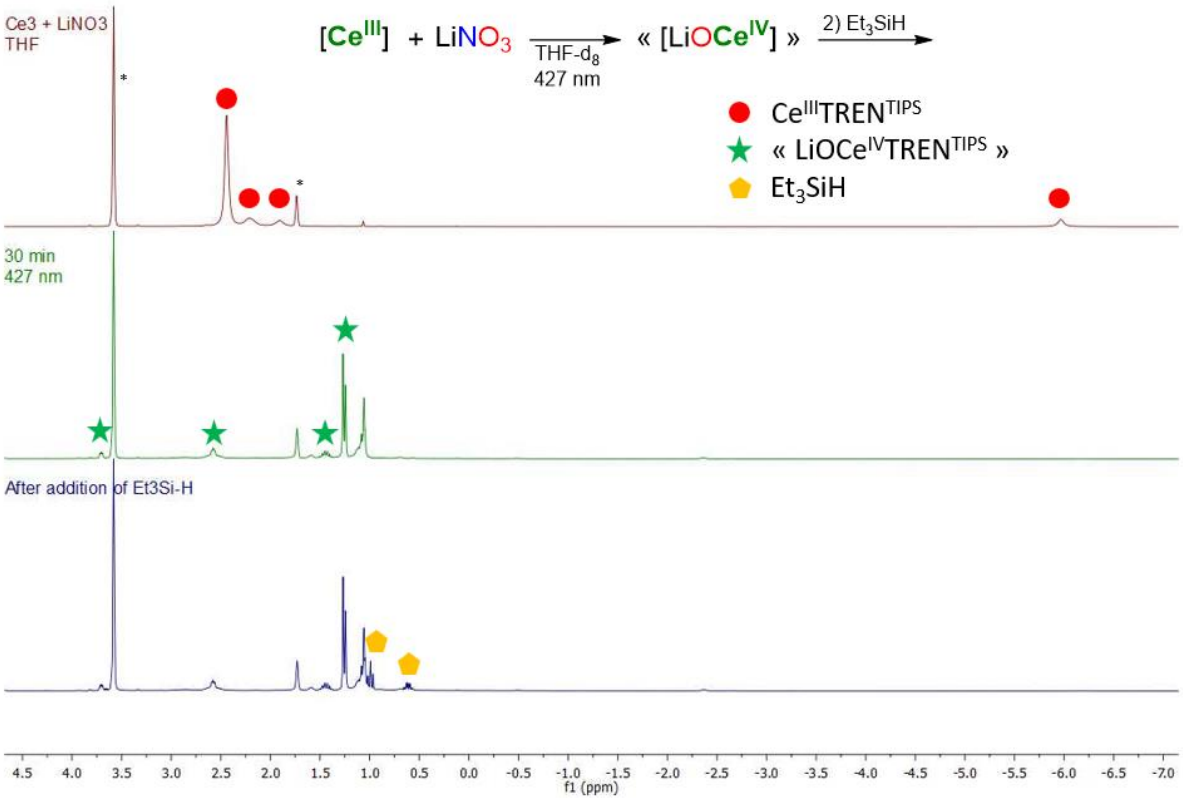

Figure S268. ^{1}H NMR spectra of photoirradiation at 427 nm of a mixture of **1** and $LiNO_3$ without 12-crown-4 in THF-d_8, and subsequent addition of triethylsilane. Solvent residual peaks are indicated with *

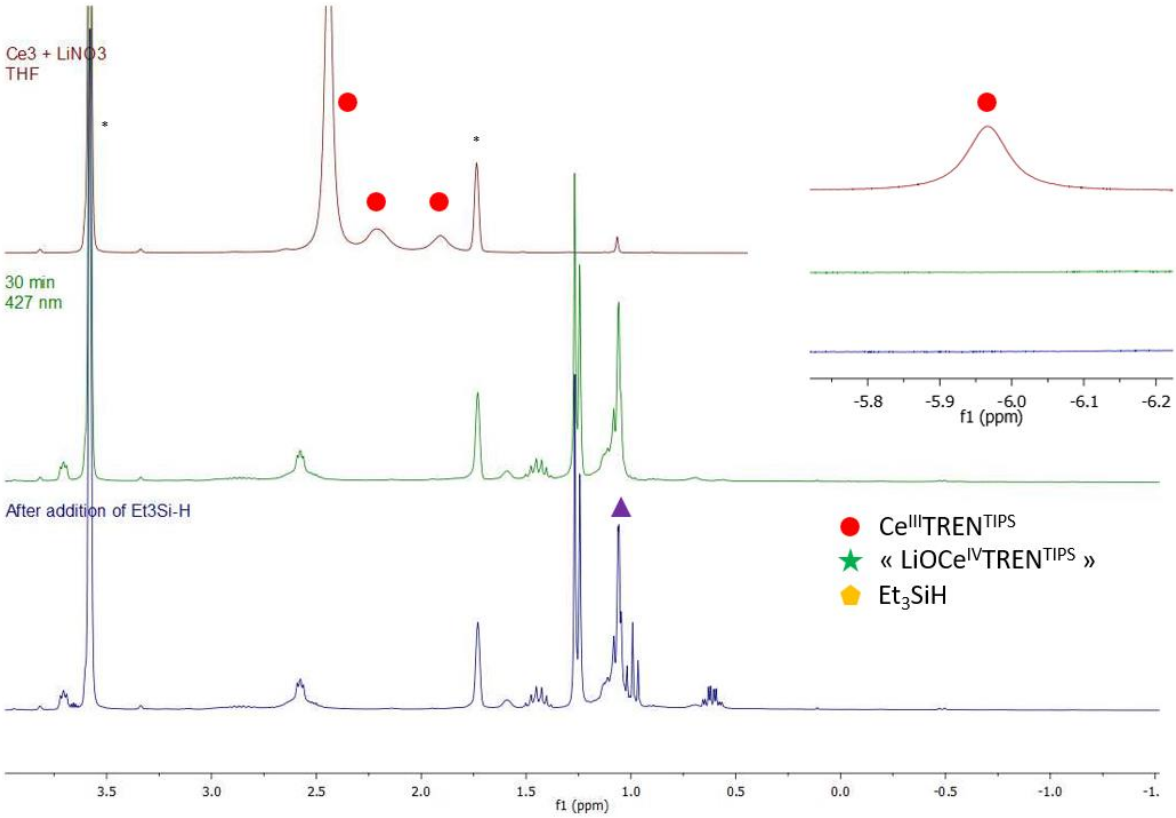

Figure S269. ^{1}H NMR spectra of photoirradiation at 427 nm of a mixture of **1** and $LiNO_3$ without 12-crown-4 in THF-d_8, and subsequent addition of triethylsilane. Zoom between -1.5 and 3.8 ppm. Solvent residual peaks are indicated with *

Institut Polytechnique de Paris
91120 Palaiseau, France

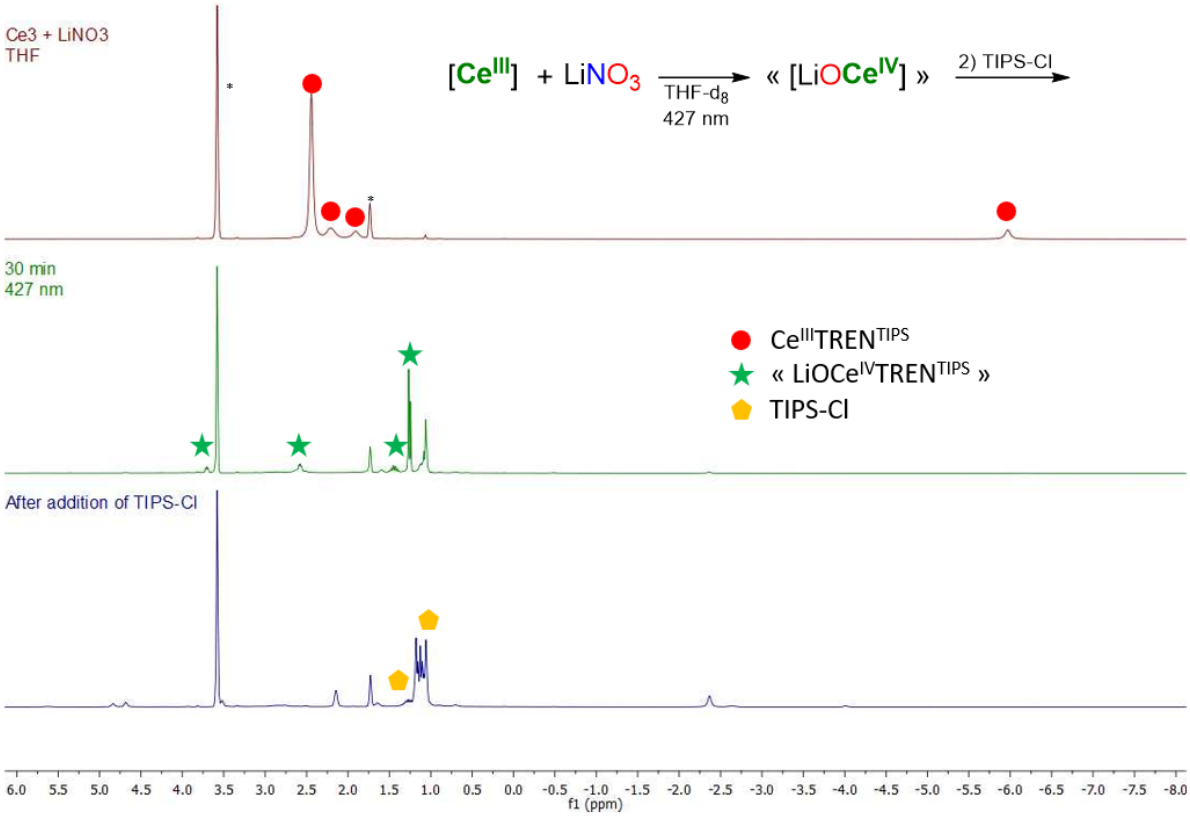

Figure S270. ^{1}H NMR spectra of photoirradiation at 427 nm of a mixture of **1** and $LiNO_3$ <u>without</u> 12-crown-4 in THF-d_8, and subsequent addition of TIPS-Cl. Solvent residual peaks are indicated with *

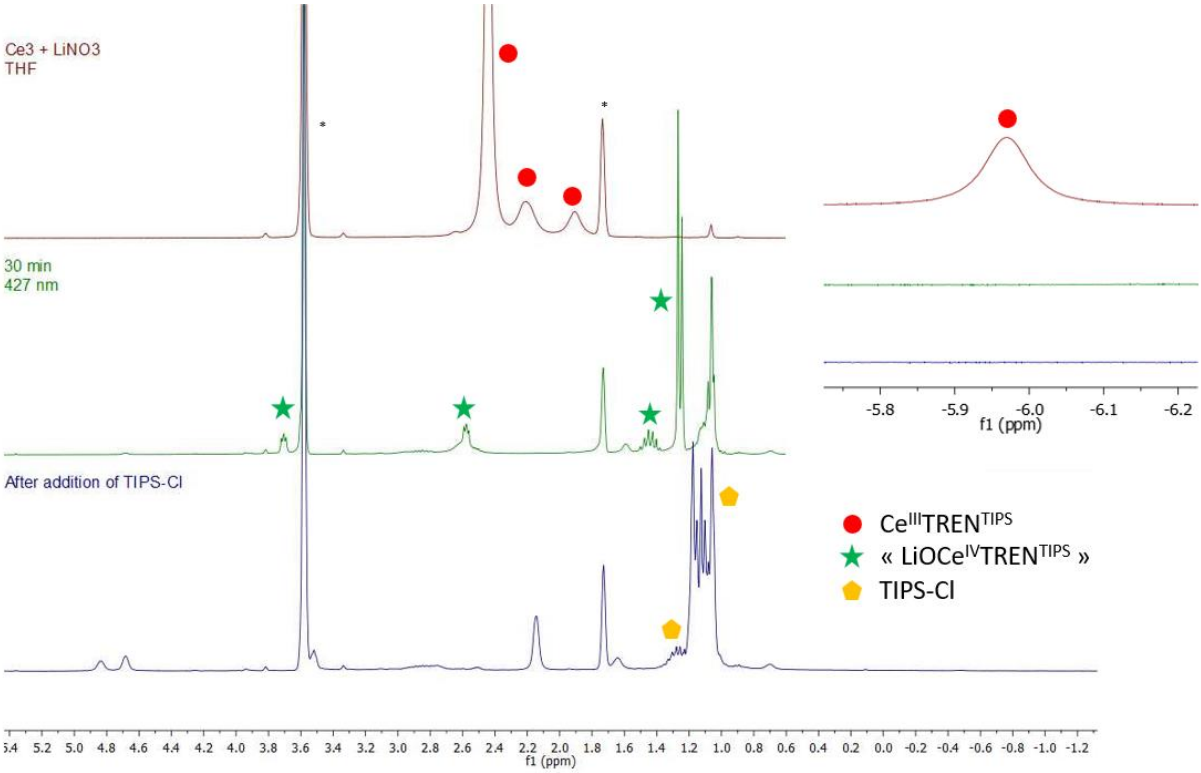

Figure S271. ^{1}H NMR spectra of photoirradiation at 427 nm of a mixture of **1** and $LiNO_3$ <u>without</u> 12-crown-4 in THF-d_8, and subsequent addition of TIPS-Cl. Zoom between -1.3 and 5.4 ppm. Solvent residual peaks are indicated with *

Institut Polytechnique de Paris
91120 Palaiseau, France

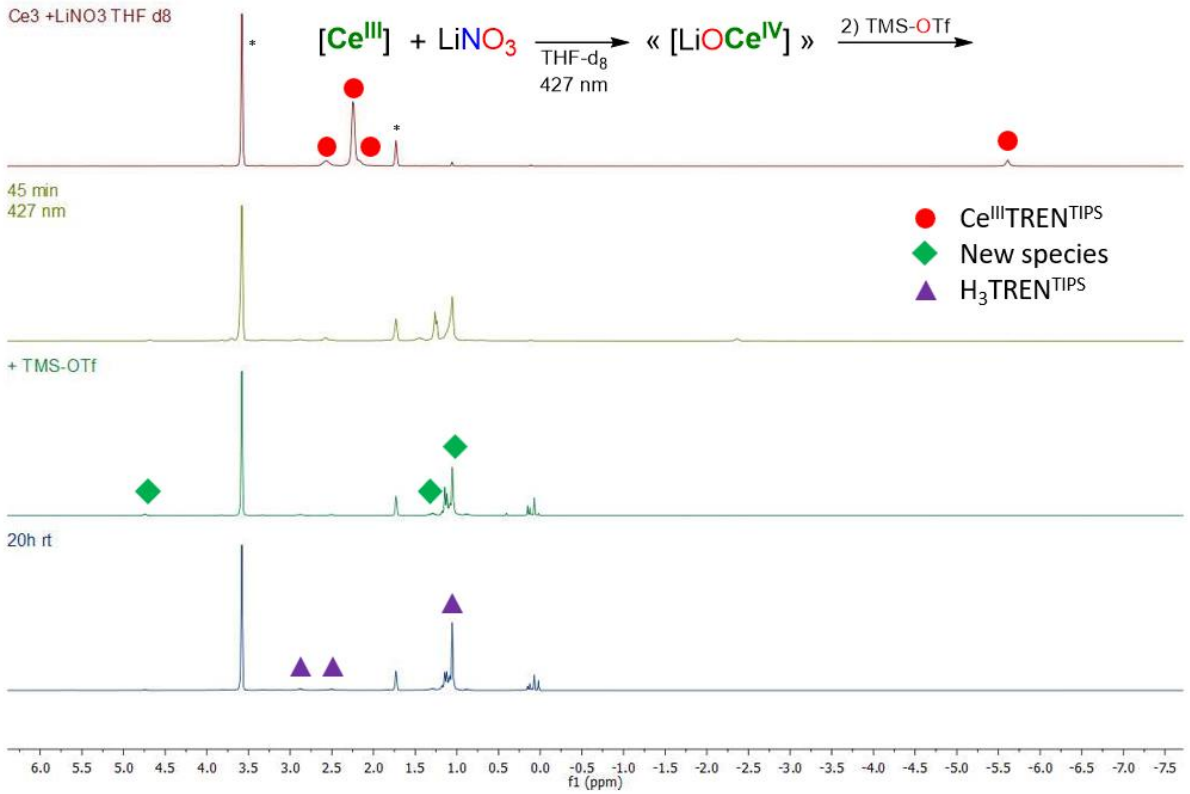

Figure S272. ^{1}H NMR spectra of photoirradiation at 427 nm of a mixture of **1** and $LiNO_3$ without 12-crown-4 in THF-d_8, and subsequent addition of TMS-OTf. Solvent residual peaks are indicated with *

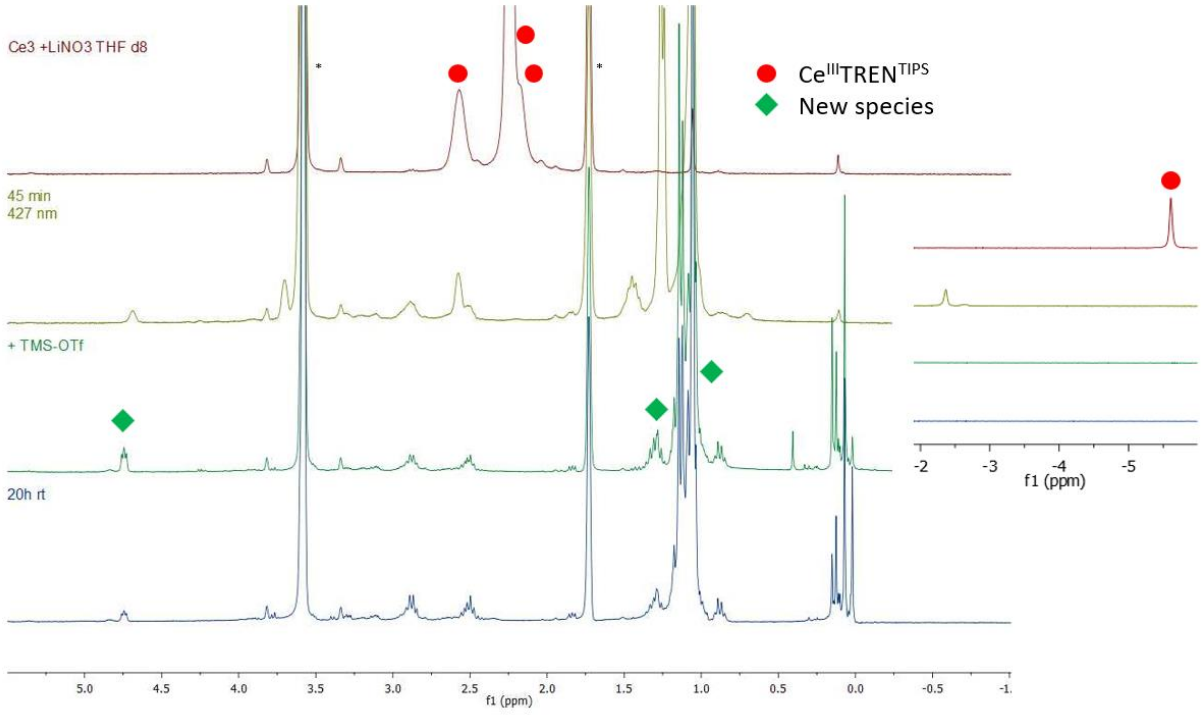

Figure S273. ^{1}H NMR spectra of photoirradiation at 427 nm of a mixture of **1** and $LiNO_3$ without 12-crown-4 in THF-d_8, and subsequent addition of TMS-OTf. Zoom between -1.0 and 5.5 ppm. Solvent residual peaks are indicated with *

Institut Polytechnique de Paris
91120 Palaiseau, France

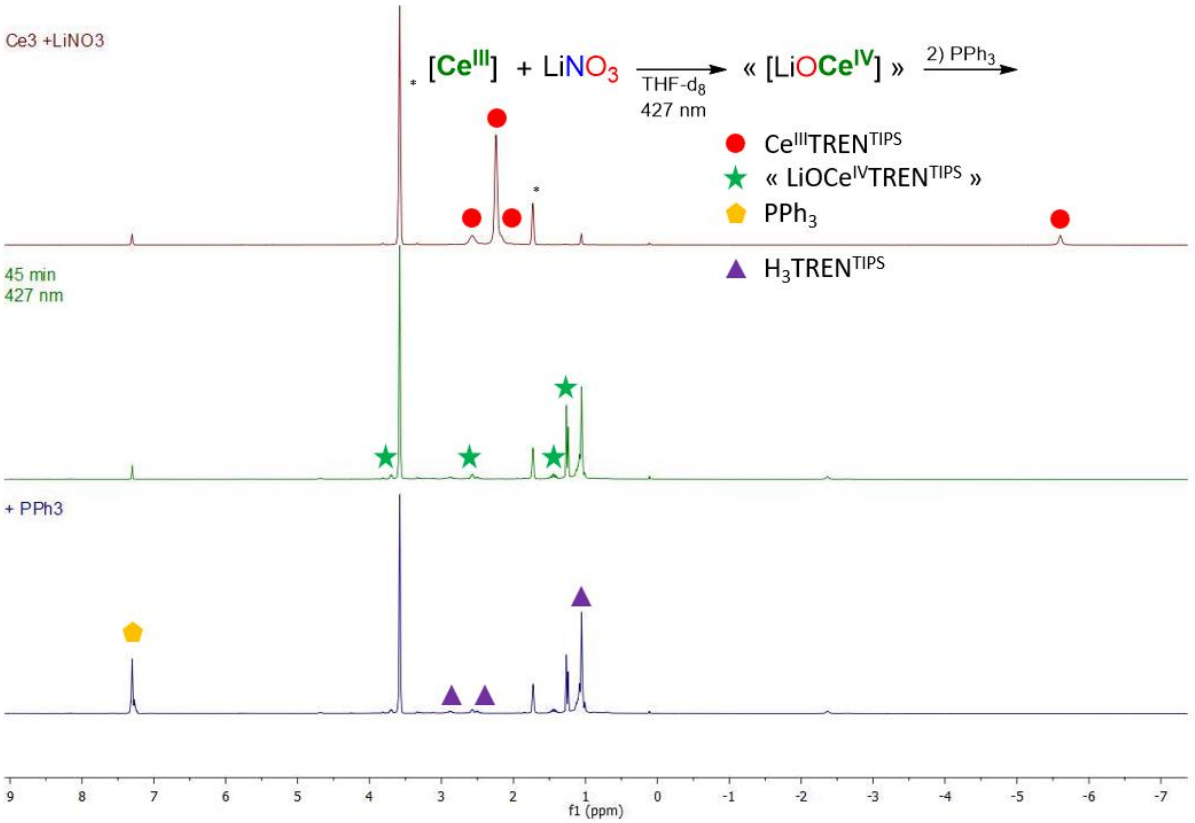

Figure S274. ^{1}H NMR spectra of photoirradiation at 427 nm of a mixture of **1** and $LiNO_3$ without 12-crown-4 in THF-d_8, and subsequent addition of PPh_3. Solvent residual peaks are indicated with *

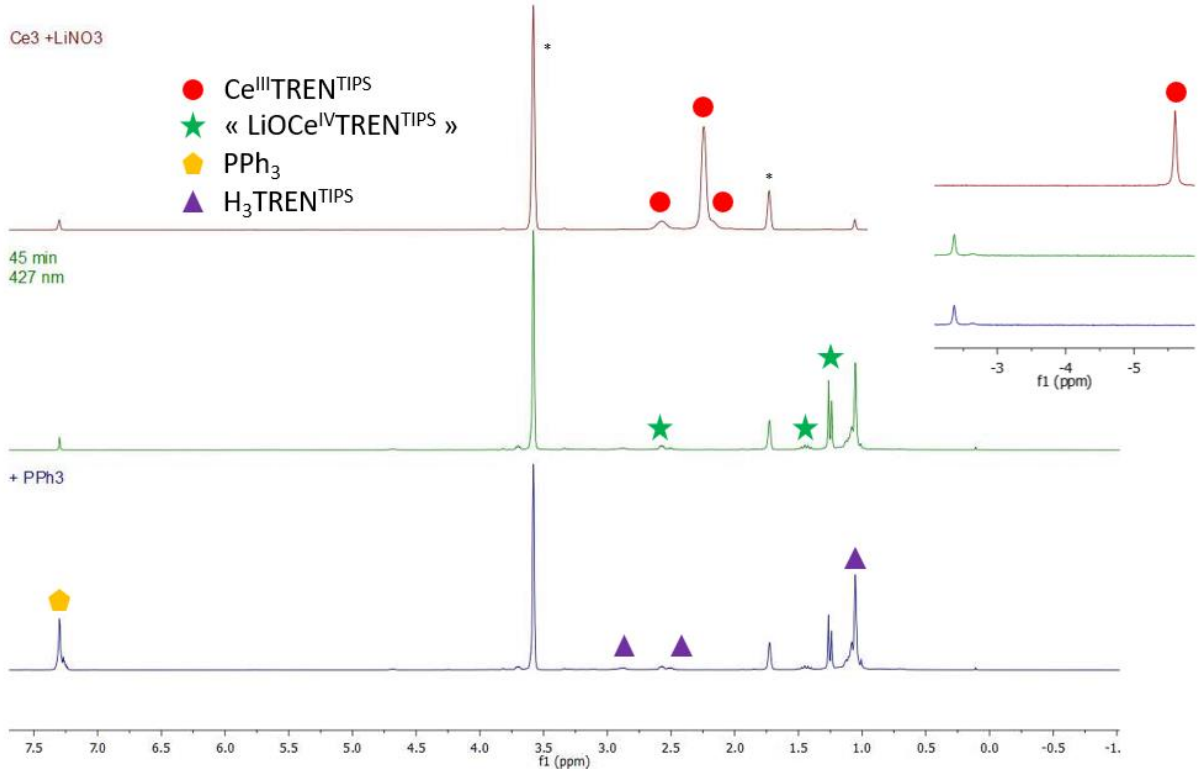

Figure S275. ^{1}H NMR spectra of photoirradiation at 427 nm of a mixture of **1** and $LiNO_3$ without 12-crown-4 in THF-d_8, and subsequent addition of PPh_3. Zoom between -1.0 and 7.5 ppm. Solvent residual peaks are indicated with *

Institut Polytechnique de Paris
91120 Palaiseau, France

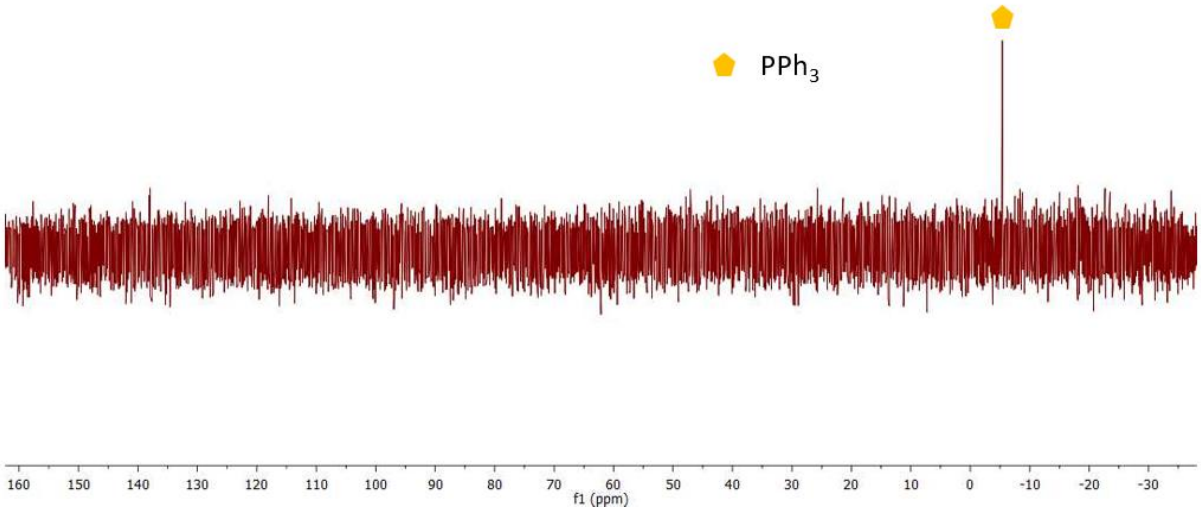

Figure S276. ^{31}P NMR spectra of photoirradiation at 427 nm of a mixture of **1** and $LiNO_3$ without 12-crown-4 in THF-d_8, and subsequent addition of PPh_3

Institut Polytechnique de Paris
91120 Palaiseau, France

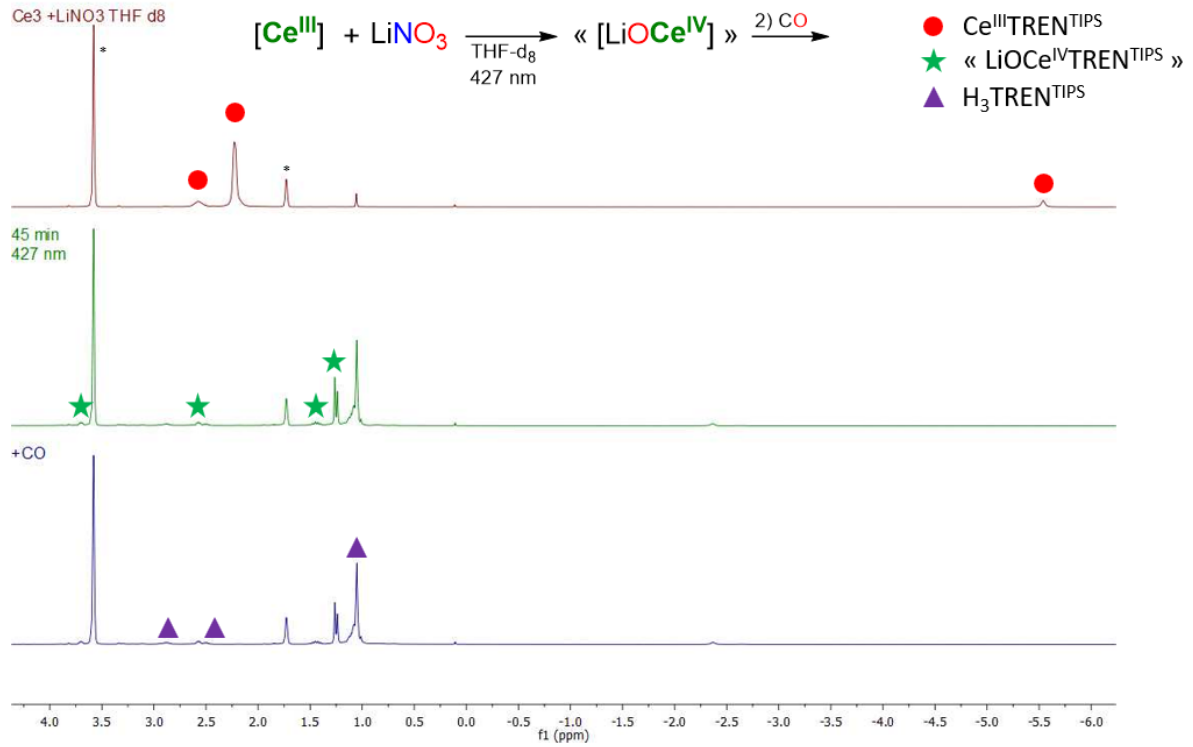

Figure S277. ^{1}H NMR spectra of photoirradiation at 427 nm of a mixture of **1** and $LiNO_3$ without 12-crown-4 in THF-d_8, and subsequent addition of CO. Solvent residual peaks are indicated with *

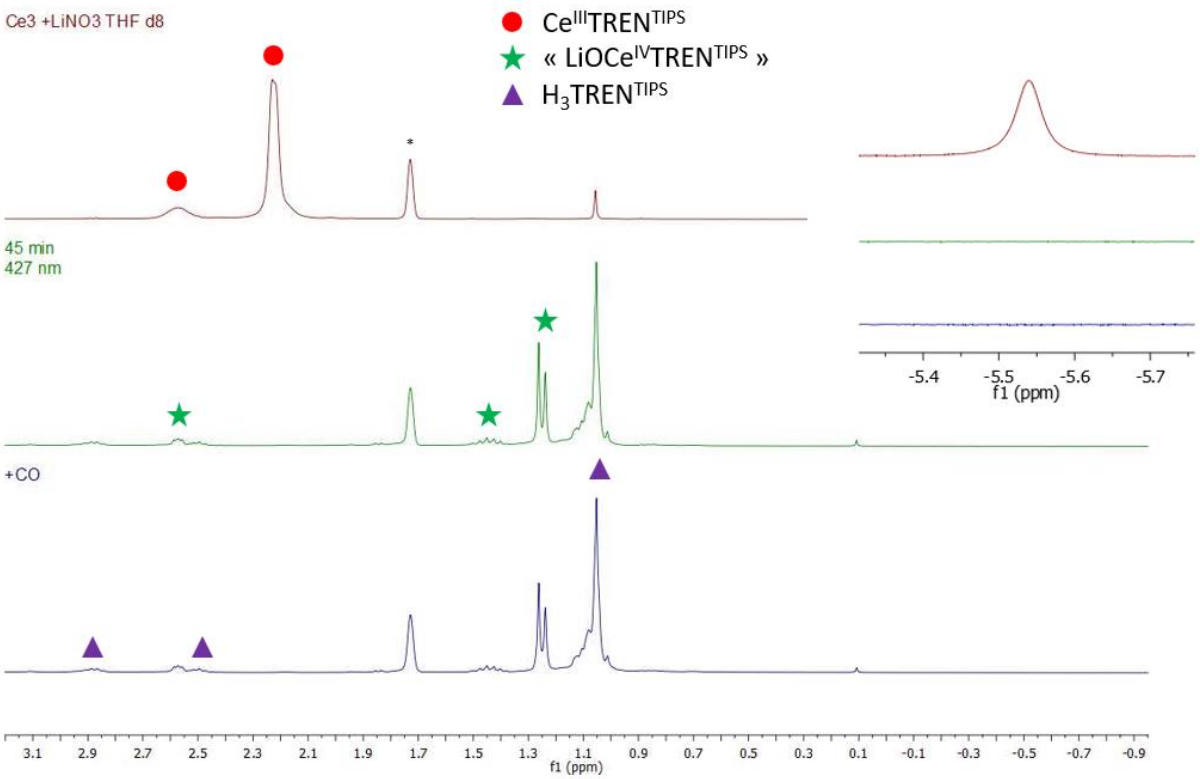

Figure S278. ^{1}H NMR spectra of photoirradiation at 427 nm of a mixture of **1** and $LiNO_3$ without 12-crown-4 in THF-d_8, and subsequent addition of CO. Zoom between -1.0 and 3.2 ppm. Solvent residual peaks are indicated with *

Institut Polytechnique de Paris
91120 Palaiseau, France

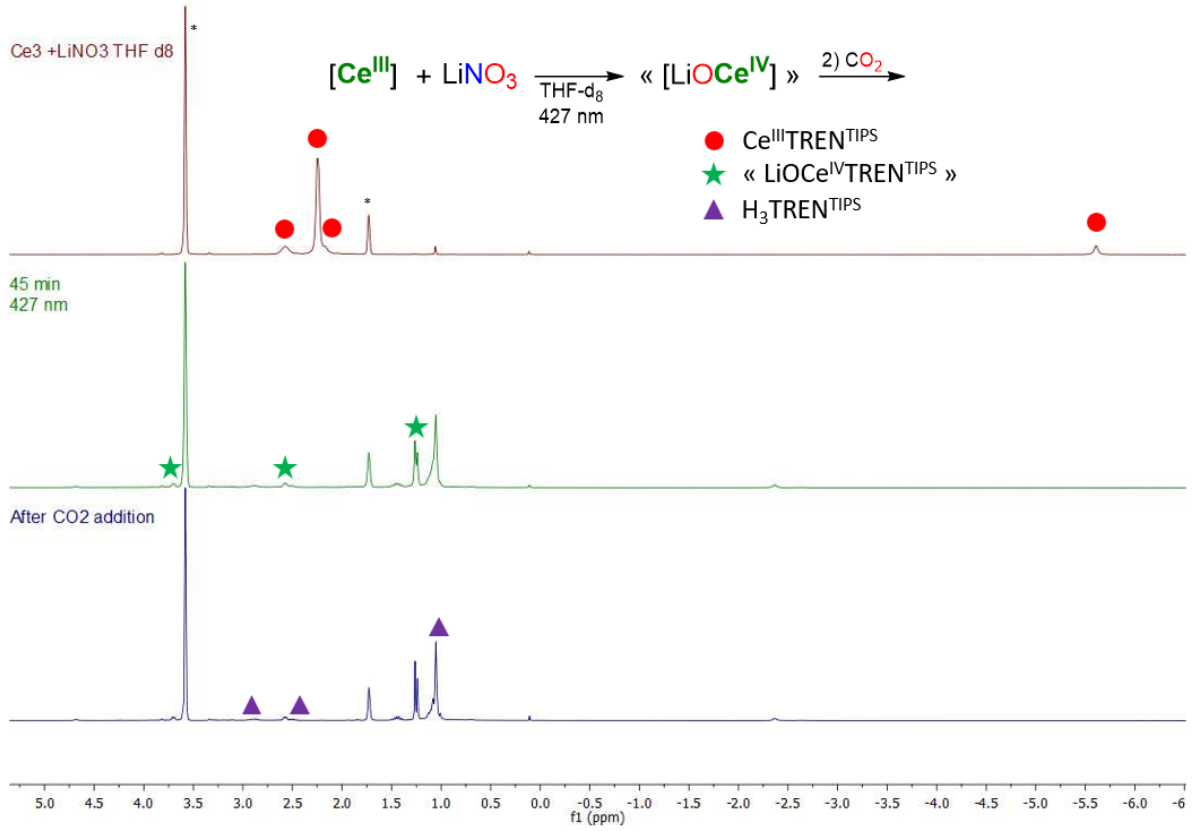

Figure S279. ^{1}H NMR spectra of photoirradiation at 427 nm of a mixture of **1** and $LiNO_3$ <u>without</u> 12-crown-4 in THF-d_8, and subsequent addition of CO_2. Solvent residual peaks are indicated with *

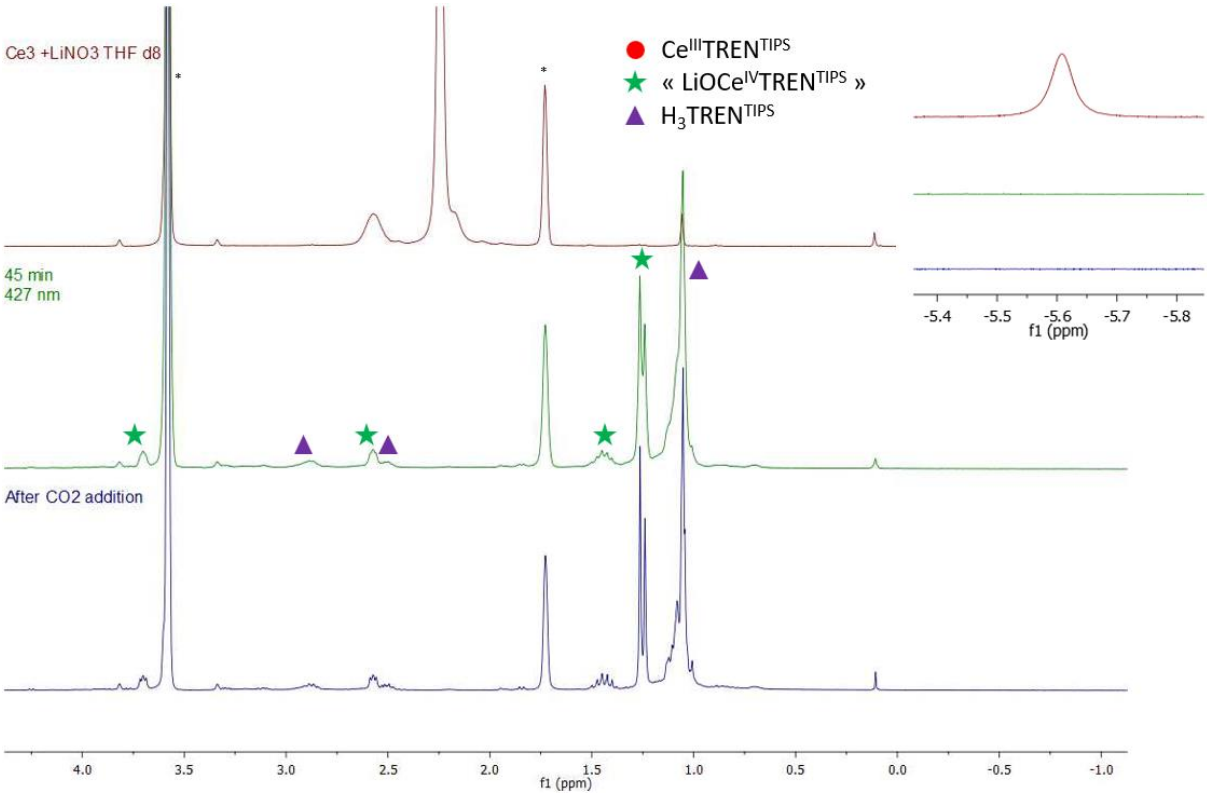

Figure S280. ^{1}H NMR spectra of photoirradiation at 427 nm of a mixture of **1** and $LiNO_3$ <u>without</u> 12-crown-4 in THF-d_8, and subsequent addition of CO_2. Zoom between -1.0 and 4.5 ppm. Solvent residual peaks are indicated with *

Institut Polytechnique de Paris
91120 Palaiseau, France

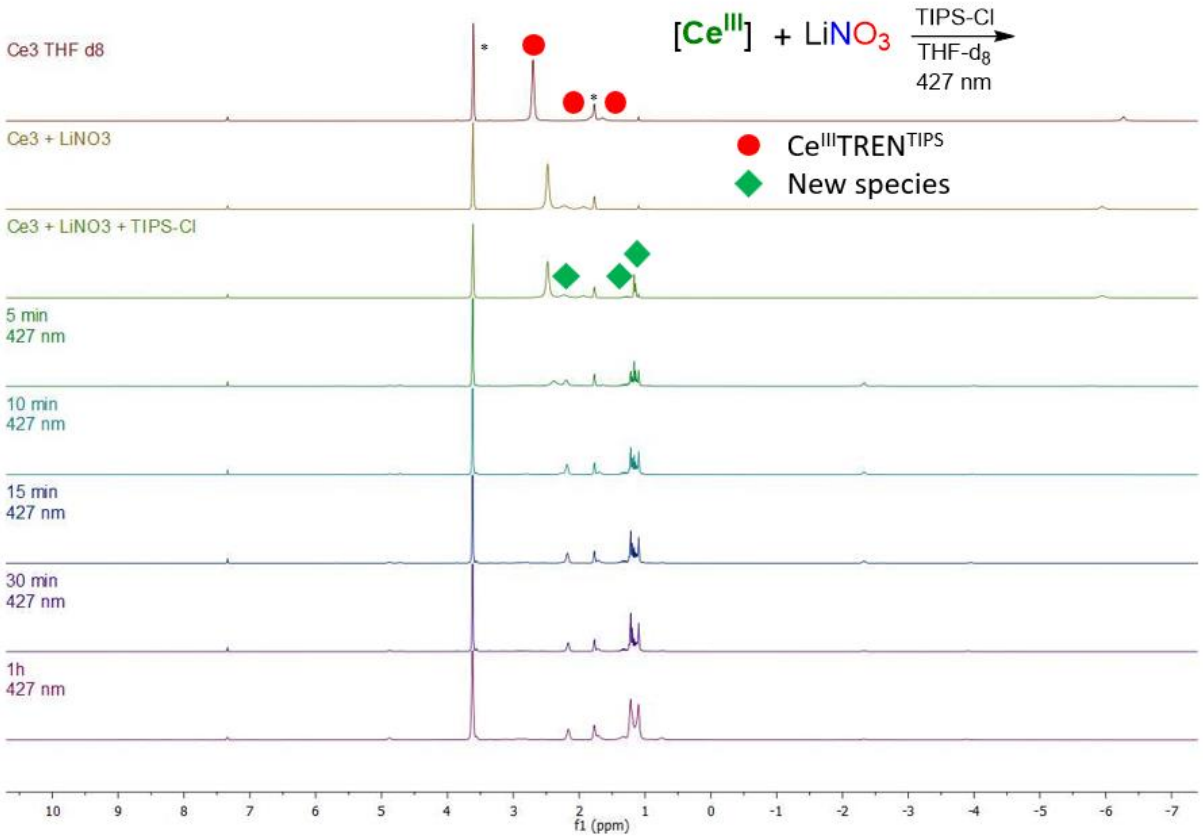

Figure S281. ^{1}H NMR spectra of photoirradiation at 427 nm of a mixture of **1** and $LiNO_3$ in the presence of TIPS-Cl in THF-d_8. Solvent residual peaks are indicated with *

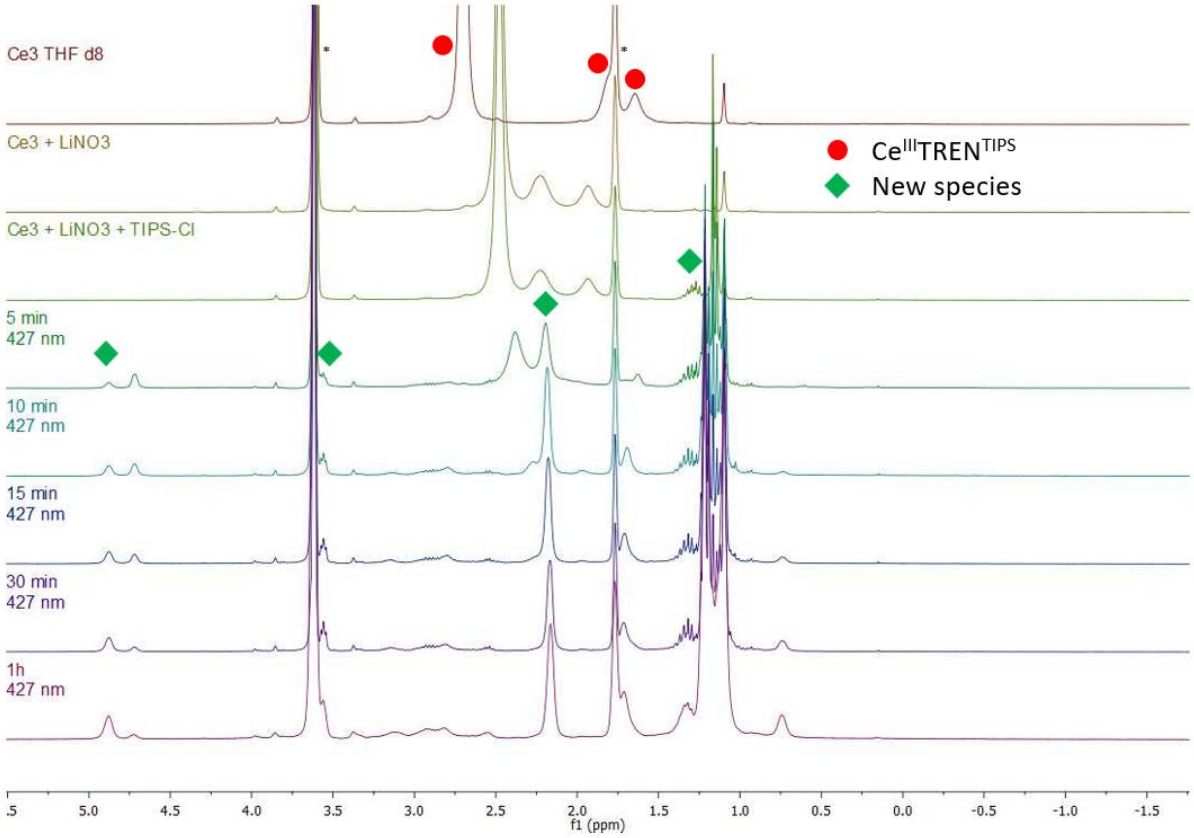

Figure S282. ^{1}H NMR spectra of photoirradiation at 427 nm of a mixture of **1** and $LiNO_3$ in the presence of TIPS-Cl in THF-d_8. Zoom between -1.5 and 5.5 ppm. Solvent residual peaks are indicated with *

Institut Polytechnique de Paris
91120 Palaiseau, France

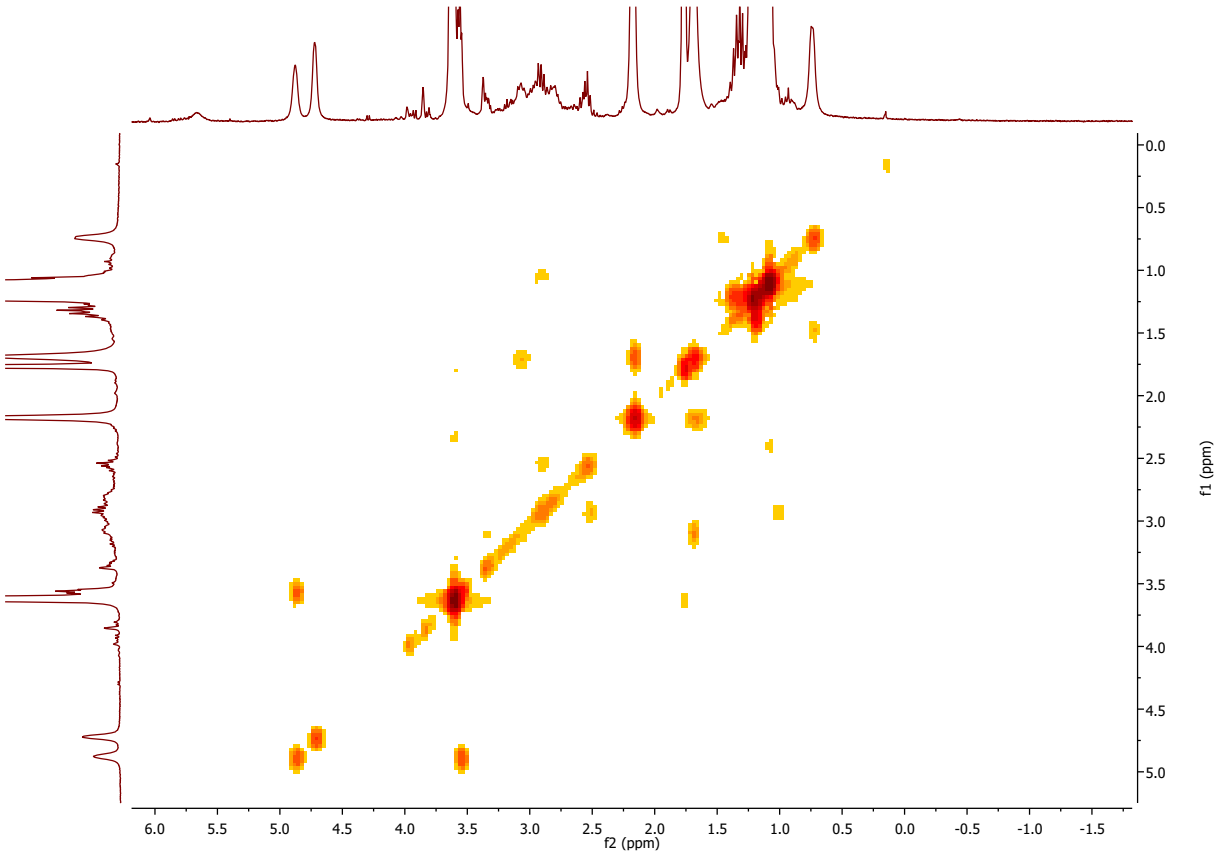

Figure S283. ^{1}H-^{1}H COSY spectrum of photoirradiation at 427 nm of a mixture of **1** and $LiNO_3$ in the presence of TIPS-Cl in THF-d_8. Zoom between -1.5 and 5.5 ppm

f) Successive additions of $LiNO_3$ on 1

Institut Polytechnique de Paris
91120 Palaiseau, France

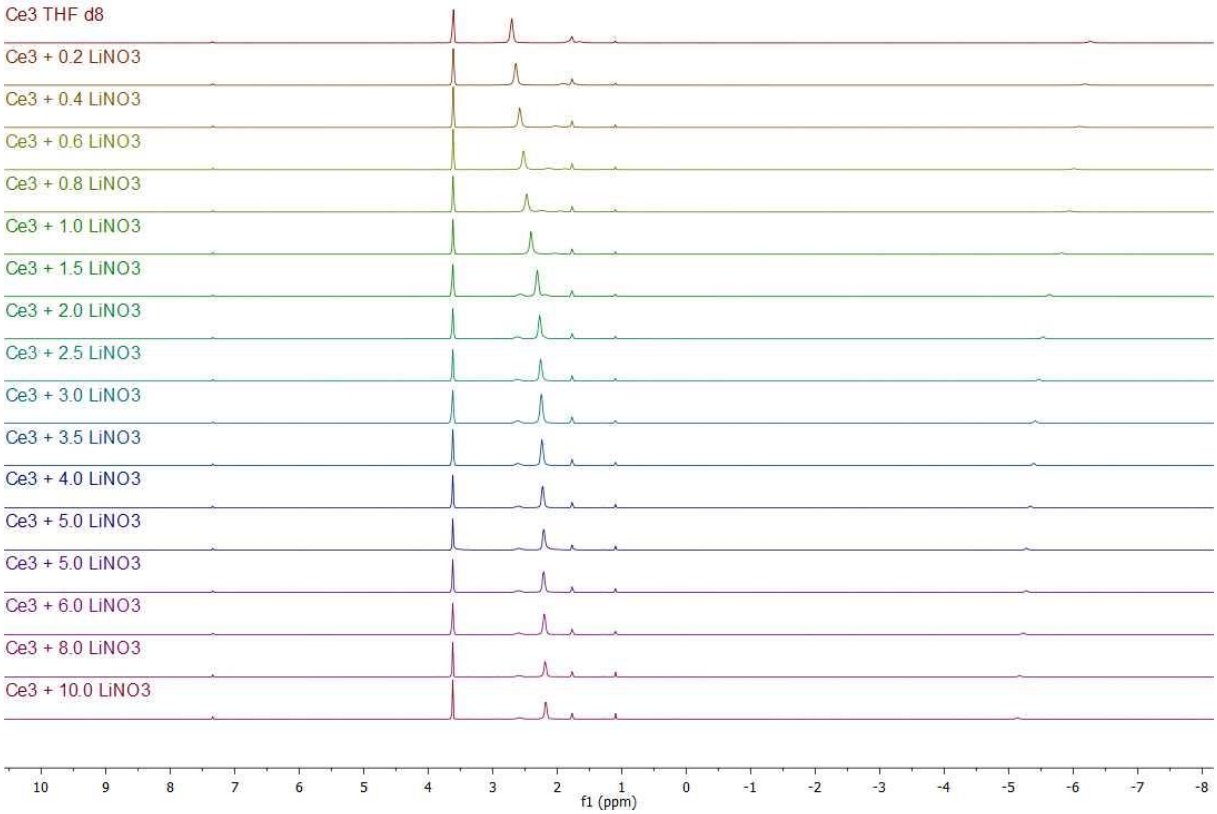

Figure S284. ^{1}H NMR spectrum of the successive additions of a concentrated solution of $LiNO_3$ in THF-d_8 to a solution of **1** in THF-d_8. Solvent residual peaks are indicated with *

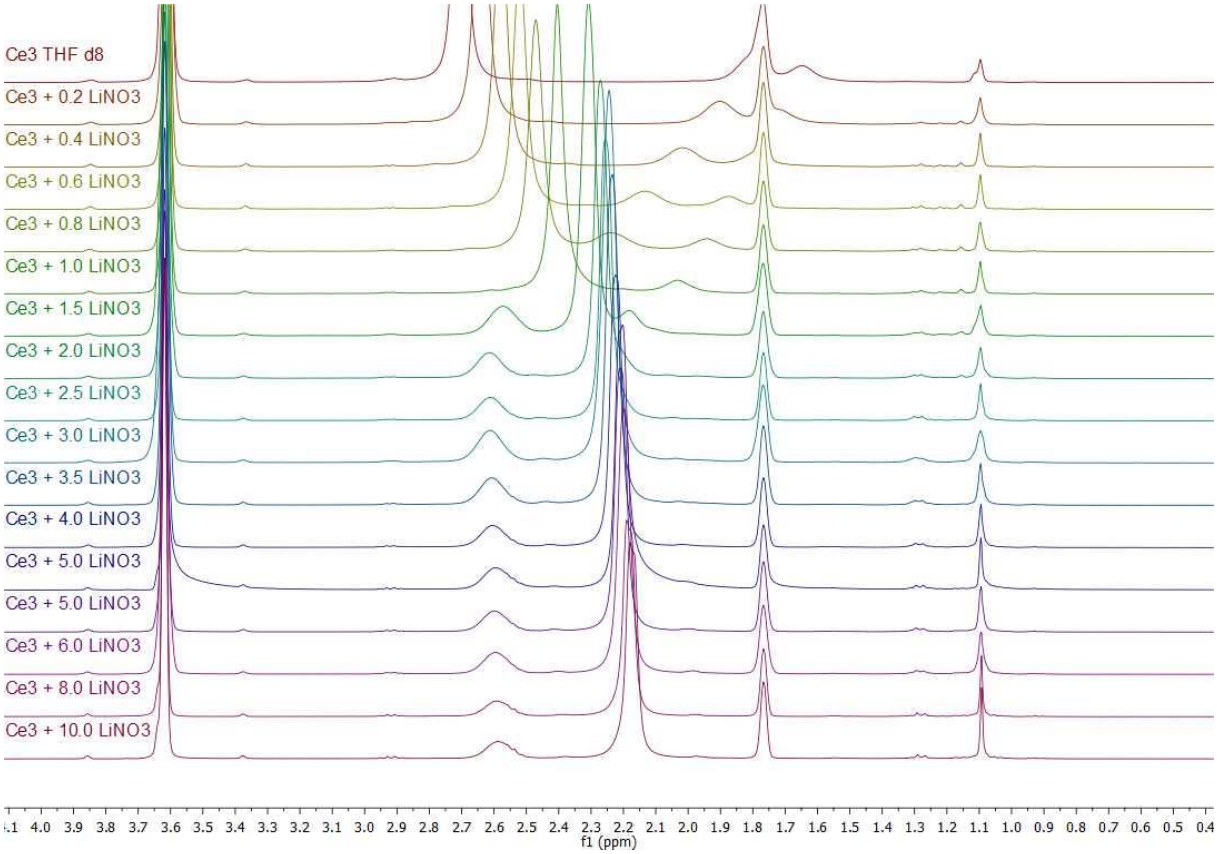

Figure S285. ^{1}H NMR spectrum of the successive additions of a concentrated solution of $LiNO_3$ in THF-d_8 to a solution of **1** in THF-d_8. Zoom between 0.4 and 4.1 ppm. Solvent residual peaks are indicated with *

Institut Polytechnique de Paris
91120 Palaiseau, France

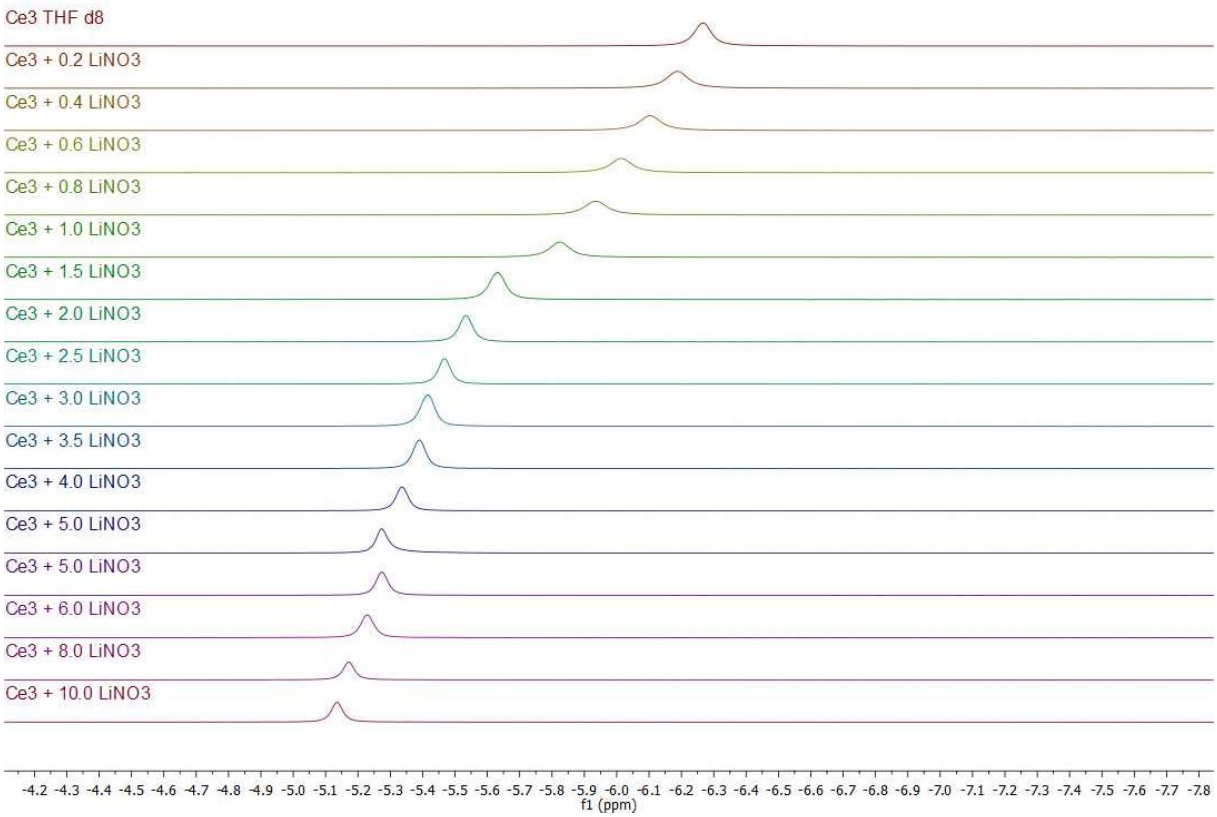

Figure S286. ^{1}H NMR spectrum of the successive additions of a concentrated solution of $LiNO_3$ in THF-d_8 to a solution of **1** in THF-d_8. Zoom between -7.8 and -4.2 ppm. Solvent residual peaks are indicated with *

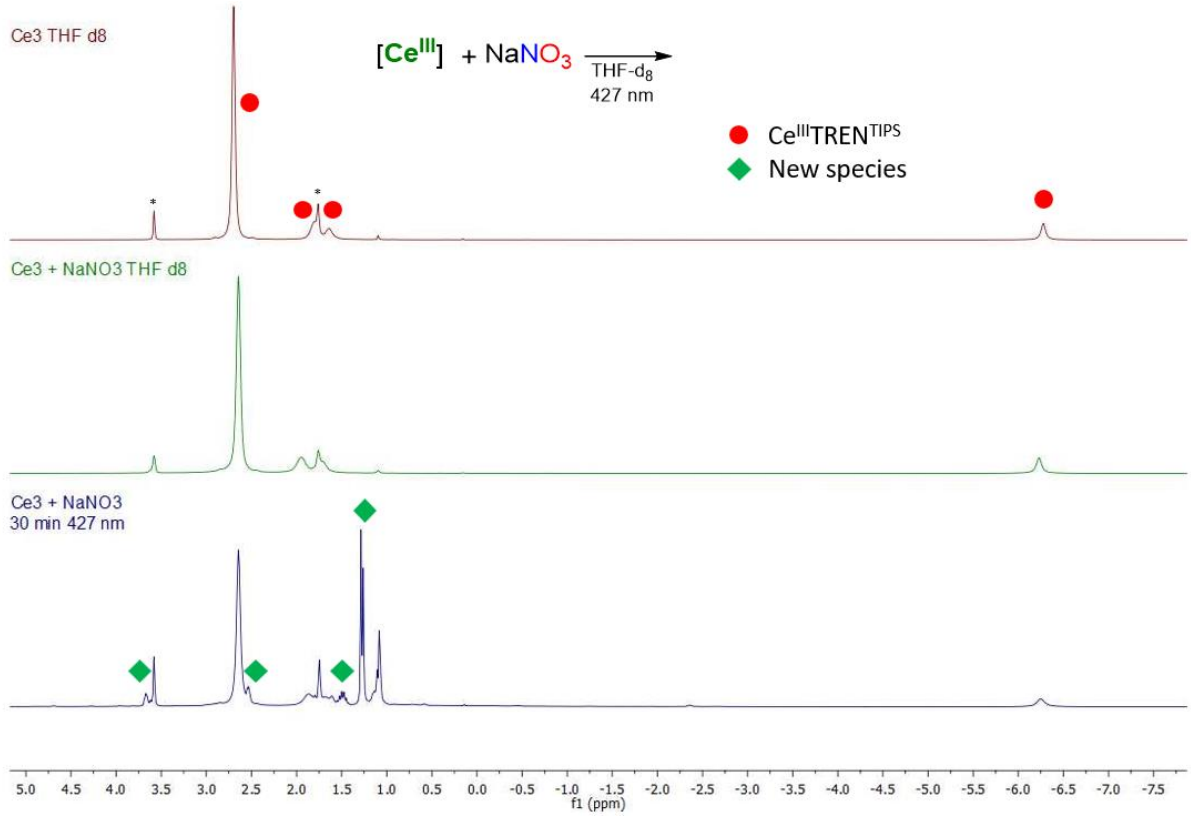

Figure S287. ^{1}H NMR spectrum of a mixture of **1**, $NaNO_3$ and 15-crown-5 in THF-d_8. Solvent residual peaks are indicated with *

Institut Polytechnique de Paris
91120 Palaiseau, France

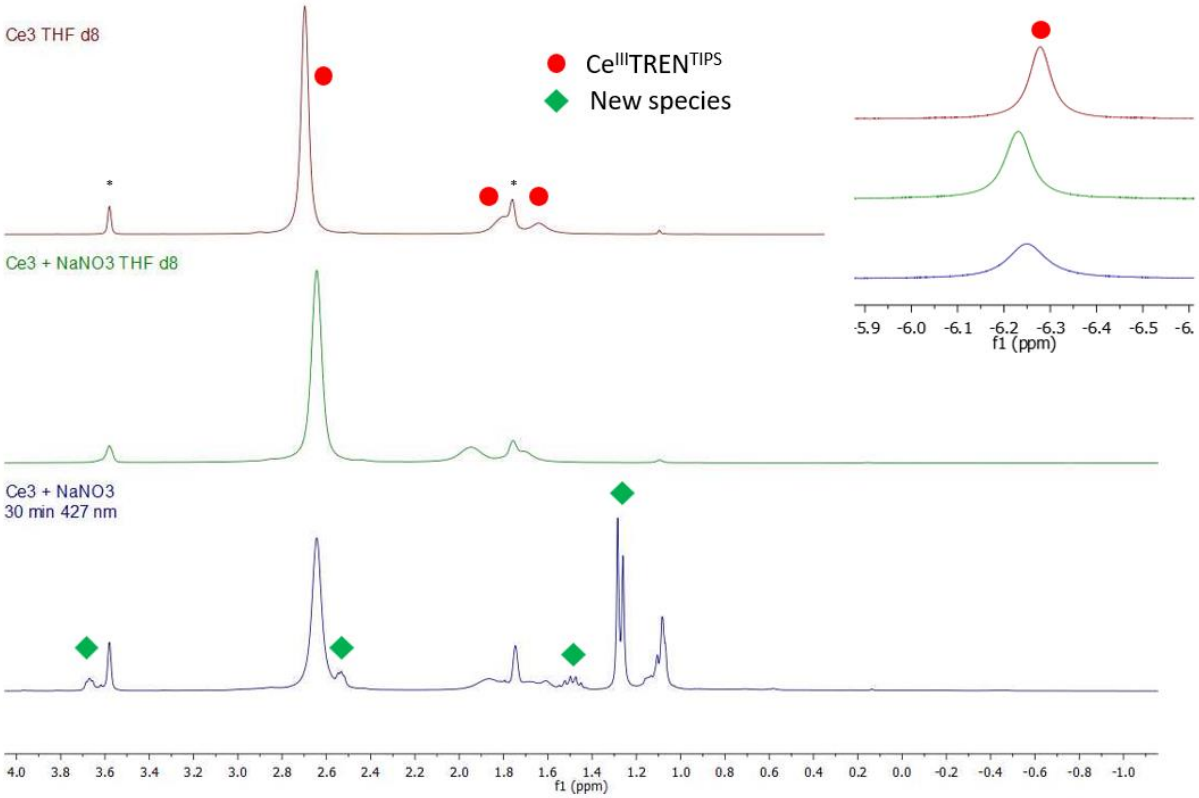

Figure S288. ^{1}H NMR spectrum of a mixture of **1**, $NaNO_3$ and 15-crown-5 in THF-d_8. Zoom between -1.0 and 4.0 ppm. Solvent residual peaks are indicated with *

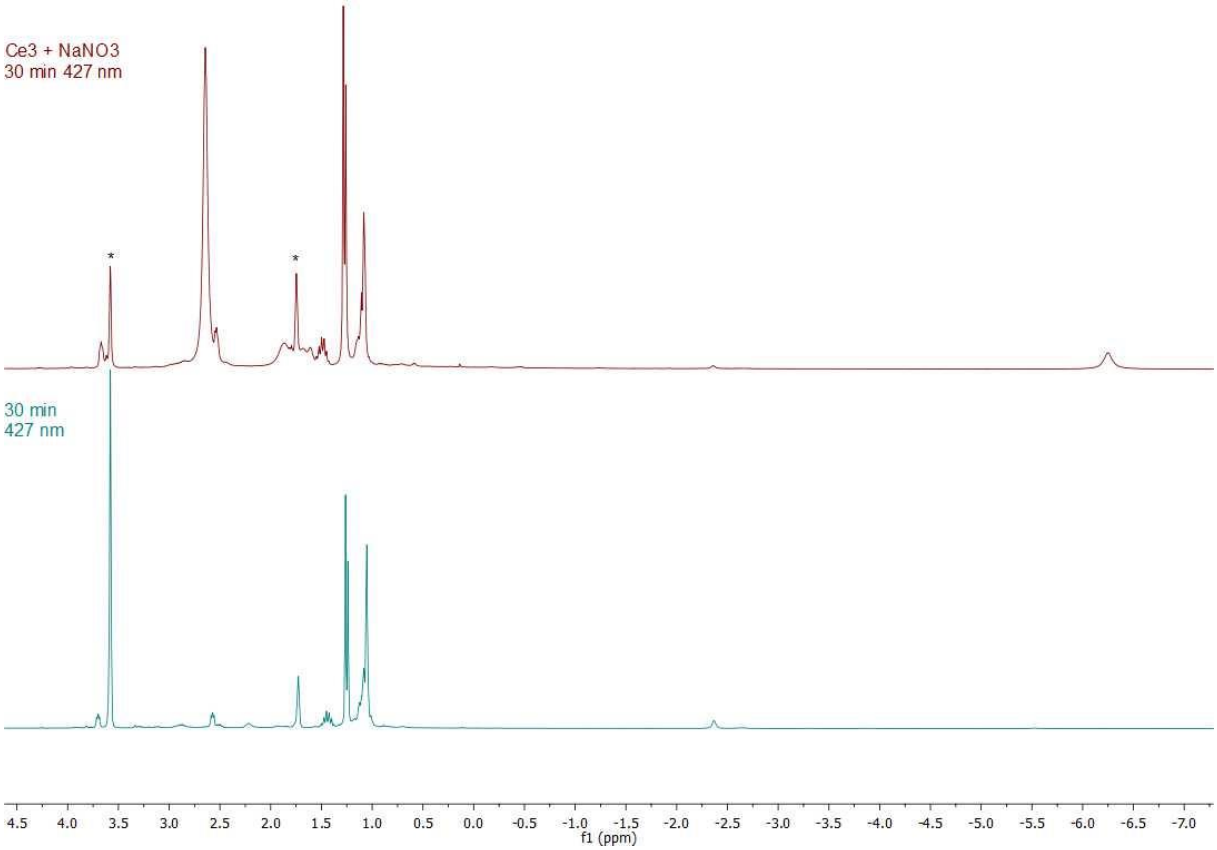

Figure S289. Comparison of photochemical reactions of 1 with $NaNO_3$ (top) and $LiNO_3$ (bottom) for 30 minutes at 427 nm. Solvent residual peaks are indicated with *

Institut Polytechnique de Paris
91120 Palaiseau, France

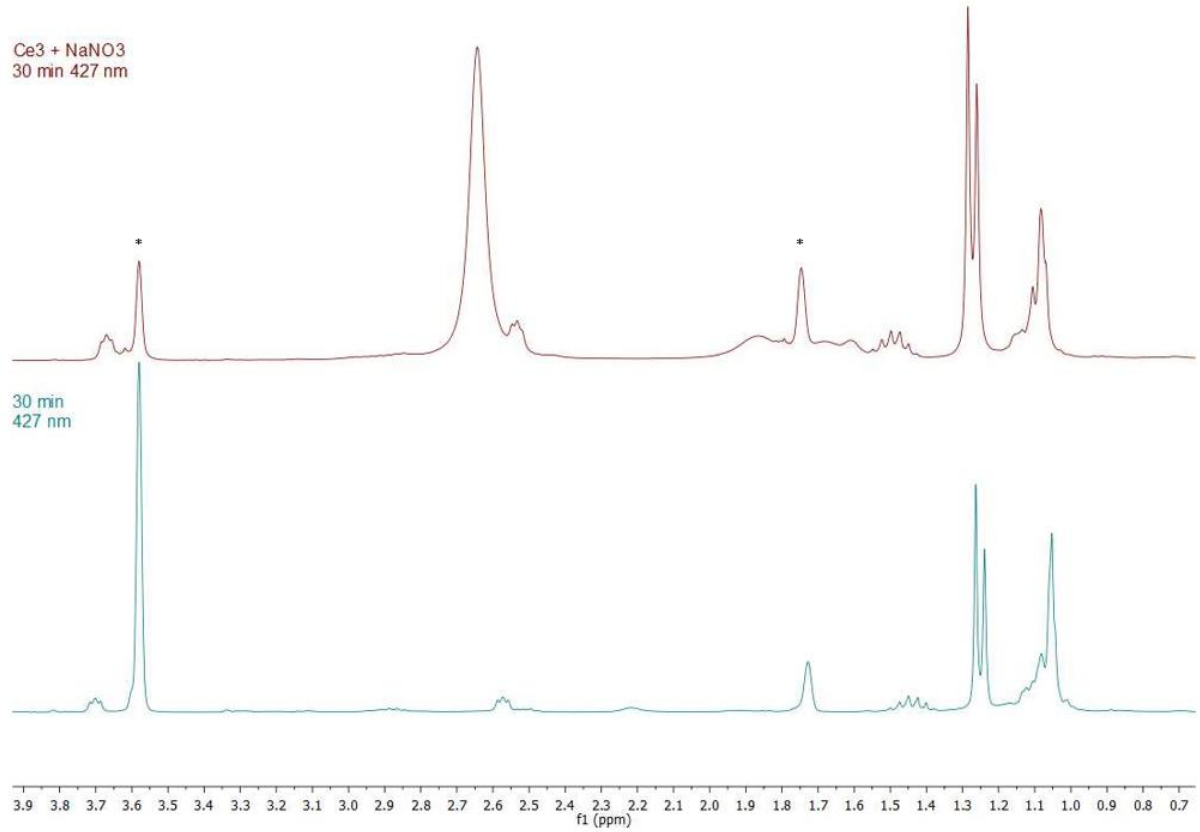

Figure S290. Comparison of photochemical reactions of 1 with $NaNO_3$ (top) and $LiNO_3$ (bottom) for 30 minutes at 427 nm. Zoom between 0.7 and 3.9 ppm.

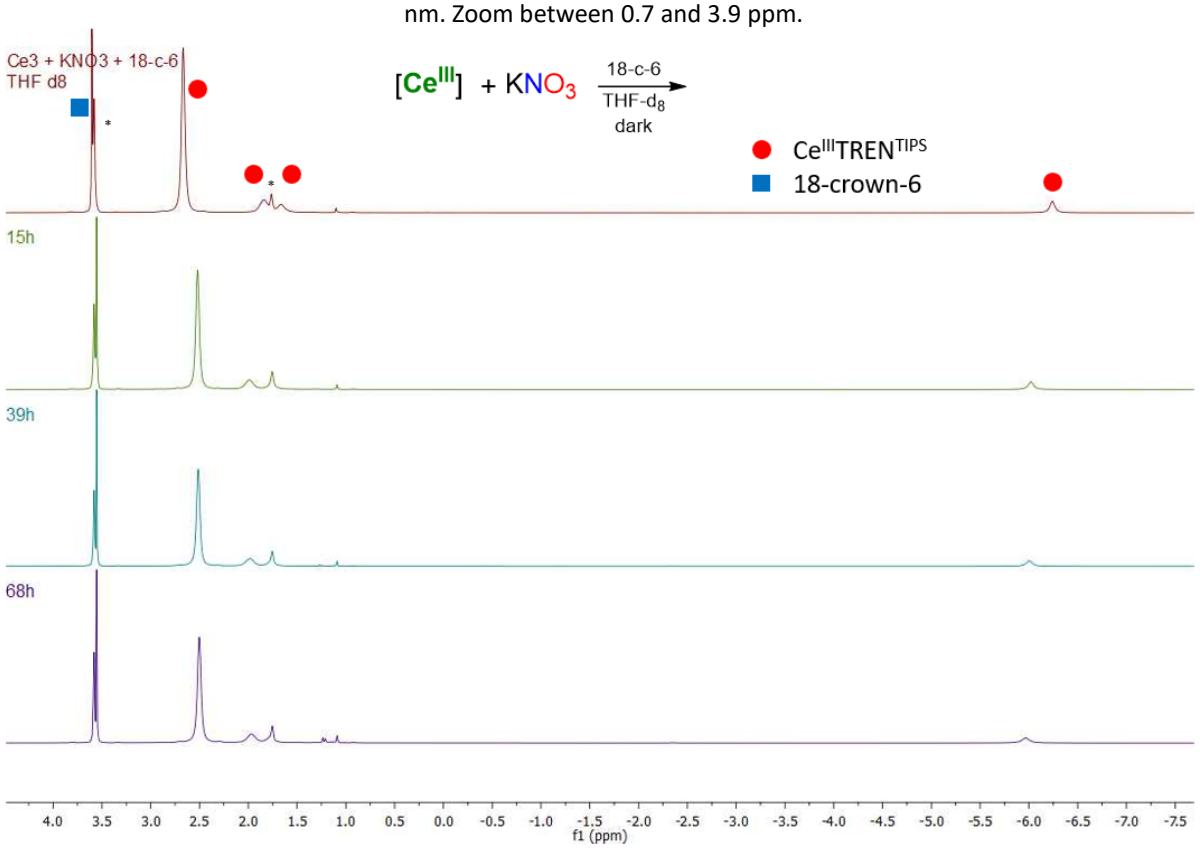

Figure S291. ^1H NMR spectrum of a mixture of **1**, KNO_3 and 18-crown-6 in THF-d_8. Solvent residual peaks are indicated with *

Institut Polytechnique de Paris
91120 Palaiseau, France

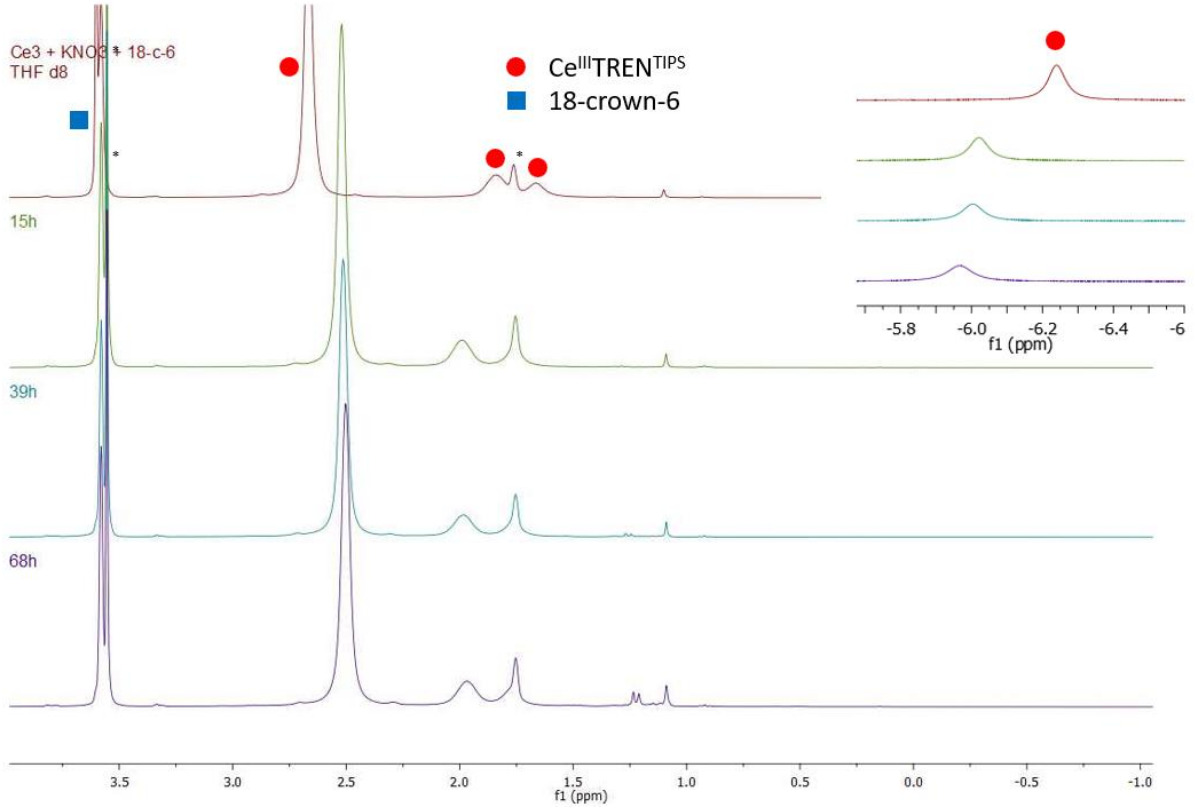

Figure S292. ^{1}H NMR spectrum of a mixture of **1**, KNO_3 and 18-crown-6 in THF-d_8. Zoom between -1.0 and 3.7 ppm. Solvent residual peaks are indicated with *

III. Crystal structure data for Part I

Identification code	1-NO_3	1-NO_3-12c4
Empirical formula	$C_{45}H_{99}CeLiN_5O_6Si_3$	$C_{49}H_{107}CeLiN_5O_{11}Si_3$
Formula weight	1037.62	1173.72
Temperature/K	150	150
Crystal system	Triclinic	Monoclinic
Space group	P-1	$P2_1/n$
a/Å	11.5120(12)	20.1260(10)
b/Å	13.0258(14)	16.2994(6)
c/Å	20.691(2)	20.3557(11)
α/°	80.110(9)	90
β/°	76.957(9)	109.605(4)
γ/°	73.234(8)	90
Volume/Å^3	2875.2(6)	6290.4(5)
Z	2	4
ρ_{calc} g/cm^3	1.199	1.239
μ/mm^{-1}	0.898	0.834
F(000)	1.110	2508.0
Radiation	Mo Kα (λ = 0.71073)	Mo Kα (λ = 0.71073)
2Θ range for data collection/°	4.304 to 58.48	4.248 to 58.656
Index ranges	-15 ≤ h ≤ 15, -17 ≤ k ≤ 15, -27 ≤ l ≤ 28	-25 ≤ h ≤ 27, -21 ≤ k ≤ 22, -27 ≤ l ≤ 27
Reflections collected	41993	106217
Independent reflections	14088 [R_{int} = 0.0601, R_{sigma} = 0.0407]	15991 [R_{int} = 0.0524, R_{sigma} = 0.0575]

Data/restraints/parameters	14088/13/807	15991/562/920
Goodness-of-fit on F2	1.023	0.945
Final R indexes [I>=2σ (I)]	R_1 = 0.0539, wR_2 = 0.1420	R_1 = 0.0365, wR_2 = 0.0799
Final R indexes [all data]	R_1 = 0.0596, wR_2 = 0.1485	R_1 = 0.0663, wR_2 = 0.0867
Largest diff. peak/hole / e Å^{-3}	2.15/-1.45	1.37/-0.98

Table S57. Crystal data and structure refinement for **1-NO_3** and **1-NO_3-12c4**

Identification code	2-O
Empirical formula	$C_{45}H_{99}CeLiN_4O_6Si_3$
Formula weight	1023.61
Temperature/K	150
Crystal system	orthorhombic
Space group	Pbca
a/Å	17.6599(4)
b/Å	18.2148(3)
c/Å	34.7508(9)
α/°	90
β/°	90
γ/°	90
Volume/Å^3	11178.3(4)
Z	8
ρ_{calc} g/cm^3	1.216
μ/mm^{-1}	0.922
F(000)	4384.0
Radiation	Mo Kα (λ = 0.71073)
2Θ range for data collection/°	4.472 to 58.564
Index ranges	-24 ≤ h ≤ 23, -24 ≤ k ≤ 13, -43 ≤ l ≤ 47
Reflections collected	71704
Independent reflections	14131 [R_{int} = 0.0228, R_{sigma} = 0.0211]
Data/restraints/parameters	14131/358/713
Goodness-of-fit on F2	0.989
Final R indexes [I>=2σ (I)]	R_1 = 0.0487, wR_2 = 0.1270
Final R indexes [all data]	R_1 = 0.0666, wR_2 = 0.1391
Largest diff. peak/hole / e Å^{-3}	0.43/-1.40

Table S58. Crystal data and structure refinement for **2-O**

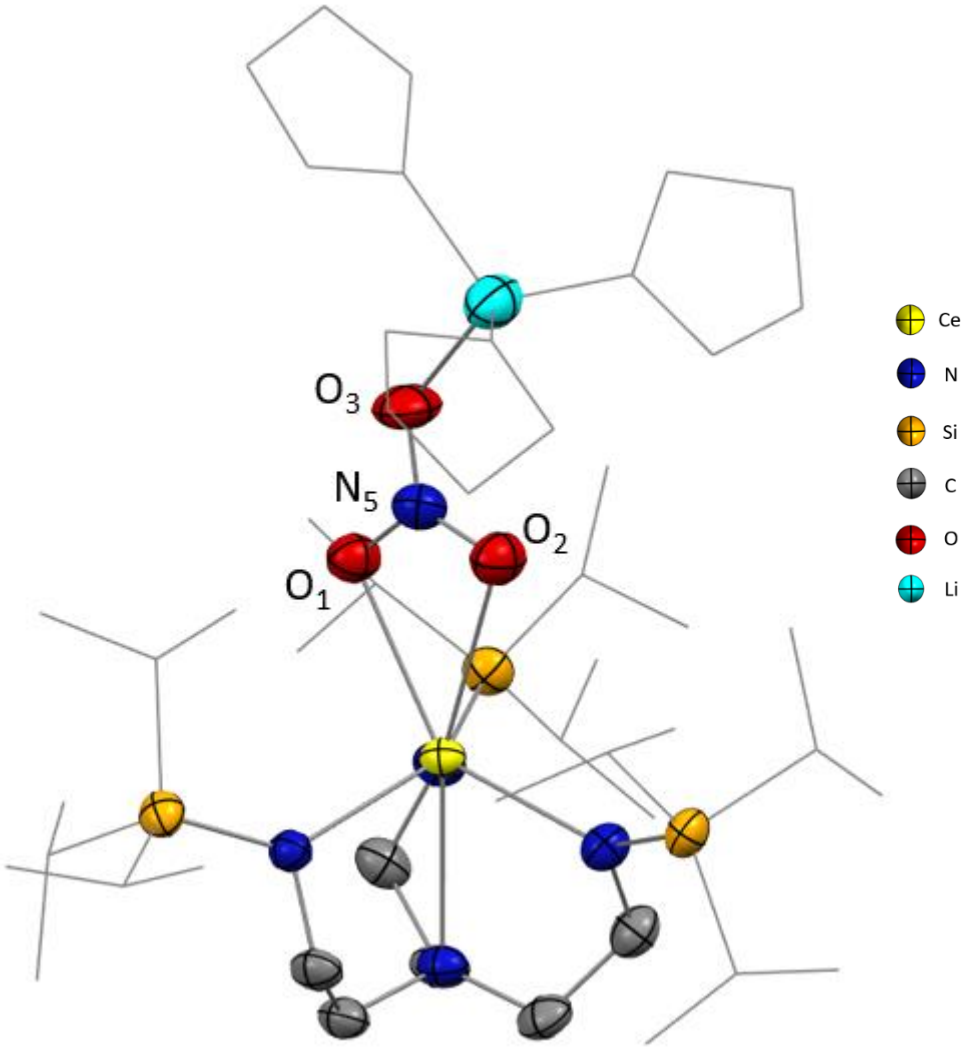

Figure S293. Structure of **1-NO$_3$**. Displacement ellipsoids are represented at 50% probability. Hydrogen atoms have been omitted for clarity, and isopropyl groups and THF molecules have been represented in wireframe style

Bond	Length (Å)	Bonds	Angle (°)
Ce-O_1	2.743(3)	C_1-N_1-Ce	107.9(2)
Ce-O_2	2.656(3)	C_3-N_2-Ce	108.6(2)
Ce-N_1	2.378(3)	C_5-N_3-Ce	111.3(2)
Ce-N_2	2.393(3)	Ce-Cent-N_4	173.7
Ce-N_3	2.372(3)	O_1-Ce-O_2	47.0(1)
Ce-N_4	2.672(3)		
N_1-Si_1	1.708(3)	**Bond**	**Mean value (Å)**
N_2-Si_2	1.716(3)	Ce-$N_{equatorial}$	2.381(5)
N_3-Si_3	1.710(3)	Ce-N_{plane}	0.792
N_1-C_1	1.479(5)	N-Si	1.711(5)
N_2-C_3	1.481(4)	N-O in NO_3	1.249(7)
N_3-C_5	1.471(4)		
O_1-N_5	1.261(4)		
O_2-N_5	1.246(4)		
O_3-N_5	1.237(4)		
O_3-Li_1	1.913(8)		

Table S59. Selected bond lengths and angles for **1-NO$_3$**

Institut Polytechnique de Paris
91120 Palaiseau, France

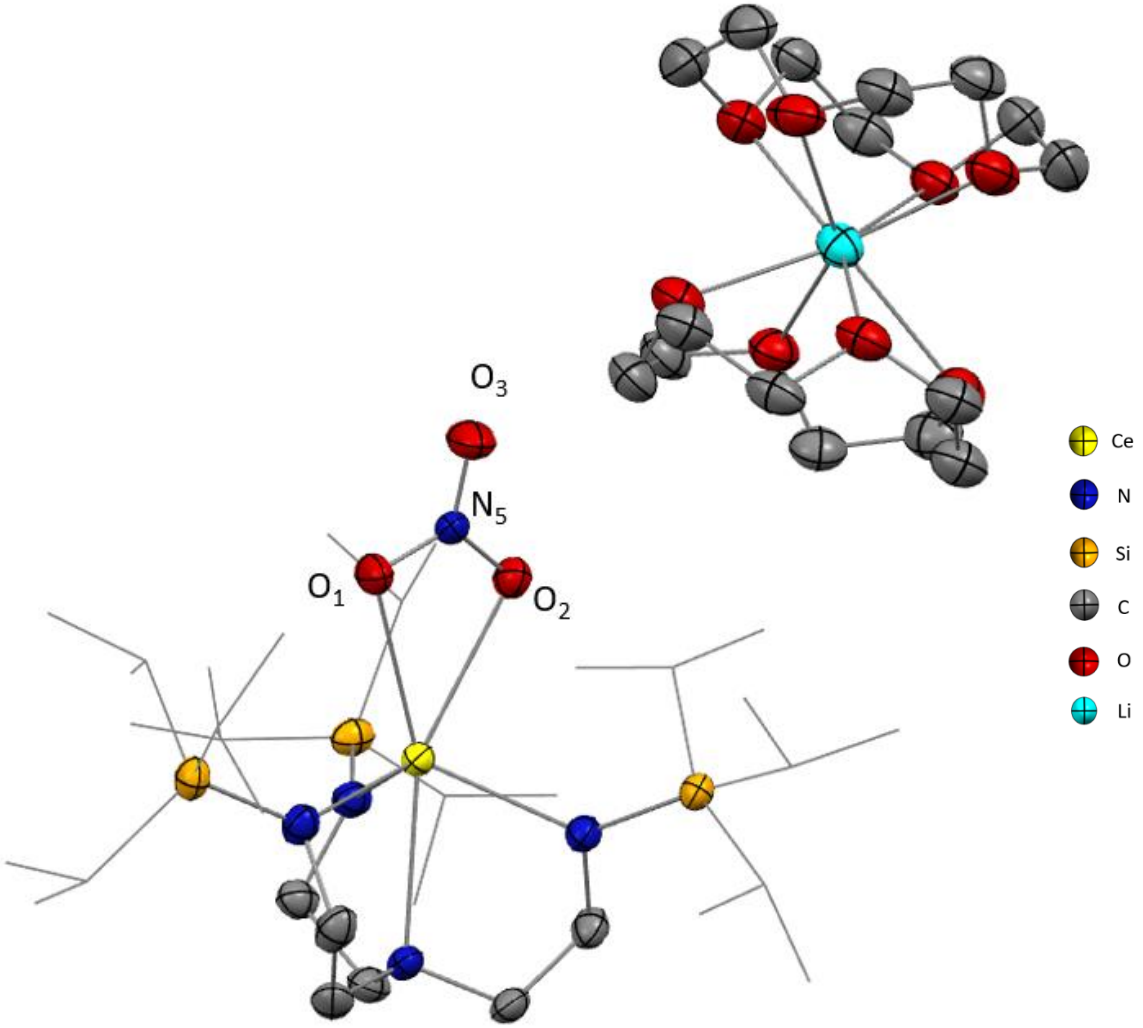

Figure S294. Structure of **1-NO_3-12c4**. Displacement ellipsoids are represented at 50% probability. Hydrogen atoms have been omitted for clarity, and isopropyl groups have been represented in wireframe style. The molecule presents a slight disorder on 12-crown-4, which was modelled but not plotted for clarity

Bond	Length (Å)	Bonds	Angle (°)
Ce-O_1	2.6695(17)	C_1-N_1-Ce	107.5(2)
Ce-O_2	2.6392(18)	C_3-N_2-Ce	107.8(2)
Ce-N_1	2.393(2)	C_5-N_3-Ce	109.2(2)
Ce-N_2	2.3871(19)	Ce-Cent-N_4	176.6
Ce-N_3	2.384(2)	O_1-Ce-O_2	48.0(5)
Ce-N_4	2.6679(19)		
N_1-Si_1	1.707(2)	**Bond**	**Mean value (Å)**
N_2-Si_2	1.705(2)	Ce-$N_{equatorial}$	2.388(4)
N_3-Si_3	1.713(2)	Ce-N_{plane}	0.788
N_1-C_1	1.480(3)	N-Si	1.708(4)
N_2-C_3	1.481(3)	N-O in NO_3	1.249(5)
N_3-C_5	1.478(3)		
O_1-N_5	1.277(2)		
O_2-N_5	1.256(2)		
O_3-N_5	1.213(3)		

Table S60. Selected bond lengths and angles for **1-NO_3-12c4**

Institut Polytechnique de Paris
91120 Palaiseau, France

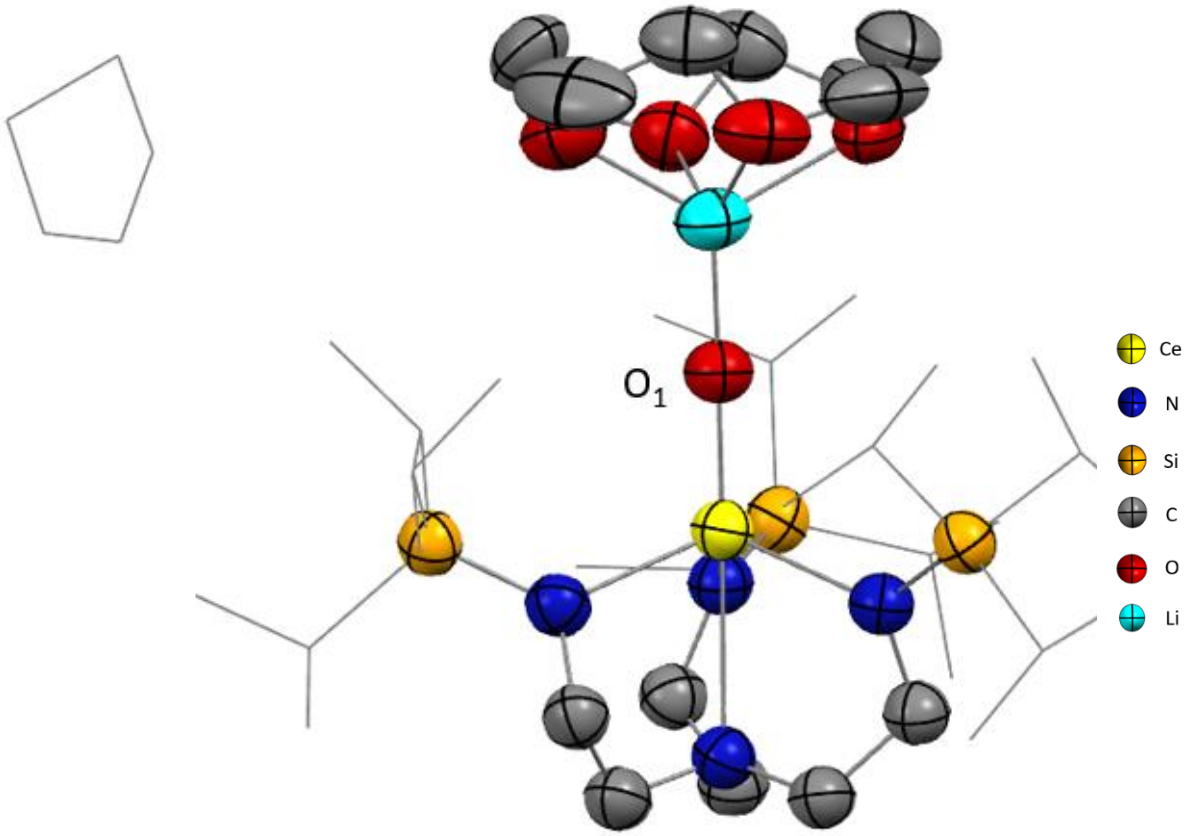

Figure S295. Structure of **2-O**. Displacement ellipsoids are represented at 50% probability. Hydrogen atoms have been omitted for clarity, and isopropyl groups and THF molecules have been represented in wireframe style. The molecule presents a slight disorder on 12-crown-4 and THF moieties. The disorder was modelled but not plotted for clarity. NB : THF molecule is coordinated to a lithium cation of another unit

Bond	Length (Å)	Bonds	Angle (°)
Ce-O_1	1.910(2)	C_1-N_1-Ce	110.1(2)
Ce-N_1	2.367(3)	C_3-N_2-Ce	112.7(2)
Ce-N_2	2.358(3)	C_5-N_3-Ce	112.1(2)
Ce-N_3	2.336(3)	Ce-Cent-N_4	173.4
Ce-N_4	2.716(2)	O_1-Ce-Li	1.6(2)
N_1-Si_1	1.711(3)		
N_2-Si_2	1.718(3)	**Bond**	**Mean value (Å)**
N_3-Si_3	1.716(3)	Ce-$N_{equatorial}$	2.354(6)
N_1-C_1	1.484(4)	Ce-N_{plane}	0.804
N_2-C_3	1.476(4)	N-Si	1.715(6)
N_3-C_5	1.470(4)		

Table S61. Selected bond lengths and angles for **2-O**

Institut Polytechnique de Paris
91120 Palaiseau, France

IV. UV-visible and IR spectroscopy data for Part I.a

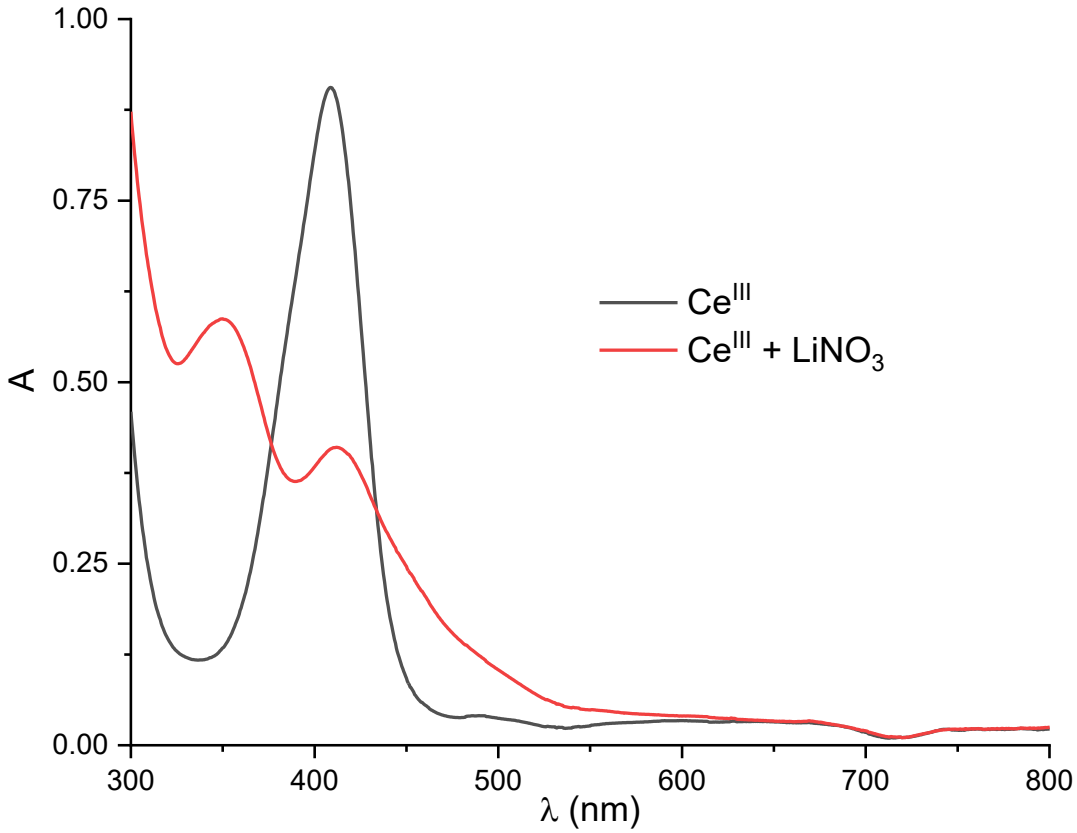

Figure S296. UV-visible spectrum of the reaction between **1** and 1 equivalent of $LiNO_3$ in THF at 1.5 $mmol.L^{-1}$

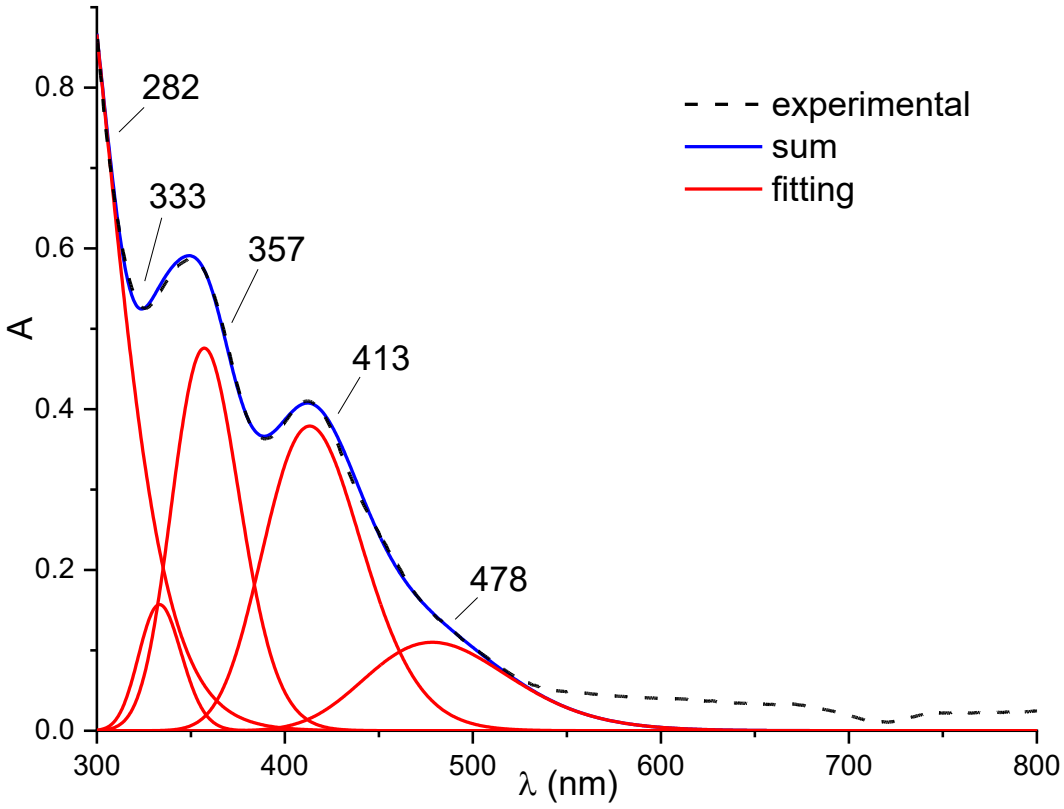

Figure S297. Deconvoluted spectrum of *in situ* generated **1-NO_3** in THF at $1.5.10^{-3}$ $mol.L^{-1}$

Institut Polytechnique de Paris
91120 Palaiseau, France

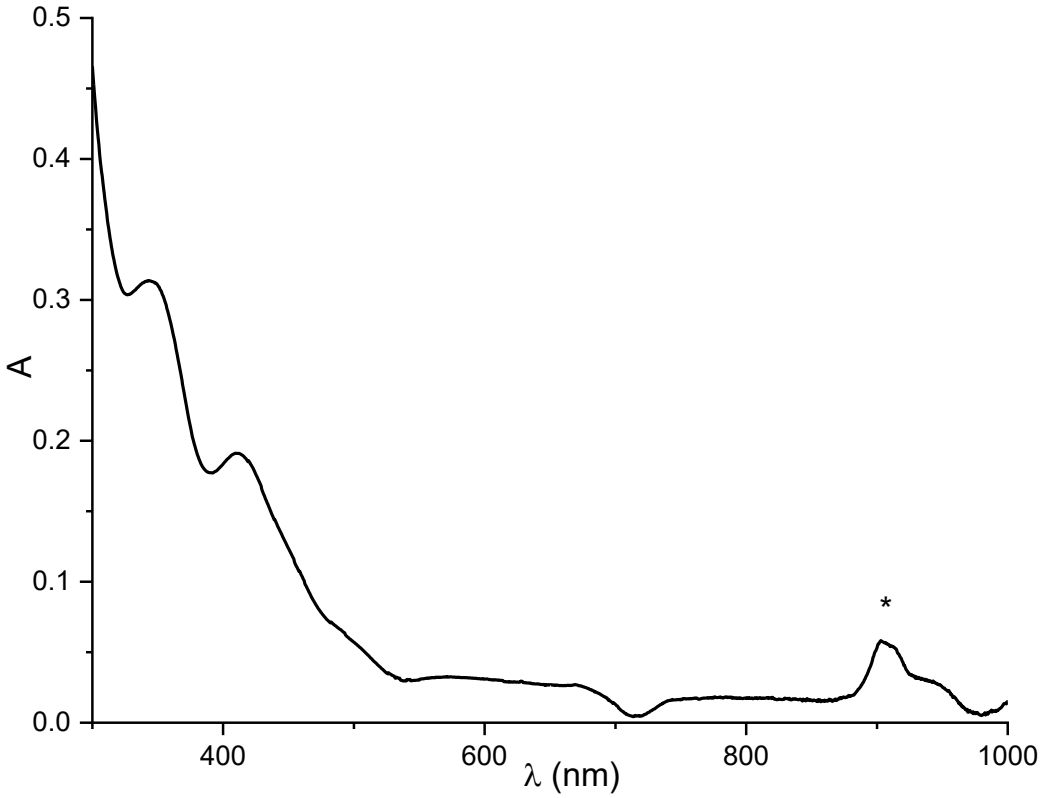

Figure S298. UV-visible spectrum of **1-NO_3-12c4** in THF at 4.10^{-4} mol.L^{-1}. * denotes an artefact of the system

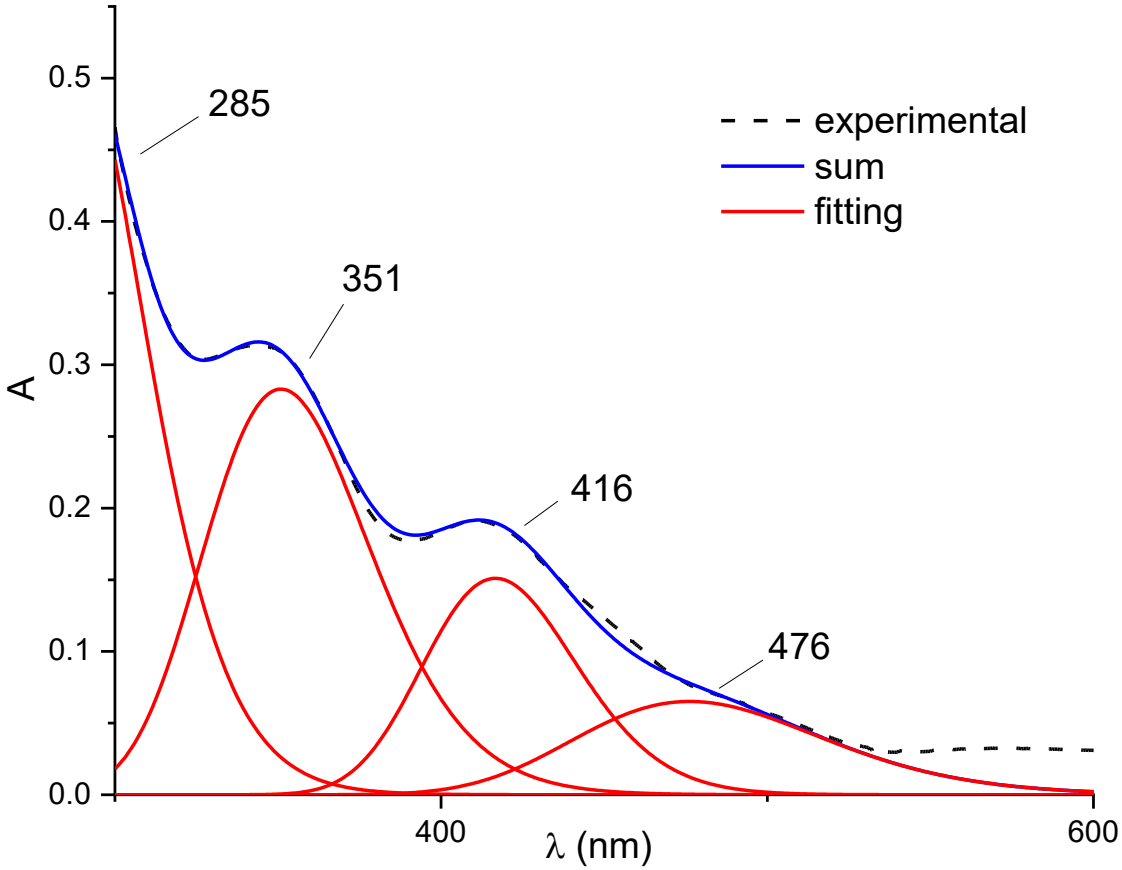

Figure S299. Deconvoluted spectrum of **1-NO_3-12c4** in THF at 4.10^{-4} mol.L^{-1}

Institut Polytechnique de Paris
91120 Palaiseau, France

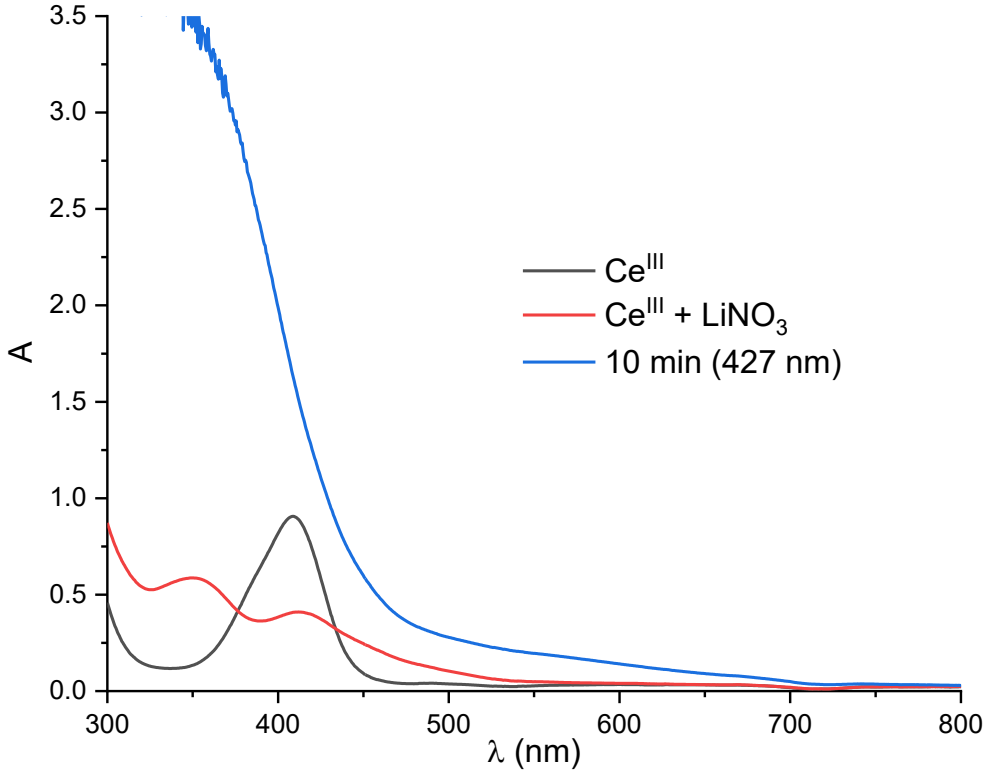

Figure S300. UV-visible monitoring of the photochemical reaction between **1** and $LiNO_3$ at $1.5.10^{-3}$ $mol.L^{-1}$ and irradiation at 427 nm for 10 minutes

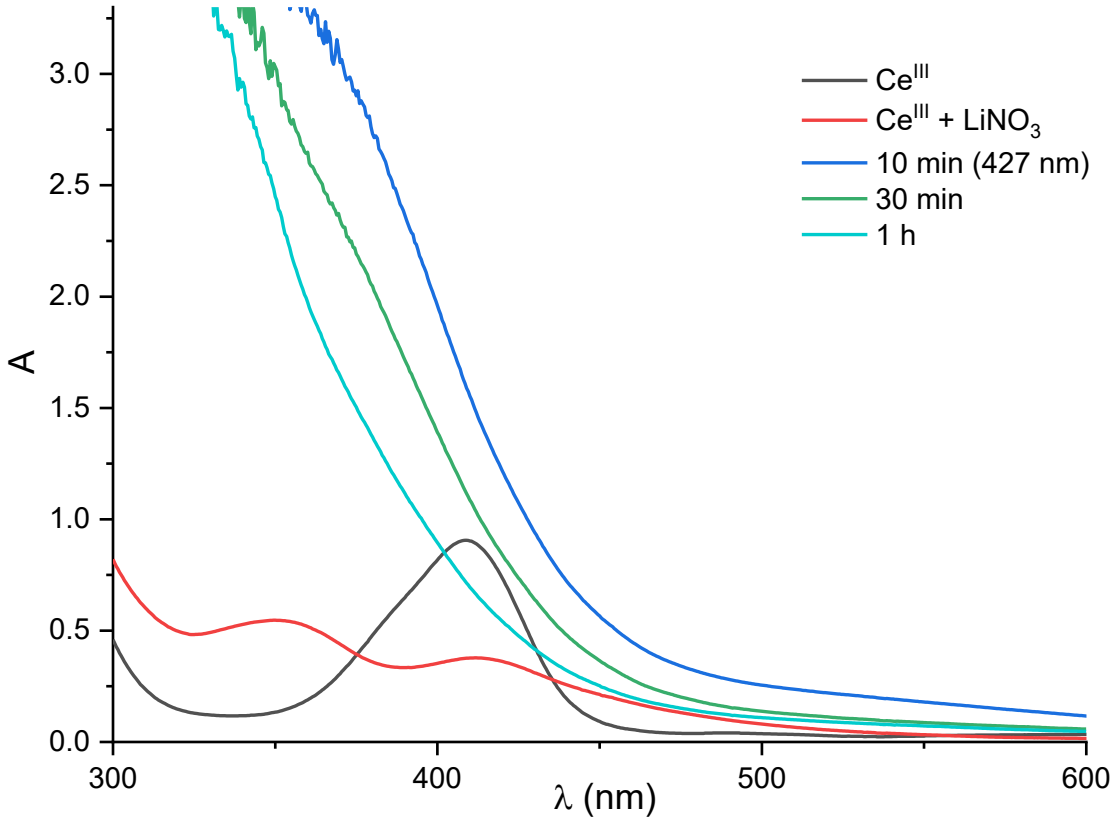

Figure S301. UV-visible monitoring of the photochemical reaction between **1** and $LiNO_3$ at 1.5 $mmol.L^{-1}$ and irradiation at 427 nm

Institut Polytechnique de Paris
91120 Palaiseau, France

Experimental section for Chapter IV

Part I.b

Institut Polytechnique de Paris
91120 Palaiseau, France

I. NMR data for Part II

a) Reactivity of 1 with inorganic nitrites

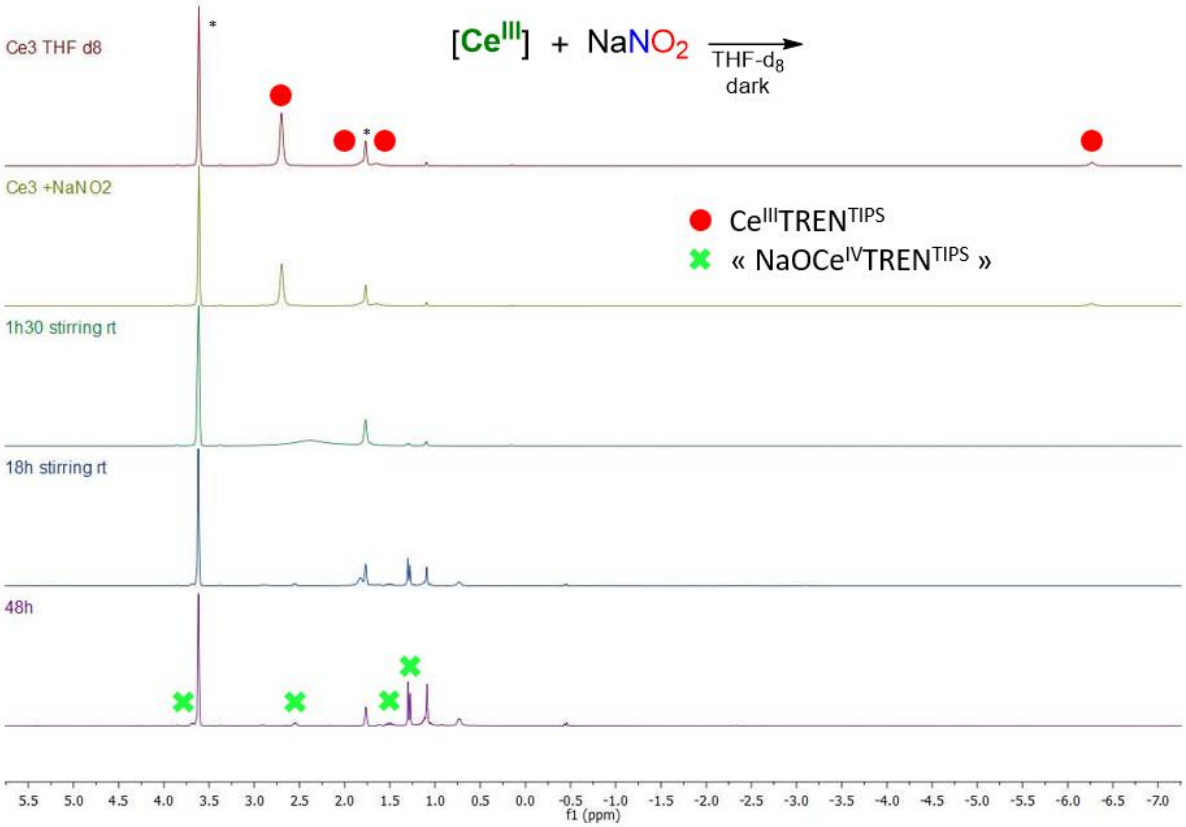

Figure S302. ^{1}H NMR spectrum of the reaction between **1** and $NaNO_2$ in THF-d_8. Solvent residual peaks are indicated with *

Institut Polytechnique de Paris
91120 Palaiseau, France

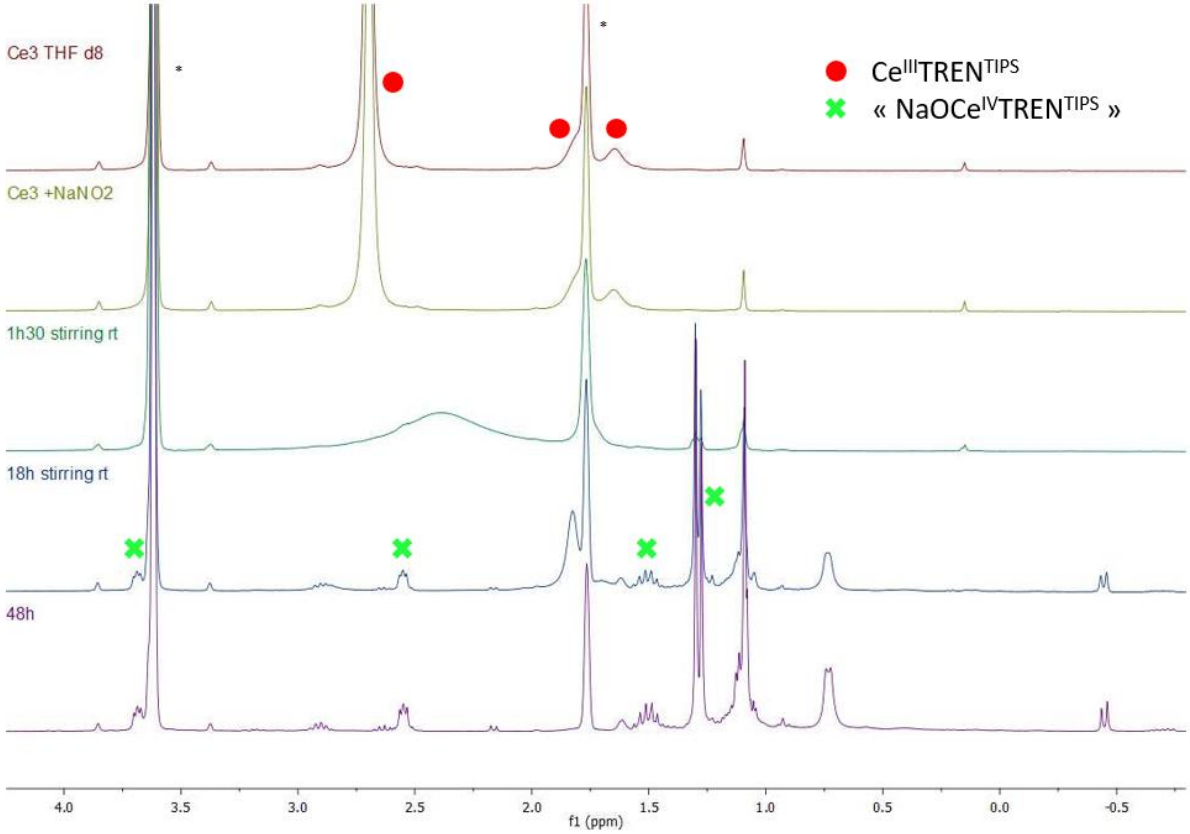

Figure S303. ^{1}H NMR spectrum of the reaction between **1** and $NaNO_2$ in THF-d_8. Zoom between -1.0 and 4.0 ppm. Solvent residual peaks are indicated with *

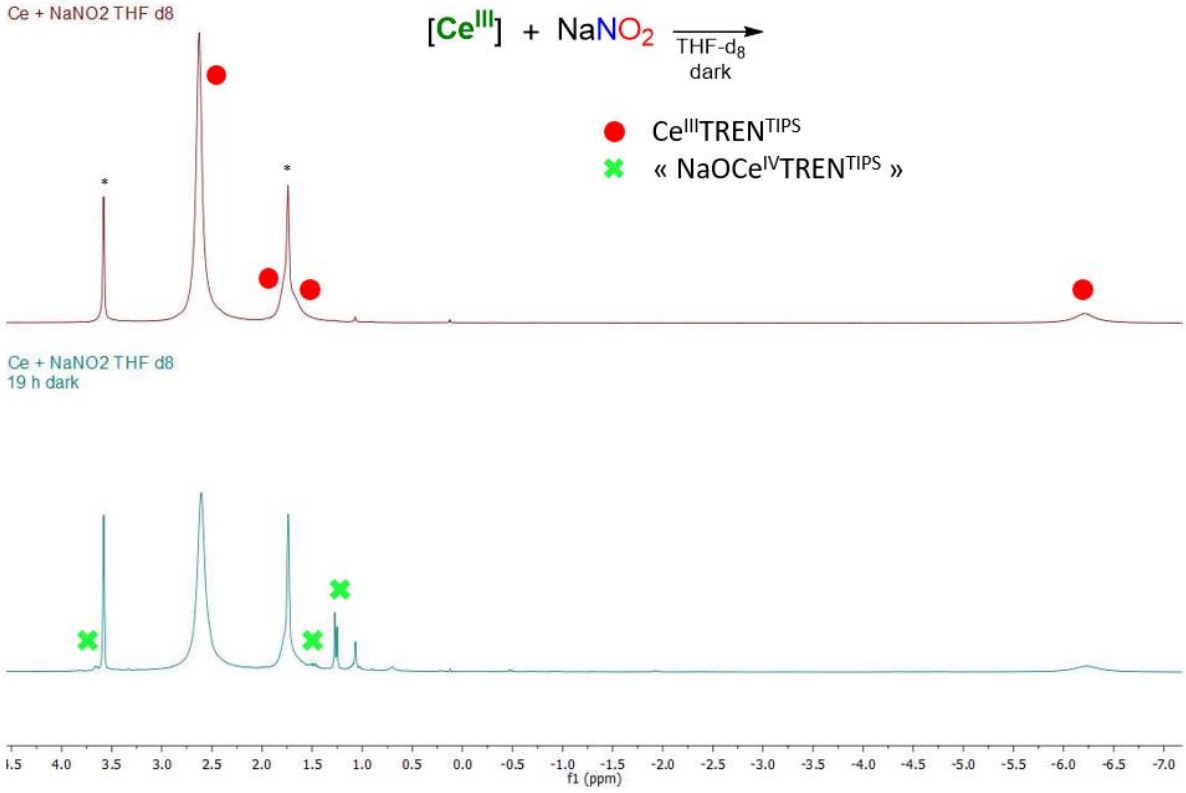

Figure S304. ^{1}H NMR spectrum of the reaction between **1** and $NaNO_2$ in THF-d_8. Solvent residual peaks are indicated with *

Institut Polytechnique de Paris
91120 Palaiseau, France

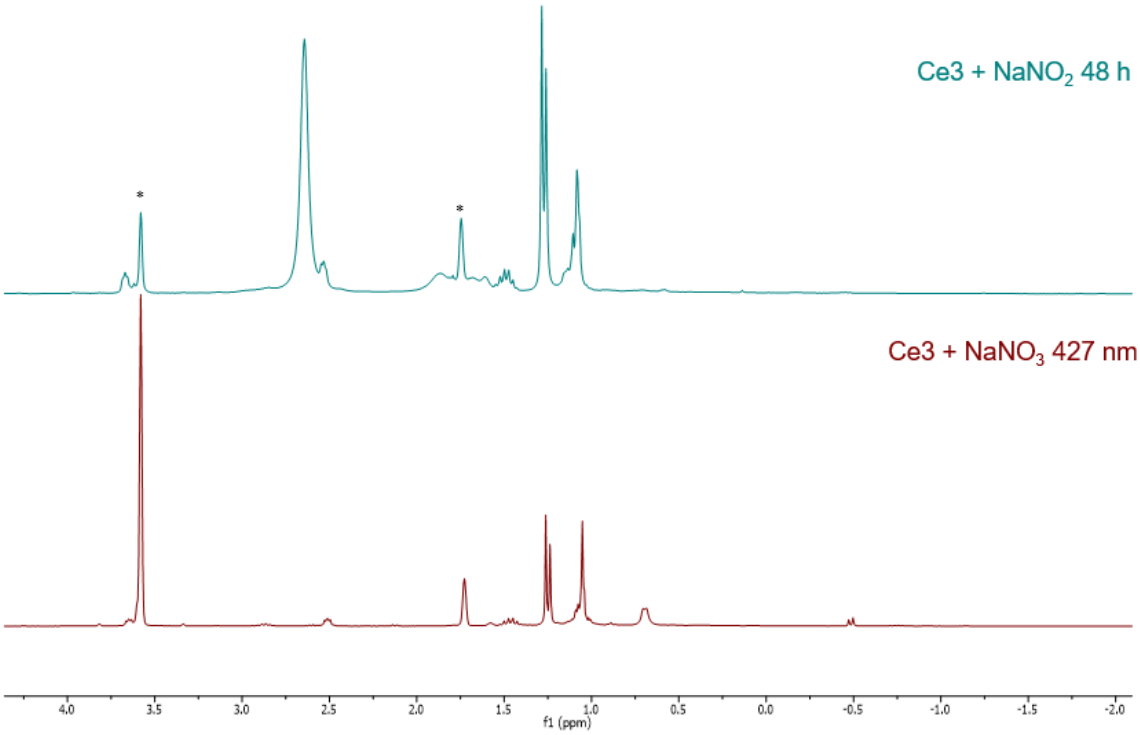

Figure S305. Comparison between the ^{1}H NMR spectra of **1** and $NaNO_2$ after 48 h in the dark (top) and the NMR of **1** and $NaNO_3$ after 30 min of irradiation at 427 nm. Solvent residual peaks are indicated with *

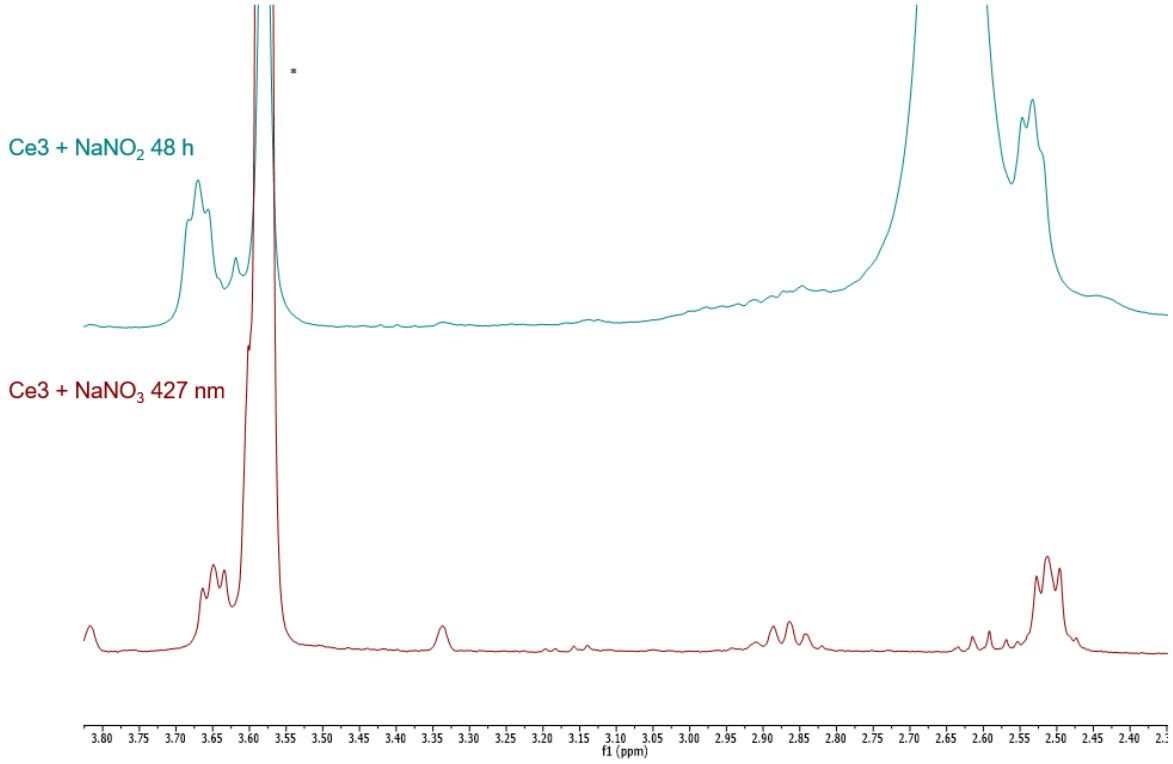

Figure S306. Comparison between the ^{1}H NMR spectra of **1** and $NaNO_2$ after 48 h in the dark (top) and the NMR of **1** and $NaNO_3$ after 30 min of irradiation at 427 nm. Zoom between 2.4 and 3.9 ppm. Solvent residual peaks are indicated with *

Institut Polytechnique de Paris
91120 Palaiseau, France

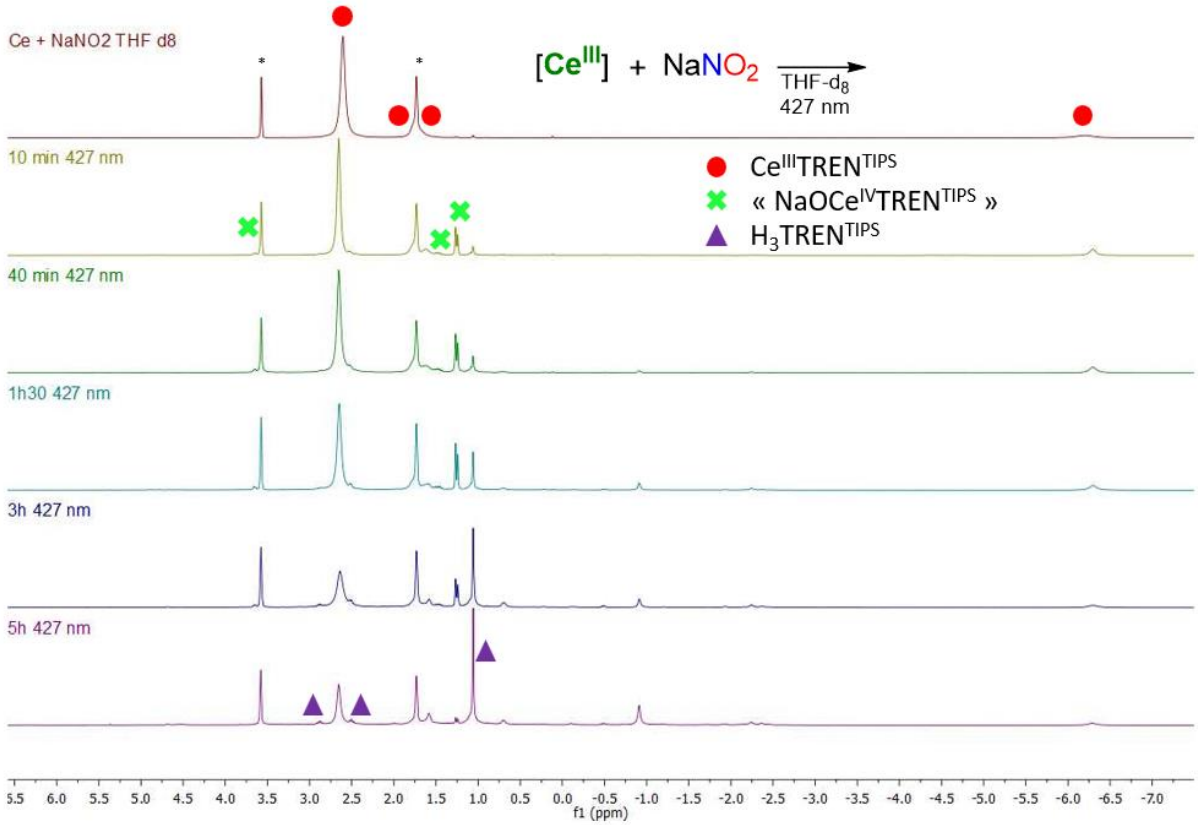

Figure S307. ^{1}H NMR spectrum of the photochemical reaction between **1** and $NaNO_2$ in THF-d_8. Solvent residual peaks are indicated with *

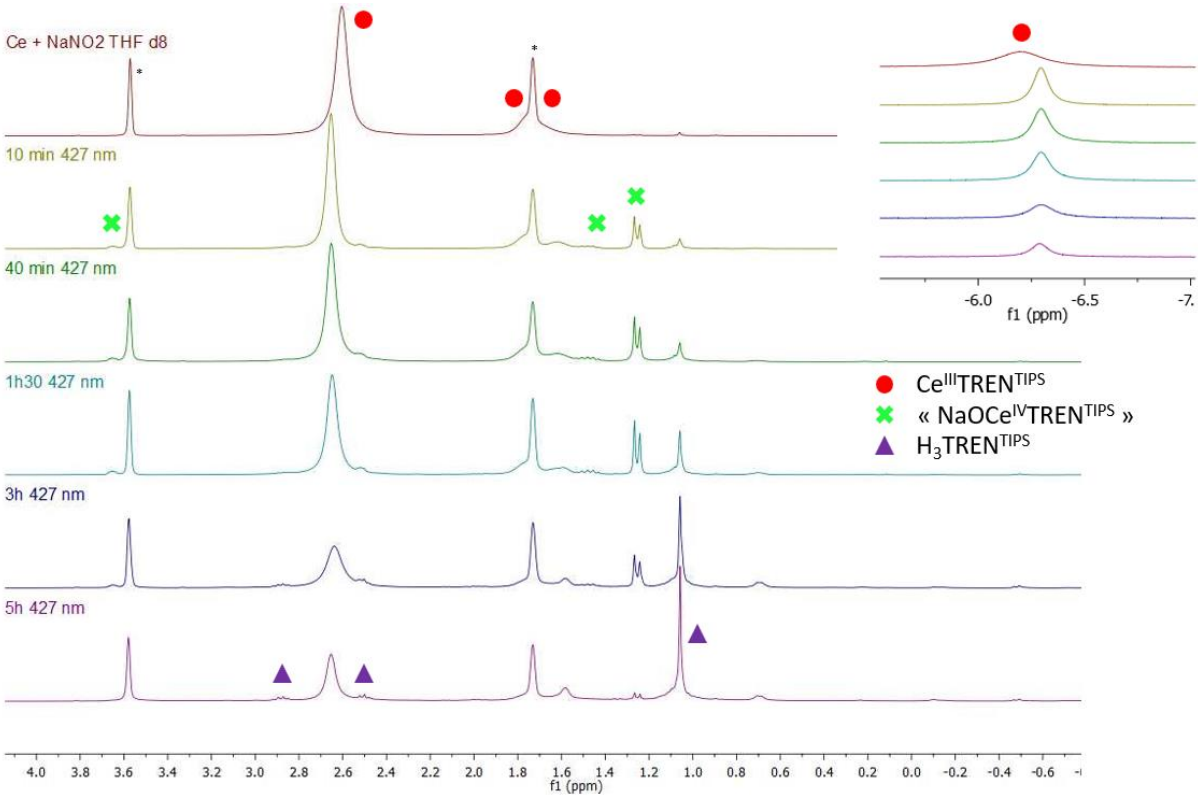

Figure S308. ^{1}H NMR spectrum of the photochemical reaction between **1** and $NaNO_2$ in THF-d_8. Zoom between -0.8 and 4.2 ppm Solvent residual peaks are indicated with *

Institut Polytechnique de Paris
91120 Palaiseau, France

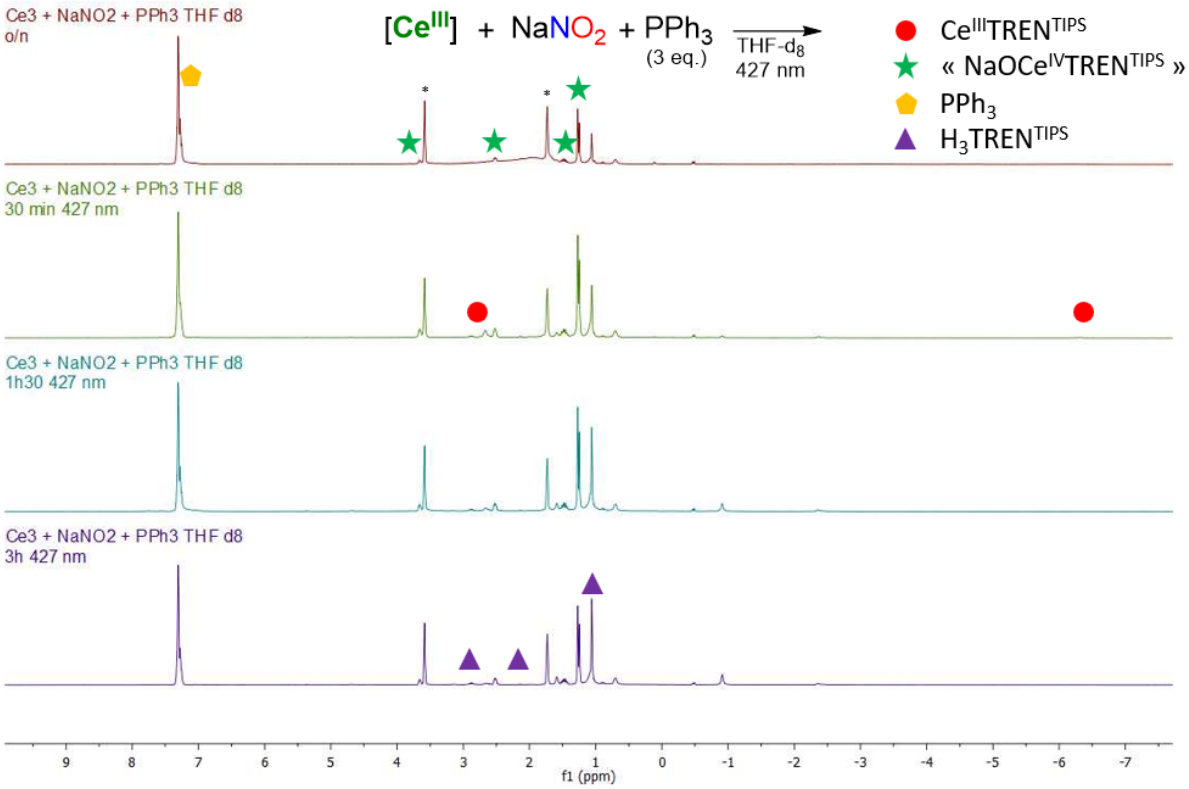

Figure S309. ^{1}H NMR spectrum of the photochemical reaction between **1** and $NaNO_2$ in the presence of PPh_3 in THF-d_8. Solvent residual peaks are indicated with *

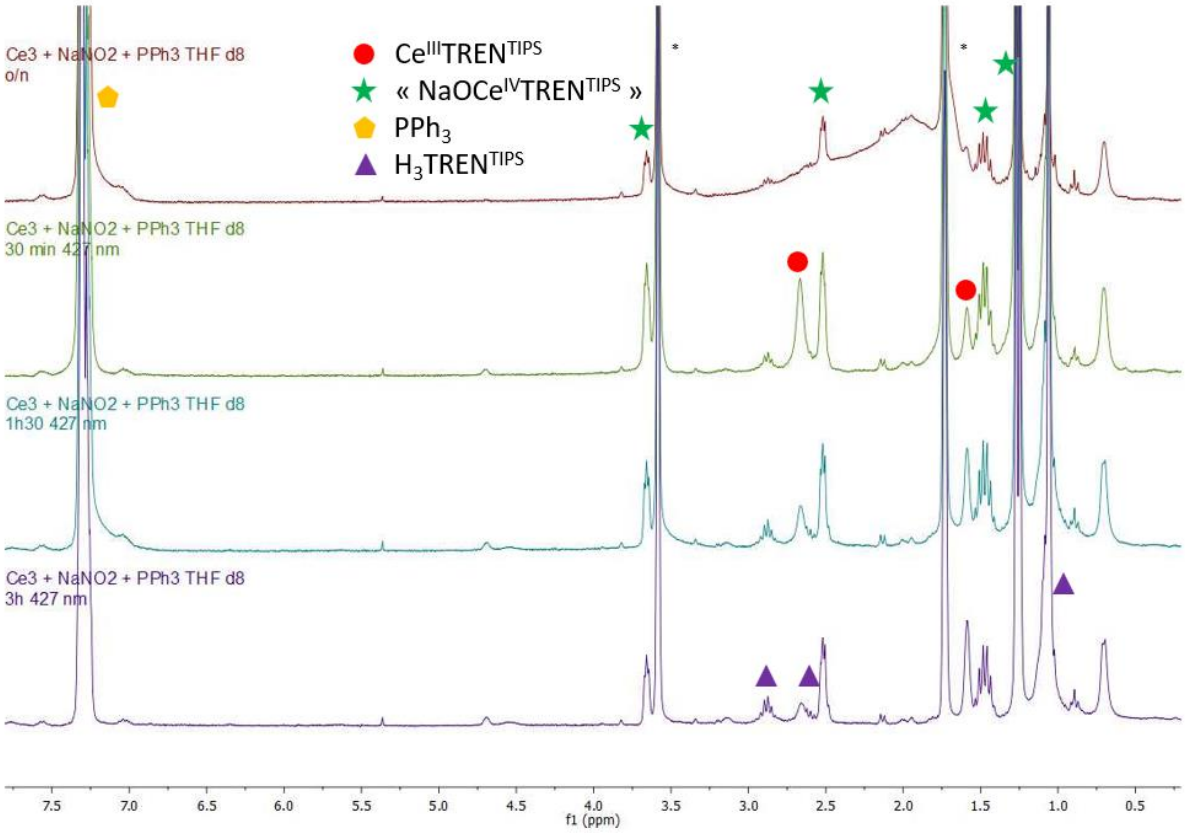

Figure S310. ^{1}H NMR spectrum of the photochemical reaction between **1** and $NaNO_2$ in the presence of PPh_3 in THF-d_8. Zoom between 0.1 ppm and 8.0 ppm. Solvent residual peaks are indicated with *

b) Reactivity with N_2O

Institut Polytechnique de Paris
91120 Palaiseau, France

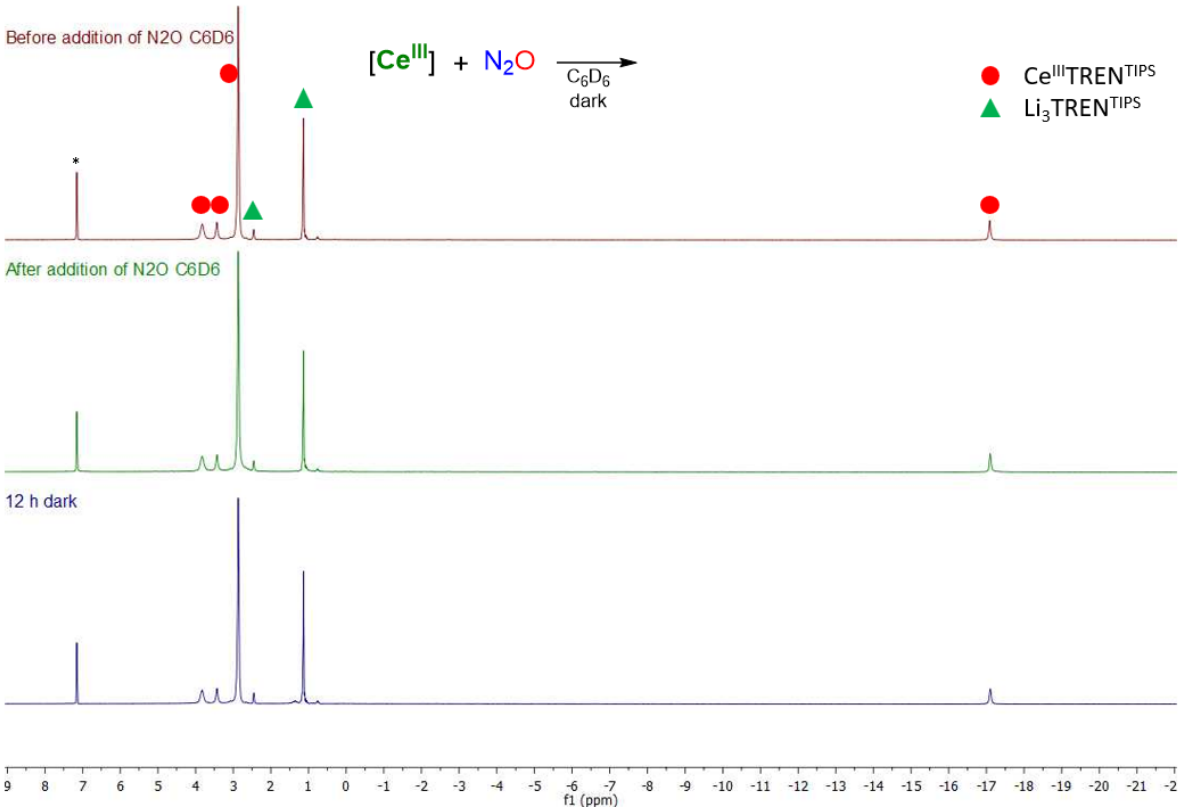

Figure S311. ^{1}H NMR spectrum of the reaction between **1** and N_2O in C_6D_6. Solvent residual peak is indicated with *

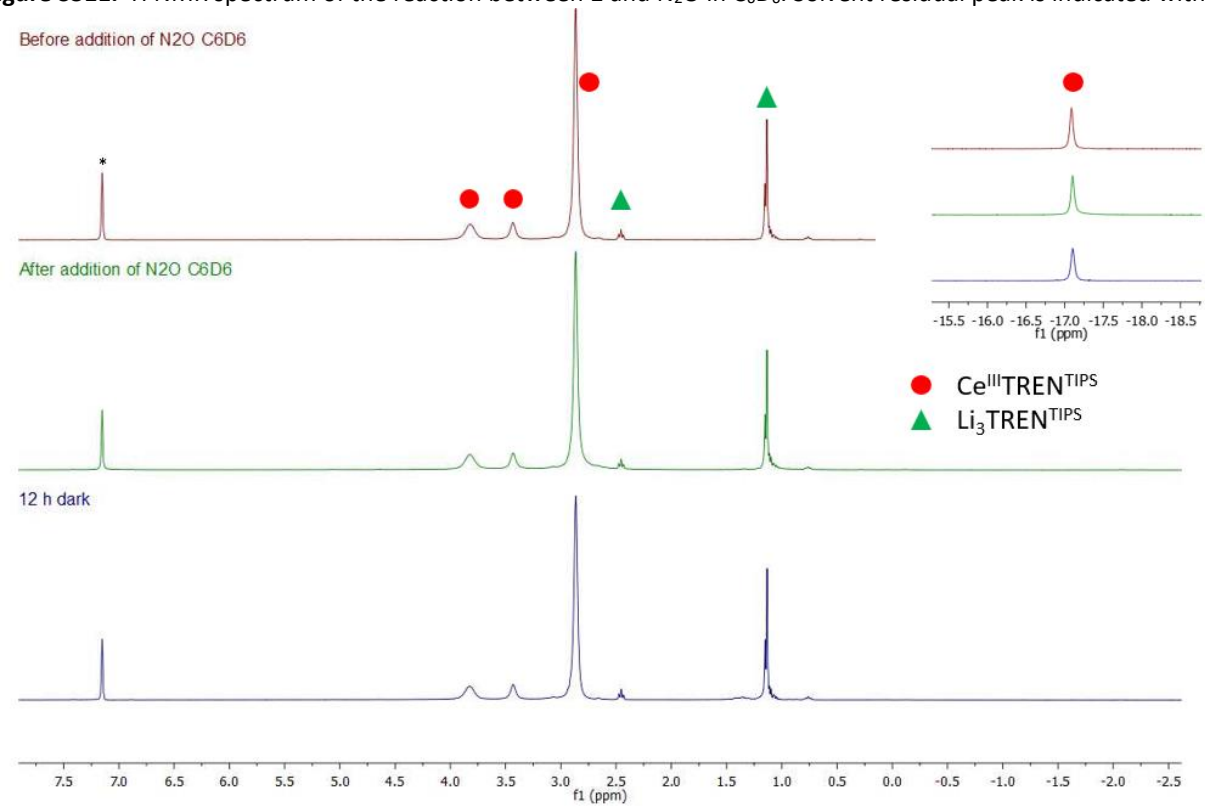

Figure S312. ^{1}H NMR spectrum of the reaction between **1** and N_2O in C_6D_6. Zoom between -2.5 and 8.0 ppm. Solvent residual peak is indicated with *

Institut Polytechnique de Paris
91120 Palaiseau, France

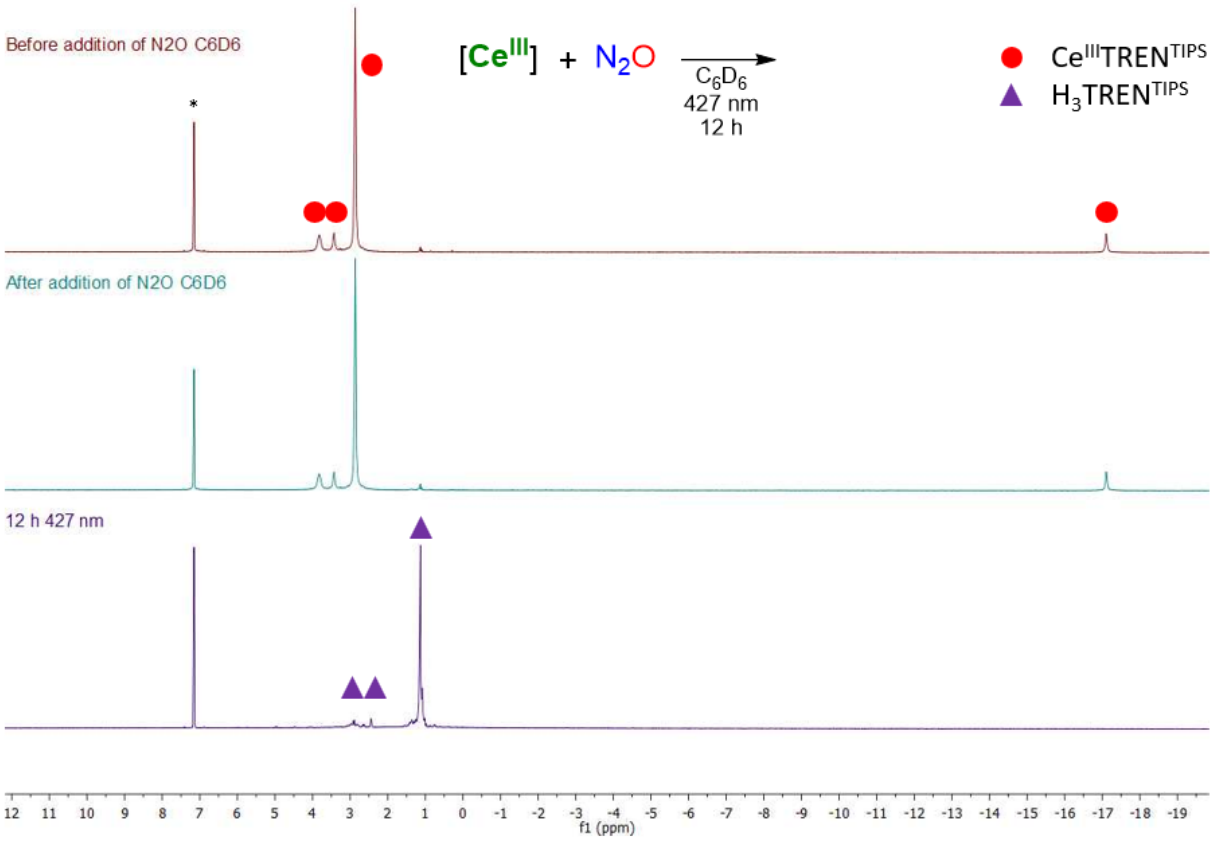

Figure S313. ^{1}H NMR spectrum of the photochemical reaction between **1** and N_2O in C_6D_6. Solvent residual peak is indicated with *

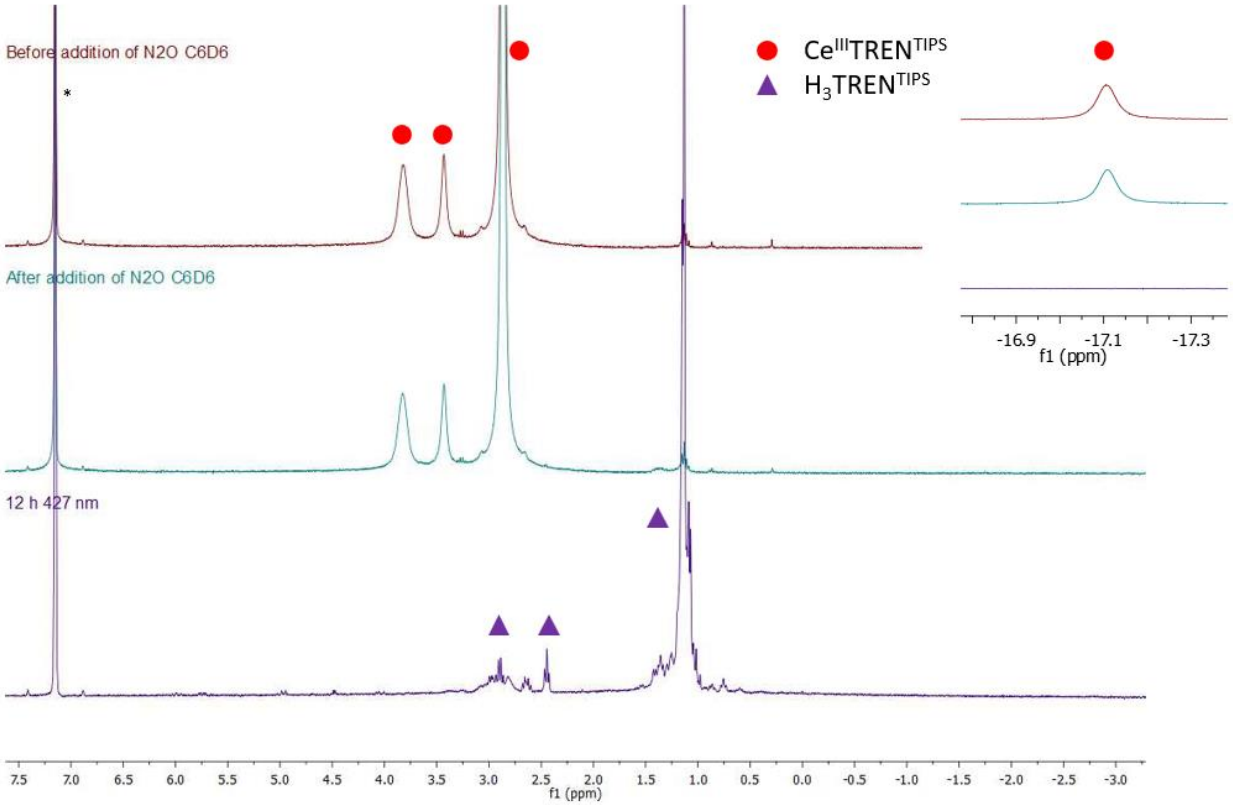

Figure S314. ^{1}H NMR spectrum of the photochemical reaction between **1** and N_2O in C_6D_6. Zoom between -3.5 and 7.5 ppm. Solvent residual peak is indicated with *

Institut Polytechnique de Paris
91120 Palaiseau, France

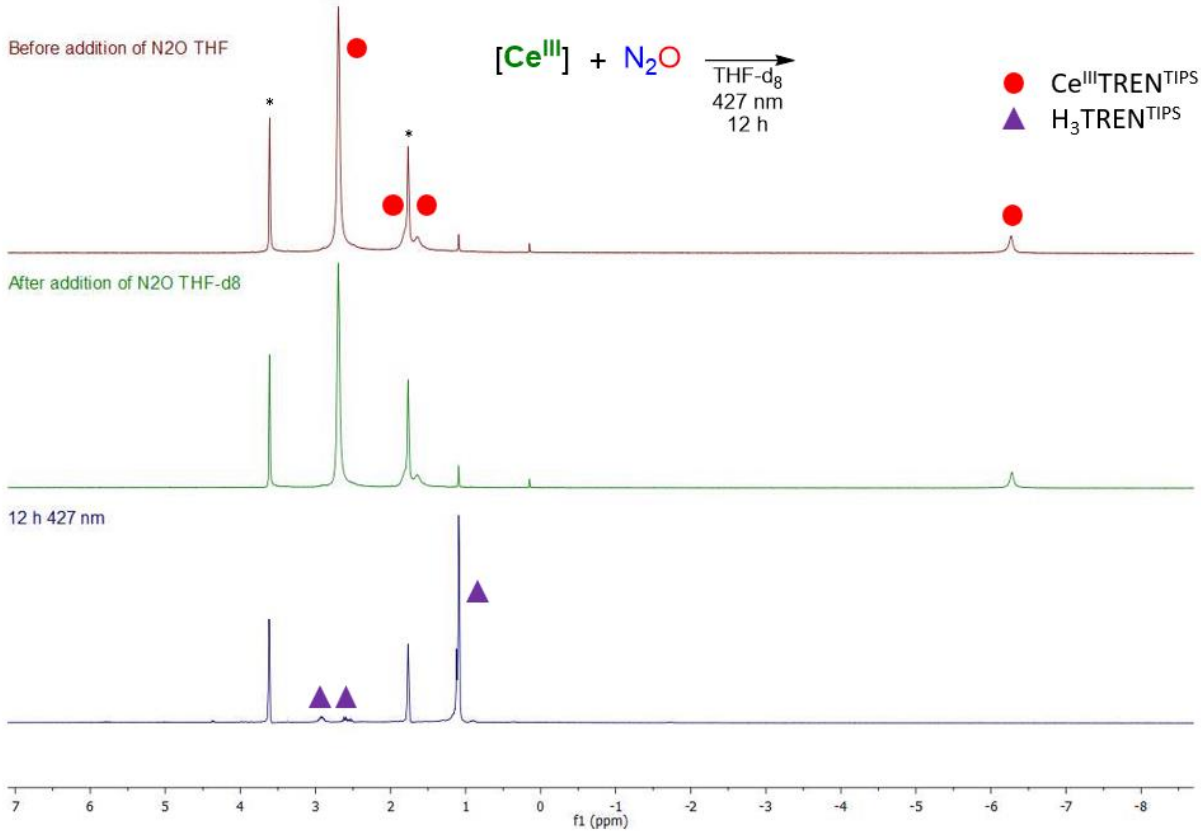

Figure S315. ^{1}H NMR spectrum of the photochemical reaction between **1** and N_2O in THF-d_8. Solvent residual peaks are indicated with *

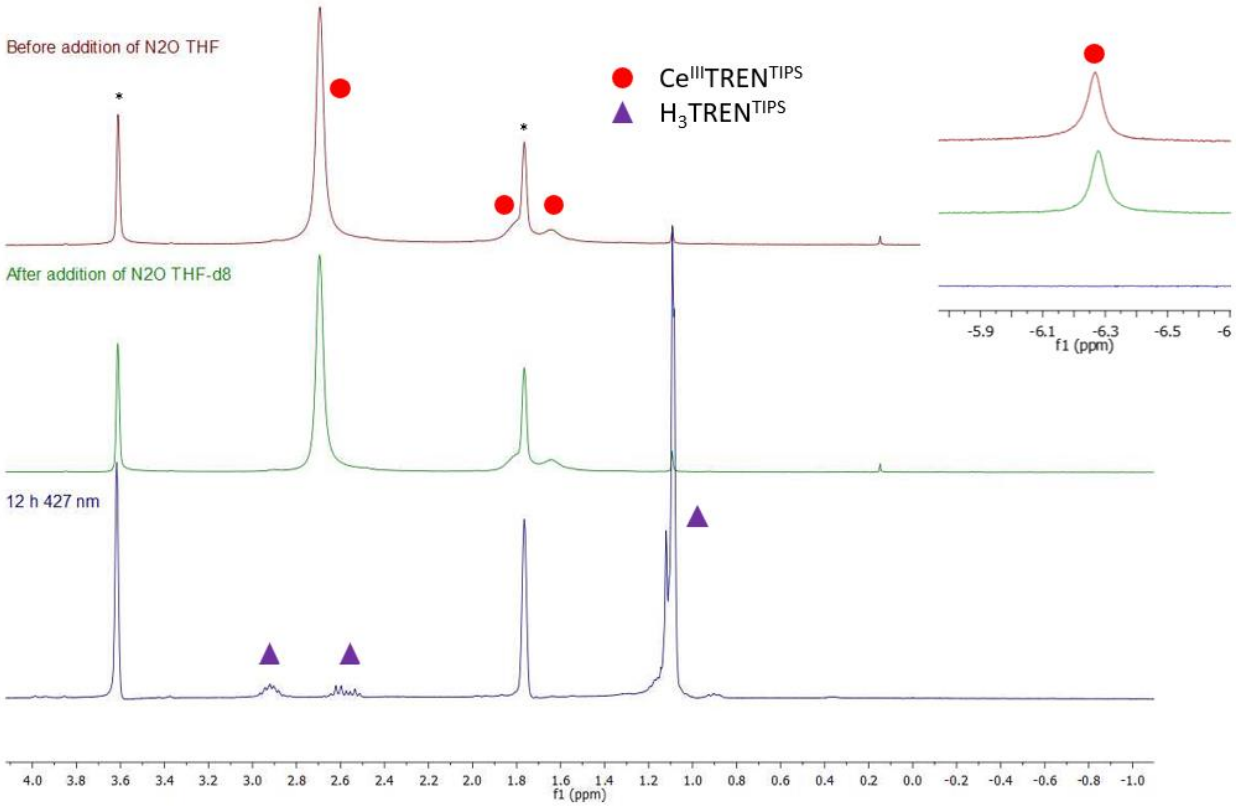

Figure S316. ^{1}H NMR spectrum of the photochemical reaction between **1** and N_2O in THF-d_8. Zoom between -1.0 and 4.2 ppm. Solvent residual peaks are indicated with *

c) Attempts of trapping experiments

Institut Polytechnique de Paris
91120 Palaiseau, France

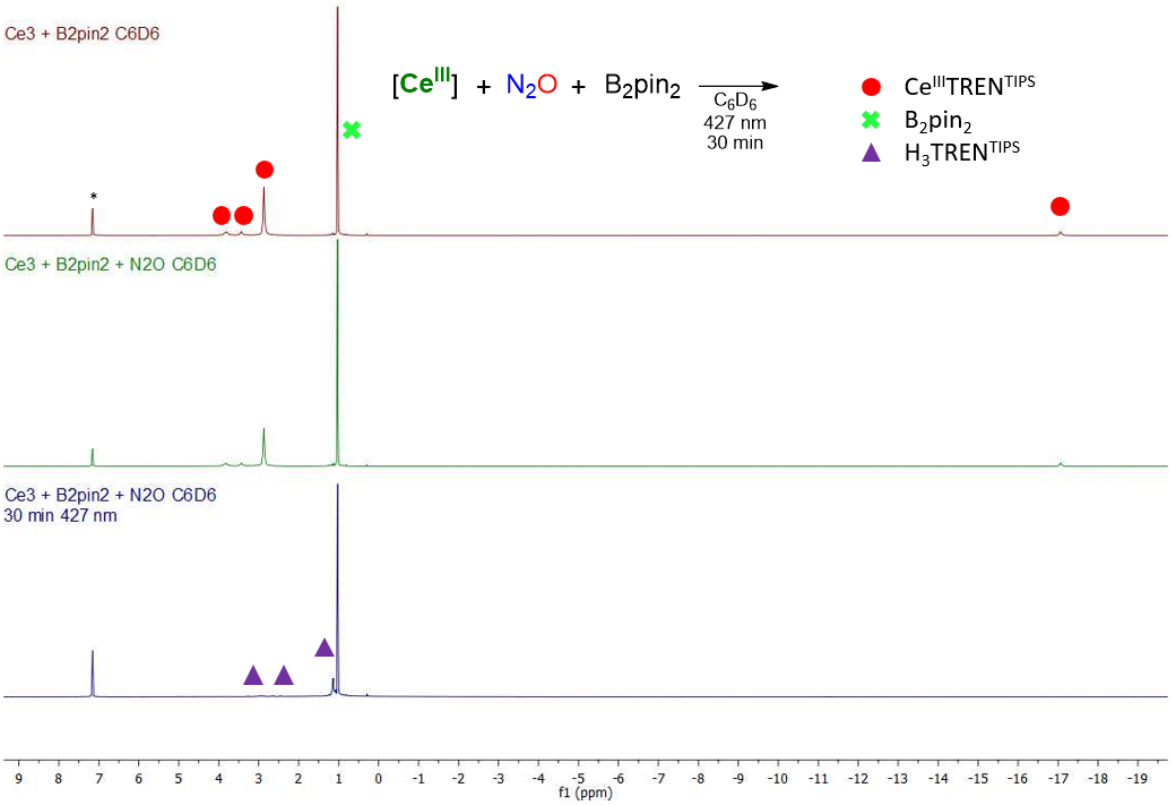

Figure S317. ^{1}H NMR spectrum of the photochemical reaction between **1** and N_2O in the presence of B_2pin_2 in C_6D_6. Solvent residual peak is indicated with *

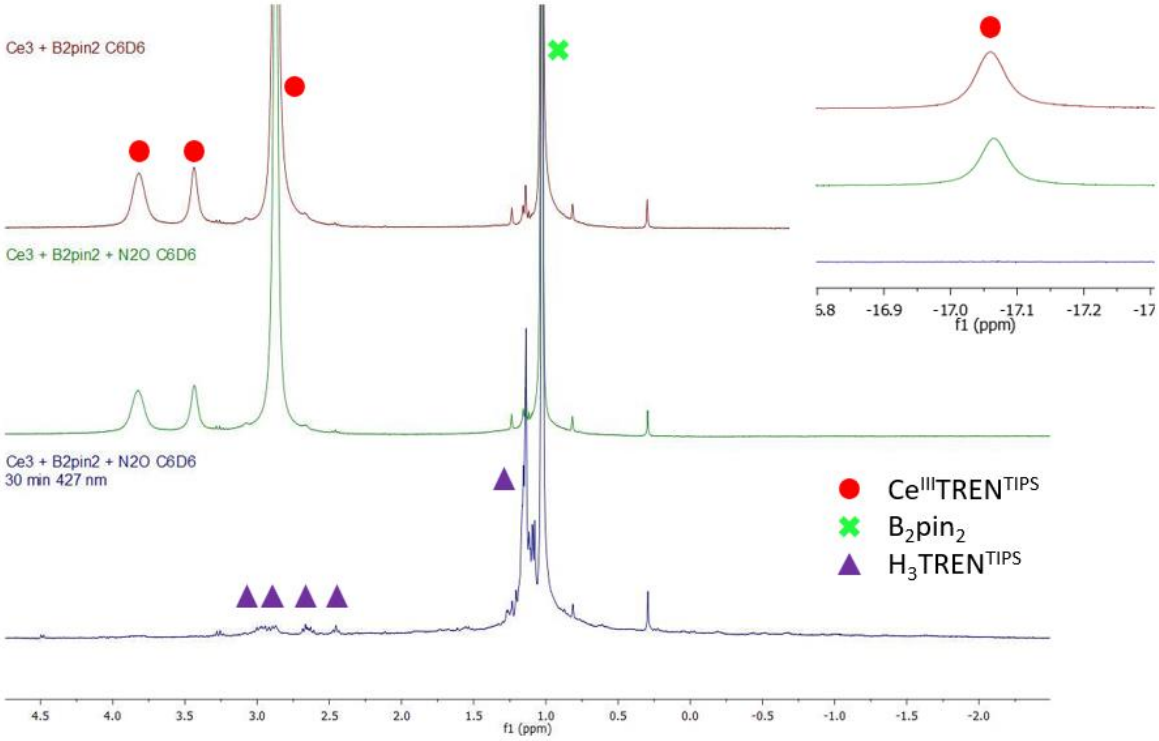

Figure S318. ^{1}H NMR spectrum of the photochemical reaction between **1** and N_2O in the presence of B_2pin_2 in C_6D_6. Zoom between -2.5 and 4.5 ppm. Solvent residual peaks are indicated with *

Institut Polytechnique de Paris
91120 Palaiseau, France

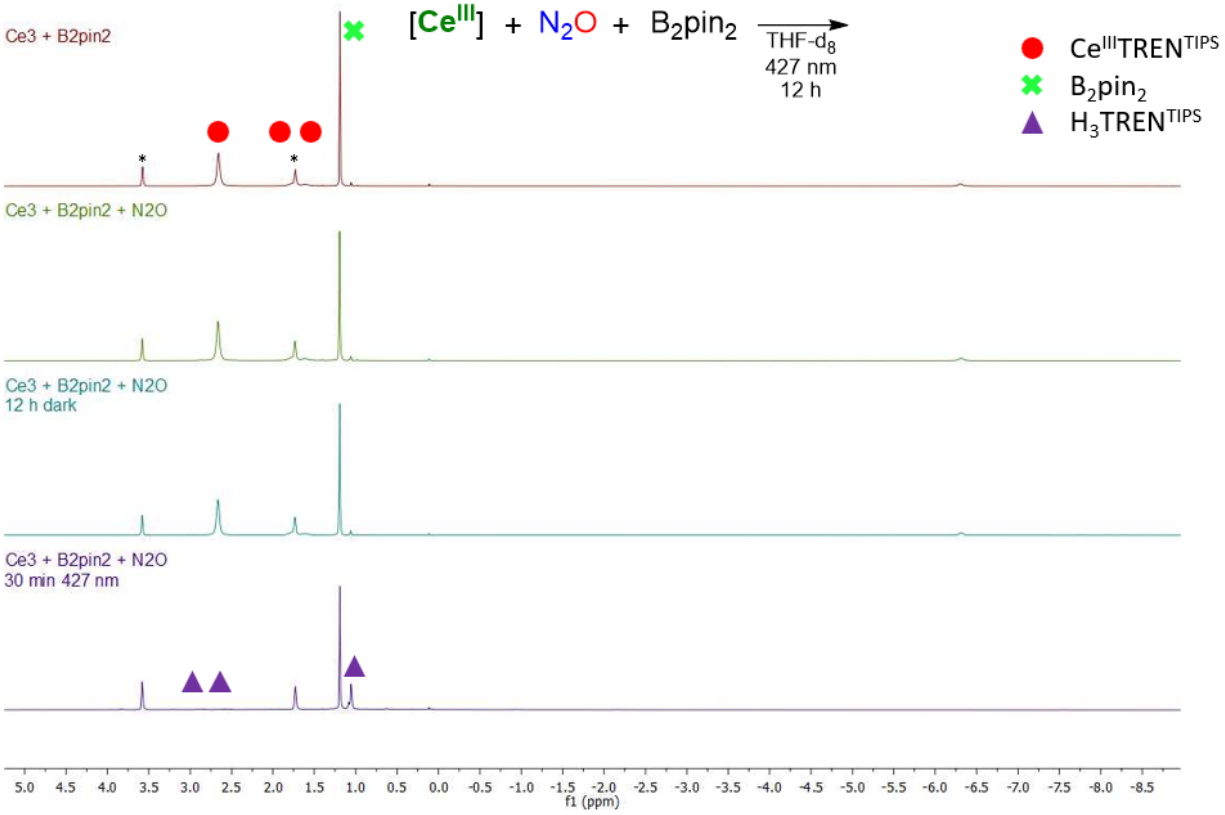

Figure S319. ^{1}H NMR spectrum of the photochemical reaction between **1** and N_2O in the presence of B_2pin_2 in THF-d_8. Solvent residual peaks are indicated with *

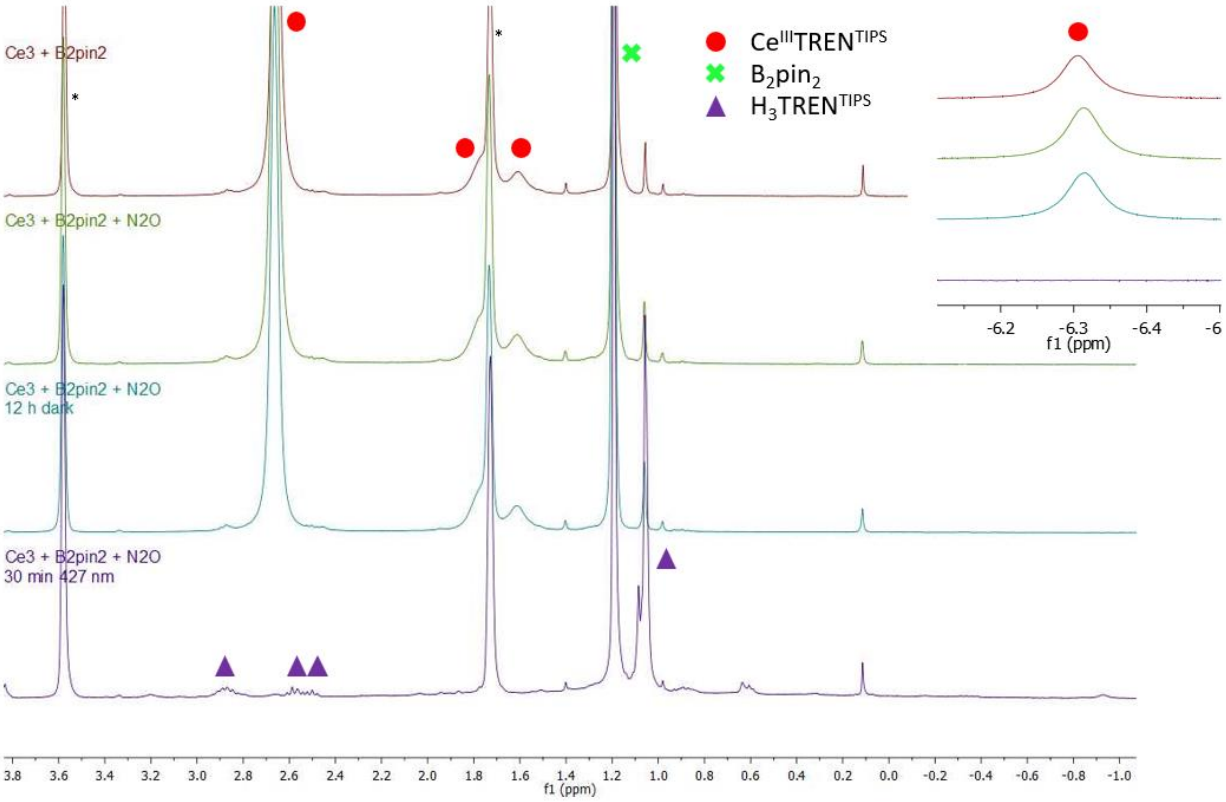

Figure S320. ^{1}H NMR spectrum of the photochemical reaction between **1** and N_2O in the presence of B_2pin_2 in THF-d_8. Zoom between -1.0 and 4.0 ppm. Solvent residual peaks are indicated with *

Institut Polytechnique de Paris
91120 Palaiseau, France

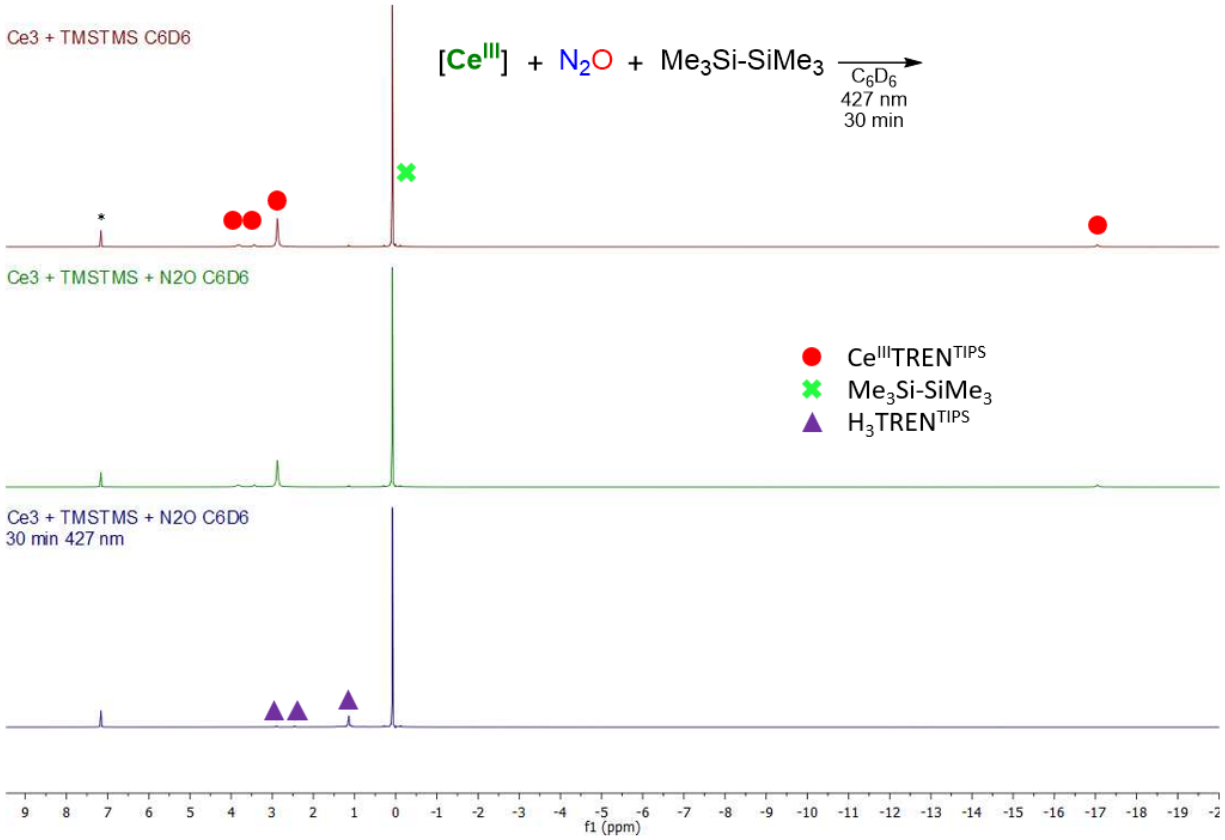

Figure S321. ^{1}H NMR spectrum of the photochemical reaction between **1** and N_2O in the presence of $Me_3Si\text{-}SiMe_3$ in C_6D_6. Solvent residual peak is indicated with *

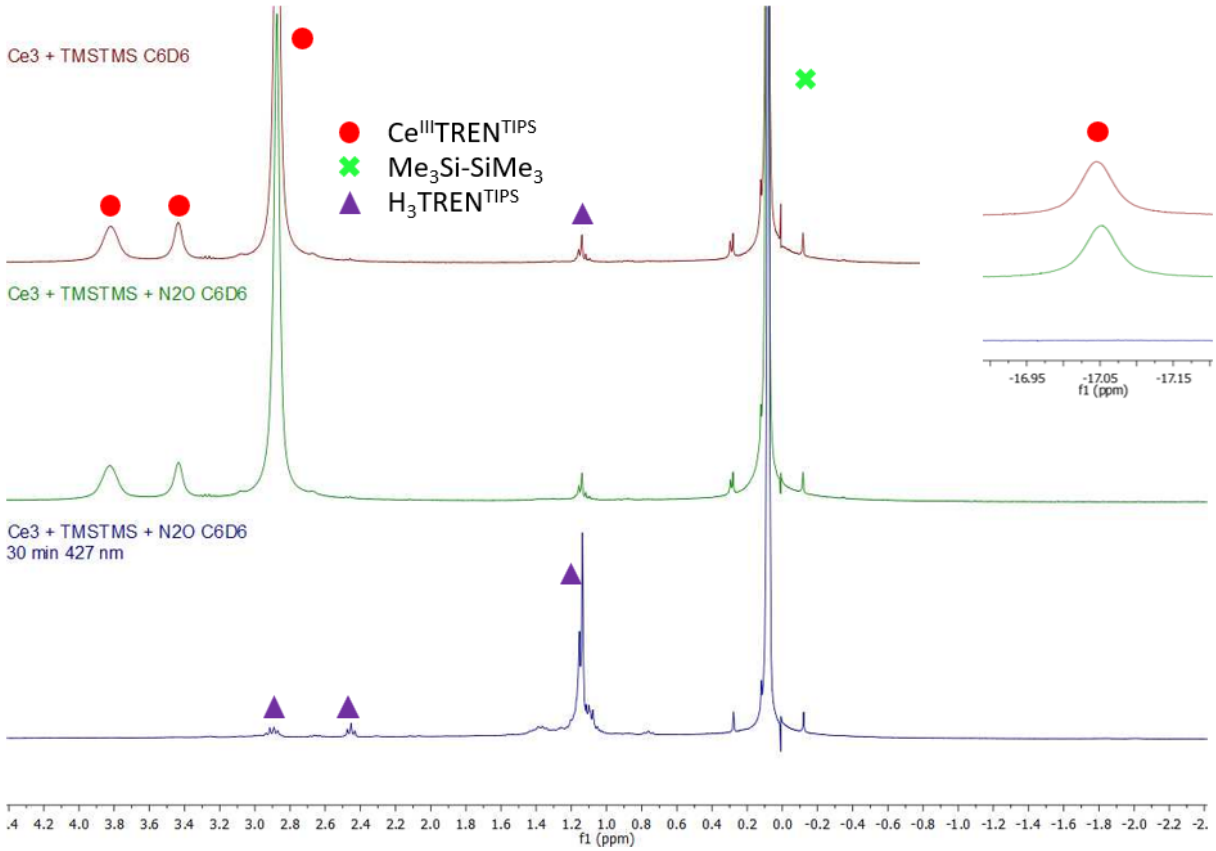

Figure S322. ^{1}H NMR spectrum of the photochemical reaction between **1** and N_2O in the presence of $Me_3Si\text{-}SiMe_3$ in C_6D_6. Zoom between -2.4 and 4.4 ppm. Solvent residual peak is indicated with *

Institut Polytechnique de Paris
91120 Palaiseau, France

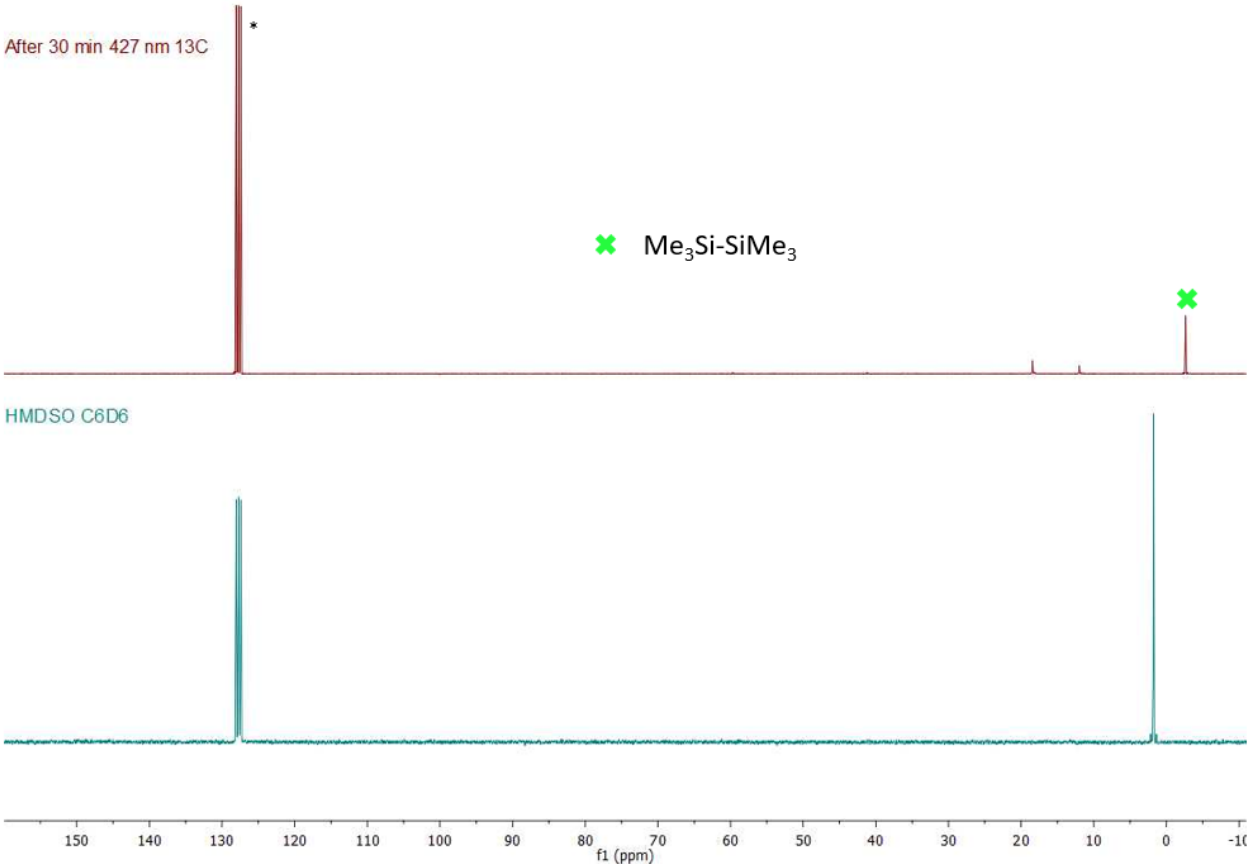

Figure S323. ^{13}C NMR spectrum of the photochemical reaction between **1** and N_2O in the presence of $Me_3Si\text{-}SiMe_3$ in C_6D_6 (HMDSO = hexamethyldisiloxane $Me_3Si\text{-}O\text{-}SiMe_3$). Solvent residual peak is indicated with *

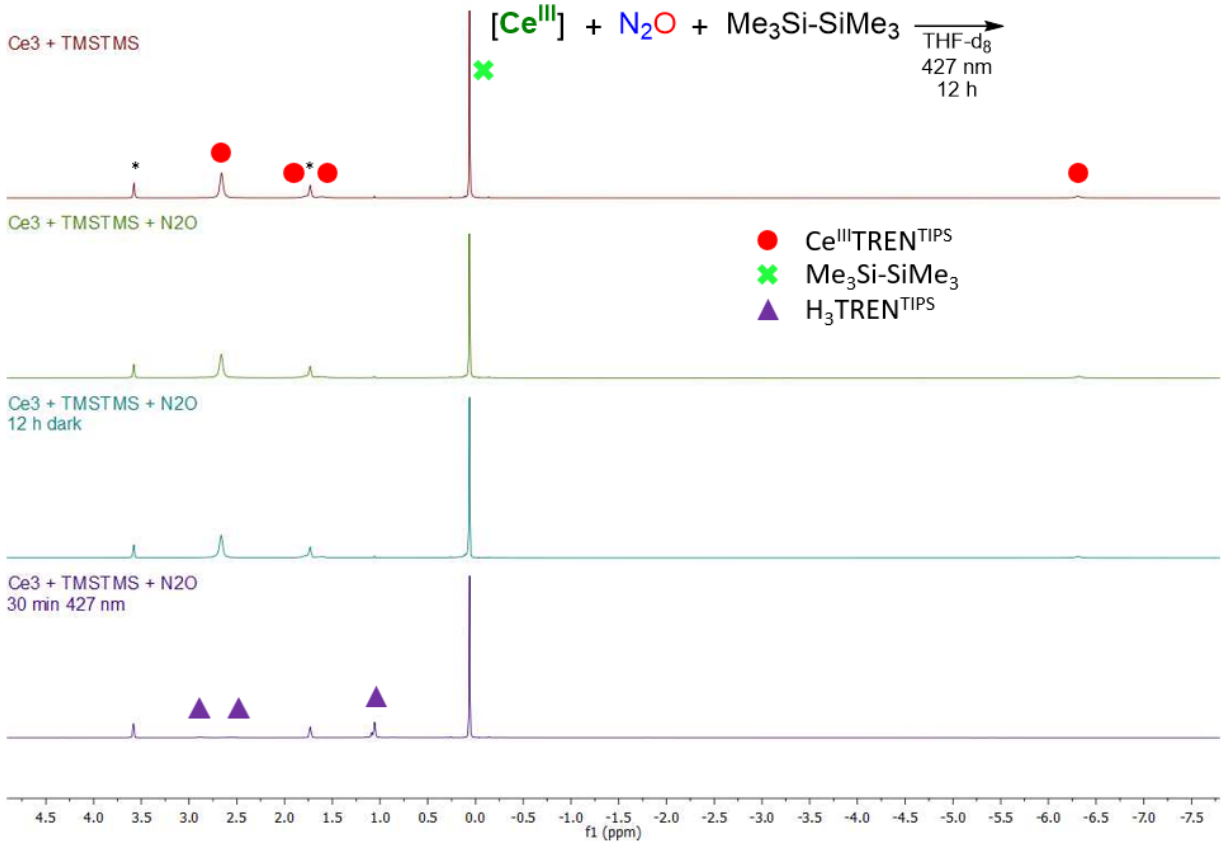

Figure S324. ^{1}H NMR spectrum of the photochemical reaction between **1** and N_2O in the presence of $Me_3Si\text{-}SiMe_3$ in THF-d_8. Zoom between -1.0 and 4.5 ppm. Solvent residual peaks are indicated with *

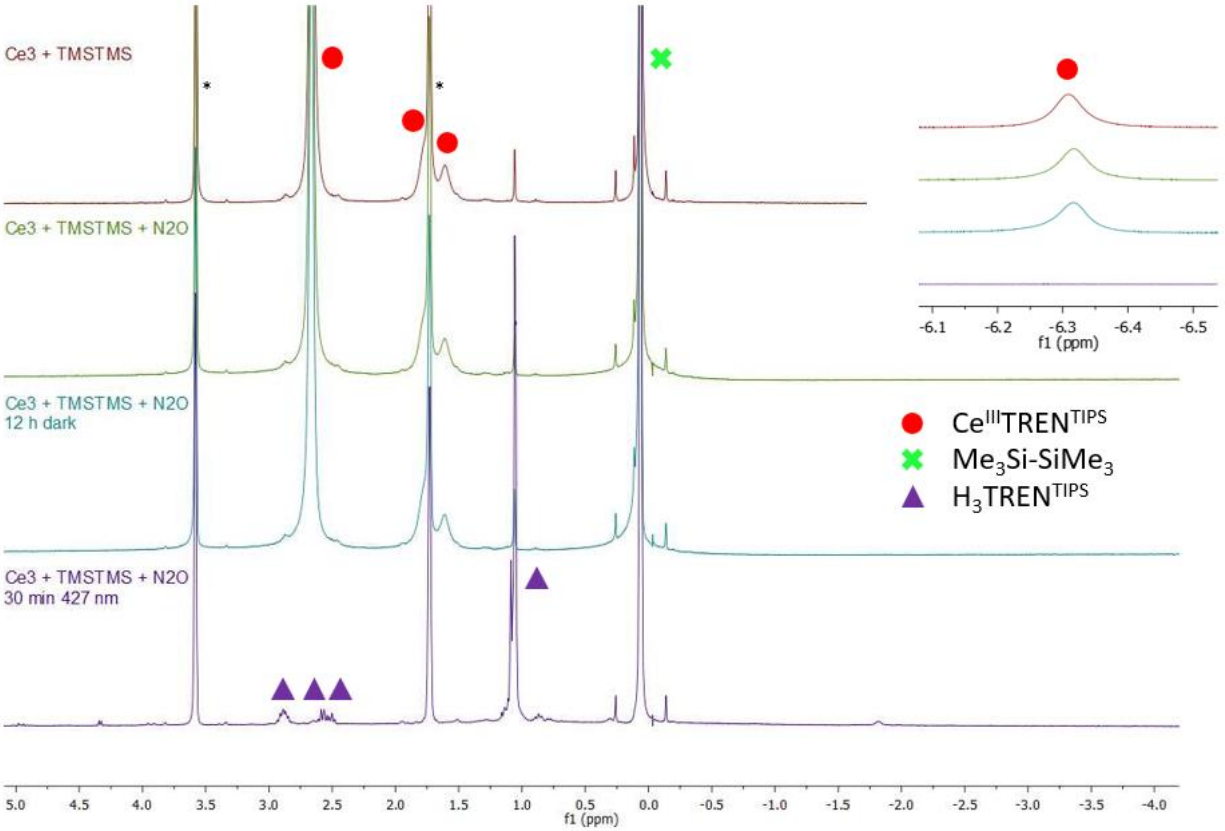

Figure S325. ^{1}H NMR spectrum of the photochemical reaction between **1** and N_2O in the presence of $Me_3Si\text{-}SiMe_3$ in THF-d_8. Zoom between -4.0 and 5.0 ppm. Solvent residual peaks are indicated with *

Institut Polytechnique de Paris
91120 Palaiseau, France

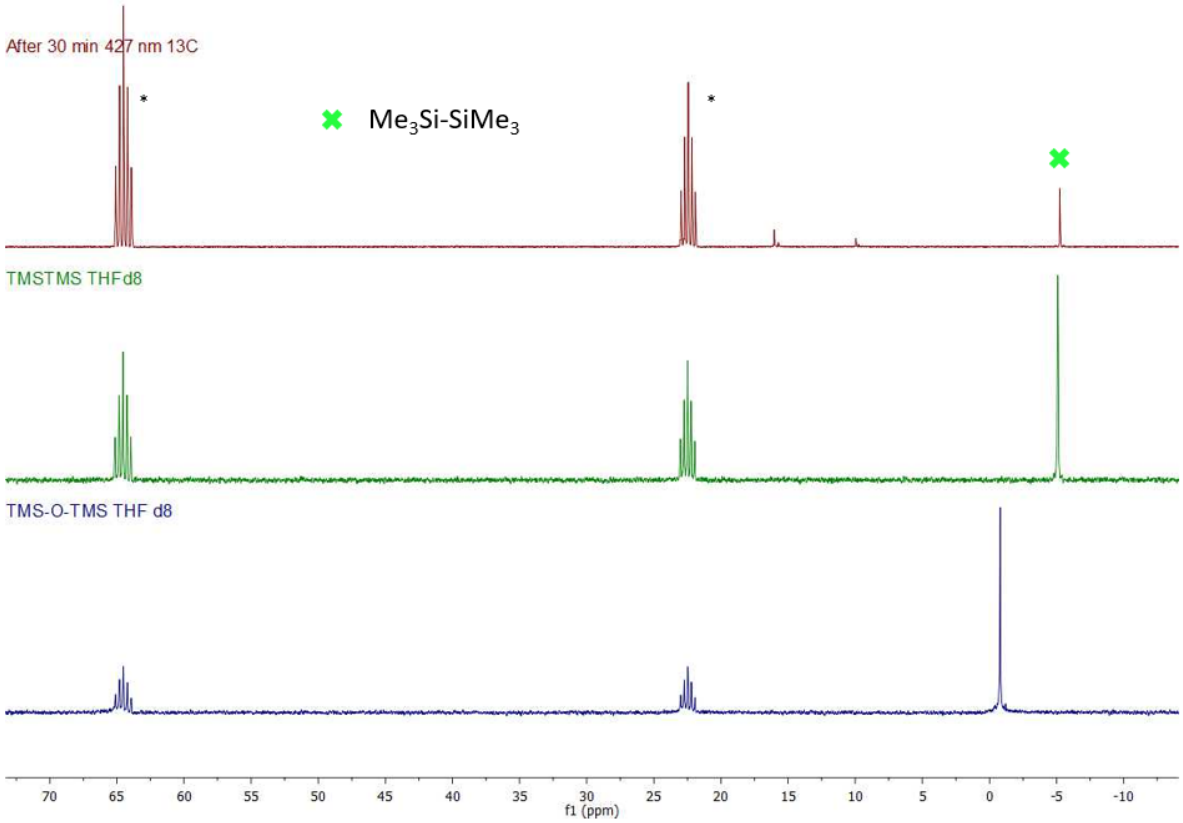

Figure S326. ^{13}C NMR spectrum of the photochemical reaction between **1** and N_2O in the presence of $Me_3Si\text{-}SiMe_3$ in THF-d_8. Solvent residual peaks are indicated with *

Institut Polytechnique de Paris
91120 Palaiseau, France

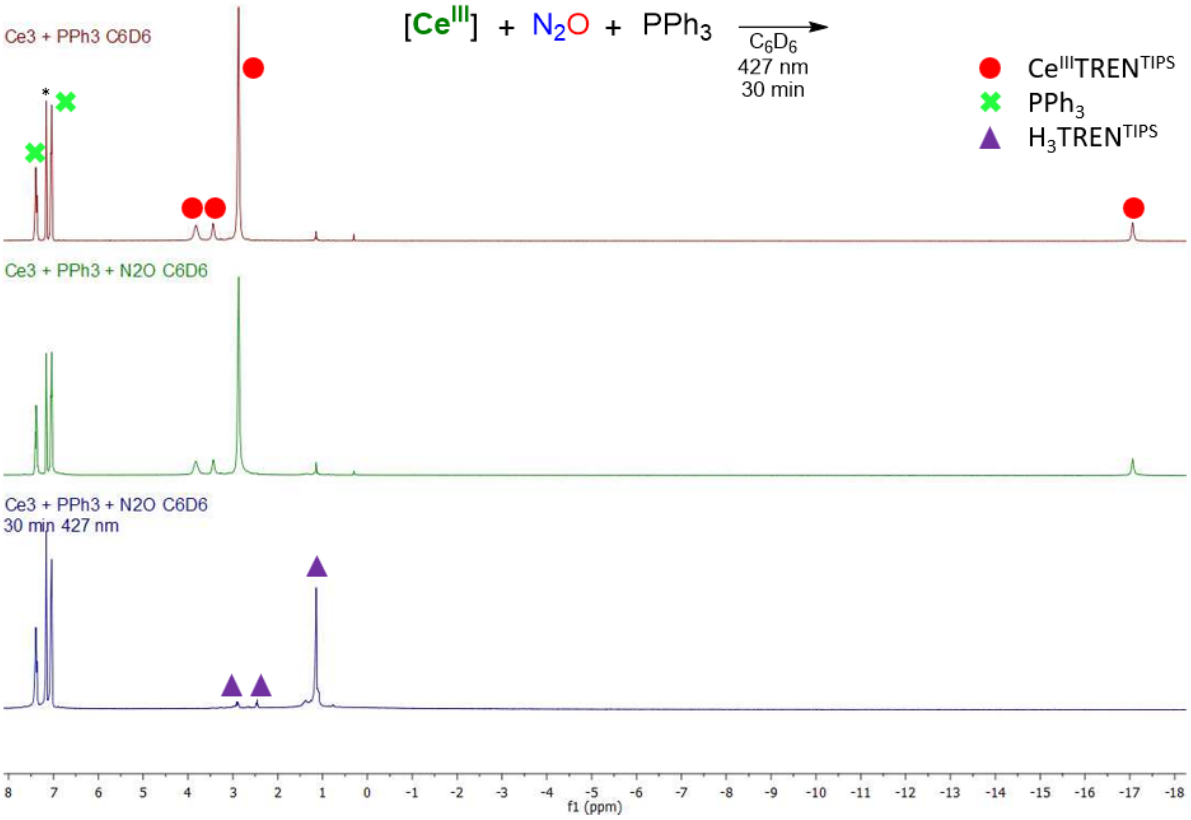

Figure S327. ^{1}H NMR spectrum of the photochemical reaction between **1** and N_2O in the presence of PPh_3 in C_6D_6. Solvent residual peak is indicated with *

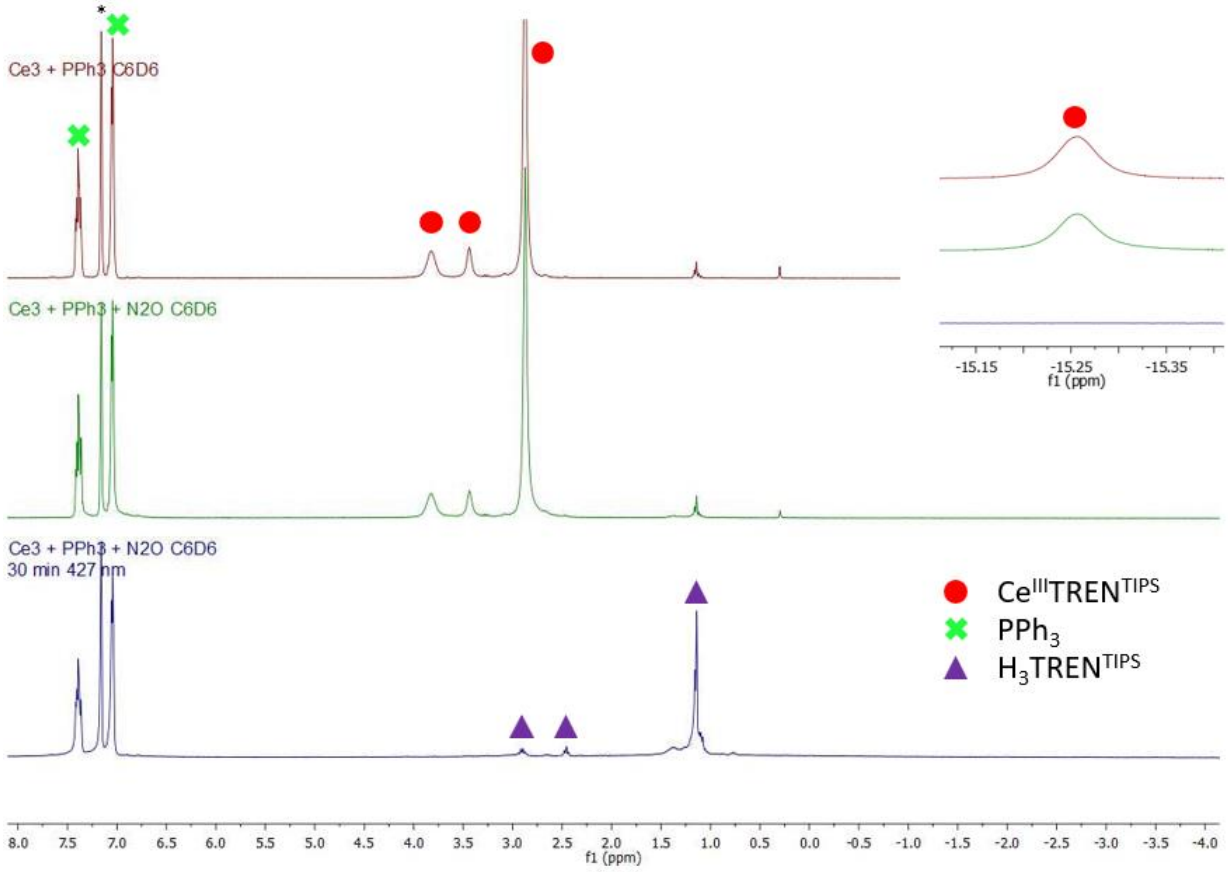

Figure S328. ^{1}H NMR spectrum of the photochemical reaction between **1** and N_2O in the presence of PPh_3 in C_6D_6. Zoom between -4.0 and 8.0 ppm. Solvent residual peak is indicated with *

Institut Polytechnique de Paris
91120 Palaiseau, France

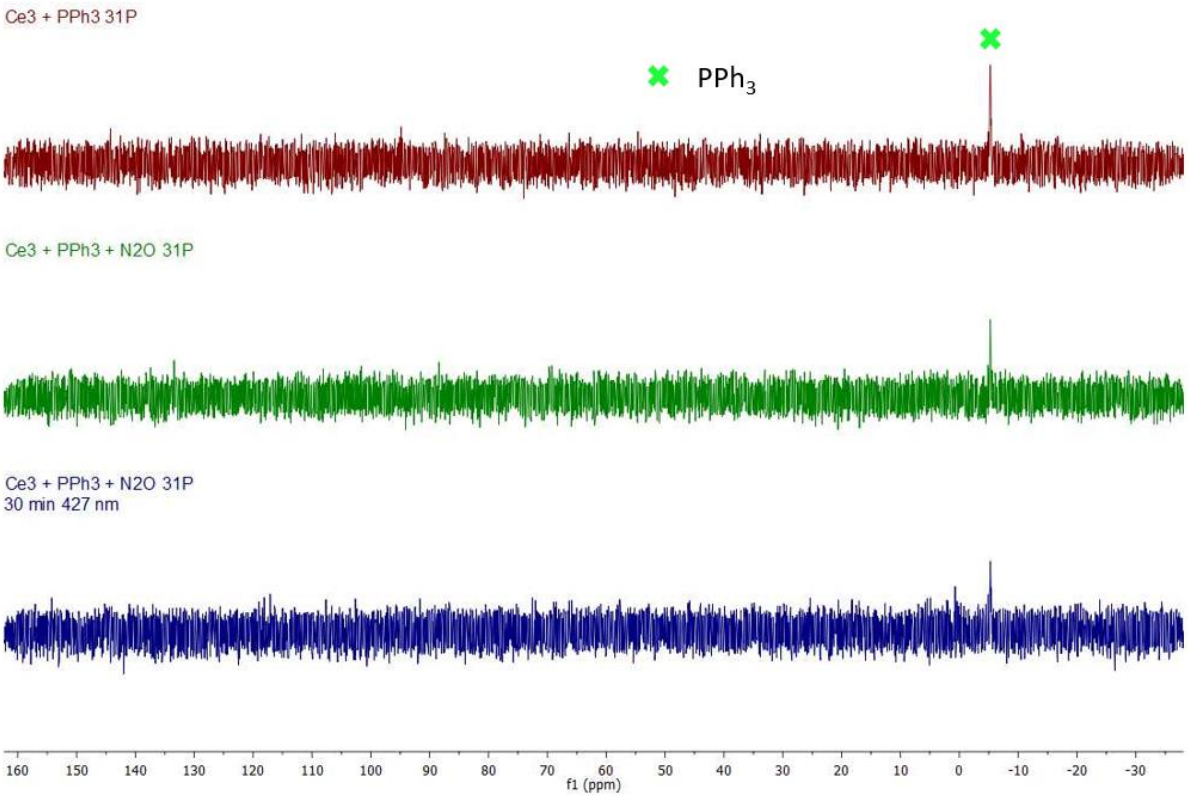

Figure S329. ^{31}P NMR spectrum of the photochemical reaction between **1** and N_2O in the presence of PPh_3 in C_6D_6

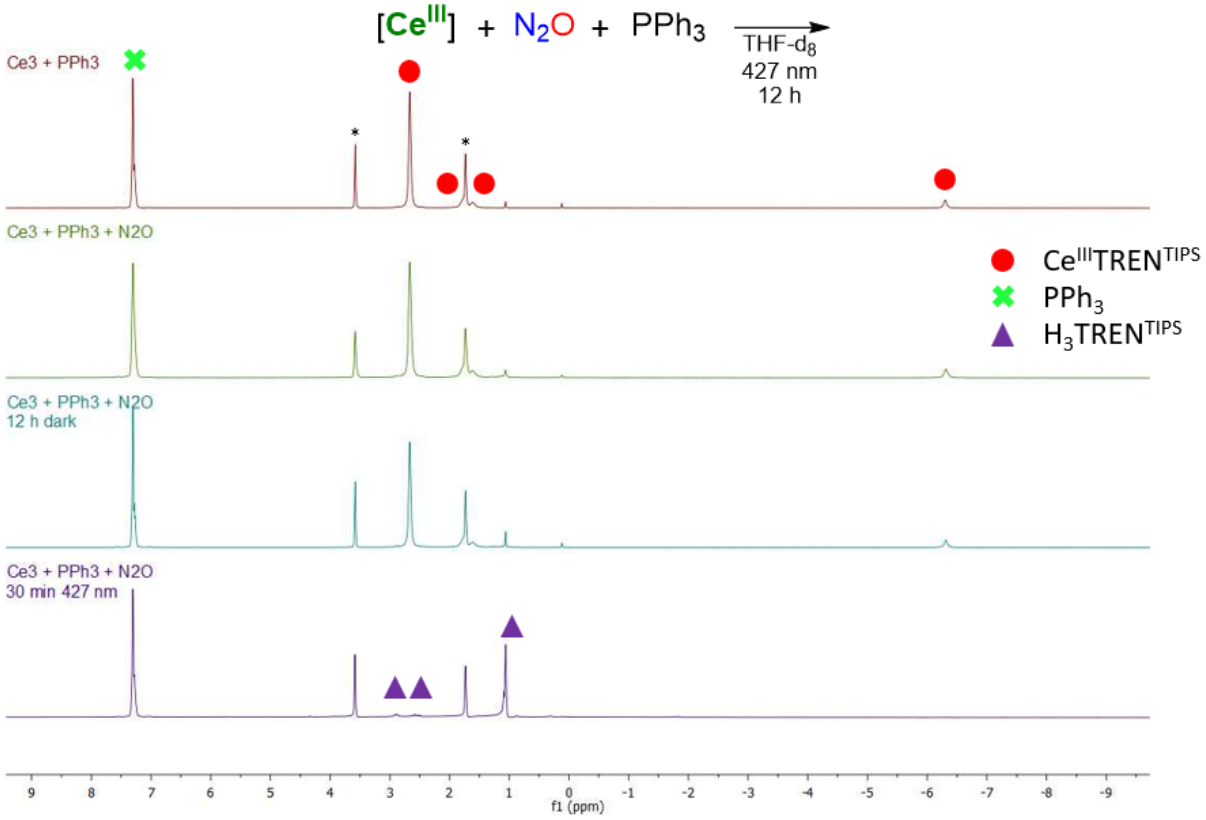

Figure S330. ^{1}H NMR spectrum of the photochemical reaction between **1** and N_2O in the presence of PPh_3 in THF-d_8. Solvent residual peaks are indicated with *

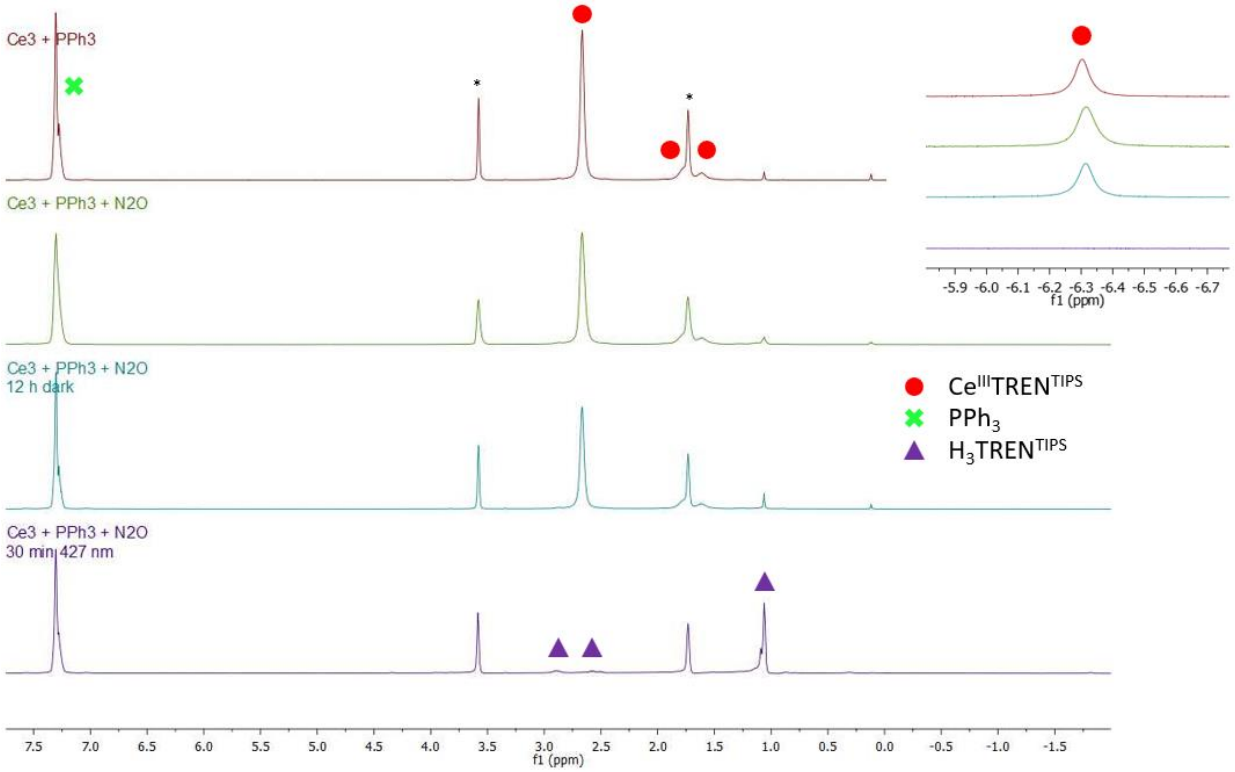

Figure S331. ^{1}H NMR spectrum of the photochemical reaction between **1** and N_2O in the presence of PPh_3 in THF-d_8. Zoom between -2.0 and 8.0 ppm. Solvent residual peaks are indicated with *

Institut Polytechnique de Paris
91120 Palaiseau, France

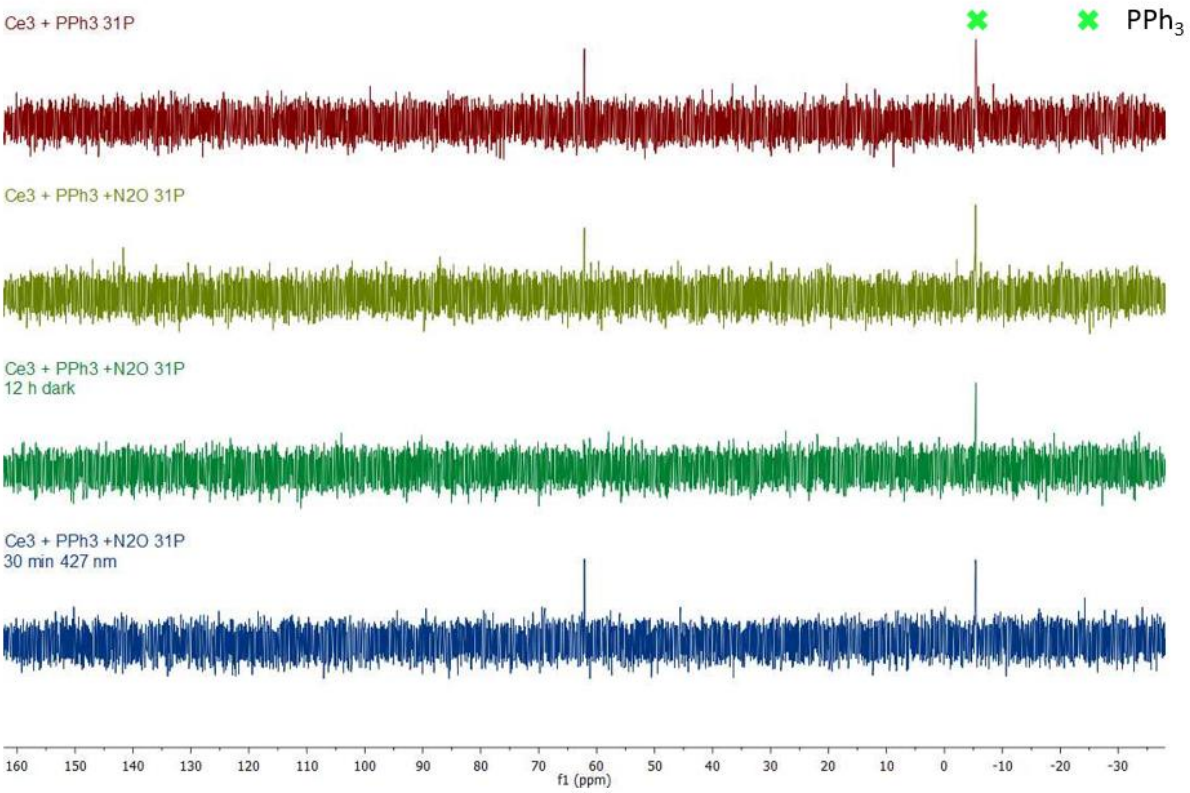

Figure S332. ^{31}P NMR spectrum of the photochemical reaction between **1** and N_2O in the presence of PPh_3 in THF-d_8

II. Gas chromatography analysis for N_2O reactivity

Institut Polytechnique de Paris
91120 Palaiseau, France

a) General procedure

Two solutions of **1** in THF were prepared inside a glovebox filled with N_2 by dissolving 30 mg (40 µmol) of crystals in 0.5 mL of THF. The two solution were degassed thrice using freeze-pump-thaw technique, and N_2O (1.5 bar absolute, excess) was added to both solutions at room temperature. One tube was irradiated at 427 nm for 30 min, while the other one was kept in the dark for the same duration. After 30 min, each tube was plugged to a micro-GC device, and the tubing was purged about 20 times with vacuum-argon cycles. Chromatogram of the tubing under argon was performed after the purging cycles (herein referred to as "blank") with the method described below. After recording of the blank, tubing was pressurised with argon (1 bar absolute), and the NMR tube was opened in the tubing to release overpressure. Micro-GC analysis was started while keeping the NMR tube open during the injection period.

Method :

General parameters :

- gas : argon and helium mixture
- inject time : 30 ms
- backflush time : 11 s
- injector temperature : 70 °C
- TCD temperature : 70 °C
- TCD Delta temperature : 20 °C
- sample pump : 15 s
- sample inlet heater : disabled

Temperature gradient :

- ramp rate : 0 °C.s^{-1} ; ramp time : 70 s ; hold time : 12 s
- ramp time : 1.5 °C.s^{-1} ; ramp time : 100 s ; hold time : 70 s

b) Gas chromatograms

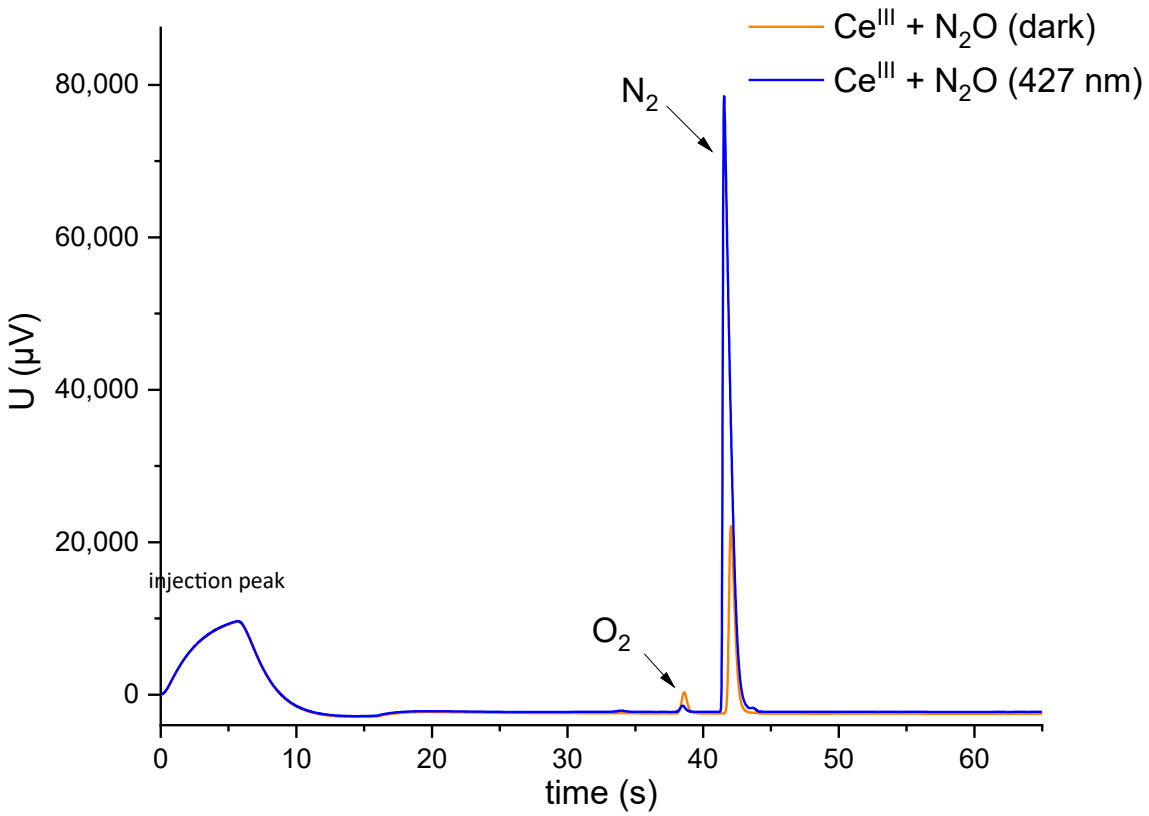

Figure S333. GC analysis (module A) of the atmosphere of the reaction medium containing a solution of **1** and N_2O (1.5 bar absolute) in THF left in the dark for 30 min (orange) and irradiated at 427 nm for 30 min (blue)

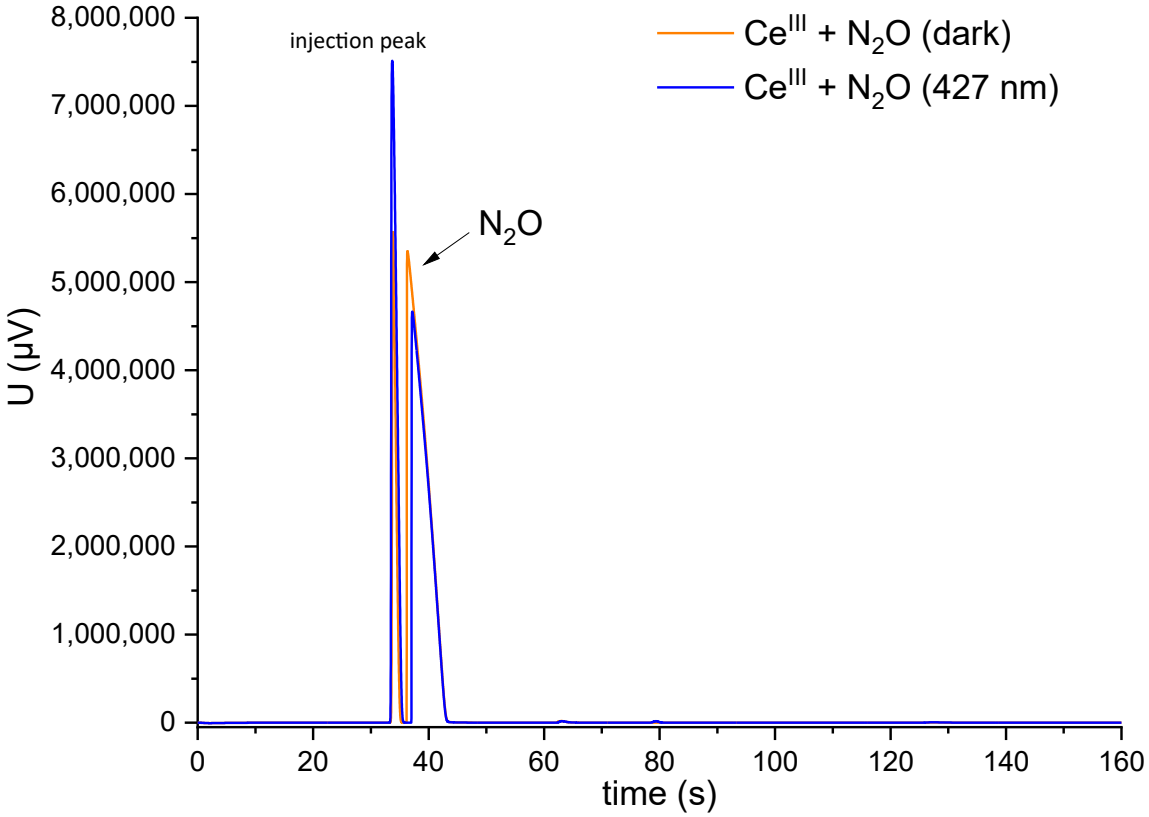

Figure S334. GC analysis (module B) of the atmosphere of the reaction medium containing a solution of **1** and N_2O (1.5 bar absolute) in THF left in the dark for 30 min (orange) and irradiated at 427 nm for 30 min (blue)

Area ($\mu V.s^{-1}$)	Dark		Irradiation at 427 nm	
Gas	**Blank**	**Dark**	**Blank**	**Irradiation**
O_2	340	2,790	176	791
N_2	542	25,516	373	102,643
N_2O	0	19,843,485	0	15,111,637

Table S62. Area values of chromatographic peaks from the reaction between **1** and N_2O in THF

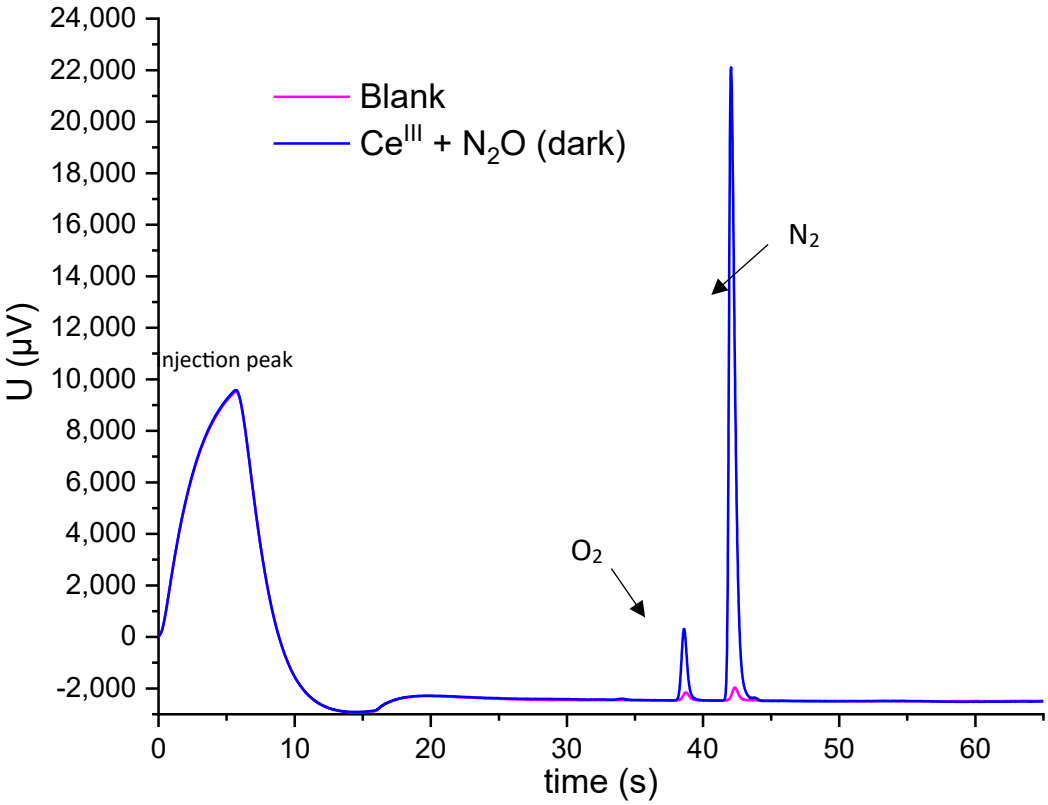

Figure S335. GC analysis (module A) of the atmosphere of the reaction medium containing a solution of **1** and N_2O (1.5 bar absolute) in THF left in the dark for 30 min (blue) and the corresponding blank of the system (magenta)

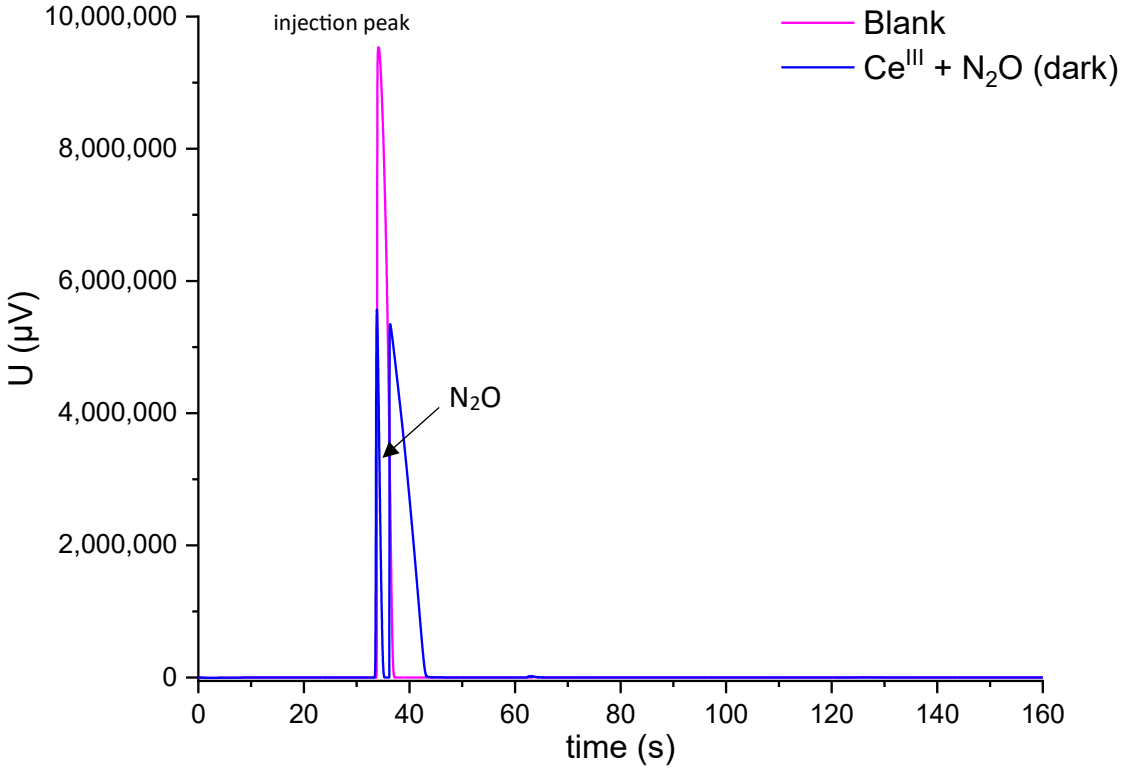

Figure S336. GC analysis (module A) of the atmosphere of the reaction medium containing a solution of **1** and N_2O (1.5 bar absolute) in left in the dark for 30 min (blue) and the corresponding blank of the system (magenta)

Institut Polytechnique de Paris
91120 Palaiseau, France

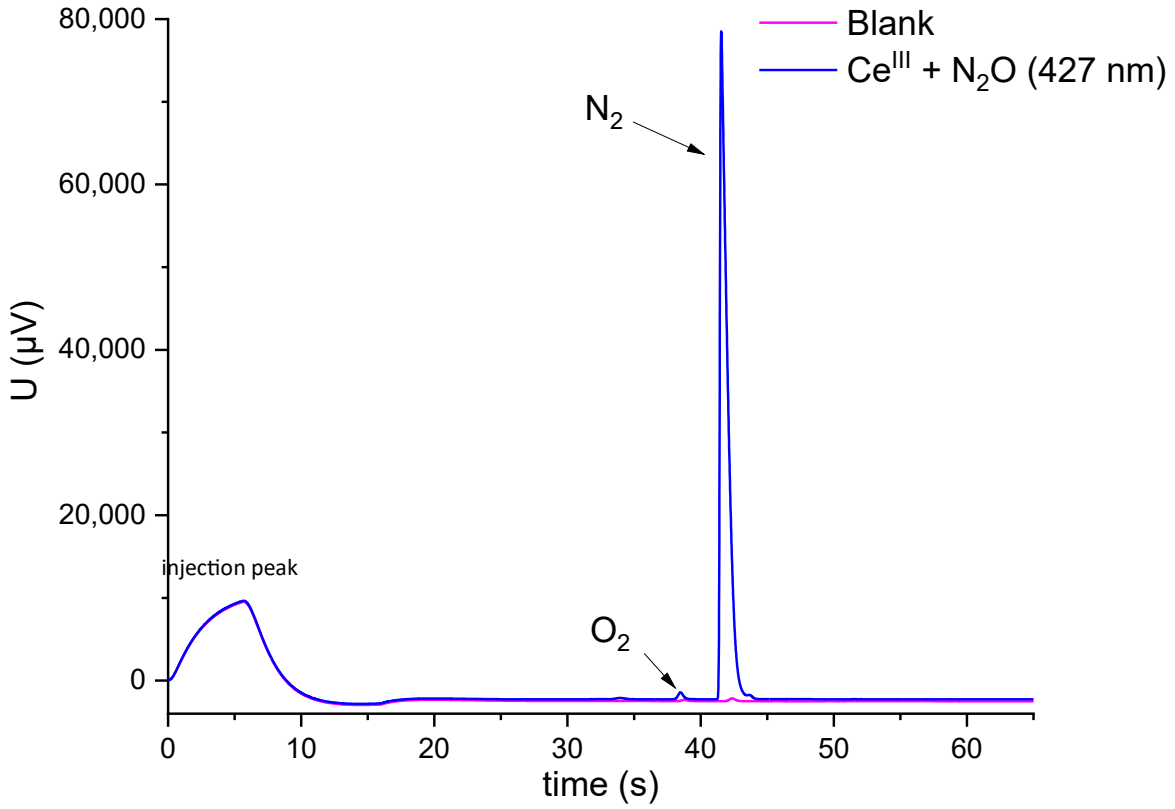

Figure S337. GC analysis (module A) of the atmosphere of the reaction medium containing a solution of **1** and N_2O (1.5 bar absolute) in THF irradiated at 427 nm for 30 min (blue) and the corresponding blank of the system (magenta)

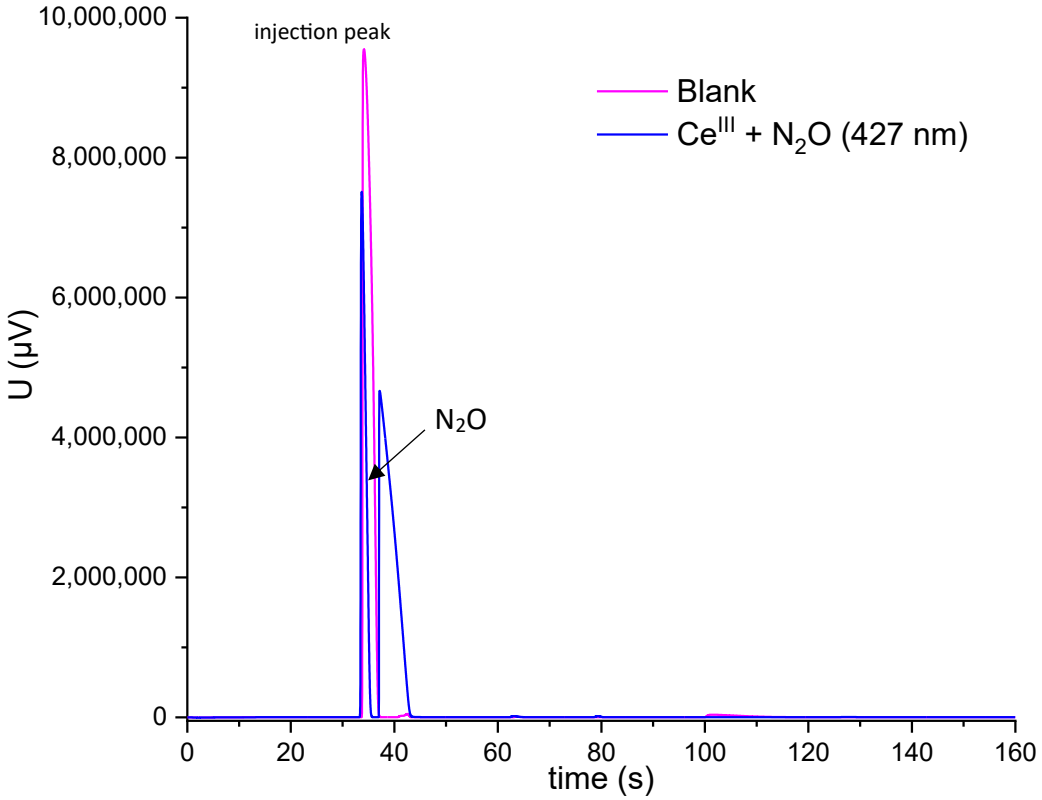

Figure S338. GC analysis (module A) of the atmosphere of the reaction medium containing a solution of **1** and N_2O (1.5 bar absolute) in THF irradiated at 427 nm for 30 min (blue) and the corresponding blank of the system (magenta)

Institut Polytechnique de Paris
91120 Palaiseau, France

Experimental section for Chapter IV

Part II

Institut Polytechnique de Paris
91120 Palaiseau, France

I. NMR data for part IV

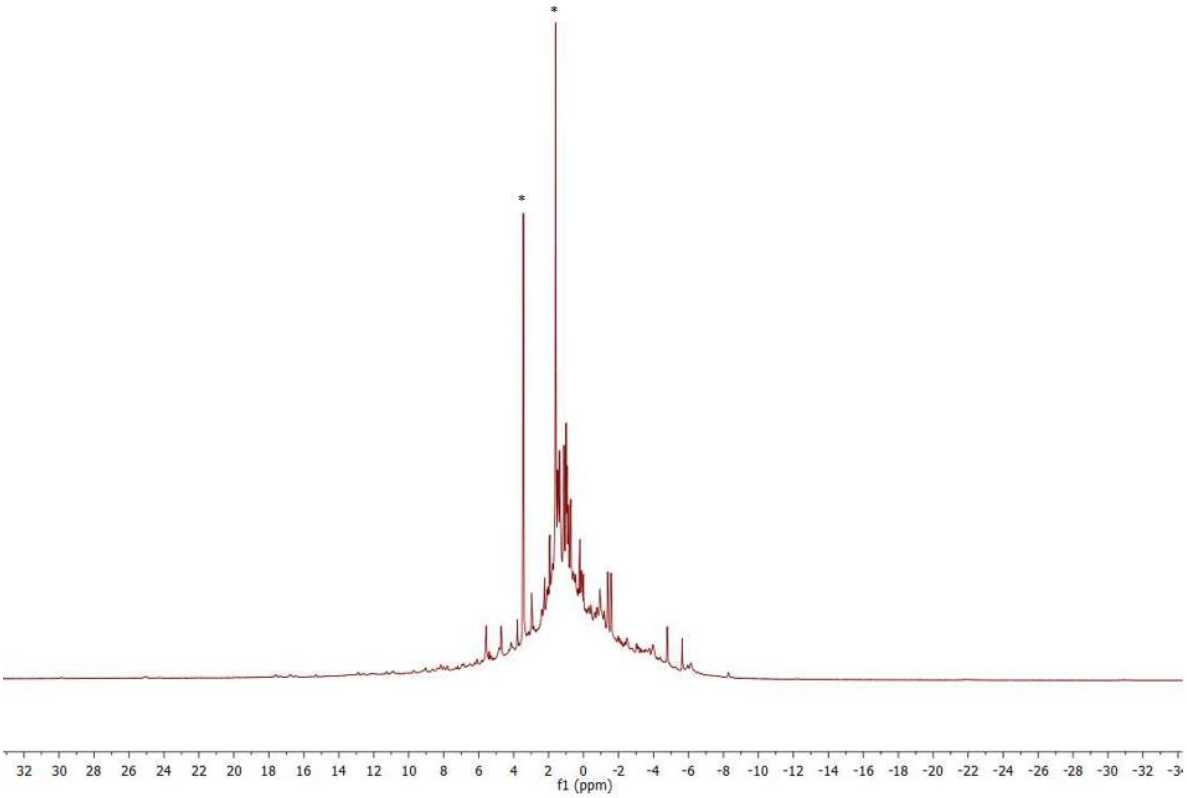

Figure S339. ^{1}H NMR spectrum of the *in-situ* reaction between **1** and CO_2 (excess) in THF-d_8. Solvent residual peaks are indicated with *

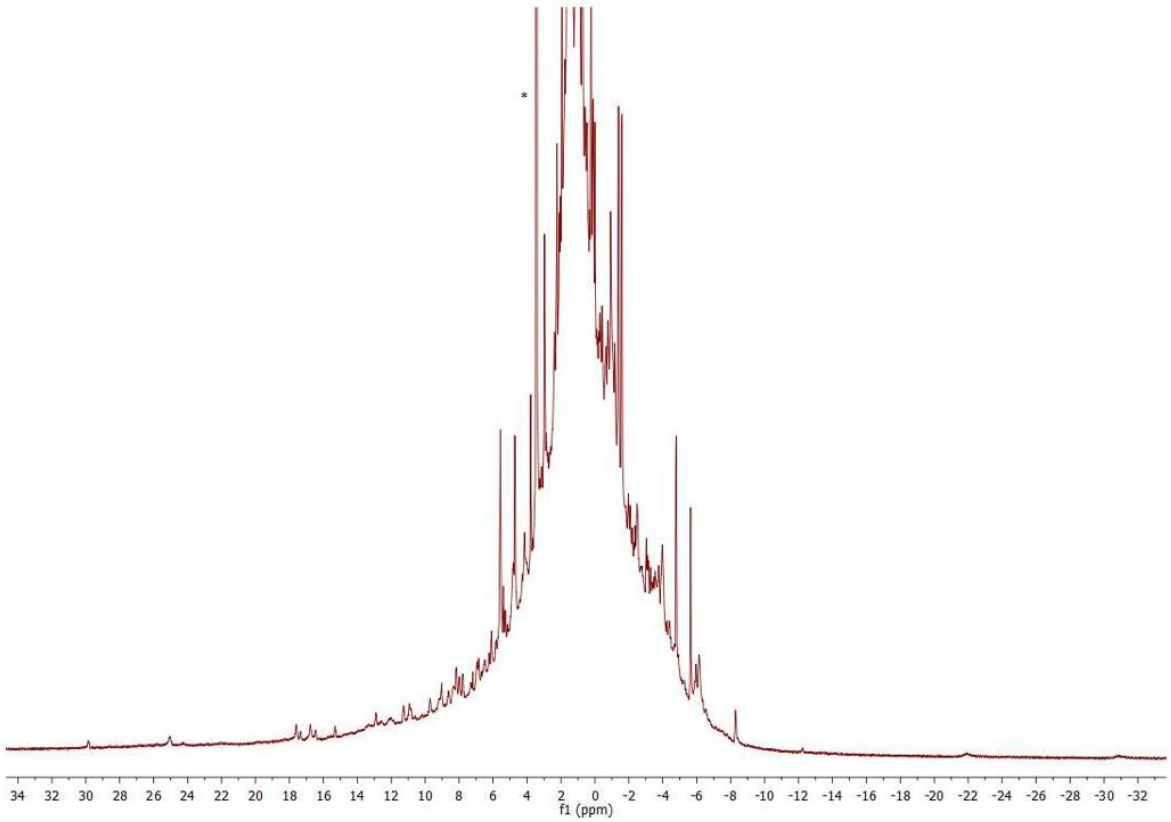

Figure S340. ^{1}H NMR spectrum of the *in-situ* reaction between **1** and CO_2 (excess) in THF-d_8. Solvent residual peaks are indicated with *

Institut Polytechnique de Paris
91120 Palaiseau, France

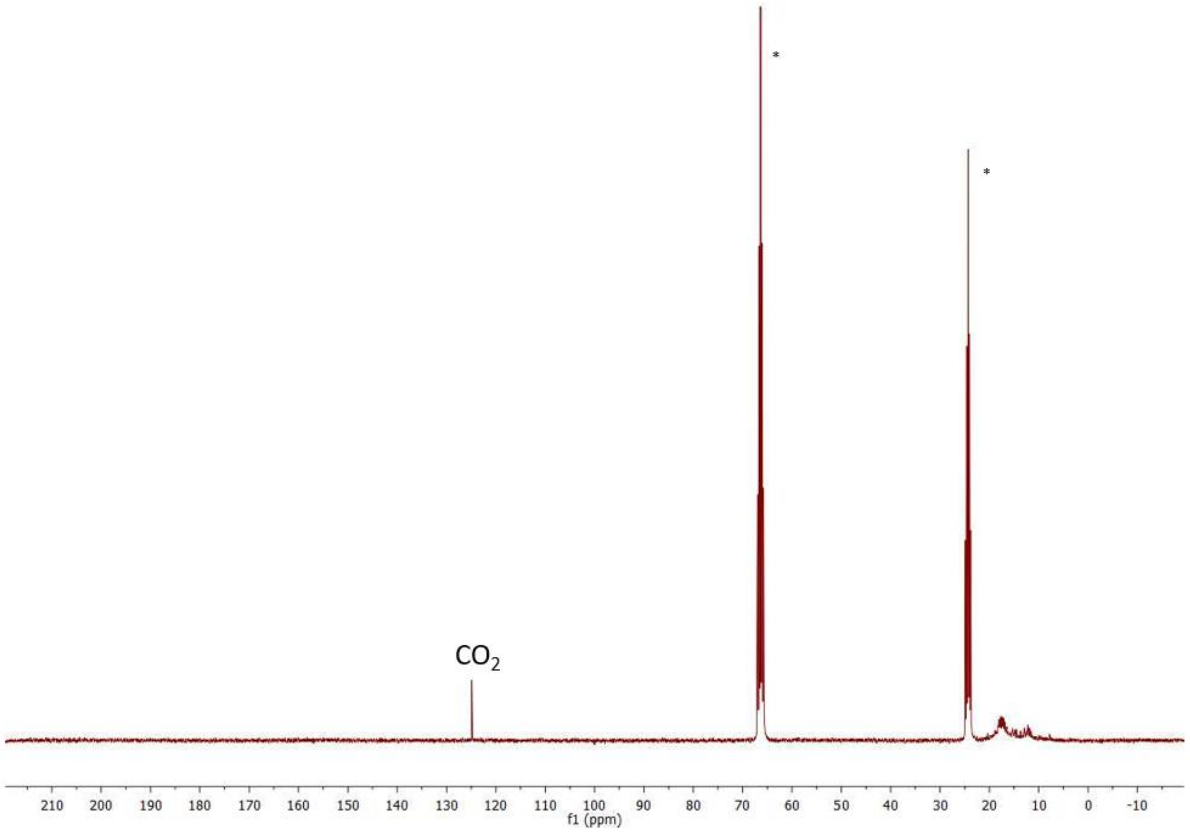

Figure S341. ^{13}C NMR spectrum of the *in-situ* reaction between **1** and CO_2 (excess) in THF-d_8. Solvent residual peaks are indicated with *

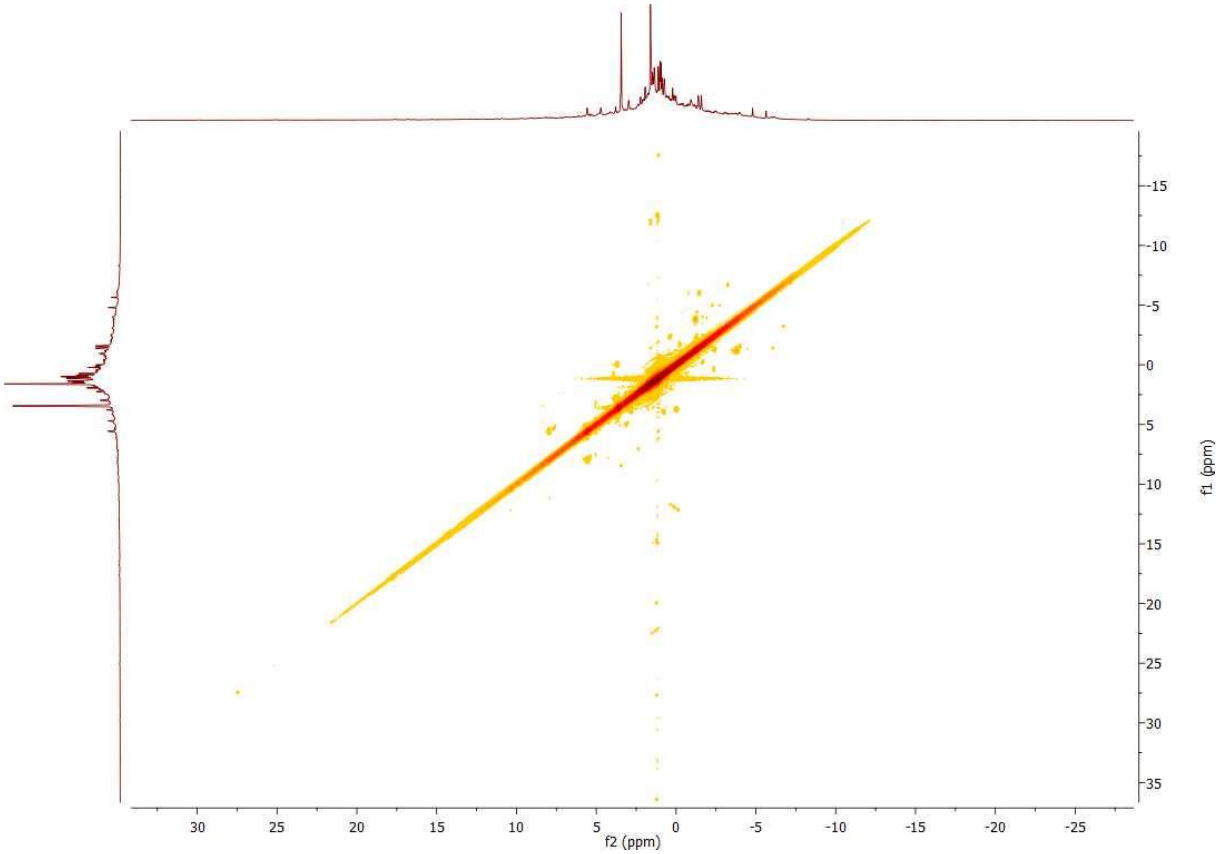

Figure S342. ^{1}H-^{1}H COSY spectrum of the *in-situ* reaction between **1** and CO_2 (excess) in THF-d_8

Institut Polytechnique de Paris
91120 Palaiseau, France

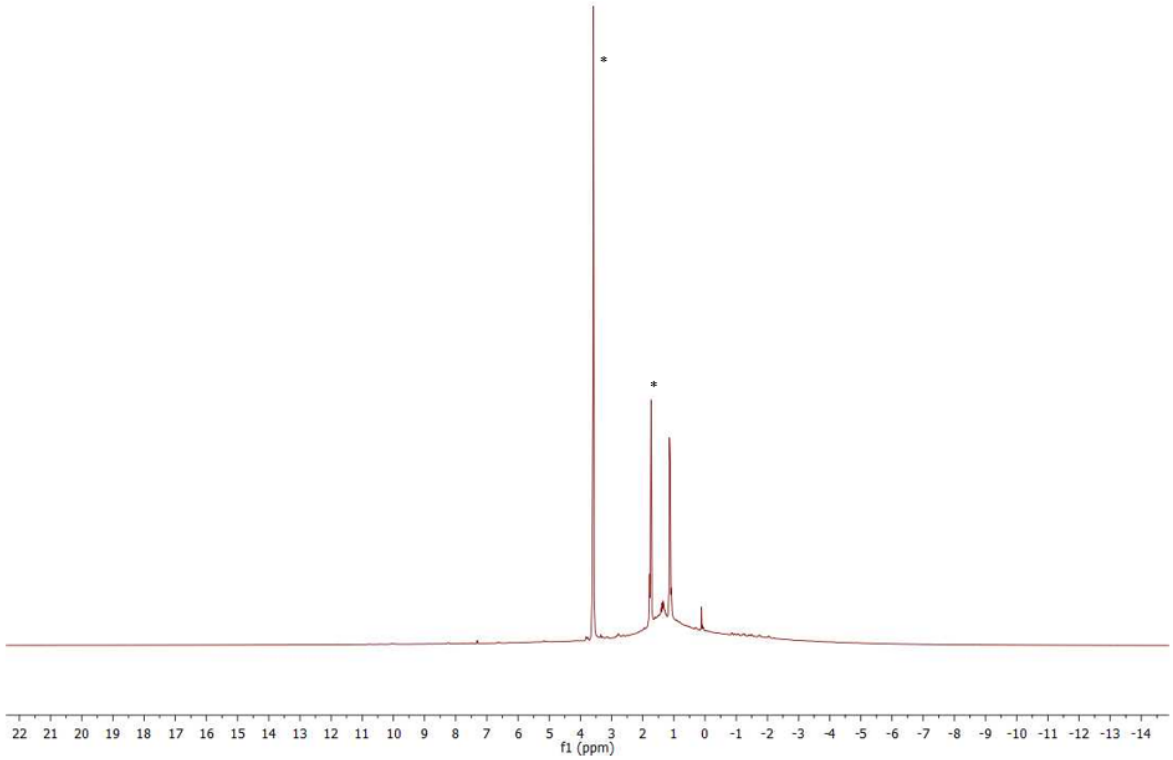

Figure S343. ^{1}H NMR spectrum of the white powder obtained by evaporation after reaction between **1** and CO_2 (excess) in THF-d_8. Solvent residual peaks are indicated with *

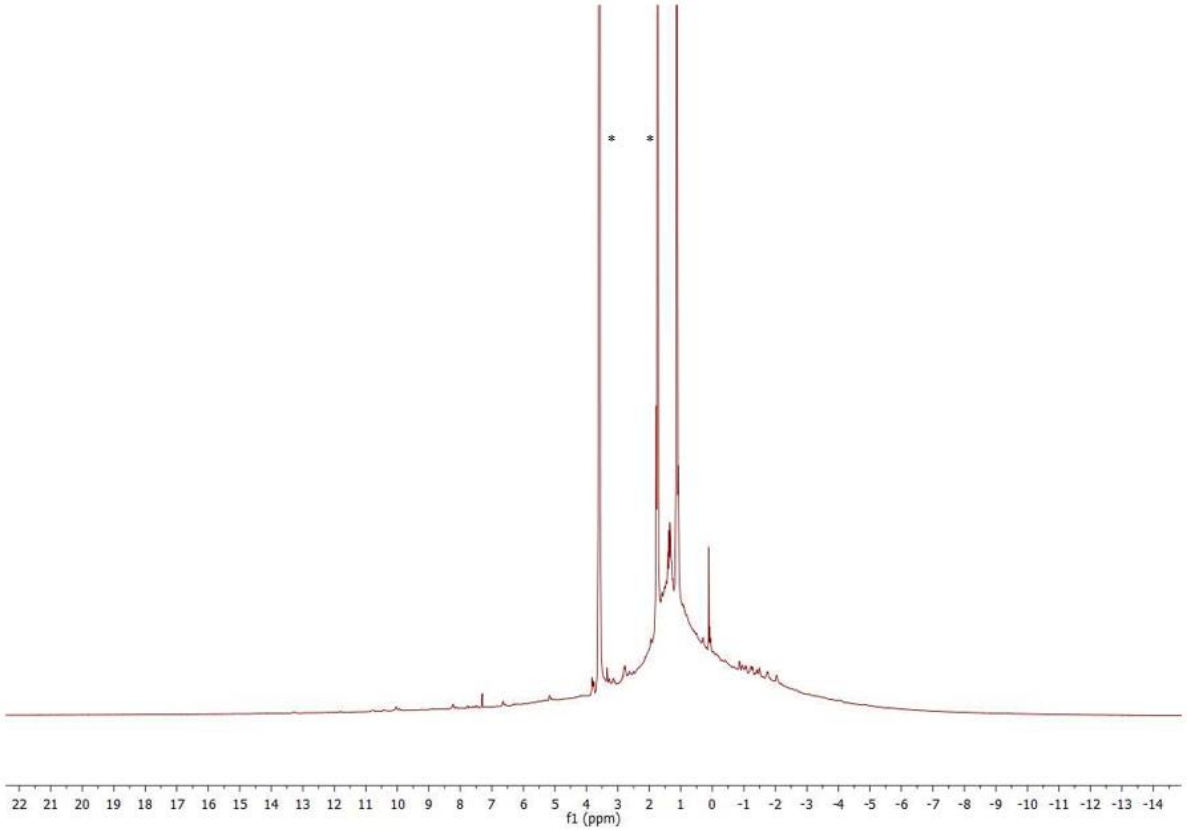

Figure S344. ^{1}H NMR spectrum of the white powder obtained by evaporation after reaction between **1** and CO_2 (excess) in THF-d_8. Solvent residual peaks are indicated with *

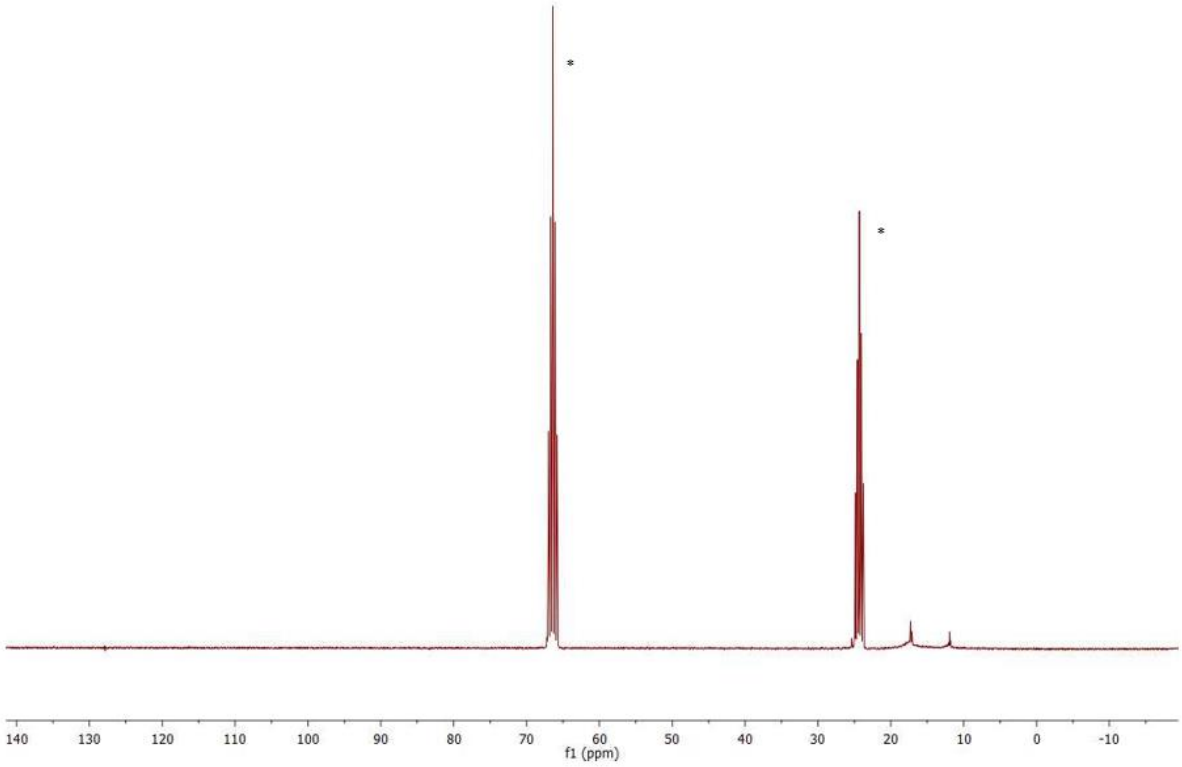

Figure S345. ^{13}C NMR spectrum of the white powder obtained by evaporation after reaction between **1** and CO_2 (excess) in THF-d_8. Solvent residual peaks are indicated with *

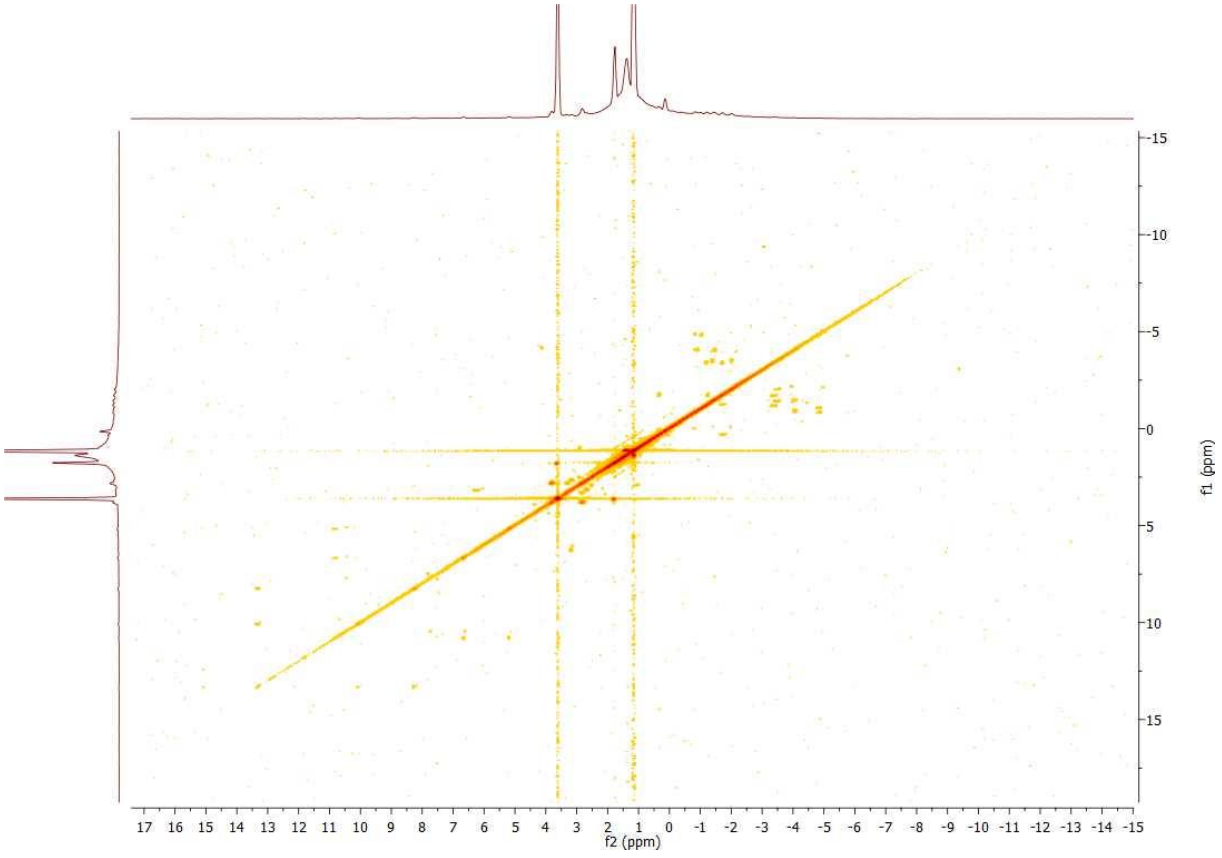

Figure S346. ^{1}H-^{1}H COSY spectrum of the white powder obtained by evaporation after reaction between **1** and CO_2 (excess) in THF-d_8.

Institut Polytechnique de Paris
91120 Palaiseau, France

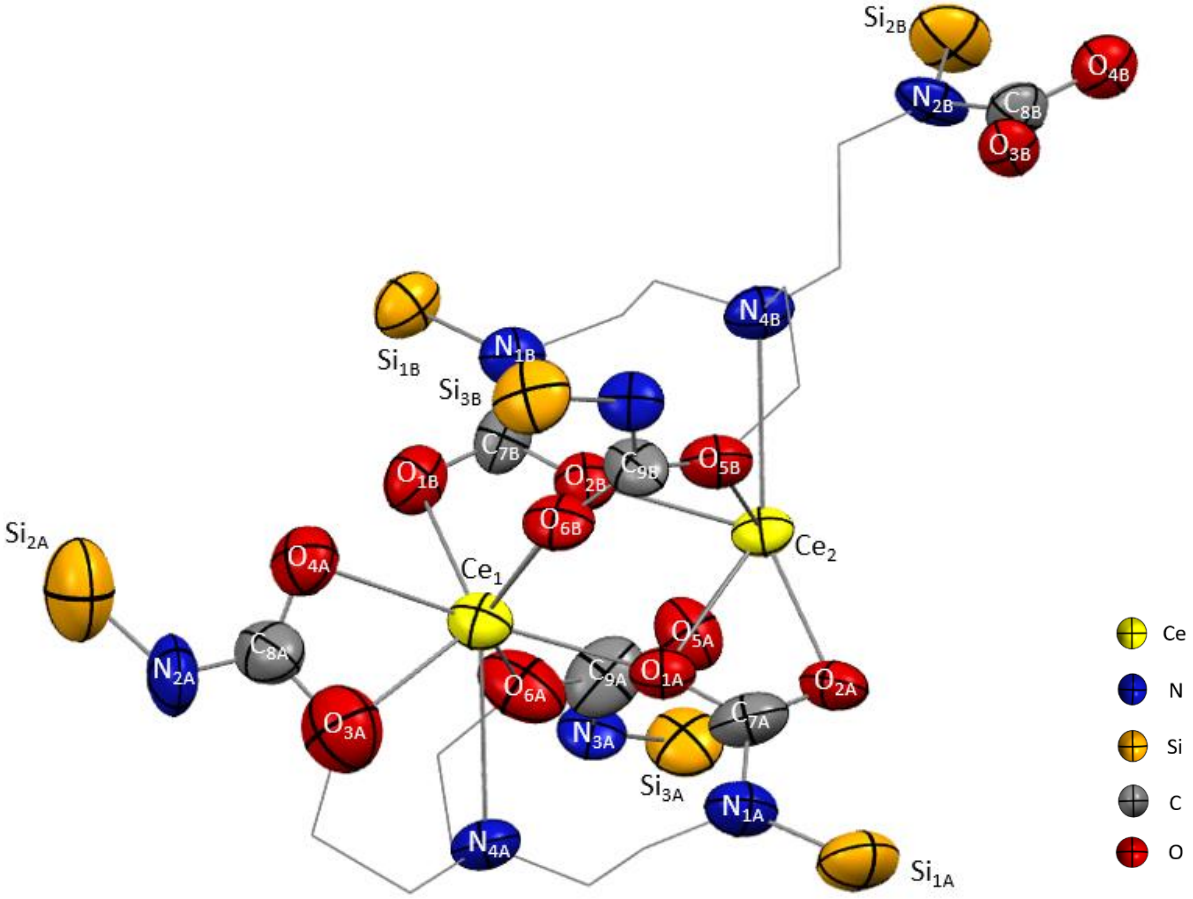

Figure S347. Simplified structure for **1-CO_2**. Displacement ellipsoids are represented at 50% probability. Hydrogen atoms and isopropyl groups have been omitted for clarity, carbons from TREN moiety have been represented in wireframe style. For the full structure, see **Figure S349**)

Bond		Length (Å)	Bonds	Angle (°)
Ce_1-O_{1A}		2.458(12)	O_{2A}-C_{8A}-O_{4A}	115.7(19)
Ce_1-O_{3A}		2.454(16)	O_{1B}-C_{7B}-O_{2B}	120.3(15)
Ce_1-O_{4A}		2.579(12)	O_{1A}-C_{7A}-O_{2A}	124.8(16)
Ce_1-O_{6A}		2.517(12)	O_{6B}-C_{9B}-O_{5B}	126.7(13)
Ce_1-O_{1B}		2.529(11)	O_{3B}-C_{8B}-O_{4B}	120.3(13)
Ce_1-O_{2B}		2.593(10)	O_{6A}-C_{9A}-O_{5A}	129.0(16)
Ce_2-O_{2A}		2.499(11)		
Ce_2-O_{5A}		2.404(11)	O_{3A}-Ce_1-O_{4A}	52.7(5)
Ce_2-O_{2B}		2.395(10)	O_{2A}-Ce_2-O_{1A}	52.5(4)
Ce_2-O_{4B}		2.479(9)		
Ce_2-O_{5B}		2.573(10)	Ce_1-O_{1A}-Ce_2	106.6(4)
Ce_1-N_{4A}		2.925(12)	Ce_1-O_{2B}-Ce_2	106.9(4)
Ce_2-N_{4B}		2.863(11)		
Ce_1-Ce_2		4.0081(13)		
	C_{8A}-O_{3A}	1.37(2)		
	C_{8A}-O_{4A}	1.27(2)		
κ^2	C_{8B}-O_{3B}	1.241(15)	**Bond**	**Mean value (Å)**
	C_{8B}-O_{4B}	1.324(18)	N-Si	1.727(35)
			N-C_{CO2}	1.37(5)
	C_{9A}-O_{5A}	1.38(2)		
μ-κ^2(O,O')	C_{9A}-O_{6A}	1.25(2)		
	C_{9B}-O_{5B}	1.273(18)		
	C_{9B}-O_{6B}	1.248(18)		
	C_{7A}-O_{1A}	1.30(2)		
μ-κ(O):κ^2(O,O')	C_{7A}-O_{2A}	1.22(2)		
	C_{7B}-O_{1B}	1.270(19)		
	C_{7B}-O_{2B}	1.288(18)		

Table S63. Selected bond lengths and angles for **1-CO_2**. For the different CO_2 binding mode discrimination, see **Figure S348**

Institut Polytechnique de Paris
91120 Palaiseau, France

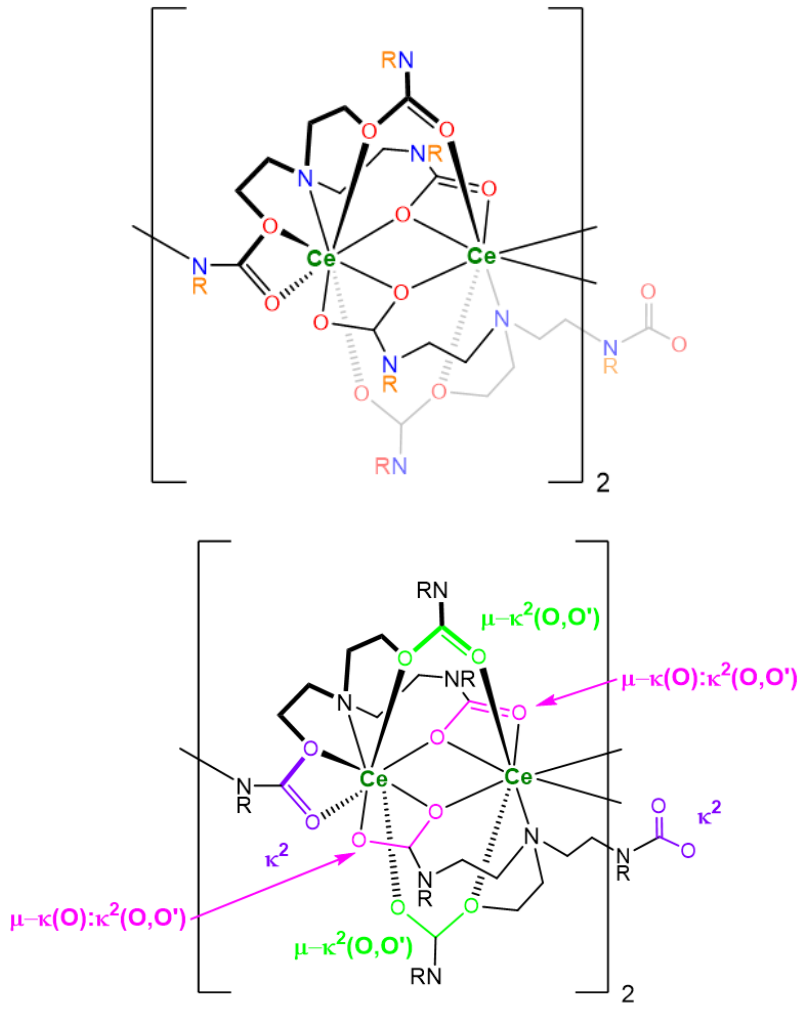

Figure S348. Naming of the different CO_2 binding modes in **1-CO_2**

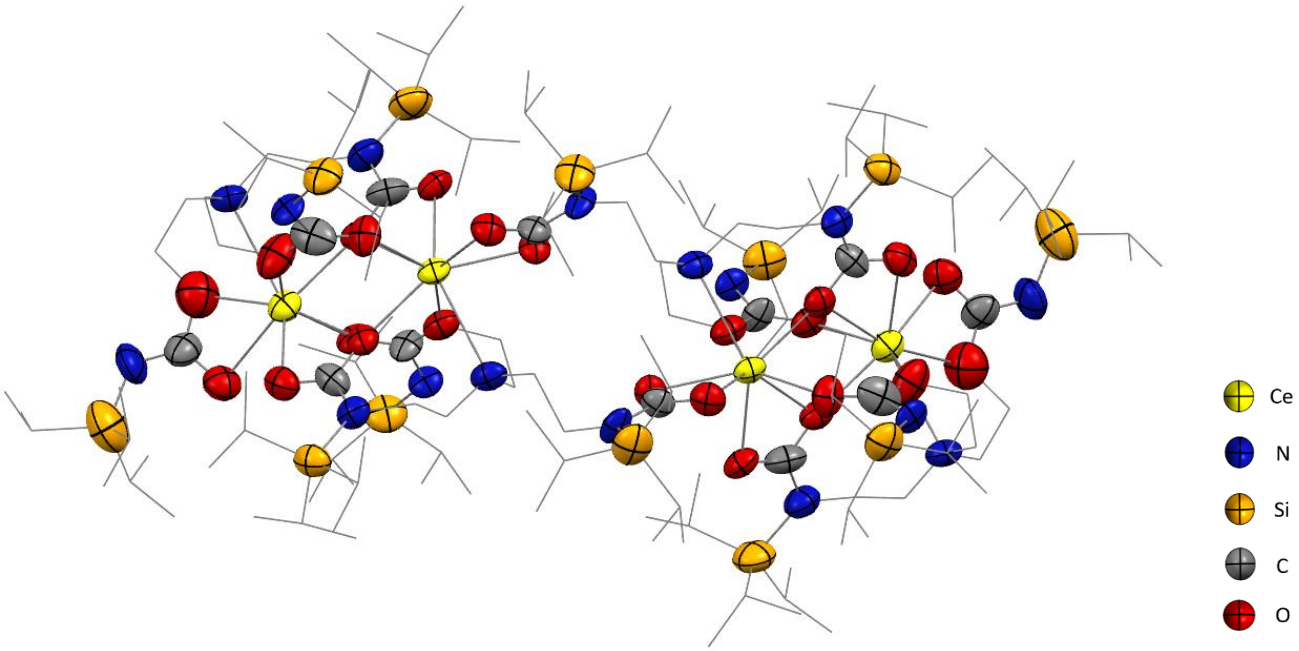

Figure S349. Structure of **1-CO_2**. Displacement ellipsoids are represented at 50% probability. Hydrogen atoms have been omitted for clarity, and isopropyl groups have been represented in wireframe style

II. UV-visible spectroscopy data for Part IV

Institut Polytechnique de Paris
91120 Palaiseau, France

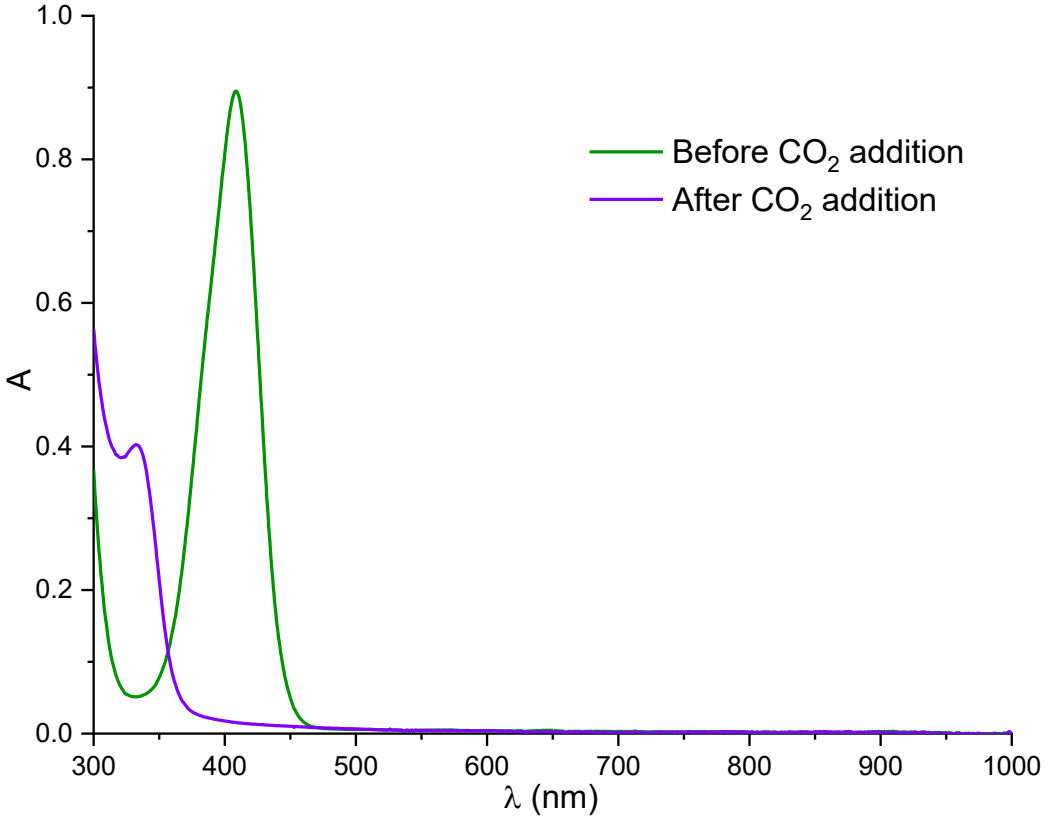

Figure S350. UV-visible spectrum before (green) and after (purple) addition of CO_2 to a solution of **1** in THF (about 1.5 mmol.L^{-1})

Institut Polytechnique de Paris
91120 Palaiseau, France

Institut Polytechnique de Paris
91120 Palaiseau, France

Experimental section for Chapter IV

Part III

Institut Polytechnique de Paris
91120 Palaiseau, France

I. Spectral data for Part III

a) General procedure

A solution of **1** (10 mg, 13µmol) in toluene-d_8 was degassed thrice using freeze-pump-thaw technique and cooled down to -79 °C. O_2 (1.2 bar absolute, about 3 eq.) was added at -79 °C. The reaction medium was carefully homogenised, and stored at -79 °C for 24 h. ^{1}H NMR spectrum was recorded at -20 °C and the VT NMR presented in **Figure S352** was recorded.

XRD suitable crystals were grown from a solution of **1** in pentane under excess O_2 atmosphere stored at -79 °C for 5 days in a J. Young NMR tube.

b) VT NMR of bridging complex

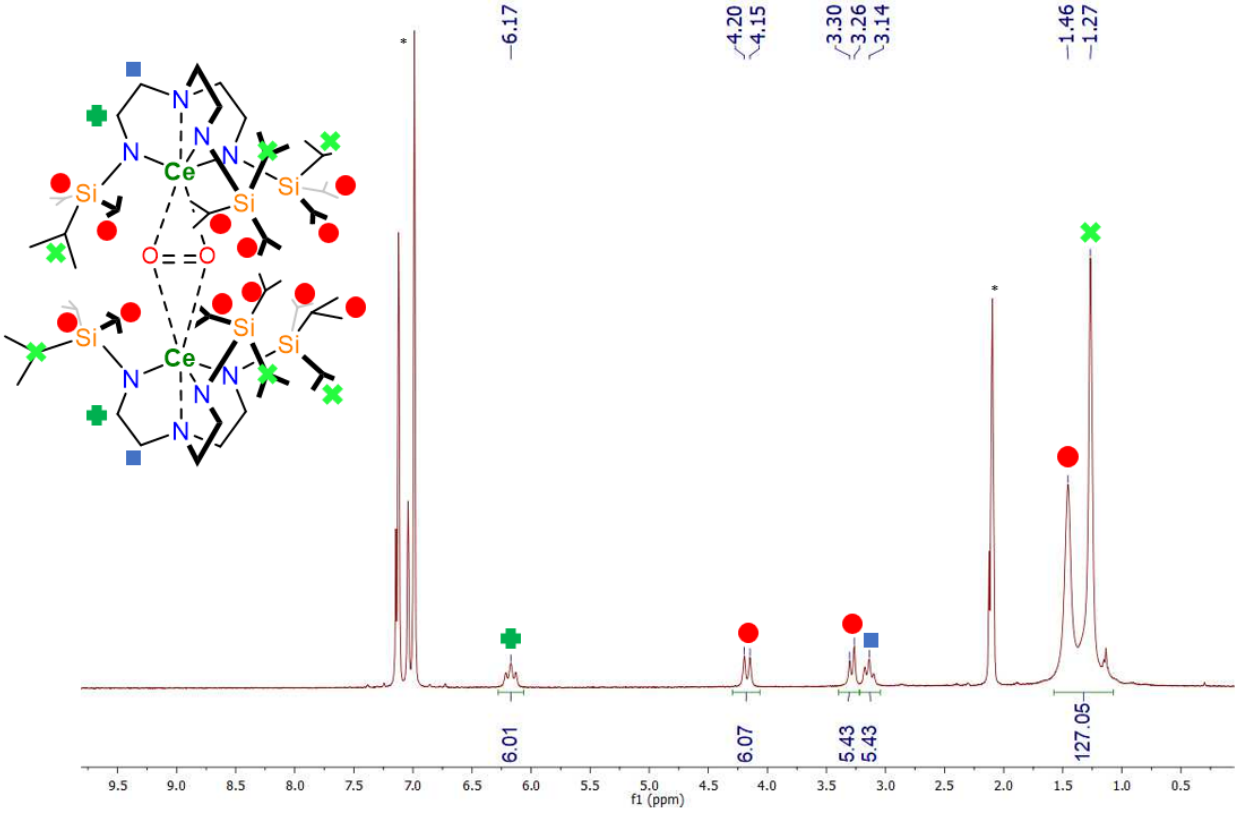

Figure S351. ^{1}H NMR of *in situ* **2-O₂** in toluene-d_8 at -20 °C. Green crosses are related to TIPS moiety pointing out from the coordination sphere of the complex, and red circle for the one closer to the reduced dioxygen moiety. Solvent residual peaks are indicated with *

^{1}H NMR (300 MHz, Toluene-d_8) δ 6.17 (s, J = 12.9 Hz, 6H), 4.17 (d, J = 14.7 Hz, 6H), 3.28 (d, J = 11.8 Hz, 6H), 3.14 (s, J = 10.7 Hz, 6H), 1.05-1.60 (2 × s, 126H)

Institut Polytechnique de Paris
91120 Palaiseau, France

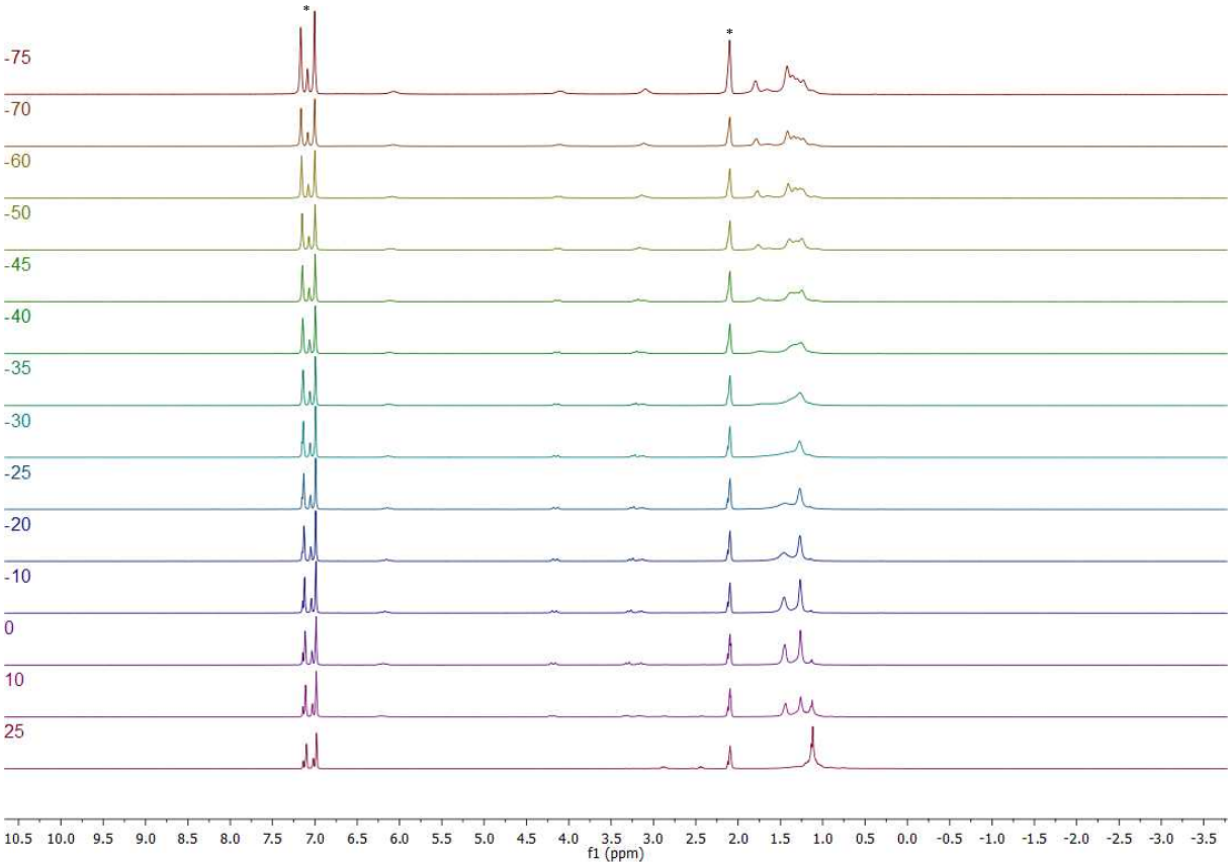

Figure S352. ^{1}H VT NMR of in situ generated **2-O$_2$** complex in toluene-d$_8$ from -75°C to 25 °C. Solvent residual peaks are indicated with *

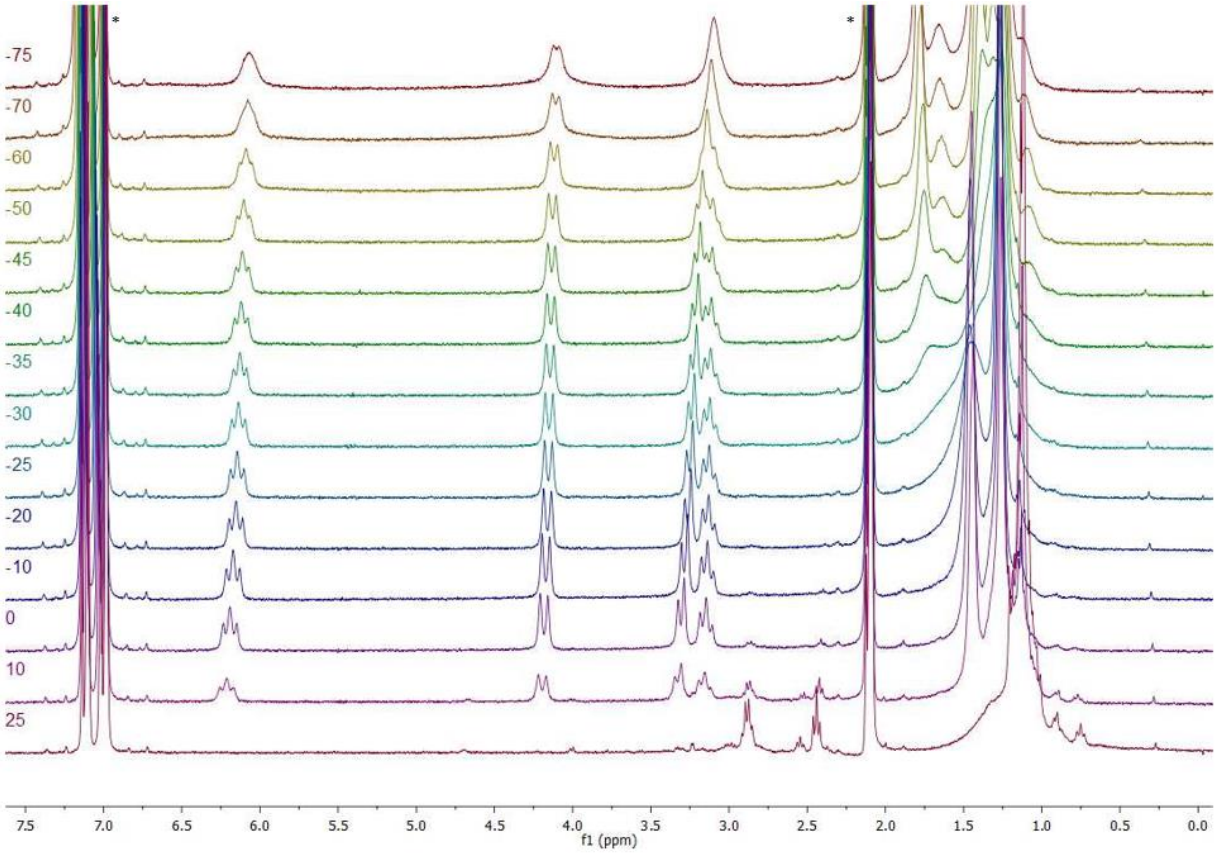

Figure S353. ^{1}H VT NMR of in situ generated **2-O$_2$** complex in toluene-d$_8$ from -75°C to 25 °C. Zoom between 0.0 and 7.5 ppm. Solvent residual peaks are indicated with *

Institut Polytechnique de Paris
91120 Palaiseau, France

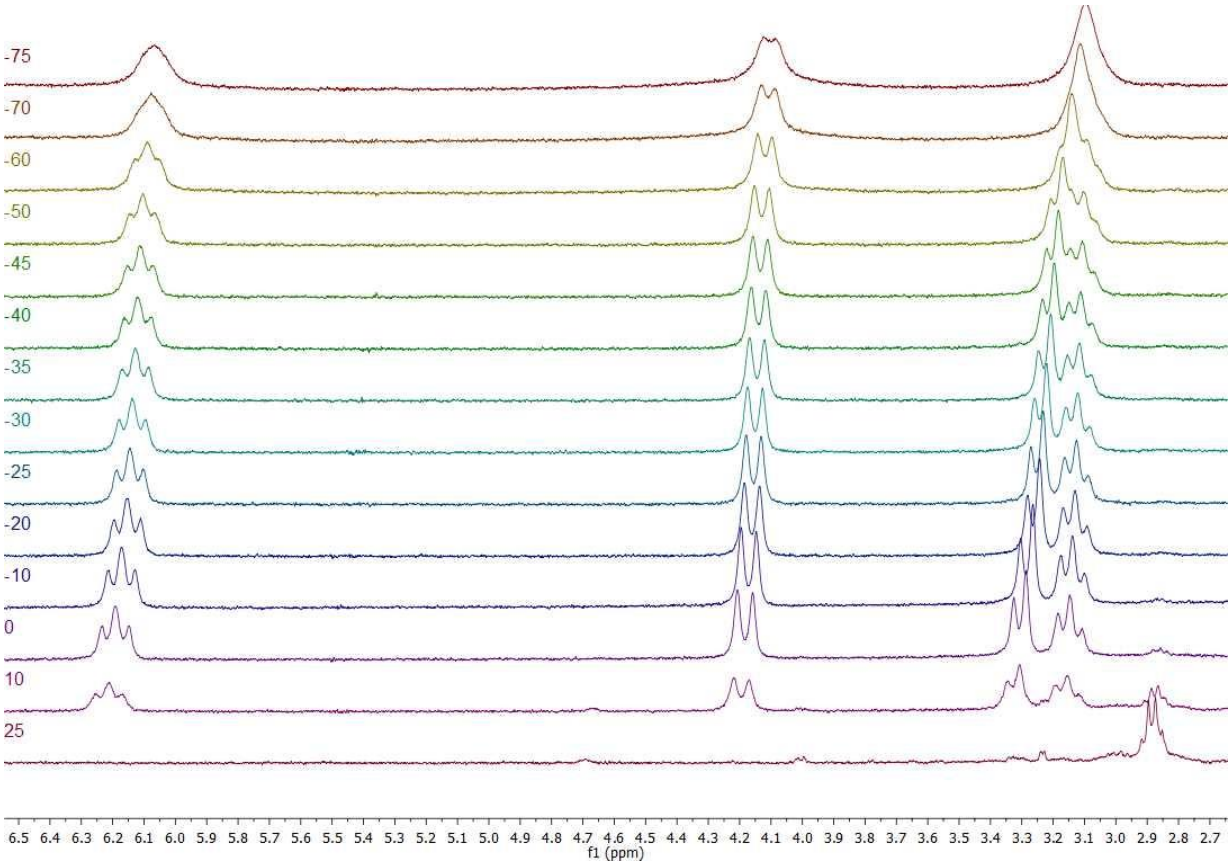

Figure S354. ^{1}H VT NMR of in situ generated **2-O$_2$** complex in toluene-d$_8$ from -75°C to 25 °C. Zoom between 2.7 and 6.5 ppm

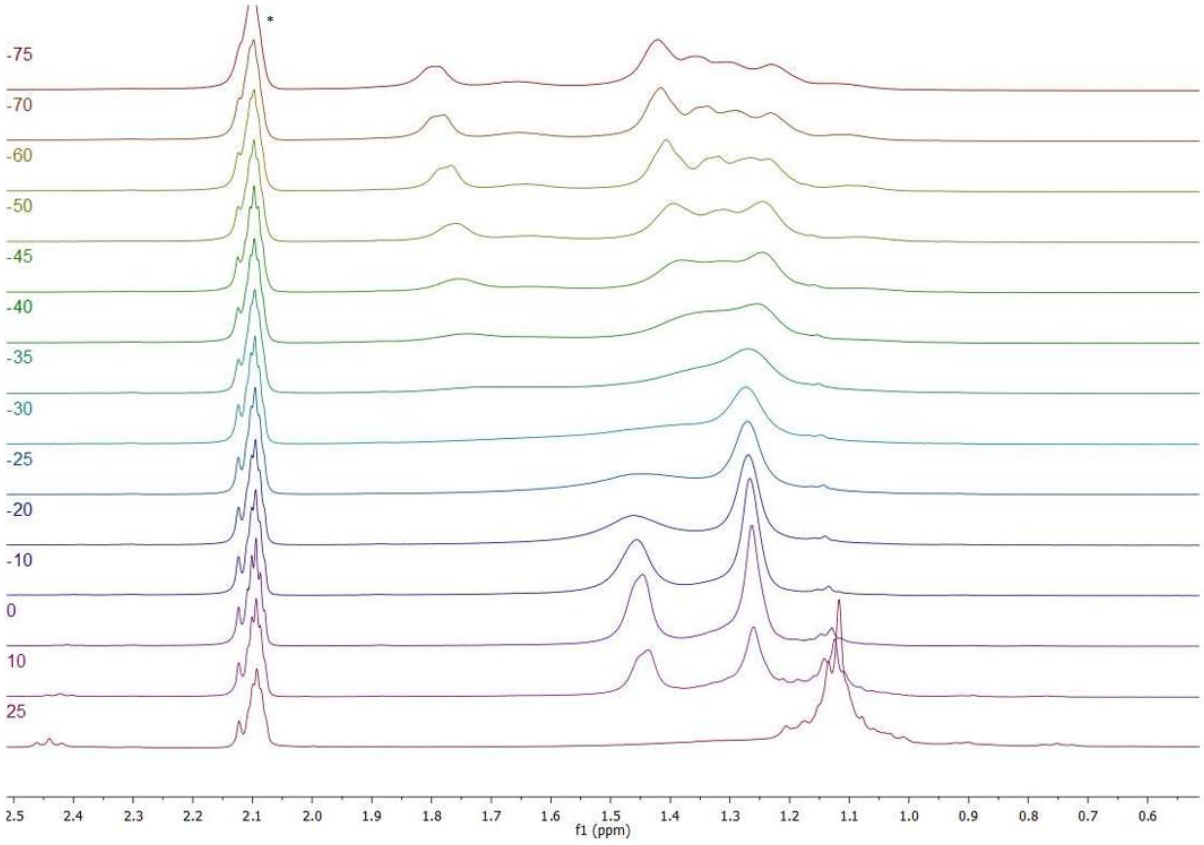

Figure S355. ^{1}H VT NMR of in situ generated **2-O$_2$** complex in toluene-d$_8$ from -75°C to 25 °C. Zoom between 0.5 and 2.5 ppm. Solvent residual peak is indicated with *

Institut Polytechnique de Paris
91120 Palaiseau, France

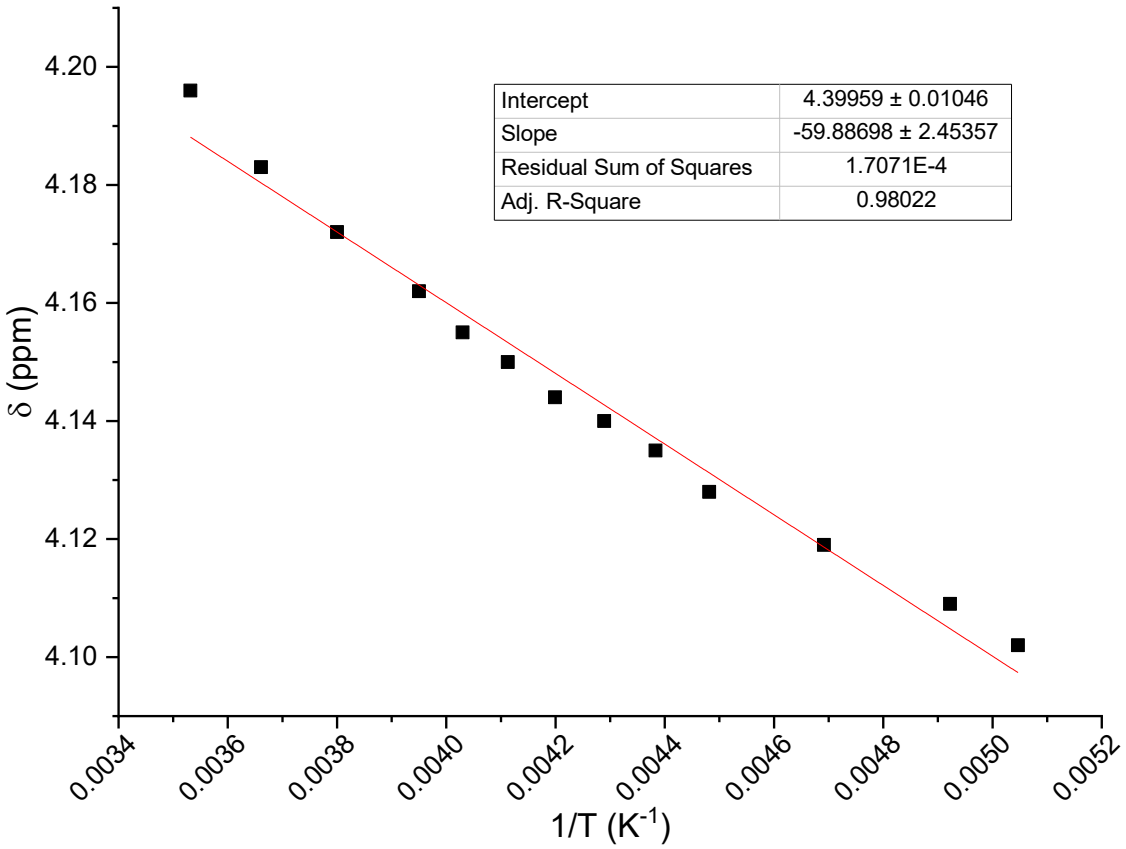

Figure S356. Evolution of the chemical shift of the peak around 4.15 ppm in ^{1}H NMR of complex **2-O₂** as a function of 1/T.

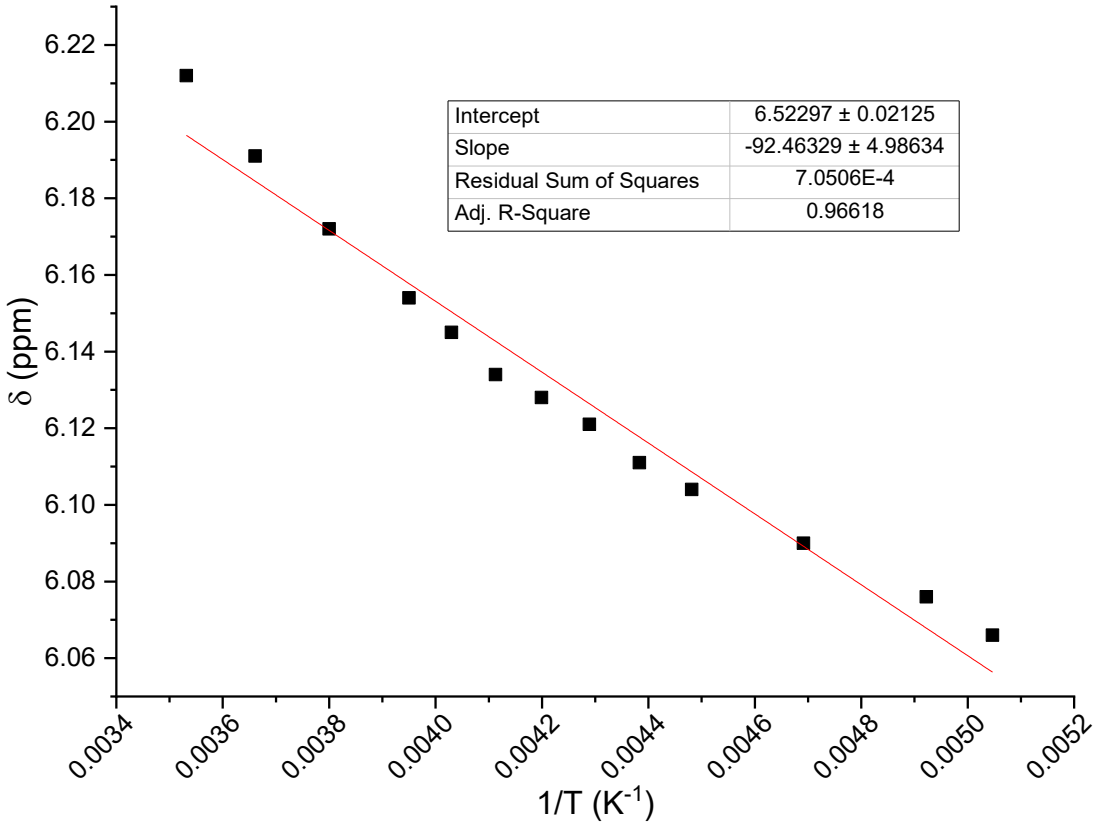

Figure S357. Evolution of the chemical shift of the peak around 6.15 ppm in ^{1}H NMR of complex **2-O₂** as a function of 1/T

c) Trapping attempts of the reduced dioxygen species

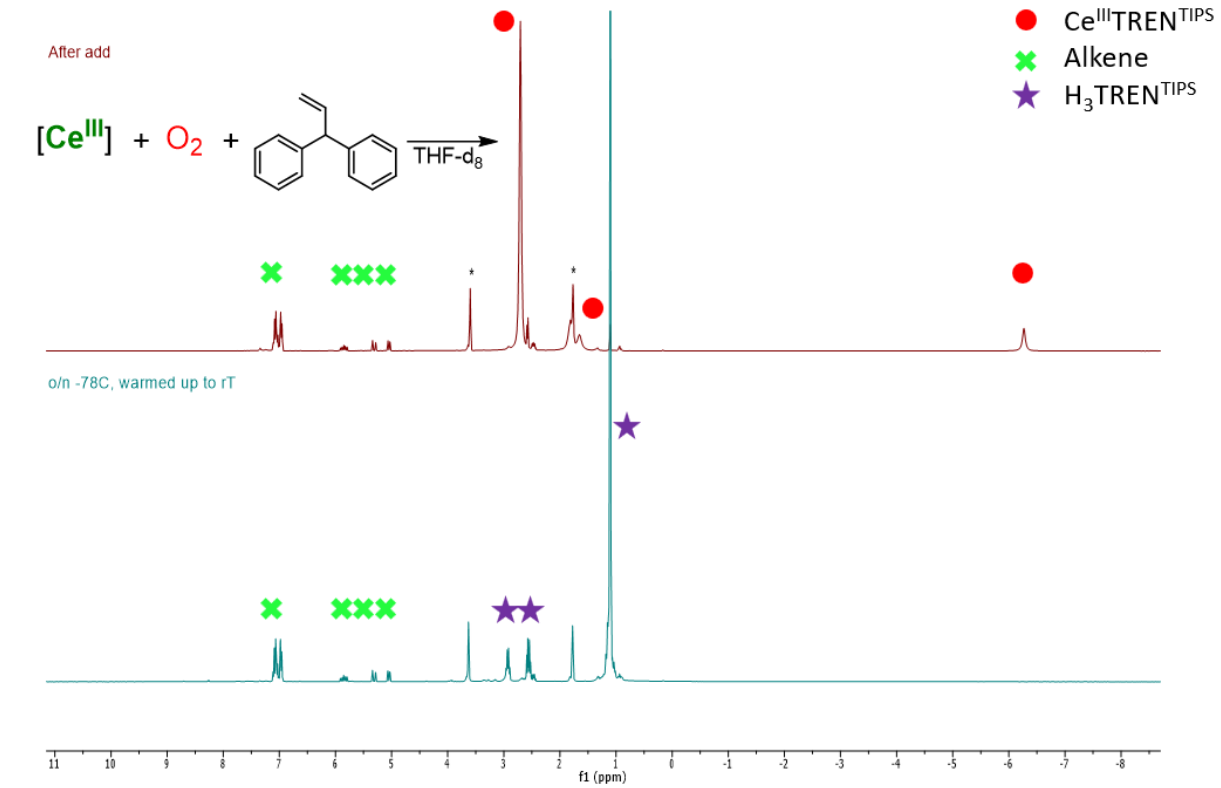

Figure S358. ^{1}H NMR spectrum of reaction of **1** with O_2 in the presence of 1,1'-(2-Propenylidene)bis[benzene] in THF-d_8 before (top) and after addition of O_2 and warming up to room temperature (bottom). Solvent residual peaks are indicated with *

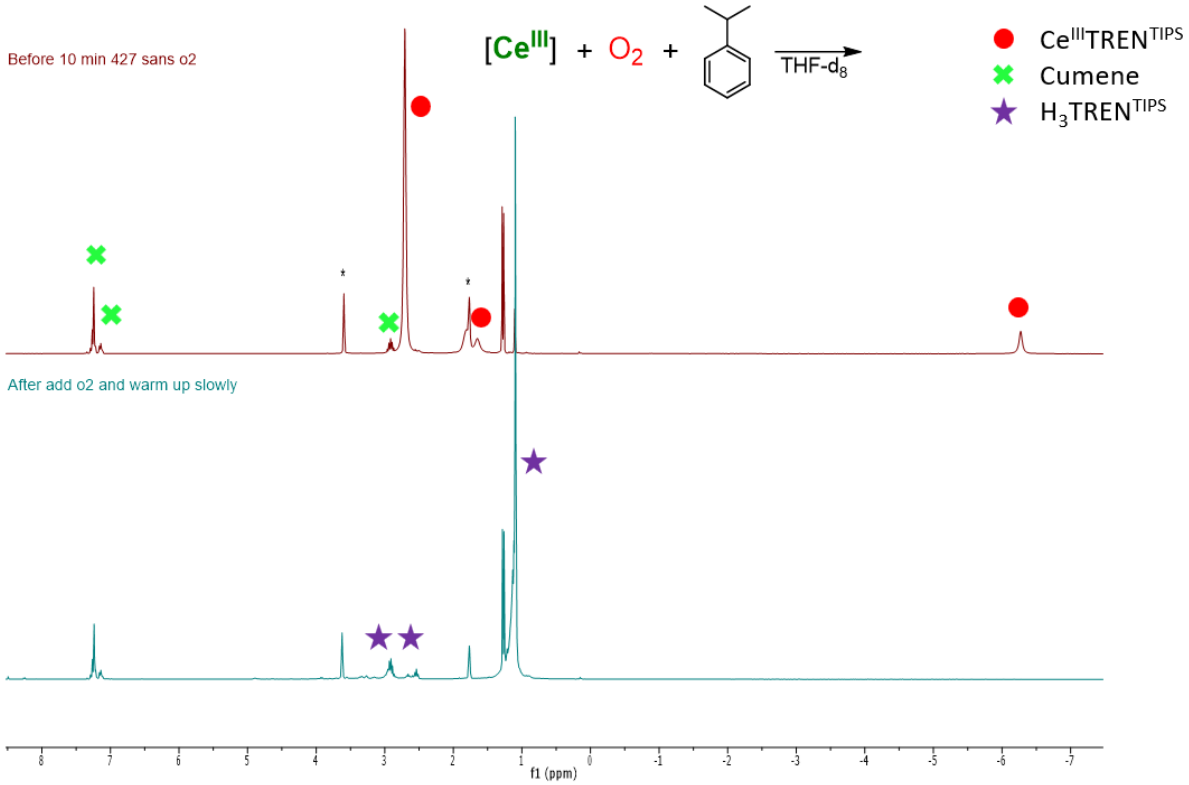

Figure S359. ^{1}H NMR spectrum of reaction of **1** with O_2 in the presence of cumene in THF-d_8 before (top) and after addition of O_2 and warming up to room temperature (bottom). Solvent residual peaks are indicated with *

Institut Polytechnique de Paris
91120 Palaiseau, France

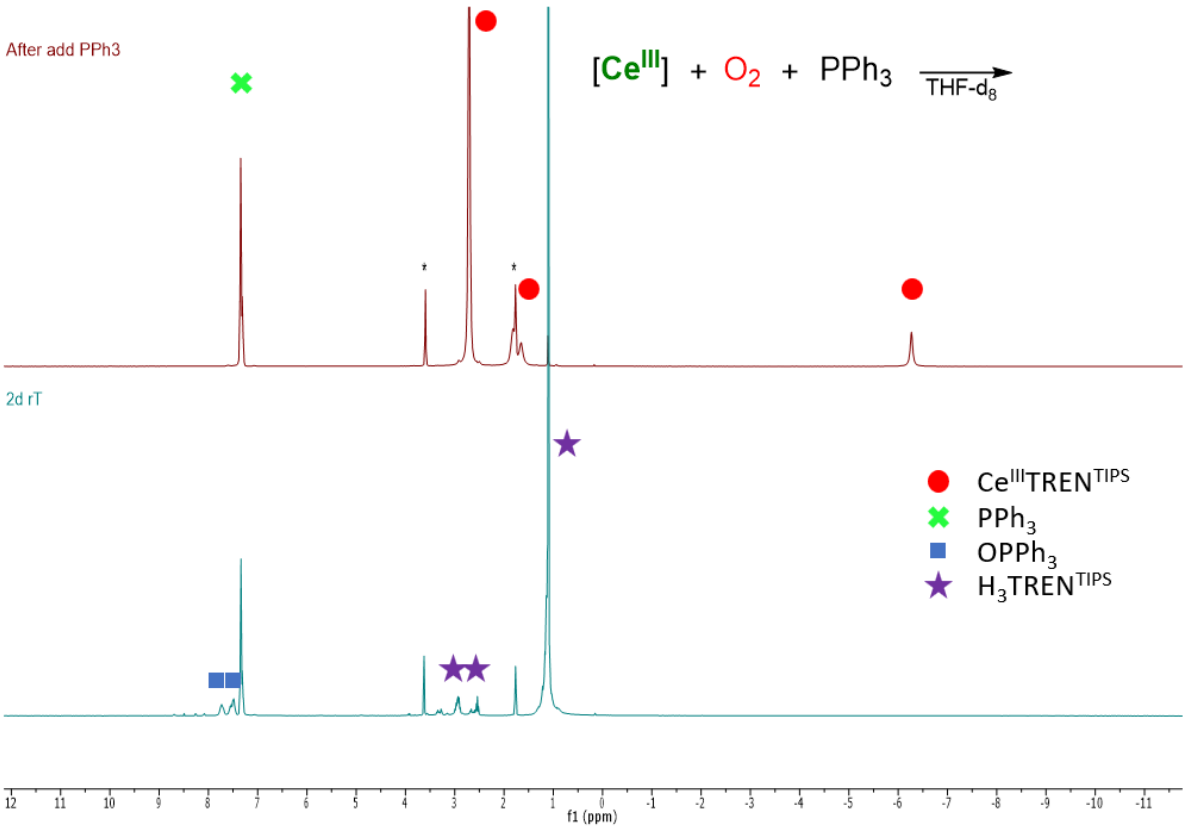

Figure S360. ^{1}H NMR spectrum of reaction of **1** with O_2 in the presence of triphenylphosphine in THF-d_8 before (top) and after addition of O_2 and warming up to room temperature (bottom). Solvent residual peaks are indicated with *

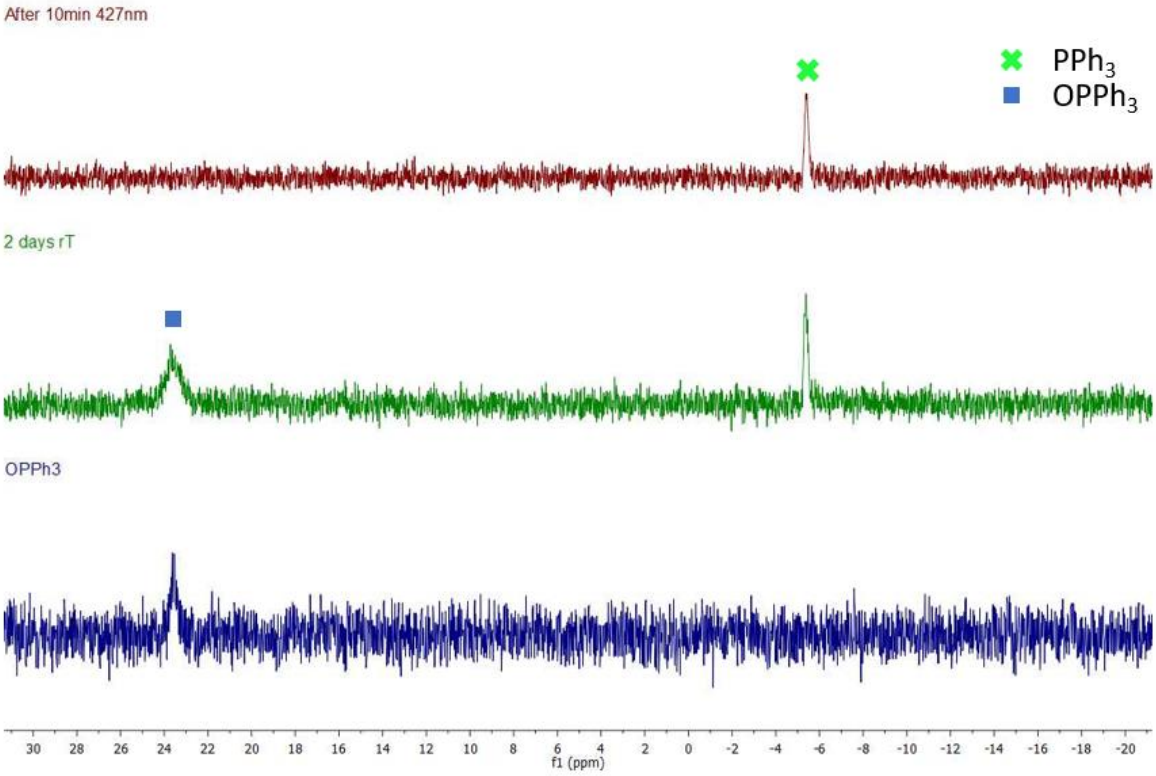

Figure S361. ^{31}P NMR of the reaction medium before (top) and after O_2 addition to a solution of **1** and PPh_3 in THF-d_8, warming up to room temperature, and 2 days of rest. ^{31}P NMR of $OPPh_3$ (bottom) in THF-d_8 is given for reference

Institut Polytechnique de Paris
91120 Palaiseau, France

II. Crystal structure data for Part III

Identification code	**2-O_2**
Empirical formula	$C_{66}H_{150}Ce_2N_8O_2Si_6$
Formula weight	1536.71
Temperature/K	150
Crystal system	Monoclinic
Space group	Cc
a/Å	24.9295(10)
b/Å	15.6869(4)
c/Å	25.2077(10)
α/°	90
β/°	115.720(3)
γ/°	90
Volume/Å^3	8881.2(6)
Z	4
ρ_{calc} g/cm^3	1.149
μ/mm^{-1}	1.132
F(000)	3272.0
Radiation	Mo Kα (λ = 0.71073)
2Θ range for data collection/°	5.194 to 50.054
Index ranges	-28 ≤ h ≤ 29, -18 ≤ k ≤ 18, -29 ≤ l ≤ 29
Reflections collected	32186
Independent reflections	14463 [R_{int} = 0.1088, R_{sigma} = 0.1881]
Data/restraints/parameters	14463/139/780
Goodness-of-fit on F2	0.976
Final R indexes [I>=2σ (I)]	R_1 = 0.1063, wR_2 = 0.2389
Final R indexes [all data]	R_1 = 0.1611, wR_2 = 0.2654
Largest diff. peak/hole / e Å^{-3}	1.52/-1.03
Flack parameter	0.10(4)

Table S64. Crystal data and structure refinement for **2-O_2**

Institut Polytechnique de Paris
91120 Palaiseau, France

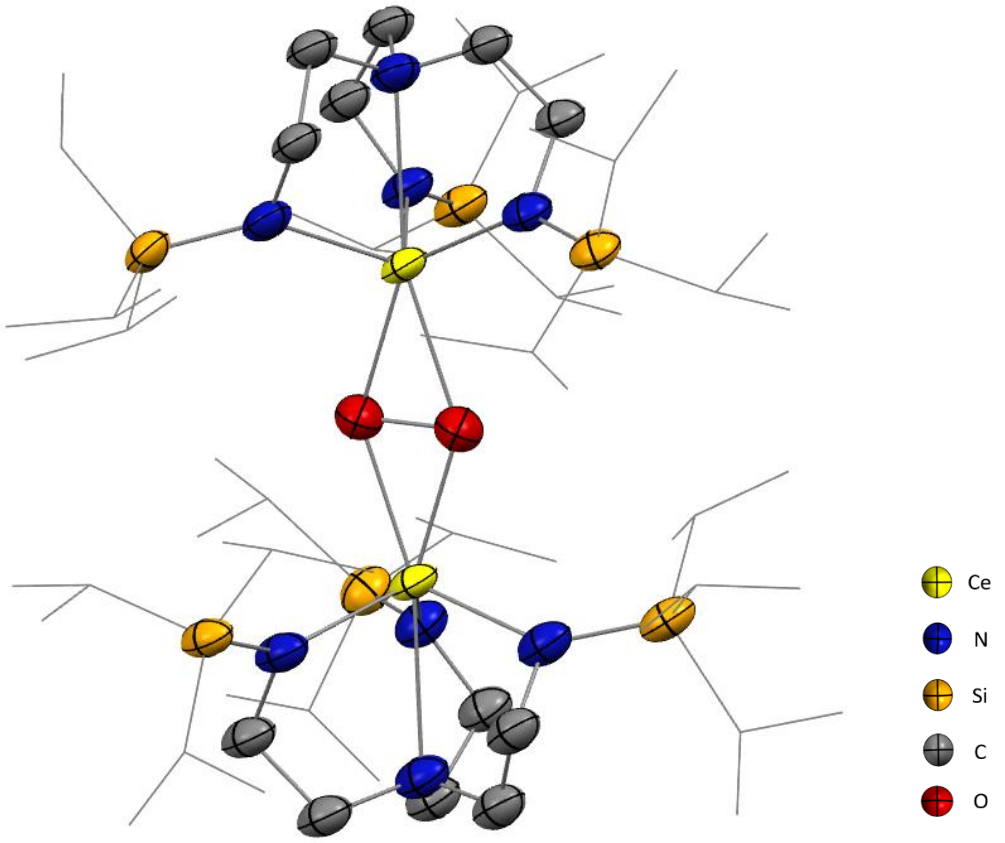

Figure S362. Structure of **2-O₂**. Displacement ellipsoids are represented at 50% probability. Hydrogen atoms have been omitted for clarity, and isopropyl groups have been represented in wireframe style. The molecule presents a slight disorder on isopropyl groups, and on dioxygen centre. The disorder was modelled but not plotted for clarity.

Bond	Length (Å)
Ce_1-O_1	2.43(4)
Ce_1-O_2	2.31(4)
Ce_1-O_3	2.42(4)
Ce_1-O_4	2.31(4)
Ce_2-O_1	2.30(4)
Ce_2-O_2	2.44(4)
Ce_2-O_3	2.32(4)
Ce_2-O_4	2.42(4)
O_1-O_2	1.50(3)
O_3-O_4	1.49(3)
Ce_1-N_{4A}	2.72(2)
Ce_2-N_{4B}	2.75(2)

Bonds	Angle (°)
C_1-N_1-Ce	108.7
C_3-N_2-Ce_1	108.0
C_5-N_3-Ce_1	107.9
Ce_1-$Cent_N$-N_{4A}	178.1
Ce_2-$Cent_N$-N_{4B}	176.5
O-Ce_1-N_{1A}	109.3(23)
O-Ce_1-N_{2A}	109.7(23)
O-Ce_1-N_{3A}	113.7(22)
O-Ce_2-N_{1B}	112.1(23)
O-Ce_2-N_{2B}	109.5(23)
O-Ce_2-N_{3B}	110.7(22)

Bond	Mean value (Å)
Ce-$N_{equatorial}$	2.27(5)
Ce-N_{plane}	0.828
Ce-$Cent_{O1\text{-}O2}$	2.25
Ce-$Cent_{O3\text{-}O4}$	2.25
Ce-O	2.37(12)
N-Si	1.75(5)

Table S65. Selected bond lengths and angles for **2-O₂**. Absence of A/B labelling indicates a mean of the measured values

Institut Polytechnique de Paris
91120 Palaiseau, France

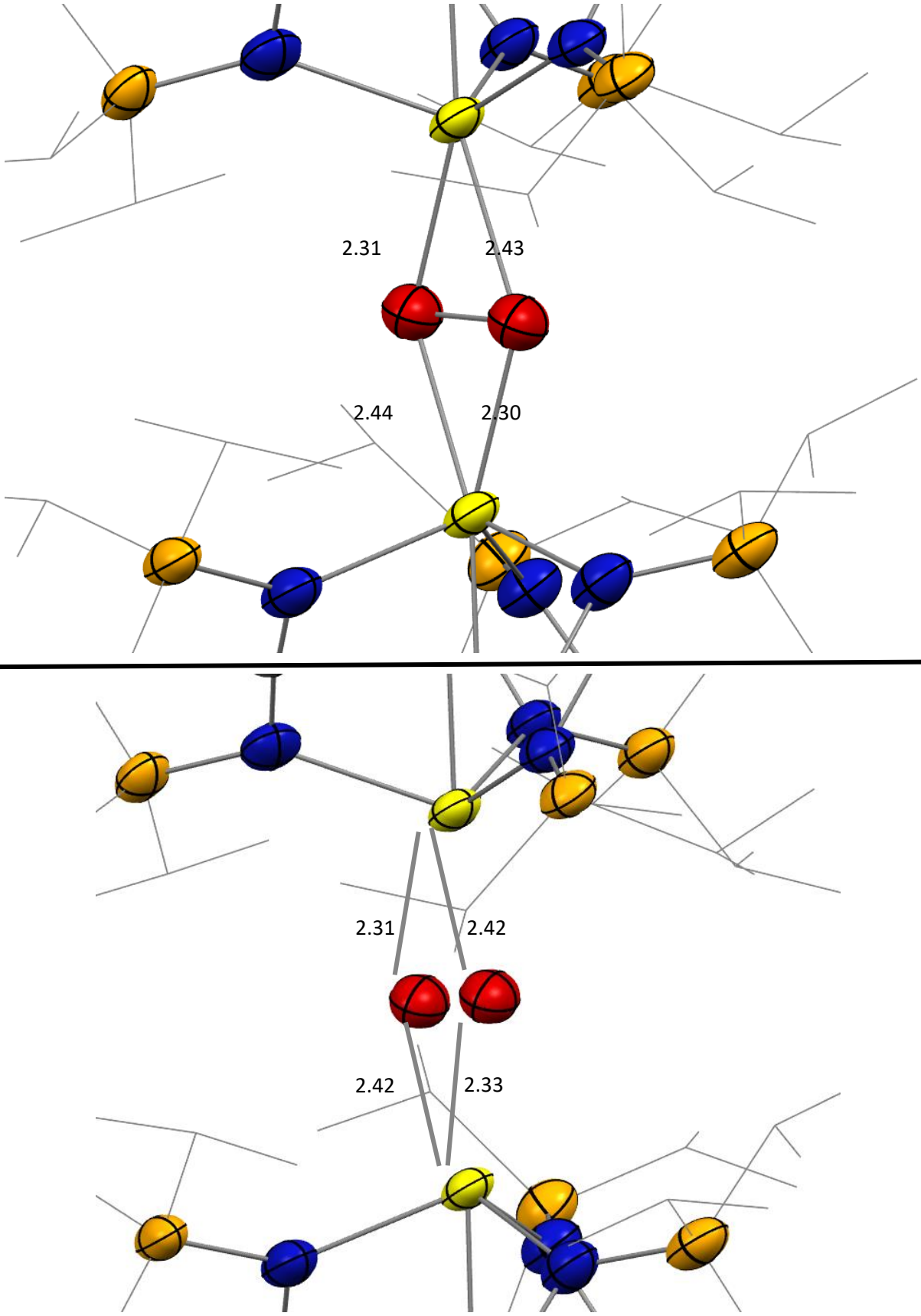

Figure S363. Display of the Ce-O bond distances of the two disordered positions of dioxygen molecule in **2-O_2** (distances are indicated in Å)

Institut Polytechnique de Paris
91120 Palaiseau, France

Appendix

I. Rehm-Weller formalism 464
a) Demonstration of the equation 464
b) Estimation of the work function ωf 465
c) Interpretation of the kinetics 465
II. Transient Absorption Spectroscopy 466
III. Time-Correlated Single Photon Counting 467

Institut Polytechnique de Paris
91120 Palaiseau, France

I. Rehm-Weller formalism

a) Demonstration of the equation

All explanations given below are based on the work of Chibisov, Braslavsky, Kavarnos, and Rehm-Weller.[1-4]

Let it be a general reaction involving an electron donor (D) and an electron acceptor (A):

$$D + A \rightarrow D^{\cdot+} + A^{\cdot-}$$

In the framework of the Koopmans' theorem,[696] the free energy needed to transfer one electron between the donor and acceptor is

$$\Delta G = IP_D - EA_A$$

Where IP_D is the ionization potential of D and EA_A is the electron affinity of A.

If the donor is excited using light irradiation with an energy $E_{0\rightarrow0}$, the ionization potential of D is decreased by the amount of energy absorbed ($IP_D^* = IP_D - E_{0\rightarrow0}$), and the free enthalpy of the reaction with an excited donor D^* is:

$$\Delta G^* = IP_D - E_{0\rightarrow0} - EA_A$$

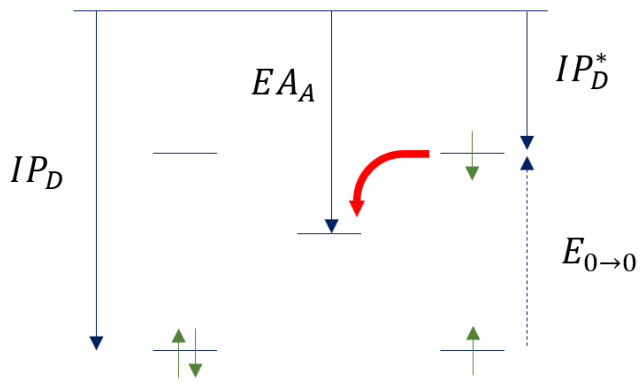

Figure S364. Adapted from Kavarnos[695].

So far, the reaction was considered to occur in the gas phase. In a dielectric medium with a dielectric constant ε, the solvated radical-ion pair is separated by a distance a, leading to a Coloumbic interaction between the two species:

$$\Delta G^* = IP_D - E_{0\rightarrow0} - EA_A - \frac{e^2}{\varepsilon a}$$

Finally, solvation-free enthalpies of the two radicals have to be considered:

$$\Delta G^* = IP_D - E_{0\rightarrow0} - EA_A - \frac{e^2}{\varepsilon a} + \Delta G(A^{\cdot-}) + \Delta G(D^{\cdot+})$$

There is a linear relationship between IP_D and $E_{1/2}(D/D^{\cdot+})$, and EA_A and $E_{1/2}(A^{\cdot-}/A)$:

$$IP_D = E_{1/2}(D/D^{\cdot+}) - \Delta G(D^{\cdot+}) + const$$

$$EA_A = E_{1/2}(A^{\cdot-}/A) + \Delta G(A^{\cdot-}) + const$$

Institut Polytechnique de Paris
91120 Palaiseau, France

Leading to the final expression of the free enthalpy of the photochemical electron transfer:

$$\Delta G^* = E_{1/2}(D/D^{\cdot+}) - E_{1/2}(A^{\cdot-}/A) - E_{0\to0} - \frac{e^2}{\varepsilon a}$$

N.B.: according to IUPAC nomenclature, this expression should not be called the Rehm-Weller equation.[694]

Furthermore, the actual reaction taking place is the following:

$$D^* + A \to D^{\cdot+} + A^{\cdot-}$$

And the associated free enthalpy

$$\Delta G^* = E_{1/2}(D^*/D^{\cdot+}) - E_{1/2}(A^{\cdot-}/A) - E_{0\to0} - \frac{e^2}{\varepsilon a}$$

By identifying with equation (1), we finally obtain:

$$E_{1/2}(D^*/D^{\cdot+}) = E_{1/2}(D/D^{\cdot+}) - E_{0\to0} - \frac{e^2}{\varepsilon a}$$

And the work function is defined as $\omega_f = \frac{e^2}{\varepsilon a}$

b) Estimation of the work function ω_f

Considering $\varepsilon = \varepsilon_r \varepsilon_0$ with ε_r being the relative permittivity of the solvent (here THF, $\varepsilon_r = 7.58$)[6] and $\varepsilon_0 = 8.85.10^{-12}\ N.m^2.C^{-2}$, and a being the distance separating the ion-radical pair, it can be assumed that $a \approx 15\ nm$ that is the size of $Ce^{III}TREN^{TIPS}$, **1**. Thus:

$$\omega_f < 0.09\ V$$

c) Interpretation of the kinetics

For an outer sphere electron transfer, the kinetic constant of the redox reaction k_{act} is following the Arrhenius law:

$$k_{act} = A.e^{\frac{-\Delta G^{\ddagger}}{RT}}$$

where $\Delta G^{\ddagger}$ is the free enthalpy of the redox reaction, A a constant, R the gas constant and T the temperature in Kelvin. $\Delta G^{\ddagger}$ is linked to the solvent reorganization energy λ_0 and the free enthalpy change $\Delta G°$:

$$\Delta G^{\ddagger} = \frac{(\lambda_0 + \Delta G°)^2}{4\lambda_0}$$

Assuming the reorganization of solvent around the different chlorobenzene derivatives is similar, the difference between the reduction kinetics of two chlorobenzenes derivatives will be dictated by the relative redox potential of the substrates, therefore to the electron-withdrawing or donating nature of the group in the para position.

II. Transient Absorption Spectroscopy

Transient Absorption Spectroscopy (TAS) is a pump-probe spectroscopic technique used to study non-emissive short-lived species, especially the excited states of molecules. Initially, a fraction of molecules is promoted to an excited state by an excitation pulse (*pump*). After a short delay, a low intensity pulse (*probe*) is sent to the sample.

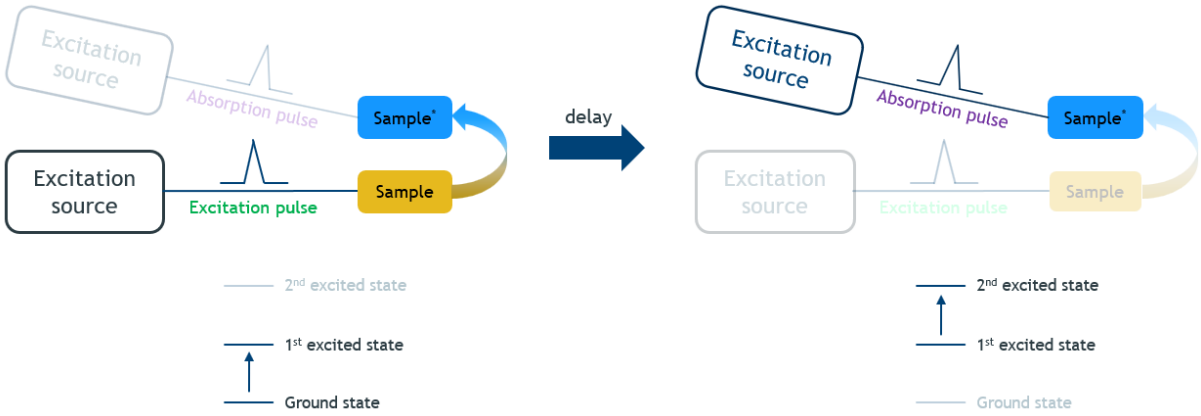

Figure S365. Principle of Transient Absorption Spectroscopy

The difference in absorption between the ground state and excited state affords a graph similar to **Figure S366**, which allows to determine the lifetime of the excited state. In **Figure S366**, the lifetime observed was perfectly identical to the luminescence lifetime associated to $^2D \rightarrow {}^2F$ emission, which showed that no lower non-emissive state (*dark state*) was present. In general, recording a spectrum at several emission wavelengths would allow to measure the absorption spectrum of a species generated by excitation at a designated wavelength (see **Figure S367**).

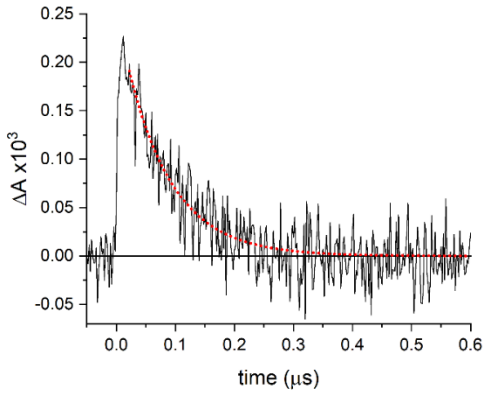

Figure S366. Measurement of the difference in absorption at 530 nm before and after excitation at 355 nm for a solution of **1** in pentane (luminescence correction was applied)

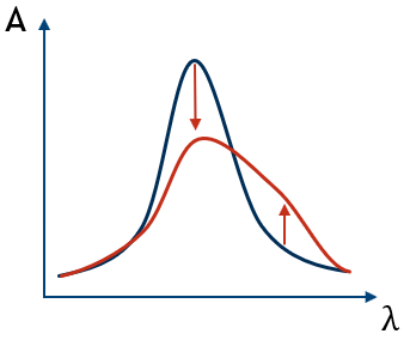

Figure S367. Example of evolution of absorption spectra before (blue) and after (red) absorption of the excitation pulse

Institut Polytechnique de Paris
91120 Palaiseau, France

III. Time-Correlated Single Photon Counting

Time Correlated Single Photon Counting (TCSPC) is a spectroscopic technique used to measure short luminescence lifetimes (10^{-12}-10^{-6} s) from the emission of a very short laser impulsion. During the measurement, the laser emits two impulsions simultaneously : one reference pulse, which starts the timer upon reaching the detector, and a second pulse exciting several molecules of the sample, which will emit a signal after a certain delay (see **Figure S368**). Upon detection of this latter signal, the timer will stop and measure the time difference between the reference and the "sample" pulse.

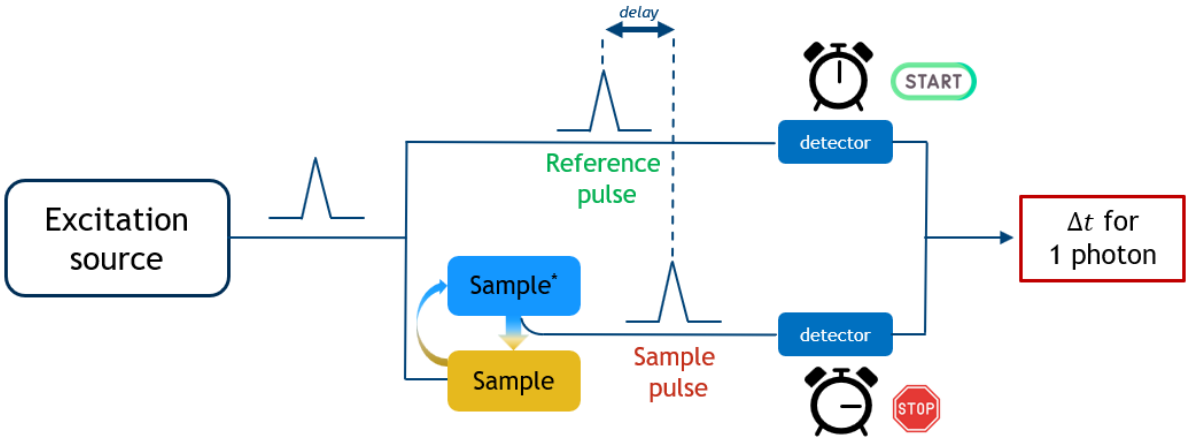

Figure S368. Principle of TCSPC. Adapted from Edinburgh Instruments[7]

As emission of a photon by luminescence is a stochastic process, repeating this procedure many times (typically 10^6) gives a probabilistic representation of the emission process, which follows a first order kinetic (see **Figure S369**Figure S369.) and allows for the determination of the luminescence lifetime τ_{lum} after fitting.

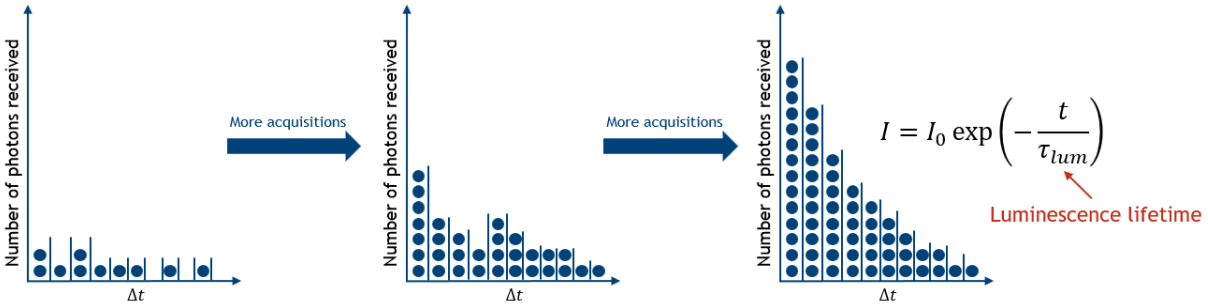

Figure S369. Evolution of the histogram of number of photons received as a function of the time difference between reference and sample pulse

TCSPC is particularly interesting to measure luminescence lifetimes, as it uses low intensity sources (preventing degradation of the molecules and therefore allowing for longer measurements), and does not rely on the intensity of the light emitted (only on the time delay).

IV. Script for EPR fitting

a) Script for data from Bruker spectrometers (DTA and DSC files)

```
                        %%   Adrien COMBOURIEU, April 2024  %%
% https://easyspin.org/easyspin/documentation/

%%   Importing experimental data
clf
clear
clc
[C,spc,param] = eprload(XXX.DTA');    % change the path to the file
B=C/10                                % converts in mT
clc
xlabel('Field (mT)')
ylabel('Intensity')
hold on                 % allows to stack several spectra
plot(B,spc,'DisplayName','off')     % adds a name for each plot, do not remove
                                    DisplayName; here, name is "off"
legend      % plots legend

%%   Definition of the system for the simulation

clf
Sys.g = 2.006
Sys.Nucs = '14N,1H';   %nuclei present
Sys.n =[1 1]          % number of each nucleus
Sys.Abund=[0.996 1]   % abundancy of each nucleus

Sys.A = mt2mhz([1.2;0.4])    % /!\ always in MHz !!!

Sys.lwpp = [0.129 0.1];       % width of the peak
Exp.Range = [min(B) max(B)];    % experimental range of B
Exp.mwFreq = str2double(erase(param.FrequencyMon, ' GHz')) ;   % experimental frequency
of the spectrometer
figure(2);

xlabel('Field (mT)')
ylabel('Intensity')
garlic(Sys,Exp);            % simulation in solution. For solids or anisotropic
compounds, use pepper
hold on
plot(B,spc, 'DisplayName','exp');    % plotting experimental data to compare. Name =
"exp"
legend

%%   Automatic fitting
Sys0 = Sys;

    % Indicate here what you want to vary. Values are the range around
    % value indicated above in "Sys" e.g.    g = 2.006 +/- 0.01 here
Vary.g = 0.01
Vary.A = 0.2
Vary.lwpp = [0.05 0.05]

% Finally, we specify the fitting algorithm and what should be fitted.
FitOpt.Method = 'simplex fcn'; % simplex algorithm, searches for local minimum.
FitOpt.AutoScale = 'maxabs';
```

```
esfit(spc,@garlic,{Sys0,Exp},{Vary},FitOpt);     % Opens the automatic fitting window.
                                                 don't forget to change to pepper if
                                                 needed


                % Don't forget to export the best parameters !


 %%     Printing the optimized simulation alongside experimental data

clf
plot(B,fit1.fit, 'DisplayName','simulation')
xlabel('Field (mT)')
ylabel('Intensity')
hold on
plot(B,spc, 'DisplayName','experimental')
legend


%%     Save in .txt file
data_exp = [B(:) spc(:)];
save('XXX\Exp.txt', 'data_exp', '-ascii');

data_simu = [B(:) fit1.fit(:)];
save('XXX\Simu.txt', 'data_simu', '-ascii');
```

b) Script for data from JEOL spectrometers (txt files without B values)

x_val_0.txt contains the field values not included in the export file from JEOL spectrometer. They can be generated using a Python script file

```
                    %%   Adrien COMBOURIEU, April 2024  %%
% https://easyspin.org/easyspin/documentation/

%%   Importing experimental data
clf
clear
clc
B = textread("XXX\x_val_0.txt")    % change the path to the file
spc = textread("XXX\index_0.txt")
clc
xlabel('Field (mT)')
ylabel('Intensity')
hold on                 % allows to stack several spectra
plot(B,spc,'DisplayName','off')    % adds a name for each plot, do not remove DisplayName;
here, name is "off"
legend      % plots legend

%%   Definition of the system for the simulation

clf
Sys.g = 2.0021
Sys.Nucs = '14N';   %nuclei present
Sys.n =[1]          % number of each nucleus
Sys.Abund=[0.996]   % abundancy of each nucleus

Sys.A = mt2mhz([1.365])    % /!\ always in MHz !!!


Sys.lwpp = [0.0697 0.0379];       % width of the peak
Exp.Range = [min(B) max(B)];    % experimental range of B
Exp.mwFreq = 9.221255000 ;   % experimental frequency of the spectrometer
figure(2);

xlabel('Field (mT)')
ylabel('Intensity')
garlic(Sys,Exp);          % simulation in solution. For solids or anisotropic compounds,
use pepper
figure(1);
plot(B,spc, 'DisplayName','exp');     % plotting experimental data to compare. Name =
"exp"
legend


%%   Automatic fitting
Sys0 = Sys;

    % Indicate here what you want to vary. Values are the range around
    % value indicated above in "Sys" e.g.    g = 2.006 +/- 0.01 here
Vary.g = 0.001
```

```
Vary.A = 2
Vary.lwpp = [0.0697 0.0379]


% Finally, we specify the fitting algorithm and what should be fitted.
FitOpt.Method = 'simplex fcn'; % simplex algorithm, searches for local minimum.
FitOpt.AutoScale = 'maxabs';

esfit(spc,@garlic,{Sys0,Exp},{Vary},FitOpt);     % Opens the automatic fitting window.
don't forget to change to
                                                 % pepper if needed


                        % Don't forget to export the best parameters !



 %%     Printing the optimized simulation alongside experimental data

clf
plot(B,fit1.fit, 'DisplayName','simulation')
xlabel('Field (mT)')
ylabel('Intensity')
hold on
plot(B,spc, 'DisplayName','experimental')
legend



%%
data_exp = [B(:) spc(:)];
save('XXX.txt\Exp.txt', 'data_exp', '-ascii');

data_simu = [B(:) fit1.fit(:)];
save('XXX.txt\Simu.txt', 'data_simu', '-ascii');
```

c) Script file to slice EPR kinetic data

This script was largely written by Dr. Alexandre Dézaphie to extract each spectrum from EPR kinetic analyses and generate the B values associated to each spectrum in a separate file.

```
#Alexandre Dézaphie & Adrien COMBOURIEU, 2025
import os
import numpy as np

os.chdir(' Path_to_file ')
print(os.getcwd())

ldir = [x for x in os.listdir() if 'keyword_in_directory_name' in x]

print(ldir)

lfile = []
for x in ldir:
    lfile += ['%s/text1/%s'%(x,y) for y in os.listdir('%s/text1'%x)  if '2d.txt' in
y]


print(lfile)
if 'out' not in os.listdir():
    os.mkdir('out')

for i in range(len(lfile)):
    name = lfile[i].split('/')[0]+'_'+lfile[i].split('/')[-1]
    print(name)
    f = open(lfile[i]).read().split('\n')
    count = 0

    if name not in os.listdir('out/'):
        os.mkdir('out/%s'%name)


    x = []
    x.append(float(f[11].split('=')[-1]))
    x.append(float(f[12].split('=')[-1]))
    print(x)


    for j in range(len(f)):

        if 'data[' in f[j] and 'Real' in f[j]:
            index = int(f[j].split(']')[0].split('.')[-1])


            mylist = np.linspace(x[0],x[1],index)

            h = open('out/%s/x_val_%d.txt'%(name,count),'w')
```

```
for p in range(len(mylist)):
    h.write(str(mylist[p])+'\n')

g = open('out/%s/index_%d.txt'%(name,count),'w')
count += 1
for k in range(index):
    g.write(f[j+k+1]+"\n")
g.close
```

Institut Polytechnique de Paris
91120 Palaiseau, France

d) Script to automatically fit the kinetics and extract the weight of each system

```
%%   Adrien COMBOURIEU, June 2025  %%

% https://easyspin.org/easyspin/documentation/

%%   Importing experimental data
clf ; clear; clc ; close all;
rtdir = "F:\Z\EPR\X\out\9-Jan-2025_PhNO2_kin.0.2d.txt";
B = textread(fullfile(rtdir, "x_val_0.txt"));    % change the path to the file
spc = textread(fullfile(rtdir, "index_0.txt"));
xlabel('Field (mT)');
ylabel('Intensity');
hold on ;                % allows to stack several spectra
plot(B,spc,'DisplayName','off')     % adds a name for each plot, do not remove
DisplayName; here, name is "off"
legend;      % plots legend

%%   Definition of the system for the simulation

Exp.Range = [min(B) max(B)];    % experimental range of B
Exp.mwFreq = 9.216164;   % experimental frequency of the spectrometer

Sys.g = 1.9962;
Sys.Nucs = '14N,1H,1H,1H,1H,1H';   %nuclei present
Sys.n =[1 1 1 1 1 1];          % number of each nucleus
Sys.Abund=[0.996;1;1;1;1;1];   % abundancy of each nucleus
Sys.A = mt2mhz([1.449;0.371;0.364;0.117;0.122;0.375]);    % /!\ always in MHz !!!
Sys.lwpp = [0.044 0.052];       % width of the peak
Sys.weight = 0.95;

Sys2=Sys;
Sys2.g =2.0022;
Sys2.A= mt2mhz([1.200;0.390;0.383;0.120;0.134;0.411]);
Sys2.lwpp = [0.058 0.057];
Sys2.weight = 1-Sys.weight;



figure(1);
xlabel('Field (mT)')
ylabel('Intensity')
[B1,spc1]=garlic(Sys,Exp);
garlic(Sys,Exp);
hold on
plot(B,spc*100, 'DisplayName','exp');    % plotting experimental data to compare. Name
= "exp"
legend

figure(2);
xlabel('Field (mT)')
ylabel('Intensity')
[B2,spc2]=garlic(Sys2,Exp);            % simulation in solution. For solids or
anisotropy, use pepper
garlic(Sys2,Exp);
hold on
plot(B,spc*100, 'DisplayName','exp');    % plotting experimental data to compare. Name
= "exp"
legend
```

Institut Polytechnique de Paris
91120 Palaiseau, France

```
%% Pre-optimization
clearvars fit1.pfit(length(Sys.A)+4) fit1.pfit(length(fit1.pfit)) Vary1 Vary2;
Vary1.g = 0.0005;
Vary1.A = [0.5;0.5;0.5;0.5;0.5;0.5];
Vary1.lwpp = [0.01 0.01];
Vary1.weight = 0.15;

Vary2.g = 0.0005;
Vary2.A = [0.5;0.5;0.5;0.5;0.5;0.5];
Vary2.lwpp = [0.01 0.01];
Vary2.weight = 0.15;

FitOpt.Method = 'simplex dint';
FitOpt.AutoScale = 'lsq';
esfit(spc,@garlic,{{Sys,Sys2},Exp},{{Vary1,Vary2}},FitOpt);

%%     Updating the initial parameters
Sys.g = fit1.pfit(1);
for n = 1:length(Sys.A)
    Sys.A(n) = fit1.pfit(n+1);
end
Sys.lwpp = [fit1.pfit(length(Sys.A)+2) fit1.pfit(length(Sys.A)+3)];
Sys.weight = fit1.pfit(length(Sys.A)+4);
figure(1);
plot(B,spc,'DisplayName','off'); hold on;
garlic(Sys,Exp);

Sys2.g = fit1.pfit(length(Sys.A)+5);
for n = 1:length(Sys2.A)
    Sys2.A(n) = fit1.pfit(n+length(Sys.A)+5);
end
Sys2.lwpp = [fit1.pfit(length(fit1.pfit)-2) fit1.pfit(length(fit1.pfit)-1)];
Sys2.weight = fit1.pfit(length(fit1.pfit));
figure(2);
plot(B,spc,'DisplayName','off'); hold on;
garlic(Sys2,Exp);

%%   Automatic fitting
clf; close all;
clearvars Vary1 Vary2 ;
Sys.weight = fit1.pfit(length(Sys.A)+4);
Sys2.weight = fit1.pfit(length(fit1.pfit));
Sys0 = Sys;
xfiles = natsortfiles(dir(fullfile(rtdir, 'x_val*.txt')));
yfiles = natsortfiles(dir(fullfile(rtdir, 'index*.txt')));
weights = zeros(length(xfiles),2);
weights_temp = zeros(length(xfiles),2); %include this line only for the
%first use of the program
Sys.weight = 0.9
Sys2.weight = 0.1
Vary1.weight = 0.1;
Vary2.weight = 0.1;
FitOpt.Method = 'simplex dint';
FitOpt.AutoScale = 'lsq';
FitOpt.Verbosity = 0;
FitOpt.TolFun = 5E-5;
FitOpt.TolEdgeLength = 5E-6;
FitOpt.x = 'x_val_0.txt'

for k = 1:length(xfiles)
    x_k = textread(fullfile(xfiles(k).folder,xfiles(k).name));
```

```
    spc_k = textread(fullfile(yfiles(k).folder,yfiles(k).name));
    plop_k = esfit(spc_k,@garlic,{{Sys,Sys2},Exp},{{Vary1,Vary2}},FitOpt);
    figure(k); hold on; xlabel('Field (mT)'); ylabel('Intensity')
    plot(x_k,spc_k, 'DisplayName','experimental');
    plot(x_k,plop_k.fit, 'DisplayName','simulation'); legend;
    weights(k,1) = plop_k.pfit(1)/(plop_k.pfit(1)+plop_k.pfit(2)); %creates a matrix
with weight values
    weights(k,2) = plop_k.pfit(2)/(plop_k.pfit(1)+plop_k.pfit(2))
    Sys.weight =  weights(k,1)-0.14;  %bias to follow the appearance of system alpha
    Sys2.weight =  weights(k,2)+0.14;

end
weights
weights_temp - weights
writematrix(weights,"F:\Z\EPR\X\out\9-Jan-2025_PhNO2_kin.0.2d.txt\PhNO2_weights.csv");
disp('Optimisation finished !')
```

References

(1) Chibisov, A. K. Electron Transfer in Photochemical Reactions. *Russ. Chem. Rev.* **1981**, *50* (7), 615–629. https://doi.org/10.1070/RC1981v050n07ABEH002656.

(2) Braslavsky, S. E. Glossary of Terms Used in Photochemistry, 3rd Edition (IUPAC Recommendations 2006). *Pure Appl. Chem.* **2007**, *79* (3), 293–465. https://doi.org/10.1351/pac200779030293.

(3) Kavarnos, G. J. Fundamental Concepts of Photoinduced Electron Transfer. In *Photoinduced Electron Transfer I*; Mattay, J., Ed.; Dewar, M. J. S., Dunitz, J. D., Hafner, K., Itô, S., Lehn, J.-M., Niedenzu, K., Raymond, K. N., Rees, C. W., Vögtle, F., Series Eds.; Topics in Current Chemistry; Springer Berlin Heidelberg: Berlin, Heidelberg, 1990; Vol. 156, pp 21–58. https://doi.org/10.1007/3-540-52379-0_2.

(4) Rehm, D.; Weller, A. Kinetics of Fluorescence Quenching by Electron and H-Atom Transfer. *Isr. J. Chem.* **1970**, *8* (2), 259–271. https://doi.org/10.1002/ijch.197000029.

(5) Koopmans, T. Über die Zuordnung von Wellenfunktionen und Eigenwerten zu den Einzelnen Elektronen Eines Atoms. *Physica* **1934**, *1* (1–6), 104–113. https://doi.org/10.1016/S0031-8914(34)90011-2.

(6) Washington University. *Dielectric Constant of Common Solvents*. https://depts.washington.edu/eooptic/linkfiles/dielectric_chart%5B1%5D.pdf.

(7) *TCSPC - What is Time-Correlated Single Photon Counting? - Edinburgh Instruments*. https://www.edinst.com/resource/tcspc-what-is-time-correlated-single-photon-counting/ (accessed 2025-04-17).

Résumé de la thèse en français

Ce travail de thèse s'inscrit dans la suite des récents développements très originaux en photochimie de complexes de cérium notamment des réactions de réductions photoinduites par des complexes de cérium(III), qui ont démontré leur potentiel dans de possibles stratégies de dépollution à la fois de dérivés halogénés et de molécules polluantes comme le méthane. Le choix du ligand s'est porté sur un ligand tripodal azoté (tris-(2-aminoéthyl)amine, TREN), combinant un effet donneur des amidures avec l'effet chélate et un fort encombrement stérique (groupements triisopropylsilyle, TIPS) pour augmenter le pouvoir réducteur du $Ce^{III}TREN^{TIPS}$, contrôler la coordination des substrats et permettre une solubilité importante dans des solvants apolaires.

La synthèse du complexe a nécessité des optimisations centrées essentiellement sur la nature du précurseur, afin d'éviter toute pollution ultérieure causée principalement par des sels de lithium. Une étude préliminaire des propriétés de coordination et d'oxydo-réduction du $Ce^{III}TREN^{TIPS}$ a permis d'isoler une variété de complexes de cérium (III) et cérium (IV), notamment par oxydation avec différents substrats (dérivés halogénés, sels d'argent, sels de cuivre, quinones). La possibilité d'échanger le ligand fluorure par d'autres groupements en utilisant des dérivés de triméthylsilyle a également été brièvement abordée, se basant sur des travaux préexistants.

Le potentiel d'oxydoréduction du complexe sous irradiation, particulièrement bas (-3.2 V *vs.* ferrocène/ferrocénium) évalué à l'aide du formalisme de Rehm-Weller, est de l'ordre de grandeur des métaux alcalins et des meilleurs complexes de cérium (III) reportés dans la littérature. Cette caractéristique a été appliquée à la déhalogénation de Polluants Organiques Persistants (POP) organochlorés, ainsi qu'à une variété d'autres molécules organochlorées, et de dérivés organofluorés (polyfluoro-aromatiques et trifluorométhylaromatiques) proches des polluants fluorés (PFAS) dont l'absence de méthode de dégradation non-polluante reste problématique. Cette réduction, suivie par Résonance Magnétique Nucléaire (RMN) de l'hydrogène, a pu être faite rapidement dans des conditions douces, bien que la nature des produits de dégradation reste à déterminer. Des adaptations en catalyse ont également été investiguées en utilisant un dérivé silylé (le tris(triméthylsilyl)silane) afin de fournir l'hydrogène nécessaire à la déhalogénation, et de réduire le cérium (IV) formé par le radical silylé formé. Plusieurs dérivés borés ont aussi été étudiés afin de valoriser le radical formé pour réaliser une borylation de Miyaura photoinduite, de manière similaire à des travaux précédents par l'équipe de E. J. Schelter.

Parallèlement, le $Ce^{III}TREN^{TIPS}$ a démontré sa capacité à réduire des composés nitro, présents dans la majorité des explosifs utilisés et dont l'épandage dans l'environnement crée une pollution persistante et difficile à traiter. En présence de $Ce^{III}TREN^{TIPS}$, les composés nitroaromatiques étudiés sont réduits en deux systèmes radicalaires distincts relativement stables (quelques heures), dont les proportions relatives varient en fonction du substituant en position para, et en fonction du temps. Une interconversion entre les deux systèmes a pu être mise en évidence en utilisant la Résonance Paramagnétique Electronique (RPE) et la spectroscopie UV-visible. La réactivité des nitroalcanes a également été investiguée, et une différence de réactivité entre le 2-méthyl-nitropropane et le nitrométhane a été observée (besoin d'irradiation *vs*. sans irradiation). Un couplage déshydrogénant avec le nitrosobenzene a également été démontré, et constitue le seul exemple d'une telle réactivité avec ce substrat dans la littérature.

Plusieurs oxydes d'azote présents au sein du cycle de l'azote ont été dégradés photochimiquement par le complexe. La réduction photochimique des nitrates et la formation d'un complexe de cérium-oxo ont permis d'améliorer significativement une méthode existante, et pourraient constituer une porte d'entrée prometteuse dans la réduction par étape des nitrates en diazote. A cet effet, la réduction des nitrites a également été démontrée à la fois en présence et en l'absence d'irradiation, conduisant également

probablement à la formation d'un complexe de cérium-oxo. Le protoxyde d'azote a pu de même être rapidement réduit en diazote sous irradiation lumineuse, permettant de montrer la possibilité de dégrader des composés problématiques pour l'environnement comme les nitrates.

Ces différentes réactivités très prometteuses ont participé à illustrer l'éventail des possibilités du $Ce^{III}TREN^{TIPS}$ pour la dégradation de polluants problématiques et de poser les bases de nouvelles réactivités innovantes faisant usage d'un métal abondant dans des conditions douces.

ECOLE DOCTORALE

Titre : Etude du comportement redox d'un complexe photoactif de cérium(III) pour la réduction de polluants

Mots clés : cérium, photochimie, réduction, polluants, terre rare

Résumé : Ce travail de thèse s'inscrit dans la suite des récents développements en photochimie de complexes de cérium notamment des réactions de réductions photoinduites par des complexes de cérium(III). Le choix du ligand s'est porté sur un ligand tripodal azoté (tris-(2-aminoéthyl)amine, TREN), combinant un effet donneur des amidures avec l'effet chélate et un fort encombrement stérique (groupements triisopropylsilyle) pour augmenter le pouvoir réducteur du $Ce^{III}TREN^{TIPS}$, contrôler la coordination des substrats et permettre une solubilisation dans des solvants apolaires. Le potentiel d'oxydoréduction du complexe sous irradiation, particulièrement bas (-3.2 V *vs.* ferrocène/ferrocénium), est de l'ordre de grandeur des métaux alcalins et des meilleurs complexes de cérium (III) reportés dans la littérature. Cette caractéristique a été appliquée à la déhalogénation de polluants organiques persistants (POP) organochlorés et de molécules organofluorées proches des polluants fluorés (PFAS) dont l'absence de méthode de dégradation non-polluante reste problématique. Parallèlement, le $Ce^{III}TREN^{TIPS}$ a démontré sa capacité à réduire des composés nitro, présents dans la majorité des explosifs utilisés et dont l'épandage dans l'environnement crée une pollution persistante et difficile à traiter, en radicaux nitro stables caractérisés par résonance paramagnétique électronique. Enfin, les oxydes d'azote présents au sein du cycle de l'azote (nitrates, nitrites, protoxyde d'azote) ont été dégradés photochimiquement par le complexe, permettant une fois de plus d'illustrer l'éventail des possibilités du $Ce^{III}TREN^{TIPS}$ pour la dégradation de polluants problématiques et de poser les bases de nouvelles réactivités innovantes faisant usage d'un métal abondant dans des conditions douces.

Title : Redox behaviour investigation of a photoactive cerium(III) complex for the chemical reduction of pollutants

Keywords : cerium, photochemistry, reduction, pollutants, rare-earth

Abstract : This thesis follows on from recent developments in the photochemistry of cerium complexes, in particular photoinduced reduction reactions by cerium(III) complexes. The choice of ligand fell on a tripodal nitrogen ligand (tris-(2-aminoethyl)amine, TREN), combining an amide donor effect with the chelate effect and a high steric hindrance (triisopropylsilyl groups) to increase the reducing power of $Ce^{III}TREN^{TIPS}$, control substrate coordination and enable solubilization in apolar solvents. The especially low redox potential of the complex under irradiation (-3.2 V *vs.* ferrocene/ferrocenium) is close to alkali metals and the best cerium (III) complexes reported in the literature. This reactivity has been applied to the dehalogenation of organochlorinated persistent organic pollutants (POPs) and organofluorinated molecules close to fluorinated pollutants (PFAS), for which the absence of non-polluting degradation methods remains a problem. Similarly, $Ce^{III}TREN^{TIPS}$ was shown to reduce nitro compounds, present in the majority of explosives that create persistent pollution that is difficult to treat, into stable nitro radicals characterized by electron paramagnetic resonance. Finally, the nitrogen oxides present in the nitrogen cycle (nitrates, nitrites, nitrous oxide) were photochemically degraded by the complex, once again illustrating the range of possibilities offered by $Ce^{III}TREN^{TIPS}$ for the degradation of problematic pollutants, and laying the foundations for new innovative reactivities using an abundant metal under mild conditions.

Institut Polytechnique de Paris
91120 Palaiseau, France